Ioffe Institute
1999

7th INTERNATIONAL SYMPOSIUM

NANOSTRUCTURES: PHYSICS AND TECHNOLOGY

REPORT DOCUMENTATION PAGE

Form Approved OMB No. 0704-0188

1. AGENCY USE ONLY (Leave blank)	2. REPORT DATE	3. REPORT TYPE AND DATES COVERED
	1999	Conference Proceedings

4. TITLE AND SUBTITLE

7th International Symposium: Nanostructure: Physics and Technology

5. FUNDING NUMBERS

F61775-99-WF030

6. AUTHOR(S)

Conference Committee

7. PERFORMING ORGANIZATION NAME(S) AND ADDRESS(ES)

Ioffe Institute
26 Polytechnicheskaya
St. Petersburg 194021
Russia

8. PERFORMING ORGANIZATION REPORT NUMBER

N/A

9. SPONSORING/MONITORING AGENCY NAME(S) AND ADDRESS(ES)

EOARD
PSC 802 BOX 14
FPO 09499-0200

10. SPONSORING/MONITORING AGENCY REPORT NUMBER

CSP 99-5030

11. SUPPLEMENTARY NOTES

12a. DISTRIBUTION/AVAILABILITY STATEMENT

Approved for public release; distribution is unlimited.

12b. DISTRIBUTION CODE

A

13. ABSTRACT (Maximum 200 words)

The Final Proceedings for 7th International Symposium: Nanostructure: Physics and Technology, 14 June 1999 - 18 June 1999

This is an interdisciplinary conference. Topics include Physics of heterostructures with quantum wells and superlattices; transport phenomena in nanostructures; 2D electron gas; far-infrared phenomena in nanostructures; physics of heterostructures with quantum wires and quantum dots; single electron phenomena in nanostructures; nanostructure technology; tunneling technology; excitons in nanostructures; laser and optoelectronic devices base on nanostructures; nanostructure characterization and novel atomic-scale probing techniques; physics of silicon-based nanostructures and nanostructure devices.

14. SUBJECT TERMS

EOARD, Semiconductors, Microelectronics, Nanotechnology

15. NUMBER OF PAGES

565

16. PRICE CODE

N/A

17. SECURITY CLASSIFICATION OF REPORT	18. SECURITY CLASSIFICATION OF THIS PAGE	19. SECURITY CLASSIFICATION OF ABSTRACT	20. LIMITATION OF ABSTRACT
UNCLASSIFIED	UNCLASSIFIED	UNCLASSIFIED	UL

NANOSTRUCTURES:
PHYSICS AND TECHNOLOGY

7th International Symposium

St Petersburg, Russia, June 14–18, 1999

Co-Chairs
Zh. Alferov
L. Esaki

PROCEEDINGS

Ioffe Institute
St Petersburg, 1999

The Seventh Symposium is held in the year of the 275th anniversary of the Russian Academy of Sciences—highest scientific society and principal coordinating body for research in natural and social sciences, technology and production in Russia. Founded in St Petersburg in 1724 by Peter the Great, the Academy was later known under various names and regained the present name in 1991. The first Academy building in St Petersburg is shown in the centre of the anniversary logo.

ISBN 5-86763-008-0

The International Symposium "Nanostructures: Physics and Technology" is held annually since 1993. The first Symposium was initiated by Prof. Zh. Alferov and Prof. L. Esaki who are its permanent co-chairs. By tradition the Proceedings of the Symposium is published before the beginning of the meeting.
More detailed information on the Symposium is presented on the World Wide Web
http://www.ioffe.rssi.ru/NANO-99/

This volume was composed at the Information Services and Publishing Department of the Ioffe Institute from electronic files submitted by the authors. When necessary these files were converted into the Symposium LaTeX 2_ε style without any text revisions. Only minor technical corrections were made by the composers.

Information Services and Publishing Department
Ioffe Physico-Technical Institute
26 Polytechnicheskaya, St Petersburg 194021, Russia
Phones: (812) 247 2617, 247 9932
Fax: (812) 247 2135, 247 1017
E-mail: vgrig@eo.ioffe.rssi.ru

Printed in Russian Federation

The Symposium is held under the auspices of
the Russian Academy of Sciences

Organizers

Ioffe Physico-Technical Institute
Scientific Engineering Center for Microelectronics at the Ioffe Institute

in association with

Research Council for the Project "Physics of Solid State Nanostructures" at the Ministry of Science and Technologies of Russia
and
the institutions of the Russian Academy of Sciences
Division of General Physics and Astronomy
St Petersburg Scientific Center

Acknowledgments

The Organizers gratefully acknowledge the following for their contribution to the success of the Symposium:
Ministry of Science and Technologies of Russia
Russian Foundation for Basic Research
AIXTRON AG, Germany
European Office of Aerospace Research and Development
Air Force Office of Scientific Research
United States Air Force Research Laboratory
United States Army Research, Development and Standardization Group (UK)
United States Office of Naval Research, Europe

Location and Date

The Symposium is held in St Petersburg's recreation area Repino on June 14–18, 1999.

Programme Committee

R. Suris, Chair (*St Petersburg*)
L. Asryan, Secretary (*St Petersburg*)

Zh. Alferov (*St Petersburg*)
A. Andronov (*Nizhnii Novgorod*)
N. Bert (*St Petersburg*)
A. Chaplik (*Novosibirsk*)
V. Dneprovskii (*Moscow*)
B. Egorov (*St Petersburg*)
A. Gippius (*Moscow*)
Yu. Gulyaev (*Moscow*)
S. Gurevich (*St Petersburg*)
L. Keldysh (*Moscow*)
Yu. Kopaev (*Moscow*)
P. Kop'ev (*St Petersburg*)
Z. Krasil'nik (*Nizhnii Novgorod*)
V. Kulakovskii (*Chernogolovka*)
M. Kupriyanov (*Moscow*)
V. Mokerov (*Moscow*)
V. Panov (*Moscow*)
E. Poltoratskii (*Moscow*)
N. Samsonov (*Moscow*)
N. Sibel'din (*Moscow*)
V. Timofeev (*Chernogolovka*)
B. Zakharchenya (*St Petersburg*)

Organizing Committee

M. Mizerov, Chair (*Center for Microelectronics*)
B. Egorov, Secretary (*Ioffe Institute*)
L. Asryan (*Ioffe Institute*)
D. Donskoy (*St Petersburg Scientific Center*)
V. Grigor'yants (*Ioffe Institute*)
P. Kop'ev (*Ioffe Institute*)
N. Sibel'din (*Lebedev Physical Institute*)
E. Solov'eva (*Ioffe Institute*)
V. Zayats (*Division of General Physics and Astronomy*)

AIXTRON Young Scientist Award

This year the Symposium Programme Committee and the Board of AIXTRON AG (Germany) established a special award to honour a young scientist who will present at the Symposium the best paper in the field of solid state nanostructures. The award consists of a diploma and a $500 reward sponsored by AIXTRON.

The awardee will be selected by the Award Committee nominated by the Programme Committee. The Chair of the Award Committee will announce the winner at the Award Ceremony scheduled for the last day of the Symposium.

Award Committee

Zh. Alferov, Chair (*Russia*)

A. Andronov (*Russia*)
M. Heuken (*Germany*)
Yu. Kopaev (*Russia*)
J. Lott (*USA*)
H. Sakaki (*Japan*)
R. Suris (*Russia*)

Contents

Opening Session

Quantum Wires and Quantum Dots

Transport in Nanostructures

Lasers and Optoelectronic Devices

2D Electron Gas

Ordered Arrays of Nanoparticles

Nanostructure Characterization and Novel Atomic-Scale Probing Techniques

Tunnelling Phenomena

General Properties of Low-Dimensional Structures

Microcavities and Photonics Crystals

Silicon Based Nanostructures

Quantum Wells and Superlattices

Excitons in Nanostructures

Far-Infrared Phenomena in Nanostructures

Nanostructure Devices

Nanostructure Technology

Unprinted Papers

The papers listed below are included in the Symposium Programme, but not printed in the Proceedings, as the authors had not submitted electronic files in due time.

OS.01I *B. Shklovskii*
Wigner crystal everywhere: quantum dots, neutron stars and DNA

QWR/QD.01I *S. Tarucha*
Correlated electrons in quantum dot atoms and molecules

QWR/QD.04I *V. V. Kulakovskii et al.*
Excitons and multi-excitons in II–VI and III–V semiconductor quantum dots in magnetic field

NC.01I *J. C. Maan*
High magnetic fields to study materials properties and physics of semiconductor nanostructures

NT.23p *L. G. Rotkina, et al.*
C_{60} based microlithography: new method of nanofabrication

LOED.02I *M. Grundmann*
Gain in quantum dots lasers

CS.01I *H. Sakaki*
10 nm-scale epitaxial quantum dots and electron population control for physics and device studies

CS.02I *G. Abstreiter*
Optical spectroscopy of individual semiconductor quantum dots

CS.03I *P. Solomon*
A topic will be defined later

7th Int. Symp. "Nanostructures: Physics and Technology"
St Petersburg, Russia, June 14–18, 1999

II–VI laser heterostructures with different types of active region

S. V. Ivanov, A. A. Toropov, T. V. Shubina, S. V. Sorokin, A. V. Lebedev, I. V. Sedova and P. S. Kop'ev
Ioffe Physico-Technical Institute, St Petersburg, Russia

Abstract. We report on the recent development of II–VI room temperature (RT) blue-green lasers based on both (Zn,Mg)(S,Se) and (Be,Mg,Zn)Se material systems, grown by molecular beam epitaxy (MBE). A novel concept of the laser structure design, aimed at enhancement of the degradation stability, is suggested and realized. It involves a combination of alternately-strained short-period superlattice (SL) waveguide (like ZnSSe/ZnCdSe or BeZnSe/ZnCdSe) (for protecting the laser active region from outside penetration of defects) with a single 2–3 ML thick CdSe/ZnSe fractional monolayer (FM) active region transformed under certain MBE conditions into the dense array of 10–50 nm-size CdSe-rich self-organized nanoislands providing effective carrier localization and spatial separation of radiative recombination sites and defects in the active region. As a result, significantly improved optical and electronic confinement as well as high quantum efficiency have been obtained, leading to the lowest ever reported threshold power density ($< 4\,\mathrm{kW/cm^2}$, 300 K) of ZnMgSSe SL FM laser, the highest characteristic temperature ($T_0 = 360$ K at RT) and maximal operational temperature (140°C) of the BeMgZnSe SL QW laser diode. First cw RT laser diodes with the FM active region have been demonstrated. All SL FM lasers have revealed the increased degradation stability with respect to conventional ZnSe-based SCH lasers.

1 Introduction

II–VI wide bandgap heterostructures still remain the only semiconductor system suitable for fabrication of commercial green laser diodes for projection television and other applications requiring the whole set of laser wavelengths in the visible spectral range. Despite the numerous efforts made during the last few years towards optimization of conventional ZnSe-based quantum well (QW) laser diodes, the progress in the lifetime increase is still rather slow [1, 2]. The main origin of the relatively fast laser degradation has been found by Nakano [2] to be non-radiative recombination enhanced defect reactions in the active region due to the very low defect activation threshold typical for the wide bandgap II–VI's.

This paper presents a novel concept of the active region design for II–VI lasers, aimed at increase in their lifetime. The key points are (i) preventing the active region from outside penetration and development of extended and point defects and (ii) spatial separation of the radiative recombination and defect-containing sites in the active regions. The former problem is solved by incorporation of alternately-strained (Zn,Cd)Se/ZnSSe (or BeZnSe/ZnSe) short-period superlattice (SL) waveguide in the ZnMg(Be *or* S)Se/ZnCdSe separate confinement heterostructure (SCH) QW lasers, which results simultaneously in an improvement of the electronic and optical confinement. An exchange of the ordinary QW recombination region for a 2–3 monolayer (ML) thick CdSe fractional monolayer (FM) inserted in a ZnSe QW produces a satisfactory solution of the latter problem due to a transformation of CdSe FM under certain growth conditions into the array of self-organizing CdSe-rich nanoislands, which suppress dramatically the migration of non-equilibrium carriers to defects. It is expected also that using the Be chalcogenides with highest lattice rigidity among II–VI's contributes to raising the activation energy of defects formation and development [3].

2 Experiment

The (Zn,Mg)(S,Se)-based optically pumped laser structures were grown by molecular beam epitaxy (MBE) pseudomorphically on GaAs(001) substrates at a substrate temperature of 270–280°C for a study of properties of the novel active region itself. The (Be,Mg,Zn)Se-based laser diodes with the SL waveguide and different recombination regions were fabricated as well. The details of MBE growth and composition control of the S- and Be-containing laser structures have been published elsewhere [4, 5]. Besides the 0.5 μm-buffer and 0.1 μm-top $Zn_{0.92}Mg_{0.08}S_{0.15}Se_{0.85}$ layers, the optically pumped SL QW lasers include a 0.2 μm thick $ZnS_{0.14}Se_{0.86}$/(Zn, Cd)Se SL waveguide lattice-matched to GaAs as a whole and a single 7 nm-ZnCdSe QW in the middle. The CdSe mole fraction in the QW and SL has been varied from 0 to 0.27, which allows one to cover the lasing wavelength range from 470 to 523 nm. The active region of the CdSe FM laser structure contains 10 nm ZnSe QW as a matrix for a 2.8 ML CdSe insertion, surrounded by the 3 nm-$ZnS_{0.14}Se_{0.86}$/5 nm-ZnSe SL. The BeMgZnSe/ZnCdSe SCH laser diode structure contains a (1 nm-$Be_{0.05}Zn_{0.95}Se$/1.5 nm-ZnSe)$_{82}$ SL waveguide centered with either a 4 nm-$Zn_{0.63}Cd_{0.37}Se$ QW or a 10 nm-ZnSe QW incorporating the similar 2.6 ML CdSe FM sheet. The laser diode structure also involves 1 μm-thick wider-bandgap n- and p-$Be_{0.05}Mg_{0.06}Zn_{0.89}Se$ cladding layers, doped with iodine and nitrogen, respectively, as well as a ZnSe/BeTe:N modulation doped graded short-period SL capped with a highly p-doped BeTe:N/ZnTe:N contact structure. The details of MBE growth of the CdSe FM active region as well as the calibration procedure have been described elsewhere [6].

Transmission electron microscopy (TEM), including high resolution (HR) TEM, and x-ray diffraction (XRD) measurements were employed to characterize the laser structure parameters and structural quality. The cw and time resolved (20 ps) photoluminescence (PL) facilities were used for optical and transport studies. Lasing characteristics of the optically pumped lasers were studied using a N_2 laser with a 8 ns pulse width. The injection laser samples were fabricated by standard photolithography of stripe contacts and measured as described elsewhere [7].

3 Short-period alternately-strained superlattice waveguide

The general design, growth peculiarities and some properties of the alternately-strained II–VI SL and multiple QW (MQW) structures have been reported elsewhere [8, 9]. As

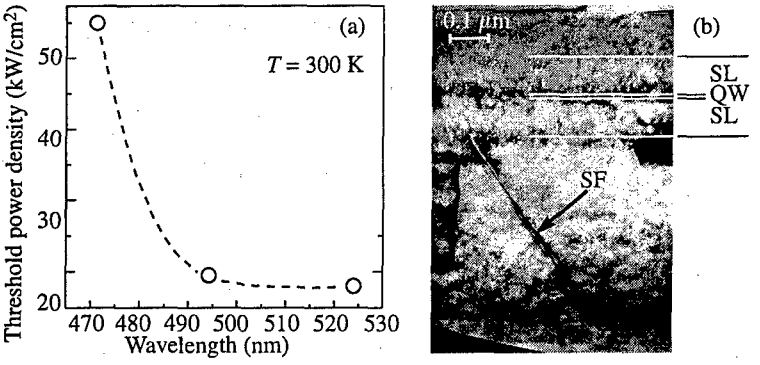

Fig. 1. (a) Room temperature threshold power density as a function of lasing wavelength for three SL QW laser structures with different compositions of (Zn,Cd)Se QW. (b) Cross-sectional TEM image of one of the structures, SF is a stacking fault.

has been shown in [8], the ZnSSe/ZnCdSe alternately-strained SLs and MQWs possess higher critical thickness's as compared to bulk layers with the same lattice mismatch and even exceed the theoretically estimated SL and MQW critical thickness's. The cross-sectional TEM image of the SCH SL QW structure, given in Fig. 1(b), demonstrates the great potential of the SL in protecting the laser active region from the extended defect (stacking fault) penetration. The threshold power density vs lasing wavelength is presented in Fig. 1(a) for three SL QW lasers demonstrating efficient room temperature (RT) operation ($P_{th} < 20\,kW/cm^2$) within a wide blue-green range (490–523 nm). These P_{th} values are among the lowest ever reported for optically pumped II–VI QW lasers, indicating improved electronic confinement for holes at the optimal optical confinement [10] as well as lowered concentration of non-radiative recombination centers in the QW.

Despite the lowest heavy-hole (*hh*) miniband in ZnSe-based SLs is rather narrow (typically $\sim$ 10 meV) due to the large effective mass ($0.6m_0$), extremely efficient carrier transport across the SLs has been observed by temperature-dependent cw and time-resolved (TR) PL measurements [11, 12]. Calculations of the band line-ups and confinement energies for a wide range of the ZnSSe/ZnCdSe SL structure parameters (thickness's and alloy compositions) show that the energy gap between the top of the lowest *hh* miniband, where exciton is essentially localized, and the bottom of the rather wide (30–100 meV) light-hole (*lh*) miniband does not exceed 10–15 meV. It provides efficient thermal occupation of the *lh* states with increasing temperature. This process appears to be responsible for the thermally-activated transfer of holes along the growth direction, followed by their capture into the QW and energy relaxation down to the lowest *hh* QW level.

The novel concept of the SL waveguide has been successfully realized in the RT BeMgZnSe/ZnCdSe SCH QW injection lasers by employing the BeZnSe/ZnSe alternately-strained SL surrounding deep ZnCdSe QW. The structures demonstrate a typical threshold current density of about 750 A/cm^2 (lowest value achieved is $\sim$ 450 A/cm^2) and threshold voltages around 7 V, which is mainly caused by still not completely optimized p-type doping of a cladding layer and optical confinement. The lasing spectra are presented in the inset of Fig. 2. However, some other parameters of the devices are not typical and are determined by the specific design of the active region. Figure 2 shows the temperature dependence of threshold current density of the SL QW laser diode with significantly enhanced characteristic temperature (up to $T_0 = 307$ K at RT), as compared to that of a conventional bulk-waveguide structure ($T_0 \sim 160$ K). This effect is associated namely with the improved electronic confinement of holes by the SL waveguide. For temperatures below 80 K, the threshold current has been found to decrease with increasing temperature, which is attributed to the thermally-activated carrier transport being even more efficient for the Be-contained SLs. In addition, a buried-ridge-waveguide laser diode with a 1 μm-stripe width yields T_0 as high as 360 K at and above RT, enabling pulsed laser operation up to 140°C [13]. These values are the highest ever reported for II–VI laser diodes.

4 CdSe/ZnSe fractional monolayer active region

It has recently been found that single CdSe/ZnSe FM structures exhibit bright excitonic PL, maximized in the vicinity of the CdSe critical thickness ($\sim$ 3 ML) ($\lambda \sim 520$ nm) [14]. The evolution of an intrinsic morphology and optical properties of single CdSe/ZnSe FM nanostructures and FM SLs within the CdSe nominal thickness range of 0.1–3.6 ML has been studied in detail by TEM, HR TEM, XRD, PL and TR PL in Refs. [6, 14–18]. A cross-sectional TEM image of the FM laser active region comprising both the SL waveguide and a single 2.8 ML CdSe FM recombination region is presented in Fig. 3(a). It demonstrates

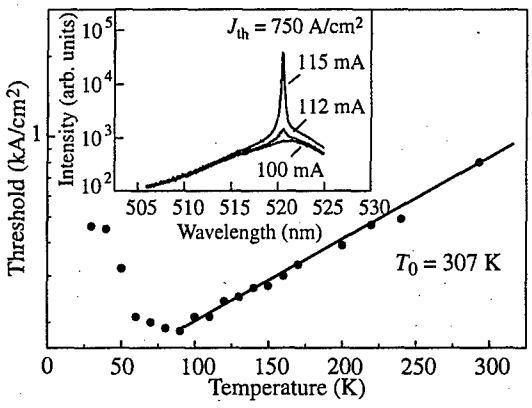

Fig. 2. Temperature dependence of threshold current density of BeMgZnSe SL QW laser diode. Inset shows its RT pulse lasing spectrum.

clearly visible elastic strain modulation of a thickness of the CdSe FM region, which can be attributed to the randomly distributed flat CdSe-enriched islands observed in the plan-view TEM picture (Fig. 3(b)). The plan-view TEM image shows the formation of 10–40 nm lateral size CdSe-based self-organized islands of about 2×10^{10} cm^{-2} density. Only $\sim$ 15% of the islands (the largest ones) look relaxed, whereas other 85% seem to be pseudomorphic. No extended defects are observed outside the large CdSe-based islands. The HR TEM study of single 2–3 ML CdSe/ZnSe FM structures revealed additionally a high density ($\sim 10^{11}$ cm^{-2}) of smaller CdSe-rich islands (8 $\pm$2 nm in lateral size), either separate or located within the larger islands as Cd composition fluctuations, which can contribute to the low energy PL tail of the structures. We believe that the dominant amount of deposited Cd is concentrated in the 2D-islands of ultra-thin QWs characterized by specific exciton localization potential due to Cd content fluctuations.

Lasing characteristics of the optically pumped ZnMgSSe laser with the CdSe FM active region are summarized in Fig. 3(c). The structure demonstrates about a 5-fold decrease in the RT threshold power density, down to $P_{th} = 3.9\,\mathrm{kW/cm^2}$ at $\lambda \sim 523$ nm, as compared

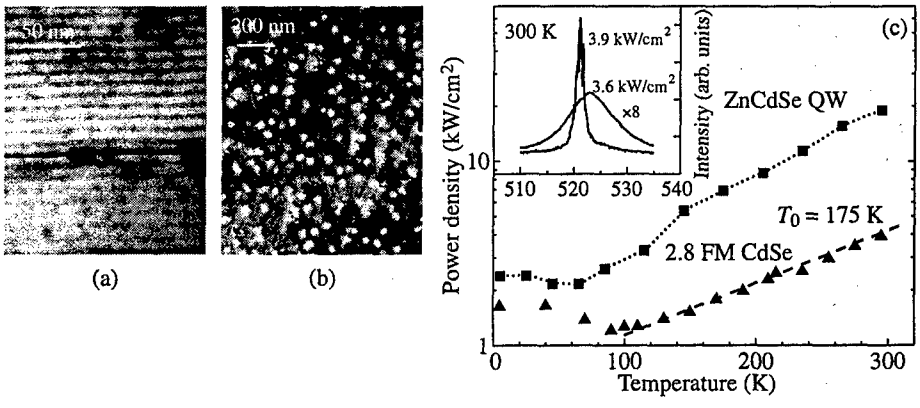

Fig. 3. Cross-sectional (a) and plan-view (b) TEM images of laser structures with 2.8 ML CdSe/ZnSe FM active region. (c) Temperature dependence of threshold power density for FM (triangle) and QW (square) laser structures. RT FM laser generation spectra are presented in the inset.

to the SL QW lasers operating at the same wavelength. The temperature dependences of threshold power density for both FM and QW laser structures are non-monotonic with noticeable minima at ~ 100 K and ~ 70 K, respectively, which can be attributed to different values of the *hh–lh* SL miniband gap governing the onset of the thermally-activated vertical carrier transport through the SLs. In addition, the FM laser does not show any noticeable degradation under the 25-fold threshold pumping power (~ 100 kW/cm^2) during 24 hours, whereas a conventional QW laser under the even more gentle conditions degrades completely within 1 hour. We speculate that the extremely low threshold of optically-pumped lasers and the enhanced degradation stability are related to the CdSe-based dot-like islands operating as efficient localization and recombination sites for the non-equilibrium carriers and preventing their migration to the larger relaxed islands and other defect regions, where they could decay non-radiatively, activating the defect development [19].

Figure 4(a) presents the cross-section TEM image of the BeMgZnSe laser diode active region comprising both the SL waveguide and the single 2.6 ML CdSe FM recombination region, which demonstrates the characteristic strain-field modulation of the FM region thickness. One should stress that the CdSe FM laser diode is the only among the series of RT SCH diodes, which has demonstrated a cw operation (see Fig. 4(b)), at all other equal conditions. Thus, first RT cw BeMgZnSe/(Zn)CdSe FM laser diodes have been fabricated.

5 Conclusions

In summary, we have presented a novel design of room-temperature ZnSe-based blue-green lasers using an alternately-strained SL waveguide, which demonstrate low (< 20 kW/cm^2) threshold power densities within the 470–523 nm range for optically pumped lasers and very high characteristic temperature (360 K at RT) due to the enhanced electronic confinement. The strained SL shows significantly increased stress stability and possibility of protecting the active region from the propagation of extended defects. In addition, the efficient mechanism of thermally-activated hole transport across the SL has been observed. Finally, employing a 2–3ML CdSe/ZnSe FM recombination region instead of a QW provides the lowest RT threshold power density ever reported for ZnSe-based lasers along with the enhanced degradation stability for both the optically and injection pumped lasers.

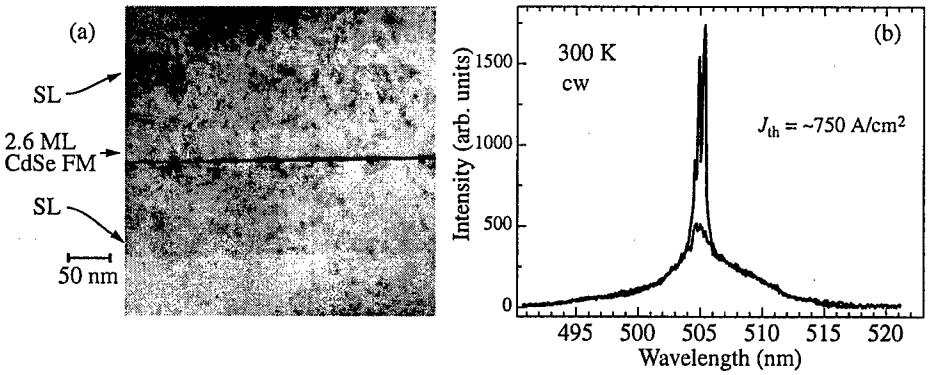

Fig. 4. Cross-section TEM image of the CdSe FM laser diode structure (a) and its cw RT electroluminescence spectra below and above threshold (b).

Acknowledgements

Authors appreciate greatly the technological and experimental collaboration with H.-J. Lugauer, G. Reusher, M. Keim, A. Waag and G. Landwehr (Universität Würzburg), G. R. Pozina, J. P. Bergman and B. Monemar (University of Linköping), N. Peranio, A. Rosenauer, D. Gerthsen (Universität Karlsruhe). Authors are thankful to A. A. Sitnikova for the TEM characterization of the structures, and N. D. Il'inskaya for the laser diode processing. This work has been supported in part by the RFBR grants, the Program of Ministry of Science of RF "Physics of solid-states nanostructures" as well as the Volkswagen-Stiftung.

References

[1] E. Kato, H. Noguchi, M. Nagai *et al.*, *Electron. Lett.* **34**, 282 (1998).
[2] K. Nakano, *Proc. 2nd Int. Symp. on Blue Laser and Light Emitting Diodes,* Chiba, 1998, p. 395.
[3] A. Waag, Th. Litz, F. Fischer *et al.*, *J. Cryst. Growth* **184/185**, 1 (1998).
[4] S. Ivanov, S. Sorokin, I. L. Krestnikov *et al.*, *J. Cryst. Growth* **184/185**, 70 (1998).
[5] A. Waag, F. Fischer, K. Schüll *et al.*, *Appl. Phys. Lett.* **70**, 1 (1997).
[6] S. V. Ivanov, A. A. Toropov, T. V. Shubina *et al.*, *J. Appl. Phys.* **83**, 3168 (1998).
[7] S. Ivanov, A. Toropov, S. Sorokin *et al.*, *Appl. Phys. Lett.* **73**, 2104 (1998).
[8] T. V. Shubina, S. V. Ivanov, A. A. Toropov *et al.*, *J. Cryst. Growth* **184/185**, 596 (1998).
[9] S. V. Ivanov, A. A. Toropov, S. V. Sorokin *et al.*, *Semicond.* **32**, 1137 (1998).
[10] A. A. Toropov, S. V. Ivanov, T. V. Shubina *et al.*, *Proc. Int. Symp. Nanostructures: Physics and Technology*, 1997 p. 210.
[11] A. Lebedev, S. Sorokin, A. Toropov *et al.*, *Acta Physica Polonica A* **94** (2), 421 (1998).
[12] A. Toropov, T. V. Shubina, A. V. Lebedev *et al.*, *Proc. 2nd Int. Symp. Blue Laser and Light Emitting Diodes*, Eds. K.Onabe *et al.*, (1998, Chiba, Japan), p. 254.
[13] M. Legge, S. Bader, G. Bacher *et al.*, *ibid*, p. 409.
[14] A. A. Toropov, S. V. Ivanov, T. V. Shubina *et al.*, *Jpn. J. Appl. Phys.* **38**, 566 (1999).
[15] A. A. Toropov, S. V. Ivanov, T. V. Shubina *et al.*, *J. Cryst. Growth* **184/185**, 293 (1998).
[16] I. Sedova, T. Shubina, S. Sorokin *et al.*, *Acta Physica Polonica A* **94** (3), 519 (1998).
[17] A. A. Toropov, T. V. Shubina, S. V. Sorokin *et al.*, *Phys. Rev. B* **59**, 2510 (1999).
[18] N. Peranio, A. Rosenauer, D. Gerthsen *et al.*, *Submitted to Phys. Rev. Lett.* (1999).
[19] S. V. Ivanov, A. A. Toropov, S. V. Sorokin *et al.*, *Appl. Phys. Lett.* **74**, 498 (1999).

7th Int. Symp. "Nanostructures: Physics and Technology"
St Petersburg, Russia, June 14–18, 1999

QWR/QD.021

Electronic properties and many-body effects in quantum dots

Satyadev Nagaraja and *Jean-Pierre Leburton*
Department of Electrical & Computer Engineering and
Beckman Institute for Advanced Science & Technology
University of Illinois at Urbana-Champaign, Urbana, IL 61801, USA

Abstract. We investigate the shell structure and electron-electron interaction in planar quantum dots within the density functional theory. We observe that the Coulomb repulsion does not alter the shell structure when the dot is symmetric in the two-dimensional (2D) plane. If the dot is asymmetric, no pre-determined shell structure emerges except when Coulomb repulsion leads to accidental *Coulomb degeneracies*. Our investigations on double-quantum dots reveal double electron charging for weak inter-dot coupling, and a significant spin polarization in accordance with Hund's rule. Both these features disappear when interdot coupling is made stronger.

Introduction

Zero-dimensional (0D) systems, such as quantum dots have been the subject of intense research in recent years [1–4], owing to novel fundamental physical phenomena as well as their potential for many exciting applications in optics and electronics [5–7]. In this work, we investigate the influence of the confining potential and electron-electron interaction in the formation of shell structure in single planar quantum dots (PQD), and the role of many body interaction, especially the effect of electron spin, on the charging behavior of coupled PQDs. Planar quantum dots are defined by electrostatically depleting a two-dimensional electron gas beneath negatively biased metal gates on top of the stucture. We consider two PQD configurations: a square-gate dot which, when empty, has a nearly circularly symmetric confining potential, and a quad-gate dot which has a rectangular symmetry. Additionally, we investigate the charging properties of a double PQD.

1 Dot structures

The devices investigated here are shown in Fig. 1 (notice the $y-$axis is in the vertical direction). They consist of an inverted GaAs/$Al_{0.3}Ga_{0.7}As$ heterostructure which confines the electrons to a 2D gas at the interface. In our model, the simulated structure consists of a 22.5-nm layer of undoped $Al_{0.3}Ga_{0.7}As$, followed by a 125-nm layer of undoped GaAs and finally an 18 nm GaAs cap layer. The cap layer is uniformly doped to 5×10^{18} cm^{-3} so that the conduction band edge is just above the Fermi level at the GaAs-cap layer–undoped GaAs boundary. The inverted heterostructure is grown on a GaAs substrate and charge control is achieved by varying the voltage on the back gate, V_{back}. The first quantum dot shown in Fig. 1(a) has a 240×240 nm^2 square open area at the top bordered by a 65-nm thick gate. The quad-gate device shown in Fig. 1(b) has four gate pads with 45-nm stubs protruding into the channel; the dimensions of the open area on the top are 230×408 nm^2. The separation between the pads along the (longer) $z-$direction is 90-nm. The schematic of the coupled dot structure is shown in Fig. 1(c). The two dots are defined by biasing the ten metallic gates, with the coupling between them varied by means of the voltage, V_t, on the tuning gates.

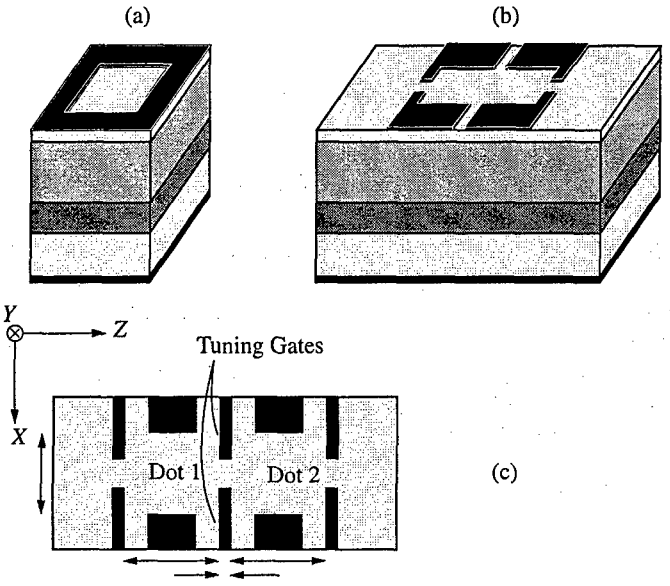

Fig. 1. Schematic representation of (a) a square and (b) a quad gate quantum dot device with layer structure (c). Schematic representation along the $x - z$ plane.

2 Computational model

In order to study the electronic properties of the quantum dot, the 3D Schrödinger and Poisson equations are solved for the central 0D region within the density functional theory [8]. The Hamiltonian ($\hat{H}^{\uparrow}$ and $\hat{H}^{\downarrow}$ for spin $\uparrow$ and spin $\downarrow$ electrons, respectively) is given by:

$$\hat{H}^{\uparrow(\downarrow)} = -\frac{\hbar^2}{2}\nabla\left[\frac{1}{m^*(\mathbf{r})}\nabla\right] + E_c(\mathbf{r}) + \mu_{xc}^{\uparrow(\downarrow)}[n,\zeta] \tag{1}$$

where $m^*(\mathbf{r})$ is the position dependent effective mass of the electron in the different materials, $E_c(\mathbf{r}) = \phi(\mathbf{r}) + \Delta E_{os}$ the conduction band edge, where $\phi(\mathbf{r})$ is the electrostatic potential, and ΔE_{os} the conduction band offset. $\mu_{xc}^{\uparrow(\downarrow)}[n,\zeta]$, the exchange and correlation potential, is a functional of the total electron density $n(\mathbf{r})$ $(= n^{\uparrow}(\mathbf{r}) + n^{\downarrow}(\mathbf{r}))$ and the spin polarization parameter $\zeta = \frac{n^{\uparrow}(\mathbf{r}) - n^{\downarrow}(\mathbf{r})}{n^{\uparrow}(\mathbf{r}) + n^{\downarrow}(\mathbf{r})}$, and has been parametrized by Ceperley and Alder [9].

The 3D Poisson equation for the electrostatic potential $\phi(\mathbf{r})$ reads:

$$\nabla[\epsilon(\mathbf{r})\nabla\phi(\mathbf{r})] = -\rho(\mathbf{r}) \tag{2}$$

where, the charge density $\rho(\mathbf{r})$ is given by $e[p(\mathbf{r}) - n(\mathbf{r}) + N_D^+(\mathbf{r}) - N_A^-(\mathbf{r})]$. Here, $\epsilon(\mathbf{r})$ is the permittivity of the material and a function of $y-$ only throughout this work, $p(\mathbf{r})$ the hole concentration, $n(\mathbf{r})$ the total electron concentration, and $N_D^+(\mathbf{r})$ and $N_A^-(\mathbf{r})$ the ionized donor and acceptor concentrations, respectively.

The Schrödinger equation is solved self-consistently with the Poisson equation by the Iterative Extraction Orthogonalization Method (IEOM) [10]. A detailed discussion of these methods and as well as the schemes employed to determine the number of electrons at equilibrium may be found in references [11] and [12].

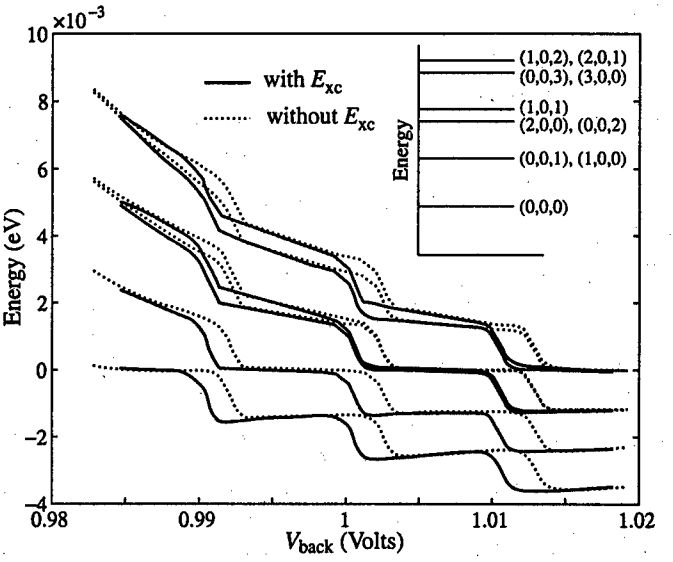

Fig. 2. Variation of the single-particle energy levels with V_{back} for the square-gate dot. The zero of the energy scale corresponds to the Fermi level. The inset shows the schematic of the energy spectrum for the empty ($N = 0$) dot with level ordering.

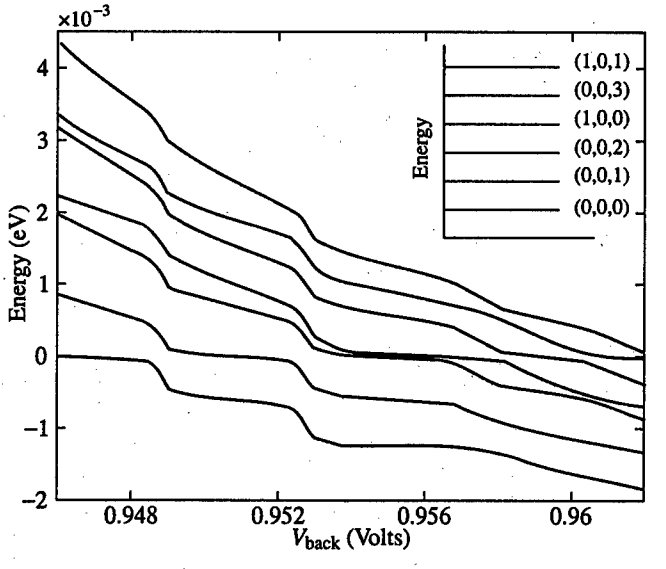

Fig. 3. Variation of the single-particle energy levels with V_{back} for the square-gate dot. The zero of the energy scale is the Fermi level. The inset shows the schematic of the energy spectrum for the empty ($N = 0$) dot with level ordering.

3 Results

3.1 Single quantum dots: shell structure vs. electron-electron interaction

It is well known that the conduction band edge for a grid-gate dot is quasi-parabolic at low energies for $N = 0$ [13, 14].

The evolution of the single-particle energy levels as a function of V_{back} is illustrated in Fig. 2 which shows a staircase variation of the first ten levels. Individual spin states have not been resolved in this diagram. It is seen that at $V_{\text{back}} = 0.985$ V the levels are well separated, but when the ground state, (0, 0, 0) [15], crosses the Fermi level, it "sticks" to this levels over a voltage range which corresponds to the charging of the first two electrons in the dot. This produces a change in slope of the upper levels which remain well separated from the first level. Meanwhile, the third and fourth levels which are respectively threefold and fourfold degenerate, and accomodate up to 6- and 8-electrons, each split into two new levels. This effect is due to the Coulomb interaction between carriers which induces some anharmonicity in the confining potential and lifts the degeneracy of the (101)-state with the (200)- and (002)-states, on one hand, and the degeneracy of the (201)- and (102)-states with the (003)- and (300)-states on the other (Fig. 2 inset). However, because of the conservation of the square symmetry of the (002)- and (200)-, the (300)- and (003)-, and the (201)- and (102)-states remain degenerate, respectively. Also visible in Fig. 2 is the influence of electron exchange-correlation which shifts all the single particle levels to lower energy because of the attractive nature of this many-body interaction.

In contrast to the square-gate dot, the quad-gate dot depicted in Fig. 1(b), has no energy level degeneracies due to its rectangular geometry, and hence no shell structure as shown schematically in the inset of Fig. 3 with the ordering of the energy levels. Fig. 3 shows the variation of the single-particle energy spectrum with V_{back} for the quad-gate dot. The variation is qualitatively similar to the square-gate device except that each curve now represents a spin-degenerate level which reduces the shell structure to a simple superposition of doubly degenerate (due to spin) states. Because the ratio between the sides of the rectangle is incommensurable, accidental degeneracies of states are absent from this spectrum for $N = 0$. However, they do appear for higher N as the electron-electron interaction distorts the self-consistent potential. One such instance is seen for $0.943\,\text{V} \leq V_{\text{back}} \leq 0.946$ V, where the third and fourth energy levels which converge at low bias cannot cross over on the Fermi level during the charging of the dot. The anamolous "Coulomb degeneracy" is caused solely by the repulsive Coulomb interaction between levels.

3.2 Double dot

Figure 4(a) shows the *Coulomb staircase* indicating the variation of the number of electrons in the double dot (Fig. 1(c)) with V_{back} at $V_t = -0.67$ V. For $V_{\text{back}} = 0.9769$ V, $\epsilon_{\text{LAO}}(0.5)$ is just negative, implying that the dot can accept one electron in the lowermost $1s-$like state. Since the interdot coupling is very weak each of the dots can be charged simultaneously with an electron each of spin $\uparrow$ resulting in N jumping from zero to two. This simultaneous (double) charging persists as long as the two dots are isolated. However, as V_{back} is increased to 0.9804 V, when the next charge degeneracy point occurs, only one of the dots can be charged (with a $\downarrow$ electron) but not both, due to increased Coulomb repulsion between the dots. Overcoming this repulsion requires a 0.1 mV increment in V_{back} resulting in the termination of double charging, which is evident as a narrow step for $N = 3$. At $V_{\text{back}} = 0.9805$ V, Dot 2 also can be charged with a $\downarrow$ electron increasing N to 4. Similar behavior is seen for 5th and 6th spin $\uparrow$ electrons, which occupy the first excited (p_z-like) states in Dots 1 and 2, respectively. The Coulomb repulsion between them is overcome

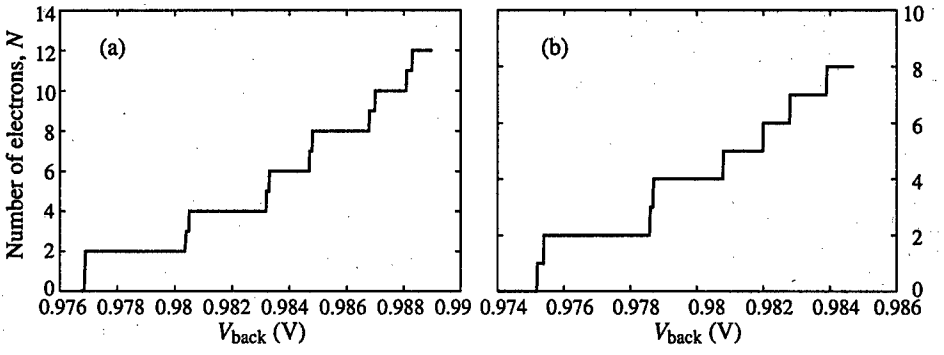

Fig. 4. Coulomb staircase diagram for the double-dot for (a) $V_t = -0.67$ V. The transitions that do not follow Hund's rules are shown in dashed lines. (b) $V_t = -0.60$ V.

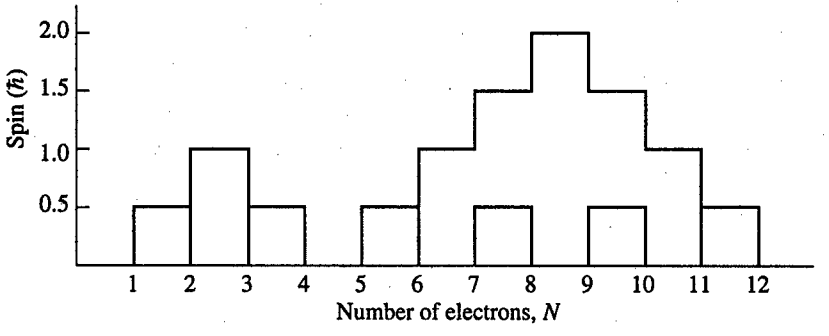

Fig. 5. Variation of the total electron spin S in the double dot with N for $V_t = -0.67$ V (solid line) $V_t = -0.60$ V (dashed line).

by a 0.1 mV increment in V_{back}. Using Hund's rule arguments, the 7th and 8th electrons are also of $\uparrow$ spin occupying the degenerate p_x-like states in Dots 1 and 2 [16]. Thus the ground state configuration for $N = 8$ is spin polarized with four electrons having $\uparrow$ spin. The $N = 9$ through $N = 12$, complete the half occupied second shells in the two dots eventually reverting the double dot system to an unpolarized state. When the interdot coupling is increased, as in Fig. 4(b), by making V_t more positive, double charging disappears. So also spin polarization in the dot, as the energy levels are reordered and the degeneracies of the first excited states in both the dots are lifted. Fig. 5 shows the variation of total spin in the dot for $V_t = -0.67$ V and $V_t = -0.60$ V. For weak coupling the total spin of the dot increases in steps of $\hbar/2$ from 0 at $N = 5$ to $2\hbar$ at $N = 8$ as the second shell in each of the dots is half filled with spins of all the electrons being parallel. For an increase in the coupling strength between the dots such a spin polarization of the dot is precluded by a lifting of degeneracy of the p_x- and p_z-states of the first shell and the total spin is never greater than $\hbar/2$.

4 Conclusions

We have investigated the shell structure in planar single quantum dots and observed that it remains largely unaltered by electron-electron interaction when the dots have a cylindrical

symmtery, but are drastically altered and lead to accidental degeneracies when the two-dimensional symmetry is lacking. In double-PQDs, we observe double electron charging for weak inter-dot coupling, which is terminated as the coupling increases. Furthermore, in the weak coupling regime, the dot becomes strongly spin polarized for $N = 8$ in accordance with Hund's rules. An increase in inter-dot coupling reverts the dot into an unpolarized spin state.

Acknowledgements

We would like to thank L. Fonseca, I. H. Lee and R. M. Martin for valuable discussions, and Y. H. Kim for making available the LSDA subroutines. This work is supported by NSF Grant No. ECS 95-09751. One of us (S.N.) would like to acknowledge support from the Beckman Institute Research Assistantship program.

References

[1] C. W. J. Beenakker, *Phys. Rev. B* **44**, 1646 (1991).
[2] D. V. Averin, A. N. Korotkov and K. K. Likharev, *Phys. Rev. B* **44**, 6199 (1991).
[3] U. Meirav and E. B. Foxman, *Semicond. Sci. Tech.*, **10**, 255 (1995).
[4] R. J. Haugh, R. H. Blick and T. Schmidt, *Physca B* **212**, 207 (1995).
[5] D. Leonard, K. Pond and P. M. Petroff, *Phys. Rev. B* **40**, 11687 (1994).
[6] K. Imamura, Y. Sugiyama, Y. Nakata, S. Muto and N. Yokoyama, *Jpn. J. Appl. Phys* **34**, 1445 (1995).
[7] J. Jimenez, L. R. C. Fonseca, D. J. Brady, J. P. Leburton, D. E. Wohlert and K. Y. Cheng, *Appl. Phys. Lett.* **71**(25), 3558 (1997).
[8] R. O. Jones and O. Gunnarsson, *Rev. Mod. Phys.* **61** (3), 689–746 (1989).
[9] J. P. Perdew and Z. Zunger, *Phys. Rev. B* **23**, 5048 (1981).
[10] R. Kosloff and H. Tal-Ezer, *Chem. Phys. Lett.* **127**, 223 (1986).
[11] D. Jovanovic and J. P. Leburton, *Phys. Rev. B* **49**, 7474 (1994).
[12] S. Nagaraja, J. P. Leburton and R. M. Martin, *unpublished* 1999.
[13] A. Kumar, S.E. Laux and F. Stern, *Phys. Rev. B* **42**, 5166 (1990).
[14] S. Nagaraja, P. Matagne, J. P. Leburton, Y. H. Kim and R. M. Martin, *Phys. Rev. B* **56**, 15572 (1997).
[15] we follow the (n_x, n_y, n_z) representation of the wavefunction with n_x, n_y and n_z representing the number of nodes of the wavefunctions along $x-$,$y-$, and $z-$ directions, respectively.
[16] S. Tarucha, D. G. Austing, T. Honda, R. J. van der Hage and L. P. Kouwenhoven, *Phys. Rev. Lett.* **77**, 3613 (1996).

7th Int. Symp. "Nanostructures: Physics and Technology"
St Petersburg, Russia, June 14–18, 1999

Quantum dots formed by ultrathin CdSe-ZnSe insertions

M. Straßburg, R. Engelhardt, R. Heitz, U. W. Pohl, S. Rodt, V. Turck,
A. Hoffmann, D. Bimberg, I. L. Krestnikov†, N. N. Ledentsov†, Zh. I. Alferov†,
D. Litvinov‡, A. Rosenauer‡ and D. Gerthsen‡
Institut für Festkörperphysik, Technische Universität Berlin,
Hardenbergstr. 36, 10623 Berlin, Germany
† Ioffe Physico-Technical Institute, St Petersburg, Russia
‡ Laboratorium für Elektronenmikroskopie der Universität Karlsruhe,
Kaiserstr. 12, Postfach 6980, 76128 Karlsruhe, Germany

Abstract. We review on experimental and theoretical studies on a new type of quantum-dot (QD) structures obtained growing ultrathin, i.e. below the critical thickness for 2D-3D transition, strained narrow gap insertions. The formation of dense arrays (up to 10^{12} cm^{-2}) of nanoscale two-dimensional islands formed by submonolayer (SML) or slightly above-1 ML CdSe insertions in a wide gap II-VI matrices is revealed in processed high-resolution transmission electron microscopy images. In the case of stacked sheets of SML insertions, the islands in the neighboring sheets are formed predominantly in correlated or anticorrelated way for thinner and thicker spacer layers, respectively. By monitoring of sharp lines due to single QDs using cathodoluminescence the 3D confinement is confirmed. We manifest significant squeezing of the QD exciton wavefunction due to lateral confinement in magneto-optical experiments. Different polarization of photoluminescence (PL) emission recorded in edge geometry for vertically-uncoupled and coupled QDs confirms the QD nature of excitons. We show complete suppression of lateral motion of excitons bound to islands in case of wide-gap (ZnMgSSe) matrices.
A resonant (0-phonon) lasing is observed in ultrathin CdSe insertions and proves the lifting of the **k**-selection rule for QD excitons. Lack of exciton screening in QDs up to high excitation densities enables strong resonant modulation of the refractive index in stacked ultrathin insertions and allows realization of resonant (excitonic) waveguiding and lasing. This enables the realization of a new type of heterostructure laser operating without external optical confinement by layers having lower average refractive indices or a new type of a surface-emitting laser.

1 Introduction

Quantum dot heterostructures [1, 2], i.e. semiconductor structures providing confinement in all three dimensions, present an ultimate limit of size quantization in solids and result in the strongest possible modification of electronic properties as compared to quantum wells and wires. The recent breakthrough in device application of QDs is mostly related to Stranski–Krastanow growth, resulting in the formation of 3D islands on top of a wetting layer [1]. 1.3 μm-emitting GaAs-based lasers with parameters, superior to those in InP-based quantum well (QW) lasers are created [3]. With regard to this progress, there are many attempts to apply similar concept to widegap lasers based on II–VI material systems and group-III nitrides [4, 5]. The CdSe/ZnMgSSe system represents the best choice to study physical mechanisms of lasing in wide-gap compounds and, with regard to the extended history of investigations [6], can be considered as a model system. For fabrication of CdSe/ZnSe QDs two principally different growth modes have been introduced. The Stranski–Krastanow mode results for the CdSe/ZnSe system in the formation of islands with a diameter being typically larger than 30 nm [7]. Such II–VI islands are too large as

compared to Bohr-diameter in ZnSe (9 nm [8]) to provide significant quantization. Another way to fabricate quantum wires and QDs has been proposed by using submonolayer (SML) narrow gap insertions [9–11]. It was shown that such islands having a height of 1 ML are providing a uniform size (width of about 4 nm for InAs elongated islands on GaAs (100) surface) [10]. The increased exciton binding energy [12] and oscillator strength [13] have been demonstrated. An island of such a size can be used very effectively to localize ZnSe excitons, which have Bohr-radii of about 4.5 nm [8].

The proposal for formation of such islands in case of II–VI SML insertions as well as demonstration of high exciton oscillator strength and lifting of **k**-selection rule for such structures has been given in [14]. This idea, however, was met with criticism, as the mechanisms used for III–V growth were believed to be hardly possible for II–VI materials [15]. However, high-resolution transmission electron microscopy images and studies of the influence of deposition conditions on SML luminescence confirmed formation of nanoscale islands having a lateral size of 4–5 nm [16]. These islands have been revealed both in case of MBE [17] and MOCVD [18] growth. Similar CdSe islands having two-dimensional shape and a size of about 5 nm have been recently reported for MBE growth using migration-enhanced MBE mode [19]. Formation of uniform nano-islands can be explained by kinetic [20] or equilibrium models [21, 22].

A different interpretation of the CdSe-ZnSe SML growth was given by Toropov *et al.* [23], who proposed that uniform quasi-alloy coverage is formed for CdSe SML depositions for average thickness below 0.7 ML. As opposite, for deposition above 0.7 ML formation of large mesoscopic islands with dimensions much larger than exciton Bohr-radii is proposed. The density and the size of these islands has believed to be about 3×10^9 cm^{-2} and 20–60 nm, respectively [4].

2 Self-organization of two-dimensional islands

Spontaneous formation of ordered arrays of islands has been long studied theoretically and experimentally (see e.g. review in: [24]). The formation of ordered ("parquet") structures on crystal surfaces has been shown to occur when two phases with different values of intrinsic surface stress (τ_{ij}) are coexisting on the surface [25]. For strained above-monolayer-high 2D islands the total energy minimum for particular island size always exists [26].

In case of stacked arrays of 2D nano-islands it was predicted, that correlated growth prevails at small spacer layer thicknesses, while anticorrelated growth occurs for thicker spacers [27]. This effect has been observed experimentally using processed high-resolution transmission electron microscopy [28]. As opposite, in publications by Toropov et al. [23, 29] anticorrelated growth of mesoscopic islands has been claimed for small spacer layer thicknesses.

3 Structural characterization of ultrathin insertions

Processed high-resolution transmission electron microscopy (HRTEM) arises as a powerful tool to reveal the structural properties of structures with ultrasmall QDs. In Fig. 1 we show a processed HRTEM images obtained using DALI procedure [30] for a stacked SML-CdSe/ZnMgSSe structure with 30 Å spacer thickness. The image was taken by a projection of a relatively thick foil of 12–20 nm, where many islands are captured. This may also contribute to the smaller contrast in comparison to a SML-CdSe/ZnSe structure with the same spacer thickness [17]. A color-coded map corresponding to the local lattice parameter in growth direction is shown. The DALI processing allows clear visualization of QDs as

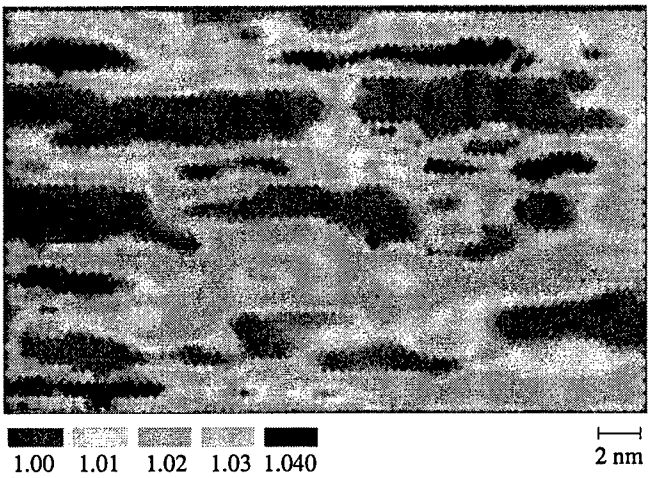

Fig. 1. The color-coded map of the local lattice parameter (LLP) in growth direction digitally processed from a HRTEM image of a stacked submonolayer-CdSe/ZnMgSSe structure.

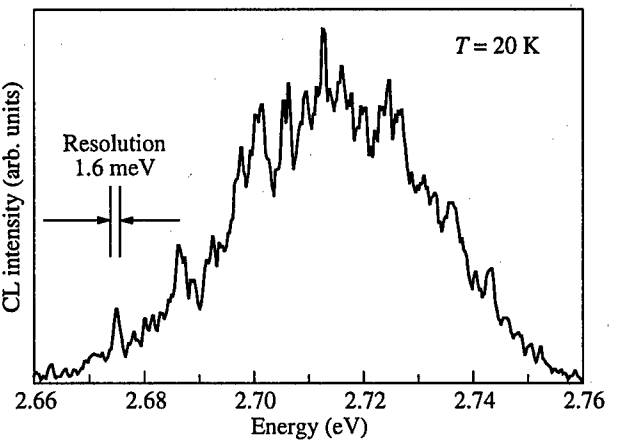

Fig. 2. Cathodoluminescence (CL) spectra of single 1 ML CdSe insertion in a ZnSSe at $T = 20$ K. The sharp luminescence lines in the spectra originate from single QDs.

local regions with increased local lattice parameter. The image reveals planar islands with a lateral size of only a few nanometers. According to the larger island size distribution in the case of quaternary spacer, the FWHM of the PL band is much broader [31] than observed for ZnSe spacers [17].

Similar conclusions can be deduced from the color-coded maps of the total local lattice displacement with respect to the lattice of the buffer layer [17]. In the case of CdSe/ZnSe structures HRTEM investigations were performed for samples with different spacer thicknesses [28, 32, 33]. Here, a correlated growth of islands was observed for spacer layer thickness < 3 nm, while anticorrelated growth occurs for spacers thicker than 3 nm. The lateral size of the QDs is about 4–5 nm in the case of ZnSe matrix. Essentially the same size of the CdSe island has been revealed in [19]. For MOCVD-grown QDs the lateral size varies between 2 and 6 nm and, thus, the PL emission from ultrathin (0.5–2 ML) insertions is broader [34].

4 Emission of individual QDs

0D confinement of excitons at 2D nano-islands must produce an atom-like energy spectrum of excitons [35] leading to the appearance of discrete energy levels of QDs. In the case of a very dense array of QDs, e.g., as formed by ultrathin insertions, it is very difficult to resolve luminescence lines corresponding to individual QDs. Such a result has been achieved in spot-focus CL studies. The luminescence spectrum of a MOVPE-grown sample [34] with a $\sim$ 1 ML CdSe insertion in a ZnSSe matrix is depicted in Fig. 3. The FWHM of the sharp emission lines, corresponding to spatially resolved luminescent areas, are limited by the spectral resolution of the setup. Ultrasharp luminsescence lines due to single QDs and a high density of nanoscale QDs formed by 1–2 ML CdSe deposition in a ZnSe matrix using MBE-growth has been proven in [19].

5 Polarization of edge emission and symmetry of the heavy hole wavefunction in QDs

Polarization of the luminescence in edge geometry enables a clear distinction between the QW and QD cases. According to Kane's selection rule, the heavy hole exciton luminescence in QWs must be completely TE polarized. As opposite to the QW case, a significant contribution of TM emission has been observed (Fig. 3), pointing to a significant role of exciton lateral confinement. The most remarkable observation has been done for polarization of edge emission in case of vertically-coupled QD states (see Fig. 3(c)). This emission is predominantly TM polarized. This indicates that the heavy-hole wavefunction is more extended in the growth direction and a has cylindrical shape. A similar effect has been observed in case of vertically-coupled InGaAs-GaAs Stranski–Krastanow QDs [36].

The extension of the exciton wavefunction in uncoupled and coupled QD structures was estimated from the Zeeman behavior with B applied parallel to the growth direction [37]. Following Ref. [38], the lateral extension of the exciton wavefunctions was estimated from the diamagnetic shifts to be $\sim$ 5.5 nm and $<$ 3 nm for uncoupled and coupled QDs, respectively, being smaller then the bulk Bohr-diameter (9 nm) [8]. These results are in good agreement with the lateral dimensions of the 2D islands observed in cross-sectional HRTEM images [28], supporting the corresponding localization of the excitons.

6 Matrix effects: lack of QD exciton transport in the case of wide gap matrix

Despite of the observation of luminescence lines due to single QDs, energy transfer processes can still be very pronounced. This results in a faster tunneling to neighboring larger QDs, having lower exciton transition energy, similar to the case of neighboring thicker and thinner quantum wells. Thus, ground state transitions can be revealed in PLE spectra [32]. This is very different from the case of InAs-GaAs Stranski–Krastanow QDs, where ground state transition is not resolved in PLE spectra, while it is observed in absorption and luminescence spectra [39]. It was observed, however, that by cladding QDs by a wider-gap ZnMgSSe matrix, one can suppress tunneling of excitons and thus realize a true QD-like PLE spectrum [31]. In this case the first peak in PLE spectrum coincides with the first excited state in QD.

7 Lasing mechanism in II–VI QDs

In bulk material direct radiative recombination of excitons with finite **k**-vector, which dominates at high temperatures and high excitation densities, is forbidden. Another particle, e.g. a LO-phonon is necessary to accommodate the exciton **k**-vector [40]. Thus, exciton-phonon scattering processes dominate the gain mechanism in II–I materials, where exciton

Bohr radii are small and densities necessary to screen excitons are higher than the excitation density at gain threshold [41]. At even higher excitation densities, exciton-exciton and exciton-electron scattering processes dominate. These processes shift the lasing wavelength typically by one or two LO-phonon energies towards longer wavelength as compared to exciton energy revealed in absorption spectrum. In QDs, however, the lasing mechanism must have principally excitonic (or biexcitonic) character, as excitons can not be screened in QDs and the **k**-selection rule is not appropriate.

8 Waveguiding and lasing

High exciton oscillator strength in case of stacked dense arrays of QDs and the experimentally proven resonant character of lasing up to room temperature [31] stimulated an idea of creating a new type of a laser based on the concept of resonant waveguiding and lasing. It was shown that a significant enhancement of the refractive index originates on the low energy side of the absorption spectrum in accordance with Kramers–Kronig relations [42]. This fact enables waveguiding in a small spectral window without external waveguides. Absorption measurements [43] demonstrated maximum absorption coefficients of the order of 10^5 cm^{-1} in the case of stacked SML QDs. This fact agrees with the estimation of the

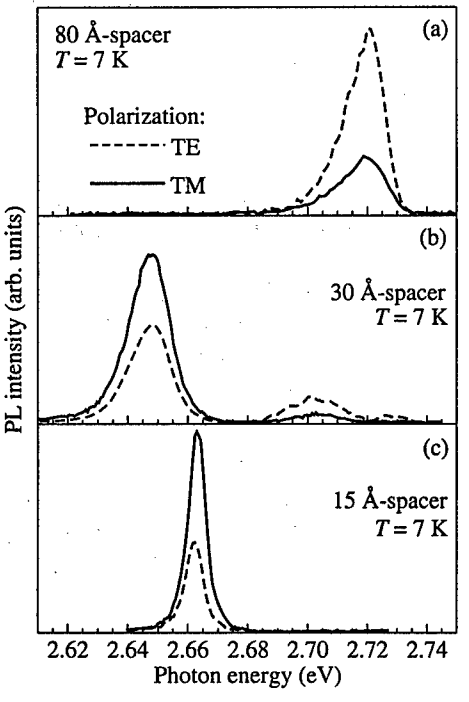

Fig. 3. Linearly polarized photoluminescence (PL) of structures with 80 Å, 30 Å and 15 Å spacers measured in edge geometry. The polarization changes from mostly TE for uncoupled islands (80 Å spacers) to mostly TM (accompanied by a red shift) for vertically coupled islands (15 Å spacers). The 30 Å spacer sample shows emission from both types of islands.

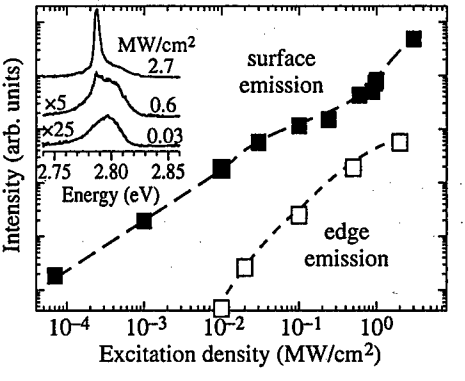

Fig. 4. Surface and edge emission of a stacked SML-CdSe structure with ZnMgSSe barriers as a function of the excitation density. The spectra are vertically displaced for clarity. The superlinear growth and the narrowing of the surface emission occurs, when edge emission saturates. The inset shows the surface emission.

exciton oscillator strength from the optical reflectance spectra and correspond to the values of the refractive index enhancement of about 0.2–0.3. Lasers based on the resonant waveguiding were demonstrated to be exceptionally promising both for II–VI [31] and III–V [44] SML structures.

9 Surface lasing without Bragg mirrors and self-adjustment of cavity

High exciton absorption coefficients in arrays of QDs allow to achieve lasing in case of very short cavity lengths in edge geometry, or realize surface lasing in vertical geometry when no highly-reflecting Bragg mirrors is used. E.g., just ZnSe/GaAs and ZnSe/air interfaces allowing to achieve about 30% reflectivity each made it possible to have surface lasing in structures with 20-fold stacked CdSe SML insertions [32]. The surface emission in dependence of the excitation density is depicted in Fig. 4.

In the case when the gain in the active medium is small, the modulation of refractive index, caused by changing gain with increase in the excitation density (chirp) is small. If the gain is high, then the shift of the cavity modes with the excitation density increase can be very significant [32]. This allows to achieve self-adjustment effect between the cavity mode and the gain spectrum. In this case the cavity mode wavelength tunes with excitation density rise, until it reaches the spectral region, where gain is able to overcome external losses.

Currently photopumped GaN-based surface emitting laser, emitting in the blue spectral range, is realized using similar concept [45]. Using of low reflectivity lower AlGaN/GaN Bragg reflector allowed to achieve room temperature surface lasing [46].

10 Conclusion

To conclude, we discussed optical properties of ultrathin CdSe insertions in a ZnSe matrix. These insertions represent dense arrays of two-dimensional nano-islands with a size comparable to the exciton Bohr-radius. The QD nature is proven by direct observation of luminescence lines from single QDs, by resonant character of gain and by lateral squeezing of excitons revealed in magneto-optical studies. New effects led to fabrication of unique devices such as resonantly-waveguiding lasers and cavity-self-adjusted surface-emitting lasers without Bragg reflectors.

Acknowledgments

This work was supported by the Russian Foundation on Basic Research, the Program of Ministry of Science of Russian Federation "Physics of solid-states nanostructures" and Deutsche Forschungsgemeinschaft (DFG). We gratefully acknowledge S. V. Ivanov and S. V. Sorokin for expert MBE growth. N.N.L. is supported by Guest Professorship Program of DAAD.

References

[1] D. Bimberg, M. Grundmann and N. N. Ledentsov, *Quantum Dot Hetrerostructures*, John Wiley & Sons, Chichester, p. 328, 1999.
[2] U. Woggon et al., *J. Lum.* **70**, 269 (1996).
[3] Yu. M. Shernyakov et al., *Electronics Lett.* (in print).
[4] S. V. Ivanov et al., *Appl. Phys. Lett.* **74**, 498 (1999).
[5] S. Nakamura et al., *Appl. Phys. Lett.* **70**, 2753 (1997).
[6] for a review see e.g., J. Gutowski et al., *J. Crystal Growth* **184/185**, (1998).
[7] M. Arita et al., *Jpn. J. Appl. Phys.* **36**, 4097 (1997).

[8] J. Puls et al., *Phys. Rev. B* **57**, 14749 (1998).
[9] O. Brandt et al., *Surf. Sci.* **267**, 319 (1992).
[10] V. Bressler-Hill et al., *Phys. Rev. B* **50**, 8479 (1994).
[11] P. D. Wang et al., *Appl. Phys. Lett.* **64**, 1526 (1994).
[12] P. D. Wang et al., *Phys. Rev. B* **50**, 1604 (1994).
[13] M. V. Belousov et al., *Phys. Rev. B* **51**, 14346 (1995).
[14] N. N. Ledentsov et al., *Appl. Phys. Lett.* **69**, 1343 (1996).
[15] K. P. O'Donnel and U. Woggon, *Appl. Phys. Lett.* **70**, 2765 (1997).
[16] N. N. Ledentsov et al., *Appl. Phys. Lett.* **70**, 2766 (1997).
[17] M. Strassburg et al., *Appl. Phys. Lett.* **72**, 942 (1998).
[18] U. W. Pohl et al., *J. Cryst. Growth* **195**, 569 (1998).
[19] T. Kümmell et al., *Appl. Phys. Lett.* **73**, 3105 (1998).
[20] V. Bressler-Hill et al., *Phys. Rev. Lett.* **74**, 3209 (1995).
[21] N. N. Ledentsov et al., *Solid State Electron.* **40**, 785 (1996).
[22] V. A. Shchukin et al., *Optical Properties of Low Dimensional Semiconductors*, G. Abstreiter, A. Aydinli, and J.-P. Leburton, Eds., NATO ASI Series. Series E: Applied Sciences, Vol. 344. pp. 257-302, Kluwer Academic Publishers, Dordrecht, The Netherlands 1997.
[23] A. A. Toropov et al., *J. Crystal Growth* **184/185**, 293 (1998).
[24] V. A. Shchukin and D. Bimberg, *Rev. Mod. Phys.* (1999) (in print).
[25] V. I. Marchenko, *JETP Lett.* **33**, 381 (1981).
[26] J. Tersoff and R. M. Tromp, *Phys. Rev. Lett.* **70**, 2782 (1993).
[27] V. A. Shchukin et al., *Phys. Rev. B* **57**, 12262 (1998).
[28] M. Strassburg et al., *Proc. 24th Int. Conf. on the Physics of Semiconductors*, Jerusalem, Israel, August 2-7, 1998.
[29] A. A. Toropov et al., *Phys. Rev. B* **59**, R2510 (1999).
[30] A. Rosenauer et al., *Optik* **102**, 63 (1996).
[31] I. L. Krestnikov et al., *J. Cryst. Growth* **184/185**, 545 (1998).
[32] I. L. Krestnikov et al., *Phys. Rev. B* (1999) (in print).
[33] I. L. Krestnikov et al., Proc. 24th Int. Conf. on the Physics of Semiconductors, Jerusalem, Israel, August 2-7, 1998.
[34] R. Engelhardt et al., *J. Cryst. Growth* **184/185**, 311 (1998).
[35] M. Grundmann et al., *Phys. Rev. Lett.* **74**, 4043 (1995).
[36] Yu Ping et al., *Phys. Rev. B* (1999) (in print).
[37] M. Straßburg et al., *J. Electr. Mat.* (1999) (in print).
[38] I. E. Itskevich et al., *Appl. Phys. Lett.* **70**, 505 (1997).
[39] N. N. Ledentsov et al., *Proc. 22nd Int. Conf. on the Physics of Semiconductors*, Vancouver, Canada, 1994, D. J. Lockwood, ed. (World Scientific, Singapore, 1995), vol. 3, p. 1855.
[40] E. Gross, S. Permogorov and A. Razbirin, *J. Phys. Chem. Solids* **27**, 1647 (1966).
[41] C. Benoit a la Guillaume, J. M. Denber and F. Salvan, *Phys. Rev.* **177**, 567 (1969).
[42] Zh. I. Alferov et al., *Superlattices and Microstructures* **15**, 65 (1994).
[43] G. N. Aliev et al., *J. Cryst. Growth* **184/185**, 315 (1998).
[44] N. N. Ledentsov et al., *Appl. Phys. Lett.* **74**, 161 (1999).
[45] A. V. Sakharov et al., *Appl. Phys. Lett.*, (in print).
[46] I. L. Krestnikov et al., *Appl. Phys. Lett.*, (in print).

7th Int. Symp. "Nanostructures: Physics and Technology"
St Petersburg, Russia, June 14–18, 1999

Spin separation in self-organized quantum dots under optical orientation of electrons

V. K. Kalevich, K. V. Kavokin, M. Paillard†, X. Marie†, P. Le Jeune†, T. Amand†, M. N. Tkachuk, V. M. Ustinov, N. N. Ledentsov and B. P. Zakharchenya

Ioffe Physico-Technical Institute, St Petersburg, Russia
† Laboratoire de Physique de la Matière Condensée CNRS-UMR 5830 INSA, Complexe scientifique de Rangueil, 31077 Toulouse cedex, France

Introduction

Optical methods, widely used in studying the arrays of self-organized semiconductor quantum dots (QDs), are even more effective when they are supplied with measuring polarization, which provides an access to additional degrees of freedom related to carrier spins [1]. In our previous work [2], we have shown that time-resolved picosecond techniques allow to observe transients of polarization of electrons in QDs under optical orientation conditions. The present work is aimed at studying the dynamics of population of discrete energy levels by spin-polarized electrons in QDs. In particular, we present a detailed study of "spin separation", i.e. redistribution of the average spin of electrons among their energy levels as a result of energy relaxation limited by Pauli's principle. Saturation of the QD ground state at high excitation intensities results in the rapid vanishing of the mean spin of electrons in this state. At the same time, the electron spin polarization at higher energy levels dramatically increases, reaching values close to 100%, which is normally forbidden by optical selection rules. We present time dependences of the circular polarization of luminescence, which reflects the electron spin state, measured over a wide spectral range under various excitation densities. A simple theoretical model is discussed that qualitatively describes the experimental results.

Experimental

The results presented below are obtained on MBE-grown $In_{0.5}Ga_{0.5}As$ QDs embedded in a GaAs matrix. An active region, which consisted of 6 planes of QDs separated by 50 Å GaAs spacers, was inserted into the middle of a 0.2 μm undoped GaAs layer confined by AlAs(2 nm)/GaAs(2 nm) superlattices. Each QD plane was formed by deposition of 4 monolayers of $In_{0.5}Ga_{0.5}As$ [4]. Circularly polarized beam of a tunable Ti-sapphire laser producing 1.2-ps long light pulses with a repetition rate of 82 MHz was used to excite the investigated structure. The time resolution of the experimental setup, based on the up-conversion technique, was limited by laser pulse duration. The luminescence was registered along the growth axis in back-scattering geometry. The degree of circular polarization of luminescence, ρ, was measured. As follows from measurements of spin beats in a strong magnetic field [2], the polarization of holes in our experiments can be neglected, and the polarization of luminescence is determined by polarization of electrons, P_e, only: $\rho = P_e$.

Normalized luminescence spectra obtained under excitation of carriers in the GaAs matrix are shown in Fig. 1. Spectrum 1, recorded under continuous wave (cw) excitation with a low pump density $W = 0.1$ W/cm^2, results from the emission of ground-state electrons and holes [2]. We associate the presence of two strongly overlapping lines in

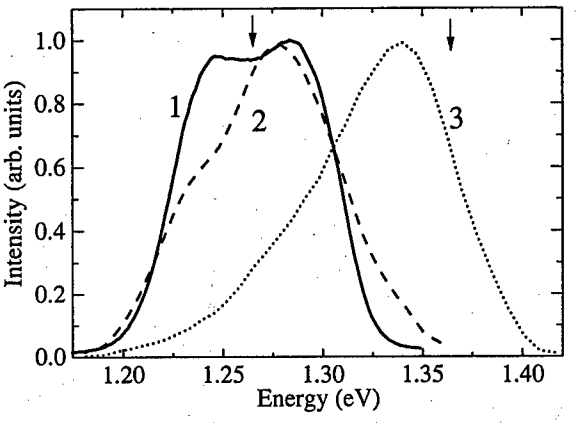

Fig. 1. Photoluminescence spectra of $In_{0.5}Ga_{0.5}As/GaAs$ QDs at excitation energy E_{exc} = 1.531 eV, T = 10 K. 1—cw excitation with power density 0.1 W/cm^2; 2 and 3—pulse pumping with power densities 0.1 and 3.0 MW/cm^2, time delay after excitation pulse equals 200 ps.

this spectrum with radiative recombination of two groups of dots having different mean sizes. Spectra 2 and 3 are registered under pulse excitation with W = 0.1 MW/cm^2 and W = 3.0 MW/cm^2, respectively. A significant blue shift of the luminescence line (up to 60 meV), arising with increase in pulse intensity, is due to the filling of the ground states of electrons and holes and to the appearance of an intense light emission from the excited states. Fig. 2 shows the time dependence $\rho(t)$ measured at two different energies of detection E_{det} (marked by arrows in Fig. 1). It can be seen from Fig. 2 that at the high-energy edge of the luminescence line the polarization first increases up to the maximum value near 70% (curve 1), and then slowly decreases. On the contrary, at the low-energy edge, ρ drops down to values which are close to zero at high excitation density (curve 2). Characteristic times of the fast increase and decrease coincide with the saturation time of the ground state. The latter, determined from the increase of the luminescence intensity (curve 3), appears to be 25 to 40 ps. Further slower decrease of polarization in curves 1 and 2′ is governed by the spin relaxation time of electrons that is of the order of 300 to 400 ps.

Model and discussion

The qualitative explanation of the different behavior of polarization at the high-and low-energy sides of the QDs spectra is as follows. The electrons, generated in the GaAs barrier by circularly polarized light, have a spin polarization equal to 50% [3], and preserve it when trapped by QDs. By virtue of Pauli's principle each energy level in the QD can contain no more than two electrons with opposite spins. As at P_e = 50% there are three times more electrons with spin $-1/2$ than with spin $+1/2$, so energy relaxation will lead to a predominant population of higher energy levels by electrons with spin $-1/2$. This results in increased polarization of luminescence which may exceed 50% (see curve 1 in Fig. 2). On the contrary, with increase in the concentration of photoexcited carriers, the radiation from the ground state becomes non-polarized, since two electrons occupying this state have opposite spins. This is also observed experimentally (see curve 2 in Fig. 2). If the time of inter-level relaxation of electrons is finite, then under pulsed excitation the initial polarization of luminescence is governed by electrons coming from barriers: $\rho(t = 0) = 50\%$. This determines the initial increase of ρ at high E_{det} and decrease of ρ at low E_{det}, corresponding to recombination from the ground state. The effect is demonstrated

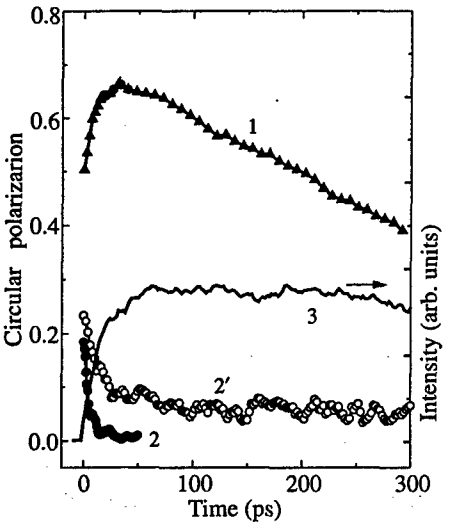

Fig. 2. Luminescence circular polarization dependence on time delay at two detection energies E_{det}. $E_{exc} = 1.531$ eV, $T = 10$ K. Solid lines are drown to guide the eye. E_{det} (eV): 1—1.363; 2, 2′, 3—1.265. W (MW/cm^2): 1, 2—1.5; 2′, 3—0.8.

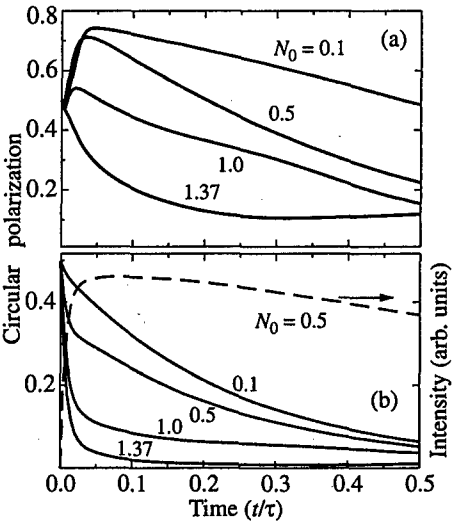

Fig. 3. Calculated dependence $\rho(t)$ at different excitation densities for: (a) excited state, (b) ground state. τ is the electron lifetime. N_0 are given with respect to the concentration of QDs. Dashed line is the luminescence intensity at $N_0 = 0.5$.

by experimental curves 1 and 2 in Fig. 2 and by theoretical curves in Fig. 3.

The main question arising when one attempts to describe the transient population of an ensemble of QDs, is to what extent the dots can be considered as isolated from each other. The answer determines the type of statistics applicable. In our case, QDs were vertically coupled, forming linear clusters, or short wires, 6 dots in each. In principle, electrons could move from one dot to another within the cluster, but probabilities of such transitions are not known. For this reason, we have considered two extreme cases, namely, isolated and strongly coupled QDs.

To describe an ensemble of dots isolated from each other, we have used the master equation approach suggested by Bimberg *et al.* [5]. In this approach, probabilities of occupation of all possible states of a dot are calculated as functions of time. As distinct from [5], we additionally distinguish these states by spin. Considering for simplicity dots with 2 electron levels, we get 16 possible electron configurations. In addition, there are two functions describing concentrations of spin-up and spin-down electrons in the reservoir (=barrier): N_1 and N_2. Dot states are coupled by single-electron transitions: 1) capture from the reservoir to the first or the second level, 2) recombination, 3) spin relaxation within a level, 4) inter-level energy relaxation (transition from the second level to the first without changing spin). In total, there are 18 differential equations describing time evolution of the spin system. This set of coupled equations has been solved numerically under initial conditions corresponding to empty dots and the reservoir filled according to optical selection rules: $N_1(t = 0) = 3N_0$, $N_2(t = 0) = N_0$. Polarizations and intensities of luminescence from the first and second levels calculated at different values of N_0, assuming realistic values of relaxation times, are presented in Fig. 3.

For the case of strongly coupled dots, the electron levels belonging to different dots

form narrow bands. This situation would be close to the one considered by Dyakonov and Perel' [6] for bulk semiconductors, but for delta-shaped density of states, typical of quantum-dot systems. In order to describe time dependent electron polarization in this case ("wire" model), we have used rate equations for concentrations of electrons with both spin directions on the first and second levels. Numerical results of this model are similar to those shown in Fig. 3. The most pronounced difference between the models occurs at low exciting intensities. In the "dot" model the polarization of the second level decreases with increase in intensity, being limited by 80%. In the "wire" model the polarization of the excited level increases with increase of pumping, coming to 100%, and then decreases with further increase in carrier concentration due to the saturation of the second level.

Both models give qualitative agreement with the experiment. To conclude on validity of a specific model, additional experiments with isolated QDs are required.

It should be noted that the spin-dependent population of excited electron levels must lead to the dependence of their radiation intensity on the mean spin of carriers and, therefore, on the polarization of the exciting light. Within both our models, this effect does show up if the polarization of the exciting light is changed from the circular to the linear one.

Acknowledgments

The authors are grateful to I. A. Merkulov, E. L. Ivchenko, A. E. Tsatsul'nikov, A. E. Zhukov, A. R. Kovsh for fruitful discussions. Partial support of the RFBR (grant 99-02-18082) is acknowledged.

References

[1] R. I. Dzhioev, B. P. Zakharchenya, E. L. Ivchenko et al., *JETP Lett.* **65**, 804 (1997).

[2] V. K. Kalevich, M. N. Tkachuk, P. Le Jeune, X. Marie and T. Amand, Proc. Int. Conf. *Physics at the Turn of the 21th Century*, St.-Petersburg, Russia (1998), to be published in Physics of the Solid State, **41**, N5, 117 (1999).

[3] *Optical Orientation*, ed. F. Meier and B. Zakharchenya, Modern Problems in Condensed Matter Sciences, North-Holland, Amsterdam, vol. 8 (1984).

[4] A. Yu. Egorov, A. E. Zhukov, P. S. Kop'ev, N. N. Ledentsov, M. V. Maximov and V. M. Ustinov, *Semiconductors* **28**, 809 (1994).

[5] M. Grundmann and D. Bimberg, *Phys. Rev. B* **55**, 9740 (1997).

[6] M. I. Dyakonov and V. I. Perel', *JETP Lett.* **13**, 144 (1971).

7th Int. Symp. "Nanostructures: Physics and Technology"
St Petersburg, Russia, June 14–18, 1999

LO phonon mediated relaxation in InP self assembled quantum dots in electric field

I. E. Kozin†‡, I. V. Ignatiev†‡, S. Nair†, H.-W. Ren†, S. Sugou† and Y. Masumoto†¶

† Masumoto Single Quantum Dot project, ERATO, JST, Japan
‡ Institute of Physics, St Petersburg State University, Russia
¶ Tsukuba University, Japan

Abstract. Strong LO phonon resonances are found in the photoluminescence spectra of InP self-assembled quantum dots under an applied bias. These arise from fast phonon assisted relaxation when the applied bias suppresses the photoluminescence.

Introduction

In the optical spectra of semiconductor quantum dot structures with not very high quantum yield of the photoluminescence (PL), features due to optical phonon mediated relaxation of excitation are observed [1]. In high quality structures, on the other hand, when the main recombination channel for excited electron hole pairs is radiative, there are no such features. In present work we found that applying an electric field to InP QDs leads to decreasing of the quantum yield. As a result, features caused by LO phonons become observable in the PL spectra.

1 Experimental result

The studied heterostructure QDP1779 was grown by gas source molecular beam epitaxy on an n^+ GaAs substrate. The QDs were formed by the deposition of InP on the InGaP layer and covered by the top InGaP layer. The areal density of the QDs is about 10^{10} cm^{-2}. Average base diameter is $\approx$ 50 nm and height is $\approx$ 10 nm. The sample was provided with a semi-transparent gold Shottky contact on the top surface and an ohmic contact on the back surface.

The PL spectra were recorded by using a cw Ti:sapphire laser, a double monochromator U1000 and a photon counting system with cooled GaAs photomultiplier tube. All the measurements were done at 5 K.

The PL spectra of the InP QDs under negative bias ("−" is on the top of the sample) are shown in Fig. 1(a). Without bias there are no strong features in the spectrum. When a negative bias is applied the intensity of the PL decreases and distinct resonances appear in the spectrum. As the negative bias is increased, these resonances grow in intensity relative to the rest of the PL band. However, under rather strong bias ($U_{\text{bias}} < -1.0$ V) intensities of the resonances start to decrease. Energy gaps between the laser line and the resonances approximately correspond to the 1LO and 2LO phonon energies in InP. As is seen from Fig. 1(b), the 1LO resonance has a rather complicated structure. A decomposition of this structure into Gaussian functions give the phonon energies 41.0 meV, 43.7 meV, 45.3 meV, 47.2 meV and 48.0 meV. The spectral shape of the 2LO resonance is reproduced by the convolution of the 1LO resonance.

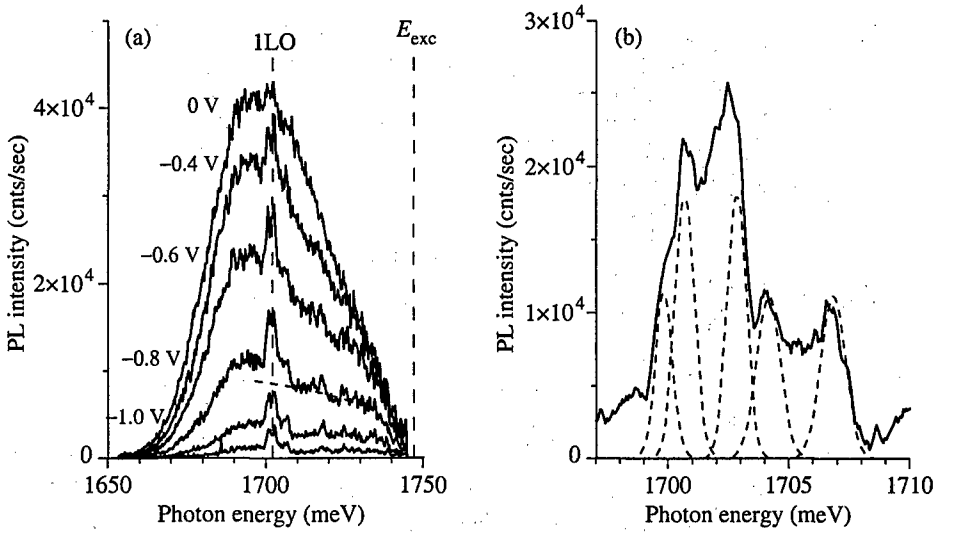

Fig. 1. (a) Dependence of the PL spectrum on the applied electric field. The excitation energy is 1747 meV. The positions of the excitation photon energy and the 1LO resonances are marked by the vertical dashed lines. (b) Part of the PL spectra around the 1LO resonance ($E_{exc} = 1747$ meV, $U_{bias} = -0.8$ V). A decomposition of the resonance into Gaussians is shown by the dotted lines. The signal was accumulated by the detection of the PL from the large illuminates sample area of about 0.03 mm^2. A background signal is substrated according the dashed line shown in the Fig. 1(a).

In Fig. 2(a) the dependence of the QDs PL spectra on the excitation photon energy E_{exc} is shown. The energy positions of the 1LO and 2LO resonances follow E_{exc}. Phonon energies determined by the Gaussian decomposition of the resonances do not depend on E_{exc}. The intensity of the resonances depends on their position with respect to the PL band. The integral intensity of the 1LO resonance has a spectral dependence that coincides very well with the PL spectrum (Fig. 2(b)). The 2LO resonance becomes weak when it goes out of the PL band.

2 Discussion

The presented experimental data strongly suggest that the observed resonances are caused by LO phonon mediated relaxation processes rather than by phonon sidebands of the resonant PL or by resonant Raman scattering. An applied bias leads to the suppression of the PL from the QDs due to the activation of various nonradiative processes.

The rates of these processes become comparable or higher than the phonon relaxation rates of the hot carriers under the increase of negative bias. It is known that a relaxation involving the LO phonons is faster than the acoustic phonons [2]. Therefore the PL in the region of the LO resonance is not suppressed so strong as in the region formed by the acoustic phonon relaxation.

For semiquantitative analysis we consider a simple model illustrated in Fig. 2. Due to small depth of the hole potential well in QDs [3] an applied bias activates a tunneling of the holes from the QDs into barrier layer. A tunneling rate exponentially depends on bias U in low rate limit: $\gamma_t = \gamma_t(\infty) \cdot e^{-U_0/U}$ [4].

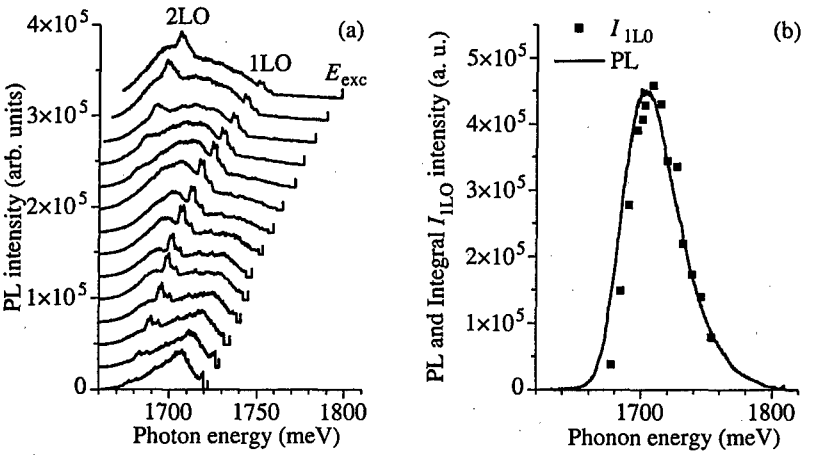

Fig. 2. (a) Dependence of the PL spectra on the excitation energy E_{exc}. $U_{bias} = -0.8$ V. (b) The spectral dependences of the QDs PL under high E_{exc} and zero bias (solid line) and the integral intensity I_{LO} of the 1LO resonance (solid squares).

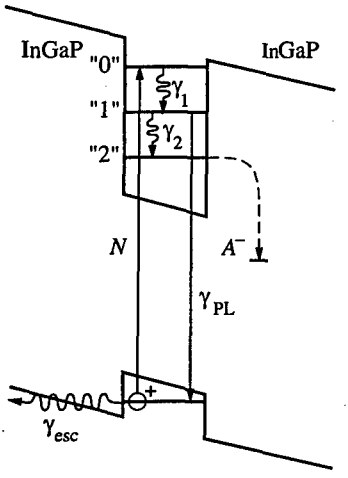

Fig. 3. A simplified model of the PL suppression in electric field.

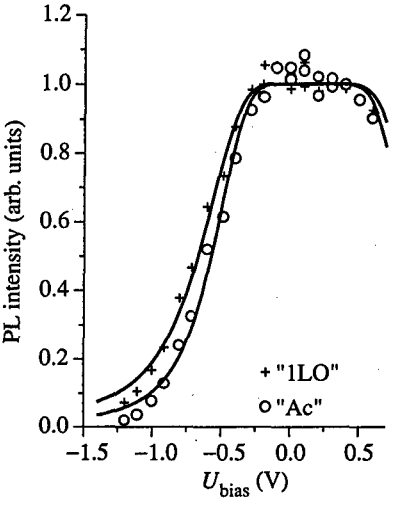

Fig. 4. The dependence of the normalized PL intensity I^*_{PL} on U_{bias} in the "1LO" and "Ac" spectral regions fitted by the expression (1).

An analysis shows that the PL suppression can be modelled as

$$I_{PL}(U) = \frac{I_{PL}(0)}{(1 + a \cdot e^{-U_0/U}) \cdot (1 + b \cdot e^{-U_0/U})}. \qquad (1)$$

Here a, b and U_0 are the fitting parameters. As an example, in Fig. 2 a normalized PL intensity $I^*_{PL} = \frac{I_{PL}(E,U)}{I_{PL}(E,0)}$ in dependence on U_{bias} is presented for two neighboring spectral

ranges $\Delta E = 35-38$ meV ("Ac" range) and $\Delta E = 44-47$ meV ("1LO" range) under the excitation photon energy $E_{exc} = 1747$ meV.

It is seen that the fitting reproduces well the general behavior of PL and its difference for "Ac" and "1LO" spectral ranges in spite of many simplifications used in the model. A good agreement between the experimental data and a fitting is observed also for the spectra recorded at the other E_{exc}.

A discovered phenomenon presents an interesting possibility to study the different resonances in the PL spectra. As is seen in Fig. 1(b), a PL spectrum in the region of the LO resonance is formed by the several peaks. According the data [5, 6], two lowest peaks with the energy distance from E_{exc}, $\Delta E = 41.0$ meV and $\Delta E = 43.7$ meV are maybe caused by the LO phonons of the InP QDs in Γ and **X** (or **L**) points of Brillouin zone. The former peaks at 45.3 meV, 47.2 meV and 48.0 meV are caused by the LO phonons of the InGaP surrounding material.

In the frame of the proposed attribution, an observation of the intensive peaks in PL spectra caused by the LO phonons of the InGaP layers is evidence a strong penetration of the electron (and maybe hole) wave functions into barrier layer.

3 Conclusion

Our experimental data show that the observation of LO resonances is in PL is possible if the quantum yield is not high. It is a good test of the optical quality of the structure. The study of the resonance structure gives useful information about the phonons in InP QDs and the surrounding material.

References

[1] R. Heitz, M. Veit, et al. *Phys. Rev. B* **56**, 10435 (1997).
[2] M. Vollmer, E. J. Mayer, W. W. Rulle, A. Kurtenbach and K. Eberl, *Phys. Rev. B* **54**, R17292 (1996).
[3] C. Pryor, M.-E. Pistol and L. Samuelson, *Phys. Rev. B* **56**, 10404 (1997).
[4] L. D. Landau and E. M. Lifshitz, *Quantum Mechanics*, 3rd edition, sec. 50 (Pergamon Press, 1977).
[5] A. Mooradian and G. B. Wright, *Solid Phys. Commun.* **4**, 431 (1966)
[6] A. Igelmund and A. Hausmann *Z. Phys B* **30**, 111 (1978).

7th Int. Symp. "Nanostructures: Physics and Technology"
St Petersburg, Russia, June 14–18, 1999

Temperature studies of single InP quantum dots

Valéry Zwiller, Mats-Erik Pistol, M. A. Odnoblyudov†‡ and Lars Samuelson
Solid State Physics, Lund University, Box 118, S-22100 Lund, Sweden
† Department of Theoretical Physics, Lund University, S-223 62, Lund, Sweden
‡ Ioffe Physico-Technical Institute, St Petersburg, Russia

In order to extract maximum information from photoluminescence studies of quantum dots, single dot studies have been performed. These studies do not suffer from fluctuations in the sizes of the dots or from variations in the environement of different quantum dots. We have performed experiments on single InP/GaInP quantum dots. The spectra always reveal several emission lines [1], no matter how much the excitation intensity is reduced, at least 4 or 5 irreducible lines are observed with an energy spacing of the order of 10 meV. The linewidth of the peaks is about 2 meV which is much larger than $k_B T$ at the experimental temperature of $T = 5$ K [1].

Information on the size and geometry of our self-assembled InP Quantum Dots grown on GaInP lattice matched to GaAs has been published elsewhere [2]. Atomic Force Microscopy (AFM) imaging of uncapped InP quantum dots shows a truncated pyramid shape with a characteristic elongation in the [110] direction [2, 3] (see Fig. 1), and is confirmed on capped samples by Transmission Electron Microscopy. AFM shows that most of the QDs are elongated in the [110] direction. The fully developped dots are typically 15 nm high and 60 by 40 nm at the base.

The sample was grown by Metal Organic Vapor Phase Epitaxy (MOVPE) at 580 °C. First, a 300 nm thick layer of GaInP was deposited on GaAs. The quantum dots were then produced by the deposition of 2.4 monolayers of InP, followed by a growth interupt of 12 seconds before the sample was capped by 300 nm of GaInP.

Experiments were performed to obtain the PL spectra of single quantum dots at various temperatures, from 5 K to 85 K. The sample was placed in a continuous flow helium cryostat. The average distance between the quantum dots was 10 microns which is more than the spatial resolution of the system (1 micron). In all measurements, the luminescence was collected using a 20x microscope objective. The excitation source was a frequency doubled Nd:YAG laser emitting at 532 nm. The emitted luminescence was dispersed by a 46 cm monochromator and was detected using a CCD camera, using typically 1 hour integration time. All the measurements presented here were made on single InP quantum

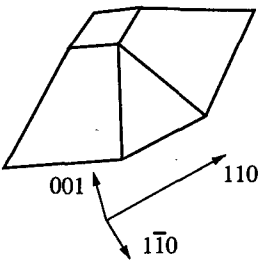

Fig. 1. Geometry of InP quantum dots. The dots are elongated in the [110] direction and have a typical height of 15 nm. The average base width is 40 nm and the average length is 55–65 nm.

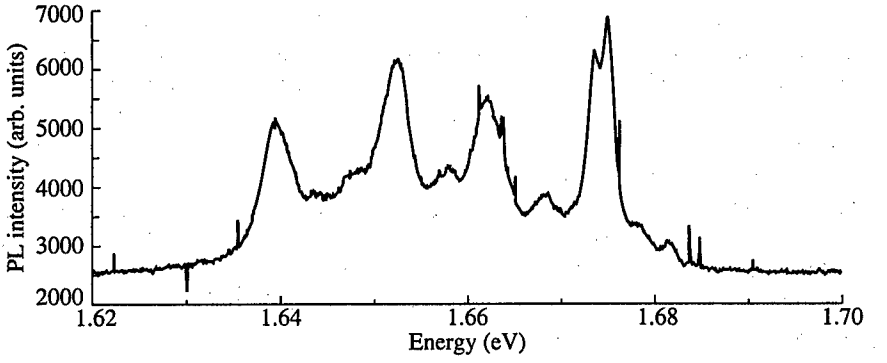

Fig. 2. A typical single dot spectrum, obtained at 5 K. Several peaks are visible, no matter how much the excitation intensity is reduced.

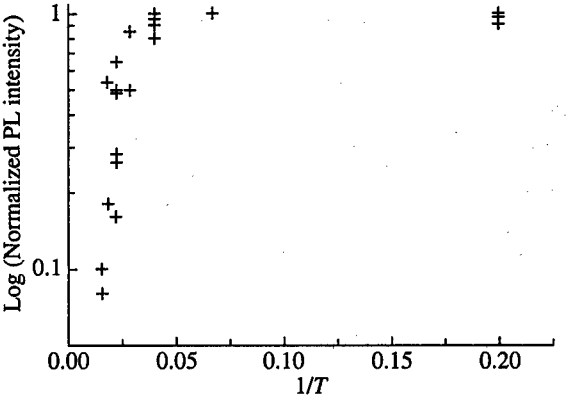

Fig. 3. Dependence of the photoluminescence emission intensity of a single InP quantum dot vs. temperature. Values were plotted for several emission lines.

dots. The excitation intensity was kept constant at about 0.1 W cm^{-2} while the temperature was increased in steps of 10 degrees.

Figure 2 shows a typical spectrum of an InP quantum dot obtained under low excitation intensity. The emission spans 40 meV and presents several peaks. With increasing temperature, all the lines are seen to decrease in intensity. This behavior has been observed to be the same in a dozen of dots.

Figure 3 is a plot of the intensity of different lines from different quantum dots measured at different temperatures. The log of the intensity is plotted against the inverse of the temperature. It is seen that all lines have a similar behavior and that an activation energy of about 1 meV can be deduced from these values.

Calculations of the energy levels for this type of quantum dots have been made, taking into account the strain and the piezoelectric field, using 6 bands **k.p** theory, within the envelope function approximation [4]. It was shown that the electrons are confined in the dot, while the holes states are localized at the base and at the top of the dot. The electron binding energy is about 210 meV [5] and the hole binding energy is about 120 meV. In the case of the valence band, the confinement is only due to strain[4]. In addition to these single particle binding energies, Coulomb attraction is expected to add a further 30 meV

to the exciton binding energy [6]. It can be expected that an increase in the temperature of the system will result in a decrease of the hole population, explaining the decrease of the photoluminescence intensity. However, the observed activation energy of temperature quenching would suggest a hole binding energy of about 1 meV, which is much lower than the binding energy due to the Coulomb attraction of the electron (i. e. assuming that the single-particle binding energy of the hole is zero). This shows that the activation energy is not due to thermal escape of the holes, and that some other mechanism is at work. Similar effects have been observed in quantum wells, and have been attributed to thermally activated non-radiative defects. This appears unlikely in this case since every dot would have to be associated with a defect. Possibly the interfaces, the edges or the corners of the dots may act as defects.

References

[1] D. Hessman, P. Castrillo, M.-E. Pistol, C. Pryor and L. Samuelson, *Appl. Phys. Lett.* **69**, 749 (1996).

[2] K. Georgsson, N. Carlsson, L. Samuelson, W. Seifert and L. R. Wallenberg, *Appl. Phys. Lett.* **67**, 2981-2 (1995).

[3] M.-E. Pistol, J.-O. Bovin, A. Carlsson, N. Carlsson, P. Castrillo, K. Georgsson, D. Hessman, T. Junno, L. Montelius, C. Persson, L. Samuelson, W. Seifert and L. R. Wallenberg, *23rd Int. Conf. on the Physics of Semiconductors* **2**, 1317-20 (1996).

[4] C. Pryor, M-E. Pistol and L. Samuelson, *Phys. Rev. B* **56**, 10404-10411 (1997).

[5] S. Anand, N. Carlsson, M.-E. Pistol, L. Samuelson and W. Seifert, *Appl. Phys. Lett.* **67**, 3016 (1995).

[6] C. Pryor, *Phys. Rev. B* **57**, 7190-7195 (1998).

7th Int. Symp. "Nanostructures: Physics and Technology"
St Petersburg, Russia, June 14–18, 1999

Stark shift of individual quantum dots

Mats-Erik Pistol, Dan Hessman, Craig Pryor and Lars Samuelson
Solid State Physics, Lund University, Box 118, S-22100 Lund, Sweden

Abstract. We have studied the influence of electric field on the emission properties of individual quantum dots of InP, inbetween barriers of GaInP. The emission shifts with applied electric field, due to the quantum confined Stark effect. We find that higher energy lines quench at high field. In addition a change in the linewidth of the emission is found for high electric fields.

Introduction

Optical investigations of semiconductor quantum dots has recently become an active area of research. In particular, the investigation of individual quantum dots has determined that the linewidth of the emission is very narrow in a variety of systems [1, 2]. Spectroscopy under different perturbations such as electric field [3] and magnetic field [4] for InAs quantum dots coherently embedded in GaAs have been performed. We will here describe the results of the influence of electric field on InP quantum dots embedded in GaInP, lattice matched to GaAs.

Experimental details

The sample we used was grown by metal-organic vapour phase epitaxy, and contained InP quantum dots in GaInP, lattice matched to GaAs (n-type). The dots are shaped like truncated pyramids, and have a typical height of 15 nm [6] Gold was evaporated on the surface to form a transparent Schottky contact. The emission was excited by a frequency-doubled YAG-laser emitting at 532 nm. A typical measurement temperature was 5 K. Since this was a low density sample, a microscope was used to separate the emission spectra from individual dots. The emission was excited by a frequency-doubled YAG-laser emitting at 532 nm. A typical measurement temperature was 5 K. An applied bias of 1 V corresponds to an open-circuit situation under illumination.

Results

Figure 1 shows emission spectra of one InP quantum dot as a function of applied bias. The peaks shift to higher energy with increasing electric field (which corresponds to decreasing applied bias). This is opposite to the conventional Stark shift in e.g. atoms which decrease the transition energies with increasing field. The quantum dots are however not symmetric in the z-direction (the growth direction) and there is thus no symmetry argument for a conventional sign of the Stark shift. At zero electric field, calculations show that the electron wavefunction is localised centrally in the quantum dots, whereas the hole wavefunction is localised mainly at the bottom of the pyramid [5]. For increasing electric field (pointing out of the substrate) the hole wavefunction will be localised more centrally in the pyramid, experiencing a higher potential. Another observation is that the higher energy peaks quench with increasing field. Similar behaviour has been observed for defects and was attributed to field assisted tunneling which is more effective for higher energy states. Although we

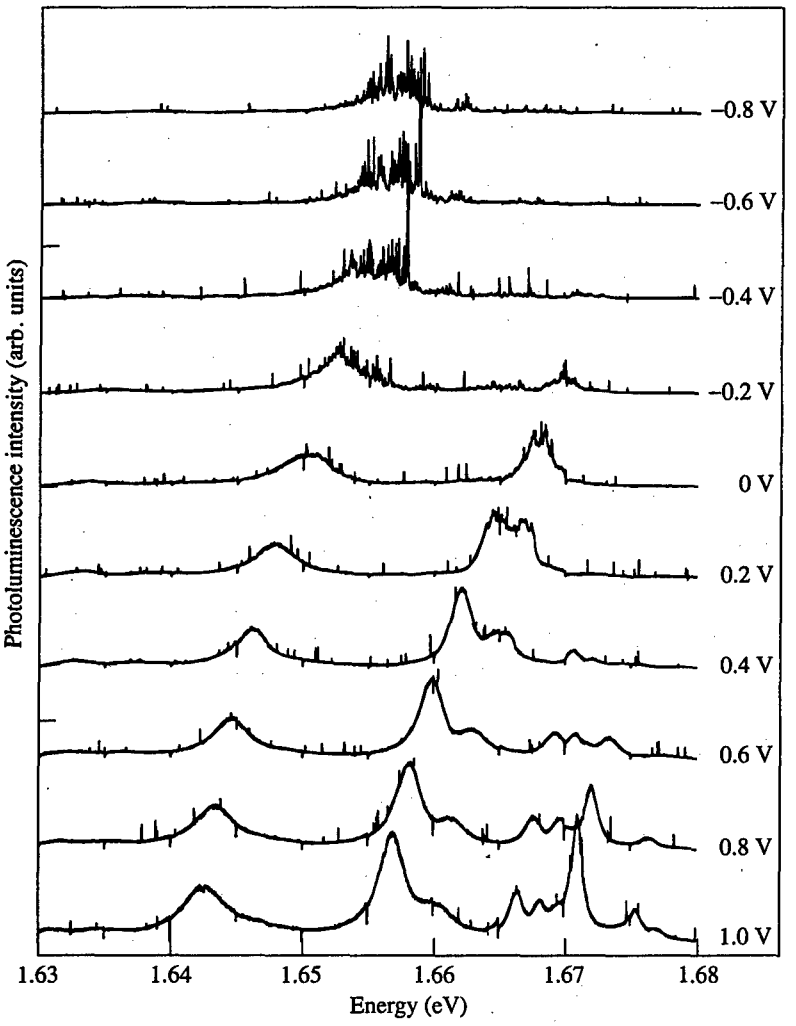

Fig. 1. Photoluminescence spectra of an InP quantum dot as a function of applied bias. The emission consists of several lines which show a Stark shift.

do not know the origin of the multiple lines, this observation supports an electronic origin. At the highest field, we observe that the originally quite broad lines split into sharp lines. We have calculated the carrier concentration in the sample as a function of electric field and illumination. We find that the carrier concentration decreases rapidly with increasing electric field, in particular for electrons. We attribute the broadening at zero electric field to interactions between carriers in the quantum dot and carriers in the wetting layer or the barrier. Similar phenomena have previously been observed in the InAs system [1].

We have calculated the transition energies as a function of the electric field. The model is an 8-band k.p model in conjunction with the envelope function approximation and includes a realistic shape of the dots, strain and piezoelectric polarisation. For electric fields however, we have introduced infinite barriers, in order to get bound states instead of resonances. In order to obtain the electric field, we solved the Poisson equation using a

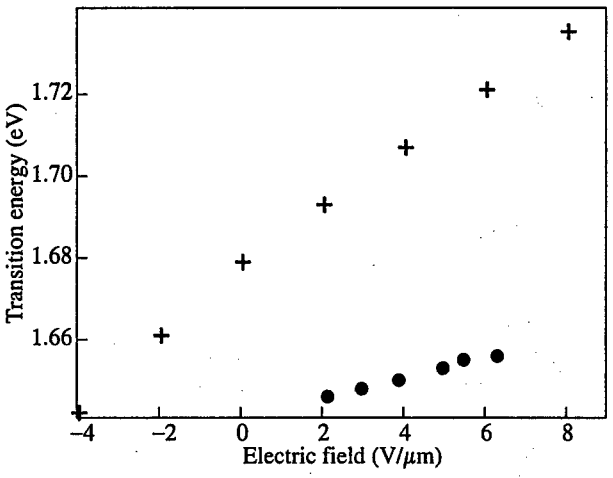

Fig. 2. Calculated (crosses) and measured (filled circles) transition energies as a function of electric field.

drift-diffusion model which also takes into account the photo-generated carriers. Figure 2 shows a comparison of the calculated and the experimental transition energies. We consider the agreement to be good and we attribute the remaining differences primarily to the difficulty of modelling the field correctly as well as to the use of infinite barriers in the calculation.

Acknowledgements

This work was performed within the Nanometer Structure Consortium in Lund and was supported by the National Swedish Science Foundation, the Technical Science Foundation and the Foundation for Strategic Research

References

[1] L. Landin, M. M. Miller, M.-E. Pistol, C. E. Pryor and L. Samuelson *Science* **280**, 262 (1998).
[2] D. Hessman, P. Castrillo, M. E. Pistol, C. Pryor and L. Sameulson, *Appl. Phys. Lett* **69**, 749 (1996).
[3] S. Raymond, J. P. Reynolds, J. L. Merz, S. Fafard, Y. Feng and S. Charbonneau, *Phys. Rev. B* **58**, 13415 (1998).
[4] M. Bayer, T. Gutbrod, A. Forchel, V. D. Kulakovskii, A. Gobunov, M. MIchel, R. Steffe and K. H. Wand, *Phys. Rev. B* **58**, 4740 (1998).
[5] C. E. Pryor, M.-E. Pistol and L. Samuelson, *Phys. Rev. B* **56**, 10404 (1997).
[6] K. Georgsson, N. Carlsson, L. Samuelson, W. Seifert and L. R. Wallenberg, *Appl. Phys. Lett* **67**, 2981 (1995).

7th Int. Symp. "Nanostructures: Physics and Technology"
St Petersburg, Russia, June 14–18, 1999

Optical and magnetic resonance investigations on Mn doped CdS nanocrystals

D. M. Hofmann†, A. Hofstaetter†, F. Henecker†, B. K. Meyer†,
N. G. Romanov‡, A. I. Ekimov‡, T. Gacoin#, G. Counio# and J. P. Biolot#
† 1. Physics Institute, University of Giessen, Heinrich-Buff-Ring 16,
D-35392 Giessen, Germany
‡ Ioffe Physico-Technical Institute, St Petersburg, Russia
# Laboratoire de Physique de la Matiere Condensee, CNRS UMR 7643,
Ecole Polytechnique, 91128 Palaiseau Cedex, France

Abstract. Mn doped CdS nanocrystals have been studied by electron paramagnetic resonance and optically detected magnetic resonance. It was found that Mn^{+2} which is located in the centre of the nanocrystals or on near surface positions create the large polarisation of the excitonic sublevels of the nanocrystals.

Introduction

The doping of sulfide nanocrystals with isoelectronic Mn has reached attention as it results in a bright yellow luminescence with quantum efficiencies of about 20% [1]. The emission originates from the $^4T_1 - ^6A_1$ crystal field transition of Mn^{2+} and peaks around 2.1 eV.

Electron paramagnetic resonance (EPR) is an appropriate tool to study the local environment of Mn^{2+} in the nanocrystals, i.e. to get information whether Mn^{2+} is located inside the nanocrystals, or near the surface, or is purely located in the matrix in which the nanocrystals are typically dispersed [2, 3]. A direct correlation to the optical properties of the nanocrystals can be obtained by optically detected magnetic resonance (ODMR). We will show that in an external magnetic field the absorption of the quantum confined states of the nanocrystals are polarised by the orientation of the spins of paramagnetic Mn^{2+} (electron spin 5/2). For low doping concentrations (one Mn per nanocrystal) ODMR shows Mn^{2+} located on tetrahedral sites in the CdS lattice (hyperfine splitting 6.9 mT). For higher Mn concentrations (three Mn per nanocrystal) Mn^{2+} which is located near the surface of the nanocrystals dominates the spectrum (hyperfine splitting 9.5 mT).

1 Experimental

The CdS:Mn nanocrystals were synthesised as follows. In a first step the precipitation of the particles is achieved in ethylene glycol by the simple mixing of one solution containing cadmium and manganese acetate and the other containing sodium sulfide. The cadmium concentration is constant to 0.1 mol/l, and the manganese concentration is varied from 0 to 0.4 mol/l. The sulfide concentration is stoichiometric. A turbid yellow-orange suspension is obtained, consisting of partially agglomerated crystallites. The solution is centrifuged and washed two times with methanol. The deagglomeration of the particles into a clear colloid is then obtained through a thermal treatment of the precipitate for 1 hour in triethylenephosphate at 215 °C. The disjunction of the particles occurs through the grafting of phosphate molecules at the surface of the particles. The obtained colloidal solution can

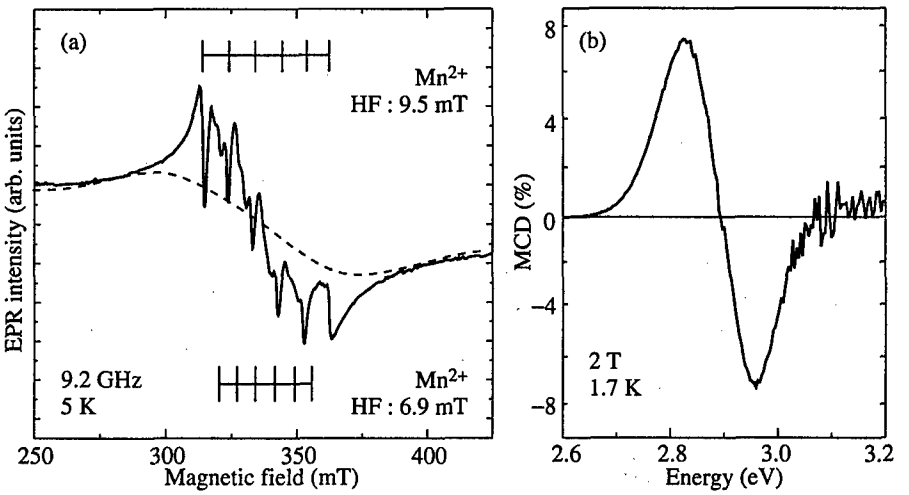

Fig. 1. (a) Electron paramagnetic resonance (EPR) spectrum of CdS nanocrystals doped with three Mn per nanocrystal. (b) Magnetic circular dichroism (MCD) of the excitonic absorption of CdS:Mn nanocrystals.

be destabilised upon the addition of heptane in excess. The flocculate is then washed two more times with heptane, and the resulting powder can be dispersed in methanol with high concentrations (> 1 mol/l).

Further incorporation of the particles in sol-gel silica matrices can be achieved using the process described in previous works [4, 5].

EPR experiments were performed on a commercial Bruker 300E spectrometer equipped with a Oxford ESR 900 flow cryostat. The setup for the optical detection of magnetic resonance (ODMR) consists of a Helium bath cryostat with a superconducting magnet. The maximum magnetic field is 4 T, the microwave frequency 24 GHz. The magnetic circular dichroism (MCD) of the absorption was detected by a photo-elastic modulator (50 kHz) in combination with a linear polarizer.

2 Results and discussion

Figure 1 shows a typical EPR spectrum of CdS nanocrystals doped with on average 3 Mn ions per quantum dot. The procedure to determine the Mn concentration is described in detail in Ref. [5]. The spectrum consists of three overlapping signals.
(a) A six line pattern of Mn^{2+} with a hyperfine splitting of 6.9 mT. This hyperfine splitting is typical for Mn^{2+} located on cation sites in tetrahedral semiconductors, thus it has been attributed to Mn^{2+} in or near the centre of the nanocrystals [2].
(b) A Mn^{2+} spectrum with a hyperfine splitting of about 9.5 mT. The increased hyperfine interaction is an indication for a reduced covalent bonding of Mn, which is likely to be the case for Mn located near the surface of the nanocrystals.
(c) A broad unresolved spectrum which arises from Mn-Mn dipolar interactions similar to heavily doped bulk materials, or Mn^{2+} located in an environment of varying crystal field strength, i.e. amorphous material, like the matrix in which the nanocrystals are embedded.
These three signals are always present in our samples, independent of the Mn doping concentration. But it should be noted that signal (a) is more intense compared to signal (b) for nanocrystals which are doped only with one Mn per nanocrystal.

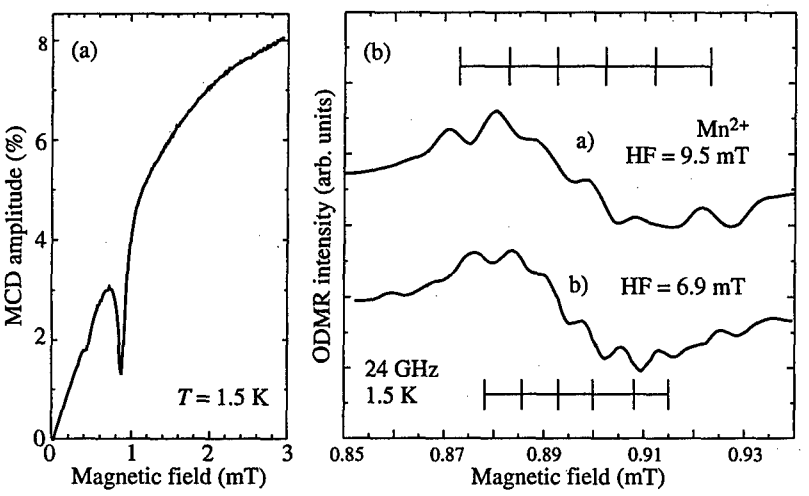

Fig. 2. (a) Optically detected magnetic resonance (ODMR) spectrum of CdS nanocrystals doped with Mn, detected on the excitonic MCD (24 GHz, 100 mW). (b) ODMR spectra measured with low microwave power (−30 dB) of CdS nanocrystals doped with three Mn (a) and one Mn (b) per nanocrystal.

The presence of Mn in the nanocrystals largely modifies its near bandgap magneto-optical absorption properties. A giant splitting of the exciton spin sublevels is observed which results in a MCD signal of several percent intensity [6]. The MCD has a derivative lineshape typical for excitonic transitions, Fig. 2. The centre position is at 2.9 eV indicating that the first transition of the quantum confined states of the nanocrystals is shifted about 500 meV to higher energies compared to the CdS bulk value. The energy position corresponds to an average diameter of the nanocrystals of 3.2 nm.

In order to prove that Mn^{2+} is responsible for this effect we performed ODMR experiments. The spectrum taken at high microwave powers (100 mW, 24 GHz) is shown in Fig. 3. The lineshape of the MCD as a function of the magnetic field follows a Brillouin function behaviour with $S = 5/2$. At the magnetic field position corresponding to $g \approx 2.0$ a strong resonance is observed reducing the MCD about 70%, at half field position an additional weaker resonance can be noticed, typical for high spin systems. To observe structure in the $g \approx 2.0$ resonance the microwave power has to be reduced considerably. Figure 4(a) shows the spectrum of the sample doped with three Mn per nanocrystal at −30 dB microwave power.

The structure of Mn^{2+} with the large hyperfine (HF) splitting of 9.5 mT is visible. For the sample doped with only one Mn per dot (Fig. 4(b)) we find Mn^{2+} with 6.9 mT hyperfine splitting, but also Mn^{2+} with HF = 9.5 mT is also present, however, in lower intensity. These results show directly that Mn^{2+} either located in the centre of the nanocrystals or near the surface create the large polarisation of the excitonic levels of the quantum dots.

Switching the microwave power on/off and monitoring the recovery of the MCD signals allows to get information on the spin lattice relaxation times. We found for both cases of high and low Mn doping that the spin lattice relaxation is faster than 10 ms, which is the time resolution of the experimental setup due to the Lock-In technique. However, the ODMR signal intensity is usually weaker in the highly doped samples which may indicate a faster

spin relaxation due to Mn-Mn interactions.

Acknowledgements

A. I. Ekimov would like to thank the Humboldt foundation for support. N. G. Romanov would like to thank the "Deutsche Forschungsgemeinschaft".

References

[1] R. N. Baragava, D. Gallaghter, X. Hong and A. Nurmiko, *Phys. Rev. Lett.* **72**, 416 (1994).
[2] T. A. Kennedy, E. R. Glaser, P. B. Klein and R. N. Bhargrava, *Phys. Rev. B* **52**, R14356 (1995).
[3] D. M. Hofmann, A. Hofstaetter, U. Leib, B. K. Meyer and G. Counio, *J. Cryst. Growth* **184/185**, 383 (1998).
[4] G. Counio, S. Esnouf, T. Gacoin and J.-P. Biolot, *J. Phys. Chem.* **100**, 20021 (1996).
[5] G. Counio, T. Gacoin and J. P. Biolot, *J. Phys. Chem. B* **102**, 5257 (1998).
[6] D. M. Hofmann, F. Leiter, B. K. Meyer, A. I. Ekimov, Al. Efros, M. Rosen, T. Gacoin, G. Counio and J. B. Biolot, submitted to Phys. Rev.

7th Int. Symp. "Nanostructures: Physics and Technology"
St Petersburg, Russia, June 14–18, 1999

A new type of surface waves on the open metallized nanowires

N. S. Averkiev, *S. O. Kognovitsky*, R. P. Seisyan and V. V. Travnikov
Ioffe Physico-Technical Institute, St Petersburg, Russia

Abstract. The present work is devoted to the investigation of light interaction with a grating array of metallized nanowires on a semiconductor surface. Specular reflection spectra of such structures for two orthogonal incident light polarizations have been studied as a function of geometrical parameters of structures. Very strong polarization contrast in some spectral intervals has been found. A specific type of "grating surface" waves has been proposed to explain the obtained results. The calculation of reflectivity spectra for TE and TM polarizations has been performed using the effective anisotropy layer model.

Introduction

Specific optical properties of periodical arrays of open metallized semiconductor nanowires are due to both the grating effect and peculiarities of light interaction with metals (for example the scattering on surface plasmon polaritons (SPP)). In particular, the specific "grating" electromagnetic waves may be excited. As follows from [1], one of such modes may be a hybrid combination of the sliding diffraction mode with waveguide modes localized at the grooves. SPPs on the surface of the deep sinusoidal metal grating may form standing waves with an essentially unhomogeneous distribution of the energy density across the grating groove direction [2]. In this work, it is shown that a specific "grating surface" electromagnetic wave (GSEMW) may propagate along the surface of the short-period lamellar grating and perpendicular to the wire direction. This wave is a coupling state of standing waves localized at deep grating grooves and surface electromagnetic waves of a plasmon type on the metal-air interface of wire tops.

1 Experiment

To investigate optical properties of wire arrays, the set of open metallized lamellar gratings was fabricated. Initial gratings were manufactured from a semi-insulating GaAs by the method of the reactive ion etching through the strip mask made with using the optical interference lithography. Then these semiconductor gratings were covered by an Au layer with the help of the thermal vacuum evaporation. Two values of the Au layer thicknesses were used. On the tops of wires and on the bottoms of intervals between wires, the Au layer thickness (d) was either $d \approx 60$ nm or $d \approx 25$ nm. The corresponding thickness (g) of Au on side (vertical) walls of wires was either $g \approx 25$ nm or $g \leq 15$ nm. The obtained gratings consisted of wires of almost rectangular cross-sections. The wire width was equal to about half of the grating period. The structures from the grating set are varied in period ($p = 250, 310, 370, 420$ nm), in depth ($h = 80, 200, 280$ nm) and in thickness of Au.

Spectra of the specular reflection from grating samples were measured in the wide range of wavelengths (400–1500 nm) at room temperature. Experiments were carried out at the strict normal incidence to sample surfaces of the collimated (0.5°) beam of the white light. The polarization of both incident and reflected beams was chosen either parallel (TE) or perpendicular (TM) to the wire direction. The obtained results are presented as spectral dependencies of the ratio between the reflectivity of TE polarized light (R_{TE}) and the reflectivity of TM polarized light (R_{TM}).

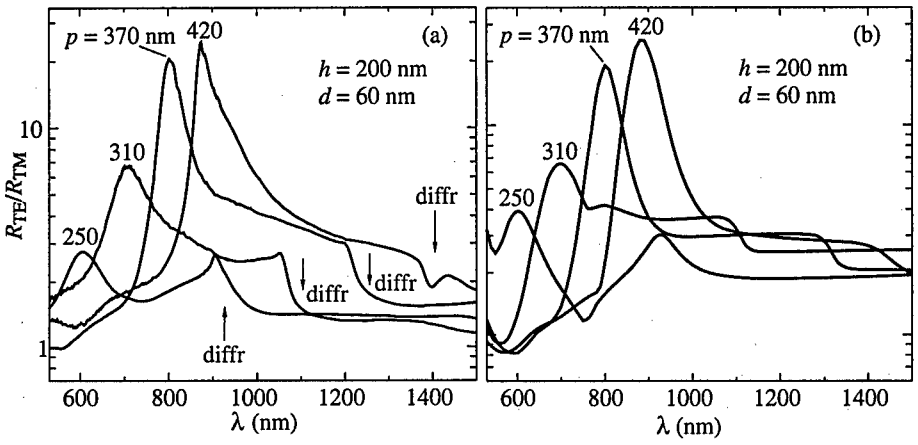

Fig. 1. The measured (a) and calculated (b) spectral dependence of the ratio between the reflectivities of TE and TM polarized light for structures with different grating periods.

The series of the strong maxima have been found in the polarization contrast spectra. The values of some maxima achieve 100 for the case of the deep grating (h = 200, 280 nm). For shallow gratings (h = 80 nm), these maxima are much smaller. Their spectral position does not depend practically on the wire height and thickness of the Au layer, but it strongly depends on the grating period (Fig. 1(a)). These maxima appear due to existence of corresponding minima in the reflection spectra for the perpendicular polarization (TM).

2 "Grating surface" electromagnetic waves

We have associated the origin of minima in TM reflection spectra with a leakage of a part of the intensity of the perpendicular polarized (TM) incident beam to the specific waves of a surface type named below as the "grating surface" electromagnetic waves (GSEMW). These waves propagate along the grating surface and perpendicular to the wire direction. GSEMWs are coupling states of surface electromagnetic waves of a plasmon type on the metal-air interface of wire tops and waveguide-type waves localized at deep grating grooves. The waves inside grooves are standing along the normal to the grating surface and polarized perpendicular to the wire direction. Propagation of GSEMW crosswise the wire direction is synchronized by the grating period so that longitudinal components of the wave electric field E inside adjacent air intervals between wires are oppositely oriented. Because of this, the surface wave period must be equal to two grating periods. This fact is in a good agreement with theoretical predictions that the waves of a surface type appear to exist on arrays of metallic wires in the range of incident light wavelength greater then two grating periods [3]. At normal light incidence, a standing superposition of GSEMWs is excited.

The short-period deep grating structure may display itself as an effective homogeneous anisotropic uniaxial medium with average optical parameters. The method of evaluation of effective refractive indexes of such medium was described in [4] and was used at studies of bulk wave reflection from surface gratings.

We have proposed to use the approach of effective medium for analysis of surface type waves. The well known dispersion dependence of a surface electromagnetic wave [5] may be applied to the surface wave which is localized on the interface between the effective

medium of grating and air. By this means, the wavelength of GSEMW may be estimated as:

$$\lambda_{\text{surf}} = 2\pi / Re\left(2\pi\sqrt{\varepsilon_{\text{eff}}/(\varepsilon_{\text{eff}}+1)}/\lambda\right), \tag{1}$$

where λ is the wavelength of the incident light in vacuum, ε_{eff} is the effective complex dielectric constant of grating top. For waves propagating across the wire direction, the ε_{eff} may be consisted with using "geometry averaging":

$$\varepsilon_{\text{eff}} = ((p-b)\varepsilon_{\text{air}} + b\varepsilon_{\text{Au}})/p, \tag{2}$$

where p is the grating period, b is the wire width, ε_{Au} is the complex dielectric constant of Au [6], ε_{air} is the air dielectric constant chosen equal to 1.

In according with the proposal model of GSEMW, the wavelength of this wave is equal to two grating periods: $\lambda_{\text{surf}} = 2p$. In this manner, the values of wavelengths of the incident light corresponding to the resonant excitation of GSEMWs may be found for all fabricated gratings from Eq. (2). These values coincide well with the spectral positions of main maxima in the experimental polarization contrast spectra ($R_{\text{TE}}/R_{\text{TM}}$). This points to the fact that these maxima are largely due to efficient interaction of GSEMWs with the incident light polarized perpendicular to the wire direction at the corresponding frequencies. This interaction plays a significant role in formation of polarization anisotropy of reflecting properties of metallized short-period deep gratings.

3 Analysis of the polarization anisotropy of reflectivity spectra

Besides excitation of GSEMWs, the polarization anisotropy of reflection is determined by other mechanisms like interference and diffraction. It is important to separate the contribution of GSEMW excitation. For this purpose, specular reflectivity spectra were calculated for cases of TE and TM polarized insident light (R_{TE} and R_{TM}) in the framework of the effective layers model [11].

Effective medium of the gratings is considered as consisting of three effective homogeneous anisotropic layers lying on the GaAs substrate. These layers are short-period gratings composed of: (1) Au tops of wires separated by air intervals, (2) GaAs wires with gilded walls also separated by air intervals, (3) Au wires lying on air interval bottoms and separated by GaAs. Each layer ($s = 1, 2, 3$) is described by two effective complex dielectric constants $\varepsilon_s^{\text{TE}}$ and $\varepsilon_s^{\text{TM}}$ for the light polarized parallel and perpendicular to the wire direction respectively:

$$\varepsilon_s^{\text{TE}} = [(p-b)\varepsilon_s^{\text{spl}} + (b-2g)\varepsilon_s^{\text{wire}} + 2g\varepsilon_{\text{Au}}]/p, \tag{3}$$

$$\varepsilon_s^{\text{TM}} = p/\left((p-b)/\varepsilon_s^{\text{spl}} + (b-2g)/\varepsilon_s^{\text{wire}} + 2g/\varepsilon_{\text{Au}}\right), \tag{4}$$

where $\varepsilon_1^{\text{wire}} = \varepsilon_{\text{Au}}$, $\varepsilon_{2,3}^{\text{wire}} = \varepsilon_{\text{GaAs}}$, $\varepsilon_{1,2}^{\text{spl}} = \varepsilon_{\text{air}}$, $\varepsilon_3^{\text{spl}} = \varepsilon_{\text{Au}}$.

The difference between $\varepsilon_s^{\text{TE}}$ and $\varepsilon_s^{\text{TM}}$ determines the polarization anisotropy of reflectivity of grating in a wide spectral range.

Reflectivity for each light polarization (R_{TE} and R_{TM}) has been calculated taking into account the reflections from four surfaces of effective anisotropic layers. Light interference between these surfaces influences strongly on reflectivity in the particular spectral range. This influence is found significantly different for TE and TM cases.

The contribution of the interaction of the light with GSEMWs into the formation of the polarization anisotropy may be described by the decrease of both the transmittance and the

reflectivity of the top boundary of the upper layer ($s = 1$) for the TM polarized light in the vicinity of GSEMW resonance excitation.

The diffraction has a large influence on the reflectivity spectra shape. The diffraction into the air is absent at the experimental geometry under study. But the diffraction into the substrate takes place in certain spectral ranges. This leads to a leakage of a part of incident light intensity to diffraction orders. In calculations of spectra this fact may be taken into account by the decrease of reflectivity from the bottom of the lowest effective layer ($s = 3$) of the structure when forming diffracting beams in the vicinity of this layer.

In this way the spectral dependence of the reflectivity ratio R_{TE}/R_{TM} has been calculated using real geometrical structure parameters and optical properties of structure materials. The set of the polarization contrast spectra obtained by this manner is shown in Fig. 1(b).

The comparison between experimental data and the calculations allows to clear the origin of several spectral features. The occurrence of long-wavelength spectral peculiarities in the range of the GaAs transparency (marked on the experimental spectra as "diffr") is determined by the light diffraction to the substrate. Short-wavelength minima in the polarization contrast spectra are largely due to the light interference.

4 Conclusion

A new type of the "grating surface" electromagnetic waves with wavelengths exceeding the grating period has been identified. We have suggested a new method of description of electromagnetic waves on the surface of short-period deep gratings using an effective medium model. This method is characterized by a simplicity and a versatility. A good agreement between experimental and calculated data has shown the significant role of the excitation of GSEMWs in the formation of reflection spectra from the structures with open metallized nanowires. The influence of interference and diffraction light on polarization anisotropy of reflectivity has determined.

The authors wish to thank Prof. V. A. Kosobukin for useful discussion and Dr. L. G. Rotkina for the important contribution to fabrication of investigated samples. One of the authors (R.P.S.) wishes to thank Professor A. A. Maradudin for interesting discussion.

References

[1] T. Lopez-Rios et al., *Phys. Rev. Lett.* **81**, 665 (1998).
[2] R. A. Watts, T. W. Preist and J. R. Sambles, *Phys. Rev. Lett.* **79**, 3978 (1997).
[3] V. P. Shestopalov et al., Diffraction of waves on grating, *Izd. Khar'kovskogo Universiteta*, Khar'kov, 1973, (in Russian).
[4] P. Yeh, *Optics Communications* **26 (3)**, 289 (1978).
[5] V. M. Agranovich, *Uspekhi Fizicheskikh Nauk* **115**, 199 (1975), (in Russian).
[6] P. B. Johnson and R. W. Christy, *Phys. Rev. B* **6**, 4370 (1972).

7th Int. Symp. "Nanostructures: Physics and Technology"
St Petersburg, Russia, June 14–18, 1999

Mechanisms of Auger recombination in semiconductor quantum wires

E. B. Dogonkine, A. S. Polkovnikov and G. G. Zegrya
Ioffe Physico-Technical Institute, St Petersburg, Russia

Abstract. The principal mechanisms of Auger recombination (AR) of nonequilibrium carriers in cylindrical quantum wires (QWRs) are investigated. It is shown that there exist two different Auger recombination mechanisms of (i) quasithreshold and (ii) thresholdless types. These mechanisms originate from the existence of barriers but have different nature. The quasithreshold mechanism is caused by confinement of carriers within the region of a quantum wire which makes the quasi-momentum conservation law approximate and enhances AR process. With increase of the wire radius this process turns to the threshold one. The thresholdless mechanism relates to the violation of the momentum conservation law at the heteroboundary and disappears with the radius tending to infinity.

Introduction

There are two main processes of Auger recombination (AR) in narrow gap semiconductors. The first of them corresponding to recombination of an electron and heavy hole and excitation of another electron is CHCC process. The second CHHS Auger process relates to the transition of a heavy hole to the spin-orbit split-off band. Contrary to bulk semiconductors, the transversal momentum component doesn't conserve in heterostructures thus allowing the thresholdless Auger process to appear [1, 2]. In [3, 4] it was shown that there are three types of AR processes in planar quantum wells (QWs): (i) threshold, (ii) quasithreshold (iii) thresholdless. It is shown that in QWRs there is a similar quasithreshold mechanism becoming 3D Auger process in the limit of a wire with the infinite radius. The AR mechanism of thresholdless type differs from those in a QW because there are two different channels (i) with transfer of a large linear momentum to the excited particle (like in planar QWs) and (ii) with transfer of an angular momentum (which is the only possible channel for quantum dots). These channels have different dependences on barrier heights in the conduction and valence bands.

1 Eigenstates of carriers in a quantum wire

Commonly the basis wave functions in the conduction and valence bands are taken in the form of eigenfunctions of the angular momentum but in the case of cylindrical symmetry it is natural to use another basis [5]:

$$|s\uparrow\rangle,\ |s\downarrow\rangle,\ |p_+\uparrow\rangle,\ |p_+\downarrow\rangle,\ |p_-\uparrow\rangle,\ |p_-\downarrow\rangle,\ |z\uparrow\rangle,\ |z\downarrow\rangle, \tag{1}$$

where $|p_+\rangle = 1/\sqrt{2}|(x+iy)\rangle$, $|p_-\rangle = 1/\sqrt{2}|(x-iy)\rangle$. This procedure excretes eigenfunctions having definite projections of linear and angular momenta on the wire axis. In this basis, dependences of wave functions on the z coordinat, where z-axis is parallel to the axis of the wire, and the axial angle take a simple form. For example the eigenstate in a

bulk semiconductor corresponding to the heavy hole is:

$$\begin{bmatrix} 0 \\ 0 \\ -2iq\,J_{m-3/2}(k\rho)\exp\left(i(m-3/2)\phi\right) \\ k_h\,J_{m-1/2}(k\rho)\exp\left(i(m-1/2)\phi\right) \\ 0 \\ -k_h\,J_{m+3/2}(k\rho)\exp\left(i(m+3/2)\phi\right) \\ \sqrt{2}k_h\,J_{m-1/2}(k\rho)\exp\left(i(m-1/2)\phi\right) \\ 0 \end{bmatrix} \exp(iqz) \tag{2}$$

(where J_m is Bessel function of the mth order). We derive boundary conditions from the continuity of the probability flux density and, following the method elaborated by Burt [6], from integrating Kane's equations across the heteroboundary that give continuity of the following functions:

$$\vec{\psi},\ \frac{d\psi_z}{d\rho},\ m_l^{-1}\mathrm{div}\vec{\psi} \tag{3}$$

where m_l is the mass of light hole in the case of zero constant of spin-orbit interaction [3, 4]. Contrary to situation in QWs [3, 4], the states with different parities cannot be separated even for heavy holes. Therefore, the dispersion equations become rather cumbersome. For example, the simplest one determining the ground state of heavy holes takes the form:

$$\begin{aligned} &\left(\frac{K_{-1}(\kappa_h R)}{J_{-1}(k_h R)} - \frac{K_1(\kappa_h R)}{J_1(k_h R)}\right)\left(\frac{K_2(\kappa_h R)}{J_2(k_h R)} - \frac{K_0(\kappa_h R)}{J_0(k_h R)}\right) \\ &\quad = \frac{4q^2}{\kappa_h^2 k_h^2}\left(k_h\frac{K_{-1}(\kappa_h R)}{J_{-1}(k_h R)} - \kappa_h\frac{K_0(\kappa_h R)}{J_0(k_h R)}\right)\left(k_h\frac{K_2(\kappa_h R)}{J_2(k_h R)} - \kappa_h\frac{K_1(\kappa_h R)}{J_1(k_h R)}\right), \end{aligned} \tag{4}$$

where k and κ are the transversal momentum components inside and outside the wire respectively, K_m is McDonald function of the mth order.

2 Matrix element of Auger recombination

The wave functions of carriers have conserved values of z-components of linear and angular momentum. Performing Fourier transform of Coulomb potential along ρ and ϕ coordinates we obtain:

$$\int_0^{2\pi} d\phi \int_{-\infty}^{\infty} dz \frac{e^{im\phi+iqz}}{|\vec{r}_1 - \vec{r}_2|} = \begin{cases} 4\pi I_m(q\rho_1)K_m(q\rho_2),\ \rho_1 \le \rho_2 \\ 4\pi K_m(q\rho_1)I_m(q\rho_2),\ \rho_1 > \rho_2 \end{cases} \tag{5}$$

(where I_m is the modified Bessel function of the mth order). Obviously, the matrix element of AR automatically yields conservation laws for the linear and angular momentum. We use the approximation $V_c, V_v \ll E_g$, where V_c and V_v are the barrier offsets in the conduction and valence bands, respectively. Procedures of evaluating the matrix element for CHCC and CHHS Auger processes are similar and only CHCC matrix element will be discussed further for the sake of simplicity. For the thresholdless AR process relating to the carrier scattering at the heteroboundary we obtain:

$$\begin{aligned} M^{(1)} = \frac{8\pi e^2}{\kappa_0(q^2+k_4^2)}\psi_{1s}(R)\psi_{4s}(R)\left\{qRK_{m-1}(qR)\left[\frac{3V_c+V_v}{4E_g}\right]\right. \\ \left. + mK_m(qR)\frac{3V_c}{4E_g}\right\}\int_0^R \psi_3^*(\rho)\psi_2(\rho)\rho d\rho. \end{aligned} \tag{6}$$

where both the discontinuity of the wave functions and their derivatives give contribution to this matrix element. The first term in the curly brackets, proportional to the linear momentum q, is similar to that existing in QWs. The second one, proportional to angular momentum m, is analogous to the thresholdless mechanism in quantum dots. For the quasithreshold process we have:

$$M^{(2)} = \frac{4\pi e^2}{\kappa_0(q^2+k_4^2)} \int_0^R \psi_4^*(\rho)\psi_3^*(\rho)\psi_2(\rho)\psi_1(\rho)\rho d\rho. \tag{7}$$

This matrix element, proportional to $\delta(k_4 - k_3)$ in the limit $R \to \infty$, turns to the threshold matrix element in a bulk semiconductor. More detailed analysis of matrix elements of thresholdless and quasithreshold types can be found in [7].

3 Rate of Auger recombination

To calculate the rate of AR in the first order of perturbation theory, the probabilities of transition should be averaged over all initial states of carriers with appropriate weight-occupation numbers and summed over all final states:

$$G = \frac{2\pi}{\hbar} \sum_{\mathbf{k}_1,\mathbf{k}_2,\mathbf{k}_3,\mathbf{k}_4} \langle M^2 \rangle f_1 f_2 (1-f_3)(1-f_4)\delta(E_3+E_4-E_1-E_2), \tag{8}$$

here f_1, f_2 are the occupancies of the initial states and f_3, f_4 are those of the final states, $\langle M^2 \rangle$ is the sum of squared Auger matrix elements over spins of the initial and final states. The expression for the rate of Auger process can be derived analytically from (8) but it is rather cumbersome. It is natural to use Auger recombination coefficient C given by:

$$G = Cn^2 p \quad \text{and} \quad G = Cp^2 n$$

for the CHCC and CHHS Auger processes, respectively, where n and p are the 1D densities of electrons and holes. Following [3, 4] we present the coefficient of AR in the form

$$C = C_1 + C_2, \tag{9}$$

where the coefficients C_1 and C_2 correspond to the thresholdless and quasi-threshold Auger processes with the matrix elements M_1 and M_2, respectively. For example, the thresholdless and quasithreshold coefficients for CHCC process are:

$$C_1 \approx \frac{24e^4}{\kappa_0^2}\frac{\hbar^3\gamma^4}{E_g^5}\frac{F(\Delta_{so}/E_g)}{R^5}\frac{k_c^2 J_0^4(k_c R)}{(J_0^2(k_c R)+J_1^2(k_c R)+K_0^2(\kappa_c R)+K_1^2(\kappa_c R))^2} \times \left\langle \left(\left[\frac{3V_c+V_v}{4E_g}\right]^2 + \frac{m^2}{q^2R^2}\left[\frac{3V_c}{4E_g}\right]^2 \right) \frac{k_h^2 q^2}{(q^2+k_4^2)^3 k_f(q)} \right\rangle, \tag{10}$$

$$C_2 \approx \frac{6e^4}{\kappa_0^2}\frac{\hbar^3\gamma^4}{E_g^5}\frac{F(\Delta_{so}/E_g)}{R^5}\frac{k_c^2 J_0^4(k_c R)}{(J_0^2(k_c R)+J_1^2(k_c R)+K_0^2(\kappa_c R)+K_1^2(\kappa_c R))^2} \times \left\langle \frac{k_h^2}{(q_h^2+k_h^2)k_f(q)}\frac{\sin^2(k_f-k_h)R}{(k_f(q)-k_h)^2} \right\rangle, \tag{11}$$

where

$$F(x) = \frac{(1+x/3)(1+x)}{(1+2x/3)(1+x/2)} \frac{1+7x/9+x^2/6}{(1+x/4+x^2/6)}\,, \quad k_f(q) = \sqrt{\frac{2E_g^2}{\hbar^2\gamma^2} \frac{1+\Delta_{so}/2E_g}{1+\Delta_{so}/3E_g} - q^2},$$

the angular brackets denote averaging over the heavy-hole distribution function and k_c is the transversal momentum component of the electron in the ground level.

4 Summary

Our analysis has shown that there exist two different AR mechanisms in semiconductor heterostructures with QWRs: thresholdless and quasithreshold. The thresholdless AR process has two channels. The first of them can be associated with the thresholdless AR process in QWs and the second one can with AR in quantum dots. It is shown that these channels have differrent dependences on barrier heights for electrons and holes in QWRs. The thresholdless coefficient tends to zero and the quasithreshold one becomes the 3D Auger process in the limit of a wire with infinite radius.

The authors would like to acknowledge the Russian Foundation for Basic Research (Grants 97-02-18151, 98-07-90336, 99-02-16796) and the Russian State Program: Physics of Solid State Nanostructures (Grants 97-1035 and 97-0003) for the support of this work.

References

[1] G. G. Zegrya and V. A. Kharchenko, *Sov. Phys. JETP* **74**, 173 (1992).
[2] M. I. Dyakonov and V. Yu. Kachorovskii, *Phys. Rev.* **B49**, 17130 (1994).
[3] G. G. Zegrya and A. S. Polkovnikov, *Zh. Exp. Teor. Fiz.* **113**, 1491 (1998) [*JETP* **86**, 815 (1998)].
[4] A. S. Polkovnikov and G. G. Zegrya, *Phys. Rev.* **B58**, 4039 (1998).
[5] P. C. Sercel and K. J. Vahala, *Phys. Rev.* **B42**, 3690
[6] M. G. Burt, *J. Phys.: Condens. Matter* **4**, 6651 (1992).
[7] E. B. Dogonkin, A. S. Polkovnikov, G. G. Zegrya, *JETP* to be published.

7th Int. Symp. "Nanostructures: Physics and Technology"
St Petersburg, Russia, June 14–18, 1999

"Unusual" temperature behavior of the photoluminescence of the InP and InGaAs quantum dots under quasiresonance excitation

V. Davydov†, *I. V. Ignatiev*†‡, I. E. Kozin†‡,
J.-S. Lee†, H.-W. Ren†, S. Sugou† and Y. Masumoto†¶
† Single Quantum Dot project, ERATO, JST, Japan
‡ Institute of Physics, St.-Petersburg State University, Russia
¶ Institute of Physics, University of Tsukuba, Japan

Abstract. A few "unusual" temperature effects are observed in the photoluminescence (PL) spectra and PL kinetics of heterostructures with self-assembled InP and InGaAs quantum dots (QDs) under the excitation within the PL band of QDs. It is found that the temperature rise leads to a *considerable increase* of the Stokes part of the PL. The analysis of this phenomenon and PL kinetics is based on the assumption about the slow relaxation of hot carriers.

Introduction

The usual method of PL excitation through the barrier interband transitions involves many relaxation processes for hot carriers. On the contrary, the excitation in the spectral region of the QD absorption creates the carriers inside QDs. Therefore, only a few relaxation processes occur prior to the radiative recombination of the electron-hole pairs. These processes can be studied in detail on different excitation conditions, at various temperatures, and under external electric field [1], etc.

In this paper we study the temperature dependences of the QDs PL and also its kinetics under the resonant excitation of QDs. They reveal a "strange" behavior—apparent increase of the PL intensity with increased temperature. This behavior can be explained only assuming a slow energy relaxation of the photogenerated carriers.

1 Experimental

Several samples with InP and $In_{0.5}Ga_{0.5}As$ QDs were studied. They all reveal very similar temperature behavior of the PL. Here we show only a few examples of the experimental data. The samples with the $In_{0.5}Ga_{0.5}As$ QDs (No 140, No 141, and No 153) were grown by the MOVPE method on the semiinsulating (100) GaAs substrate. The QD layer is sandwiched by undoped GaAs epitaxial layers. The QD areal density was $\rho_{QD} = 5 \times 10^9\,cm^{-2}$ for No 140, $10^{10}\,cm^{-2}$ for No 141 and $2\times^9\,cm^{-2}$ for No 153. The structure with the InP QDs was grown by means of MOVPE (sample QDPG0298, $\rho_{QD} = 3 \times 10^9\,cm^{-2}$) and GS MBE (sample QDP1779, $\rho_{QD} = 10^{10}\,cm^{-2}$) on n^+ (100) GaAs substrates.

The PL spectra were measured by using a cw Ti:sapphire laser, a double monochromator U1000, and a photon counting system with cooled GaAs and InGaAs photomultiplier tubes. The sample temperature was varied using the Oxford gas-flow optical cryostat ("Optistat") in the range of 5–280 K.

The PL kinetic was studied using a picosecond Ti:sapphire laser (pulse duration 5 ps), a double monochromator with zero dispersion (spectral resolution 0.5 nm), and a streak camera. The time resolution of the setup was about 20 ps.

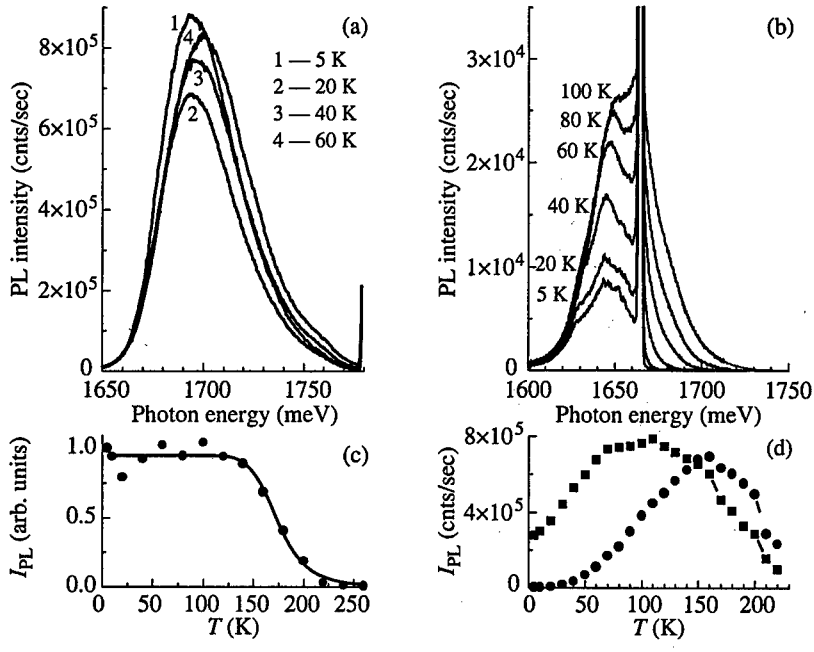

Fig. 1. General PL behavior of InP QDs at various temperatures. (a) PL under nonresonant excitation of $E_{exc} = 1784$ meV. (b) PL under resonant excitation of $E_{exc} = 1687$ meV. (c) $I_{PL}(T)$ under nonresonance excitation. Fitting by a model taking account of the activation energy type nonradiative process. (d) Dependence of integral Stokes (squares) and anti-Stokes (circle) PL intensity on temperature under resonance excitation.

2 Experimental results and analysis

The PL spectra of the sample QDPG0298 with InP QDs are shown in Fig. 1. Similar data for InGaAs QDs are presented in Fig. 2.

The main feature of the PL spectrum under resonance excitation at low temperature (Figs. 1(b) and 2(b)) is the presence of a dip between the laser line and the Stokes PL peak. This shows that the energy relaxation rate is small for small energy distance between levels in the QDs.

The temperature dependences of the integral PL intensity $I_{PL}(T)$ are different from each other for the nonresonance and resonance excitation (Fig. 1(c,d) and Fig. 2(b)). In the case of nonresonance excitation, a usual behavior with *decreasing* intensity at fairly high temperatures is observed. It can be explained by the process of thermostimulated quenching and described by the thermoactivation formula $I_{PL}(T) = I_{PL}(0)/[1 + a \cdot \exp(-\Delta E/kT)]$.

For the resonance excitation (Fig. 1(b,d) and Fig. 2(a)), *an increase* of the PL intensity is observed up to rather high temperatures. The integral intensity $I_{PL}(T)$ increases typically by 3–5 times for the most of the samples studied. We suppose that at low temperature a considerable fraction of the PL is resonant one and is covered by the exciting laser line. This is possible provided that the energy relaxation rate is comparable with or smaller than the radiative recombination rate. At elevated temperatures, the relaxation becomes faster due to the activation of the stimulated photon emission processes.

To prove this assumption, we have studied the time-resolved PL. The PL kinetics for the sample QDP1779 with the InP QDs are shown in Fig. 3. The PL intensity from a single

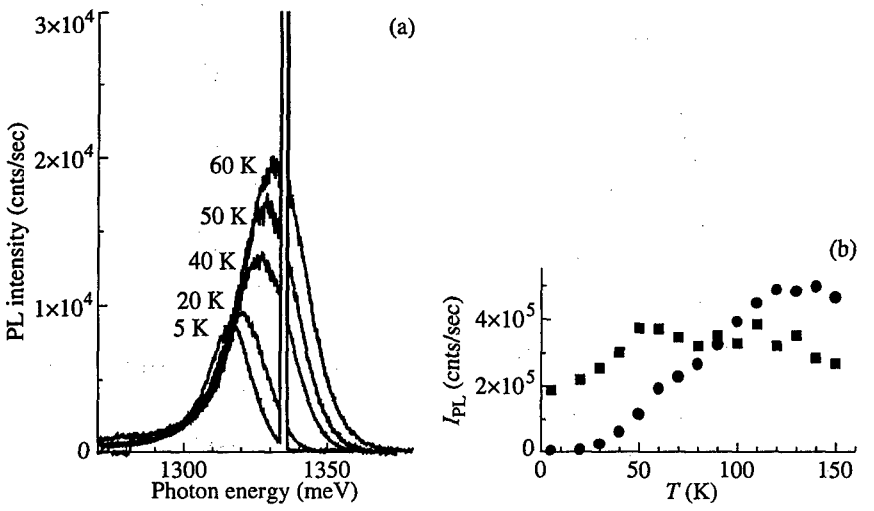

Fig. 2. General PL behavior with changing temperature for InGaAs QDs. (a) PL under resonant excitation $E_{exc} = 1334$ meV. (b) Dependence of integral Stokes and anti-Stokes PL intensity on temperature under resonance excitation ($E_{exc} = 1334$ meV).

layer of QDs is too weak compared with the background of the scattered laser light to detect directly the resonance PL. However, the spectral dependence of the kinetics reveals an increase of the decay time with increasing energy gap between the wavelengths of detection and excitation (Fig. 3(b)).

In our case, there is no grounds to anticipate energy transfer between the QDs, since the above effects are observed in structures with the areal densities of QDs varying by an order of magnitude. By this reason, the spectral diffusion can be related only to relaxation inside the QD.

As the temperature increases, the PL decay time τ becomes longer (Fig. 3(c)). This effect is usual for the system with continuous spectrum of energy states [2]. In the case of QDs, with a discrete spectrum of energy states, it can be explained by thermally activated population of nonradiative states. As the theoretical calculations [3, 4] show these states can be formed by the hole localization in small part of QDs. The temperature dependence $\tau(T)$ can be approximated in this case by the formula $\tau(T) = \tau(0)/(1 - ae^{-\Delta E/kT})$ which fits well the experimental data.

Under resonance excitation, increase of the temperature gives rise to the PL in the short-wavelength part of the spectrum above the exciting line (anti-Stokes PL, AS PL). Its behavior is rather different for the InP and InGaAs QDs and cannot be explained by taking into account only the Boltzmann statistics and the density of states extracted from the PLE spectra. We think that the AS PL profile is affected also by spectral distribution of the radiative recombination rate.

3 Conclusion

The above experimental data show that the behavior of the QDs ensemble is very similar in some aspects to behavior of a quantum-mechanical system with continuous energy spectrum. However, the physical origin of such a behavior has different nature and is related to slow relaxation of hot carriers, presumably due to their strong localization. There is no evidence for energy transfer between the QDs up to the temperatures when the PL

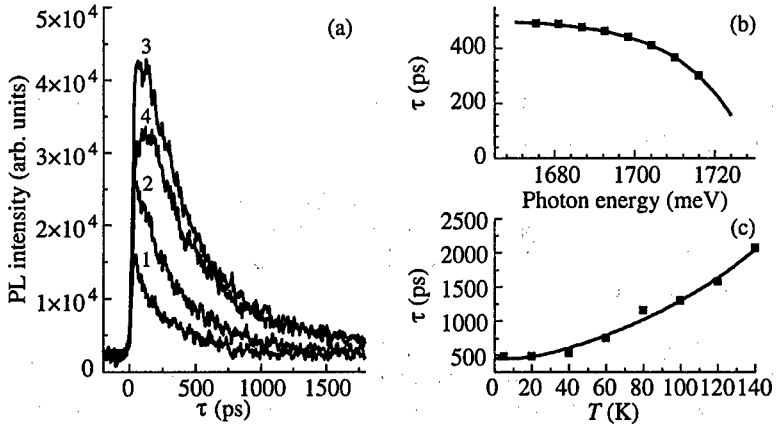

Fig. 3. (a) PL kinetics curve for the various detection energies. $E_{exc} = 1724$ meV, $E_{PL} = 1716.3$ meV for curve 1, 1710.3 meV—2, 1692.8 meV—3, 1681.4 meV—4. (b) Dependence of the τ on the detection energy at low temperature ($T = 5$ K). (c) Dependence of the τ of the PL at $E_{PL} = 1687.1$ meV on the temperature.

quenching starts.

References

[1] I. E. Kozin, I. V. Ignatiev, S. Nair, H.-W. Ren, S. Sugou and Y. Masumoto *This volume p. 24*
[2] J. Martinez-Pastor, A. Vinattieri et al., *Phys. Rev.* B **47**, 10455 (1993).
[3] C. Ulrich, S. Ves et al., *Phys. Rev. B* **52**, 12212 (1995).
[4] C. Pryor, M.-E. Pistol and L. Samuelson, *Phys. Rev. B* **56**, 10404 (1997).

7th Int. Symp. "Nanostructures: Physics and Technology"
St Petersburg, Russia, June 14–18, 1999

Effect of GaAs (001) surface misorientation on the emission from MBE grown InAs quantum dots

V. P. Evtikhiev, *I. V. Kudryashov*, E. Yu. Kotel'nikov, A. K. Kryganovskii, A. S. Shkolnik, A. N. Titkov and V. E. Tokranov
Ioffe Physico-Technical Institute, St Petersburg, Russia

Abstract. The photoluminescence (PL) is used to study the capped InAs QDs single sheet array MBE grown on the vicinal GaAs (001) surfaces misoriented to the [010] direction by 0, 2, 4, 6 degree. The misorientation leads to the blue shift and the narrowing of InAs QDs PL lines and makes PL efficiency higher. These effects are related, respectively, with the smaller size and higher size uniformity of the InAs QDs and reduction of the number of large InAs islands on the misoriented surfaces. It was found that decrease of the growth interruption time between the end of QDs growth and start of the GaAs layer overgrowth makes these modifications of the PL spectra with surface misorientation stronger and efficiency of the PL higher.
With the use of misoriented substrates, single sheet QDs laser with threshold current density of 210 A/cm^2 at room temperature was realized.

Introduction

Self-assembled quantum dots (QDs) arrays attract much attention due to the interest in their potential device applications [1-2]. However, to realize the high performance optical devices based upon QDs it is necessary to win the high size uniformity and high internal quantum efficiency of the QDs. Our preliminary AFM studies on the open InAs QDs arrays [3] have shown that it is possible to improve homogeneity and reach higher density of QDs growing them on the vicinal GaAs (001) surfaces misoriented to the [010] direction. This possibility originates from a specific patterning of the surfaces misoriented to the [010] direction. On such misoriented surfaces there appear multiatomic steps going to the [110] and [$\bar{1}$10] directions.

In that work we studied the photoluminescence (PL) of the capped InAs QDs single sheet array MBE grown on the vicinal GaAs (001) surfaces misoriented to the [010] direction.

1 Experimental procedure

The two sets of samples were grown by molecular beam epitaxy (MBE) in Stransky–Krastanow growth mode. Each set of samples consists of four samples, which were prepared via simultaneous InAs QDs single sheet array growth on four GaAs substrates misoriented by 0, 2, 4 and 6 degrees to the [010] direction. Two sets of samples differ only by the interruption time (T_{int}) between the end of QDs growth and start of the GaAs layer overgrowth. For the first set $T_{\text{int}} = 15$ min and for the second one $T_{\text{int}} = 10$ s. The thickness of the InAs deposition was 2.9 ML. The growth temperature of InAs QDs was 470°C and the III–V elements flux ratio was equal 2. In the grown heterostructures the InAs QDs single sheet array was confined by GaAs barriers (200 Å) which were surrounded by the AlAs/GaAs superlatticies and cladding $Al_{0.7}Ga_{0.3}As$ layers.

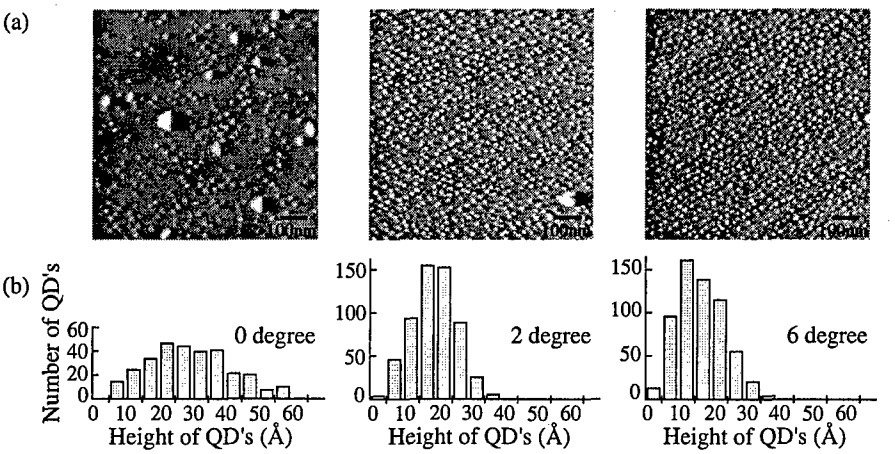

Fig. 1. (a) AFM images of the open InAs QDs arrays on the GaAs surfaces misoriented to the [010] direction by 0, 2 and 6 degrees. (b) the dependence of the InAs QDs height distributions on the angle of misorientation.

2 Results and discussions

In the Fig. 1(a) we show atomic force microscopy (AFM) images of the open InAs QDs arrays on the GaAs surfaces misoriented to the [010] direction by 0, 2 and 6 degrees. Fig. 1(b) presents the dependence of the InAs QDs height distributions on the angle of misorientation. It is clearly seen that misorientation of the GaAs substrate already on small angles results in the reduction of the number of large InAs islands on the surface and leads to higher density and better size uniformity of InAs QDs. Simultaneously, QDs become smaller.

In the Fig. 2 we present the PL spectra for capped InAs QDs. The position of the PL line maximum and the full width on the height middle (FWHM) of the PL lines versus angle of misorientation are shown in the Fig. 3. For both the series of spectra the misorientation of the substrate leads to blue shift of the maximum and decrease of the FWHM of PL lines. These effects can be naturally explained by the decrease of the sizes and better size uniformity for the InAs QDs on the misoriented surfaces what was revealed for the open QDs arrays in Fig. 1. It is important to note that the observed effects depend on the growth interruption time Tint and are less pronounced in the samples for which T_{int} was longer. The last observation directly demonstrates an importance of the kinetic processes on the surface in the formation of the InAs QDs.

Let us remind that on the exactly oriented GaAs(001) surface adatom diffusion at the chosen growth conditions is fast. At the same time on the misoriented surfaces patterned with the dense net of terraces, adatom surface diffusion between terraces should be much slower, since adatom migration between terraces occurs mainly through the gateways connecting terraces [4]. The increase of the misorientation angle makes terraces and gates smaller and causes progressive suppression of the adatom migration. In this connection, the effect of interruption time on the PL spectra should be small for exactly oriented surfaces and became stronger on the misoriented surfaces. However, with the further increase of the misorientation angle it again should become weaker. This behaviour has been found experimentally. The comparison of the data in Fig. 3 shows that effect of the growth interruption time is stronger for sample with 2 degree misorientation.

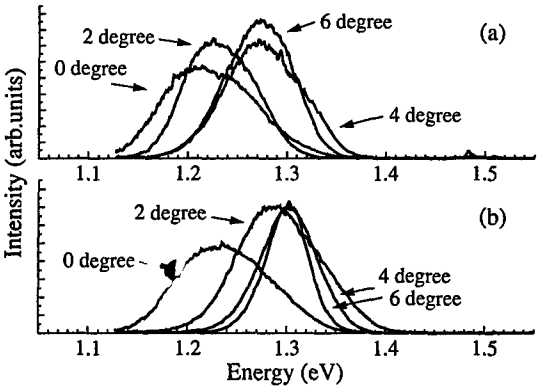

Fig. 2. The PL spectra recorded at $T = 77$ K for the samples with the growth interruption time $T_{int} = 15$ min (a) and $T_{int} = 10$ s (b).

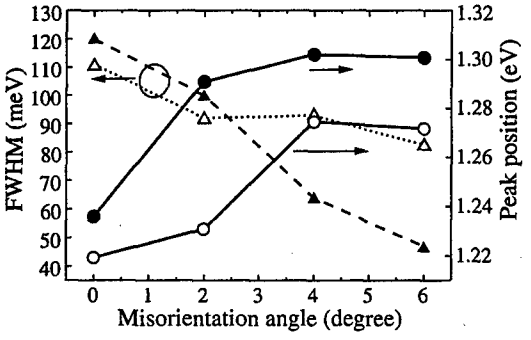

Fig. 3. The position of the PL line maximum (full circles for the samples with the growth interruption time $T_{int} = 15$ min, open circles for $T_{int} = 10$ s) and FWHM of the PL line (full triangles for the samples with the growth interruption time $T_{int} = 15$ min, open triangles for $T_{int} = 10$ s).

So, we imply that QDs formation on the misoriented surface comprise two main stages with different characteristic times. First process is very quick. The self-assembled QDs array with high density and high uniformity appear on this stage. On the second, much longer stage QDs increase in sizes due to QDs interactions. This interaction occurs via surface migration of adatoms between QDs. The changes in the QDs morphology on this second growth stage determine variations in the position and width of the QDs PL lines for samples grown with longer interruption time. So, the misorientation creates a new, much slower time scale for this stage of the QDs formation because of the suppression of the adatom migration between terraces on the misoriented surfaces.

The suppression of the adatom migration on the misoriented surfaces also allows essentially decrease the density of the large InAs islands. These large islands contain dislocations and usually are considered as efficient centres of nonradiative recombination.

The application of the GaAs(001) substrates misoriented to the [010] direction permits to win the better uniformity and higher density of QDs arrays with high internal quantum efficiency. We successfully used such substrates for the fabrication of laser heterostructures with a single sheet QDs array. Obtained for such laser structures good internal quantum efficiency and FWHM values of 40 meV permitted to realise classical QDs laser with low threshold current density [5]. The broad area (100 μm) lasers with high reflecting mirror

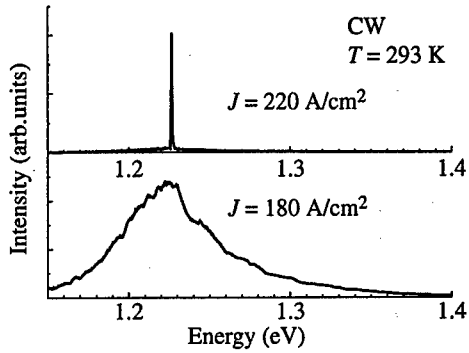

Fig. 4. The electroluminescence and lasing spectra for the broad area (100 μm) lasers with high reflecting mirror coating mode from 4 degree misoriented substrate.

coating made from 4 degree misoriented substrate show the threshold current density of 210 A/cm^2 at room temperature. The electroluminescence and lasing spectra of such laser are presented in Fig. 4.

3 Conclusion

We have found that misorientation of GaAs(001) substrates to the [010] direction leads to the blue shift and the narrowing of the InAs QDs PL lines. The observed effects are related with the decrease of sizes and better size uniformity of the InAs QDs grown on such substrates. The modifications in the InAs QDs morphology arise due to the suppression of the adatom diffusion on the misoriented GaAs surface and become stronger with the increase of misorientation angle and the decrease of the MBE growth interruption time T_{int}. The substrate misorientation gives also a new, much slower, time scale for the QDs redistribution by sizes and makes weaker the QDs coalescence process. High quantum efficiency can be reached for QDs grown on the misoriented substrates.

We successfully used the MBE growth of the InAs QDs on the GaAs (001) substrates misoriented to the [010] direction for fabrication of classical QDs laser diodes. The low threshold current densities were achieved for the broad area laser diodes.

Work has been supported by the Russian Foundation for Basic Research and the Program of Ministry of Science of RF "Physics of solid-states nanostructures".

References

[1] Y. Arakawa and H. Sakaki, *Appl. Phys. Lett.* **40** 939 (1982).
[2] L. V. Asryan and R. A. Suris, *Semicond. Sci. Techn.* **11** 554 (1996).
[3] V. P. Evtikhiev, A. K. Kryganovskii, A. B. Komissarov, A. N. Titkov, M. Ichida and A. Nakamura. *Inst. Phys. Conf. Ser.* **155** 351 (1996).
[4] V. P. Evtikhiev, V. E. Tokranov, A. K. Kryzhanovski, A. M. Boiko, R. A. Suris, A. N. Titkov, A. Nakamura and M. Ichida. *Semicond.* **32** 765 (1998).
[5] V. P. Evtikhiev, I. V. Kudryashov, E. Yu. Kotel'nikov, V. E. Tokranov, A. N. Tarasov and Zh. I. Alferov. *Semicond.* **32** 1323 (1998).

7th Int. Symp. "Nanostructures: Physics and Technology"
St Petersburg, Russia, June 14–18, 1999

Cold anti-Stokes photoluminescence of InP self-assembled quantum dots in the presence of electric current

H.-W. Ren†, S. Sugou†, Y. Masumoto†, *I. Ignatiev*†‡ and I. Kozin†‡
† Single Quantum Dot project, ERATO, JST, Japan
‡ Institute of Physics, St.-Petersburg State University, Russia

Abstract. An intense anti-Stokes photoluminescence is observed in a structure with InP quantum dots in the presence of a direct electric current and cw optical pumping below the lowest electron hole transition in the quantum dots. A simple model is proposed for the explanation of the observed phenomenon. Its essential point is the existence of deep level defects around the QDs.

Introduction

A cold anti-Stokes photoluminescence (AS PL) has been observed in various semiconductor heterostructures [1–5]. Usualy Auger and two-step excitation mechanisms are discussed to be responsible for this effect. On the other hand, there is a well known electroluminescence (EL) effect which occurs when an electric current flows through a specially designed heterostructure like laser diode. In the present work, we show that in structures with InP quantum dots (QDs) it is possible to observe a strong AS PL at low temperature when the optical pumping and electric current are applied to the structure simultaneously. There is no AS PL if one of the actions is absent.

1 Experimental

We studied the heterostructure schematically drawn in the inset of the Fig. 1(a). It was grown by gas source molecular beam epitaxy on a n^+ GaAs substrate. The QDs were formed by the deposition of InP on the InGaP layer and covered by the top InGaP layer. The areal density of QDs is about 10^{10} cm^{-2}. The average base diameter is $\approx$ 50 nm and the height is $\approx$ 10 nm. The studied sample was supplied with a semitransparent gold Shottky contact on the top surface and an ohmic contact on the back surface.

The PL and PL excitation (PLE) spectra were recorded by using the setup including a double monochromator U1000, a cw Ti:sapphire laser and a photon counting system with a cooled GaAs photomultiplier tube. All the measurements were done at the sample temperature of 5 K.

2 Experimental results

In Fig. 1(a) the PL spectra of InP QDs are shown. They were recorded at resonant (a) and nonresonant (b) laser excitation with constant intensity and different electric currents I in the range of 0–1000 μA/mm^2. It is found that under positive $U_{\text{bias}} > 0.7$ V ("+" on the top of the sample) the electric current through the sample increases rapidly. AS PL appears synchronously with the electric current and its intensity also increases rapidly with the bias. At $I = 1000$ μA/mm^2, the integral intensity of AS PL under resonant excitation (Fig. 1(a)) exceeds that of the Stokes PL without the electric current. This means that the observed

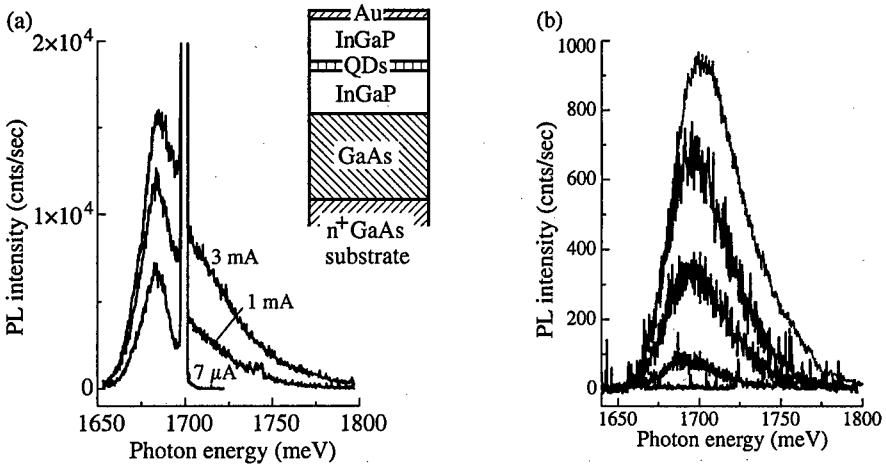

Fig. 1. (a) Stokes and anti-Stokes PL of InP QDs under resonant excitation in the presence of an electric current through the heterostructure (excitation photon energy $E_{exc} = 1700$ meV and excitation power $P_{exc} = 100$ W/cm^2). Inset: A simplified structure of the studied sample. (b) AS PL at the low energy excitation ($E_{exc} = 1494$ meV, $P_{exc} = 500$ W/cm^2) under different electric currents trough the sample (from the bottom to the top: 130 μA, 290 μA, 1030 μA, and 3300 μA). The sample area is $S = 3$ mm^2. The Stokes PL spectrum of QDs under the high photon energy excitation ($E_{exc} = 1800$ meV) is shown by a dotted line for comparison.

effect is very strong. Under negative bias, the AS PL is not observed and the Stokes PL decreases [6].

AS PL is observed under the optical excitation with photon energy E_{exc} much lower than the energy of photons emitted by QDs. The PL excitation (PLE) spectrum of the sample is shown in Fig. 2. It should be stressed that AS PL is observable under excitation in the whole transparent region of the sample (including GaAs). Moreover there are no features in PLE spectrum at the GaAs exciton position pointed by the vertical bar in Fig. 2.

3 Analysis

The experimental data presented above can be explained in the following simple model shown schematically in Fig. 3. We suppose that there are a number of deep defect levels around the QDs. The first hint on the existence of the deep levels was found by the observation of Franz–Keldysh oscillations in such kind of structures [7]. Laser light produces transitions between the valence band of the InGaP barrier and defect levels and creates holes which fall into the QDs. The electric current supplies the QDs with electrons. Their recombination with photocreated holes produces AS PL.

There are some features in this model. In steady state conditions we should suppose a presence of an optical transition between the deep levels and the conduction band levels of InGaP (shown by the dashed arrow in Fig. 3) to avoid an accumulation of electrons in the deep level centers. In this sence, AS PL is produced by a two step optical excitation and the electric current. But experimental data shows that the intensity of AS PL is roughly proportional to the optical pump power density ranging from 100 to 1000 W/cm^2.

AS PL also depends roughly linearly on the electric current ranging from 50 to 1000 μA/mm^2. Assuming the efficiency of the electron capturing process by QDs to

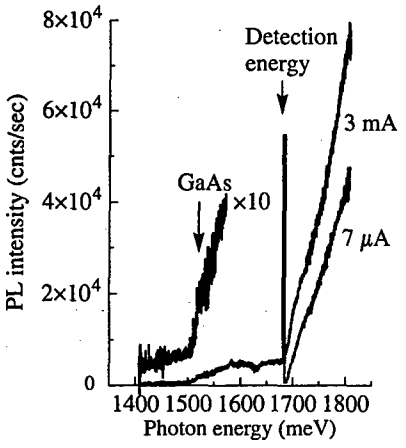

Fig. 2. The PLE spectra of the InP QDs under weak and strong electric currents through the sample. The vertical bar shows the energy position of the GaAs exciton.

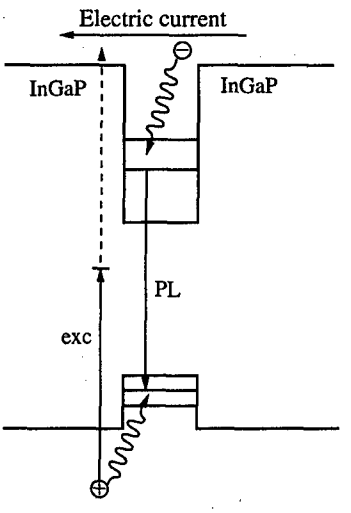

Fig. 3. A simplified model of the processes involved in the observed phenomenon.

be equal to the area of QDs divided by that of the sample we can estimate the number of captured electrons per second per dot to be $n_e = 6 \times 10^6$ for $I = 100\ \mu A/mm^2$. This value of n indicates that the nonradiative channel for electron relaxation is very slow. The nonradiative channel for holes is also slow, because the light excitation intensity of 100 W/cm^2 corresponds to 4×10^6 photons per second per dot. Taking also into account the rather high quantum efficiency of the PL from QDs [6], we can assume that the deep centers are located in the barrier layer, outside the QDs, but close to the QDs layer.

The observation of the AS PL signal in a wide spectral region of excitation (Fig. 3) can be explained by the broad energy distribution of the initial states for optical pumping belonging to the valence band of InGaP. Therefore we cannot say anything about the energy distribution of the deep level states.

Under resonance excitation, a strong increase of the Stokes PL at positive bias is observed. This effect is very similar with the temperature increase of the PL observed by us [8]. We think that under resonant excitation a considerable fraction of the PL is a resonant PL hidden by the scattered laser line if there is no electric current. Under applied bias, the electrons supplied by electric current accelerate the relaxation processes due to electron-electron collisions. As a result, a resonant PL is transformed in nonresonant one that causes an increasing of the nonresonant PL.

4 Conclusion

The study performed shows that in structures with InP QDs between InGaP barrier layers, there are defects with deep levels which are located around the QDs. Optical transitions from the InGaP valence band states to the deep levels create the holes which are captured by the QDs. The holes recombine with electrons supplied by the electric current. This process is observable as AS PL. The discovered phenomenon shows that the optical property of InP QDs are essentially affected by the defects in the QDs layer even in high quality structures.

The nature of these deep levels is unknown and further study is needed.

References

[1] W. Seidel, A. Titkov, J. P. Andre, P. Voisin and M. Voos, *Phys. Rev. Lett.* **73**, 2356 (1994).
[2] R. Hellmann, A. Euteneuer A, et al. *Phys. Rev. B* **51**, 18053 (1995).
[3] F. A. J. M. Driessen, H. M. Cheong et al. *Phys. Rev. B* **54**, R5263 (1996).
[4] J. Zeman, G. Martinez, P. Y. Yu and K. Ushida, *Phys. Rev. B* **55**, R13428 (1997).
[5] Cho Yong-Hoon, D. S. Kim et al. *Phys. Rev. B* **56**, R4375 (1997).
[6] I. E. Kozin, I. V. Ignatiev, S. Nair, H.-W. Ren, S. Sugou and Y. Masumoto *This volume p. 24.*
[7] Y. Masumoto, V. Davydov, I. Ignatiev, H.-W. Ren and S. Sugou, *Jpn. J. Appl. Phys.* **38**, 2290 (1999).
[8] V. Davydov, I. V. Ignatiev, I. E. Kozin, J.-S. Lee, H.-W. Ren, S. Sugou, Y. Masumoto *This volume p. 46.*

7th Int. Symp. "Nanostructures: Physics and Technology"
St Petersburg, Russia, June 14–18, 1999

Photoluminescence of InAs/GaAs quantum dots in the presence of subband 1.06 μm excitation

D. A. Mazurenko†‡, A. V. Scherbakov†, A. V. Akimov†, D. L. Fedorov‡, A. J. Kent§ and M. Henini§

† Ioffe Physico-Technical Institute, St Petersburg, Russia

‡ Baltic State Technical University, St Petersburg 198005, Russia

§ Physics Department, Nottingham University, Nottingham NG7 2RD, UK

Optical properties of InAs/GaAs self-assembled quantum dots (QDs) have been intensively studied during last several years which is mainly due to the promising applications of QD's structures as lasers with low threshold current [1]. Most of the experiments in this field are aimed on the studies of the electron-hole radiative recombination in QDs. However it is obvious that there exist non-radiative recombination channels which limit a quantum efficiency of QD's photoluminescence (PL) and thus increase a threshold for lasing. Apparently, these nonradiative processes are connected with the defects which are formed during the growth of QDs [1, 2]. In PL experiments these defects play a role of traps for photoexcited electrons and holes and thus decrease the number of carriers which recombine radiatively in QDs. A lifetime of the carrier trapped to the defect may be very long and, in principle, it becomes possible to release a trapped carrier by means of subband ($\hbar\omega_1 < E_g$, E_g — the band gap of InAs QD) optical excitation and thus to increase the PL quantum efficiency. The enhancement of quantum efficiency induced by the subband excitation was demonstrated earlier in epitaxially grown bulk GaAs [3]. In QDs such experiments were not carried out to our knowledge.

Here we present the first studies of the effect of additional subband excitation $\hbar\omega_1 = 1.17$ eV ($\lambda = 1.06$ μm) on the PL of self-assembled InAs/GaAs QDs. We experimentally observe that PL intensity increases in the present of subband $\hbar\omega_1$ excitation and the relative increase up to 40% is obtained. We study the dependence of the relative increase of PL intensity on the density of $\hbar\omega_1$ excitation and observe the saturation of the relative increase of PL intensity at high power of subband light. The qualitative analysis of the experimental results is based on the model of photoionization of deep traps as a result of subband excitation.

Our studies had been made on sample with 10 layers of InAs QDs grown by Stranski–Krastanow method on (311) surface of semiinsulating GaAs substrate and coated by 100 Å GaAs layer. Experiments are carried out at $T = 77$ K. The cw-Ar ($\hbar\omega_0 = 2.41$ eV) or He-Ne ($\hbar\omega_0 = 1.96$ eV) lasers are used for the interband PL excitation. This optical source creates free carriers in GaAs barriers which are captured to InAs QDs and recombine radiatively. For subband excitation we use cw-YAG:Nd laser ($\hbar\omega_1 = 1.17$ eV). The beams from the both lasers are focused on the input of the 0.2 mm diameter optical fiber and thus transferred to the surface of the sample with InAs/GaAs QDs.

We present the results of stationary experiments when the PL intensity is constant in time and all transient processes after switching on/off the subband excitation are over. Figure 1 shows the measured PL spectra for the studied sample. Solid line is the spectrum measured without subband excitation. Typical inhomogeniously broadened PL spectral line is observed. The width of PL line FWHM = 52 meV indicates the relatively good quality of QD sample. The dashed line in Fig. 1 shows the PL spectrum when the sample

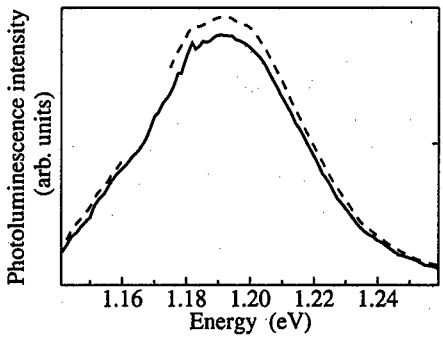

Fig. 1. Luminescence spectra of QD sample in the absence, $P_1 = 0$ (solid line), and in the presence, $P_1 = 250$ W/cm^2, (dashed line), of subband optical $\hbar\omega_1 = 1.17$ eV excitation. The density of interband $\hbar\omega_0 = 1.96$ eV excitation $P_0 = 0.17$ W/cm^2.

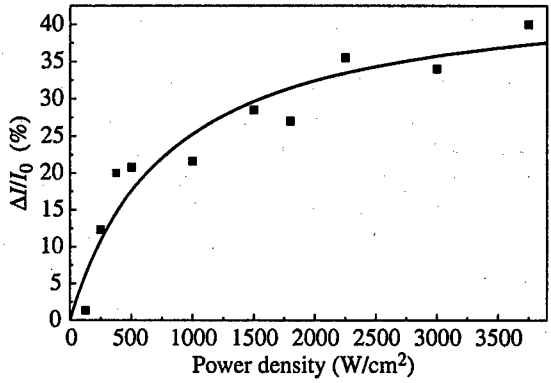

Fig. 2. The dependence of the relative increase of PL intensity $\Delta I/I_0$ on the density of subband $\hbar\omega_1 = 1.17$ eV excitation for $P_0 = 0.2$ W/cm^2, $\hbar\omega_0 = 1.96$ eV. Solid line shows calculated dependence.

is excited additionally by subband light (density on the sample $P_1 = 250$ W/cm^2). The relative increase $\Delta I/I_0 \sim 10\%$, of PL intensity ($\Delta I = I - I_0$) is observed. The subband excitation does not change the shape of PL line and thus the relative increase $\Delta I/I_0$ does not depend on the detected wavelength, $\hbar\omega_d$, of PL. We observe the relative increase of PL present for both interband excitations $\hbar\omega_0 = 2.41$ eV (Ar-laser) and $\hbar\omega_0 = 1.96$ eV (He-Ne laser). No PL is detected for $P_0 = 0$ at any value of P_1.

The dependence of relative increase $\Delta I/I_0$ on the subband excitation density P_1 for low interband excitation density, $P_1 = 0.2$ W/cm^2 is shown in Fig. 2. It is seen that this dependence is sublinear and $\Delta I/I_0$ increases rapidly only for low $P_1 < 500$ W/cm^2. For higher $P_1 > 500$ W/cm^2 $\Delta I/I_0$ shows a tendency to a saturation at the value of $\Delta I^{\max}/I_0 \approx 40\%$. It has been noted that a big relative increase $\Delta I/I_0$ is observed only for low densities of interband excitation. Really we observed that $\Delta I/I_0$ decreases from 40% up to 4% when P_0 increases from 0.045 W/cm^2 to 1 W/cm^2.

The main idea of the explanation of the observed PL enhancement effect is similar to the case of bulk GaAs [3] and is based on the photoionisation effect of deep traps which capture the photoexcited carriers. The details of capture and recombination processes on these deep traps are not understood. Thus we limit our discussion by a simple model where

only one type of carriers (electrons) are captured to one type of the deep traps. We assume that the capture of an electron to a deep trap takes place from a QD and a subband excitation releases a trapped carrier to the GaAs conduction band. Then the released carrier may be again captured to a QD and thus take part in the radiative recombination. Hence the PL intensity increases. The carriers are excited in the GaAs barriers with the generation rate $g \propto P_0$. Electrons and holes may be captured to QDs or to other defects and surface states. We consider QD structures with high PL quantum efficiency and thus assume that carriers from GaAs barriers are mostly captured to the wetting layer and then, from the wetting layer, they are effectively captured to QDs. In our model an electron may tunnel from a QD to a trap and the rate of this process is the main parameter which limits the quantum efficiency.

The proposed simple model gives results which are in a good qualitative agreement with the experimental observation which is demonstrated in Fig. 2. The solid curve shows the calculated dependence $\Delta I/I_0$ on P_1 using this model. Qualitatively the saturation at high P_1 means that all trapped electrons are released and thus recombine radiatively in QD before the nonradiative recombination on a trap takes place. In this case the quantum efficiency of the PL becomes unity. Obviously, this will not happen if the capture processes to other defects or surface states are present. The analysis show that qualitatively the enhancement of PL quantum efficiency and the saturation at high P_1 still takes place but the value of $\Delta I/I_0$ becomes smaller with the increase role of surface and defects non-radiative recombination.

We, however, do not exclude other models which qualitatively may give the PL quantum efficiency enhancement. Photoionisation of QDs in the presence of subband excitation may play a certain role in high quality QD structures and low P_0. In this case the subband induced release of an electron from a QD will increase the chance of meeting a hole in another QD. The subband excitation, in principle, may also change the surface and local electric fields which may result in the changes of the defects and surface capture rates.

In summary we experimentally observe the increase of the PL intensity in InAs/GaAs self-assembled QDs induced by subband 1.06 μm optical excitation. For low interband excitation density the relative increase reaches the value of 40%. The relative increase of PL intensity saturates at high density of subband excitation. We would like to point that the present observation may be useful in the attempts to decrease the threshold current density in QD lasers.

We acknowledge A. A. Kaplyanskii, L. Eaves, V. P. Evtihiev, and P. S. Kop'ev for fruitful discussions. The work is supported by the Russian Foundation for Basic Research (No 99-02-18276).

References

[1] N. N. Ledentsov, V. M. Ustinov, V. A. Shchukin., P. S. Kop'ev, Zh. I. Alferov and D. Bimberg, *Semiconductors* **32**, 343 (1998).

[2] M. M. Sobolev, A. R. Kovsh, V. M. Ustinov, A. Yu. Egorov, A. E. Zhukov, M. V. Maksimov and N. N. Ledentsov, *Semiconductors* **31**, 1074 (1997).

[3] A. V. Akimov and V. G. Shofman. *J. Luminescence* **53**, 335 (1992).

7th Int. Symp. "Nanostructures: Physics and Technology"
St Petersburg, Russia, June 14–18, 1999

Cladding layer effect on the reflectance and transmission spectra in the CdTe/CdZnTe MQWs

D. B. Turchinovich†, V. P. Kochereshko†, H. Mariette‡, R. T. Cox§ and Y. Merle d'Aubigne‡

† Ioffe Physico-Technical Institute, St Petersburg, Russia

‡ Laboratoire de Spectrometrie Physique, Universite Joseph Fourrier Grenoble I and CNRS, Boite Postale 87, F-38402 Saint Martin d'Heres Cedex, France

§ CEA/Departement de Recherche Fondamentale sur la Matiere Condensee, 17, rue de Martyrs, F-38054 Grenoble Cedex, France

Recently it was shown that the oscillator strength of an exciton resonance in a MQW system depends not only on a QW width, but on a period of MQW structure as well [1]. The exciton-photon coupling has been found to enhance in a MQW structure with a period equal to one half and is weakened in a structure with a period equal to one fourth of a light wavelength in a barrier material. Thus, the coupling effect between photon modes and an exciton in a QW depends crucially on the optical path of the incident light.

In the present paper the cladding layer effect on the reflectance and transmission spectra in the CdTe/CdZnTe MQWs has been studied. It is known from the literature [2] that the reflectance lineshape in the exciton resonance region is emission-like when the wave, reflected from the surface and the one, reflected from the QW are in the same phase, i.e. when the distance between the QW and the surface is equal to $n\lambda/2$, where n is an integer (Bragg conditions). However, the reflectance lineshape shows an absorption-like nature when this distance is equal to $(2n+1)\lambda/4$, i.e. both waves have opposite phases (anti-Bragg conditions).

We studied the reflectance and transmission spectra of the $CdTe/Cd_xZn_{1-x}Te$ ($x = 0.13$) MQW structures. The experiments were carried out at the temperatures of 1.6 K and 77 K. The structures studied consist of the two QWs of the different widths ($L_z = 58$ Å and $L_z = 74$ Å) sandwiched by the $3\lambda/4$-thick cladding layer, $\lambda/4$-thick barrier (where λ is light wavelength in the barrier material), and the $CdTe/Cd_yZn_{1-y}Te$ substrate ($y = 0.12$).

The main point of the investigation was to study the modification of the reflectance spectra and to find out the dependence of the exciton resonance parameters (radiation damping and oscillator strength) on the optical path of the light. By tuning the incidence angle we varied the optical path and, consequently, tuned the phase difference, which resulted in a modification of the reflectance lineshape. The existence of two QWs of the different widths placed on the different distances from the surface allowed us to monitor the modification of the reflectance lineshape at different incident angles. In the transmission experiment it was shown that at the Bragg conditions the exciton resonance line is more distinct than that at the anti-Bragg conditions.

The reflectance and transmission spectra of the two structures, each containing two QWs, are shown in the Fig. 1(a) and (b). In the structure presented in the Fig. 1(a) the 74 Å QW is placed on the distance of $3\lambda/4$ from the surface and the 58 Å QW is on the distance of λ from the surface. In the Fig. 1(b) the positions of the QWs are inverted.

From the comparison of Fig. 1(a) and (b) one can see that for the QW placed on the $3\lambda/4$ distance from the surface the amplitude of an exciton resonance lineshape, and consequently its oscillator strength is sufficiently (about 1.5 times) greater than that of the QW placed on

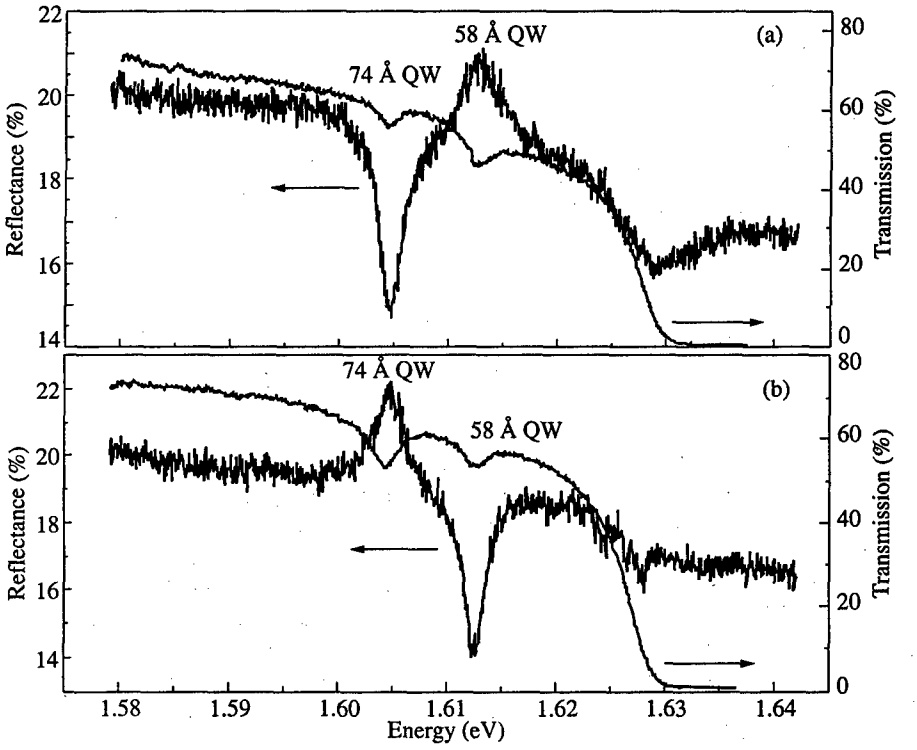

Fig. 1. Reflection and transmission spectra measured at 77 K at normal light incidence. (a) in this sample the 74 Å-thick QW is placed on the $3\lambda/4$ distance from the surface and the 58 Å-thick QW is placed on a λ distance from the surface. (b) in this sample the 58 Å-thick QW is placed on the $3\lambda/4$ distance from the surface and the 74 Å-thick QW is placed on a λ distance from the surface.

the λ distance from the surface, and this effect is defined completely by the surface-to-QW distance of the sample.

Thus, the oscillator strength of an exciton in a single QW is defined not only by the overlap of the electron and hole wavefunctions as was believed recently, but is defined by the electromagnetic field distribution in a structure as well.

References

[1] V. P. Kochereshko, G. R. Pozina, E. L. Ivchenko, D. R. Yakovlev, A. Waag, W. Ossau, G. Landwehr, R. Hellman, and E. O. Göbel, in *Proc. 22nd Int. Conf. on the Physics of Semiconductors*, Vancouver, 1994, ed. D. J. Lockwood (World Scientific, Singapore, 1995), p. 1372.

[2] Y. Merle d'Aubigne, A. Wasiela, and H. Mariette, *Phys. Rev. B* **54**, 19, 14003 (1996).

7th Int. Symp. "Nanostructures: Physics and Technology"
St Petersburg, Russia, June 14–18, 1999

Photoluminescence study of electronic structure of InAs quantum dots grown on GaAs vicinal surfaces

S. Yu. Verbin, B. V. Novikov, R. B. Juferev, Yu. Stepanov, A. B. Novikov, Dinh Son Thach, I. Shchur, V. G. Talalaev, G. Gobsch†, R. Goldhahn†, N. Stein†, A. Golombek†, G. E. Cirlin¶, V. G. Dubrovskii‡, V. N. Petrov‡, A. E. Zhukov¶, A. Yu. Egorov¶ and V. M. Ustinov¶

Institute of Physics, St. Petersburg State University, 198904 Russia
† Institut für Physik, Technische Universität, 98684 Ilmenau, Germany
‡ Institute for Analytical Instrumentation of RAS, 198103 Russia
¶ Ioffe Physico-Technical Institute, St Petersburg, Russia

Abstract. Photoluminescence (PL) study results of InAs/GaAs quantum dot (QD) arrays on vicinal GaAs(100) substrates at InAs thickness fixed to 1.8 monolayers are reported. It is shown that at T = 4 K PL peaks from QDs are blue-shifted and their full width at half maxima decreases as substrate misorientation angle towards various directions raises from 0 to 7 degrees. The intensity of this emission band decreases at the temperature rise and at $T > 80$ K two bands with longer wavelength are clearly observed in PL spectra too. The excitation intensity and temperature dependences of PL spectra at 4–300 K indicate that observed PL spectra structure can be explained by the emission from both lowest and excited levels of QDs with average size 8–9 nm.

Introduction

One of the most promising ways to fabricate nanostructures is the direct QDs formation due to self-organization effects during molecular beam epitaxial (MBE) growth in mismatched heteroepitaxial systems. Spontaneous formation of the arrays of three dimensional islands was observed in various semiconductor systems, in particular InAs/GaAs (see e.g. review [1] and references therein). The properties of InAs/GaAs QDs were studied by various methods. However, the main attention was paid to the study of nanoobjects obtained by conventional MBE on singular GaAs(100) surfaces. Recent study (see e.g. [2, 3]) shows that the growth on vicinal substrates and/or the use of submonolayer migration enhanced epitaxy (SMEE) technique for QDs fabrication lead to the formation of QDs with lower deviation from mean size and to the decreasing of threshold current density at laser generation. The electronic structure of such QDs system is studied in particular *via* PL spectra. These spectra are complex enough and it is the subject of discussion so far [4, 5]. The aim of this work is the PL study of InAs/GaAs QD arrays obtained by SMEE on the GaAs(100) misoriented substrates in dependence on the excitation intensity and temperature.

1 Experiment and results

The structures consist of the InAs QDs confined from both sides with wide-gap GaAs and $Al_{0.25}Ga_{0.75}As$/GaAs superlattices (5 pairs, 2 nm/2 nm each) on GaAs (100) semi-insulating substrates misoriented towards [001], [010], [011], [00$\bar{1}$] and [0$\bar{1}$1] direction by 0° (singular substrates) — 7° are used. The samples growth has been written in detail in [2].

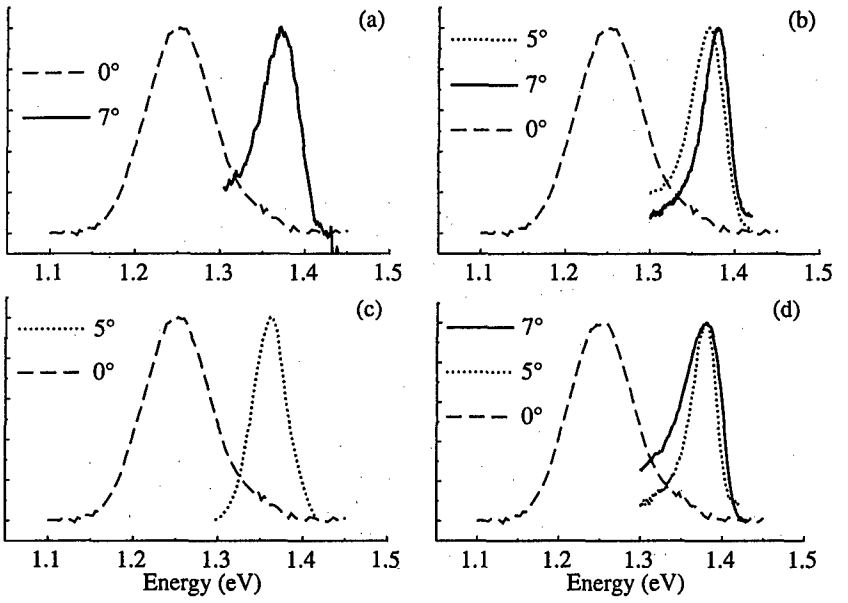

Fig. 1. PL spectra of InAs/GaAs sample with the singular surface and surface misoriented towards various directions. (a) [00$\bar{1}$], (b) [010], (c) [011], (d) [0$\bar{1}$1]) at $T = 4$ K.

The QDs emission band with the intensity maximum near 1.25 eV is observed in typical PL spectra of samples with singular surfaces at $T = 4$ K. Besides this broad band the lines of GaAs exciton and impurity emission with maxima near 1.5 eV are observed.

Monotonous shift of intensity maximum from 1.25 eV to 1.38 eV and decrease of emission band full width at half maxima (FWHM) have been observed as misorientation angle increases from 0° to 7° towards [001] direction. Strong decrease of FWHM in dependence of the misorientation angle is attributed to the size distribution narrowing while the average lateral size of QDs decreases [2]. The angle dependence of PL spectra is qualitatively the same for another directions too but with the higher width of QDs emission band (Fig. 1).

Besides the dominating emission band (1.38 eV) the longwave tail is observed in PL spectra at $T < 80$ K. Up to five weak maxima were observed in this tail for some samples with maximum misorientation angle. The intensity of shortwave band (1.38 eV) drastically decreases at 4 K $< T <$ 80 K and the longwave bands dominate in PL spectra at $T > 80$ K. We have found from temperature dependence of shortwave band intensity that activation energy for this band is nearly 5 meV.

The QDs emission complex curve can be fitted by a sum of Gaussian contours in the whole temperature range 80–300 K. The most longwave band is broader than shortwave band. The temperature shift of longwave band maximum at $T > 80$ K is few times higher than temperature shift of GaAs bandgap. The temperature shift of most shortwave band maximum (1.38 eV) observed at temperatures 4–80 K is higher than temperature shift of GaAs bandgap too. The relative intensity of shortwave PL bands goes up with the increase of excitation intensity at $T > 80$ K (Fig. 2).

While further excitation intensity increases these QDs emission bands also saturate and in this case GaAs substrate emission dominates in PL spectra. Excitation spectra of QDs

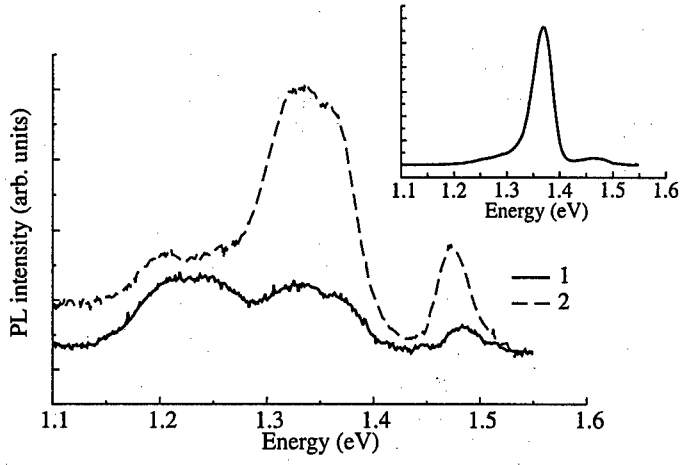

Fig. 2. Dependence of PL spectra of InAs/GaAs sample (7°, [001]) on excitation intensity (1—100 mW, 2—400 mW) at $T = 170$ K. Insert — this sample PL spectrum at $T = 10$ K and excitation intensity 100 mW.

emission bands has been measured too and energy relaxation with LO-phonons emission has been observed.

2 Discussion

We believe that results obtained confirm our explanation of the shape of PL spectra of QDs on vicinal surfaces by the emission from both lowest and excited levels of QDs [5]. It has been shown in models [6–8] that at non-resonant excitation excited levels in the QDs can be populated even in the case of empty lower levels. This situation may appear if recombination rate of excited states in the QD is higher than the rate of interlevel transitions.

We suppose that the most shortwave PL band observed at low temperatures is the emission of excited state of the QDs. This band intensity decreasing observed as temperature rises may be explained by faster thermal depopulation of excited levels. PL band maxima positions are fitted by the theoretical calculations [9] if QDs lateral size is near 8–9 nm. The excitation intensity dependence of PL spectra at $T > 80$ K is then explained by saturation of lower levels.

Taking into account also the spectral dispersion of QDs levels energy due to QDs size distribution the greater red shift of QDs emission band maxima observed at PL spectra depending on the temperature may be the evidence of thermal redistribution in the nonuniformly broadened system of QDs levels.

3 Conclusions

To conclude, we have studied PL spectra of InAs QDs grown by SMEE method on the vicinal GaAs(100) substrates with inclination angles towards various directions up to 7°. It is shown that PL peaks become narrower and are shifted towards shorter wavelengths with the rise of misorientation angle at fixed amount of InAs deposited. The excitation intensity and temperature dependences of PL spectra at 4–300 K indicate that the structure observed can be explained by the emission from both lowest and excited levels of QDs with average size 8–9 nm.

Aknowledgments

Authors thank Dr. A. O. Golubok for helpful discussion. This work was partially supported by Russian Foundation "Integration of Fundamental Science and High School 1997–2000" (grant No 326.75) and Russian Foundation for Fundamental Research (grant No 99-02-17780).

References

[1] N. N. Ledentsov, V. M. Ustinov, V. A. Shchukin, P. S. Kop'ev, Zh. I. Alferov and D. Bimberg, *Semiconductors* **32**, 343 (1998).

[2] R. B. Juferev, A. B. Novikov, B. V. Novikov, S. Yu. Verbin, Dinh Son Thach, G. Gobsch, R. Goldhahn, N. Stein, A. Golombek, G. E. Cirlin, V. G. Dubrovskii and V. N. Petrov, *Proc. 6th Int. Symp. "Nanostructures: Physics and Technology" (St Petersburg)* p. 204, 1998.

[3] V. P. Evtikhiev, I. V. Kudryashov, E. Yu. Kotel'nikov, V. E. Tokranov, A. N. Titkov, I. S. Tarasov and Zh. I. Alferov, *Semiconductors* **32**, 1323 (1998).

[4] A. F. Tsatsul'nikov, B. V. Volovik, N. N. Ledentsov, *et al. Semiconductors* **32**, 84 (1998).

[5] B. V. Novikov, R. B. Juferev, S. Yu. Verbin, *et al. Proc. 24th Int. Conf. on Semiconductors (Ierusalem)* (1998) (in press).

[6] U. Bockelmann, *Phys. Rev.* **B48**, 17637 (1995).

[7] F. Adler, M. Geiger, A. Bauknecht, F. Scholz, H. Schweizer, M. H. Pilkuhn, B. Ohnesorge and A. Forschel, *J. Appl. Phys.* **80**, 4019 (1996).

[8] M. Grundmann and D. Bimberg, *Phys. Rev.* **B55**, 9740 (1997).

[9] M. Grundmann, N. N. Ledentsov, O. Stier, D. Bimberg, V. M. Ustinov, P. S. Kop'ev and Zh. I. Alferov, *Appl. Phys. Lett.* **68**, 979 (1996).

7th Int. Symp. "Nanostructures: Physics and Technology"
St Petersburg, Russia, June 14–18, 1999

Photoluminescence study of InP nanoscale islands grown by MOVPE in InGaAs/GaAs matrix

D. A. Vinokurov, V. A. Kapitonov, Z. N. Sokolova and I. S. Tarasov
Ioffe Physico-Technical Institute, St Petersburg, Russia

Abstract. Photoluminescence study (PL) of the self-assembling Stranski–Krastanov growth of InP nanoscale islands embedded in $In_{0.49}Ga_{0.51}P$ matrix by low pressure metal organic vapor phase epitaxy are presented. The temperature and the excitation level dependencies of the external quantum efficiency of these structures were investigated. InP nanoislands demonstrate a high quantum efficiency at 77 K and high PL wavelength temperature stability.

Introduction

The self-assembling homogeneous and coherent nanoscale islands (NSIs) formation in strongly strained semiconductors have been a subject of intensive investigation due to the 3D confinement of carriers in island's volume. Recently the quantum dot lasers with low threshold current and high characteristic temperature have been presented for In(Ga)As/GaAs growth system [1]. But the most short-wavelength laser structures with InP NSI active region embedded in $In_{0.49}Ga_{0.51}P$ matrix matching to GaAs (100) substrate grown by MBE have exhibited the pulse generation only at 90 K [2]. For increasing of working temperature of such structures it is necessary to study the temperature and power dependencies of external quantum efficiency.

1 Experimental

In this paper we present external quantum efficiency as a function of the temperature and the excitation level in heterostructures with InP NSI grown by low pressure MOVPE [3]. Structures with InP NSI grown by MOVPE [3–5] demonstrated that: (i) the energy peak is not shifted with the increase of amount of deposited island material, (ii) the quantum efficiency at 77 K is very high. Fig. 1 demonstrates the temperature dependence of photoluminescence (PL) peak for InP NSI with nominal deposition thickness of 5MLs at excitation level 50 W/cm^2. This structure revealed 30% of the external quantum efficiency at 77 K. The temperature dependence of InP NSI peak is more smooth than that of InGaP matrix and compressive strained quantum well with 6 MLs thickness (calculated) (Fig. 1).

Fig. 2 shows the temperature dependence of external quantum efficiency (η) for the structure of 5 MLs InP nominally. PL efficiency falls drastically with measuring temperature increase. The characterization temperature T_0 for this structure [$\eta = \eta_0 \exp(-T/T_0)$] decreases from 61 K to 13 K that may be connected with the increase of the electron leakage from NSI into the InGaAs matrix [6]. Low temperature (77 K) PL spectra of InP NSIs with deposition thickness of 3 ML (solid lines) and 5 ML (dash lines) at various excitation levels are shown in Fig. 3. These spectra are the superposition of two PL peaks: NSI and wetting layer. At low excitation level ($P = 10{-}30\,\mathrm{W/cm^2}$) only NSI peak is observed and therefore the position of PL peaks of these two structures is the same. The increase of excitation level results in the appearance and enhancement of the short-wavelength peak

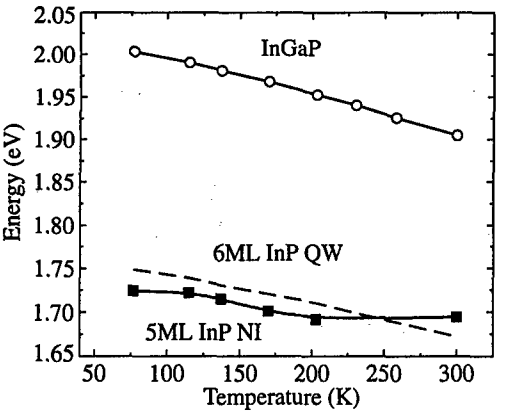

Fig. 1. PL temperature dependence for 5 ML InP NSI (solid square), InGaP matrix (open circle) and 6 ML Quantum Well (dash line), $P = 50\,\mathrm{W/cm^2}$.

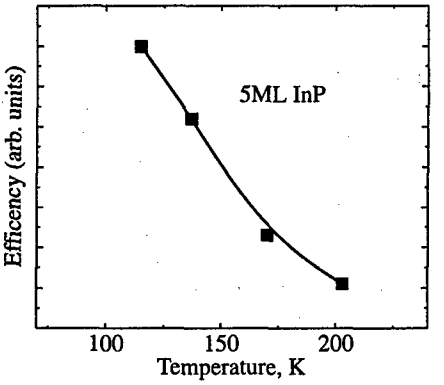

Fig. 2. Temperature dependence of quantum efficiency of 5 ML InP NSI, $P = 50\,\mathrm{W/cm^2}$.

corresponding to the wetting layer radiation and further to the saturation of radiative NSI transitions. More strong spectral shifts for the structure with 3 ML deposition thickness compared with 5 ML ones can be explained by lower island density in 3 ML structure and therefore luminescence saturation of InP NSI occurs at lower excitation density.

In Fig. 4 the temperature dependencies of the PL spectra of the structures with 3 ML deposition thickness and 5 $\mathrm{kW/cm^2}$ excitation level are displayed. As the temperature increases the wetting layer short-wavelength peak decreases; at $T > 230$ K only one peak connected with NSIs in PL spectrum is detected. In our opinion this phenomenon is related with the more intensive electron leakage from the wetting layer into the InGaP matrix in comparison with InP NSI at temperature increase.

2 Conclusions

The external quantum efficiency measurements as a function of the temperature and excitation level were performed. It was shown that InP NSIs grown by MOVPE method [4] were formed as coherent islands. The amount of deposited material influences only on the density of the NSIs but not on there size. Grown InP NSIs demonstrated high quantum efficiency at 77 K and high wavelength temperature stability at low excitation level. At

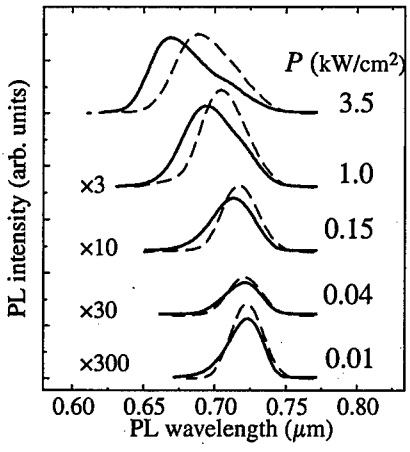

Fig. 3. 77 K PL spectra of 3 ML (solid line) and 5 ML (dash line) InP NSIs at different excitation level.

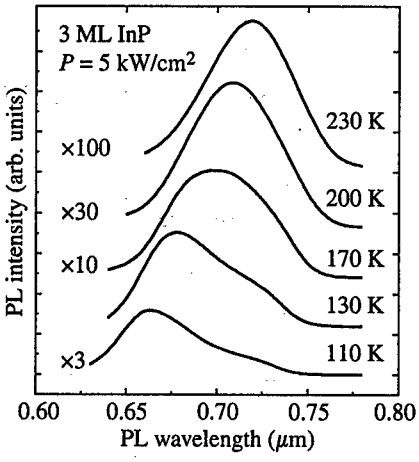

Fig. 4. PL spectra of 3 ML InP NSI s at high excitation level (5 kW/cm^2) for different measuring temperatures.

high excitation level the InP NSI luminescence was saturated and wetting layer radiation became dominant. The rise of the external quantum efficiency at 300 K and suppression of InP NSI emission saturation can be probably achieved by the increase of a number of separated InP layers or using more wide-gap materials for matrix, e.g. (AlGa)InP.

This work was supported by the Russian Foundation for Basic Research, grant No 98-02-18266.

References

[1] N. N. Ledentsov, V. M. Ustinov, V. A. Shchukin, et al., *Semiconductors* **32**, 385 (1998).
[2] M. K. Zundel, N. Y. Jin-Phillipp, F. Phillipp, et al., *Appl. Phys. Lett.* **73**, 1784 (1998).
[3] O. V. Kovalenkov, D. A. Vinokurov, D. A. Livshits, et al., *Proc. 23rd Int. Symp. Compound Semiconductors*, St. Petersburg, Russia, September 23-27, 1996, Inst. Phys. Conf. Ser., N 155: Chapter 3, p. 271.
[4] D. A. Vinokurov, V. A. Kapitonov, O. V. Kovalenkov, et.al., *Pis'ma ZhTF* **24**, (16) 1 (1998).
[5] W. Seifert, N. Carlsson, M.-E. Pistol, et al., *Appl. Phys. Lett.* **67** (8) 1166 (1995).
[6] D. A. Vinokurov, V. A. Kapitonov, D. A. Livshits, et al., *Semiconductors* **33** (1999), (to be published).

7th Int. Symp. "Nanostructures: Physics and Technology"
St Petersburg, Russia, June 14–18, 1999

Raman study of the topology of InAs/GaAs self-assembled quantum dots

G. Zanelatto, Yu. A. Pusep, N. T. Moshegov†‡, A. I. Toropov‡, P. Basmaji† and *J. C. Galzerani*

Universidade Federal de São Carlos, 13565-905 São Carlos, SP, Brasil
† Instituto de Fisica de São Carlos, Universidade de São Paulo,
13560-970 São Carlos, SP, Brasil
‡ Institute of Semiconductor Physics, 630090 Novosibirsk, Russia

Abstract. The topology of self-assembled InAs/GaAs quantum dots was studied by resonant Raman scattering caused by the interface modes localized near the edges of the dots. Evidences were found that on both sides of the InAs layer containing the dots, their topologies show some resemblances. In addition, in the multilayered systems the evidence of the coalescence of the dots (which form vertical columns) in neighbor layers separated by the distance smaller than 25 monolayers was obtained.

The self-assembled InAs/GaAs quantum dots which are formed during the 3D overgrowth of highly mismatched materials have been extensively studied over last years because of their promising device potentialities. Nevertheless, the process of formation of the self-assembled quantum dots is not yet well understood although it evidently influences their electronic characteristics. The widely accepted point of view is that pyramidal InAs dots are formed on a thin ($\approx$ 1.5 ML thick) InAs wetting layer (see [1] and references herein). However, recent studies using cross-sectional tunneling microscopy [2, 3] and scanning transmission electron microscopy [4, 5] presented direct evidences that due to the segregation the InAs dots in forms of lenses or disks are rather embedded within the wetting layer and not on it. Moreover, as it has been shown in [4], the process of the capping of the InAs dots with GaAs changes their volume due to the redistribution of InAs from the dots to the GaAs capping layer. Obtaining information about the formation of the quantum dots in this case is very difficult. Therefore, any application of spectroscopic methods, which are simple to use, to study the topology of the self-assembled quantum dots is indispensable.

In this communication we present the Raman spectra of the InAs/GaAs self-assembled quantum dots showing that the topologies of the dots are somewhat similar on both sides of the InAs layer where they are formed. This implies in a difference between the material of the dots and the one of the wetting layer, which can be caused by a strong modification of the wetting layer between the dots due to the segregation, as it has been established in [2–5].

In order to study the topology of the InAs/GaAs quantum dots we measured the Raman scattering of the interface vibrational modes localized near the edges of the dots. The contribution of these modes to the Raman scattering, being proportional to the density of the dots, has been shown to appear at the resonance with electron excitations confined in the InAs dots [6]. Thus, the Raman lines associated with such interface modes can serve as indicators of the presence of the quantum dots.

The InAs/GaAs heterostructures containing the self-assembled InAs quantum dots were grown on (001)-oriented GaAs substrates by molecular beam epitaxy via Stranski–Krastanov growth. Structures with and without 500 Å thick cap GaAs layers were grown

under the same growth conditions; the last ones were characterized by an atomic force microscope (AFM) Digital Instruments Nanoscope IIIa using the tapping mode. Samples both with a single InAs layer containing quantum dots and with multilayers separated by different GaAs spacers were investigated.

The single layer dots were grown with the nominal thicknesses of InAs 2, 2.5, and 3 ML's at the temperature $T = 500\,^{\circ}\mathrm{C}$ and the As_4 background pressure $P_{As} = 8 \times 10^{-6}$ Pa. The multilayered dot structures were grown as following: after the growth of a GaAs/AlAs superlattice and a GaAs buffer, the temperature of the substrate was reduced to 450–470 °C and the InAs layer with the nominal thickness 3 ML's was deposited. The process of the formation of the dots was controlled by reflection high-energy electron diffraction (RHEED) oscillations. A transition from streaked to spotty RHEED pattern indicating a formation of the 3D islands was observed after the deposition of an effective thickness of InAs equal to 1.8 ML. The growth was interrupted for 30 s after the deposition of the nominal thickness of InAs; then the GaAs spacer of the corresponding thickness was grown and the process was repeated in order to obtain the multilayered structure. During the growth the fluxes of InAs and GaAs were fixed at 0.1 and 0.35 ML/s respectively, while $P_{As} = 2 \times 10^{-6}$ Pa. Finally, the structure was capped with 500 Å of GaAs.

The Raman scattering was performed at $T = 8$ K with a Jobin-Yvon U-1000 double-grating spectrometer supplied with a conventional photon counting system. A Ti-sapphire tuned laser pumped with an Ar^+ ion laser was used for excitation near the $E_0 + \Delta_0$ resonance of the InAs quantum dots. The cross-polarized Raman spectra were measured in order to avoid photoluminescence.

In order to obtain information about the InAs/GaAs interface we compared the Raman spectra of the samples grown with and without the GaAs capping layer. We expect that in the case of a plane InAs/GaAs interface, the interface vibrations associated with the edges of the dots would contribute to the Raman spectra in the capped samples and would not in the samples without capping layers.

As it has been shown in [6], the interface modes associated with the InAs quantum dots are seen in Raman scattering in resonance with the $E_0 + \Delta_0$ electron excitations confined in the dots ($E_{ex} \approx 1.72$ eV, as measured in [7]). At such a resonance excitation the GaAs bulk phonons are week and they are detected as a shoulder at the high frequency side of the Raman line corresponding to the first interface mode [6]. The obtained Raman spectra are plotted in Fig. 1. In all the samples grown with the capping layer the Raman lines caused by the GaAs-like interface modes were observed. The first interface modes located at 293 cm^{-1} reveal larger intensities as compared to the high-index ones. Although with smaller intensities, identical lines were found in all the uncapped samples. This result testifies to the formation of the edges between the dots and the underlying GaAs (similar to those between the dots and the capping layer), which can appear due to the modification of the InAs wetting layer between the dots. As it has been shown in [2]-[5], the segregation strongly alters the contents of the wetting layer between the dots; as a consequence, the InAs dots become effectively embedded within the InGaAs wetting layer giving rise to the relevant interface modes. Actually, in this case the interface modes are localized at the edges formed by the boundary between the dots and the InGaAs wetting layer. Analyzing the ratios of the Raman line intensities measured in the uncapped quantum dots to the capped ones, we can conclude that the larger this ratio, the sharper the edges corresponding to the top of the dots relative to the edges of their bases embedded in the wetting layer.

It is worth mentioning, that the InAs-like interface modes were also found in the Raman spectra of the samples under investigation. However, due to their relatively weak intensity

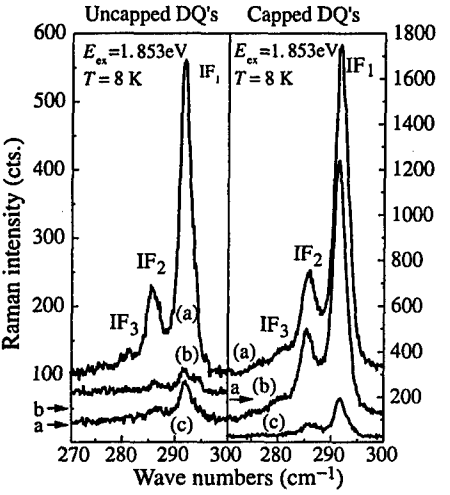

Fig. 1. The GaAs-like interface modes measured at $T = 8$ K in the single layer InAs/GaAs heterostructures containing self-assembled quantum dots grown with nominal thicknesses of InAs: (a) 2 ML's, (b) 2.5 ML's, (c) 3 ML's. The right panel shows the samples with the GaAs capping layer, while on the left one the spectra of the uncapped samples are presented. Arrows show positions of the zero intensities for the corresponding spectra, which were shifted up.

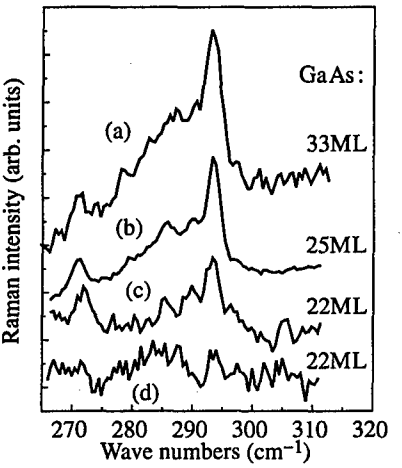

Fig. 2. The GaAs-like interface modes measured at $T = 8$ K in the multilayered InAs/GaAs heterostructures with the 2 ML's thick InAs layers separated by GaAs spacers with different thicknesses: (a) 33 ML's ($E_{ex} = 1.75$ eV), (b) 25 ML's ($E_{ex} = 1.78$ eV), (c) 22 ML's ($E_{ex} = 1.78$ eV), (d) 15 ML's ($E_{ex} = 1.77$ eV); the numbers of periods are: 15, 10, 7, and 7 respectively.

we could not include them in the analysis.

In addition, we studied the interface modes in the multilayered systems containing self-assembled quantum dots. The Raman spectra measured in the samples with different thicknesses of the spacers between the quantum dot layers are depicted in Fig. 2. As it is seen, for thicknesses of the spacers smaller than 25 ML's, the intensities of the interface modes decrease with the decrease of the spacer thicknesses. This occurs because at small

thicknesses of the spacers the InAs dots in vertical columns formed by aligned growth of neighbor layers coalesce (or they are close to coalescence), thus decreasing the density of the tips responsible for the relevant interface modes. At the spacer thicknesses equal to 15 ML's a significant number of dots coalesce resulting in very weak intensities of the interface modes. Thus, this shows that Raman spectroscopy can serve as a tool to characterize the separation of the quantum dots in multilayer systems.

To summarize, by Raman spectroscopy of the interface modes localized near the edges of the InAs/GaAs self-assembled quantum dots we found an evidence of the similar topologies of the quantum dots on both sides of the layer where they are formed. We showed that the Raman scattering is a tool sensitive enough to analyze the separation between the quantum dots in multilayered systems.

The financial support from CNPq, FAPESP, and CAPES is gratefully acknowledged.

References

[1] M. Grundmann, O. Stier and D. Bimberg, *Phys. Rev.* **B52**, 11969 (1995).
[2] W. Wu, J. R. Tucker, G. S. Solomon and J. S. Harris, Jr., *Appl. Phys. Lett.* **71**, 1083 (1997).
[3] B. Legrand, B. Grandidier, J. P. Nys, D. Stievenard, J. M. Gerard and V. Thierry-Mieg, *Appl. Phys. Lett.* **73**, 96 (1998).
[4] P. D. Siverns, S. Malik, G. McPherson, D. Childs, C. Roberts, R. Murray, B. A. Joyce and H. Davock, *Phys. Rev.* **B58**, 10127 (1998).
[5] P. B. Joyce, T. J. Krzyzewski, G. R. Bell, B. A. Joyce and T. S. Jones, *Phys. Rev.* **B58**, R15981 (1998).
[6] Yu. A. Pusep, G. Zanelatto, S. W. da Silva, J. C. Galzerani, P. P. Gonzalez-Borrero, A. I. Toropov and P. Basmaji, *Phys. Rev.* **B58**, R1770 (1998).
[7] S. W. da Silva, Yu. A. Pusep, J. C. Galzerani, D. I. Lubyshev, P. P. Gonzalez-Borrero and P. Basmaji, *J. Phys. Condens. Matter* **9**, L13 (1997).

7th Int. Symp. "Nanostructures: Physics and Technology"
St Petersburg, Russia, June 14–18, 1999

QWR/QD.20p

Electron in quasiplane superlattice of cylindric quantum dots

G. Zegrya†, *M. Tkach*‡, O. Makhanets‡ and V. Zharkoy‡
†Ioffe Physico-Technical Institute, St Petersburg, Russia
‡ Chernivtsi State University, 2 Kotsubinsky str., 274012, Chernivtsi, Ukraine

Abstract. The theory of electron spectrum in quasiplane superlattice of cylindric quantum dots is built using the modified method of augmented plane waves. It is established that quasiplane energy bands arise only when the ratio between cylinder height and radius of base is bigger than some critical value.

Experimental investigation of periodical semiconductor quantum dots structures started recently [1]. The theory of quasiparticle spectra in such systems and in quantum well superlattices is not established yet.

The theory of electron spectrum in quasiplane quantum superlattice of cylindric quantum dots (Fig. 1) is built. It is assumed that cylindric quantum wells superlattice (CQWS) is embedded into vacuum. The quantum well is a cylinder of height h and radius a; c-distance between the nearest borders of two neighbour dots. Effective mass of electron in the well is μ_1 and in the matrix-μ_2. Well and matrix potentials respectively the vacuum are $(-V_1)$ and $(-V_2)$ consequently. The CQWS system is assumed as infinitly deep potential well because the vacuum surrounding CQWS is a strong potential barrier.

In order to obtain the electron spectrum one has to solve the stationary Schrödinger equation with Hamoltonian

$$\hat{H} = -\frac{\hbar^2}{2}\left(\vec{\nabla}_{xy\varphi}\frac{1}{\mu(x,y)}\vec{\nabla}_{xy\varphi} + \frac{1}{\mu(x,y)}\frac{\partial^2}{\partial z^2}\right) + U(x,y,z). \tag{1}$$

In Cartezian coordinate system where OZ axis is directed along the axial axis of cylinder and OXY plane crossing the middle of cylinders height the potential $U(x,y,z)$ can be written in the form

$$U(x,y,z) = U(x,y) + \begin{cases} 0 & z < h/2 \\ \infty & z \geq h/2 \end{cases} \tag{2}$$

$$U(x,y) = \begin{cases} -V_1 & x,y \ \textit{inside the wells} \\ -V_2 & x,y \ \textit{outside the wells} \end{cases} \tag{3}$$

Introducing the electron average effective mass $\overline{\mu} = (\mu_1+\mu_2)/2$ the electron wave function is found as

$$\psi(x,y,z) = \psi_{||}(x,y)f(z) \tag{4}$$

where

$$f(z) = \begin{cases} \sqrt{\frac{2}{h}}\cos\frac{\pi n}{h}z & n = 1,3,5,\ldots \\ \sqrt{\frac{2}{h}}\sin\frac{\pi n}{h}z & n = 2,4,6,\ldots \end{cases} \tag{5}$$

Thus equation (1) can be rewritten in the form

$$\left\{-\frac{\hbar^2}{2}\left(\vec{\nabla}_{xy}\frac{1}{\mu(x,y)}\vec{\nabla}_{xy}\right) + U(x,y) - E_\perp^0\right\}\psi_\perp^0 = 0 \tag{6}$$

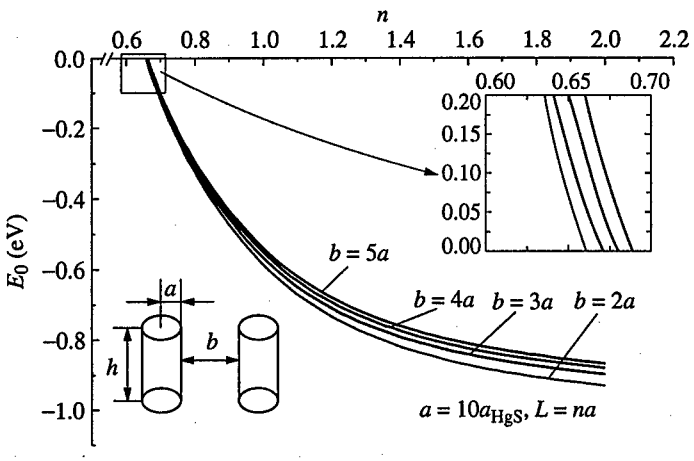

Fig. 1. Electron qround zone dependence on distance between nearest wells, $L = 2\rho_0$.

where

$$E_{\perp}^{0} = E^{0} - \frac{\pi^2\hbar^2}{2\bar{\mu}h^2}n^2. \tag{7}$$

Further equation (6) is solved using the modified method of augmented plane waves (established recently in [2]) for the plane superlattice of circle quantum wells. According to this method one has to write the Schrödinger equation for the wave function inside the plain circle quantum well. In polar coordinate system for the radial function $f_m(\rho)$ it is written as

$$\left\{-\frac{\hbar^2}{2\mu_1}\left[\frac{1}{\rho}\frac{d}{d\rho}\left(\rho\frac{d}{d\rho}\right) - \frac{m^2}{\rho^2}\right] - U_0 + \frac{\pi^2\hbar^2}{2\bar{\mu}h^2}n^2 - E^0\right\} f_m(\rho) = 0 \tag{8}$$

where $U_0 = U_1 - U_2$.

When the energy $\varepsilon = -E < 0$ the solution of equation (8) is Bessel function

$$f_m(\rho) = J_m(\alpha\rho) \tag{9}$$

where

$$\alpha = \sqrt{2\mu_1\hbar^{-2}a^{-2}(U_0 - \epsilon) - \frac{\mu_1}{\bar{\mu}}\frac{n^2}{h^2}}. \tag{10}$$

One can obtain the electron spectrum in quasiplane superlattice of cylindric quantum dots using the function (9) together with the plane waves in modified method of augmented plane waves.

The calculations was performed for the system of β-HgS dots embedded into β-CdS matrix. The results are shown in Figs. 1 and 2. The main conclusions are following.

It is clear from Fig. 1 that plane enrgy bands of superlattice arise only at some critical minimal ratio between cylinder height (h) and radius of base (a); the distance (b) between the neighbour dots is arbitrary. It is clear from physical considerations because at small sizes of any quantum well it cannot produce the bound state creating the band due to the interaction with the other wells.

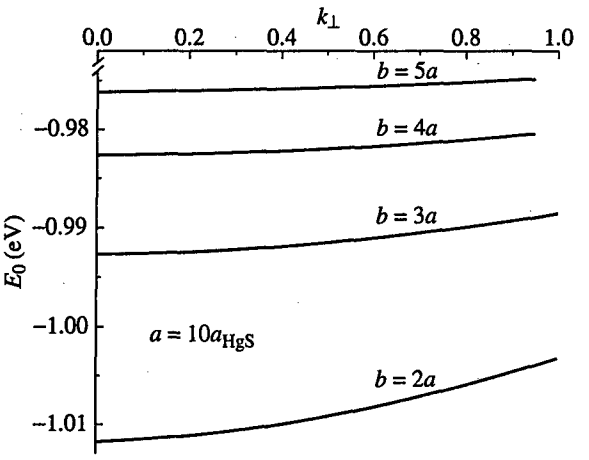

Fig. 2. Electron qround zone dependence on distance between nearest wells, $L = 2\rho_0$.

Figure 2 shows the electron ground band dependence on the distance between the nearest wells (b). It is clear that (b) decreasing shifts the band into the region of lower energies. and increasing its width at the fixed sizes of the well. Physically it means that (b) decreasing is equivalent to the decreasing of barrier height. The electron breely moves in the superlattice i.e. its effective mass of plane movement is decreasing.

References

[1] N. Ledentsov, V. Ustinov, V. Shchukin, P. Kop'ev, Zh. Alferov and D. Bimberg, *Fiz. Tekh. Poluprovod.* **32**, 4 (1998).

[2] G. Zegrya, V. Golovach, M. Tkach, I. Pronyshyn and O. Makhanets, *Fiz. Tekh. Poluprovod.* **34**, 4 (1999).

7th Int. Symp. "Nanostructures: Physics and Technology"
St Petersburg, Russia, June 14–18, 1999

Nonlinear conductance of quantum wires normally pinched-off by surface potential

K. S. Novoselov, Yu. V. Dubrovskii, V. A. Sablikov†, D. Yu. Ivanov, E. E. Vdovin, Yu. N. Khanin, V. A. Tulin, D. Esteve‡ and S. Beaumont§
Institute of Microelectronics Technology RAS,
142432 Chernogolovka, Moscow District, Russia
† Institute of Radioengineering and Electronics RAS,
141120 Fryazino, Moscow District, Russia
‡ Quantronics Group in Service de Physique de l'Etat Condense, Commissariat a l'Energie Atomique Saclay F-91191, Gif-sur-Yvette Cedex, France
§ Department of Electronics and Electrical Engineering, University of Glasgow, Glasgow G128QQ, United Kingdom.

In this work the studies of the nonlinear transport in quantum wires patterned from wafers with a high mobility two-dimensional electron gas by means of E-beam lithography and following chemical etching are presented. The wires studied were normally pinched-off by surface potential under equilibrium conditions. Stepwise increase of the differential conductance $g = dI/dV$ from zero to a approximately constant value G_0 at a certain critical voltage V_c was detected. The critical voltage V_c and G_0 dependence of the wire width was studied. This observation are similar to the findings of L. P. Kouwenhoven *et al.* [1] on quantum point contacts when they were slightly pinched-off by application of the appropriate split-gate voltage. Unexpectedly we also found the change of the magnitoresistance sign with the reverse of the magnetic field direction in the nonlinear conductance regime. It happened only when magnetic field was in the 2DEG plane and normal to the wire. The possible reasons of loosing the inversion symmetry point in the wires under high voltage biases are discussed. The wires with different lithographic width 0.50 μm, 0.52 μm, and 0.54 μm and 0.8 μm length were fabricated from a GaAs/GaAlAs heterostructure with a high-mobility two- dimentional electron gas (2DEG) located 100 nm below the surface (the electron density $N_{2D} = 3.1 \cdot 10^{11}$ cm^{-2} at $T = 4.2$ K with mobility $1.4 \cdot 10^6$ cm^2/Vs corresponding to the mean free of 9 μm). In fact, the real width of the wire was about 0.25 μm (determined from the scanning electron microscopy micro graph) when lithographic width was 0.54 μm. It should be noted that surface depletion in our samples was about 150 nm from the wires sidewalls. Thus the parabolic quantum well was created in the wire with 1D quantization as the result.

Fig. 1 shows the $I-V$ characteristics for samples with lithographic width 0.5 μm, 0.52 μm and 0.54 μm. All the measures are held at 4.2 K. All of our samples demonstrate a stepwise increase of the differential conductance $g = dI/dV$ from zero to a approximately constant value G_0 (various for all samples) at a certain critical voltage V_c. The critical voltage V_c increases strongly with decreasing of the lithographic width of the wires. Moreover, the value G_0 shows evident correlation with the lithographic width of the samples—slightly increases with incresing width. Note that the $I-V$ characteristics are not antisymmetric, and the critical voltage V_c is slightly different (about 10 mV) for positive and negative bias.

It should be marked that critical voltage V_c and G_0 after heating and following cooling down were slightly different. The degradation of our samples with the number of the temperature cycles led to slight V_c decrease and G_0 increase.

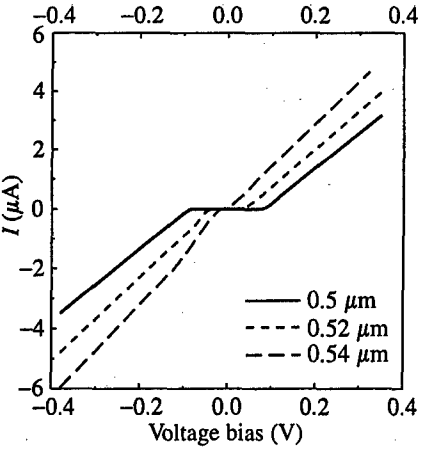

Fig. 1. Current-voltage characteristics for samples with lithographic width 0.5 μm (solid curve), 0.52 μm (dotted curve), 0.54 μm (dashed curve).

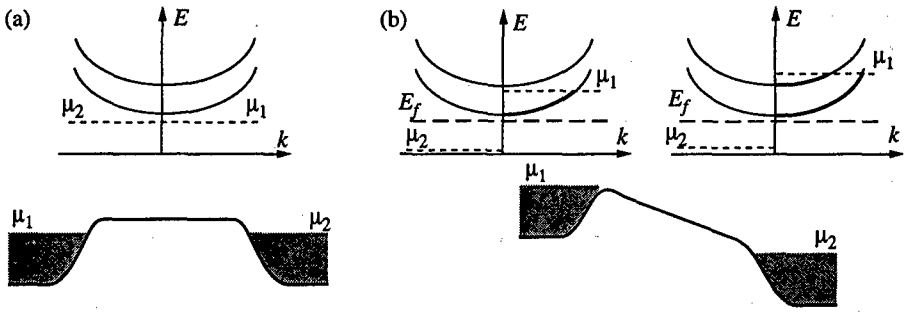

Fig. 2. Upper picture—subband occupation at the bottleneck in the absence (a) and in the presence (b) of the voltage bias. Lower picture—the schematic band diagram of our samples bottleneck in the absence (a) and in the presence (b) of the voltage bias.

To understand the main features in the $I-V$ characteristics we use a simple model following the work of L. P. Kowenhoven *et al.* [1]. Fig. 2(a) shows the schematic zone structure of our samples at zero voltage bias. Due to the lateral confinement 1D subbands are formed. Apart from the lateral confinement, the surface depletion reduces the electron density in the wire. On entering the wire, in the absence of the voltage bias, the bottom of the 1-st subband rises relatively to the bulk 2DEG Fermi level, as a combine result of the increased lateral confinement and electrostatic barrier.

In the presence of the voltage bias the bottom of the 1-st subband descending relative to the chemical potential in the emitter—μ_2. At the critical voltage bias V_c the maximum of the potential barrier, where the 1-st subband bottom has an energy E_1, occurs lower than μ_2. Extrapolating an approach valid in the linear transport regime, following Kouwenhoven, the current is given by

$$I = \frac{2e}{h}[\mu_1 - E_1]$$

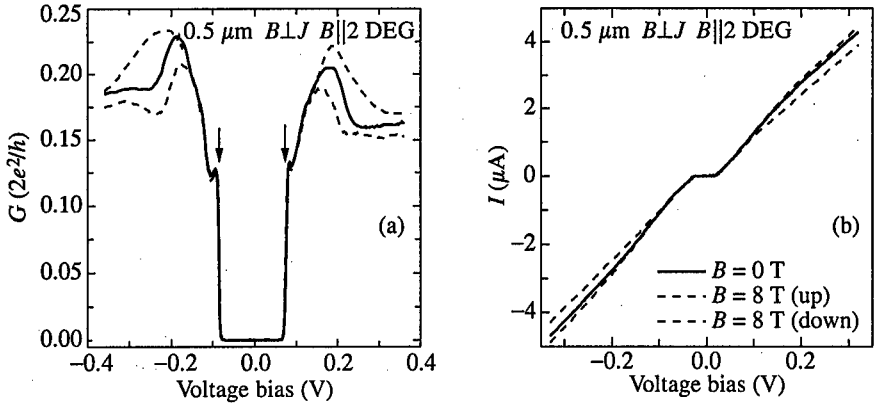

Fig. 3. Differential conductance of the samples with lithographic width 0.5 μm, solid curve—without magnetic field, dotted and dashed curve—in the magnetic field 8 T (a). Current-voltage characteristics for the samples with lithographic width 0.5 μm, solid curve—without magnetic field, dotted and dashed curve—in the magnetic field 8 T (b). For the dashed curves magnetic field is oriented in the 2DEG plane and normal to the wire, whereas for the dotted curves the direction of magnetic field was reversed.

and the conductance is given by

$$G = \frac{dI}{dV} = m\frac{2e^2}{h}.$$

Here m is a phenomenological parameter between 0 and 1, describing the fraction of total voltage V, which drops on the left of the bottleneck.

It should be noted, that according with calculation in our samples the distance between 1D levels is about 0.8 meV. Thus we can expected that even at voltages just slightly over the V_c there are a number of 1D levels lies under the chemical potential in the emitter—μ_2. So we can write, that at voltage bias, where the linear regime is approach the differential conductance is given by $G = m\frac{2e^2}{h}n$. Here n is the number of subbands lying under the μ_2.

In Fig. 3(a) the solid curve shows the differential conductance versus voltage bias for the sample with lithographic width 0.5 μm. One can see the local maximum close to the pinch-off voltage. At higher voltages the differential conductance reach maximum ($\approx 0.2\frac{2e^2}{h}$), and then fall down to the constant value $\approx 0.15\frac{2e^2}{h}$.

At the moment we can't explain the peaks on the curve of the differential conductance versus voltage bias. But we can propose, that at so high voltage bias (0.2 V) the real space transfer could be included into the consideration. Electrons get energy in the electric field and can be transferred from the quantum well into the AlGaAs modulated doped region above or below the 2DEG layer. For example, electrons can be transferred in to the doped region close to the surface, where the electrons mobility is smaller then for the electrons in the quantum well. Thus the differential conductance drops into the constant value.

The behaviour of our samples in the presence of a magnetic field is rather unexpected. In Fig. 3(b) the $I-V$ characteristics for the sample with lithographic width 0.5 μm in the absence (solid curve) and in the presence (dashed and dotted curve) is shown. For the dashed curve the magnetic field is oriented in the 2DEG plane and normal to the

wire, whereas for the dotted curve—in the reverse direction. At low voltage bias near the pinch-off no magnetoresistance is detected. But at higher voltages, when the conductance reach maximum value, the magnetoresistance can be easily seen. As one can see the magnetoresistance change it's sign as the magnetic field change it's direction to the opposite. Besides this, the sign of the magnetoresistance depends of the current direction. The relative negative magnetoresistance is approximately 4%, whereas the positive is about 12%.

For magnetic field parallel to the wire the magnetoresistance does not change sign with reversing magnetic field direction.

At voltages, when the magnetoresistance is obvious, part of the electrons is out of the quantum well, and the transport is not one dimensional. Depending on its direction magnetic field (when perpendicular to the current and in plane of the 2DEG) shifts the maximum of the electron density in the real space up or down with respect to the surface. If the maximum of the spatial electron density located closer to the scattering centres the electron mobility decreases, the magnetoresistance is positive and *vice versa.*

Thus we have investigated the conductance of the quantum ballistic transport pinched off in equilibrium. Our data are explained by simple model of L. P. Kouwenhoven *et al.* The effect of magnetoresistance sign reversing with reversing the current flow or magnetic field direction in nonlinear region has been found.

This work was partly supported by the INTAS (grant 96-0721), RFBR (98-02-17642), and national program "Physics of Solid State Nanostructures" (97-1057) (Russia).

References

[1] L. P. Kouwenhoven, B. J. van Wees *et al.*, *Phys. Rev. B* **39**, 8040 (1989).

7th Int. Symp. "Nanostructures: Physics and Technology"
St Petersburg, Russia, June 14–18, 1999

Mesoscopic superconductors in proximity to nanomagnets

V. T. Petrashov†‡, *I. A. Sosnin*†‡, I. Cox†, A. Parsons† and C. Troadec†
† Royal Holloway, University of London, Egham, Surrey, TW20 0EX, UK
‡ Institute of Microelectronics Technology, Chernogolovka, Moscow, 142432, Russia

Abstract. We report a study of electron transport through mesoscopic superconducting (aluminium) wires with ferromagnetic (nickel) and superconducting electrodes in the temperature range of 0.28–1.5 K in magnetic fields up to 5 T. We observe spectacular changes in the differential voltage-current charachteristics, dV/dI vs I, when the measuring current is injected from the ferromagnetic electrodes: the dV/dI curves become non-symmetric with respect to the current direction and show the regions with negative differential resistance. The peaks corresponding to the superconducting transition split into two with separation depending on the external magnetic field and the polarisation of current. We attribute the effects to the nonequilibrium spin polarization induced by the current from the ferromagnetic electrode and the effects of the saturation magnetisation leading to the Zeeman splitting of the quasiparticle spectrum in the adjacent superconductor.

Introduction

Properties of a ferromagnetic/superconductor interface have been extensively studied over the past years. In early experiments by Tedrow and Meservey with low transparency interfaces, the tunneling from ferromagnetic (F) into superconductor (S) was used to calculate density of states for spin-up and spin-down electron bands in the ferromagnet [1]. The model employed the Zeeman splitting of quasiparticle spectrum in the superconductor. Recently, major experimental efforts have been applied to study F/S systems with high transparency clean interfaces. It was found that the superconducting correlations penetrate in the ferromagnet over surprisingly large distance [2-4]. By matching Andreev reflection coeficients at the interface, it was possible to extract the spin polarization of the current [5]. On the other hand, spin accumulation in non-magnetic media over the distance of spin-relaxation length imposes a nonequilibrium magnetic moment, which depends on amplitude and sign of spin polarisation [6]. In our experiment with clean interfaces we observed the Zeeman splitting in the critical current of superconducting transition due to strong magnetic field from the ferromagnet. The geometry of electrodes allowed us to vary the polarisation of measuring current. We found the value of the splitting depending on the polarisation. The essential difference of our experiment is the presence of strong gradient of magnetic field. For the first time the effect of the magnetic field gradient in mesoscopic systems was observed.

1 Experimental

The samples were fabricated using standard e-beam lithography. The geometry of the structures is shown in Fig. 1. The width of the wires was about 100 nm. The first layer was a 40 nm thick Ni film in contact with golden pads made using photo-lithography. The length-to-width ratio for the Ni wire was about 20. The second layer was 55 nm thick Al film with small area of the interface to Ni of about 100×100 nm^2. Before the deposition of the second layer, the contact area was Ar^+ plasma etched to obtain a clean interface between

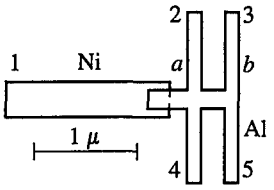

Fig. 1. Sample geometry. 1—Nickel electrode; 2–5—Aluminium electrodes. The voltage U_{23} is measured as a function of current I_{45} or I_{15} applied to part *ab*.

the two metals. A special study of the interface quality using SIMS spectra showed that total amount of oxigen between the layers correspond to less than 8% of one monolayer.

The measurements were carried out in the temperature range from 0.28 K to 1.5 K and in magnetic fields up to 5 T applied perpendicular to the substrate. The voltage U_{23} was measured as a function of current I_{45} or I_{15} applied to part *ab*. To change the ratio of spin polarised to non-spin polarised current, additional current Ibias was supplied between points 1, 4. The resistivity, ρ, of the Ni and Al films was about 50 $\mu\Omega$cm and 1.3 $\mu\Omega$cm, with the diffusion constants, D, equal to 14 cm^2/s and 106 cm^2/s, respectively, calculated using ρl value for Ni, 1.5×10^{-11} Ωcm^2 [13a] and Al, 3.2×10^{-12} Ωcm^2 [13b]. The critical temperature of the Al wires was about 1.0 K. We believe that this lower-than-usual value was due to the proximity to the ferromagnetic conductors.

2 Results

Figure 2(a) shows experimental normal/superconducting phase diagrams of an Al wire, obtained by measuring differential resistance versus applied dc current at different external magnetic fields. The peaks on the diagrams correspond to critical current of a superconducting transition. Figure 2(b) shows results of calculation of critical current, taking into account Zeeman splitting and angular dependence of critical magnetic field. The fit is in excellent agreement with experiment.

Figure 3 presents the effect of bias current applied to electrodes 1 and 4. It is seen, that the peaks can split in two with the distance between them depending on I_{bias}. When the direction of I_{bias} and I_{45} or I_{15} in electrode 4 coincide, the spin-polarization of the resulting current through *ab* does not change. Hence position of peaks A depend very little on bias current. On the contrary, when I_{bias} and $I_{4,5}$ or $I_{1,5}$ in electrode 4 are of opposite direction, so that spin polarization in ab increases as Ibias increases. As a result of that we see strong critical current suppression with larger splitting (peaks B on Fig. 3).

3 Discussion

To understand main features of experimental phase diagram, it is important to take into account that nanomagnet can produce rather strong and nonuniform magnetic field next to the mesoscopic superconductor. In this case, external magnetic field is not only directly influence the superconductor but also change the direction of magnetisation in the ferromagnet, which in turn affects the superconductor. To simulate this situation, we take the following model. Our Ni nanomagnet is a single-domain ferromagnetic with easy axis along the wire, i.e. pointing onto the superconductor. External magnetic field is then perpendicular to easy axis. As it increases, the saturation magnetisation vector rotates toward the direction of external field while staying the same in absolute value. The effective magnetic field, H^*, acting on the superconductor from the nanomagnet we take equal to component of induction inside ferromagnet normal to the interface and neglect H inside the ferromagnet.

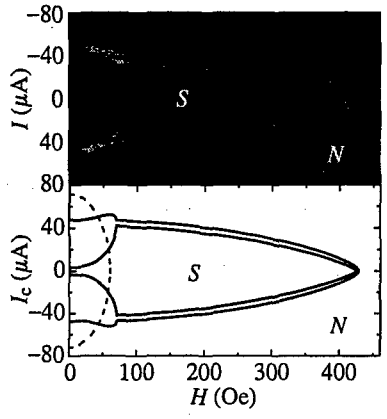

Fig. 2. (a) The current-magnetic field normal/superconducting phase diagram taken at $T = 0.27$ K. Colour represents value of dV/dI in arbitrary units. Measuring current is I_{15}. (b) Calculated dependence of reduced critical current.

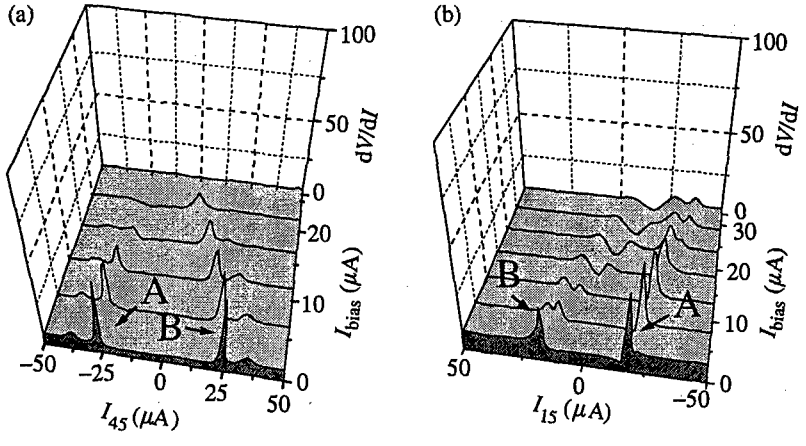

Fig. 3. (a) dV/dI vs I_{45}, (b) dV/dI vs I_{15}. Curves taken at $T = 0.27$ K, $H = 200$ Oe. Bias current applied to electrodes 1 and 4. Peaks A: direction of I_{bias} and I_{45}, I_{15} in electrode 4 is the same; peaks B, opposite.

The angular dependence of critical magnetic field $H_c(\theta)$ we take [7]

$$\left|\frac{H_c(\theta)\cos(\theta)}{H_{c\perp}}\right| + \left(\frac{H_c(\theta)\sin(\theta)}{H_{c//}}\right)^2 = 1 \tag{1}$$

The dependence of the superconducting gap (on the magnetic field close to the transition we approximate as,

$$\Delta(H) = \Delta_0\left[1 - \left(\frac{H^*(H)}{H_c}\right)^2\right]^{1/2} \pm \mu_B H^*(H), \tag{2}$$

where the second term is due to the Zeeman splitting of the quasiparticle spectrum. We take that critical current $I_c(H) \propto \Delta^{3/2}(H)$ (see for example [7]). The result of this fitting is

shown as solid lines in Fig. 2. We used the following parameters in calculation: $\Delta_0 = 1.7$ K, $H_{c\perp} = 430$ Oe, $H_{c\parallel} = 1800$ Oe, H_{rot}=70 Oe, $B_s = 6000$ Gs. Though the model describes well the main features of the phase diagrams, it does not account for additional peaks marked in Fig. 2. We believe that the origin of these could be a strong gradient of magnetic field, causing an additional force equal to acting in opposite directions on electrons with opposite spins. This results in different effective electric field acting on spin-up and spin-down electrons, leading to additional peaks on the phase diagram. However, to calculate this effect one need to know exactly the distribution of magnetic field. The experiments to measure this distribution directly using Lorentz microscopy are under way.

4 Conclusion

We measured normal/superconducting phase diagram of a mesoscopic superconductor in proximity to a nanomagnet. We observed a Zeeman splitting of quasiparticle spectrum in the superconductor. The position of the peaks on the diagrams corresponded to critical current of a superconducting transition. The proposed model, taking into account the effect of magnetic field of a nanomagnet and angular dependence of a critical field, explains well the main features. However, additional peaks are probably due to strong gradients of magnetic field. Using bias current, that allowed us to change the polarisation of measuring current, we showed that the splitting depends on spin polarisation, what supports our model.

The work was funded within EPSRC grant No GR/L94611.

References

[1] R. Meservey and P. M. Tedrow, *Physics Reports* **238**, 173 (1994).
[2] V. T. Petrashov, V. N. Antonov, S. Maksimov and R. Shaikhaidarov, *JETP Lett.* **59**, 551 (1994).
[3] M. Giroud, H. Courtois, K. Hasselbach, D. Mailly and B. Pannetier, *Phys. Rev. B* **58**, 11872 (1998).
[4] V.T. Petrashov et al, in press.
[5] S. K. Upadhyay, A. Palanisami, R. N. Louie and R. A. Burman, *Phys. Rev. Lett.* **81**, 3247 (1998).
[6] M. Johnson, *Phys. Rev. Lett.* **70**, 2142 (1993).
[7] M. Tinkham, *Introduction to Superconductivity*, 2nd edition, 1996.

7th Int. Symp. "Nanostructures: Physics and Technology"
St Petersburg, Russia, June 14–18, 1999

Transport properties of InAlAs/InGaAs/InP graded channel pseudomorphic high electron mobility structures

N. A. Maleev†, A. E. Zhukov†, A. Yu. Egorov†, A. R. Kovsh†, V. M. Ustinov†, P. S. Kop'ev†, Y. Wu‡, R. Zhang‡ and S. F. Li‡

† Ioffe Physico-Technical Institute, St Petersburg, Russia

‡ Hebei Semiconductor Research Institute, 050051, Shijiazhuang, P.R.China

Pseudomorphic $In_{0.52}Al_{0.48}As/In_xGa_{1-x}As$ heterostructures on InP (with $x > 0.53$) have emerged as excellent candidates for high-frequency field effect transistors [1]. The influence of the indium content and the channel thickness on the carrier concentration and mobility of PHEMT structures with constant In concentration has been investigated by several authors (for reference see [1]). For example, Drouot *et al.* [2] reported the electron mobility as high as $15000\,cm^2/V \cdot s$ for the carrier concentration of $2.4 \times 10^{12}\,cm^{-2}$ at 300 K for $InAlAs/In_{0.75}Ga_{0.25}As$ structures with a 10-nm wide channel. Another possible approach to design pseudomorphic HEMT structures is based on graded $In_xGa_{1-x}As$ channel [3]. That structure demonstrated, for instance, the electron mobility of $12700\,cm^2/V \cdot s$ for the carrier concentration of $3.0 \times 10^{12}\,cm^{-2}$ at 300 K.

In the present study we study the effect of the composition profile of graded $In_xGa_{1-x}As$ channel on the electron mobility. We also investigated the influence of the buffer layer on transport properties and effect of InGaAs cap layer on the results of Hall measurements.

Experimental samples were grown using a Riber 32P MBE system. The substrates were semi-insulating "epi-ready" InP(100) wafers. All the samples were grown at $500° \pm 5°C$. Lattice-matched InGaAs was used as a buffer layer for the most of structures. While an InAlAs buffer layer is typically used in InAlAs/InGaAs HEMT structures, the alternative way is to use InGaAs or InP buffer [4]. To eliminate the effect of shunting conductivity through the barrier layer, no heavily doped cap InGaAs layer was grown in the most of the structures. The thickness of the InAlAs spacer layer (4 nm) and the sheet concentration of Si atoms in δ-layer ($4 \times 10^{12}\,cm^{-2}$) were chosen to achieve the concentrations in the channel of about $2.5 \times 10^{12}\,cm^{-2}$. Hall measurements were performed on square samples using the Van der Pauw technique.

The general scheme of the investigated heterostructures is shown in Fig. 1. All graded channel structures have nearly the same compositional profile of the channel consisting of the flat part with the maximal InAs mole fraction of 0.72 with the thickness L_{flat} sandwiched between two gradient parts ($x = 0.53 \div 0.72$) with the thickness L_{grad}. Varying the values of L_{flat} and L_{grad} results in different shapes of the channel profile from pure rectangular to triangular (V-shaped).

The Hall results obtained for standard lattice-matched, pseudomorphic and graded channel pseudomorphic structures are given in Table 1. The maximal mobility observed in the lattice-matched HEMT structure was $9330\,cm^2/V \cdot s$ (sample A), whereas the use of the pseudomorphic channel allowed us to increase it up to $11700\,cm^2/V \cdot s$ (sample F).

The main difference between the graded channel and conventional pseudomorphic HEMTs is that the two-dimensional electron gas (2DEG) of graded channel structures is mostly centered in the region with higher In concentration and effectively shifted from the heterointerface. As a result of the increased separation between the 2DEG and the

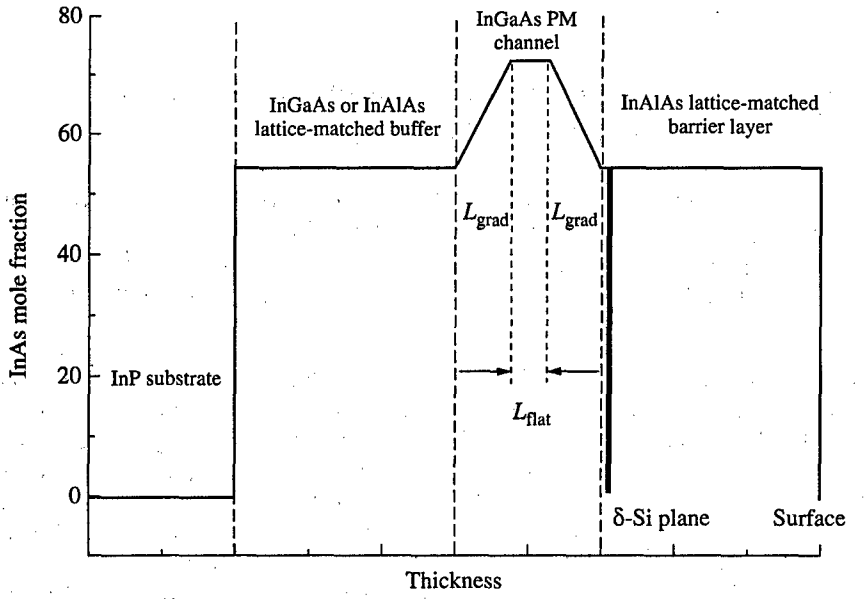

Fig. 1. Compositional profile of the investigated heterostructures.

Table 1. Structures specific parameters and the results of Hall measurements (300 K).

Sample	Channel shape	L_{grad}, nm	L_{flat}, nm	⟨L⟩, nm	Δ, nm	Buffer thickness	μ, $cm^2/V \cdot s$	n_s, 10^{12} cm^{-2}
A	Lattice-matched	—	—	—	—	250 nm	9330	2.45
B	V-shaped	10.2	0	10.2	10.2	230 nm	11900	2.49
C	V-shaped	10.2	0	10.2	10.2	50 nm	12400	2.60
D	U-shaped	8.7	3.7	12.4	10.6	230 nm	12800	2.53
E	U-shaped	4.4	8.3	12.7	8.6	50 nm	11000	2.64
F	Rectangular	0	13.6	13.6	6.8	50 nm	11700	2.44
G	U-shaped + cap layer	8.7	3.7	12.4	10.6	50 nm	9420	3.52

InAlAs/InGaAs heterointerface both the Coulomb scattering and the scattering due to heterointerface roughness are reduced. All graded channel structures demonstrate the mobility higher than 11000 $cm^2/V \cdot s$. It is clearly seen from Table 1 that increase in the mobility well correlates with the increase in the effective separation from the interface $\Delta = L_{flat}/2 + L_{grad}$ and the effective thickness of the pseudomorphical channel $\langle L \rangle = L_{flat} + L_{grad}$ (keeping the channel thickness below the critical layer thickness). The optimal channel structure demonstrates the electron mobility as high as 12800 $cm^2/V \cdot s$ for the carrier concentration of 2.53×10^{12} cm^{-2} (sample D) which is among the best results ever reported for PHEMT structures.

Co-existence of two conducting paths associated with 2DEG and incompletely depleted δ-layer results in the well known reduction in Hall mobility as compared to that expected for the pure channel conductivity. However, the effect of heavily doped InGaAs cap layer is usually underestimated because the application of this cap layer leads also to strong

decrease in the height of surface potential. We investigated the effect of the cap layer on the Hall measurement results. PHEMT structure G has the same design as D but, in addition, the 7-nm InGaAs cap layer heavily doped with Si (4×10^{18} cm^{-3}) was grown on the top. In our structures the typical sheet channel concentration from Hall measurements is $(2.4 \div 2.8) \times 10^{12}$ cm^{-2}. The appearance of some parallel conductivity through the barrier layer in the structure with cap n^+ layer results in increase in the measured Hall sheet concentration from 2.53×10^{12} to 3.52×10^{12} cm^{-2} and decrease in the measured Hall mobility from 12800 to 9400 cm^2/V · s (samples D and G, respectively).

Most of device-oriented structures are based on an InAlAs buffer layer since the use of InGaAs leads to insufficient pinch-off characteristics due to spreading of the channel electrons over this InGaAs buffer layer. However, this problem can be effectively overcome by strong reduction of the thickness of InGaAs buffer. In this case the potential barrier at the interface of semi-insulating InP substrate prevents electron spreading.

To study the effect of the buffer layer thickness, several HEMT structures were grown on very thin (50 nm) InGaAs buffer layer. The comparison shows that the thickness of the InGaAs buffer layer can be reduced from 230 nm to at least 50 nm with no pronounced effect on concentration in the channel. At the same time, the mobility increases slightly, most probably due to the elimination of the effects of small lattice mismatch and better carrier localization in the region with high In composition.

In conclusion, we studied the effect of the composition profile of pseudomorphic channel on transport properties of InGaAs/InAlAs structures. The increase in the effective separation of 2DEG from the heterointerface and the channel thickness was shown to be the key point to achieve the maximal mobility. The possibility to achieve excellent transport properties in structures with very thin InGaAs buffer layer is shown.

References

[1] *Compound semiconductor electronics: the age of maturity*, Ed. M. Shur, World Scientific, 1996.

[2] V. Drout, M. Gendry, C. Santinelli, X. Letartre, J. Tardy, P. Viktorovitch, G. Hollinger, M. Ambri and M. Pitaval, *IEEE Trans. Electron. Dev.* **TED-43**, 1326–1335 (1996).

[3] K. B. Chough, C. Caneau, W.-P. Hong and J.-I. Song, *IEEE Electron. Dev. Lett.* **EDL-15**, (1994).

[4] Y. F. Yang, C. C. Hsu and E. S. Yang, *Electron. Lett.* **30**, 1894–1895, (1994).

7th Int. Symp. "Nanostructures: Physics and Technology"
St Petersburg, Russia, June 14–18, 1999

Coulomb drag in double layer systems with correlated disorder

I. V. Gornyi†, A. G. Yashenkin‡ and D. V. Khveshchenko§
† Ioffe Physico-Technical Institute, St Petersburg, Russia
‡ Petersburg Nuclear Physics Institute, Gatchina, St. Petersburg 188350, Russia
§ NORDITA, Blegdamsvej 17, DK-2100 Ø, Copenhagen, Denmark

Abstract. We study the effect of correlations between impurity potentials in different layers on the Coulomb drag in a double-layer semiconductor electron system. It is found that for strongly correlated potentials the drag in the diffusive regime is considerably enhanced as compared to conventional predictions. The appropriate experimental conditions are discussed, and the new experiments are suggested.

Introduction

Over the past decade the frictional drag in double-layer two-dimensional electron systems has been a subject of extensive experimental [1] and theoretical [2, 3, 4] studies. This phenomenon is manifested in the appearance of current I_2 or voltage V_2 in the "passive" layer 2 when the applied voltage V_1 causes the current I_1 to flow in the "active" layer 1. The strength of the drag is characterized by either transconductivity $\sigma_{21} = (I_2/V_1)_{V_2=0}$ or transresistivity $\rho_{21} = (V_2/I_1)_{I_2=0}$, which are related one to another as $\rho_{21} = -\sigma_{21}(\sigma_{11}\sigma_{22} - \sigma_{12}\sigma_{21})^{-1} \approx -\sigma_{21}\sigma_{11}^{-2}$ where σ_{ii} are the intrinsic conductivities of the layers.

In the absence of tunneling, the drag arises due to interlayer momentum transfer mediated by inelastic scattering (mainly, Coulombic) of carriers that belong to different layers. In the conventional theory [2], the carriers in each layer are scattered by their own impurity potentials. As a result, the processes contributing to σ_{21} can be understood in terms of coupling between *independent* thermal density fluctuations in different layers. The phase space available to the thermal excitations is small and limited by energies $\omega < T$. Therefore, the drag effect rapidly vanishes with decreasing temperature. For instance, $\rho_{21} \propto T^2$ ($T^2 \ln T$) in a clean (dirty) normal metal [2] and $\rho_{21} \propto T^{4/3}$ for composite fermions in double-layers of electrons in the half-filled Landau levels [3]. However, the recent experiments [5] have demonstrated that the transresistivity does not vanish at low temperatures.

The picture of independent impurity potentials used in Refs. [2, 3] is well justified in the case of the standard experimental geometry [1], where two Si delta-doped layers (DDLs) are situated on the outer sides of the double quantum well. The DDLs not only serve as the reservoirs supplying carriers but also introduce disorder in the form of a smooth random potential (SRP) of the ionized donors. Moreover, due to the efficient screening the carriers in each quantum well experience only a SRP created by the nearest DDL.

Instead, one can consider an alternative geometry where a single DDL is located in the middle between the two electron layers, so that the SRPs in both layers are almost identical. This setup gives one an opportunity to study a new type of coherent effects in systems with spatially separated carriers. This case is obviously beyond the conventional theoretical description [2, 3].

In the present work we investigate the influence of correlations between the impurity potentials in different layers on the transresistivity. We focus our attention onto the case of a long characteristic time, τ_g, at which the carriers feel the difference between the SRPs in the two layers ($\tau_g \gg \tau_{\rm tr}$, where $\tau_{\rm tr}$ is the transport scattering time in each layer). We show that in this case the drag is strongly enhanced in comparison to the non-correlated situation. This enhancement is due to a possibility of a coherent motion of carriers propagating in different layers and feeling nearly the same random potential. As a result, the effective time of their interaction increases considerably. This gives rise to the new behavior of the transresistivity

$$\rho_{21}^{\rm corr} \simeq -\frac{\pi^4}{24}\frac{\hbar}{e^2}\frac{\ln(T\tau_g)}{(k_{\rm F}d)^4(\kappa l)^2}, \quad \tau_g^{-1} \ll T \ll \tau_{\rm tr}^{-1}, \tag{1}$$

$$\rho_{21}^{\rm corr} \simeq -\frac{\pi^4}{6}\frac{\hbar}{e^2}\frac{(T\tau_g)^2}{(k_{\rm F}d)^4(\kappa l)^2}, \quad T \ll \tau_g^{-1}. \tag{2}$$

Here, $l = v_{\rm F}\tau_{\rm tr}$ is the electron mean free path, $k_{\rm F}$ ($v_{\rm F}$) is the Fermi momentum (velocity), d is the interlayer distance (throughout this paper we assume $l \gg d$), and κ is the Thomas-Fermi momentum. This term yields the dominant contribution to ρ_{21} within the entire experimentally accessible temperature range, provided that the system remains in the diffusive regime, $T \ll \tau_{\rm tr}^{-1}$. We specify the experimental conditions necessary for the observations of the behavior described by Eqs. (1) and (2), and predict a suppression of these regimes by a weak magnetic field.

Calculations

The new correlation effects for the transconductivity are described by diagrams with two electron loops (one current vertex per each), connected not only by the interlayer Coulomb interaction lines but also by the impurity lines combining into the interlayer Diffusons and Cooperons. After the summation over electron frequencies and momenta, the non-zero contribution of these diagrams to the DC transconductivity takes the form

$$\sigma_{21}^{\rm corr} = \frac{4e^2}{\pi\hbar T}\int \frac{D(dq)}{Dq^2 + \tau_g^{-1} + \tau_\varphi^{-1}} \int_0^\infty \frac{d\omega}{\sinh^2\frac{\omega}{2T}} \,{\rm Im}\Psi_c(\mathbf{q},\omega)\,{\rm Im}\Lambda_c(\mathbf{q}.\omega), \tag{3}$$

The quantities Ψ_c and Λ_c are given by

$$\Psi_c(\mathbf{q},\omega) = \psi\left(\frac{Dq^2 - i\omega + \tau_g^{-1} + \tau_\varphi^{-1}}{4\pi T} + \frac{1}{2}\right),$$

$$\Lambda_c(\mathbf{q},\omega) = 2\left[\ln\frac{\varepsilon_0}{T} + \lambda_{21}^{-1} - \Psi_c(\mathbf{q},\omega) + \psi(1/2)\right]^{-1},$$

where ψ is the digamma function, $\varepsilon_0 \propto \varepsilon_{\rm F}$ is the upper energy cutoff, τ_φ is an inelastic phase-breaking time, and λ_{21} is the effective interaction constant:

$$\lambda_{21} = (4\pi^2\nu_{\rm F})^{-1}\langle V_{21}(\mathbf{p}-\mathbf{p}')\rangle_{\mathbf{p},\mathbf{p}'}.$$

Assuming that the screening is strong enough, $\kappa d \gg 1$, and $k_{\rm F}d \gg 1$, one finds $\lambda_{21} \simeq \pi(4k_{\rm F}d\kappa d)^{-1}$.

Evaluation of the integrals in Eq. (3) yields

$$\rho_{21}^{\text{corr}} \simeq -\frac{2\pi^2}{3}\frac{\hbar}{e^2}\frac{1}{(k_F l)^2[\lambda_{21}^{-1} + \ln(\varepsilon_0/T)]^2}\ln\frac{T\tau_\varphi\tau_g}{\tau_\varphi + \tau_g} \tag{4}$$

at $\tau_g^{-1} \ll T \ll \tau_{\text{tr}}^{-1}$, and

$$\rho_{21}^{\text{corr}} \simeq -\frac{8\pi^2}{3}\frac{\hbar}{e^2}\frac{(T\tau_g)^2}{(k_F l)^2[\lambda_{21}^{-1} + \ln(\varepsilon_0\tau_g)]^2} \tag{5}$$

at lower temperatures. These equations constitute our main result. Under realistic experimental conditions (see below) the value of λ_{21}^{-1} is sufficiently large for one to neglect the logarithmic terms in the denominators of Eqs. (4) and (5). Also, since the interlayer decoherence time τ_g is temperature independent, the argument of the logarithmic function in the numerator of Eq. (4) is linear in temperature provided that $\tau_g \ll \tau_\varphi$. Then Eqs. (4) and (5) reduce to Eqs. (1) and (2), respectively.

Discussion and experiments

Now let us compare these equations with the results of the standard theory [2]:

$$\rho_{21}^{\text{conv}} = -\frac{\hbar}{e^2}\frac{\pi^2\zeta(3)}{16}\frac{1}{(k_F d)^2(\kappa d)^2}\left(\frac{T}{\varepsilon_F}\right)^2. \tag{6}$$

We see that at $T \ll \tau_{\text{tr}}^{-1}$ our result exceeds the conventional one: in the interval $\tau_g^{-1} \ll T \ll \tau_{\text{tr}}^{-1}$ the correlation effects lead to the smoother T-dependence, while at $T \ll \tau_g^{-1}$ the prefactor of the T^2-dependence is $(\tau_g/\tau_{\text{tr}})^2$ times greater in our case.

The expression (3) resembles the Maki-Thompson correction to the conductivity of a single-layer system [6]. However, in that case the corresponding processes yield a small correction to the Drude term while in the double-layer system they determine the leading contribution to σ_{21}. Also, in our situation there exists the temperature-independent quantity τ_g resulting in a new behavior at $\tau_g \ll \tau_\varphi$ and $T \ll \tau_g^{-1}$.

The origin of the interlayer decoherence time τ_g can be explained as follows. Consider two coherent electron waves propagating in slightly different random potentials ($u+\delta u$ and $u-\delta u$). After passing through the distance of order of the SRP correlation length a they acquire a random phase difference $\Delta\phi \sim (2\delta u)v_F^{-1}a$. This leads to the electron's phase diffusion with the diffusion coefficient $D_{\text{ph}} = (\Delta\phi)^2 v_F a^{-1}$, and provides a complete loss of phase coherence over the time $\tau_g \sim D_{\text{ph}}^{-1}$.

A perpendicular magnetic field leads to a suppression of the transresistivity, since one has to replace τ_g^{-1} by $\tau_H^{-1} = 4DeH/(\hbar c)$ in Eq. (1) at $\tau_g^{-1} \ll \tau_H^{-1} \ll T$ and in Eq. (2) at $T, \tau_g^{-1} \ll \tau_H^{-1}$.

Now we discuss the experimental conditions under which the above theory applies. For the standard geometry we have found that the condition $\tau_g \gg \tau_{\text{tr}}$ can never be satisfied as long as $\kappa d > 1$. We note, however, that unavoidable substrate roughnesses may lead to the *correlated* interface roughnesses of both quantum wells, thanks to the long-range character of the deformation field. Then in very clean samples where the interface roughness becomes the main scattering mechanism one can expect some coherence of the kind described in this work to occur even in the conventional geometry.

The situation is different for the suggested geometry with a single DDL located *between* the two quantum wells. Introducing a finite width of the DDL δ we find that the condition $\tau_g \gg \tau_{tr}$ can be rewritten as $2(k_F\delta)^2 \ll \min[1, \kappa d]$. For $\kappa \sim 0.02$ Å^{-1}, $k_F \sim 0.015$ Å^{-1}, $\delta \sim 10$ Å, and $d \sim 400$ Å the above criteria are fulfilled, and there exists the regime of temperatures described by Eq. (1). Note that it might be easier to observe this regime in dirty samples (yet with $l \gg d$). For $l \sim 5000$ Å (which implies $\tau_{tr}^{-1} \sim 4$ K and $\tau_g^{-1} \sim 0.2$ K) Eq. (1) yields ρ_{21} of the order of a few mΩs within the entire temperature range $\tau_{tr}^{-1} > T > \tau_g^{-1}$, whereas the conventional theory would predict a rapid decay of the transresistivity from $\rho_{21} \sim 1$ mΩ at $T \sim \tau_{tr}^{-1}$ to $\rho_{21} \sim 3\mu\Omega$ at $T \sim \tau_g^{-1}$.

Acknoledgments

We gratefully acknowledge useful discussions with A. P. Dmitriev, M. I. Dyakonov, V. Yu. Kachorovskii, A. V. Subashiev, and I. Ussishkin. This work has been supported by INTAS Grant No 97-1342, and in part by RFBR and by the Program "Physics of Solid State Nanostructures" (Grant No 1001).

References

[1] P. M. Solomon *et al., Phys. Rev. Lett.* **63**, 2508 (1989); T. J. Gramila *et al., Phys. Rev. Lett.* **66**, 1216 (1991);

[2] A.-P. Jauho and H. Smith, *Phys. Rev. B* **47**, 4420 (1993); K. Flensberg *et al., Phys. Rev. B* **52**, 14761 (1995); A. Kamenev and Y. Oreg, *Phys. Rev. B* **52**, 7516 (1995).

[3] I. Ussishkin and A. Stern, *Phys. Rev. B* **56**, 4013 (1997); Y. B. Kim and A. J. Millis, cond-mat/9611125.

[4] I. Ussishkin and A. Stern, *Phys. Rev. Lett.* **81**, 3932 (1998); F. Zhou and Y. B. Kim, cond-mat/9897321; Y. Oreg and A. Kamenev, *Phys. Rev. Lett.* **80**, 2421 (1998).

[5] M. P. Lilly *et al., Phys. Rev. Lett.* **80**, 1714 (1998).

[6] K. Maki, *Progr. Theor. Phys.* **39**, 897 (1968); R. S. Thompson, *Phys. Rev. B* **1**, 327 (1970); A. I. Larkin, *Pis'ma Zh. Eksp. Teor. Fiz.* **31**, 239 (1980) [*Sov. Phys. JETP Lett.* **31**, 219 (1980)].

7th Int. Symp. "Nanostructures: Physics and Technology"
St Petersburg, Russia, June 14–18, 1999

Quantum transport theory for semiconductor superlattices

P. Kleinert† and V. V. Bryksin‡
† Paul-Drude-Institut für Festkörperelektronik, Hausvogteiplatz 5-7, 10117 Berlin, Germany
‡ Ioffe Physico-Technical Institute, St Petersburg, Russia

Abstract. The Kadanoff–Baym–Keldysh non-equilibrium Green's function technique is used to study quantum transport within the lowest miniband of semiconductor superlattices (SLs) under high-electric fields. Both intra-collisional field effects (ICFEs) and lifetime broadening are taken into account. An inevitable extension of the generalized Kadanoff–Baym ansatz is discussed. The collisional broadening of electro-phonon resonances due to scattering on impurities is calculated. Even if the mean impurity scattering strength is considerably smaller than the miniband width, the oscillatory current anomalies, which result from ICFEs, are completely smeared out.

1 Introduction

If the Bloch frequency $\Omega = eEd/\hbar$ (E is the electric field strength and d the SL period) is larger than some effective scattering rate, $1/\tau$, carriers confined to the lowest miniband are expected to be Bragg reflected before being scattered by phonons or imperfections in the crystal. This gives rise to Bloch oscillations and to the formation of a Wannier–Stark (WS) ladder. The electric field induced WS localization results in non-analytic resonant-type anomalies in the current-voltage characteristic (I–V), known as electro-phonon resonances [1]. Whereas these current anomalies have been observed in narrow band semiconductors, there are no experiments that clearly demonstrate such quantum effects in the SL transport. To resolve this puzzle we develop a quantum transport theory that treats simultaneously electro-phonon resonances as well as scattering induced lifetime broadening.
There is a fundamental problem that arises when the collisional broadening is taken into account within a consequent quantum-mechanical approach. As the eigenenergies of the system are no longer sharp, the electron distribution function depends explicitly on a time variable even for stationary transport problems. This expresses the non-Markovian character of the transport. For a non-degenerate electron gas a solution of the Dyson equation can be searched for by employing the following extended generalized Kadanoff–Baym (KB) ansatz

$$\widetilde{G}^{<}(\boldsymbol{k},t) = -\widetilde{G}^{>}(\boldsymbol{k},t) f\left(\boldsymbol{k} - \frac{e\boldsymbol{E}}{2\hbar} \mid t \mid, t\right), \tag{1}$$

where we introduced the notation

$$\widetilde{G}^{\gtrless}(\boldsymbol{k},t) \equiv G^{\gtrless}\left(\boldsymbol{k} - \frac{e\boldsymbol{E}}{2\hbar}t, t\right), \text{ with } \widetilde{G}^{\gtrless}(\boldsymbol{k},t)^{*} = -\widetilde{G}^{\gtrless}(\boldsymbol{k},-t). \tag{2}$$

$G^{\gtrless}$ are the closed-time path Green's functions. If the collisional broadening plays only a minor role, the explicit time dependence in the distribution function disappears ($f(\boldsymbol{k},t) \to f(\boldsymbol{k})$) and Eq. (1) becomes identical with the well known generalized KB ansatz [2], which has been used in the literature to study quantum transport in semiconductors. Unlike the early KB ansatz, which has fundamental limitations, the generalized KB ansatz is fully

consistent with the dynamical structure of the theory and agrees exactly with results derived from the Liouville equation for the density matrix. This ansatz takes the causality for the time evolution of the particle propagator properly into account and follows unambiguously from the symmetry properties of the electron system in an external electric field. If, however, lifetime broadening becomes important, the generalized KB ansatz no longer solves the kinetic equation and one has to determine a distribution function $f^{\gtrless}(\boldsymbol{k} - e\,\boldsymbol{E} \mid t \mid/2\hbar, t)$ that depends explicitly on a time variable. This leads to additional complications because a closed equation cannot be derived for the distribution function $f^{\gtrless}(\boldsymbol{k}, t = 0)$ which is used to calculate the current density.

In this paper we will study the damping of electron-phonon resonances in the SL transport. We will show below that such resonances survive only when the lifetime broadening is extremely small. In this case $f(\boldsymbol{k}, t)$ is nearly independent of t and the kinetic equation simplifies accordingly.

2 Numerical results and discussion

We consider a simple tight-binding energy band of the SL

$$\varepsilon(\boldsymbol{k}) = \varepsilon(\boldsymbol{k}_\perp) + \varepsilon(k_z) = \frac{\hbar^2 \boldsymbol{k}_\perp^2}{2m^*} + \frac{\Delta}{2}(1 - \cos k_z d), \tag{3}$$

where m^* is the effective mass and Δ the miniband width. $\widetilde{G}^{>}$ is calculated from the Dyson equation under the condition $G^{<} \sim 0$, which holds true for a non-degenerate electron gas. In quasi-classical approximation and for elastic scattering on impurities we get

$$\widetilde{G}^{>}(\boldsymbol{k}, t) = -i \exp\left[\frac{i}{\hbar}\int_{-t/2}^{t/2} d\tau\varepsilon\left(\boldsymbol{k} - \frac{e\,\boldsymbol{E}}{\hbar}\tau\right) - s(\varepsilon(\boldsymbol{k}_\perp)) \mid t \mid\right], \tag{4}$$

where the damping function $s(\varepsilon)$

$$s(\varepsilon) = \frac{m^* u^2}{\pi^2 \hbar \Delta d}\int_{\max(0,\varepsilon-\Delta)}^{\varepsilon+\Delta} d\varepsilon' K\left(\sqrt{1 - \left(\frac{\varepsilon - \varepsilon'}{\Delta}\right)^2}\right), \tag{5}$$

is proportional to the scattering strength u^2. K is the complete elliptic integral of the first kind. The current density is calculated from the stationary electron distribution function, which is the solution of a kinetic equation. Integrating by parts, we obtain

$$j_z = -\frac{e}{\hbar V}\sum_{\boldsymbol{k}} \varepsilon(k_z)\frac{\partial f(\boldsymbol{k}, t = 0)}{\partial k_z}, \tag{6}$$

where V is the volume of the crystal. The collision integral can be introduced in Eq. (6) when $\partial f(\boldsymbol{k}, 0)/\partial k_z$ is replaced by the right-hand side of the kinetic equation. In the case of high electric fields and weak scattering ($\Omega\tau > 1$) we get

$$j_z = \frac{e m^* n_s \omega_0^2 \Gamma}{2\pi\hbar^4 k_B T d}\frac{1}{1 - e^{-\beta}}\sum_{l=-\infty}^{\infty}\frac{1}{\pi}\int_0^\pi dz\, l J_l^2\left(\frac{\Delta}{\hbar\Omega}\sin z\right)\int_0^\infty d\varepsilon d\varepsilon' e^{-\varepsilon'/k_B T}$$

$$\times\left\{\frac{s(\varepsilon, \varepsilon')}{(l\Omega + (\varepsilon' - \varepsilon)/\hbar - \omega_0)^2 + s(\varepsilon, \varepsilon')^2} + \frac{e^{-\beta} s(\varepsilon, \varepsilon')}{(l\Omega + (\varepsilon' - \varepsilon)/\hbar + \omega_0)^2 + s(\varepsilon, \varepsilon')^2}\right\}, \tag{7}$$

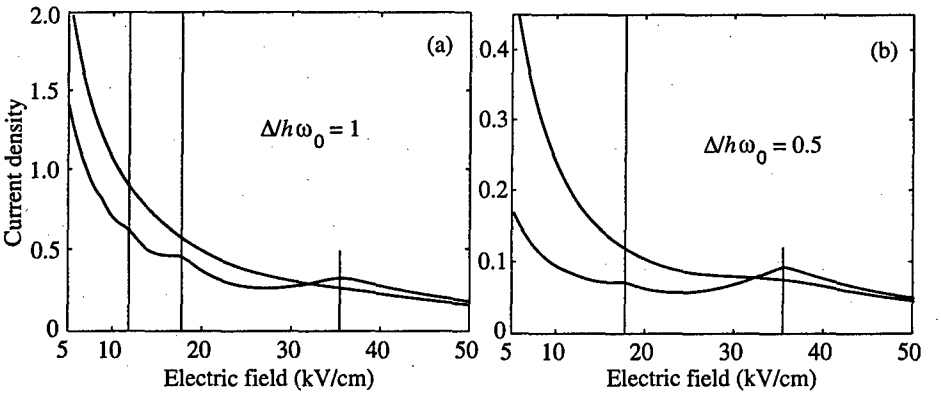

Fig. 1. (a) Field dependence of the dimensionless current density j_z/j_{z0} with $j_{z0} = em^*n_s\omega^2\Gamma/2\pi\hbar^3 d$ for $\Delta/\hbar\omega_0 = 1$ and $\hbar\omega_0/k_BT = 5$. The scattering strength parameter $m^*u^2/\pi^2\Delta d$ is given by 0.005 and 0.05 for the solid and dashed line, respectively.
(b) The same as in (a) for $\Delta/\hbar\omega_0 = 0.5$.

where the lateral electron distribution function has been replaced by the Boltzmann distribution. n_s is the sheet density, Γ the coupling constant, ω_0 the phonon frequency, $\beta = \hbar\omega_0/k_BT$, and $s(\varepsilon, \varepsilon') = s(\varepsilon) + s(\varepsilon')$.
Within our approach we obtained a broadened Lorentzian energy conservation in Eq. (7). This approximation has the defect that higher and higher energy states become populated because the Lorentz curve falls off only gradually. To avoid this run-away effect the explicit time dependence of the distribution function has to be retained. In our present analytic study, however, we will not address the details of such an analysis, but present some numerical results that reveal already the main features of ICFEs and collisional broadening in the SL transport.

Numerical results calculated from Eq. (7) are shown in Figs. 1 (a) and (b) for $\Delta/\hbar\omega_0 = 1$ and 0.5, respectively. Vertical lines mark the positions of electro-phonon resonances at $E = \hbar\omega_0/led$ with $l = 1, 2, 3$ (for d we used 10 nm). The solid lines have been calculated for the case when the impurity scattering strength is much smaller than the miniband width ($m^*u^2/\pi^2\Delta d = 0.005$). In this case weak current oscillations appear, which, however, are rapidly smeared out, when the impurity strength becomes slightly larger. This is shown by the dashed lines, which have been calculated for $m^*u^2/\pi^2\Delta d = 0.05$. The lifetime broadening effect, obtained from the microscopic model, seems to be larger than phenomenological estimates suggest. This is due to the fact that in Eq. (7) both energy integrals are affected by the damping function $s(\varepsilon)$.
Our numerical results demonstrate that current oscillations, which are due to ICFEs, occur only, when the lifetime broadening is extremely small. This might be the reason, why quantum mechanical current oscillations have not been observed in high-field transport measurements in SLs until now.

In conclusion we believe that our quantum-mechanical approach, which accounts for both ICFEs and collision broadening, can be used to study the stationary transport in other nanostructure devices, too.

References

[1] V. V. Bryksin and Y. A. Firsov, *Sov. Phys. - JETP* **34**, 1272 (1971); [*JETP* **61**, 2373 (1971).]
[2] P. Lipavsky and V. Spicka and B. Velicky, *Phys. Rev. B* **34**, 6933 (1986).

7th Int. Symp. "Nanostructures: Physics and Technology"
St Petersburg, Russia, June 14–18, 1999

Influence of structural transition in metal on charge transport in nanocrystal metal-polymer-metal system

A. N. Lachinov†, T. G. Zagurenko†, V. M. Kornilov† and R. Z. Valiev‡
† Institute of Physics of Molecules and Crystals,
Ufa Research Center, RAS, 450000 Ufa, Russia.
‡ Institute of Physics of Advanced Materials, UGATU,
450000, Ufa, Russia.

The paper presents the results of the investigation of influence of the structural transitions in nanocrystal metals on the electrical conductivity in a nanocrystal metal-polymer-metal system (NM-P-M). The experiment idea was as follows. The structural transitions in the nanocrystal metal induced by a magnification of its grain size at specific temperatures should lead to a modification (decreasing) of the work function ϕ_m. When such a metal is in contact with the electroactive polymer, the change in (m should lead to a change in the polymer space charge and as a result to a change in the charge carrier injection conditions. In the present work the nanocrystal metals (Cu, Ni) were selected as electrodes. The nanocrystal state is nonequilibrum in these metals and the rather small heating to $T \approx 0.4T_{cr}$ gives rise to restoring of the initial structure [1]. The nanocrystal structure was identified by methods of the electronic microscopy and X-ray structure analysis. As it was shown earlier [2], an ultra fine-grained structure is formed in Cu and Ni as a result of the intensive plastic deformation of torsion (IPD). The resulting nanocrystal structure has a size of grains of about 100 nm, high level of the crystal lattice microdistortions, nonequilibrum grain boundaries, high density of the grain-boundary dislocations, increased static and dynamic atomic displacements. During the last years the IPD method was successfully used for obtaining the nanostructures in various metals and alloys [1, 2]. IPD can cause the modification of the material work function on 0.1 eV and more [1, 3]. It was expected, that the heating would induce restoring the initial (m value, which will affect the electrical current in NM-P-M system. The measurements of the current were carried out using the technique described in [4]. As a polymer the films of polyphthalidilidenbiphenylilene (PPB) of about 0.8 μm thick were used. This polymer reveals insulator-metal transition.

Figure 1 shows the temperature dependence of the current I(T) flowing through a NM-P-M system. When the copper is used as NM, the raise in temperature does not change the current up to $T_1 = 145$°C. In the range of temperatures $T_1 = 145$°C–$T_2 = 175$°C $I(T)$ dependence reveals a peak with a maximum at $T_{\max} \approx 160$°C. The similar behavior is observed when the nanocrystal Ni is used as the electrode. In the latter case the maximum of the current is observed at $T_{\max} \approx 215$°C. The similar experiments were carried out using Cu an Ni with equilibrium grain structure instead of nonequilibrium nanocrystal samples. In these experiments the following samples were used:

1. The initial large-grain metal, from which afterwards the nanocrystal samples were obtained.
2. Heat-treated nanocrystal samples. (The samples were treated during 30 min at 500°C, which, as is known [1], completely destroys the nanocrystal structure.) The measurements revealed no temperature singularities in the system conductivity in the investigated tem-

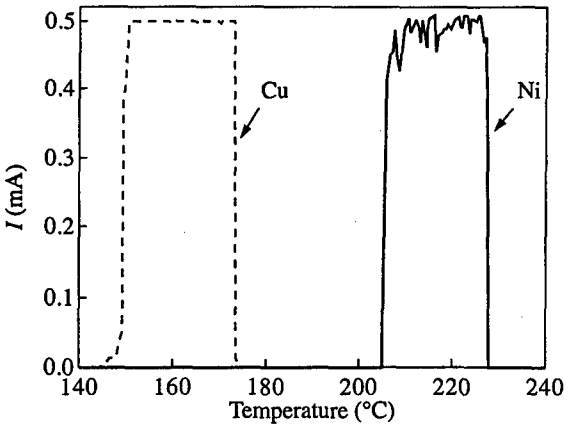

Fig. 1. Temperature dependence of current flowing through the polymer film. Solid line—upper electrode is nanostructural Cu, dashed line—nanostructural Ni. Polymer film thickness 2 μm; lower electrode V; applied voltage 5 V; heating rate 8°C/min.

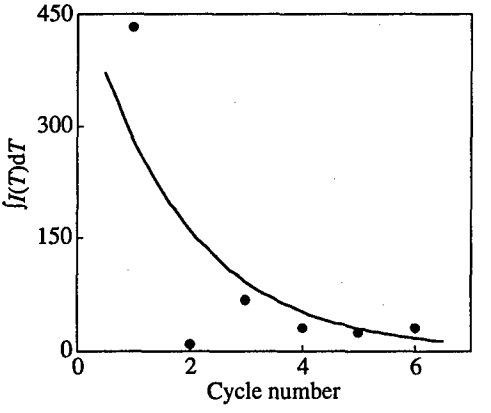

Fig. 2. Integral $I(T)$—cycle number dependence. Film thickness 2 μm; upper electrode—nanostructural Cu; lower electrode V; applied voltage 5 V; heating rate 8°C/min.

perature range. The microstructure evolution of the nanocrystal Cu and Ni during heating was explicitly investigated in papers [3, 5] using mentioned above methods and also using differential scanning calorimetry technique. The results obtained testify to intensive relaxation processes associated with a transformation of the defect structure during low temperature heat-treatment. These processes are observed in the temperature ranges of 100–200°C for Cu and of 180–220°C for Ni. These temperature ranges are close to those, in which mentioned above conductivity peculiarities are detected. It allows us to make a conclusion that the mechanisms initiating these modifications are similar and are caused by the temperature transformation of the microstructure of the metal samples.

Multiple measurements of $I(T)$ dependence on the same sample showed that with the increase in the measurement cycles the decrease in the amount of the charge flowing through the sample is observed down to some minimal value which corresponds to the

current flowing through the sample at room temperature. It, apparently, reflects that fact, that for identical conditions of measurements in multiple cycles, the relative changes in the work function decrease (1,2) as the sample structure approaches equilibrium state. It is necessary to pay attention to some peculiarities of the dependence represented in Fig. 2.
1. During one cycle of heating the sample does not return to the equilibrium state. The full transition occurs during several cycles.
2. As a rule, the maximum characteristic temperature, at which the current singularity is registered, is observed in the first cycles of measurements.
3. With the increase in the number of cycles the downward tendency for the characteristic temperature is observed. Simultaneously the extension of the temperature range occurs, in which the effect is observed. In accordance with (1, 2) in addition to the work function the electrical field should influence the injection current. This influence was estimated by integrating $IU(T)$ on dT in the range of (T_0, T_n) depending on the voltage applied. This integral is proportional to the net charge, passing through the sample in the given temperature range. T_0 and T_n—boundary temperatures of the experimental interval, $IU(T)$—the temperature dependence of the current at voltage U on the electrodes. The analysis of the experimental results showed, that for $U < 0.1$ V the magnitude of the charge flowing through the sample is constant. In the range of voltages of 0.1 V $< U <$ 5 V superlinear increase in the net charge passing through the polymer is observed. Above 5 V the dependence approaches the linear. The similar dependence is observed practically on all samples. The investigations performed indicate, that the use of a thin polymer film of PPB type in M-P-M heterostructure allows to study surface transformations in metal electrodes caused by structural transitions. This method is very sensitive, simple in a realization and consequently can appear rather effective.

The work is supported by grant from RFBR No. 96-02-19208, 98-03-33322.

References

[1] R. Z. Valiev, I. V. Alexandrov and R. K. Islamgaliev, *Processing and Properties of Nanostructured Materials Prepare by Sever Plastic Deformation. Nanostructured Materials* (ed. G. M. Chow and N. I. Noskova), Kluwer Academic Publ., 121 (1998).
[2] R. Z. Valiev, A. V. Korznikov and R. R. Muljukov, *FMM* **6**, 70 (1992).
[3] V. Yu. Gertsman, R. Birringer, R. Z. Valiev and H. Gleiter, *On the Structure and Strength of Ultrafine-grainde Cooper Produced by Sever Plastic Deformation, Ser. Met. Mater.* **30**, 229-234 (1994).
[4] V. M. Kornilov and A. N. Lachinov, *JETP* **111**, (4) 1513 (1997).
[5] R. K. Islamgaliev, F. Chmelik and R. Kuzel, *Mater. Sci. Eng.* **A234**, 335 (1997).

7th Int. Symp. "Nanostructures: Physics and Technology"
St Petersburg, Russia, June 14–18, 1999

Influence of a built-in potential on electron transport properties of metallic ballistic structures, as evidence of quantum-well effect

G. M. Mikhailov†, I. V. Malikov†, A. V. Chernykh†, E. Olsson‡ and L. Ryen§
† Institute of Microelectronic Technology RAS, 142432 Chernogolovka, Moscow District, Russia
‡ Angstrom Laboratory, Uppsala University, Uppsala, Sweden
§ Chalmers University of Technology, Gothenburg, Sweden

When an electron mean free path becomes comparable to or exceeds the structure dimensions, both inner and outer surface electron scattering begins to determine conducting properties of the multilayered structures. Electron conductivity becomes to be characterised by surface dominated electron transport, and differs essentially from that determined by the bulk structure. Under the conditions, when spatial quantisation of electron momentum due to effect of inner and outer surface potentials comes into the play, the new features are introduced into sliding electron transport of both thin films and nanostructures, composed from the metals. It may lead to the properties, that are unusual for metallic conductors. Here, we present the results of electron transport investigation of Mo-Nb ballistic structures and the effect of interface electron scattering, controlled by built-in potential.

Growth and fabrication. Epitaxial growth of Mo and Nb was performed in super high vacuum chamber by step by step laser ablation of the targets from high purity Nb and Mo onto hearted till 750 °C sapphire ($\bar{1}012$) substrate [1]. At first, the Mo film of 35 nm thick was grown, followed by thin Nb interlayer deposition by single laser pulses target ablation, and, finally, deposition of the second Mo layer of 35 nm thick was performed. The XRD and cross sectional TEM were used for characterization of grown tri-layered films. It is seen from the Fig. 1 that the X-ray peaks (002) and (011) of Mo/Nb/Mo and single-layered Mo film are close each other. Cross-sectional TEM investigations do not reveal

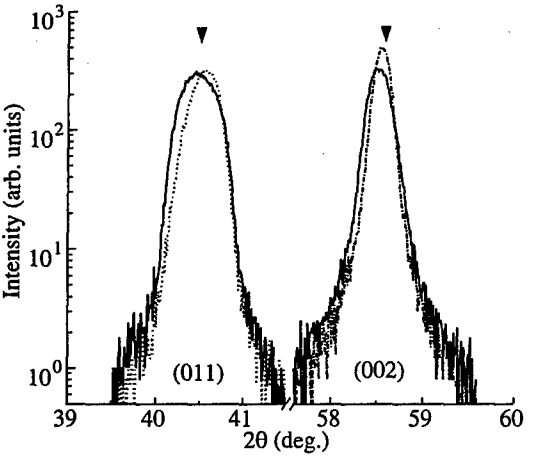

Fig. 1. The XRD $\omega - 2\theta$ scan of peaks (002) and (011) Mo/Nb/Mo film (solid lines), and single layered Mo film (dotted lines). Down triangles show the peak position of the bulk Mo single crystal.

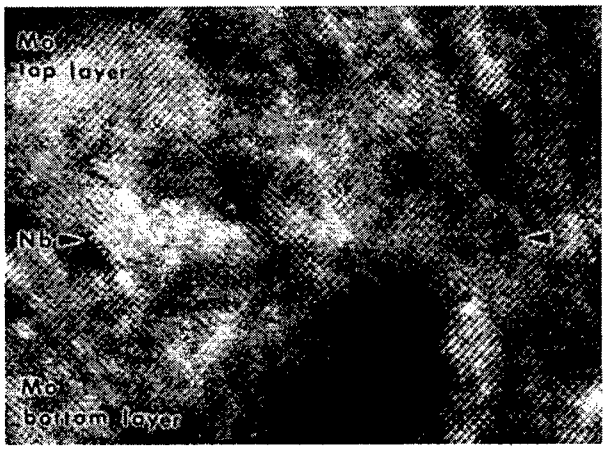

Fig. 2. Cross section of Mo/Nb/Mo film with interlayer Nb thickness in two monolayers. Arrows show Nb minimum of interlayer position. The sample corresponds to the specific resistance oscillation, depicted in Fig. 3 (see text for details).

both distinctive structural defects, associated with thin Nb interlayer, and any difference of the bulk structure between top and bottom Mo layers (Fig. 2). The nanostructures were fabricated down to 200 nm lateral resolution using subtractive electron lithography process, developed earlier [2], additional lithography process was used for Nb leads fabrication.

Electron transport. Specific resistance of tri-layered Mo/Nb/Mo films, determined from lateral electron transport measurements, oscillates upon Nb interlayer thickness with monolayer (0.16 nm) periodicity. It is in effect from room to 9.5 K temperature. The film specific resistance at room temperature differs from that of Mo bulk singlecrystal only in 15%. Min-

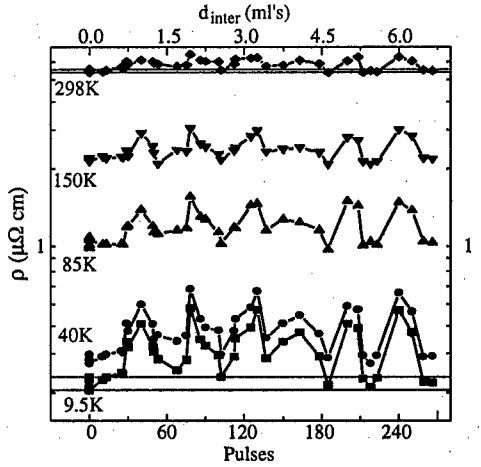

Fig. 3. Specific resistivity of tri-layered Mo(35 nm)/Nb(d)/Mo(35nm) epitaxial films as a function of interlayer Nb thickness (top axis) at the temperatures 298, 150, 85, 40 and 9.5 K. The Nb layer thickness depends on the number of laser pulses during Nb layer growth (bottom axis). Vertical lines are specific resistivity of single layer Mo(001) film of 70 nm thick, defined from controlled experiments.

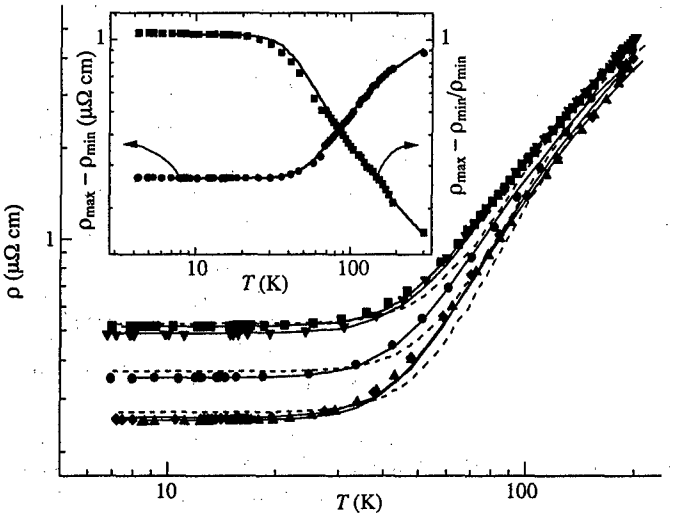

Fig. 4. Temperature dependence of specific resistance in maximum, minimum and in intermediate position of oscillation. (See text for details.)

imum of specific resistivity of tri-layered films corresponds to the Nb thickness with the "half" of each next grown Nb monolayer. It is equal to the specific resistance of single-layered Mo films of 70 nm thick, while for "complete" Nb monolayer growth (maximum) it corresponds to that of Mo single-layered film of 35 nm thick.

Such type behavior is also found in temperature dependence of tri-layered film specific resistance. The amplitude of an oscillation does not exceed more than 15% of specific resistance at 298 K and comes to 100% as the temperature decreases to 9.5 K. Its absolute values are shown in the inserting to the Fig. 4 together with its relative values.

The specific resistance of tri-layered Mo(35 nm)/Nb/Mo(35 nm) films in minimum (diamonds) goes together with that (down triangles) of single-layered Mo film of 70 nm thick and in maximum (squares) with that (up-triangles) of 35 thick. The intermediate values between maximum and minimum (circles) of oscillation are also shown. We used formulae of [3] to fit experimental data, using temperature dependence for bulk mean free path of the film as for bulk Mo single crystal [4] and taking into account both surface scattering and transverse momentum quantisation of sliding electrons [2]. Fitting curves are shown in Fig. 4 and in its inserting as the solid lines. The fitting parameters describe increasing of specific resistivity in each oscillation as an effect of the interface (interlayer) scattering, which we attribute to the built-in potential. Quantum corrections are not small. For comparison we also applied well known effective mean free path model (dashed lines) to fit experimental data. However, it was in lower fitting accuracy. All of these results, together with that of structural characterization (Figs. 1–2) of the films, unambiguously prove that the built-in potential, formed by Nb interlayer, affects on the sliding electron transparency (reflection) through the Nb interlayer, spatial quantisation of transverse electron momentum is important too.

As it will be seen below, the effect of built-in potential is also significant for electron transport through the contact between the strips of nanometer scale. Figure 5 presents the volt-current (V–I) characteristics of the cross type nanostructure composed of epitaxial Mo and disordered Nb strips. The unusual for metals diode effect, appearing as an asymmetric V–I curve, was found. It depends on the temperature and mean free path (m.f.p.) of

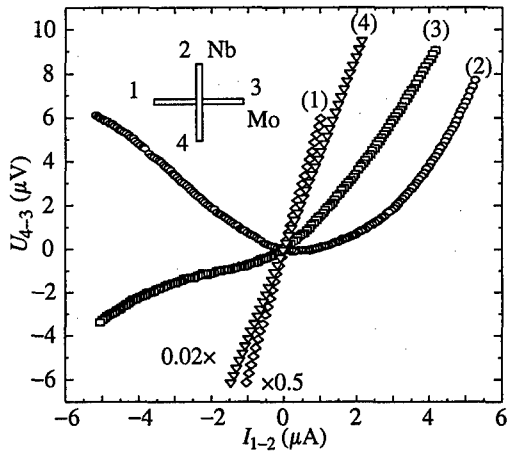

Fig. 5. Bending volt-current characteristic for asymmetric Mo (001)-Nb cross nanostructure with the 400 nm lead width, measured above superconducting transition. Diamonds (1)-Mo strip with effective residual m.f.p. $L_{\text{eff}} \sim 550$ nm at $T = 298$ K, Circles (2)—Mo with $L_{\text{eff}} \sim 550$ nm at $T = 9.5$ K, Squares (3)—Mo with $L_{\text{eff}} \sim 170$ nm at $T = 9.5$ K, Up triangles (4)—Mo with $L_{\text{eff}} \sim 60$ nm at $T = 9.5$ K.

electrons in the epitaxial Mo strip.

We consider the diode effect to be due to the dependence of an electron transparency through the contact area, controlled by built-in contact potential between Mo and Nb strips, both on the direction and the magnitude of the current, passing through the contact area.

New types of metallic low-dimensional structures fabricated on the basis of high-quality epitaxial refractory-metal films possess new properties that are unusual for metallic conductors. It can be attributed to the realisation of the ballistic limit in electron transport leading to sliding electrons come into play and a spatial quantisation of an electron momentum is important. Under this condition, the scattering of conducting electrons is controlled also by the properties of the built-in potential. It gives rise to new phenomena in electron transport of metallic conductors associated with this mechanism.

References

[1] I. V. Malikov and G. M. Mikhailov, *J. Appl. Phys.* **82**, 5555 (1997).

[2] G. M. Mikhailov, L. I. Aparshina, S. V. Dubonos, Yu. I. Koval, I. V. Malikov and A. V. Chernykh, *Nanotechnology* **9**, (1) 1 (1998).

[3] G. M. Mikhailov, I. V. Malikov and A. V. Chernykh, *Pis'ma JETP* **66**, 693 (1997).

[4] N. V. Volkenstine, L. S. Starostina, V. E. Startsev and E. P. Romanov, *Fiz. Met. & Metal.* **18**, 888 (1964).

7th Int. Symp. "Nanostructures: Physics and Technology"
St Petersburg, Russia, June 14–18, 1999

Low flicker noise GaN/AlGaN heterostructure field effect transistors with submicrometer channel

S. Morozov, A. Balandin†, S. Cai†, R. Li†, Yu. Dubrovskii, K. L. Wang†, G. Wijeratne† and C. R. Viswanathan†
Institute of Microelectronics Technology RAS,
142432 Chernogolovka, Russia
† Electrical Engineering Department, University of California-Los Angeles
Los Angeles, California 90095-1594

1 Introduction

Recently, wide bandgap compound semiconductors demonstrated potential for high frequency and high power density device applications. These materials offer several inherent advantages, such as higher breakdown voltage, higher thermal conductivity, comparable carrier mobility, and high saturation velocity. GaN is among those which show a great promise for microwave applications.

Development of high performance microwave technology requires detailed knowledge of the noise behavior of the devices. Particularly, it is important to know the value of flicker noise, e.g. $1/f$ noise, since this type of noise is the limiting figure for all kinds of HEMTs and MOSFETs.

In this paper we report investigation of $1/f$ flicker noise in GaN/$Al_{0.15}Ga_{0.85}N$ doped channel heterostructure field effect transistors (referred as GaN HFET).

2 Device structure and measurements

The layered structure was fabricated by MBE on a sapphire substrate. A 1.0 μm thick i-GaN buffer layer was followed by 50 nm thick n-GaN layer with the doping level of 5×10^{17} cm^{-3}, and 3 nm thick i-$Al_{0.15}Ga_{0.85}N$ undoped spacer layer. On top, there was 30 nm thick $n-Al_{0.15}Ga_{0.85}N$ layer with the doping level of 2×10^{18} cm^{-3}. The barrier and channel doping resulted in a sheet electron concentration of about 1.6×10^{13} cm^{-2}. Electron Hall mobility was determined to be 460 cm^2/Vs at room temperature.

Devices selected for this study had a fixed gate length $L_G = 0.25$ μm. A device with $L_{DS} = 3$ μm had the drain current $I_{DS} = 0.55$ A/mm at the gate bias $V_{GS} = -3.0$ V. The maximum transconductence (for negative gate biases) was $g_m = 102$ mS/mm (at $V_{GS} = -5$ V). A device with $L_{DS} = 2$ μm had the maximum transconductence (for negative gate biases) $g_m = 133$ mS/mm at $V_{GS} = -3$ V ($L_G = 0.25$ μm).

We have examined a large number of devices with the gate width $W = 2 \times 40$ μm, and four different source — drain separation distances $L_{SD} = 2$; 3; 4; and 5 μm. All examined devices were made on the same wafer. For these devices we obtained experimental dependence of the equivalent input referred noise power spectrum on frequency, gate and drain voltages. The measurements were carried out for both the linear region of the device operation corresponding to low drain-source voltage, V_{DS}, and the onset of the saturation region of operation (subsaturation) corresponding to $V_{DS} = 5$ V.

The slope ν of the $1/f^{\nu}$ dependence in all spectra is very close to 1, although varies for

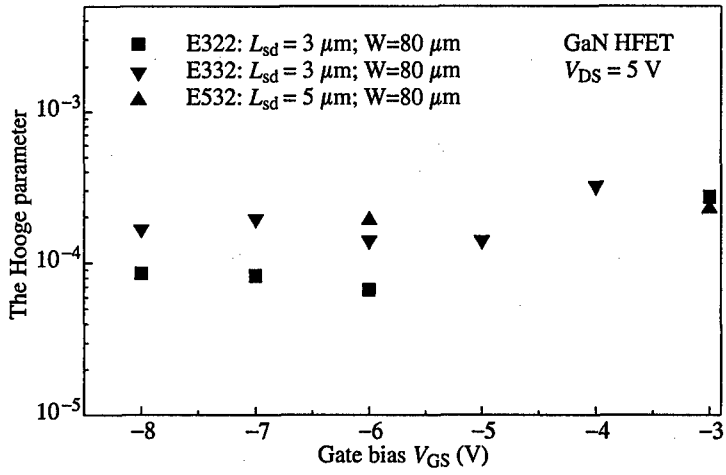

Fig. 1. Hooge parameter α_H as a function of the gate bias. The results are shown for three devices biased at $V_{DS} = 5$ V. The gate dimensions are 0.25 μm × 80 μm.

different devices and gate bias values. We did not observe any clear trace of the generation-recombination ($g - r$) bulges in the noise spectra.

The equivalent input-referred noise spectral density was obtained from the drain current noise spectral density using the regular relation

$$S_{V_{eq}} = \frac{S_{I_D}}{g_m^2}, \tag{1}$$

where $S_{V_{eq}}$ is the equivalent input-referred noise spectral density, S_{I_D} is the drain current noise spectral density, and g_m is the transconductance of the device.

At relatively small absolute values of the gate bias $|V_{GS}|$, the noise spectral density S_V is gate bias dependent, and decreasing with a higher negative bias. At high absolute values of the gate bias when the channel is almost pinched off, the noise density is about the same for different values of V_{GS}. This type of behavior was characteristic for all examined transistors.

In order to have quantitative characteristic of the overall noise in the device, we use the Hooge parameter α_H [1] introduced via the equation

$$\frac{S_{I_D}}{I_D^2} = \frac{\alpha_H}{Nf}, \tag{2}$$

where f is the frequency, N is the total number of carriers under the gate calculated from the drain-source current at which the noise was measured. The number of carriers in homogeneous samples can be expressed as

$$N = \frac{L^2}{Re\mu}. \tag{3}$$

Here μ is the mobility in the conducting channel, R is the resistance between two device terminals, and L is the channel length. Two quantities (R and μ) in Eq. (3) are determined

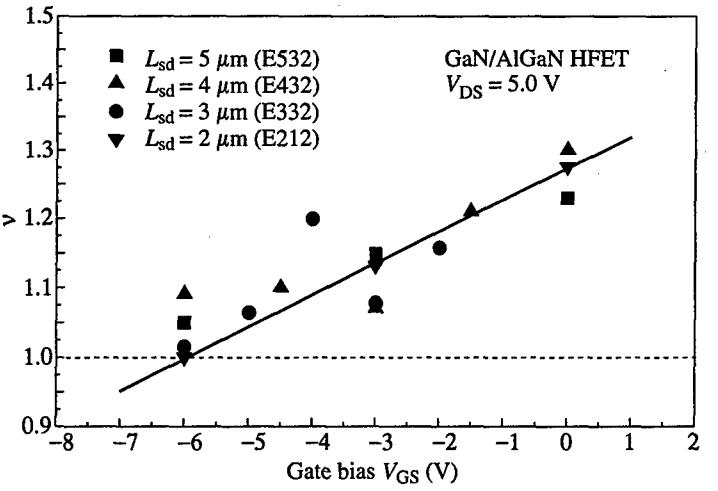

Fig. 2. Dependence of the exponent ν of the $1/f^{\nu}$ noise power density on the gate bias. The results are shown for four devices with different L_{DS}. All four devices are biased at $V_{DS} = 5$ V. The exponent ν approaches 1 with more negative bias.

experimentally. The resistance is found at a given V_{DS} during the noise measurements, while the mobility is determined for the layered structure using the Hall measurements. The gate leakage current for the devices was small (less then 1%), and hence its effect on their noise performance was neglected. Finally, the Hooge parameter was calculated using Eqs. (1)–(3) for different devices and bias points. The results for $V_{DS} = 5$ V are given in Fig. 1. Despite some variations of the of the α_H parameter values, they are all close to 10^4. It is also seen that α_H almost does not depend on the gate bias. For all examined values of L_{DS}, the Hooge parameter was in the same range and did not show any clear trend. Based on this, we concluded that the source — distance separation does not strongly affect low-frequency noise performance of GaN HFETs.

One should note that the Hooge parameter α_H in our analysis was used as a figure of merit for purpose of comparison with other published results, and was not intended to suggest the mobility fluctuation model and not carrier density fluctuation noise model for our devices [2].

In an attempt to clarify the origin of the low-frequency noise in our devices, we extracted the exponent ν of the $1/f^{\nu}$ noise power density for all examined devices and studied its gate bias dependence. The ν vs. V_{GS} dependences are shown in Fig. 2 for four devices with different L_{DS}. All four devices are biased at $V_{DS} = 5$ V. One can see that ν is in the range of $1.0 < \nu < 1.3$ and decreases with increasing (more negative) gate bias. Such a dependence of the magnitude of the $1/f^{\nu}$ noise spectral density can be most easily interpreted in terms of the modified carrier density fluctuation model [3] which is an extension of the well-established McWhorter formalism. The modified carrier-density fluctuation model explains the liner dependence of the exponent ν on the gate bias by the nonuniformity of the trap distribution. The argument is that trap density across the band gap varies with energy, and the band bending with increasing gate voltage will change the number of effective traps, and thus the time constants contributing to $1/f^{\nu}$ noise. Since the quality of GaN/AlGaN heterojunctions remains rather poor, we expect a lot of imperfections (traps) nonuniformly

distributed both in energy and space. Due to this reason, the above interpretation of the pronounced ν dependence on the gate bias seems very realistic.

Conclusions

We have carried out a detailed investigation of the low-frequency noise characteristics of GaN HFETs grown on sapphire substrate. Our results indicate that the average value of the Hooge parameter α_H of GaN HFETs is on the order of 10^{-4}. This low value of the $1/f$ noise is comparable to the noise level in conventional GaAs FETs. The latter indicates possibility of the use of microwave GaN HFETs in communication systems, particularly those requiring high power density and high temperature operation. The presented results also allow to model the noise response of the devices for different gate and drain biases and device geometrical dimensions.

This work was, in part, supported by the DoD MURI-ARO program on "Low-Power/Low-Noise Electronic Technology for Mobile Communications" and by CRDF-RFBR (Grant RP1-220).

References

[1] F. N. Hooge, T. G. M. Kleinpenning and L. K. J. Vandamme, *Rep. Prog. Phys.* **44**, 479 (1981).
[2] L. K. J. Vandamme, *Solid State Electron.* **23**, 317 (1980).
[3] Z. Celik-Butler and T. Y. Hsiang, *Solid State Electron.* **30**, 419 (1987).

7th Int. Symp. "Nanostructures: Physics and Technology"
St Petersburg, Russia, June 14–18, 1999

Influence of a magnetic field on the Coulomb drag between quantum wires in the ballistic regime

O. E. Raichev† and *P. Vasilopoulos*‡
† Institute of Semiconductor Physics, Pr. Nauki 45, 252650, Kiev, Ukraine
‡ Concordia University, Physics Department, 1455, de Maisonneuve Blvd W., H3G 1M8, Montreal, Canada

Abstract. The influence of a magnetic field H on the Coulomb drag between quantum wires is studied theoretically for low temperatures, when the electron motion along the wires is nearly ballistic. A considerable decrease of the drag transresistance is found as a result of the suppression of backscattering in electron-electron collisions at $H \sim 1$ T.

Introduction

The Coulomb drag in spatially separated low-dimensional electron systems has received a great deal of attention and has nearly developed into a separate field; a recent review is found in Ref. [1]. In particular, the drag between quantum wires was studied theoretically [2] assuming scattering of the carriers, e.g., by impurities. It is however, difficult to check experimentally these results in microstructural samples because the actual double-quantum-wire systems [3] are normally shorter than 1 μm and electron transport there is either ballistic or mesoscopic.

Recently, Gurevich *et. al.* [4], demonstrated the possibility of the drag effect in the regime in which most of the electrons travel through the wire ballistically. However, a few of the electrons experience backscattering due to the interaction with the electrons of the other wire, and this modifies the time-averaged distribution functions in such a way that the drag effect appears. Such a ballistic Coulomb drag (BCD) has not yet been observed experimentally. However, further theoretical studies of the BCD are important because they would bring new information and thereby stimulate experimental work in this new area. In this paper we investigate the effect of a magnetic field H applied perpendicular to the plane of the wires on the BCD. The backscattering processes, which are essential for the drag effect to appear, are suppressed by the magnetic field because the spatial overlap between the forward- and backward-propagating electron states decreases as the states tend to localize near the opposite edges of each wire. For this reason, we claim that the BCD will be suppressed and our aim is to study this suppression quantitatively.

Below we present the double-quantum-wire model and derive a general expression for the drag transresistance ρ_D. Then we give the numerical results for the magnetic-field dependence of ρ_D and a brief discussion.

1 General formalism

We use a model of a four-terminal double-quantum-wire system, similar to those investigated in the "directional coupler" problem [3]. Two closely spaced quantum wires (numbered 1 and 2) with parabolic confinement along the y direction are contacted independently to four leads at $x = -L/2$ and $x = L/2$, where L is the length of the wires. The leads

have potentials $v_1(\pm L/2) = v_{1\pm}$, and $v_2(\pm L/2) = v_{2\pm}$. Applying the bias $v_{2-} - v_{2+}$ to the leads of wire 2 (drive wire) we obtain the current I flowing through wire 2; this current induces a voltage $v_{1-} - v_{1+}$ in wire 1 (drag wire). This is the typical setup for drag measurements [1]. We assume that the barrier between the wires is high enough to allow the neglect of tunneling.

The wave functions $\Psi_{jnk}(x, y) = e^{ikx}\chi_{jnk}(y)$ (n is the Landau-level number, $j = 1, 2$, and k is the wave vector) of electrons, confined by the potentials $U_j = \varepsilon_j^0 + m\Omega_j^2(y - y_j)^2/2$ in the presence of a perpendicular magnetic field H, are given by $\chi_{jnk}(y) = (\pi^{1/2}\ell_j 2^n n!)^{-1/2} H_n((y - Y_j)/\ell_j)) \exp(-(y - Y_j)^2/2\ell_j^2)$. The corresponding spectrum $\varepsilon_{jn}(k)$ (spin splitting is neglected) reads

$$\varepsilon_{jn}(k) = \varepsilon_j^0 + \hbar\omega_j(n + 1/2) + (\hbar^2/2m_j)(k - y_j/\ell_c^2)^2, \tag{1}$$

Here $\omega_j^2 = \omega_c^2 + \Omega_j^2$, $\omega_c = eH/mc$ is the cyclotron frequency $m_j = m\omega_j^2/\Omega_j^2$, $\ell_c = \sqrt{\hbar/m\omega_c}$ is the magnetic length, $\ell_j^2 = \hbar/m\omega_j$, and $Y_j = [\Omega_j^2 y_j + \hbar\omega_c k/m]/\omega_j^2$ are the positions of the centers of the oscillators. Since we do not consider electron transitions between the wires, we will shift the wave vectors $k - y_1/\ell_c^2 \to k$ for wire 1 and $k - y_2/\ell_c^2 \to k$ for wire 2. Then the centers of the oscillators will read $Y_j = y_j + (\hbar\omega_c/m\omega_j^2)k$. We also assume that only the lowest Landau levels of both wells are populated ($n = 0$) and omit the index n.

If the distribution functions $f_{jk}(x) \equiv f_{jk}$ change over distances much longer than both the electronic wavelength π/k and the characteristic radius of the interaction potential, we can write the Boltzman kinetic equations as

$$\frac{\hbar k}{m_j}\frac{\partial f_{jk}(x)}{\partial x} = -\frac{4\pi}{\hbar}\sum_{j'k'q}\left|M_{kk'q}^{jj'j'j}\right|^2 \delta(\varepsilon_{jk} + \varepsilon_{j'k'} - \varepsilon_{j,k-q} - \varepsilon_{j',k'+q})$$
$$\times[f_{jk}(1 - f_{j,k-q})f_{j'k'}(1 - f_{j',k'+q}) - f_{j,k-q}(1 - f_{jk})f_{j',k'+q}(1 - f_{j'k'})]. \tag{2}$$

where the collision integrals account only for electron-electron scattering. The Coulomb matrix elements $M_{kk'q}^{jj'j'j}$ are given by

$$M_{kk'q}^{jj'j'j} = \frac{2e^2}{\kappa}\int dy \int dy' K_0(|q||y - y'|)\chi_{jk}(y)\chi_{j'k'}(y')\chi_{j'k'+q}(y')\chi_{jk-q}(y). \tag{3}$$

Here κ is the dielectric constant and K_0 is the modified Bessel function. In the one-dimensional case the intrawire ($j = j'$) part of the collision integral vanishes due to the restriction $q = k - k'$ following from the energy conservation law in Eq. (2). The exchange part (not written in Eq. (2)) vanishes for the same reasons.

It is convenient to write separately the distribution functions for the forward- and backward-moving electrons as $f_{j|k|}^{>} = f_{jk}|_{k>0}$ and $f_{j|k|}^{<} = f_{jk}|_{k<0}$, respectively. For these functions the boundary conditions are given in the Landauer-Buttiker approach by $f_{jk}^{>}(-L/2) = f(\varepsilon_{jk} - e\delta v_{j-})$ and $f_{jk}^{<}(L/2) = f(\varepsilon_{jk} - e\delta v_{j+})$, where $\delta v_{j\pm} = v_{j\pm} - v$, v is the equilibrium potential, $f(\varepsilon) = [e^{(\varepsilon - ev)/T} + 1]^{-1}$, and T is the temperature. For $j = 1$ and $j = 2$, Eq. (2) gives two coupled kinetic equations, whose solution allows to express the unknown potentials v_{1-} and v_{1+} through the fixed v_{2-} and v_{2+} values and thereby calculate the BCD.

2 Calculation of transresistance, results, and discussion

If most of the electrons move through the wires balistically, Eq. (2) can be solved by simple iterations. The zero-order approximation gives $f_{jk}^{>}(x) = f(\varepsilon_{jk} - e\delta v_{j-})$ and $f_{jk}^{<}(L/2) = f(\varepsilon_{jk} - e\delta v_{j+})$. Substitution of these functions in the collision integral gives non-zero contribution for the interwire collisions with backscattering. Taking into account that $v_{1-} - v_{1+}$ is considerably smaller than $v_{2-} - v_{2+}$ due to the assumed weak Coulomb coupling, we finally obtain, in the linear approximation

$$f_{1k}^{>}(x) = f(\varepsilon_{1k} - e\delta v_{1-}) + (m_1/\hbar k)\lambda_{>}(k)e(v_{2-} - v_{2+})(x + L/2), \tag{4}$$

$$f_{1k}^{<}(x) = f(\varepsilon_{1k} - e\delta v_{1+}) + (m_1/\hbar k)\lambda_{<}(k)e(v_{2-} - v_{2+})(x - L/2), \tag{5}$$

where $\lambda_{>}(k)$ and $\lambda_{<}(k)$ are determined by the Coulomb matrix elements and the equilibrium distribution functions only. The current flowing in the drag wire is given by $I_D = e/\pi \int dk(\hbar k/m_1)[f_{1k}^{>}(x) - f_{1k}^{<}(x)]$ (this current does not depend on x due to the property $\int dk[\lambda_{>}(k) - \lambda_{<}(k)] = 0$, which follows from detailed balance). The drag transresistance is given by $\rho_D = -(v_{1-} - v_{1+})/I$ and the ballistic current I by $I = (v_{2-} - v_{2+})/R_0$, where $R_0 = h/2e^2$ is the resistance quantum. From the requirement $I_D = 0$ we obtain

$$\rho_D = \frac{4e^2 m_0 L}{\hbar\kappa^2 T}\int_0^\infty dk \int_0^\infty dk' q_{kk'}^{-1} f(\varepsilon_{1k}) f(\varepsilon_{2k'})[1 - f(\varepsilon_{1k_1})][1 - f(\varepsilon_{2k_2})]$$

$$\times \left[\int\int \frac{dy dy'}{\pi \ell_1 \ell_2} K_0(q_{kk'}|y_1 - y_2 + y - y'|) Q_1(k, k_1, y) Q_2(-k', -k_2, y')\right]^2. \tag{6}$$

Here $q_{kk'} = m_0(k/m_1 + k'/m_2)$, $k_1 = k' + \eta(k' - k)$, $k_2 = k + \eta(k' - k)$, $Q_j(p, p', y) = \exp\{-[(y - (\omega_c/\omega_j)\ell_j^2 p)^2 + (y + (\omega_c/\omega_j)\ell_j^2 p')^2]/2\ell_j^2\}$, $m_0 = 2m_1 m_2/(m_1 + m_2)$ and $\eta = (m_1 - m_2)/(m_1 + m_2)$.

Below we analyze in detail the case when the confining potentials are identical in both wires; this entails $m_1 = m_2$, $\ell_1 = \ell_2 = \ell$, $\Omega_1 = \Omega_2 = \Omega$, and $\omega_1 = \omega_2 = \omega$. We also assume that both the temperature T and splitting energy $\Delta = \varepsilon_1^0 - \varepsilon_1^0$ are small in comparison with the Fermi energy ε_F defined as $\varepsilon_F = ev - (\varepsilon_1^0 + \varepsilon_2^0)/2 - \hbar\omega/2$. These assumptions mean that the k and k' values contributing to the integrals are in narrow regions near $\sqrt{2m_0\varepsilon_F}/\hbar$, and the integrals over k and k' are calculated easily. We obtain

$$\rho_D = \frac{e^2 m^{3/2}\omega^3 LT}{2\sqrt{2}\pi\hbar^2\kappa^2\Omega^3\varepsilon_F^{3/2}} \frac{(\Delta/2T)^2}{\sinh^2(\Delta/2T)} \exp\left(-\frac{8\omega_c^2\varepsilon_F}{\hbar\omega\Omega^2}\right)$$

$$\times \left[\int_{-\infty}^{\infty} du e^{-u^2/2} K_0\left(\sqrt{8\omega\varepsilon_F/\hbar\Omega^2}\,|w/\ell + u|\right)\right]^2, \tag{7}$$

where $w = |y_1 - y_2|$ is the distance between the centers of the wires and u a dimensionless variable. Equation (7) demonstrates a significant suppression of the drag effect by the magnetic field, mostly due to the exponential factor and the increase, with H, of the argument of K_0. The decrease of ρ_D starts as $\rho_D(H) - \rho_D(0) \sim -H^2$ and becomes exponential with increasing H. The characteristic H for this suppression is determined by the Fermi energy and wire parameters. It is estimated as $H = (mc/e)\sqrt{\hbar\Omega^3/8\varepsilon_F}$ and is of the order of 1 T for typical wire parameters. Another less important factor, which contributes to the magnetic-field dependence of the BCD transresistance is the dependence

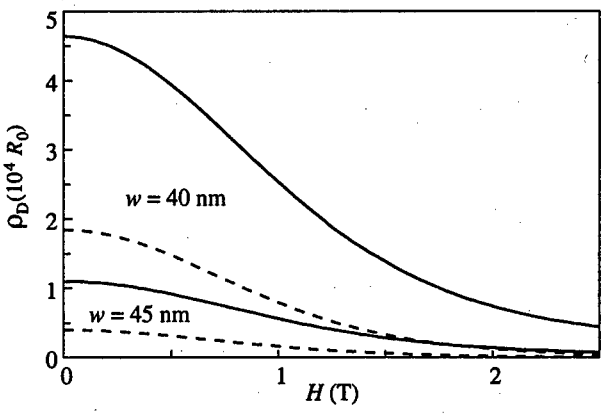

Fig. 1. Dependence of the transresistance ρ_D on the magnetic field H at two different Fermi energies $\varepsilon_F(0) = 3$ meV (solid) and $\varepsilon_F(0) = 4$ meV (dashed). The two upper curves correspond to $w = 40$ nm and the two lower ones to $w = 45$ nm.

of ε_F on H. It is taken below as $\varepsilon_F(H) - \varepsilon_F(0) = -\hbar(\omega - \Omega)/2$, under the assumption that v is constant.

In Fig. 1 we show the field dependence of ρ_D (in units of $h/2e^2$) for the resonance condition $\Delta = 0$ for which the drag is maximal [4]. The curves are plotted for two different values of $\varepsilon_F(0)$ and w shown in the caption. The other parameters used, common to all curves, are $\hbar\Omega = 5$ meV, $T = 1$ K, $m = 0.067$ of the free electron mass, $\kappa = 13$, and $L = 0.5$ μm. Although the variations of both ε_F and w considerably modify ρ_D, they do not influence the field dependence qualitatively.

In summary, we have theoretically demonstrated the magnetic-field induced suppression of the drag effect between two quantum wires in the ballistic transport regime. This suppression results from that of backscattering in the interwire Coulomb collision processes and is significant at $H \sim 1$ T. We hope that these results will stimulate further experimental investigations of electron transport in double-quantum-wire systems.

References

[1] A. Rojo *et al.*, *J. Phys.: Condens. Matt.* **11**, R31 (1999).
[2] H. C. Tso and P. Vasilopoulos *Phys. Rev. B* **45**, 1333 (1992); Yu. M. Sirenko and P. Vasilopoulos *ibid* **46**, 1611 (1992); B. Tanatar *ibid* **58**, 1154 (1998).
[3] J. A. del Alamo and C. C. Eugster, *Jpn. J. Appl. Phys.* **34**, 4439 (1995).
[4] V. I. Gurevich, V. B. Pevzner, and E.W.Fenton *J. Phys.: Condens. Matter* **10**, 2551 (1998).

7th Int. Symp. "Nanostructures: Physics and Technology"
St Petersburg, Russia, June 14–18, 1999

Scattering processes in the structures with one-dimensional lateral superlattice

E. L. Shangina
Ryazan State Medical University, 391000 Ryazan, Russia

1 Introduction

The semiconductor nanostructures with artificial periodic potential in lateral plane are considered as very attractive objects in both fundamental and applied investigations. To construct a periodic potential relief, various methods are employed [1, 2]. Let us consider the structures with lateral superlattice created by wire-like doping of a vicinal i-GaAs surface [3, 4]. After deposition of a fraction of Si (or Sn) monolayer on the i-GaAs δ-doping plane having well-formed set of monolayer steps, both migration process of Si (Sn) adatoms and their segregation to the step edges are observed; thus we deal with the self-organized wire-like doping. The typical terrace step width is $\sim$ 8 nm for Si doping, $\sim$ 50 nm for Sn doping on vicinal (001) GaAs surfaces. The overall view of the structure considered is shown in Fig. 1, Fig. 2 represents the calculated potential and the electron distribution in the GaAs(0.3°, δ-Sn) structure for the doping level $N_D \approx 1.8 \times 10^{12}$ cm^{-2}. The distribution law of impurity atoms on the step of vicinal plane was approximated by Gaussian law: $N_D(x) \sim \exp\{-(x - d/2)^2/2\sigma^2\}$, where d is the width of the vicinal plane step and σ is the standard deviation of distribution. The width of terrace steps is set to be 53 nm, which corresponds to the case of the 0.3°-off GaAs(001) surface.

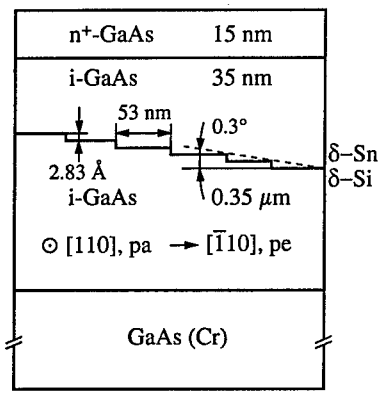

Fig. 1. The overall view of the structure with δ-Sn layer on i-GaAs vicinal plane.

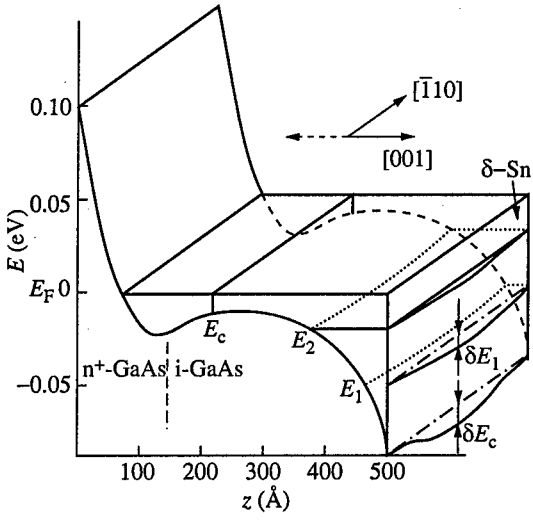

Fig. 2. The band diagram $E_c(x, z)$ and electron wave functions in the GaAs(0.3°, δ-Sn) structure. The modulation of conduction band edge E_c and size-quantized levels E_1, E_2 in the [1̄10] direction is shown.

The structures of this kind revealed the anomalies of kinetic effects [4]: the "giant" negative magnetoresistance (up to 28% for the [110] direction) and the anisotropy of conductivity in the whole ranges of both electric fields $E = 0$–7 kV/cm, magnetic fields $B = 0$–40 T, temperatures $T = 0.39$–293 K. To explain the anomalies observed complex investigations of scattering mechanisms of electrons in the GaAs(0.3°, δ-Sn) structure are needed.

The aim of this work is the modeling of various scattering processes in the structures with wire-like doping with subsequent comparison between calculated data and results of experimental observation of magnetoconductivity, Shubnikov–de Haas oscillations and photoluminescence spectra.

2 Scattering processes

It is obviously to suppose that the leading mechanism of electron scattering in the structures with wire-like doping is the inter- and intrasubband scattering by the random fluctuations of potential relief connected with the presence of ionized Sn impurity. In these conditions when some subbands are filled, the corresponding relaxation times $\tau_{t\alpha}$ of carriers momentum are given by the equation

$$\tau_{t\alpha} P_{\alpha\alpha} - \sum_{\alpha' \neq \alpha} P_{\alpha\alpha'} \tau_{t\alpha'} = 1 \tag{1}$$

where α is the number of the subband.

The probabilities of the corresponding transients $P_{\alpha\alpha}$ can be written within the framework of the Born approximation in the low-temperature limit of scattering on ionized impurity [5]:

$$P_{\alpha\alpha} = \frac{1}{2\pi\hbar E_{F_\alpha}} \int_0^{2k_{F_\alpha}} \frac{\langle |U_1(q)| \rangle^2 q^2 dq}{\varepsilon^2(q)\sqrt{4k_{F_\alpha}^2 - q^2}}$$

$$+ \sum_{\alpha' \neq \alpha} \frac{1}{2\pi\hbar E_{F_\alpha}} \int_{|k_{F_\alpha} - k_{F'_\alpha}|}^{k_{F_\alpha} + k_{F'_\alpha}} \frac{\langle |U'_1(q)| \rangle^2 dq 2k_{F_\alpha}^2}{\varepsilon^2(q)\sqrt{4k_{F_\alpha}^2 - \left[q + \frac{k_{F_\alpha}^2 - k_{F'_\alpha}^2}{q}\right]^2}} \tag{2}$$

$$P_{\alpha\alpha} = \frac{1}{2\pi\hbar E_{F_\alpha}} \int_{|k_{F_\alpha} - k_{F'_\alpha}|}^{k_{F_\alpha} + k_{F'_\alpha}} \frac{\langle |U'_1(q)| \rangle^2 (k_{F_\alpha}^2 + k_{F'_\alpha}^2 - q^2) dq}{\varepsilon'^2(q)\sqrt{4k_{F_\alpha}^2 - \left[q + \frac{k_{F_\alpha}^2 - k_{F'_\alpha}^2}{q}\right]^2}} \tag{3}$$

where E_{F_α} and k_{F_α} are the Fermi energy and the Fermi wave vector, respectively, q is the scattering wave vector, $\langle |U'_1(q)| \rangle$ is the Fourier transform of the potential of electron-ionized impurity interaction, $\varepsilon'(q)$ is the dielectric constant of electron gas. But it should be noted that there is the complementary scattering mechanism of electrons in the GaAs(0.3°,δ-Sn) structure. The spatial quasiperiodic modulation of quantum size levels $\delta E_\alpha(r)$ because the quasiperiodic modulation of impurity distribution $\Delta N_D(r)$ in the δ-doping plane is observed; these fluctuations work as a scattering potential:

$$\delta E_\alpha(r) = \frac{\partial E_\alpha}{\partial N_D} \Delta N_D(r). \tag{4}$$

For a quantum well of triangular shape the variational approach gives us the expression for the first size-quantized level:

$$E_0(r) = \left(\frac{\pi^2 2\hbar e^2}{\chi\sqrt{m^* n_D(r)}}\right)^{2/3}. \tag{5}$$

As the impurity distribution has the Gaussian form their autocorrelation function may be expressed as (in the δ-doping plane):

$$\langle \Delta N_D(r)\Delta N_D(r')\rangle = (N_D^{\max})^2\left(1-2e^{-\lambda^2/8\sigma^2}\right)^2 \exp\left[-\frac{(r-r')^2}{\lambda^2}\right] \tag{6}$$

where $\langle \ldots \rangle$ means an ensemble average.

From Eqs. (4), (5) and (6), the square of the 2D scattering matrix element M_R^2 for the electrons of the first subband can be written as

$$M_R^2 = \pi\left(\frac{2\pi^2\hbar e^2 N_D^{\max}}{\chi\sqrt{m^*}}\right)^{4/3}\left(1-2e^{-\lambda^2/8\sigma^2}\right)^2 \lambda^2 e^{-q^2\lambda^2/4} \tag{7}$$

where $\boldsymbol{q} = \boldsymbol{k} - \boldsymbol{k}'$ is the 2D scattering wave vector and $q = |\boldsymbol{q}|$. In these conditions, the inverse of the transport relaxation time $\tau_t^{LS}(E)$ due to the scattering by quasiperiodic fluctuations of potential profile in the $[\bar{1}10]$ direction is then given by

$$\frac{1}{\tau_t^{LS}(E)} = \frac{m^*}{2\hbar}\left(\frac{2\pi^2 e^2 N_D^{\max}}{\chi\sqrt{m^*\hbar}}\right)^{4/3}\lambda^2\left(1-2e^{-\lambda^2/8\sigma^2}\right)^2\int \frac{e^{-q^2\lambda^2/4}}{\varepsilon^2(q)}(1-\cos\theta)d\theta \tag{8}$$

where θ is the scattering angle. Thus, the mobility μ_{LS} limited by quasiperiodic scattering may be expressed as

$$\mu_{LS} = \frac{e}{m^*}\langle\tau_t^{LS}\rangle. \tag{9}$$

3 Results and discussion

The numerical calculations of the subband relaxation times $\tau_{t\alpha}$ restricted by the impurity scattering have been realized according to Eq. (1)–(3). The values of both the the amplitude of the self-consistent wave function $\xi_{s\alpha}(z)$ and the concentration of electrons from size-quantized levels in the GaAs(0.3°, σ-Sn) structure have been used in the calculations. The values $\tau_{t1} = 1.3 \times 10^{-12}$ s, $\mu_1 = 3500\,\mathrm{cm^2/V\,s}$ and $\tau_{t2} = 2.2 \times 10^{-12}$ s, $\mu_2 = 5800\,\mathrm{cm^2/V\,s}$ have been obtained for the electrons of the first subband and the second one, correspondingly. These values are very close to the experimental data $\langle\mu^{pa,pe}\rangle = (2{-}7.4) \times 10^3\,\mathrm{cm^2/V\,s}$.

Thus, the physical mechanism restricting the electron mobility in the GaAs(0.3°, σ-Sn) structure is the scattering by the ionized impurity which creates the σ-shape quantum well immediately. But the investigations of the complementary mechanism—electrons scattering by the quasiperiodical fluctuations of potential relief—are still needed.

The parametrical dependences $\tau_t^{LS}(N_D, \sigma, \lambda, T)$ have been calculated according Eq. (7), (8) for the structures with wire-like doping. The data are presented in Fig. 3. It has been shown by calculations that the low-temperature transport relaxation times of electrons τ_t^{LS} in these structures are in the range $\sim 10^{-11}{-}10^{-12}$ s for $N_D = (1{-}3) \times 10^{12}\,\mathrm{cm^{-2}}$,

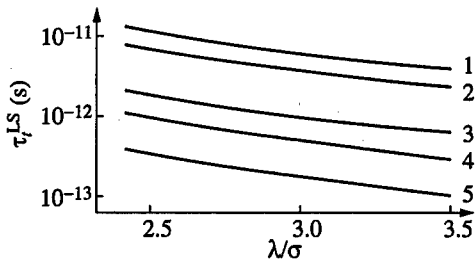

Fig. 3. Calculated parametrical dependences of the transport relaxation time $\tau_t^{LS}(N_D, \sigma\lambda, T)$. T = 4.2 K. λ, nm: 1, 2—53, 3—45, 4, 5—40. N_D, cm^{-2}: 1—1×10^{12}, 2, 3, 4—1.4×10^{12}, 5—3×10^{12}.

$\lambda = 40-53$ nm, and $\sigma = (0.3-0.4)\lambda$. thus, the scattering by quasi-periodical fluctuations of potential relief must be taken into account in the modeling of kinetics effects in the wire-like doped structures without one-dimensional channels. It should be noted that the procedure of relaxation times calculation must be modified in respect to the Eq. (4)–(8) in the case when the carriers sense the superlattice potential i.e. the mean free path length is more than the superlattice period [6]. Moreover, the calculations procedure changes if we take into consideration the real (not triangular) shape and finite depth of the quantum well created by wire-like doping; it is the subject of the further investigations.

References

[1] B. Etienne, F. Laruelle, Z. Wang, L. Sfaxi, F. Lelarge, F. Petit, T. Melin and A. Cavanna, *Semicond. Sci. Technol.* **11**, 1534 (1996).

[2] Zh. I. Alferov, A. Yu. Egorov, A. E. Zhukov, S. V. Ivanov, P. S. Kop'ev, N. N. Ledentsov, B. Ja. Meltzer and V. M. Ustinov, *Sov. Phys.-Semicond.* **26**, (1992).

[3] Y. Takagaki, K. J. Friedland and K. Ploog, *Appl. Phys. Lett.* **64**, 3258 (1994).

[4] V. I. Kadushkin, E. V. Klyshevich, E. L. Shangina and F. M. Tsahhaev, *Phys. Low-Dim. Struct.* **3/4**, 135 (1998).

[5] V. I. Kadushkin, E. V. Klyshevich, E. L. Shangina and F. M. Tsahhaev, *Phys. Low-Dim. Struct.* **11/12**, (1998).

[6] A. Ya. Shik, *Sov. Phys.-Semicond.* **7**, 261 (1973).

7th Int. Symp. "Nanostructures: Physics and Technology"
St Petersburg, Russia, June 14–18, 1999

Progress in red vertical cavity surface emitting lasers

J. A. Lott
Air Force Institute of Technology, Wright-Patterson AFB, Ohio USA

Abstract. The development of red vertical cavity surface emitting lasers with peak emission wavelengths from 620 to 690 nm is reviewed. The performance characteristics of state-of-the-art gain guided and selectively oxidized device structures are presented.

1 Introduction

Red (620–700 nm) vertical cavity surface emitting lasers (VCSELs) are candidates for plastic fiber communications, compact disk and digital video disk holographic heads, medical diagnostics, and optical alignment and interconnects. The devices consist of an AlGaInP quantum well optical cavity active region surrounded by AlGaAs distributed Bragg reflectors (DBRs). To avoid absorptive losses, the AlAs mole fraction (x) of the higher index/lower bandgap $Al_xGa_{1-x}As$ DBR quarter-wave layer is increased as the desired emission wavelength is decreased. As determined from Fig. 1, this requires that $x > 0.4$ for peak emission wavelengths below 700 nm. The value of x should increase to about 0.6 for peak emission at 630 nm.

Optically-pumped "visible" (peak emission at 740 nm) VCSELs were first reported in 1987 [1], followed by AlGaAs VCSEL diodes (770 nm) in 1991 [2] and AlGaInP VCSEL diodes (639–661 nm) in 1993 [3]. Many other reports of visible VCSELs have followed [4–8]. As with near-infrared (800-1000 nm) VCSELs, improved performance has

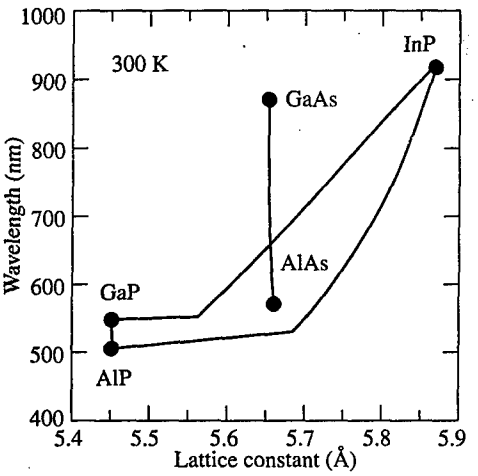

Fig. 1. Photon wavelength vs. lattice constant for AlGaAs and AlGaInP.

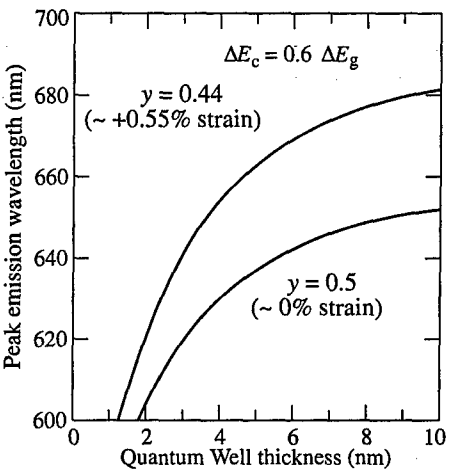

Fig. 2. Calculated room temperature peak emission wavelength vs. QW thickness. The curves are for $Ga_yIn_{1-y}P$ ($y = 0.44, 0.5$) QWs with $(Al_{0.5}Ga_{0.5})_{0.5}In_{0.5}P$ barrier layers.

been obtained by moving from simple pillar structures to gain-guided proton implanted structures, and to new native Al-oxide structures [9]. Other parallel improvements include DBR interface grading and pulse doping schemes. This paper reviews the development and performance characteristics of proton implanted and native Al-oxide red VCSEL structures from 1991 to the present.

2 Device structures

The VCSELs are grown by low pressure metalorganic vapor phase epitaxy on (100) (n^+)GaAs substrates, misoriented 5° or 10° toward the (111)A. The top (n) and bottom (p) DBRs are composed of $Al_xGa_{1-x}As$ ($x = 0.5$ or 0.6)/$Al_xGa_{1-x}As$ ($x = 0.92$ or 1.0) with graded interfaces. The p-dopant is C, while the n-dopant is Si. The first low index DBR layer on top of the optical cavity is composed of $Al_xGa_{1-x}As$ ($x = 1.0$). The one-lambda optical cavity active region has three or four, 6–8 nm-thick, $Ga_yIn_{1-y}P$ ($y = 0.42-0.5$) QWs surrounded by undoped $(Al_{0.5}Ga_{0.5})_{0.5}In_{0.5}P$ barrier layers. For reference, Fig. 2 shows the calculated peak emission wavelength for example AlGaInP QW active regions as a function of QW thickness.

The optical properties of AlGaInP are influenced by an ordered phase that occurs naturally, under certain crystal growth conditions, on the group III sublattice [10]. Long range ordering is directly related to a reduction in the GaInP energy bandgap (up to ~ 130 meV) as compared to fully disordered (random) epitaxial layers. The effects of ordering are clearly observed in the photoluminescence (PL) spectra of Fig. 3. The PL peaks in curves (b) and (d), as compared to those in curves (a) and (c), are broadened and shifted toward longer wavelengths, indicating increased ordering. In this case, a reduction in ordering is obtained by increasing the misorientation of the substrates from 2° to 5° off (100), and increasing the growth temperature from 675 to 750 °C.

The 2-inch diameter wafers are grown without rotation, resulting in a thickness variation along the centerline from front to back. This is an important research technique for fabricating prototype devices, allowing the characterization of devices with varying mismatch

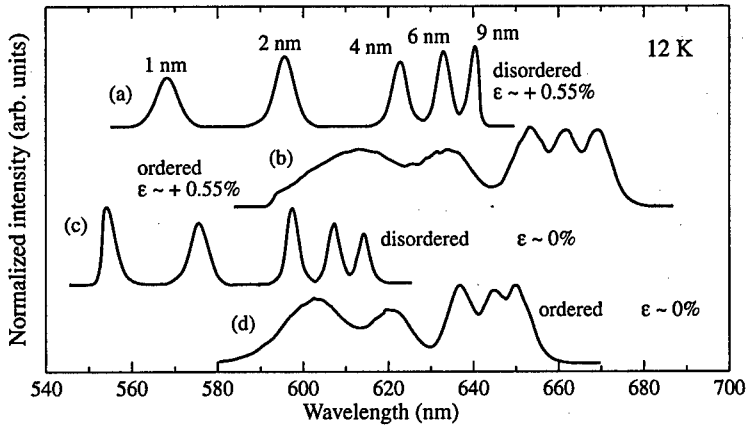

Fig. 3. Photoluminescence of AlGaInP QW heterostructures with five $Ga_yIn_{1-y}P$ QWs that are 9, 6, 4, 2, and 1 nm thick, separated by 60 nm thick $(Al_{0.7}Ga_{0.3})_{0.5}In_{0.5}P$ barrier layers. Curves (a) and (c): $T_g = 750\,°C$, 6° off (100) substrate. Curves (b) and (d): $T_g = 675\,°C$, 2° off (100) substrate.

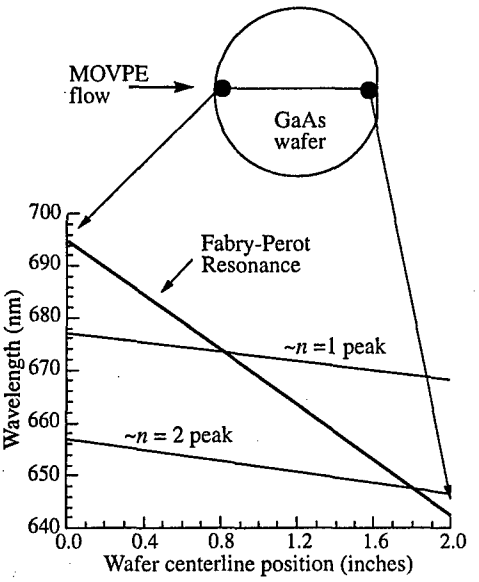

Fig. 4. Schematic of the variation in Fabry–Perot resonance wavelength and peak QW transition wavelengths across an unrotated red VCSEL wafer (n = 1 and n = 2 refer to the first and second quantized state QW transitions).

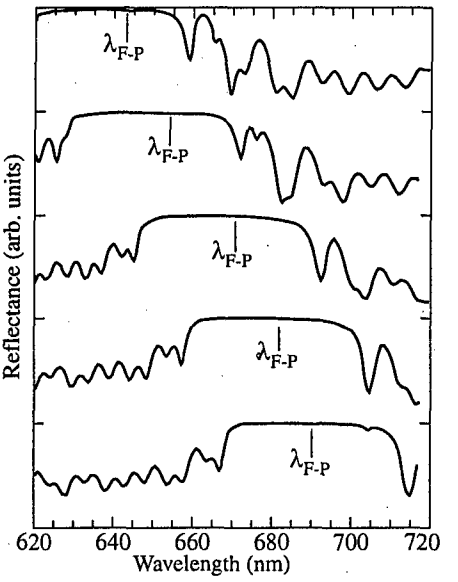

Fig. 5. Measured reflectance spectra (at normal incidence) at five approximately equally spaced points across a nonrotated red VCSEL wafer.

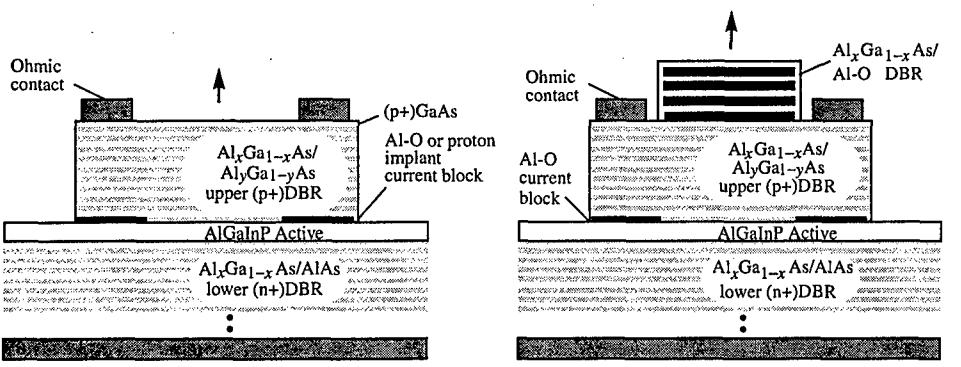

Fig. 6. Schematic diagrams of a proton implanted (gain guided) or Al-oxide red VCSEL (left), and a selectively oxidized red VCSEL with a partial top Al-oxide DBR (right).

between the Fabry–Perot resonance and the QW gain peak. Figure 4 shows the measured variation in Fabry–Perot resonance and peak gain for a typical wafer. The small variation in QW gain results primarily from a change in GaInP QW composition across the nonrotated wafer. The measured reflectance spectra for an example nonrotated red VCSEL wafer is shown in Fig. 5. The wafers are fabricated into ion implanted or selectively oxidized Al–O structures as shown in Fig. 6. The fabrication proceeds in a manner similar to that described in [6–9].

Table 1. Typical CW performance characteristics of proton implanted (H^+) and selectively oxidized (Al–O) VCSELs at 300 K. The emission apertures are approximately $5 \times 5\,\mu m^2$. The maximum power conversion efficiency is given by η_{max}. The maximum output power P_{max} is for the fundamental transverse mode.

	690 nm		650 nm		630 nm	
	H^+	Al–O	H^+	Al–O	H^+	Al–O
I_{th} (mA)	1.2	0.5	3.5	0.8	5.2	2.1
V_{th} (V)	2.4	2.0	2.7	2.2	3.1	2.2
P_{max} (mW)	6.5	9	1.0	2	0.1	0.35
η_{max} (%)	18	45	5	35	0.5	12

3 Performance characteristics

Typical continuous wave (CW) performance characteristics for selectively oxidized red VCSELs are shown in Fig. 7 and Fig. 8. As with red edge-emitting lasers, the maximum output power decreases and the threshold current increases as the emission wavelength decreases. A summary comparison between implanted and selectively oxidized VCSELs is given in Table 1 (for structures based on Fig. 6, left). The values are the averages of 20 randomly selected devices emitting within 5% of the given peak wavelength. The gain guided device performance rivals that of conventional gain guided infrared (850, 980 nm) VCSELs circa 1992. The selectively oxidized red VCSEL performance for emission at 690 nm is roughly equal to the best state-of-the- art infrared VCSELs emitting at 850 nm. Life tests were performed on the 690 nm Al-oxide VCSELs at 50 °C. After 2000 hours, the threshold currents and voltages, and peak output powers remain within 3% of their starting values.

4 Resonant mode blueshifts in microcavity VCSELs

Conventional planar VCSELs support a single longitudinal optical mode and one or more transverse optical modes. Intracavity Al-oxide layers are selectively positioned within a VCSEL to form both a current aperture and a cylindrical or rectangular waveguide. A Microcavity VCSEL is formed when the radius of the VCSEL's transverse aperture is on the

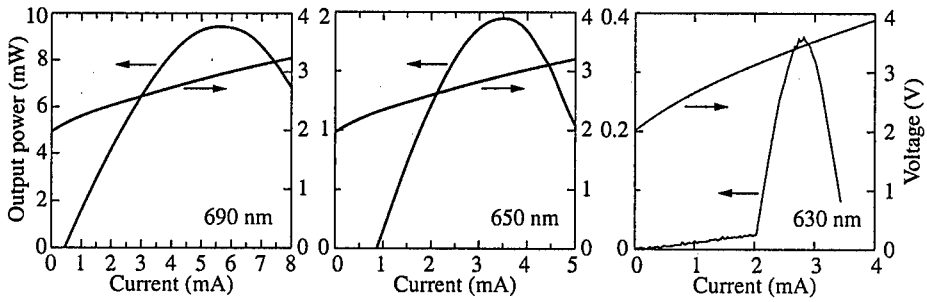

Fig. 7. Room temperature L–I characteristics for selectively oxidized red VCSELs emitting at 690, 650, and 630 nm. The oxide apertures are approximately $5 \times 5\,\mu m^2$.

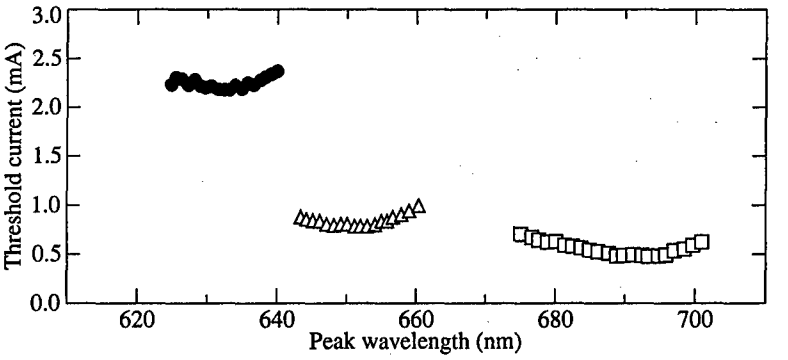

Fig. 8. Room temperature threshold current versus peak emission wavelength for selectively oxidized red VCSELs emitting near 690, 650, and 630 nm. The oxide apertures are approximately $5 \times 5\,\mu m^2$.

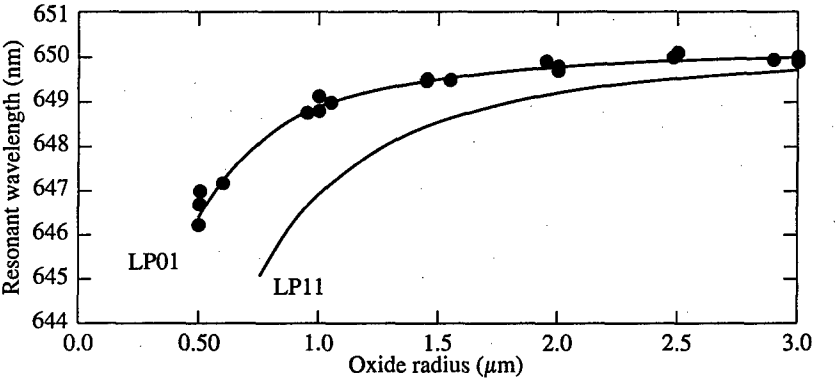

Fig. 9. Calculated (solid lines) and measured (dots) room temperature resonant emission wavelength as a function of oxide aperture radius for selectively oxidized red VCSELs designed for large area emission at 650 nm. The fundamental (LP01) and first higher order mode (LP11) are shown.

order of the thickness of the VCSEL's longitudinal resonant microcavity [11]. The lasing modes for large area VCSELs are one-dimensional quasi-plane waves, whereas the lasing modes of microcavity VCSELs are true three-dimensional modes. From a purely optical point of view, the resonant modal wavelengths of red and near infrared VCSELs blueshift as the aperture radius decreases below about 5 μm. Consider a circularly symmetric, oxide aperture VCSEL designed for large area emission at 650 nm (Fig. 6, left). Figure 9 is a plot of the calculated [12] (and measured) resonant mode blueshift for this VCSEL as the radius of the oxide aperture is varied from 3 μm down to 0.5 μm. The fundamental and first higher order modes for the 650 nm VCSEL are illustrated in Fig. 10.

5 Conclusion

Red AlGaInP/AlGaAs VCSELs have reached maturity and are ready to be used in a variety of photonic systems. Superior overall performance is obtained for devices with emission wavelengths from 660 to 690 nm. Devices emitting between 630 to 660 nm will eventually become commercially viable. Future optical interconnect and related photonic systems may well be based on dense arrays of red or infrared VCSELs. When implementing these

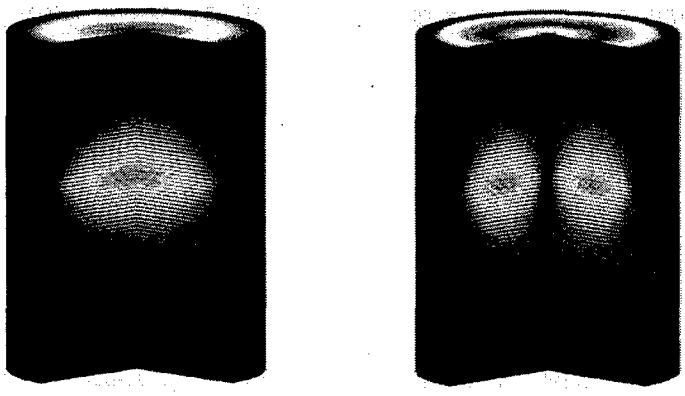

Fig. 10. Calculated fundamental mode (LP01, left) and first higher order mode (LP11, right) optical energy profile for a 650 nm selectively oxidized (single Al–O layer) VCSEL. The energy distribution on the top surface is amplified in order to illustrate the emitted mode.

arrays with small diameter VCSELs, one may need to account for resonant mode blueshifts (along with resonant mode redshifts due to device heating).

References

[1] P. L. Gourley and T. J. Drummond, *Appl. Phys. Lett.* **50**, 1225 (1987).

[2] Y. H. Lee, B. Tell, K. F. Brown-Goebeler, R. E. Leibenguth and V. D. Mattera, *IEEE Phot. Tech. Lett.* **3**, 108 (1991).

[3] J. A. Lott and R. P. Schneider, Jr., *Electr. Lett.* **29**, 830 (1993).

[4] B. Tell, R. E. Leibenguth, K. F. Brown-Goebeler and G. Livescu, *IEEE Phot. Tech. Lett.* **4**, 1195 (1992).

[5] K. H. Gulden, M. Moser, S. Luscher and H. P. Schweizer, *Electr. Lett.* **31**, 2176 (1995).

[6] J. A. Lott, *Proc. 22nd Int'l Symp. Comp. Semi.* Cheju Island, Korea (Aug 1995).

[7] K. D. Choquette, R. P. Schneider, Jr., M. Hagerott Crawford, K. M. Geib and J. J. Figiel, *Electr. Lett.* **31**, 1145 (1995).

[8] W. W. Chow, K. D. Choquette, M. H. Crawford, K. L. Lear and G. R. Hadley, *IEEE J. Quant. Electr.* **33**, 1810 (1997).

[9] M. H. MacDougal, G. M. Yang, A. E. Bond, C.-K Lin, D. Tishinin and P. D. Dapkus, *IEEE Phot. Tech. Lett.* **8**, 310 (1996).

[10] R. P. Schneider, Jr., E. D. Jones, J. A. Lott and R. P. Bryan, *J. Appl. Phys.* **72**, 5397–5400 (1992).

[11] M. J. Noble, J.-H. Shin, K. D. Choquette, J. P. Loehr, J. A. Lott and Y.-H. Lee, *IEEE Photon. Tech. Lett.* **10**, 475 (1998).

[12] M. J. Noble, J. P. Loehr and J. A. Lott, *IEEE J. Quant. Electr.* **34**, 1890 (1998).

7th Int. Symp. "Nanostructures: Physics and Technology"
St Petersburg, Russia, June 14–18, 1999

Temperature dependence of spontaneous emission and threshold characteristics for 1.3 μm InGaAs/GaAs quantum dot GaAs-based lasers

D. L. Huffaker, O. Shchekin, G. Park, Z. Z. Zou, S. Csutak and D. G. Deppe
Microelectronics Research Center, The University of Texas at Austin
10100 Burnet Rd., Bldg. 160, M.S. R9900 Austin, TX 78758, USA

Quantum dot (QD) active regions are rapidly advancing for use in semiconductor lasers [1–2]. The atomic-like density of states promises several improvements in laser diode performance including ultralow threshold current density and temperature insensitive threshold. Another important characteristic is the possibility for extended wavelength ($\lambda > 1.1$ μm) emission from GaAs-based devices [3–5]. This has been demonstrated in a QD vertical cavity surface emitting laser that emits at 1.15 μm [6], a resonant cavity QD photodetector operating at 1.27 μm [7] and more recently in edge-emitting lasers that use low loss cavities and operate at the wavelength of 1.31 μm at room temperature [8].

Here, we present data characterizing the temperature dependence of spontaneous emission and lasing characteristics for 1.3 μm InGaAs/GaAs quantum dot (QD) GaAs-based lasers. While efficient ground state emission is achieved at 80 K, the spontaneous efficiency decreases with increasing temperatures. Similarly, ultralow threshold current density (20 A/cm^2) is obtained at 77 K. Although the lasing threshold remains temperature insensitive to 200 K, it increases rapidly at higher temperatures. With high reflectivity coated facets, room temperature threshold current densities as low as 90 A/cm^2 are achieved. We have modeled these device characteristics as a function of temperature. From our analysis, we attribute these temperature characteristics to an increased nonradiative recombination rate from the QD higher energy levels and wetting layer. Our results suggest that very low threshold current density can be obtained at room temperature once nonradiative recombination is eliminated.

The QD active region is grown by molecular beam epitaxy in a GaAs barrier region surrounded by a $Al_{0.20}Ga_{0.80}As$ average composition waveguide region and a $Al_{0.70}Ga_{0.30}As$ cladding region. The InGaAs QDs are formed from a total of 11 monolayers of In, Ga and As deposited by sub-monolayer depositions [5]. A QD density of 10^{10} dots/cm^2 is measured using atomic force microscopy. Broad-area edge-emitters are fabricated. Devices with very short cavity length ($L < 1.0$ mm), in which lasing is inhibited due to edge loss, have been studied in spontaneous emission. Longer cavities are studied as lasers both with and without high reflectivity (HR) coated facets.

The electroluminescence output power is measured versus current and converted to efficiency versus current density. The results are shown in Fig. 1. At 80 K, the peak efficiency is 0.5% at 5 A/cm^2 which corresponds to ground state emission. We believe this represents close to 100% internal quantum efficiency. With increased current density and subsequent increased level filling the efficiency drops to 0.20% at 100 A/cm^2. This indicates that an increased nonradiative recombination rate exists for the higher energy levels even at low temperatures. At 160 K, the peak efficiency drops to 0.34% at 5 A/cm^2. At 250 K and 300 K, the peak efficiencies are 0.11% and 0.04% at current densities of 10 A/cm^2 and 40 A/cm^2, respectively. This indicates that temperature dependent nonradiative recombination is present in the QDs. Furthermore, we see that the radiative efficiencies vary for samples which are grown under similar conditions. Room temperature electrolumines-

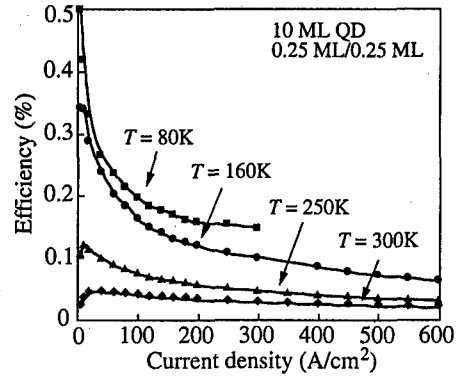

Fig. 1. Spontaneous efficiency versus current density measured for several temperatures. Two trends are observed. The ground state efficiency decreases with increasing temperature, and the efficiency at each temperature decreases with increasing current density.

cence efficiencies as high as 0.20% have been measured [5]. Therefore, we attribute the nonradiative recombination to point defects on the QD surface or within the QD bulk [9].

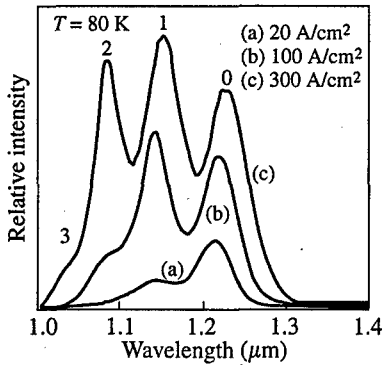

Fig. 2. Spontaneous emission spectra at 80 K for three different current densities.

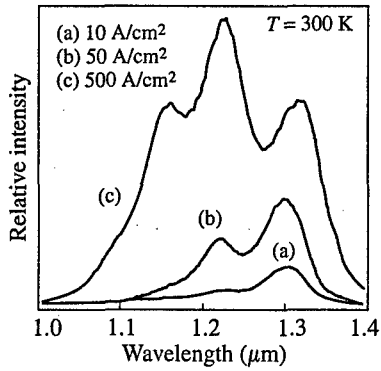

Fig. 3. Spontaneous emission spectra at 300 K for three different current densities.

To evaluate level filling, we measured spontaneous emission spectra for different current densities and different temperatures. Figure 2 shows spontaneous emission spectra at three different current densities for $T = 80$ K. At 5 A/cm^2 (spectra not shown) only the ground state is excited with a 40 meV linewidth centered at 1.22 μm. With increasing current to 20 A/cm^2, the first excited state, at 1.14 μm is partially filled. At 100 A/cm^2 and 200 A/cm^2, the second and third excited states at 1.09 μm and 1.04 μm, respectively, are filled. At 300 K, the spectra has similar behavior. Figure 3 shows 300 K spontaneous spectra from the same device measured at 10 A/cm^2, 50 A/cm^2 and 500 A/cm^2. The ground state emission peak occurs at 1.31 μm with a 40 meV linewidth. We observe that higher current densities are necessary to achieve bandfilling, which is consistent with a reduced electroluminescence efficiency. At both 80 K and 300 K, the higher energy levels begin to fill before the ground state saturates.

Figure 4 shows light versus current curves and spectra measured under room-temperature pulsed conditions for a QD laser ($L = 2.76$ mm) with high reflectivity (HR) coated facets. These lasers are made from the same epitaxial wafer as the shorter devices characterized in

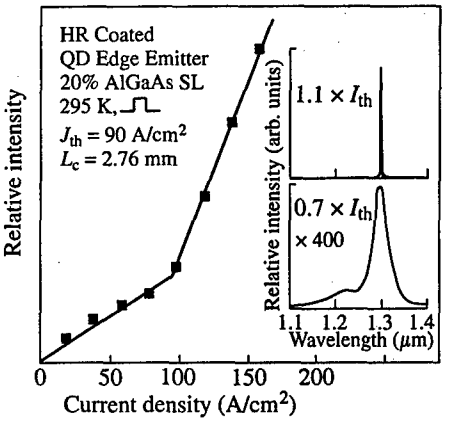

Fig. 4. Light versus current and spectral data taken at 300 K under pulsed operation. The laser is 2.76 mm long with HR-coated facets. The threshold is 90 A/cm^2 and the lasing wavelength is 1.31 μm.

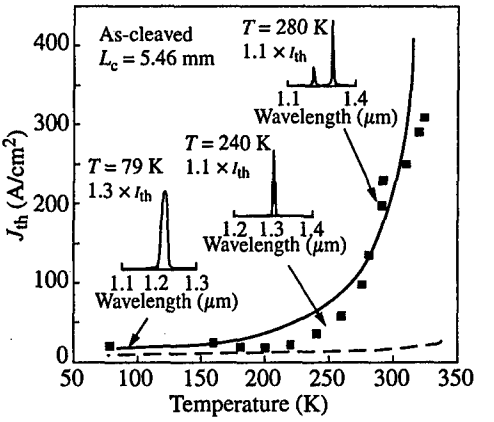

Fig. 5. Threshold current density versus temperature for a 5.46 mm long cavity with as-cleaved facets. Lasing occurs on the ground state for temperatures from 79 K to 280 K and on the first excited state for temperatures higher than 280 K. The solid curve shows calculated threshold current density versus temperature. The dashed curve shows calculated threshold current density if the nonradiative recombination rate is zero.

Figs. 1–3. A low threshold current density of 90 A/cm^2 is achieved at the 1.31 μm lasing wavelength. With HR coatings, this laser will operate from the ground state throughout the range of operation (up to 325 K). The upper limit of the temperature range is set by the dewar.

The temperature dependence of threshold from 77 K to 324 K for a longer cavity (L = 5.46 mm) with as-cleaved facets, also from the same wafer, is shown in Fig. 5. Spectral data at three different temperatures are shown as insets. At 79 K the threshold current density is 20 A/cm^2. From T = 79 K up to T = 200 K the threshold is nearly independent of temperature. Within this range, the carriers occupy the ground states of dots where the nonradiative recombination rate is low. At temperatures higher than 220 K, the threshold increases quickly due to increased carrier occupation of the higher energy levels and the wetting layer which causes increased nonradiative recombination. The spectral insets show that lasing occurs on the ground state within the temperature range of 79 K to 280 K and on the first excited state for higher temperatures. At 79 K, the carriers are confined to individual QDs with a low probability of escape relative to the radiative recombination. The lasing spectrum is therefore multimode and broad due to spectral hole burning [10]. At 240 K, the spectrum shows a decreased number of lasing modes due to thermal coupling of the QD ensemble through the wetting layer [11]. At 280 K, the spectrum shows both the ground state and the first excited state lasing simultaneously. Above 280 K, the laser operates from the first excited state.

We have performed extensive modeling of the temperature characteristics for 1.3 μm QD lasers based on a 2D harmonic oscillator density of states [9]. The model accounts for carrier scattering and radiative and non-radiative recombination between the QD energy levels. Material parameters such as non-radiative and radiative recombination rates and scattering rates are determined by fitting calculated data to experimental data. In order to

limit the number of adjustable parameters, we have assumed symmetrical electron and hole levels and scattering rates. Despite the assumption, we can achieve reasonable agreement with experimental data such as electroluminescence efficiencies, spontaneous spectra and threshold current densities. In Fig. 5, we show the calculated threshold current density overlaid on the experimental data points. The solid curve shows the calculated threshold current density using a nonradiative recombination rate that is consistent with our experimental data. The dashed curve shows the calculated threshold current density assuming that the nonradiative recombination rate equals zero. The model indicates that the increase in threshold with increasing temperature is due to an increasing population of higher energy levels and that carriers in higher energy levels have a higher nonradiative recombination rate due to an increased number of nonradiative recombination paths compared to radiative recombination paths. Our results therefore predict quite low threshold current density at room temperature if nonradiative recombination is eliminated from the QDs. We will discuss the model and calculated parameters as well as QD crystal growth in more detail during the presentation.

Acknowledgments

This work has been supported by the National Science Foundation and the State of Texas Advanced Research Program.

References

[1] N. Kirstaedter, N. N. Ledentsov, M. Grundmann, D. Bimberg, V. M. Ustinov, S. S. Ruvimov, M. V. Maximov, P. S. Kop'ev, Zh. I. Alferov, U. Richter, P. Werner, U. Gosele and J. Heydenreich, *Electron. Lett.* **30**, 1416 (1994).

[2] H. Shoji, K. Mukai, N. Ohtsuka, M. Sugawara, T. Uchida and H. Ischikawa, *IEEE Phot. Tech. Lett.* **7**, 1385 (1995).

[3] K. Mukai, O. Nobuyuki, S. Mitsuru and S. Yamzaki, *Jpn. J. Appl. Phys.* **33**, L1710 (1994).

[4] R. Mirin, J. Ibbetson, K. Nishi, A. Gossard and J. Bowers, *Appl. Phys. Lett.* **67**, 3795 (1995).

[5] D. L. Huffaker and D. G. Deppe, *Appl. Phys. Lett.* **73**, (1998).

[6] D. L. Huffaker, H. Deng and D. G. Deppe, *IEEE Phot. Tech. Lett.* **10**, 185 (1998).

[7] J. C. Campbell, D. L. Huffaker, H. Deng and D. G. Deppe, *Electron. Lett.* **33**, 1337 (1997).

[8] D. L. Huffaker, G. Park, Z. Zou, O. Shchekin and D. G. Deppe, *Appl. Phys. Lett.* **73**, (1998).

[9] D. G. Deppe, D. L. Huffaker, S. Csutak, Z. Zou, G. Park and O. B. Shchekin, *submitted to IEEE J. Quantum Elect.*

[10] G. Park, D. L. Huffaker, Z. Zou, O. B. Shchekin and D. G. Deppe, *IEEE Phot. Techn. Lett.* **11**, (1999) (accepted for publication).

[11] A. E. Zhukov, V. M. Ustinov, A. Y. Egorov, A. R. Kovsh, A. F. Tsatsulnikov, N. N. Ledentsov, S. V. Zaitsev, N. Y. Gordeev, P. S. Kopev and Zh. I. Alferov, *Jap. J. Appl. Phys.* **37**, 4216 (1997).

7th Int. Symp. "Nanostructures: Physics and Technology"
St Petersburg, Russia, June 14–18, 1999

Surface-mode lasing from optically pumped InGaN/GaN heterostructures

A. V. Sakharov, W. V. Lundin, V. A. Semenov, A. S. Usikov, N. N. Ledentsov, A. F. Tsatsul'nikov, Zh. I. Alferov, A. Hoffmann† and D. Bimberg†
Ioffe Physico-Technical Institute, St Petersburg, Russia
† Institute für Festkörperphysik, Technische Universität Berlin, Hardenbergstr. 36, D-10623 Berlin, Germany

Devices based on III-nitride compound semiconductors have been rapidly and successfully developed in recent years as highly efficient emitters of visible light. Long-lived blue laser diodes [1] along with high brightness blue, green, and most recently, amber light emitting diodes have been demonstrated. GaN-based surface emitting lasers have attracted wide attention because of naturally integrated mirrors, low beam divergence and possibilities to fabricate dense two-dimensional arrays of short-wavelength semiconductor lasers important for high-density high-speed optical storage applications. At the same time, fabrication of such devices was thought to be very complicated in view of the necessity to epitaxially grow conductive and highly reflective quarter wave Bragg mirrors based on GaN/AlGaN materials.

On the other hand, it was demonstrated, that ultrahigh modal gain in structures with stacked dense arrays of wide-gap II–VI quantum dots (QDs) allows to realize ultrahigh gain coefficients and achieve surface lasing even without using of Bragg reflectors [2]. It was shown also, that ultrathin InGaN deposits result in spontaneous formation of dense arrays of nanoislands [3]. Moreover, spontaneous spinodal decomposition of the InGaN alloys also favors formation of QD-like structures [4, 5]. Indeed, high modal gain in 0.1 μm-thick InGaN layers at high excitation densities allowed some authors [6, 7] to observe stimulated emission in vertical direction. At the same time no evidence of the importance of the feedback in the system resulting in appearance of lasing modes was given. In this work we fabricated and study optical properties of the structure composed of closely packed stacks of ultrathin InGaN insertions. We demonstrate possibility to achieve ultrahigh material gain in the system and achieve surface lasing. Characteristic typical for QD lasers temperature dependence of threshold excitation density and gain-spectrum — cavity mode self-adjustment effects are observed.

The samples used in this work were grown on (0001)-oriented sapphire substrates by low pressure metalorganic chemical vapour deposition technique and employing an AlGaN nucleation layer deposited at 530 °C [8]. Ammonia, trimethylindium (TMI), trimethylgallium (TMG) and thrimethylaluminum (TMA) were applied as component precursors. Purified hydrogen and argon were used as carrier gases. Argon was used as a bubbling gas for TMI while hydrogen was used as a bubbling gas for TMG and TMA. Samples consist of a 2.5 μm GaN layer deposited at 1050 °C at pressure 200 mbar using H_2 as carrier gas, a InGaN/GaN active region formed by temperature cycling at 600 mbar pressure using Ar as carrier gas, and a 0.1 μm GaN cap layer deposited at 1050 °C. Active region consisted of thin (25 nm) intermediate InGaN layer with low indium composition (8%) deposited at 800 °C followed by superlattice composed of 12 periods. The superlattice is formed due to temperature cycling from 730 to 860 °C, resulting in a strongly modulated In compositional profile, as In incorporates only at low temperatures. During the growth of the active region

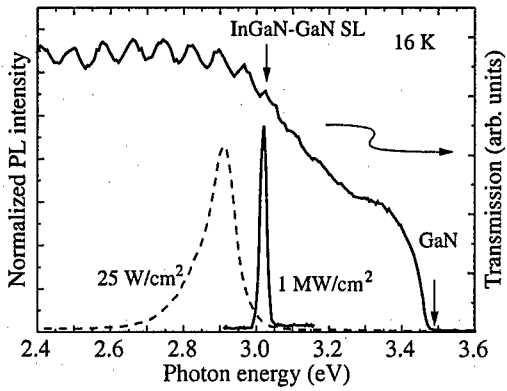

Fig. 1. Low temperature PL spectra at low excitation density, surface lasing and transmission spectra of structure under study.

TMI and TMG flows were constant. It was shown [3–5] that low temperature growth of InGaN leads to formation of dense array of In-rich nanoclasters (quantum dots).

The period of the superlattice obtained from XRD data was 12 nm, that in a good agreement with value estimated from the TMG flow. Average In content in the active region obtained from XRD was 8%. The width of the InGaN insertion estimated from temperature monitoring is about 4 nm. Photoluminescence (PL) measurements were performed in the temperature range 16–300 K by using close-cycle He cryostat. The samples were excited by He-Cd laser (325 nm, 25 mW) or by pulsed N_2 laser (337.1 nm, 1.5 kW). The laser beam was focused into a spot with a diameter of 400 μm. The laser light intensity was attenuated using a set of neutral density filters. The emission was coupled into MDR-23 spectrometer and detected by cooled photomultiplyer.

The low-temperature photoluminescence, surface lasing and optical transmission spectra are shown in Fig. 1. The PL spectrum shows a single peak with tails exhibiting near exponential behavior on both high and low energy side. A significant energy shift between PL maximum and the onset of the InGaN absorption in the transmission spectra strongly support formation of In-rich nanodomains. At large excitation densities, PL emission narrows and its intensity strongly increases. The PL maximum intensity shifts to the high energy side of the luminescence band at low excitation density, but still remains on the low energy side with respect to the onset of the InGaN-GaN SL-induced absorption.

The dependence of PL intensity on excitation density at 150 K is shown in Fig. 2(a). PL spectra for different excitation density are shown in Fig. 2(b). It can be seen that in all the spectra the PL is modulated by Fabry–Perrot microcavity modes formed by GaN/Al_2O_3 interface and GaN surface. It is clearly seen that at high excitation densities (> 600 kW/cm^2) one of the resonator modes starts to dominate in the PL spectra and its peak intensity grows superlinearly. Single-mode emission together with strong increase in the slope efficiency indicate the presence of the feedback in this system despite of the remarkably low finesse of the cavity. To the best of our knowledge, it is the first demonstration of lasing in vertical direction for structures with quantum-size InGaN/GaN insertions.

We also note that stimulated emission in edge direction was observed at excitation densities of about one order of magnitude lower than those for vertical lasing. Simultaneously with appearance of a narrow line in edge geometry we observed saturation of spontaneous recombination. Thus for vertical lasing, stimulated emission in edge geometry may play a

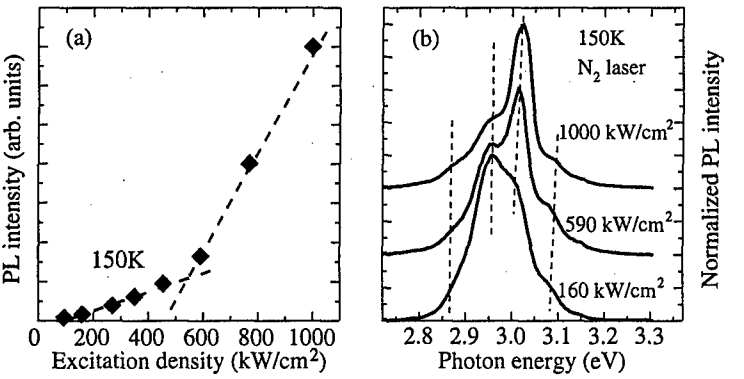

Fig. 2. Photoluminescense intensity *versus* excitation density (*a*) and PL spectra (*b*) taken at 150 K.

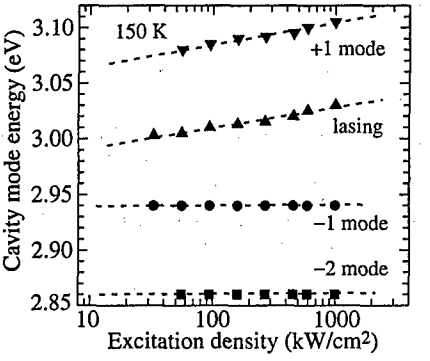

Fig. 3. Cavity modes position of Fabry–Perrot cavity versus excitation density.

negative role.

The threshold gain necessary to achieve surface lasing (g_{th}) can be written as:

$$g_{th} = \frac{1}{2L} \ln\left(\frac{1}{R_1 R_2}\right)$$

where R_1 and R_2 are reflectivity coefficients of both interfaces forming the cavity, and L the cavity length. We can neglected internal losses in GaN in this case. We estimate the reflectivity coefficients to be 2.4% for GaN/Al_2O_3 and 17% for GaN/air interfaces using the refractive indexes of unity for air, 2.4 for GaN, and 1.75 for sapphire. Then, taking into account that the active region, resulting in gain, has a thickness of 0.15 μm, we obtain the value of 2×10^5 cm^{-1} for the threshold gain.

In addition we observe short-wavelength shift of the cavity modes with increase in the excitation density (see Fig. 2(b)). The largest shift (2.6 nm) was observed for the high-energy modes, while the low energy modes does not shift. This effect can be described via Kramers–Kroning equations, and can be explained by a strong modulation of the absorption/gain curve in the vicinity of the lasing energy.

Figure 3 demonstrates the dependence of cavity modes on excitation density for a broader range of excitation densities. The effect of interaction of gain spectrum and cavity modes is characteristic for QD vertical cavity lasers surface emitting lasers and was reported for injection lasers based on InGaAs/GaAs quantum dots [9], and II–VI QD structures under photoexcitation.

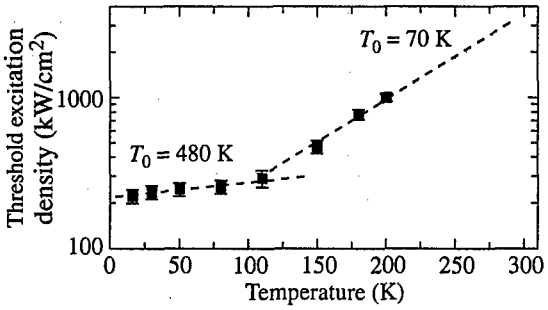

Fig. 4. Temperature dependence of threshold excitation density.

Temperature dependence of the threshold excitation density for vertical lasing is shown in Fig. 4. In a temperature range between 16 and 120 K the threshold excitation density remains weakly affected, while it increases at higher temperatures. The temperature dependence can be extrapolated in two ranges via empirical equation:

$$P_{\text{th}} = P_0 \times \exp\left(\frac{T}{T_0}\right)$$

with $T_0 = 480$ K in the low temperature range and $T_0 = 70$ K in the high temperature range. Similar temperature dependencies was reported for InGaAs-GaAs quantum dot lasers [9]. Increasing of the threshold excitation density at higher temperatures can be explained by thermal evaporation of carriers from QDs [10].

To conclude we have demonstrated vertical lasing without Bragg reflectors in structure with multiple InGaN/GaN insertions. Laser action is confirmed by superlinear dependence of the output intensity versus excitation density and by appearance of a single lasing mode defined by a vertical Fabry–Perrot cavity formed by GaN/air and GaN/Al_2O_3 interfaces. Effect of interaction of gain spectrum and cavity modes is demonstrated.

This work was supported by Project NATO SfP-972614.

References

[1] S. Nakamura, *et al.*, *Appl. Phys. Lett.* **72**, 2014 (1998).
[2] I. L. Krestnikov, *et al.*, *Phys. Rev. B in print* (1999).
[3] K. Tachibana, *et al.*, *Appl. Phys. Lett.* **74**, 383 (1999).
[4] S. Nakamura, *et al.*, *Appl. Phys. Lett.* **70**, 2753 (1997).
[5] A. Vertikov, *et al.*, *Appl. Phys. Lett.* **73**, 493 (1998);
K. Tachibana, *et al.*, *Appl. Phys. Lett.* **74**, 383 (1999);
R. W. Martin, *et al.*, *Appl. Phys. Lett.* **74**, 263 (1999).
[6] S. T. Kim, H. Amano, I. Akasaki, *Appl. Phys. Lett.* **67**, 267 (1995).
[7] M. Asif Khan, *et al.*, *Appl. Phys. Lett.* **65**, 520 (1994).
[8] J. Christen, *et al.*, Physica E **2**, 557 (1998).
[9] N. N. Ledentsov, *et al.*, *Semicond. Sci. Technol.* **13**, 99 (1999).
[10] N. Kirstaedter, *et al.*, *Electron. Lett.* **30**, 1416 (1994).

7th Int. Symp. "Nanostructures: Physics and Technology"
St Petersburg, Russia, June 14–18, 1999

3.3 W injection heterolaser based on self-organized quantum dots

A. R. Kovsh, D. A. Livshits, A. E. Zhukov, A. Yu. Egorov, V. M. Ustinov, M. V. Maximov, N. N. Ledentsov, P. S. Kop'ev, Zh. I. Alferov and D. Bimberg†
Ioffe Physico-Technical Institute, St Petersburg, Russia
† Institute für Festkörperphysik, Technische Universität Berlin,
Hardenbergstr. 36, D-10623 Berlin, Germany

Presently there is a strong interest to semiconductor self-organized quantum dots [1]. The delta-like density of states as a function of energy is expected to provide a very high differential gain above the transparency leading to significant reductions in threshold current in appropriately designed lasers compared with their bulk and quantum well counterparts [2]. Up to now the significant progress in this field is achieved. Ground state lasing is realised in various material systems with the lowest values of threshold current density of 63 A/cm^2 [3] and 11 A/cm^2 [4] at room and liquid nitrogen temperatures, respectively.

At the beginning of investigation of QDs the possibility to achieve a high output power in QD laser diodes has not been studied in detail. In 1997 we have reported on room temperature continuous wave lasing with the output power of the order of 1 W in laser based on InGaAs/AlGaAs QDs [5]. Improving the design of the QD active region proposed in [6] allowed us to increase this value up to 1.5 W. In this work we report on the QD laser demonstrating maximum output power 3.3 W.

One of the dominant mechanisms limiting power of semiconductor laser is spectral hole burning [7], associated with the finite capture time of charge carriers on the active states. Since the capture time in InGaAs QDs is relatively large (30–40 ps [8]) and the QDs themselves are characterized by a certain number of states determined by their areal density, the perspective of using the QD lasers for high-power applications was unclear. The number of QD states can be increased by stacking the QD sheets [9] or using the vicinal surfaces for the QD formation [10]. In [6] we have proposed the alternative way to increase the areal density of QDs. The basic idea of the method is to use denser InAlAs QDs as the centres for stimulated formation of InGaAs QDs. Finally, the array of composite vertically coupled QDs is formed. The areal density is set by the InAlAs islands, whereas the optical transition energy is determined by the InGaAs QDs. Following this method we have formed the active region of the laser studied in the present work. The structure was grown by solid source molecular beam epitaxy (MBE) in Riber 32 apparatus on n^+-GaAs(100) substrate in standard GRIN SCH design. The scheme of the structure under investigation and the cross-section of the active region are shown in Fig. 1. The active region was inserted into the middle of the 0.5 μm $Al_{0.15}Ga_{0.85}As$ waveguide. It consisted of the array of composite vertically-coupled InAlAs/InGaAs QDs. First three QD layers were formed by successive deposition of 5.3 monolayers of InAlAs and after that three rows of InGaAs QDs were grown. 5 nm layers of $Al_{0.15}Ga_{0.85}As$ separated the QD rows. QD formation was monitored in situ by the characteristic transition of the high electron energy diffraction (HEED) pattern. The substrate temperature was 485, 700, and 600 °C during the growth of the active region, cladding layers, and waveguide, respectively. The whole structure was grown under MBE standard As-rich conditions. Broad area laser diodes (stripe width 100 μm) were fabricated. No coating was deposited on facets.

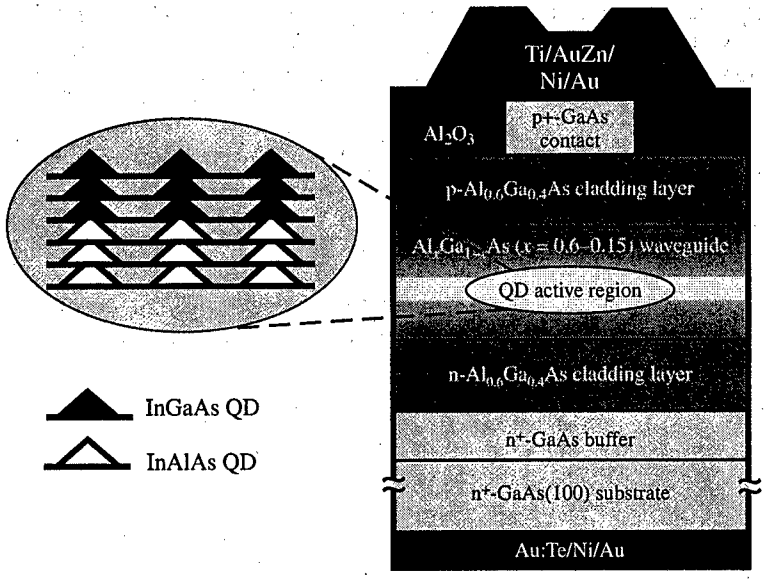

Fig. 1. The scheme of the laser based on composite vertically-coupled InAlAs/InGaAs QDs in AlGaAs matrix.

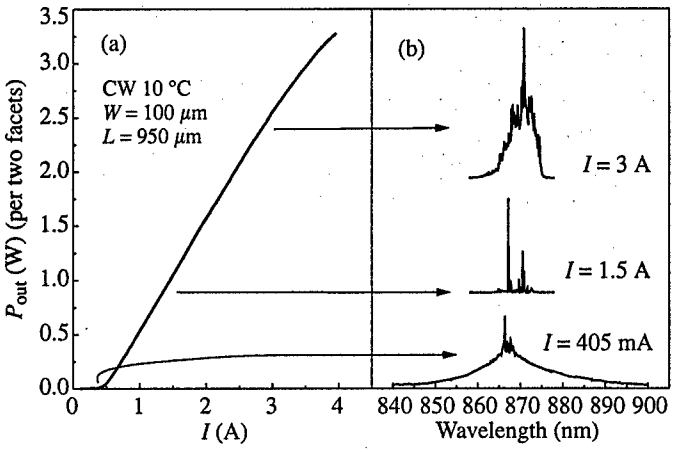

Fig. 2. (a) Light output power (P_{out}) dependence on continuous wave (CW) drive current per both facets at heat sink temperature of 10 °C; (b) lasing spectra recorded at corresponding current.

Continuous wave (CW) light output power (P_{out}) per both facets as a function of the drive current is presented in Fig. 2(a). The heat sink temperature was 10°C. The lasing spectra taken at several values of drive current are shown in Fig. 2(b). The threshold current (I_th) was 402 mA, that corresponds to the current density of 423 A/cm^2. The 405 mA spectrum was recorded just above the threshold. Stimulated emission arises at the maximum of spontaneous emission, thus, one can conclude that lasing proceeds via the QD ground states. $P_{out}-I$ dependence becomes sublinear from 2.7 A due to the heating of the active region. One can see that the laser demonstrates the maximum output power as high as 3.28 W. The differential efficiency was estimated to be 73%.

Increasing the QD areal density allowed us to increase the maximum current flowing through the structure, since this current is limited by the finite amount of QDs themselves and relatively slow capture of carriers into them. Moreover, this leads to the decrease in population of the wetting layer and matrix states at the same pumping level, that in its turn, results in the reduction of parasitic current and structure overheating caused by recombination via upper states. Both these facts are very important to achieve high output power.

Thus, in this work we demonstrated room temperature CW lasing via the QD states with the maximum output power as high as 3.3 W. This result points out that QDs can be used as an active region of injection lasers for high-power applications. We believe that further progress can be achieved by optimizing both the design of active region and the fabrication of laser diodes.

Acknowledgements

This work is supported by the Program of the Ministry of Science of Russia "Physics of Solid State Nanostructures" and INTAS 96-0467.

References

[1] L. Goldstein, F. Glas, J. Y. Marzin *et al.*, *Appl. Phys. Lett.* **47** (10), 1099 (1985).
[2] M. Asada, Y. Miyamoto, Y. Suematsu *et al.*, *J. Quant. El.* **QE-22**, 1915 (1986).
[3] V. M. Ustinov, A. Yu. Egorov, A.R. Kovsh *et al.*, *J. Cryst. Growth* **175/176**, 689 (1997).
[4] V. M. Ustinov, A. E. Zhukov, A. Yu. Egorov *et al.*, *Electron. Lett.* **34** (7), 670 (1998).
[5] M. V. Maximov, Yu. M. Shernyakov, N. N. Ledentsov *et al.*, *Proc. 6th Int. Symp. "Nanostructures: Physics and Technology", St. Petersburg, June 22-26, 1998* , p. 202.
[6] A. R. Kovsh, A. E. Zhukov, A. Yu. Egorov, *et al.*, *Semiconductors* **32** (9), 997 (1998).
[7] T. Makino, J. D. Evans and G. Mak, *Appl. Phys. Lett.* **71** (20), 2871 (1997).
[8] N. Kirstaedter, O. Schmidt, N. N. Ledentsov *et al.*, *NY, USA: IEEE* **1**, 290 (1995).
[9] Q. Xie, A. Madhukar, P. Chen and N. Kobayashi *et al.*, *Phys. Rev. Lett.* **75**, 2542 (1995).
[10] V. P. Evtikhiev, I. V. Kudryashov, E. Yu. Kotel'nikov *et al.*, *Semiconductors* **32**, 1323 (1998).

7th Int. Symp. "Nanostructures: Physics and Technology"
St Petersburg, Russia, June 14–18, 1999

1.06 and 1.3 μm resonant cavity-enhanced photodetectors based on InGaAs quantum dots

I. L. Krestnikov, N. A. Maleev, M. V. Maximov, A. F. Tsatsul'nikov, A. E. Zhukov, A. R. Kovsh, I. V. Kochnev, N. M. Shmidt, N. N. Ledentsov, V. M. Ustinov, P. S. Kop'ev, Zh. I. Alferov and D. Bimberg†
Ioffe Physico-Technical Institute, St Petersburg, Russia
† Institute für Festkörperphysik, Technische Universität Berlin, Hardenbergstr. 36, D-10623 Berlin, Germany

Photodetectors operating at the optimum wavelength for high-bit-rate, long-haul optical transmission systems (1.06, 1.3 and 1.55 μm) are of great practical importance and a subject of significant interest in research. To date, most of this work has utilized the InP/InGaAsP materials system, as the bandgap of the InGaAsP alloy can be adjusted to produce light emitters and detectors in the required wavelength range while keeping lattice matching with the InP substrate. On the other hand, using the strained InGaAs quantum dots (QDs) on GaAs substrates also allows to achieve the required wavelength range [1, 2]. The next step to improve photodetectors is to use a three-dimensional (3D) optical confinement for photons. It has been shown that the use of a Fabry–Perot resonant microcavity leads to an enhancement of the quantum efficiency, improved bandwidth, and better wavelength selectivity [3]. Distributed Bragg reflectors (DBRs) which are necessary for efficient microcavity resonators can be hardly obtained in the InGaAsP system due to low difference of refractive indices. While the GaAs/AlAs DBRs of good quality can be easily prepared. Taken together these facts: appropriate wavelength of the QD transitions and high performance GaAs/AlAs DBRs, one can conclude that the InGaAs/GaAs/AlAs system on a GaAs substrate is very beneficial for designing and fabricating the resonant cavity-enhanced (RCE) photodetectors [4, 5]. In this work we discuss optical properties of the structures with GaAs/AlAs DBRs and InGaAs QDs used as an active medium of the device.

The schematic view of the studied structures is shown in Fig. 1. First, bottom GaAs/AlAs DBR was grown on the GaAs (100) substrate by metal-organic chemical vapor deposition (MOCVD) (structure A) or molecular beam epitaxy (MBE) (structures B and C). Structure A consisted of 25 AlAs/GaAs periods, structure B—12 periods and structure C—22 periods. Then, a GaAs $2\lambda/n$ (n—refractive index, $\lambda = 1.3\,\mu$m for structures A and B and $\lambda = 1.06\,\mu$m for structure C) cavity region was grown by MBE for all structures. The special growth technique was used for structure A [6]. InGaAs QDs were introduced in the center of the cavity. Details of QDs growth are described elsewhere [1, 2]. The bottom part of the cavity was n-doped by Si and the top part was p-doped by Be. QDs were placed in an undoped layer having a 0.1 μm thickness. Together with the structure A a satellite structure without bottom DBR was grown during the same epitaxial run. For photocurrent measurements intracavity ohmic contacts were fabricated. Top SiO_2/ZnS DBRs (4 pairs) were deposited on structures B and C by thermal evaporation. Photoluminescene (PL) was excited by an Ar^+ laser (100 W/cm^2). A double-pass monochromator and a Ge-photodetector were used as detecting system. Light of a tungsten lamp was used for reflectivity measurements. For photocurrent investigations a light of the tungsten lamp passed through the monochromator and was focused on the RCE photodetector (1 mW/cm^2) by a microscope.

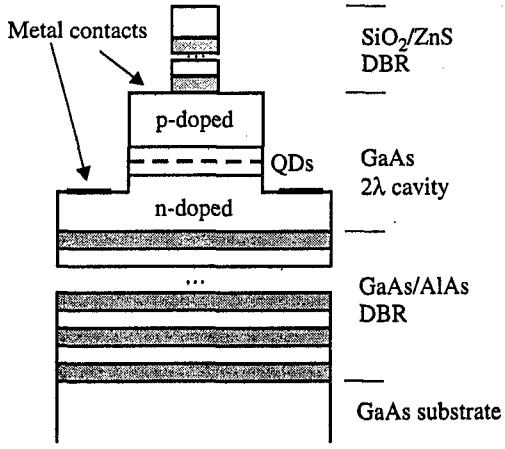

Fig. 1. Schematic view of the resonant cavity-enhanced photodetector structure.

In Fig. 2 PL spectra of structure A and its satellite (*a*) and an optical reflectance (OR) spectrum of structure A (*b*) are shown. The shape of the OR spectrum is defined by the GaAs/AlAs DBR which provides a very high reflectivity (better than 99.5%) as the sufficient number of periods in the DBR (25 GaAs/AlAs pairs) was grown. A cavity dip is not seen in the OR spectrum due to the low reflectivity of the air/GaAs interface. According to our computer simulations, the value of the dip is about 0.5% and cannot be well-resolved with our set-up.

PL spectrum of the satellite structure is typical for InGaAs QDs having optical transitions in the 1.3 μm-range [1], while the PL spectrum of structure A is dramatically changed by the DBR. The main peak is narrowed and its intensity is an order of magnitude higher than

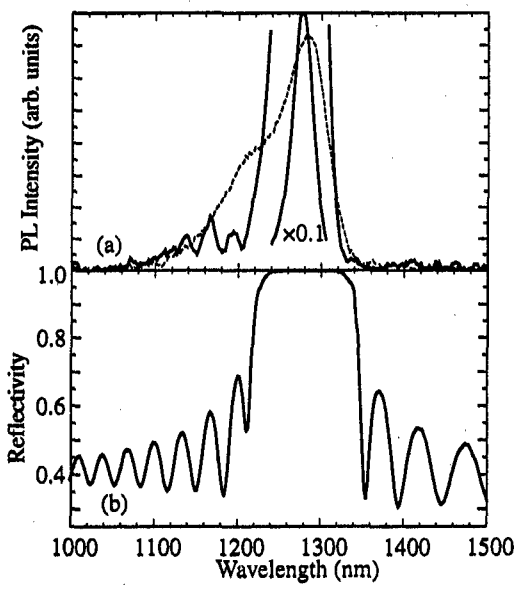

Fig. 2. Photoluminescence spectra of structure A and its satellite at 300 K (*a*) and optical reflection spectrum of structure A (*b*).

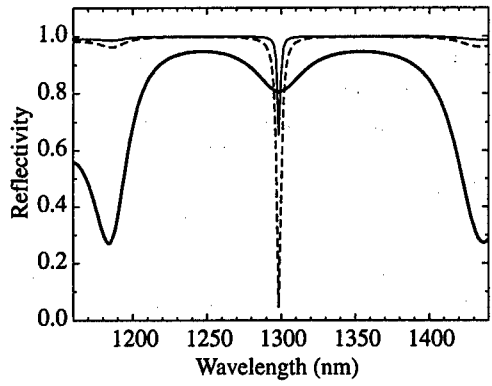

Fig. 3. Calculated optical reflectance (OR) spectra for structure B without (thick line) and with (thin line) top dielectric distributed Bragg reflector (DBR). Dashed line presents a calculated OR spectrum with top dielectric DBR having an antireflection coating.

that in the satellite structure. It can be explained by the formation of a standing wave in the microcavity at the resonant wavelength. In this case the line broading is caused only by finesse of the cavity. The second manifestation of the influence of DBR on the PL spectrum is the intensity oscillations on the short wavelength side of the peak. These oscillations are in an agreement with those in the OR spectrum. Thus, the effects of the resonant cavity-enhancements are evident even without the highly-reflecting top DBR. However, in this case the bandwidth is not narrow enough. To define proper parameters of the top dielectric (SiO_2/ZnS) DBR we performed a computer simulation of the OR spectra and the distribution of the electromagnetic field in the structure B.

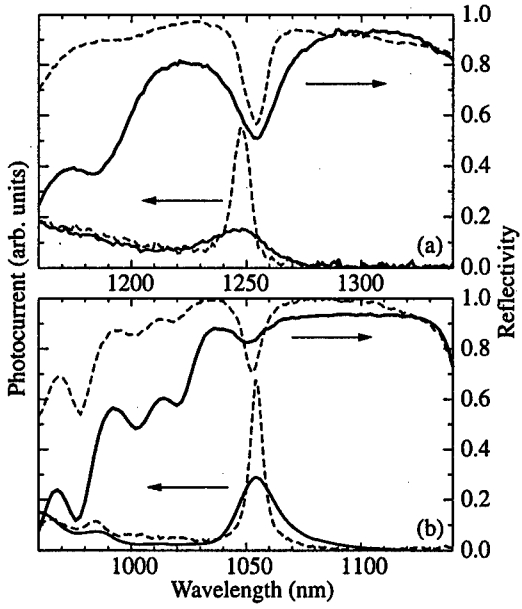

Fig. 4. Dependence of photocurrent *versus* wavelength and OR spectra for structures B (*a*) and C (*b*) without (solid line) and with (dotted line) top dielectric DBR.

The calculated OR spectra are shown in Fig. 3. As opposite to the case of the 25 pair AlAs/GaAs DBRs, in the case of only 12 pairs DBRs, the cavity dip is clearly seen in the calculated spectrum even without the top dielectric DBR (thick line). Using the top dielectric DBR dramatically improves the finesses of the cavity. It results in a narrowing of the cavity dip and in increase of its depth (thin line). However, due to the high reflectivity of the top DBR the most of the incident photons are reflected even at the resonant wavelength. To avoid the lose of the incident light it is possible to use an antireflection coating which is formed by increasing the thickness of the top ZnS layer up to the $\lambda/2n$ value. In the OR spectrum it results in a pronounced increase of the depth of the cavity dip (dashed line). In this case the most of the incident photons enters the structure and is adsorbed by QDs. This effect is also confirmed by the calculations of distribution of the intensity of the electromagnetic field in the structure. In the case of antireflection coating, the electromagnetic field intensity in the active region is much stronger than in the opposite case. Thus, for our devices we used dielectric DBR with top ZnS layer having a $\lambda/2n$ thickness.

Figure 4 shows dependence of photocurrent *versus* wavelength and OR spectra for structures B (*a*) and C (*b*) without (solid line) and with (dotted line) top dielectric DBR. One can see a resonant peak in photocurrent, which corresponds to the cavity dip in the OR spectra. Some detuning in wavelengths is caused by non-uniformity of the thicknessess of the epitaxial layers. As it follows from the calculations, the use of top dielectric DBR with antireflection coating results in an increase in depth and narrowing of the photocurrent peak. To improve these sensitivity of the device further, making it more attractive for device applications, it is necessary to use higher quality DBRs (similar to used in structure A). To overcome the problem of the slow growth rate in MBE, a set of structures with DBRs, having a large number of periods, were grown using MOCVD. The active region with QDs was grown by MBE on top of DBRs. Now these structures are under investigation.

In summary, we have fabricated RCE photodetectors with AlAs/GaAs DBRs and InGaAs QDs used as an active medium operating at 1.06 and 1.3 μm wavelengths.

This work was supported by RFBR and Volkswagen Foundation.

References

[1] A. E. Zhukov, *et al. Semiconductors* **33**, 167 (1999)

[2] M. V. Maximov, *et al. Proc. 24th Int. Conf. on the Physics of Semiconductors, Jerusalem, August 2-7, 1998* (World Scientific, 1998), *in print*

[3] A. Chin and T. Chang, *J. Vac. Sci. Tech.* **8**, 339–342 (1990).

[4] O. Baklenov, *et al. Electron. Lett.* **34**, 694–695 (1998).

[5] J. C. Campbell, *et al. Electron. Lett.* **33**, 1337–1339 (1997).

[6] N. A. Maleev, *et al. Proc. 6th Int. Symp. "Nanostructures: Physics and Technology", St. Petersburg, June 22-26, 1998* , pp. 297–299.

7th Int. Symp. "Nanostructures: Physics and Technology"
St Petersburg, Russia, June 14–18, 1999

Lasing from quantum dots formed by activated alloy spinodal decomposition on InAs stressors

M. V. Maximov†, Yu. M. Shernyakov†, A. F. Tsatsul'nikov†, B. V. Volovik†, D. A. Bedarev†, I. N. Kaiander†, N. N. Ledentsov†‡, A. E. Zhukov†, A. R. Kovsh†, V. M. Ustinov†, P. S. Kop'ev†, Zh. I. Alferov† and D. Bimberg‡

† Ioffe Physico-Technical Institute, St Petersburg, Russia

‡ Institut für Festkörperphysik, Technische Universität Berlin, D-10623 Berlin, Germany

Abstract. We demonstrate injection lasing in structures with a novel type of quantum dots (QDs) formed by activated spinodal decomposition on InAs stressors. At low temperatures the lasing is observed via the first exited QD exciton state with the lasing wavelength of 1.1 μm. With temperature increase lasing switches to higher energy states but remains up to room temperature. Simultaneous lasing via two energy states is also observed.

In recent years significant progress is achieved in fabrication, experimental and theoretical studies of lasers based on self-organized quantum dots [1–3]. Quantum dots (QDs) provide an ultimate limit of size quantization in solids, and, thus, an extreme modification of electronic properties as compared to bulk crystals. The δ-function like density of states and strong confinement of electron and hole wavefunctions in a QD result in a dramatically increased exciton oscillator strength, ultrahigh material and differential gain and can lead to reduced threshold current density and its improved temperature stability for proper device geometry. Threshold current densities as low as 60 A/cm^2 at room temperature are realized four side cleaved samples [2]. High internal (> 96%) and differential (70%) efficiencies are obtained for shallow mesa InGaAs-AlGaAs lasers based on vertically coupled QDs. It is experimentally proven that QD lasers provide ultrahigh material gain of 10^5 cm^{-1} and differential gain of 10^{-13} cm^{-2} in agreement with theoretical predictions [1].

Besides their fundamental advantages QDs allows to achieve emission at longer wavelength as compared to quantum well (QW) devices. Recently it has been well understood that in case of formation of a free-standing three-dimensional island on a lattice-mismatched substrate most of the strain can relax elastically, as opposite to the case of pseudomorphic layer growth, where strain relaxation can occur only via dislocation formation. In case of three-dimensional growth coherent narrow gap islands with sufficiently large volume can be formed, and, after overgrowth, longer wavelengths emission for the given narrow gap insertion and the wide gap matrix can be realized. This can be used to extend the operation wavelength of GaAs-based light emitters and photodetectors up to 1.3 μm [4] and even up to 1.75 μm [5]. Optoelectronic devices that emit or detect in the 1.3 μm wavelength range are technologically important for use in high-bit-rate, long-haul transmission lines and application that require transparent optical propagation through Si. Until recently only InP/InGaAsP material system has been utilized to fabricate 1.3 and 1.55 μm devices. On the other hand GaAs-based device technology is, in general, both cheaper and more advanced than that of InP and permits cost-efficient production of vertical cavity devices. Recently room-temperature lasing at the wavelength of 1.31 μm has been achieved via

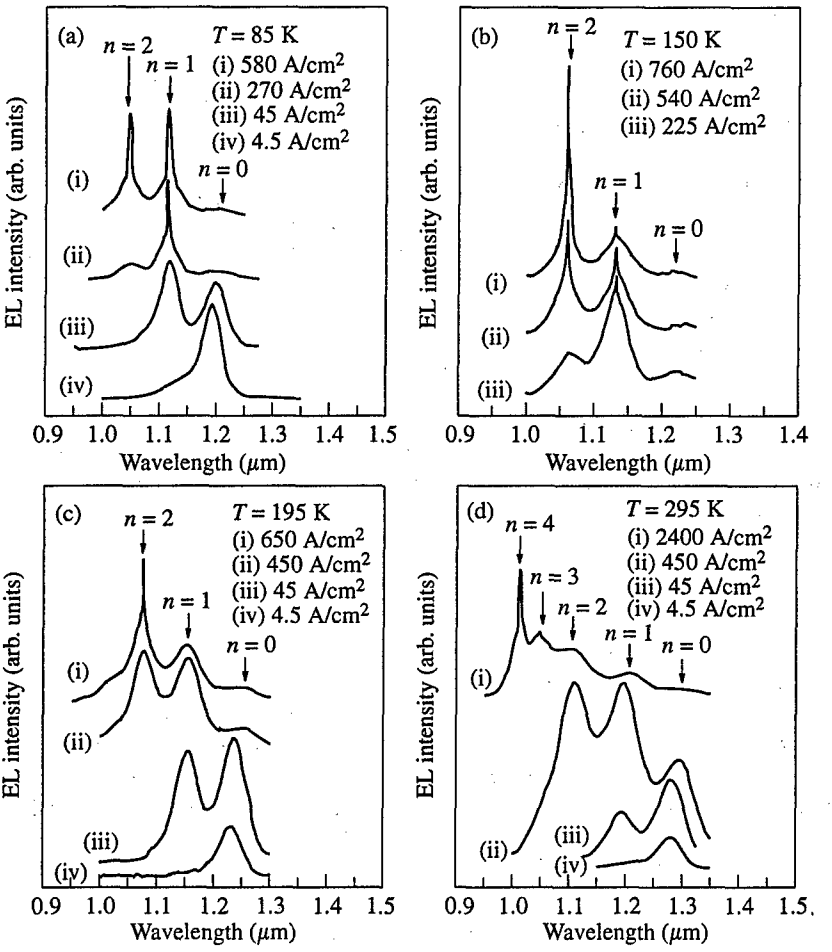

Fig. 1. Electroluminescence spectra for QD structure at different temperatures.

the $In_{0.5}Ga_{0.5}As/GaAs$ quantum dots with ultra-low (10 A/cm^2) threshold current nearly temperature insensitive up to 200 K [4].

In spite of the numerous advantages of QDs devices there still exists, however, a problem to bring unique results realized for QD lasers in the low temperature range to room temperature, where the characteristics of QD lasers are only approaching to those of the best quantum well (QW) devices. Thus, it seems to be very important to develop novel approaches for QD fabrication.

In this study we propose to fabricate QDs by activated InGaAs spinodal decomposition using sheet of predeposited InAs stressors [6, 7]. The details of MBE growth are presented elsewhere [7]. In this study we will focus on electroluminescence properties of these structures.

Figure 1(a) shows the spontaneous emission spectra for the laser samples with four cleaved sides at 85 K. At the current density of 4.5 A/cm^2 the emission is mainly from the ground states at $\sim$ 1.2 μm with a full width at half-maximum of about 30 meV. A band filling with increasing current occurs, which shows the first excited state at 1.12 μm and the second excited state at 1.05 μm. The peaks due to the emission from different QDs

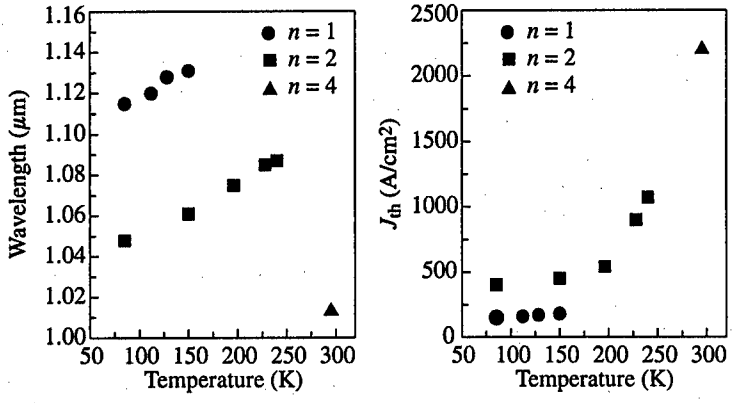

Fig. 2. Temperature dependences of the lasing wavelength and threshold current.

energy levels are well resolved and energy separation between ground and first and first and second energy levels can be estimated as 77 meV and 70 meV correspondingly.

At about 150 A/cm^2 lasing starts via the first excited level. At current densities higher than 400 A/cm^2 an additional lasing line due to the lasing via the second excited level appears in the spectra. Since the self-organized QD has the atomic-like density of states maximal gain increases with n as degeneracy of electron levels. At higher temperatures devices exhibit lasing via the $n = 2$ transition (Fig. 1(b)), and then via the $n = 3$ and $n = 4$ transitions at room temperature (Fig. 1(d)).

The temperature dependencies of the threshold current and wavelength are shown on Fig. 2. The threshold currents for $n = 1$ and $n = 2$ transitions are temperature independent up to 200 K due to the very deep confinement potential for these dots. At higher temperatures there is a significant increase in the threshold current density. Since at high temperatures lasing occurs via excited (i.e. shallower) energy levels we attribute this behavior to carrier escape from QDs to the GaAs waveguide region.

Even at low temperatures the $n = 0$ transition has insufficient gain to lase in the present structure. We believe that the main reason is low QD density of approximately 1×10^{10} cm^{-2} in this structure. Recent theoretical studies revealed that characteristics of the QD lasers (material gain, characteristic temperature (T_0), threshold current density (J_{th}), etc.) depend significantly on parameters characterizing arrays of QDs, such as surface density of QDs, size dispersion, QD localization energy, and structure geometry [8, 9]. One of the most important parameters is the dots surface density and optimization of this quantity can affect the device performance very significantly. It was shown that there exists a minimal surface density required to attain lasing at given inhomogeneous line broadening and total losses. The optimal surface density minimizing the J_{th} was estimated to be on the order of 10^{11} cm^{-2} for realistic QD size dispersion and typical losses [8]. As the typical density of InGaAs QDs is usually smaller than this value, the gain for the ground state transition may be not sufficient to overcome losses. Thus one can assume that after the QD density is increased high quality devices with low thresholds and high temperature stability can be realized.

To conclude we have studied the laser with active region based on quantum dots formed by activated alloy spinodal decomposition on InAs stressors. The lasing wavelength is 1.1 μm at 80 K which is to our knowledge significantly longer than that for quantum wells in the same material system. The threshold current has low temperature sensitivity up to 200 K.

Parts of this work are supported by Volkswagen Stiftung, INTAS-96-OPEN-467, BMBF, Russian Foundation for Basic Research. N.N.L. is grateful to the Alexander von Humboldt Foundation.

References

[1] M. Asada, Y. Miyamoto and Y. Suematsu, *IEEE J. Quantum. Electron.* **QE-22**, 1915 (1986).

[2] N. N. Ledentsov, V. M. Ustinov, A. Yu. Egorov, A. E. Zhukov, M. V. Maximov, I. G. Tabatadze and P. S. Kop'ev, *Semiconductors* **28**, 832 (1994).

[3] D. Bimberg, N. Kirstaedter, N. N. Ledentsov, Zh. I. Alferov, P. S. Kop'ev and V. M. Ustinov, *IEEE J. Sel. Top. Quantum Electron.* **3**, 196 (1997).

[4] D. L. Huffaker, G. Park, Z. Zou, O. B. Shchekin. and D. G. Deppe, *Appl. Phys. Lett.* **73**, 2564 (1998).

[5] M. V. Maximov, A. F. Tsatsul'nikov, B. V. Volovik, D. A. Bedarev, A. Yu. Egorov, A. E. Zhukov, A. R. Kovsh, N. A. Bert, V. M. Ustinov, P. S. Kop'ev, Zh. I. Alferov, N. N. Ledentsov, D. Bimberg, I. P. Soshnikov and P. Werner, *Proc. ICPS24, Jerusalem, August 2-7*, 1998 (World Scientific, 1998).

[6] I. L. Krestnikov, A. V. Sakharov, N. N. Ledentsov, I. P. Soshnikov, Yu. G. Musikhin, A. R. Kovsh, V. M. Ustinov, I. V. Kochnev, P. S. Kop'ev, Zh. I. Alferov and D. Bimberg *Proc. 6th Int. Symp. "Nanostructures: Physics and Technology", St. Petersburg, Russia,* June 22-26, 1998, p. 257-259, 1998.

[7] A. F. Tsatsul'nikov, N. A. Bedarev A. R. Kovsh, P. S. Kop'ev, N. N. Ledentsov, N. A. Maleev, Yu. G. Musikhin, M. V. Maximov, V. M. Ustinov, B. V. Volovik and A. E. Zhukov, this volume p. 139.

[8] L. V. Asryan and R. A. Suris, *IEEE J. Selec. Top. Quantum Electron.* **3**, 148 (1997).

[9] M. Grundmann and D. Bimberg, *Jap. J. Appl. Phys.* **36** part 1, 4181 (1997).

7th Int. Symp. "Nanostructures: Physics and Technology"
St Petersburg, Russia, June 14–18, 1999

1.3 μm emission from 2 ML InAs quantum dots in a GaAs matrix

A. F. Tsatsul'nikov, N. A. Bedarev, A. R. Kovsh, P. S. Kop'ev, N. N. Ledentsov, N. A. Maleev, Yu. G. Musikhin, M. V. Maximov, A. A. Suvorova, V. M. Ustinov, B. V. Volovik, A. E. Zhukov, D. Bimberg† and P. Werner‡

Ioffe Physico-Technical Institute, St Petersburg, Russia
† Institut für Festkörperphysik, Technische Universität Berlin, Hardenbergstr. 36, D-10623 Berlin, Germany
‡ Max-Planck-Institut für Mikrostrukturphysik, 06120 Halle, Germany

Significant interest in self-assembled quantum dots (QDs) fabricated in situ during deposition of thin strained layer on a surface of a lattice-mismatched material is related to unique properties of these QDs and extraordinary device expectations [1]. One of the possibilities is to widen the emission range on GaAs substrates up to 1.6–1.8 μm. Recently, lasing at 1.3 μm was realized in such QD structures [2]. This laser was based on $In_{0.5}Ga_{0.5}As$ QDs which were grown by molecular enhanced epitaxy and effective thickness of InGaAs layer was 11 monolayers (MLs). Alternative way to shift the emission band is to lower the band gap of the matrix by inserting the InAs QDs in a narrow InGaAs quantum well (QW) [3]. Additionally to the narrowing of the matrix material band gap, the spinodal decomposition of the InGaAs alloy on stressors can be responsible for the long-wavelength shift of the emission. These effects potentially allow to utilize QDs formed on the initial stage of islands formation (effective thickness of the InAs layer is about 2 MLs ≈ 6 Å). Exactly these QDs are usually used for applications in injection lasers. This is related to the coherent nature of small QDs and low probability of formation of dislocated clusters. Small QDs are usually characterized by high surface density and fast carrier capture and relaxation processes. In this work we investigated the structural and optical properties of InAs QDs inserted in (In,Al,Ga)As QWs as a function of effective thickness of the InAs layer and the composition and thickness of QW. All samples were grown by molecular beam epitaxy on GaAs(100) substrates. Active region contains InAs QDs which were overgrown by $In_xGa_yAl_{1-x-y}As$ QW. Effective thicknesses of the InAs layer (d_{InAs}), and the QW region (L_{QW}) and the InAs (x) and AlAs (y) contents of the QWs for the investigated structures are summarized in the Table, where the data of transmission electron microscopy (TEM) are represented: QD density (ρ_{QD}), density of threading dislocations (ρ_{disl}) and linear density of in-plane misfit dislocations formed due to QDs (ρ_{lin}). The table also shows the results of optical studies: PL peak wavelength (PL_{max}), integral intensity of the ground state QD PL (I_{gs}), integral intensity of the PL (I_{int}) line, and the ratio of the intensities of the ground state QD PL and higher-energy lines due to smaller dots and excited states (I_{gs}/I_{ex}).

To realize a significant shift of the PL line from 1.1 μm for 2ML InAs QDs towards the 1.3 μm wavelength these 2ML QDs were overgrown by InGaAs QW with relatively large InAs content (samples #1 and #2). As it is seen from the Table 2 ML InAs QDs covered by 40 Å $In_{0.40}Ga_{0.60}As$ QW emit at 1.3 μm (samples #1 and #2). Sample #1 is characterized by high QD density (more than 10^{11} cm^{-2}), but the high InAs mole fraction in QW leads to the strong increase in dislocation density and degradation of optical properties (decrease of integral PL intensity). Using of submonolayer (sml) deposition mode (sample #2) for InGaAs QW allows to decrease ρ_{lin} and ρ_{disl} and to increase the PL efficiency (Fig. 1).

Table 1.

Sample	#1	#2	#3	#4	#5	#6	#7	#8
d_{InAs}, Å	6	6	6.5	7.5	8	9	9	6
x	0.4	0.4	0.18	0.18	0.18	0.18	0.12	0.15
y	–	–	–	–	–	–	–	0.15
L_{QW}, Å	40	40 sml	25	25	25	25	60	40
ρ_{QD} 10^{10} cm^{-2}	12	6.1	3.4	–	4.3	–	3.6	2.8
ρ_{lin} 10^{4} cm^{-1}	4.8	3.3	2.3	–	2.7	–	4	0.83
ρ_{disl} 10^{8} cm^{-2}	180	14	no	–	1.4	–	15	1.8
PL_{max}, μm	1.30	1.31	1.24	1.26	1.27	1.27	1.30	1.32
I_{gs}	0.2	4	7	8	6	5	6.5	10
I_{int}^{I}	0.5	8	20	20	15	10	10	15
I_{gs}/I_{ex}	0.5	1.0	0.5	0.7	0.75	1.2	1.7	1.9

To investigate the influence of QD and QW parameters on structural and optical properties we changed the effective thickness of the deposited InAs layer keeping the constant parameters of InGaAs coverage (samples #3–6). One can see from the Table that, increase in the QD InAs layer thickness to 8 Å results in a shift of PL maximum to 1.27 μm and in an appearance of strong PL lines related to excited states in this case. Further increase in the InAs average thickness to 9 Å does not cause any significant shift of the emission band, but results in a decrease in the intensity of the excited state PL with respect to the ground state emission. In spite of the decrease in the integral intensity of the PL emission, the intensity of the ground state line remains constant. To shift the PL maximum further the InAs content in the QW was decreased and the QW thickness was increased (sample #7). This structure demonstrated 1.3 μm PL (Fig. 1) but was characterized by a high density of threading dislocations which is comparable with the case of sample #2 containing 2 ML QDs covered with an $In_{0.4}Ga_{0.6}As$ layer.

Thus, both methods (utilizing small and larger QDs) allow to realize 1.3 μm emission and results in comparable structural and optical quality. However, the possibility to reduce the defect density to acceptable levels is not evident in these approaches. We found also that the dependence of the PL peak energy on In composition, or thickness of the InGaAs layer is not monotone. There exist a critical composition for the fixed thickness (or a critical thickness for the fixed composition, e.g. 4 nm for 20% InAs content), when the PL maximum shifts back to smaller wavelength with increase in either thickness or composition. We attribute this effect to appearance of high concentration of dislocated clusters which accumulate In from the InGaAs strained regions in their vicinity.

To reach the 1.3 μm range we also used additions of Al in the InGaAs alloy. Al additions are known to enhance the effect of decomposition of strained InGaAlAs QWs [4]. The effect is observed also for thick (In,Al)As layers [5]. Spontaneous formation of compositionally-modulated structures is reported by us earlier for InGaAs quantum wells, but the effect was less pronounced in that case [6]. In the present work the InAs QDs was used as strained precursors to stimulate the decomposition intentionally. This allows, using small (6 Å) QDs and 40 Å $In_{0.15}Ga_{0.7}Al_{0.15}As$ QW (sample #8) to reach wavelength of

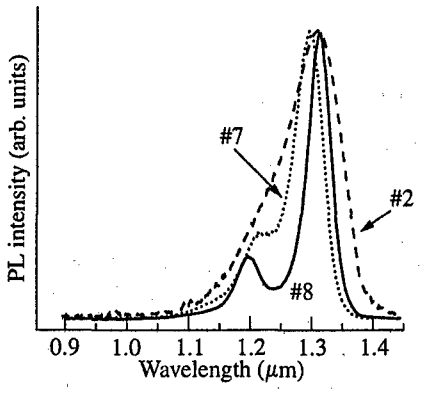

Fig. 1. PL spectra of investigated samples at $T = 300$ K.

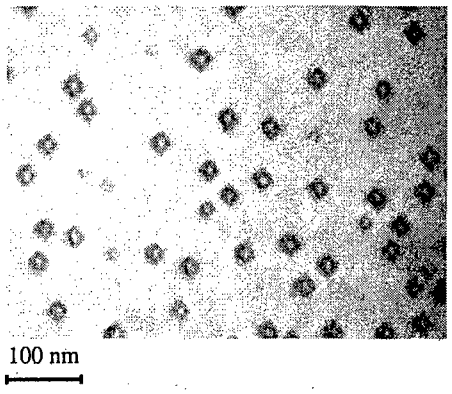

Fig. 2. TEM image of the sample #8.

1.3 μm (Fig. 1). This structure is characterized by relatively small density of 19 nm-large QDs (Fig. 2) but also, by low ρ_{lin} and ρ_{disl}. Small concentration of dots indicates that some dots can be dissolved during the overgrowth process as it is also can be seen for other samples. This structure demonstrated a high intensity ratio between ground state 1.3 μm PL and high-energy PL peak. A relatively weak decrease of the PL intensity by one order of magnitude at moderate excitation densities is observed with temperature increase up to 300 K. Thus, addition of Al does not result in a strong degradation of quality of the alloy, deposited at the relatively low substrate temperature. Thus, we studied dependence of structural and optical properties of the structures with InAs QDs embedded in (In,Ga,Al)As QW and demonstrated the possibility to reach the 1.3 μm emission range by using 2 ML InAs QDs as stressors for stimulated alloy decomposition.

This work was supported by Russian Foundation for Fundamental Research, the Program of the Ministry of Science of RF "Physics of Solid-State Nanostructures", INTAS-96-0467 and Volkswagen Foundation.

References

[1] Y. Arakawa and H. Sakaki, *Appl. Phys. Lett.* **40**, 939–941 (1982).
[2] D. L. Huffaker et al., *Appl. Phys. Lett.* **73**, 2564–2566 (1998).
[3] A. E. Zhukov et al., *Fiz. Tekhn. Poluprov.* **33**, 180–183 (1999).
[4] I. L. Krestnikov et al, *Proc. of the 6th Int. Symp. "Nanostructures: Physics and Technology"*, St. Petersburg, Russia, June 22-26, 1998, pp. 257–259.
[5] S. W. Jun et al., *Appl. Phys. Lett.* **68**, 3443–3445 (1996).
[6] N. N. Ledentsov et al., *Appl. Phys. Lett.* **70**, 2888–2890 (1997).

7th Int. Symp. "Nanostructures: Physics and Technology"
St Petersburg, Russia, June 14–18, 1999

QW diode laser modulation by lateral gain tailoring

Ju. V. Alekseeva, M. S. Shatalov and S. A. Gurevich
Ioffe Physico-Technical Institute, St Petersburg, Russia

Abstract. We present a new modulation technique by the control of lateral modal gain profile in four-terminal stepped-mesa diode laser. The simulation of the high frequency laser characteristics is performed on the basis of a computer model of stripe geometry diode laser which takes into account lateral effects. Modulation bandwidth of 11 GHz for ridge laser can be extended for 5–6 GHz by employing a newly developed stepped-mesa laser design. Moreover, nearly flat small signal modulation response with 3 dB bandwidth as high as 38 GHz can be obtained by making use of modulation of the lateral gain profile.

Introduction

Nowadays, very high speed diode lasers are required to satisfy the rapid increase in transmission speed of long haul fiber optic network. Long (1.3 μm or 1.55 μm) wavelength semiconductor lasers with 30 GHz direct modulation bandwidth were recently reported [1]. Several attempts to further increase the 3 dB bandwidth under direct modulation were made [2, 3] using specially designed MQW structures. Structures with optimized MQW profile and doping levels were suggested and bandwidth of 40 GHz was obtained for devices lasing at 1.1 μm [2]. Tunneling injection lasers on 0.98 μm emission wavelength were proposed and 3 dB bandwidth of 48 GHz was demonstrated. However, it is hardly possible to significantly improve the direct modulation bandwidth by further optimization of the MQW structure design. Use of other modulation schemes such as push-pull modulation [4], reflection coefficient modulation [5] or confinement factor modulation [6] allows to improve the modulation performance with respect to direct modulation. In this paper we report on the design and high frequency performance of novel four-terminal stepped-mesa diode laser.

1 Laser design

The device is designed on the basis of the ridge laser with two additional side electrodes used for confinement factor modulation [6]. The laser is a multiple quantum well structure containing three InGaAsP ($\lambda = 1.3$ μm) QWs 1% compressive strained and four InGaAsP ($\lambda = 1.1$ μm) barriers lattice matched to InP. Fabry–Perot cavity is 150 μm long and has two cleaved mirrors with reflectivity coefficients of about 0.32. Central electrode, 2 μm wide, is surrounded by 1.5 μm wide stairs etched in upper cladding. The central contact is for pumping and/or direct modulation and side electrodes are for applying additional bias and/or modulating signals. The schematic representation of four-terminal stepped-mesa diode laser is depicted in Fig. 1. The main advantage of the laser geometry is the specific stepped-mesa profile of central electrode which allows to maintain specific lateral profile of the optical gain. The lateral overlap of injected carriers with the optical mode profile can be substantially increased with respect to traditional ridge or buried laser structures. This allows to improve the high frequency laser performance even under direct modulation. The use of additional side electrodes leads to tailoring of lateral shape of modal gain at

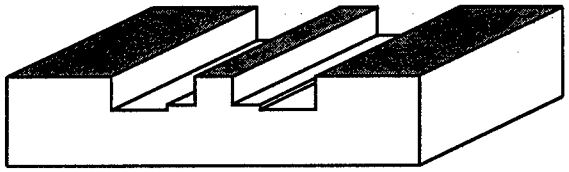

Fig. 1. Schematic representation of four-terminal stepped-mesa laser diode.

high speed. Direct modulation regime as well as modulation by the signal applied to the side electrodes can be realized in this structure. By using two simultaneous signals applied to the central and to the side electrodes, the output power waveform correction can be performed [6].

2 Results and discussion

The analysis of the laser operation is done using the computer model of laterally nonuniform ridge laser. This model accounts for all lateral effects which take place in a typical ridge laser such as lateral pumping current spreading in contact and upper cladding layers and carrier drift and diffusion in undoped SCH and MQW layers. The model includes in a phenomenological way the processes of carrier capture and escape in/out of QWs.

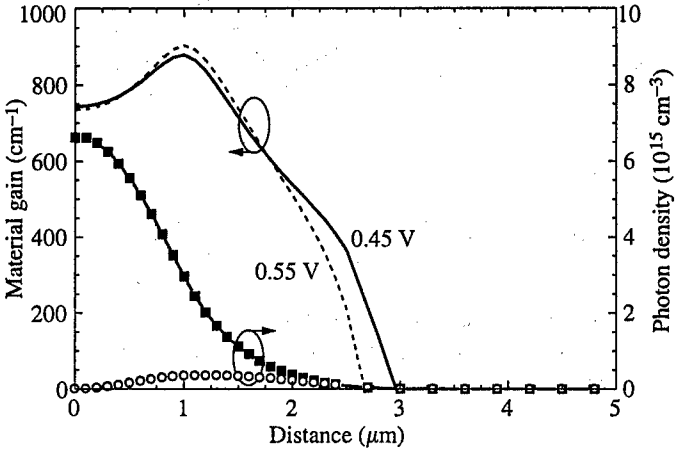

Fig. 2. Lateral distributions of material gain (lines) in four-terminal stepped-mesa structure at different voltages applied to the side contacts. The photon densities in zero- (solid symbols) and first-order (open symbols) lateral modes correspond to 0.55 V side voltage.

Due to the axial symmetry, the simulations are performed only for the right-hand side of the laser structure and then the lateral distributions obtained are extended to the whole device to calculate the total output power. The lateral distribution of material gain at different bias applied to the side contacts is plotted in Fig. 2. The photon density profiles in zero- and first-order lateral modes are also presented in Fig. 2. The mode profiles are assumed to be fixed by the index steps in deeply etched mesa structure and independent of pumping and side bias. As can be seen in this figure, lateral gain profile changes with the side voltage in very special manner. In the center of the mesa ($x = 0$) high photon density drastically reduces the effective carrier lifetime leading to the clamping of the carrier density. Due to this the material gain also becomes fixed in the center of the mesa. The gain is allowed to

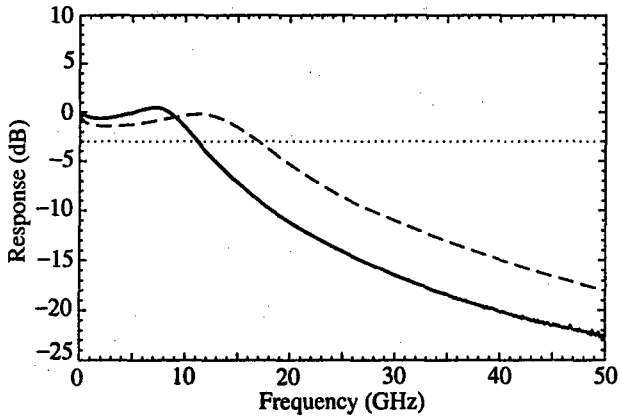

Fig. 3. Simulated small signal direct modulation responses of simple ridge (solid) and stepped-mesa (dash) structures.

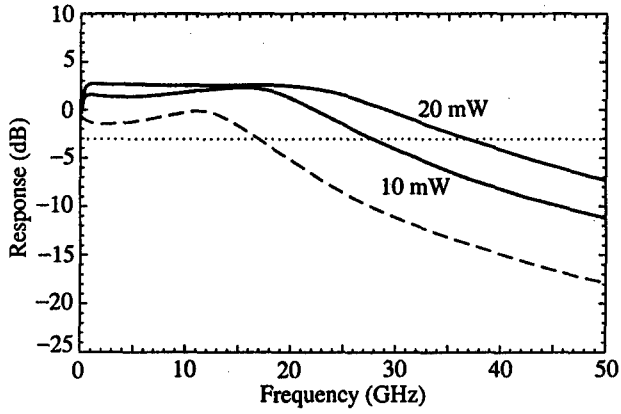

Fig. 4. Simulated small signal responses of a stepped-mesa structure under modulation by the side voltage (solid) at different output power levels. Direct modulation response at 10 mW (dash) is shown for comparison.

change only in the areas under the steps of the mesa. The proper design of the width and height of these steps results in a very efficient lateral gain tailoring by the side voltage.

Fig. 3 shows the small signal direct modulation responses for two cases of laser geometry. The first is a simple 2 μm wide ridge and the second is a stepped-mesa etched to the same depth as the ridge. It is clear from Fig. 3 that direct modulation bandwidth improves in stepped-mesa device, which is due to lateral redistribution of the injected carriers. The 3 dB bandwidth of 11 GHz in ridge laser can be extended for 6 GHz by using the stepped-mesa structure.

The high speed performance of a stepped-mesa laser improves significantly when the modulating voltage signals are applied to the side electrodes. The comparison of simulated small signal responses under direct (pumping current) and side voltage modulation is presented in Fig. 4. The cut-off frequency of 28 GHz is achieved at 10 mW output power under the modulation of the lateral gain distribution, while the direct modulation bandwidth is only 17 GHz. At higher output power, the 3 dB bandwidth of 38 GHz is obtained.

3 Summary

We have analyzed the design features and high frequency performance of a four-terminal stepped-mesa diode laser. It is shown that with the use of stepped-mesa structure the intrinsic response of the laser can be extended towards higher frequency even under direct modulation. The modulation by the signals on side electrodes of the device results in a very broad modulation bandwidth by means of lateral gain tailoring. The modulation response with 3 dB bandwidth as high as 38 GHz can be obtained on the structure initially having only 11 GHz cut-off frequency.

This work is supported by INTAS grant 93-0049 ext.

References

[1] Y. Matsui et. al. *IEEE Phot. Techn. Lett.* **9**, 25-27 (1997).
[2] S. Weisser et. al. *IEEE Phot. Techn. Lett.* **8**, 608–610 (1996).
[3] X. Zhang et. al. *IEEE J. Sel. Top. Quantum Electron.* **3**, 309–314 (1997).
[4] M. C. Nowell et. al. *IEEE J. Sel. Top. Quantum Electron.* **1**, 433–441 (1995).
[5] E. Goutain et. al. *Electron. Lett.* **32**, 896–897, (1996).
[6] S. A. Gurevich et. al. *Int. J. High Speed Electron. Syst.* **8**, 547–574 (1997).

7th Int. Symp. "Nanostructures: Physics and Technology"
St Petersburg, Russia, June 14–18, 1999

Peculiarities of radiative recombination in BeMgZnSe/ZnCdSe injection lasers

V. I. Kopchatov, N. Yu. Gordeev, S. V. Ivanov, P. S. Kop'ev,
H.-J. Lugauer†, G. Reuscher†, A. Waag† and G. Landwehr†
Ioffe Physico-Technical Institute, St Petersburg, Russia
† Physikalisches Institut der Universität Würzburg, Am Hubland,
D-97074 Würzburg, Germany

Introduction

The wide band-gap II–IV compounds are considered to be most suitable for manufacturing light emitting diodes (LED) and lasers emitting in a short wavelength range of visible spectrum. Now the utmost interest to such lasers is related to a potential opportunity for creation large-color-screen projection television. Recently, due to the relatively fast progress in the improvement of the structural properties of (Mg,Zn,Cd)(S,Se) heterostructures several groups have reported on lasing both at low [1, 2] and room temperature (RT) [3]. But short lifetime of injection blue-green lasers at RT still limits their commercial application [4].

In this paper we report on study of the main characteristics of RT injection lasers based on BeMgZnSe/ZnCdSe separated confinement heterostructure (SCH).

1 Experimental

The laser BeMgZnSe/ZnCdSe SCH investigated was grown by molecular beam epitaxy (MBE) pseudomorphically to a GaAs (001) substrate at substrate temperature of 270–280 °C. The MBE growth and composition control of Be-chalcogenides based heterostructures have been published elsewhere [5]. The active region of the laser diode structure contains a (10 Å-$Be_{0.05}Zn_{0.95}Se$/15 Å-ZnSe)$_{82}$ superlattice (SL) waveguide lattice-matched to GaAs as a whole, centered with a 2.6 ML-CdSe/10 nm-ZnSe nanostructure. Details of structural and optical characteristics of the active region have been given elsewhere [6]. The structure also involves around 1 μm-thick wider bandgap n- and p-$Be_{0.05}Mg_{0.06}Zn_{0.91}Se$ cladding layers, doped with iodine and nitrogen, respectively, as well as a top ZnSe/BeTe:N modulation doped graded SL capped with a 10 nm-BeTe layer for the low-resisitvity ohmic contact fabrication.

Laser samples of 20 μm-wide stripe geometry were investigated. The lasers were pumped by pulsed current (0.2–2.0 μs pulse duration, 50–1000 Hz repetition frequency). All experiments were carried out at RT.

2 Results and discussion

The dependence of the threshold current density (J_{th}) versus output optical losses is shown in Fig. 1. As follows from it, J_{th} is characterized by an abrupt growth with increasing the losses. The similar drastic increase in J_{th} has been observed earlier and is typical for SCH with quantum well [7].

Electroluminescence (EL) spectra of experimental sample at different pumping currents are also presented in Fig. 1. As is seen, the position of the EL peak is shifted slowly in

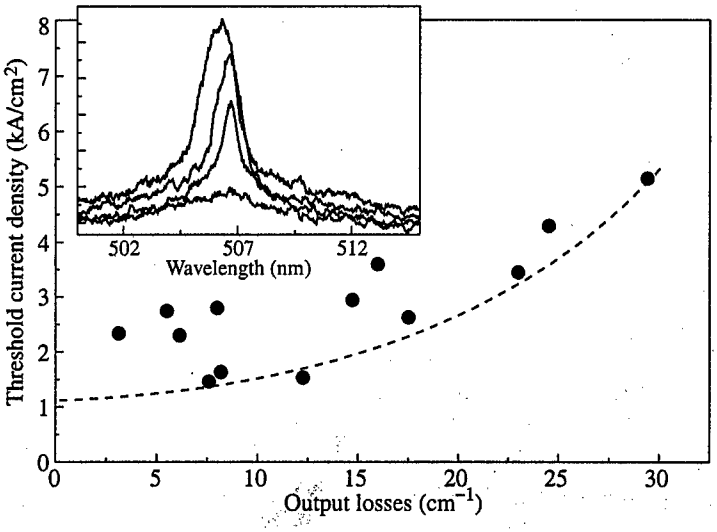

Fig. 1. Threshold current density as a function of output optical losses. Electroluminescence spectra of experimental sample at different pumping current ($0.98I_{th}$, I_{th}=265 mA, $1.1I_{th}$, $1.5I_{th}$) are shown in the insert.

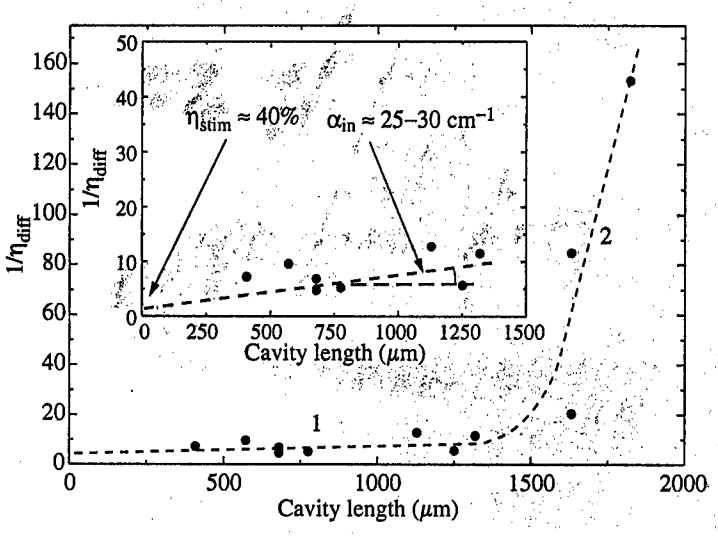

Fig. 2. Inverse differential quantum efficiency of stimulated emission vs laser cavity length.

the short-wavelength direction with increasing the pumping current. It may be attributed to rising an inversion level in the structure.

To determinate the internal quantum efficiency of stimulated emission (η_{stim}) and the internal cavity losses (α_{in}) the differential quantum efficiency — η_{diff} (DQE) was studied. We should note that despite the known structural imperfection of the studied heterostructure (stacking fault density is in excess of 10^6 cm^{-2}) the η_{diff} as high as 21% per both facets has been obtained. The cavity length dependence of the inverse differential quantum efficiency of the stimulated emission is plotted using experimental data (see Fig. 2).

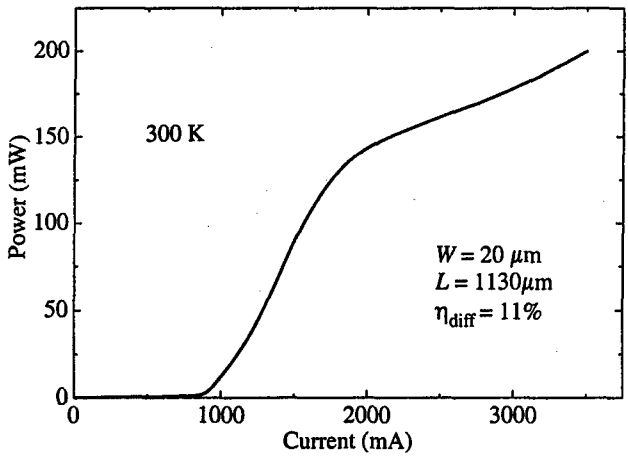

Fig. 3. Light-current characteristic of BeMgZnSe/ZnCdSe laser in quasi-CW regime.

It should be noted that the internal quantum efficiency of stimulated emission is limited by the value of 40%. The rest 60% of emitted photons contribute to a spontaneous recombination. It may be explained by inhomogeneous CdSe-based active region. As follows from Fig. 2 (slope 1), the intrinsic cavity losses reach the value of $25 \div 30$ cm^{-1}, which can obviously be lowered by an optimization of the waveguide geometry (e.g. using wider band-gap emitter). Increasing cavity length (slope 2) up to 1500 μm leads to drastic fall of the DQE (and respectively to rising the inverse DQE). We attribute it with the micro- and especially macro-defects which began to be significant in long lasers.

Using the value of α_{in} and the plot from Fig. 1 allow us to estimate the transparency current density. It has been found to be as high as $\approx$1 kA/cm^2. It can be supposed that improvement both the composition and the uniformity of active region will significantly reduce this value.

In spite of the rather high threshold current density and significant internal cavity losses we succeed in obtaining the quasi-CW laser operation. In that measurements the samples were bonded stripe down to the cooper using indium solder. The light output power reaches 200 mW per facet (Fig. 3), which is the record value ever reported for BeMgZnSe/ZnCdSe blue-green lasers.

No reflecting materials to cover laser mirrors were used. Pumping current pulse had a 2 μs duration and a 1 kHz repetition frequency. The saturation of light-current characteristic under the high pumping current may be attributed to the heating of the active region and neighboring layers.

3 Conclusions

EL study of the BeMgZnSe/ZnCdSe injection laser heterostructure has been performed. The RT threshold current density of $\approx$1.4 kA/cm^2 has been obtained at the lasing wavelength of 506 nm. Maximal value of the differential quantum efficiency achieved is 21% per both facets. RT light output power as high as 200 mW per facet at quasi-CW operation has been demonstrated. Potential opportunities for laser characteristics improvement in such heterostructures have been shown.

Acknowledgements

Authors are grateful to V. V. Zabrodskii and V. L. Sukhanov for precisely calibrated photodetectors. This work was supported in part by RFBR, the Program of the Ministry of Sciences of RF "Physics of Solid State Nanostructures" and the Volkswagenstiftung.

References

[1] M. A. Haase, J. Qiu, J. M. DePuydt, and H. Cheng, *Appl. Phys. Lett.* **59**, 1272 (1991).

[2] H. Jeon, J. Ding, A. V. Nurmikko, W. Xie, D. C. Grillo, M. Kobayashi, R. L. Gunshor, G. C. Hua, and N. Otsuka, *Appl. Phys. Lett.* **60**, 2045 (1992).

[3] H. Jeon, J. Ding, A. V. Nurmikko, H. Luo, N. Samarth, J. K. Furdyna, W. A. Bonner, and R. E. Nahory, *Appl. Phys. Lett.* **57**, 2413 (1990).

[4] M. Kato, H. Noguchi, M. Nagai, H. Okuyama, S. Kijima and A. Ishibashi, *Electron. Lett.* **34**, 282 (1998).

[5] A. Waag, F. Fischer, K. Schull, T. Baron, H. -J. Lugauer, Th. Litz, U. Zehnder, W. Ossau, T. Gerhardt, M. Keim, G. Reuscher, and G. Landwehr, *Appl. Phys. Lett.* **70**, 280 (1997).

[6] S .V. Ivanov, A. A. Toropov, S. V. Sorokin, T. V. Shubina, I. V. Sedova, A. A. Sitnikova, P. S. Kop'ev, Zh. I. Alferov, H. -J. Lugauer, G. Reuscher, M. Keim, F. Fischer, A. Waag, G. Landwehr, *Appl. Phys. Lett.* **74**, 498 (1999).

[7] S. V. Zaitsev, N. Yu. Gordeev, V. M. Ustinov, A. E. Zhukov, A. Yu. Egorov, M. V. Maksimov, A. F. Tsasul'nikov, N. N. Ledentsov, P. S. Kop'ev, and Zh. I. Alferov, *Semiconductors* **31**, 539 (1997).

7th Int. Symp. "Nanostructures: Physics and Technology"
St Petersburg, Russia, June 14–18, 1999

High power broadband singlelobe InGaAsP/InP superluminescent diode

N. A. Pikhtin, A. Yu. Leshko, A. V. Lyutetskiy, S. A. Shuravin,
A. L. Stankevich, N. V. Fetisova and I. S. Tarasov
Ioffe Physico-Technical Institute, St Petersburg, Russia

Abstract. Superluminescent diodes (SLDs) operating in 1300–1550 nm wavelength range with high output power (40 mW), wide spectra width (65 nm at FWHM), low modulation depth (< 1%) and singlelobe far-field pattern have been fabricated. The optimum SLD is 10° tilted mesa-stripe construction with back absorbtion section based on broad gain profile InGaAsP/InP separate confinement double heterostructure.

Introduction

Superluminescent diodes (SLD) are the optimum light sources for optical low coherence reflectometry [1] and fiber gyroscopes due to their short coherence length, low intrinsic noise and broad emission spectra. In this connection broadband SLD emitting in 1300–1550 nm wavelength range with high output optical power and effective coupling with singlemode optical fiber is of great interest.

The main problem to obtain high power superluminescent emission is to reach high optical gain within diode without optical feedback. The most effective ways of Fabry–Perot modes suppression are the following: deposition of antireflection coating on diode facets [3], introduction of unpumped absorbing region [4–5], tilted stripe formation [6].

This paper reports on the investigation and fabrication of optimum SLD construction for the achievement of maximum cw output power of singlelobe broadband superluminescent emission with low spectral modulation. SLD was based on mesastripe laser diode construction [7] on the base of InGaAsP/InP separate confinement double heterostructure (SC DH) grown by modified version of LPE technology [8]. 800 Å active layer and 1 μm waveguide thicknesses were chosen in the case of SLD construction. Mesastripe laser structure with 4 μm stripe width provides effective coupling in singlemode optical fiber with 50% coupling coefficient [7]. Laser diodes on the base of such construction have low threshold current, high internal and external quantum efficiency and high output power in single transverse mode operation [7]. Our previous investigations [9, 10] showed that such laser diodes possess anomalously wide lasing and spontaneous emission spectra. An existence of very broad gain profile [10] makes such structure very attractive for the fabrication of SLD with high output power and broad emission spectra.

1 Experimental results and discussion

To achieve superluminescent emission SC DH InGaAsP/InP mesa stripe laser diode construction was modified with the aim of lasing suppression. Influence of each introduced change in the construction on such diode output characteristics as lasing threshold current, output power and efficiency of superluminescent emission, emission spectra width and spectra modulation was examined.

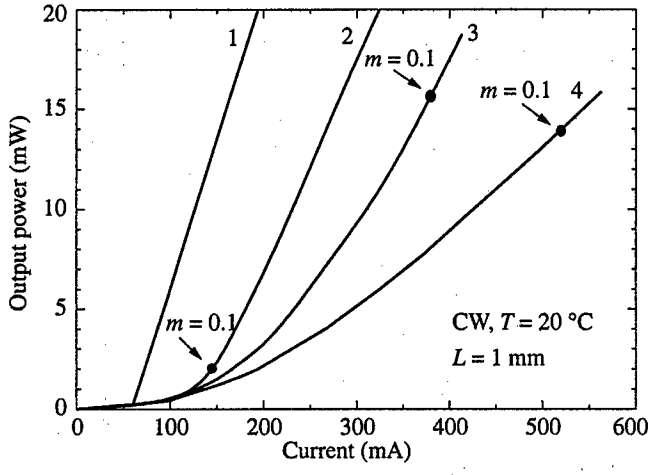

Fig. 1. CW light-current characteristics of SC DH InGaAsP/InP ($\lambda = 1.55\ \mu$m) SLD of mesa construction with tilted stripe angle α: 1—$\alpha = 0°$ (laser diode), 2—$\alpha = 5°$, 3—$\alpha = 10°$, 4—$\alpha = 14°$.

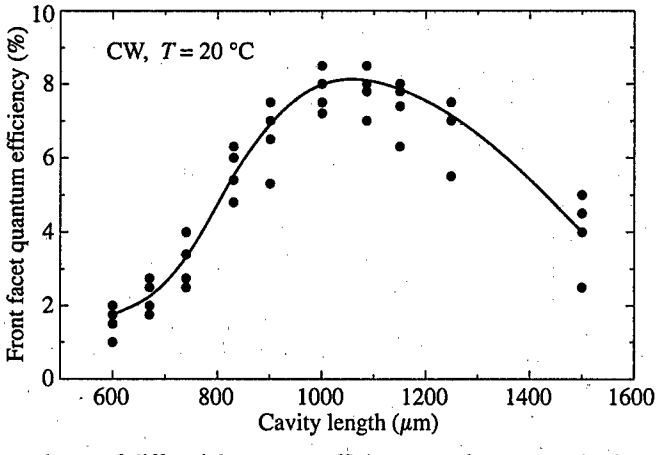

Fig. 2. The dependence of differetial quantum efficiency per facet on cavity length of 10° tilted mesastripe SC DH InGaAsP/InP ($\lambda = 1.55\ \mu$m) SLD.

Investigation of radiation characteristics of SLD with different tilted stripe angle α (from 0° to 14°) and different cavity length L allowed to determine the optimum values of those parameters (Fig. 1 and Fig. 2). They were found to be $\alpha = 10°$ and $L = 1$ mm. As it is seen in Fig. 1, superluminescent emission power increases with the increase of tilted stripe angle. Besides, emission spectra halfwidth (FWHM) decreases with the increase of pump current, and this dependence the sharper the tilted stripe angle less. At the same time the spectral modulation depth $m = (P_{max} - P_{min})/(P_{max} + P_{min})$ increases, where P_{max}, P_{min} are the maximum and the minimum peak intensities in the emission spectra. The value $m = 0.1$ was chosen as a threshold point of lasing regime (it is indicated on light-current curves in Fig. 1).

The sharp dependence of differential quantum efficiency of stimulated emission η_d on

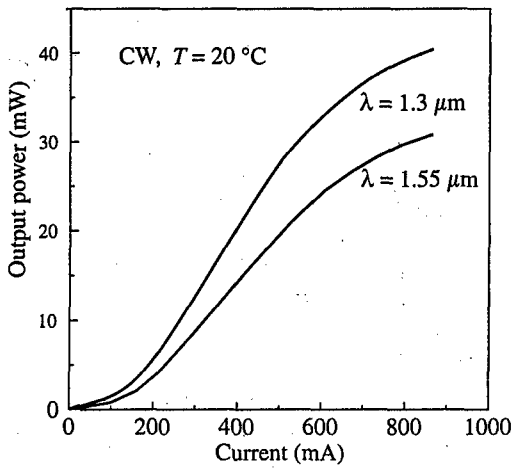

Fig. 3. Room temperature cw light-current characteristics of SC DH InGaAsP/InP (λ = 1.3–1.55 μm) SLDs with 10° tilted mesastripe (L = 1 mm) and back absorbing section (L = 300 μm).

SLD cavity length (Fig. 2) compared to laser diode one [11] is connected with single pass operation regime of SLD (η_d) decrease at short cavity length and an increase of internal optical losses (η_d decrease at long cavity length).

Maximum cw output power of superluminescent emission of tilted stripe InGaAsP/InP SLD (λ = 1.55 μm) measured at 0.1 spectra modulation depth reached 15 mW at optimum values α = 10° and L = 1 mm.

An introduction of additional back absorbing section in tilted mesa stripe SLD construction made it possible to widen the range of superluminescent emission. Such construction is similar to two-section laser diode construction described in detail in our previous work [10]. In SLD case the optimum lengths of pumped and absorbing sections were found to be 1000 μm and 300 μm, respectively. The *cw* light-currrent characteristics of two-section tilted stripe (α = 10°) InGaAsP/InP SLD are presented in Fig. 3. Such SLD construction allowed to receive 40 mW (λ = 1.3 μm) and 30 mW (λ = 1.55 μm) cw output power of superluminescent emission. Emission spectra FWHM is 60 nm (spectra modulation depth $m < 0.03$) and 65 nm ($m < 0.01$) at maximal output power P_{max} and operating output power $1/2P_{max}$, respectively. The far field pattern is singlelobe with FWHM ($\theta_{\parallel}$ = 25° and $\theta_{\perp}$ = 40°), allowing efficient coupling into singlemode optical fiber.

Deposition of antireflection (AR) coating with reflection coefficient R = 1% on the front facet of SLD didn't result in perceptible increase of output power of superluminescent emission.

Further optimization of superluminescent diode efficiency is seen in the decrease of heterostructure internal optical losses and deposition of AR coating with R less than 0.1%.

Summary

We have demonstrated high power low coherence singlelobe InGaAsP/InP (λ = 1.3 – 1.55 μm) superluminescent diode. SLD uses two-section mesa construction with 10° tilted stripe of 4 μm width and 1000 μm length and back absorbing region of 300 μm length. CW output powers as high as 40 mW (λ = 1.3 μm) and 30 mW (λ = 1.55 μm)

were achieved. Emission spectra halfwidth is 65 nm with spectral modulation of less than 0.01. Singlelobe far-field pattern allows efficient coupling into singlemode optical fiber.

References

[1] R. C. Youngquist, S. Carr and D. E. N. Davies, *Opt. Lett.* **12**, 158 (1987).

[2] W. K. Burns, C. L. Chen and P. P. Moeller, *IEEE/OSA J. Lightwave Technol.* **LT-1**, 98 (1983).

[3] I. P. Kaminow, G. Eisenstein and L. W. Stulz, *IEEE J. Quantum Electron* **QE-19**, 493 (1983).

[4] N. S. K. Kwong, N. Bar-Chaim and T. Chen, *Appl. Phys. Lett.* **54** (4), 298 (1989).

[5] H. Nagai, Y. Noguchi and S. Sudo, *Appl. Phys. Lett.* **54** (18), 1719 (1989).

[6] C. F. Lin, *Electr. Lett.* **27**, 968-970 (1991).

[7] M. A. Ivanov, N. D. Ilyinskaya, Yu. V. Ilyin, Yu. A. Korsakova, A. Yu. Leshko, A. S. Lunev, A. V. Lyutetskiy, A. V. Murashova, N. A. Pikhtin, I. S. Tarasov, *Tech. Phys. Lett.* **21** (3), 198 (1995).

[8] Zh. I. Alferov and D. Z. Garbuzov, *Fiz. Tekh. Poluprovod.* **21** (7), 824 (1987).

[9] N. A. Pikhtin, M. A. Ivanov and I. S. Tarasov, *Semiconductors* **28** (11), 1094 (1994).

[10] N. A. Pikhtin, A. Yu. Leshko, A. V. Lyutetskiy, V. B. Khalfin, N. V. Shuvalova, Yu. V. Ilyin and I. S. Tarasov, Int. Symp. *Nanostructures: Physics and Technology*, St. Petersburg, Russia, 24-28 June 1996, Abstracts, pp. 362-365 (1996).

[11] D. Z. Garbuzov, A. V. Ovchinnikov, N. A. Pikhtin, I. S. Tarasov, Z. N. Sokolova and V. B. Khalfin, *Fiz. Tekh. Poluprovod.* **25** (5), 928 (1991).

7th Int. Symp. "Nanostructures: Physics and Technology"
St Petersburg, Russia, June 14–18, 1999

Peculiarities of photoluminescence and electroluminescence properties of spontaneously formed periodical InGaAsP/GaAs structures

I. S. Tarasov†, L. S. Vavilova†, V. A. Kapitonov†, D. A. Livshits†,
A. V. Lyutetskiy†, A. V. Murashova†, N. A. Pikhtin† and G. V. Skrynnikov§
† Ioffe Physico-Technical Institute, St Petersburg, Russia

Abstract. Double heterostructures with spontaneously formed periodical (SFP) InGaAsP/GaAs active regions have been grown. The dependence of photoluminescence (PL) and electoluminescence (EL) properties of SFP InGaAsP/GaAs structures on excitation level and temperature have been investigated. From analysis of linear polarization rate spectral dependencies of PL SFP InGaAsP/GaAs structures it have been determined that domains with different solid phase composition have lattice mismatch (Δa) value of opposite sign. Threshold current density 50 A/cm^2 at 77 K have been obtained in laser structures. Strong saturation of longwavelength emission band intensity in room temperature PL and EL spectra with the increase of excitation level have been revealed.

Introduction

In our previous works [1–3] the growth method of spontaneously formed periodical (SFP) InGaAsP/GaAs structures was proposed. This method is based on the use of the spinodal decomposition effect of A^3B^5 multicomponent solid solutions [3–6]. Carried out experimental and theoretical investigations of SFP InGaAsP/GaAs structures showed that such structures consist of domains with different composition periodically interchanged in (001) and (010) directions of the the easiest compression. According to microscopic investigations the dimension of SFP InGaAsP/GaAs domains is 200–600 Å [2]. In present paper investigation of photoluminescence and electoluminescence properties of SFP InGaAsP/GaAs structures have been carried out.

1 Experimental samples

Isotype and anysotype double heterostructures with spontaneously formed periodical (SFP) InGaAsP/GaAs structures as an active region were grown. Active region thickness was 0.2–0.3 μm. Energy bandgaps of SFP InGaAsP/GaAs domains were $E_{g1} = 1.46$ eV and $E_{g2} = 1.72$ eV which correspond to longwavelength and shortwavelength emission bands in luminescence spectra of double heterostructures. Four-cleaved laser diodes were fabricated from anysotype structures. Investigation of luminescence properties of fabricated samples were studied by standard PL and EL technique. For the investigation of linear polarization rate spectral dependencies the original method we had presented in [7–8] was used.

2 Results and discussion

2.1 *Photoluminescence properties of spontaneously formed periodical InGaAsP/GaAs structures*

Typical photoluminescence spectra of SFP InGaAsP/GaAs structures at room and liquid nitrogen temperatures have longwavelength and shortwavelength emission bands corresponding to radiative recombination in domains with different solid phase composition

(E_{g1}, E_{g2}). The main peculiarity of these spectra consists in temperature dependence of longwavelength and shortwavelength emission band intensities correlation. At liquid nitrogen temperature the correlation of longwavelength and shortwavelength emission bands intensities in PL spectra of SFP structures is well expressed with simple mathematical model taking into account the dependence of thermal distribution and free carriers ejection on potential well depth (E_{g1}, E_{g2}). 77 K PL spectra of SFP structures are similar to PL spectra of InGaAsP/GaAs separate confinement double heterostructures (SC DH) with low-energy active layer (E_{g1}) and high-energy band waveguide (E_{g2}). At room temperature the intensities of longwavelength and shortwavelength emission bands become equal which doesn't correlate with PL spectra of SC DH InGaAsP/GaAs and theoretical model.

PL temperature dependence investigations of SFP InGaAsP/GaAs structures have shown that longwavelength emission band efficiency decreases more rapidly than shortwavelength one with the temperature increase. In SC DH InGaAsP/GaAs structures case the reverse dependence is observed.

The simplest explanation of this phenomenon could be the presence of defects due to non-elastic deformation of SFP structure domains. According to the "soft mode" model, in periodical structure the conjugation of lattice parameters of neighbouring domains is accompanied with an appearence of elastic deformation. However, the calculated value of lattice mismatch of SFP structure domains could reach 3% which results in non-elastic deformation of crystal lattice in the case of bulk epitaxial films [8].

For the determination of deformations in domains of SFP InGaAsP/GaAs structures the formerly designed method of determination of lattice mismatch parameter from spectral dependencies of linear polarization rate was used [8]. In PL spectra of SFP structures the spectral dependence of linear polarization rate has been observed indicating on the presence of elastic deformations. The character of PL spectral dependencies of shortwavelength and longwavelength emission bands indicates on the opposite sign of elastic deformation of domains with different composition. The obtained result confirms the theoretical model [3] and is not in agreement with supposition about the presence of non-elastic deformations in SFP structures.

77 K and 300 K PL spectra of SFP InGaAsP/GaAs structures at different excitation levels have been investigated. Excitation level has been varied from 10 W/cm^2 to 6 kW/cm^2. At 77 K the correlation of shortwavelength and longwavelength band intensities has not been changed with excitation level increase. Only longwavelength band broadening and band maximum shift have been observed. The obtained result we connected with some fluctuation of solid phase composition in the domains of SFP InGaAsP/GaAs structures. At room temperature the strong saturation of PL longwavelength band intensity with excitation level increase has been observed. To our opinion it is connected with low volume of domains responsible for longwavelength emission band in comparison with the volume of domains corresponding to shortwavelength emission band.

2.2 *Electroluminescnce properties of spontaneously formed InGaAsP/GaAs structures*

In electroluminescence (EL) spectra of SC DH SFP InGaAsP/GaAs structures shortwavelength and longwavelength emission bands have been also observed. Analogous to 77 K PL spectra in 77 K EL spectra shortwavelength and longwavelength emission bands have been observed. With an increase of pump current up to 50–80 A/cm^2 the threshold current has been reached. The correlation between lasing wavelength and threshold current has been observed. The minimum value of threshold current has been measured in the samples with maximum lasing wavelength resulting from gain saturation. The strong dependence of lasing wavelength on injection carrier concentration indicate on relatively low volume

fraction of domains with low energy solid solution composition in the whole volume of active region. At room temperature the longwavelength emission band in EL spectra has been observed only at low pump currents. With an increase of pump current longwavelength band intensity saturates and shortwavelength band intensity increases. Room temperature threshold current in four-cleaved diodes was 0.9–1.3 kA/cm^2 which is in accordance with theoretical and experimental values of threshold current densities for double heterostructure with 0.3 μm active layer thickness.

Conclusion

Investigation of linear polarization rate spectral dependencies of SFP InGaAsP/GaAs structures revealed the presence of elastic deformations with opposite sign in interchanged domains with different solid phase composition. Threshold current density 50 A/cm^2 was achieved in double heterostructures with SFP InGaAsP/GaAs active region. The observed strong saturation of longwavelength emission band intensity in temperature dependencies of PL and EL spectra is connected with relatively low volume of domains of low-energy material in SFP InGaAsP/GaAs structures. Simple theoretical evaluations showed that 4–5 times increase of low-energy material volume in SFP structure will allow to reduce threshold current density to 15–20 A/cm^2 at 77 K and to receive room temperature laser generation at 60–90 A/cm^2.

References

[1] I. S. Tarasov, L. S. Vavilova, I. P. Ipatova et al., *23 Int. Symp. on Compound Semiconductors*, ISCS-23, St Peterburg, Russia, p. 117, 1996.
[2] L. S. Vavilova, I. P. Ivanova, V. A. Kapitonov et al., *Semiconductors* **32**, 590 (1998).
[3] N. A. Bert, L. S. Vavilova, I. P. Ivanova et al., *Semiconductors* **33**, (1998).
[4] I. P. Ipatova, V. G. Malyshkin and V. A. Shchukin, *J. Appl. Phys.* **74**, 7198, (1993).
[5] Seiji Mukay, *J. Appl. Phys.* **54**, 2635 (1983).
[6] J. E. Guyer and P. W. Voovhees, *Phys. Rew. B* **54**, 11710 (1996).
[7] A. T. Gorelenok, I. S. Tarasov and A. S. Usicov, *Tech. Phys. Lett.* **7**, 452 (1981).
[8] N. A. Bert, A. T. Gorelenok, I. S. Tarasov et al., *Semiconductors* **16**, 60, (1982).

7th Int. Symp. "Nanostructures: Physics and Technology"
St Petersburg, Russia, June 14–18, 1999

Acousto-electric transport through a two-dimensional system in the nonlinear regime

A. O. Govorov†, M. Rotter‡, M. Streibl‡, C. Rocke‡, A. V. Kalameitsev†, A. Wixfor‡ and J. P. Kotthaus‡

† Institute of Semiconductor Physics, Russian Academy of Sciences, Siberian Branch, 630090 Novosibirsk, Russia

‡ Sektion Physik der Ludwig-Maximilians-Universität and Center for Nano-Science, Geschwister-Scholl-Platz 1, 80539 München, Germany

Abstract. Surface acoustic waves strongly interact with a two-dimensional electron plasma in hybrid semiconductor-piezoelectric structures. At high intensities of a surface acoustic wave, nonlinear effects play the main role: the plasma turns into moving electron stripes, the acousto-electric current reaches its maximum, and the absorption of the sound wave is strongly suppressed. The interaction between the surface acoustic wave and the photo-generated carriers results in ionization and drag of excitons. The electron-hole pairs are effectively trapped in the moving potential of the sound wave and then re-assembled into photonic signals. The photoluminescence intensity in the presence of a sound wave strongly depends on the excitation because of screening. Together with experimental data, we present a theoretical description of nonlinear phenomena using hydrodynamic approach.

Introduction

The interaction between surface acoustic waves (SAWs) and mobile carriers in quantum wells is an important method to study dynamic properties of two-dimensional (2D) systems. The SAW can trap carriers and induce acoustic charge transport (ACT) investigated in a number of systems in a view of possible device applications [1]. Also, the SAW-method was applied to study the quantum Hall effects [2, 3], electron transport through a quantum-point contact [4], lateral nanostructures [5], and commensurability effects in a 2D system [6]. However, all those experiments have been done in the regime of small signals and linear interaction.

Here we study the transition from the linear regime of acousto-electric interaction to the limit of strongly non-linear effects in a 2D electron plasma and in a system with photo-generated carriers [7–9].

1 Acousto-electric phenomena in semiconductor-piezoelectric structures

In usual GaAs-based microstructures it is very difficult to realize SAWs with high-amplitude potentials because electro-mechanical coupling in GaAs is relatively weak. The strong piezoelectric interaction is achieved in hybrid structures [7, 8] (Fig. 1), where the SAW-induced potential amplitude can be comparable with the band-gap of a semiconductor. The hybrid structure is fabricated by the epitaxial lift-off (ELO) technique [10] and includes a semiconductor layer tightly bound to a piezoelectric host crystal ($LiNbO_3$) by the van der Waals forces. The semiconductor layer contains a InGaAs-AlGaAs quantum well (QW) with a high-quality 2D electron gas (2DEG), to which Ohmic contacts are formed. The distance between the QW and the piezocrystal is just 32 nm, whereas the distance between

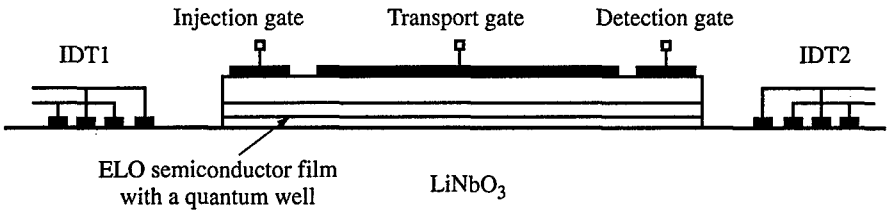

Fig. 1. The cross section of a hybrid semiconductor-piezoelectric structure.

the QW and the top transport gate is $d = 450$ nm. By changing the transport-gate voltage V_t we can tune the electron density in a QW. In this structure, travelling SAWs can induce very strong piezoelectric fields in the semiconductor layer due to the strong piezoelectricity of the host $LiNbO_3$-crystal. The SAW is induced and detected by the metal interdigital transducers, IDT1 and IDT2, respectively, at room temperatures [8].

1.1 Acoustic charge transport

Transport properties of a 2DEG in the presence of a SAW can be examined by the injection and detection top gates (Fig. 1). The transport gate is kept at a negative voltage, $V_t = -8$ V, so that the QW is depleted. The negative bias at the injection gate is removed for a short moment (0.3 μs) and electrons are injected into the QW. The SAW flushes a certain amount of injected electrons. These electrons are trapped in the moving potential of the SAW and transported through the sample to the detection gate. The detection gate acts as a Schottky diode charge detector and the electron signal is read out by an oscilloscope. The signal on the detection gate as a function of the time has a form of a peak with a maximum at $t = t_m$. The detection time t_m strongly depends on the SAW intensity, indicating a nonlinear interaction. In Fig. 2 we show the dependence of the ACT-signal velocity, $v = L/t_m$, from the SAW-intensity [8]. Here L is the spacing between the injection and transport gates. The amplitude of the SAW potential Φ_0 is calculated from the SAW intensity I_{saw}. With increasing potential Φ_0 the signal velocity first increases and finally saturates at the sound velocity v_s. This indicates that the intense SAW completely traps injected electrons into piezopotential minimums.

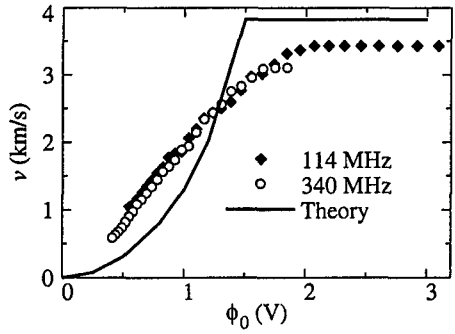

Fig. 2. The measured velocity of acoustic charge transport as a function of the SAW-potential amplitude for two SAW frequencies [8]. Theoretical data are also shown.

1.2 SAW absorption

The SAW can be strong enough to break up an initially homogenous 2D plasma into moving stripes. Here we study the transmission of a SAW through a 2DEG. The density of a 2DEG

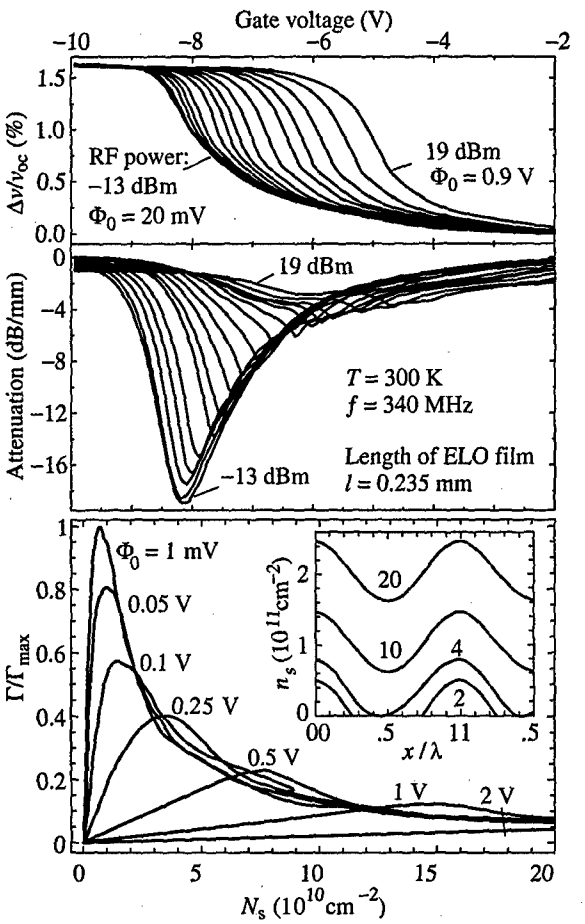

Fig. 3. The measured attenuation and the velocity change of a SAW, Δv, as a function of the gate voltage for different SAW-intensities. The lower part shows the calculated attenuation as a function of the electron density. In the insert we plot the function $n_s(x)$. The numbers attached to the plots correspond to N_s in units of 10^{10} cm^{-2} [8].

N_s is varied by the transport-gate voltage. It is known that, at small SAW-intensities, the sound attenuation by electrons Γ as a function of the conductivity σ exhibits a maximum at $\sigma = \sigma_m$ [11], where $\sigma_m = \epsilon_{eff} v_s/(2\pi)$ and ϵ_{eff} is the effective dielectric constant. At high SAW amplitudes the attenuation is strongly modified: Γ is suppressed and its maximum is shifted to higher conductivity. The attenuation for different SAW-intensities is plotted in Fig. 3 as a function of the transport-gate voltage, which determines the conductivity and the electron density in a 2DEG [8].

In order to understand these phenomena we develop a nonlinear theory for acousto-electric effects in 2D [12]. Most of previous theoretical studies on SAW interactions in a 2D plasma [11] relate to the linear regime of interaction, when the equilibrium 2D density N_s is much larger than the perturbation $\delta n_s(x,t)$ caused by a SAW. Here x and t are the in-plane coordinate and the time, respectively. However, in our system, the SAW-potential amplitude is so large that $N_s \sim \delta n_s$. The electron dynamics in our system is described by

non-linear hydrodynamic equations. In the long wave-length limit, $kd \ll 1$, the electron-density distribution can be found from the equation [8]

$$en_s(x_1)\mu\left[\frac{4\pi ed}{\epsilon_s}\frac{dn_s(x_1)}{dx_1} + E_0 \sin(kx_1)\right] + ev_s n_s(x_1) = A_0, \quad (1)$$

where A_0 is a constant. Here k is the wave vector of a SAW, $x_1 = x - v_s t$, E_0 is the amplitude of a SAW electric field, and μ and ϵ_s are the electron mobility and the semiconductor dielectric constant, respectively. The solution of Eq. (1) should be periodic. Numerical solutions for various average 2D densities $N_s\langle n_e(x_1)\rangle$ are shown in the inset of Fig. 3. Here the brackets $\langle \ldots \rangle$ denote the average over the wave length. It can be seen that the electron system forms separated stripes for small values of N_s. $\Phi_0 = E_0/k$ is the amplitude of the SAW potential. It follows from Eq. (1) that in the regime of separated strips the average local velocity of the electron plasma, $v = \langle v_e(x_1)\rangle$, is at its maximum and equal to the sound velocity v_s. Similar behavior was described in Ref. [13] for 3D.

In Fig. 2, we also plot the calculated average velocity v as a function of the potential Φ_0 using the parameters $N_s = 2.5 \times 10^{10}$ cm^{-2} and $\mu = 5000$ cm^2/Vs. Our relatively simple model reproduces the experimental behavior well. The saturation of v reflects the formation of electron stripes.

The absorption of a SAW by electrons is given by the equation $Q = \langle jE_{saw}\rangle$, where j is the electron current and E_{saw} is the SAW electric field. The non-linear absorption coefficient, $\Gamma = Q/I_{saw}$, as a function of N_s was calculated using the solutions of Eq. (1) (Fig. 3). In the limit of high Φ_0 the absorption coefficient is given by $\Gamma = Q_{max}/I_{saw} \propto 1/I_{saw}$ and decreases with increasing SAW-intensity I_{saw} [8, 13]. Theory and experiment are in good agreement: in intense SAWs the calculated absorption coefficient is strongly suppressed and the maximum of $\Gamma(N_s)$ is shifted to higher N_s. In the limit of large N_s, an asymptotic solution of Eq. (1) was given in Ref. [14] without noting the condition $\sigma_m \ll \sigma$. Also, the Weinreich relation [15] can be very useful to describe the non-linear regime [13, 16].

The shift of the SAW-velocity due to the electron plasma is shown in the upper part of Fig. 3. With increasing I_{saw} the curves are shifted towards larger conductivity σ (Fig. 3) which can be understood in terms of screening effects.

2 Interaction of acoustic waves with photo-generated carriers

In recent experiments on semiconductor QWs Rocke and co-authors [9] have demonstrated that a photonic signal can be transformed into electron-hole pairs, transported over a macroscopic distance across a sample, and then re-assembled again into light. A strong potential superlattice induced by a SAW spatially separates electrons and holes and thus the life-time is increased by a few orders of magnitude. In contrast to ACT of unipolar charges [1], in this case, the SAW transports two types of carriers, electrons and holes. This experiment develops the principles for realization of photonic memory devices and delay lines.

Another type of experiments deals with the SAW absorption and the phase shift due to the interaction with photo-generated carriers in semiconductor QWs [17, 18]. In the pump-probe experiments [17], a first intense SAW ionizes photo-generated excitons and a second low-intensity SAW is absorbed by electron-hole pairs. Thus, the ionization process due to the piezoelectric fields can be directly observed. At low temperatures in relatively wide QWs, the SAW can induce exciton localization and drag due to the quantum confined Stark effect [18, 20].

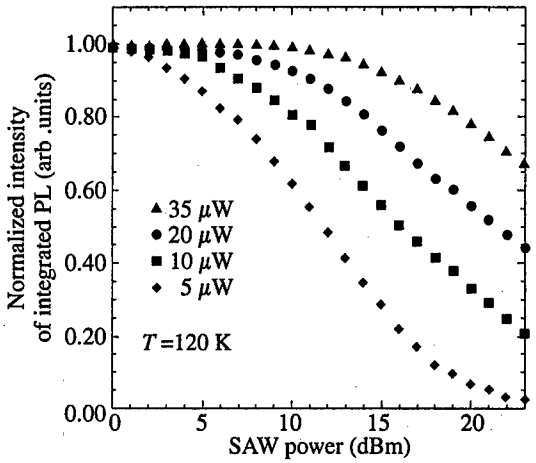

Fig. 4. The photoluminescence intensity of a GaAs-based QW as a function of the SAW power for different laser intensities [19].

At high temperatures the SAW interacts mostly with free electrons and holes. The amplitude of the SAW-potential in the presence of photo-generated carriers in the linear regime is given by $\Phi = \Phi_0/|1 + i\sigma/\sigma_m|$, where σ is the conductivity of an electron-hole plasma. σ_m is relatively low and corresponds to the densities 10^9-10^{10} cm^{-2}. In optical experiments, the photo-generated electron density can be larger than the above numbers and thus the plasma can effectively screen the SAW potential. The importance of the screening effects in the photoluminescence (PL) spectra of QWs is seen from the experimental data shown in Fig. 4. Here we see that the PL intensity strongly decreases with increasing SAW power due to spatial separation of electrons and holes. At high laser intensities suppression of the PL due to the SAW is not so effective: the PL intensity starts to decrease at higher I_{saw}. Thus, at high laser intensities, the photo-generated plasma can effectively screen the SAW potential and prevent suppression of the PL. These preliminary data on acousto-optical interactions show that the screening effect in the presence of a SAW can be utilized to realize optical nonlinearity.

Acknowledgements

We gratefully acknowledge financial support by the Bayerische Forschungsstiftung FOROPTO.

References

[1] M. J. Hoskins, H. Morko and B. J. Hunsinger, *Appl. Phys. Lett.* **41**, 332 (1982); W. J. Tanski, S. W. Merritt, R. N. Sacks, D. E. Cullen, E. J. Branciforte, R. D. Caroll and T. C. Eschrich, *Appl. Phys. Lett.* **52**, 18 (1988).

[2] A. Wixforth, J. P. Kotthaus and G. Weimann, *Phys. Rev.* **B40**, 7874 (1989).

[3] R. L. Willett, R. R. Ruel, K. W. West and L. N. Pfeiffer, *Phys. Rev. Lett.* **71**, 3846 (1993).

[4] V. I. Talyanskii, J. M. Shilton, M. Pepper, C. G. Smith, C. J. B. Ford, E. H. Linfield, D. A. Richie and G. A. C. Jones, *Phys. Rev.* **B56**, 15180 (1997).

[5] G. R. Nash, S. J. Bending, Y. Kershaw, K. Eberl, P. Grambow, and K. von Klitzing, *Surf. Sci.* **361/362**, 668 (1996).

[6] J. M. Shilton, D. R. Mace, V. I. Talyanskii, M. Pepper, M. Y. Simmons, A. C. Churchill and D. A. Ritchie, *Phys. Rev.* **B51**, 14770 (1995).

[7] M. Rotter, C. Rocke, S. Böhm, A. Lorke, A. Wixforth, W. Ruile and L. Korte, *Appl. Phys. Lett.* **70**, 2097 (1997).
[8] M. Rotter, A. V. Kalameitsev, A. O. Govorov, W. Ruile and A. Wixforth, *Phys. Rev. Lett.* **82**, 2171 (1999).
[9] C. Rocke, S. Zimmermann, A. Wixforth and J. P. Kotthaus, *Phys. Rev. Lett.* **78**, 4099 (1997).
[10] E. Yablonovich, D. M. Hwang, T. J. Gmitter, L. T. Florez and J. P. Harbison, *Appl. Phys. Lett.* **56**, 2419 (1990).
[11] K. A. Ingebrigtsen, *J. Appl. Phys.* **41**, 454 (1970); A. V. Chaplik, *Sov. Tech. Phys. Lett.* **10**, 584 (1984).
[12] In 3D systems a nonlinear theory of acousto-electric interactions was developed in a number of papers, see e.g. V. L. Gurevich and B. D. Laikhtman, *Sov. Phys. JETP* **19**, 407 (1964); J. R. A. Beale, *Phys. Rev.* **135**, 1761 (1964); P. N. Butcher and N. R. Ogg, *Brit. J. Appl. Phys. (J. Phys. D)*, Ser. 2, Vol. 1, 1271 (1968); P. K. Tien, *Phys. Rev.* **171**, 970 (1968).
[13] Yu. V. Gulyaev, *Fiz. Tekhn. Poluprovod.* **12**, 415 (1970) [*Sov. Phys. Semicond.*].
[14] V. A. Vyun, Proceed. of *IEEE Ultrasonic Symposium* (France, 1994), p. 441.
[15] G. Weinreich, *Phys. Rev.* **107**, 317 (1957).
[16] M. Rotter et al., will be submitted to *Appl. Phys. Lett.*
[17] C. Rocke, A. O. Govorov, A. Wixforth, G. Böhm and G. Weimann, *Phys. Rev.* **B57**, R6850 (1998).
[18] M. Streibl et al., in preparation.
[19] M. Streibl, C. Rocke, A. O. Govorov and A. Wixforth, Proceed. of *IEEE Ultrasonic Symposium* (Japan, 1998), in press.
[20] S. Zimmermann, A. O. Govorov, W. Hansen, J. P. Kotthaus, M. Bichler and W. Wegscheider, *Phys. Rev.* **B56**, 13414 (1997).

7th Int. Symp. "Nanostructures: Physics and Technology"
St Petersburg, Russia, June 14–18, 1999

The plateau-insulator phase transition in the quantum Hall regime

R. T. F. van Schaijk†, A. de Visser†, S. Oltshoorn‡, H. P. Wei§
and A. M. M. Pruisken†
† University of Amsterdam, Valckenierstraat 65,
1018 XE Amsterdam, The Netherlands
‡ High Field Magnet Laboratory, University of Nijmegen, Toernooiveld,
6525ED Nijmegen, The Netherlands
§ Department of Physics, Indiana University, Bloomington, Indiana 47405

Abstract. We report experiments on the plateau-insulator transition in a low mobility $In_{0.53}Ga_{0.47}As$/ InP heterostructure. An exponential law describes the resistance ρ_{xx} and we extract a critical exponent $\kappa = 0.55 \pm 0.05$ which is slightly different from the established value $\kappa = 0.425 \pm 0.04$ for the plateau transitions. Upon correction for the temperature dependence of the critical conductance σ^*_{xx}, our data indicate that the plateau-plateau and plateau-insulator transitions are in the same universality class.

Introduction

In the field of two dimensional electron gases the nature of the transitions between adjacent quantum Hall plateaus (PP transition) is an ardent topic of research. Experiments on low mobility $In_{.53}Ga_{.47}As$/InP heterostructures are a remarkable demonstration of a quantum phase transition indicating that the quantum Hall steps become infinitely sharp as the temperature T approaches absolute zero [1–2]. The maximum slope in the Hall resistance ρ_{xy} with varying magnetic field B was shown to diverge algebraically in T, $(d\rho_{xy}/dB)_{\max} \sim T^{-\kappa}$, while the half width $\Delta(B)$ of the longitudinal resistance ρ_{xx} was shown to vanish like $\Delta B \sim T^{\kappa}$. In both cases the critical exponent $\kappa = 0.42$.

Due to the short-range random alloy potential scattering, the low-mobility InGaAs/InP structure shows a wide range in T for studying scaling phenomena. This is in sharp contrast to high mobility GaAs/AlGaAs heterostructures where the long-range potential fluctuations dramatically complicate the observability of the critical phenomenon [3–4]. Nevertheless, the PP transitions in GaAs heterostructures have been studied extensively. In these experiments, the same value of $\kappa \approx 0.42$ was found but for a few samples only and for a small range in lowest T [4]. However, in most of the samples simple data fitting produced κ's ranging from 0.2 up to 0.9. These results are Landau level dependent and even for a given Landau level the ρ_{xx} and ρ_{xy} data give rise to different values for κ [5].

The focus in the last few years has been on transport in the lowest Landau level. Mostly samples of lower density were used [6–7]. The resistance data look quite different from those of the other Landau levels since the transition is between a quantum Hall (plateau) phase and an insulator (PI transition).

One of the most important predictions of the renormalization theory is that the PP and PI quantum phase transitions are in the same universality class [2]. This stipulates that the same κ be observed as T approaches absolute zero. In the experiments of Refs [6–7] a comparison between the PP and PI transitions within the same sample was either not possible or not drawn. Recently, an interesting empirical result for the lowest Landau level ρ_{xx} has been reported [8]. For arbitrary samples at finite T, the ρ_{xx} data seems to depend linearly rather than algebraically on T, indicating that the problem is generically the same for all GaAs

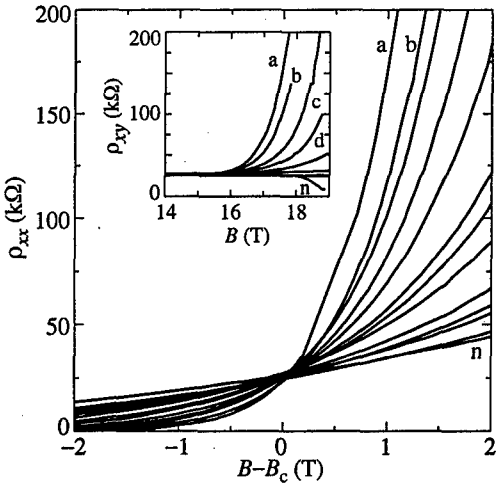

Fig. 1. Resistivity ρ_{xx} and Hall resistance ρ_{xy} (inset) versus magnetic field. B_c is the critical magnetic field defined in the text. The curves are labelled a,b,...,n and the corresponding temperatures are 0.13, 0.21, 0.26, 0.35, 0.47, 0.59, 0.83, 1.04, 1.4, 1.5, 1.9, 2.2, 3.1 and 4.2 K.

samples. Once again, the experimental design has overlooked an essential requirement for studying scaling phenomena: the importance of short-range random potential scattering — an essential prerequisite for sample choice.

1 Experimental results

We have measured the critical aspects of the PI transition and these are compared with the PP transition measured on the same sample. We benefit from the fact that our sample has been studied before [9]. In particular, the exponent κ for the PP transitions was found to be 0.42 and 0.20 for spin polarized and spin degenerate Landau levels respectively. The mobility of the sample was $\mu \approx 16000\,\mathrm{cm}^2/\mathrm{Vs}$ at $T = 4.2$ K. The electron density is $2.2 \times 10^{11}\ \mathrm{cm}^{-2}$ which means that the PI transition occurs at $B \approx 16$ T.

The experiments were carried out in a Bitter magnet ($B = 20$ T) using a plastic dilution refrigerator (0.1–2 K) and a bath cryostat (1.5–4.2 K). The magneto transport properties were measured with a standard ac-technique with a frequency of 6 Hz and an excitation current of 5 nA. The main experimental results are presented in Fig. 1 where the resistivity ρ_{xx} and Hall resistance ρ_{xy} (inset) are plotted versus magnetic field. The ρ_{xx} data is plotted as function of $B - B_c$, where B_c separates the insulating phase at high B and the quantum Hall phase at lower B. The maximum value of the conductivity, the critical conductivity σ^*_{xx}, defines the critical field B_c.

The ρ_{xy} is at low T clearly not quantised through the metal-insulator transition. Theoretically the expectation is that ρ_{xy} is quantised through the transition. The divergence of the Hall resistance means that it is not a Hall insulator according to the definition of Kivelson et al. [10].

From the σ_{xx} and σ_{xy} data the critical exponent can be extracted in a similar fashion as was done previously for the ρ_{xx} and ρ_{xy} data for the PP transitions [1]. For the T dependence of the σ_{xx} peak width, we obtain $\Delta B \sim T^{\kappa}$, with an exponent $\kappa = 0.465 \pm 0.05$. For the T dependence of the Hall conductivity is found, $(d\sigma_{xy}/dB)_{\min} \sim T^{-\kappa}$ with $\kappa = 0.435 \pm 0.05$. In the inset of Fig. 2 the width ΔB versus T is plotted for the PI as well as

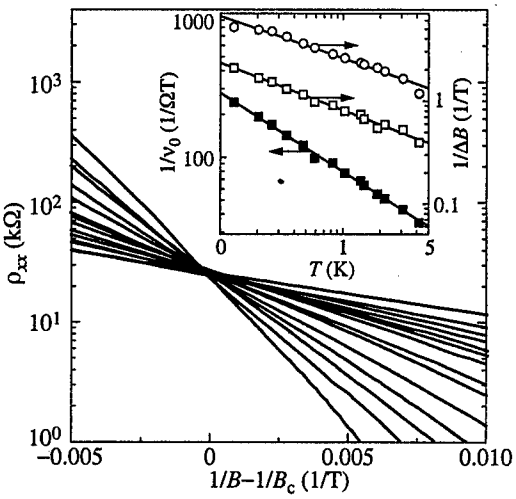

Fig. 2. ρ_{xx} data on a logarithmic scale versus inverse magnetic field. The labels and temperatures are the same as in Fig. 1. Inset: Left axis: $1/\nu_0$ vs T for the $1 \rightarrow 0$ PI transition (full squares, $\kappa' = 0.55$). Right axis: $1/\Delta B$ vs T for the $2 \rightarrow 1$ plateau transition (open circles, $\kappa = 0.42$) and the PI transition (open squares, $\kappa = 0.46$).

the PP ($2 \rightarrow 1$) transition. The latter was derived for the half width of ρ_{xx} and gave a critical exponent of $\kappa = 0.425 \pm 0.05$. The exponents $\kappa = 0.465 \pm 0.05, 0.435 \pm 0.05$ and 0.425 ± 0.05 are all the same, within the experimental error, indicating that the PP and the PI transition are transitions with the same scaling behaviour.

In Fig. 2 the resistivity is plotted on a log scale as function of the difference $1/B - 1/B_c$. The resistivity can be described by the following equation:

$$\rho_{xx}(\nu, T) = \rho^*_{xx} \exp[-\Delta\nu/\nu_0(T)] \tag{1}$$

The slope (ν_0) of the straight lines around zero can be accurately determined at each T. In the inset of Fig. 2 $1/\nu_0$ is plotted versus T on a log-log scale. The data nicely follow a power law behaviour $1/\nu_0 \sim T^{-\kappa'}$ with $\kappa' = 0.555 \pm 0.05$. This value differs from the expected value $\kappa = 0.42$ by more than the experimental error. The data can not be described with a linear law $\nu_0 = \alpha T + \beta$ as proposed by Shahar *et al.* [8].

This linear dependence on T does not describe the asymptotics of the quantum phase transition at zero Kelvin. Instead it is semiclassical in nature and typically observed at finite T on samples with predominantly slowly varying potential fluctuations [3].

2 Discussion

In the next part we address the origin of the difference in exponents. The transport data of the PI transition can be accurately described by Eq. (1), where ρ^*_{xx} denotes the critical resistance. It can be written as $\rho^*_{xx} = \sigma^*_{xx}/(\sigma^{*2}_{xx} + 1/4)$. Both quantities are weakly dependent on T and this dependence is not simply irrelevant as thought previously. It turned out to be marginal and it accounts for the difference in the observed exponents, as follows:

$$\kappa = \kappa' - [d \ln(\sigma^{*2}_{xx} + 1/4)/d \ln T] \tag{2}$$

Equation (2) shows how a relatively weak T dependence in σ^*_{xx} can lead to different exponents extracted from different quantities. In Fig. 3 $1/\nu_0$ versus T on a log-log scale is

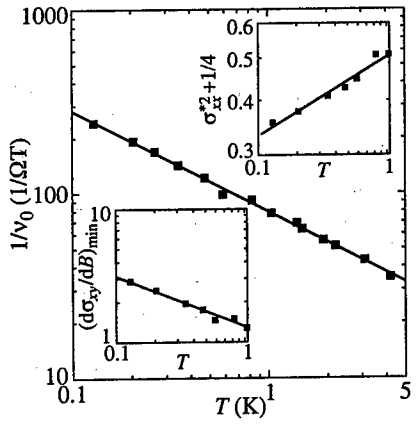

Fig. 3. $1/\nu_0$ vs T for the PI transition (full squares, $\kappa' = 0.55$). Upper inset: $\ln(\sigma_{xx}^{*2} + 1/4)$ vs T. The slope of the straight line equals 0.15. Lower inset: $(d\sigma_{xy}/dB)_{\min}$ vs T. The slope of the straight line equals 0.43.

replotted. The solid line gives $\kappa' = 0.55$. In the upper inset the low T data for $\ln(\sigma_{xx}^{*2}+1/4)$ versus $\ln T$ is shown and a slope of 0.155 ± 0.03 is obtained. According to Eq. (2) $\kappa = 0.40$, which should be compared with the low T dependence of $(d\sigma_{xy}/dB)_{\min}$ (see lower inset Fig. 3).

In summary our results show that the PP and PI transition have the same scaling behaviour. We have shown that the effective exponent $\kappa' = 0.55$ of the PI transition is due to the T dependence of the critical conductance σ_{xx}^*. Weak macroscopic inhomogeneities in the sample cause the lack of universality in σ_{xx}^*. By combining the results of the PP and PI transitions we conclude that $\kappa = 0.42$ stands for the universal critical exponent of the quantum phase transition.

References

[1] H. P. Wei, D. C. Tsui, M. A. Paalanen and A. M. M. Pruisken, *Phys. Rev. Lett.* **61**, 1294 (1988).
[2] A. M. M. Pruisken, *Phys. Rev. Lett.* **61**, 1297 (1988).
[3] A. M. M. Pruisken, B. Skoric and M. A. Baranov, cond-mat/9807241.
[4] H. P. Wei, S. Y. Lin, D. C. Tsui and A. M. M. Pruisken, *Phys. Rev.* **B45**, 3926 (1992).
[5] S. Koch, R. J. Haug, K. v. Klitzing and K. Ploog, *Phys. Rev.* **B43**, 6828 (1991).
[6] H. W. Jiang, C. E. Johnson, K. L. Wang and S. T. Hannahs, *Phys. Rev. Lett.* **71**, 1439 (1993).
[7] W. Pan, D. Shahar, D. C. Tsui, H. P. Wei and M. Razeghi, *Phys. Rev.* **B55**, 15431 (1997).
[8] D. Shahar, M. Hilke, C. C. Li, D. C. Tsui, S. L. Sondhi, J. E. Cunningham and M. Razeghi, *Solid State Commun.* **107**, 19 (1998).
[9] S. W. Hwang, H. P. Wei, L. W. Engel, D. C. Tsui and A. M. M. Pruisken, *Phys. Rev.* **B48**, 11416 (1993).
[10] S. Kivelson, D. H. Lee and S. C. Zhang, *Phys. Rev.* **B46**, 2223 (1992).

7th Int. Symp. "Nanostructures: Physics and Technology"
St Petersburg, Russia, June 14–18, 1999

High-frequency hopping conductivity of two-dimensional electronic system in GaAs/AlGaAs heterostructures (acoustical method)

I. L. Drichko, A. M. Diakonov, V. D. Kagan, V. V. Preobrazenskiy†,
D. A. Pristinski, *I. Yu. Smirnov* and A. I. Toropov†
Ioffe Physico-Technical Institute, St Petersburg, Russia
† Semiconductors Physics Institute of SD RAS, 630090, Novosibirsk, Russia

Introduction

In the Quantum Hall regime when the Fermi level is situated between two adjacent Landau bands, the electrons are localized. This fact is confirmed by numerous direct current (DC) measurements of the resistivity of the high-mobility 2-dimensional systems in a magnetic field at low temperatures (see, for example, [1]). In this case DC conductivity seems to be of a hopping nature. However, the origin of the localized states is very difficult to determine in this experiments. The study of high-frequency conductivity $\sigma_{xx}^{\mathrm{hf}}$ proved to be useful in solving of this problem.

If the electrons are "free" the high-frequency conductivity $\sigma_{xx}^{\mathrm{hf}}$ should be the same as $\sigma_{xx}^{\mathrm{dc}}$, measured in DC experiment, and the difference between $\sigma_{xx}^{\mathrm{hf}}$ and $\sigma_{xx}^{\mathrm{dc}}$, from the other hand, points to the carrier localization. The high-frequency conductivity can be obtained from the propagation measurements of a surface acoustic wave (SAW). When a SAW propagates along the surface of a piezoelectric on which a semiconducting heterostructure with 2-dimensional electrons is superimposed, the elestic wave is accompanied with an alternating electric field. This field penetrates into the 2-dimensional conductivity canal, thus producing currents, Joule losses, and the SAW attenuation. Sound velocity changes also.

All these effects are governed by the high-frequency conductivity of a 2-dimensional system, and consequently if one observes Shubnikov–de Haas oscillations of the 2-dimensional system DC resistance in a magnetic field, similar oscillations should manifest themself in the SAW attenuation coefficient Γ and relative velocity change $\Delta V/V$.

In present work Γ and $\Delta V/V$ have been measured in a magnetic field up to 7 T on the GaAs/AlGaAs heterostructures with sheet densities $n = (1.3{-}7)\cdot 10^{11}\ \mathrm{cm}^{-2}$ and mobilities $\mu = (1{-}2)\cdot 10^5\ \mathrm{cm}^2/\mathrm{V}\cdot\mathrm{s}$.

Experimental results and discussion

The high-frequency conductivity is generally a complex value: $\sigma_{xx}^{\mathrm{hf}} = \sigma_1 - i\sigma_2$. For Γ and $\Delta V/V$ in this case we have:

$$\Gamma = 8.68\frac{K^2}{2}kA\frac{\dfrac{4\pi\sigma_1}{\varepsilon_s V}t(k)}{\left[1+\dfrac{4\pi\sigma_2}{\varepsilon_s V}t(k)\right]^2+\left[\dfrac{4\pi\sigma_1}{\varepsilon_s V}t(k)\right]^2}, \qquad (1)$$

$$A = 8b(k)(\varepsilon_1+\varepsilon_0)\varepsilon_0^2\varepsilon_s\exp[-2k(a+d)],$$

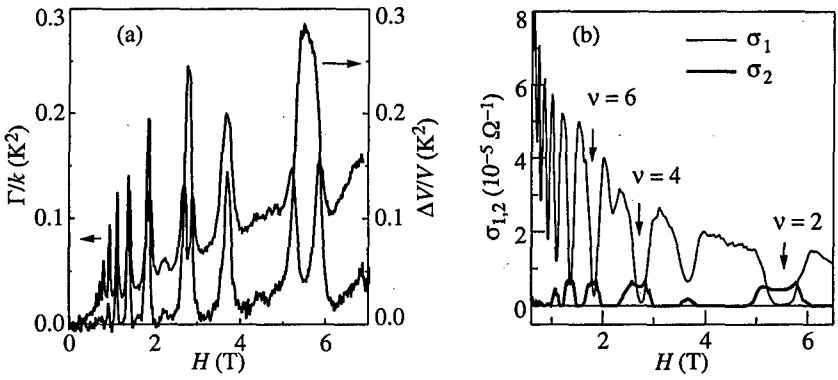

Fig. 1. (a) The experimental dependencies of Γ and $\Delta V/V$ on magnetic field H at $T = 1.5$ K, ($f = 30$ MHz). (b) The dependencies of σ_1 and σ_2 on H at $T = 1.5$ K, ($f = 30$ MHz).

$$\frac{\Delta V}{V} = \frac{K^2}{2} A \frac{\frac{4\pi\sigma_2}{\varepsilon_s V} t(k) + 1}{\left[1 + \frac{4\pi\sigma_2}{\varepsilon_s V} t(k)\right]^2 + \left[\frac{4\pi\sigma_1}{\varepsilon_s V} t(k)\right]^2},$$

where K^2 is the electromechanic coupling constant of $LiNbO_3$, k and V are wavevector and velocity of SAW, respectively, a is the gap between the piezoelectric and the heterostructure, d is the depth at which the 2-dimensional canal is burried, ε_1, ε_0, and ε_s are the dielectric constants of lithium niobate, vacuum and gallium arsenide respectively, b and t are some complex functions of a, k, ε_1, ε_0, ε_s.

In Fig. 1(a) the magnetic field dependencies of $\Gamma/(4.34AK^2k)$ and $(\Delta V/V)/(AK^2/2)$ for a sample with the carrier density $n = 2.7 \cdot 10^{11}$ cm^{-2} and mobility $\mu = 2 \cdot 10^5$ cm^2/V$\cdot$s are shown. One can see that these values oscillate with magnetic field, and for large filling factors the attenuation and velocity change peak do coinside, whereas for little filling factors the velocity change maxima coinside with the minima of the attenuation. Such a behaviour of these values could be explained sufficiently well by the (1).

The Eq. (1) provide us with σ_1 and σ_2 from the experimentally measured Γ and $\Delta V/V$. In Fig. 1(b) the dependencies of σ_1 and σ_2 on a magnetic field at $T = 1.5$ K are shown. As one can see, $\sigma_2 = 0$ in the magnetic field region where the Fermi level lies within the Landau band (semi-integer filling factors). From the experiment the results of which are shown in Fig. 2(b) it follows that the electrons are delocalized in this magnetic field region, and the conductivity is determined by its real part $\mathrm{Re}\,\sigma_{xx}^{\mathrm{hf}} = \sigma_1$, which is of the same value as the DC conductivity $\sigma_{xx}^{\mathrm{dc}}$.

With the further increase of the magnetic field the Fermi level leaves the Landau band, a metal-dielectric transition takes place, and the electrons become localized in the random fluctuation potential of the charged impurities. In the vicinity of the transition, in the dielectric side of it, a discrepancy between the conductivity values is observed, so that $\sigma_1 > \sigma_{xx}^{\mathrm{dc}}$. In this case Γ still could be considered by the $\sigma_{xx}^{\mathrm{dc}}$ at the percolation level, but into Eq. (1) a factor less than 1 should enter, whose physical meaning is: the part of the area occupied by the "lakes of electrons" [2].

In the magnetic fields corresponding to the small integer filling factors the Fermi level is in the middle position between the Landau bands. One can see in Fig. 2(b) that in this

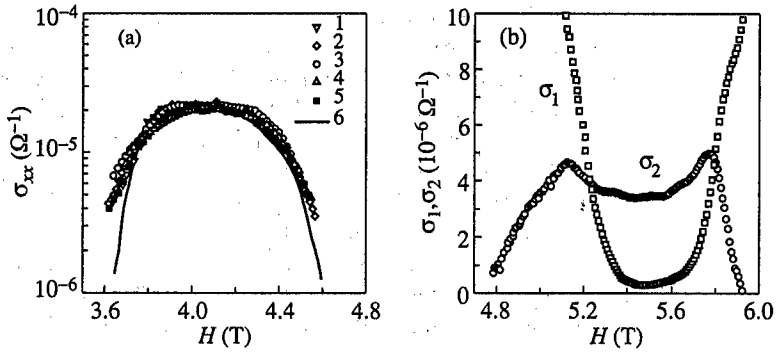

Fig. 2. (a) σ_{xx}^{dc} (solid line) and σ_1 versus H near the region of delocalized states. The symbols correspond to frequences f (MHz) and vacuum gap widths a (in μm): 1—213 and 0.3, 2—30 and 0.5, 3—150 and 0.3, 4—30 and 0.4, 5—90 and 1.2, $T = 4.2$ K. The sample has $n = 7 \cdot 10^{11}$ cm^{-2}. (b) The $\sigma_1(H)$ and $\sigma_2(H)$ at $T = 1.5$ K near the filling factor $\nu = 2$ for the sample with $n = 2.7 \cdot 10^{11}$ cm^{-2}, $f = 30$ MHz.

case σ_2 is far from being equal to zero, but to the contrary, is nearly an order higher than σ_1. According to Efros [3] such a relation between conductivities: $\sigma_1/\sigma_2 \sim 0.1$ ($f = 30$ MHz) can exist in the case of high frequency hopping conductivity, when the electrons are localized on the separate impurity atoms, that is so-called "two-site absorption". High-frequency hopping conduction occurs by electronic transitions between localized states with close energies. The states that are optimal for such transitions form compact pairs lying at a considerable distance from each other. There are no transitions between pairs, so that the pairs cannot give rise to transport of current in a static field, although a high-frequency field effects transitions within pairs, thereby producing polarization. Transitions within pairs can occur both with and without the help of phonons. In the former case, called the relaxation case, the energy E required for the transition of an electron within a pair is on the order of kT. At frequencies $\omega < \omega_{ph}$ and $\hbar\omega < kT$, where $\omega = 2\pi f$ is the SAW frequency, w_{ph} is the characteristic phonon frequency order of 10^{12}–10^{13} s^{-1}, relaxation absorption dominates, and we shall be discussing precisely this case. For this mechanism the following relation holds:

$$\begin{aligned} \mathrm{Re}\,\sigma_{xx}^{hf} &= \sigma_1 = \frac{\pi^2}{8}\frac{\xi\omega e^4}{\varepsilon_s} r_\omega^2 g_0^2, \\ \mathrm{Im}\,\sigma_{xx}^{hf} &= \sigma_2 = \frac{\pi}{2}\omega\frac{e^4}{\varepsilon_s} g_0^2 \left[\frac{r_\omega^3}{3} + r_T^3\right]. \end{aligned} \tag{2}$$

$$\begin{aligned} r_w &= \frac{\xi}{2}\ln\left(\frac{\omega_{ph}}{\omega}\right) \\ r_T &= \xi \ln\frac{J_0}{T};\ J_0 \simeq \varepsilon_B. \end{aligned}$$

Where ξ is the localization length, r_w is the distance between localized states within one pair, e is the electron charge, $g_0 = dn/dE_F$ is the density of states, ε_B is the Bohr energy. As one can see from (2), σ_1 does not depend on a temperature. In our experiment at high

magnetic fields (small filling factors) σ_1 is independent of a temperature in the 1.5–3 K interval. This fact is also in favour of the hopping nature of the high-frequency conductivity.

With the aid of (2) one can estimate the localization length ξ. If for g_0 one takes $g_0 = m^*/\pi\hbar^2 = 1.8 \cdot 10^{25}\,\mathrm{cm}^{-2}/\mathrm{erg}$, from (2) it follows that $\xi = (3.0 \pm 0.3) \cdot 10^{-6}\,\mathrm{cm}$ (5.5 T) and $\xi = (3.6 \pm 0.4) \cdot 10^{-6}\,\mathrm{cm}$ (2.7 T). It should be noticed that for the same magnetic field these values differ only slightly from the magnetic length $\ell_B = \sqrt{\hbar c/eH}$ ($1.1 \cdot 10^{-6}$ cm (5.5 T), $1.56 \cdot 10^{-6}$ cm (2.7 T)) and the cyclotron radius $R_c = 2\nu/k_F$ in this sample ($2.4 \cdot 10^{-6}$ cm (5.5 T) and $4.7 \cdot 10^{-6}$ cm (2.7 T).

The $\sigma_1(T, H)$ and $\sigma_2(T, H)$ dependencies could be qualitatively explained by the change with T and H of the pair number actual for hopping. As T and H changes the number of localized electrons at the Fermi level varies due to the thermal activation to the upper Landau level.

Acknowledgements

The work is supported by RFFI No 98-02-18280 and MNTRF No 97-1043 grants.

References

[1] M. Furlan, *Preprint Cond-mat* 9712304 (1997).

[2] I. L. Drichko, A. M. D'yakonov, A. M. Kreshchuk, T. A. Polyanskaya, I. G. Savel'ev, I. Yu. Smirnov and A. V. Suslov, *Fiz. Tekh. Poluprovodn.* **31**, 451 (1997).

[3] A. L. Efros, *Zh. Eksp. Teor. Fiz.* **89**, 1057 (1985).

7th Int. Symp. "Nanostructures: Physics and Technology"
St Petersburg, Russia, June 14–18, 1999

Reduction of the intersubband scattering delta doped layers by the Lorentz-force of an in-plane magnetic field

P. M. Koenraad†, A. F. W. van de Stadt†, J. H. Wolter† A. Dekeyser‡,
R. Bogaerts‡ and F. Herlach‡
† COBRA Inter-University Research Institute, Eindhoven Uiniversity of Technology,
P.O. Box 513, 5600 MB Eindhoven, the Netherlands
‡ Department Natuurkunde, University of Leuven, Celestijnenlaan, B-3001, Belgium

Abstract. In structures with a narrow delta doped layer we observe a strong anisotropy in the magnetoresistance when the current is applied either parallel or perpendicular to the in-plane magnetic field. This anisotropy is absent in structures with thick doping layers. By a detailed analysis of the solution of the Boltzmann transport equation we were able to show that the anisotropy is due to a reduction in the intersubband scattering. The reduction of the intersubband scattering is due to the fact that the Lorentz-force pushes electrons, which move perpendicular to the in-plane magnetic field direction, away from the layer of ionized impurities.

Introduction

The diamagnetic shift is well known to give rise to subband depopulation when an in-plane magnetic field is applied to a 2D system with more than a single subband occupied. The depopulation of a subband leads to so-called diamagnetic Shubnikov–de Haas oscillations that are observable in the magnetoresistance. Already in 1986 Reisinger and Koch [1] calculated a universal depopulation diagram for delta doped structures. This diagram predicts the magnetic field value at which the depopulation of a subband will occur. By now the R & K diagram has become the standard for the study of depopulation effects in delta doped structures in many III/V semiconductors. It has however never been tested in the high magnetic limit where we can expect the depletion of the first excited subband.

1 Experiments

Using pulsed magnetic fields up to 50 T we have studied in detail the validity of the R&K diagram for GaAs structures with single and coupled delta doped layers. When the current is applied either parallel or perpendicular to the in-plane magnetic field we observe a strong anisotropy for the depopulation of the $n = 1$ subband in structures with a single narrow delta doped layer, see Fig. 1(a). This anisotropy is absent in structures with a thick doping layer, see Fig. 1(b). The dependence of the anisotropy on the layer thickness is observed in samples with a higher doping concentration. A similar effect is also observed for coupled delta doped layers where we find a strong anisotropy when the delta layers are strongly coupled but where the anisotropy disappears when the coupling between the layers becomes weaker.

For a large number of samples with a narrow doping profile, i.e. a width of 2 nm, we have determined the inflection point on the negative slope of the diamagnetic Shubnikov–de Haas oscillations. Normally this inflection point is considered to coincide with the magnetic depopulation. As is shown in Fig. 2 the deviation from the calculated values can be quite large and the apparent depopulation of the $n = 1$ subband seems to depend on the orientation of the current with respect to the magnetic field.

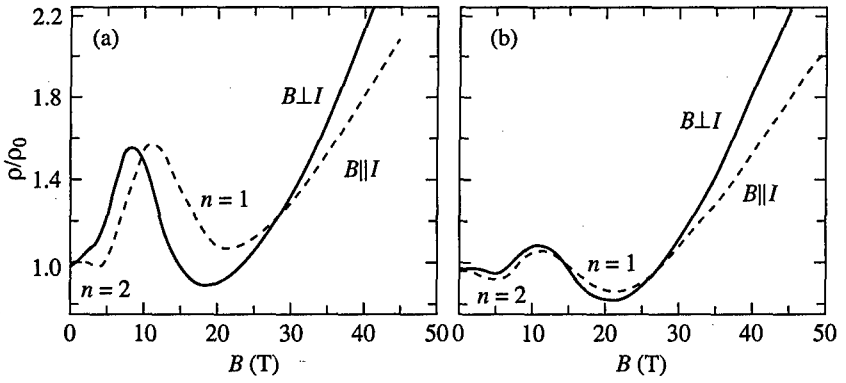

Fig. 1. Diamagnetic Shubnikov–de Haas oscillations measured in a sample with a narrow doping profile (a) and a thick doping profile (b). The current is applied either parallel or perpendicular to the in-plane magnetic field. The doping density is 2×10^{12} cm^{-2} for both samples. The sample in (a) has a width of the doping layer of 2 nm whereas the width of the sample in (b) is close to 6 nm.

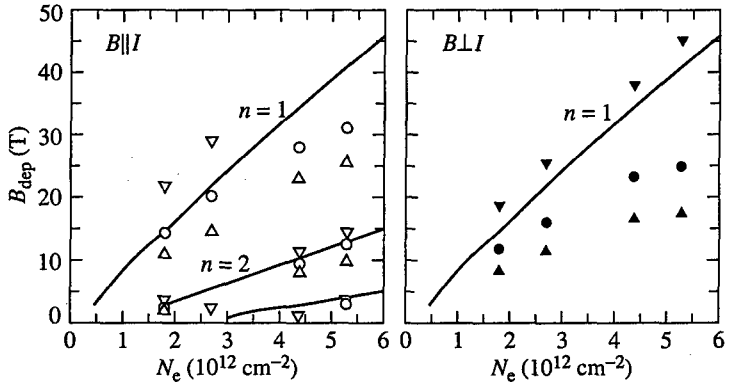

Fig. 2. Comparison of the minimum (▽), inflection point (○) and the maximum (△) in the diamagnetic Shubnikov–de Haas oscillations measured in samples with a narrow doping profile. The current is applied either parallel (a) or perpendicular (b) to the in-plane magnetic field.

2 Analysis and discussion

We have solved the Boltzmann-transport equation in order to calculate the transverse and longitudinal magnetoresistivity components, i.e. the current perpendicular or parallel to the in-plane magnetic field. The calculation of these magnetoresistivity components is rather complicated as we have to deal with anisotropic Fermi-contours, a finite number of occupied and empty subbands, etc. The calculations show that a depopulation is observable in the magnetoresistivity by a drop in the resistivity because the intersubband scattering disappears when the Fermi energy drops below the $n = 1$ subband. Similar results for a heterostructure were obtained by Ensslin *et al.* [2]. Our detailed analysis showed that the observed anisotropy and the deviation of the observed depopulation field value from the R&K value is due to a strong reduction of the intersubband scattering previous to the actual crossing of the Fermi-energy with the bottom of the $n = 1$ subband. The reduction of the intersubband scattering turns out to be due a Lorentz force induced shift of the wavefunction when the in-plane magnetic field is applied perpendicular to the movement of the electrons.

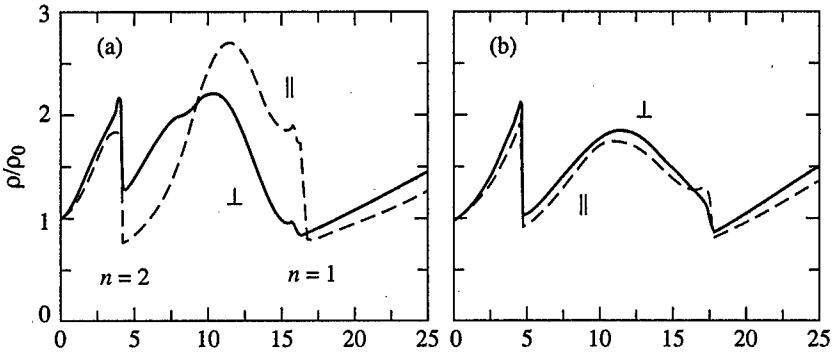

Fig. 3. Calculated diamagnetic Shubnikov–de Haas oscillations for a structure with single delta doped layer of (a) 2 nm and (b) 10 nm thick. The calculations are normalized by the magnetoresistance at zero magnetic field.

Due to this shift the overlap between the wavefunction of the $n = 1$ subband and the layer of ionized impurities is strongly reduced. This strong reduction in the overlap gives rise to a near complete annihilation of the intersubband scattering between the two lowest subbands. This mechanism only works in structures that have a narrow distribution of the ionized impurities. As is shown in Fig. 3 the numerically obtained magnetoresistivity curves agree nicely with the experimentally observed curves in structures with different doping layer thicknesses. In structures with a narrow doping profile the anisotropy is large whereas it is almost absent in structures with a thick doping profile. Similar results where obtained in structures with different separations between two coupled delta layers.

3 Conclusions

In structures with delta doped layers we measured the longitudinal and transversal magnetoresistance.when an in-plane magnetic field is applied. We observed a strong anisotropy for these two components of the magnetoresistance in structures with single narrow doped layers or in structures with strongly coupled delta doped layers. The apparent depopulation that is determined from the diamagnetic Shubnikov–de Haas oscillations also deviates from the theorectical predicted values in these structures. All these effects are mainly due to a Lorentz force induced shift of the wavefunction when an electron moves perpendicular to the in-plane magnetic field direction.

References

[1] H. Reisinger and F. Koch, *Surf. Sci.* **170**, 397 (1986).
[2] K. Ensslin, A. Wixford, M. Sundaram, P. F. Hopkins, J. H. English and A. C. Gossard, *Phys. Rev. B* **47**, 1366 (1993).

7th Int. Symp. "Nanostructures: Physics and Technology"
St Petersburg, Russia, June 14–18, 1999

Role of intensive intersubband transitions in Shubnikov–de Haas oscillations and in weak localization

N. S. Averkiev, L. E. Golub and S. A. Tarasenko
Ioffe Physico-Technical Institute, St Petersburg, Russia

Abstract. Shubnikov–de Haas conductivity oscillations are calculated taking into account intensive intersubband transitions between levels of size quantization in a quantum well and compared with anomalous magnetoresistance under weak localization conditions.

Introduction

The most widely used nanostructures characterization method is investigation of their properties in magnetic field. The Shubnikov–de Haas effect and the anomalous magnetoresistance measurements in weak filed are often applied.

In the ultra-quantum case of one size-quantized subband filling these phenomena are investigated very well both theoretically and experimentally. At two and more subbands occupation the new peculiarities appear in these effects caused by intersubband transitions. For instance, if the scattering cross-section is anisotropic then conductivity of the 2D electron gas is not reduced to the sum of conductivities in each subband. Therefore one has to take into account intersubband transitions in the weak localization theory, Shubnikov–de Haas effect and quantum Hall effect to determine exactly such parameters as carrier concentration, diffusion coefficient and spin relaxation times.

In this report the role of intersubband transitions is demonstrated in anomalous magnetoresistance effect and Shubnikov–de Haas oscillations.

1 Weak localization

It has been shown [1] that in the case of intensive intersubband transitions the anomalous conductivity in weak manetic field B is described by the standard expression:

$$\sigma(B) - \sigma(0) = \frac{e^2}{4\pi^2\hbar}\left[2\,f_2\left(\frac{B}{B_\varphi + B_\parallel}\right) + f_2\left(\frac{B}{B_\varphi + B_\perp}\right) - f_2\left(\frac{B}{B_\varphi}\right)\right], \quad (1)$$

where

$$B_\varphi = \frac{\hbar c}{4eD\tau_\varphi}, \qquad B_{\parallel,\perp} = \frac{\hbar c}{4eD\tau_{\parallel,\perp}}, \quad (2)$$

the function f_2 is given by: $f_2(x) = \ln x + \psi(1/2 + 1/x)$, and $\psi(y)$ is a Digamma-function. Here τ_φ is a phase relaxation time and $\tau_{\parallel,\perp}$ are the longitudinal and transverse spin relaxation times where the role of the indicated axis plays the normal to the QW plane. D is an averaged diffusion coefficient, determining the whole conductivity of the system. It is important to note that this average is not reduced to the half-sum of the diffusion coefficients in each subband. The relaxation rates τ_φ, $\tau_\parallel$ and $\tau_\perp$ are also quantities averaged over subbands.

Thus the intensive intersubband transitions change essentially the dependence of conductivity on magnetic field. Instead of two contributions like Eq. (1) from each subband with six characteristic magnetic fields one has three parameters averaged over two subbands.

2 Shubnikov–de Haas effect

Since periods of Shubnikov–de Haas oscillations are determined by crossing of Landau levels in each subband by the Fermi level the intersubband transitions do not change the functional dependence of conductivity on the magnetic field. However the contributions of each size-quantized subband depend both on the transitions intensity and on the angle dependence of scattering cross-section. In this report the case of isotropic scattering is considered for simplicity.

The expression for the dissipative conductivity has a view:

$$\sigma_{xx} = \frac{n_1 e^2 \tau_1/m}{1+(\omega_c\tau_1)^2}\left\{1-2\frac{(\omega_c\tau_1)^2}{1+(\omega_c\tau_1)^2}\left[\left(1-\frac{\tau_1}{\tau_{12}}\right)\delta_1+\frac{\tau_1}{\tau_{12}}\delta_2\right]-\frac{\tau_1}{\tau_{12}}(\delta_1-\delta_2)\right\}$$
$$+\frac{n_2 e^2 \tau_2/m}{1+(\omega_c\tau_2)^2}\left\{1-2\frac{(\omega_c\tau_2)^2}{1+(\omega_c\tau_2)^2}\left[\left(1-\frac{\tau_2}{\tau_{12}}\right)\delta_2+\frac{\tau_2}{\tau_{12}}\delta_1\right]-\frac{\tau_2}{\tau_{12}}(\delta_2-\delta_1)\right\}, \quad (3)$$

where m is the electron effective mass, ω_c is its cyclotron frequency, $n_{1,2}$ and $\tau_{1,2}$ are respectively concentration and momentum relaxation time in the first and second subbands, and τ_{12} is the intersubband transition time. The oscillating parts are given by:

$$\delta_1 = 2\cos\left(2\pi\frac{E_F}{\hbar\omega_c}\right)\exp\left(-\frac{\pi}{\omega_c\tau_1}\right), \quad \delta_2 = 2\cos\left(2\pi\frac{E_F-\Delta}{\hbar\omega_c}\right)\exp\left(-\frac{\pi}{\omega_c\tau_2}\right), \quad (4)$$

where E_F and $E_F - \Delta$ are Fermi levels reckoned from bottoms of the first and second subbands of size quantization. Here Δ is the energy distance between subbands.

The peculiarity of Eq. (3) is that the main signal with the frequency $2\pi E_F/\hbar$ is modulated by the slow changing oscillation even at low occupation of the excited subband: $E_F - \Delta \sim n_2 \ll n_1$.

Acknowledgements

This work was financially supported by the Russian Foundation for Basic Research (grant 98-02-18424) and by the Program "Physics of Solid State Nanostructures" (grant 97-1035).

References

[1] N. S. Averkiev, L. E. Golub and G. E. Pikus, *Solid State Commun.* **107**, 757 (1998); *Semiconductors* **32**, 1087 (1998).

7th Int. Symp. "Nanostructures: Physics and Technology"
St Petersburg, Russia, June 14–18, 1999

High-temperature conductance quantization: the case of quasi-2D percolating structures

D. A. Bakaushin†, A. S. Vedeneev†, V. E. Sizov†, B. A. Aronzon‡,
N. K. Chumakov‡, A. B. Davydov‡ and E. Z. Meilikhov‡
† Institute of Radioengineering & Electronics RAS, Fryazino, Moscow reg., Russia
‡ RSC "Kurchatov Institute", Moscow, Russia

Investigation of electron properties of disordered quasi-2D semiconductor objects is caused by fundamental interest to regularities of metal-to-insulator transition, which specifics is determined by both the system dimension and disorder parameters. Also known that up-to-date FETs (based on selectively doped semiconductor structures) are naturally disordered due to elevated impurity content. Effects of disorder are stronger when the gate voltage is lower, that is a case of weaken electron screening of the fluctuation potential (FP) induced by chaotic ensemble of built-in charges (ionized impurities).

The situation when conductance of disordered systems has the percolation character is of peculiar interest. In this case one should expect manifestation of both finite (macroscopic) spatial scales of self-averaging of the system resistance and local regions, where the regions determine a value of the resistance.

The report is devoted to consideration of electron transport properties of quasi-2D systems in dependence on disorder parameters controlled by built-in charges and (in gated structures) by electron screening of the FP [1]. Main experiments were performed on model objects. There are Si-MNOS structures with inversion n-channel, which allow variation of concentration of the FP sources ($10^{11}-10^{13}$ cm^{-2}) by controllable injection of electrons from Si onto traps at SiO_2-Si_3N_4 interface. At temperatures $T = 4.2-300$ K the conductance of inversion channel G vs. the gate voltage V_g was studied.

It was established that decreasing of the FET's gate length (from 100 to 5 μm) leads to strong changing of the $G(V_g)$ dependence: it manifests a region of quasi-plateau at $G \sim e2/h$. The peculiarity at G values being of an order of the conductance quant is a typical feature of FETs with relatively short (0.5–10 μm) but wide (50–1000 μm) gate and elevated concentration of built-in charges ($> 10^{12}$ cm^{-2}) [2]. It was observed in FETs with different material of semiconductor substrate and under-gate insulator, sign and effective mass of charged carriers, and nature of the FP sources, particularly in the GaAs-AlGaAs HEMTs, GaAs-MESFETs with bull or delta- doping, and even in Si-MOS FETs with inversion p-channel, regardless to the gate length-to-width relation.

We associate the peculiarity to be caused by transition from the 2D-regime of electron transport (high gate voltage, the FP is screened by 2D electrons) to the percolation-like quasi-1D regime at reduced V_g. Mechanism of this transition in percolating systems is discussed. Conducting paths are thought to be formed by wells of the chaotic potential relief connected by pass regions. We hope that the wells are responsible for macroscopic spatial scales of these paths, while the passes control a character of the system conductance.

Using computer simulation following analysis has been performed:
– spatial and energy scales of the FP;
– parameters and conductance of the passes;
– percolating characteristics of systems with fixed sizes (incoherent mesoscopics).

In frames of the percolation model under consideration we have determined conditions where
– electron transport is carried out along single paths and has reduced percolation level;
– the passes controlling the single path conductance are really manifest themselves as quantum-sized micro-constrictions even at elevated temperatures (up to room temperatures).

By this way we show that quasi-2D systems disordered by electrostatic FP could have quantum quasi-1D character of conductance regardless to their micrometer sizes.

The work is supported by grants of the RFBR No 98-02-6747 and Physics of Solid Nanostructures No 97-10-81.

References

[1] B. A. Aronzon, E. Z. Meilikhov, D. A. Bakaushin, A. S. Vedeneev and V. V. Ryl'kov, *JETP-Letters* **66**, 668 (1997).
[2] B. A. Aronzon, D. A. Bakaushin, A. S. Vedeneev, V. V. Ryl'kov and V. E. Sizov, *Semiconductors* **31**, 1261 (1997).

7th Int. Symp. "Nanostructures: Physics and Technology"
St Petersburg, Russia, June 14–18, 1999

Antidot lattice in QHE regime: macroscopic limit

E. M. Baskin and *M. V. Entin*
Institute of Semiconductor Physics, RAS, Siberian Branch,
Pr. Lavrentyeva, 13, Novosibirsk, 630090, Russia

Abstract. QHE is studied in 2D system with antidots. The size of antidots is considered large compared with quantum and relaxation lengths. In this limit the electric field in the system is described by a continuity equation. It is found, that the electric field in the system without conducting boundaries can be expressed through that in the same system without magnetic field. The electric field and the current density are found in structures, containing one and two antidots and in a round disk with point contacts as well.

Introduction

The different descriptions of quantum Hall effect (QHE) results in the same quantization. They are microscopic approach, based on local relation between the electric field and the current density, the edge current approach, attributing the Hall quantization to the boundary currents, and the macroscopic approach.

Unlike the standard theories of QHE, based on microscopic consideration of conductivity tensor in a homogeneous electric field not taking into account the spatial fluctuations of external field, some recent works consider the Hall quantization as a macroscopic phenomenon, using the quantized Hall conductivity and zero drift conductivity of an ideal system as a zero approximation, and solving the problem of current flow in a mixture of Hall conductors and normal metal [1] or Hall conductors on different plateaus [2, 3]. This approach gave so called "semicircle" relation between the Hall and drift components, not containing the Plank constant, correctly describing the experimental data both for integer and fractional Hall effect.

The purpose of the present paper is the study of electric field and current distribution of nonhomogeneous quantum Hall system. We shall consider the quantum Hall system as a mixture of an homogeneous Hall conductor and insulating phase, neglecting the screening length. Really, such system represents, for example, the QH system with strong doping and compensation, where the insulating domains are formed by randomly reduced density of donors. In particular, in the extreme quantum limit (one partly filled Landau level) the system can be considered as a mixture of insulating domains, where the first Landau level is empty and QHE insulator domains, where the first Landau level is filled. The other example provides the hand-made potential relief of so called antidot lattice, where the problem of current flow has independent meaning, in particular for the QHE breakdown s[4].

1 Reduction of current and electric field distribution to zero-magnetic field problem.

We consider the 2D Hall conductor with common insulator inclusions. We based on the local expression for the density of current $\mathbf{j} = \hat{\sigma}\nabla\phi$ obeying the continuity equation $\nabla\mathbf{j} = 0$ with boundary conditions $(\mathbf{jn}) = 0$, where $\hat{\sigma} = ||\sigma_{ij}||$ is the conductivity tensor, ϕ is potential and $\mathbf{n}$ is a normal to the insulator boundary. The continuity equation gives the Laplace equation for potential $\sigma_{xx}\Delta\phi = 0$.

Unlike the usual formulation of conditions of problem of field distribution, *including* extended conducting contacts, the problem with insulating boundaries (and may be point current contacts) has a very simple solution. It can be found by mapping the problem with magnetic field to the same one without magnetic field, solved by means of the theory of analytical functions.

Consider the holomorphic function $w = \phi_0 + i\psi_0$, where ϕ_0 and ψ_0 satisfy the boundary conditions

$$\mathbf{n} \times \nabla\phi_0 = 0 \qquad \mathbf{n}\nabla\psi_0 = 0, \qquad \int \nabla\psi_0 \, dS/S = \mathbf{E}_0, \tag{1}$$

where S is the sample area, the mean electric field $\mathbf{E}_0$ is applied along x axes.

The potential ψ_0 supplied by expression for current $\mathbf{j} = \sigma\nabla\psi_0$, corresponds to the problem of current flow in a medium with local longitudinal conductivity σ with insulator inclusions in the absence of magnetic field. The potential ϕ_0 corresponds to current flow in conducting medium with ideally-conducting inclusion of the same form. This potential is also the solution of current flow problem in ideal QHE system ($\sigma_{xx} = 0$) with insulating inclusion.

Let the function ϕ is defined by an equation

$$\phi = \sin\alpha \, \phi_0 + \cos\alpha \, \psi_0 = Im(e^{i\alpha} w). \tag{2}$$

The function ϕ satisfies the condition $\mathbf{n}\hat{\sigma}\nabla\phi = 0$ if the angle α is

$$\cos\alpha = \frac{\sigma_{xx}}{\sqrt{\sigma_{xx}^2 + \sigma_{xy}^2}}, \qquad 0 < \alpha < \pi/2. \tag{3}$$

As a result, the solution of the boundary problem ϕ with magnetic field B differs from that without magnetic field ψ_0 by the rotation of the vector of electric field in any point on the angle α: $\mathbf{E}(\mathbf{r}, B) = \hat{U}(\alpha)\mathbf{E}(\mathbf{r}, 0)$, where $\hat{U}(\alpha)$ is a matrix of rotation on angle α.

2 Electric field and current distribution in confined systems

Three problems of field and current distribution were solved analitically. One is the density of current in a round quantum disk with point tunnel contacts. Another are current and field distribution around one and two antidots. The figures showes the equipotential lines and lines of current in these cases. As seen from figures, the magnetic field does not change the current distribution for the fixed current on the external boundary and leads to the rotation of electric field, while the fixed external field results in the rotation of the whole picture of current together with the current on the boundary.

3 Discussion

Besides the considered cases of field and current distribution, the analytical solutions of field and current distribution problems can be found for domains with known conformal map. For example, it can be done for insulator inclusion with fractal form [6].

Another problem, which is tightly bound with considered here, is the problem of effective conductivity of antidot system in QHE regime [7]. We expressed the effective Hall and drift conductivities of Hall conductor through the effective conductivity of geometrically equivalent system in zero magnetic field. It is important to emphasize that in the QHE plateau regime when the local drift conductivity goes to zero, the effective drift and Hall

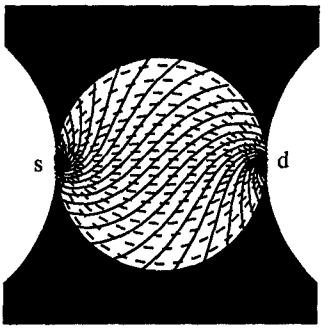

Fig. 1. Equipotential lines (solid) and current lines (dashed) in a round large quantum dot with two tunnel contacts, according to analytic formulae $j_x - ij_y = 2aJ[\pi(a^2 - z^2)]^{-1}$, $\phi = J\pi^{-1}(\sigma_{xx}^2 + \sigma_{xy}^2)^{-1/2}\mathrm{Re}[\exp(-i\alpha)\log(a - z) - \log(a + z)]$. J is the overall current, $z = x + iy$. The angle α is $\pi/4$.

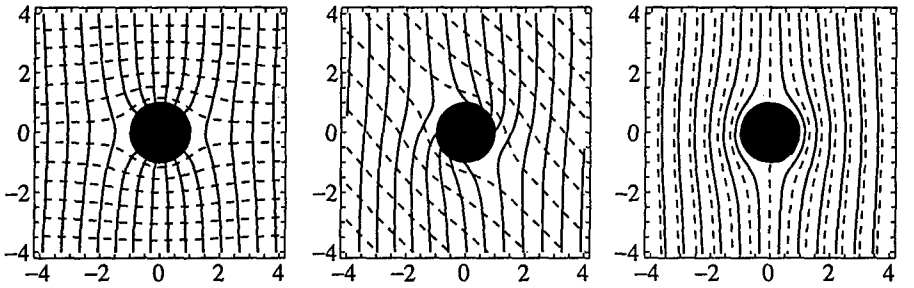

Fig. 2. Current and field distribution around one antidot (black), determined by formula $E^*(z) = E^*(\infty) - E(\infty)e^{-2i\alpha}a^2/z^2$, where $E(z) = E_x + iE_y$. The mean electric field has x-direction. The angle α runs from left to right values 0 ($B = 0$), $\pi/4$ and $\pi/2$ (Hall plateau).

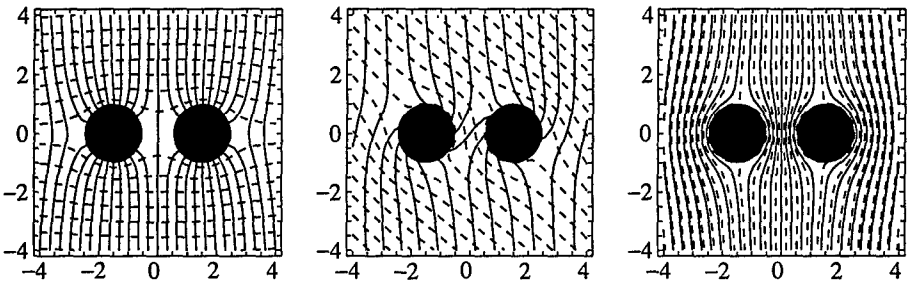

Fig. 3. The same as Fig. 2 for two antidots. The field distribution is found analogically to [5].

conductivities coincide with local ones. We also used the solution of current and field distribution problem for description of QHE breakdown in antidot arrays.

The work was partially supported by Russian Foundation for Basic Researches (Grant 970218397) and Federal Program "Physics of Solid-State Nanostructures". One of us (E.M.B.) was supported also by INTAS Grant No 960730.

References

[1] V. E. Arkhincheev and E. G. Batyev, *Solid State Commun.* **12**, 1059 (1989).
[2] A. M. Dykhne and I. M. Ruzin, *Phys. Rev. B* **50**, 2369 (1994).
[3] I. M. Ruzin and S. Feng, *Phys. Rev. Lett.* **74**, 154 (1995).
[4] G. Nachtwei, G. Lutjering, D. Weiss, Z. H. Liu, K. von Klitzing and C. T. Foxon, *Phys. Rev. B* **55**, 6731 (1997).
[5] E. M. Baskin and M. V. Entin, *Physics of low-dimensional structures*, 1/2, 17 (1997).
[6] M. B. Hastings and L. S. Levitov, *Physica D* **116**, 224 (1998).
[7] E. M. Baskin and M. V. Entin, *submitted to JETP*.

7th Int. Symp. "Nanostructures: Physics and Technology"
St Petersburg, Russia, June 14–18, 1999

Real-space transfer of electrons under a random potential: a possible mechanism of current instability in heterostructures

V. I. Borisov, V. A. Sablikov, A. I. Chmil' and I. V. Borisova
Institute of Radioengineering & Electronics, Russian Academy of Sciences
Vvedenskii sq. 1, Fryazino, Moscow region, 141120, Russia.

Abstract. A possible mechanism of lateral current instability observed in GaAs/AlGaAs heterostructures is proposed. The mechanism has to do with electron transfer in a heavily doped layer of AlGaAs, which is strongly compensated due to the presence of DX-centers. The heating of electrons in the percolation cluster net and the transfer of these electrons to the random potential wells results in the appearance of a hidden negative differential conductivity. The formation of an electric field domain brings about the conductivity collapse of the 2D electron gas. Experimental results proving this mechanism are given.

Introduction

The electric instability is known to be observed in GaAs/AlGaAs heterostructures under certain conditions. In particularly, it results in the almost complete current collapse through 2D electron gas. Although this is a dramatic and very important phenomenon, its nature is not yet understood.

In this paper a possible mechanism for this instability is proposed and experimental results confirming it are given. We suppose that the instability is caused by real space transfer of electrons in a long-range random potential in a heavily doped layer of AlGaAs. Heating the electrons in the percolation claster results in their transfer to random wells where they become localized. This process gives rise to an N-type negative differential conductivity and an electric field domain formation. One wall of the domain, which is enriched with electrons, blocks the conductivity of 2D electrons.

1 Experimental

The modulation doped heterostructures GaAs/$Al_{0.25}Ga_{0.75}As$ were obtained by MBE. The instability was observed in structures with heavy doping of AlGaAs ($\sim 5 \cdot 10^{18}$ cm^{-3}), suitably large thickness of the AlGaAs layer ($\geq$ 500 Å) and the spacer ($\sim$ 150 Å) under temperatures less than 300 K. The amplitude of the current oscillations increases, and its frequency decreases, with lowering the temperature. Various types of current instabilities can be observed, depending on the experimental conditions. In particular, these include continuous oscillations of the current, or, under temperatures less than 150 K, a periodic current collapse with a characteristic turn-off time of $\sim 2 \cdot 10^{-8}$ sec. Fig. 1 shows the time evolution of the current in the case where a small dc voltage and a large-amplitude voltage pulse was applied to the structure, which triggered the current collapse. A strong decrease of current takes place under the pulse action, and afterwards the conductivity relaxes. Analysis shows the characteristic relaxation time to have a temperature-dependence with an activation energy of approximately 30 meV. This implies that the current electrons become localized under the pulse action, and that the bond energy does not correspond to any known defect level in the AlGaAs/GaAs heterostructure. We show that this energy is close to the random potential amplitude.

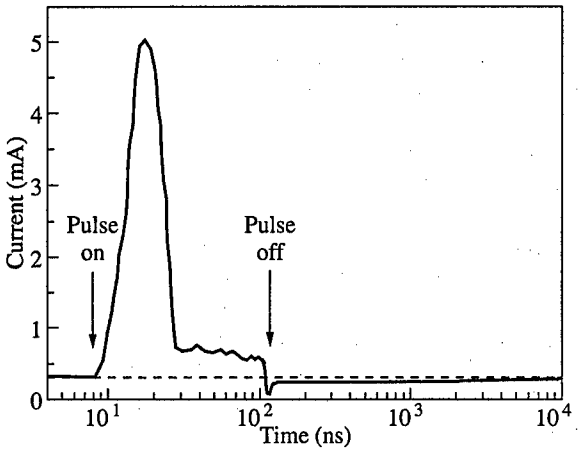

Fig. 1. Evolution of the current during the collapse and subsequent recovery of conductivity. $T = 77$ K, the voltage pulse amplitude is $U = 90$ V, distance between contacts is 5 mm.

2 Real-space transfer in random potential

We draw attention to the fact that AlGaAs layer contains a layer which is not depleted with electrons and this layer is heavily doped and strongly compensated semiconductor due to presence of both shallow donors (Si atoms) and deep levels of DX centers. The concentration of DX centers is not fixed because they are created by Si atoms which are displaced in the cell and capture two electrons. However the concentration of charged DX^- centers is very close to that of donors so that the large-scale random potential appears. The amplitude of the random potential is determined by the fluctuation of the DX^--center concentration and screening by the 2D electrons. The amplitude of the large-scale potential fluctuation is estimated as

$$\varphi(R_s) \approx \frac{e}{\epsilon}\left(\frac{\pi a N_{\mathrm{Si}}}{2}\right)^{1/2},$$

where a is the thickness of undepleted layer, R_s is the spatial scale of fluctuations, $R_s \approx (2d + a)$, ϵ is the semiconductor's dielectric constant. The random potential amplitude is evaluated numerically as $\varphi \sim 70$ meV and spatial scale is $R_s \sim 600$ Å, i.e. the large-scale potential is close to its maximum value determined by the binding energy of DX centers and essentially exceeds the temperature.

The conduction in an AlGaAs layer occurs through a percolation cluster net. As the temperature dependence of conductivity does not exhibit activation behavior, it seems likely that the level of a chemical potential is greater than the percolation level. However, the chemical potential cannot greatly exceed this level, because otherwise the average concentration of free electrons would be too high. Thus, electrons in percolation clusters move without having to overcome any barriers. Percolation clusters are surrounded by a multitude of random potential wells, in which the electrons are localized.

The height of the potential barriers separating electrons in clusters from the electrons in the wells is evaluated by $\varphi(R_s)$. The mobility of electrons in clusters is expected to be rather high, and hence noticeable heating of electrons by an external electric field occurs. Under such conditions the nonlinearity of conductivity is governed by real space transfer of the heated electrons from the cluster net to the wells. The electrons coming into the wells dissipate their energy via phonons and thus cease to participate in conduction. In such a

way, a priming negative differential conductivity appears.

Above mechanism is also similar to the known mechanism for N-shaped current-voltage characteristics in semiconductors with repulsive impurity centers. Random potential wells play the role of capturing centers in our case.

3 The current instability

The essential difference of the system we consider here, from the well investigated case of real space transfer of electrons in heterostructures [1] consists in the fact that the potential relief is not fixed and is changed when the electron density is redistributed between the cluster and wells. The electron transition to wells results in a change of the latter's potential, and correspondingly in a change in the barrier the electrons must overcome. The number of electrons in a well under non-equilibrium conditions is determined by the balance of electron flows from a cluster into wells and in the opposite direction.

The heating of electrons in the percolation cluster and their transfer to adjacent random wells results in a priming N-type negative differential conductivity in AlGaAs layer. The process is initiated in those places where the conductivity is the lowest one. The electron transfer to the wells leads to the conductivity decrease, which gives rise to a local increase in the electric field and the electron heating and so on. The evolution of instability can be accompanied both by oscillations of a current and the formation of the high field domain.

The threshold electric field F_c for the instability to appear is estimated as

$$F_c \approx \left(\frac{(2\alpha + 1 + k) n_0 T}{3 e \mu_n \tau_\varepsilon N} \right)^{1/2}, \tag{1}$$

where μ_n is the electron mobility, τ_ε is the energy relaxation time of electrons, $\alpha = e^2 N w/(4CT)$ is a dimensionless parameter, $N = mT/(\pi\hbar^2)$ is the effective density of states in the two-dimensional case, w is the characteristic well size, C is the specific capacitance (per unit length) of wells with respect to a cluster (of magnitude $C \sim 1$, because cross-sectional sizes of a barrier and wells are of the same order of magnitude. n_0 is the two-dimensional concentration of electrons in a cluster, $k \sim 1/2$. Using the reasonable values of parameters: $\tau_\varepsilon = 3 \cdot 10^{-12}$ sec, $\mu_n = 10^4$ cm^2/Vsec, $n_0 \approx N$, the threshold field may be evaluated as $F_c = 500$ V/cm for $T = 200$ K. The average electric field along a layer may be noticeably lower.

The instability in a AlGaAs layer has a crucial influence onto the conductivity of the whole heterostructure, owing to its effect onto 2D electron gas. This effect is determined by two main processes.

The first process is connected to the domain. One of the domain wall accumulates a positive charge while the other wall is charged negatively. The electric field of the negatively charged domain wall pushes out electrons from the quantum well and blocks current through 2D electron gas. Apparently, this is a reason for the collapse of current to occur.

The second process is connected to the presence of the ohmic contacts, which connect the 2D electron layer with highly doped AlGaAs layer. The transfer of the electrons from a cluster into the wells of a random potential results in the violation of an equilibrium between the electrons in a cluster net and the 2D electron gas. This causes the electrons from a quantum well to pass into the cluster net where they are warmed up by the applied electric field and transferred to the wells of a random potential and so on.

The offered mechanism allows one to explain qualitatively the main features of the observed instability. We have done two additional experiments to conform this mechanism of instability.

An effect of homogeneous illumination on the instability was investigated. We have found that the variation in the threshold field caused by illumination correlate directly with photoconductivity of 2D electrons studied in [2]. An increase in the 2D electron density results in increasing the threshold field. This correlation may be understood taking into account that in this case the equilibrium between the electrons in a cluster net and the 2D electron gas is violated. This causes the electrons from a quantum well to pass into the cluster net. A rise in the electron concentration in the cluster net according to the equation (1) results in the rise of threshold voltage.

The second experiment was done using the local illumination of the sample by a focused radiation of the He-Ne laser under the conditions of a current collapse. We found that the full recovery of the conductivity appears if a light spot has a certain position. This position depends on the amplitude of impulse voltage. This fact allows us to conclude that the distribution of the electric field in a sample is non-uniform and that this non-uniformity is not connected to any technological defects. It can be connected to formation of high field domain in the AlGaAs layer.

The present work is supported by RFBR (grant No 97-02-17999), MSTP "Physics of solid-state nanostructures" (grant No 97-1054) and Program "Atomic surface structures" (grant No 5.3.99).

References

[1] Z. S. Gribnikov, K. Hess and G. A. Kosinovsky, *J. Appl. Phys.* **77**, 1337 (1995).
[2] V. I. Borisov, V. A. Sablikov, I. V. Borisova and A. I. Chmil', *FTP* **6**, 1 (1999).

7th Int. Symp. "Nanostructures: Physics and Technology"
St Petersburg, Russia, June 14–18, 1999

Electrostatics and kinetics of 2D electrons in lateral superlattices on vicinal planes

A. V. Chaplik and *L. I. Magarill*
Institute of Semiconductor Physics, RAS, 630090 Novosibirsk, Russia

Abstract. The potential of one-dimensional lateral superlattice screened by two-dimensional electron gas located in close proximity is found. The periodic potential created by the superlattice effects on the kinetic and optical properties of the electron system. Magnetoreflectance, Faraday rotation angle and ellipticity of the reflected electromagnetic field are calculated.

Introduction

One of possible ways to fabricate short periodic lateral superlattice (SL) is segregation of charged impurities on vicinal planes of crystals (see Fig. 1). The terraced interface of a heterojunction is populated by donors nonuniformly. The latters tend to aggregate themselves at the edges of the terraces forming the chains of positive charges. As a result, the 2D electrons residing close to the interface "see" a one-dimensional periodic potential $V(x)$ with the period a determined by the angle of disorientation of the vicinal plane (see e.g. [1, 2, 3]).

Usually the potential $V(x)$ is represented by its Fourier components $V^{(r)}$ which are just given parameters of the theory. In the present paper we, first of all, calculate the potential $V(x)$ accounting for the screening effects in 2D electron gas. Then we consider magnetooptical phenomena in 1D lateral SL.

1 Screened potential of 1D SL

Consider a periodic set of charged filaments parallel to the y-axis and placed in the plane $z = 0$. The linear density of charge at each filament is ξ. In the plane $z = -\Delta$ we have strongly degenerate 2D electron gas. The problem is to find the self-consistent potential $V(x)$ and areal density of electrons $\sigma(x)$ in the plane $z = -\Delta$.

The electrostatic problem with *finite* screening is, generally speaking, nonlinear because the density of charge depends on the potential. However, a lucky exception is the Thomas–Fermi limit for 2D electron gas. Indeed, the areal density of 2D electrons $n(\mathbf{r})$ is given by ($T \to 0$)

$$n(\mathbf{r}) = \frac{m^*}{\pi\hbar^2}[\mu + e\varphi(\mathbf{r})]\vartheta[\mu + e\varphi(\mathbf{r})], \tag{1}$$

where $\vartheta(t)$ is the Heaviside step function, μ is the chemical potential. For a single charged filament placed at the distance Δ above the 2D degenerate electron gas one has

$$\varphi(x; z = -\Delta) = -2\xi e^{\kappa\Delta} Re\{e^{-i\kappa x} Ei[\kappa(x - i\Delta)]\}, \tag{2}$$

where $Ei(t)$ is the exponential integral. After summation over all the filaments arranged in the periodic set with the period a we arrive eventually at the formula for the potential of SL

$$V(x) = \frac{\pi\xi}{\kappa a}\int_0^\infty dz \frac{e^{-z}\sinh[2\pi(\Delta + z/\kappa)/a]}{\cosh[2\pi(\Delta + z/\kappa)/a] - \cos^2(\pi x/a)}. \tag{3}$$

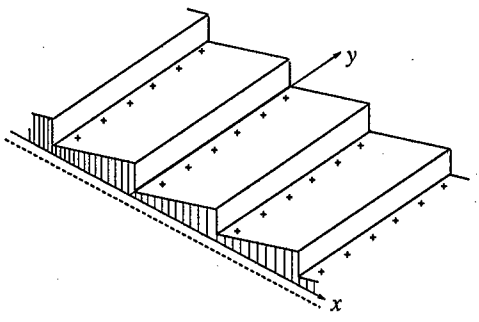

Fig. 1. Two-dimensional electron gas at a vicinal surface; + charged donors, − electrons.

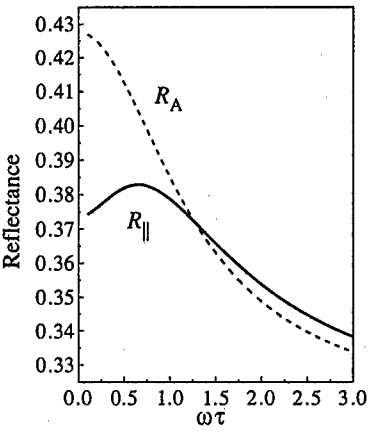

Fig. 2. Frequency dependence of the reflectance at $B = 0$. Here and in the following figures solid (dash) line corresponds to $R_\parallel$ ($R_\perp$).

The Fourier components $V^{(r)}$ of the potential (3) can be calculated analytically. For example,

$$V^{(1)} = \frac{\pi\xi}{\kappa a}\frac{e^{-2\pi\Delta/a}}{1+2\pi/\kappa a}.$$

2 Dynamic conductivity of 1D SL

In this section the expressions for components of a dynamic magnetoconductivity tensor $\sigma(\omega, \mathbf{B})$ of 1D lateral superlattice are derived. The linearized kinetic equation for a degenerate ($T = 0$ K) electron system subject to a laterally modulating potential $V(x)$, a constant uniform magnetic field $\mathbf{B}$ (axis z) and a microwave field $\mathbf{E}(t) = Re(\mathbf{E}_\omega e^{-i\omega t})$ reads:

$$\hat{\mathcal{L}}_\omega \chi \equiv \left[v(x)\cos\varphi\frac{\partial}{\partial x} + \left(\frac{\partial v}{\partial x}\sin\varphi + \omega_c\right)\frac{\partial}{\partial\varphi} + \frac{1}{\tau}\left(1 - \int_0^{2\pi}\frac{d\varphi}{2\pi}\right) - i\omega\right]\chi = -e\mathbf{E}_\omega \mathbf{u} v(x). \tag{4}$$

Here $\mathbf{u}$ is the unit vector ($\mathbf{u} = (cos\varphi,\ \sin\varphi)$), $v(x) = v_F\sqrt{1 + eV(x)/E_F}$ is the magnitude of the electron velocity (v_F is the Fermi velocity), $\omega_c = eB/m^*c$ is the cyclotron frequency, τ is the relaxation time (assumed to be constant).

We assume the lateral potential $V(x)$ to be weak that allows one to solve Eq. (4) perturbatively. To the lowest order in V we come to the following expression for magnetoconductivity:

$$\sigma_{ij}(\omega, \mathbf{B}) = \frac{\sigma_0\eta}{\eta^2+\gamma^2}\left\{ d_{ij} - \frac{\eta d_{ix}d_{xj}q^2l^2}{2(\eta^2+\gamma^2)}\sum_{r=-\infty}^{\infty} r^2\frac{|eV^{(r)}|^2}{E_F^2}\cdot\frac{S(rqv_F/\omega_c)}{1 - S(rqv_F/\omega_c)}\right\} \tag{5}$$

$$S(z) = \eta\sum_{n=-\infty}^{\infty}\frac{J_n^2(z)}{n^2\gamma^2+\eta^2}.$$

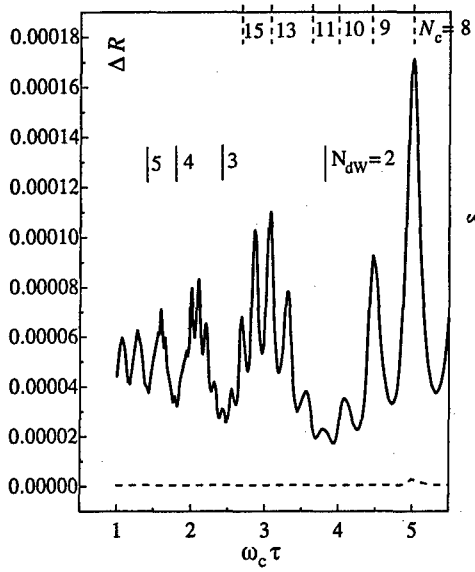

Fig. 3. Magnetic field dependence of $\Delta R(B) = R(B) - R^{(0)}(B)$ for for $\omega\tau = 40$. Solid ticks indicate the positions of dynamic Weiss oscillations followed from Eq. (6), dashed ticks mark CR harmonics ($\omega = N_c\omega_c$).

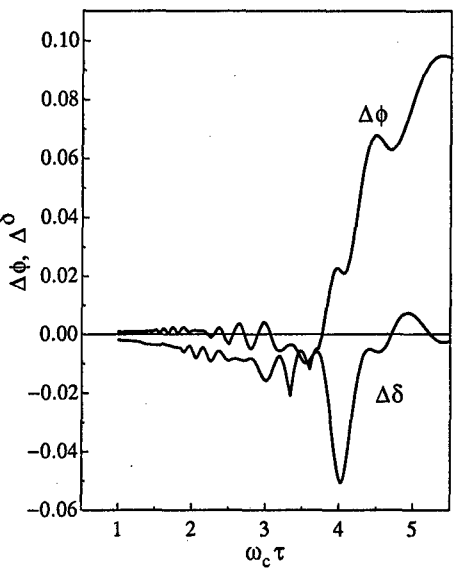

Fig. 4. Magnetic field dependence of the Faraday rotation angle ϕ and ellipticity δ for $\omega\tau = 4$.

Here $q = 2\pi/a$, $\sigma_0 = N_s e^2\tau/m^*$, $d_{xx} = d_{yy} = 1$, $d_{yx} = -d_{xy} = \gamma/\eta$, $\gamma = \omega_c\tau$, $\eta = 1 - i\omega\tau$, $l = v_F\tau$ is the free path length, $J_n(z)$ are Bessel functions.

3 Magnetoreflectance and Faraday effect

The expressions (5),(6) allows us to find the reflectance R, Faraday rotation angle ϕ and ellipticity δ.

The results of numerical computations are depicted in Figs. 2–4. For calculations the following parameters have been used: $\mu = 5 \cdot 10^4$ cm^2/V·s ($\tau = 1.9ps$), $m^* = 0.067m_0$, $N_s = 4 \cdot 10^{11}$ cm^{-2} ($E_F = 14.29$ meV, $v_F = 2.74 \cdot 10^7$ cm/s), $a_0^* = 10.12$ nm, $a = 32$ nm, $\Delta = 75$A, $\xi = 2 \cdot 10^5$ e/cm, $n = 3.58$f. At $B = 0$ we plot $R_\parallel$ and $R_\perp$ as functions of the frequency ω (Fig. 2). For y-polarized incident wave we have conventional monotonic Drude behavior $R_\perp \equiv R^{(0)}(\omega)$; we denote by $R^{(0)}$ the reflectance of the unmodulated system. However for x- polarized case the effect of lateral SL results in the curve $R_\parallel(\omega)$ with maximum at $\omega\tau \sim 1$. In the magnetic field the results essentially depend on the interplay of parameters ω, $\omega_0 = 2\pi v_F/a$ and τ. In the frequency region $1 \ll \omega\tau \ll \omega_0\tau$ (for chosen parameters $\omega_0\tau = 72.4$), a picture of beatings occurs: the envelope function connected with the cyclotron resonance (CR) and its harmonics modulates conventional Weiss oscillations. An example of $R(B)$ corresponding to the case $\omega \lesssim \omega_0(\omega\tau = 40)$ is shown in Fig. 3. Under given frequency CR harmonics are modulated by the envelope function with minima which obey the relation

$$2\frac{v_F}{a}\Phi\left(\frac{\omega}{\omega_0}\right) = \omega_c\left(N_{dW} - \frac{1}{4}\right), \tag{6}$$

where $\Phi(x) = \sqrt{1-x^2} - x \arctan(1/x^2 - 1)$, $N_{dW} = 1, 2 \ldots$. Here we have the manifestation of so called dynamic Weiss oscillations. The possibility of observation of Weiss-type oscillations in dynamic regime has been predicted in [4]. At $\omega > \omega_0$ only CR harmonics with the exponential envelope function are left (no Weiss oscillations).

Similar oscillation behavior due to the periodic lateral potential can be also observed in other magnetooptical values, as a transmittance, Faraday rotation angle etc. B-dependence of the Faraday rotation angle and ellipticity in a reflected electromagnetic wave is shown in Fig. 4. In the accepted scale the results for two polarizations coincide very closely.

Acknowledgements

The financial support of RFBR (grant No 96-15-96323) and NWO is gratefully acknowledged.

References

[1] J. H. Neave et al, *Appl. Phys. Lett.* **47**, 100 (1985).
[2] T. Fukui, H. Saito, V. Tokur, *Jap. Appl. Phys.* **27**, L320 (1988).
[3] V. I. Kadushkin, A. P. Senichkin, *Sov. Phys.- Semicond.* **24**, 2080 (1990).
[4] L. I. Magarill, I. A. Panaev, and S. A. Studenikin, *J. Phys.: Cond. Matt.* **7**, 1101 (1995).

7th Int. Symp. "Nanostructures: Physics and Technology"
St Petersburg, Russia, June 14–18, 1999

Anomalous magnetoconductance due to weak localization in 2D systems with anisotropic scattering: computer simulation

A. V. Germanenko, V. A. Larionova, G. M. Minkov and S. A. Negashev
Institute of Physics and Applied Mathematics, Ural State University
620083 Ekaterinburg, Russia

Abstract. The results of computer simulation of particle motion over the plane with randomly distributed scatters are presented. They are used to analyse the influence of scattering anisotropy on the negative magnetoresistance due to weak localisation. It is shown that the magnetic field dependence of magnetoresistance in this case can be described by the well known expression, obtained in the diffusion limit for isotropic scatternig, but with the prefactor less than unity and breaking-phase length which differs from the true value.

Introduction

Quantum correction to the conductivity arises from interference of electron waves scattered along closed trajectories in opposite directions. An external magnetic field applied perpendicular to the 2D layer destroys the interference and suppresses the quantum correction. This results in anomalous negative magnetoresistance, which is experimentally observed in many 2D systems. This phenomenon is usually described in the framework of quasiclassical approximation which is justified under the condition $k_F l \gg 1$, where k_F is the Fermi wave vector, l is the mean free path. In this case the conductivity correction is expressed through the classical probability density W for an electron to return to the area of the order $\lambda_F l$ around the start point [1–3].

$$\delta\sigma = -\sigma_0 \frac{\lambda_F l}{\pi} W, \sigma_0 = \frac{e^2}{2\pi\hbar} k_F l. \quad (1)$$

This expression allows to calculate the conductivity correction at an arbitrary magnetic field [4]. Analitical expressions are derived only for some specific cases: (i) in the diffusion limit, i.e. at $B \ll B_{tr}$ and $l \ll l_\varphi$ [1, 2], where l_φ is the phase-breaking length due to inelastic processes, and $B_{tr} = \Phi_0/2\pi l^2$, $\Phi_0 = \pi\hbar c/e$; (ii) in the high-field limit, i.e. at $B \gg B_{tr}$ [3].

To our knowledge, this problem has been solved only for the case of random distribution of scattering centers and isotropic scattering. As a rule, these conditions are not fulfilled in real semiconductor structures. First of all, in semiconductors the scattering by ionized impurities dominates at low temperatures. This scattering is strongly anisotropic, in particular in heterostructure with a remote doping layer. Besides, the impurity distribution is correlated to some extend due to Coulomb repulsion of the impurity ions at growing temperatures. In the present work the role of scattering anisotropy in the quantum correction to the conductivity is investigated through a computer simulation.

1 Simulation details

To find the values of the mean free path l and probability density W in (1), we have simulated the motion of a particle in the 2D plane with scattering centers in it. The plane is

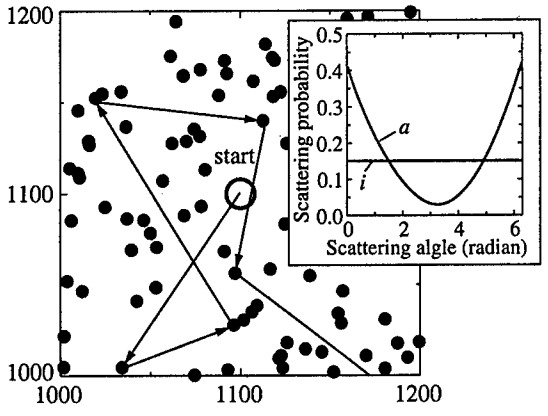

Fig. 1. A fragment of the lattice with scattering centers. Lines show closed trajectories. In the inset the angle dependences of scattering probability for the isotropic (curve *i*) and anisotropic (curve *a*) scattering mechanisms are presented.

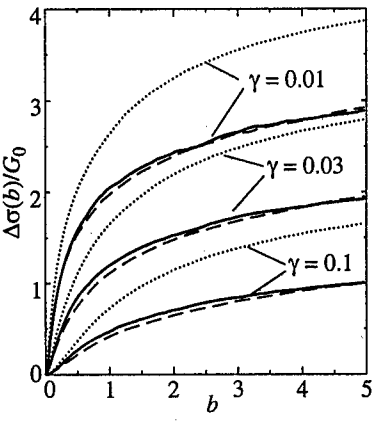

Fig. 2. The dependences $\Delta\sigma(b) = \delta\sigma(b) - \delta\sigma(0)$ for the isotropic (dashed curves) and anisotropic (solid curves) scattering mechanisms, which are calculated with the angle dependences of scattering probabilities presented in the inset in Fig. 1. Dotted curves are the results of diffusion approximation (3).

a 3000 × 3000 lattice. The scatters are randomly distributed in the lattice sites. The whole scatters number is 2×10^4. Every scatter covers seven lattice parameters in diameter. The start point of particle motion is chosen in a scatter near the centre of the lattice. We suppose the particle to move linearly between two sequential collisions with scatters (Fig. 1). The collisions change the motion direction according to given angle dependence of scattering probability. A trajectory is considered to be closed if after a number of collisions $n < n_{\max}$ it passes near the start point at the distance less than $d/2$. Since d has to be small enough, we choose d of about the scatter diameter. We assume that the particle never returns to the area of the start point at $n > n_{\max} = 1000$ or when it escapes the lattice. An estimation shows that both assumptions introduce the error in $\delta\sigma$ less than one percent at $\gamma = l/l_\varphi > 0.01$.

The simulation has been carried out for two different scattering mechanisms: isotropic and anisotropic. For the isotropic scattering corresponding to a short-range scattering potential, the scattering probability does not depend on the scattering angle (the curve *i* in the inset in Fig. 1). For the anisotropic scattering we have used the angle dependence of scattering probability presented by the curve *a*. It is close to that in heterostructures with a doped barrier, where impurities are spaced from the 2D gas. The curve *a* corresponds, for example, to the 2D structure with impurity density of about 10^{12} cm^{-2} and a spacer of 50 Å thick.

To calculate the conductivity correction in a magnetic field, we have modified the expression (1) by including the magnetic field in it according to a standart procedure. The final expression for the conductivity correction in the magnetic field can be written as:

$$\frac{\delta\sigma(b)}{G_0} = -\frac{2\pi l}{d \cdot N} \sum_i \cos\left(\frac{bS_i}{l^2}\right) \exp\left(-\frac{l_i}{l_\varphi}\right), \qquad (2)$$

where summation runs over all closed trajectories among a total number of trajectories N

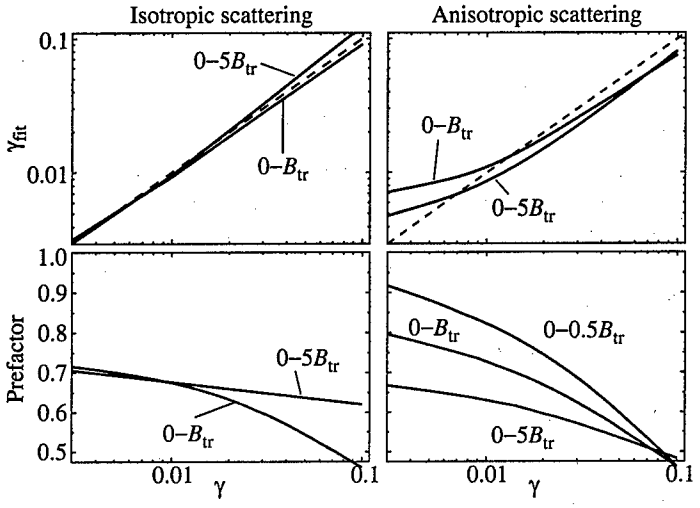

Fig. 3. The results of fitting of simulated curves (solid and dashed curves in Fig. 1) by expression (3). Dashed lines in upper figures correspond to $\gamma_{fit} = \gamma$.

($N = 10^6$ in our calculations), $b = B/B_{tr}$, $G_0 = e^2/2\pi^2\hbar$, S_i and l_i stand for the area and length of the i-th trajectory, respectively, the exponent accounts for the phase breaking. Note that in (2) l denotes the mean free path connected with the transport relaxation time.

2 Results and discussion

The results of simulation, obtained for different γ values, are presented in Fig. 2. Let us consider, at first, the results for the isotropic scattering (dashed curves). They are in a good agreement with the results of numerical calculation carried out beyond the diffusion limit [4]. This lends support to the validity of the method used. Here the results of calculation in the diffusion limit ($b \ll 1$, $\gamma \ll 1$), obtained through the well-known expression

$$\frac{\Delta\sigma(b)}{G_0} = \psi\left(\frac{1}{2}+\frac{\gamma}{b}\right) - \psi\left(\frac{1}{2}+\frac{1}{b}\right) - \ln(\gamma), \tag{3}$$

are shown too. As is clearly seen, the conditions, under which the expression (3) works well, are very rigorous: even for $\gamma = 0.01$ and $b < 1$ the formula (3) gives evidently larger value of $\Delta\sigma(b)$ than that in our simulation.

The solid curves in Fig. 2 are the results of our simulation for the anisotropic scattering mechanism. The closeness of these results to those, obtained for isotropic scattering, stands out. At first glane it seems to be surpising. The introduction of anisotropy in scattering process decreases the probability of returning to the start point area, because the scattering for small angles dominates in this case and in the average the particle moves to greater distance from the start point after each collision. As is seen from (1), the decreasing of W has to lead to decreasing in $\delta\sigma$. However, this decreasing is compensated by the increasing of transport length l, which is averaged with the weight $(1 - \cos(\theta))$ when integration runs over the scattering angle θ. Thus, the introduction of anisotropy of scattering does not dramatically change the negative magnetoresistance (at least up to $b = 5$).

One can now attack the results of simulation as experimental ones. Let us describe our curves by expression (3) in the usual fashion. We have introduced a numerical multiplier (so-called prefactor) in (3) and used it and γ as fitting parameters. The results of such data

processing are presented in Fig. 3. The curves labels show the magnetic field ranges, in which the fitting procedure has been carried out. In spite of strong difference between the simulation results and those given by (3) (see dotted and other curves in Fig. 2), the fitting value of $\gamma_{\rm fit}$ is very close to γ, used in our simulation for both isotropic and anisotropic scattering mechanisms. The difference between γ and $\gamma_{\rm fit}$ is less than 10% for the isotropic scattering and 40–50% for the anisotropic one. The value of prefactor is less than 1 and decreases with increasing γ.

Thus, (i) the use of expression (3) to determine the phase-breaking length (or time) from the magnetic field dependence of anomalous magnetoconductance in semiconductor structures, where scattering is anisotropic, can give the error of about 40–50%, (ii) the fact that the prefactor is less than 1 can be related not only with e-e interaction influence as it is frequently supposed, but with poor fulfilment of the condition $l \ll l_\varphi$ and strong anisotropy of scattering as well.

Acknowledgements

This work was supported in part by the RFBR through Grants 97-02-16168, 98-02-17286, the Russian Program *Physics of Solid State Nanostructures* through Grant 97-1091, and the Program *University of Russia* through Grant 420.

References

[1] L. P. Gorkov, A. I. Larkin and D. E. Khmelnitskii, *JETP Lett.* **30**, 248 (1979).
[2] S. Chakravarty and A. Schmid, *Phys. Reports* **140**, 193 (1986).
[3] M. I. Dyakonov, *Solid State Commun.* **92**, 711 (1994); A. P. Dmitriev *et al. Phys. Rev. B* **56**, 9910 (1997).
[4] H.-P. Wittman and A. Schmid, *J. Low. Temp. Phys.* **69**, 131 (1987).

7th Int. Symp. "Nanostructures: Physics and Technology"
St Petersburg, Russia, June 14–18, 1999

Unusually wide plateau of the quantum Hall effect in a quasi bilayer hole system inside the p-GeSi/Ge/p-GeSi quantum well

M. V. Yakunin†, Yu. G. Arapov†, O. A. Kuznetsov‡ and V. N. Neverov†
† Institute of Metal Physics RAS, Ekaterinburg, GSP-170, 620219, Russia
‡ Scientific-Research Institute at Nizhnii Novgorod State University, Russia

Abstract. An unusually wide plateau of the integer quantum Hall effect (for the filling factor $\nu = 1$) has been revealed in a wide *p*-GeSi/Ge/*p*-GeSi quantum well. This plateau exists in one of two metastable states of the sample, for which a symmetric quasi-double-quantum-well system is formed inside the Ge layer due to the hole-hole repulsion. The plateau exists not only within a magnetic field range corresponding to the quantum-Hall liquid, but extends beyond it into a so-called quantized Hall insulator phase. According to the existing theories, this extra wide plateau may be indicative of a kind of disorder, characterized by a certain distribution of fluctuations in their size and carrier density.

Magnetic field dependence of the low temperature quantum magnetotransport in a 2D charge carrier gas is described by a series of alternating electron phases, each dependent on the degree and character of disorder in the system [1]. The *high disoder* system under weak magnetic field B exhibits a divergently growing longitudinal ρ_{xx} resistivity with decreasing temperature T, but a temperature independent classical linear $\rho_{xy}(B)$ Hall resistivity [2–5], this phase being called a Hall insulator [1]. A high (giant) negative magnetoresistivity is usually observed in this field range for high disorder systems. At the higher fields the Hall resistivity $\rho_{xy}(B)$ passes into a faint plateau of the quantum Hall effect (QHE), concomitant with a rather weak $\rho_{xx}(B)$ minimum, indicating a transition into a QH-liquid phase. This phase terminates with a transition to a high-field insulator phase, characterized again by a divergent $\rho_{xx}(B, T)$, but either divergent and T-dependent [3, 4], or finite linear [5] Hall magnetoresistance. The electronic phase transitions are marked with the node points, through which all the $\rho_{xx}(B)$ traces for different temperatures pass. In the *moderate disorder* system, with mobilities of the order of 10 $m^2/V{\cdot}s$ (implying an n-type GaAs-based system), quite distinct integer QHE (IQHE) plateaux are observed at milli-Kelvin temperatures with almost vertical interplateau transitions [6]. In the *most perfect* systems, with mobilities $\geq$ 100 $m^2/V{\cdot}s$, the IQHE plateau widths decrease with increasing mobility, forming interplateau intervals of a quasi-linear $\rho_{xy}(B)$ dependence, which are in fact filled with the fractional QHE (FQHE) states [7]. IQHE in these systems terminates at a high field side with a linear $\rho_{xy}(B)$ dependent part broken by the FQHE peculiarities, and it is from this linear part the transition into an insulating phase occurs for the low disorder systems [8].

Since the IQHE plateau widths depend nonmonotonously on disorder the questions arise: what is the maximum IQHE plateau width possible and under what conditions would it realize? While the principal limit exists for the maximum IQHE plateau widths with filling factors $\nu > 1$, which is determined by a simple condition $\Delta\nu = 1$ (spin-split case) stemmed from the periodic intersections of the Fermi level with the Landau levels, the situation isn't that trivial for the $\nu = 1$ case. At first sight, maximum width possible for this plateau is determined by the same condition $\Delta\nu = 1.5{-}0.5 = 1$, implying that

delocolized states are located in energy close to the centers of both the lowest Landau levels. In fact, the bending upward of this plateau observed until recently [9] always started at $\nu > 0.5$. Anyhow, it was implied conventionally that this plateau couldn't extend into a high field insulating phase over the phase transition point, since the plateau at the fundamental $\rho_{xy} = h/e^2$ value has been considered the feature of the QHE-phase only.

Some recent results contradict this postulate. First, it was found that the $\nu = 1/3$ FQHE plateau extends beyond the high field phase transition point [10]. Later similar result was obtained for a $\nu = 1$ IQHE plateau in a GaAs/AlGaAs heterostructure with mobility as low as $\mu = 1.1$ m^2/V·s [11]. Both results [10, 11] have been obtained for n-type conductivity. It is worth noting that investigations of a $\nu = 1$ QH state in a low mobility GaAs/AlGaAs n-type heterostructure may be problematic due to a small g-factor resulting in a hardly resolved spin sublevels (considering that transition between 0^+ and 0^- sublevels is responsible for this QH state). Probably by that reason a more spectacular result was achieved on a p-type heterostructure (Ge/GeSi) [12] with the $\nu = 1$ QH plateau reaching from 2.5 T till the maximum 10 T field measured.

As it follows from a theoretical analysis of the insulator neighboring of the QH phase [13] based on a random network of paddles, the QH plateau indeed may extend into an insulating phase with its width being dependent on the relative abundance of different density puddles, which depends in turn on the distribution of potential fluctuations. Interplay between percolation via the network and coupling of the puddles by tunneling results in that the smaller puddle sizes allow a larger regime of the quantized Hall insulator phase. Considering the high sensitivity of the plateau width to the details of the disorder potential in the sample, together with a very poor number of experimental results available, we think that new results on this account would be of a great importance. We have observed an unusually wide Hall plateau in the low temperature measurements performed on Ge/p-$Ge_{1-x}Si_x$ multi-quantum-well selectively doped heterostructures [14], and it was revealed under rather specific conditions — as a component of a bistable state.

Here we analyze these results in view of the T-dependence of $\rho_{xx}(B)$ to separate different electronic phases. The results were obtained on the samples 451b4 and 451a4 of a big family investigated: see [14, 15] for a more detailed sample description. These two samples differ from the others by rather wide wells of 35.5 nm and lower hole densities $p_s = 1.4 \cdot 10^{15}$ m^{-2} (other parameters: number of repetitions 36, $x = 0.097$ and $\mu = 1.4$ m^2/V·s). A bistable behavior of these samples was revealed in the high field range at low temperatures characterized by two metastable states (see Fig. 1(a) for the sample 451b4; sample 451a4 is cut from the same wafer and exhibits similar results): (i) a QH state with holes divided into two 2D sublayers in each Ge layer and (ii) a classical state with undivided hole gas in a layer. The former state implies an existence of some self-stabilizing mechanism, probably connected with the weak tunneling through the barrier between two equivalent states in the sublayers. Going out of the balance drives the system into the state with a single conducting gas in a Ge layer and to destruction of the QH regime. This implies the change of the potential profile in the well due to the hole gas redistribution in the direction normal to the interface [14]. The bistable behavior in asymmetric double-quantum-wells (DQW) was revealed in a number of works [16].

Comparing our results for the DQW state with the results [12] a good resemblance could be seen, although we have a somewhat lower precision for the ρ_{xy} value within the plateau due to the multilayered structure of the samples and the metastability of the quasi-DQW state: with a very weak (here) or absent [12] $\nu = 2$ (related to a single 2D gas) QH state an extremely wide $\nu = 1$ plateau exists; the low field border of the plateau is located in the

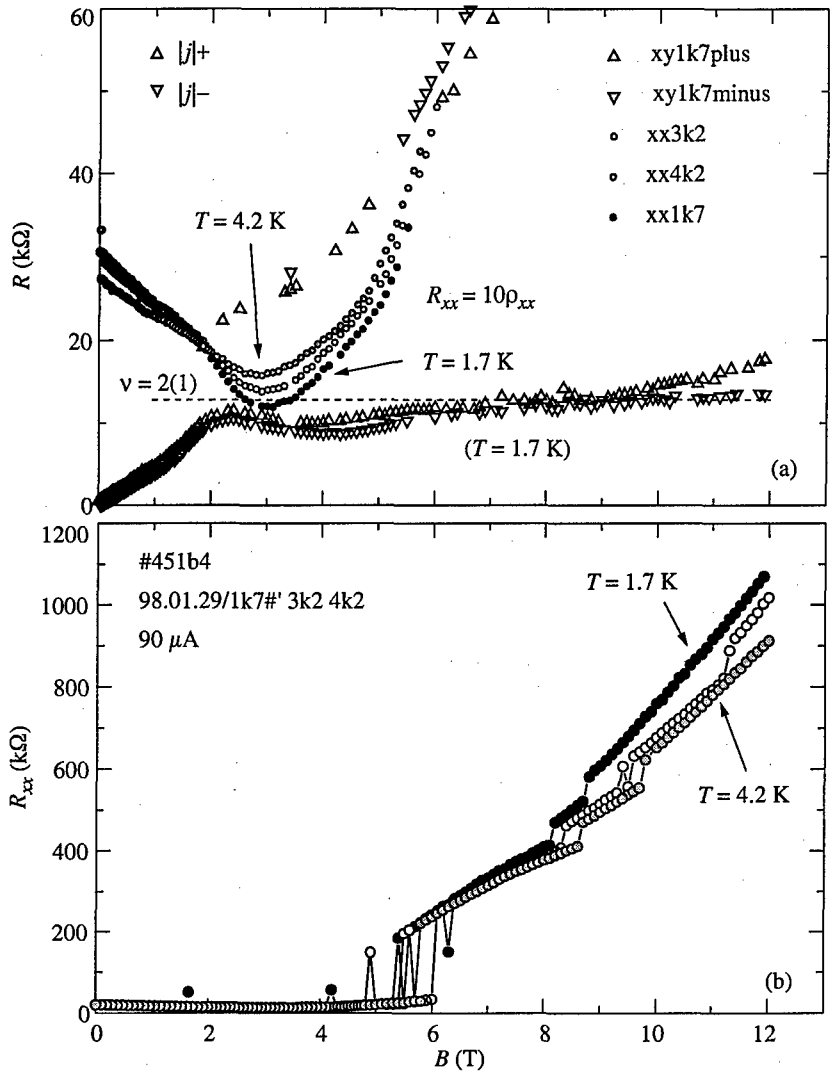

Fig. 1. (a) Bistability in the Hall resistance of sample 451b4. The dash line marks the ρ_{xy} value for the first plateau, calculated per a Ge layer ($h/2e^2$). The scale for ρ_{xx} is a factor of 10 enlarged. (b) $R_{xx}(B)$ as measured for $T = 1.7$, 3.2 and 4.2 K.

vicinity of the low field node point present in the $\rho_{xx}(B, T)$ set of traces. As for the high field node, the unstable $\rho_{xx}(B)$ behavior hampers to determine it exactly, but we can see for sure that this node does exist in the vicinity of $B = 6$ T: it follows particularly from that the $\rho_{xx}(B)$ trace for the lowest temperature measured $T = 1.7$ K is the lowest one in the minimum at $B = 3$ T, but it is the highest one at the high field region (Fig. 1(b)). Thus the plateau extends above the QH phase into the state of quantized Hall insulator [13] in our results, as well as in [12]. Also we can see that the value of resistance in the high field node is several times higher than it is in the low field node. Analyzing other works we can conclude that the values of ρ_{xx} are approximately equal in both nodes for the high

disorder samples [2–5], but the low field node goes down relative the high field node for the lower disorder, receding from the fundamental value h/e^2: see [9], also such an asymmetry appears in [12] for the higher hole densities regulated by the gate voltage. We've observed a higher difference in the ρ_{xx} values in the nodes that reflects a lower disorder in our sample than in [12]. The latter is confirmed by the existence of a weak $\nu = 2$ peculiarity and by the lower $\rho(B = 0)$ values.

Finally, it's worth noting that, like in our work, the measurements in [12] were done on the GeSi/Ge/GeSi heterosystem with a p-type conductivity, but with a substantial difference: in contrast to our samples with symmetrically doped QWs, their structures were single side doped, that resulted in an initially asymmetric QW potential relief. Similar potential profile is expected to exist in our samples in the single-component metastable state. Surprising is that we've obtained a qualitatively different result, namely a classical behavior, in this state. This yields an additional argument in favor of an important role of the disorder characteristics for the description of samples and emphasizes insufficiency of characterizing the sample by such macro parameters as the mobility and the carrier density only.

The work is supported by RFBR, Grants No 98-02-17306 and 99-02-16256.

References

[1] S. Kivelson, D. H. Lee and S. C. Zhang, *Phys. Rev. B* **46** 2223 (1992).
[2] H. W. Jiang, C. E. Johnson, et. al., *Phys. Rev. Lett.* **71** 1439 (1993).
[3] T. Wang, K. P. Clark, G. F. Spencer, et. al., *Phys. Rev. Lett.* **72** 709 (1994).
[4] R. J. F. Hughes, J. T. Nickolls, et al., *J. Phys.: Condens. Matter.* **6** 4763 (1994).
[5] C. H. Lee, Y. H. Chang, Y. W. Suen and H. H. Lin, *Phys. Rev. B* **56** 15238 (1997).
[6] see e.g., M. A. Paalanen, D. C. Tsui and A. C. Gossard, *Phys. Rev. B* **25** 5566 (1982); G. Ebert, K. v. Klitzing, et al., *Solid State Commun.*, **44** 95 (1982).
[7] see e.g., H. L. Stormer, A. Chang, D. C. Tsui et al., *Phys. Rev. Lett.* **71** 1439 (1993); T. Sajoto, Y. W. Suen et al., *Phys. Rev. B* **41** 8449 (1990).
[8] H. C. Manoharan, Y. W. Suen et al., *Phys. Rev. Lett.* **77** 1813 (1996).
[9] see e.g., L. W. Wong, H. W. Jiang and W. J. Schaff, *Phys. Rev. B* **54** 17323 (1996).
[10] D. Shahar, D. C. Tsui, M. Shayegan et al., *Science* **274** 589 (1996).
[11] D. Shahar, D. C. Tsui et al., *Solid State Commun.* **102** 817 (1997).
[12] M. Hilke, D. Shahar, S. H. Song, D. C. Tsui, Y. H. Xie and Don Monroe, *Cond-mat./* 9810172;*Proc. 24-th Int. Conf. Phys. Semicond.* (Jerusalem, 1998).
[13] E. Shimshoni and A. Auerbach, *Phys. Rev. B* **55** 9817 (1997).
[14] M. V. Yakunin, Yu. G. Arapov et al., *Proc. 6th Internat. Symp. "Nanostructures: Physics and Technology"* (St. Petersburg, 1998) p. 462; *Izv. Rossiiskoi Akademii Nauk, Ser. Fiz.* **63** 334 (1999).
[15] Yu. G. Arapov, V. N. Neverov, G. I. Harus, N. G. Shelushinina, M. V. Yakunin and O. A. Kuznetsov, *Semiconductors* **32** 649 (1998).
[16] see e.g., Y. Takagaki, K. J. Friedland et al., *J. Phys.: Condens. Matter.* **10** 8305 (1998); M. I. Stockman, L. N. Pandey et al., *Phys. Rev. B* **48** 10966 (1993) and references therein.

7th Int. Symp. "Nanostructures: Physics and Technology"
St Petersburg, Russia, June 14–18, 1999

2D lattices of ferromagnetic nanoparticles as supermagnetics

A. A. Fraerman, S. A. Gusev, I. M. Nefedov, I. R. Karetnikova, L. A. Mazo, M. V. Sapozhnikov, Yu. N. Nozdrin, I. A. Shereshevskii and L. V. Suhodoev
Institute for Physics of Microstructures, RAS,
GSP-105, Nizhny Novgorod, 603600, Russia

The interest in the systems of nanosize magnetic particles is accounted for by their potentiality as ultrahigh density magnetic recording media. It is assumed that each particle carries one bit of information and the maximal density of data recording can be increased to 10^{10} bit/cm^2. There are two basic limitations set on the geometrical sizes of such systems. First, the size of the particles should not be too small, as the lifetime of a particle with the assigned magnetic moment is $\sim \exp(KV/T)$, where K is the constant of the magnetic anisotropy, V the particle volume, T the temperature. The effect of the thermally induced rotation of the particle magnetic moment is called superparamagnetism. Second, the field of particles interaction in recording media must be much smaller than the energy of magnetic anisotropy. Otherwise, the particles demonstrate a collective behavior. One fundamental type of interaction between single-domain particles is the dipole interaction. The energy of two-particle interaction has the form

$$E = \frac{1}{2}\sum D_{ik}(\vec{x}-\vec{y})M_i(\vec{x})M_k(\vec{y}), \quad D_{ik}(\vec{x}) = \frac{\delta_{ik}}{x^3} - \frac{3x_i x_k}{x^5} \tag{1}$$

where $M_i(\vec{x})$ is the i-th component of the magnetic moment of a particle at point $\vec{x}$. It follows from (1) that to decrease the interaction energy one has to increase the interparticle distance. If there is a strong interaction in the system of superparamagnetic particles the unusual situation is possible. Indeed, the particle interaction energy can be neglected at rather high temperatures, and the system goes to a superparamagnetic state. With a decrease of the temperature the system became ordered due to the dipole interaction of particles. Such a state of the system was defined as supermagnetic [1]. The critical temperature of transition into this state depends on the characteristic value of the dipole interaction between particles

$$T_c \simeq M_o^2 V^2/R^3 \tag{2}$$

and for typical values of magnetization $M_o \simeq 1000$ G, $V \simeq 10^{-18}$ cm^3 and interpartical distance $R \simeq 10^{-5}$ cm, T_c is about to 100 K.

Due to anisotropic character of the dipole interaction (1) the type of the long-range order essentially depends on the parameters of a lattice. For example, two-dimensional lattices with a rhombic unit cell can have a ground state with both the ferromagnetic- and the antiferromagnetic type of ordering depending on a rhombicity angle [2]. It means that by varying a 2D lattice symmetry, a particle size and interparticle distance one can, in principle, create magnetics with assigned properties.

In this work we report some results of our investigations into such systems. We focussed on a investigation of 2D lattices with a rectangular unit cell. The easy magnetization axis in these systems is directed along the short side of the unit cell. The antiferromagnetic type of dipole ordering in the neighboring chains of the particles corresponds to the ground state at $T = 0$. Let us consider a simple case of noninteracting chains. At finite temperature

and zero external field there is no long-range order in this system. Despite the fact that the small perturbations spectrum does not have an acoustic branch, the long-range order is destroyed by nonlinear excitations (solitons). Fig. 1 presents the results of numerical simulation of the magnetization distribution in a dipole chain at a finite temperature. Note

Fig. 1. The thermoiduced soliton pair in dipole chain (computer simulation).

that the picture is similar to the one when the field is applied in the plane perpendicular to the chain.

The long-range order in 2D-system appears due to interaction of the chains. The chain interaction leads to interesting features of the hysteresis loop when the field is directed along the chains. In Fig. 2 we provide the results of numerical simulation for a system consisting of 80 chains, each having 6 dipoles (the ratio of the unit cell sides is 1:2). We can see that

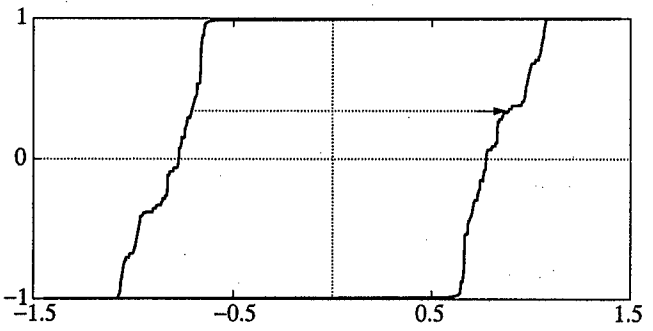

Fig. 2. The numerical simulation of the hysteresis loop in field directed along the chains.

the hysteresis loop is essentially a number of steps that correspond to the magnetization reversal of one chain. A similar dependence was studied in [3] for other systems and was called a "devil staircase". With a change of the derivative sign of the external field the system goes from one branch of the hysteresis loop to the other (shown by the dotted line in Fig. 2). These are, briefly, our ideas about the behavior of 2D lattices with a rectangular unit cell.

Two-dimensional lattices of nanosize magnetic particles were formed by the electron lithography method from permalloy films (Ni_3Fe) that were laser deposited on a substrate. Patterns were produced using C_{60} fullerene films as negative electron resists and Ti films as transmitting layer. In this way it is possible to form 2D lattices consisting of cylinder-shaped particles with a 15 to 100 nm diameter and a height equal to the thickness of the original (Ni_3Fe) film. According to the available data, the particles of this size should be considered single-domain ones. In the study of the magnetic properties we used a difference scheme comprising two semiconductor (InSb) Hall sensors with common potential contacts and independent current contacts. The size of the Hall cross of the sensors was $50 \times 100\ \mu$m, the thickness was $10\ \mu$m. The system under study was produced in the working zone of one sensor. The developed method allows to measure the magnetic field component perpendicular to the sensor plane in a wide temperature range. Figures 3 and 4 show the magnetization curves of a sample for different orientations of the external magnetic field

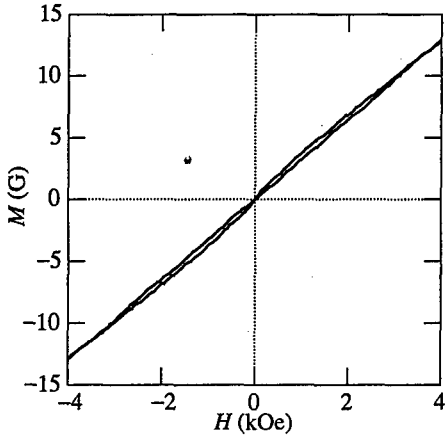

Fig. 3. The dependence of M_z on the magnetic field with $\theta = 45°$, $\phi = 0°$.

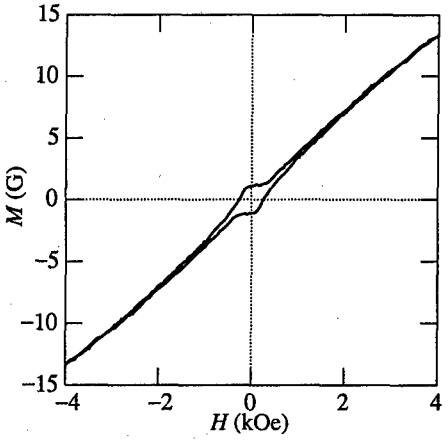

Fig. 4. The dependence of M_z on the magnetic field with $\theta = 45°$, $\phi = 90°$.

and $T = 4.2$ K. The particles form a lattice with a rectangular unit cell, 90×180 nm. The particles radius is 20 nm and the height is 45 nm.

The external field direction is characterized by two angles, θ and ϕ, where θ is the angle measured from the normal to sample and ϕ is the azimuthal angle measured from the axis directed parallel to the particle chains. The dependence of the magnetization curves on field orientation relative to the lattice axes cannot be interpreted in terms of individual particle properties and is a manifestation of the collective behavior of the particles. Note that the hysteresis loop in Fig. 4 has a remanent magnetization. This is likely to be connected with formation of nonuniform states (solitons) in the system of interest, which is close to a 1D system. When a field is applied perpendicular to the chains, there are two equilibrium states in the dipole chain, that have the same energy and differ in the sign of the longitudinal component of the magnetization. Hence, a temperature-induced domain formation is possible in these orientations. Measurements of the magnetization curves of a particle lattice with a square unit cell provide indirect evidence of the proposed hypothesis, as they have shown absence of remanent magnetization for any orientation of the external field. Numerical simulation also confirms the absence of solitons in a square lattice of dipoles.

In Figure 5 the magnetization curve for $\theta = 90°$, $\phi = 0°$ is presented. It is peculiar in that the magnetic susceptibility depends on the sign of change of the magnetic field.

The lower branch of the hysteresis loop corresponds to the increasing of the magnetic field, the upper one corresponds to the magnetic field decrease. If one changes the derivative sign of the magnetic field, the system goes from the one branch to the other. As was mentioned above, such a behavior is determined by multistability of the system. The question of whether or not this system undergoes a transition into a superparamagnetic state can be solved by investigating the temperature dependence of the observed effects. That such a dependence exists is proved by the qualitative changes occurring in the magnetization curve of a rectangular unit cell sample with an increase in the sample temperature to 77 K.

We believe that from the fundamental standpoint the obtained results are of great interest as an example of the behavior of a two-dimensional system with the exactly known inter-

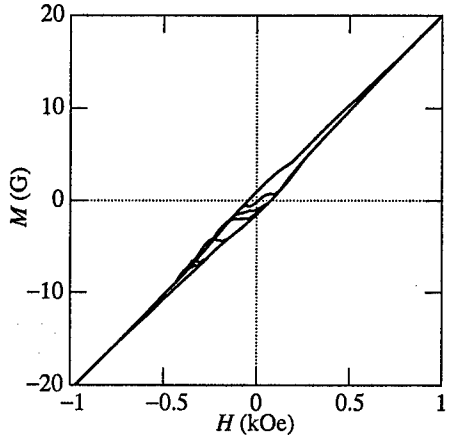

Fig. 5. The dependence of M_z on the magnetic field with $\theta = 90°$, $\phi = 0°$.

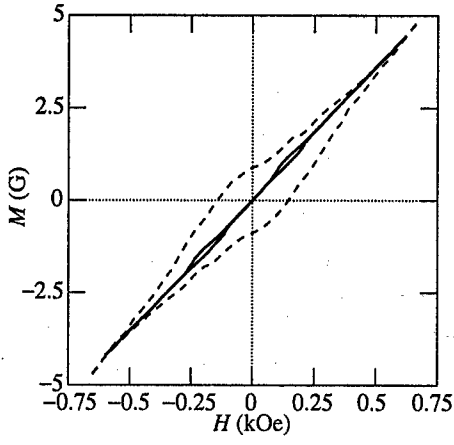

Fig. 6. The hysteresis loop change with a temperature (dashed line 4.2 K, solid line 77 K.

action. The samples, their fabrication technology and measurements could prove useful for ultrahigh density magnetic recording media under active development currently.

Acknowledgments

This work was performed as part of Project 98-02-16183 of the Russian Foundation for Basic Research and the program "Physics of Solid-State Nanostructures", Grant 98074.

References

[1] S. Morup, *Europhys. Lett.* **28**, 671 (1994).
[2] V. M. Rosenbaum, V. M. Ogenko and A. A. Chuiko, *Usp. Fiz. Nauk* **161**, 79 (1991).
[3] P. Bak and R. Bruinsma, *Phys. Rev. Lett.* **49**, 249 (1982)

7th Int. Symp. "Nanostructures: Physics and Technology"
St Petersburg, Russia, June 14–18, 1999

Fabrication and magnetic properties of 2D arrays of nanoparticles

S. A. Gusev , S. V. Gaponov, A. A. Fraerman, L. A. Mazo, M. V. Sapozhnikov, Yu. N. Nozdrin and L. V. Suhodoev
Institute for Physics of Microstructures, RAS,
GSP-105, Nizhny Novgorod, 603600, Russia

Several procedures can be chosen to create structures consisting of nanosized particles: chemical decomposition with the STM tip [1], self-organizing deposition on the crystal surfaces, the laser interference irradiation of solid mixture films [2] etc. However, till now electron-beam lithography remains one of the basic technique for the fabrication of ultrasmall structures, because only e-beam lithography ensures controllable dimensions, shape and position of particles. In specific cases using conventional processing with the positive resist poly(methyl methacrylate) (PMMA) it is possible to fabricate the structure with features less than 10 nm [3]. Unfortunately the large sizes of PMMA molecules (up to 100 nm) reduce the reproducibility of nanostructures dimensions and are severely limit an assortment of objects, that can to make by this manner. The small size of C_{60} molecules and the ability of fullerides to modify their physical and chemical properties under exposure to photon irradiation or electrons [4, 5] make it possible to use this material for high resolution nanofabrication. In the present paper we demonstrate the capabilities e-beam lithography with fullerens on an example of creation of two-dimensional periodical systems of nanosizes magnetic particles (nanomagnets). The main steps of the procedure for manufacture permalloy nanoparticles are thin films deposition, exposure by e-beam, development and two-stage etching. The choice of Ni_3Fe in this study has been dictated by magnetic experiment requirements, and it was discussed in [6]. We have used double-layer mask containing the C_{60} film as a sensitive layer and Ti film as a transmitting layer. Permalloy and Ti films have been prepared by pulse laser evaporation on the substrate at room temperature. Fulleride films were deposited by sublimation of a C_{60} powder (purity is 0.98, synthesised in ICMOC RAS, N. Novgorod) at temperature 350 °C in vertical reactor with hot walls and supplied with cooling holder for the substrate. The thickness of magnetic layers was varied from 20 to 70 nm due to magnetic experiments requirements. The thickness of masking films was 20 nm for the C_{60} layer and 30 nm for Ti film.

The fullerides were patterned in the JEM-2000EX electron microscope with scanning electron microscopy (SEM) mode and by 200 kV e-beam, which diameter was it is possible to change from 10 nm and over. Accordingly results in Ref. [5] the threshold of sensitivity the fulleride is about 0.01 C/cm^2, we have got one the same order of value in our experiments. Usually the doses for practical usage were 0.05 ... 0.1 C/cm^2, because it assured the reproducibility and uniformity of patterns sizes. Electron beam irradiation of C_{60} films reduces the solubility of fullerenes in organic solvents. The most likely reasons of changes of the solubility are electron induced polymerization C_{60} molecules accompanied partially graphitization ones [5, 7]. Exposed samples were developed in the toluene during 1 min, and then patterns were transferred into the Ti layer by plasma etching with CF_2Cl_2 atmosphere. The ended step of fabrication the magnetic particles is the Ar^+ ion milling of Ni_3Fe films, using this double-layered mask. By carefully monitoring the elemental composition of samples by means EDS qualitative microanalysis and checking up the morphology of particles by SEM, we can better detect the end points of plasma etching and ion milling

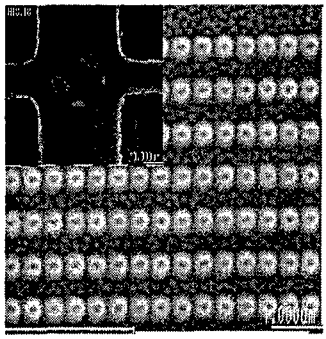

Fig. 1. SEM microphotography array of magnetic nanoparticles, top view. On an insert in the upper left corner of the figure array of magnetic nanoparticles with rectangular lattice on the Hall magnetometer (are seen Moire patterns between a lattice and raster of SEM).

processes. However, usually we have done some overmilling at the last step, to prevent presence any magnetic substance between the particles we make. Some SEM images of arrays of ferromagnetic particles are present at Fig. 1. The real shape of ferromagnetic core is a disc, which thickness equals the thickness of initial permalloy film, and it is a small part (approximately one third) of the visible height of a particle on the microphotograph. Also it is possible to fabricate magnetic columns by this procedure, but we didn't tried to create ones with aspect ratios more than 3:1, when diameters not exceeded 20 nm.

The smallest particle's diameter was about 10 nm, we have prepared by this method, and the distance between boundaries of particles was the same value. Moreover, we believe, that such ultrasmall size of magnet isn't the limit of this technique. Really, the main factor determining the ability of lithography is the resolution of resist. Using C_{60} we found, that the patterns by diameter less than 10 nm and the minimal distance between them 5–6 nm can be obtained in reproduced manner. However the observation, microphotography and correct measurements sizes of this kind objects is the special metrological task, which to us for the present did not uniquely to be decided.

The measurements of the magnetic properties were provide using the commercial Hall magnetometer. Difference scheme, consisting of two semiconductor (InSb) Hall sensors with common potentional contacts and independent current contacts was used [6]. The system of particles investigated was formed in the working zone of one of the sensors (Fig. 1).

As the used method allows to measure only the z-component of the magnetization, we provide our investigation with the three orientation of the external magnetic field: (i) the field is perpendicular to the sample plane ($\theta = 0°$); (ii) the field is directed at 45 degree to the sample plane along the short side of the rectangle cell ($\theta = 45°$, $\phi = 0°$); (iii) the field is directed at 45 degree to the sample plane along the long side of the rectangle cell ($\theta = 45°$, $\phi = 90°$). The results of this measurements for $T = 4.2$ K are represented in Figs. 2 and 3.

The difference in the magnetization curves indicates the collective behavior of the system, which is the result of the dipole-dipole interaction between particles. The hysteresis if the field directed at $\theta = 45°$, $\phi = 0°$ (Fig. 2) is the attribute of the easy axis of the magnetization which is directed along the short side of the rectangle cell. The remanent magnetization is absent in this case. The curve for $\theta = 45°, \phi = 90°$ (Fig. 3) have hysteresis

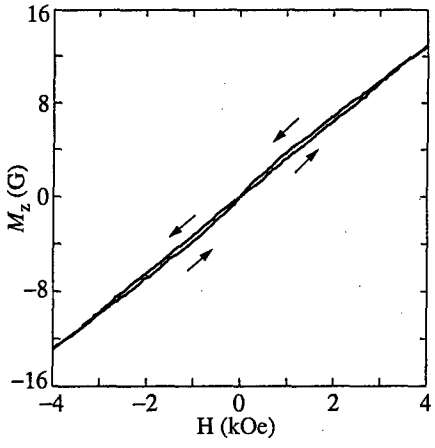

Fig. 2. The dependence of M_z on the magnetic field with $\theta = 45°$, $\phi = 0°$.

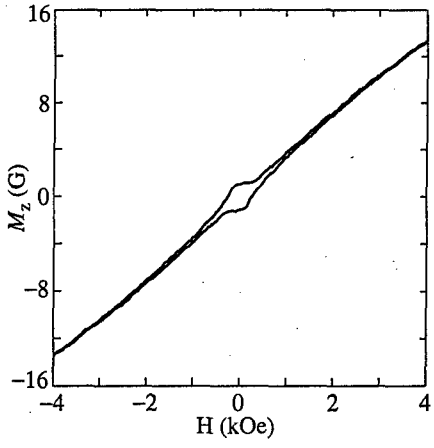

Fig. 3. The dependence of M_z on the magnetic field with $\theta = 45°$, $\phi = 90°$.

in the weak magnetic field with the remanent magnetization which is approximately 0.05 of the saturation magnetization, one equals 35 G. The remanemt magnetization apparently is reasoned by the nonuniform states which are appear in this case.

Now we study the applicability of fullerides technology for creation nanoparticles of another metals and semiconductors (GaAs, InSb, Ge, Si, Co, Cr etc). The details of this investigation we'll publish elsewhere.

Acknowledgements

This work was performed as part of Project 98-02-16183 of the Russian Foundation for Basic Research and the program "Physics of Solid-State Nanostructures", Grant 98074.

References

[1] A. D. Kent, S. Von Molnar, S. Gider and D. D. Awschalom, *J. Appl. Phys.* **76**, 6656 (1994).
[2] Yu. K. Verevkin, S. A. Gusev, V. N. Petryakov and N. I. Polushkin, *Abst. of XVI International Conf. Coherent and Nonlinear Optics* **39** (Moscow-1998).
[3] D. R. Cumming, S. Thoms et al., *Appl. Phys. Lett.* **68**, 322 (1996).
[4] Y. B. Zhao, P. M. Poirier et al., *Appl. Phys. Lett.* **64**, 577 (1994).
[5] T. Tada and T. Kanayama, *Jpn. J. Appl. Phys.* **35**, L63 (1996).
[6] S. A. Gusev, L. A. Mazo, I. M. Nefedov, Yu. N. Nozdrin, M. V. Sapozhnikov, L. V. Sukhodoev and A. A. Fraerman, *JETP Lett.* **68**, 509 (1998).
[7] V. M. Mikushin and V. V. Shnitov, *Solid State Phys.* **39**, 187 (1997) (in Russian).

7th Int. Symp. "Nanostructures: Physics and Technology"
St Petersburg, Russia, June 14–18, 1999

Granulated metallic nanostructure fabricated by laser ablation

V. M. Kozhevin, D. A. Yavsin, S. A. Gurevich, V. M. Kouznetsov,
V. M. Mikushkin, S. Yu. Nikonov, A. N. Titkov and A. V. Ankudinov
Ioffe Physico-Technical Institute, St Petersburg, Russia

Abstract. A new method for the fabrication of monodisperse metallic nanostructures is described. The method is based on laser ablation of Cu target and subsequent fission of the splashed liquid Cu drops resulting from drops charging in the laser torch plasma up to instability threshold. The monodisperse charged nanoparticles produced by fission are directed to the substrate by the external electric field. The final stage of structure formation is free air oxidation of the deposited film. The structures were studied by SEM, AFM, surface profilometry, and XPS methods. It is shown that the film consists of closely packed spherical Cu nanoparticles, about 6 nm in diameter, covered by the Cu_2O layer of the thickness of 0.8 nm. Average gap between the neighbouring nanoparticles is controlled by laser beam intensity and it can be changed from $\delta x \approx 1$ nm to $\delta x \approx 4$ nm. The fabricated films can consist of one or several monolayers of oxidized Cu granules.

Introduction

The fabrication of granulated metallic nanostructures has gained considerable attention because of their potential use for designing of novel types of electronic devices. In particular, such structures are promising for fabrication of single-electron devices operating at elevated temperatures [1]. To fabricate these devices one needs to produce monodisperse metallic granules with typical size less then 10 nm. For this it would be necessary to use either a nm-resolution lithography or to use a source of nanoparticles together with manipulation techniques, allowing for proper particle positioning, or to employ nanoparticles self assembling. These techniques could not be referred as well developed ones, therefore, novel approaches towards nanostructure fabrication and manipulation are needed. We report on novel method of granulated nanostructure fabrication based on laser ablation of metallic target and discuss the results of this structure studies.

1 The method of structure formation

The experimental structures were fabricated using the method described previously in [2]. This method is based on laser ablation of metallic target with further fission of splashed liquid metallic drops in laser torch plasma. The beam from pulsed AIG Nd^{3+} laser was introduced into the vacuum chamber through the side port and focused on the Cu target to produce the power density about 10^9 W/cm^2. The vacuum chamber was pumped down to 10^{-5} Pa. Illumination of the target by intense laser beam results in surface heating, melting, and evaporation of the target material. In the laser torch, besides of ionised Cu vapours, liquid Cu drops of submicron size arise due to instability of the melt surface layer. These drops get charged in plasma and, if the plasma electron temperature is high enough, became to be unstable [3]. The analysis shows that the electron temperature should be as high as 60 eV to generate capillary instability of the drops and to produce their subsequent fission. The process of drop fission is of cascade type and it stops when the drop size reduces down to the critical value, $d_{crit} \approx 10$ nm. This critical size is determined by autoelectronic charge

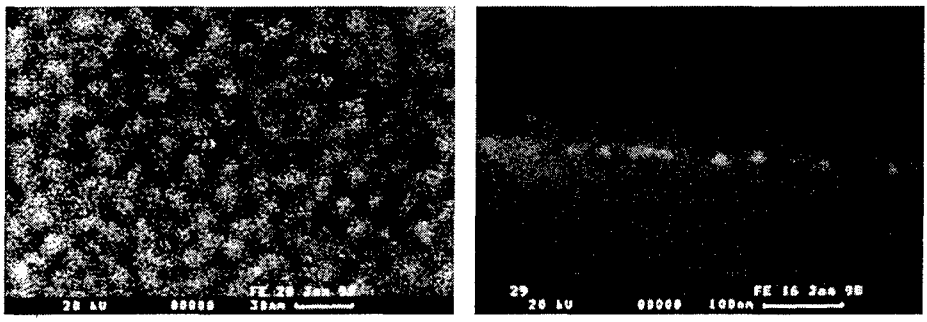

(a) (b)

Fig. 1. SEM image of fabricated monolayer. (a) plain view and (b) cross view.

emission from the surface of the drop. As a result, relatively big initial drops with wide size dispersion turn on the set of nearly monodisperse nanoparticles. The nanoparticles formed near the target are still charged and thus their movement can be controlled by the external electric field. To collect nanoparticles on the substrate the DC voltage (1–3 kV) was supplied between the target and the anode where substrate was fixed. It is to note that the above voltage was not enough to direct the big drops to the substrate. In this way the additional mechanism for the particle size separation was realised.

The particles were deposited on the alumina, silicon, and oxide-passivated silicon substrates. The final stage of the process was free air oxidation of the nanostructure. The described method allows to fabricate films which consist of one or several monolayers of the nanometric granules and, what is more, the number of monolayers is controlled by the process duration. Below, we discuss the results of structure studies of oxidized granulated films.

2 Experimental results and discussion

Fig. 1(a) shows the SEM plain view of the fabricated granulated film. As one can see in this figure, the granules are closely packed and the characteristic size of individual granules can be estimated as 10 nm. Analysis of SEM images of the structures obtained under different conditions, at different values of the laser beam intensity, showed that the nanoparticles of about 10 nm in diameter exist only if laser beam intensity exceeds certain critical value I_{cr}. Above this threshold the particles size is nearly constant.

Estimations show that experimental value of I_{cr} is just the intensity needed to heat the electrons in the laser torch plasma up to the temperature $T_e \approx 60-70$ eV. As we have mentioned above this temperature is desired to charge the initial "big" drops up to capillary instability threshold [4] and initiate drops fission. Another observation resulted from the analysis of SEM images is that the distance between the centres of neighbouring granules grows from the 8 nm to 12 nm with the increase of the laser beam intensity from I_{cr} to $2I_{cr}$. This can be explained by more intensive target evaporation in the case of more powerful laser beams. As a result, at higher laser pulse power the deposited drops are separated by larger amount of atomic size Cu particles. Fig. 1(b) displays the cross-sectional SEM image of the film shown in Fig. 1(a) (deposition during 3 minutes, pulse repetition frequency is 28 Hz). It is clearly seen that this film consists of one monolayer of closely packed spherically shaped granules. With the accuracy provided by SEM images we can conclude that all the fabricated nanostructures are monodisperse.

The monolayer films were analysed by AFM. Experiments performed with the tip having

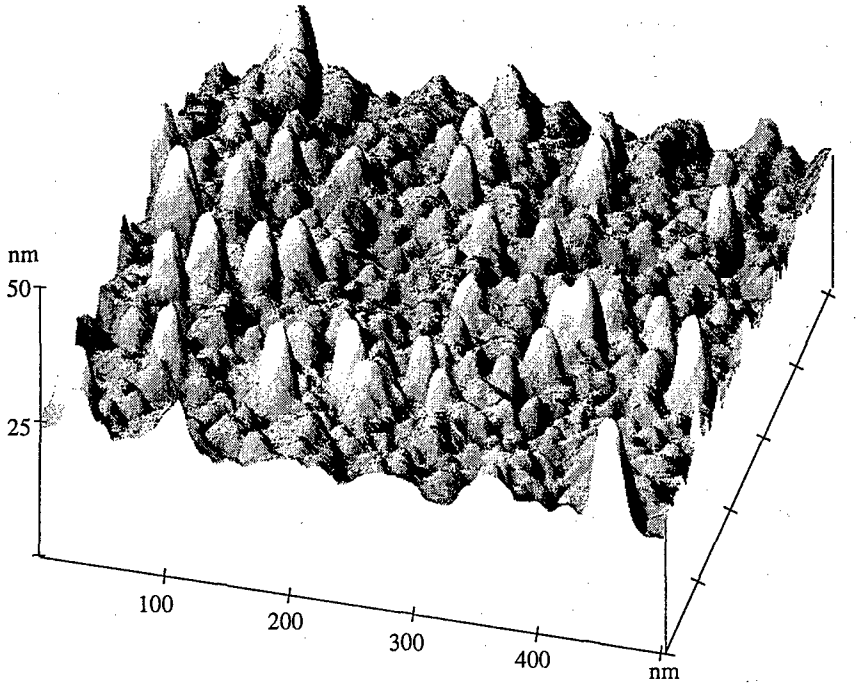

Fig. 2. AFM image of fabricated monolayer.

the end radius $\approx$ 40 nm show that the amplitude of the surface modulation is not more the 1 nm and characteristic lateral size of surface inhomogenity is about 40 nm. Using of sharper tip with the end radius $r \approx 10$ nm gives the surface modulation depth 5 nm and the size of surface inhomogenity 15 nm (Fig. 2). The results of both AFM measurements can be explained taking into account that the tip is in contact simultaneously with several closely packed granules and assuming the mean granule diameter 8 nm, which is consistent with SEM observation.

Measurements of the film thickness were done by DEKTAK profilometer. First, the strips of granulated film were formed on the substrate surface by lift-off technique. Then, to increase the structure rigidity the structure was covered by the thin SiO_2 layer. Three different samples were fabricated, keeping the laser beam intensity close to I_{cr} and varying the time of deposition: (1) 3 minutes, (2) 3 minutes deposition—30 minutes interval, four times repeated for the total deposition of 12 min., and (3) continuous deposition during 12 minutes. The measured thickness of the first film is $H_1 > 8$ nm, the second film has the thickness $H_2 > 20$ nm, and the third film thickness is $H_3 > 19$ nm. Noting that the granule size is typically 8 nm, the thickness of the first film corresponds to one monolayer of granules. The data on the second film thickness can be understood if we propose that the film consists of four layers of granules, closely packed so that in each layer the gap between the neighbouring granules is about $\delta x > 1$ nm. Comparing the data on the second and the third films one can conclude that the film thickness depends only on the total time of deposition.

The information about the chemical composition of the granulated films was obtained by using XPS measurements of monolayer films. Analysis of the photoelectron spectra shows that the film consist mainly of the copper and the oxygen. The fraction of oxygen measured

in as-made films (free air oxidized) is 16%, whereas measurements of the films pre-etched by the Ar+ ions (0.5 nm removed) give the oxygen content 10%. It should be noted that oxidized thin film can contain only Cu_2O oxide because $Cu_2 \rightarrow CuO$ reaction is possible only in the oxide layer with the thickness exceeding 250 nm [4]. To estimate the thickness of the Cu_2O layer we assumed that spherical granules are oxidized homogeneously from the surface. In this case the oxygen content 16% corresponds to the thickness of Cu_2O spherical layer $dR > 0.8$ nm. Removing 0.5 nm of the material from the upper part of the granules by surface etching results in reducing of the oxygen percentage. The experimental value of oxygen content 10% is in a good agreement with the estimation based on the assumption of homogeneous surface oxidation.

Summing up, the granulated Cu films fabricated by laser ablation consists of the monodisperse spherical Cu granules, 6 nm in diameter, covered by 0.8 nm thick Cu_2O layer. Each monolayer of such granules is closely packed. The gap between the neighbour granules depends on the deposited mass of vaporised Cu and is controlled by the laser beam intensity. This distance increases from $dx > 1$ nm for $I > I_{cr}$ up to $dx > 4$ nm for $I > 2I_{cr}$. Due to the possibility of close control of structure parameters such films are of interest for the study of transport properties of low dimensional nanostructures.

This work was supported in part by RFBR grant No 98-02-18210, the Program of the Ministry of Science of RF "Physics of Solid-State Nanostructures" grants Nos 97-2014, 97-1035, State Program "Micro- and Nanoelectronic Technology" grant 151/57/1.

References

[1] E. Bar-Sadeh, Y. Goldstein, C. Zhang, H. Deng, B. Abeles and O. Millo, *Phys. Rev.* **B50**, 8961 (1994).

[2] S. A. Gurevich, V. M. Kouznetsov, V. M. Kozhevin, D. A. Javsin, D. A. Zakheim, V. V. Khorenko and I. V. Rozhansky, 6th International Symposium *Nanosructures: Physics and Technolody*, St. Petersburg, Russia, p. 344, 1998.

[3] A. I. Grigor'ev, S. O. Shiryaeva, S. S. Verbitskii and J. Coll, *Interface Sci.* **146**, 137 (1990).

[4] B. V. Nekrasov, *Basics of General Chemistry*, Moscow, Vol. 3, p. 50, 1965.

7th Int. Symp. "Nanostructures: Physics and Technology"
St Petersburg, Russia, June 14–18, 1999

Three-dimensional (3D) arrays of silicon nanosize elements in the void sublattice of artificial opals

V. N. Bogomolov†, N. A. Feoktistov†, V. G. Golubev†, J. L. Hutchison‡, *D. A. Kurdyukov*†, A. B. Pevtsov†, J. Sloan‡ and L. M. Sorokin†
† Ioffe Physico-Technical Institute, St Petersburg, Russia
‡ Department of Materials, Oxford University, Parks Road, Oxford OX1 3PH, UK

Abstract. Silicon is now the most important material in modern solid state electronics. Regular systems of silicon nanoclusters containing up to 10^{14} cm^{-3} elements have been fabricated in a sublattice of opal voids. Structural studies of samples by TEM, HREM and Raman measurements were carried out. The regular lattices of Pt-Si junctions were obtained and their current-voltage characteristics (CVC) were investigated.

Introduction

Contemporary solid-state electronics is based on planar technology. Transition to 3D systems of semiconductor devices is necessary for futher increase of the volumetric density of elements. By using 3D dielectric matrices similar to opal, it may be possible to obtain three-dimensional ensembles of semiconductor nanodevices with density of elements as high as 10^{14} cm^{-3}.

1 Experimental

To fabricate semiconductor nanocomposites we used 'monocrystals' of synthetic opals having optically perfect structure [1]. The opals consist of 250 nm diameter close packed amorphous silica spheres and have regular sublattice of voids (45–90 nm) up to 26% accessible to filling by other substances [2].

To incorporate silicon into opal samples the thermal CVD technique was used [3]. The CVD-reactor consisted of a quartz tube with an external heater, through which a gas mixture of SiH_4 (5%) and Ar was passed. An opal plate was placed perpendicularly to gas flow. The reactor design excluded of a gas flow around a sample. As a result of silane thermal decomposition a silicon film was deposited on the inner surface of opal cavities. The conditions of decomposition were isothermal.

To increase the volume fraction of nanocrystalline silicon phase the samples were annealed at $T = 800$°C and pressure about 1 Torr.

The silicon structure was determined by TEM, HREM and Raman measurements. Electron microscopes JEM4000EXII and JEM2010EX equipped with EDX attachment for element analysis in the object region with size 3–5 nm were used. The microstructure images both in diffraction contrast and high resolution modes were taken.

The sample intended for structure analyses was grinded on abrasive paper with the grain size 5 μm up to thickness 70–80 μm. Plates with the linear sizes no more than 3 mm (diameter of a sample holder) were cut out. Further thinning was carried out by Ar^+-ion milling up to thickness, transparent for electrons.

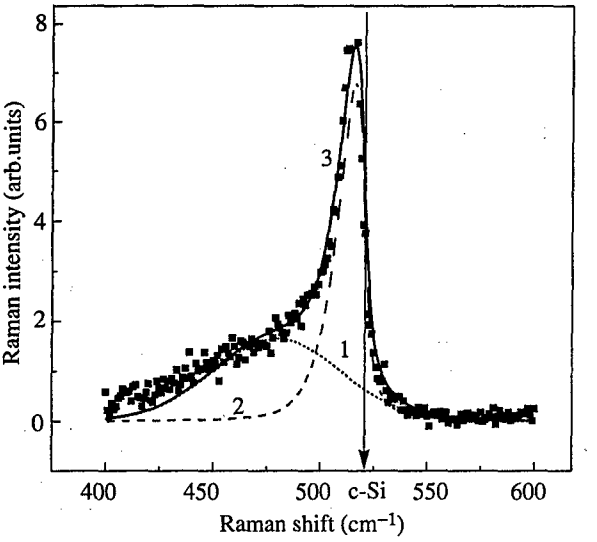

Fig. 1. Raman spectrum of a nanocomposite 'opal-silicon'. 1—'amorphous component' of a spectrum, 2—'nanocrystalline component', 3—'total' spectrum. The phonon frequency corresponding to c-Si is marked.

The Raman measurements were carried out in the backscattering geometry. The spectral resolution was 5 cm^{-1} and the scanning accuracy was about 1 cm^{-1}. The spectra were excited by the 4888 Å line of argon-ion laser.

The samples were filled with platinum to fabricate metal-semiconductor-metal (MSM) junctions. An opal was impregnated with a solution of platinum tetrachloride in ethanol, and then $PtCl_4$ was reduced with hydrogen.

2 Results and discussion

Figure 1 shows the Raman spectrum of an annealed sample. The narrow peak, associated with Raman-active TO phonon mode of crystalline silicon is seen to shift to the low frequency range as compared with a bulk silicon.

Such a transformation of the spectrum testifies to formation of a nanocrystalline phase of silicon [4]. Analysis of Raman spectra within the framework of the model of a strong spatial confinement of optical phonons has allowed to estimate both the average size $L \approx$ 4 nm and volume fraction $\chi = 52\%$ of crystallites in amorphous-nanocrystalline silicon system [5, 6, 7].

TEM study of unannealed sample have shown, that as-deposited silicon film was amorphous with rarely distibuted Si crystallites with sizes about 3–5 nm.

In annealed samples silica spheres are covered uniformly with a 20–25 nm-thick layer of mixed amorphous-nanocrystalline silicon (Fig. 2(a), diffraction contrast mode). The composition was specified by EDX spectrum. Structure state of Si was determined by microdiffraction patterns taken for the large crystals which found to be point patterns with orientation (110).

It is seen (Fig. 2(a)), that Si film on a sphere surface has more dark contrast than sphere itself. The black areas represent the separate grains of nanocrystalline silicon of various

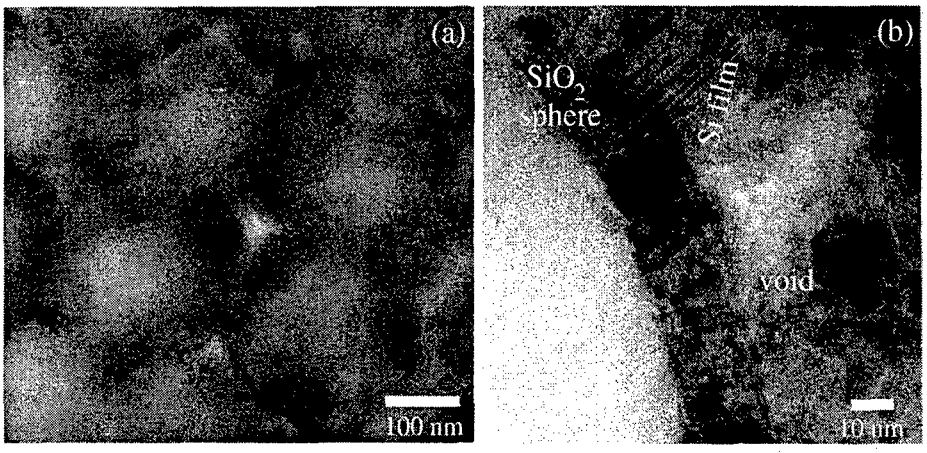

Fig. 2. (a) TEM image of annealed sample 'opal-Si'. (b) HREM image of silicon film on the surface of SiO_2 sphere.

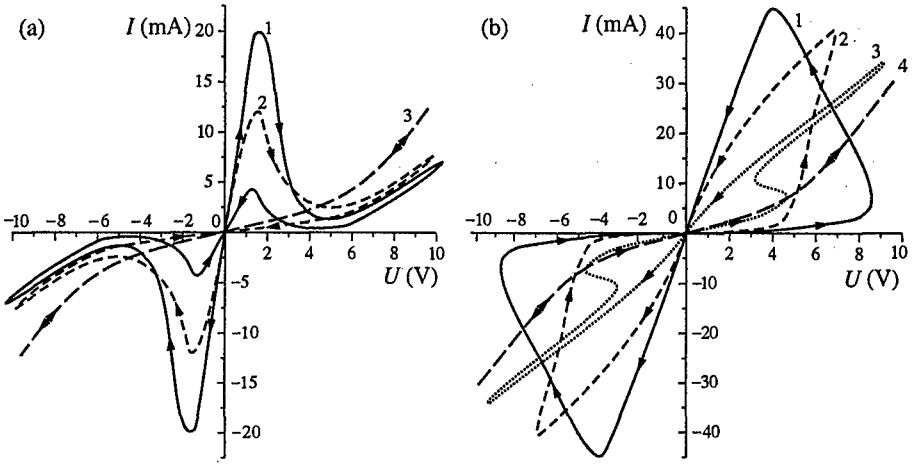

Fig. 3. N-shaped (a) (1—0.1 Hz, 2—100 Hz, 3—10 kHz) and N-S-shaped (b) (1—0.01 Hz, 2—1 Hz, 3—100 Hz, 4—10 kHz) CVC of nanocomposites 'opal-Si-Pt' with different fill factors.

size which are in exact Bragg reflection.

HREM silicon film image (Fig. 2(b)) shows, that the separate grains have single crystal structure over all thickness of the silicon layer. The large grains have hexagon shape. The interface 'Si crystal layer–amorphous silica sphere' is well seen.

In most cases on a silicon film surface there is an amorphous layer, which appears to be silicon dioxide arising as a result of oxidation of the silicon film surface due to surrounding. Its thickness reaches about one thirds of Si film thickness.

The average crystallite sizes are varied from 4 to 10 nm. It is to be noted, that as the thickness of silicon layer exceeds $\approx$ 25 nm and becomes compared with the void size, the cavities in an opal are filled by silicon not completely. Figure 2 illustrates this fact as well.

The empty volume is accessible to fill by other substances. For example, platinum

clusters can be impregnaged into the rest volume. Figure 3(a,b) shows current-voltage characteristics of the nanocomposites 'opal-Si-Pt'. The type of CVC depends on fill factor of Pt. That behaviour of CVC is defined by redistribution of carriers on the Pt-Si interface.

3 Conclusion

It is shown, that the thermal CVD technique allows to deposit the 20–25 nm-thick uniform silicon film on the inner surface of void sublattice of artificial opals. It is established that the thickness of the silicon film and degree of filling can be simple varied by both the duration of the thermal CVD process and the thickness of the opal sample. It, in turn, allows to create 3D multilayer planar structures. 3D arrays of Pt-Si junctions were designed. The structures fabricated is found to have S- or N-like CVC.

Acknowledgements

This work was supported by the Russian R&D Program 'Nanostructures' under Grant No 97-2016 and RFBR Grant No 98-02-17350.

References

[1] V. N. Bogomolov, D. A. Kurdyukov, A. V. Prokofiev and S. M. Samoilovich, *JETP Lett.* **63**, 496 (1996).
[2] V. N. Bogomolov and T. M. Pavlova, *Semiconductors* **29**, 826 (1995).
[3] V. N. Bogomoliov, V. G. Golubev, N. F. Kartenko, D. A. Kurdyukov, A. B. Pevtsov, A. V. Prokofiev, V. V. Ratnikov, N. A. Feoktistov and N. V. Sharenkova. *Techn. Phys. Lett.* **24**, 326 (1998).
[4] Z. Igbal and Veprek, *J. Phys. C: Solid State Phys.* **15**, 377 (1992).
[5] L. H. Campbell and P. M. Fauchet, *Solid State Commun.* **58**, 739 (1986).
[6] A. B. Pevtsov, V. Yu. Davydov, N. A. Feoktistov and V. G. Karpov, *Phys. Rev.* **B52**, 955 (1995).
[7] V. G. Golubev, V. Yu. Davydov, A. B. Pevtsov and N. A. Feoktistov, *Phys. Solid State* **38**, 1197 (1997).

7th Int. Symp. "Nanostructures: Physics and Technology"
St Petersburg, Russia, June 14–18, 1999

The preparation of ordered colloidal magnetic particles by magnetophoretic deposition

Andrei Susha†‡, Dangsheng Su¶ and *Michael Giersig*‡
† Permanently address: Physico-Chemical Research Institute,
Belarusian State University Leningradskaya 14, 220080 Minsk, Belarus
¶ Humboldt Universität zu Berlin, Institute of Physics,
Invalidenstraße 110, 10115 Berlin, Germany
‡ Hahn-Meitner-Institut, Glienicker Straße 100, 14109 Berlin, Germany

Abstract. The preparation of ordered two-dimensional (2-D) magnetic nanoparticles using a magnetophoretic technique is reported. The quality of the ordering can be readily observed by electron microscope and the lattice constants determined by electron diffraction. Using image processing, it can be shown that the cobalt particles condense into hexagonal close packing and also that the crystallographic axes of the individual cobalt particles are randomly oriented. The equilibrium distance between the particles corresponds approximately to the size of the absorbed stabilisers and the strength of the magnetic field. The method is of general interest as a means of preparing monolayer films of nanosized magnetic particles such as cobalt or iron oxide.

1 Results and discussion

Cobalt nanoparticles were prepared by thermolysis of dicobaltoctacarbonyls in an organic carrier at 110 °C in presence of two different surfactants. The surfactants used were sodium-bis 2-(ethyl-hexyl) sulfosuccinate (Co I) and oleoylsarcosine (Co II). As a result ferrofluids (FF) of saturation magnetization of at least 20 mT were obtained. After the reaction non-stabilised particles were separated in an external magnetic field. After that, the stable ferrofluid was diluted with toluene in a ratio of 1:100. The composition of the particles (core and shell) was analysed by chemical and physical methods. The results corresponded to the magnetic properties of the core. Furthermore, magnetite particles were prepared by co-precipitation. The particles were modified by an inner surfactant layer of lauric acid and an outer layer of an ethoxylated alcohol. Aqueous base FF of a saturation magnetization by 100 mT were obtained. For observations all FF were highly diluted with the carrier.

Observation by high resolution transmission electron microscopy (HRTEM) (Fig. 1 and Fig. 2) showed Co particles well isolated and regularly dispersed in the surfactant with a narrow size distribution of about 8 nm ± 6% (Co I) and 12 nm ± 5% (Co II) in diameter. The sizes of the particles deduced from the analysis of the magnetic susceptibilities and magnetisation curves are consistent with those measured by HRTEM.

The distribution of the particle magnetic moments in ferrofluids reconstructed from the magnetization curves is in a good agreement with those computed from the particle sizes on HRTEM-images.

We have used the small nanoparticles for the creation of two dimensional arrays. The magnetic particles were ordered by drying a drop (5 μL) on a carbon-coated grid in the presence of an external magnetic field of ca. 0.8 T, which was created by placing the grid between two magnets.

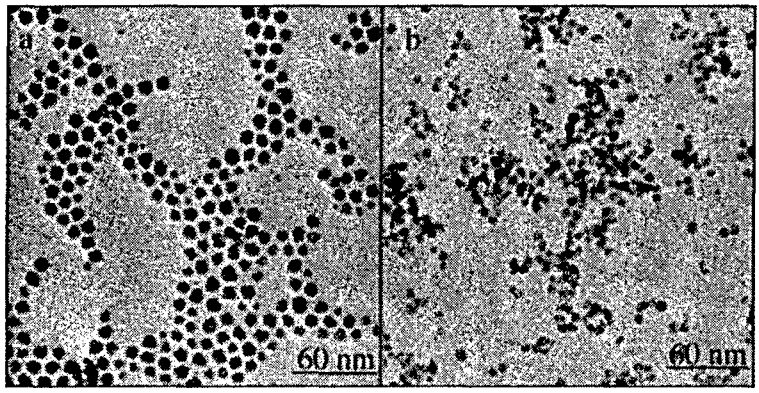

Fig. 1. Low magnification TEM micrograph of small Co particles in different solutions: (a) Co I; (b) Co II.

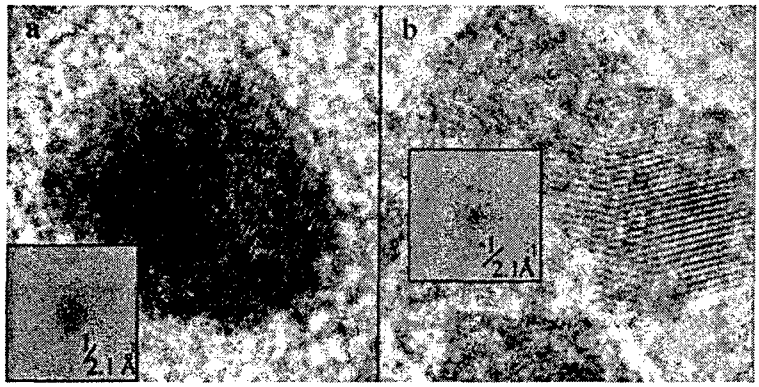

Fig. 2. HRTEM micrograph of two Co particles from the pictures Fig. 1 and Fig. 2 respectively.

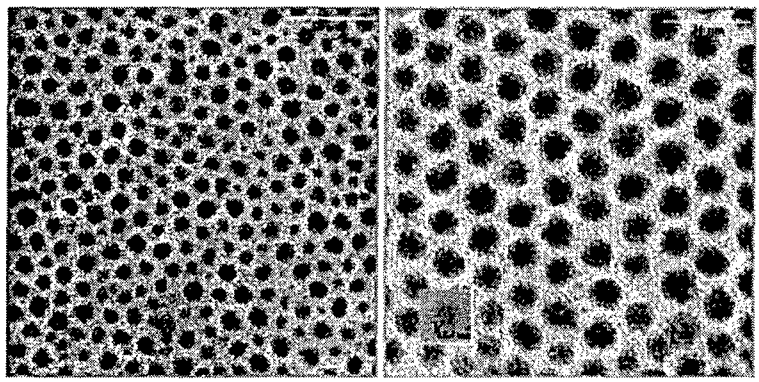

Fig. 3. TEM micrograph of 2-D ordering of Co nanoparticles by using an external magnetic field.

Figure 3 shows two TEM images of 2-D orderd Co particles at different magnetic field strengths.

References

[1] G. Schmid Ed., *Clusters and Colloids, from Theory to Application*, V.C.H. Weinheim, 1994.
[2] K. A. Eason, K. J. Klabunde, C. M. Sorensen and G. C. Hadjipanayis, *Polyhedron* **13**, 1197 (1995).

7th Int. Symp. "Nanostructures: Physics and Technology"
St Petersburg, Russia, June 14–18, 1999

Structure of stacked InAs quantum dots in a Si matrix: HRTEM experimental results and modeling

N. D. Zakharov†, P. Werner†, V. M. Ustinov‡, G. E. Cirlin‡, O. V. Smolski‡, D. V. Denisov‡, Zh. I. Alferov‡, N. N. Ledentsov§, R. Heitz§ and D. Bimberg§

† Max-Planck Institute of Microstructure Physics, Halle/Saale, Germany
‡ Ioffe Physico-Technical Institute, St Petersburg, Russia
§ Technical University of Berlin, Germany

Abstract. A quantum dot structure containing two layers of small coherent InAs clusters embedded into Si single crystal matrix was grown by MBE. The structure of these clusters was investigated by high resolution transmission electron microscopy. The quality of the grown structure severely depends on the substrate temperature, growth sequence, and the geometrical parameters of the sample. Investigation demonstrate that Si crystal can incorporate only a limited volume of the deposited InAs in a form of coherent clusters.

Introduction

There is a strong interest in combining unique properties and flexibility of III–V materials with silicon technology, which is ideally suited for microelectronics. Until now most of researchers are concentrated on growth of thick layers of III–V materials on silicon [1]. More recently, the idea of using of ultra-small coherent III–V narrow gap crystallites (quantum dots) coherently inserted in the silicon matrix has been proposed [2]. Scanning tunnelling microscopy studies demonstrates that small InAs quantum dots (QDs) can be, indeed, formed on the Si(100) surface, and, after overgrowth with Si, these QDs demonstrate intense and broad luminescence line at about 1.3 μm at 10 K [3]. Despite of the high importance of these spectroscopic results no direct proof of the coherent nature of the InAs insertions in a silicon matrix was given.

The aim of this paper is to demonstrate the possibility to characterise InAs insertions in a Si matrix using high resolution transmission electron microscopy (HRTEM), to prove the coherent nature of InAs inclusions, to compare experimentally derived and simulated HRTEM images to draw conclusions on the QD size, and to demonstrate the possibility of growth of coherent multiple InAs insertions in a Si matrix for applications in micro- and optoelectronics.

Experimental

The samples were grown using a molecular beam epitaxy (MBE) on Si (100) substrates. The variable parameters were the substrate temperature during growth, the InAs growth rate, the average thickness of the insertion and the arsenic pressure during growth. Two samples (A and B) were mostly investigated in this work (Fig. 1). The crystalline quality of the structure and the composition of the grown layers were investigated by HRTEM and the energy-dispersive X-ray spectroscopy (EDX). Computer simulations of HRTEM images were performed by using MacTempas program package [4].

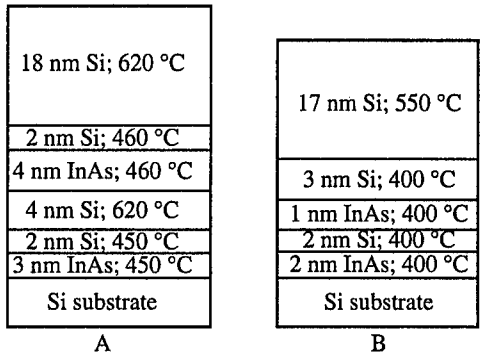

Fig. 1. Sequence and thickness of the layers in two MBE grown structures: A and B.

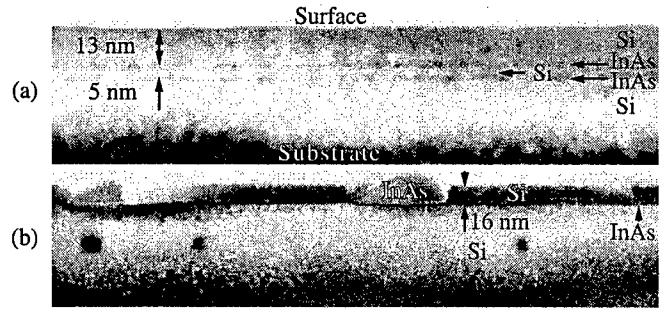

Fig. 2. Cross section TEM images of the specimen A (a) and B (b). Two layers of InAs clusters are marked by arrows in (a).

Results

A cross section TEM image of sample A taken at low magnification is shown in Fig. 2(a). Two InAs insertions exhibiting dark contrast are marked by arrows. One can also notice that the effective thickness of the InAs insertions is well below 4 nm, indicating that only a small part of the deposited InAs was incorporated into the structure after Si overgrowth. The reason for this is the increase of the substrate temperature after the InAs deposition and overgrowth of ultra-thin (2 nm) Si layer. We found this step to be important to keep the high quality of the structure, because part of the excess of deposited InAs is effectively evaporated at 620 °C. In the case of the sample B, where the InAs and Si deposition occurred at lower temperature (Fig. 2), the most of InAs is concentrated in large dislocated clusters. In this case it is clearly seen that the Si overgrowth does not take place in the vicinity of the InAs clusters. Moreover, only the lower InAs layer shows a coherently incorporated InAs clusters. At the surface specimen contains a high density of shallow pits (16 nm deep) partly occupied by large InAs precipitates. Plan-view TEM images of these precipitates demonstrate a square-type Moir^ pattern with a spacing corresponding to the misfit between Si and InAs. EDX spectra taken from these precipitates in the transmission mode demonstrate pronounced In and As peaks. To analyse the lattice structure and size of the InAs clusters incorporated in the Si matrix in sample A, cross-section samples have been investigated by HRTEM (Fig. 3). Contrast features having a size of about 3 nm in diameter and laterally separated from each other by 0.5-1 nm can be clearly seen (see arrows in Fig. 3). To understand the origin of these contrast features computer simulations

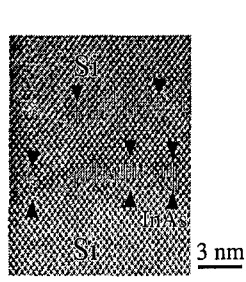

Fig. 3. Cross section image of the sample A taken at high resolution. InAs clusters are marked by arrows.

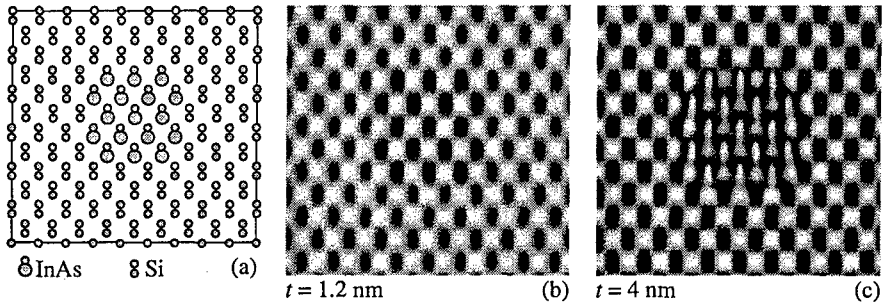

Fig. 4. Atomic model of the InAs cluster in a Si matrix (a) and two high resolution images simulated for crystallite size of 1.2 (b) and 4 nm (c).

of the small InAs cluster in Si matrix have been done. The crystallographic model of the InAs cluster used for the calculations is shown in Fig. 4(a). The model represents the case, when Si atoms are substituted with InAs molecules, reducing the symmetry of the matrix. The HREM simulations are carried out for imaging conditions close to the experimental ones (Scherzer defocus) and for different foil thickness (Fig. 4(b,c)). For the small thickness (t = 1.2 nm) the contrast is fairly low, as it may be expected, while in the case of thicker crystal (t = 4 nm) the theoretical image demonstrates rather good agreement with experimental one (Fig. 3).

Discussion

To summarise the results one can conclude that layers of coherent InAs insertions can be successfully fabricated in a single-crystalline silicon matrix. Quality of the grown structure severely depends on the substrate temperature, growth sequence, and geometrical parameters of the sample. In addition to STM results, one can also conclude that the Si crystal lattice can only adopt a limited volume of the deposited InAs in a form of coherent clusters. If the deposited InAs layer is too thick, large dislocated InAs precipitates are formed accumulating excess of InAs during Si overgrowth. We also note that the total area occupied by the shallow pits (see Fig. 2(b)) was about 2 times lower in sample A than in B. Besides, these pits in sample A are almost empty, while in the sample B they always contain relaxed InAs clusters. Thus, high temperature step in Si overgrowth is essential to evaporate the excess amount of InAs.

From the above considerations, and taking into account the STM data [3] it appears that the average thickness of deposited InAs, the thickness of the Si spacer between the InAs insertions, the substrate temperature during the InAs deposition and Si overgrowth should

be optimised to obtain high quality structures with multiple InAs insertions in Si.

References

[1] S. F. Fang, K. Adomi, S. Iyer, H. Morkož, H. Zabel, C. Choi and N. Otsuka, *J. Appl. Phys.* **68**, R31-R58 (1990).

[2] N. N. Ledentsov, *Proceedings of the 23rd International Conference on the Physics of Semiconductors*, Berlin, Germany, July 21–26, 1996, Ed. by M. Scheffler and R. Zimmermann (World Scientific, Singapoure, 1996), v. 1, p. 19.

[3] G. E. Cirlin, V. G. Dubrovskii, V. N. Petrov, N. K. Polyakov, N. P. Korneeva, V. N. Demidov, A. O. Golubok, S. A. Masalov, D. V. Kurochkin, O. M. Gorbenko, N. I. Komyak, V. M. Ustinov, A. Yu. Egorov, A. R. Kovsh, M. V. Maximov, A. F. Tsatsul'nikov, B. V. Volovik, A. E. Zhukov, P. S. Kop'ev, Zh. I. Alferov, N. N. Ledentsov, M. Grundmann and D. Bimberg, *Semicond. Science and Technol.***13**, 1262 (1998).

[4] R. Kilaas, *Proc. 45th Annual EMSA Meeting*, ed. G. W. Bailey. San Francisco Press, San Francisco 1987, p. 66.

7th Int. Symp. "Nanostructures: Physics and Technology"
St Petersburg, Russia, June 14–18, 1999

Cross-sectional atomic force microscopy of ZnSe-based laser diodes

A. V. Ankudinov, A. N. Titkov, T. V. Shubina, S. V. Ivanov, P. S. Kop'ev, H.-J. Lugauer†, A. Waag† and G. Landwehr†
Ioffe Physico-Technical Institute, St Petersburg, Russia
† Physical Institute, University of Würzburg, 97074 Würzburg, Germany

Abstract. Cleaved facets of ZnBeMgSe-based lasers with different design of active region have been studied by means of the cross-sectional atomic force and lateral (friction) force microscopy (AFM and LFM). A difference in friction coefficients has been successfully exploited to image basic layers of the laser diodes. The Be-containing cladding layers and the waveguide area are revealed as regions of lower friction as compared to a GaAs substrate. Elastic strains accumulated at the layer boundaries are displayed via nanometer-high steps and undulations forming in the morphology of the cleaved facets. A remarkable reduction of the elastic strain in the active region containing a (Zn, Cd)Se quantum well has been found for the laser with the specially designed alternately-strained superlattice in the waveguide.

Introduction

The cleavage of an ideally perfect crystal is expected to be atomically plain and to exhibit no structure [1]. Contrary to that an epitaxial semiconductor heterostructure is obviously not the ideal crystal and usually consists of alternatively strained heterolayers. Recent cross-sectional atomic force microscopy (AFM) studies of such heterostructures have revealed an existence on cleaved facets of the nanometer-high topographic singularities placed along the interfaces [2–4]. A possible mechanism of the relief formation on the cleavages of strain compensated heterostructures is an elastic relaxation of the surface due to strain variations in underlaying layers [2]. For strained heterostructures another scenario was also proposed, including cleavage crack deviation at the interface between two materials with different fracture toughness due to occurence of a plastic deformation by the glide of misfit dislocations [3]. Thus, AFM topography data may be used to extract a valuable information on the structural properties of the constituent layers of the heterostructure. The AFM data may be completed if lateral force microscopy (LFM) mode measuring frictional forces is used. The friction force may vary between different materials and utilization of the LFM mode permit one to distinquish different semiconductor layers on cleaved facets [3, 4].

We applied cross-sectional AFM for the characterization of the cleavages of ZnSe-based laser diode heterostructures, which still remain the main candidates for fabrication of a commercial injection laser for the green (490–550 nm) spectral region [5]. However, for the successful development of those devices it is still necessary to increase an onset energy of appearance and development of the extended defects in ZnSe-based materials and to suppress their propagation and multiplication in a laser device [6]. A promising approach to solve these problems is to employ Be-containing compounds. The beryllium-based chalcogenides (e.g. BeMgZnSe) are expected to increase significantly the covalent component of the bond, hence "hardening" the material [7, 8]. In addition, an efficient gradual strain redistribution in the active region of the II–VI lasers is proposed by incorporation of

specially designed alternately-strained superlattice (AS SL) waveguide, lattice-matched to a GaAs substrate [9].

Experimental results and discussion

We have investigated three BeMgZnSe/ZnCdSe-based laser heterostructures with different active region design. The first one of a conventional type involves a 0.2 μm $Be_{0.03}Zn_{0.97}Se$ bulk waveguide centered with a 4 nm–$Zn_{0.63}Cd_{0.37}Se$ quantum well (QW) and surrounded by 1 μm thick widebandgap n- and p-BeMgZnSe cladding layers doped with iodine and nitrogen, respectively. In the second structure the bulk waveguide is exchanged by a (1 nm-$Be_{0.05}Zn_{0.95}Se$/1.5 nm-ZnSe)$_{82}$ AS SL lattice-matched to GaAs as a whole. Contrary to the second structure, the third one contains a 2.8 ML-CdSe/10 nm-ZnSe fractional monolayer (FM) nanostructure instead of the conventional QW. The growth conditions and composition control for the structures have been reported elsewhere [7, 8, 10, 11].

The cross-sections of laser heterostructures were prepared by cleavage in air. The samples thinned to approximately 200 μm were placed on the polished brass plate face down. The cleavage was initiated by pressing the cutter on the GaAs substrate along the ⟨110⟩ direction. The freshly cleaved samples were studied in air by AFM (P-4 SPM, NT-MDT) operating in contact mode. Commercial Si triangular cantilevers were used with a normal elastic constant of 0.68 N/m and with the radius of curvature of the tip less than 40 nm. LFM images were obtained when scanning in the direction nearly perpendicular to the longest axis of the cantilever. To minimize the cross-talk between normal and lateral deflections of the cantilever a low scanning speed of about 1 μm/s was employed.

Fig. 1 presents cross–sectional AFM data and a schematic band energy diagram for the laser heterostructure with the CdSe/ZnSe FM active region. AFM topography image of laser cleavage presented in Fig. 1(b) reveals two singularities on the cleavage surface: (i) 0.2 nm-high ridge and (ii) 0.5 nm-high step, running parallel to the heterostructure interfaces identified by their distances from the top cleavage edge (not included in the image). The ridge is placed at the center of the waveguide area (W), while the step coincides with the II–VI/GaAs interface. The linear dimensions of the ridge and step may be better seen in the AFM profile (Fig. 1(c) taken along A–A line in the AFM topography image.

The LFM image taken simultaneously with AFM topography from the same cleavage area is shown in Fig. 1(d). Here the darker grey tone corresponds to smaller lateral deflecton of the cantilever and, hence, to smaller friction force. The observed contrast arises mainly from the lateral variations in friction between the tip and underlying layers, which was confirmed by a reversal of the image grey contrast when the scanning direction was reversed [12]. The friction force is characterized by the value of the current arising in the deflection detector of the SPM device when cantilever twists due to lateral forces. Variation of the friction force (in the units of the deflection detector current) in the direction normal to the interfaces is shown in Fig. 1(e). The presented plot is averaged over the whole studied cleavage area. The mean friction force on GaAs is taken as a zero level. The detectable differences in friction, when crossing the laser interfaces, are found, which provides explicit visualization of the basic layers of the laser structure in good agreement with the laser diagram in Fig. 1(a). Similar surface morphology and friction force behaviour have been found for the cleavages of the rest two laser structures. However, the conventional type laser demonstrates a much higher step of 1.7 nm at the QW position instead of the low 0.2 nm ridge.

Before discussing the obtained topography data, it is interesting to note that the friction force on the II–VI layers, demonstrated by the cleavages of all the studied laser structures, is

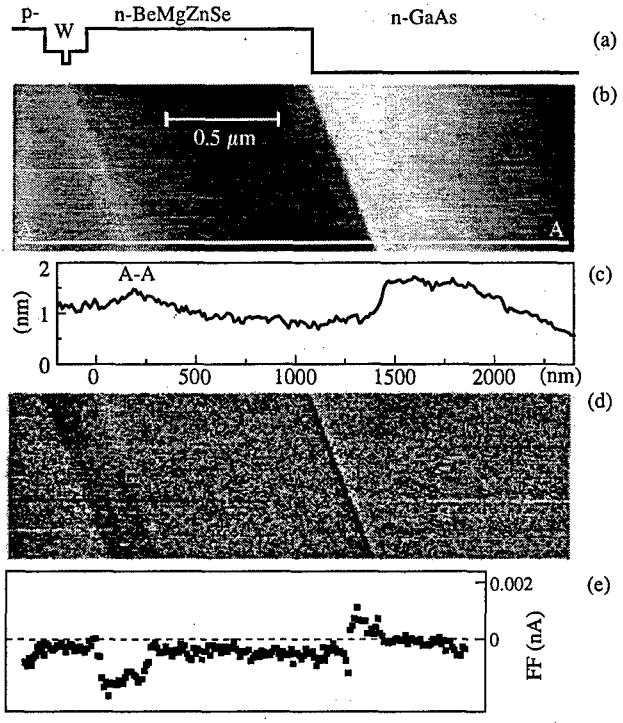

Fig. 1. (*a*) the conduction band energy diagram for the laser structure of the third type; (*b*) AFM topography image of laser cleavage; (*c*) the AFM profile taken along A–A line in the AFM topography image; (*d*) the LFM image taken in parallel with AFM topography image from the same cleavage area; (*e*) graph of the averaged fricition force signal across the interfaces.

smaller than that on the GaAs substrate. In general, one could expect the contrary relation, since ZnSe is considerably softer than GaAs [3]. One should propably take into account different structural properties of oxides formed at ZnSe and GaAs, which may enlarge or even reverse somehow the contrast. This broblem certainly needs a separate study. However, the comparative study of S-contained and Be-contained II–VI heterostructures shows that the Be incroporation, even at the level of several percents, increases the hardness of the II–VI epilayers [13]. The additional confirmation is provided by Fig. 1(d) and 1(e), where the area of ZnBeSe waveguide is characterized by the lowest friction force. An introduction of softening Mg to the cladding layers enhances the friction on these layers, but the presence of the Be still remains the friction force lower than that at the GaAs substrate.

The character of singularities occuring on the cleavages of the laser stuctures allows one to elucidate directly the strain distribution in the active region of the structures. Two studied QW laser structures have nearly the same lattice mismatch 2% between the waveguides and 4 nm-QWs. On the other hand, a total energy of deformation related to the 2.6 ML CdSe insertion (7% of lattice mismatch) is of the order of that accumulated by the thicker QWs of the lower Cd content. For the laser of conventional type, the 1.7 nm high step has been found at the interface between waveguide and the QW. Earlier it was found that the step height increases with the mismatch value [3], and thus, with the total energy of deformation. The step may appear to reduce the elastic strains at the QW/waveguide interface in the case

when the release of strain energy is larger than an increase in free surface energy. For both laser structures with AS SL waveguide we did not found any high step, but only a small undulation in waveguide area of the cleavage. This observation leads us to the conclusion about a considerable reduction of the total energy of deformation in the active region due to redistribution or "smoothing" of the elastic strain over the whole waveguide. It means that AS SL play a special role of the strain redistributing spring. By the way, the resulting diminished strains in the waveguide region can initiate an expansion of the SL waveguide area over cleavage surface, which is revealed as the ridge in the AFM image in Fig. 1(b) and (c).

It is interesting to note that the height of the observed surface singularities did not change notably along the interfaces, but the singularity shape did. In the case of step, we observed an abrupt change in the step side orientation. A ridge structure could transform into a double ditch. We believe that these local transformations in the cleavage morphology are related to some structural defects at the interfaces.

Conclusion

Our work demonstrates possibilities of AFM and LFM studies of the heterostructure cleavages as a powerful alternatives to conventional epilayer thickness determination and strain detection techniques, like SEM and TEM.

The authors would like to thank A. K. Kryzhanovsky for writing a program of statistic processing of images. This work was supported in part by RFBR, the Program of the Ministry of Sciences of RF "Physics of Solid State Nanostructures" and the Volkswagenstiftung.

References

[1] J. Friedel, *Dislocations* Ch. 12, Cleavage, Pergamon Press Ltd. 1964.
[2] J. Chen, *et al. Appl. Phys. Lett.* **72**, 1727 (1998).
[3] G. Bratina, *et al. Phys. Rev. B* **52**, R8625 (1995).
[4] I. Suemune and M. Hoshiyama, *Jpn. J. Appl. Phys.* **33**, Part 1, 3748 (1994).
[5] E. Kato, *et al. Electron. Lett.* **34**, 282 (1998).
[6] A. Ishibashi, M Ukita and S. Tomita, ICPS23 (1996).
[7] A. Waag, *et al. Appl. Phys. Lett.* **70**, 1 (1997).
[8] A. Waag, *et al. J. Cryst. Growth* **184/185**, 1 (1998).
[9] S. V. Ivanov, *et al. Appl. Phys. Lett.* **73**, 2104 (1998).
[10] S. Uvanov, *et al. J. Cryst. Growth* **184/185**, 70 (1998).
[11] S. V. Ivanov, *et al. Appl. Phys. Lett.* **74**, 498 (1999).
[12] J. Ogletree, R.W. Carpick, M. Slameron, *Rev. Sci. Instr.* **67** (9), 3298 (1996).
[13] A.V. Ankudinov *et al.*, to be published elsewere.

7th Int. Symp. "Nanostructures: Physics and Technology"
St Petersburg, Russia, June 14–18, 1999

Low temperature scanning tunneling spectroscopy of different individual impurities on GaAs (110) surface and in subsurface layers

N. S. Maslova†, V. I. Panov†, V. V. Rakov†, *S. V. Savinov*†, A. Depuydt‡ and C. Van Haesendonck‡

† Chair of Quantum Radio Physics, Moscow State University, 119899 Moscow, Russia

‡ Laboratorium voor Vaste-Stoffysica en Magnetisme, Katholieke Universiteit Leuven, B-3001 Leuven, Belgium

In present work we would like to present the results of low temperature STM and STS investigations of (110) surface of GaAs monocrystals doped with impurities of different kind.

All the experiments were performed using home build low temperature STM with sample cleavage mechanism [1]. Monocrystal GaAs samples with different dopants were cleaved in situ after cooling down to liquid helium temperature therefore exposing clean (110) plane. In our experiments we have used GaAs crystals doped with Te and double doped (compensated) with Si and Zn. To the best of our knowledge STM investigation of double doped samples were performed for the first time.

The most striking observations can be summarized as following. In STM images donor impurities in GaAs such as Te and Si looks like rather weakly localized circular features with diameter approximately 4 nm (Figs. 1, 2). STM image of acceptor impurity, such as Zn, has more complicated structure with both both strongly and weakly localized parts

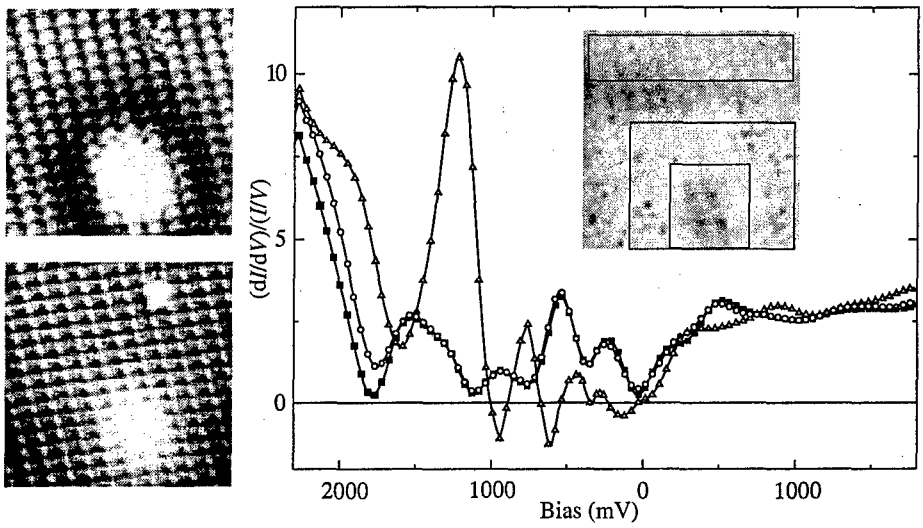

Fig. 1. Tunneling conductivity spectra near Te atom on (110) GaAs surface at temperature 4.2 K. Insert depicts the slice of 40 by 40 tunnelling conductivity curves array taken at −2 V. Each curve is the result of averaging over surface area which is marked by numbers. STM images of surface area 5.8×5.8 nm in size where spectroscopic data was acquired at sample bias: a) −1.5 V; a) +1 V.

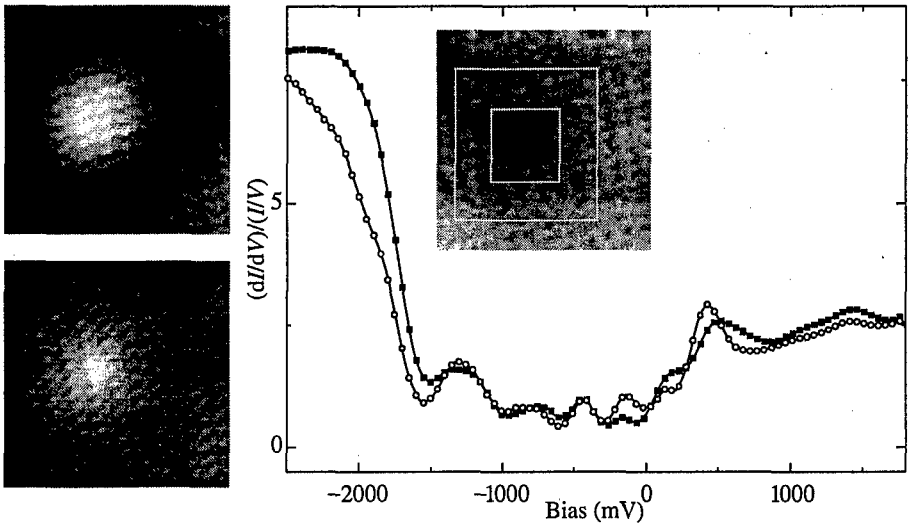

Fig. 2. Tunneling conductivity spectra near Si atom on (110) GaAs surface at temperature 4.2 K. Insert depicts the slice of 40 by 40 tunnelling conductivity curves array taken at −2 V. Each curve is the result of averaging over surface area which is marked by numbers. STM images of surface area 5.8×5.8 nm in size where spectroscopic data was acquired at sample bias: a) −1.5 V; a) +1 V.

and localization radius of about 2 nm (Fig. 3). For negative sample bias donor impurities are seen as a round hillocks surrounded by circular depression, which can be ascribe to the presence of charge density oscillations (Friedel oscillations) [2]. For positive sample bias the corrugation height is smaller and charge oscillations are absent. Donor impurities behave in the same way when they are located in the first or in up to fourth subsurface layer [3].

In general there is no direct evidence in which layer doping atom is located, at the same time symmetry arguments can be used. It was shown that Zn atoms on GaAs surface produces triangle like features. That is why we ascribe defect in Fig. 3 to the Zn atom located on the surface. In opposite to donor atoms, STM image of Zn acceptor is seen as round hollow feature at positive sample bias and as triangle like hillock surprisingly surrounded by round depression. At the same time STM image of Zn atom located below the surface strongly depends on the depth. In general case STM/STS images of impurities in GaAs matrix depends on the depth below the surface, i.e. the number of surface-subsurface layers the impurity is located in, which can be ascribed to different spatial structure of selfconsistent potential caused by induced impurity and/or STM tip charges [4].

Analyzing our results of STM/STS investigations of diferent doping atoms we found out some general similarities in behavior of tunneling conductivity spectra. STS images of all impurities show shift of gap edges as well as changes in semiconductor gap width. We ascribe the observed results to charge induced band bending caused by localized charges on the impurity and/or on the STM tip apex [5]. Tunneling conductivity curves measured above all types of impurities (despite of their positive/negative charge) reveal peaks inside the fundamental band gap in the range from −1.2 V to −1.5 V, near the valence band edge. We suppose that this behavior of tunneling conductivity is also connected with Coulomb interaction of localized charges which shifts impurity levels towards gap edge where tunneling current grows most rapidly with tunneling bias resulting in strong selfconsistent

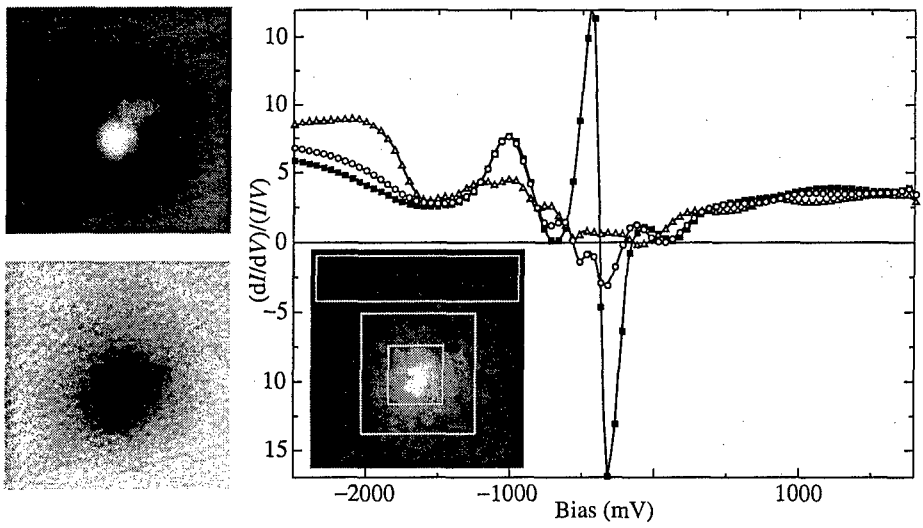

Fig. 3. Tunneling conductivity spectra near Zn atom on (110) GaAs surface at temperature 4.2 K. Insert depicts the slice of 40 by 40 tunnelling conductivity curves array taken at −2 V. Each curve is the result of averaging over surface area which is marked by numbers. STM images of surface area 5.8×5.8 nm in size where spectroscopic data was acquired at sample bias: a) −1.5 V; a) +1 V.

changes of localized charge.

For acceptor impurities there are as positive peaks as negative dips on tunneling conductivity curves in the range from −.2 V to −1 V. This is the bright demonstration that tunneling conductivity is not proportional to the sample local density of states in the presence of localized states. We suppose that charge effects can lead to non-monotone dependence of impurity level energies on applied bias voltage, which results in negative tunneling conductivity. Negative slope of $I-V$ curves can be caused by switching on and off of resonant channels connected with impurity localized states. The energy of such states depends on the value of induced charge, localized in tunneling junction area, which in turn depends on tunneling bias [6]. Thus changes in voltage, applied to the junction, can drive localized state to and out of resonance during $I-V$ dependence measurement.

Acknowledgements

The work in Moscow has been supported by the Russian Ministry of Research (Surface atomic Structures, grant 95-1.22; Nanostructures, grant 1-032) and the Russian Foundation of Basic Research (RFBR, grants 96-0219640a and 96-15-96420). The work at the KU Leuven has been supported by the Fund for Scientific Research–Flanders (FWO) as well as by the Flemish Concerted Action (GOA) and the Belgian Inter-University Attraction Poles (IUAP) research programs. The collaboration between Moscow and Leuven has been funded by the European Commission (INTAS, project 94-3562).

References

[1] S. I. Oreshkin, V. I. Panov, S. V. Savinov, S. I. Vasiliev, A. Depuydt and C. Van Haesendonck, *Pribory i Technica Experim.* **4**, 145 (1997).

[2] M. C. M. M. van der Wielen, A. J. A. van Roij and H. van Kempen, *Phys. Rev. Lett.* **76**, 1075 (1996).

[3] A. Depuydt and C. Van Haesendonck, N. S. Maslova, V. I. Panov, S. V. Savinov and P. I. Arseev, *Phys. Rev. B* (submitted).
[4] P. I. Arseev, N. S. Maslova and S. V. Savinov, *JETP Lett.* **68**, 239 (1998).
[5] N. S. Maslova, V. I. Panov, S. V. Savinov, A. Depuydt and C. Van Haesendonck, *JETP Lett.* **67**, 130 (1998).
[6] A. Depuydt, N. S. Maslova, V. I. Panov, V. V. Rakov, S. V. Savinov and C. Van Haesendonck, *Appl. Phys. A* **66**, 171 (1998).

7th Int. Symp. "Nanostructures: Physics and Technology"
St Petersburg, Russia, June 14–18, 1999

Second harmonic generation probing of MnAs/Si(111) heterostructures

A. G. Banshchikov, *A. V. Kimel*, V. V. Pavlov, R. V. Pisarev,
N. S. Sokolov and Th. Rasing†
Ioffe Physico-Technical Institute, St Petersburg, Russia
† Research Institute for Materials, KUN, 6525 ED Nijmegen, The Netherlands

Abstract. Ferromagnetic-semiconductor heterostructures MnAs/Si(111) have been studied by using the optical second harmonic generation and the linear magneto-optical Kerr effect. Magnetic and crystallographic contributions to the SHG are separated on the base of rotational anisotropy method. Magnetic hysteresis loops measured by the SHG and the Kerr effect exhibit different behavior due to a different sensitivity of two optical techniques to the interface, surface and bulk properties.

Introduction

Magneto-electronics based on new types of nanostructures is rapidly developing brunch of technique. Ferromagnetic-semiconductor heterostructures are a subject of intensive investigations due to their great potential for new optical and electronic devices, such as nonvolatile magnetic memory monolithically integrated with Si or GaAs in one chip, magneto-optical memory, magnetic sensors coupled with semiconductor circuits and spin-polarized transport devices [1]. For this kind of devices it is important to monitor the interface and bulk magnetic properties of the ferromagnetic films.

For centrosymmetric media the second harmonic generation (SHG) is only allowed in the electric-dipole approximation for surfaces and interfaces, where the space-inversion-symmetry operation is broken [2]. Thus SHG is expected to be sensitive to a few monolayers at surfaces and interfaces. It has been experimentally shown that the source of magnetization-induced SHG signal for Co films is bound to the interface region of less than 6 monolayers [3]. On the other hand, the linear magneto-optical Kerr effect (MOKE) is formed in the thickness range of the penetration depth of light $\alpha = \lambda/(4\pi k)$ [4], where λ is the wavelength of light and k is the absorption coefficient. We suggest that SHG and MOKE methods can provide complementary results due to their different probing regions.

The nonlinear optical polarization excited in a noncentrosymmetric magnetic medium can be written in the electric-dipole approximation as [5]

$$P_i^{2\omega} = \varepsilon_0 \chi_{ijk}^{(2)} E_j E_k + \varepsilon_0 \chi_{ijkl}^{(3)} E_j E_k M_l,$$

where E_j and E_k are the incident optical electric fields at the fundamental frequency ω and $\mathbf{M}$ is the spontaneous magnetization. The nonlinear tensors $\chi_{ijk}^{(2)}$ and $\chi_{ijkl}^{(3)}$ describe the crystallographic and magnetic parts of $\mathbf{P}^{2\omega}$, respectively. These tensors are complex in the absorption region of crystals, what allows interference between crystallographic and magnetic contributions to SHG.

In the paper we present results on the SHG and MOKE studies MnAs/Si(111) heterostructures.

1 Experiment and samples

Below the critical temperature $T_C = 45°$ C, MnAs has the hexagonal structure of NiAs-type (point group $6/mmm$) and ferromagnetic state with an "easy plane" type of magnetic anisotropy coinciding with the (0001) crystal plane. At T_C, a first order phase transition occurs to the paramagnetic structure of MnP-type having the point group mmm. Heterostructures CaF_2/MnAs/Si(111) have been grown by the molecular-beam-epitaxy method. After standard chemical cleaning, silicon substrates were loaded into the growth chamber and cleaned thermally at 1250° C in ultra high vacuum. This procedure provides atomically cleaned Si(111) surfaces with a 7×7 superstructure. The thickness of MnAs films was in the range of 12–400 nm. A cap layer of CaF_2 (thickness 4–12 nm) was used for protection. The crystalline quality of Si substrates and the growth of ferromagnetic films and cap layers was monitored *in situ* by reflection high energy electron diffraction. For the SHG and MOKE experiments, we used a Ti:sapphire laser, with 100 fs pulse width at 80 MHz repetition rate (see Ref. [5]). All experiments have been done in reflection at a wavelength of 800 nm and at an angle of incidence of 45°.

2 Results and discussion

In Fig. 1 the anisotropy of SHG in CaF_2(4 nm)/MnAs(35 nm)/Si(111) structure is shown for the two directions of **M** in the plane of incidence (longitudinal geometry) as a function of crystal rotation angle φ around the sample surface normal. Measurements have been done for the *P*-input polarization of the fundamental light and *S*- (Fig. 1(a)) and *P*- (Fig. 1(b)) output polarizations of the SH light. In case of the *PS* combination of polarizations the magnetic contribution to SHG survives and it is possible to separate it from the crystallographic one. The experimental data are well described by the equation $I^{2\omega} = [A\cos(3\varphi) + B]^2$, where A and B are the constants describing the anisotropic and isotropic contributions to the SHG, respectively. In case of *PS* combination of polarizations B depends linearly on M, but if the combination is *PP* then B is independent on M and is purely crystallographic. The best fit is shown by the solid line for $+M$ and by the dashed line for $-M$ in Fig. 1(a). The anisotropic contribution to the SHG arises partially from the MnAs/Si interface and the Si(111) surface characterized by the point group $3m$ (about 30% of Si surface was not covered by MnAs during deposition). For this polar group there are four independent components of $\chi^{(2)}_{ijk}$ ($xxx = -xyy = -yyx = -yxy$, $yyz = xxz = xzx = yzy$, $zxx = zyy$, zzz [6]). The isotropic magnetic contribution to SHG is most probably related to the CaF_2/MnAs magnetic interface. This interface dominates over MnAs/Si interface due to a strong absorption of the pump beam in the MnAs film ($k = 2.8$ at $\lambda = 800$ nm [7]).

Fig. 2 shows the rotational anisotropy of the SH *P*-polarized intensity for the CaF_2(8 nm)/MnAs(70 nm)/Si(111) structure for the *P*-polarized fundamental light. In this structure MnAs film is sufficiently thick to cancel the contribution from MnAs/Si interface. Thus in this case the SHG may arise only from CaF_2/MnAs interface. Possible polar group for this interface is $6mm$, therefore the SHG should exhibit an isotropic behavior. In the transversal geometry (**M** is perpendicular to the plane of incidence) there is a noticeable magnetic contribution to the SHG (see Fig. 1(a)). In the longitudinal geometry magnetic contribution to SHG vanishes, in accordance with the symmetry properties of $\chi^{(3)}_{ijkl}$.

For the azimuthal angle position of crystal $\varphi = 210°$, where the magnetic contrast has a maximum value (see Fig. 1(a)), we measured the SHG and MOKE hysteresis loops shown in Fig. 3(a) for CaF_2(4 nm)/MnAs(35 nm)/Si(111) structure. There is a pronounced difference between the coercive fields measured by the two methods. This difference is

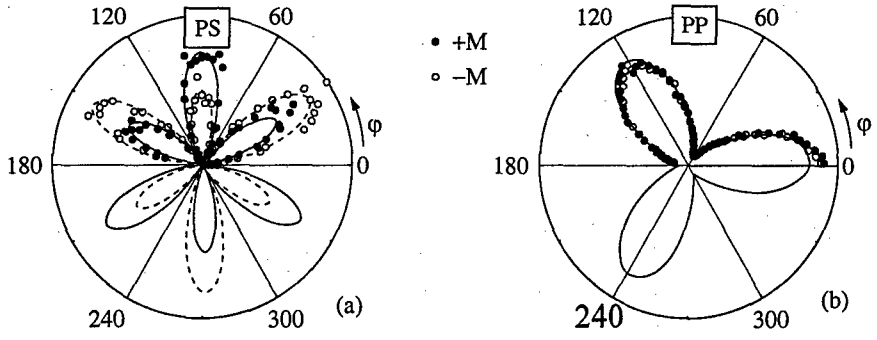

Fig. 1. Rotational anisotropy of the SH intensity in longitudinal geometry for CaF_2(4 nm)/MnAs(35 nm)/Si(111) structure for *PS* (a) and *PP* (b) input-output combinations of polarizations.

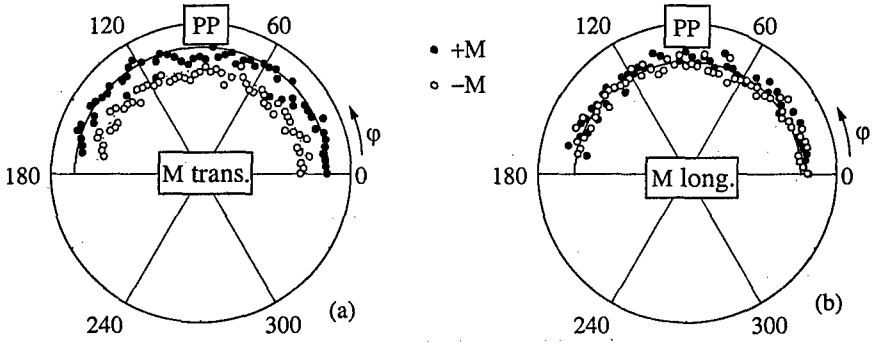

Fig. 2. Rotational anisotropy of SH intensity in (a) transversal and (b) longitudinal geometries for CaF_2(8 nm)/MnAs(70 nm)/Si(111) structure for *P*-input and *P*-output polarizations.

stronger for CaF_2(8 nm)/MnAs(70 nm)/Si(111) structure (Fig. 3(b)). Moreover, the SHG hysteresis loop is shifted in the direction of positive value of magnetic field.

In conclusion, CaF_2/MnAs/Si(111) heterostructures have been studied by using the two complementary magneto-optical techniques. Anisotropic pattern of SH rotational

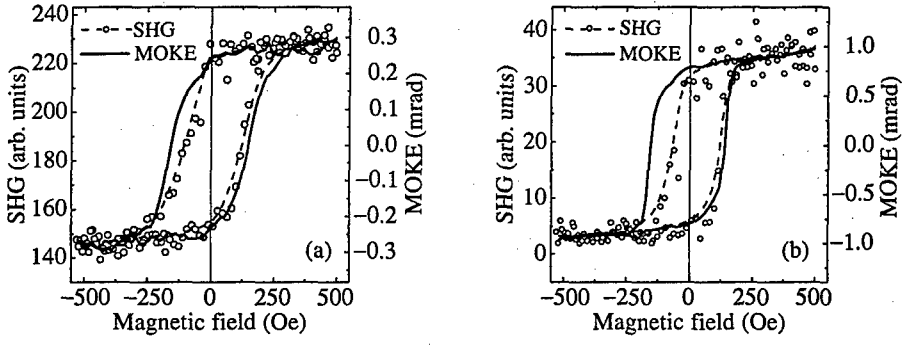

Fig. 3. Comparison of magnetic hysteresis loops measured using the SHG (dots and dashed lines are guide for eye only) and the Kerr effect (solid lines) for (a) CaF_2(4 nm)/MnAs(35 nm)/Si(111) and (b) CaF_2(8 nm)/MnAs(70 nm)/Si(111) structures.

anisotropy has been observed for CaF_2(4 nm)/MnAs(35 nm)/Si(111) structure, whereas for CaF_2(8 nm)/MnAs(70 nm)/Si(111) it was found to be isotropic. In both cases the crystallographic and magnetic contributions to the SHG have been separated on the base of model calculations. It was found that the SHG hysteresis loop differs from the MOKE one for the structures under study. Taking into account a sensitivity of the SHG and MOKE to the CaF_2/MnAs interface and the bulk of MnAs films, respectively, we can make conclusions about difference in magnetic properties of probed areas of the ferromagnetic films.

Acknowledgements

The work has been supported by the Russian Foundation for Basic Research, the INTAS and the Joint Dutch-Russian Project.

References

[1] G. A. Prinz, *Physics Today* **48**, N4, 58 (1995).
[2] Y. R. Shen, *The Principles of Nonlinear Optics* (J. Wiley and Sons, New York, 1984).
[3] H. A. Wierenga, W. de Jong, M. W. J. Prins, Th. Rasing, R. Vollmer, A. Kirilyuk, H. Schwabe and J. Kirschner, *Phys. Rev. Lett.* **74**, 1462 (1995).
[4] V. E. Zubov and A. D. Modestov, *Opt. Spectr.* **82**, 64 (1997).
[5] V. V. Pavlov, R. V. Pisarev, A. Kirilyuk and Th. Rasing, *Phys. Rev. Lett.* **78**, 2004 (1997).
[6] R. R. Birss, *Symmetry and Magnetism* (North-Holland, Amsterdam, 1966).
[7] A. M. Stoffel and J. Schneider, *J. Appl. Phys.* **41**, 1407 (1970).

7th Int. Symp. "Nanostructures: Physics and Technology"
St Petersburg, Russia, June 14–18, 1999

Electronic structure of stacked self-organized InAs/GaAs quantum dots

P. N. Brunkov†‡, A. Patanè‡, A. Levin‡, A. Polimeni‡, L. Eaves‡, P. C. Main‡, Yu. G. Musikhin†, A. R. Kovsh†, V. M. Ustinov† and S. G. Konnikov†

† Ioffe Physico-Technical Institute, St Petersburg, Russia
‡ School of Physics and Astronomy, University of Nottingham, NG7 2RD Nottingham, UK

Abstract. Capacitance and conductance-voltage characteristics have been measured at various frequencies and temperatures for a Schottky barrier structure containing three sheets of self-organized InAs quantum dots in an n-GaAs matrix. The capacitance of the structure consists of bulk and quantum dot contributions, whereas the conductance mainly depends on the electron transfer out of the dots, which is a function of the balance between measurement frequency and the thermionic emission rate of carriers from quantum dots. An analysis of the temperature-dependent conductance of the structure gives information about the electronic structure and electron emission rate from the quantum dots.

Introduction

In the last few years considerable attention has been given to both experimental and theoretical studies of electronic structure of self-organized quantum dots (QDs) [1-4]. Recently it was shown that when the distance between adjascent QD layers is below 100 Å the vertical alignment of the QDs is observed, resulting in a change in the electronic structure of the stacked QDs [1, 2]. In this paper we provide an analysis of the frequency- and temperature-dependent capacitance (C) and conductance (G) of structures with stacked InAs QDs incorporated in an n-type GaAs matrix. This approach allows us to study the electronic structure and dynamic features of electron trapping into the stacked QDs.

1 Results and discussion

The samples with embedded sheets of self-organized InAs QDs in an n-GaAs matrix, were grown by molecular beam epitaxy on n^+-GaAs (001). The QD section consists of three sheets of InAs QDs with a 50 Å thick GaAs spacer inserted between successive InAs island layers. The QD section was sandwiched between a 0.5 μm-thick GaAs cap and a 1 μm-thick GaAs buffer layer. Both the cap and buffer layers were uniformly doped with Si at 2×10^{16} cm^{-3} except for 100 Å thick undoped spacers on each side of the QD section. Schottky barriers were made by depositing Au through a shadow mask (350 μm diameter). The $C(V)$ and $G(V)$ characteristics were measured over a frequency range f from 10 kHz to 1 MHz using an HP4275A LCR meter. The amplitude of the measuring signal ($V_{\rm osc}$) was 10 mV.

At 100 K there is a plateau from -2.0 V to -3.6 V in the $C(V)$ characteristic related to the discharging of the QDs (Fig. 1(a)) [4]. For temperatures below 70 K, the plateau in the $C(V)$ characteristic is suppressed and a peak appears in $G(V)$ (Fig. 1). The capacitance is measured by superimposing a small ac signal $V_{\rm osc}$ at a frequency f on the applied dc reverse bias $V_{\rm rev}$. Note that $V_{\rm osc}$ causes a modulation of the charge both at the edge of the space charge region ($dQ_{\rm 3D}$) and at the point where the the bulk chemical potential (μ) in the

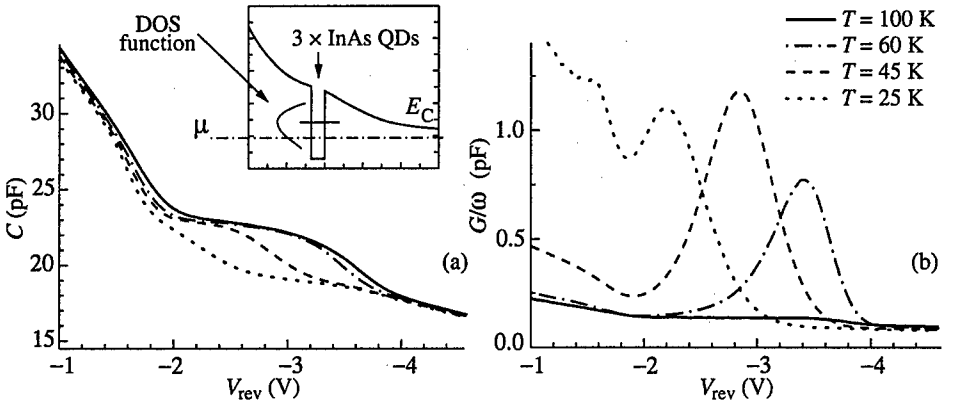

Fig. 1. Temperature dependence of (a) the $C(V)$ and (b) the $G(V)$ characteristics of QD structures measured at $f = 100$ kHz. The insert shows the conduction band diagram of the structure. The horizontal line represents the electron subband energy level E_{qd} in the QDs.

GaAs matrix crosses the density of electron states (DOS) in the QD layer (dQ_{qd}) (inset in Fig. 1).

To reach equilibrium between the QD layer and adjacent GaAs layers, the thermionic emission rate of electrons (e_n) from the QDs must be much higher than $\omega = 2\pi f$. The thermionic emission rate depends exponentially both on the temperature and the energy of the QD electron levels:

$$e_n = e_{n0} \exp \frac{-(E_C - E_{qd})}{kT}, \tag{1}$$

where $E_C - E_{qd}$ is the QD energy level with respect to the bottom of the conduction band and e_{n0} is a characteristic parameter of the QDs.

As the temperature decreases, e_n becomes smaller than ω, i.e. carriers freeze onto the QD levels [4]. This manifests itself as a decrease of the width of the capacitance plateau (Fig. 1(a)) and the appearance of a peak in the $G(V)$ characteristics (Fig. 1(b)). G/ω as a function of bias goes through a maximum when $\omega/e_n = 2$ [5]. The conductance peak moves to higher V_{rev} as temperature increases, since the array of QDs has a Gaussian DOS function and deeper (which means lower thermal activation rates) states contribute to the signal at higher V_{rev} (inset in Fig. 1).

The steady state occupation probability of the electron levels in the QDs is determined at a given temperature by the Fermi–Dirac function, depending on the relative positions of the electron level in the QDs (E_{qd}) and the bulk chemical potential μ in the GaAs matrix [4]. The sheet concentration of QDs was found to be $N_{qd} = 5 \times 10^{10}$ cm^{-2} from plan-view transmission electron microscopy. The DOS in the QD sheet may be approximated by a Gaussian function, which describes the spread of energies associated with the distribution of QD sizes [1]. By fitting the $C(V)$ characteristic measured at 100 K (Fig. 2(a)) to a quasi-static model [4] we find that the DOS in the QD layer corresponds to a Gaussian distribution with centre at $E_{qd} = 70$ meV from the bottom of the GaAs conduction band and standard deviation of $\Delta E_{qd} = 80$ meV. Calculation of the $C(V)$ characteristics of the QD structure shows that the region of quasi-constant capacitance from −2.2 to −3.6 V (Fig. 2(a)) is associated with a decrease in the concentration of electrons in the plane of the quantum dots with increasing reverse bias V_{rev} (Fig. 2(b)). This allows us to estimate

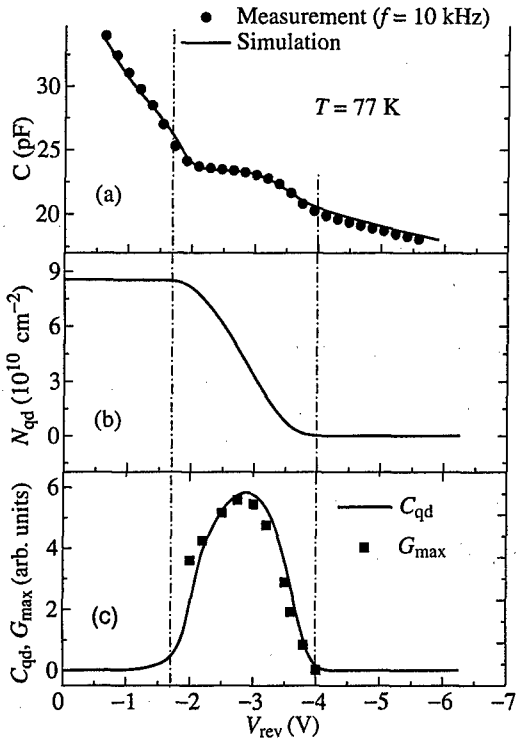

Fig. 2. (a) $C(V)$, (b) $N_{qd}(V)$, and (c) $C_{qd}(V)$ characteristics of the QD structure obtained at T = 80 K: experimental data (•) and model calculations (—) for $N_{qd} = 5 \times 10^{10}$ cm^{-2}, $E_{qd} = 70$ meV, and $\Delta E_{qd} = 80$ meV.

the capacitance related to QDs as $C_{qd} = qdN_{qd}/dV$ (Fig. 2(c)), where q is the electron charge. From the model it follows that the $C_{qd}(V)$ has a peak at $V_{rev} = -2.8$ V, when the Fermi level crosses the maximum of the DOS in the QD layer.

The thermionic emission rate depends exponentially on both the temperature and the energy of the QD electron levels (Eq. (1)). Therefore, by varying the measurement frequency and the temperature, we can control the C_{qd}. Figure 3 shows (a) $C(T)$ and (b) $G(T)$ characteristics of the QD structure measured at $V_{rev} = -2.8$ V. The temperature at which the feature due to the C_{qd} recovers in Fig. 3(a) depends on the measurement frequency. Each step in capacitance corresponds to a peak in conductance (Fig. 3(a,b)). Fig. 3(c) shows G/T of the QD structure at 100 kHz and at various V_{rev}. As V_{rev} is changed from -1.7 V to -4.0 V the position of the conductance peak moves to higher temperature and the activation energy, Δ_A, determined from the Arrhenius plot (insert to Fig. 3(c)), changes from 12 meV to 61 meV. The amplitude of the conductance peak has a maximum at $V_{rev} = -2.8$ V (Fig. 3(c)), because the conductance is proportional to the $C_{qd}(V)$ (Fig. 2(c)) and therefore reflects the DOS in the QD layer [5].

At $V_{rev} = -2.8$ V, $\Delta_A = 23$ meV, which is 47 meV lower than E_{qd} determined from the quasi-static analysis. The discrepancy may be due to the presence of an excited state between the ground state in the QDs and the bottom of the GaAs conduction band. In addition, there is a high electric field around the QD layer, which results in reduction of the

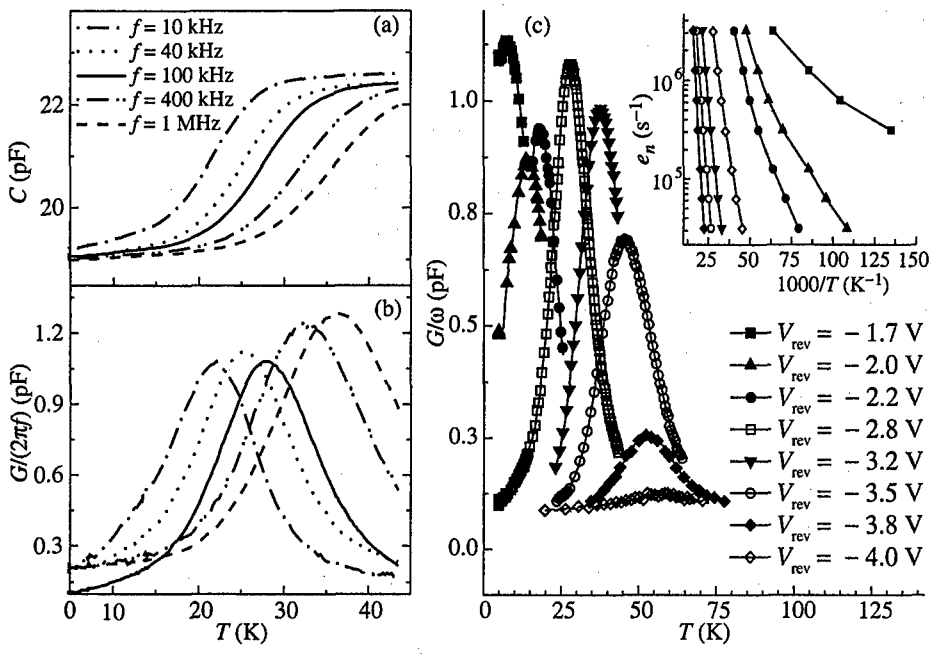

Fig. 3. (a) $C(T)$ and (b) $G(T)$ characteristics of QD structure at $V_{rev} = -2.8$ V. (c) Temperature dependence of conductance measured at 100 kHz as a function of the V_{rev}. Insert shows Arrhenius plot of the emission rates.

activation energy.

2 Conclusions

We have investigated the frequency-dependent admittance spectra of an n-GaAs structure containing self-organized InAs QDs. We find that the the quantum dot contribution to $C(T)$ and $G(T)$ characteristics depends on the relation between the thermionic emission rate e_n of electrons from QDs and the angular measurement frequency ω. Analysis of the admittance spectra provides information about the electron emission rate from the QDs. Since the array of self-organized QDs has a Gaussian DOS, we can study different parts of the QD energy spectrum by changing V_{rev}.

The authors would like to thank EPSRC, Royal Society (UK), and FAPESP (Brazilian Funding Agency) for partial financial support.

References

[1] D. Bimberg, M. Grundmann and N. N. Ledentsov, *Quantum Dot Heterostructures* John Wiley, 1998.
[2] G. S. Solomon, J. A. Trezza, A. F. Marshall and J. S. Harris Jr, *Phys. Rev. Lett.* **76**, 952 (1996).
[3] J. Kim, L.-W. Wang, and A. Zunger, *Phys. Rev. B* **57**, R9408 (1998).
[4] P. N. Brounkov, A. Polimeni, S. T. Stoddart, M. Henini, L. Eaves, P. C. Main, A. R. Kovsh, Yu. G. Musikhin and S. G. Konnikov, *Appl. Phys. Lett.* **73**, 1092 (1998).
[5] E. H. Nicollian and A. Goetzberger, *Bell Sys. Techn. J.* **46**, 1055 (1967).

7th Int. Symp. "Nanostructures: Physics and Technology"
St Petersburg, Russia, June 14–18, 1999

Atomic force microscopy characterization of nanostructured materials using selective chemical etching

A. A. Bukharaev, N. I. Nurgazizov, A. A. Mozhanova and D. V. Ovchinnikov
Kazan Physical Technical Institute, RAS, 420029 Kazan, Russia

Abstract. Atomic force microscopy and selective chemical etching were used to estimate the shape and sizes of the buried αFe nanoparticles created by ion bombardment in silica glasses. *In-situ* and *ex-situ* AFM measurements were performed. New data about distribution of nanoparticles and radiation induced defects both in a plane and on depth were obtained by these methods.

Introduction

Atomic-force microscope (AFM) allows to obtain the three-dimensional images of a surface of solid state with nanoscale resolution. However in a usual mode with the help of AFM it is possible to obtain data only about surface of solid samples, because AFM cantilever tip can not "glance" in deeper near-surface layers of substance. The level-by-level removal of superficial layers, for example with the help of their dissolution or chemical etching in liquid environment, allows to take off this restriction. This method is especially effective for study of nanostructured materials which have different rate of dissolution of separate nanofragments. The selective chemical etching of the surface of such sample can reveal thin structure of such substance in this case. It is essential, that as it is possible to carry out researches with AFM in liquid environment so there is an opportunity to observe transformation of the surface during etching in *in-situ* mode in a real time scale.

Experiments and discussion

We created a special measuring cell for work in aqueous solution of HF on Russian commercial scanning probe microscope P4-SPM-MDT for study of selective chemical etching in a real time scale in *in-situ* mode. Thermal drift of the AFM image obtained with the help of such cell in *in-situ* mode did not exceed 0.1 mm/hour due to special methods of fastening of a sample and cantilever, that allowed to study transformation of the same area of the surface with the size 1×1 mm within 2–3 hours, receiving the AFM image in every 2 minutes. Thus, it was possible to obtain up to 60 images of the same surface place during its chemical etching. Videoclips were created, which displayed transformation of a surface during etching, using computer animation methods on the basis of these images. Microscope worked in a contact mode, so as the cantilever tip constantly touched the surface during scanning. Olympus Si_3N_4 cantilevers were used. The experiments have shown, that weak acid solutions (with HF concentration up to 1 %) practically do not damage the tip of such cantilever. Besides, the experiments *ex-situ* were carried out, when the sample was taken out from a solution after etching during certain time and the measurements were performed with P4-SPM-18RM microscope in tapping mode.

In the present work the above mentioned methods were used for investigation of internal structure of silica glasses and SiO_2 layers with 100 nm thickness formed on Si. Samples

were irradiated using the ILU-3 accelerator with Fe^+ of 40 keV energy and the fluence up to 2×10^{17} ion/cm^2.

In our previous works [1] it was shown, that bombardment of silica glasses by Fe^+ ions of 40 keV can create ferromagnetic αFe nanoparticles in a surface layer at depth up to 60 nm. The presence of ferromagnetic αFe particles in near-surface layers was confirmed by the optical and FMR measurements. The lateral sizes of particles were appreciated with the help of transmission electron microscopy and were in range from 10 up to 100 nm [1]. However one could know the thickness and depth of particles placement only from the indirect data. It is known, that in HF acid the low-soluble protective film is formed on the surface of some metals [2], besides as we have showed earlier [3] the etching rate of SiO_2 containing of the radiation defects induced by ion bombardment is higher for some times, than in case of nonimplanted SiO_2. By virtue of this it is possible to assume, that implanted SiO_2 will be dissolved faster than αFe in HF and αFe nanoparticles will occur on the surface during SiO_2 dissoluting, what can be found out with the help of AFM.

Really, after etching in HF of approximately 5–10 nm of implanted SiO_2 on its surface there were characteristic protrusions, which can be connected with metal nanoparticles appeared on the surface (Fig. 1). The characteristic shape of protrusions observed in Fig. 1 (as a trapeze) is a result of known effect of convolution of the pyramidal AFM tip and the spherical particle [4]. The similar shape of the AFM images was observed by us earlier during obtaining of the images of spherical Ni particles in contact mode [4]. The *ex-situ* measurements in tapping mode (when the tip radius was about 10 nm) have shown, that the lateral sizes of such protrusions are in range from 40 up to 100 nm. In view of effect of convolution it means, that the real horizontal sizes of nanoparticles are in range of 20–80 nm, that is enough well agree with the obtained earlier data about the lateral sizes of buried αFe nanoparticles.

During layer-by-layer removal of SiO_2, forces attaching the particle to the surface obviously decrease after an output of the buried particle from the surface. In this case, interaction between the cantilever tip and such particle during scanning can appear enough to remove the particle from the surface. In *in-situ* experiments this phenomenon was observed distinctly. For example: on the series of AFM images (Fig. 1), consistently obtained on the same place it is well visible how the particles designated by numbers 1–6 disappear. For these cases it is possible to distinctly observe the moment of pushing out the particle by the AFM tip from the surface. As a result of removal only the left part of the particle is visible in the AFM image and the right part of the image of the particle is absent after pushing out the particle by the tip. It is defined by a trajectory of movement of the tip along the surface during scanning (scan lines are parallel to the ordinate axis and the image is formed from left to right). By estimating the height of the relief before and after nanoparticle removal it is possible to make a conclusion about its thickness, which for different particles was from 5 up to 20 nm.

It is essential, that after etching of approximately 30 nm of implanted layer of SiO_2, when almost all αFe nanoparticles were disappeared from the surface (at the same time the characteristic FMR signal and the optical absorption from iron nanoparticles vanish) active formation of a microrelief which difference of heights reaches 40 nm still proceeds. It is well visible from **rms** dependence on time constructed on the basis of the obtained images. Non-uniform distribution of radiation-induced defects in glass located on depth from 30 up to 60 nm is the reason of it. Those areas of glass where the higher radiation defect concentration were etched faster. Smooth surface was formed again after complete dissolution of the radiation damaged layer, which thickness was close to the maximum

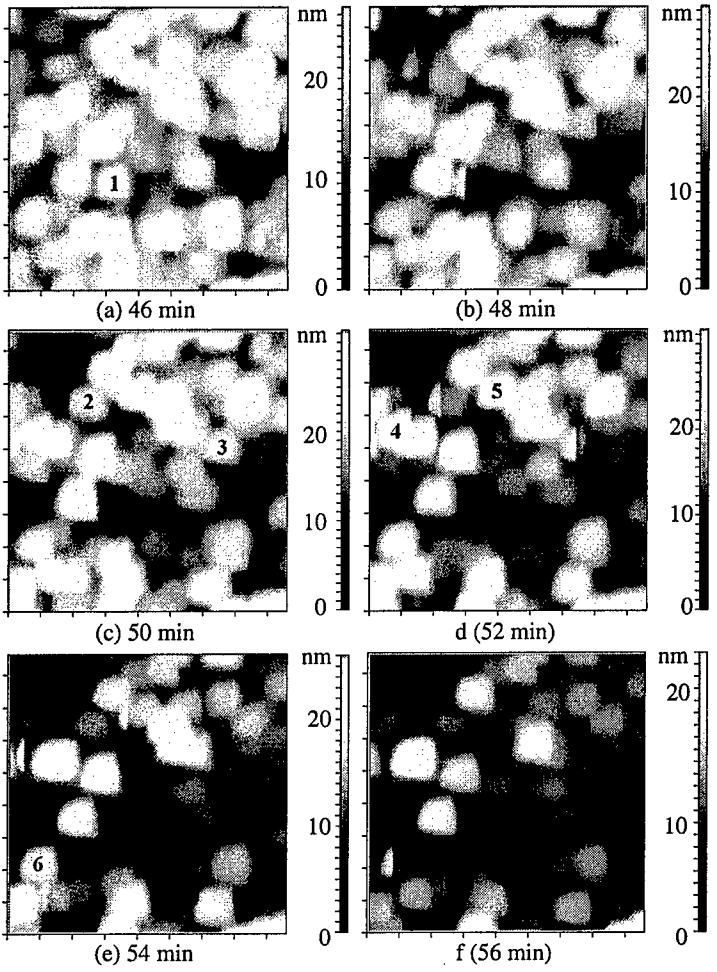

Fig. 1. The series of the AFM images shows the transformation of the same area (860×860 nm) of SiO_2 with αFe nanoparticles during the chemical etching, when the tip apex are pushing out some of the protrusions corresponding to the nanoparticles (with numbers 1–6). In brackets there was indicated the time from start of the chemical etching process.

depth of penetration of Fe^+ in glass during ion bombardment.

Thus, AFM research of the surface chemical etching *in-situ* and *ex-situ* have allowed to estimate not only lateral sizes of nanoparticles buried in glass, but also to establish their thickness and to delineate the distribution of nanoparticles and radiation defects induced by ion bombardment both in a plane and on depth.

Acknowledgements

The work is supported by Russian Basic Research Foundation (Grant 98-03-32753) and Russian Ministry of Sciences (Grant 02.04.3.1.40.E.22).

References

[1] A. A. Bukharaev, A. V. Kazakov, R. A. Manapov and I. B. Khaibullin, *Sov. Phys. Solid State* **33** *4*, 578 (1991).

[2] N. L. Glinka *General Chemistry*, Leningrad: Chemistry, 1986.

[3] A. A. Bukharaev, A. A. Bukharaeva, N. I. Nurgazizov and D. V. Ovchinnikov, *Technical Physics Letters* **24** *11*, 863 (1998).

[4] A. A. Bukharaev, E. F. Kukovitskii, D. V. Ovchinnikov, N. A. Sainov and N. I. Nurgazizov, *Physics of Solid State* **39** *11*, 1846 (1997).

7th Int. Symp. "Nanostructures: Physics and Technology"
St Petersburg, Russia, June 14–18, 1999

Ionized states in the III–V heterostructure measured by low-temperature capacitance spectroscopy with optical excitation

V. Davydov†‡, H.-W. Ren†, S. Sugou†¶ and Y. Masumoto†§
† Single Quantum Dot Project, ERATO, JST, Tsukuba Research Consortium, Ibaraki 300-26, Japan
‡ On leave from S. I. Vavilov State Optical Institute, St Petersburg, Russia
¶ Opto-Electronics Research Laboratories, NEC Corporation, Tsukuba, Ibaraki 305, Japan
§ Institute of Physics, University of Tsukuba, Ibaraki 305, Japan

Abstract. The photo-capacitance spectroscopy at low temperature is shown to be a sensitive technique for characterization of the semiconductor structures. This technique was applied to the study of III–V heterostructure with InP quantum dots. Several types of the deep states which can be photo-ionized were found in the structure. Some of this states shows sensitivity to photon energies far below the bandgap of all materials involved.

Introduction

Capacitance spectroscopy and its various modification such as deep level transitional spectroscopy (DLTS) provides a powerful tool for the characterization of the semiconductor structures [1]. However the basic theory of such a measurements is rooted on the classical notions of the thermal ionization of donors or acceptors. This approach gives the elegant tools, such as depletion layer approximation, but at the same time imposes the serious restrictions which results, for example, in the poor resolution of DLTS.

This restrictions can be easily overcame by mere changing the measurement conditions further away from the thermal equilibrium. Probably the most clear and widely adopted example of this "nonequilibrium philosophy" is the technique of photo-conductive measurements of bulk semiconductors. By using the nonequilibrium photons, it allows investigation of the states over the entire bandgap at a single temperature chosen from the considerations of the detection convenience.

The increasing complexity of interesting subjects for modern semiconductor science and applications demands further sophistication of the investigation techniques in the same direction, that is, away from the equilibrium. One possible way is the using of ultrashort optical pulses, which can reveal processes as fast as interband relaxation [2]. Another quite successful approach, low-temperature capacitance spectroscopy [3], has an advantage of detecting tunnel current which is more selective than thermocurrent and also does not require the electrical conductance of the whole sample. Recently this technique was used [4] for study of the charged states of InAs self-assembled quantum dots (QDs).

In this work we are presenting an attempt to apply the similar technique to the heterostructures with InP QDs which studies are more difficult because of generally worse quality of ternary composition barriers and interference from the bulk GaAs substrate which interband transitions overlap with the optical transitions in the QDs.

1 Experimental

The sample used for this experiment is grown by the gas source molecular beam epitaxy on the GaAs n-doped substrate and contains GaAs buffer with short GaAs/AlAs superlattice inside, $In_{0.5}Ga_{0.5}P$ barrier separated from the buffer by thin AlAs layer, and the single layer of InP QDs covered by the second half of the barrier layer. Detailed microphotograph of the sample is presented elsewhere [5]. The gold electrode with transparency of about 5% and area of 10 mm^2 is deposited on the top of sample, and back side of the substrate is coated by the indium.

This sample is mounted in the optical cryostat filled by a superfluid helium and both sample surfaces are wired to the outside by separate shielded conductors. Both shields are grounded and connected to the cryostat body. The substrate contact is used for applying the sweepable DC bias to the sample with small 100 kHz AC modulation added via the differential amplifier. The top semitransparent contact is connected to the input terminal of the current amplifier at the virtual ground potential. When reverse bias is applied, a considerable leakage current occurs through the point defects shunting the epitaxial layers. Loop for this current is completed through the low output impedance of differential amplifier and low input impedance of current amplifier.

The signal from the current amplifier is fed to the lock-in detector which is referenced by the same 100 kHz modulation. Quadrature component of the current is proportional to the capacity of the sample. This component is fed to the second lock-in detector which reference is locked to the light chopper modulating the sample illumination. Thus, the second lock-in records the sample capacitance change by the action of light. The CW Ti:sapphire laser and the combination of incandescent lamp and monochromator are used as tunable light sources.

2 Results and discussion

Capacitance–voltage profile of this sample, measured at 2 K, is essentially flat and even non-monotonous in the domain of reverse bias. This is the direct consequence of inapplicability of the depletion layer approximation at low temperatures.

The photo-capacitance–voltage (ΔC versus V) profiles excited by the laser light of different wavelengths are presented in Fig. 1. The traces were recorded by linearly sweeping the bias voltage back and forth, and some traces indicate a hysteresis-like splitting which represents the very slow (comparing with the sweep rate of about 1 V/s) charging and discharging processes in the sample. Note that the photo-capacitance is always positive, that is the additional light can only release additional charge.

The traces show a number of peaks at different voltages. In view of the logarithmic scale in the figure, these peaks are rather sharp providing good resolution of this technique. The width of sharpest feature is comparable to the modulation amplitude. Whereas the position of the peaks requires for interpretation some additional electrostatic considerations, the area below each peak

$$\Delta Q = \int \Delta C \, dV \tag{1}$$

represents the amount of mobile charge released by the illumination because the electrostatic equation $Q = CV$ due to its integral nature is insensitive to the details of charge distribution.

The physical origin of this peaks owes to the presence of internal potential profile in the semiconductor structures which is affected by the external bias. The capacitance measuring technique is sensitive only to the mobile charge, which is constituted from carriers located in

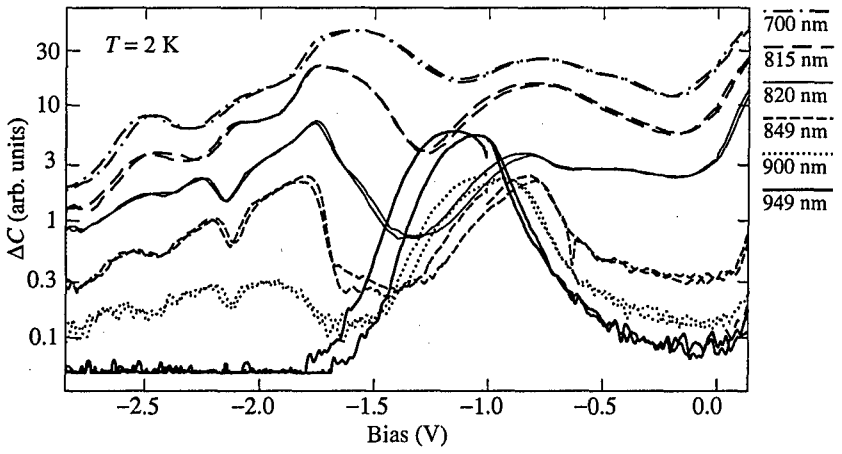

Fig. 1. Photo-capacitance as function of applied bias for different laser wavelengths. Laser power is about 0.6 μW/cm^2 and chopping frequency is 15 Hz for all traces.

the flat regions of the profile. Different portions of the profile are flattened under the different bias, providing a means for the selecting different layers of the sample. Monochromatic light gives an additional selectivity.

The most interesting result is that considerable photo-capacitance signal is observed even when the excitation light falls below the GaAs bandgap, where the sample should be totally transparent. This is a clear indication of the presence of deep states which were also observed in our studies on anti-Stokes photoluminescence [6]. Moreover, the amplitude of the most prominent peak around -1.0 V bias is increasing with longer wavelengths, which means that photo-generated mobile carriers can accumulate during the time comparable to the light chopping period. An additional experiment with the lamp and monochromator as light source has shown that amplitude of this peak continue to grow with decreasing the chopping frequency down to few mHz and that the photo-capacitance signal can be excited with photons as low as 1.0 eV.

3 Conclusion

This work presents the low temperature photo-capacitance spectroscopy as a powerful tool for investigation of the complex semiconductor heterostructures. This technique is used to study the epitaxial structure with InP QDs. A number of types of defects which can be photo-ionized is found in the sample. Some of this defects are sensitive to the infrared light far below the band to band absorption of any material in the structure. Exact identification of this defects needs further investigation.

Acknowledgments

We thank Dr. M. Mizuta and Dr. Y. Mochizuki for interest in this work and fruitful discussions.

References

[1] P. Blood and J. W. Orton, *The Electrical Characterization of Semiconductors: Majority Carriers and Electron States* Academic Press, 1984.

[2] J.-C. Diels and W. Rudolph, *Ultrashort Laser Pulse Phenomena*, Academic Press, 1996.
[3] L. Jacak, P. Hawrylak and A. Wójs, *Quantum Dots* Springer, 1998.
[4] K. H. Schmidt, G. Medeiros-Ribeiro and P. M. Petroff, *Phys. Rev. B* **58**, 3597 (1998).
[5] Y. Masumoto, V. Davydov, I. Ignatiev, H.-W. Ren and S. Sugou, *Jpn. J. Appl. Phys.* **38**, 2290 (1999).
[6] Y. Masumoto, H.-W. Ren, S. Sugou, I. Ignatiev and I. Kozin, This volume p. 54.

7th Int. Symp. "Nanostructures: Physics and Technology"
St Petersburg, Russia, June 14–18, 1999

Electron tunnelling at surfaces of Mott insulating *d*- and *f*-metal oxides: the *ab-initio* interpretation of STM images

S. L. Dudarev, M. R. Castell, G. A. D. Briggs and A. P. Sutton
Department of Materials, University of Oxford, Parks Road,
Oxford OX1 3PH, United Kingdom

Abstract. In this communication we describe recent progress in the first-principles theoretical modelling of surface electronic structure and elevated temperature atomically-resolved STM images of surfaces of semiconducting *d*- and *f*-metal oxides. The presence of strong electron correlations in the $3d$ and $5f$ shells of metal ions in NiO, CoO and UO_2 makes conventional computational methods based on the local spin density approximation (LSDA) of density functional theory unsuitable for *ab-initio* calculations of the surface electronic structure of these oxides. By using the LSDA+U approach, which combines LSDA with the Hubbard U term, we explain the origin of the contrast reversal of experimental STM images of the NiO (001) surface. We also show how the symmetry of surface states is responsible for the order of magnitude difference in the contrast of STM images of NiO (001) and CoO (001) surfaces, and we describe how theoretical simulations make it possible to identify the atoms that are seen in STM images of the (111) surface of UO_2.

Introduction

Antiferromagnetic insulating transition metal oxides form a class of compounds whose electronic structure cannot be described using conventional band theory. The origin of the insulating behaviour of those oxides was explained in 1937 by Peierls who pointed out that band theory fails when the inter-site tunneling of electrons is suppressed by the on-site Coulomb repulsion between electrons. The anomalous electronic behaviour of transition metal oxides associated with strong electron correlations in the $3d$ shell, also manifests itself in compounds containing ions of actinide elements. Metal ions in actinide oxides (for example, in UO_2) contain partly filled $5f$-shells where electrons are localized in the vicinity of atomic cores. The magnitude of the Hubbard parameter U describing the strength of electron-electron interaction in the $5f$ shell is comparable with the magnitude of U characterizing the $3d$ electrons in transition metal oxides.

So far, experimental and theoretical studies of transition metal and actinide oxides were mainly focused on their *bulk* properties. In our work [1, 2, 3] we investigate the *surface* properties of the $3d$ and $5f$ oxides. This field has recently attracted attention of many research groups worldwide. This stems from the interest in magnetic properties of metal oxides that are being considered as potential components of future media storage devices. Interest in surface properties of uranium oxides is driven by the recent discovery of unusually high catalytic activity of their surfaces. Transition metal oxides are also known to be catalytically active, and there is evidence for the existence of a link between the unusual surface properties displayed by the $3d$ and $5f$ oxides and the role played by strong electron correlations in the formation of surface electronic states in these materials.

1 Electronic structure and tunnelling at oxide surfaces

Evaluating the tunneling current using the Bardeen approxiamtion, we arrive at

$$I(L \to R) = \frac{2\pi}{\hbar} \sum_{L,R} (n_L - n_R) \, |M_{LR}|^2 \delta(E_R - E_L), \tag{1}$$

where matrix element M_{LR} is given by

$$M_{LR} = \frac{\hbar^2}{2m} \int_A d^2A \left[\Psi_L(\mathbf{A}, z_A) \frac{\partial}{\partial \mathbf{r}} \Psi_R^*(\mathbf{A}, z_A) - \Psi_R^*(\mathbf{A}, z_A) \frac{\partial}{\partial \mathbf{r}} \Psi_L(\mathbf{A}, z_A) \right]. \tag{2}$$

Integration in (2) is performed over an arbitrary surface A separating the entire space into the left-hand and right-hand side parts, one including the tip and the other including the sample, in such a way that the effective *one-electron* potential vanishes everywhere at this surface. Formula (2) shows that in order to interpret an STM image, it is often *sufficient* to investigate the asymptotic behaviour of the real space distribution of the density of electronic states in the vacuum gap separating the STM tip and the surface.

For many metallic and band insulating surfaces the effective one-electron states can be found using conventional density-functional techniques based on the local density approximation. However, predictions of metallic ground states for CoO and UO_2 and the near metallic ground state for NiO made using LSDA shows that this strategy cannot be followed in an investigation of the electronic structure of $3d$ and $5f$ oxide materials. In our work we use the LSDA+U method [4] that has proved to be successful in addressing a number of fundamental issues relevant to the *bulk* properties of UO_2 and NiO [5, 6]. The LSDA+U method combines the LSDA treatment of electron correlations in delocalized s and p orbitals with the spin-unrestricted Hartree–Fock (UHF) treatment of localized d or f orbitals. In practical calculations, the UHF correction amounts to the renormalization of the matrix of the LSDA potential [6] (the correction applies only to the spatially localized d and f orbitals)

$$V_{jl}^{\sigma} \equiv \frac{\delta E_{LSDA+U}}{\delta \rho_{lj}^{\sigma}} = \frac{\delta E_{LSDA}}{\delta \rho_{lj}^{\sigma}} + (\tilde{U} - \tilde{J}) \left[\frac{1}{2} \delta_{jl} - \rho_{jl}^{\sigma} \right], \tag{3}$$

where ρ_{jl}^{σ} is the density matrix of electrons occupying partly filled electronic shells of metal ions (the $5f$ shell in UO_2 and the $3d$ shell in NiO and CoO).

2 Electronic states at NiO(100), CoO(100) and UO_2(111) surfaces

Atomically-resolved images of the (100) surface of NiO obtained by Castell *et al* [1] exhibit the reversal of image contrast occurring as a function of the sign of the bias applied to the sample. Image contrast observed at a positive sample bias is significantly higher than the contrast of images observed at a negative sample bias. To explain this effect, in Fig. 1 we plotted the real space distributions of the density of filled and empty surface electronic states of NiO calculated using the LSDA+U approach. These distributions show that, on one hand, at positive applied bias electrons tunnel predominantly into the empty $3d_{3z^2-r^2}$ states localized on nickel sites. On the other hand, at negative applied bias the main contribution to the tunneling current comes from the states localized on oxygen sites. Fig. 1 shows that image contrast should be expected to be significantly lower in the latter case than in the

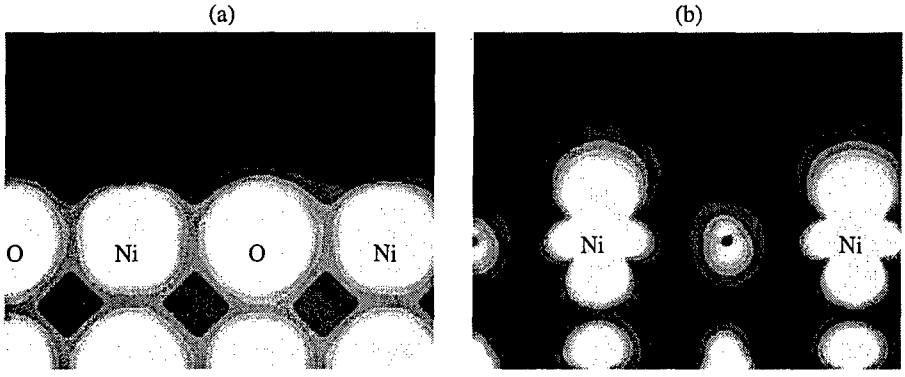

Fig. 1. Valence electron charge density distribution (a) calculated numerically for the NiO(001) antiferromagnetically ordered surface and the distribution of the density of *empty* states (b) calculated for the same surface by integrating over a 1 eV energy interval corresponding to the bottom of the conduction band.

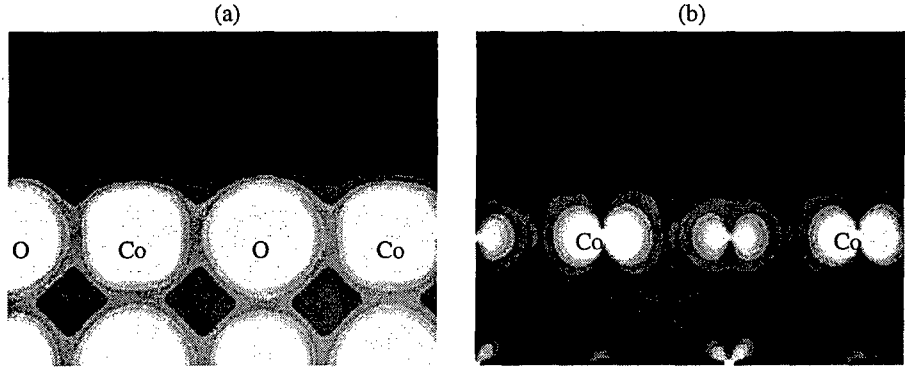

Fig. 2. Charge density distribution (a) and the density of empty electronic states (b) calculated for the antiferromagnetically ordered CoO(001) surface.

former one, in agreement with experimental observations. In experiments [7] conducted on NiO(100) and CoO(100) surfaces we compared the contrast of STM images of the two surfaces obtained under similar experimental conditions. While the atomically resolved images of CoO and NiO looked similar, we observed a significant difference in the atomic corrugation heights. To explain this phenomenon, we have carried out a first-principles investigation of the electronic structure of the CoO(100) surface. The results shown in Fig. 1 and Fig. 2 illustrate the difference in the symmetry of low-lying *d*-states forming the bottom of the conduction band of NiO and CoO. This difference is responsible for the order of magnitude difference in the contrast of experimental STM images observed for the two surfaces [7].

In Ref. [2] we reported the atomically resolved STM images of uranium dioxide $UO_2(111)$. The interpretation of these images is less straightforward since oxygen ions on the (111) surface of the fluoride structure of UO_2 are situated above uranium ions (see Fig. 3). However, the density of states plot shown in Fig. 3 proves that uranium ions still

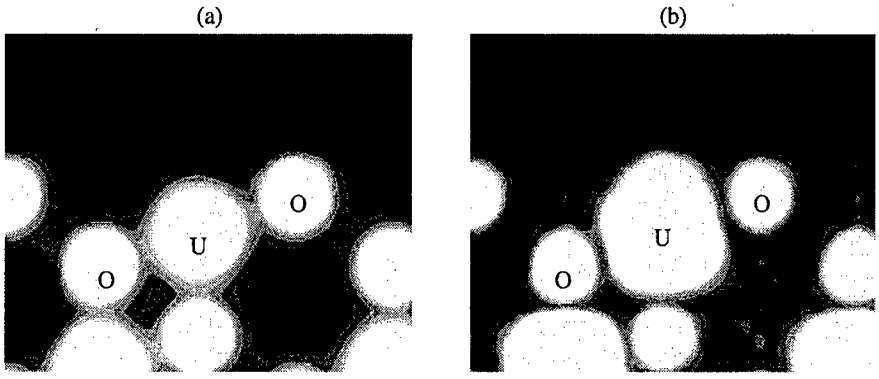

Fig. 3. Charge density distribution (a) and the density of empty electronic states (b) calculated for the antiferromagnetically ordered $UO_2(111)$ surface.

give the dominant contribution to the tunneling current observed at a positive applied bias. In summary, in this communication we described applications of the LSDA+U method to surfaces of Mott insulating transition metal and actinide oxides and showed how a combination of novel experimental information with the first-principles theoretical modelling gives rise to a new method of investigation of the electronic structure of this unusual class of oxide materials.

Acknowledgements

Computations were performed in the Materials Modelling Laboratory of the Department of Materials at the University of Oxford. This work was financially supported by BNFL and by the EPSRC through grant GR/M34454.

References

[1] M. R. Castell, P. L. Wincott, N. G. Condon *et al*, *Phys. Rev. B* **55**, 7859 (1997).
[2] M. R. Castell, S. L. Dudarev, C. Muggelberg *et al*, *Appl. Phys. A* **66**, S963 (1998); *J. Vac. Sci. Tech. A* **16(3)**, 1055 (1998).
[3] S. L. Dudarev, A. I. Liechtenstein, M. R. Castell *et al*, *Phys. Rev. B* **56**, 4900 (1997).
[4] V. I. Anisimov, J. Zaanen, O. K. Andersen, *Phys. Rev. B*, **44**, 943 (1991)
[5] S. L. Dudarev, D. Nguyen Manh and A. P. Sutton, *Philos. Mag. B* **75**, 613 (1997).
[6] S. L. Dudarev, G. A. Botton, S. Y. Savrasov *et al*, *Phys. Rev. B* **57**, 1505 (1998).
[7] M. R. Castell, S. L. Dudarev, G. A. D. Briggs and A. P. Sutton, *Phys. Rev. B* **59**, (1999), in press.

7th Int. Symp. "Nanostructures: Physics and Technology"
St Petersburg, Russia, June 14–18, 1999

X-ray reciprocal space mapping of coincided As-clusters/GaAs and δ-InAs/GaAs superlattices grown at low temperature

N. N. Faleev†, V. V. Chaldyshev†, V. V. Preobrazhenskii‡, M. A. Putyato‡, B. R. Semyagin‡ and Y. Takeda§

† Ioffe Physico-Technical Institute, St Petersburg, Russia
‡ Institute of Semiconductor Physics, 630090, Novosibirsk, Russia
§ Nagoya University, 464-8603, Nagoya, Japan

Abstract. X-ray reciprocal space mapping was employed to assess the crystalline quality of the δ-InAs/GaAs superlattices grown at low temperatures and structural transformations related to formation of As-cluster/GaAs superlattices upon post-growth anneal.

Introduction

During the last few years InAs/GaAs superlattices with thin InAs layers have attracted much attention due to interesting electronic and optical properties. While perfect GaAs films are normally produced by molecular-beam epitaxy (MBE) at ~ 600 °C, the InAs/GaAs superlattices are grown at a reduced temperature (normally 400–500 °C) in order to eliminate indium segregation and produce abrupt interfaces. A decrease in the growth temperature leads to an increase of point defect concentration. When the temperature is extremely low (~ 200 °C), a high arsenic excess is incorporated in the growing film and the concentration of arsenic antisite defects is as high as 10^{20} cm^{-3} [1]. A post-growth anneal of the GaAs films grown at low temperature (LT) results in precipitation of the excess arsenic. The annealed LT GaAs exhibits a very high electrical resistivity and extremely short carrier lifetime [2]. This material is promising for application in ultra-fast devices.

The system of nano-scale arsenic clusters in the annealed LT GaAs films is random. It has been shown recently that InAs δ-layers can be used to form two-dimensional cluster sheets in the GaAs matrix [3] and superlattices of these sheets coincided with the initial δ-InAs/GaAs superlattices [4]. In this paper we employed x-ray reciprocal space mapping to assess the crystalline quality of both the initial δ-InAs/GaAs superlattices grown at low temperatures and As-cluster/GaAs superlattices formed by the post-growth anneal.

1 Experimental

The δ-InAs/GaAs superlattices were grown by MBE at 150 and 200 °C. The nominal thickness of the InAs δ-layers was ~ 1 monolayer. The thickness of the GaAs spacers was 30 and 50 nm. All the samples were cut into several parts, one of them was kept as-grown, the other were annealed at 400, 500, or 600 °C.

X-ray diffraction (XRD) studies were carried out using high-resolution, double-crystal diffractometers. Studies of superstructural ordering and measurements of reciprocal space mapping (RSM) of diffracted intensity were made using a double-crystal $\theta-\theta$ diffractometer with a twofold channel-cut Ge (001) monochromator crystal. $\omega - 2\theta$ and ω-scanning techniques for rocking curves (RCs) and the $\theta-2\theta(\omega)$ technique for RSM registration were used. Cu$K_{\alpha 1}$ radiation was used for the measurements. A narrow receiving slit in front of

the detector enabled separation of the coherent and diffuse components of the diffracted x-ray beam.

2 Results and discussion

The structures investigated have high crystal lattice perfection, which was demonstrated by measurements at a high angular resolution (about 1.0 arcsec) in the vicinity of GaAs (004) reflection. The parameters of crystal perfection are determined from the extended interference patterns arising from structures under Bragg diffraction conditions. This means that the density of small structural defects in as grown samples is insignificant. Furthermore, coarse defects such as dislocations are entirely absent. The elimination of grown-in structural defects in these samples and the high degree of crystal lattice perfection enable structural investigations and modelling of samples containing real quantum-sized objects with extremely high accuracy. In the case of perfect structures, the main structural features observed in experiments must be correlated with the real structures of scattering objects, including quantum sized objects. Wide-angle XRD RCs have shown the existence of superstructural ordering along the direction of epitaxial growth for both investigated samples. The coherent approximation of the dynamical theory of XRD based on Takagi's equations [5] was used for the simulation of RCs. Fitting of RCs has shown that the period of multilayer structures is close to the value estimated from the growth conditions, and that the average thickness of the InAs layers is about 0.20–0.25 nm, which is close to the expected value. Evaluation of the roughness of the interfaces in the periodic parts of structures has been obtained from the entire angular range of coherent RCs. It was shown that the roughness of the InAs/GaAs interfaces of the as-grown samples is equivalent to about 3–4 monolayers and is typical for a GaAs(001) surface [6].

Figs. 1 and 2 show the RSM of diffracted intensity in the vicinity of GaAs(004) reflection for two samples grown at different temperatures. For as-grown samples one can see a large number of superlattice interference peaks and low diffuse scattering. This is clear evidence of high crystalline quality of these samples in spite of a very high concentration of excess-arsenic-related point defects ($(1-2) \times 10^{20}\,\mathrm{cm}^{-3}$). The annealing at 600 °C leads to a significant diminishing of the interference patterns and strong increasing of diffuse scattering (part (b) in Figs. 1 and 2). The diffuse scattering is symmetrically distributed around GaAs(004) and zero-order superlattice (0SL) peaks. In as-grown samples the point defects do not influence the crystal perfection of as-grown samples, and the planarity and roughness of the InAs/GaAs interfaces. The scale of non-uniformity of deformation fields around the interfaces is comparable with the roughness of the interfaces. Formation of As clusters at the InAs δ-layers upon annealing leads to increasing roughness of the interfaces. In addition, migration of native point defects causes enhanced In-Ga intermixing. These processes produce a significant distortion of the local strains around the δ-layers and, as a result, lead to the intensive diffuse scattering in the vicinity of central diffraction peaks, and to diminishing extension of interference patterns.

A strong lattice relaxation was detected after annealing of the samples. The lattice parameter of the annealed material is slightly less than that of stoichiometric one. This relaxation was stronger for the sample grown at lower temperature. However, comparison of experimental date in Figs. 1 and 2 shows that the spatial distribution of the x-ray diffracted intensity is very similar for the samples grown at 150 and 200 °C. The decrease of the growth temperature by 50 °C results in the increase of the excess arsenic by the factor of two. However, higher supersaturation by excess As causes more intensive precipitation rate and the sheet cluster concentrations at InAs δ-layers turn out to be approximately equal in

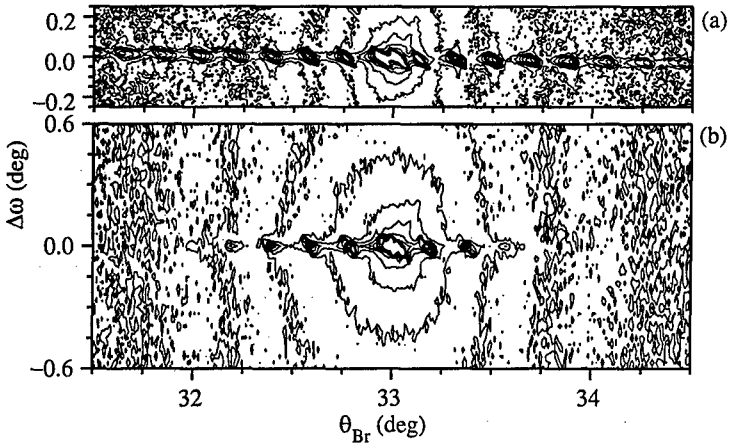

Fig. 1. X-ray reciprocal space mapping in the vicinity of GaAs(004) for the sample grown at 200 °C before (a) and after (b) annealing at 600 °C.

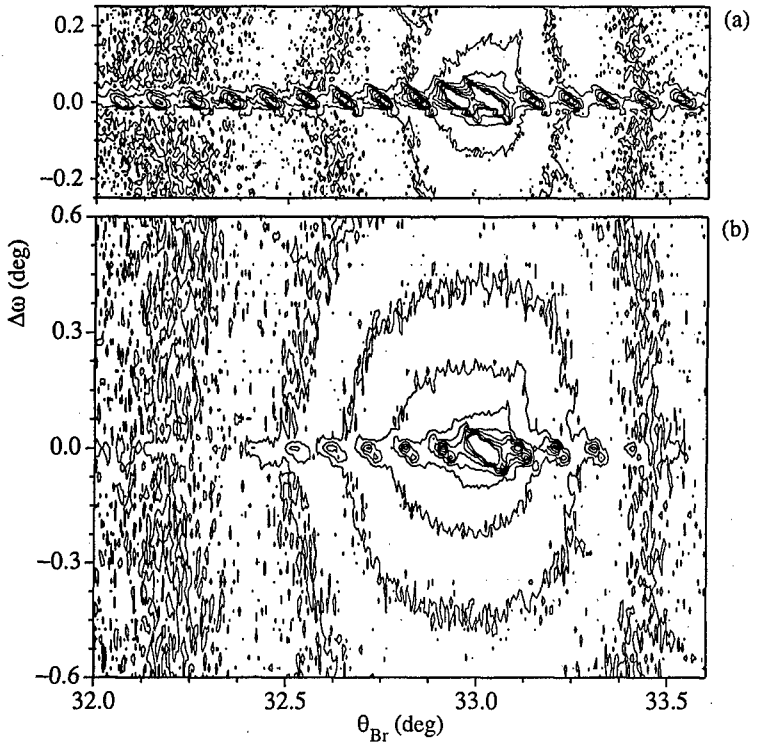

Fig. 2. X-ray reciprocal space mapping in the vicinity of GaAs(004) for the sample grown at 150 °C before (a) and after (b) annealing at 600 °C.

both samples. Analysis of reciprocal space patterns shows that formation of nano-scale As clusters does not produce extended defects such as dislocations and stacking faults.

3 Conclusions

Multilayer δ-InAs/GaAs periodical structures grown by MBE at low temperature were studied by high resolution x-ray diffraction methods. It was shown that in spite of the initial high concentration of point defects in these structures they have high crystal lattice perfection and flat abrupt interfaces. A strong increase in the x-ray diffuse scattering was detected by reciprocal space mapping of the samples annealed at 500 and 600 °C. This effect is accompanied by remarkable decrease of the interference patterns. Both phenomena can be attributed to increasing roughness of the interfaces due to formation of As clusters superlattices coincided with the initial δ-InAs/GaAs periodical structures. Formation of nano-scale clusters was found to produce no extended defects such as dislocations and stacking faults. The lattice parameter of the clusters contained material is slightly less than that of stoichiometric one.

Acknowledgment

This work was conducted under the visiting fellow program of the Monbusho Project Venture Business Laboratory at Nagoya University and supported in part by the Daiko Foundation and grant of JSPS. This work was also supported in part by grants from the Russian Foundation for Basic Research, and by grants from the Ministry of Science of the Russian Federation (Research programs: "Fullerenes and Atomic Clusters" and "Physics of Solid State Nanostructures").

References

[1] N. A. Bert, V. V. Chaldyshev, A. E. Kunitsyn, Yu. G. Musikhin, N. N. Faleev, V. V. Tretyakov, V. V. Preobrazhenskii, M. A. Putyato and B. R. Semyagin, *Appl. Phys. Lett.* **70**, 3146 (1997).

[2] F. W. Smith, A. R. Calawa, C. L. Chen, M. J. Mantra and L. J. Mahoney, *Electron. Dev. Lett.* **9**, 77 (1988).

[3] N. A. Bert, V. V. Chaldyshev, D. I. Lubyshev, V. V. Preobrazhenskii and B. R. Semyagin, *Semiconductors* **29**, 2232 (1995).

[4] V. V. Chaldyshev, N. A. Bert, A. E. Kunitsyn, Yu. G. Musikhin, V. V. Preobrazhenskii, M. A. Putyato, B. R. Semyagin, V. V. Tretyakov and P. Werner, *Semiconductors* **32**, 1161 (1998).

[5] S. Takagi, *J. Phys. Soc. Jpn.* **26**, 1239 (1969).

[6] D. Suzuki, H. Yamaguchi and Y. Horikoshi, *Jpn. J. Appl. Phys.* **37**, 758 (1998).

7th Int. Symp. "Nanostructures: Physics and Technology"
St Petersburg, Russia, June 14–18, 1999

Resonant tunneling through GaAs quantum well with embedded InAs quantum dots

E. E. Vdovin, Yu. N. Khanin, K. S. Novoselov, D. Yu. Ivanov, Yu. V. Dubrovskii, L. Eaves†, P. C. Main†, A. Patanè†, A. Polimeni†, M. Henini†, J. Middleton† and G. Hill‡

Institute of Microelectronics Technology RAS, 142432 Chernogolovka, Russia
† The School of Physics and Astronomy, University of Nottingham,
Nottingham NG7 2RD, United Kingdom
‡ Department of Electrical and Electronic Engineering,
University of Sheffield, Sheffield S1 3RD, United Kingdom

In recent years there has been great interest in the properties of heterostructures containing self assembled InAs quantum dots (QD) [1–8]. To identify their electronic states, photoluminescence (PL) and PL excitation spectroscopies [1–3], capacitance spectroscopy [4], far-infrared spectroscopy [5], and resonant tunneling via InAs QD [6, 7] have been performed.

InAs QD in semiconductor nanostructures can be used to monitor their physical properties. For example, Main *et al.* [8] have used InAs QD to probe the local density of states of a two-dimensional electron system at all energies from the sub-band edge to the Fermi energy. On the other hand, double-barrier heterostructures (DBHS) have been studied extensively due to the resonant tunneling phenomenon exhibited in these systems, leading to numerous potential applications in ultra high-speed electronic devices. In the present work we are concerned with a study of the tunneling current through a GaAs-$Al_{0.4}Ga_{0.6}As$ double-barrier heterostructure with InAs QD embedded in the well region.

The samples were grown by molecular-beam epitaxy on a $n^+(100)$ GaAs substrate. The structure consisted (in the order of growth) of a lightly Si-doped, 300-nm-thick GaAs layer ($N_d = 3 \cdot 10^{18}\,cm^{-3}$), a 50.4-nm-thick GaAs layer ($N_d = 2 \cdot 10^{17}\,cm^{-3}$), a 50.4-nm-thick undoped GaAs layer; a 8.3-nm-thick $Al_{0.4}Ga_{0.6}As$ barrier layer; a 5.6 nm undoped GaAs layer, 1.8 monolayers (ML), or 2.3 ML InAs with growth rate 0.13 ML/s to form InAs QD, a 5.6-nm-thick undoped GaAs layer, a 8.3-nm-thick $Al_{0.4}Ga_{0.6}As$ barrier layer, a 50.4 nm undoped GaAs layer, a 50.4-nm-thick GaAs layer ($N_d = 2 \cdot 10^{17}\,cm^{-3}$), a 300-nm-thick GaAs layer ($N_d = 3 \cdot 10^{18}\,cm^{-3}$) cap-layer. A control sample, lacking the InAs layer but identical otherwise, was also grown.

Ohmic contacts were obtained by successive deposition of AuGe/Ni/Au layers and subsequent annealing. Mesa-structures were fabricated by conventional chemical etching.

The current-voltage ($I-V$) characteristics at 4.2 K of the samples with 200 μm mesa diameter are shown in Fig. 1. Curve 1 corresponds to the sample without QD, and curves 2 and 3 to the samples with 1.8 ML and 2.3 ML of InAs in the centre of the QW respectively. The sample without QD has three resonant peaks due to tunneling via quantum-well quasi-bound states. The second and the third resonances exhibit bistability in the form of strong hysteresis in the $I-V$ curves arising from the electrostatic effects of a buildup of negative space charge in the quantum well when biased at resonance [9]. In the $I-V$ curves of the samples with QD the first resonance is suppressed and only wide shoulders are left in the appropriate voltage bias region. The second resonance is roughly at the same bias for the 1.8 ML sample as for the one without QD, and apparently weaker for the 2.3 ML sample.

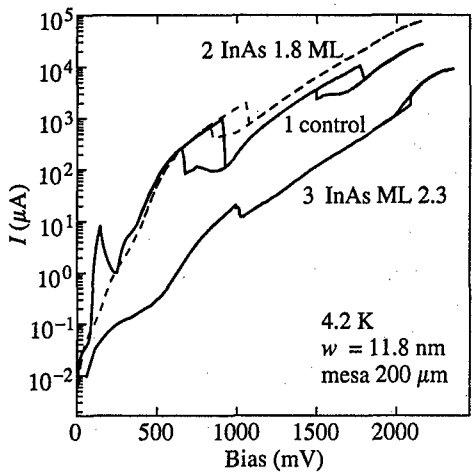

Fig. 1. $I-V$ characteristics of the experimental devices at 4.2 K.

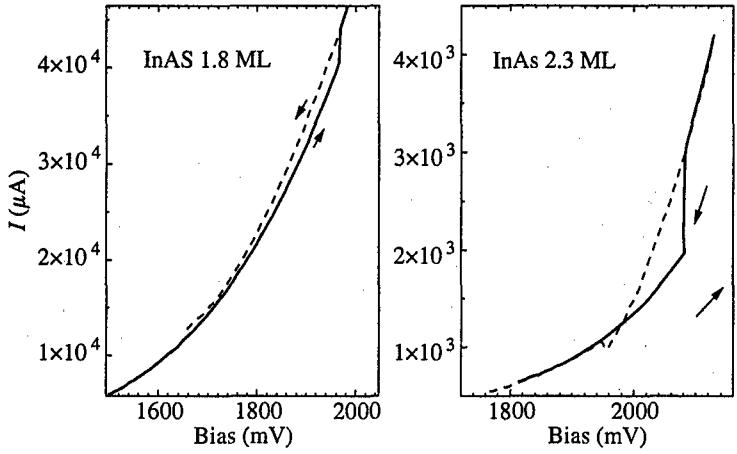

Fig. 2. $I-V$ characteristics in the region of the "inverted bistability" of the samples with different QD embedded in the well.

The third resonances of both QD samples display an unusual shape and are shown in more detail in Fig. 2.

To explain the difference between hows the first and second resonances appear in the $I-V$ curves of the different samples it is enough to take into account the influence of the localised perturbation generated by the InAs QD. It is strong for the first resonance associated with the first quasibound state when the wave function has the amplitude maximum coincident with the QD location in the well. It is weaker for the second resonance since the density maximum of the electronic wave function for the second subband is located far from the centre of the QW.

The distinguishing feature of the third resonances of the samples with QD is that the off-resonant current is greater then the on-resonant one when the bias is swept from low to higher voltage. Similar behaviour of the current near the second resonance was observed previously [10] on asymmetric double barrier structures when the bias was swept in the

reverse direction and was termed "inverted bistability". The effect arose from the additional charge buildup in the lowest subband in the well on resonance originating from inelastic, intersubband electron transfer in the well. In contrast, in the off-resonant condition, the energy of the top of the second barrier is lowered so that off-resonant electrons have only to pass one barrier, while on-resonant electrons must pass two barriers. We argue that the interplay of the intersubband scattering rates is strongly increased by the presence of the perturbation potential from the QD and relative positions of the subband levels in the wells could create the "inverted bistability" with the shapes found in the present work.

Thus we have investigated the electron resonant tunneling through the GaAs quantum wells with embedded InAs quantum dots. It was found that the localised perturbation generated by the InAs quantum dots strongly influences the wave functions of the subband states in the quantum wells. The "inverted bistability" of the third resonance was observed for the samples with quantum dots. The shape of the resonances on the $I-V$ curves under "inverted bistability" differs from that previously observed adding to the collection of the butterfly-like resonances on the double barrier structures.

This work was partly supported by the INTAS-RFBR (grant 95-849), RFBR (98-02-17642), national program "Physics of solid state nanostructures" (97-1057) (Russia), and by EPSRC(UK).

References

[1] S. Fafad, D. Leonard, J. L. Merz, *et al.*, *Appl. Phys. Lett.* **65**, 1388 (1994).
[2] J. Y. Marzin, J. M. Geraad, A. Izrael, *et al.*, *Phys. Rev. Lett.* **73**, 716 (1994).
[3] R. Leon, S. Fafad, D. Leonard, *et al.*, *Appl. Phys. Lett.* **67**, 521 (1995).
[4] R. N. Brunkov, A. Polimeni, S. T. Stoddart, *et al.*, *Appl. Phys. Lett.* **73**, 1092 (1998).
[5] H. Draxler, D. Leonard, W. Hansen, *et al.*, *Phys. Rev. Lett.* **73**, 2252 (1994).
[6] M. Narihiro, G. Yusa, Y. Nakamura, *et al.*, *Appl. Phys. Lett.* **70**, 105 (1997).
[7] K. A. Benedict, A. S. G. Thornton, T. Ihn, *et al.*, *Physica B* **256-258**, 519-522 (1998).
[8] P. C. Main, A. S. G. Thornton, T. Ihn, *et al.*, *Physica B* **256-258**, 507-513 (1998).
[9] M. L. Leadbeater, L. Eaves, P. E. Simmonds, *et al.*, *Solid-State Electron.* **31**, 707 (1988).
[10] M. L. Leadbeater, L. Eaves, M. Henini, *et al.*, *Solid-State Electron.* **32**, 1467 (1989).

7th Int. Symp. "Nanostructures: Physics and Technology"
St Petersburg, Russia, June 14–18, 1999

The step-like features on the I–V curves of the resonant tunneling diodes: current vortexes?

V. A. Volkov, M. Feiginov, *Yu. V. Dubrovskii*†, V. G. Popov†, E. E. Vdovin†, L. Eaves‡, P. Main‡, M. Henini‡, A. K. Geim§, J. K. Maan§ and M. S. Skolnick¶

Institute of Electronics and Radioengineering RAS, Moscow 103907, Russia
† Institute of Microelectronics Technology RAS,
142432 Chernogolovka, Russia
‡ The School of Physics and Astronomy, University of Nottingham,
Nottingham NG7 2RD, United Kingdom
§ High Field Magnet Laboratory, Research Institute for Materials,
University of Nijmegen, 6525 ED Nijmegen, The Netherlands
¶ Department of Physics, University of Sheffield,
Sheffield S3 3JD, United Kingdom

Since the pioneering work of Tsu and Esaki [1], where the idea of the resonant tunneling diode was proposed, an enormous number of publications have been dedicated to its study. The range of the considered phenomena extends from the background physics to the design of sophisticated devices. Generally, transport through double barrier resonant tunneling structures (DBRTS) is considered as one-dimensional. Only recently few researchers begun to consider the lateral (in the plane of the barriers) current distribution [2, 3].

Here we present resonant tunneling current measurements in DBRTSs of various diameters, but with otherwisethe identical structure. I–V curves of samples with large diameters demonstrate step-like features in the negative differential conductance (NDC) region of the I–V curve. The features could be distinguished from the similar ones related to external circuit oscillations. It is shown that self-excitation of the current vortexes in the barrier region could be a possible reason for the observed step-like phenomena.

The samples were grown by MBE and are symmetric $GaAs/Al_{0.4}Ga_{0.6}As$ DBRTSs with 8.2 nm thick barriers and a quantum well of width 11.8 nm. The barriers are separated from the highly doped bulk contact regions by 30 nm thick undoped GaAs spacer layers. Samples of 5, 10, 20, 50 and 100 μm diameters were fabricated.

Fig. 1 shows I–V curves of a DBRTS with 10 μm diameter in various magnetic fields perpendicular to the current flow. The I–V curves coincide with that of a 5 μm diameter structure normalized to the mesa area. Magnetic field is applied to change the value of negative differential conductance σ which is the critical parameter in the theory of the external circuit oscillations. The variation of the I–V curves with magnetic field have been earlier studied in detail [4]. In that case it was discussed in terms of the Lorenz force with the help of a simple graphical model used for the description of the conservation laws describing the tunneling. It was shown that the in-plane magnetic field broadens the resonance: it moves to the right and decreases in amplitude. The same is observed in our structures.

All the I–V curves of the 10 μm and 5 μm structures are stable in the NDC region. There are no hysteresis or step-like features, which would appear if the external circuit oscillated [5]. It can be shown that the stability condition for the simple equivalent circuit

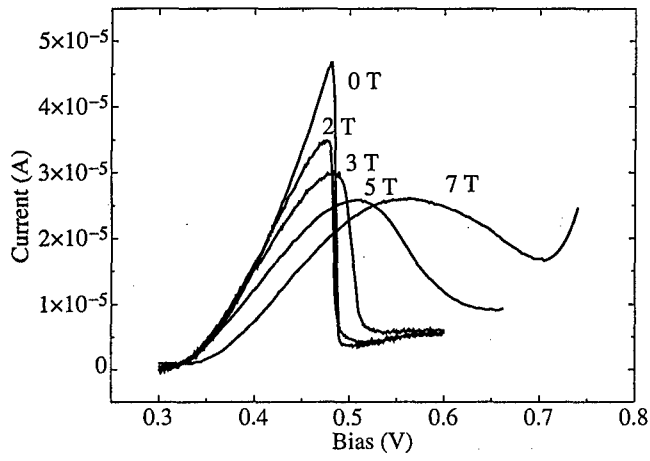

Fig. 1. Current-voltage characteristics of the DBRTS with 10 μm mesa diameter in the different magnetic fields perpendicular to the current flow. $T = 4.2$ K.

of a sample load resistor (R) in series with an inductor (L), and parallel to a sample capacitance (C) is

$$| \sigma | \leq \frac{R C}{L}, \tag{1}$$

The sample in this circuit is considered as a resistor with negative differential conductance σ.

It is clear from Fig. 1 that $| \sigma |$ decreases with magnetic field. We can consider the measured I–V curves of the 10 μm structure as the intrinsic ones of our DBRTS in so far as there are no oscillations in the NDC region. With the increase of the magnetic field from 0 to 7T, $| \sigma |$ decreases 100 times. This means that the stability condition should be fulfilled for all the samples with diameters up to 100 μm in magnetic field B=7T in the same experimental environment. This may not be true for smaller magnetic fields and below we focus on the data when the stability condition is satisfied.

Fig. 2 shows I–V curves measured on 20, 50 and 100 μm diameter samples in a magnetic field of $B = 7$ T. The currents are normalized to 10 μm mesa diameter. All the curves were measured with the same external circuit. Step-like features in the NDC region appear and the number of steps is roughly proportional to the mesa diameter. Using a standard oscilloscope we did not observe any oscillations in the NDC regions of the I–V curves shown in Fig. 2.

To emphasize the above observations Fig. 3 shows the differential conductance of the 10 μm sample in $B = 2$ T, and that if the 20 μm sample in $B = 7$ T. The 20 μm sample has one step in the NDC region when $| \sigma |$ is much less then the maximum negative differential conductance of the 10 μm structure.

We argue that one of the possible reasons for appearance of the observed steps is the following. Let's choose the the growth direction as the z-axis, and the y-axes along the magnetic field B. It is natural to suppose that the local intrinsic I–V curve has a form analogous to that shown in the Fig. 1. Fluctuations of the charges in the semiconductor regions can build up under certain conditions due to the fact that σ is negative. In more formal language that means that the so-called junction plasmons [6, 7] are unstable. In the vicinity of an arbitrary point on the I–V curve (V_0, j_0) the build up of the instability

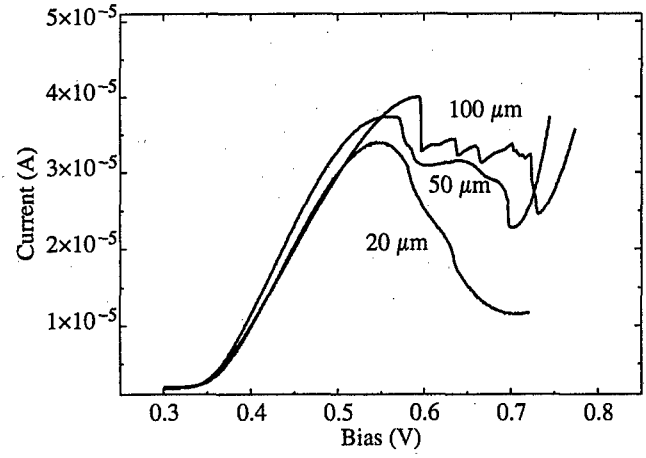

Fig. 2. Current–voltage characteristics measured on 20, 50 and 100 μm samples in magnetic field of $B = 7$ T perpendicular to the current flow. The currents are normalized to 10 μm mesa diameter. $T = 4.2$ K.

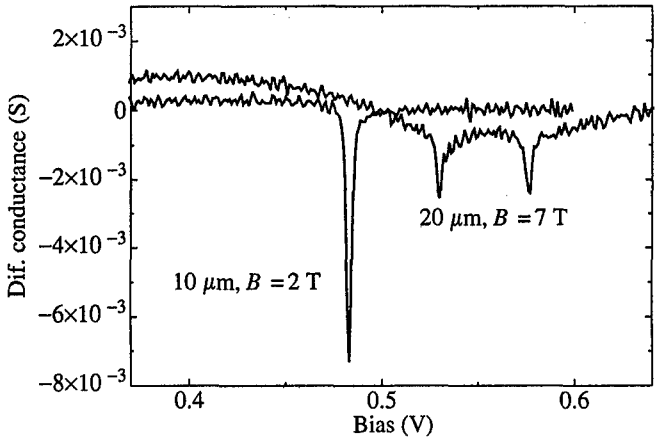

Fig. 3. Differential conductance of the 10 μm sample in the field of $B = 2$ T, and of the 20 μm sample in the field of $B = 7$ T. $T = 4.2$ K.

can lead to a current vortex. The fact that the current lines are closed means that the current fluctuations in the x-direction (δj_x) in the upper n-GaAs layer are closed in the z-direction through the fluctuation of the tunnel current (δj_z). The fluctuations $\delta j_z = \sigma \delta V$ and $\delta j_x = \sigma_{xx} \delta E_x$ are connected with each other by the continuity equation: $\delta j_x + \delta j_z = 0$. Taking into account that the fluctuation of the lateral electric field is $\delta E_x \approx \delta V / L_x$, one can obtain an assessment of the lateral size of the vortex:

$$L_x(B) \approx \frac{\sigma_{xx}(B)}{\sigma(B)}. \tag{2}$$

In our samples we estimate L_x is of the order of 100 μm in $B = 7$ T. If the diameter of the DBRTS is less than L_x the vortexes cannot appear and there are no steps in the I–V

curve. If the diameter increases or $L_x(B)$ diminishes, at first one vortex appears, then two vortexes, etc. Each one of them is accompanied by a step-like feature on the I–V curve.

Thus we have found the step-like features in the I–V curves of double-barrier resonant tunneling structures. These cannot readily be explained in terms of external circuit oscillations. A theoretical model is proposed that the appearance of the step-like features in the negative conductance region of the I–V characteristics is due to the self-excitation of current vortexes in the barrier region of the DBRTS.

This work was partially supported by INTAS-RFBR (grant 95-849), RFBR (98-02-17642 and 99-02-17592), and National program "Physics of solid state nanostructures" (grants 97-1057 and 96-1019). Yu.V.D. acknowledges the Royal Society for the financial support.

References

[1] R. Tsu and L. Esaki, *Appl. Phys. Let.* **22**, 562 (1973).
[2] C. Zhang, M. L. F. Lerch, A. D. Martin et al., *Phys. Rev. Lett.* **72**, 3397 (1994).
[3] M. N. Feiginov and V. A. Volkov, *JETP Lett.* **68**, 662 (1998).
[4] M. L. Leadbeater, L. Eaves, P.E. Simmonds et al., *Solid-State Electron.* **31**, 707 (1988).
[5] T. C. L. G. Sollner, *Phys. Rev. Lett.* **59**, 1622 (1987).
[6] V. I. Talyanskii, *JETP* **101**, 1846 (1992).
[7] S. A. Mikhailov and V. A. Volkov, *JETP Lett.* **61**, 508 (1995).

7th Int. Symp. "Nanostructures: Physics and Technology"
St Petersburg, Russia, June 14–18, 1999

Quantum-well plasma instability in the resonant tunneling regime

M. N. Feiginov†, V. A. Volkov†, L. Eaves‡ and J. K. Maan§
† Institute of Radioengineering and Electronics of RAS,
11 Mokhovaya st., Moscow, 103907, Russia
‡ University of Nottingham,
Nottingham NG7 2RD, United Kingdom
§ High Field Magnet Laboratory, University of Nijmegen,
6525 ED Nijmegen, the Netherlands

Abstract. The resonant tunneling is accompanied by the accumulation of the 2D electrons in the well between the barriers of the double-barrier heterostructures. It leads to the $I-V$ curve of Z-type in the high-quality structures. We have shown that it also leads to the instability of the 2D plasmons in the quantum well. The build up of the instability can give rise to the lateral static domains in the tunnel current, that in its turn results in the kinks in the region of the central arm of Z of the $I-V$ curve.

As a rule the double-barrier resonant tunneling structures (DBRTS) have the $I-V$ curves of N-type [1]. However in the high quality structures the accumulation of the 2D electrons in the quantum well (QW) of the DBRTS is to result in the transformation of the $I-V$ curve of N-type to that of Z-type [2]-[6]. If one uses the ordinary experimental technique (say, the load line is close the vertical one), it is seen as hysteresis or bistability in the $I-V$ curve. A new experimental technique has been proposed recently, where a negative load resistance is realized [7]. The technique allows one to measure the $I-V$ curves of Z-type. An additional peak in the region of the central arm of Z was observed with the help of the technique [8]. The interpretation of the experimental results [7], [8] depends on the solution of the stability problem of the homogeneous (along the QW) distribution of the currents and charges in the DBRTS with respect to the inhomogeneous perturbation in the Z-type region of the $I-V$ curve. The first part of the paper is devoted to the solution of the problem. The problem is formulated in the terms of the 2D plasmons – low-frequency charge oscillations in the QW. The second part of the paper is devoted to the the static nonlinear nonhomogeneous distribution of the tunnel current and charge density in the QW.

1 The spectrum of 2D plasmons in the QW

We consider the DBRTS in the sequential tunneling model. The set of equations describing the time and spatial (x, y) distribution of the currents and potentials in the QW consists of the material Eq. (1), continuity Eq. (2), the Eq. (3) that follows from the Poisson equation in the local capacitance approximation, the equations for the emitter-well (J_{ew}) (4) and well-collector (J_{wc}) (5) tunnel currents, respectively:

$$\frac{\partial \mathbf{J}}{\partial t} + \nu \mathbf{J} = \frac{\sigma \nu}{e} \nabla E_{fw}, \tag{1}$$

$$-e\frac{\partial}{\partial t} N_{2D} + \nabla \mathbf{J} = J_{ew} - J_{wc}, \tag{2}$$

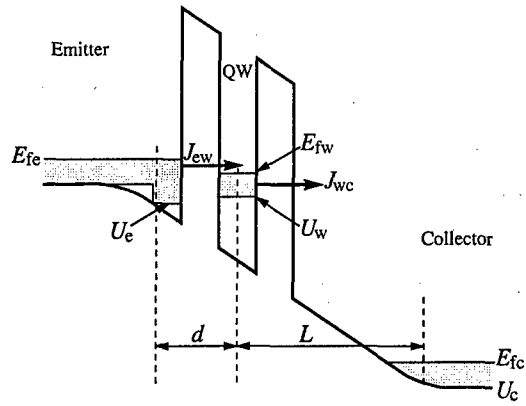

Fig. 1. The energy diagram of the DBRTS in the regime of the resonant tunneling.

$$V - V_0 = \frac{e^2}{C} N_{2D} - \left(E_{fe}^0 - E_{fc}^0\right) \frac{d}{L+d}, \tag{3}$$

$$J_{ew} = -\left[E_{fe} - E_{fw} - (E_{fe} - U_w)\,\theta(U_w - E_{fe})\right] \rho_{2D} \frac{e}{\tau_e} \tilde{\theta}(V), \tag{4}$$

$$J_{wc} = -N_{2D} \frac{e}{\tau_c}, \tag{5}$$

see the notations in Fig. 1. $\mathbf{J}(x, y)$ is the density of the 2D current in the QW; $V = U_w - U_e$. For simplicity we supposed that the bottom of the 2D subband in the QW is higher than the Fermi energy in the emitter, when the energy shift due to the external bias (V_{ext}) is equal to zero, $V = V_0$ in the case. ρ_{2D} is the 2D density of states in the QW, $N_{2D} = [E_{fw} - U_w]\rho_{2D}$ is the local 2D concentration of the electrons in the QW, τ_e and τ_c are the life times of electrons in the QW due to the tunneling to the emitter and collector, respectively. $C = \epsilon(L + d)/4\pi Ld$, $\nu = 1/\tau$ is the reciprocal momentum relaxation time in the QW, $\sigma = N_{2D}e^2/m^*\nu$ is the static 2D conductance of the QW. The form-factor $\tilde{\theta}(V)$ describes the broadening of the resonant levels. If the broadening is neglected, $\tilde{\theta}(V) = \theta(V)$, where $\theta(V)$ is the step function. One gets the known Z-type $I-V$ curve from the set of Eqs. (1)–(5) if all the variables are supposed to be static and homogeneous (we use the superscript "0" for the solution).

Linearizing the Eqs. (1)–(5) in the vicinity of the homogeneous static solution, one gets [9] the set of equations describing the screened 2D plasmon in the QW. The dispersion Eq. of the 2D plasmons is:

$$(\omega + \imath\nu)\,(\omega + \imath\nu_T) = \frac{\sigma^0 \nu}{C} \left(1 + \frac{C}{e^2 \rho_{2D}}\right) q^2, \tag{6}$$

$$\nu_T = \frac{1}{\tau_c} + \frac{\tilde{\theta}(V^0)}{\tau_e} + \frac{e^2 \rho_{2D}}{C} \left[\frac{\tilde{\theta}(V^0)}{\tau_e} - \frac{\left[E_{fe} - U_e - V^0\right]}{1 + \tilde{\theta}(V^0)\tau_c/\tau_e} \frac{\tilde{\theta}'(V^0)}{\tau_e}\right], \tag{7}$$

here q is the 2D wavevector of the plasmons. The plasmons are unstable in time when $Im(\omega) > 0$. The analysis of the Eqs. (6) and (7) (see [9]) shows that 2D plasmons are unstable in the central arm of Z of the $I-V$ curve: (i) in the case of $-\nu < \nu_T < 0$ provided

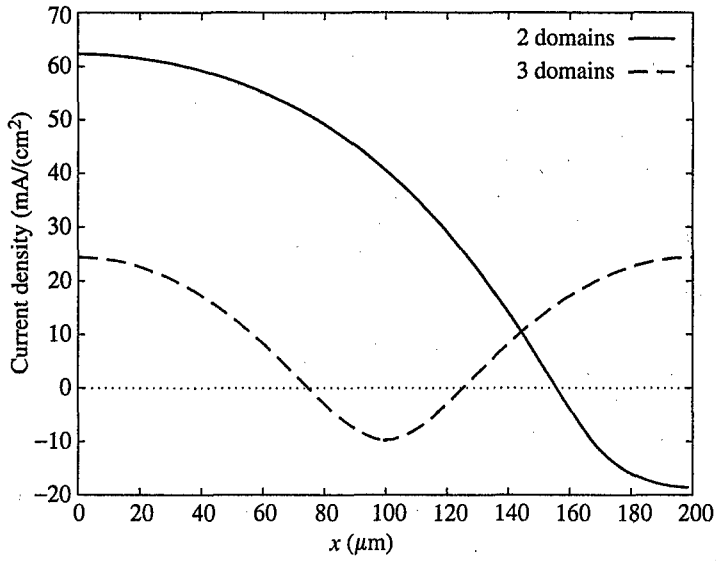

Fig. 2. The deviation of the tunnel current from the homogeneous solution in the case of 2 domains (full curve) and 3 domains (dashed curve).

$q < q_0$ (i.e. the width of DBRTS is sufficiently large: $W > \pi/q_0$); (ii) in the case of $-\nu_T > \nu$ and arbitrary values of W and q; here

$$q_0 = \sqrt{-\frac{\nu_T C}{\sigma^0}\left(1+\frac{C}{e^2\rho_{2D}}\right)^{-1}}. \tag{8}$$

The instability does not depend on the external circuit. For the parameters of DBRTS taken from Refs. [7, 8] length $\pi/q_0 \approx 150\,\mu$m.

2 Inhomogeneous nonlinear solution

If $-\nu < \nu_T < 0$ the 2D plasmons build up without oscillations in time in the central arm of Z of the $I-V$ curve. The increase in amplitude should be stopped by the nonlinear effects. The nonlinear static solutions follow from the set of Eqs. (1)–(5). They describe the domain-like distribution of the tunnel current and the 2D charge in the QW. For the illustration of the phenomenon we present here the calculation result of the inhomogeneous tunnel current distribution (see Fig. 2) and the $I-V$ curve (see Fig. 3). The parameters of the DBRTS where taken from the papers [7, 8]. Due to the appearance of the domain structure in the tunnel current, the kinks appear in the central arm of Z of the $I-V$ curve (see Fig. 3) that qualitatively corresponds to the experimentally observed [8] features of the $I-V$ curve of Z-type.

3 Conclusions

We have shown that in the high quality DBRTS with the $I-V$ curve of Z-type, the 2D screened plasmons are unstable in the central arm of the Z in the following cases: (i) in the structures of any width (W) if $\nu_T < -\nu$; (ii) in sufficiently wide structures ($W > \pi/q_0$)

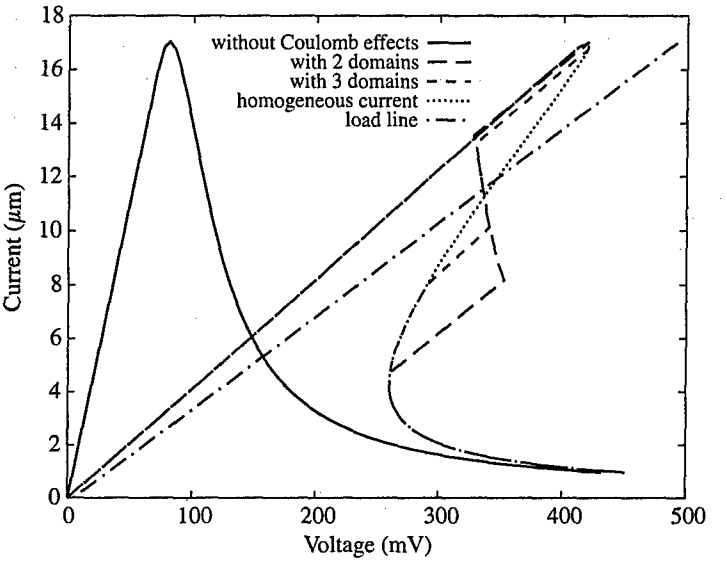

Fig. 3. The $I-V$ curves of the DBRTS.

if $-v < v_T < 0$. The instability does not depend on the external circuit and the load resistance may be positive as well as negative. The build up of the instability can give rise to the static domains in the tunnel current, that in its turn results in the kinks in the Z-region of the $I-V$ curve. The result is in a qualitative agreement with the experiment [8].

The work is partially supported by INTAS-RFBR (No 95-0849) and RFBR (No 99-02-17592).

References

[1] H. Mizuta and T. Tanoue, *The Physics and Applications of Resonant Tunneling Diodes* Cambridge University Press, 1995.
[2] F. W. Sheard and G. A. Toombs, *Appl. Phys. Lett.* **52**, 1228 (1988).
[3] V. J. Goldman, D. C. Tsui and J. E. Cunningham, *Phys. Rev. Lett.* **58**, 1256 (1987).
[4] A. Zaslavsky, V. J. Goldman, D. C. Tsui and J. E. Cunningham, *Appl. Phys. Lett.* **53**, 1408 (1988).
[5] R. K. Mains, J. P. Sun and G. I. Haddad, *Appl. Phys. Lett.* **55**, 371 (1988).
[6] H. L. Berkowitz and R. A. Lux, *J. Vac. Sci. Technol.* **B5**, 967 (1987).
[7] A. D. Martin, M. L. F. Lerch, P. E. Simmonds and L. Eaves, *Appl. Phys. Lett.* **64**, 1248 (1994).
[8] C. Zhang, M. L. F. Lerch, A. D. Martin, P. E. Simmonds and L. Eaves, *Phys. Rev. Lett.* **72**, 3397 (1994).
[9] M. N. Feiginov and V. A. Volkov, *JETP Lett.* **68** (8), 633 (1998).

7th Int. Symp. "Nanostructures: Physics and Technology"
St Petersburg, Russia, June 14–18, 1999

Scanning tunneling microscope investigations of local photoconductivity in InGaAs/GaAs quantum-dimensional nanostructures

V. Ya. Aleshkin, A. V. Biryukov, S. V. Gaponov, Z. F. Krasil'nik
and *V. L. Mironov*
Institute for Physics of Microstructures of the Russian Academy of Science, 603600 Nizhny Novgorod, GSP-105, Russia

Abstract. We demonstrate a possibility of using a scanning tunneling microscope (STM) for high spatial resolution study of photoconductivity spectra of quantum-dimensional structures. Measurements of the photoconductivity spectra from quantum dots located near a sample surface reveal some features related to the energy spectra of these quantum dots.

The conventional methods for study of photoconductivity and photoluminescence of quantum well/dot semiconductor structures provide test-area — averaged data, which largely overestimate the characteristic lateral scales in a structure, namely, quantum dot sizes, scale of quantum well doping inhomogeneities, etc. [1, 2]. Application of probe microscopy techniques allows to appreciably upgrade spatial resolution by decreasing the aperture of a beam of exciting or detected radiation. Major advances in this area are associated with the use of a near-field optical microscope for investigation of photoconductivity [3, 4] and photoluminescence [5, 6] of quantum-dimensional structures. However, we believe that most promise is involved in a study of local photoconductivity of such structures by photoresponse in the scanning tunneling microscope (STM) tunnel current, since using a tunneling contact as photocurrent detector allows to confine the probe area to one quantum dot.

In the present paper we report the results obtained in a research of local photoconductivity of $In_xGa_{1-x}As/GaAs$ quantum wells and quantum dots, using STM in combination with an optical system [7]. A halogen lamp radiation passed through a monochromator was used as optical pump. The monochromatic radiation was then carried by a multicable waveguide to the substrate of a semiconductor structure, that served as a filter cutting off quanta of light with an energy larger than the GaAs forbidden gap width. Therefore, photocarriers were generated only in $In_xGa_{1-x}As$. Investigations included $In_xGa_{1-x}As/GaAs$ epitaxial structures [2] of n-type conductivity, whose tunneling contact I–V characteristic is typical for the Schottky barrier. The probe was held over surface via an STM feedback system at j_t = const and at voltage corresponding to the direct branch of the I–V curve. The photocurrent was measured as a difference between the current in the I–V curve backward branch for a excited contact and the dark current.

Spatial resolution in this method depends, in the first place, on diffusion processes of photocarriers determining the photocurrent flow through a tunneling contact. The character of the diffusion processes largely depends on the depth of a quantum structure location relative to the near-surface space charge area (SCA). If a quantum well is outside the SCA, the size of the area from which photocarriers are collected on the STM probe is determined by the diffusion length of the carriers in a GaAs overgrown layer and in a $In_xGa_{1-x}As$ well. If a quantum structure is inside the SCA, spatial resolution primarily depends on such factors as photocarriers transit in a strong near-surface field and their capture at deep surface states. For quantum dots located near the surface the role of duffusion processes

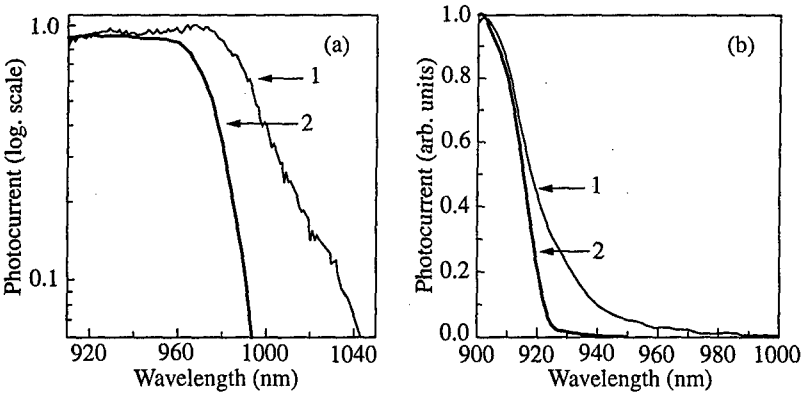

Fig. 1. Photoconductivity spectra of structures containing a GaAs/InGaAs quantum well (a) and a layer of GaAs/InAs quantum dots (b). The thickness of the GaAs overgrown layer is 250 and 320 nm, respectively. Curves 1 are obtained in the conventional technique of photocurrent measurements on macrocontacts. Curves 2 are yielded by measuring a local photoresponse in STM.

is insignificant, and spatial resolution can in principle be upgraded to the size of the wave function of minority carriers.

The experiments have demonstrated a rather strong dependence of the STM photocurrent value on the intensity and wavelength of exciting radiation. Fig. 1 shows the photoexcitation spectra from an $In_xGa_{1-x}As/GaAs$ heterostructure with a quantum well located at $\sim$ 250 nm depth (a) and from a heterostructure containing a layer of InAs quantum dots in GaAs at $\sim$ 320 nm depth (b). The STM spectra were compared with the ones obtained in the conventional technique of measuring a photocurrent via $\sim$ 500 μm diameter macrocontacts deposited onto sample [2]. As was shown in the experiments, the STM photoconductivity spectra feature a sharper long-wave end which is responsible for absorption of light at size-quantization levels. This may be accounted for by the fact that the region from which photocarriers are collected on the STM probe is by far smaller than the sizes of macrocontacts and, hence, the spectrum is less blurred through fluctuations of the $In_xGa_{1-x}As$ layer thickness and composition.

In Fig. 2(a) there is a photoconductivity spectrum from the layers of quantum dots grown near a sample surface. To prevent oxidation such structures were immersed in oil immediately after growth, so the spectra were taken from the tunneling contact made through an oil interlayer. For quantum dots grown near a sample surface diffusion processes were insignificant and one could observe a fine structure of the long-wave end of photoexcitation (shown by arrows in the figure), which is believed to correspond to the size quantization levels in quantum dots and in a thin wetting layer of InAs.

Along with the spectral measurements we investigated the distribution inhomogeneity of a photoresponse across sample surfase. To this effect, in the course of scanning we interrupted the feedback loop in each point of the frame and recorded the current value in the backward branch of the semiconductor curve. Fig. 2(b) exemplifies a photoresponse distribution across the surfase of a structure containing a quantum well at a 250 nm depth. The dark spots indicate the no-response areas of the structure. The image contrast may depend on both quantum well inhomogeneity and local properties of the overgrown layer. Therefore, a correct interpretation will require further research on the morphology and properties of the overgrown layer.

In summary, a possibility of using STM for high spatial resolution of local photocon-

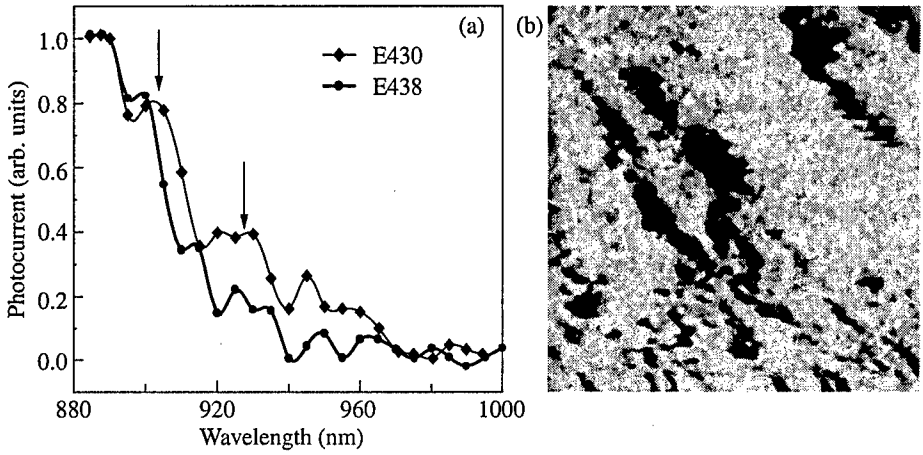

Fig. 2. (a) STM spectra of photoconductivity for structures with InAs/GaAs quantum dots located near sample surface. The thickness of the overgrown layer for sample E438 is 2 nm, for sample E430—1.5 nm. (b) Photoresponse distribution across the surface of a sample containing a quantum well at a 250 nm depth. Frame size is 1×1 μm.

ductivity in quantum-dimensional structures is reported. For structures with quantum dots grown on sample surface the probe area can be confined to one quantum dot, which allows investigations of individual energy spectrum for this dot.

Acknowledgements

The authors are thankful to D. Revin for assistance in this work, to A. Murel for providing the data on photoconductivity mesurements on macrocontacts, and to O. Khrykin and V. Danil'tsev for providing experimental samples.

This work was supported by the State Committee Science and Technology programme "Fundamental metrology" (project 3.45) and the RFBR grants No. 96-02-16990a, 98-02-16625.

References

[1] A. W. Leitch and H. L. Ehlers, *Infrared Phys.* **6**, 28 433–440 (1998).

[2] V. Ya. Aleshkin, D. M. Gaponova, S. A. Gusev et al., *Phys. & Tech. Semicond.* **1**, 32 111–116 (1998).

[3] S. K. Buratto, J. W. P. Hsu, E. Betzig and J. K. Trautman, et. al., *Appl. Phys. Lett.* **21**, 65 2654-2656 (1994).

[4] M. S. Ünlü, B. B. Goldberg and W. D. Herzog, *Appl. Phys. Lett.* **13**, 67 1862-1864 (1995).

[5] T. D. Harris, D. Gershoni, L. Pfeiffer, M. Nirmal, et al., *Semicond. Sci. Technol.* **11**, 1569-1574 (1996).

[6] A. Chavez-Pirson, J. Temmyo, H. Kamada, H. Gotoh and H. Ando, *Appl. Phys. Lett.* **26**, 72 3494-3496 (1998).

[7] D. G. Volgunov, S. V. Gaponov, V. F. Dryakhlushin, et al., *Instruments and Experimental Techniques* **2**, 41 123-128 (1998).

7th Int. Symp. "Nanostructures: Physics and Technology"
St Petersburg, Russia, June 14–18, 1999

Tunneling between strongly localized two-dimensional electron systems

Yu. V. Dubrovskii, E. E. Vdovin, Yu. N. Khanin, V. G. Popov,
D. Yu. Ivanov, D. K. Maude†, J.-C. Portal†, L. Eaves‡, P. C. Main‡,
M. Henini‡, J. Middleton‡, A. K. Geim¶, J. K. Maan¶ and G. Hill§
Institute of Microelectronics Technology RAS, 142432 Chernogolovka, Russia
† Grenoble High Magnetic Field Laboratory, MPI-CNRS,
BP166 38042 Grenoble Cedex 9, France
‡ The School of Physics and Astronomy, University of Nottingham,
Nottingham NG7 2RD, United Kingdom
¶ High Field Magnet Laboratory, Research Institute for Materials,
University of Nijmegen, 6525 ED Nijmegen, The Netherlands
§ Department of Electrical and Electronic Engineering, University of Sheffield,
Sheffield S3 3JD, United Kingdom

Over the last decade, various authors have shown that [1–7] both resonant and many-body effects play an essential role in tunnelling between parallel two-dimensional electron gases (2DEG). In earlier work [1] resonant tunnelling between different two-dimensional (2D) subbands as well as inter and intra Landau level tunnelling in a magnetic field normal to the 2D-plane were thoroughly investigated. It was shown [2] that the in-plane magnetic field also strongly influence resonant tunneling between two 2DEGs as it requires the conservation of both energy and in-plane momentum. The so-called Coulomb gap in the tunneling density of states was observed as the suppression of the tunneling current by a magnetic field for equilibrium tunneling between 2D-electron systems [3–6]. There is a general agreement that the observed suppression is related to the in-plane Coulomb correlation between 2D electrons in a high magnetic field. Another manifestation of the Coulomb correlation was found in double barrier resonant tunneling devices [7] where the voltage position of the resonant current peak shifted to higher voltage bias in a magnetic field. Recently it was shown [8] that weak disorder influences the suppression of the tunneling current and gives rise to a linear dependence of the gap magnitude on magnetic field in the ultraquantum limit (filling factor $\nu < 1$) while a square root dependence was observed [5, 7] for high quality 2DEGs.

In this work we present tunneling current measurements between strongly disordered two-dimensional electron systems (2DES) in a magnetic field parallel to the current. To form the 2DES we used Si donors sheets (δ-doped layers) with the donor concentration slightly above metal-insulator transition in the corresponding electron system [9, 10]. In a high enough magnetic field all the electrons in the studied δ-doped layers were strongly localized. In our experiments electron transport along the layers did not contribute to the measured current due to the special structure arrangement [8] (pure vertical transport). This allows us to measure for the first time the equilibrium current which is proportional to the tunneling density of states of the strongly localized 2D electron systems in a magnetic field.

The sample grown by MBE was a single barrier GaAs/$Al_{0.4}Ga_{0.6}As$/GaAs heterostructure with a 12 nm thick barrier. The barrier was separated from the highly doped bulk contact regions by 50 nm thick undoped GaAs spacer layers. Si donors sheets with concentration of 3×10^{11} cm^{-2} were located 5 nm from each side of the barrier. Measurements of the Shubnikov–de-Haas like oscillations in the tunneling current gave the same electron sheet

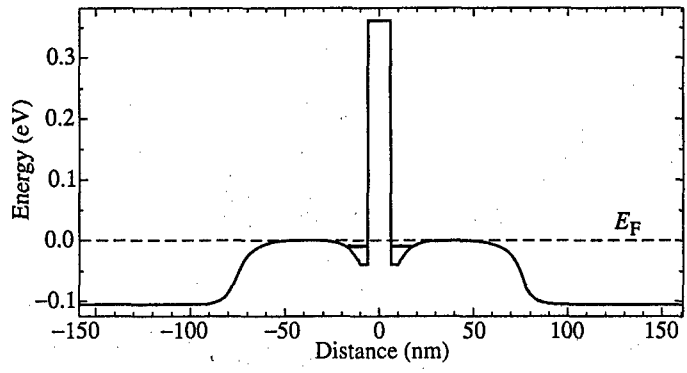

Fig. 1. Schematic band diagram of the structure at zero bias.

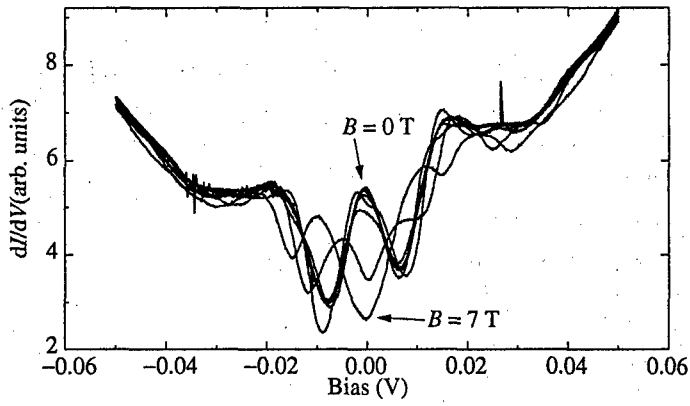

Fig. 2. The tunneling differential conductance as a function of external voltage in different magnetic fields up to 7 T. Magnetic field step between the curves is 1 T.

concentrations as the donor doping levels. Samples studied had 100 μm mesa diameters. The schematic band diagram of the structure under zero bias is shown in Fig. 1.

Figures 2 and 3 show the differential conductance versus external voltage at various magnetic fields. In zero magnetic field the differential conductance has a peak at zero voltage and two pronounced shoulders at higher voltages of both polarities. We argue that the zero voltage peak reflects resonant tunneling between ground states of the 2DEGs, and the shoulders are due to resonant tunneling between subbands of different indexes (0-1 transition). For our structure the metal-insulator transition is expected for a critical field about 5 T when the magnetic length becomes equal to the average donor separation.

The experimental curves could be described in principle on the interplay of resonance tunneling between different Landau levels taking into account the existence of two-dimensional subbands with higher indexes and the self-consistent redistribution of the electrons between accumulation layers as the density of states is modulation by the magnetic field.

In this work we concentrate on the equilibrium tunneling processes around zero bias. In magnetic fields around the critical value, the tunneling differential conductance exhibits a minimum at zero bias. At the same time only the lowest energy Landau levels in the respective layers are occupied (the spin splitting is not resolved) and as the result there is the minimum in the density of states around the Fermi level. The tunneling differential

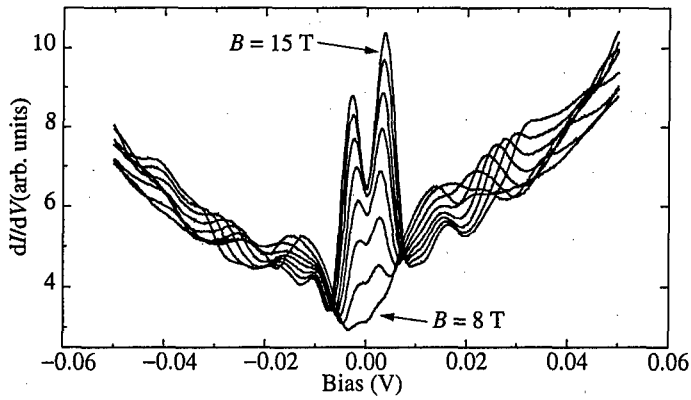

Fig. 3. The tunneling differential conductance as a function of external voltage in different magnetic fields from 8 T to 15 T. Magnetic field step between the curves is 1 T.

conductance at low voltage directly reflects the joint density of states at the Fermi levels in the 2D electron layers. With a futher increase of the magnetic field, the minimum of the differential conductance at zero bias gradually converts to a maximum reflecting again the density of states at the Fermi level. At the same time a dip at zero bias appears which reflects the gap in the tunneling density of states around the Fermi level of the strongly localized 2D electron systems.

The distance between maxima is well described by the expression $\Delta = (0.30 \pm 0.01)\hbar\omega_c$, where ω_c is the cyclotron frequency. It is difficult to compare this value with current theories because as far as we know there are no calculations of the gap dependence on the magnetic field for the strongly localized system. We would like only to emphasise that the measured dependence surprisingly coincides with the gap dependence on the magnetic field found for tunneling between slightly disordered 2D electron systems $\Delta = (0.28 \pm 0.02)\hbar\omega_c$ [8] for $\nu < 1$.

Thus we have investigated equilibrium tunnelling between strongly localized 2D electron systems in a high magnetic field in the structure with pure vertical transport. High magnetic field suppresses equilibrium tunneling creating a gap in the tunneling density of states which depends linearly on magnetic field.

This work was partly supported by the INTAS-RFBR (grant 95-849), RFBR (98-02-17642, 98-02-22008), PICS-CNRS (628), and national program "Physics of the solid state nanostructures" (97-1057).

References

[1] W. Demmerle, J. Smoliner, G. Berthold *et al.*, *Phys. Rev. B* **44**, 3090 (1991).
[2] G. Rainer, J. Smoliner, E. Gornik *et al.*, *Phys. Rev. B* **51**, 17642 (1995).
[3] J. P. Eisenstein, L. N. Pfeiffer, and K. W. West, *Phys. Rev. Lett.* **69**, 3804 (1992).
[4] J. P. Eisenstein, L. N. Pfeiffer, and K. W. West, *Phys. Rev. Lett.* **74**, 1419 (1995).
[5] K. M. Brown, N. Turner, J. T. Nicholls *et al.*, *Phys. Rev. B* **50**, 15465 (1994).
[6] N. Turner, J. T. Nicholls, E. H. Linfield *et al.*, *Phys. Rev. B* **54**, 10614 (1996).
[7] J. G. S. Lok, A. K. Geim, J. C. Maan *et al.*, *Phys. Rev. B* **56**, 1053 (1997).
[8] Yu. V. Dubrovskii, E. E. Vdovin, Yu. N. Khanin *et al.*, *Pis'ma v ZhETF* **69**, 237 (1999).
[9] Qiu-Yi Ye, A. Zrenner, F. Koch and K. Ploog, *Semicond. Sci. Technol.* **4**, 500 (1989).
[10] A. Zrenner, F. Koch, J. Leotin *et al.*, *Semicond. Sci. Technol.* **3**, 1132 (1988).

7th Int. Symp. "Nanostructures: Physics and Technology"
St Petersburg, Russia, June 14–18, 1999

Resonant tunneling through single thin barrier heterostructure with spacer layers

Yu. N. Khanin, E. E. Vdovin, Yu. V. Dubrovskii, D. K. Maude†, J.-C. Portal† and T. G. Andersson‡

Institute of Microelectronics Technology RAS, 142432 Chernogolovka, Russia
† Grenoble High Magnetic Field Laboratory, MPI-CNRS,
BP166 38042 Grenoble Cedex 9, France
‡ Department of Physics, Chalmers University of Technology,
S-412 96 Göteborg, Sweden

At first sight tunneling through single barrier heterostructure is a simple problem solved on first pages of any quantum mechanics textbook. However, undoped spacer layers between a barrier and highly doped contact regions are incorporated usually in real structures to avoid dopants diffusion into barrier materials. The existence of the spacer layers immediately makes the problem of tunneling through a single barrier structure more complicated and many different phenomena could appear to accompany a simple tunneling process. For example, reflection of electrons from highly doped contact regions could give rise to additional tunnel resonances observed in $I-V$ tunnel characteristics [1]. Recently we indicated that residual light doping of a barrier gives rise to extra current around zero external voltage bias due to the appearance of the accumulation layers on both sides of the 5 nm thick barrier and additional resonant tunneling conductance between these build-in two dimensional electron layers [2].

In this work we present tunneling current measurements on the structure with very thin 2.5 nm barrier identical otherwise to used in the previous work [2]. We have found that additional conductance in this structure at zero bias is as large as 25% without magnetic field and reaches 100% in the magnetic field $B = 8$ T parallel to the tunneling current. We argue that build-in accumulation layers transfer the single barrier structure to resonant tunneling triple barrier structure where spacer layers play role of the external barriers. This model at least qualitatively explains all our findings.

The heterostructures used for the fabrication of experimental samples were grown by the MBE on a (100)-oriented Si doped n^+-type GaAs wafer ($N_d = 2 \cdot 10^{18}\,cm^{-3}$) at the substrate temperature 570°C. The structure consisted (in the order of growth) of a lightly Si-doped, a 50-nm–thick GaAs layer ($N_d = 2 \cdot 10^{16}\,cm^{-3}$), a 10-nm–thick undoped GaAs layer; a 2.5-nm–thick AlAs barrier layer; a 10-nm–thick undoped GaAs layer; a 50-nm–thick lightly doped GaAs layer ($N_d = 2 \cdot 10^{16}\,cm^{-3}$); and a 0.4-mm–thick GaAs cap-layer ($N_d = 2 \cdot 10^{18}\,cm^{-3}$). Ohmic contacts were obtained by successive deposition of AuGa/Ni/Au layers and annealing at $T = 400$°C. A mesa–structure 100 μm in diameter was fabricated by conventional chemical etching.

We measured dependences of current,and differential conductivity dI/dV on a voltage bias in magnetic fields up to 15 T at 4.2 K. The dependence of the differential conductivity dI/dV was measured by lock-in technique.

Figure 1(a) shows the differential tunneling conductance G as a function of bias V_b at various magnetic fields $B \parallel J$ up to 8 T. As can be seen in Fig. 1(a) the conductance peak with the amplitude $\Delta G/G \approx 0.25$ was observed at $B = 0$ T near zero voltage. The conductance peak becomes narrower and its magnitude increases with increasing magnetic field. For

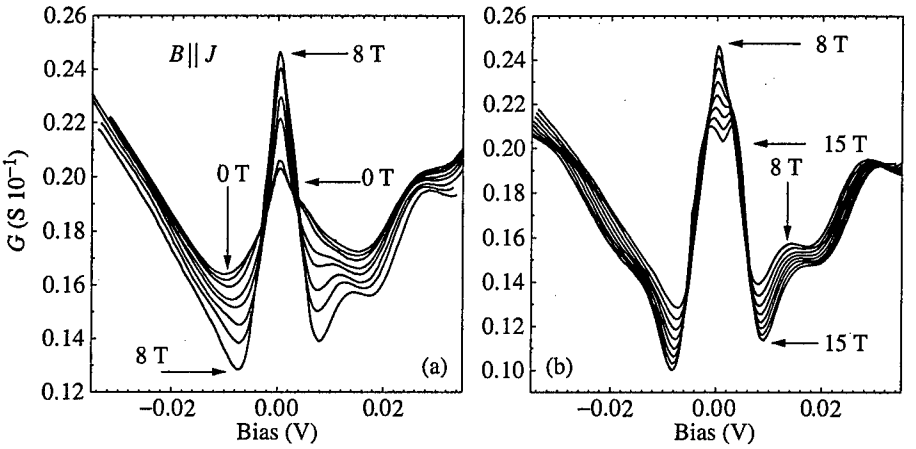

Fig. 1. (a) Tunneling differential conductance as a function of external voltage bias without and in different magnetic fields $B \parallel J$ up to 8 T. Magnetic field step between the curves is 1 T. (b) Tunneling differential conductance as a function of external voltage bias in different magnetic fields $B \parallel J$ from 8 T to 15 T. Magnetic field step between the curves is 1 T.

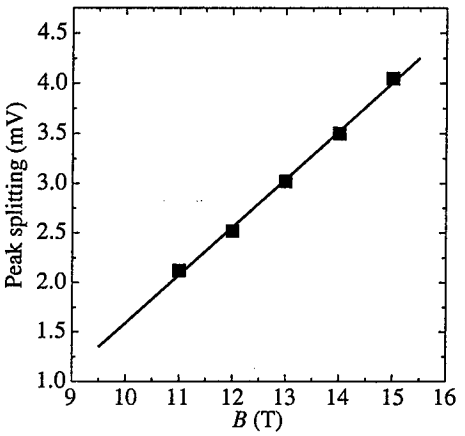

Fig. 2. Magnetic field dependence of the zero bias conductance peak Δ splitting.

higher magnetic fields as can be seen in Fig. 1(b) the magnitude of the conductance peak decreases smoothly with increasing magnetic field from 8 T to 11 T. Then in magnetic field higher then 11 T a dip around zero bias appears in the $G(V_b)$ characteristics. With increasing magnetic field both the depth of the dip and the separation of the surrounding peaks become larger. Thus over the range of magnetic field from 11 T to 15 T the conductance peak splits. The magnetic field dependence of the conductance peak splitting Δ are shown in Fig. 2, that is voltage separation between small conductance peaks around zero voltage. The the peak splitting increases linearly with magnetic field increase. Taking into account the leverage factor in the structure, $\Delta(B)$ dependence are described by the expression $\Delta \approx 0.15\hbar\omega_c$.

Figure 3 shows the experimental conductance characteristics $G(V_b)$ at various magnetic fields $B \perp J$ up to 8 T. The conductance peak decrease with increasing magnetic field and disappears at $B \approx 4$ T. With further increase of magnetic field the conductance at zero bias

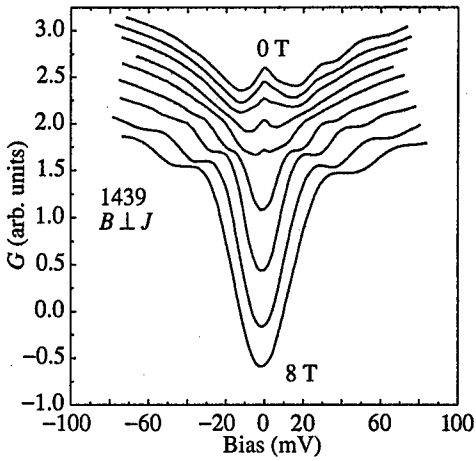

Fig. 3. Tunneling differential conductance as a function of external voltage bias without and in different magnetic fields $B \perp J$ up to 8 T. Magnetic field step between the curves is 1 T. The curves are shifted vertically for clarity.

rapidly falls down.

As was mentioned above all the observed features are typical for triple barrier structure in resonance at zero bias voltage bias. Increase of the tunnel conductance with parallel to the current magnetic field higher then 4 T and following decrease reflects the density of states at the Fermi level when only last Landau level is occupied in the accumulation layers. The splitting of conductance peak around zero bias in a magnetic field higher 11 T is due to the suppression of tunneling current between 3D and 2D states first observed by Ashoori *at al.* [3]. The suppression of tunnel conductance by in-plane magnetic field is typical for 2D–2D tunneling processes [4].

Thus we have studied the tunneling in a single thin barrier heterostructure with spacer layers. All findings are explained in terms of resonant tunneling through triple barrier structure.

This work was partly supported by the INTAS–RFBR (grant 95–849), RFBR (98-02-17642, 98-02-22008), PICS–CNRS (628), and national program "Physics of the solid state nanostructures" (97-1057).

References

[1] Yu. V. Dubrovskii, Yu. N. Khanin, E. E. Vdovin *et al.*, *Surf. Sci.* **361/362**, 213 (1986).
[2] Yu. V. Dubrovskii, Yu. N. Khanin, T. G. Andersson, U. Genser, D. K. Maude, and J.-C. Portal, *ZhETP.* **109**, 868 (1996).
[3] R. C. Ashoori, J. A. Lebens, N. P. Bigelov, and R. H. Silsbee, *Phys. Rev. Lett.* **58**, 1497 (1991).
[4] J. P. Eisenstein, T. G. Gramila, L. N. Pfeiffer, and K. W. West, *Phys. Rev. B* **44**, 6511 (1991).

7th Int. Symp. "Nanostructures: Physics and Technology"
St Petersburg, Russia, June 14–18, 1999

Intersubband resonant polaron in near-surface δ-doped GaAs

I. N. Kotel'nikov†‡ and V. A. Volkov†

† Institute of Radioengineering and Electronics of the RAS, Moscow 103907, Russia
‡ International Laboratory of High Magnetic Fields and Low Temperatures, Wroclaw, Poland

Abstract. The many-body features of tunnel spectra of Al/δ-GaAs are measured. The in-plane magnetic field shifts the 2D subband energies, with the diamagnetic shift of empty subband (E_1) is greater than that of the filled subband (E_0). The anticrossing of the terms $E_1(B) - \hbar\omega_{LO}$ and $E_0(B) + \hbar\omega_{LO}$ is observed (here $\hbar\omega_{LO}$ is the LO phonon energy; zero energy of the subband bottoms is at Fermi level E_F). The effect is attributed to the strong intersubband polaron interaction at double resonance conditions: $E_1 - E_F = \hbar\omega_{LO}$ and $E_1 - E_0 = 2\hbar\omega_{LO}$.

Introduction

The tunneling spectroscopy is extensively used for investigations of many-body effects. There are well-known polaron singularities in the tunnel spectra (TS) of 3D systems. For example, in n-GaAs Schottky-barrier tunnel junctions these features were found at the energies $E_F \pm \hbar\omega_{LO}$ [1], where $\hbar\omega_{LO} = 36.5$ meV. The singularities are weak in the 3D case.

We studied stronger LO-phonon singularities in TS of quasi-2D systems, namely, in δ-doped GaAs near Al/GaAs interface. In the system there are two 2D-subbands, the partly filled E_0 subband and the empty E_1 subband. The diamagnetic shift of subband energies induced by the in-plane magnetic field B [2] was used for the tuning of the intersubband energy $E_1(B) - E_0(B)$. The intersubband-resonance polaron effect was observed for the first time.

1 Samples and conditions of measurements

The tunnel structures Al/δ-GaAs were prepared on semi-insulating (100) GaAs substrate by the method of molecular beam epitaxy (MBE). The δ-doped layer was formed at the distance of $L = 20$ nm from Al/GaAs interface at the temperature 570°C. The density of the Si atoms in the δ-layer was $5.2 \cdot 10^{12}$ cm^{-2} and acceptor concentration in epitaxial layer was about 10^{15} cm^{-3}. Deposition of Al from the Knudsen cell took place directly in the MBE chamber after the cleaning procedure and cooling of the substrate down to 100°C. Al/δ-GaAs tunnel junctions with the diameter of Al gate 0.7 mm were formed and Au-Ge-Ni ohmic contacts to the δ-layer were prepared. The 1st and 2nd derivatives of $I-U$ characteristic of the junction were measured. The magnetic field experiments were carried out in International Laboratory of High Magnetic Fields and Low Temperatures (Wroclaw, Poland) at $T = 1.6$ K and $T = 4.2$ K in $B \leq 15$ T. The Shubnikov–de Haas-like oscillations were observed in TS at $B \parallel I$ and $U = 0$ and the density $n = 1.1 \cdot 10^{12}$ cm^{-2} of 2D electrons in the δ-layer under Al gate was determined from these data.

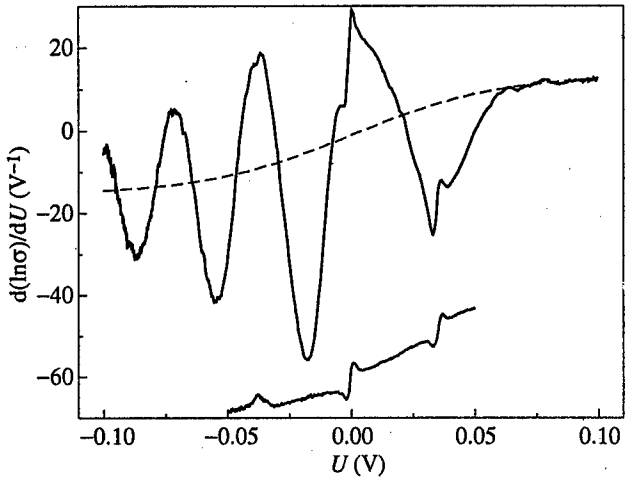

Fig. 1. The tunnel spectra of Al/δ-GaAs (upper curve) and Al/n-GaAs (lower curve shifted on $-50\,\mathrm{V}^{-1}$) junctions at $T = 4.2\,\mathrm{K}$ and $B = 0$. Dashed line is the background curve F. The positive bias U corresponds to electron tunneling from GaAs into Al electrode.

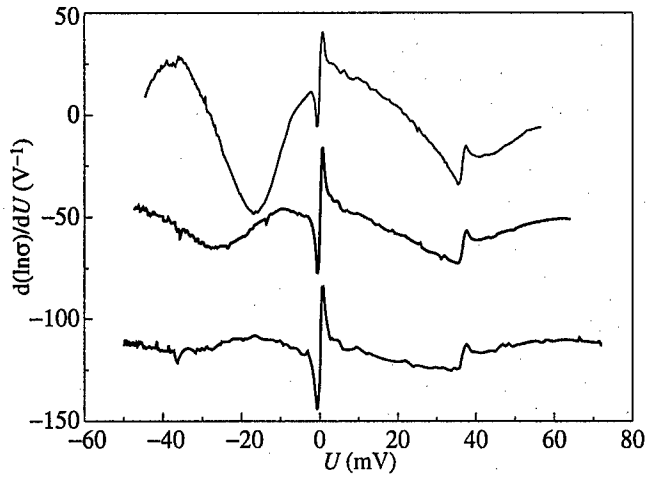

Fig. 2. The tunnel spectra with subtraction of the background curve $F(U)$. The upper curve corresponds to the magnetic field $B = 0$ (shift along Y-axis is equal to 0), for the middle curve $B = 7.8\,\mathrm{T}$ ($-50\,\mathrm{V}^{-1}$), and for the lower curve $B = 10.7\,\mathrm{T}$ ($-110\,\mathrm{V}^{-1}$).

2 Results and discussions

The typical tunnel spectrum of Al/δ-GaAs at $B = 0$ and $T = 4.2\,\mathrm{K}$ is shown in Fig. 1. The many-body features are observed in TS: zero-bias anomaly (ZBA) and phonon lines at $eU = \pm\hbar\omega_{\mathrm{LO}}$. The latter were associated with electron-optical phonon self-energy (polaron) effects as was first suggested for 3D GaAs in [1]. The TS of the Al/n-GaAs junction (see the lowest curve in Fig. 1) shows that the many-body singularities in 3D and 2D tunnel junctions are qualitatively the same. The strong dips in TS are related with the bottoms E_i of the two-dimensional subbands in the δ-layer. It is well known [3] that the tunnel conductance in i-subband $\sigma_i(U) \propto \rho_{||i}(E_i, U) \cdot D(E_i, E_{\mathrm{F}} - eU)$, where

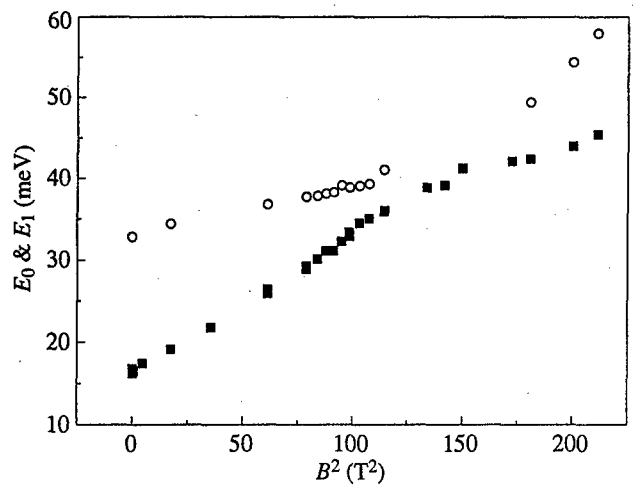

Fig. 3. The magnetic field ($B \perp I$) dependences of the subband energies E_0 ('o', shift $2\hbar\omega_{LO} = 73$ meV) and E_1 ('■') for Al/δ-GaAs tunnel junction. The Fermi energy of δ-GaAs is accepted as zero of the energy scale.

$\rho_{||i} = \left(m/\pi\hbar^2\right) \Theta\left(E_F - eU - E_i\right)$ is the two-dimensional density of states and D is the barrier transmission. Thus, the positions U_i of dips in TS $d(\ln\sigma)/dU$ can be used to determine the subband energies E_i in 2DEG. The dips at $U > 0$ and $U < 0$ correspond to full and empty subbands, respectively. According to Fig. 1, only one subband E_0 is occupied in our samples and the value of Fermi energy is $\simeq$ 40 meV. This value gives 2DEG density $\simeq 1.2 \cdot 10^{12}\,\mathrm{cm}^{-2}$ in agreement with our Shubnikov–de Haas tunneling measurements.

The magnetic field applied in the plane of the δ-layer ($B \perp I$) "pushes out" two-dimensional subbands from the quantum well of the δ-layer (diamagnetic shift [4]) and reduces the magnitude of the dips in TS. Fig. 2 shows this behavior of TS for subbands E_0 and E_1 where the background curve $F(U)$ was subtracted. The curve $F(U)$ can be seen in Fig. 1 (dashed line). This background curve does not depend on magnetic field B as it results from our experiments. We used the curves $d(\ln\sigma)/dU - F$ in the data treatment to obtain the dependence of the minimum position of the dips $eU_i = -E_i$ on the magnetic field.

The dependencies $E_0\left(B^2\right)$ and $E_1\left(B^2\right)$ are shown in Fig. 3 where E_0 is shifted up on 73 meV. In the low field range the usual diamagnetic shift [4, 5] is observed: $\Delta E_i = e^2 \Delta z_i^2 B^2/2m$. Here $\Delta z_i = (\langle z_i^2\rangle - \langle z_i\rangle^2)^{0.5}$ is the spread of i-subband wave function at $B = 0$ in the direction z perpendicular to δ-layer. For our samples Δz_0 and Δz_1 are determined from the slope of the curves in Fig. 3 near the $B = 0$ region and are equal to 6.4 and 11 nm, respectively. These values are obtained for GaAs electron effective mass $m = 0.07 m_0$. The energy E_1 reaches the optical phonon energy at $B = B_c \cong 11$ T.

At $B > B_c$, when $E_1(B) \geq \hbar\omega_{LO}$, the slopes of E_0 and E_1 are drastically changed. That means the renormalization of the 2DEG spectrum above the threshold field B_c. The anti-crossing of terms in Fig. 3 corresponds to the double resonance:

$$E_1(B) - E_0(B) = 2\hbar\omega_{LO}$$
$$E_1(B) - E_F = \hbar\omega_{LO}$$

The effect can be interpreted as the observation of the intersubband resonant polaron.

The results are in semiqualitative agreement with the model of the resonant polaron interaction in two-level electron 3D system [6]. The corresponding 2D theory is absent, but we expect that the 2D polaron resonance could be stronger than that in 3D case [7].

We are grateful to Yu. V. Fedorov and A. V. Hook for preparation of the samples in MBE chamber, A. Ya. Shul'man for helpful discussions and V. G. Mokerov for support of this work. The work has been partly supported by INTAS-RFBR (Project No 97-11475) and RFBR (No 97-02-17750 and No 99-02-17592).

References

[1] J. W. Conley and G. D. Mahan, *Phys.Rev.* **161** 681 (1967).
[2] A. Zrenner, H. Reisinger, F. Koch, K. Ploog and J. C. Maan, *Phys. Rev.* **B33** 5607 (1986).
[3] D. J. BenDaniel and C. B. Duke, *Phys. Rev.* **160** 679 (1967).
[4] D. C. Tsui, *Solid State Commun.* **9** 1789 (1971).
[5] F. Stern and W. E. Howard, *Phys. Rev.* **163** 816 (1967).
[6] I. B. Levinson and E. I. Rashba, *Usp. Fiz. Nauk* **111** 683 (1973) [in Russian].
[7] A. Petrou and B. D. McCombe, in: *Landau Level Spectroscopy*, ed. Landwehr G. and Rashba E.I. Elsevier Science Publishers B.V., 1991, Chapter 12.

7th Int. Symp. "Nanostructures: Physics and Technology"
St Petersburg, Russia, June 14–18, 1999

Investigation of the characteristics of interband resonant tunnelling diodes with modified barriers

I. Lapushkin†, *A. Zakharova*† and V. Gergel‡
† Institute of Physics and Technology of the Russian Academy of Sciences, Nakhimovskii Avenue 34, Moscow 117218, Russia
‡ Institute of Radioengineering and Electronics of the Russian Academy of Sciences, Mokhovaya Str. 11, Moscow 103907, Russia

Resonant tunnelling structures (RTS) with type II heterojunctions made from InAs, AlSb, GaSb materials have been intensively studied for the last ten years experimentally and theoretically (see, for example, [1–4]). These RTS which operation is based on the overlapping of the InAs conduction band and GaSb valence band exhibit negative differential resistance (NDR) with high values of peak-to-valley (P/V) current ratio and can be useful for practical applications. Especially high values of P/V current ratio (20 at room temperature and 88 at liquid nitrogen temperature [1]) were achieved for InAs/AlSb/GaSb RTS in which the electrons from InAs contact layer heavily doped by donors tunnel through the quasibound states in the valence band quantum well of the GaSb layer into the states in the conduction band of the second InAs contact layer. Several modifications of this structure were considered to enlarge the value of P/V current ratio. The utilization of the strained GaAsSb layer instead of the GaSb quantum well layer or the inserting the AlAs monolayers into the structure [2, 3] results in increasing the P/V current ratio. In this paper we propose a modification of an InAs/AlSb/GaSb RTS, which implies the replacing the AlSb barriers by AlGaSb barriers. We show that this modification can significantly enlarge the values of P/V current ratio.

Our consideration of the InAs/AlSb/GaSb and InAs/AlGaSb/GaSb RTS is based on the model for self-consistent calculation of the I–V characteristics of these diodes, proposed in [4], where the theoretical I–V characteristics of realistic InAs/AlSb/GaSb RTS were investigated and good quantitative agreement with the experiment was achieved for the values of peak and valley current density for the first time. The only difference from the model described in [4] consists in the method of the resonant tunnelling current calculation. Here the resonant interband tunnelling current through the light hole states in the well is obtained in terms of the tunnelling probability, while in [4] this current component is obtained in terms of tunnelling times using the transfer Hamiltonian approach. The calculated conduction and valence band diagram of the InAs/AlGaSb/GaSb RTS is shown in Fig. 1.

The I–V characteristics of the symmetrical InAs/AlSb/GaSb and InAs/$Al_{0.4}Ga_{0.6}Sb$/-GaSb RTS with 25 Å wide-gap barrier layers made from AlSb and AlGaSb, respectively, and 65 Å quantum wells made from GaSb at room temperature are shown in Fig. 2. The other parameters of the InAs/AlSb/GaSb RTS are as in [1]. Curves 1 and 2 correspond to the InAs/AlSb/GaSb and InAs/AlGaSb/GaSb RTS, respectively. The InAs/AlGaSb/-GaSb RTS includes two InAs contact layers doped by donors with the concentration equal 2×10^{18} cm^{-3} and two 100 Å lightly doped spacer layers with the donor concentration equal 2×10^{16} cm^{-3}. The value of the peak current density for the InAs/AlSb/GaSb RTS is in a reasonable quantitative agreement with the experiment [1]: the calculated and measured values are approximately equal to 10^3 A/cm^2 and 200 A/cm^2, respectively.

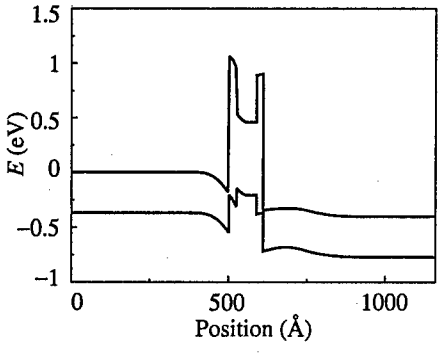

Fig. 1.

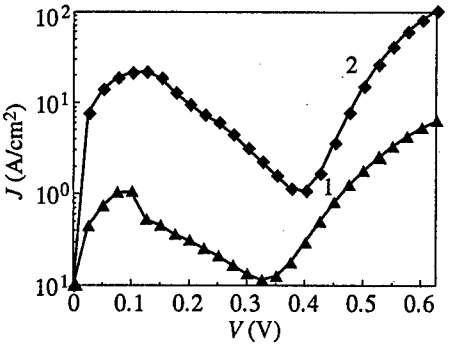

Fig. 2.

Excellent agreement with the experimental results is obtained for the value of P/V current ratio: the theoretical value is equal to 9, while the observed value equals 9.5 [1]. The calculated peak current density and P/V current ratio for the InAs/AlGaSb/GaSb RTS are about 2×10^4 A/cm^2 and 20, respectively, that are essentially greater than those for the InAs/AlSb/GaSb RTS.

The total tunnelling current density for each curve shown in Fig. 2 is the sum of different interband and intraband tunnelling current components as described in [4]. The interband tunnelling current components through the light and heavy hole states in the well make a contribution to the peak current density. The valley current is conditioned by the interband tunnelling processes through the heavy hole states in the valence band quantum well, interband tunnelling from the light hole states in the well which become lower than the conduction band edge of the left spacer near the barrier and intraband tunnelling from the states in the valence band of the left contact or spacer layer into the states in the GaSb quantum well. For high values of the external bias, only two current components are significant: the hole intraband tunnelling current and the interband tunnelling current from the light hole states in the well which are lower than the conduction band edge of emitter. The energy gap of the $Al_xGa_{1-x}Sb$ material is less than that of the AlSb. For this reason the transparency of the $Al_xGa_{1-x}Sb$ barriers is greater than that of the AlSb barriers. For this reason the current density increases with x decreasing. The peak current density enlarges greater than the valley current density, that results in the increasing the value of P/V current ratio.

In order to achieve high values of peak current density and P/V current ratio we investigated different symmetrical and asymmetrical InAs/$Al_xGa_{1-x}Sb$/GaSb RTS for $x \approx 0.4$ at room and liquid nitrogen temperature. The I-V characteristics of the RTS with 20, 25 and 30 Å left barrier, 65 Å quantum well and 20 Å right barrier at lattice temperature $T = 300$ K are shown in Fig. 3. Curves 1, 2 and 3 correspond to the diodes with 20, 25 and 30 Å left barriers, respectively. Fig. 4 represents the values of peak current density J_p (curve 1) and P/V current ratio J_p/J_v (curve 2) versus the left barrier thickness d_1. The value of J_p decreases, while the value of P/V current ratio enlarges as the left barrier thickness increases. The value of peak current density as high as 42 kA/cm^2 is obtained for the InAs/AlGaSb/GaSb RTS with $d_1 = 20$ Å, the corresponding value of $J_p/J_v = 12$. For the InAs/AlGaSb/GaSb RTS with $d_1 = 30$ Å the values of P/V current ratio equal 35 and peak current density equal 14 kA/cm^2 are achieved. Hence the values of peak current density and P/V current ratio can be significantly enlarged due to utilization of the AlGaSb

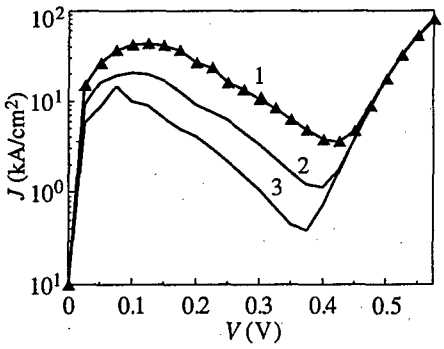

Fig. 3.

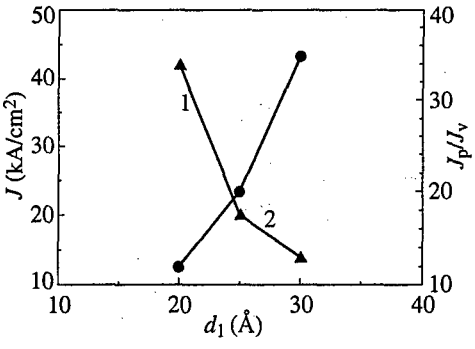

Fig. 4.

barriers instead of AlSb barriers.

The I–V characteristics of the InAs/AlGaSb/GaSb RTS with 65 Å quantum well and 20 Å right barrier at liquid nitrogen temperature are shown in Fig. 5. Curves 1, 2 and 3 represent the characteristics of the diodes with 20, 25 and 30 Å left barriers, respectively. The dependencies of the peak current density (curve 1) and P/V current ratio (curve 2) on the left barrier thickness are presented in Fig. 6. The peak current density increases only slightly with the lattice temperature decreasing. The values of J_p/J_v are much greater for the I–V curves obtained at $T = 77$ K. For the InAs/AlGaSb/GaSb RTS with $d_1 = 30$ Å the P/V current ratio as high as 800 is achieved. This value is much greater than all known experimental values for RTS. The interband tunnelling current components through the light and heavy hole states in the quantum well, which compose the total tunnelling current density for the values of external bias up to the voltage corresponding to the valley current, depend slightly on the value of T. These current components drop as the voltage increases for the values of external bias greater than the voltage corresponding to the peak current density. In the NDR region the intraband tunnelling current from the states in the valence band of the left spacer or contact layer into the empty states in the valence band quantum well switches on with the voltage increases, because is lowered the hole quasi-Fermi level and increases the number of empty quasibound states in the well. This current increases with the voltage increasing that results in the observed values of valley current. The hole intraband tunnelling current drops exponentially with the temperature decreasing since decreases exponentially the number of empty states below the hole quasi-Fermi level in the GaSb quantum well. For this reason the hole intraband tunnelling current switches on at considerably greater values of external bias at $T = 77$ K than those at $T = 300$ K. This results in the increase of P/V current ratio.

Note that if the interband resonant tunnelling current through the light hole states in the well is obtained in terms of tunnelling times as in Ref. [4] the calculated values of P/V current ratio at $T = 77$ K are much greater than those shown in Fig. 6. This is due to the fact that in this case the tunnelling current through the light hole states drops to zero when the quasibound state level becomes lower than the conduction band edge of the left spacer layer near the barrier. For this reason in all calculations of the I–V characteristics in this paper the resonant tunnelling current was obtained in terms of the tunnelling probability. We believe that the phonon-assisted processes can not enlarge considerably the values of valley current and reduce the values of P/V current ratio for the investigated RTS with sufficiently thin barrier layers. In the region of valley current the phonon-assisted interband tunnelling

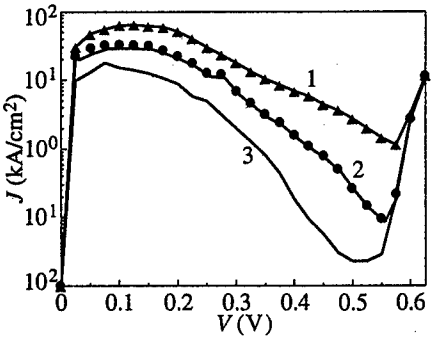

Fig. 5.

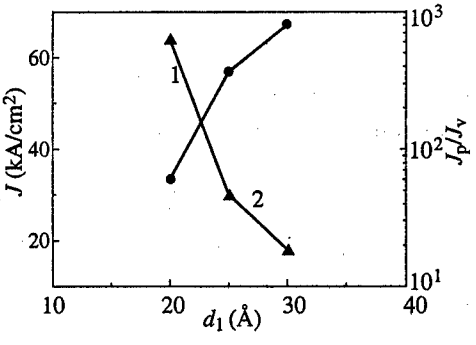

Fig. 6.

into the light hole quasibound states in the quantum well are forbidden, because all these states are below the conduction band edge of the left spacer layer near the barrier. Only the phonon-assisted interband tunnelling processes into the heavy hole states in the well can occur. These processes are not dominant, because the interband tunnelling processes without scattering are not forbidden. The phonon-assisted processes in this case can be dominant for interband transitions from the InAs conduction band into the states in the valence band of GaSb, if the thickness of the AlGaSb barrier layer is greater than 100 Å (see [5]).

In summary, we investigated theoretically the I-V characteristics of the InAs/AlSb/GaSb and InAs/AlGaSb/GaSb RTS at room and liquid nitrogen temperature. It was shown that the values of the peak current density and P/V current ratio can be essentially enlarged by employing AlGaSb barriers instead of AlSb barriers. For the InAs/AlGaSb/GaSb RTS the values of P/V current ratio greater than all until now known experimental values for RTS were obtained.

Acknowledgements

This work was partially supported by Russian Foundation for Basic Research under grant No 97-02-16438a.

References

[1] J. R. Södestr, D. H. Chow and T. C. McGill, *Appl. Phys. Lett.* **55**, 1094 (1989).
[2] J. N. Schulman, D. H. Chow and T. C. Hasenberg, *Solid-St. Electron.* **37**, 981 (1994).
[3] S. Tehrani, J. Shen, H. Goronkin, M. Hoogstra and T. X. Zhu, *Inst. Conf.* Ser. **136**, 209 (1994).
[4] I. Lapushkin, A. Zakharova, V. Gergel, H. Goronkin and S. Tehrani, *J. Appl. Phys.* **82**, 2421 (1997).
[5] A. Zakharova, *J. Phys.: Condens. Matter* **9**, 4635 (1997).

7th Int. Symp. "Nanostructures: Physics and Technology"
St Petersburg, Russia, June 14–18, 1999

Dynamics and stability of lateral current density patterns in resonant-tunneling structures

M. Meixner†, *P. Rodin*‡, E. Schöll† and A. Wacker†
† Institut für Theoretische Physik, Technische Universität Berlin,
Hardenbergstrasse 36, D-10623, Berlin, Germany
‡Ioffe Physico-Technical Institute, St Petersburg, Russia

Abstract. We study lateral current density patterns in a double-barrier resonant tunneling structure with a bistable Z-shaped current-voltage characteristic. It is shown that for a positive load the external circuit provides a positive feedback upon the dynamics of the current pattern. This leads to accelerated motion of lateral switching fronts which switch the device from the low–conductivity to the high–conductivity state, and vice versa. Negative feedback and stabilization of a stationary front can be achieved by implementation of an active external circuit simulating a negative load.

Dynamical charge accumulation within the potential well of a double barrier resonant-tunneling structure (DBRT) leads to an electrostatic feedback mechanism which increases the energy of the quasi-bound state supporting resonant tunneling conditions for higher applied voltages. This mechanism may result in the intrinsic bistability of the DBRT where a high current and a low current state coexist for the same applied voltage u, and the current-voltage characteristic becomes Z-shaped, instead of N-shaped, thus exhibiting hysteresis upon voltage sweep [1]. Recently it has been pointed out [2, 3] that such bistability provides the basis for lateral pattern formation in the DBRT. Lateral current density patterns are characterized by a current density profile which varies in the plane perpendicular to the current flow reflecting spatial coexistence of the two stable states. The formation of such patterns is similar to the appearence of stationary current filaments and travelling fronts in the case of an S-shaped current-voltage characteristic [4]. It is known that the stability and dynamics of current density patterns in bistable semiconductors cannot be understood without taking into account the circuit conditions [4, 5, 6]. In this contribution we analyze lateral current density patterns in the DBRT and their dependence upon the feedback provided by the external circuit.

For a given applied voltage u the internal state of the DBRT can be parameterized by the electron concentration $n(x, t)$ in the quantum well described by the continuity equation [7]

$$\frac{\partial n}{\partial t} = \frac{1}{e}\left(J_{\mathrm{ew}}(n, u) - J_{\mathrm{wc}}(n)\right) + D(n)\frac{\partial^2 n}{\partial x^2}, \tag{1}$$

where J_{ew} and J_{wc} are the emitter-well and the well-collector current densities, respectively, corresponding to vertical transport (along the z-axis), and the last term describes lateral transport (in the x-direction parallel to the quantum well plane; the width w of the sample along the other lateral direction is supposed to be small). Generally, the combination of lateral diffusion and drift in the well plane effectively results in a term with a nonlinear diffusion coefficient $D(n)$ [7, 2, 3]. We have derived approximate expressions for J_{ew} and

J_{wc} for a symmetric structure assuming sequential tunneling:

$$J_{ew}(n,u) = \frac{e}{\hbar}\Gamma_L \cdot \left[\varrho\Delta\frac{\arctan(2\Delta/\Gamma) - \arctan(2\Omega/\Gamma)}{\pi} + \varrho\frac{\Gamma}{4\pi}\ln\frac{\Delta^2 + (\Gamma/2)^2}{\Omega^2 + (\Gamma/2)^2}\right] \cdot f_W,$$

$$J_{wc}(n) = \frac{e}{\hbar}\Gamma_R \cdot n, \tag{2}$$

$$\Delta \equiv E_F - E_W + \frac{u}{2} - \frac{en}{C_{int}},\ \Omega \equiv \frac{u}{2} - \frac{en}{C_{int}} - E_W,\ C_{int} \equiv \frac{\varepsilon\varepsilon_0}{d},\ \varrho \equiv \frac{m}{\pi\hbar^2},\ f_W \equiv 1 - \frac{n}{\varrho\Delta}.$$

Here E_F is the Fermi level in the emitter, E_W is the energy of the quasibound state in the well with respect to the bottom of the well, Γ is the total broadening of the quasibound state, Γ_L and Γ_R are the linewidths corresponding to escape via the emitter and collector barriers, respectively, ρ is the two-dimensional density of states, ε and ε_0 denote the relative and absolute permittivity, respectively, m is the effective electron mass, C_{int} is the capacitance of the well, d is the effective thickness of the barriers, and f_W is the effective filling factor of the states in the well. Δ and Ω denote the energy of the quasibound state with respect to the Fermi level and bottom of the conductance band in the emitter, respectively. The corresponding spatially homogeneous current-voltage characteristic $J(u) = J_{ew} = J_{wc}$ is shown in Fig. 1(a).

The dynamics of the voltage across the device $u(t)$ is described by Kirchhoff's equation for the external circuit (see [7]):

$$RC\frac{du}{dt} = U_0 - u - Rw\int_0^L \frac{J_{ew} + J_{wc}}{2}dx, \tag{3}$$

where U_0 is the applied bias voltage, R is the load resistance, L and w are the lateral sample length and width, respectively, and C is the total differential capacitance of the external circuit and the DBRT.

Eqs. (1),(2),(3) represent an example of a bistable medium with global coupling studied for stationary current density patterns in [6]. For $R > 0$ any stationary pattern in such a system is unstable [6]. Another important class of lateral patterns constitutes of travelling fronts corresponding to the propagation of the high current density state into the low current density state (hot front, front velocity $v > 0$) or vice versa (cold front, $v < 0$), i.e., they describe electronic switching processes between the off and the on state. Previously, we have numerically studied the propagation of planar (1D) fronts in a different semiconductor model (thyristor) with a Z-shaped bistability [9]. The main results of [9] may be applied to the DBRT as well. The $v(u)$ dependence for the DBRT is shown in Fig. 1(b). The speed and the direction of front propagation can be easily controlled by the voltage u. For a certain voltage the velocity is zero, i.e., the front becomes stationary, while for smaller voltages ($v > 0$) the front switches the system to the on state, and for larger voltage ($v < 0$) the front switches the system off. The dynamics of u due to the external circuit Eq. (3) leads to a nonlocal coupling of the front propagation since u depends on the integral value of the current density over the cross-section and, therefore, on the front position. This results in a feedback on the front dynamics. The negative slope $dv/du < 0$ leads to acceleration of both hot (Fig. 1(c)) and cold (Fig. 1(f)) fronts if the DBRT is operated via an external load resistance $R > 0$. Decelerated motion and stabilization of stationary front patterns (Fig. 1(d,e)) can be achieved by an implementation of active external circuits simulating a negative load $R < 0$ and negative capacitance $C < 0$ [8]. The front slows down and eventually becomes stationary. Oscillatory front dynamics is possible for a sufficiently

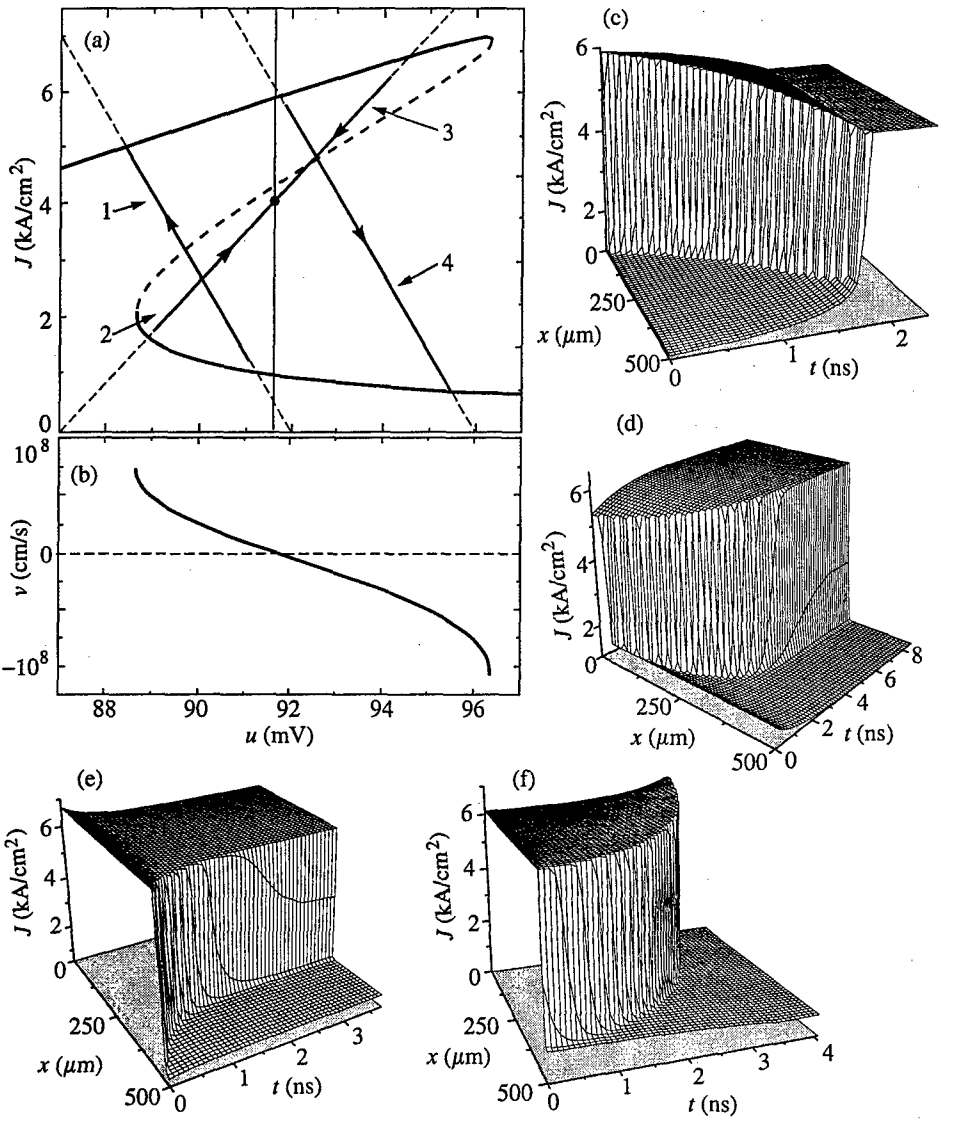

Fig. 1. (a) Current-voltage characteristic $J(u)$ calculated for the DBRT with $E_F = 5$ meV, $E_W = 40$ meV, $\Gamma = 1$ meV, $\Gamma_L = \Gamma_R = 0.5$ meV, $\varepsilon = 12$, and $m = 0.067$ (for GaAs). (b) The dependence of the front velocity v on u for the voltage-controlled regime; $v > 0$ corresponds to a hot front. (c,d) accelerated and decelerated hot fronts for $R > 0$ (load line 1 in the (J, u)-plane: $U_0 = 92$ mV, $RLw = 7.8 \cdot 10^{-11}\,\Omega \cdot \mathrm{m}^2$) and $R < 0$ (load line 2: $U_0 = 87$ mV, $RLw = -1.3 \cdot 10^{-10}\,\Omega \cdot \mathrm{m}^2$), respectively; (e,f) decelerated and accelerated cold fronts for $R < 0$ (load line 3: $U_0 = 87$ mV, $RLw = -1.3 \cdot 10^{-10}\,\Omega \cdot \mathrm{m}^2$) and $R > 0$ (load line 4: $U_0 = 96$ mV, $RLw = 7.8 \cdot 10^{-11}\,\Omega \cdot \mathrm{m}^2$), respectively. In these simulations $RC = 10^{-12}$ s which corresponds to an instantaneous global feedback on front dynamics. Here we assume a diffusion constant $D = D_0 = 1\,\mathrm{m}^2/\mathrm{s}$ inside the well. For different values of D the length and velocity has to be rescaled by a factor $\sqrt{D/D_0}$.

large capacitance C. In conclusion, this offers convenient control of lateral switching in the DBRT.

References

[1] V. J. Goldmann, D. C. Tsui and J. E. Cunningham, *Phys. Rev. Let.* **58**, 1256 (1987).
[2] B. Glavin, V.Kochelap and V. Mitin, *Phys. Rev. B* **56**, 13346 (1997).
[3] D. Mel'nikov and A. Podlivaev, *Semiconductors* **32**, 206 (1998).
[4] V. L. Bonch-Bruevich, I. P. Zvyagin, and A. G. Mironov *Domain Electrical Instabilities in Semiconductors* (Consultant Bureau, New York, 1975);
E. Schöll, *Nonequilibrium Phase Transitions in Semiconductors* (Springer, Berlin 1987).
[5] E. F. Bass, V. S. Bochkov and Yu. Gurevich, *Sov. Phys. JETP* **31**, 972 (1970).
[6] A. Alekseev, S. Bose, P. Rodin and E. Schöll, *Phys. Rev. E* **57**, 2640 (1998).
[7] A. Wacker and E. Schöll, *J. Appl. Phys.* **78**, 7352 (1995).
[8] A. Martin, M. Lerch, P. Simmonds and L. Eaves, *Appl. Phys. Lett.* **64**, 1248 (1994).
[9] M. Meixner, P. Rodin and E. Schöll, *Phys. Rev. E* **58**, 2796 (1998).

7th Int. Symp. "Nanostructures: Physics and Technology"
St Petersburg, Russia, June 14–18, 1999

Tunneling quantum current in carbon nanotube's junctions

S. S. Savinskii†, N. V. Khokhriakov† and S. Melchor‡
† Udmurt State University, 426034, Izhevsk, Russia
‡ Granada University, E–18071–Granada, Spain

Theoretical possibility of making carbon nanotubes based nanoelectronic devices with strong non-linear and multifunctional electronic properties is discussed in the report. It may be realised by joining nanotubes of different chiralities and consequently electronic characteristics (from typical semiconductors to semimetals, see for example [1]). Nanotubes of distinct radii and chiralities may be joined through a connecting surface representing a carbon structure packed by penta-, hexa- and heptagons [2].

In the literature [3] to analyse theoretically quantum current in two nanotube junction the direct diagonalization of electronic Hamiltonian of finite carbon cluster with junction structure containing 700 atoms is performed. Then the eigenvectors obtained are used to calculate the electric current under a voltage applied. Similar investigations of the current in three or more nanotubes junctions are absent in the literature. To investigate electric current in nanotube's junctions we use a phenomenological approach allowing analyse the current states in the nanotube junctions from known electron eigenfunctions of isolated nanotubes and presupposed nature of transition amplitude.

Let there are N single-layer and sufficiently long carbon nanotubes of different chiralities and radii connected between itself through transition surface area hereinafter named "connection area" (see Fig. 1). The transition amplitude between quantum states of different nanotubes is assumed to be small, that allows us to neglect the alternative electron transitions between chosen two states via interstitial ones. Hereinafter we denote the π-electron wave functions and quantum states energies of nanotube with number γ as $|\, k, m, n, \gamma\rangle$ and $E_{kmn\gamma}$ correspondingly, where $n = 1, 2$ is zone number in expression (1) for the signs $(-)$ and $(+)$. The π-electron states of the ideal nanotube are classified by two quantum numbers k, m, $\hbar k$ is the momentum of the electron along the axis of the cylinder, $\hbar m$ is the angular momentum, $\hbar$ is Planck's constant. The expressions for the π-electron wave functions of the ideal nanotube in tight-binding approximation may be found in our previous work [4], here we give only expression for the electron energy

$$\begin{aligned} E^{\pm}_{k,m} &= E_\pi \pm |\mathbf{H}_{01,k,m}| \\ \mathbf{H}_{01,k,m} &= \beta_0 + \exp(-im\varphi_2 - ikz_2)(\beta_1 + \beta_2 \exp(-im\varphi_1 - ikz_1), \end{aligned} \tag{1}$$

where E_π is the diagonal matrix element of the Hamiltonian, β_0, β_1, β_2 are the nonzero matrix elements based on the nearest neighbours atomic orbitals, the difference between the matrix elements depends on parameter a/R, where a is the nearest neighbour distance, R is nanotube's radius.

Apply at nanotube's ends electric potentials φ_γ, where $\gamma = 1, \ldots N$ (see Fig. 1), and suppose that the potentials in the nanotubes are constants, all voltage drop is only in the junction region. Transition matrix element $T^{k'm'n'\gamma'}_{kmn\gamma}$ between quantum states of different nanotubes $|\, k, m, n, \gamma\rangle$ and $|k', m', n', \gamma'\rangle$ (see Fig. 2) is assumed to be small. Suppose that quantum numbers correspond to electron moving to the contact, whereas k', m', n', γ' correspond to moving from the contact.

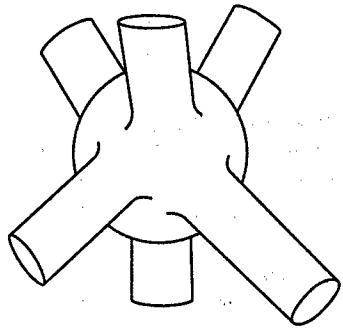

Fig. 1. Nanotube's contact area.

Using Fermi's formula for the transitions in the continuous spectra per unit time (see for example [5]) and taking into account multi-channel character of the electron transitions we obtain for the quantum current in the tube with number γ following expression

$$J_\gamma(\varphi_1 \ldots \varphi_2) \cong \frac{2\pi e}{\hbar} \int \sum_{m,n,m',n',\gamma'} \left| T^{k'm'n'\gamma'}_{kmn\gamma} \right|^2 D_{mn\gamma}(E + e\varphi_\gamma)$$
$$\times D_{m'n'\gamma'}(E + e\varphi_{\gamma'}) \left[f(E - \mu_\gamma + e\varphi_\gamma) - f(E - \mu_{\gamma'} + e\varphi_{\gamma'}) \right] dE \quad (2)$$

f is the Fermi–Dirac function, $D_{mn\gamma}(E)$ is partial electronic states density in the tube γ, equal to the number of states per unit energy interval on the equidistant line number m (see Fig. 2) with zone number n, e is the absolute value of electron charge. Function $D_{mn\gamma}(E)$ may have singularity at the energy E_{*m}, where the electron velocity along the tube axis become zero and partial density disconverges as $|E - E_{*m}|^{-1+1/2j}$, $j = 1, 2, 3, \ldots$. In expression (2) transitions between quantum states $|k, m, n, \gamma\rangle$ and $|k', m', n', \gamma'\rangle$ satisfy the energy conservation low $E_{kmn\gamma} + e\varphi_\gamma = E_{k'm'n'\gamma'} + e\varphi_{\gamma'}$; μ_γ is the chemical potential of isolated tube γ. For the ideal nanotubes the chemical potentials are the same and equal E_π, but in the case of doped or defective nanotubes are different.

The most simple analysis of the expression (2) may be performed for two nanotubes connection ($N = 2$). Supposing that chemical potentials of both tubes and potential φ_1 are zero, denoting the potential difference $\varphi_2 - \varphi_1$ through V, we obtain from (2) at zero temperature

$$J(V) \cong \frac{2\pi e}{\hbar} \int_0^{eV} \sum_{m,n,m',n'} \left| T^{k'm'n'2}_{kmn1} \right|^2 D_{mn1}(E) D_{m'n'2}(E + eV) dE. \quad (3)$$

Integral (3) may disconverge if singularities of functions $D_{mn1}(E)$ and $D_{m'n'2}(E + eV)$ coincide, that appear for discrete voltages with step of eV equal to energy distance

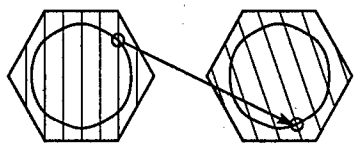

Fig. 2. Allowed states in the Brillouin zone for ideal nanotubes (6,0) and (6,2). The curves are level curves of the π-electron energy. The arrow denotes a quantum transition between nanotube's states.

$E_{*m'+1} - E_{*m'}$ between singularities of partial electron density function, depending on parameter a/R. More detailed analysis of the integral (3) disconvergency requires analytical investigation of the matrix element square dependence on the energy. If one of the joined tubes is metallic and the other has an energy gap then the current (3) is zero in the interval eV equal to the energy gap width. Change of the voltage sign leads to change of zone numbers of electron transition. The last may be cause of nonsymmetric current–voltage characteristic $I(V)$ because transition matrix element depends on the zone numbers the transition is realised between.

We discussed briefly peculiarities of two nanotubes junction current — voltage characteristic $I(V)$. In the many tube junction additive contributions from the different pairs of nanotubes make analysis of expression (2) more complicated, but nonmonotone dependence $I(V)$ in tubes, associated with electron states density singularities and presence of band gaps is summarised.

References

[1] M. S. Dresselhaus, G. Dresselhaus and P. C. Eklund, *Science of Fullerenes and Carbon Nanotubes* Academic Press, San Diego, 1996.
[2] L. Chico, V. H. Crespi, L. X. Benedict et al., *Phys. Rev. Lett.* **76**, 971 (1996).
[3] R. Saito, G. Dresselhaus and M. S. Dresselhaus, *Phys. Rev. B* **53**, 2044 (1996).
[4] S. S. Savinskii and N. V. Khokhryakov, *JETP* **84**, 1131 (1997).
[5] L. D. Landau and E. M. Lifshitz, *Quantum Mechanics*, Pergamon Press, New York 1977.

7th Int. Symp. "Nanostructures: Physics and Technology"
St Petersburg, Russia, June 14–18, 1999

Virtual-tunneling-assisted vertical conduction in superlattices with intentional disorder

I. P. Zvyagin
Faculty of Physics, Moscow State University, 119899 Moscow, Russia

Abstract. A new mechanism of vertical conduction in superlattices with intentional disorder is discussed. We show that at low temperatures the conductance of these structures can be mostly determined by phonon-assisted transitions between the second-nearest wells in the vicinity of the well with the highest size-quantization level. Such transitions involve virtual transitions to the state of the intermediate well and are characterized by a low activation energy and specific dependence of the vertical conductance on the scale of disorder.

1 Introduction

Superlattices with intentional disorder (SLID) and multiple quantum well structures, in which disorder was introduced by random controlled variations of the well widths in the process of structure deposition, were first discussed in [1] and were experimentally realized in [2, 3]. Vertical conduction (in the direction of the SLID growth axis) in such structures was studied by optical methods, in particular, stationary and picosecond luminescence spectroscopy, and also by direct measurements of the vertical conductance. The conductance measurements for Si-doped GaAs/GaAlAs SLID revealed some unusual features [4, 5]. Thus at low temperatures the temperature dependence of the conductance was practically nonactivated (quasimetallic) even for structures with large disorder, namely, when the width of the distribution of size quantization levels exceeded the estimated miniband width. Even though the Coulomb fields arising from the electron redistribution between the wells can give rise to an appreciable suppression of disorder (narrowing of the level distribution) [6], the explanation of the relatively weak temperature dependence of the conductance still remains problematic.

The wave functions of electronic states in SLID can be written in the form $\psi_{\lambda \mathbf{k}_\parallel} = NU_\lambda(z) \exp(i\mathbf{k}_\parallel \rho)$, where N is the normalization factor, z is the coordinate in the SLID growth direction, ρ is the in-plane position vector, $U_\lambda(z)$ is the eigenstate corresponding to the solution of the one-dimensional problem with the potential $V(z) = \sum_n V_n(z)$ describing the modulation of the conduction band edge, and $V_n(z)$ is the potential of the n th well (we set $V_n(z) = 0$ in the barrier regions). The functions $U_\lambda(z)$ are localized and for small overlap of wave functions of the neighboring wells, we can use the basis of "atomic-like" wave functions localized at the corresponding wells. Since for the structures of the type studied in [4] the contributions >from higher subbands are negligible, we can take only the lowest subband into account and write $\lambda = n$. For SLID the vertical conduction is usually controlled by phonon-assisted tunneling between neighboring wells. As in the standard hopping theory (e.g., see [7, 8]), the low-field problem can be reduced to the equivalent resistance network, with resistances expressed in terms of resulting transition rates between the wells (the difference from the standard hopping problem is that we have to sum over the initial and final states of the wells). Thus, for the resistance $R_{nn'}$ connecting the wells

n and n' we have

$$R_{nn'}^{-1} = (e^2/kT) \sum_{\mathbf{k}_\parallel, \mathbf{k}'_\parallel} W_{n\mathbf{k}_\parallel, n'\mathbf{k}'_\parallel} f_{n\mathbf{k}_\parallel}(1 - f_{n'\mathbf{k}'_\parallel}), \tag{1}$$

where $\mathbf{k}_\parallel$ is the two-dimensional momentum in the well plane, $W_{n\mathbf{k}_\parallel, n'\mathbf{k}'_\parallel}$ is the probability of phonon-assisted transitions from the state $n'\mathbf{k}'_\parallel$ to the state $n\mathbf{k}_\parallel$ and $f_{n\mathbf{k}_\parallel}$ is the equilibrium average occupation number of the state $n\mathbf{k}_\parallel$. If the higher level (say, E_n) lies above the Fermi level μ, then (for $E_n - \mu \gg kT$) we have $R_{nn'} = R_0 \exp\{-(E_n - \mu)/kT\}$, where the preexponential factor R_0 depends on the overlap of the wave functions of neighboring wells and only weakly depends on energy and temperature. In the nearest-neighbor approximation, the network is quasi-one-dimensional, and its resistance is given by the sum of series resistances connecting of the neighboring wells of the chain. Clearly, if the scatter of the energy levels is greater than the miniband width and kT, then the total resistance is determined by a critical well (or by a small number of critical wells) with adjoining largest resistances. These resistances exponentially depend on temperature and it follows that the temperature dependence of the total vertical conductance is activated, with the activation energy determined by the position of the highest energy levels relative to the Fermi level. However, with lowering temperature the vertical conductance can be controlled by parallel shunt resistances corresponding to second-neighbor phonon-assisted transitions. In fact, the critical resistances exponentially increase and the level separation for transitions between wells lying on different sides of the critical one (and hence the activation energy) is typically smaller for these transitions. We shall see that the most probable transitions involve virtual intermediate-well states.

2 Probability of second-neighbor phonon-assisted transitions via virtual states

Let us consider a three-well configuration representing the critical region consisting of the critical well 2 with a high level E_2 lying above the Fermi level and two adjacent wells 1 and 3 with lower levels. Next, let $u_n(z)$ and E_n be the wave functions and energies corresponding to the solution of the one-dimensional problem with a single nth well (we assume that $E_2 > E_3 > E_1$). Taking the overlap into account, we can construct the hybridized wave functions corresponding to the solution of the three-well problem. Thus, for level separations exceeding the transfer integrals $t_{mn} = \int dz\, u_m(z) \tilde{V}_n(z)\, u_n(z)$, where $\tilde{V}_n(z) = \sum_{n' \neq n} V_{n'}(z)$, the lowest energy state is mostly localized at well 1 and the corresponding wave function is

$$U_1(z) = N_1\{u_1(z) + c_{12}u_2(z)\}, \tag{2}$$

where N_1 is the normalization factor and $c_{12} = t_{12}/(E_2 - E_1)$. Here we have omitted the transfer integrals between wells 1 and 3 and as usually neglected the nonorthogonality integrals with the functions $u_n(z)$. Similarly, we can write out the expressions for the wave functions $U_2(z)$ and $U_3(z)$ localized at the wells 2 and 3.

The phonon-assisted transition probability, which involves the spatial displacement between wells 1 and 3 is expressed in terms of the matrix element

$$\begin{aligned} I_{3\mathbf{k}_\parallel, 1\mathbf{k}'_\parallel} &= \int dz U_1(z) H_{e,ph}^{\mathbf{k}_\parallel \mathbf{k}'} U_3(z) \\ &= N_1 N_3 \{c_{12} \int dz u_2(z) H_{e,ph}^{\mathbf{k}_\parallel \mathbf{k}'_\parallel} u_3(z) + c_{32} \int dz u_1(z) H_{e,ph}^{\mathbf{k}_\parallel \mathbf{k}'_\parallel} u_2(z)\}, \end{aligned} \tag{3}$$

where $H_{e,ph}^{\mathbf{k}_\parallel \mathbf{k}'_\parallel} = \int \mathbf{d}\rho \, \exp\{i(\mathbf{k}_\parallel - \mathbf{k}'_\parallel)\rho\} H_{e,ph}$ and $H_{e,ph}$ is the Hamiltonian of the electron-phonon interaction.

Expression (3) describes the amplitude of the transition between wells 1 and 3 as the sum of contributions of the two channels, the first one corresponding to the succession of virtual tunneling from 1 to 2 succeeded by phonon-assisted transition from 2 to 3 and another one corresponding to phonon-assisted transition from 1 to 2 succeeded by tunneling from 2 to 3. Note that for our system the probability of direct phonon-assisted transition from 1 to 3 is small compared to that of the process described by Eq. (3). In fact, the integrals involving the functions $u_1(z)$ and $u_3(z)$ are proportional to the overlap factor $\exp\{-\alpha(2w + L)\}$, where α is the inverse wave function decay length in the barrier region, w is the barrier width and L is the well width. On the other hand, the product of the overlap factors appearing in Eq. (3), $\exp(-2\alpha w)$, is much greater so that for $\exp(-\alpha L) \ll 1$ the probability of the direct transition from 1 to 3 is negligible. This is in contrast to the conventional situation in the problem of hopping between localized states, where usually the probability of direct phonon-assisted transition between distant sites is much larger than that for transitions involving virtual states.

The shunt resistance R_{13} for the processes involving virtual states is defined by (1), where the transition probabilities are expessed in terms of the modulus of the matrix element (3) squared. Provided that $(E_3 - E_1) > kT$, we obtain that the conductivity is activated with the activation energy $E_3 - \mu$, which is smaller than the activation energy $E_2 - \mu$ for the conduction mode with nearest-well transitions in the critical region. Another difference between the nearest-well and distant-well conduction modes is a different scaling behavior as the disorder energy (the width of the level distribution) is varied. As follows >from the corresponding dependence of $|c_{12}|^2$, the preexponential factor of the conductance is inversely proportional to the disorder energy squared whereas the activation energy scales as the disorder energy. Note that the usual experimentally studied structures with the number of the wells of the order 100 [4] are mesoscopic and can have widely fluctuating conductances for various realizations of the size quantized level distribution. The scaling behavior of the conductance can, however, be checked for these structures if one uses series of structures similar to those described in [4] with different disorder energies for the same random realization.

3 Discussion

The scaling behavior of the preexponential factor of the conductance is expected to become evident in the case of small activation energies. The activation energy can be small if the energies E_1, E_3 for the states localized on different sides of the critical well lie below the Fermi level. Actually, the levels E_1, E_3 can correspond to hybridized states of several wells (clusters) rather than to individual wells adjacent to the critical one. If the miniband width for the corresponding regular SL (or the transfer energy) is not too small compared with the disorder energy, then the average number of sites in the clusters is sufficiently large; then for the most probable realization of disorder the lowest energies of hybridized states of the clusters adjoining the critical well lie below the Fermi level. In this case the nonactivated temperature dependence of the vertical conductance is expected.

Acknowledgements

This work was supported by the Russian Foundation for Basic Research, the Ministry of Education and the program "Universities of Russia".

References

[1] J. D. Dow, S. Y. Ren and K. Hess, *Phys. Rev. B* **25**, 6218 (1982).
[2] A. Chomette, B. Deveaud, A. Regreny and G. Bastard, Phys. Rev. Lett. **57**, 1464 (1986).
[3] T. Yamamoto, M. Kasu, S. Noda and A. Sasaki, *J. Appl. Phys.* **68**, 5318 (1990).
[4] G. Richter, W. Stolz, S. Koch, P. Thomas, K. Maschke and I. P. Zvyagin, *Superlattices and Microstructures* **22**, 475 (1997).
[5] M. Lee, S. A. Solin and D. R. Hines, *Phys. Rev. B* **48**, 11921 (1993).
[6] I. P. Zvyagin and M. A. Ormont, *The 24th Int. Conf. on the Physics of Semiconductors, August 2-7, 1998, Jerusalem, Israel* , Abstracts, p. Tu-P87.
[7] B. I. Shklovskii and A. L. Efros, *Electronic Theory of Doped Semiconductors* (in Russian), Moscow, Nauka, 1979.
[8] V. L. Bonch-Bruevich, I. P. Zvyagin, R. Keiper, A. G. Mironov, B. Esser and R. Enderlein, *Electronic Theory of Disordered Semiconductors* (in Russian), Moscow, Nauka, 1981.

7th Int. Symp. "Nanostructures: Physics and Technology"
St Petersburg, Russia, June 14–18, 1999

GPLDS.01p

Spin and energy resolved near-threshold electron photoemissionfrom strained GaAs/GaAsP heterostructure

H.-J. Drouhin†, G. Lampel†, *Yu. A. Mamaev*‡ A. V. Subashiev‡
and Yu. P. Yashin‡
† Laboratoire de Physique de la Matière Condensée,
UMR 7643-CNRS, Ecole Polytechnique, 91128 Palaiseau, France
‡ St Petersburg State Technical University, 195251 St Petersburg, Russia

Abstract. High resolution energy distribution curves (EDC) and a polarization versus energy distribution curves (PEDC) of the electrons, photoemitted from strained GaAs/GaAsP are presented. We have found that in the vicinity of the photothreshold the polarization does not vary across the EDC both at room and 120 K temperatures of the cathode, which shows that no depolarization occurs in the band bending region (BBR). The EDC are interpreted in terms of the competition between the electron tunneling in vacuum and hopping between the states in the band-bending region localized by the fluctuation potential.

Introduction

The photoemission from the stressed film is understood as a the three-step process, consisting of: (i) electron excitation under optical pumping, (ii) electron relaxation to the local equilibrium state and capture in the BBR, and finally, (iii) electron escape into vacuum throughout the BBR [1]. The details of the third step, i.e. electron kinetics in the BBR is still a rather controversial matter. Experimental investigations of the EDC and PEDC curves performed in unstrained GaAs cathodes showed, that, for the near bandgap excitation the electron energy distribution is spread over a broad energy band with a width close to the value of NEA [2]. It is shifted below the position of conduction-band minimum in the bulk. The polarization of the emitted electrons in this band is strongly dependent on the excitation energy, but not on the emitted electron energy. This facts may suggest that the electron energy relaxation in the BBR occurs via hopping between electronic states localized in the surface plane by the strong fluctuation potential introduced by the random spatial distribution of the ionized acceptors and donors in the BBR [3]. The localization suppresses the spin and energy relaxation processes, while the spread of the energies of the loclalized states provides broad EDC.

In this paper we report the first experimental results for the energy and polarization distribution curves of the electrons, photoemitted from a highly strained GaAs layer. We show that the observations are in line with the model of the highly localized electron states in the BBR.

1 Results

The experimental set-up was described in [2]. The sample is illuminated by σ^+ or σ^- circularly polarized light from a Ti:Sapphire or He-Ne laser normal to its surface. The photoemitted electrons are energy selected by a cylindrical 90° electrostatic deflector operating in the constant-energy mode. The full width at half maximum of the transmission function is $\Delta E \simeq 20$ meV. The polarization of the energy selected electrons is measured by a Mott detector. The sample under investigation was a 140 nm thick GaAs overlayer MOCVD

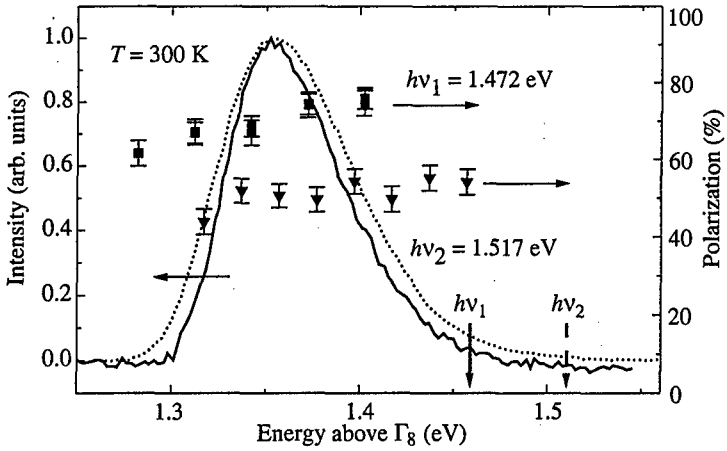

Fig. 1. Electron energy distribution and polarized electron distribution of the emitted electrons for GaAs/GaAsP strained cathode, normalized to the maximum value for two excitation energies, $T = 300$ K, energy resolution is 20 meV. Maximum position of the EDC is shown by arrow.

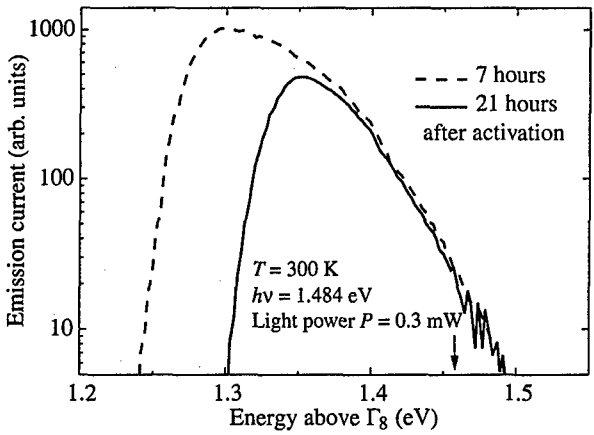

Fig. 2. Evolution of the electron energy distribution upon the degradation of the GaAs/GaAsP photocathode at $T = 300$ K, excitation energy is 1.484 eV; light power 0.01 mW. Dashed line — 7 hours, solid line — 21 hours after the activation. Band gap value is shown by arrow.

grown on a $GaAs_{0.72}P_{0.28}$ buffer at the top of commercial GaAs (001) wafer. The details of the sample structure were described in [4]. NEA state was achieved by activation of atomically clean surfaces with cesium and oxygen. The quantum yield at the poarization maximum was not less than 3×10^{-4}.

The EDC and PEDC data at room temperature are presented in Fig. 1 for two excitation energies. The position of the EDC peak is shifted down in energy as in most unstressed GaAs cathodes, though the EDC are rather narrow (FWHM does not exceed 100 meV) at room temperature. Similar curves are observed at 120 K. Besides, we have found that in the studied sample the shape of the EDC peak does not change noticeably in the excitation range in the vicinity of the photothreshold $E_g - 0.02\,\text{eV} \ll h\nu \ll E_g + 0.07\,\text{eV}$, where $E_g = 1.47$ eV. The E_g value of the film was determined by fitting of the polarization and

quantum yield spectra to the spectra calculated in the diffusion model [5]. It is clearly seen that the polarization remains constant across EDC, so that no depolarization effects for the electrons in BBR region are registered. As a result the integrated values of the electron polarization for the $P(h\nu)$ spectrum and the P values measured at the EDC maximum (both at 20, and 80 meV resolutions) are found to be about equal at given $h\nu$.

Typical EDC spectra for the excitation energy ($h\nu = 1.484$ eV) above E_g, $h\nu - E_g \geq$ 150 mev taken in 7 and 21 hours after activation are presented in Fig. 2. The degradation of the strained-layer photocathode sample is found to be accompanied by a cut off in the low-energy part of EDC, which manifests the decrease of the effective NEA. The NEA decrease is known to be a result of the activation layer degradation due to the cesium-oxygen disbalance. In our case the degradation was accompanied by a considerable shift of the EDC low-energy threshold to the high-energy side, while the EDC high-energy edge does not change.

2 Discussion

The electronic potential in the BBR near the surface fluctuates substantially due to random distribution of ionized acceptors and Cs-originated donor centers. Therefore all the electronic states in the BBR below a certain energy defined as an electron Mobility Edge (ME) are localized also in the surface plane by the potential fluctuations. The density of the localized states $g(\epsilon)$ below the ME is a rapidly decreasing function of the localization energy ϵ in the bang gap (measured downwards from the ME). To obtain analytical results it is convenient to approximate it by an exponent, $g(\epsilon) = g_0 \exp(-\epsilon/\gamma)$, where g_0 is the density of states at the ME energy. The estimated and measured time of the electron emission from the BBR in vacuum $\tau_{\text{emi}} \approx 10$ ps is much larger that the time of the delocalized electron energy relaxation due to the emission of the phonons, whereas below ME the electron energy relaxation is suppressed since the number of the final localized states in the nearest vicinity of a given localized state is diminishing with energy. The emitted electron energy distribution is formed as a result of competition of the processes of the electron emission in vacuum and the electron hopping down in energy in the tail states. We will assume the probability for the electron to emit a phonon $\tau_{\text{hop}}^{-1}(\epsilon)$ to be proportional below ME to the average density of the final electron states. Similar model was developed for interpretation of the luminescence spectra in mixed crystals in Ref. [6].

In the case when the emitted phonon energy is smaller than the EDC pear width, the calculated electron emission current energy dependence $J_{\text{emi}}(\epsilon)$ is

$$J_{\text{emi}}(\epsilon) = J_{\text{emi}}(0) \exp\left[\frac{\epsilon}{\gamma} - \alpha\left(\exp\left(\frac{\epsilon}{\gamma}\right) - 1\right)\right], \tag{1}$$

where the parameter α is given by $\alpha = 2\tau_{\text{hop}}(0)\gamma/(\tau_{\text{emi}}\delta^2 g_0 a_0^2)$, τ_{emi} is the time of the electron emission from the BBR in vacuum, δ is the average emitted phonon energy, and a_0 is the average localization radius of the tail states at the emission peak energy. The results of the calculation of the EDC together with the experimental curve are shown in Fig. 3. It is seen that the shape of the experimental EDC is susessfuly reproduced. The fitting of the Eq. (1) dependence to experimental data gives $\gamma = 30$ meV, $\alpha = 0.08$, in line with theoretical estimations.

The depolarization decline below the conduction band energy is the consequence of the localization of the electron states in this energy region, since the main D'yakonov-Perel' spin-relaxation mechanism is not effective for the localized states. The changes of the EDC with temperature are found to be mainly due to the thermal variation of the band gap.

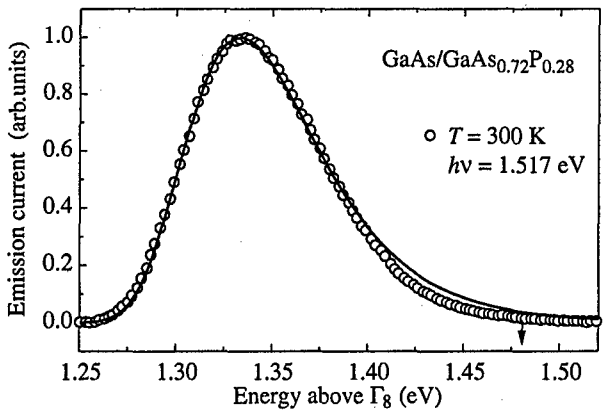

Fig. 3. Experimental electron energy distribution curve $T = 300$ K, together with results of the calculation (solid line) using the localized states model. Band gap value is shown by arrow.

In conclusion, the EDC and PEDC measurements for the strained GaAs layer surface activated to NEA, demonstrate the electron capture to the band bending region before emission. The shape of the energy distribution peak is in good agreement with the results of the model of the emission from the states localized in the surface plane by the fluctuations of the surface potential. The localization is also manifested by switching off the spin relaxation across the emission peak.

Acknowledgments

This work was supported by the Russian State Programs "Physics of Solid State Nanostructures" under grant 97-1091 and "Surface Atomic Structures" under grant 2.6.99. One of us (Yu. M.) is thankful to Swiss National Science Foundation (grant 7IP 51742) for travel support and to Ecole Polytechnique, France, for the support, which made possible to perform joint experiments. HJD thanks the Délégation Générale pour l'Armement for support.

References

[1] See e.g., A. V. Subashiev, Yu. A. Mamaev, Yu. P. Yashin and J. E. Clendenin, *Phys. Low-Dim. Structures* **1/2**, 1 (1999), and references therein.

[2] H.-J. Drouhin, C. Hermann and G. Lampel, *Phys. Rev. B* **31**, 3859 (1985); *B* **31**, 3872 (1985).

[3] A. V. Subashiev, *Proc. of the Low Energy Polarized Electron Workshop* LE-98, St. Petersburg, 1998, ed. Yu. A. Mamaev et al., SPES-Lab-Pub., 1998, p. 125.

[4] Yu. A. Mamaev, Yu. P. Yashin, A. V. Subashiev et al., *Phys. Low-Dim. Structures* **7**, 27 (1994).

[5] B. D. Oskotskij, A. V. Subashiev and Yu. A. Mamaev, *Phys. Low Dim. Struct.* **1/2**, 77 (1997).

[6] E. L. Ivchenko et al., *Phys. Solid State* **36**, 218 (1994).

7th Int. Symp. "Nanostructures: Physics and Technology"
St Petersburg, Russia, June 14–18, 1999

Symmetry of the GaAs crystal with δ-doping Si layers and its influence on the band structure

Yu. E. Kitaev†, M. F. Kokorev‡ and P. Tronc§
† Ioffe Physico-Technical Institute, St Petersburg, Russia
‡ Radioengineering and Electronics Department, State Electrotechnical University, 197367 St. Petersburg, Russia
§ Laboratoire d'Optique Physique, ESPCI, 10 rue Vauquelin, 75005 Paris, France

Abstract. The GaAs crystals are shown to lower symmetry from T_d to D_{2d} or C_{2v} when inserting a δ-layer with odd or even number of Si planes respectively. These symmetry changes correspond to uniaxial or plane distortion of the GaAs lattice in the neighbourhood of a δ-layer. The band shifts of GaAs induced by the insertion of δ-layers are estimated.

Introduction

The progress in MBE and MOCVD technologies allowed to fabricate semiconductor heterostructures with a spatial scale comparable with a crystal lattice constant [1]. It has been pointed out [2, 3] that the continuum models (such as envelope-function method, effective-mass method [4] etc.), which proved to be effective for heterostructures with thick layers, failed to describe adequately the physical properties of nanostructures. For heterostructures with thick layers, the validity of continuum models results from translational symmetry in each layer which breaks only at interfaces. As a result, the description of such structures is based on the parameters of constituent bulk crystals.

However, for heterostructures with ultrathin layers (comprising several atomic planes) the translational symmetry along the direction perpendicular to the layers is lost in any individual layer because the thickness of a layer is comparable with the lattice constant. Moreover, interface regions become comparable with a layer thickness. Therefore, to study the properties of such systems we should start with determination of their crystal structure (space group and atomic arrangement within a primitive cell), i.e. to treat them as new crystals with own symmetry.

The performed analysis shows [3] that in superlattices (SL), new periodicity arises along the growth direction accompanied by a change of their point symmetry. In general, the space group and atomic arrangement over the Wyckoff positions in the primitive cell turn out to be functions of the SL growth direction and numbers of monolayers of constituent bulk materials forming the SL. As a result, a symmetry of a SL can be described by one of the 230 (three-dimensional three-periodic) space groups.

In contrast, in δ-doped systems, the periodicity along the direction perpendicular to the layers disappears.

1 Symmetry of the GaAs crystal with Si δ-layers

A GaAs crystal with a Si δ-layer is a 3D system with 2D translational symmetry. The symmetry of such systems is described by one of the 80 diperiodic groups in 3D [5]. The

Table 1. Symmetry of the GaAs crystal with Si δ-layers.

No of Si planes n	Space group G	Point group G_0	Bravais lattice	Atomic arrangement
bulk	T_d^2	T_d	fcc	1a(000)–Ga(T_d); 1c$\left(\frac{1}{4}\frac{1}{4}\frac{1}{4}\right)$-As($T_d$);
1	DG59	D_{2d}	square	1a(000)–$Si_{Ga/As}$(D_{2d}); 2f$\left(\frac{1}{2}\frac{1}{2}z\right)$-Ga/As($C_{2v}$);
	$P\bar{4}m2$			2g$\left(0\frac{1}{2}z\right)$-As/Ga($C_{2v}$)
2	DG23	C_{2v}	primitive	1a(00z)–Si_{Ga}(C_{2v}); 1c$\left(0\frac{1}{2}z\right)$–$Si_{As}$ (C_{2v});
	P2mm		rectangular	1b$\left(0\frac{1}{2}z\right)$-As($C_{2v}$); 1d$\left(\frac{1}{2}\frac{1}{2}z_1\right)$-Ga($C_{2v}$);
				1d$\left(\frac{1}{2}\frac{1}{2}z_2\right)$-Ga($C_{2v}$)
3	DG59	D_{2d}	square	1a(000)-Si_{Ga} (D_{2d}); 2g$\left(0\frac{1}{2}z_1\right)$-$Si_{As}$ (C_{2v});
	$P\bar{4}m2$			2f$\left(\frac{1}{2}\frac{1}{2}z\right)$-Ga($C_{2v}$); 2g$\left(0\frac{1}{2}z_2\right)$-As($C_{2v}$)

typical representatives of the δ-Si:GaAs structure with one and two Si planes constituting a δ-layer are shown in Fig. 1.

We determined that the crystal structure of such a system (space group and arrangement of atoms over the Wyckoff positions) depends on the number n of Si atomic planes in a δ-layer. The results of the analysis are presented in Table 1. The Wyckoff positions and their coordinates follow notations of [5].

Notice, that our analysis is valid for any crystal with a zinc-blende structure including GaN, InN, InAs etc.

From Table 1, one can see that the introduction of one (odd) Si plane reduces the point symmetry of the GaAs bulk crystal from T_d to D_{2d} whereas the introduction of two (even) planes from T_d to C_{2v}. Thus, in the case of odd number of Si planes, the x and y axes are equivalent whereas they become inequivalent for even number of Si planes. For $n = 1$, we have considered two cases: Si substitutes Ga or As (Si_{Ga} or Si_{As}, respectively). In both cases, the symmetry remains the same but Ga and As atoms in adjacent planes interchange their symmetry positions.

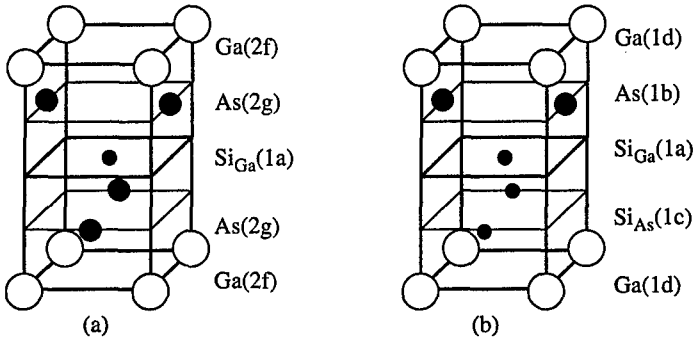

Fig. 1. The crystal structures of the GaAs crystal with one (a) and two (b) Si planes in a δ-layer.

2 Influence of Si δ-layer-induced lattice distortions on band structure

We can see that the introduction of one (odd) Si atomic plane in a bulk GaAs is equivalent (from the point of view of symmetry) to uniaxial deformation of the bulk crystal whereas the introduction of two (even) Si atomic planes corresponds to plane deformation. This modifies the valence (VB) and conduction band (CB) states.

As an example, we estimate the band shifts induced by lattice distortions along the [001] direction due to the insertion of a δ-layer with one Si plane (see Fig. 2). In case of uniaxial deformation, the shifts of conduction band (CB), heavy-hole (HH), light-hole (LH) and spin-orbit split-off (SO) bands measured from the CB bottom and VB top at zero strain (without a δ-layer), ΔE (CB), ΔE (HH) and ΔE (LH,SO), are given by [6]

$$\Delta E(\mathrm{CB}) = \frac{2}{3}E_{\mathrm{H}}, \tag{1a}$$

$$\Delta E(\mathrm{HH}) = -\frac{1}{3}E_{\mathrm{H}} - E_{\mathrm{U}}, \tag{1b}$$

$$\Delta E(\mathrm{LH,SO}) = -\frac{1}{3}E_{\mathrm{H}} - \frac{1}{2}\left[(\Delta - E_{\mathrm{U}}) \mp (9E_{\mathrm{U}}^2 + 2E_{\mathrm{U}}\Delta + \Delta^2)^{1/2}\right] \tag{1c}$$

where $E_{\mathrm{H}} = 2a[(C_{11} - C_{12})/C_{11}]\epsilon_{\mathrm{Ga/As}}$, $E_{\mathrm{U}} = -b[(C_{11} + 2C_{12})/C_{11}]\epsilon_{\mathrm{Ga/As}}$; $\epsilon_{\mathrm{Ga/As}}$ is the strain induced by a Si plane substituting Ga or As planes, C_{11} and C_{12} are elastic constants, a and b are hydrostatic and shear deformation potentials, respectively, Δ is spin-orbit split-off energy.

We estimate the strain $\epsilon_{\mathrm{Ga/As}}$ in the neighbourhood of a δ-layer as a relative difference of corresponding covalent tetrahedral radii:

$$\epsilon_{\mathrm{Ga/As}} = (r_{\mathrm{Si}} - r_{\mathrm{Ga/As}})/2r_{\mathrm{Si}}. \tag{2}$$

For GaAs, taking the values of covalent tetrahedral radii ($r_{\mathrm{Si}} = 1.17$ Å, $r_{\mathrm{Ga}} = 1.26$ Å and $r_{\mathrm{As}} = 1.17$ Å) from [7], the values of elastic constants ($C_{11} = 1.188 \times 10^{12}$ dyn/cm^2, $C_{12} = 0.538 \times 10^{12}$ dyn/cm^2) and deformation potentials (a = −8.9 eV, b = −1.73 eV) as well as spin-orbit split-off energy (Δ = 0.34 eV) from [6], we obtain the values for band

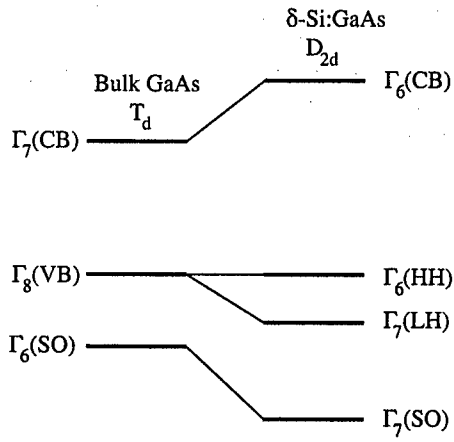

Fig. 2. GaAs band state modification induced by insertion of one Si plane (band shifts correspond to Table 2).

Table 2. CB and VB shifts (in eV) in GaAs regions in the neighbourhood of a δ-layer.

	Si at Ga position	Si at As position
$\epsilon_{Ga/As}$	–0.038	0.0043
E_H	0.374	0.0416
E_U	–0.127	–0.0141
ΔE(CB)	0.249	0.028
ΔE(HH)	0.002	0.002
ΔE(LH)	–0.150	–0.028
ΔE(SO)	–0.571	–0.354

shifts in GaAs regions in the neighbourhood of a δ-layer given in Table 2. Note that the case of even numbers of Si planes is more sophisticated: the plane deformation arises that induces anisotropy in the xy plane.

From the above results, we see that in the case of Si substituting Ga the band gap strongly increases whereas for Si at As sites the band shifts are much smaller. This leads to changes of band populations, mobility and other kinetic coefficients in the neighbourhood of a δ-layer [8]. The lattice distortion extends over tens of lattice constants. Thus, these effects are to be taken into account when analyzing the properties of nanostructures.

Acknoledgements

The authors acknowledge the Russian Ministry of Education Grant 97-5-5.3-19. One of us (PT) wishes to thank the French Embassy in Moscow for the support.

References

[1] K. Ploog, *J. Cryst. Growth* **81**, 304 (1987).
[2] M. Di Ventra and K. A. Mader, *Phys. Rev. B* **55**, 13148 (1997).
[3] Yu. E. Kitaev, A. G. Panfilov, P. Tronc and R. A. Evarestov, *J. Phys.: Condens. Matter* **9**, 257 (1997); *ibid* **9**, 277 (1997).
[4] G. Bastard, *Wave mechanics applied to semiconductor heterostructures* (Les Ulis, Editions de Physiques, 1992).
[5] E. A. Wood, *Bell Syst. Techn. J.* **43**, 541 (1964).
[6] I. Suemune, *Phys. Rev. B* **43**, 14099 (1991).
[7] C. Kittel, *Introduction to Solid State Physics* (Wiley, New York, 1976).
[8] G. L. Bir and G. E. Pikus, *Symmetry and deformation effects in semiconductors* (Nauka, Moscow, 1972) (in Russian).

7th Int. Symp. "Nanostructures: Physics and Technology"
St Petersburg, Russia, June 14–18, 1999

Observation of negative persistent photoconductivity in GaAs delta-doped by Sn

V. A. Kulbachinskii†, V. G. Kytin†, R. A. Lunin†, A. V. Golikov†, A. V. Demin†, V. G. Mokerov‡, A. S. Bugaev‡, A. P. Senichkin‡, P. M. Koenraad#, R. T. F. van Schaijk§ and A. de Visser§

† Low Temperature Physics Department, Moscow State University, 119899, Moscow, Russia

‡ Institute of Radioengineering and Electronics, RAS, Moscow, Russia

Physics Department,Eindhoven University of Technology, The Netherlands

§ Van der Waals-Zeeman Institute,University of Amsterdam, The Netherlands

Abstract. GaAs δ-doped structures with various Sn doping densities have been grown on vicinal substrates. The observed at low temperatures negative persistent photoconductivity in heavily δ-doped samples is connected with increase of electron concentration and decrease of electron mobilities. Such effect may occur when the correlations among charged shallow donors and DX^--centers are destroyed via photoexcitation of electron out of the DX^--centers. The observed in samples with electron concentration less than $8 \times 10^{12}\,\mathrm{cm}^{-2}$ effect of positive persistent photoconductivity may be explained by spatial separation of photogenerated carriers.

Introduction

Tin is rarely been used for δ-doping in GaAs because of its high segregation ability [1]. On the other hand with tin it's possible to obtain very high electron densities [2]. The structures with Sn δ-doping on vicinal GaAs substrates show a perspective for obtaining one-dimensional electronic channels [3]. The only positive persistent photoconductivity have been observed for δ-doped GaAs(Si) samples [4].

1 Samples

All investigated structures were grown by MBE on GaAs substrates misoriented 3° from (001) plane towards (110) basal plane. On semi-insulating GaAs (Cr) substrate a buffer layer of i-GaAs (width 450 nm) was grown. At a temperature of $\approx$ 450°C a tin layer was deposited in the presence of an arsenic flux. The structures were covered by a layer of i-GaAs (width 40 nm) and a cap layer n-GaAs (width 20 nm) with a concentration of silicon $2 \times 10^{18}\,\mathrm{cm}^{-3}$. The design density of tin in the δ-layer varied from $10^{14}\,\mathrm{cm}^{-2}$ in sample No 1 down to $2.5 \times 10^{12}\,\mathrm{cm}^{-2}$ in sample No 4. Some parameters of sample are shown in Table 1. Resistance was measured in plane of Sn delta-layer. The effect of photoconductivity was investigated for Hall bar samples with the current channel in the [110] direction.

2 Results

The influence of the illumination on the resistance of the samples has been investigated at temperatures $T = 4.2$ K and $T = 77$ K for light wavelengths λ from 650 nm to 1700 nm. The resistance of the samples No 1 and No 2 with high electron density (more

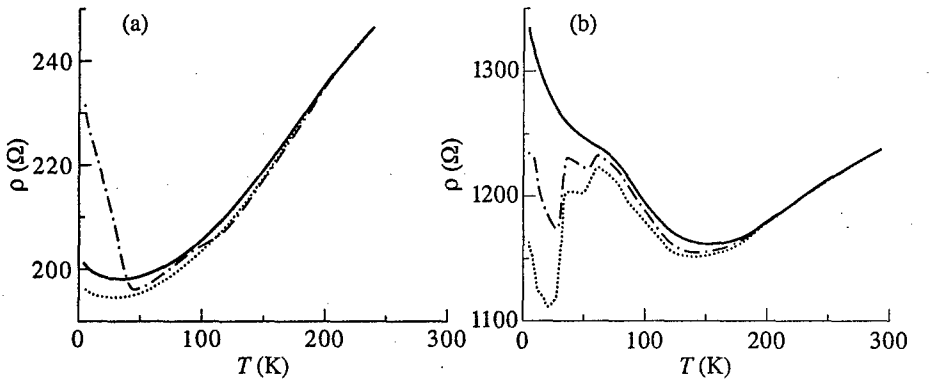

Fig. 1. Temperature dependence of resistance for sample No 1 (a) and No 3 (b) in darkness (solid lines) and after illumination at $T = 4.2$ K by light with wavelength $\lambda = 791$ nm (dashed lines) and $\lambda > 1120$ nm (dashed-dotted lines).

than 10^{13} cm^{-2}) drops rather rapidly under illumination by light with wavelength less than approximately 835 nm ("short wavelength" radiation), reaches the minimum and than increases much slower. This growth of resistance saturated at value bigger than the value of the resistance in darkness. The resistance under illumination by light with wavelength more than 835 nm ("long wavelength" radiation) increases directly from the value in darkness. After illumination at $T = 4.2$ K the resistance does not change in darkness during more than 5 hours (negative persistent photoconductivity — NPPC).

The resistance of the samples No 3 and No 4 with electron density less than 10^{13} cm^{-2} decreases after both type of illumination, but the saturated value of resistance after illumination by "short wavelength" radiation is less then the value of resistance after illumination by "long wavelength" radiation. After switching off the illumination the resistance of samples relaxes to the darkness value during several hours (positive persistent photoconductivity — PPPC).

The temperature dependence of resistance, measured in darkness and during heating with rate 3 K/min after illumination at $T = 4.2$ K by light passed through silicon plate ($\lambda > 1120$ nm) and through interference filter 783 nm $< \lambda <$ 799 nm, are shown on Fig. 1 for samples No 1 and No 3. For heavily doped sample No 1 the effect of NPPC is observed at temperatures less then 40 K, that is near the characteristic temperature for population of DX-centers in Sn-doped GaAs (60 K according to Ref. [5]). In all samples the photoconductivity is persistent at temperatures less then 180 K.

The investigation of Shubnikov–de Haas effect shows that for PPPC effect the frequencies in Fourier spectrum are changed weakly, but for NPPC effect the frequencies (and consequently the electron concentration in subband) increase compared to darkness case (Fig. 2). The quantum mobilities of electrons in subbands increase slightly (mainly in upper subbands) for PPPC effect and decrease in lower subbands for NPPC effect. The Hall mobilities of electrons also increase after illumination by "short wavelength" radiation and decrease after illumination by "long wavelength" radiation (Table 1).

3 Discussion

The effect of PPPC may be explained by photogeneration of electron-hole pairs in investigated structures. The electrons flow towards the δ-layer, and the holes recombine with the

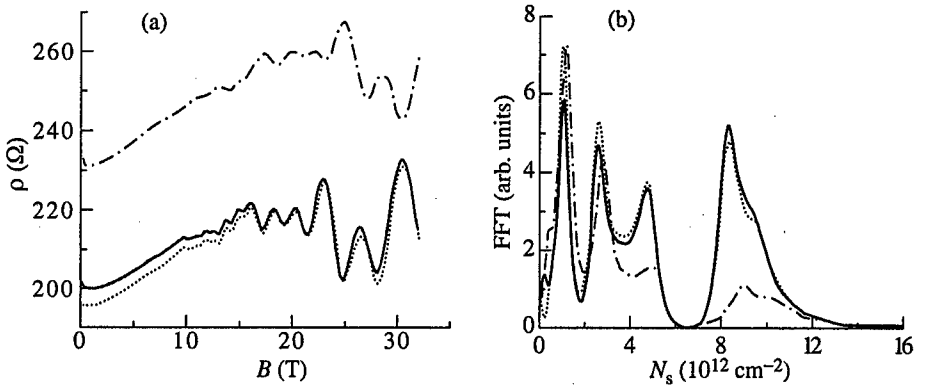

Fig. 2. Magnetoresistance of sample No 1 (a) and Fourier spectrum of Shubnikov–de Haas oscillations (b) in darkness (solid lines) and after illumination by light with wavelength $\lambda = 791$ nm (dashed lines) and $\lambda > 850$ nm (dashed-dotted lines) at $T = 4.2$ K.

Table 1. Resistance ρ, electron Hall concentration n_H, sum of the Shubnikov–de Haas concentrations n_{SdH} in all subband and Hall mobility μ_H at temperature $T = 4.2$ K for samples Nos 1–3 in darkness and after illumination by light with wavelength $\lambda = 791$ nm and $\lambda > 850$ nm.

Sample number	Illumination	ρ (Ω)	n_H (10^{12} cm^{-2})	μ_H (cm^2/Vs)	Σn_{SdH} (10^{12} cm^{-2})
	darkness	202	31.5	981	26.2
1	$\lambda = 791$ nm	198	31.6	1000	26.2
	$\lambda > 850$ nm	240	30.4	857	27.9
	darkness	384	25.8	631	25.9
2	$\lambda = 791$ nm	367	24.9	683	26.0
	$\lambda > 850$ nm	422	26.0	571	29.6
	darkness	1330	8.03	586	8.28
3	$\lambda = 791$ nm	1173	8.62	618	8.39
	$\lambda > 850$ nm	1235	8.81	574	8.38

charged acceptors in the buffer GaAs layer or flow towards the substrate. In the saturation case the conduction band in the GaAs buffer layer is flattened, and the additional electron concentration equals $\Delta n_S = \epsilon\epsilon_0 \Delta V/ed = 1.2 \times 10^{11}$ cm^{-2}, where d is the width of buffer layer, $\Delta V = 0.75$ V is the potential corresponding to energy level of chrome in substrate.

The relaxation of PPPC in darkness (Fig. 3) is good fitted by dependence

$$\sigma(0) - \sigma(t) = A \ln\left(1 + \frac{t}{\tau}\right) \tag{1}$$

that is characteristic for spatial separation of photogenerated carriers [6]. The "long wavelength" radiation possibly ionize the deep levels in substrate and does not neutralize the acceptors ($N_a \approx 2 \times 10^{10}$ cm^{-2}) in buffer layer.

The NPPC effect is connected with increase of electron concentration and decrease of electron mobilities in heavily δ-doped samples. Such effect may occur when the corre-

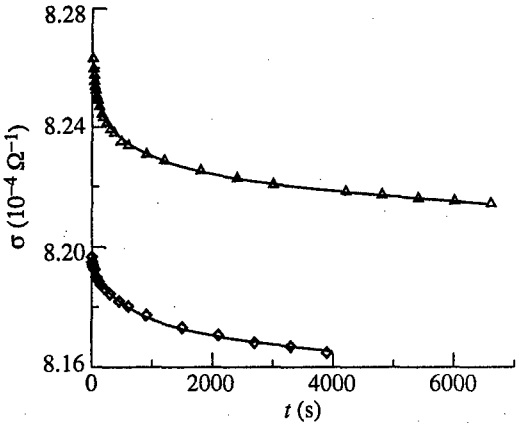

Fig. 3. The time dependence of conductivity of sample 3 in darkness after illumination by light with $\lambda = 791$ nm (triangles) and $\lambda > 1120$ nm (squares) at $T = 77$ K. Solid lines are a theoretical fitting to expression (1) with $\tau = 23$ s for $\lambda = 791$ nm and $\tau = 68$ s for $\lambda > 1120$ nm.

lations among charged shallow donors and DX^--centers is destroyed via photoexcitation of electron out of the DX^--centers [7, 8]. However we cannot exclude that Sn form in GaAs neutral DX^0-centers and after photoionization these metastable centers scatter the electrons much stronger.

The work was supported by the Russian Foundation for Basic Research (Grant No 97-02-17396) and by the Dutch organizations N.W.O. and F.O.M.

References

[1] J. J. Harris et. al., *J. Appl. Phys. A* **33**, 87 (1984).
[2] V. A. Kulbachinskii et. al., *Proceedings of 6th Int. Symp. "Nanostructures: Physics and Technology"*, St. Petersburg, Russia p. 293, 1998.
[3] A. de Visser, et al. *Pis'ma Zh. Eksp. Teor. Fiz.* **59**, 340 (1994); *JETP Lett.* **59**, 363 (1994).
[4] S. Arscott, M. Missous, L. Dobaczewski, *Semicond. Sci. Technol.* **7**, 620 (1992).
[5] M. Baj and L. H. Dmowski, *J. Phys. Chem. Solids* **56**, 589 (1995).
[6] H. J. Queisser and D. E. Theodorou, *Phys. Rev. B* **33**, 4027 (1986).
[7] E. Buks, M. Heiblum and H. Shtrikman, *Phys. Rev. B* **49**, 14790 (1994).
[8] J. M. Shi et al., *Phys. Rev. B* **55**, 13093 (1997).

7th Int. Symp. "Nanostructures: Physics and Technology"
St Petersburg, Russia, June 14–18, 1999

GPLDS.04p

Effective-mass approximation for electrons in ultrathin heterolayers

E. E. Takhtamirov and *V. A. Volkov*
Institute of Radioengineering and Electronics of RAS,
Mokhovaya 11, 103907 Moscow, Russia

Abstract. It was shown that the usually employed model of rectangular potentials in the effective-mass equations generally fail for ultrathin layers, of width of the order of the lattice constant. There are additional terms, which play minor role for thick quantum wells and barriers, that may have drastic influence on electron states in semiconductor nanostructures with ultrathin layers. The terms are defined with details of the microscopic structure of heterointerfaces. It was shown that allowance for these terms may turn a barrier layer into an effective quantum well binding electrons, and vice versa.

Presently the progress in crystal growth technology allows to compose high-quality heterostructures containing ultrathin layers, of width of the order of the lattice constant a, and experimentally investigate the electron states in such structures (see e. g. [1]). The effective-mass approximation (EMA) based on the envelope-function method is not applicable for description of electron states in quantum wells (or barriers) of width of the order of a is a commonly held view (see e. g. [2]). On the other hand, it is received that EMA works "surprisingly well" for nanostructures composed of thick layers even with atomically abrupt heterointerfaces (see e. g. [3]). Accepting these standpoints, one still may set at least two questions: "What are the reasons leading to the first statement?" and "What is the accuracy of EMA when it is used to consider electron states in a quantum well of some width L?" The main goal of the work is to answer these questions and formulate envelope-function equations applicable for ultrathin heterolayers.

In [4] it has been shown that the usually employed model of rectangular potentials (just a set of Heaviside step-functions $\Theta(z - z_i)$) and position-independent effective mass parameters in the effective-mass equations describing electron states in semiconductor nanostructures may be used as a *zero*-order approximation, with the small parameter $a\bar{k}$, where $1/\bar{k}$ is the characteristic size of the envelope function. Thus the only input parameters needed to solve the problem of electron states within the accuracy are the bulk effective masses of one of the constituents and the band offsets. The EMA of such grade of accuracy does not allow to describe some fine effects like 2D Brillouin zone-center mixing of light and heavy holes in (001) A_3B_5 nanostructures, mixing of different valleys induced by broken translation symmetry of the structures, *etc.* But for eigenvalues of the electron states it provides one with an approximately correct solution. This takes place only for heterostructures composed of layers of width $L \gg a$ each.

It is evident that the rectangular profile of the heterostructure potential is an approximation. As the width of the layers decreases, the number of atoms in the layers become comparable with the number of heterointerface atoms, and the simple model will inevitably fail even for the eigenvalues. The detailed microscopic structure of the heterointerface is unknown. So it is desirable to describe it with a set of a few parameters that should be taken from the experiment along with other parameters like effective masses and band offsets. Of course, the parameters will definitely depend on the heterostructure growth process, but

similar situation exists for the band offsets: the heterointerface dipole may affect it considerably. From this point of view the properly constructed EMA that takes into account real heterointerface structure, being still very simple and allowing plain inclusion of external potentials, would have no drawbacks when compared to other empirical instruments like tight-binding or pseudopotential methods [5].

The appropriate solution to the problem may be found if we pay attention to the *first*-order EMA in small parameter $a\bar{k}$ that allows for microscopic structure of heterointerfaces (we considered lattice-matched A_3B_5 materials only). This approximation grade will play a role of the basic EMA for structures with ultrathin layers. The structure of the proper equations is the following. The kinetic energy operator has its usual bulk form, but the effective potential energy consists of the "usual" rectangular term and some Dirac δ-functions at the heterointerfaces. For example, for conduction band Γ-states in a symmetric quantum well (or barrier) of width L it has the following form:

$$U_c(z) = \Delta U_c\,[\Theta(z) - \Theta(z-L)] + d_1\,[\delta(z) + \delta(z-L)]\,. \tag{1}$$

Here ΔU_c is the band offset, for the barrier $\Delta U_c > 0$ and for the quantum well $\Delta U_c < 0$, and the parameter d_1 is defined with details of the microscopic structure of the heterointerface. This parameter may be roughly estimated as $d_1 \sim a\Delta U_c$. For its experimental evaluation it may be important that d_1 should take different values for different nanostructure growth crystal orientations. To illustrate this, we will consider its microscopic structure. If we put down the potential of the heterostructure with a single heterojunction in the following model form [6]:

$$U(\mathbf{r}) = U_1(\mathbf{r}) + G(z)\,[U_2(\mathbf{r}) - U_1(\mathbf{r})] \equiv U_1(\mathbf{r}) + G(z)\delta U, \tag{2}$$

where $U_1(\mathbf{r})$ and $U_2(\mathbf{r})$ are the periodic potentials of the semiconductors forming the heterojunction, and $G(z)$ is the form-factor appearing like a smeared step-function (Oz is the growth axis), then

$$d_1 = \Delta U_c \int_{-\infty}^{+\infty} (G(z) - \Theta(z))\,\mathrm{d}z$$

$$- \sum_{j=\pm1,\pm2,\pm3\ldots} \frac{\langle c \mid \delta U \cos(Kjz) \mid c\rangle}{Kj} \int_{-\infty}^{+\infty} \frac{\mathrm{d}G(z)}{\mathrm{d}z} \sin(Kjz)\,\mathrm{d}z, \tag{3}$$

where $\mid c\rangle$ is the periodic part of the band edge Bloch function of one of the materials (from (2) it follows that $\Delta U_c = \langle c \mid \delta U \mid c\rangle$), and value of K depends on the heterostructure growth crystal orientation:

$$K = \begin{cases} 4\pi/a, & Oz \parallel [001]; \\ 4\pi\sqrt{2}/a, & Oz \parallel [110]; \\ 2\pi\sqrt{3}/a, & Oz \parallel [111]. \end{cases} \tag{4}$$

The effective potential energy written in the form (1) may be used both for thick and ultrathin layers. In the former case the term proportional to d_1 plays a role of a small correction, but in the latter case this term is important, and as $L\bar{k}_z \ll 1$, the potential energy may be written in the form where only one parameter describes both the usual and interface contributions:

$$U_c(z) = b_1\delta(z - L/2), \tag{5}$$

where

$$b_1 = 2d_1 + \Delta U_c L. \tag{6}$$

Phenomenologically such form of the potential energy of ultrathin quantum wells has beed proposed to use in [7].

The sign of d_1 has nothing in common with the sign of ΔU_c, and, as a consequence, it is possible that while the potential of a thick layer does not produce a bound state (that is $\Delta U_c > 0$), there will be such states in a similar structure with an ultrathin layer (so that $b_1 < 0$).

In conclusion, we have shown that the model of rectangular potentials in the effective-mass equations generally fail for ultrathin layers, of width of the order of the lattice constant. The reason of this lies in its over-simplified treatment of the heterointerfaces. Allowance for additional interface potentials may have drastic influence on eigenvalues of electron states in such nanostructures. These interface potentials are defined with details of the microscopic structure of heterointerfaces as well as the heterostructure growth crystal orientation. The potentials may reveal themselves in the following: it is possible that while the potential of a thick layer does not produce a bound state, there will be such states in a similar structure with an ultrathin layer, and vice versa.

The work was supported by RFBR-INTAS (No 95-0849), RFBR (No 99-02-17592) and Federal Program "Physics of Solid State Nanostructures" (No 96-1019).

References

[1] R. Schwabe *et al.*, *J. Appl. Phys.* **77**, 6295 (1995).
[2] D. M. Wood and A. Zunger, *Phys. Rev. B* **53**, 389 (1996).
[3] M. G. Burt, *J. Phys.: Condens. Matter.* **4**, 6651 (1994).
[4] E. E. Takhtamirov and V. A. Volkov, *Phys. Low-Dim. Struct.* **1/2** (1999) (to be published).
[5] M. Di Ventra and A. Baldereschi, *Proc. ICPS-23* (Berlin 1996), World Scientific, 1996, p. 1719.
[6] V. A. Volkov and E. E. Takhtamirov, *Usp. Fiz. Nauk* **167**, 1123 (1997) (*Physics-Uspekhi* **40**, 1071 (1997)).
[7] I. Yassievich and U. Rössler, *J. Phys.: Condens. Matter.* **6**, 7927 (1994).

7th Int. Symp. "Nanostructures: Physics and Technology"
St Petersburg, Russia, June 14–18, 1999

Polariton effects in optical spectra of microcavities

S. Rudin† and T. L. Reinecke‡
† U. S. Army Research Laboratory, AMSRL-SE-EP, Adelphi, Maryland 20783, USA
‡ Naval Research Laboratory, Washington, D. C. 20375, USA

The coupling between electronic excitations and optical modes have been of considerable interest in studies of atoms in optical cavities and optical excitations in semiconductor microcavities. The electromagnetic spectra of atoms in optical cavities exhibit splittings due to the coupling of the atomic dipole transitions with the radiation field [1, 2]. These coupled modes are called the vacuum field Rabi oscillations and the splittings between them are the vacuum field Rabi splittings. In case of electronic excitations in semiconductor microcavities the optical modes are coupled to excitons and the exciton-photon modes are often called cavity polaritons [3, 4]. These couplings are important for understanding such effects as optical bistability and laser action.

In many theoretical studies of coupled modes the electronic excitations were represented by a two-level system (a spin model). In this representation the higher lying states of the excitation are neglected. The difference in energy of the two levels is taken to be the excitation energy between the lowest two states of the atom, ΔE_a, or the excitation energy of an exciton in a semiconductor, $E_g - E_b$, where E_g is the band gap and E_b is the exciton binding energy. Systems with N two-level systems coupled to an electromagnetic mode with non-zero linewidth have been sudied in the literature [5] where it has been shown that the Rabi splitting is proportional to $\sqrt{N}$. The linewidth of the optical mode represents, for example, the finite Q of the cavity.

Harmonic oscillators can also be used to represent the atomic excitations, and this representation offers greater ease of mathematical treatment than does the spin representation. The oscillator exhibits vacuum field Rabi oscillations when coupled to a quantized electromagnetic mode, although it does not exhibit driven Rabi oscillations in external fields [1]. Here we present a quantum mechanical treatment of the vacuum field Rabi splitting using an N harmonic oscillators model including finite linewidts of the electronic and optical modes. Actually, we consider two models. In the first one the interacting modes representing photons and excitons are each coupled to a source of dissipation [6]. In the second model the photon is taken to be coupled to a continuum of the electromagnetic states into which the cavity photon state can "leak", or tunnel [7, 8].

The Hamiltonian is that of the set of N harmonic oscillators with excitation energies ω_1, all coupled to one oscillator representing the cavity photon with excitation energy ω_0. In the resonant approximation, which is sufficient for ω_0 close to ω_1, the Hamiltonian is given in terms of creation and annihilation operators as

$$H_{\rm osc} = \hbar\omega_0 a_0^+ a_0 + \sum_{i=1}^{N} \hbar\omega_1 a_i^+ a_i - \frac{\hbar\alpha}{2} \sum_{i=1}^{N} (a_0^+ a_i + a_i^+ a_0) \qquad (1)$$

where α is proportional to the oscillator strength of the electronic transition and depends on the cavity geometrical parameters [4, 8].

In the first model [6] each of the oscillators is coupled linearly to a loss mechanism giving rise to two damping coefficients, β_0 for the photon and β_1 for each of the electronic

excitations. To simplify the results, here we assume the near resonance condition $\omega_0 \approx \omega_1$. Following the procedure given in Ref. [6], we obtain $N-1$ degenerate frequencies and two different resonance frequencies. The difference between the resonance frequencies is the Rabi oscillation frequency of the interacting system. It is given, approximately, by

$$\Delta\omega \approx \sqrt{\alpha^2 N - \frac{1}{4}(\beta_0 - \beta_1)^2}. \tag{2}$$

The Rabi splitting, on the other hand, is obtained from the position of the peaks in the optical spectrum and will be different from $\Delta\omega$ in Eq. (2).

We obtain the absorption spectrum as the imaginary part of the susceptibility which is evaluated as the Fourier transform of the dipole-dipole correlation function. The result is

$$\chi''(\omega) = \frac{N}{8} \frac{\beta_1(\omega-\omega_1)^2 + \beta_0\alpha^2 N/4}{[(\omega-\omega_1)^2 - \alpha^2 N/4 - \beta_0\beta_1/4]^2 + (\beta_0+\beta_1)^2(\omega-\omega_1)^2/4}. \tag{3}$$

The absorption spectrum has a doublet lineshape and the Rabi splitting is given by the difference between the peaks. If the damping coefficients β_0 and β_1 are much smaller than $\alpha\sqrt{N}$ the widths of the two peaks are approximately $(\beta_0+\beta_1)/2$.

In the second model [7, 8] we consider coupling of the cavity photon to the continuum of the electromagnetic excitations described by operator $b(\Omega)$ where Ω is the continuum of frequencies, $0 < \Omega < \infty$. The coupling of the cavity optical mode a_0 to b is given by

$$\int_0^\infty \mathrm{d}\Omega \left[V(\Omega)a_0^+ b(\Omega) + V^*(\Omega)b^+(\Omega)a_0\right]. \tag{4}$$

The coupling of a_0 to N oscillators a_i is the same as in Eq. (1). We find that the absorption spectrum lineshape in this model has the same form as in Eq. (3) where photon linewidth, β_0, is replaced by a term determined by V in Eq. (4).

The emission spectrum can be found by evaluating the distribution of energies in the spectrum of the outside photons, represented by operators b, in the time $t \to \infty$ limit. At $t = 0$ the cavity polaritons are assumed to have an equilibrium distribution at a given temperature [8]. In this way we obtain a frequency dependence of the emission spectrum which has a doublet lineshape. In the case of the laterally patterned semiconductor microcavities we have obtained the dependence of the Rabi splitting of the ground state polariton on the lateral size of a cavity studied in Ref. [4] and have found good agreement with the experimental results.

Acknowledgment

T.L.R. was in part supported by the U.S. Office of Naval Research.

References

[1] G. S. Agarwal, *J. Opt. Soc. Am* **B2**, 480 (1985).
[2] Y. Zhu, D. J. Ganthier, S. E. Moriu, Q. Wu. H. J. Carmichael and T. W. Mossber. *Phys. Rev. Lett.* **64**, 2499 (1990).
[3] C. Weisbuch, M. Nishioka, A. Ishikawa and Y. Arakawa, *Phys. Rev. Lett.* **69**, 3314 (1992).
[4] T. Gutbrot, M. Bayer, A. Forchel, J. P. Reithmaier, T. L. Reinecke, S. Rudin and P. A. Knipp, *Phys. Rev. B* **57**, 9950 (1998).
[5] G. S. Agarwal, *Phys. Rev. Lett.* **53**, 1732 (1984).
[6] S. Rudin and T. L. Reinecke, to be published in *Phys. Rev. B.*
[7] U. Fano, *Phys. Rev.* **124**, 1866 (1961).
[8] L. C. Andreani, V. Savona, P. Schwendimann and A. Quattropani, *Superlattices and Microstructures* **15**, 453 (1994).

7th Int. Symp. "Nanostructures: Physics and Technology"
St Petersburg, Russia, June 14–18, 1999

Dressed polariton emission in III–V semiconductor doped with quantum wells or quantum dots

M. Singh, W. Lau and J. Desforges
Department of Physics, University of Western Ontario, London, Canada

The most interesting phenomena in photonic band gap materials are the formation of photon-atom bound states and suppression of spontaneous emission from the photon-atom bound state [1]. Recently, Rupasov and Singh have studied the quantum electrodynamics of a two-level atom placed within a frequency dispersive medium whose polariton spectrum contains a energy gap [2]. They found that if the atomic resonance frequency lies within the gap, then the spectrum of the system contains a polariton-atom bound state with an eigenfrequency lying within the gap. The radiation and medium polarization of the bound state are localized in the vicinity of the atom. In photonic band gap materials, the existence of the photonic band gap is due to multiple photon scattering by spatially correlated scatters, while in dispersive media such as semiconductors and dielectrics, the energy gap is caused by photon coupling to an elementary excitation (excitons, optical phonons etc.) of the media.

The aim of the present paper is to study the dressed polalriton emission in III–V semiconductors doped with two-level quantum wells or dots. Making use of the spherical harmonic representation and the dipole resonance approximation, we derive an effective model Hamiltonian of the system, which, in the limiting case of empty space, coincides with the model Hamiltonian obtained in liturature. To find the self energy function of the system we diagonalize exactly the Hamiltonian in the one-polariton sector of the entire Hilbert space. To study the spontaneous decay rate of an initially excited dressed state of the polariton system, we consider that the resonance frequencies of a quantum dot lies either inside or outside the polariton gap. We obtain for the first time the dynamic Stark effect due to polariton dressed states. This effect is very similar to that of photon-atom dressed states in quantum optics. We also study the spontaneous decay rate of a system doped with two quantum dots. We consider the case in which one quantum dot is in the excited state while the other is in the ground state with no polaritons present in the system and the resonance frequencies of two dots lie in the polariton continuous spectra. It is found that when the distance between the two dots becomes very large, the spontaneous decay rate of the excited state is equal to that of the single dot case. For very small distances, it is found that the rate of spontaneous emission from the symmetric state is two times that of the single dot case. This phenomenon in quantum optics is called superradiance. For the polariton-dot system in the antisymmetric state, the spontaneous emission rate is found to be zero. This phenomenon is related to subradiance in quantum optics. Numerical calculations are performed for spontaneous decay rate of an excited state in GaSb and GaAs.

References

[1] S. John, *Phys. Rev. Lett.* **58**, 2486 (1987); E. Yablonovitch, et al, *Phys. Rev. Lett.* **67**, 2295 (1991).
[2] V. I. Rupasov and M. Singh, *Phys, Lett. A* **222**, 258 (1996).

7th Int. Symp. "Nanostructures: Physics and Technology"
St Petersburg, Russia, June 14–18, 1999

Light localization in a disordered photonic crystal

Yu. A. Vlasov†, M. A. Kaliteevski‡ and *V. V. Nikolaev*
Ioffe Physico-Technical Institute, St Petersburg, Russia
† Present address—NEC Research Institute, 4 Independence Way, Princeton, NJ 08540
‡Also at Department of Physics, University of Durham, South Road, Durhama DH1 3LE, UK

Abstract. It is known that photonic Bloch states can become strongly localized near the bandedges in a disordered photonic crystal. We show that Bloch states are disrupted and the new localization regime establishes when local fluctuations of the bandedge frequency caused by randomization of refractive index profile becomes as large as the bandgap width.

Introduction

Light localization in disordered media [1] can be caused when constructive interference of backscattered waves brings transport to a complete halt (strong or Anderson localization). In this regime the transport mean free path l becomes as short as the wavelength of the wave λ and the Ioffe-Regel criterion for localization (IR) $kl < 1$ is satisfied [2], where $k = 2\pi/\lambda$. During last decades there has been a considerable interest in experimental verification of light localization. We present the results of theoretical analysis aimed at the investigation of the "subtle interplay of order and disorder" in disturbed periodic-on-average 3D photonic crystal [3], which is required for observation of Anderson localization of photons.

1 Theory

As a model system we choose synthetic opals [4], which are composed of nearly monodisperse (standard deviation δ about 5%) submicron silica spheres, closely packed in a face centered cubic (fcc) lattice with a period of ≈ 200 nm. For numerical simulations we use routine one-dimensional transfer matrix method [5], in which experimental 3D fcc structure is modeled by a refractive index profile, which is periodic only in the [111] direction. In order to incorporate the actual experimental parameters of the system into the calculation scheme (spheres radius R and volume packing fraction β) the profile is calculated as $n(z) = S_{sp}(z)n_a + (1 - S_{sp}(z))n_b$, where $S_{sp}(z)$ is relative area cross-section of the spheres in a (111) plane calculated as a function of the distance along the [111] z direction. Refractive indices of the spheres ($n_a = 1.37$) and surrounding media ($n_b = 1.47$) are chosen close to experimental values [4]. The calculated transmission spectrum of an ideal periodic structure exhibits a gap, centered at reduced frequency $\nu_0 = 0.60$ (in units of c/a, where c is speed of light, a - fcc lattice constant). Its relative width $\Delta\nu/\nu_0$ about 1% with a midgap value of imaginary wavevector of 1300 cm^{-1}.

The disorder is incorporated in the model in analogy with the experimental case of opals by a random distribution of the spheres diameters δ, which was chosen to be flat for simplicity. We find that presence of disorder leads to exponential decay of light with thickness not only within the former gap of the periodic structure, but also in the former passbands, thus significantly broadens the gap. The attenuation length is usually defined as

$\xi^{-1} = -\langle \ln T \rangle / L$, where L being the sample thickness and brackets denote the ensemble averaging over various (in general infinite) different random configurations [5]. The general tendency for increased transmission at the midgap and decreased at the bandedges, already pointed out in the bibliography [5], is also found in the system studied. It is commonly believed that this counterintuitive effect (increasing transmission with increase of disorder) is the result of the increased photonic DOS due to appearance of strongly localized photonic bandtail states, which fill the gap [5]. In what follows we will present an alternative analysis of light localization in disturbed periodic structures.

2 First localization regime, $\delta \ll \Delta\nu/\nu_0$

We believe, that, depending on the amount of disorder δ, at least two quite different localization regimes builds up consequently. Indeed in our model system the deviation δ of the spheres radius R results in a local deviation of fcc lattice constant $a = 2\sqrt{2} \cdot R$ and in a corresponding local fluctuation of the photonic bandedge frequency. This forms a random profile of refractive index on which the wave is scattered. In the case $\delta \ll \Delta\nu/\nu_0$ the waves at the bandedges can be well described by the wavevector k_{cryst} of the average periodic structure and the modified IR criterion [3] $k_{\text{cryst}} l < 1$ can be applied for the analysis of localization. Figure 1(a) represents the lower envelope of the calculated electric field profile inside the opal structure for the frequency $\nu_0 = 0.596$ in the passband near the conduction band edge for different values of disorder. Note that the profiles presented are averaged over 200 random configurations thus reflecting the band structure of the averaged periodic system. It is seen that in a perfect periodic structure ($\delta = 0$), the wave is nearly a standing at a given frequency (curve 1). The corresponding periodic envelope function is defined by $k_{\text{cryst}} = 1.9 \cdot 10^5\ \text{cm}^{-1}$. The incorporation of disorder leads to a rapid destruction of coherence (note the vanishing amplitude of the low-frequency periodic modulation in curves 2-5). Low-frequency periodic envelope still exists, however, for some value of disorder, which means that the modified IR criterion [3] $k_{\text{cryst}} l < 1$ can still be applied. Note, that l corresponds now to the mean free path in which this coherent Bloch state is disrupted. For example $\delta = 0.5\%$ for curve 2 and the corresponding l can be estimated to be 10^{-3} cm, which gives $k_{\text{cryst}} l \approx 100$. As the frequency approaches the bandedge, k_{cryst} approaches zero. Therefore for a 1D crystal there always exists such a frequency region close to the bandedge where $k_{\text{cryst}} l < 1$. In order to obtain strong spatial localization in a 3D periodic structure, it is necessary to achieve energy coincidence of such localization regions at the bandedges for all the directions, which is the condition reminiscent of that for opening up of the omnidirectional PBG [3].

3 Second regime of localization, $\delta > \Delta\nu/\nu_0$

A qualitatively different regime builds up when $\delta > \Delta\nu/\nu_0$. The local fluctuations of the bandedge frequency are so large that they exceed the whole width of the gap. For frequencies in the former passbands, a nonzero probability appears for finding large, sufficiently ordered regions, which act as, even disordered, Bragg mirrors (frequencies fall in the gap). As a result, exponential attenuation of the wave appears in configurationally averaged intensity curves (see curves 4–6 in Fig. 1(a)) even at frequencies in the passbands of periodic structure. For a single configuration, however, sharp resonant modes appear in transmission spectrum, in which the transmission approaches unity. It is the Thouless criterion of localization [6], which we use to examine such states. It requires essentially that the width of energy levels be as small in comparison to the energy spacing between them in order to prevent tunneling between states and to block the transport. We calculate the field profile for a

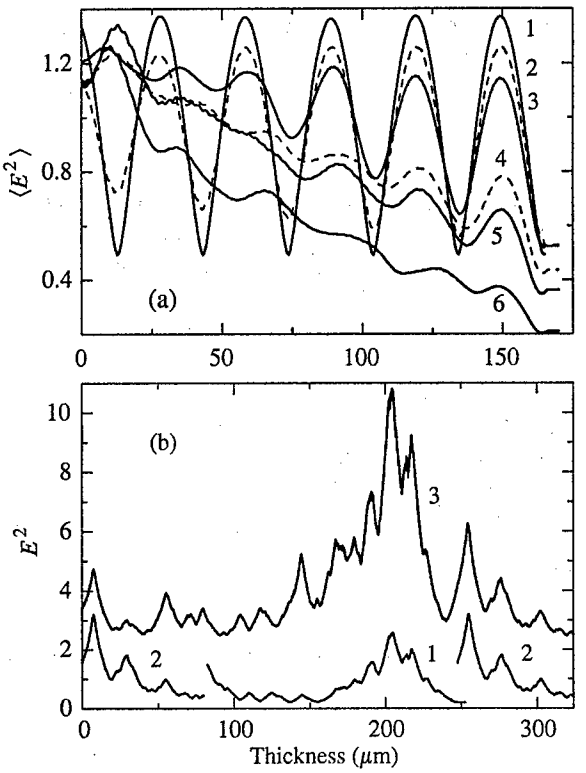

Fig. 1. Electric field intensity profiles for the frequency $\nu_0 = 0.596$ in the passband. (a) Averaged over 200 random configurations. The standard deviation δ of the spheres diameter is 1—0%, 2—0.5%, 3—1%, 4—3%, 5—4%, 6—6%. (b) For a single configuration of disorder of $\delta = 20\%$. Curve 3 corresponds to the structure of 330 μm thickness combined from the structure 1 of 165 μm thickness at the center and two structures 2 of 82.5 μm stacked to it from both sides.

single realization of disorder in a $L = 165$ μm thickness sample (see curve 1 in Fig. 1(b)). The realization is chosen the same as for spectrum in the inset of Fig. 1 for frequency $\nu_0 = 0.596$, for which the resonant state exists. The resulting field profile (see curve 1 in Fig. 1(b)) do exhibit exponential tails, which localize the wave function to a small space volume. Then two identical layers of 82.5 μm thick (see curve 2) are added to this structure on both sides and the resulting field profile is calculated for the whole composite sample of 330 μm (see curve 3). It can be clearly seen from a comparison of curves 1 and 3 that initial state retain completely its initial shape. This indicates that the state 1 "feel" its environment only through exponential tails and is relatively insensitive to the background beyond the localization length, which can be defined now as an exponent in the tail region of the profiles for a single realization of disorder (about 8 μm for curve 1). To obtain complete localization in this sense in a 3D structure, it is necessary to create analogous localized states at the same frequency for all other directions (and polarizations), which spatially overlap. This can be achieved in a disordered 3D photonic crystal with a gaps for different directions, which are energetically overlapping. This condition is also very similar to that for opening up a complete PBG, except that the widths of the perturbed gaps can be significantly larger in disordered crystal, thus facilitating spatial localization.

In conclusion, two different regimes of light localization in a disordered photonic crystal

are identified, which builds up consequently depending on the amount of disorder compared with the normalized width of the gap in corresponding periodic structure. This comparison can be applied to gaps for different directions and, therefore, it remains valid for the photonic crystal of any dimensionality.

Acknowledgments

We would like to thank O. Z. Karimov for technical assistance in transmission measurements. Fruitful discussions with V. N. Astratov, A. A. Kaplyanskii, I. P. Ipatova and E. L. Ivchenko are gratefully acknowledged. This work was supported in part by the RFBR, Grant No. 960217928.

References

[1] D. S. Wiersma et al., *Nature* **390**, 671 (1997).
[2] A. F. Ioffe and A. R. Regel, *Prog. Semicond.* **4**, 237 (1960).
[3] S. John, *Phys. Rev. Lett.* **58**, 2059 (1987).
[4] Yu. A. Vlasov et al., *Phys. Rev. B* **55**, 13357 (1997).
[5] A. R. McGurn et al., *Phys. Rev. B* **47**, 13120 (1993); V. D. Freilikher et al., *Phys. Rev. E* **51**, 6301(1995).
[6] D. J. Thouless, *Phys. Rep.* **13C**, 93 (1974).

7th Int. Symp. "Nanostructures: Physics and Technology"
St Petersburg, Russia, June 14–18, 1999

Light-emitting nanocomposite films on the base of silicon nitride and silicon oxynitride layers

V. G. Baru†, A. P. Chernushich†, M. I. Elinson†, V. A. Jitov†, V. I. Pokalyakin†, G. V. Stepanov†, A. A. Timofeev‡ and L. Yu. Zaharov†

† Institute of Radioengineering and Electronics, RAS, 103907 Moscow, Russia

‡ Moscow Engineering and Physics Institute, 115409 Moscow, Russia

Abstract. The silicon nanostructures on the base of SiN_x and SiN_xO_y with room temperature luminescence in visible part of spectrum were obtained. The regimes of deposition and annealing allowed adjusting excess of Si and structure of layers and essentially influenced on their electrical, optical and luminescent properties. The mechanisms of photo and electroluminescence and paths of the Si light source realization are discussed.

The creation of silicon efficient sources of visible light compatible with modern silicon technology has a science and practical significance in connection with perspective of their using for optical interconnection in Very Large Scale Integration (VLSI) and other applications [1–3]. Therefore the search for new Si-based material with room temperature luminescence in visible part of a spectrum is very actual. In this work it was obtained and investigated the luminescent Si nanostructure on the base of thin SiN_x and SiN_xO_y layers. The layers were deposited on different substrates by ion-plasma sputtering of Si target by Ar ions in controlled atmosphere of N_2 and O_2 gases. The regimes of deposition and annealing allowed adjusting excess of Si and essentially influenced on the structure of layers and their electrical, optical and luminescent properties. The layer structure was investigated by TEM and AFM. It was found that layers contain Si nanocrystals with average size about 2–20 nm in dependence of Si excess and the preparation conditions.

The layer with low Si excess show the visible photoluminescence (PL) in wide spectral region ($\lambda = 400-800$ nm). The vacuum annealing ($T = 1100°C, t = 10$ min.) of samples results in sharp increasing of PL especially in PL peak region ($\lambda = 500-600$ nm). The optical properties of layers (transmission and reflection) do not change essentially. In Fig. 1 and Fig. 2 shown the spectra of PL and transmission before and after vacuum annealing.

The electroluminescence (EL) was investigated on cSi-SiN_x-Au structures. The light was observed trough the semi-transparent Au top contact. The conductivity of layers with low Si content was very low before annealing. The annealing activated the carrier injection and conductivity and visible EL appeared at forward polarity of voltage-current characteristic. The quantum efficiency in such layers was not more than 10^{-6}. We associate the PL and EL mechanisms and peculiarity of optical properties of layers with low Si excess with formation in such layers Si nanocrystals with size quantum spectrum. The short time annealing improves the layer structure, passivate the nanocrystal-matrix interface and suppress the non-radiating recombination in such layers.

The different results were obtained on the layers with high Si excess. In such layers was observed the essential decreasing of PL intensity up to PL disappearance and drastic increasing of EL intensity at reverse polarity of voltage-current characteristic (at negative polarity on cSi substrate in pSi-SiN_x-Au structure). The typical EL spectrum for such structure shown in Fig. 3. The quantum efficiency in such layers was reached 10^{-4}. The

substrate heating ($T = 200-300°C$) during the layer deposition result to increasing of EL efficiency.

The vacuum annealing influenced noticeably on optical properties, in particular increased the transmission on the whole spectrum, and decreased the EL efficiency. The observed effects are due to significant modifications of a layer structures with increasing of Si excess. The TEM and microdifraction patterns shown that the main part of Si excess are exist as large (10 and more nm) amorphous and crystalline clusters and also in state of supersaturated solid solution in matrices. The annealing results in dissociation of solid solution and partly Si crystallization. We connect the PL suppress with imperfection of layer structure, worsening of condition of quantum confinement in nanocrystals and increasing

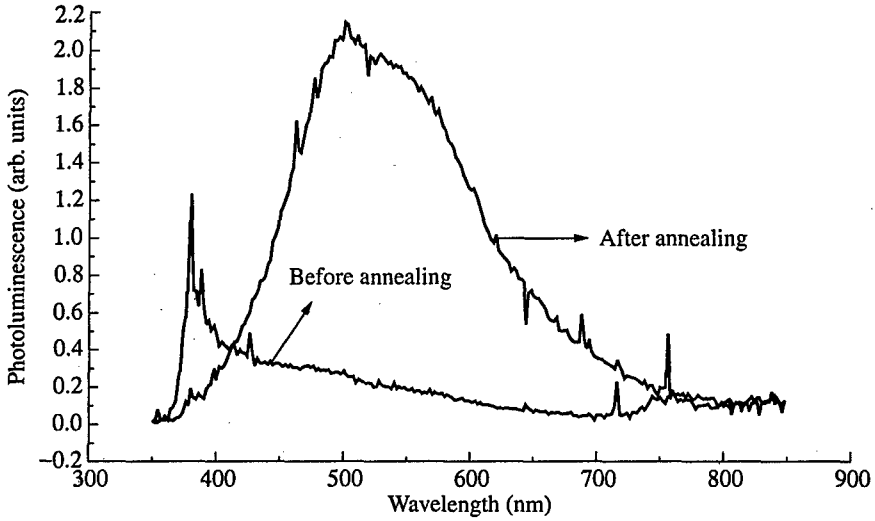

Fig. 1. The photoluminescence spectra before and after vacuum annealing.

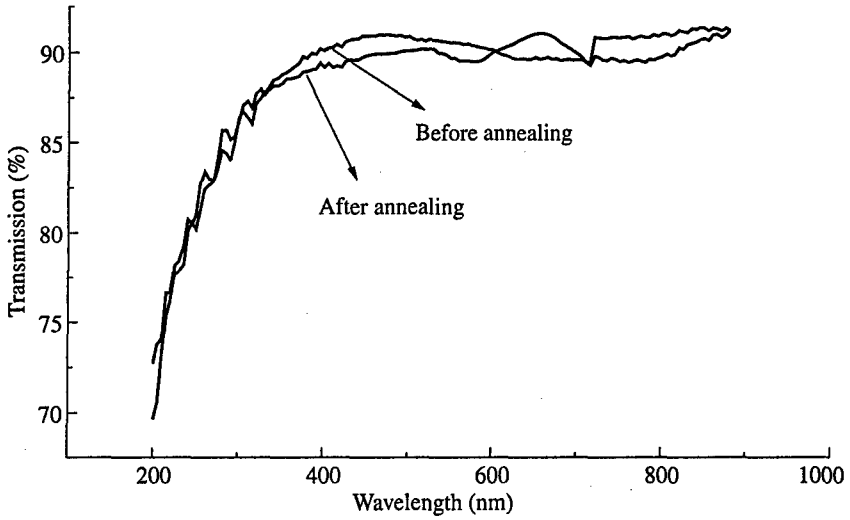

Fig. 2. Spectra of the optical transmission before and after vacuum annealing.

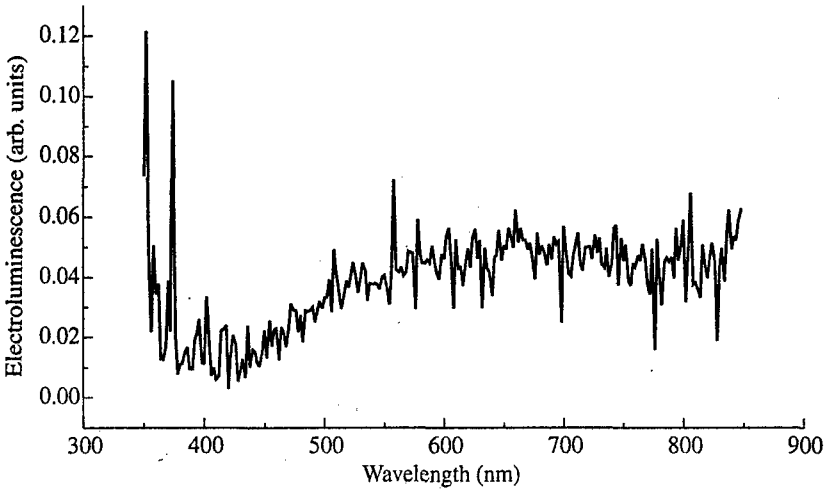

Fig. 3. Spectrum of the electroluminescence.

of the non-radiating recombination. The increasing of EL can be connected with sharp rise of carriers injection and conductivity in such layers, appearance of regions with high local electrical field, avalanche ionization and microplasma formation. The paths of increasing PL and EL quantum efficiency and perspectives of realization Si LED are discussed.

This work was financially supported by Ministry of Science and Technology Policy of the Russian Federation (program "Physics of Solid State Nanostructures") and by European Community (INCO-COPERNICUS).

References

[1] J. Linnros and N. Lalic, *Appl. Phys. Lett.* **66**, 3048 (1995).
[2] A. Loni et al., *Electron. Lett.* **31**, 1288 (1995).
[3] L. Tsybeskov et al., *Appl. Phys. Lett.* **68**, 2058 (1996).

7th Int. Symp. "Nanostructures: Physics and Technology"
St Petersburg, Russia, June 14–18, 1999

Second harmonic generation in porous silicon multilayer periodic structures

A. B. Fedotov, L. A. Golovan', *P. K. Kashkarov*, N. I. Koroteev,
M. G. Lisachenko, A. N. Naumov, D. A. Sidorov-Biryukov,
V. Yu. Timoshenko and A. M. Zheltikov
M. V. Lomonosov Moscow State University, Faculty of Physics
and International Laser Center, 119899, Moscow, Russia

Abstract. In the paper second harmonic (SH) generation in a photonic bandgap structure was investigated. The intensity of SH from a multilayer structure exceeds the intensity of SH from both homogeneous layer of porous silicon and a single crystal silicon (100) substrate. The SH generation efficiency was found to be sensitive to parameters of photonic bandgap structures. The dependence of the SH signal on the azimuthal rotation angle is isotropic. SH radiation is polarized in the plane of incidence. The SH intensity is a nonmonotonic function of the angle of incidence, reaching its maximal value at the angle of incidence corresponding to the minimal phase mismatch in the multilayer periodic structure.

Introduction

In last decade porous silicon (PS) became a material attracting great attention. Due to its well-developed surface, possibility of nanocluster formation and simplicity of production PS is a very perspective material for various technological applications [1]. One of them is a fabrication of multilayer periodic structures of PS alternate layers of different porosity. Such structures have a photonic bandgap and may be used as Bragg reflectors, microcavities, control of short laser pulse parameters and so on [2, 3, 4]. That is why it is important to elicit the ability to apply PS photonic bandgap structures for nonlinear optical process controlling. For this purpose dispersion properties of a periodic structure may be used [5].

Second harmonic (SH) generation in homogeneous porous silicon layer was found to be very inefficient [6]. This fact is due to an optical isotropy of PS on a wavelength scale. The way to increase SH efficiency proposed in the paper is a fabrication of multilayer periodic structure with appropriate parameters.

1 Experimental

The multilayer structure was made by an electrochemical etching of a crystalline silicon wafer in HF ethanol solution (1:1). To fabricate the structure alternate pulses of current density 5 and 105 mA/cm^2 were used. Varying the duration of the current pulses, we were able to control the layer depths. Single crystal silicon wafer with (100) surface orientation was used as a substrate. Three structures were produced (samples A, B and C), each of them consisted of 12 pairs of layers alternating refractive indices. Porosities of layers are 70% (refractive index $n_1 = 1.4$) and 80% (refractive index $n_2 = 1.2$). The obtained samples are Bragg reflectors, their reflection spectra are shown in Fig. 1.

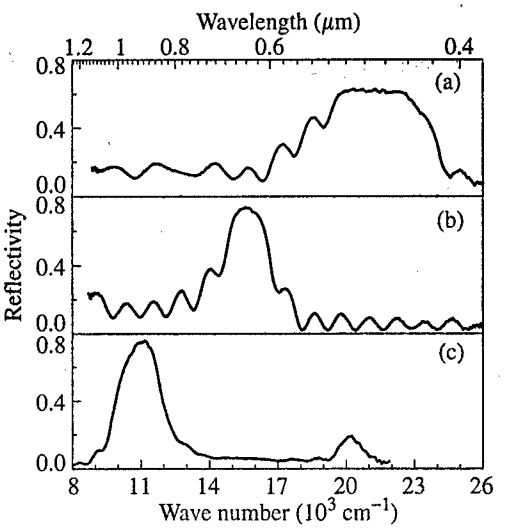

Fig. 1. Reflection spectra of structures A (*a*), B (*b*) and C (*c*) at normal light incidence.

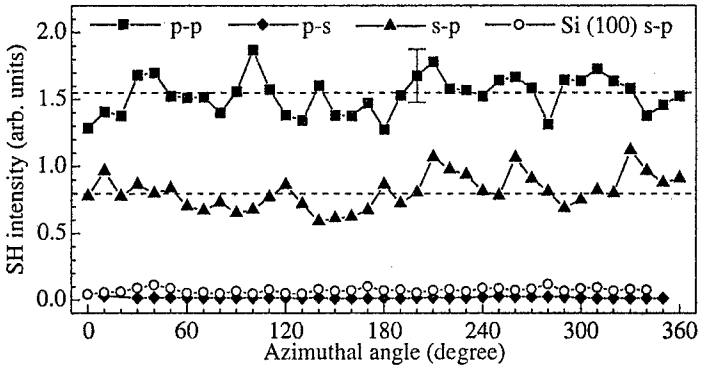

Fig. 2. The dependences of the SH signal of the sample A on the azimuthal angle at different polarizations of fundamental and SH intensities. For comparison the dependence for a single crystal silicon surface (100) is shown.

2 Results and discussion

The dependence of the SH intensity on the azimuthal rotation angle for the sample A is shown in Fig. 2. One can see that the dependence is isotropic. Another important result is a polarization of the SH radiation in the plane of incidence. Besides, the SH generation is more efficient when the pumping radiation is polarized in the plane of incidence. These effects may be explained by properties of PS layers: optical isotropy in directions perpendicular to the normal to the surface and formation of silicon nanoclusters along the normal to (100) surface. It is worth noting that the SH intensity from PS structure exceeded the SH intensities both from a crystalline silicon surface (100) (see Fig. 2) and homogenous PS layer.

The SH generation efficiency was found to be sensitive to parameters of the photonic bandgap structures. The dependences of the SH intensities on the angle of incidence θ for structures A, B and C are shown in Fig. 3. The dependence is nonmonotonic, for the sample

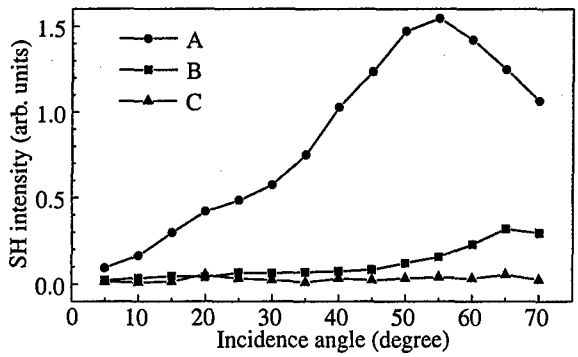

Fig. 3. The dependence of the SH intensity on the angle of pumping radiation incidence for samples A, B, and C.

A maximal signal is reached at the angle of incidence about $\theta = 55°$. For the samples B and C the SH signals are much weaker and their maxima are reached at greater angles of incidence.

The analysis of phase mismatch of fundamental and SH radiation in such structures was carried out. The dispersion in a periodic structure was taken into consideration. According to our calculation the angle of minimal phase mismatch in structure A is 50° what is close to the experimental results.

Thus, it was found in experiment that in porous silicon multilayer periodic structure SH generation takes place, its efficiency exceeds those of crystalline silicon substrate and homogenous porous silicon layer. The SH generation efficiency depends on parameters of multilayer periodic structures. The isotropic azimuthal dependence of the SH signal is obtained. The SH intensity is a nonmonotonic function of the angle of incidence. Carried out modeling shows that SH intensity reached its maximal value at the angle of incidence corresponding to the minimal phase mismatch in the multilayer periodic structure.

Acknowledgements

This work was partially supported by the State Scientific and Technical Programmes (Russia) "Physics of Solid Low-Dimensional Structures", "Atomic Surface Structures" and the Russian Foundation for Basic Research.

References

[1] A. G. Gullis, L. T. Canham, P. D. J. Calcott, *J. Appl. Phys.* **82**, 909 (1997).
[2] L. Pavesi, *La Rivista del Nuova Cimento* **20**, ser. 4, No 10, 1 (1997).
[3] W. Theiß, *Surf. Sci. Rep.* **29**, 91 (1997).
[4] A. M. Zheltikov, N. I. Koroteev, S. A. Magnitskiy and A. V. Tarasishin, *Quantum Electronics* **28**, 861 (1998).
[5] N. Bloembergen and A. J. Sievers, *Appl. Phys. Lett.* **17**, 483 (1970).
[6] L. A. Golovan', A. V. Zoteev, P. K. Kashkarov and V. Yu. Timoshenko, *Tech. Phys. Lett.* **20**, 334 (1994).

7th Int. Symp. "Nanostructures: Physics and Technology"
St Petersburg, Russia, June 14–18, 1999

SBNS.03p

Optical second harmonic generation studies of the dc-electric field screening in Si–SiO_2 multiple quantum wells

V. V. Savkin†, A. A. Fedyanin†, F. A. Pudonin‡, A. N. Rubtsov†
and O. A. Aktsipetrov†
† Department of Physics, Moscow State University, 119899, Moscow, Russia
‡ Lebedev Physical Institute of RAS, Leninsky pr. 53,
117924, Moscow, Russia

Abstract. Dc-electric field screening in the Si–SiO_2 multiple quantum wells is studied by optical second harmonic generation. Experimentally observed oscillations in the nonlinear response, inconsistent with semiclassical description of screening, are explained within the Tomas-Fermi approach.

The significant attention has been given recently to the study of the influence of the external electric field on the nonlinear-optical properties of the solids. In particular, the electric field effects in low-dimensional systems such as multiple quantum wells (MQWs) and superlattices are of interest. The optical second-harmonic generation (SHG) is sensitive to the symmetry properties, as a consequence practically there is no SHG signal from the centrosymmetric material. Dc-electric field induced SHG (EFISH) is determined by polarization $P_{2\omega}$ as $P_{2\omega} = \chi^{(3D)}(\omega, \omega, 0)E_\omega E_\omega E_0$, where $\chi^{(3D)}$ is nonlinear susceptibility, E_ω and E_0 are fundamental and dc-electric field. To interpret EFISH results in low-dimensional structures it is important to know the screening of the electric field in the structure.

In this paper, we present the description of screening of dc-electric field in MQWs. The basic method of research of screening electric field in Si–SiO_2 MQWs is EFISH. 40 pairs of amorphous Si–SiO_2 layers were evaporated by RF-sputtering on the vicinal (100) silicon wafer (Fig. 1). The parameters of radiation and sample are shown in Fig. 2. The dependence of the SHG intensity on the azimuthal angle and on the dc-electric field applied to the MQWs has been studied in transmission through the multilayered structure and in parallel polarizations of the fundamental and SHG wave. Azimuthal dependence reveals a two-fold symmetry and is completely anisotropic. The dependence of the SHG intensity on the dc-electric field applied to the MQWs presented in Fig. 2 has been studied in maximum of anisotropic dependence.

This oscillatoric dependence is interpreted as the feature of the screening of dc-electric field in layered structure of the MQWs. Note that classical screening gives essentially monotonic dependence, which is inconsistent with the experimental data. The electrostatic problem is solved in assumption that there is no current through the sample. Nevertheless, the electrons are supposed to come in wells due to the tunneling. Discrete analogue of the Poisson equation in two-dimensional case with boundary conditions is used to obtain the the electrostatic potential $\varphi(n)$ as function of a discrete variable n, which numbers n-th quantum well and the dependence of the electrostatical field E_0 on the voltage applied to the MQWs U. It is shown that the dependence of the electrostatical field E_0 on the voltage U have got oscillatoric behavior when $d + D\frac{\varepsilon_1}{\varepsilon} > \varepsilon a_0$, where d and D — thickness of the Si and SiO_2 layers, respectively, ε and ε_1 are their static dielectric constants, a_0—Bohr

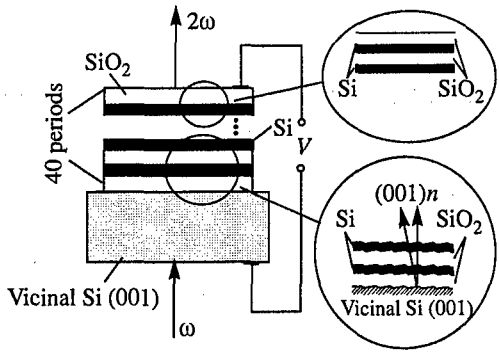

Fig. 1. Structure of the sample and geometry of experiment.

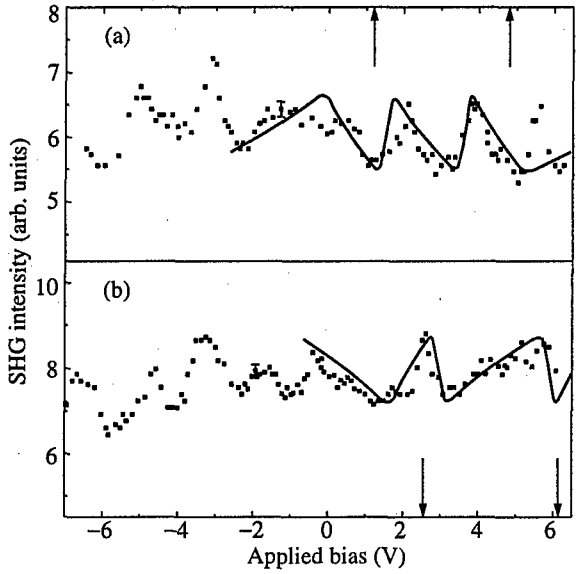

Fig. 2. The SHG intensity as a function of voltage. Experiment—square. Theory—solid line. Parameters of samples and radiation: (a) $d_{Si} = 1.1$ nm, $D_{SiO_2} = 3$ nm, $d_{Si(001)} = 10^5$ nm, (b) $d_{Si} = 1.1$ nm, $D_{SiO_2} = 5$ nm, $d_{Si(001)} = 10^5$ nm; $\lambda_\omega = 1064$ nm. Arrows indicate the region of validity of the model.

radius. This oscillatoric dependence $\varphi(n)$ appears due to excluding of the self-action in the Tomas–Fermi description. The screening in the single well is described using Hartree approach.

The azimuthal anisotropic dependence allows to assume that internal layers of the MQWs possess the small initial miscut (Fig. 1) with $2/m$ symmetry. However the external layers possess ∞/m symmetry. For the transmission geometry only $2/m$ layers contribute to the EFISH response. In this assumption the theoretical dependence of the SHG intensity on the external bias is obtained. Fig. 2 shows this dependence. The arrows indicate the region of validity of the model. The fit reveals good agreement to experimental data.

7th Int. Symp. "Nanostructures: Physics and Technology"
St Petersburg, Russia, June 14–18, 1999

Polarization anisotropy of photoluminescence of oxidized silicon nanocrystals

O. M. Sreseli†, D. I. Kovalev† and G. Polisski‡
† Ioffe Physico-Technical Institute, St Petersburg, Russia
‡ Department für Physik E16, Universität München,
D-85747 Garching, Germany

Abstract. Photoluminescence polarization and its anisotropy from oxidized silicon nanocrystals has been investigated.Unusual polarization anizotropy was observed under excitation with linear polarized light and large differences between excitation and detection energies. Oxide shell is shown to produce some effects enhancing the probability of no-phonon quasi-direct radiative transitions in nanocrystals. The observed anisotropy is explained by the anisotropy of heavy hole exciton in a quantum box.

Introduction

Porous Si is known to have a good memory of the linear polarization of the light used to excite the photoluminescence (PL).A review of this effect can be found in [1]. It has been established that polarization is due to an axial nanocrystallite (NC) asymmetry. For the colloidal particles having a spherical shape the polarization is totally absent [2]. In elongated nanocrystals (NCs), the anisotropy may have two origins, the electron confinement [3] or the effect of the depolarizing field created by the light-induced charges on the interfaces [4, 5]. Because of the difference in the optical dielectric constants inside and outsite the NCs, a depolarizing field appears when NCs are excited by light. It reduces the electric field inside the NCs, and the reduction is the smallest along the long NC axis. Light absorption is the largest in the NCs with the long axes aligned in the direction of the electric field of the exciting light. The excited NCs emit light also with preferential polarization along the long axis. The PL from the ensemble of randomly oriented NCs becomes thus polarized along the direction of linear polarization of the exciting light. Polarization degree of PL is isotropic in a sample plane, and anisotropy of polarization may appear only in the presence of anisotropic distribution of elongated NCs. For example, the artificially induced anisotropy of the NC distribution is reported in [6]. The anisotropy due to electronic confinement in elongated NCs seems to be effective for quasiresonant excitation of PL. The polarization studies achieved in these conditions reveal the symmetry of the ground states in Si NCs [7].

In this paper we study the PL polarization of oxidized silicon NCs prepared by thermal oxidation of porous-Si layer. We present an unusual behavior of the PL polarization at both non-resonant and quasiresonant PL excitation by linear polarized light. Appearence of polarization anisotropy in these cases is discussed in terms of dielectric model and quantum confinement.

1 Experiment

The porous-Si layers were made from the (100)Si wafers by conventional technique, the details of the sample preparation can be found elsewhere [8]. Oxidation was carried out in

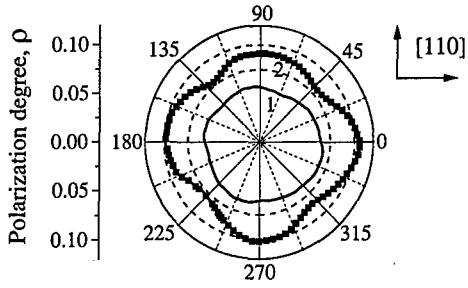

Fig. 1. Polar diagram of the PL polarization in porous Si prepared on (100)substrate. $\lambda_{ex} = 442$ nm (2.8 eV), $\lambda_{det} = 650$ nm (1.9 eV). (1) before oxidation; (2) after oxidation at 200°C, 5 min.

oxygen atmosphere at 200°C. The PL was excited by the linearly polarized light from the He-Cd laser (442 nm—non-resonant excitation) or from He-Ne laser (633 nm—resonant excitation). The polarization of the exciting light, $\vec{e_{ex}}$ lies in the surface plane of the layer, and its orientation with respect to crystalline axis can be changed by rotating the sample. The polarization degree is defined as

$$\rho = (I_{\parallel} - I_{\perp})/(I_{\parallel} + I_{\perp})$$

where $I_{\parallel}(I_{\perp})$ is the PL intensity polarized parallel (perpendicular) to $\vec{e_{ex}}$.

Measurements were done at 300 K. Details of setup are ascribed in [7].

2 Results and discussion

Angular dependences of the PL polarization under non-resonant excitation of the sample before and after oxidation are shown in Fig. 1. The isotropy of ρ in the (100) plane of porous layer (curve 1) was shown in [1, 9] and indicates the random orientation of the luminecing NCs in this plane.

After oxidation one may expect two effects: the reduction of NC sizes and, in the case of homogenious oxidation, the increase of their asymmetry (the ratio of long to short axis dimensions becomes larger). We see the first effect as shifting of PL spectrum to short-wave region and the second effect causes the enhancement of ρ (compare curve 1 and 2 in Fig. 1). When (100) plane is excited after oxidation procedure, the polarization anisotropy appears (curve 2 in Fig. 1). This is an unusual phenomenon for non-resonant excitation, since there is a great energy difference between exciting and emitting photons. We have studied this anisotropy at different wavelengths of detection (Fig. 2(a)). The polarization memory is higher when $\vec{e_{ex}}$ is parallel to [110] direction and has a minimum when $\vec{e_{ex}}$ is parallel to [100]. With increasing of the wavelength the degree of polarization decreases, but its anisotropy becomes more pronounced. The polarization anisotropy may be induced by structural anisotropy of NCs in case of different oxidation rates along different crystallographic axes. But the rates depend strongly on oxidation conditions. It is not straightforward to extent the data obtained for flat and polished crystallographic planes of c-Si on arbitrary NC curved surfaces.

Before discussing the second possible reason—electronic confinement—we investigated polar diagrams of PL polarization at resonant PL excitation (Fig. 2(b)). Resonant excitation of oxidized samples gives enhanced PL polarization degree and pronounced polarization anisotropy which does not decrease with increasing λ_{det}. Again ρ is higher in

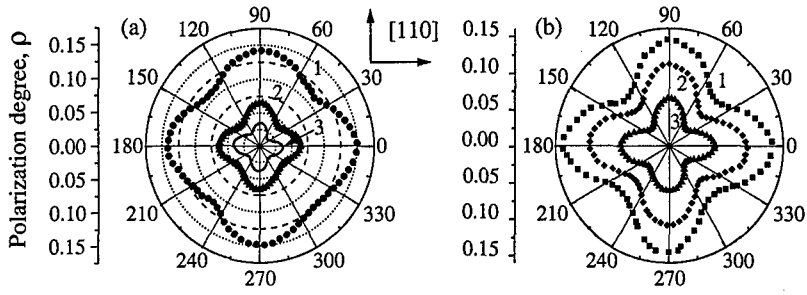

Fig. 2. Polar diagrams of the PL polarization in oxidized Si NCs under non-resonant (a) and resonant (b) conditions; (a) λ_{ex} = 442 nm (2.8 eV), λ_{det}: 1—550 nm (2.25 eV); 2—700 nm (1.77 eV); 3—750 nm (1.65 eV); (b) λ_{ex} = 633 nm (2.8 eV), λ_{det}: 1—670 nm (1.85 eV); 2—700 nm (1.77 eV); 3—750 nm (1.65 eV).

[110] direction. Under resonant conditions the dependence of ρ on the crystalline axes reflects the warping of the heavy hole sub-band [7]. Under resonant excitation, the absorption takes place in states which are close to the ground state of the exciton. In a quantum box the ground state would have a nature of the heavy holes because their confinement is smaller. Along the [110] direction the heavy hole mass is larger than along the [100] direction. For the same NC size, the absorption will be higher in the [110] aligned NC, because in the quantum box the density of states is higher along this direction. This anisotropy must dissapear for detection energies far from the excitation ones. In [7] this occurs at differences $\Delta = E_{ex} - E_{det}$, equal to 0.2–0.3 eV. At higher Δ, for lower detection energies, contributions from light hole excitons become important. In the light hole band the mass along [100] is larger than the mass along [110], and ρ becomes greater in [100] direction [7, 10]. In our experiments anisotropy of polarization memory is well-defined till $\Delta = 0.5$ eV (setup limitation), not to mention anisotropy under non-resonant excitation at Δ, equals to 1–1.5 eV. We explain our results by enhancement of no-phonon quasi-direct radiative transitions. It was shown theoretically [11] and experimentally [12] that in smaller Si NCs the probability of no-phonon transition increases with respect to phonon-assisted processes. For confinement energies above 0.7 eV the no-phonon transitions begin to dominate. Oxidation, first, increases the confinement energy due to reduction of NC sizes, second, increases asymmetry of NC and localization of the exciton along its longer axis. For the same confinement energies no-phonon transitions are some times stronger in Si NCs having a SiO_2 cover [12]. So even at large Δ we see anisotropy of polarization due to asymmetry of Si heavy hole band. We assume also that larger NCs oxidize with greater rates than the smaller ones and have larger SiO_2 cover. This explains why at one excitation energy ρ does not decrease with increasing λ_{det} (increasing Δ).

Thus, we have observed polarization anisotropy in photoluminescence of Si oxidized NCs and explained it in frame of quantum confinement model.

Acknowledgements

This work was partly supported by the grant "Solid State Nanostructures".

References

[1] F. Koch, D. Kovalev, B. Averboukh, G. Polisski and M. Ben-Chorin, *J. Luminescence* **70**, 320 (1996).

[2] L. E. Brus, P. E. Szajovski, W. L. Wilson, T. D. Harris, S. Schupller and P. Sitrin, *J. Am. Chem. Soc.* **117**, 2915 (1995).
[3] Al. L. Efros and A. V. Rodina, *Phys. Rev.* **B47**, 10005 (1993).
[4] D. Kovalev, B. Averboukh, M. Ben-Chorin, J. Diener, F. Koch, Al. L. Efros, M. Rosen, N. A. Gippius and S. G. Tikhodeev, *Appl. Phys. Lett.* **67**(11), 1585 (1995).
[5] A. P. Lavallard and R. A. Suris, *Solid State Commun.* **25**, 267 (1995).
[6] G. Polisski, A. V. Andrianov, D. Kovalev and F. Koch, *Braz. J. of Physics* **26**(1), 189 (1996).
[7] D. Kovalev, M. Ben-Chorin, J. Diener, B. Averboukh, G. Polisski and F. Koch, *Phys. Rev. Lett.* **79**(1), 119 (1997).
[8] G. Polisski, F. Koch, O. M. Sreseli and A. V. Andrianov, *Semiconductors* **31**(3), 304 (1997).
[9] A. V. Andrianov, D. Kovalev and I. D. Yaroshetskii, *Phys. Solid State* **35**, 1323 (1993).
[10] G. Polisski, B. Averboukh, D. Kovalev and F. Koch, *Advances in Microcrystalline and Nanocrystalline Semiconductors - 1996*, Ed. P. M. Fauchet, R. W. Collins, P. A. Alivisatos, I. Shimizu, J.-C. Vial. **452**, 541 (1997).
[11] M. S. Hybertsen, *Phys. Rev. Lett.* **72**, 1514 (1994).
[12] D. Kovalev, H. Heckler, M. Ben-Chorin, G. Polisski, M. Schwartzkopff and F. Koch, *Phys. Rev. Lett.* **81**, 2803 (1998).

7th Int. Symp. "Nanostructures: Physics and Technology"
St Petersburg, Russia, June 14–18, 1999

The influence of deposition parameters on the structure of nanocrystalline silicon

E. I. Terukov†, *V. Kh. Kudoyarova*†, V. Yu. Davydov†,
K. V. Koughia‡, G. Weiser§ and H. Mell§
† Ioffe Physico-Technical Institute, St Petersburg, Russia
‡ St Petersburg Pediatric Academy, 194100 St Petersburg, Russia
§ Philipps University of Marburg, Marburg, Germany

Abstract. Nanocrystalline silicon films have been produced by PECVD method in $SiH_4 + H_2$ gas mixtures. Raman spectra, IR absorption and absorption edge of the films have been investigated in a function of such deposition parameters as the gas dilution ratio, H_2O contamination, the deposition temperature (T_s) and the material of the substrate. The study of IR spectra has showed the presence of bonded hydrogen, with the total concentration (C_H) varying from 4 to 13 at.%. The analysis of Raman spectra has revealed that the films contain nanocrystallites embedded in amorphous matrix. The size of crystallite (R) has been evaluated from the shift of the peak in Raman spectra corresponding to crystalline phase and has been found to be in a range 38–57 Å. The volume fraction of crystallites (X_c), which varied from 15% to 81%, has been estimated from the intensity of this peak. Both values, X_c and R, are primarily influenced by H_2O contamination, while the effect of T_s is less pronounced. The size of crystallites displays also a strong dependence of the substrate material. IR investigations show that at $T_s = 160$°C amorphous matrix contains polymeric phase which disappears at $T_s = 340$°C.

Introduction

The intensive investigations of silicon films containing nanocrystals was stimulated by the discovery in 1990 by L. T. Canham [1] of photoluminescence in visible region at room temperature in porous silicon. This phenomenon implied the possibility of creation of silicon based photoelectronic devices. Further investigations have revealed that the intensity and wavelength of photoluminescence are closely connected with the size (R) and volume fraction of nanocrystals (X_c) [2]. When produced by other methods, the silicon films consist of mixtures, where nanocrystals and microcrystals are embedded in amorphous phase. At low X_c amorphous phase plays a role of a bounding tissue while at high X_c it becomes just an interface between crystals. Thus, one of the urgent technological problems is how to control the size of and the concentration of nano- and microcrystals.

In present work we demonstrate the results of our investigations concerning optical properties of silicon films produced by Plasma Enhanced Chemical Vapor Deposition (PECVD) and show that these films contain a large fraction of nano- and microcrystallites included in amorphous tissue. We show also that the concentration and the size of crystallites may be effectively changed by variation of deposition parameters.

1 Experimental techniques

The nc-Si:H films were prepared by PECVD method. The mixture of $SiH_4 + H_2$ was used as the initial gas. The dilution ratio (SiH_4/H_2) was varied from 0.5 to 1.5. In some experiments the initial gas was contaminated by H_2O. The quartz and silicon single crystals were used

as the substrates and the deposition temperature (T_s) was varied from 160 to 340°C. The deposition parameters are summarized in the Table 1.

The films structure was investigated by Raman spectroscopy. The spectra were measured in automated installation based on DFS-24 spectrometer. The definition was not less than 3 cm^{-1}. The excitation was done by Ar^+ laser at wavelength 4880 Å. The measurements were carried out at minimum intensity to avoid the heating of the sample. The method of R and X_c calculation from Raman spectra is described in details in [3].

IR spectroscopy was used for the determination of hydrogen concentration (C_H) and bonding configurations. C_H was determined from integrated absorption at 630 cm^{-1} (for oxygen free samples) or 2090 cm^{-1} (for samples contaminated by oxygen).

Optical gap was determined from optical transmission measurements and was calculated from Tauc plot [4]: $\sqrt{\alpha h\nu} = f(h\nu)$.

2 Results and discussion

2.1 The influence of the initial gas dilution by hydrogen on the films structure

In this section we discuss the changes in nc-Si:H films structure caused by the dilution of initial gas by hydrogen. Figure 1 displays Raman spectra of PECVD nc-Si:H corresponding to TO-phonon absorption. It can be clearly seen that the spectrum consists of two lines with substantially different width. The broad line may be associated with the amorphous phase and is centered at about 480 cm^{-1}. The narrow one is situated at approximately 517.5 cm^{-1} and reflects the presence of crystalline phase. The interpretation of Raman

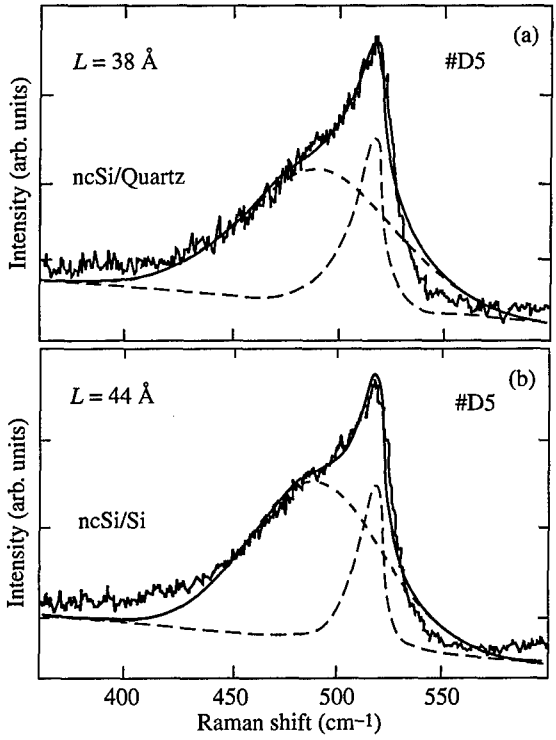

Fig. 1. Raman spectra of silicon films of mixed composition deposited on different substrates. (a) quartz. (b) c–Si.

Table 1. Deposition parameters and characteristics of nanosilicon films.

		Samples					
		D1	D2	D3	D4	D5	D6
Dilution ratio	SiH_4/H_2	1.5	1.0	0.5	0.5	0.5	0.5
Deposition temperature	T_s, °C	160	160	160	160	340	340
Thickness	d, μm	1.3	0.95	0.85	0.85	0.52	0.48
Deposition rate	v, Å/s	0.80	0.58	0.35	0.37	0.28	0.21
Size of nanocrystals on quartz	R, Å	49	50	57	38	44	54
Volume fraction of nc on quartz	X_c	0.78	0.75	0.74	0.15	0.50	0.81
Size of nanocrystals on c–Si	R, Å	40	37	49	36	38	49
Volume fraction of nc on c–Si	X_c	0.78	0.80	0.76	0.40	0.56	0.82
Hydrogen concentration	C_H at%	4.8	6.7	9.0	13.0	4.1	2.8
Oxygen concentration	C_O at%	—	—	—	0.4	1.4	—
Optical gap	E_g^{opt}, eV	—	1.94	—	—	—	1.74

spectra in accordance with the method developed in [3] allowed us to evaluate the size of nanocrystals (R) and their volume fraction (X_c). Our data show that the dilution of SiH_4 by H_2 leads to increase of R from 49 to 57 Å, while X_c remains approximately unchanged ~ 0.7. IR investigations reveal that the amorphous phase consists of silicon bonded with hydrogen in monomer Si–H and polymer $(Si-H_2)_n$ configurations. The gas dilution by hydrogen leads to further polymerization what corresponds to the increase of absorption coefficient at $\sim 2090\,cm^{-1}$ and $\sim 890\,cm^{-1}$.

2.2 The influence of deposition temperature

At permanent deposition condition the T_s increase from 160°C to 340°C influences the nanocrystallites very slightly. X_c varies from 0.74 to 0.81 and R from 57 to 54 Å. But the subsequent changes of amorphous phase are much greater. The T_s growth leads to disappearing of polymer chains, what is detected as the absence of IR absorption at 800–900 cm^{-1}. At greater T_s H is distributed on crystal grains in Si–H form.

2.3 The influence of H_2O contamination

In accordance with our experiments the greatest changes of nanocrystal phase were caused by the presence of H_2O vapour in initial gas what leads to substitution of hydrogen atoms by O–H groups. As can be seen in Table 1 R may be varied by this method from 57 to 38 Å with simultaneous change of X_c from 0.74 to 0.15. The amorphous phase is also remarkably reconstructed: the total concentration of H is increased, and as a considerable amount of the oxygen enters in the network in Si–O–Si form, what leads to growth of the absorption at 1080 cm^{-1}.

2.4 The influence of substrate material

To understand the role of substrate material in nanocrystals formation the films were deposited on quart and silicon single crystal (c–Si). The Table 1 illustrates that on the c–Si the size of nanocrystals is $\sim 6-10$ Å greater than on the quartz, while their concentration remains nearly the same. It may be explained in the following way. The initial concentration of nanocrystals seems to be equal for both substrates but their following growth is faster on c–Si substrate due to higher thermal conductivity of c–Si and hence higher mobility of radicals participating in the growth of nanocrystals.

3 Conclusions

In accordance with our results we can conclude:
— PECVD method permits to produce the silicon films of mixed composition with characteristic size of nanocrystallites ranging from $\sim$ 30 to $\sim$ 60 Å by use of $SiH_4 + H_2$ gas mixtures.
— The size of nanocrystallites, the structure of amorphous phase and the film growth rate may be varied by the dilution of silane by hydrogen.
— The structure of amorphous phase is much more sensitive to deposition temperature than that of crystalline phase.
— The size and the concentration of nanocrystallites are two times less in the films produced from silane contaminated by H_2O.
— The size of nanocrystallites on c–Si substrates is greater than on quartz substrates.

Acknowledgments

This work is supported by the grant INTAS 97-1910.

References

[1] L. T. Canham, *Appl. Phys. Lett.* **57**, 1046 (1990).
[2] S. Tong, X. Lin, L. Wang, F. Yan and X. Bao, *Appl. Phys. Lett.* **69**, 596 (1996).
[3] V. G. Golubev, V. Yu. Davydov, A. V. Medvedev, A. B. Pevtsov and N. A. Feoktistov, *Phys. Solid State* **39**, 11197 (1997).
[4] J. Tauc, *Optical Properties of Amorphous Semiconductors* in *Amorphous and Liquid Semiconductors*, Plenum Press, London and New York (1974), p. 159.

7th Int. Symp. "Nanostructures: Physics and Technology"
St Petersburg, Russia, June 14–18, 1999

Radiative processes in InGaN quantum wells

P. G. Eliseev
Center for High Technology Materials, University of New Mexico, Albuquerque, NM 87106 U.S.A. (on leave from P. N. Lebedev Physics Institute, Moscow)

Abstract. Light-emission properties of InGaN quantum wells are reviewed and discussed including performance in wide range of temperatures (up to 450 K). The typical anomaly of "blue" temperature-induced shift of the luminescence spectral peak is explained in terms of the band-tail model. The model is applied to the InGaN active medium in LEDs and in lasers. The tail states are associated with composition variations in the alloy. They seem to be favorable for efficient radiative recombination.

1 Introduction

Most of new impressive achievements in the short-wavelength semiconductor optoelectronics (high-efficiency violet, blue and green LEDs [1], UV and purple LDs [2–5]) are associated with utilization of InGaN quantum wells (QWs). Early studies of InGaN alloy had been performed with polycrystalline films deposited on sapphire or fused quartz (see, for example [6, 7]). The wavelength coverage had been established from $\sim$ 365 nm (GaN) to $\sim$ 620 nm (InN). During last decade, the quality of InGaN material is improved significantly. Quantum efficiency of the luminescence in this material is high and comparable to that in high-quality GaAs and InGaAs.

The InGaN alloy is known as an unstable system at substantial content of indium, therefore, it can be subjected to decomposition or phase modification. Occurrence of phase separation is established under the annealing procedures [7]. Theoretically, the immiscibility in InGaN had been predicted [8]. There is no available commercial substrate material for lattice-matched growth, and most of devices are fabricated using mismatched substrates like sapphire or SiC. As a result, the lattice perfection is low, with dislocation density as high as $10^9-10^{12}\,\mathrm{cm}^{-2}$. In spite of this, InGaN QWs demonstrate excellent radiative characteristics. Nitride-based semiconductor device are expected to operate well above the room temperature. There is a challenge for future optoelectronics to face applications at elevated temperatures. InGaN-based devices are most promising candidates for this purpose [9]. In addition, semiconductor nitrides are known as piezoelectric materials [10]. Therefore, some novel properties can be expected in InGaN associated with stress-induced piezoelectric fields. Thus the understanding of radiative processes in InGaN is of great interest.

2 Quantum efficiency and high-temperature performance of LEDs

An important subject of discussion is quantum efficiency of the InGaN-based LEDs. The external quantum efficiency of visible LEDs at room temperature is 5–7% in commercial samples and up to 12% in experimental samples. Commercial LEDs shows very slow degradation or no visible degradation. Therefore, they are capable to operate long time at rather high optical output.

L–I characteristics are shown of green commercial LEDs in Fig. 1 in the temperature range [9]. The optical power measurements are made under dc injection below the current of 10 mA (current density $J \sim 14\,\mathrm{A/cm}^2$) and in pulse-current (pc) injection at higher

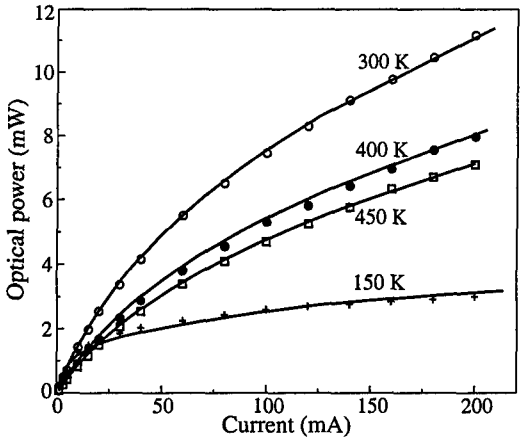

Fig. 1. Light-current characteristics of green Nichia InGaN SQW LED in temperature range up to 450 K. Curves are calculated with recombination coefficients as fitting parameters. Diode area is 7×10^{-4} cm^2.

current to avoid overheating. In addition to the power measurements the carrier lifetime is measured at 300 K. This gives sufficient experimental information to consider the recombination balance in SQW LEDs and to obtain the fitting of the room-temperature L–I curve assuming standard terms of linear non-radiative recombination, "bimolecular" radiative recombination, the Auger recombination and some higher-order recombination term which will be discussed later. For other temperatures than 300 K we perform similar analysis assuming that the radiative recombination coefficient B is in reverse proportion to the temperature as it is expected for 2D system. This theory need experimental confirmation because operating states in InGaN QWs are not obviously 2D states, but can be quantum-dot-like states. It may be reasonable for most low-energy states occupied at low current. In Ref. [11] the radiative lifetime is found to be not temperature dependent between 10 K and about room temperature in InGaN with indium content of $\sim$ 2%. This is considered as an indication on 0D nature of involved states. Therefore, the hypothesis of constant B should be also considered. The equation used in the analysis is as follows:

$$J/e = AN + BN^2 + CN^3 + DN^{4.8} + EN^9 + \ldots \qquad (1)$$

where N is 2D carrier density, A, B, C, D and E are fitting coefficients. The quantity A relates to the linear non-radiative recombination, C is the Auger coefficient, high-order coefficients D and E describe non-radiative losses due to leakage of carriers from active region and overflow losses, respectively.

The fitting parameters are shown for green LED at three temperatures in Table 1. The coefficient D is probably accounted for the leakage processes from the quantum well. Understanding that the potential barriers are very high in this structure, the leakage can be associated with not over-barrier leakage but with a transport via defects. The quantity D appears to decrease with temperature rise, whereas the contribution into the recombination balance increases. The decrease of D can be associated with a decrease of the carrier degeneracy which influence the effective height of the potential barrier for carriers. Process described by coefficient E is seen at low temperatures and disappears at room temperature. Because the small thickness of the quantum-well layer (3 nm), it can be associated with overflow when the free path of carriers is larger than QW thickness.

Table 1. Fitting parameters used to fit the L–I curves of green LED. All coefficients are used in the 2D recombination balance therefore they relate to the 2D carrier density in the QW.

Temperature, K	A, 1/s	B, cm^2/s	C, cm^4/s	D, cm$^{7.6}$/s	E, cm^{16}/s
100	$< 1\times10^{6}$	3×10^{-4}	$< 5\times10^{-18}$	$< 2\times10^{-37}$	7×10^{-86}
300	3×10^{6}	1×10^{-4}	$< 2\times10^{-17}$	5×10^{-39}	$< 1\times10^{-90}$
450	2.8×10^{7}	6.67×10^{-5}	$< 5\times10^{-17}$	4.5×10^{-39}	$< 1\times10^{-90}$

The LED performance at 450 K indicates possible high-temperature applications. In frames of above mentioned analysis we see that the internal quantum efficiency at room temperature can be estimated as 66.9% at 20 mA and 27.7% at 200 mA. At 450 K these figures are 40.3% and 18.6% respectively. The efficiency extraction and collection of photons is estimated as $\sim$ 8%. This corresponds to the external quantum efficiency of 5.35% (300 K) and 3.22% (450 K) at 20 mA. The calculated carrier lifetime in green InGaN SQW LED at 20 mA at room temperature is $\sim$ 6 ns (radiative lifetime is 9.2 ns), measured value is 6.2$\pm$0.5 ns. This shows satisfactory agreement of the proposed recombination balance with experimental data.

3 EL and PL spectra

From systematic study we point out following features of the spectra: 1) spectral peak position is typically not in agreement with nominal levels of quantum-confined states in quantum wells but is substantially red-shifted; 2) large bandwidth (typically, from $5.5kT$ to $9kT$ at 300 K in green LEDs depending on the injection current); 3) strong "blue" shift along with increase of the current (about 200 meV in green LEDs when current goes from 0.5 A/cm^2 to $\sim$ 2 kA/cm^2); 4) non-monotone (S-shaped) temperature dependence of the peak position with gradual "blue" temperature-induced shift which occurs in contrast to the expected temperature-induced band-gap shrinkage. The anomaly in the temperature behavior of the spectral peak position was reported in Ref. [12] in the study of the spontaneous electroluminescence spectra of InGaN-based SQW LEDs under strong current pulses. At low current this anomaly is even more apparent. In Fig. 2 the spectral peak position is shown in the blue LED under different values of the current. The interpretation of this behavior has been given in [13] in terms of the band-tail model.

The photoluminescence data are shown here in context of the anomaly of "blue" temperature-induced shift that was mentioned above in connection with electroluminescence. It is found in several papers that the shift is rather common in different structures: single heterostructures, double heterostructures (with over-critical bulk-like thickness up to 40–50 nm) and in quantum wells (thickness is 2–5 nm). The spectral peak position in function of temperature is shown in Fig. 3 for two different epitaxial structures. The anomaly is identified which is temperature "blue" shift in the range of 50–150 K in sapphire-substrate sample. This is not typical for undoped GaN, but is well pronounced in most InGaN luminescent structures including those in green LEDs investigated by both EL and PL characterization techniques [13]. Homoepitaxial sample does not show temperature-induced "blue shift" anomaly in the same temperature range.

4 Band-tail model

The InGaN-based materials, including both QW and more thick layers, are subjected to the significant broadening due to non-uniformity of the alloy composition (in addition to the defect-related and impurity-related broadening expected in both GaN and InGaN). In ideal

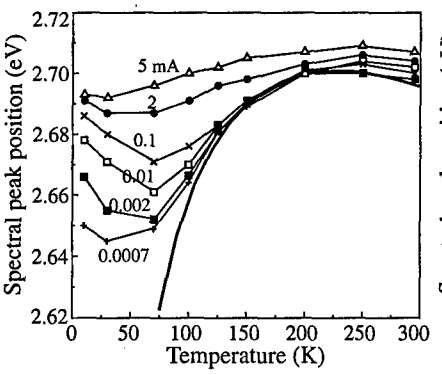

Fig. 2. EL spectral peak position of blue InGaN SQW LED at different current [13]. Thick curve is calculated according to Eq. (2). Fitting parameter s is 31.5 meV.

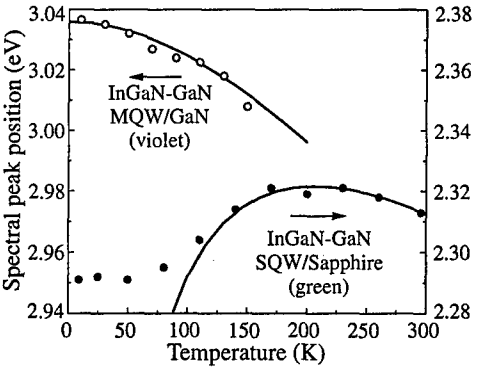

Fig. 3. PL spectral peak position of two InGaN samples: 1) open circles are for homoepitaxial MQW structure (grown by MOCVD on bulk GaN substrate obtained by sublimation method); pumping wavelength is 325 nm [18]; 2) solid circles are for green LED SQW structure on sapphire substrate; pumping wavelength is 442 nm [13].

QW, the DOS at the band edge is described by step-like function. When the energy position of the band edge varies the averaged DOS becomes to be broadened and it is non-zero below the nominal band edge. We call this range the band tail. It is occupied by the excess carriers in first, and filling of the band-tail states gives blue shift of the spectral peak. The band tail in undoped InGaN is result of "anti-phase" variations of the band edges. This means that c-band edge is going down, whereas v-band edge is going up. This is opposite case as compared with heavily doped materials, where the edges vary "in-phase". In InGaN, carriers are captured into band-tail states (captured electron-hole pairs can be considered as localized exciton) and then recombine via vertical transitions. That carrier which is captured below the mobility edge in the tail is localized. It has greater chance to recombine radiatively as compared with mobile carriers. It can not diffuse freely and can not come to nonradiative center.

Applying the Gaussian statistics for the band-gap variations, one obtains an Erf-type distribution for averaged DOS. Therefore, the asymptotic part of DOS distribution can be described in term of the Gaussian tail (with the same dispersion as that of the assumed statistics). The tail states can be occupied in non-degenerated manner like states in an ordinary band. This means that most of carriers occupy states substantially above the quasi-Fermi level F. As DOS in non-zero below this level, some of carriers are degenerated there. Therefore in general, the carriers in the tail are degenerated partially, and the non-degenerated case means only the carriers predominate in non-degenerated state. The energy distribution function $N(E, F, T)$ of carriers in the tail is blue-shifted when temperature rises, and its peak position is much higher than F. When the DOS of electron and hole tails are the Gaussian functions the spectral peak is red-shifted in respect to the energy difference E_0 between the Gaussian centers. The shift is equal to σ^2/kT, where $\sigma^2 = \sigma_e^2 + \sigma_h^2$, and σ_e^2 and σ_h^2 are dispersions of DOS functions of electrons and holes, respectively [13]. In this case the peak position corresponds to equation

$$E_{\text{peak}}(T) = E_0(0) - \alpha T^2/(T + \beta) - \sigma^2/kT, \tag{2}$$

where first and second terms in the right side are the Varshni approximation for band-gap with fitting parameters $E_0(0)$, α and β, and third term is temperature-dependent shift with band-tail parameter σ as explained above. This expression is a good approximation for low current above 100 K (non-degenerate occupation), whereas at low temperature and at high current it is not adequate because of the occupation degeneracy. We have inspected numerous reported data concerning the spectral peak position of InGaN emission (from QWs and bulky epilayer samples) versus temperature (both PL and EL measurements) and collected results of approximate analysis by the expression (2) in Table 2. Parameter $E_0(0)$ varies according to the average indium content. The band-tail parameter σ increases along with decrease of $E_0(0)$ suggesting the correlation of the composition variation with average indium content.

The Eq. (2) shows that the temperature dependence of the alloy bandgap can not be obtained from the luminescence peak position with no knowledge of σ. This explains difficulties of description of the InGaN bandgap parameters in spite of numerous PL and EL measurements published. Interesting experimental fact is that in homoepitaxial MQW samples of InGaN (grown on bulk GaN prepared by sublimation method) the "blue"-shift anomaly is not observed. Corresponding data are given in the last line in Table 2. It can be associated with lower dislocation density in bulky substrate. Simultaneously, these homoepitaxial structure does not demonstrate efficient luminescence, especially at room temperature. It seems to be an indication that tail states are favorable for radiative recombination, whereas in absence of tails, the radiative recombination is less competitive with non-radiative processes.

The band-tail approach is valid not only to InGaN quantum wells, but also to thick ("bulky") layers of InGaN grown on sapphire substrates. The approach seems to be adequate for both strained and relaxed structures. However, in non-relaxed structures the contribution of piezoelectric field is expected. The piezoeffect can produce shift of energy levels of 2D quantum-confined states that should be compared with the broadening parameter in order to understand if it is observable. There is also significant temperature-dependent homogeneous broadening of the emission band providing a masking of more fine effects. Large total spectral bandwidth of the InGaN emission is governed by both homogeneous and inhomogeneous contributions that combined in geometrical manner. Band-tail contribution into FWHM is $\sim 2.35\sigma$. As an example, in green LED, bandwidth of $\sim$ 160 meV is contributed by $\sim$ 80 meV from the band-tail broadening and $\sim$ 140 meV from the homogeneous (collisional) broadening.

5 About the role of dislocations

Dislocations can play an important role in the formation of In-rich clusters. They supply the centers of the phase precipitation and also produce a non-uniform inclusion of indium during growth. The low-temperature MOCVD epitaxial growth (typical to InGaN growth as compared with GaN growth) is shown to be associated with screw-type dislocation (spiral growth) [20, 21]. The growth rate and indium content are enhanced in vicinity of such dislocations. Therefore, dislocation density is one of important factors providing both compositional and geometrical variation in InGaN QWs. Large-size (0.1–1 μm) variations of the compositions near dislocations have been revealed by cathodoluminescent topography [21]. Probably, in homoepitaxial InGaN samples, this factor is not involved, and the tail formation is not typical. On the other hand, the efficiency of PL emission is found to be lower in homoepitaxial samples. This can be an indication that tail states are important to provide more efficient radiative recombination. Recently the comparison of

Table 2. Parameters of band tail in GaN and InGaN epitaxial structures. ΔE is the temperature-induced *blue* spectral shift; $E_0(0)$ and σ are fitting parameters (see text).

Structure	Method	Indium content, %	ΔE, meV	$E_0(0)$, eV	σ, meV
GaN, thick ($\sim 1\ \mu$m) epilayer	PL	0	~0	~3.48	< 2
InGaN, DH, d=40 nm[a]	PL	2	~3	3.432	8
InGaN:Si, SH[b]	PL	6	6	3.387	13.7
InGaN, MQW, d is not indicated[c]	PL	~20	7.6	~3.4	6.5
InGaN, SH, d=110 nm (SH #5743)	PL	8.5±1.5	20	3.34	10
InGaN, DH, d=40 nm (DH #5748)	PL	7.5±1.5	30	3.289	14.5
InGaN, SH, d=200 nm[d]	PL	20	24	3.05	16
InGaN, SQW, d=2.5 nm (LED #302)[e]	EL	15–30	52	2.78	31.5
InGaN, SQW, d=2.5 nm (LED #228)	EL	30–45	30	2.394	28.6
InGaN, SQW, d=2.5 nm (LED #229)[e]	EL	30–45	59	2.392	35
InGaN, 10-MQW, d=3 nm (Homoepitaxy)	PL	~20	0	3.036	~0

[a] Derived from PL spectral peak position plot in Ref. [11]. [b] Derived from PL measurements reported in Ref. [14]. [c] PL study reported in [15]. Peak position of 3.4 eV suggests lower In content than value of 20% indicated in the paper. [d] Derived from experimental plots in Ref. [16]. [e] Derived from EL measurements (see [13]). The In content is known rather roughly.

the InGaN QW materials has been reported with different dislocation density but on the same epitaxial wafer (prepared using so called *lateral epitaxial overgrowth* technique) [22]. It has not been found difference in optical properties of such materials and concluded that the effective band gap fluctuation in InGaN QWs is not related to threading dislocations. However, in that experiment the regions of high dislocation density are rather narrow stripes (5 μm wide) surrounded by "lateral-overgrown" low-dislocation material. Therefore, the comparable study is not easy because of scattering of both pumping and emitted light in the material. More reliable result could be obtained by comparison of characteristics of separate samples. We use this way comparing InGaN material grown on sapphire and on GaN bulk crystals. Certainly, there are also issues of different growth condition, layer thickness, and average indium content of separate samples.

6 Conclusions

Similarly to GaN, the InGaN alloy emits interband radiation in spite of very high density of defects, demonstrating low sensitivity of the radiation yield to the dislocation density. But this alloy emits even better than GaN, and it has advantage in laser diode applications. Large-scale production of short-wavelength LEDs is based on utilization of InGaN quantum wells. Commercial production of InGaN QW LDs is announced this year. In researches, the emission characteristics of InGaN are understood in terms of localized states adjacent to the nominal edge of the interband transitions in the quantum well. Our point is to treat these states as a band tail with smooth DOS distribution. A new finding is that in homoepitaxial InGaN QWs there is no anomalous "blue" temperature-induced spectral shift, which is typical for sapphire-substrate samples. This is an indication that inhomogeneous broadening can be associated with features of homoepitaxial growth (no misfit stress to the substrate, lower dislocation density). Dislocations seem to be involved in the formation of tail states, however further study is necessary for deeper understanding of their role.

Acknowledgments

Author is thankful to his colleagues by the nitride-related researches I. V. Akimova of P. N. Lebedev Physics Institute, Moscow, Russia, Dr. M. Osinski, Dr. E. Rabinovich and J. Lee of UNM, Albuquerque, NM, Prof. S. Sakai, Dr. S. Juodkazis and T. Sugahara of University of Tokushima, Japan, Dr. P. Perlin of Unipress, Warszawa, Poland. For useful discussions author thanks Dr. S. Nakamura of Nichia Res. Center, Anan, Japan, Prof. S. Fujita and Dr. Y. Kawakami of Kyoto University, Kyoto, Japan.

References

[1] S. Nakamura, M. Senoh, N. Iwasa and S. Nagahama, *Jpn. J. Appl. Phys.* **34**, L797-L799 (1995)

[2] S. Nakamura, M. Senoh, S. Nagahama, N. Iwasa, T. Yamada, T. Matsushita, H. Kiyoku, Y. Sugimoto, *Jpn. J. Appl. Phys.* **35** (1B) Pt. 2, L74-L76 (1996).

[3] I. Akasaki, S. Sota, H. Sakai, T. Tanaka, M. Koike and H. Amano, *Electron. Lett.* **32** (12) 1105-1106 (1996).

[4] S. Nakamura, M. Senoh, S. Nagahama, N. Iwasa, T. Matsushita and T. Mukai, *Proc. 2 nd Int. Symp. "Blue Lasers and Light Emitting Diodes"* Sep. 29 - Oct. 2, 1998, Chiba, Japan 371-376 (1998).

[5] S. Nakamura and G. Fasol, *The Blue Laser Diode* Springer-Verlag, Berlin, 1997.

[6] K. Osamura, K. Nakajima, Y. Murakami, P. H. Shingu, A. Ohtsuki, *Solid State Commun.* **22**, 617-621 (1972).

[7] K. Osamura, S. Naka and Y. Murakami, *J. Appl. Phys.* **46**, 3432 (1975).

[8] I. Ho and G. B. Stringfellow, *MRS Symp. Proc.* **449**, 871 (1997).

[9] I. V. Akimova, P. G. Eliseev and M. Osinski, *Quant. Electronics* (Moscow) **28** (11) 1013-1016 (1998).

[10] A. Bykhovski, B. Gelmont and M. Shur, *J. Appl. Phys.* **74**, 6734 (1993).

[11] Y. Narukawa, S. Saijou, Y. Kawakami, S. Fujita, T. Mukai and S. Nakamura, *Appl. Phys. Lett.* (1999).

[12] I. V. Akimova, P.G. Eliseev, M. A. Osinski, P. Perlin, *Quant. Electron.* **26** (12), 1039-1041 (1996).

[13] P. G. Eliseev, P. Perlin, J. Lee, M. Osinski, *Appl. Phys, Lett.* **71** (5), 5659-571 (1997).

[14] T. Taguchi, T. Maeda, Y. Yamada, S. Nakamura, G. Shinomiya, *Int. Symp. Blue Lasers and LEDs*, Chiba Univ., Japan, 1996, Proc., 372-374 (1996).

[15] K. L. Teo, J. S. Colton, P. Y. Yu, E. R. Weber, M. F. Li, W. Liu, K. Uchida, H. Tokunaga, N. Akutsu and K. Matsumoto, *Appl. Phys. Lett.* **73** (12), 1697-1699 (1998).

[16] S. Chichibu, L. Sugiura, J. Nishio, A. Setoguchi, H. Nakanishi and K. Itaya, *Proc. 2 nd Int. Symp. Blue Lasers and LEDs*, Chiba, Japan, 616-619 (1998).

[17] M. Osinski, P. G. Eliseev, P. Perlin, J. Lee, H. Sato, T. Sugahara, Y. Naoi, S. Sakai, *Adv. Program of CLEO/IQEL'1998*, San Francisco, CA, May 3-8, 1998, Pap. CWH5, pp. 107 (1998).

[18] T. Sugahara, P. G. Eliseev, H. Saeki, Y. Naoi, K. Nishino and S. Sakai, *46 th Japanese Appl. Phys. Conf.* Noda Campus, Tokyo Sci. University, March 28-31 (1999).

[19] P. G. Eliseev, I. V. Akimova, P. Perlin and M. Osinski, *3rd All-Russian Conf. Semicond. Physics*, Moscow, 1-5 Dec., 1997; Abstr., p. 88 (1997).

[20] H. Sato, T. Sugawara, Y. Naoi, S. Sakai, *Jpn. J. Appl. Phys.* **37** (4A), 2013-2015 (1998).

[21] T. Sugahara, M. Hao, T. Wang, D. Nakagawa, Y. Naoi, K. Nishino, S. Sakai, *Jpn. J. Appl. Phys.* **37** (10B), L1195-L1198 (1998).

[22] S. F. Chichibu, H. Marchand, M. S. Minsky, S. Keller, P. T. Fini, J. P. Ibbetson, S. B. Fleischer, J. S. Speck, J. E. Bowers, E. Hu, U. K. Mishra, S. P. DenBaars, T. Deguchi, T. Sota and S. Nakamura, *Appl. Phys. Lett.* **74** (10), 1460-1462 (1999).

7th Int. Symp. "Nanostructures: Physics and Technology"
St Petersburg, Russia, June 14–18, 1999

Quantum confined Pockels effect and optical polarized spectroscopy of interfaces in type-II heterostructures

E. L. Ivchenko†, V. P. Kochereshko†, A. V. Platonov†, D. R. Yakovlev‡, M. Keim‡, W. Ossau‡, A. Waag‡ and G. Landwehr‡
† Ioffe Physico-Technical Institute, St Petersburg, Russia
‡ Würzburg University , 97074 Würzburg, Germany

Abstract. We report on a strong enhancement of the Pockels effect in direct-gap type-II ZnSe/BeTe heterostructures. The effect has been found experimentally and analyzed theoretically. In quantum well structures with equivalent interfaces, say the Zn-Te and Te-Zn interfaces, the unbiased sample is optically isotropic in the plane perpendicular to the growth direction. In the presence of an electric field the electron and hole wavefunctions are pushed towards one of the interfaces and off from the other, as a result the balance is broken and the photoluminescence polarization becomes nonzero and reaches 70–80 in moderate electric fields. To describe the field-induced in-plane anisotropy in type-II heterostructures, a theoretical model has been developed which is based on the representation of optical matrix elements in the microscopical tight-binding model.

For zinc-blende heterostructures CA/C′A′ grown along the [001] principal axis, the point symmetry, C_{2v}, of a single interface is reduced as compared with the point group T_d for a bulk material and D_{2d} for a quantum well (QW) with symmetrical interfaces. It leads to new optical phenomena, in particular, to the in-plane optical anisotropy. The latter can be observed in QW structures if the normal and inverted interfaces are nonequivalent as realized on heteropairs with no-common atom or by distorting the free carrier wavefunction in an electric field and making different its values at the opposite interfaces.

Up to now, the in-plane optical anisotropy in QW structures induced by normally applied electric field, or the quantum confined Pockels effect, has been observed for two heterosystems both of them having a type-I band alignment. Kwok et al. [1] studied photoluminescence (PL) of biased GaAs/AlGaAs multiple QWs (MQWs), no noticable anisotropy was found for allowed interband transitions whereas the nominally forbidden PL peak $e2$-$hh1$ showed a substantial difference reaching 20–30% between $[1\bar{1}0]$ and [110] polarizations. Krebs et al. [2] reported the observation of a dichroism up to 11% in InGaAs/InP MQWs inserted into a p-i-n diode. The quantum confined Pockels effect in type-I heterostructures has been described [2, 3] in terms of the generalized envelope function approximation [4]. In type-I QWs, where the interband optical transitions are spatially direct, the overlap between electron and hole wave functions extends over the whole well layer which results in averaging and considerably reducing the effect of interface-induced and electric-field affected heavy-light hole mixing. On the contrary, in type-II structures the spatially-indirect transitions arise due to the electron-hole overlap only within an extremely narrow region containing the interface. Therefore, the transition oscillator strength has to be strongly correlated with anisotropic orientation of the interface chemical bonds. This is confirmed by observations of high linear polarization of the PL in InAs/AlSb [5] and ZnSe/BeTe [6] MQWs with nonequivalent normal and inverted interfaces.

In the present work we have studied the Pockels effect in type-II ZnSe/BeTe double-barrier heterostructures. Modification of the band diagram under external electric fields

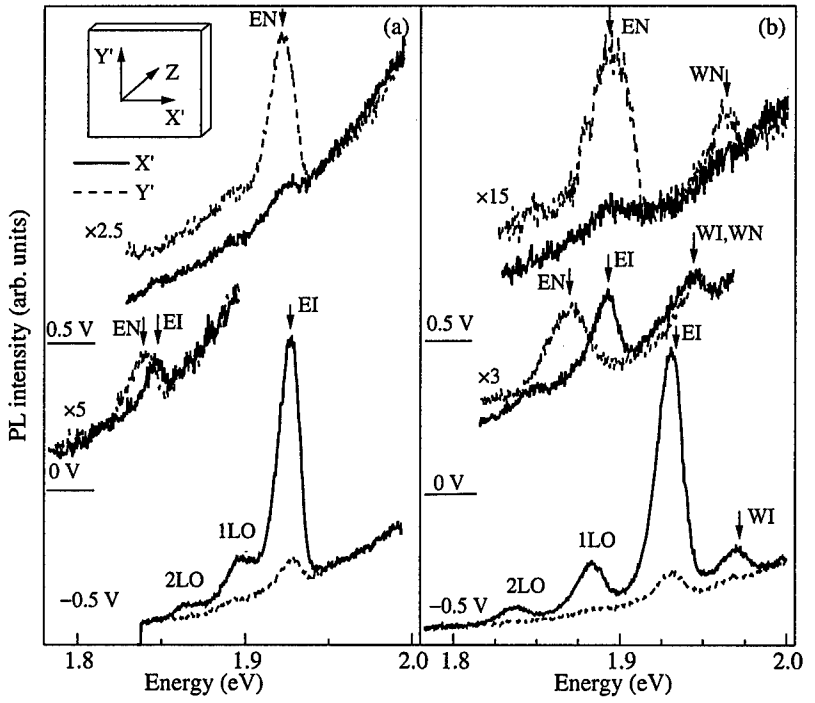

Fig. 1. The polarized PL spectra measured at different bias voltages for the analyzer orientation along the x′ and y′ axes of the sample A with $Zn_{0.9}Mn_{0.1}Se$ in the middle layer (a) and sample B with the pure ZnSe middle layer (b).

allowed us to detect signal from an individual interface and to determine orientation of chemical bonds from the induced optical anisotropy effect. A set of resonant tunneling ZnSe/BeTe double-barrier structures (DBS) were grown on GaAs:Si(001) substrates by molecular-beam epitaxy. The layer sequence is symmetric and comprises lattice matched BeZnSe:I (300 nm) contact layers, undoped ZnSe (25 nm) spacer layers, which act as electron emitters under bias voltage applied, and the BeTe/ZnSe/BeTe (4 nm/5 nm/4 nm) double-barrier structure. In sample B the central layer was of pure ZnSe while in sample A it was substituted by a $Zn_{0.9}Mn_{0.1}Se$ (5 nm) layer. For the both structures the normal (BeTe on ZnSe) and inverted (ZnSe on BeTe) interfaces are grown respectively under Zn and Te termination and contain the Zn-Te chemical bonds.

The PL spectra detected in linear polarizations along $[1\bar{1}0]$ and [110] axises are shown in Fig. 1 for the two studied structures. The emission lines under study originate from the spatially indirect transitions involving electrons from the ZnSe emitters (E) or quantum wells (W) and holes from the BeTe layers. The both samples demonstrate very similar behavior. At zero electric field pairs of PL lines at 1.84 eV for the sample A and at 1.87 eV for the sample B are due to recombination of electrons from the left- and right-hand side emitters and photoholes in BeTe (the lines EI and EN). Additionally, in the sample B a pair of the WI and WN lines at 1.95 eV involving electrons from the well layer is observed. Splitting between the EN and EI lines can be attributed to small charge-asymmetry of the emitters. Positive electric fields push off electrons from the rightmost Zn-Te interface and form a triangular potential near the leftmost Te-Zn interface pressing electrons towards the

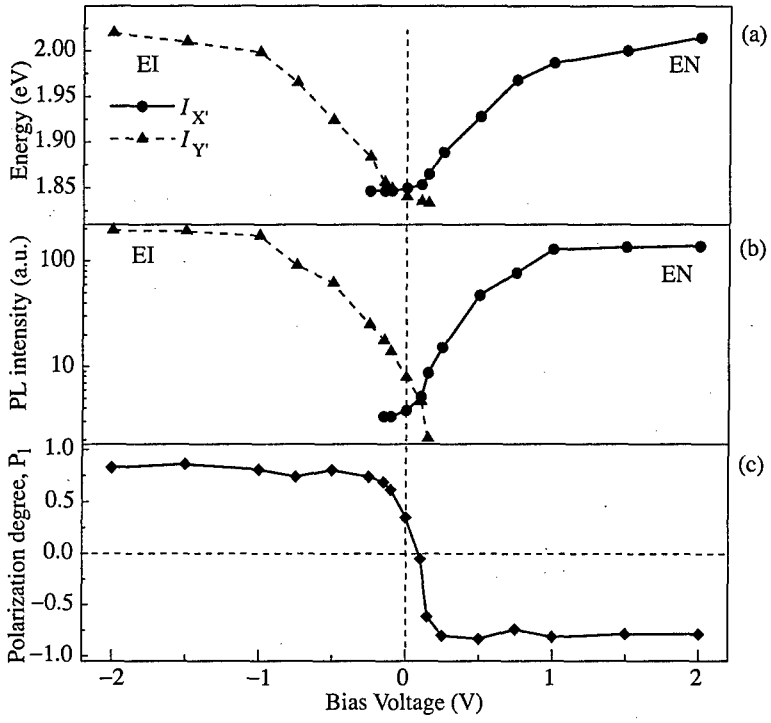

Fig. 2. Effect of the electric field on the position (a), intensity (b) and polarization (c) of the PL lines due to optical transitions from the ZnSe emmiters to the adjacent BeTe layers in the sample A.

latter. As a result the relative intensity of the EN line contributed by transitions at the Zn-Te interface increases and that for the EI line related to the Te-Zn interface vanishes. The field reversal leads to exchange of the role played by the interfaces. The bias-induced PL intensity variations and energy shifts for the EN and EI lines in the sample A are presented in Fig. 2(a) and (b). The field-induced optical anisotropy, i.e. the Pockels effect, is visualized in Fig. 2(c) as a degree of PL linear polarization in the axes $I_{1\bar{1}0}$, I_{110}. For both directions of the bias voltage the absolute value of P_l rapidly increases, saturates to 0.7−0.8 at the voltage $U \geq 0.25$ V and is almost invariable for higher U up to ±2 V. Under the same conditions the linear polarization detected in the axes [100] and [010] was absent.

In the ZnSe/BeTe system the conduction- and valence-band offsets amount to 2 eV and 1 eV respectively and the penetration depth for an electron into the BeTe layer or for a hole into the ZnSe layer is of the order of one monomolecular layer. Therefore in type II direct-gap ZnSe/BeTe heterostructures the wavefunctions of an electron and a hole participating in the spatially indirect transition overlap remarkably only over few atomic planes. In this case calculation of the interband matrix elements presupposes the knowledge of microscopic behavior of the wavefunctions at the interfaces which can be obtained by using pseudopotential or tight-binding models. From the polarization degree of 0.7−0.8 we obtain for the ratio between the indirect-transition matrix elements: $|M_{x'}/M_{y'}| = 2.4-3$ for one and the inverse value for the other interface. This means a strong in-plane anisotropy for the interband matrix elements of the velocity operator, $\mathbf{v}_{cv}$. We express the matrix elements in terms of the tight-binding parameters by using representation given in [7] and based on the quantum mechanical definition of the velocity operator $\mathbf{v} = (i/\hbar)[H\mathbf{r}]$, where

H is the tight-binding Hamiltonian.

In the nearest-neighbor sp^3 model the scalar product of $\mathbf{v}_{cv}$ and the light polarization unit vector $\mathbf{e}$ can be expanded for the electron and hole states with zero in-plane wavevector as

$$\frac{ia_0}{4\hbar}\sum_l \left[V(sa,pc)C^*_{2l,s}\left(C_{2l-1,x'}e_{x'} \pm iC_{2l+1,y'}e_{y'}\right)\right.$$
$$\left.+V(pa,sc)C^*_{2l-1,s}\left(C_{2l,x'}e_{x'} \pm iC_{2l-2,y'}e_{y'}\right)\right]. \qquad (1)$$

Here the sign $\pm$ corresponds to the transitions from the $\pm 3/2$ heavy-hole valence states to the spin-up and spin-down conduction states which are written in terms of the s-like planar orbitals ϕ_{ns} with the expansion coefficients C_{ns} and p-like planar orbitals with the expansion coefficients C_{np_j} ($j = x' \parallel [1\bar{1}0]$], $y' \parallel [110]$), the integer n is even and odd respectively for the anion and cation planes, a_0 is the lattice constant, $V(sa,pc)$ and $V(pa,sc)$ are the two linearly independent sp-interaction parameters. The terms in the sum (1) describe contributions to the optical matrix element due to particular interatomic optical transitions. It should be emphasized that the transitions $2l \leftrightarrow 2l-1$ and $2l \leftrightarrow 2l+1$ are polarized orthogonally. The experimental high degree of linear polarization can be understood taking into account that only a finite number of terms in Eq. (1) are important, say those arising due to the Se(s) $\rightarrow$ Zn(p), Zn(s) $\rightarrow$ Te(p), Te(s) $\rightarrow$ Be(p) interatomic transitions and that the product $C_{-1,s}C_{0,y'}$ exceeds $C_{-2,s}C_{-1,x'}$ and $C_{0,s}C_{1,x'}$, where $n = 0$ is assigned to the Te interface plane.

Acknowledgements

Deutsche Forschungsgemeinschaft (SFB 410), Russian Foundation for Basic Research (RFBR 98-02-18234).

References

[1] S. H. Kwok, H. T. Grahn, K. Ploog and R. Merlin, *Phys. Rev. Lett.* **69**, 973 (1992).
[2] O. Krebs, D. Rondi, J. L. Gentner, L. Goldstein and P. Voisin, *Phys. Rev. Lett.* **80**, 5770 (1998).
[3] E. L. Ivchenko, A. A. Toropov and P. Voisin, *Phys. Solid State* **40**, 1748 (1998).
[4] I. L. Aleiner and E. L. Ivchenko, *JETP Lett.* **55**, 692 (1992); E. L. Ivchenko, A. Yu. Kaminski and U. Rössler, *Phys. Rev. B* **54**, 5852 (1996).
[5] F. Fuchs, J. Schmitz and N. Herres, *Proc. 23rd Int. Conf. Phys. Semicond.* (Berlin, 1996), ed. by M. Scheffler and R. Zimmermann, World Scientific, vol. 3, p. 1803.
[6] A. V. Platonov, V. P. Kochereshko, E. L. Ivchenko, D. R. Yakovlev, W. Ossau, F. Fischer, A. Waag and G. Landwehr, *Acta Phisica Polonica A* **94**, 479 (1998).
[7] L. C. Lew Zan Voon and L. R. Ram-Mohan, *Phys. Rev. B* **23**, 15500 (1993).

7th Int. Symp. "Nanostructures: Physics and Technology"
St Petersburg, Russia, June 14–18, 1999

Impact of Fano resonances on the Wannier–Stark ladder

C. P. Holfeld†, T. W. Canzler†, D. M. Whittaker‡, F. Löser†, M. Sudžius†, K. Leo† and K. Köhler§

† Institut für Angewandte Photophysik, Technische Universität Dresden, 01062 Dresden, Germany

‡ Toshiba Research Europe Ltd., 260 Cambridge Science Park, Milton Road, CB4 0WE Cambridge, United Kingdom

§ Fraunhofer–Institut für Angewandte Festkörperphysik, 79108 Freiburg, Germany

Abstract. We report on the observation of Fano resonances in electrically biased superlattices. In such structures, Coulomb interaction couples discrete exciton states to continua of lower-lying subbands. We thus observe Fano resonances on the Wannier–Stark states. In superlattices, it is possible to continuously tune the coupling strength by sweeping the electric field. We prove this by linear absorption spectroscopy which demonstrates that the coupling and the line asymmetry change with field. We also measured the polarization decay of the Wannier–Stark transitions and found a decrease of the dephasing times for growing Fano coupling strength.

Introduction

Degeneracy of discrete states and a continuum is often found in nature. The quantum mechanical coupling of such degenerate discrete and continuous states gives rise to Fano resonances which lead to major changes of the optical spectra by quantum interference of the transition paths. Fano interference manifests itself by a strong, asymmetric deviation from the natural line shape together with a broadening due to the coupling. The quantum mechanical coupling is also expressed by a reduction to zero transition probability on one side of the resonance below the former continuum level.

Fano resonances appear in various systems since they are not restricted to a certain origin of the states or their interaction. They are indeed an universal phenomenon in physics. The theory has originally been developed by Fano to understand rare gas spectra [1]. In semiconductor physics, electron–electron and phonon–electron interaction are subject to Fano resonances. In particular, the Fano effect is generally predicted in low-dimensional semiconductors [2] since confinement usually forms excitonic subbands which are coupled by the Coulomb interaction. This has experimentally been confirmed in quantum wells [3], bulk GaAs in a magnetic field [4] and electrically biased superlattices [5]. As a new attempt, the Fano coupling strength can be manipulated by either changing the density of continuum states [6] or varying the coupling matrix element [5].

1 Fano coupling and superlattices

A Fano system needs only a few, generalized prerequisites. Consider a discrete state $|d\rangle$ which is energetically degenerate with a continuum of states $|c\rangle$ (see Fig. 1). These states are Fano coupled by an interaction Hamiltonian $\hat{V}$. Finally, the Fano system is experimentally probed by a transition from a common ground state $|g\rangle$ (transition operator $\hat{T}$). It should be noted that there is no restriction on the actual origin of both the states and the participating

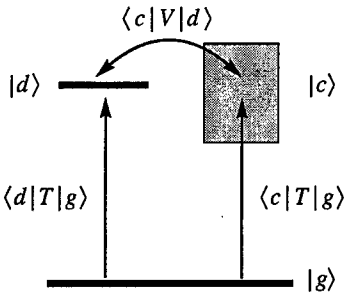

Fig. 1. Schematic overview about the energy states involved in Fano coupling.

interactions. Due to the Fano coupling $\hat{V}$, the transition paths to discrete and continuous states are no longer independent but do quantum mechanically interfere in respect to their phase-locking.

The mathematical analysis of Fano assumes a delta-like discrete state coupled to a quasi-continuous set of discrete states with an uniform density of states in the zero-spacing limit [1]. Coupling between different continuum states is neglected. The probing transition then results no longer in a sharp line. Its profile is modified by asymmetric broadening and is given by the line shape formula g:

$$g(\varepsilon) = \frac{(q+\varepsilon)^2}{1+\varepsilon^2} \qquad \varepsilon = \frac{E - E_R}{\frac{1}{2}\Gamma} \tag{1}$$

$$\Gamma = 2\pi |\langle c|\hat{V}|d\rangle|^2 \tag{2}$$

The argument ε is a normalized energy difference in respect to a resonance energy E_R in units of the spectral broadening Γ. This parameter Γ is solely dependent on the Fano coupling probability and is not influenced by the transition process. The line shape formula (1) contains also a parameter q which strongly determines the asymmetry and depends on the excitation conditions.

The Fano effect is generally predicted in low-dimensional semiconductors [2]. Here confinement splits the electronic bands into several subbands. Due to Coulomb interaction there are several bound (discrete) excitons just below every subband edge followed by an ionization continuum of unbound excitons. Thus, the discrete excitonic states are degenerate with the ionization continua of lower-lying subbands. Coupling of them is again mediated by the Coulomb interaction.

This situation is also found in superlattices. An axial electric field splits the quasi-3D miniband into an equidistantly spaced ladder of subbands, the so-called Wannier–Stark ladder (WSL). The splitting $\Delta E = eFd$ of the subbands is directly dependent on the applied electric field F (d—superlattice period). The ladder transitions are labeled with $\mathrm{hh}_{\pm n}$ according to heavy hole transitions to the nth neighbour well on the energetically raised (+) or dropped (−) side.

The discrete excitonic states are Fano-coupled to the continua of lower-lying ladder states as described in the previous paragraph. In comparison to other systems, superlattices offer the unique possibility of continuously tuning the Fano coupling by simply sweeping the applied electric field. This varies the splitting of the WSL which corresponds to a changing momentum mismatch of discrete state and continuum. We thus expect weaker Fano coupling with increasing field.

2 Results and discussion

Our measurements are carried out on GaAs/$Al_{0.3}Ga_{0.7}As$ superlattices with a barrier/well width of 17 Å or 67 Å, respectively. The temperature of the sample has been kept at approximately 10 K during mesurements. First, the field-dependent evolution of Fano resonances has been observed using a standard setup for absorption spectroscopy with correction of the halogen lamp spectrum. When applying an electric field in growth direction of the superlattice, the absorption of the miniband and of its related heavy and light hole excitons disappears. Instead the Wannier–Stark states develop as described in the previous section. An example of the obtained spectra is shown in Fig. 2. It turns out that the transitions to all ladder states exhibit a rather large line width and distinct asymmetry with the slow rise on the low-energy side. This observation is made over the whole field range where there is a pronounced oscillator strength of the transitions. The line width is found to decrease with growing field in accordance with increasing ladder spacing. Coupling of the Wannier–Stark excitons to lower subband continua is thus impeded resulting in a narrower profile.

The absorption has also been calculated theoretically for comparison. The numerics is based on the direct solution of the Schrödinger equation considering the confinement potential of biased superlattices and the presence of Coulomb interaction between electrons and holes [7]. The only free parameters are the absolute scaling of absorption and some phenomenological broadening due to interface roughness and field inhomogeneities. The calculations thus naturally include Fano resonances. A comparison of experimental and theoretical absorption spectra reveals strong correspondence. Almost all spectral details are reproduced by theory. A fit of the Fano line shape formula to the calculated spectra in the absence of extra broadening is used to obtain values of the Fano coupling parameter Γ (Eq. (1), (2)). There is a pronounced decrease of Γ with growing field supporting the experimental observation.

We have also investigated the polarization decay by means of transient four-wave mixing (FWM). These measurements are restricted to the hh_{-1} transition because it has a strong oscillator strength and a distinct dependence of the energetic position on the applied field. The spectral pulse width is set to about 7 meV (corresponding to 300 fs) thus ensuring

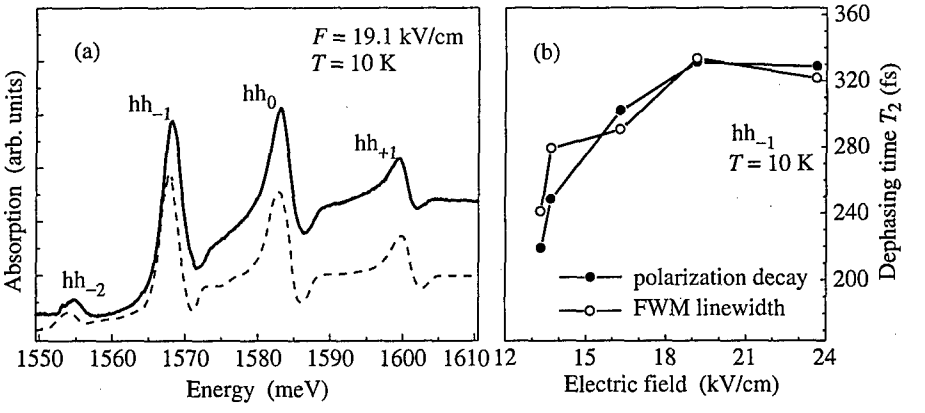

Fig. 2. (a) Example of experimental (solid line) and theoretical (dashed line) absorption spectrum of a 67/17 Å superlattice. (b) Dephasing times for the hh_{-1} transition at varying electric fields due to the decay time and linewidth of the FWM signal.

the excitation of only one Wannier–Stark transition even at a small ladder splitting. The centre of the laser is shifted approximately 2 meV below the absorption peak to prevent an incoherent carrier background. We obtain a clearly resolved decay of the FWM signal in contrast to a previous study on bulk GaAs in a magnetic field [8]. Both the rise and decay time of the signal is well above the autocorrelation limit. The polarization decay time systematically rises for stronger fields which is not expected for collisional broadening. We thus attribut the slower polarization decay to the weaker discrete state-continuum coupling $|\langle c|\hat{V}|d\rangle|^2$ resulting in a reduced Fano line width Γ.

Acknowledgements

We gratefully thank D. S. Chemla and S. Glutsch for their helpful discussions, T. Hasche and V. G. Lyssenko for experimental help. This work was financially supported by the Deutsche Forschungsgemeinschaft.

References

[1] U. Fano, *Phys.Rev.* **124**, 1866 (1961).
[2] S. Glutsch, D. S. Chemla and F. Bechstedt, *Phys. Rev. B* **51**, 16885 (1995).
[3] D. Y. Oberli *et al.*, *Phys. Rev. B* **49**, 5757 (1994).
[4] S. Glutsch *et al.*, *Phys. Rev. B* **50**, 17009 (1994).
[5] C. P. Holfeld *et al.*, *Phys. Rev. Lett.* **81**, 874 (1998).
[6] J. Faist *et al.*, *Optics Letters* **21**, 985 (1996).
[7] D. M. Whittaker, *Europhys. Lett.* **31**, 55 (1995).
[8] U. Siegner *et al.*, *Phys. Rev. Lett.* **74**, 470 (1995).

7th Int. Symp. "Nanostructures: Physics and Technology"
St Petersburg, Russia, June 14–18, 1999

Electric field induced interference impurity ionization in coupled quantum wells

Yu. A. Aleshchenko, I. P. Kazakov, V. V. Kapaev, Yu. V. Kopaev,
N. V. Kornyakov and A. E. Tyurin
P. N. Lebedev Physical Institute of RAS, 117924 Moscow, Russia

Abstract. The dramatic change of Si donor impurity ionization energy was experimentally found in GaAs/AlGaAs double-well structure. This effect accompanies the rearrangement of electronic wave function in electric field. With less than 1 V variation of the bias on the structure the impurity ionization energy falls to zero from 15.5 meV. The Stark effect should cause the variation of this parameter no more than 3 meV.

Introduction

The quantum interference of electronic states in coupled quantum wells (QWs) causes a high sensitivity of the system to the external exposures. In these circumstances even relatively weak electric field gives rise to the drastic modification of electronic wave functions (WFs) and their redislocation between QWs. We have predicted earlier [1] the effect of impurity ionization energy (E_{imp}) modification caused by such redislocation. The inversion of lower subbands of coupled QWs with their anticrossing in external field is responsible for this effect. The localized state of the electron on impurity atom which is formed mainly from the states of the lower subband changes its binding energy and the shape of WF as a result of inversion. Here we verify this effect by photoluminescence (PL) spectroscopy in GaAs/AlGaAs double-QW structure in external electric field.

1 Experimental procedure

The structure under study was grown by MBE on GaAs(100) substrate. The active layers of the structure comprised lower undoped 57 Å QW, 34 Å $Al_{0.34}Ga_{0.66}As$ barrier and 79 Å upper QW with Si δ-doping ($n = 6.3 \times 10^{11}$ cm^{-2}) in its centre. The PL was excited by 4880 Å line of Ar^+ laser at 20–90 K.

2 Experimental results

The PL peaks assignment was made by comparison of experimental spectra taken at zero bias ($U = 0$) with the results of simultaneous solution of Shrödinger and Poisson equations. The potential profile in the region of QW of the structure to be investigated as well as calculated WFs for three lower electron and heavy hole subbands at $U = 0$ are sketched in Fig. 1(a). One can see from the figure that the distortion of potential profile by built-in field causes the localization of ground state electron and hole WFs (curves 1) in different QWs. As a result the overlap integral for the transition between first electron and heavy-hole subbands (c1–h1) appears to be considerably lower than for transitions connecting second electron and first heavy-hole (c2–h1) as well as first electron and second heavy-hole (c1–h2) subbands which WFs are localized in the same QW.

The PL spectrum of the structure taken at 20 K and $U = 0$ with the excitation intensity of 4 W/cm^2 is shown in Fig. 1(b) by solid line. The narrow peak at 1.599 eV dominates

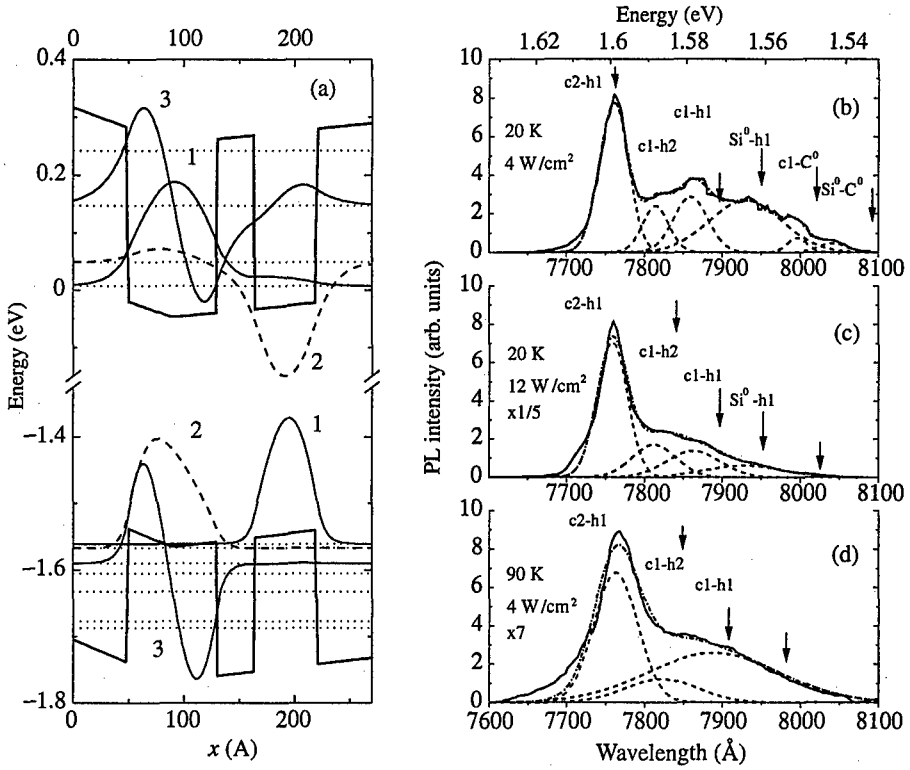

Fig. 1. Potential profile in the region of QWs and calculated WFs (a) as well as PL spectra of the structure at zero bias (b)-(d).

in the spectrum. There is a broad band containing the contributions of several overlapping peaks which is adjacent to the main peak from its low-energy side. The spectrum fits well by six Gaussians shown in Fig. 1(b) by dashed lines (dash-dotted line represents the resulting contour). The comparison of PL data with the results of calculations of the energy spectrum of the structure allows one to assign peaks at 1.599, 1.588 and 1.576 eV respectively to c2−h1, c1−h2 and c1−h1 excitonic transitions. The high intensities of c2−h1 and c1−h2 transitions correlate with the calculated distributions of WFs presented in Fig. 1(a).

PL peaks at 1.566, 1.552 and 1.543 eV which are at lower energies relative to c1−h1 transition are most probably due to impurities. In the temperature range 20–90 K all but two-particle electron-impurity complexes should be ionized. In particular, the excitonic complexes with neutral impurities which produce the dominant contribution to the impurity PL at low temperatures and high doping levels appears to be thermally dissociated. From these considerations the peak at 1.566 eV next to c1−h1 excitonic transition is most likely due to electron transition from neutral Si atoms to $h1$ subband (Si^0−h1). The peak at 1.552 eV nearest to Si^0−h1 transition is separated from c1−h1 excitonic transition by 24 eV. Since C is main background acceptor in our samples it would appear reasonable to assign peak at 1.552 eV to the c1−C^0 transition. Moreover, because of the comparable shifts of the remaing peak at 1.543 eV from c1−C^0 peak and Si^0−h1 peak relative to c1−h1 transition it is pertinent to ascribe the peak at 1.543 eV to the Si^0−C^0 transition.

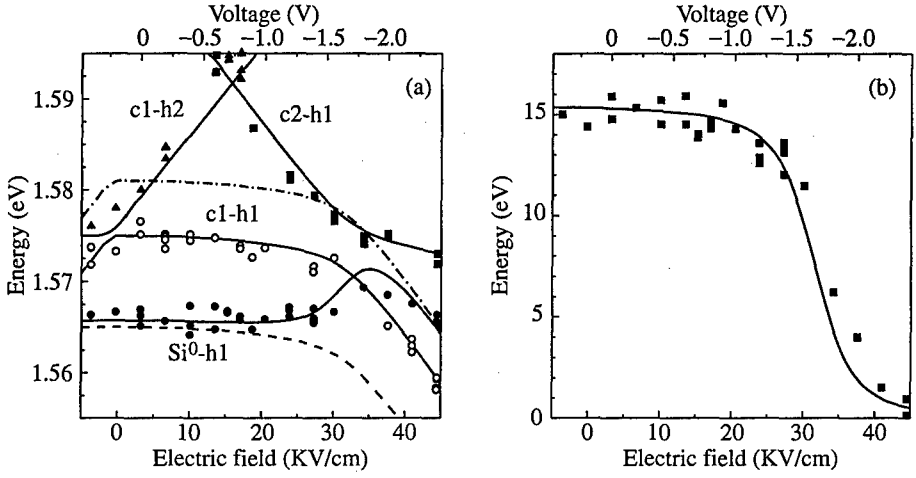

Fig. 2. Theoretical and experimental field dependences of the main transitions in PL spectrum (a) and of E_{imp} (b).

To confirm the impurity nature of low-energy peaks the excitation intensity and temperature dependences of PL were measured. As an example in Fig. 1(c) the PL spectrum of the same sample is shown but measured with the excitation intensity of 12 W/cm^2 and amplification about a fifth as large as it does in spectrum in Fig. 1(b). Indeed, as the excitation intensity increases the contribution of low-energy peaks to the spectrum diminishes as compared to that of c1−h1 transition due to finite amounts of Si donors and C acceptors in QW. Notice that because of weakness of low-energy peaks in spectrum in Fig. 1(c) the good fit in this region is provided by one peak which is designated as Si^0−h1 transition instead of three peaks in Fig. 1(b). The PL spectrum in Fig. 1(d) measured at 90 K and amplification 10 times that of spectrum in Fig. 1(b) illustrates the modification of spectrum with temperature. This spectrum is approximated well by three Gaussians (dashed lines) which are the contributions of c2−h1, c1−h2 and c1−h1 transitions at 90 K. The absence of impurity states contributions in this spectrum is explained by thermal ionization of donors and acceptors.

3 Ionization energy of Si donor

In the spectrun in Fig. 1(b) taken at $U = 0$ the Si^0−h1 peak and c1−h1 excitonic transition are 10 meV apart. One has to add to this value the exciton binding energy E_{ex} to determine E_{imp}. Our variational calculations taking into account built-in field in the structure provide $E_{\text{ex}} \approx 6$ meV, therefore, E_{imp} is close to 16 meV. This is considerably in excess of the values reported by many authors (12–13 meV). The additional increase of E_{imp} in our case is explained by δ-doping which produces the V-shaped potential in the centre of QW. This potential is responsible for the decrease of lower states energies relative to the higher states [2] and consequently for the increase of E_{imp}. According to our estimates the increase of E_{imp} is as much as 3–4 meV for our samples due to this effect.

In Fig. 2(a) the PL data (points) and the results of calculations (curves) are shown for the field dependences of the main transitions when biases from +0.4 to −2.4 V are applied to the top electrode. The anticrossing of c1−h1 and c2−h1 curves in Fig. 2(a) at the field

strength of 30 kV/cm is of significance for us since in this region the redislocation of electronic WF of lower subband from doped to undoped QW takes place. The calculation in the effective mass approximation yields $E_{\text{imp}}(F) = u^2(F)E_0$, where E_0 is impurity ionization energy in single QW with the same parameters as doped QW in our samples. The electric field F dependent coefficient $u(F)$ contains the information regarding the part of electron WF localized in doped QW. This coefficient varies from 1 to 0 and E_{imp} changes accordingly from E_0 to 0. The more sophisticated calculations in the approximation of δ-shaped potential [3] allows one to refine the previous formula and to calculate the field dependence of Si^0–h1 peak position which is shown in Fig. 2(a) by solid line. The field dependence of impurity peak position without the effect of modification of impurity ionization energy is shown by dashed line for comparison along with the field dependence of c1–h1 edge transition (dash-dotted line). The latter was obtained from the experimental field dependence of c1–h1 exciton peak position having regard to calculated E_{ex}. Referring to Fig. 2(a), in the region of 25–40 kV/cm where the redislocation of electron WF occurs the Si^0–h1 curve approaches rapidly the field dependence of c1–h1 edge transition. This is an evidence of drastic decrease of E_{imp}.

The theoretical and experimental field dependences of E_{imp} obtained as a difference between calculated field dependence of c1–h1 edge transition and the respective theoretical and experimental dependences of Si^0–h1 transitions are shown in Fig. 2(b). One can see from this figure that E_{imp} reaches 15.5 meV in the weak field but rapidly vanishes as field increases. Such dramatic change of E_{imp} is connected with electron WF redislocation with anticrossing of lower subbands in electric field and can't be explained by Stark effect. According to our estimates the latter would produce the E_{imp} variation not exceeding 3 meV.

This work has been supported in part by RFBR, Russian Programme "Physics of Solid State Nanostructures" and State Programme "Integration".

References

[1] V. I. Belyavsky, Yu. V. Kopaev, N. V. Kornyakov and S. V. Shevtsov *JETP Lett.* **61**, 1039 (1995).
[2] R. Sasagawa, H. Sugawara, Y. Ohno, et al. *Appl. Phys. Lett.* **72**, 719 (1998).
[3] Yu. A. Aleshchenko, I. P. Kazakov, V. V. Kapaev, Yu. V. Kopaev, N. V. Kornyakov and A. E. Tyurin *JETP Lett.* **69** 194 (1999).

7th Int. Symp. "Nanostructures: Physics and Technology"
St Petersburg, Russia, June 14–18, 1999

Magnetic field-induced type-I type-II transition in (ZnMn)Se/(ZnBe)Se spin superlattices

B. König, U. Zehnder, D. R. Yakovlev†, W. Ossau, T. Gerhard, M. Keim, A. Waag and G. Landwehr
Physikalisches Institut der Universität Würzburg, Am Hubland,
D-97074 Würzburg, Germany
† Ioffe Physico-Technical Institute, St Petersburg, Russia

Abstract. We have performed a magneto-optical study on spin superlattice structures fabricated on the basis of (ZnMn)Se/(ZnBe)Se. The band alignment of a $Zn_{0.91}Mn_{0.09}Se$/ $Zn_{0.972}Be_{0.028}Se$ superlattice was found to undergo a type-I to type-II transition for one of the exciton spin component. This spin superlattice formation manfests itself in an asymmetric Zeeman splitting of a spatially direct exciton resulting from a spin dependent change of the exciton binding energy. A pronounced broadening of the spatially direct exciton in reflectance and photoluminescence excitation spectra was observed when scattering in the (ZnBe)Se barriers becomes possible.

Introduction

The use of dilluted magnetic semiconductors (DMS) in nanostructures has brought a lot of new and interesting phenomena in the physics of low dimensional systems. In particular the ablity of tuning confining potentials for carriers by applying external magnetic fields which can lead to the formation of a spin superlattice has contributed in understanding the effect of quantum confinement on exciton states both in experiment and theory. The peculiar magnetic properties of DMSs stem from a strong s, p–d exchange interaction between the electron and hole states and the localized $3d$-states of the magnetic ions.

Here we have applicated (ZnBe)Se as a new non-magnetic barrier material for (ZnMn)Se and present first results of optical studies on (ZnMn)Se/(ZnBe)Se multi quantum wells (MQWs) as a novel representative for spin superlattices.

1 Experimentals

The sample under investigation was grown by molecular beam epitaxy (MBE) in a Riber system on (001)-oriented GaAs substrates. The multi quantum well (MQW) consists of 20 periods of alternating 100 Å-thick layers of $Zn_{0.91}Mn_{0.09}Se$ and $Zn_{0.972}Be_{0.028}Se$.

Optical spectra were taken at sample temperatures of 1.7 K (pumped liquid helium) and 8 K. Magnetic fields up to 7.5 T, generated by a superconducting split-coil solenoid, were applied parallel to the growth axis (Faraday geometry). An Ar-ion laser served as the pump source for a tunable dye-laser (Stilben 3) used in photo luminescence excitation (PLE) experiments. For reflectance measurements a halogen lamp was applied. The circular polarized signal was analyzed by a 1-m monochromator and detected with a charged-coupled-device (CCD) or a cooled photomultiplier tube followed by a photon counting system.

2 Results and discussion

2.1 *Photoluminescence studies*

In Fig. 1(a) we present PLE spectra of the $Zn_{0.91}Mn_{0.09}Se$/ $Zn_{0.972}Be_{0.028}Se$ MQW taken at 1.7 K for different magentic field strengths detected under σ^--polarized excitation. The strongest feature observed in the zero field spectrum at 2.83 eV is attributed to the 1s-state of the e1−hh1 exciton (denoted by X_{hh1}) in the $Zn_{0.91}Mn_{0.09}Se$ wells. By increasing the magnetic field the high energy spin-state of the X_{hh1}-exciton energetically meets with the barrier exciton at a critical magnetic field of $B_0 = 1.5\,T$. In the field range $B > B_0$ for which the ground state is taken over by the barrier exciton the further energy shift is accompanied by a rapid decrease of the absorption-maximum intensity. Fig. 1(b) shows the PLE peak positions of the various interband transitions as a function of magnetic field. We may point out that a perturbative approach which uses fixed single-particle wave functions to determine exciton binding energies is not suitable for this MQW with small band offsets. In particular the weak carrier confinement which is in the order of the exciton binding energy does not allow to treat excitonic effects as a perturbation and requires a gerneralized variational exciton wave function for an iterative numerical solution. Thus we calculated the Zeeman splitting of free electron and heavy hole (hh) states and used the constant exciton binding energy of 20 meV for all magnetic fields to meet experimental energies [solid lines in Fig. 1(b)].

The total zero-field band offset for this structure has been calculated to 34 meV using the alloy dependence of the $Zn_{1-x}Mn_xSe$ and $Zn_{1-x}Be_xSe$ band gap. Whereas the zero-field type-I band alignment is maintained for the $(-1/2, -3/2)$ exciton transition (σ^+-polarized) the effect of a magnetic field for $m_s = +1/2$-electrons and $m_j = +3/2$-holes is to decrease

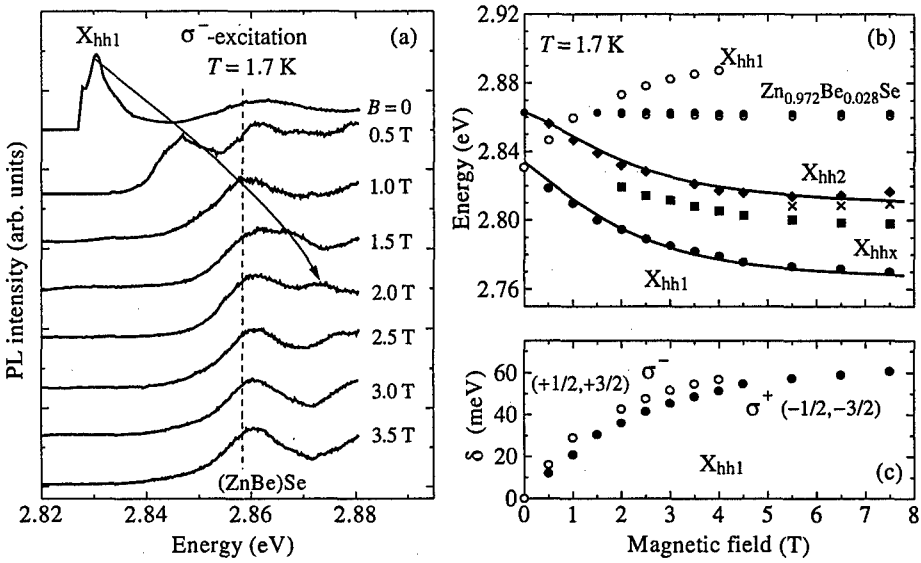

Fig. 1. (a) PLE spectra of a $Zn_{0.91}Mn_{0.09}Se/Zn_{0.972}Be_{0.028}Se$ MQW measured under σ^--excitation at 1.7 K. (b) Exciton transition energies as a function of magnetic field (σ^+: closed symbols, σ^-: open symbols). (c) Relative X_{hh1} spin splitting $\delta E = |E(0) - E(B)|$.

the respective barrier heights (σ^--polarized). At sufficient magnetic fields in the range $0 < B < B_0$ (about 0.3 T) the small valence band discontinuity is overcompensated by the heavy hole Zeeman splitting. However for a small negative valence band offset the Coulomb potential generated by the confined electrons keep the $m_j = +3/2$ holes localized in the (ZnMn)Se layers. By further increasing the magnetic field the band alignment becomes effectively type-II if the hole spin-splitting in addition compensates the exciton binding energy. It has been shown both experimentally [1, 2] and theoretically [3] that a spatially direct exciton state can be formed besides of an indirect one which is composed of an electron localized in the (ZnMn)Se layer and a hole state in the non-magnetic barrier. It is appropriate to regard the direct exciton as a metastable state as its energy lies above the energy of the indirect one. The oszillator strength (i. e. absorption coefficient) of the indirect state is expected to be not sufficient to give a signal in our PLE measurements. A clear indication for the spin dependent confinement is given by the asymmetric spin splitting $\delta E = |E(0) - E(B)|$ of the metastable X_{hh1}-exciton which differs for the $(-1/2, -3/2)$- and for the $(+1/2, +3/2)$-transition shown in Fig. 1(c). Since the Zeeman splitting of band edges is symmetric the difference in ΔE of about 7 meV (3 T) results from a magnetic field dependent exciton binding energy which increases for the lower and decreases for the upper Zeeman branch mainly caused by changes of the hole confinement.

We explain the experimentally observed weakening in the PLE maximum intensity of the $(+1/2,+3/2)$-transition by the broadening of the spatially direct exciton state. In the regime of a type-II band alignment the hole from the (ZnMn)Se layer can be scattered into the (ZnBe)Se barrier by the emission of acoustical phonons. The mechanism corresponds to the scattering of a metastable exciton into a stable exciton. Additional scattering channels become available when the energy of the metastable exciton is shifted above the energy of the barrier exciton ($B > B_0$) and hence the well exciton as a whole can scatter into exciton states of the non-magnetic barriers. For the MQW under study both scattering channes are expected to get involved in the same magnetic field range. By accounting 20 meV for the Coulomb potential (about the exciton binding energy) we estimated the band alignment to get effectively type-II at $B = 1.3\,\mathrm{T}$. This field almost coincides with $B_0 = 1.5\,\mathrm{T}$ for which the energies of the barrier and well exciton are equal. The influence of scattering on the metastable exciton is further investigated by reflectance measurement. Moreover by means of reflectance we exclude possible contributions of relaxation dynamics that may differ PLE spectra from absorption spectra.

2.2 *Reflectivity studies*

According to the temperature dependence of the Zeeman splitting it is expected with raised sample temperature to shift the critical field B_0 to higher values. We made use of this dependence to clearly identify the situation of resonant barrier and well energy in reflectance measurements. Two series of σ^--polarized spectra taken at 1.7 K and 8 K are given in Fig. 2(a) and (b). The temperature of 8 K was chosen low enough to avoid changes of the band gap or thermal broadening by exciton-phonon-interaction. In accordance with the energetic position in PLE spectra the sharp feature marked in the low temperature reflectance spectra ($B = 0$) in Fig. 2(a) is the X_{hh1}-exciton resonance. The magnetic field of 1.5 T beyond which the spectra start to be drastically altered coinsides with the critical field B_0. As previously argued the similar behaviour is observed for the 8 K-spectra shown in Fig. 2(b) at a higher critical field of $B_0(8\,\mathrm{K}) \approx 4.5\,\mathrm{T}$. In fact in the range of X_{hh1}-exciton energies taken from PLE which are labeled by arrows in Fig. 2(a) no significant resonance is observable for $B > B_0$. For both temperatures the disappearence of the X_{hh1}-resonance

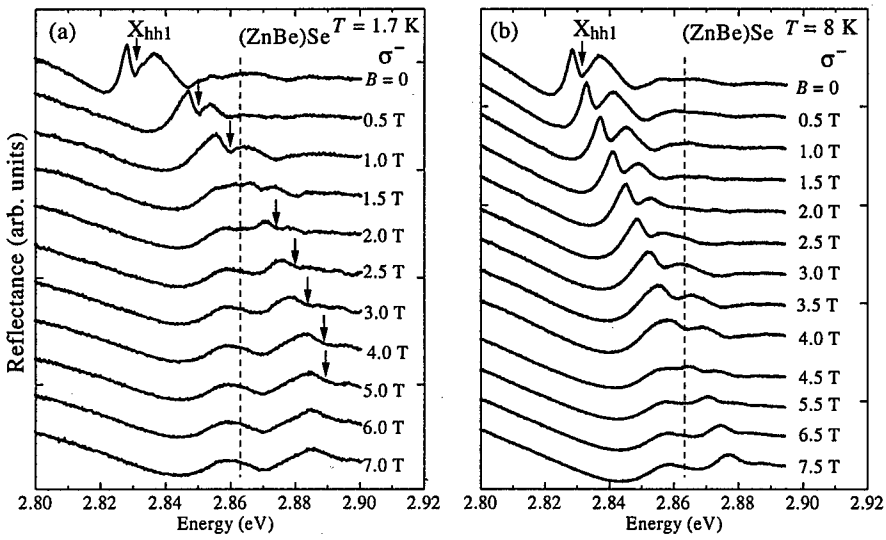

Fig. 2. σ^--polarized reflectance spectra of a $Zn_{0.91}Mn_{0.09}Se/Zn_{0.972}Be_{0.028}Se$ MQW taken a temperatures of 1.7 K (a) and 8 K (b). Arrows indicate X_{hh1}-energies determined from PLE spectra.

at $B > B_0$ is obvious due to exciton scattering into the (ZnBe)Se barriers. However the resonance keeps pronounced in σ^+-polarized spectra (not discussed here).

Acknowledgements

This work is supported by the Deutsche Forschungsgemeinschaft through Sonderforschungsbereich 410.

References

[1] W. Y. Yu, M. S. Salib, A. Petrou, B. T. Jonker and J. Warnock, *Phys. Rev. B* **55**, 1602 (1997).
[2] W. Y. Yu, S. Stoltz, A. Petrou, J. Warnock and B. T. Jonker, *Phys. Rev. B* **56**, 6862 (1997).
[3] J. Warnock, B. T. Jonker, A. Petrou, W. C. Chou and X. Liu, *Phys. Rev. B* **48**, 17321 (1993).

7th Int. Symp. "Nanostructures: Physics and Technology"
St Petersburg, Russia, June 14–18, 1999

Magneto-reflectivity studies of ZnSe/ZnMgSSe QWs with low density 2DEG

G. V. Astakhov†, D. R. Yakovlev‡, V. P. Kochereshko†, G. V. Mikhailov†, W. Ossau‡, J. Nürnberger‡, W. Faschinger‡ and G. Landwehr‡

† Ioffe Physico-Technical Institute, St Petersburg, Russia

‡ Physikalisches Institut der Universität Würzburg, 97074 Würzburg, Germany

Abstract. Magneto-reflectivity has been studied in modulation-doped ZnSe/ZnMgSSe quantum well structures with low and moderate carrier concentrations. Negatively charged exciton (trion) lines were observed in the reflectivity spectra. Magnetic-field-induced circular polarization of the trion reflection line has been found to correlate with the polarization of electron gas at filling factor $\nu < 2$.

It has been found recently that at low free electron concentration in a semiconductor quantum well (QW) the exciton-electron interaction results in the formation of bound exciton-electron complexes (trions) [1]. Such trion states were observed in II–VI (CdTe/CdZnTe and CdTe/CdMgTe) as well as in III–V (GaAs/AlGaAs) semiconductor QWs in transmission, reflection and photoluminescence spectra [1–3]. The main feature of the trion reflection (transmission) line is its strong circular polarization in magnetic fields. This polarization is due to the fact that the trion ground state is a singlet. In a sufficiently strong magnetic field and at temperatures low enough for all electrons to fall to the lowest Zeeman sublevel, only a photon with a certain circular polarization can create a trion. In the present paper we report on a magneto-reflectivity study of trion states in modulation-doped ZnSe/ZnMgSSe quantum wells (QWs) at various electron concentrations.

Samples grown by molecular-beam epitaxy on (100)-oriented GaAs substrates were 100-Å thick $ZnSe/Zn_{0.89}Mg_{0.11}S_{0.18}Se_{0.82}$ QWs with n-type modulation doping with chlorine in the barrier layer (30-Å thick doped layer separated from the QW by a 100-Å spacer). A set of structures with different concentrations of two-dimensional electron gas (2DEG) was grown. The 2DEG concentration was varied from about zero (compensated structure) up to 10^{11} cm^{-2}. We have chosen the ZnSe-based QW structures owing to the strong Coulomb interaction in this material (exciton binding energy in ZnSe is 20 meV). This leads to a strong enhancement of the exciton-electron interactions. As a result, the characteristic energy of such interactions becomes much larger than the potential fluctuations in the sample.

Figure 1 shows reflectivity spectra taken from the ZnSe/ZnMgSSe structures under study in zero magnetic field at 1.6 K. The top panel of this figure shows a reflection spectrum taken from nominally undoped structure (2DEG concentration less than 4×10^9 cm^{-2}). Only one strong line (X) ascribed to the exciton resonance is observed in the spectrum at 2.8195 eV. At higher electron concentrations an additional line attributed to the negatively charged exciton (X^-) appears in the spectra about 5 meV below the exciton resonance. With increasing electron density, the intensity of this line grows and the exciton line broadens. At an electron concentration $n_e \approx 1.5 \times 10^{11}$ cm^{-2} the intensity of the trion line much exceeds

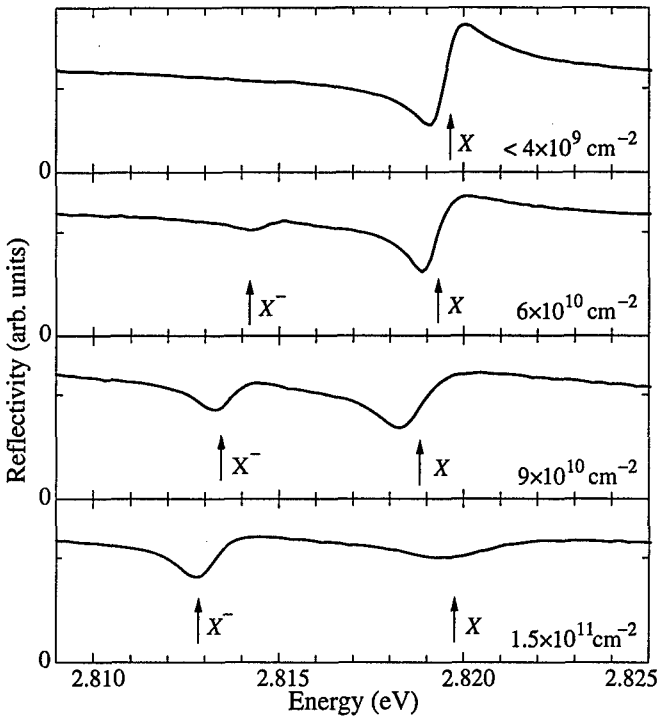

Fig. 1. Reflectivity spectra of 100-Å-thick ZnSe/$Zn_{0.89}Mg_{0.11}S_{0.18}Se_{0.82}$ single QWs with different 2DEG concentrations. The concentration increases in the direction from top to bottom panel. $T = 1.6$ K. Arrows indicate exciton X and trion X^- states.

that of the exciton line. The strong reflectance associated with the trion line indicates the fundamental character of the trion state. We believe that the trion has the same significance for 2DEG optics as the exciton for the optics of dielectrics.

In external magnetic fields, the X^- reflection line becomes strongly polarized. The degree of polarization of the X^- line is presented in Fig. 2 as a function of magnetic fields for different 2DEG concentrations. In the case of a low electron concentration in the QW ($n_e \approx 6 \times 10^{10}$ cm^{-2}—the upper panel), the magnetic field dependence of the polarization of the X^- line is described by the Brillouin function ($B_{1/2}[B] = th[\mu g_e B/kT]$, where μ is the Bohr magneton, T is temperature, and B is magnetic field) with electron g-factor $g_e = +1.15$ (dotted line). A slight disagreement between the experimental data (circles) and the Brillouin function is observed in weak magnetic fields. This disagreement becomes much more pronounced at higher electron concentrations. For the highest electron concentration ($n_e \approx 1.5 \times 10^{11}$ cm^{-2}), the X^- line is found to be completely unpolarized at $B < 3$ T. In order to describe correctly the behaviour of the X^- in a dense 2DEG in weak magnetic field, one should use the Fermi–Dirac statistics instead of the Boltzmann one for calculating the electron population of the Zeeman sublevels.

The electron spin polarization in a dense 2DEG in magnetic fields occurs when Landau levels pass through the Fermi energy. The spin polarization is zero at even filling factors (the filling factor is $\nu = n_e(hc/eB)$), when two Zeeman components of the Landau level are filled by electrons, and reaches maxima at odd filling factors. The dependences of the 2DEG

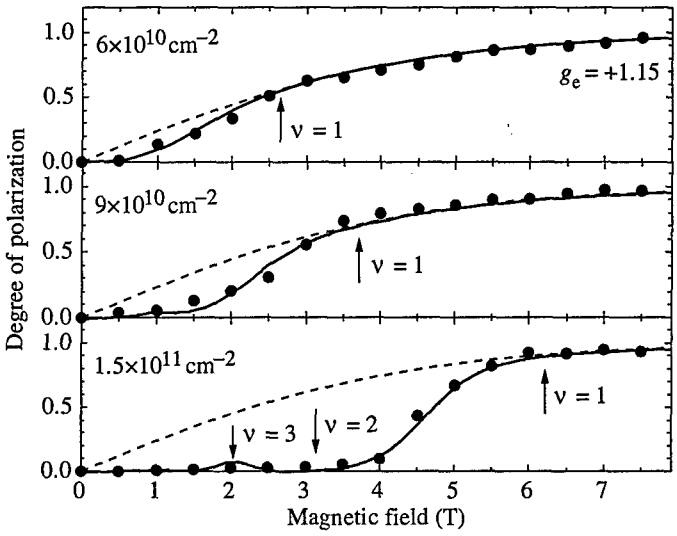

Fig. 2. Degree of polarization of the X^- line vs magnetic field in 100-Å-thick $ZnSe/Zn_{0.89}Mg_{0.11}S_{0.18}Se_{0.82}$ single QWs with different 2DEG concentrations, circles—experiment, dotted line—Brillouin function with $g_e = +1.15$, solid line—calculation using the Fermi–Dirac statistics. Arrows indicate integer values of filling factor.

polarization calculated with a Fermi–Dirac distribution of electrons in Landau levels are plotted in Fig. 2 (solid line) together with the experimentally observed circular polarization of the trion line. It can be seen that the 2DEG polarization oscillates (bottom panel), while the experimental dependence exhibits a monotonic behaviour. This experimental dependence is similar to that we would observe if only the lowest Landau level ($\nu < 2$) contributed to the polarization. This fact indicates an important role of the lowest Landau level in the trion formation, mentioned in Ref. [4]. The absence of the circular polarization of this line at filing factors $\nu > 2$ could mean that in these conditions of a dense 2DEG the observed line should be attributed to multi-electron-exciton complexes containing more than three particles. The polarization properties of such complexes must be different from those of the trions, with the binding energies being, contrariwise, very close.

The above considerations can be used to deduce the 2DEG concentration. The concentrations determined in this way are shown in Fig. 2.

In conclusion, we have carried out a magneto-optical study of ZnSe/ZnMgSSe modulation-doped QWs. In the presence of excess electrons in the QW, a line attributed to the negatively charged exciton appears in the reflectivity spectra. We have analysed the degree of polarization of the X^- line as a function of magnetic field. An optical method to determine the 2DEG concentration in quantum wells is proposed. The magnetic-field-induced circular polarization of the X^- reflection (absorption) line correlates with the polarization of the lowest Landau level. Our results support the viewpoint that the lowest Landau level is the most important for the trion state formation.

This work was supported by the NATO grant HTECH.LG 974702, Russian Foundation for Basic Research (Grants No 98-02-04089 and No 98-02-18219) and the Program "Nanostructures" of the Russian Ministry of Science and Technology.

References

[1] K. Kheng, R. T. Cox, Y. Merle d'Aubigne, F. Bassani, K. Saminadayar and S. Tatarenko, *Phys. Rev. Lett.* **71**, 1752 (1993);
G. Finkelstein, H. Shtrikman and I. Bar-Joseph *Phys. Rev. Lett.* **74**, 976 (1995).

[2] W. Ossau, D. R. Yakovlev, U. Zehnder, G. V. Astakhov, A. V. Platonov, V. P. Kochereshko, J. Nürnberger, W. Faschinger, M. Keim, A. Waag, G. Landwehr, P. C. M. Christianen, J. C. Maan, N. A. Gippius and S. G. Tikhodeev, *Physica B* **256-258**, 323 (1998).

[3] D. R. Yakovlev, G. V. Astakhov, V. P. Kochereshko, A. Keller, W. Ossau and G. Landwehr, this volume p. 393.

[4] S. Lovisa, R. T. Cox and K. Saminadayar, *Phys. Stat. Sol. (a)* **164**, 175 (1997).

7th Int. Symp. "Nanostructures: Physics and Technology"
St Petersburg, Russia, June 14–18, 1999

Hole cyclotron resonance in MQW Ge/GeSi heterostructures in quantizing magnetic fields

V. Ya. Aleshkin, V. I. Gavrilenko, I. V. Erofeeva, O. A. Kuznetsov,
M. D. Moldavskaya, V. L. Vaks and D. B. Veksler
Institute for Physics of Microstructures of Russian Academy of Sciences
GSP-105, Nizhny Novgorod, 603600, Russia

Abstract. "Quantum" cyclotron resonance of 2D holes in strained Ge/GeSi heterostructures has been investigated in frequency range $\nu = 370 \div 700$ GHz. Calculations of hole Landau levels in rectangular quantum well in strained heterostructures have been performed allowed to interpret the observed far infrared magnetoabsorption spectra.

Introduction

The two-dimensional (2D) holes in strained SiGe-based heterostructures have been found to be sensitive to band structure engineering "tools": built-in deformation and quantum confinement. The deformation results in decoupling of light and heavy hole energy subbands and in decrease of hole mass at the bottom of valence band while confinement results in mixing of light and heavy hole states. Energy-momentum law of 2D holes in strained Ge/GeSi(111) heterostructures were studied earlier [1] both theoretically and experimentally (by means cyclotron resonance (CR) at $\nu = 130$ GHz, $T = 4.2$ K, i.e. in "semiclassical" case $\hbar\omega \approx k_B T$). In undoped samples spectra the CR line of photoexcited 2D holes in Ge quantum wells (QWs) was observed corresponded to the small mass value $m_c = 0.07 m_0$. The application of lateral electric field was shown to result in the remarkable shift of the hole CR line to higher magnetic fields (up to 400%) due to the strong nonparabolicity of 2D hole dispersion.

In the first study of "quantum" CR in strained Ge/GeSi(111) system [2] selectively doped heterostructures were investigated using Fourier-transform spectrometer (cf. [3, 4]). Two CR lines were observed in the spectra in magnetic fields up to 14 T which was tentatively attributed to CR transitions from the first and the second lowest hole Landau levels. In this paper we present the study of "quantum" CR absorption in *undoped* samples that becomes possible due to the usage the more powerful radiation source: backward wave tube oscillators. The results were interpreted on the base of Landau level calculations in strained QWs.

1 Experimental

MQW Ge/$Ge_{1-x}Si_x$ heterostructure (#306, $x = 0.12$, $d_{Ge} = 200$ Å, $d_{GeSi} = 260$ Å, number of periods $N = 162$) was grown by CVD technique on Ge(111) substrate. The whole width of the structure exceeds the critical value thus providing stress relaxation between the substrate and the heterostructure and biaxial elastic deformation of Ge layers $\epsilon = 2.18 \times 10^{-3}$. The CR absorption spectra of the sample were studied in Faraday geometry at $T = 4.2$ K in the frequency range $\nu = 350 \div 700$ GHz using n-InSb detector. The sample was illuminated by LED ($\lambda \approx 0.9\,\mu$m) that was triggered at $f = 1$ kHz; thus

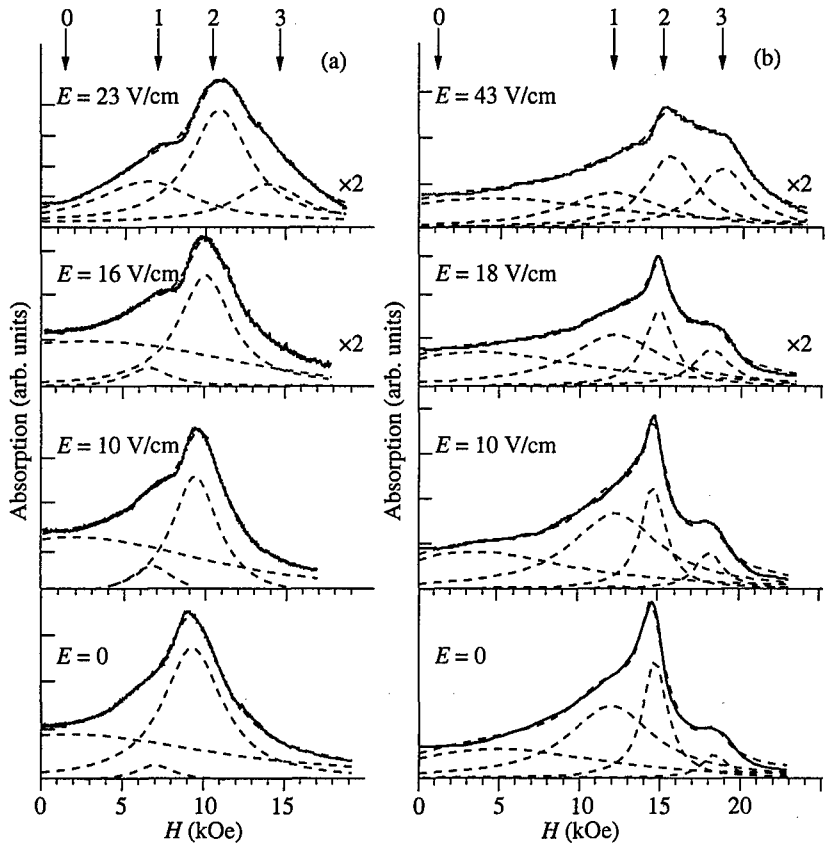

Fig. 1. CR spectra of photoexcited holes in Ge/GeSi heterostructure #306 at dc electric fields; $T = 4.2$ K; (a) $\nu = 370$ GHz, (b) $\nu = 600$ GHz. Each experimental curve (solid line) is resolved into three or four Lorentzians (dashed lines). The Lorentzians positions are marked by arrows.

all spectra were measured at the modulation of photoexcitation. Strip ohmic contacts were deposited on the sample surface to allow lateral electric field application.

The observed CR spectra are shown in Fig. 1. The lowest curves represent the spectra at zero electric field while the upper ones are obtained at some dc voltages applied to the sample. To distinguish the spectral features each curve was resolved into three or four Lorentzians; the feature positions being marked in Fig. 1 by arrows. The broad line 0 seems to results from nonresonant tails (polarization of radiation was nearly linear) of the other lines 1, 2, 3. Note that in contrast to CR in "semiclassical" case [1] dc electric field does not shift the lines but changes the relative magnitudes of lines 2 and 3. The line positions $\hbar\omega(H)$ in wide frequency range $130 \div 700$ GHz are plotted in Fig. 2. It is clearly seen that the linear extrapolation of line 1 position to $H = 0$ gives $\varepsilon = 0.85$ meV; hence this line cannot be attributed to CR of free carriers. It is natural to attribute the line 1 to transitions between excited residual shallow acceptor or A^+-center states [5] (which become populated under LED illumination) associated with two different Landau levels (cf. [6]). The line 2 corresponds to the same cyclotron mass $m_c = 0.07m_0$ both in "semiclassical" and in quantizing magnetic fields and results from CR of 2D holes occupying the lowest Landau level. At last the line 3 becomes discernible only at $\nu \geq 400$ GHz, its intensity

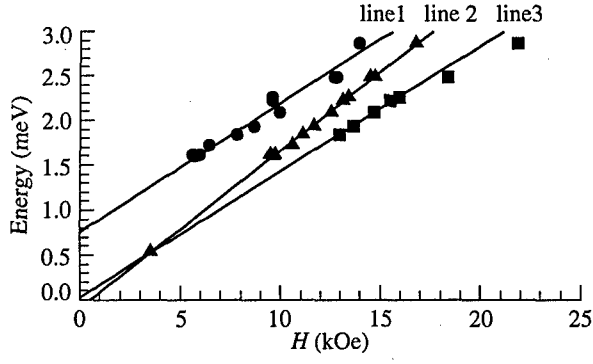

Fig. 2. Spectral positions of the absorption lines 1, 2, 3 versus magnetic field.

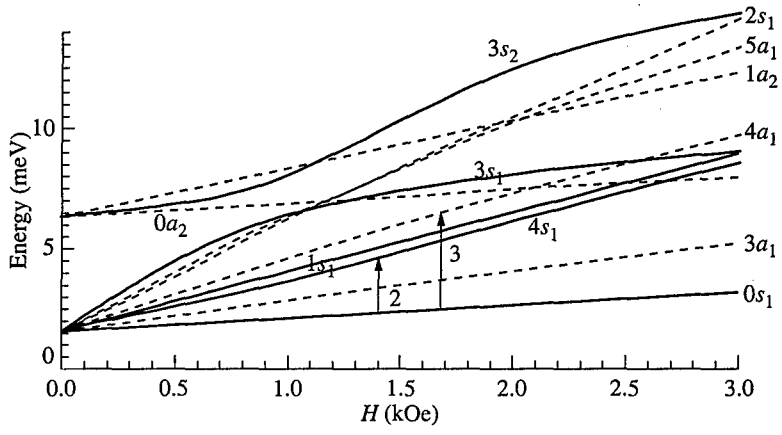

Fig. 3. Fan chart of calculated Landau levels in Ge QW for Ge/GeSi heterostructure #306. Arrows 2, 3 correspond to lines 2, 3 on Fig. 2.

being increased in comparison with that of the line 2 in dc fields. It indicates that the line 3 is associated with CR transitions of 2D holes occupying the higher Landau level (cf. [2]).

2 Calculations and comparison with the experiment

Calculations of Landau levels of 2D holes in rectangular quantum well in strained Ge/GeSi heterostructures were performed using 4×4 $\boldsymbol{k}\cdot\boldsymbol{p}$ Hamiltonian in axial approximation. The symmetry results in the conservation of the total angular momentum projection on the magnetic field direction M_j and the parity of the wave function with respect to the reflection in the plane $z = 0$ that goes through the QW center. Thus each state could be classified by eigenvalue $n = M_j + 3/2$ ($n = 0, 1, 2, \ldots$), and should be either symmetric (s) or antisymmetric (a) with respect to the plane $z = 0$. This notation is used in Fig. 3 where fan chart of lower Landau levels is plotted. The index in notation indicates the subband from which the given Landau level originates from. In Faraday geometry dipole transitions are allowed between two states of the same parity if $\Delta n = \pm 1$. As it is seen from Fig. 3 the lower Landau levels are weakly interacting and their energies depend linearly on the magnetic field up to 30 kOe. The most of photoexcited holes in our experiments populate

the lowest Landau level $0s_1$. The allowed CR transition $0s_1 \rightarrow 1s_1$ corresponds to the cyclotron mass $m_c = 0.06m_0$ that is a little bit less than observed mass for the line 2 of $0.07m_0$. Similarly the calculated mass for the allowed transition from the next Landau level $3a_1 \rightarrow 4a_1$ $m_c = 0.065m_0$ is less than the observed one for the line 3 ($0.08m_0$). It is cleally seen from Fig. 1 that the relative intensity of the line 3 increases with the heating dc electric field resulting in the populating of the upper laying Landau level $3a_1$ at the expense of devastating of the lowest one $0s_1$. The 15% discrepancy between the calculated and the observed effective mass values probably results from the neglecting of the split-off hole subband in the calculations.

The research described in this publication was made possible in part by "Physics of Solid State Nanostructures" (projects No 97-2022), "Physics of Microwaves" (project No 4.5), "Physics of Quantum and Wave Processes/Fundamental spectroscopy" (project No 08.02.043). The authors would like to acknowledge M. V. Yakunin for the fruitful discussion and A. V. Maslovskii for the collaboration in the experiments with backward wave tube oscillators.

References

[1] V. Ya. Aleshkin, N. A. Bekin, I. V. Erofeeva *et al.*, *Abstr. Int. Symp. "Nanostructures: Physics and Technology"*, St. Petersburg, p. 271, 1995.
[2] V. Ya. Aleshkin, N. A. Bekin, I. V. Erofeeva *et al.*, *Procr. Int. Symp. "Nanostructures: Physics and Technology"*, St. Petersburg, p. 137, 1997.
[3] C. M. Engelhardt, D. Tobben, M. Aschauer *et al.*, *Solid State Electron.* **37**, 949 (1994).
[4] L. K. Orlov, A. V. Potapov, R. A. Rubtsova *et al.*, *Thin Solid Films* **294**, 208 (1997).
[5] V. I. Gavrilenko, I. V. Erofeeva, A. L. Korotkov *et al.*, *JETP Lett.* **65**, 194 (1997).
[6] S. Holmes, J. P-Cheng, B. D. McCombe *et al.*, *Phys. Rev. Lett.* **69**, 2571 (1992).

7th Int. Symp. "Nanostructures: Physics and Technology"
St Petersburg, Russia, June 14–18, 1999

In-plane linear polarization of luminescence and level anticrossings in GaAs/AlAs superlattices and quantum wells

P. G. Baranov†, *N. G. Romanov*†, A. Hofsteatter‡, B. K. Meyer‡,
A. Scharmann‡, W. von Foerster‡, F. J. Ahlers# and K. Pierz#
† Ioffe Physico-Technical Institute, St Petersburg, Russia
‡ 1. Physics Institute, University of Giessen,
Heinrich-Buff-Ring 16, D-35392 Giessen, Germany
Physikalische-Technische Bundesanstalt, Braunschweig, Germany

Abstract. In-plane linear polarization of luminescence under above-band-gap excitation was investigated in type II and type I GaAs/AlAs (001) quantum wells and superlattices together with the study of level anticrossing and ODMR. Correlation of such polarization with the preferential exciton localization was found and discussed in terms of coexistence of excitons and separately localized electrons and holes. The influence of the substrate temperature on the interface quality was revealed in type I GaAs/AlGaAs quantum wells from level-anticrossing spectroscopy.

Introduction

The use of luminescence to detect magnetic resonance and level anticrossing of excitons and carriers provided a new insight in the microstructure of quantum wells (QW) and superlattices (SL) (see [1–3] and references therein). In type II SL electrons and holes are spatially separated in the adjacent AlAs and GaAs layers, respectively. In LAC and ODMR experiments a direct link was established between the order of the exciton radiative levels and the interface, normal (AlAs on GaAs) or inverted (GaAs on AlAs), where it is localized. It was established that the lowest radiative exciton level is [110]-polarized for excitons localized at the normal interface and [1$\bar{1}$0]-polarized for excitons at the inverted interface [4]. Moreover, excitons localized at the opposite interfaces were found to have different exchange splittings due to asymmetry of the interface composition profiles [5]. This made possible separate investigations of the opposite interfaces with the use of ODMR and LAC spectroscopy. Anisotropic exciton localization was also revealed in type I GaAs/AlAs and GaAs/AlGaAs quantum wells from LAC in linearly polarized light [6].

In the present paper we report on a study of in-plane linear polarization of luminescence in GaAs/AlAs QW and SL under non-resonant excitation and its correlation with the preferential localization of excitons, electrons and holes. LAC spectroscopy was also used to analyze the interface quality in type I QW.

1 Results and discussion

GaAs/AlAs and GaAs/AlGaAs QW and SL were grown by MBE technique on (001) GaAs substrates kept at $T_s = 520-680$°C. A special type II SL (P233) with a gradient of GaAs/AlAs composition in the SL plane (from 6/6.5 to 8.5/8 monolayers) was grown with $T_s = 620$°C with 30 s interruptions after GaAs layers. Actual composition of the samples was controlled by X-ray and Raman characterization. Photoluminescence was excited far above the band gap with an Ar-ion laser. LAC was recorded by monitoring linear or circular polarization of emission. 24 and 35 GHz ODMR spectra were obtained by monitoring microwave-induced variations of circularly polarized luminescence.

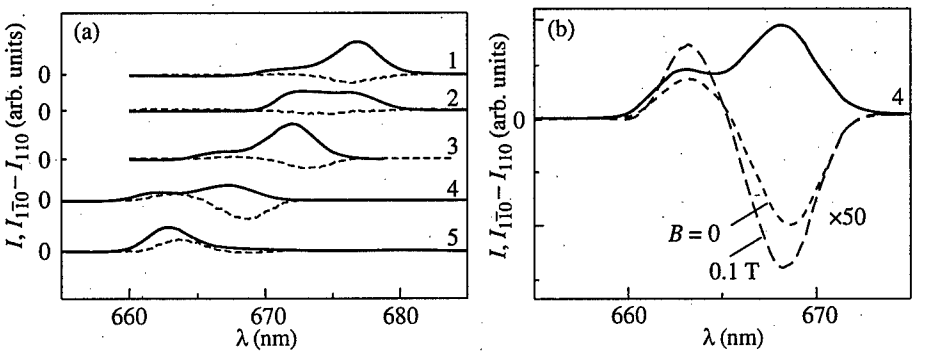

Fig. 1. (a) Emission spectra (full lines), and linear polarization of emission (dashed lines) in type II GaAs/AlAs SL P233 measured with different positions of excitation spot. (b) Linear polarization in zero magnetic field and at $B = 0.1$ T for one of the spectra shown in Fig. 1(a). $T = 1.6$ K

In all type II and type I structures we found linear polarization of the order of some per cent along [110] or [1$\bar{1}$0] directions in the SL plane. Fig. 1(a) shows luminescence spectra (full lines) and linear polarization signals (dashed lines) measured in different points of SL P233 (marked 1 to 5) which correspond to different GaAs/AlAs composition. Positive sign corresponds to polarization along [1$\bar{1}$0]. Linear polarization was found to depend on magnetic field ($B \parallel [001]$). This can be seen in Fig. 2(b) where spectral dependencies of polarization signal are plotted for zero field and $B = 0.1$ T, a value which is far enough from signals due to exciton level anticrossings.

Dependencies of the degree of polarization on magnetic field measured in the peaks of two emission lines (Fig. 1(a)) are shown in Fig. 2. Resonant LAC signals belong to excitons localized at the normal and inverted interface as marked in the picture. They have opposite signs since the order of radiative levels for two classes of excitons is inverted (see inset). The assignment of LAC was confirmed by ODMR measurements. From the values of hole g-factors and exciton exchange splitting it was concluded that emission in long-wavelength line appears from monolayer-high GaAs islands. LAC signals are superimposed on a broad line with the same shape as ODMR signal ascribed to electron–hole pairs. ODMR of electrons and holes is always observed in type II SL in addition to the exciton ODMR. A broad signal centered at $g_e \simeq 1.9$ is due to a distribution of zero-field splitting (exchange splittings) rather than a distribution of g-factors what was unambiguously confirmed by observation of multiquantum ODMR. The shape of this broad signal can be explained by a simple model of statistical distribution of interpair distances in the SL plane. This implies the existence of separately localized electrons and holes. Electrons are in AlAs layers and holes in GaAs layers which follows from the values of g-factors. Since an exchange-coupled e-h pair has the same energy level scheme as the exciton a distribution of exchange splittings averages LAC signals and gives rise to a broad line with the same shape as for ODMR. Dashed lines in Fig. 2 are result of calculations made for ODMR signal of e-h pairs.

As was shown before [6] analysis of LAC allows to obtain spectral dependencies of preferential exciton localization which depends on the interface microstructure. For a SL under consideration the ratio of exciton concentrations at the normal and inverted interfaces in the peaks of short- and long-wavelength emission lines are 1.6 and 0, respectively. Numerous measurements allowed to find a correlation between the sign and value of this

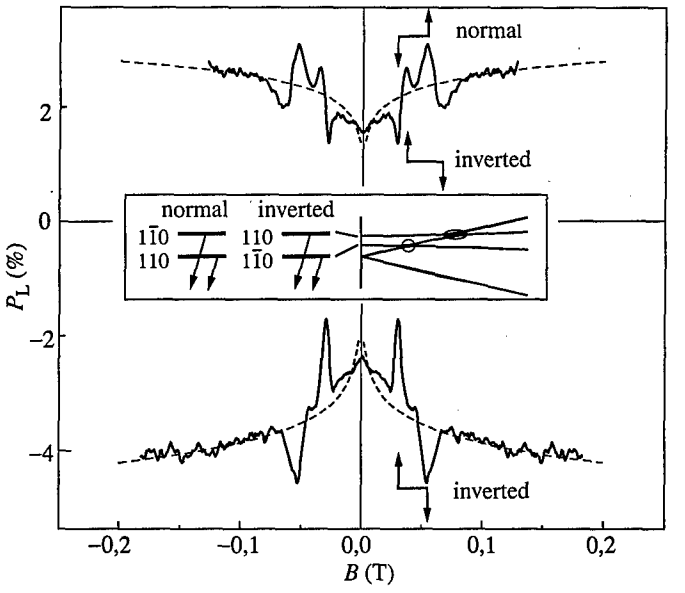

Fig. 2. Linear polarization of emission as a function of magnetic field measured in the peaks of short-wavelength (upper curve) and long-wavelength (lower curve) luminescence lines shown in Fig. 1(b). $B \parallel [001]$. $T = 1.6$ K.

polarization and relative concentrations of excitons at the opposite interfaces. Thus zero-field linear polarization can bring information on interface microroughness.

The zero-field polarization is obviously not connected with Boltzmann populations of the exciton radiative levels since its value increases with temperature. We tentatively ascribe it to distant pairs of separately localized electrons and holes. The existence of zero-field linear polarization is a manifestation of in-plane anisotropy in the distribution of the pair dipole moments.

In type I QW and SL in-plane anisotropy of the interfacial defects is responsible for anisotropic exciton localization and a splitting of exciton radiative levels. Linear polarization of emission and LAC recorded by monitoring circular and linear polarization of emission in two QW structures both containing 25 Å and 50 Å QW but grown by MBE at different substrate temperatures are shown in Fig. 3. Linear polarization along [1$\bar{1}$0] is observed, i.e. in the direction of a preferential orientation of interface defects. Increasing substrate temperature improves interfaces which is manifested in the narrowing of exciton LAC (see inset in Fig. 3(a)) and an increase of zero-field linear polarization (Fig. 1(a)). Increasing disorder of the interface in the samples grown at lower temperature is illustrated by comparison of LAC signals. It is possible that separately localized e-h pairs which were recently found in type I structures [7] contribute to zero-field linear polarization.

In conclusion, correlation of in-plane zero-field linear polarization of luminescence with the preferential exciton localization was found in type II and type I GaAs/AlAs QW and SL and discussed in terms of coexistence of excitons and separately localized electrons and holes. The influence of the substrate temperature on the interface quality was revealed in type I GaAs/AlGaAs quantum wells from level-anticrossing spectroscopy.

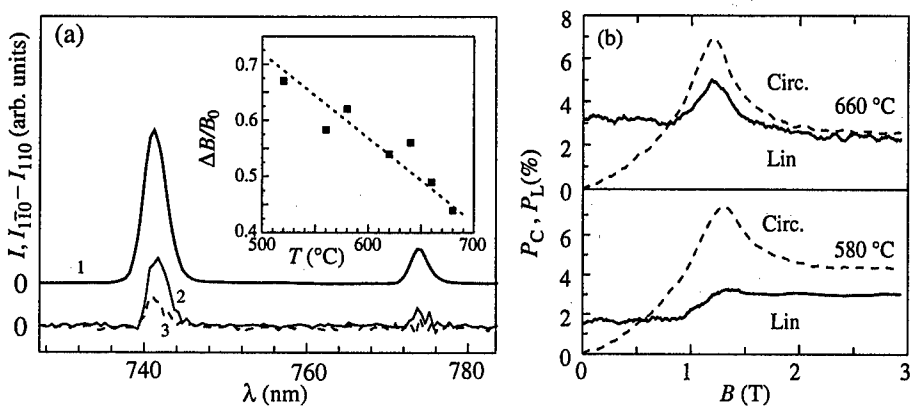

Fig. 3. (a) Emission spectra (1) and linear polarization (2,3) in two type I GaAs/AlGaAs QW samples MBE-grown at 660 °C (curves 1, 2) and 560 °C (1, 3). Inset shows a dependence of a linewidth of LAC signals recorded via circular polarization in 25 Å QW on temperature of substrate during the MBE growth. (b) Linear and circular polarization of emission in 25 Å QW for these two QW-structures. $T = 1.6$ K.

References

[1] H. W. van Kesteren, E. C. Cosman, W. A. J. A. van der Pool and C. T. Foxon, *Phys. Rev. B* **41**, 5283 (1990).

[2] P. G. Baranov, I. V. Mashkov, N. G. Romanov, P. Lavallard and R. Planel, *Solid State Commun.* **87**, 649 (1993).

[3] P. G. Baranov and N. G. Romanov in: *The Physics of Semiconductors* ed. J. Lockwood (World Scientific, 1994) v. 2, p. 1400.

[4] P. G. Baranov, I. V. Mashkov, N. G. Romanov, C. Gourdon, P. Lavallard and R. Planel, *JETP Lett.* **60**, 445 (1994).

[5] P. G. Baranov, N. G. Romanov, A. Hofstaetter, A. Scharmann, C. Schnorr, F. J. Ahlers and K. Pierz, *JETP Lett.* **64**, 754 (1996).

[6] P. G. Baranov, N. G. Romanov, A. Hofstaetter, B. K. Meyer, A. Scharmann, C. Schnorr, W. von Foerster, F. J. Ahlers and K. Pierz, in Proc. Int. Symp. *Nanostructures: Physics and Technology*, ed. Zh. Alferov and L. Esaki, St. Petersburg, 1997, p. 47.

[7] A. Frommer, E. Cohen, Arza Ron, A. Kash and L. N. Pfeiffer, *Phys. Rev B* **49**, 2935 (1994).

7th Int. Symp. "Nanostructures: Physics and Technology"
St Petersburg, Russia, June 14–18, 1999

Damping of manganese spin precession in the presence of free carriers in CdMnTe quantum wells

C. Camilleri†, *D. Scalbert*†, J. Allègre†, M. Dyakonov‡, M. Nawrocki§,
J. Cibert¶, A. Arnoult¶ and S. Tatarenko¶

† Groupe d'Etude des Semiconducteurs, UMR 5650 CNRS-Université Montpellier
2, Place Eugène Bataillon, 34095 Montpellier Cedex, France
‡ Laboratoire de Physique Mathématique, UMR 5825 CNRS-Université Montpellier
2, Place Eugène Bataillon, 34095 Montpellier Cedex, France
§ Institute of Experimental Physics, Warsaw University,
Hoza 69, 00-681 Warsaw, Poland
¶ Laboratoire de Spectrométrie Physique, UMR 5588
CNRS-Université Joseph-Fourier Grenoble, BP87, 38402 St Martin d'Hères Cedex

Abstract. The transverse relaxation time T_2 of the Mn spins has been measured by time-resolved photo-induced Kerr rotation in n-type and p-type CdMnTe quantum wells, with a magnetic field applied parallel to the quantum well plane. The dependencies of T_2 on the magnetic field and on the carrier density indicate the influence of carriers on T_2. A model, akin to dielectric relaxation, is proposed to explain qualitatively these results.

Introduction

Spin relaxation processes in quantum confined semiconductor structures are currently a subject of intense work. In particular, in heterostructures containing a dilute magnetic semiconductor the magnetic ions constitute a new channel for electrons and holes spin relaxation. This possibility has been considered theoretically [1] and explored experimentally through time-resolved luminescence polarization [2] and time-resolved circular dichroism [3]. Conversely, the spin dynamics of Mn ions in presence of a gas of electrons or holes has received little attention until now. Recent progress in the fabrication of modulation doped magnetic quantum wells of high quality should motivate such studies, where the opportunity to have a high density 2D gas of carriers strongly interacting with Mn spins is of primary importance. As an example K. Kavokin [4] has predicted profound changes of the Mn spin dynamics in the vicinity of the ferromagnetic transition recently observed in p-doped QWs [5].

Here we look for the influence of the electron or hole gas on the phase relaxation time of Mn spins T_2. The T_2 time was measured by time-resolved photo-induced Kerr rotation using a pump-and-probe setup. The gist of the method is to produce a rapidly varying effective magnetic field B_{eff}, acting as a tipping pulse for the Mn magnetization M initially aligned along the external magnetic field $B_0 \parallel$ to the QW plane. B_{eff} is produced by the spin polarized carriers, mainly the holes, which are photo-created by a circularly polarized pump pulse. $B_{\text{eff}}(t)$ will decay with the hole spin polarization on a time scale of a few ps, and M slightly tipped with respect to B_0 will continue to precess freely around B_0 for hundreds of ps. The component of M along the growth axis oscillates back and forth and manifests itself through the Kerr rotation of the polarization plane of the probe beam (Fig. 1).

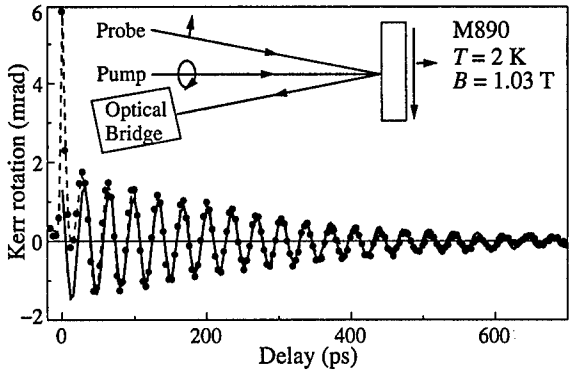

Fig. 1. Time-resolved Kerr rotation signal versus pump-probe delay. The signal oscillations reveal the Mn spin precession. The full line is a fit to the data with a damped sinusoid. The inset depicts the experimental geometry.

These experiments have been first proposed by Crooker et al. [6, 7], who studied ZnCdSe/ZnSe QWs containing MnSe monolayers or fraction of monolayers. Akimoto *et al.* did similar experiments on CdTe/CdMnTe heterostructures [8].

1 Samples and setup characteristics

We report on experiments done on two $Cd_{1-x}Mn_xTe$/CdZnMgTe QWs. One is a 80 Å width modulation doped QW of p-type with $x = 0.025$ (sample M921) and the other is a nominally undoped 50 Å QW with $x = 0.026$ (sample M890). The samples were in superfluid helium and subjected to an in-plane magnetic field up to about 1 T. Photoluminescence of the undoped QW reveals a negatively charged exciton line, an evidence that this QW contains an electron gas produced by residual donors in the barrier. The p-doped QW has a degenerate hole gas density of about 2×10^{11} cm^{-2}, estimated from the Moss-Burstein shift, and could be depleted by a weak above barrier illumination.

For the pump-probe experiments we have used 1.5 ps pulses, produced at 80 Mhz by a mode-locked Al_2O_3:Ti laser. The polarization of the pump was modulated alternatively between left and right helicities with an Elasto-Optic Modulator (EOM) operating at 50 kHz. The pump-induced rotation of the linear polarization of the probe was detected with an optical bridge (see e.g. [7]) and a lock-in amplifier fed with the reference of the EOM.

2 Results and discussion

Figure 1 shows a time-resolved Kerr rotation signal obtained on sample M890. The sharp peak at short delays contains contributions from the spin-polarized photo-created carriers which relax rapidly. Measurements of the Kerr rotation at short delays allow us to deduce the spin relaxation times τ_e and τ_h of electrons and holes. The presentation of these results is beyond the scope of this paper. At delays longer than τ_e and τ_h, typically a few ps or tens of ps, only the contribution from Mn persists. The full line in Fig. 1 is a fit to the experimental data with a damped sinusoid

$$S(t) = A_{Mn} \exp(-t/T_2) \sin(\omega t + \phi) \quad (1)$$

where ω is the Larmor frequency of the Mn spins. In order to obtain a reasonable fit we had to introduce a dephasing parameter ϕ, a fact already noticed in [7]. If ω were assumed

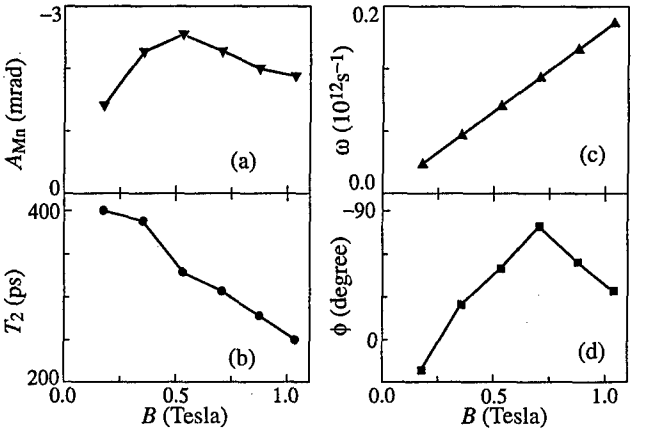

Fig. 2. Magnetic field dependence of the fitting parameters used in the damped sinusoid (see text) for nominally undoped sample (M890).

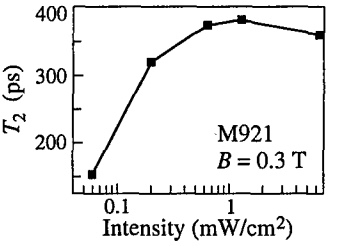

Fig. 3. T_2 versus intensity of illumination at $\lambda = 5145$ Å for the p-doped sample.

to be a constant, extrapolation back to zero would give a non-vanishing signal. Based upon this remark it was assumed in [7] that ω varies due to a time dependent demagnetizing field created by the electrons. This hypothetical field should progressively vanish as electrons recombine, producing a variation of ω during the carriers lifetime, hence a dephasing. Here we propose an alternative explanation based only on the phenomenological Bloch equations with no additional hypothesis. It can be shown that an asymmetric time dependence of $B_{\text{eff}}(t)$ in the Bloch equations leads to a non-zero dephasing given by $\tan(\phi) = -\omega\tau_h$ (mainly the holes contribute) and also predicts $A_{Mn} \propto M(\omega^2 + (1/\tau_h)^2)^{-1/2}$.

In Fig. 2 we give, for sample M890, the field dependence of the different fitting parameters which appear in Eq. (1). As expected ω increases linearly with the magnetic field (Fig. 2(c)). A_{Mn} and ϕ follow qualitatively the behavior predicted by our model, apart the value of ϕ at 0.7 T which seems too large. Using $\tan(\phi) = -\omega\tau_h$ the data of Fig. 2(c–d) yield τ_h in the range 5–15 ps in agreement with the decay of the signal observed at short delays (the point at 0.7 T was excluded). The most interesting result is the marked decrease of T_2 with increasing field. We suggest that this effect could be related to the presence of electrons in our QW. In the case of the p-type QW the influence of holes on the T_2 time is readily seen in Fig. 3, and manifests itself as an increase of T_2 when the QW is depleted by a weak above barrier illumination.

It has been known for a long time, especially in nuclear magnetism, that free carriers may enhance the spin-lattice relaxation rate of localized spins [9]. The relaxation is basically due to a simultaneous spin-flip of the carrier and of the localized spin caused by non-

diagonal terms in the spin-spin interaction. This mechanism also contributes to T_2, as phase coherence is lost during a spin-flip scattering. We may estimate the efficiency of this mechanism for Mn spins 5/2 interacting with a degenerate 2D gas [10] as

$$\frac{1}{\tau_{c-\mathrm{Mn}}} = \frac{15\pi}{2\hbar}\gamma\left(\frac{\rho}{W}\right)^2 kT. \tag{2}$$

Here γ is the carrier-Mn exchange integral, ρ is the 2D density of states for one spin sub-band, W is the QW width and T is the carrier temperature. For electrons one finds $\tau_{e-\mathrm{Mn}} \approx 100$ ns at $T = 2$ K. The holes should be much more efficient than electrons due to the 4-fold larger exchange integral, and larger density of states. We estimate $\tau_{h-\mathrm{Mn}} \approx 3$ ns. These relaxation times are too long, even for the p-type sample, to contribute significantly to the observed T_2. Additionally Eq. (2) is valid only when the conduction (or valence) band spin-splitting is smaller than the Fermi energy. When this is no longer the case the spin-flip scattering should be strongly reduced, hence the relaxation time should increase, contrary to the observed decrease of T_2 with increasing B_0 (Fig. 2(b)).

We are led to propose a new relaxation mechanism, akin to dielectric relaxation, as follows. The precessing magnetization induces a spin polarization of the carrier gas. This polarization however does not establish instantaneously, but with a delay related to the spin relaxation time τ_c of the carriers. This is a source of dissipation in the course of magnetization rotation around B_0. The damping will be maximum, as in dielectric or paramagnetic relaxation, when the condition $\omega\tau_c = 1$ is satisfied. The corresponding relaxation time can be expressed as

$$\frac{1}{\tau^*} = \omega_c \frac{\omega\tau_c}{1+(\omega\tau_c)^2} \tag{3}$$

where ω_c is the effective field created by the carriers on the Mn, expressed in frequency units. This model explains qualitatively our results, namely the decrease of T_2 with increasing field in sample M890 and with hole concentration in sample M921.

Acknowledgement

One of us (D.S.) wish to thank K. Kavokin for fruitful discussions.

References

[1] G. Bastard and L. L. Chang, *Phys. Rev. B* **41**, R7899 (1990).
[2] M. R. Freeman et al., *Phys. Rev. Lett.* **64**, 2430 (1990).
[3] R. Akimoto et al., *Phys. Rev. B* **56**, 9726 (1997).
[4] K. Kavokin, to appear in *Phys. Rev. B*.
[5] A. Haury et al., *Phys. Rev. Lett.* **79**, 511 (1997).
[6] S. A. Crooker et al., *Phys. Rev. Lett.* **77**, 2814 (1996).
[7] S. A. Crooker et al., *Phys. Rev. B* **56**, 7574 (1997).
[8] R. Akimoto et al., *Phys. Rev. B* **57**, 7208 (1998).
[9] A. Abragam, *Principles of Nuclear Magnetism*, (Clarendon Press – Oxford, 1994).
[10] M. G. Tyazhlov et al., *Phys. Rev. B* **59**, 2050 (1999).

7th Int. Symp. "Nanostructures: Physics and Technology"
St Petersburg, Russia, June 14–18, 1999

Nonparabolicities and negative hole masses in quantum wells

A. A. Gorbatsevich and O. V. Zhabitsky
Moscow State Institute of Electronic Technology, 103498, Moscow, Russia

Abstract. It is shown that negative effective masses corresponding to the in-plane motion of holes in the fourth group and zinc blend heterostructure quantum wells which are usually attributed to the nonparabolicities caused by the repulsion and/or anticrossing of heavy and light hole subbands results in to the competition of two factors: the warping of the bulk energy spectrum and the phase shift of the size-quantized momentum due to heavy-light hole mixing.

Since the early studies of semiconductor heterostructures the problem of quantum well energy spectrum calculations was of prime importance. While the conduction size-quantized subbands can be easily described and interpreted within the framework of ordinary single-band quantum mechanics with all the problems lying in the determination of effective boundary conditions for envelopes the valence band subbands are usually treated by means of numerical methods because of there complex structure. The results of such numerical simulations widely present in modern textbooks demonstrate strong nonparabolicities of energy spectrum corresponding to the in-plane hole motion which are commonly associated with heavy-light hole subbands anticrossing. A common feature of the in-plane energy spectrum is the existence of the subbands with negative hole effective masses. The mass sign change could be treated in principal as a result of heavy-light hole subbands repulsion. However detailed study of energy dispersion curves for a number of structure parameters shows that it is not necessarily the case because the value of negative hole effective mass and its existence does not directly depend on the heavy-light hole subbands separation. In the present paper we investigate the origin of hole effective mass sign inversion. It is shown that apart from the heavy-light hole anticrossing two important mechanisms take place: the warping of heavy hole bands which is present already in the bulk and the in-plane quasimomentum dependent phase shift of the quantized quasimomentum due to heavy-light hole mixing.

We start from the standard Luttinger Hamiltonian:

$$H = \begin{pmatrix} P+Q & L & M & 0 \\ L^* & P-Q & 0 & M \\ M^* & 0 & P-Q & -L \\ 0 & M^* & -L^* & P+Q \end{pmatrix}, \tag{1}$$

where:

$$P = \frac{\gamma_1}{2m_0}(k_x^2 + k_y^2 + k_z^2),$$
$$Q = \frac{\gamma_2}{2m_0}(k_x^2 + k_y^2 - 2k_z^2),$$
$$L = -\frac{i\sqrt{3}\gamma_3}{m_0}(k_x - ik_k)k_z,$$

$$M = \frac{\sqrt{3}\gamma_2}{2m_0}(k_x^2 - k_y^2) - i\frac{\sqrt{3}\gamma_3}{m_0}k_x k_y.$$

Energy spectrum of the Hamiltonian possesses two double-degenerate branches of heavy and light holes:

$$E = P \mp \sqrt{Q^2 + |L|^2 + |M|^2}. \tag{2}$$

A qualitative picture of level anticrossing can be obtained if one averages the Hamiltonian (1) over the size-quantized subband wave function localized in the well [1]. Odd terms in respect to k_z (L-terms) vanishes after this procedure. The retaining Hamiltonian can be block-diagonalized and the resulting spectrum demonstrate anticrossing of heavy and light hole subbands.

Note however that the M-term contribution to energy spectrum is of the 4-th order in respect to the in-plane quasimomentum $k_\perp$. Hence anticrossing described by the M-term in the Hamiltonian has nothing in common with possible effective mass sign change which is to be described by quadratic in $k_\perp$ terms.

Let us turn to the bulk spectrum (2). A qualitative understanding of the peculiarities of energy spectrum in size-quantized structures can be obtained if we simply take k_z equal constant k_{zn}.

To estimate the effective masses we can omit M-term in the equation (2) and expand energy expression over $k_\perp^2$ up to the first order. It is useful to present the result both in terms of Luttinger and A, B, C parameters:

$$\begin{aligned} E_{h,l} &\approx (\gamma_1 \mp 2\gamma_2)\frac{\hbar^2 k_{zn}^2}{2m_0} + \left[\gamma_1 \pm \gamma_2 \mp \frac{3\gamma_3^2}{\gamma_2}\right]\frac{\hbar^2 k_\perp^2}{2m_0} \\ &= (A \mp B)\frac{\hbar^2 k_{zn}^2}{2m_0} + \left[A \mp B \mp \frac{C^2}{2B}\right]\frac{\hbar^2 k_\perp^2}{2m_0}. \end{aligned} \tag{3}$$

The term with the coefficient γ_3 in (3) arises from the L-term in the Hamiltonian which is responsible for warping of bulk energy spectrum in the plane containing quantized z-axes. (Note that M-term also describes warping but in xy-plane dosn't contain quantized axis). It immediately follows from (3) that a negative contribution to heavy hole subband effective mass exists always. This contribution presents if and only if warping is taken into account and is absent in the so-called spherical approximation [2, 3].

For all most popular semiconductors such as $GaAs$ ($\gamma_1 = 7.65$, $\gamma_2 = 2.41$, $\gamma_3 = 3.28$), Si ($\gamma_1 = 4.22$, $\gamma_2 = 0.39$, $\gamma_3 = 1.44$), Ge ($\gamma_1 = 13.35$, $\gamma_2 = 4.25$, $\gamma_3 = 5.69$) (see e.g. [4]) this contribution exceeds the first two terms in square brackets and the coefficient at $k_\perp^2$ in (3) is negative. Because warping is the characteristic of bulk energy spectrum the coefficient at $k_\perp^2$ in (3) can be considered as a bare effective mass for the in-plane motion in quantum wells which is negative for heavy holes. In the spherical approximation ($\gamma_3 = \gamma_2$) the coefficient at $k_\perp$ in (3) is positive in common semiconductors.

In the expression (3) we don't yet take into account the dependence of size-quantized momentum k_{zn} upon $k_\perp$ which results from heavy-light hole mixing at semiconductor heterointerface. At small $k_\perp$ we can write

$$k_{zn} = k_{zn0} + \alpha L k_\perp^2, \tag{4}$$

where L is the quantum well width. It is natural to interpret the second term in (4) as a phase shift due to heavy-light hole mixing at semiconductor heterointerface. Collecting

the contributions from both (3) and (4) we obtain for the in-plane effective masses the following expressions

$$\frac{1}{m_{h\perp}} = \gamma_1 + \gamma_2 - \frac{3\gamma_3^2}{\gamma_2} + 2\alpha_{hn}(\gamma_1 - 2\gamma_2)k_{zn0}L, \tag{5}$$

$$\frac{1}{m_{l\perp}} = \gamma_1 - \gamma_2 + \frac{3\gamma_3^2}{\gamma_2} + 2\alpha_{ln}(\gamma_1 + 2\gamma_2)k_{zn0}L. \tag{6}$$

If $\alpha > 0$ then the phase shift (last term in the expressions (5), (6)) pushes the effective mass to positive values. To calculate α one should find the general solution of the Schrödinger equation with the Hamiltonian (1) satisfying proper boundary conditions. Widely accepted choice of boundary conditions for semiconductor heterostructures assumes continuity of the wave functions

$$\hat{\psi}(z_{0-}) = \hat{\psi}(z_{0+}) \tag{7}$$

and the "currents"

$$\hat{j}_-\hat{\psi}(z_{0-}) = \hat{j}_+\hat{\psi}(z_{0+}) \tag{8}$$

at the heterointerface located at z_0, where $\hat{j}$ is the "current" operator which can be obtained by the integration of the Hamiltonian over the heterointerface [2]. The problem can be studied analytically in the case of infinitely high barriers (a box or a semiconductor film). For the box boundary conditions reduces to

$$\hat{\psi}(0) = \hat{\psi}(L) = 0. \tag{9}$$

For the first time this approach was realized in [5] where however because of sign drop an erroneous conclusion was made that the highest hole subbands in *Si* and *Ge* films possesses negative (electron-like) masses. In the case of infinite barriers for the first heavy hole subband we obtain

$$\alpha_{h1} = \frac{3}{2\pi^2}\frac{\gamma_3^2}{\gamma_2^2}\sqrt{\frac{\gamma_1 + 2\gamma_2}{\gamma_1 - 2\gamma_2}}\frac{1+\cos\theta}{\sin\theta}, \tag{10}$$

where:

$$\theta = k_{zh0}\sqrt{\frac{m_l}{m_h}}L = \pi\sqrt{\frac{\gamma_1 - 2\gamma_2}{\gamma_1 + 2\gamma_2}}. \tag{11}$$

From (5), (10) it follows that for common semiconductors hole effective mass for the topmost subband is positive. However if one instead of (7), (8) takes the generalized boundary conditions [6, 7, 8] describing heavy-light hole mixing already at normal incidence ($k_\perp = 0$) the coefficient α can be depressed and the effective mass can become negative. Numerical diagonalization of matrix 16×16 resulting from the conditions (7), (8) shows that at lower barrier the $k_\perp$—independent part of quantized quasimomentum decreases. In the expression (11) it corresponds to the reduction of k_{zho} resulting in the reduction of the denominator containing sin-function in (10). So for quantum wells with finite barrier height the tendency to the negative masses in the topmost subband is further supressed. For higher subbands the expression for α is similar to (10) however its sign oscillates with subband number becuase of the variation of the sin sign as k_{zn} changes over π/L. Another source of α sign variation is the reduction of barrier height. If k_{zn} for heigher barrier slighly exceeds π/L then for smaller barrier it will pass below the π/L and the sign of α will be changed. Hence the subband curvature for different barrier height can be dufferent.

Acknowledgment

This work was supported in part by Russian MNTP Physics of Solid State Nanostructures and Federal Program "Integration".

References

[1] H. Haug and S. W. Koch, *Quantum theory of the optical and electronic properties of semiconductors* (World Scientific, Singapore, 1990).
[2] G. Bastard, J. A. Brum and R. Ferreira, *Solid State Physics* **44**, 229 (1991).
[3] M. I. Djakonov and A. V. Hayetskij *Zh. Eksp. Teor. Fiz.* **82**, 1584 (1982).
[4] P. Y. Yu and M. Cardona, *Fundamentals of Semiconductors. Physics and Materials Properties* (Springer-Verlag, Berlin, 1996).
[5] S. S. Nedorezov, *Fiz. Tverd. Tela* **12**, 2269 (1970) [*Sov. Physics Solid State* **12**, 1814 (1971)].
[6] T. Ando and S. Mori, *Surface Science* **113**, 124 (1982).
[7] E. L. Ivchenko and A. Yu. Kaminski, *Phys. Rev.* **B54**, 5852 (1996).
[8] B. A. Foreman *Phys. Rev. Lett.* **81**, 425 (1998).

7th Int. Symp. "Nanostructures: Physics and Technology"
St Petersburg, Russia, June 14–18, 1999

Phonons in wurtzite $(GaN)_m(AlN)_n$ superlattices: non-monotoneous dependence of the number of Raman-active modes on superlattice period

Yu. E. Kitaev†, M. F. Limonov† and P. Tronc‡
† Ioffe Physico-Technical Institute, St Petersburg, Russia
‡ Laboratoire d'Optique Physique, ESPCI, 10 rue Vauquelin, 75005 Paris, France

Abstract. The symmetry of wurtzite $(GaN)_m(AlN)_n$ is established to depend on the numbers of monolayers of constituent materials in the primitive cell being C_{6v}^4 (odd $m+n$) or C_{3v}^1 (even $m+n$). As a result, it was shown that the number of Raman-active modes depends non-monotonically on $m+n$.

Spectacular successes in III–V nitride technology (GaN, AlN, and InN) in recent years have fostered the growth of short-period $(GaN)_m(AlN)_n$ semiconductor superlattices (SLs) [1] which can be considered as candidates for high-efficiency blue-light-emitting devices. However, the study of their phonon spectra was hindered by absence of any symmetry analysis. In the present paper, we present a complete group-theory analysis of the $(GaN)_m(AlN)_n$ SLs including the determination of their space groups, phonon symmetries, and Raman and infrared (IR) selection rules.

We use the approach that we have elaborated upon for the $(GaAs)_m(AlAs)_n$ SLs [2]. We consider the SLs as crystals with an enlarged unit cell compared with that of the parent materials (GaN and AlN). The structure of SLs, i.e., a space group G and an arrangement of atoms over the Wyckoff positions in a primitive cell, depends on the growth direction and numbers of monolayers (m, n) of constituent materials in the formula unit. For each direction of growth, these SLs constitute several crystal families specified by different space groups. Within each family, the crystals have the same space group but differ from each other by an arrangement of atoms over the Wyckoff positions. Thus, from the crystallographic point of view the SLs with different numbers of monolayers m and n are distinct crystals, even those belonging to the same family. Such a dependence of the SL crystal structure on the numbers of monolayers strongly influences its phonon states.

Bulk GaN and AlN single crystals exist in two modifications with the zinc-blende structure (space group T_d^2) and wurtzite structure (space group C_{6v}^4). The $(GaN)_m(AlN)_n$ SLs grown from zinc-blende parent GaN and AlN crystals are isostructural with the $(GaAs)_m(AlAs)_n$ ones considered in detail in [2]. Therefore, from the point of view of symmetry, the results of the analysis of $(GaAs)_m(AlAs)_n$ can be directly applied to the zinc-blende $(GaN)_m(AlN)_n$ ones. Below, we analyze the SLs formed from wurtzite parent materials (GaN and AlN) grown along the sixfold screw axis. When analyzing the SL structure, we adopt an approximation that the atoms in SLs are on the sites of a wurtzite lattice with lattice constants a and c and internal parameter u (denoting separation between anion and cation sublattices) being averages of the corresponding parameters of GaN and AlN. The approximation is reasonable since the differences in the u, a, and c parameters of GaN and AlN are less than 1.5%, 2%, and 4%, respectively. Taking this approximation into account, the coordinates of all the atoms in the lattice are well defined. As a result, we can determine both the space group and the atomic arrangement over the Wyckoff positions for a SL with arbitrary numbers of monolayers m and n.

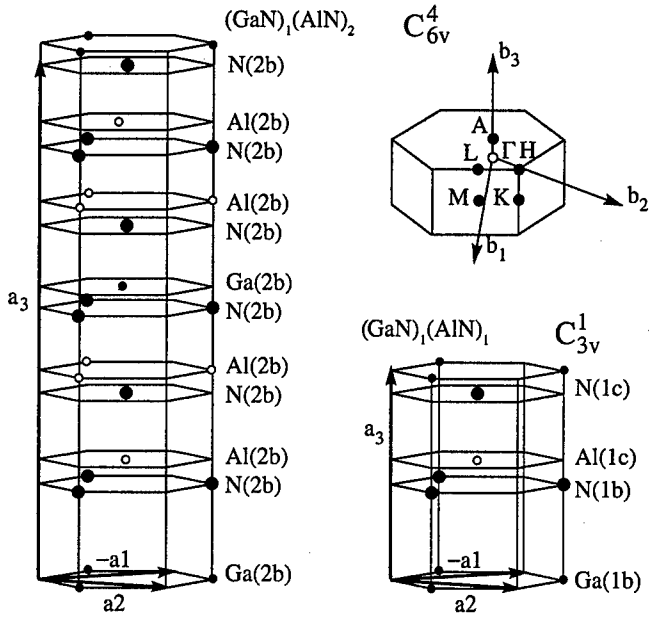

Fig. 1. The primitive unit cells of the $(GaN)_1(AlN)_1$ and $(GaN)_1(AlN)_2$ [0001] SLs and the corresponding BZ. The Wyckoff positions are given in parentheses together with the atoms.

Our analysis is valid for a SL made of two binary materials with a wurtzite structure and an identical cation or anion. If the difference in the lattice parameters between both materials cannot be neglected, our analysis remains valid at least for pseudomorphic SLs.

We have determined that the wurtzite $(GaN)_m(AlN)_n$ SL' grown along the [0001] direction form two families with space groups C^4_{6v} and C^4_{3v} (hexagonal Bravais lattice) correspoding to odd and even values of $m + n$, respectively. The crystal structures of typical representatives of these two different families are presented in Fig. 1 together with the corresponding Brillouin zone (BZ). For odd values of $m + n$, the nonsymmorphic space group C^4_{6v} of the SL is that of the bulk, the sixfold screw axis being conserved, whereas for even values of $m + n$ the improper translation $(00\frac{1}{2})$ is lost with the sixfold screw axis being replaced by the threefold rotation one. The symmetry of the latter family is described by the symmorphic C^1_{3v} space group. The atomic arrangements over the Wyckoff positions for both SL families are shown in columns 1–4 of Tables 1 and 2. The numbers preceding the chemical element symbols denote the number of such atoms at the Wyckoff positions listed in column 5 together with their coordinates and site symmetry groups.

Next we obtained the phonon symmetry in the $(GaN)_m(AlN)_n$ SLs using the method of induced band representations of space groups [3]. The results are presented in Tables 1 and 2. The symmetries of phonon modes at the symmetry points of the BZ are given by indices of small irreducible representations (irreps) (columns 7–9) induced by those irrreps β (column 6) of site symmetry groups according to which the local atomic displacements (x, y, z) are transformed. (The labelling of small irreps follows [4]).

The sets of normal modes at the symmetry points of the BZ are obtained by summing up contributions of all the atoms in the primitive cell. As a result, for the SLs with C^4_{6v} we

Table 1. Phonon symmetry in $(GaN)_m(AlN)_n$ SLs with the space group C_{3v}^1.

Atomic arrangement								
$m=1$	$m=2$	$m=2s+1$	$m=2s$	$\mathbf{q}$	β	Γ (000)	K $\left(\frac{1}{3}\frac{1}{3}0\right)$	M $\left(\frac{1}{2}00\right)$
$n=1$	$n=2$	$n=2t+1$	$n=2t$			C_{3v}	C_3	C_s
	1Ga	$\frac{m+1}{2}$Ga	$\frac{m}{2}$Ga	$1b$	$a_1(z)$	1	2	1
1Ga	1Al	$\frac{n-1}{2}$Al	$\frac{n}{2}$Al	$\left(\frac{1}{3}\frac{2}{3}z\right)$	$e(x,y)$	3	1,3	1,2
1N	2N	$\frac{m+n}{2}$N	$\frac{m+n}{2}$N	C_{3v}				
	1Ga	$\frac{m-1}{2}$Ga	$\frac{m}{2}$Ga	$1c$	$a_1(z)$	1	3	1
1Al	1Al	$\frac{n+1}{2}$Al	$\frac{n}{2}$Al	$\left(\frac{2}{3}\frac{1}{3}z\right)$	$e(x,y)$	3	1,2	1,2
1N	2N	$\frac{m+n}{2}$N	$\frac{m+n}{2}$N	C_{3v}				

Table 2. Phonon symmetry in $(GaN)_m(AlN)_n$ SLs with the space group C_{6v}^4.

Atomic arrangement								
$m=1$	$m=1$	$m=2$	$m=2s+1$	$\mathbf{q}$	β	Γ (000)	K $\left(\frac{1}{3}\frac{1}{3}0\right)$	M $\left(\frac{1}{2}00\right)$
$n=2$	$n=4$	$n=3$	$n=2t$			C_{6v}	C_{3v}	C_{2v}
2Ga	2Ga	4Ga	$2m$Ga	$2b$	$a_1(z)$	1,4	3	1,4
4Al	8Al	6Al	$2n$Al	$\left(\frac{1}{3}\frac{2}{3}z\right)$	$e(x,y)$	5,6	1,2,3	1,2,3,4
6N	10N	10N	$2(m+n)$N	C_{3v}				

have

$$\begin{aligned}
&\Gamma \to \Gamma = \Gamma_{opt} + \Gamma_{ac} = 2(m+n)(\Gamma_1 + \Gamma_4 + \Gamma_5 + \Gamma_6), \quad \Gamma_{ac} = \Gamma_1 + \Gamma_6,\\
&K \to 2(m+n)(K_1 + K_2 + 2K_3),\\
&M \to 2(m+n)(2M_1 + M_2 + M_3 + 2M_4).
\end{aligned} \tag{1}$$

whereas for the SLs with C_{3v}^1 symmetry the sets of normal modes are

$$\begin{aligned}
&\Gamma \to \Gamma = \Gamma_{opt} + \Gamma_{ac} = 2(m+n)(\Gamma_1 + \Gamma_3), \quad \Gamma_{ac} = \Gamma_1 + \Gamma_3,\\
&K \to 2(m+n)(K_1 + K_2 + K_3)\\
&M \to 2(m+n)(2M_1 + M_2).
\end{aligned} \tag{2}$$

Below, for the BZ-center phonons we give the correspondence between the two commonly used sets of irrep notations together with IR-active components and non-zero terms of the Raman tensor shown in parentheses:

$$\begin{aligned}
C_{6v}^4 : \Gamma_1 &= A_1(z; xx, yy, zz), \ \Gamma_4 = B_1(\text{silent}), \ \Gamma_5 = E_2(xx, yy, xy),\\
\Gamma_6 &= E_1(x, y; yz, xz);\\
C_{3v}^1 : \Gamma_1 &= A(z; xx, yy, zz), \ \Gamma_3 = E(x, y; xx, yy, xy, yz, xz).
\end{aligned} \tag{3}$$

From Eqs. (1)–(3) it is seen that in the C_{6v}^4 SLs there exist the E_1 modes that are Raman active in the xz and yz polarizations and nonactive in xx and yy polarizations, whereas

Table 3. Numbers of Raman and IR active modes in wurtzite $(GaN)_m(AlN)_n$ SLs.

$m+n$	bulk	2	3	4	5	6	$m+n$ (odd) (C_{6v}^4)	$m+n$ (even) (C_{3v}^1)
Raman	4	6	16	14	28	22	$[6(m+n)-2]$	$[4(m+n)-2]$
IR	2	6	10	14	18	22	$[4(m+n)-2]$	$[4(m+n)-2]$

on the C_{3v}^1 SLs all modes are Raman active in the xx and yy polarizations. Therefore, in analyzing Raman spectra it is easy to distinguish SLs with C_{3v}^1 and C_{6v}^4. Thus Raman scattering can serve as a test of SL quality since it is sensitive to a change of the SL period within a monolayer. Analyzing Eqs. (1)–(3) it is interesting to notice that, when increasing the number of monolayers $(m+n)$ in the formula unit, the number of Raman-active modes increases nonmonotonically. The results are summarized in Table 3.

It is seen that the numbers of Raman-active modes are governed by different equations: $[6(m+n)-2]$ and $[4(m+n)-2]$ for the SLs with C_{6v}^4 symmetry and C_{3v}^1 symmetry, respectively. As a result, when adding one monolayer to a SL with an odd $m+n$ value, the number of Raman-active modes decreases. At the same time, the number of IR-active modes is given by the same equation $[4(m+n)-2]$ for both SL families, i.e. it depends monotonically on the $m+n$ value.

Thus, the $(GaN)_m(AlN)_n$ SLs should be considered as crystals specified by their own space group rather than a simple superposition of bulk parent materials. We have obtained that the SLs belong to two crystal families specified by space groups C_{3v}^1 and C_{6v}^4, depending on whether $m+n$ is even or odd. The dependence of the SL point symmetry on the numbers of monolayers leads to drastic changes in the symmetry of phonon states and selection rules. As a consequence, from polarized Raman spectra one can easily distinguish the SL belonging to different families. Finally, a spectacular property of the $(GaN)_m(AlN)_n$ SLs is a nonmonotoneous dependence of the number of Raman-active modes on $m+n$, whereas the number of IR-active modes increases monotonically.

Acknoledgements

This work is supported by Russian Foundation for Basic Research (Grant No 99-02-18318). One of us (PT) wishes to thank the French Embassy in Moscow for the support.

References

[1] M. Asif Khan, J. N. Kuznia, D. T. Olson, T. George, and W. T. Pike, *Appl.Phys.Lett.* **63**, 3470 (1993).

[2] Yu. E. Kitaev, A. G. Panfilov, P. Tronc, and R. A. Evarestov, *J.Phys.: Condens.Matter* **9**, 257 (1997); *ibid.* **9**, 277 (1997).

[3] R. A. Evarestov and V. P. Smirnov, *Site Symmetry in Crystals: Theory and Applications* Vol. 108 of Springer Series in Solid State Sciences, ed. M. Cardona (Springer, Heidelberg, 1993; second edition 1997).

[4] S. C. Miller and W. F. Love, *Tables of Irreducible Representations of Space Groups and Co-Representations of Magnetic Space Groups* (Pruett, Boulder, 1967).

7th Int. Symp. "Nanostructures: Physics and Technology"
St Petersburg, Russia, June 14–18, 1999

Combined magnetopolaron in magnetooptical effects in quantum wells

L. I. Korovin†, I. G. Lang† and *S. T. Pavlov*‡
† Ioffe Physico-Technical Institute, St Petersburg, Russia
‡ P. N. Lebedev Physical Institute, 117924 Moscow, Russia

Abstract. Combined polaron states in a rectangular quantum well (QW) in a strong magnetic field directed perpendicular to the QW plane have been considered. At low temperatures these states are due to interaction of two electron energy levels (with different Landau quantum numbers (n and n_1) and different size-quantization quantum numbers (m and m_1)) with confined LO phonons under condition when the energy difference of the electron levels is close to the confined LO phonon energy. The resonant magnetic field H_{res}, at which a combined polaron forms, depends on the energy difference of the size-quantization levels and consequently depends on QW's parameters. The separation between the branches of the combined polaron energy spectrum ΔE_{res} and H_{res} as functions of the QW's width d have been calculated. It is shown that H_{res} may be reduced significantly in comparison to H_{res} for the case $m = m_1$.

In a strong magnetic field the polaron shift due to weak electron-LO phonon interaction is determined by the perturbation theory. However under condition

$$\omega_{L1} = j\Omega_e, \quad j = 1, 2, 3, \ldots . \tag{1}$$

(ω_{L1} is the LO phonon frequency, Ω_e is the electron cyclotron frequency) there appeares resonant coupling between Landau levels: an electron on the upper Landau level n emits LO phonon in a real transition and transits to the lower Landau level $n - j = n_1$. Being on the level $n - j$ the electron can absorb the earlier emitted phonon and transit on the initial level, emit a LO phonon again and so on. All these processes contribute essentially into the polaron state forming under condition (1) and they have to be taken into account.

The energy spectrum of the unperturbed electron-phonon system consists of two energy levels (one electron on the Landau level n and one electron on the Landau level $n - j = n_1$ plus one LO phonon), which intercross in the point $\Omega_e = \omega_{L1}/j$ as functions of frequency Ω_e. The transition from the unperturbed electron-phonon system to the polaron state under condition (1) means a summing up the terms of the perturbation theory sequence (on the electron-phonon coupling constant) corresponding to multiple emitting and absorption processes.

This summing results in lifting of degeneracy in the point $\Omega_e = \omega_{L1}/j$ and the polaron energy spectrum is represented by two noncrossing branches the separation between of which at the point $\Omega_e = \omega_{L1}/j$ is determined by the electron-phonon coupling constant. For the first time such polaron state was discovered in interband magnetoabsorption of bulk InSb [1].

The polaron states formation in strong magnetic fields takes place in quasi-two dimensional (2D) systems as well as in three-dimensional (3D) ones. In both 3D and 2D semiconductor structures the polaron states are very important in the frequency dependence formation of magnetooptical effects such as interband light absorption. The main difference between these systems is in the electron (hole) energy spectra: these are the one-dimensional

Landau bands in 3D case and the discrete energy levels in 2D case. This distinction results in different polaron energy spectrum splitting in the crossing point $\Omega_e = \omega_{L1}/j$ growing with the system dimensionality reduction: the energy splitting is proportional to $\sim \alpha^{2/3}$ [2] in 3D case and to $\sim \alpha^{1/2}$ [3, 4] in 2D case, where $\alpha \ll 1$ is the Frölich non-dimensional electron-phonon coupling constant.

The discribed above polaron state in a QW was called a double magnetopolaron (on the number of the intercrossing energy levels of the unperturbed electron-phonon system). More complicate polaron states are possible: triple magnetopolaron, quaternate and so on [4–6]. All these states relate to the same size-quantization energy level with the quantum number m. Therefore the resonant condition (1) does not depend on the position of the size-quantization energy level and, consequently, on the QW's width d.

However the electron (hole) energy levels in QW depend on two discrete quantum numbers: the Landau quantum number n and the size-quantization quantum number m. Therefore alongside the condition (1) it is possible performing of the other type resonant condition, when electron phonon interaction links two electron (holes) energy levels with different m and n. In this case the QW width d (and consequently the difference of the size-quantization level energies) determines the resonant magnetic field value. The role of such combined polaron states in frequency dependence formation of magnetooptical effects has been investigated.

In a QW of type I with the energy gap E_g, barriers ΔE_e and ΔE_h for electrons and holes respectively in a magnetic field **H** directed perpendicular to the QW plane the electron and hole energy spectra are discrete and have the form

$$E^e_{m,n} = \varepsilon^e_m + (n+1/2)\,\hbar\Omega_e, \quad E^h_{m,n} = E_g + \varepsilon^h_m + (n+1/2)\,\hbar\Omega_h, \quad \Omega_{e(h)} = \frac{|e|H}{m_{c(v)}c}, \quad (2)$$

where e is the electron charge, c is the velocity of light in vacuum, $m_{c(v)}$ is the electron (hole) effective mass, $\varepsilon^{e(h)}_m = \hbar\omega^{e(h)}_m$ is the electron (hole) size-quantized energy in the QW.

The resonant condition for a combined magnetopolaron is satisfied if

$$E^e_{m,n} = E^e_{m_1,n_1} + \hbar\omega_{L1}. \quad (3)$$

The resonant interaction takes place for an electron because the resonant condition does not hold for a hole due to the difference of electron and hole effective masses .

Substitution of the $E^e_{m,n}$ from Eq. (2) into Eq. (3) results into the expression for the resonant cyclotron frequency of the combined magnetopolaron

$$\Omega^{res}_e = \frac{\omega_{L1} - (\omega^e_m - \omega^e_{m_1})}{n - n_1}. \quad (4)$$

As it follows from the definition (4) there are three possible interrelations between m, m_1 and n, n_1. First, $m > m_1$ and $n > n_1$; second, $m > m_1$ and $n < n_1$; third, $m < m_1$ and $n > n_1$. The variant $m < m_1$ and $n < n_1$ leads to the negative Ω^{res}_e and must be neglected.

The first variant demands the condition

$$\hbar\omega_{L1} \geq \varepsilon^e_m(d) - \varepsilon^e_{m_1}(d). \quad (5)$$

to be satisfied. Let us suppose that the equality in Eq. (5) is performed if $d = d_{min}(m) > d'_{min}(m)$, where

$$d'_{min}(m) = (m-1)\pi\sqrt{\hbar^2/2m_c\Delta E_e} \quad (6)$$

is the value of d at which the upper level m gets out of the QW. Because the value $\varepsilon^{e}_{m}(d) - \varepsilon^{e}_{m_1}(d)$ diminishes smoothly with growing the QW width d from the value $\Delta E_e - \varepsilon^{e}_{m_1}(d'_{min}(m))$ to zero, the inequality (5) is satisfied in the interval

$$\infty > d > d_{min}(m). \tag{7}$$

If it happenes that $\hbar\omega_{L1} > \Delta E_e - \varepsilon^{e}_{m_1}(d'_{min}(m))$ (a shallow QW), the condition (5) is satisfied at $d < d_{min}(m)$, i.e. for any d when upper energy level exists in a QW.

In the second variant the condition

$$\hbar\omega_{L1} \leq \varepsilon^{e}_{m}(d) - \varepsilon^{e}_{m_1}(d), \tag{8}$$

is to be satisfied in the interval

$$d'_{min}(m) < d < d_{min}(m), \tag{9}$$

because for $d > d_{min}(m)$ the variant 2 polaron disappeares and for $d < d'_{min}(m)$ the energy level m gets out of the QW. Let us note that both variants 1 and 2 cannot be unified because they correspond to the different intersecting energy levels of the electron-phonon system.

The terms of Eq. (3) and Eq. (4) distinguish radically from Eq. (1) for the double polaron for which the resonant magnetic field value does not depend on the QW parameters. For a combined magnetopolaron the value Ω^{res}_{e} depends on both the QW width and depth, in other words every concrete QW has its own resonant magnetic field H_{res}.

There are intersections of the electron-phonon energy levels with equal numbers N of phonons. These polaron states are analogous to the weak polarons introduced in [6] when the difference of the phonon numbers, regarding to the two energy levels of the electron-phonon system, $\Delta N \neq 1$. In such a case the interlevel transitions with one LO phonon emitting are impossible. One has to take into account here the transitions through the virtual states. Then the degeneration in the crossing point is lifted, however the splitting value will be higher order on α, than $\alpha^{1/2}$.

There is also a resonant binding between the energy levels of the electron-phonon system existing at any magnetic field value. It realizes under condition

$$\hbar\omega_{L1} = \varepsilon^{e}_{m} - \varepsilon^{e}_{m_1}. \tag{10}$$

This is the case of the resonant binding between the two size-quantization energy levels with coinciding Landau quantum numbers, i.e. $n = n_1$. Eq. (4) is performed in a wide interval of QWs parameters because magnetic field compensates a divergence of an energy levels difference from the value $\hbar\omega_{L1}$.

The energy difference of two combined magnetopolaron branches is $(2 \cdot 10^{-3}-4 \cdot 10^{-3})$ eV, what is less than the appropriate value for the double magnetopolaron [6] $(3 \cdot 10^{-3}-6 \cdot 10^{-3})$ eV, nevertheless it is quite observable. But in the case of a combined magnetopolaron the resonant magnetic field H_{res} is less than H_{res} for the double polaron. H_{res} diminishes with increasing of value $j = n-n_1$ (Eq. (1)) for the double magnetopolaron but in the case of a combined magnetopolaron (Eq. (4)) $\hbar\Omega_e$ diminishes, first, with growing j and, second, due to decreasing $\hbar\omega_{L1} - (\varepsilon^{e}_{m} - \varepsilon^{e}_{m_1})$. This is so for the variant 1 of Eq. (4).

The double polaron appropriating to the lowest size-quantized energy level $m = 1$ can exist at any QW width. So long as a combined magnetopolaron is due to two size-quantized energy levels it cannot exist in the width region $d < d'(m)$, where $d'(m)$ is the QW width at which the upper energy level gets out from the QW. $d'(m)$ increases with increasing

of quantum number m. It means that the lower limit for the existance of the 1 variant combined polaron increases with $d'(m)$ increasing.

The damping of the branches of the combined polaron energy spectrum due to LO phonon inharmonicity as well as interband absorption and reflection of light by QW at an arbitrary interrelation between radiative and "phonon" lifetimes of combined polarons have been investigated.

This work has been partially supported by the Russian Foundation for Basic Research and by the Program "Solid State Nanostructures Physics" (97-1049).

References

[1] E. J. Johnson and D. M. Larsen, *Phys. Rev. Lett.* **16**, 655 (1966).

[2] L. I. Korovin, S. T. Pavlov, *Zh. Eksp. Teor. Fiz.* **53**, 1708 (1967); (*Soviet Phys.: JETP* **26**, 979 (1968)). *Pis'ma Zh. Eksp. Teor. Fiz.* **6**, 525 (1967).

[3] L. I. Korovin, S. T. Pavlov, B. E. Eshpulatov, *Fiz. Tverd. Tela* **20**, 3594 (1978) (*Soviet Phys.: Solid State* **20**, 2077 (1978)).

[4] I. G. Lang, V. I. Belitsky, A. Cantarero, L. I. Korovin, S. T. Pavlov, M. Cardona, *Phys. Rev. B* **54**, 17768 (1996); *Phys. Rev. B* **56**, 16880 (1997).

[5] L. I. Korovin, I. G. Lang, S. T. Pavlov, *Zh. Eksp. Teor. Fiz.* **111**, 2194 (1997). (*JETP* **84**, (6) 1197-1208 (1997)).

[6] L. I. Korovin, I. G. Lang, S. T. Pavlov, *Pis'ma Zh. Eksp. Teor. Fiz.* **65**, 511 (1997) (*JETP Lett.* **65**, (7), 532-536 (1997)); *Zh. Eksp. Teor. Fiz.* (1999), accepted for publication.

7th Int. Symp. "Nanostructures: Physics and Technology"
St Petersburg, Russia, June 14–18, 1999

Angular dependence of luminescence from GaAs/AlGaAs DQW

V. V. Krivolapchuk†, *E. S. Moskalenko*†, A. L. Zhmodikov†, T. S. Cheng‡ and C. T. Foxon‡

†Ioffe Physico-Technical Institute, St Petersburg, Russia
‡ Department of Physics, University of Nottingham,
University Park NG7 2RD, Nottingham, UK

This paper reports the exciton photoluminescence (PL) study of GaAs/AlGaAs double quantum well (DQW). The particular interest is paid to the luminescence behaviour of the indirect exciton (IX) consisting of the electron (e) and a hole (h) localized in the different quantum wells (QW) of the same DQW. This IX architecture leads to the existence of distinct dipole moment in the system of IX gas and moreover to the essentially longer radiative lifetime compare to the direct excitons which are composed from e and h located in the same QW. All this makes it possible to expect some new properties in the IX system. For example, the long ($\approx 1\ \mu$s) radiative lifetime allows one to create the IX gas of high density (10^{10} cm^{-2}) even at moderate pumping intensities ($\approx$ 1 mW) and as a result to expect the appearance of a new collective phase in the dense IX gas which was predicted theoretically [1]. Experimental results on the IX PL properties which can be interpreted in the frame of the manifestation of new phase in the dense IX system were published recently [2].

In this contribution we present the external electric field (V_{dc}) induced changes in the low-temperature ($T = 1.8$ K) PL spectra of IX recorded on the DQW samples (detailed sample description and experimental setup are given elsewhere [2]) as a function of an angle α in between plane of the sample and PL detection direction (optical axis). It was observed that PL spectra taken at $\alpha = 90°$ show almost no changes in the full width at half maximum (FWHM) as well as in the shape of the IX PL line which progressively shifts to low energies with increasing of V_{dc} while those taken at $\alpha = 60°$ behave in quite a different way. Namely, as V_{dc} increases, IX line shape shows more and more pronounced double peak structure which leaves only single PL line at moderate V_{dc}'s. With further increase of V_{dc} this single line consistently narrows and broadens as was reported in our earlier observation [2]. We consider this strong angular dependence originates from clearly pronounced dipole moment in the system of spatially separated excitons and discuss the experimental results in terms of radiation diagrams of variously oriented IX dipoles.

We are grateful to RFBR 98-02-18296 for the financial support.

References

[1] Yu. E. Lozovik and O. L. Berman *Sov. Phys. JETP* **111**, 1879 (1997).
[2] V. V. Krivolapchuk, E. S. Moskalenko, A. L. Zhmodikov, C. T. Foxon and T. S. Cheng *Sov. Phys. Solid State* **41**, 149 (1999).

7th Int. Symp. "Nanostructures: Physics and Technology"
St Petersburg, Russia, June 14–18, 1999

Electric field domains and self-sustained current oscillations in weakly-coupled long period GaAs/AlGaAs superlattices

Yu. A. Mityagin, V. N. Murzin, A. A. Pishchulin and I. P. Kazakov
P. N. Lebedev Physical Institute, 117924, Leninsky pr., 53, Moscow, Russia

The self-sustained current oscillations associated with electric field domains in long period GaAs/AlGaAs superlatices were investigated experimentally as well as by numerical simulation. The MBE-grown GaAs/AlGaAs superlatices (d_W = 250 Å, d_B = 100 Å, 30 periods) were lightly doped and embedded within n^+-contacts. Several (4) plateaus with pronounced oscillatory-like negative differential conductivity (NDC) structure corresponding to formation of electric field domains were observed in time-averaged I–V characteristics.

The current oscillations were observed at constant bias voltage corresponding to plateau-like regions of I–V characteristics. The fundamental oscillation frequency (between 20 kHz and 10 Mhz) increased with increasing index of subband involved in the tunneling resonance. The transition from periodic to chaotic oscillation regime was observed when bias voltage came into ranges of negative differential conductivity in I–V characteristics of the superlattice.

The periodic and strong dependence of the oscillation frequency upon the bias voltage was observed within plateau, the oscillation frequency continuously tuning within each period. The observed periodic dependence is correlating with the periodicity of NDC structure in time-averaged I–V characteristics.

The interpretation of the experiment is based on the numerical simulations within the discrete drift model of resonant tunneling and electric field domain dynamics in superlattices [1]. For the drift velocity curves used in the calculations and determined from comparison with experimental data the simulation showed that in considered case the oscillation mechanism is the oscillating of the position of the domain boundary being pinned within a few periods of the superlattice.

It is also shown that introducing into the superlattice of a single quantum well with lower dopant concentration may stimulate the self-sustained current oscillations due to domain instability in the vicinity of such a defect [2].

References

[1] Yu. A. Mityagin and V. N. Murzin, *JETP Lett.* **64**, 155 (1996).
[2] Yu. A. Mityagin, D. G. Batashov and V. N. Murzin *Physics of Low-Dimensional Structures* **1/2**, 117 (1998).

7th Int. Symp. "Nanostructures: Physics and Technology"
St Petersburg, Russia, June 14–18, 1999

Band parameters of MQWs heterostructures InGaAs/GaAs: magnetooptical study

Kh. Moumanis, R. P. Seisyan, S. I. Kokhanovskii and M. E. Sasin
Ioffe Physico-Technical Institute, St Petersburg, Russia

Abstract. Investigation of the optical absorption and magnetoabsorption spectra of a set of $In_xGa_{1-x}As/GaAs$ strained MQWs with different well widths and different Indium content x has been carried out at 1.7 K in the presence of the magnetic field up to 7.5 T. The measurements performed on the free standing samples have allowed to obtain well-resolved oscillatory spectra and to reconstruct Landau level positions. An effective masse of the electron and other parameters of the InGaAs/GaAs MQW heterostructures depending on the Indium concentration were estimated.

Introduction

The ternary alloys $In_xGa_{1-x}As$ grown on GaAs attract much attention due to their applications in micro- and optoelectronics. Precise knowledge of the band parameters of these alloys is required for these applications. Determination of band parameters is a non-trivial problem because of their dependence on the compound x. In a major part of publications on this subject, for the sake of simplicity, the linear interpolations or extrapolations are used. Sometimes this approach is too rough to yield satisfactory results. Especially, it concerns the calculation of a heavy-hole mass. Here we report a detailed investigation of the magnetoabsorption spectra usually assumed as the best source of band parameter data. Indium compound effect on the conduction and valence band effective masses in $In_xGa_{1-x}As$ alloys is under study.

Our technique is based on the low-temperature light absorption measurements in the presence of an external magnetic field. Landau oscillations in these spectra represent a signature of so-called "diamagnetic excitons" [1], which are formed at strong magnetic fields. To restore true Landau fans from the measured spectra one has to add to the experimental transition energies the calculated exciton binding energies R_B as is discussed in detail in [2]. Knowing the slope of true Landau fans, following [1, 2] one can deduce the cyclotron masses of electrons and holes.

Thus for a correct determination of the band parameters one should be able to determine R_B with a good precision. In general a binding energy is a complex function of magnetic field and all quantum numbers of the problem, $R_B(N, l, M, L_z)$, where N is a quantum number of the electron (hole) state in the well, l is a Landau quantum number, M is a momentum projection into the magnetic field direction, L_z is a width of quantum well. The inevitable mixing of light- and heavy-hole states complicates the calculation.

1 Samples and experimental procedure

The $In_xGa_{1-x}As$ samples were grown by molecular beam epitaxy on (100) oriented GaAs substrates. Characteristics of the studied samples are listed in Table 1. $Al_{0.5}Ga_{0.5}As$ 0.5 μm thick stop layers were grown in order to allow complete removing the substrates by chemical etching. This has allowed to measure all details of transmission spectra which were then used to restore the spectral dependence of the absorption coefficient in the structures.

Magneto-optical measurements have been carried out at $T = 1.7$ K in a pumped liquid Helium cryostat with a superconducting solenoid, which allowed to create magnetic fields up to 7.5 T. The free samples were immersed in the liquid helium. The spectra were obtained for left- and right-circularly polarized light in the Faraday geometry using a high-transmission diffraction monochromator.

Table 1. MQWs Indium contents x, and layer thicknesses L_z, L_B deduced from the X-ray diffraction measurements. N is the number of periods of multiple quantum well structures, FWHM is the width of the spectral lines directly deduced from the absorption spectra.

Samples	x	L_z (nm)	L_B (nm)	N	FWHM (meV)
1	0.033	9.3	89.7	30	0.8
2	0.044	8.5	83.7	20	0.9
3	0.045	9.0	82.2	20	1.1
4	0.062	8.8	75.8	20	1.7
5	0.066	6.3	79.4	20	1.6
6	0.132	4.4	14.7	30	6.6
7	0.161	7.5	33.1	30	5.0
8	0.209	5.0	13.0	30	10.3
9	0.225	4.6	23.7	30	11.9

As one can see from the Table 1, low Indium concentrations ($x = 0.033-0.066$) correspond to the best quality of samples[1] and ultra-narrow spectral lines. To exclude strain relaxation effects the barriers in multiple QW structures have been made much thicker than wells. Compound x, well width L_z and barrier width em L_B were determined with use of X-ray diffraction spectroscopy[2].

2 Results and discussion

Optical transmission spectra measured after removing a substrate without magnetic field and under $B = 1-3$ T of one for our samples are shown in Fig. 1. In [3] we have studied optical transmission spectra either before or after substrate removal. Free standing samples exhibit much more spectral details. Two kinds of spectral lines in zero field having different scales of absorption modulation can be distinguished. The low amplitude lines correspond to the transitions on the (In,Ga)As well electron level,while stronger spectral features correspond to the transitions in the GaAs barrier (4) described in the terms of the exciton-polariton branch quantization combined with weak strain effects [4]. The lines (1 and 2) are associated with HH1E1 exciton ground (1s) state and first excited (2s) state, and the series of lines correspond to the light hole exciton states LH-E1 (3). It is worth to note that for such a small In contents there are no other allowed optical transitions in the system according to the calculated energy scheme.

Magnetic fields higher than 1 T cause oscillations in the absorption spectrum (Fig. 1). A considerable number of absorption maxima are recorded, sometimes more than 20 peaks. The fact of such a large number of strong oscillations observed in the magnetoabsorption, attests rather high quality of the quantum-well layers. This oscillatory behavior of the

[1] Samples were prepared in Optical Science Center, University of Arizona, and kindly placed at our disposal by H. Gibbs and G. Khitrova.

[2] The X-ray measurements were performed with N. N. Faleev in A. F. Ioffe Physico-Technical Institute.

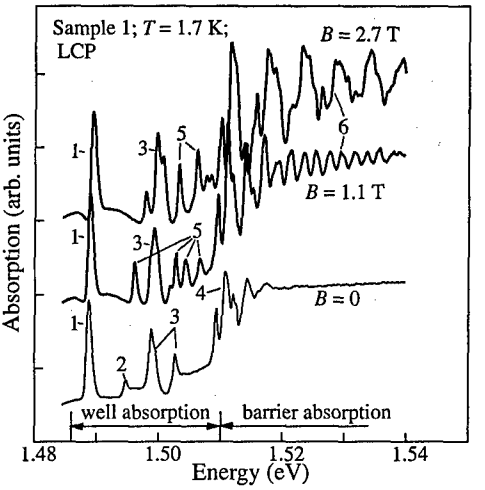

Fig. 1. Absorption spectra for MQWs $In_{0.033}Ga_{0.067}As/GaAs$ without magnetic field and under B = 1.1 T; B = 2.7 T: 1, 2—heavy hole exciton states; 3—light hole excitons; 5, 6—magnetoexciton maxima for QWs and GaAs barrier, respectively.

magnetoabsorption maxima is characteristic of the interband magnetoabsorption of quantum wells and has been observed previously in the AlGaAs/GaAs system [5]. It appears when the strong-field criterion $\beta = \hbar\Omega/2R_0 \gg 1$ (where R_0 is the binding energy of an exciton for $B = 0$ and (Ω is the sum of cyclotron frequencies of electrons and holes) is not satisfied by the excitonic ground state, and is observed only when excited states of the exciton participate in the absorption.

Heavy hole exciton transitions dominate in the magnetoabsorption spectra. To restore true Landau fans one has to add the calculated binding energies to all experimental peak energies. This, as well as the next procedure, can be assumed as a good confirmation for calculated magnetoexciton binding energies. The reconstruction of Landau fans in the units $y = \hbar\omega_0(l + 1/2)$, where $\omega_0 = eB/mc$ is the free electron cyclotron energy proportional to the magnetic field B, for all samples listed in Table 1, is shown in Fig. 2. Such scale collects all the experimental points belonging to the different Landau states into one curve, as one really can see in Fig. 2. This allows us to estimate the reduced effective mass μ of an electron and hole in the plan of the quantum well, from the slope of the reconstructed straight line for the transitions between Landau subbands $\Delta E/\Delta B$.

Unfortunately, we have not possibility to separate contributions of electron and heavy hole in the obtained reduced masses. Moreover, obtained data belong to the samples with different quantum well width L_z. After taking correction on electron nonparabolicity depending on L_z, we can choice heavy hole masses that allows us to obtain the dependence of m_c^* on the Indium concentration (see Fig. 3), which not contradict to the known dependence of m_c^* on x bulk material (for example, $m_0^{-1}m_c^* = 0.0660 - 0.0537x + 0.0116x^2$; see [6]). By such a way, we define the compositional dependence of the valence band effective masses for heavy hole: $m_0^{-1}m_{HH}^*(x) = 0.385 - 0.88x + 0.86x^2$. Comparing this value with known literature dependence for heavy hole mass, we can talk about absence of the substantional mixing of light- and heavy-hole states in given heterostructures with heavy holes strongly separated from light holes by strain. Heavy hole masses in MQW were studied theoretically in [7] taking into account both light hole tunneling and changes due to deformation of a layer. Following [7] m_{HH}^* in the first quantization level (HH1)

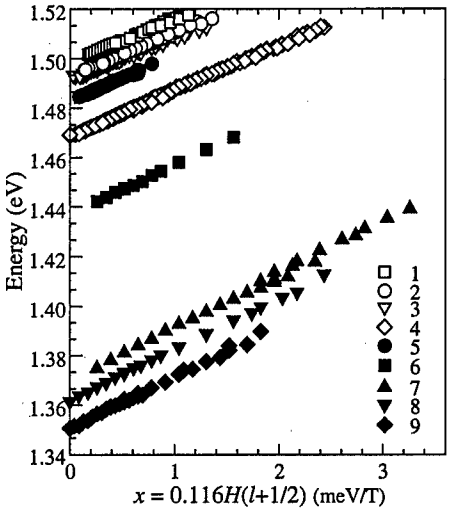

Fig. 2. Positions of maxima in the magnetoabsorption corrected for the binding energy of diamagnetic excitons plotted as a function of the cyclotron energy of a free exciton and the Landau number $(l + 1/2)$ for $In_xGa_{1-x}As/GaAs$ MQW samples listed in Table 1.

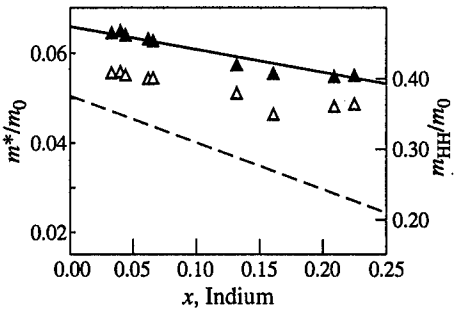

Fig. 3. Dependences of the electron and hole effective masses in $In_xGa_{1-x}As$ alloys on the Indium concentration. Triangles are reduced masses obtained directly as $\Delta E/\Delta B$ in Fig. 2, black triangles are after nonparabolicity corrections, and dotted line is supposed m^*_{HH}. Solid line is the dependence of electron effective mass from [6].

should be much higher then in unstrained QWs, approaching to the bulk mass, what largely explains the obtained result.

References

[1] R. P. Seisyan, *Spectroscopy of Diamagnetic Excitons*, Moscow: Nauka, 1984 (in Russian).
[2] A. V. Kavokin, S. I. Kokhanovskii, A. I. Nesvizhskii, M. E. Sasin, R. P. Seisyan, V. M. Ustinov, A. Yu. Egorov, A. E. Zhukov and S. V. Gupalov, *Semiconductors* **31**, 9 (1997).
[3] S. I. Kokhanovskii, K. Moumanis, M. E. Sasin, R. P. Seisyan, A. V. Kavokin, H. Gibbs and G. Khitrova, *Phys. Stat. Sol. (a)* **164**, 67 (1997).
[4] G. N. Aliev, N. V. Luk'yanova, R. P. Seisyan, M. R. Vladimirova, V. N. Bessolov, H. Gibbs and G. Khitrova. *Compound Semiconductors* vol. 155, p. 169, 1996.
[5] N. D. Il'inskaya, S. I. Kokhanovskii and R. P. Seisyan, *Semiconductors* **27**, 57 (1993).
[6] S. I. Kokhanovskii, Yu. M. Makushenko, R. P. Seisyan, Al. L. Efros, T. V. Yazeva and M. A. Abdullaev, *Sov. Phys. Semicond.* **25**, 298 (1991).
[7] L. G. Gerchikov and A. V. Subashiev, *Semiconductors* **27**, 249–256 (1993).

7th Int. Symp. "Nanostructures: Physics and Technology"
St Petersburg, Russia, June 14–18, 1999

Effect of relaxation processes on Auger recombination in semiconductor quantum wells

A. S. Polkovnikov, E. B. Dogonkine and G. G. Zegrya
Ioffe Physico-Technical Institute, St Petersburg, Russia

Abstract. In this paper we study the effect of carrier relaxation processes on Auger recombination in semiconductor quantum wells (QWs). It is shown that the calculation in the framework of the conventional perturbation theory is not applicable in the case of narrow wells and wires because of its divergence. Therefore a more rigid Green function techniques is used. The relaxation processes are shown to increase Auger recombination coefficient, however their influence becomes weaker with decrease of the QW width. The transition from the QW to the bulk case is explicitly carried out.

Introduction

It is several decades since Auger recombination (AR) was investigated in bulk semiconductors [1, 2]. It was shown that Auger process calculated in the first order of perturbation theory on Coulomb interaction has a threshold nature, i.e. its coefficient exponentially depends on temperature. In heterostructures, however, the transversal momentum component doesn't conserve thus allowing the thresholdless Auger process to appear [3, 4]. In our previous papers [5, 6] we showed that there are three different AR processes in quantum wells (QWs): (i) threshold, which is just a 2D analogue of the bulk process, (ii) quasithreshold arising from confinement of electrons and holes within the quantum well, and (iii) thresholdless which is caused by carrier scattering on the heteroboundaries. An explicit transition from the 2D to the 3D case for the CHCC Auger process carried out in [5, 6] showed that the quasithreshold and threshold mechanisms merge into the single bulk process when the QW width becomes considerably larger than the critical value given by:

$$a_c = \lambda_{Eg} \left(\frac{T}{E_{th}} \right)^{3/2} \exp \frac{E_{th}}{T}, \tag{1}$$

where $\lambda_{Eg} = 2\pi/k(Eg)$ is the wavelength of an electron having the band gap energy Eg, $E_{th} \approx \frac{2m_c}{m_h} Eg$ is the threshold energy in a homogeneous semiconductor, m_c and m_h are the electron and heavy hole masses, T is temperature in energy units. It is an easy matter to see that in semiconductors with the energy gap close to 1 eV the value of a_c can be as large as several thousands Angströms, which strongly exceeds the free path length in these semiconductors. Hence there is an obvious contradiction between this result and the common sense. The solution to this paradox is the direct taking into account of various scattering processes. Finally we note here that it is impossible to use conventional quantum mechanical perturbation analysis for this purpose. The reason is that the scattering mechanisms such as the electron(hole)-electron(hole) or electron(hole)-phonon processes become resonant and the corresponding expressions obtained in the second and higher orders of perturbation theory diverge [6].

1 Green function formalism for the calculation of Auger recombination processes

The temperature Green function formalism was firstly applied to AR processes in a homogeneous semiconductor in [7, 8]. However there was no investigation of Green function broadening due to relaxation processes on the value and temperature dependence of Auger coefficient. The author of those papers also used phenomenological expressions for the wave functions and overlap integrals rather than those obtained in the multi-band **kp**-theory. Nevertheless, a convenient method for calculating the Auger rate in any order of interaction potential is suggested there.

The expression for the recombination rate obtained in the linear response theory on Coulomb interband scattering is as follows [7]:

$$\frac{\partial N_c}{\partial t} = \int_{-\infty}^{\infty} dt e^{i\mu_\Delta t} \sum_{\lambda_i,\xi_j} \int \dots \int d\mathbf{r}_1 \cdots d\mathbf{r}_4 \Delta_{1,2,3,4} U(\mathbf{r}_1 - \mathbf{r}_2) U(\mathbf{r}_3 - \mathbf{r}_4) i G_4^R(t), \quad (2)$$

where

$$G_4^R(t) = \Theta(t) \sum_{i_1,j_1,\dots} \langle \hat{\Psi}^{\alpha+}_{\lambda_4,i_1}(\mathbf{r}_1,t) \hat{\Psi}^{\beta+}_{\lambda_3,j_1}(\mathbf{r}_2,t) \hat{\Psi}^{\beta}_{\lambda_2,j_2}(\mathbf{r}_2,t) \hat{\Psi}^{\alpha}_{\lambda_1,i_2}(\mathbf{r}_1,t)$$
$$\times \hat{\Psi}^{\gamma+}_{\xi_4,k_1}(\mathbf{r}_3,0) \hat{\Psi}^{\delta+}_{\xi_3,l_1}(\mathbf{r}_4,0) \hat{\Psi}^{\delta}_{\xi_2,l_2}(\mathbf{r}_4,0) \hat{\Psi}^{\gamma}_{\xi_1,k_2}(\mathbf{r}_3,0) \rangle \quad (3)$$

is the four particle retarded Green function, $\Theta(t)$ is the step function, $U(\mathbf{r})$ is the interaction Coulomb potential screened by the host lattice, λ_i and $\xi_j = c, v$ numerate the conduction or the valence band, $i_1, j_1, \dots$ are the spin indices [6], $\alpha, \beta, \dots$ are the indices numerating the components of wave functions in 8×8 basis [6] ($\alpha = |s\uparrow\rangle, |s\downarrow\rangle \dots$), $\Delta_{1,2,3,4} = \delta_{\lambda_2,c} + \delta_{\lambda_1,c} - \delta_{\lambda_3,c} - \delta_{\lambda_4,c}$ shows that only interband Auger transitions are responsible for the non-conservation of particles in the conduction (valence) band, $\mu_\Delta = (\mu_c - \mu_v)\left[\delta_{\lambda_4,c} + \delta_{\lambda_3,c} - \delta_{\lambda_2,c} - \delta_{\lambda_1,c}\right]$, $\hat{\Psi}(t)$ is the field operator in the modified Heisenberg picture where all terms leading to interband transition are excluded from the total Hamiltonian [7]. We note here that in a homogeneous semiconductor wave functions with different spins are orthogonal ($i_1 = i_2,\ j_1 = j_2, \dots$), however this is not the case for QWs. It was assumed that both electrons in the conduction band and holes in the valence band have Fermi-Dirac distribution with their own chemical potentials ($\mu_c \neq \mu_v$). This assertion is valid when the intraband relaxation times are much shorter than those of interband transitions.

Further simplifications come from using the mean field approximation for the four-particle Green function. In this case the function G_4^R splits into two different terms corresponding to the direct and exchange scattering processes. This approximation is justified at high temperatures when there are no coherent, e.g. excitonic, states and the vertex corrections are small. Because the relaxation time for holes is much shorter than that for electrons, we neglect by the electron scattering processes. For the sake of simplicity electrons in initial state are supposed to occupy only their ground state. However this assumption is not essential because the ground state energy can be substituted by the mean thermal one for sufficiently wide QWs. Then after some manipulations, for the recombination rate per unit square, we obtain:

$$\frac{1}{S}\frac{\partial N_c}{\partial t} \approx \frac{24\pi^3 e^4 \hbar n_c^2}{m_c E_g^2 \kappa_0^2} \sum_{nj,mi} \int_{-\infty}^{\infty} dE \int_0^{\infty} \frac{dq}{k_4} f_h(E) D_{nj,mi}(q,E)$$

$$\times\langle 2M_I^{nj}(q,k_4)M_I^{mi}{}^*(q,k_4) - M_I^{n,j}(q,k_4)M_{II}^{mi}{}^*(q,k_4)\rangle, \qquad (4)$$

where

$$M_I^{nj}(q,k_4) = \int_{-a/2}^{a/2} \psi_f^{s}{}^*(x,q,k_4)\psi_{c1}^{s}(x)\psi_{c2}^{\beta}(x)\psi_{h\,nj}^{\beta}{}^*(x,q)dx,$$

a is the QW width, M_{II} can be obtained from M_I by interchanging indices c_1 and c_2, $n_c = N_c/S$ is the 2D electron density, nj and mi numerate the energy levels and spin states of a heavy hole, $f_h(E) = \exp[(\mu_h - E)/T]$ is the hole distribution function, which are supposed to be non-degenerated for the case of simplicity, $D_{nj,mi}(q, E)$ is the spectral function, obtained from the imaginary part of a heavy hole Green function, angular brackets in (4) denote averaging over the states of localized electrons. It is to be noted that only the quasithreshold AR mechanism was taken into account in (4), because it was shown to prevail in QWs at high temperatures [6]. In general the Green function in a QW is not diagonal and the spectral function D cannot be written in a simple Lorentzian form. However, in two limiting cases of wide and narrow wells D becomes diagonal. Thus in narrow QWs there is only one energy level in the well and in wide QWs Green function becomes diagonal because of the spatial homogeneity. Therefore if instead of $D_{nj,mi}$ an expression having Lorenz form multiplied by $\delta_{n,m}\delta_{j,i}$ were used the obtained results would be accurate in both limits of narrow and wide QWs and could be considered as interpolate ones for intermediate widths. In this case it is easy to verify that the Auger coefficient is the squared matrix element of Auger transition averaged over the initial states and summed over the final states, but where instead of the δ-function representing the energy conservation law there is a spectral function. In the limit $\Gamma \to 0$ (4) turns to the coefficient obtained in the first order of perturbation theory. The expression for the quasithreshold Auger coefficient obtained in [6] can be easily generalized yielding

$$C \approx \frac{\pi^2 e^4}{\kappa_0^2}\frac{\hbar^3\gamma^4}{E_g^5}\frac{F(\Delta_{so}/Eg)}{a(a+2/\kappa_c)^2}\frac{1}{Z}\sum_n \int_0^\infty dq \int_0^\infty dE \frac{q}{q^2+k_{hn}^2}\frac{q_c^2 k_{hn}^2 + q_h^2(k_c^2 + \frac{1}{2}q_c^2)}{k_4}$$
$$\times(G_{-1} + 2G_0 + G_1)\frac{1}{\pi}\frac{\Gamma_n(q,E)}{\Gamma_n(q,E)^2 + (E - E_{hn}(q))^2}, \qquad (5)$$

where

$$G_\lambda = \frac{1 - \cos(k_4 - k_{hn} - 2\lambda k_c)a}{k_4 - k_{hn} - 2\lambda k_c}, \qquad Z = \sum_n \int_0^\infty q dq \exp\left(-\frac{E_{hn}(q^2)}{T}\right),$$

k_{hn} and E_{hn} are the wave vector and the energy of a hole at the nth level, q_c is the average longitudinal momentum of the localized electrons, $F(\Delta_{so}/Eg)$ is the multiplier close to unity introduced in [6], k_c and κ_c are the absolute values of electron transversal wavevectors in a quantum well and barrier region respectively, γ is Kane's parameter, k_4 can be determined from the following equation:

$$E_f(k_4^2 + q^2) - Eg - 2Ec = E,$$

where $E_f(k)$ is the energy of a conduction band electron. Obviously both G_λ and D in fact eliminate threshold conditions. Thus G_λ allows non-conservation of the momentum

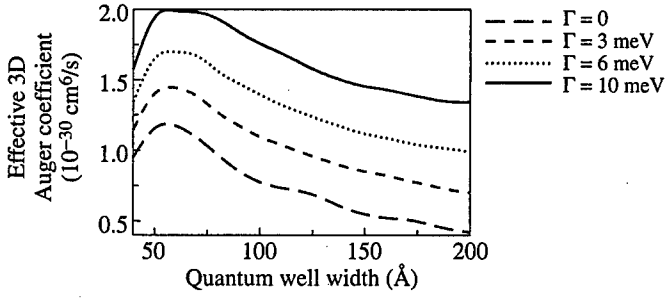

Fig. 1.

and D violates the energy conservation law. The critical quantum well thickness at which the 2D–3D transition occurs can be determined now by comparing widths of G and D. An another important feature arises from the analysis of (5). Namely, the calculations made in the framework of conventional perturbation theory wouldn't give the term Γ^2 in the denominator of the spectral function D. Because there is no threshold in sufficiently narrow wells and all values of the hole momentum q are allowed, this expression would diverge at the resonance where the denominator becomes zero. Therefore the approach based on the conventional perturbation theory is not applicable in the case of QWs.

2 Discussion

Certainly the calculation of Γ, or to be more precise of the imaginary part of the Green function, is quite a separate problem which is to be discussed elsewhere. The value of Γ obviously depends on carrier density, QW width, etc. However to illustrate the effect of relaxation processes in the QWs we consider Γ to be an external parameter and compare dependences of AR coefficient, multiplied by the squared QW width, on QW width at different Γ values (Fig. 1).

The analysis of this figure shows that in narrow QWs the finite lifetime of carriers is not very important factor and AR can be calculated in the first order of the perturbation theory, while in wide QWs Γ plays a crucial role and the more its value the less width where the 2D–3D transition occur.

The authors would like to acknowledge the Russian Foundation for Basic Research (Grants 97-02-18151, 98-07-90336) and the Russian State Program: Physics of Solid State Nanostructures (Grants 97-1035 and 97-0003) for the support of this work.

References

[1] A. R. Beattie and P. T. Landsberg, *Proc. Roy. Soc.* **A 249**, 16 (1959).
[2] B. L. Gel'mont, *Sov. Phys. JETP* **48**, 268 (1978).
[3] G. G. Zegrya and V. A. Kharchenko, *Sov. Phys. JETP* **74**, 173 (1992).
[4] M. I. Dyakonov and V. Yu. Kachorovskii, *Phys. Rev.* **B49**, 17130 (1994).
[5] G. G. Zegrya and A. S. Polkovnikov, *JETP* **86**, 815 (1998).
[6] A. S. Polkovnikov and G. G. Zegrya, *Phys. Rev.* **B58**, 4039 (1998).
[7] M. Takeshima, *Phys. Rev.* **B26**, 917 (1982).
[8] M. Takeshima, *Phys. Rev.* **B28**, 2039 (1983).

7th Int. Symp. "Nanostructures: Physics and Technology"
St Petersburg, Russia, June 14–18, 1999

Gigantic oscillations of dc-voltage in semiconductor superlattices

Yu. A. Romanov and *Ju. Yu. Romanova*
Institute for physics of microstructures, RAS, Niznii Novgorod, Russia

Abstract. Electron properties of semiconductor superlattices (SL) in an high-frequency intensive field (harmonic and biharmonic) were studed. We showed that the induced and self-induced transparency states of SL are unstable. Absolute negative conductance, unstable plasma oscillations and parametric amplificatoin of intense field harmonics destroy these states. As a result SL turns in a new state with dc-voltage and (or) non-linear plasma oscillations. The field-dependence of dc-voltage has hysteresis. The gigantic oscillations of dc-voltage arise in SL with high electron concentration. The dissipative chaos and stochastic current oscillations occurs in a very strong field.

There are three types of semiconductor superlattice (SL) transparency: selective transparency, self-induced transparency and induced transparency. Resonant building up of electrons by a harmonic electric field arises in the window of transparency and, therefore, the absorption of the electric field is maximum. The electrons can pass the energy they have taken away from the field not only to the lattice but also to another field and intensify it. This can lead to evolution of the dissipation instability and destruction of the states of transparency. The most efficient destruction mechanisms are the parametric intensification of the strong field harmonics, excitation of growing plasma oscillations and absolute negative conductance (ANC). A SL placed in a strong harmonic field turns either into a steady state or into a self-oscillation regime, or into chaotic state as a result of development of instabilities. The character of transitional processes and the final state depend on the field amplitude and the parameters of the external circuit. We have considered a broken circuit (the SL current is zero) in this paper. The SL behavior is investigated for the given strong static and biharmonic field.

$$E(t) = E_c + E_1 \cos(\omega_1 t + \delta_1) + E_2 \cos(\omega_2 t + \delta_2)$$

Then, using the numerical simulations we investigated the SL behavior in a self-consistent multi-friequency field.

We showed:

1. The transparency states of SL are unstable to quasi-static and plasma oscillations.
2. SL turns into an opaque state without current with the finite static dc-voltage as a result of the destruction of transparency. The states are resistant to quasi-static oscillations, aperiodic instabilities are absent. The stability to high-frequency oscillations depends on the resonant properties of the external circuit.
3. New regions of transparency with nonvanishing static current arise at a given static voltage across the SL. These states are unstable, too.
4. The gigantic oscillations of dc-voltage arise in SL which is in a strong external harmonic field. Their frequency can be controlled by the external circuit parameters and electron concentration.
5. In a general case the states in which SL turns under harmonic field are characterized by dc-voltage and nonlinear plasma oscillations. The dissipative chaos occurs in a very strong field.

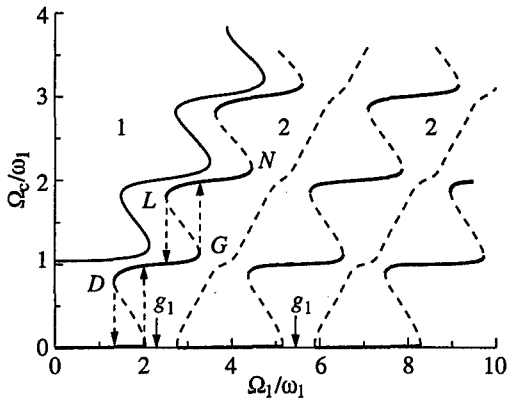

Fig. 1.

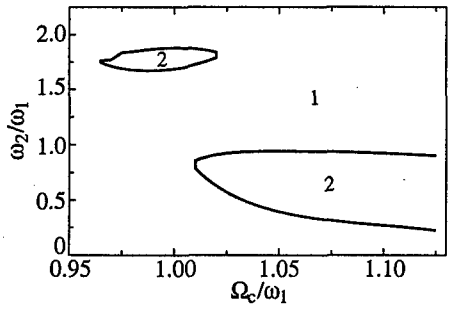

Fig. 2. The regions of negative conductivity (2) on the "step" DG. (1) is the stable region.

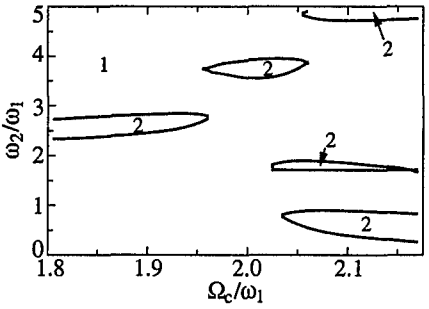

Fig. 3. The regions of negative conductivity (2) on the "step" LN. (1) is the stable region.

Figure 1 demonstrates the instability region (negative conductivity region) for the field E_1—(1) and E_2—(2) under $E_2 = 0$ and for field E_2—(2) under $E_c = 0$. The boundary curves correspond to the non-current states ($j_c = 0$), solid lines are for the steady states. Dashed lines are for the instabilities states: $\Omega_c = eE_cd$, $g_1 = eE_1d/\hbar\omega_1$, d is the SL period, $\omega_1\tau = 4$, τ is the relaxation time. Existence of g_1-regions with two and more steady states of the static EMF is the main peculiarity of the boundary lines. $V_c = (N\hbar\omega_1/e)n$, $n = 0, \pm1, \pm2 \ldots$, N is number of SL periods.

This peculiarity leads to hysteresis in the dependence $Vc(g)$ under slow modification of the amplitude of the strong field. The pointers show an example of hysteresis. Figures 2–3 depict the regions of the negative conductivity on the "steps" DG and LN respectively. They show that SL is not resistant to high frequency only, in the state with $V_c \neq 0$. Spontaneous appearance of static dc-voltage and(or) nonlinear plasma oscillations change the SL conductivity at the frequency of the strong field E_1. This leads to destruction of its transparency, a change in the intrinsic field and, hence, to gigantic ($\sim N\hbar\omega_1/e$) dc-voltage oscillations. The oscillation frequency depends on the parameters of the external circuit and may be rather high.

This work is supported by INTAS-FEBR 95-0615 grant, RFFI 96-02-19271 grant and RFFI 96-02-19284a grant.

7th Int. Symp. "Nanostructures: Physics and Technology"
St Petersburg, Russia, June 14–18, 1999

Generation and recombination in semimetallic heterostructures

M. Singh, J. Desforges and W. Lau
Department of Physics and Astrinomy, University of Western Ontario,
London, Canada

Heterojunctions InAs-GaSb belong to the most interesting objects in the modern semiconductor physics [1]. Due to the partial overlapping of the InAs conduction band with the GaSb valence band, a semimetallic electron-hole system is formed at the interface. Contrary to ordinary semimetals (Bi), electron and hole systems in these heterostructures are spatially separated. That is why the current flow through single heterojunctions and multilayer heterostructures is governed by generation-recombination processes at the InAs-GaSb interface.

The aim of the present work is to calculate the interface generation-recombination (GR) rate. We considered three band Kane model Hamiltonaian [2] and envelope-function approximation to calculate GR rate. We found that the generation-recombination processes in semimetallic heterojunctions is very different compared to ordinary semiconductors, p-n-junctions and other heterojunctions. In particular, the creation of electron-hole pairs requires no additional energy and, hence, the generation rate must have no activation temperature dependence. An electron of InAs reaching the interface can either reflect back or with some probability transmit into the valence band of GaSb. Such a transition is equivalent to a recombination of elelctron-hole pair. The process when electrons from the valence band of GaSb penetrate into InAs, is equivalent to the generation of an electron-hole pair at the interface. So, generation-recombination at the interface does not require the presence of any third body (photon, phonon, recombination center, etc.).

We applied the present theory to describe the conduction processes in heterojunctions n-InAs–p-GaSb. We found that the current-voltage characteristic of the junction n-InAs–p-GaSb has the properties of an Ohmic contact, in agreement with the experimental results [3]. As the applied voltage U increases, the current-voltage characteristic becomes non-linear and finally saturates for $eU > \Delta$ at the value, independent of the temperature. The results obtained above can also be applied to the InAs–GaSb superlattices. If the thickness of superlattice layers is of order of 100 Å or more, the superlattice is in a semimetallic state and contains alternating layers with high electron and hole concentration. It is usually assumed that the superlattice conductivity is provided by formation of electron and hole minibands. However, at large superlattice periods miniband conductivity will be very small. In this case we may expect that the conductivity in InAs layers will be provided by electrons, in GaSb — by holes and the total superlattice conductivity will be governed by generation-recombination processes at the interfaces. It will result in the superlattice resistivity per unit area equal will be proportional to the number of layers.

References

[1] M. Altarelli, in: *Optical Properties of Narrow-Gap Low-Dimensional Structures*, edited by C. M. Sotomayor Torres, et al. (Plenum Press, 1987), p. 15.
[2] P. Voisin, reference [1], p. 85.
[3] H. Sakaki, et al. *Appl. Phys. Lett.* **31**, 211 (1977).

7th Int. Symp. "Nanostructures: Physics and Technology"
St Petersburg, Russia, June 14–18, 1999

Charged excitons in ZnSe-based QWs

D. R. Yakovlev†‡, G. V. Astakhov†, V. P. Kochereshko†, A. Keller‡, W. Ossau‡ and G. Landwehr‡

† Ioffe Physico-Technical Institute, St Petersburg, Russia

‡ Physikalisches Institut der Universität Würzburg, 97074 Würzburg, Germany

Abstract. We report on magneto-optical studies of ZnSe/(Zn,Mg)(S,Se) and ZnSe/(Zn,Be,Mg)Se quantum wells with n-type and p-type modulation doping. Negatively and positively charged excitons related to the heavy-hole exciton state are found and identified by their polarization properties. Exciton and trion parameters (radiative and nonradiative dampings, g factors) are determined.

The existence of charged exciton complexes (trions) in semiconductors has been predicted by Lampert in 1958 [1]. In analogue with charged hydrogen ions H^- and H_2^+ the negatively charged exciton (X^-), consisting of two electrons and one hole, and the positively charged exciton (X^+), formed by two holes and one electron, have been suggested. However, the first clear experimental proof of the X^- existence has appeared quite recently in 1993. Kheng *et al.* reported the observation of the negatively charged exciton state in a CdTe-based quantum well (QW) structure with a two-dimensional electron gas (2DEG) of low density [2]. It follows from the calculation of the charged exciton binding energy that this complex is only weakly bound in bulk materials (about 5% of exciton Rydberg energy), which hinders its experimental observation in 3D systems. However, reduction of dimensionality of the system down to quasi-two-dimensional one strongly favors the trion stability and increases its binding energy up to 20–45% of the Rydberg energy. In recent years negatively charged excitons have been studied intensively in CdTe- and GaAs-based QWs [3, 4]. The observation of positively charged excitons has also been reported for these structures [5–7].

Being scaled with the exciton Rydberg the trion binding energy can be enhanced considerably by the proper choice of the material system. The logical step after GaAs (with exciton binding energy of 4.2 meV) and CdTe (10 meV) is to investigate ZnSe-based structures (20 meV) in order to improve the Coulomb interaction. The technique of molecular-beam epitaxy (MBE) is well developed for the growth of ZnSe-based QW structures. However, the mostly studied structures contain (Zn,Cd)Se ternary alloy QWs barriered by ZnSe layers. In these structures the exciton resonances are broadened significantly due to alloy fluctuations, which makes highly-resolved optical spectroscopy of exciton and trion states very difficult. We are aware of one report on X^- state observation in (Zn,Cd)Se/ZnSe QW only [8]. Very recently the growth of high-quality lattice-matched ZnSe/(Zn,Mg)(S,Se) QWs with exciton inhomogeneous broadening less than 1 meV has been published [9, 10]. In this paper we report on magneto-optical studies of negatively and positively charged excitons in ZnSe/(Zn,Mg)(S,Se) and ZnSe/(Zn,Be,Mg)Se QWs. Trion states related to both heavy-hole and light-hole excitons are found and their parameters are examined as a function of QW width and in external magnetic fields.

A set of $ZnSe/Zn_{0.86}Be_{0.06}Mg_{0.08}Se$ single QW (SQW) structures with QW width varied from 30 Å up to 200 Å was grown by MBE on (100) GaAs substrates. The ZnSe QWs were confined by 1000 Å thick barriers. A total band gap discontinuity between QW

and barrier materials of 230 meV is distributed in ratio 70/30 between the conduction and valence bands. The structures were nominally undoped. $ZnSe/Zn_{0.89}Mg_{0.11}S_{0.18}Se_{0.82}$ SQWs were also grown by MBE on (100) GaAs substrates. ZnSe SQWs were located between $Zn_{0.89}Mg_{0.11}S_{0.18}Se_{0.82}$ barriers of 1000 Å- and 500 Å thickness. The total band gap discontinuity of 200 meV is distributed about equally between the conduction and valence band edges. Results for three structures are reported here. The first one is nominally undoped with a residual concentration of the 2DEG in the 100 Å SQW $n_e \leq 10^{10}\,\mathrm{cm}^{-2}$ due to the weak n-type background conductivity of the barriers. The second structure has $n_e = 9 \times 10^{10}\,\mathrm{cm}^{-2}$ provided by a modulation doped layer (30 Å thick, Cl doped to a level of $5 \times 10^{17}\,\mathrm{cm}^{-3}$) separated by a 100 Å spacer from a 100 Å SQW. The third sample was p-type doped with nitrogen through the whole thickness of the barrier layers excluding an 120 Å SQW and 30 Å spacers on both sides of the SQW. The carrier concentration of the two-dimensional hole gas (2DHG) is about $n_h \approx 3 \times 10^{10}\,\mathrm{cm}^{-2}$. Photoluminescence (PL), reflectivity and spin-flip Raman scattering (SFRS) spectra were measured at 1.6 K and in magnetic fields up to 7.5 T applied perpendicular to the QW plane (Faraday geometry). Circularly polarized light was analyzed by means of achromatic quarter-wave plates. The signal was dispersed by a 1-m spectrometer and detected by either a charge-coupled device (CCD) or by a photomultiplier.

In Fig. 1(a,b) PL and reflectivity spectra of 30 Å- and 200 Å thick QWs are plotted. In low-temperature emission spectra two lines corresponding to the heavy-hole exciton (X) and X^- are clearly seen (detailed identification of the optical resonances by means of magneto-optics in fields up to 20 T was reported in Ref. [10]). For the 200 Å the X^-

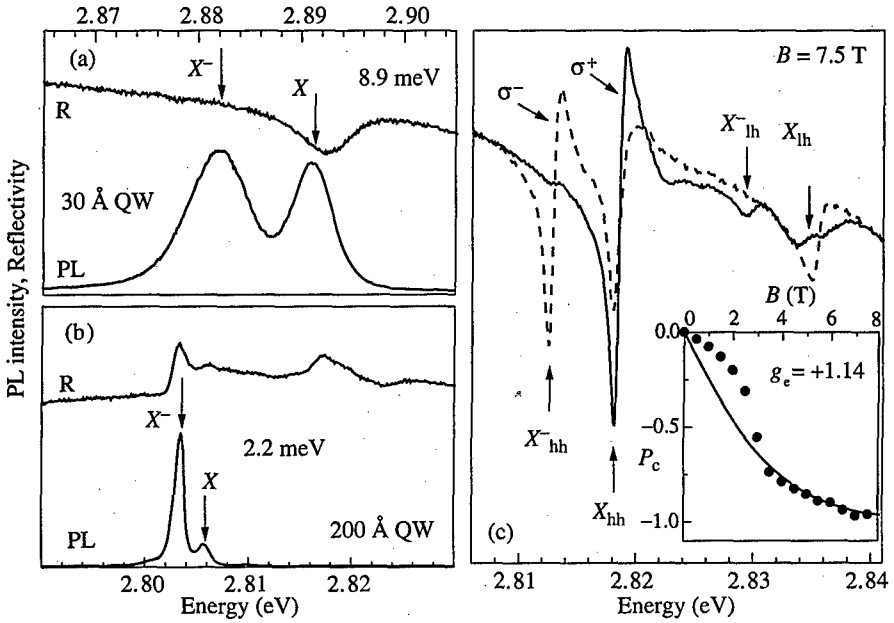

Fig. 1. Photoluminescence and reflectivity spectra of $ZnSe/Zn_{0.86}Be_{0.06}Mg_{0.08}Se$ SQWs with well width of 30 Å (a) and 200 Å (b) taken at 1.6 K and at a zero magnetic field. In the panel (c) reflectivity spectra of a 100 Å thick $ZnSe/Zn_{0.89}Mg_{0.11}S_{0.18}Se_{0.82}$ SQW with $n_e \approx 9 \times 10^{10}\,\mathrm{cm}^{-2}$ detected in two circular polarizations are presented. An inset shows the polarization degree of X^-_{hh} transition: experimental data (circles) and calculated dependence (solid line).

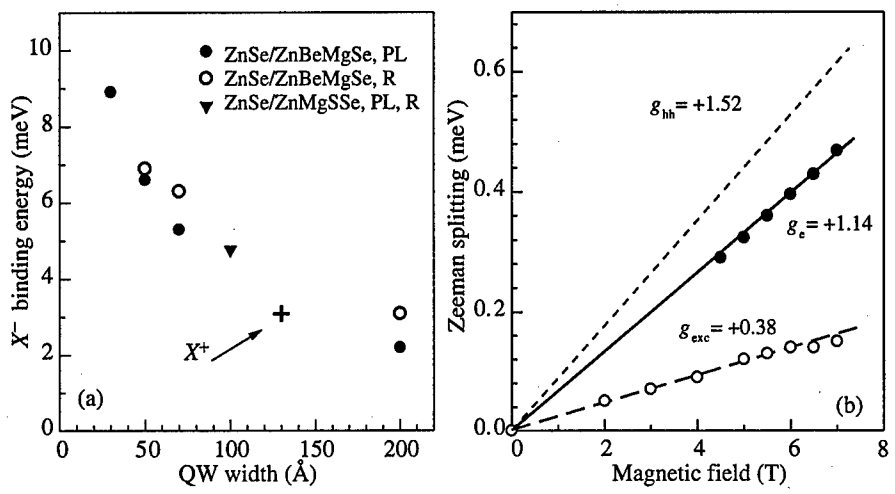

Fig. 2. (a) Trion binding energies as a function of QW width for the studied ZnSe-based structures. Data points evaluated from photoluminescence (PL) and reflectivity (R) spectra are shown. (b) Zeeman splittings of heavy-hole excitons and carriers in a 100 Å thick $ZnSe/Zn_{0.89}Mg_{0.11}S_{0.18}Se_{0.82}$ SQW. Experimetal data are shown by circles and linear interpolations are represented by lines.

line is also intensive in the reflectivity spectrum, however, it is not detectable for the 30 Å QW. The main reason for that is a difference in 2DEG concentrations (we estimate from the optical spectra $n_e \geq 10^{11}$ cm^{-2} for the 200 Å QW and $n_e \leq 10^{10}$ cm^{-2} for the 30 Å QW), which in these nominally undoped structures is supplied by shallow donors of the barrier layers. In narrow QWs the electron quantum-confined energy level is higher than the barrier donor levels and electron collection into the QW is reduced significantly.

The binding energy of the X^- state defined as the energy difference between X^- and X is plotted in Fig. 2(a) as a function of QW width. It increases by a factor of 4 with well width reduction from 200 Å down to 30 Å and amounts to 9 meV. For the 100 Å QW the X^- binding energy is 17% of the exciton binding energy in the QW, which value of 30 meV was determined from the magneto-exciton fan chart [10].

In Fig. 2(b) experimental results on the Zeeman splitting of the exciton and carriers in the 100 Å $ZnSe/Zn_{0.89}Mg_{0.11}S_{0.18}Se_{0.82}$ QW are collected. The exciton splitting with a g factor $g_{exc} = +0.38$ was deduced from the reflectivity spectra and that of the electron with $g_e = +1.14$ was measured by means of SFRS. The heavy-hole g factor was calculated by means of the equation $g_{hh} = g_{exc} + g_e = +1.52$ [11].

The strong polarization of the X^- absorption in magnetic fields is a fingerprint of the trion which allows to distinguish clearly trion resonance from the excitonic one [2]. This is due to the singlet spin structure of the trion ground state, i.e. spins of two electrons involved in the X^- complex should be oriented antiparallel. As a result, when a 2DEG is totally polarized by the magnetic field X^- can be excited optically only for one circular polarization of light (namely the σ^- polarization in ZnSe-based QWs with a positive electron g factor $g_e = +1.14$ measured by SFRS (see Fig. 2(b)). At 7.5 T the X^-_{hh} transition in the reflectivity spectra is totally polarized (see Fig. 1(c)). Its oscillator strength became twice stronger in σ^- polarization, comparing with the zero field value, and vanishes for σ^+ polarization keeping the integral oscillator strength constant.

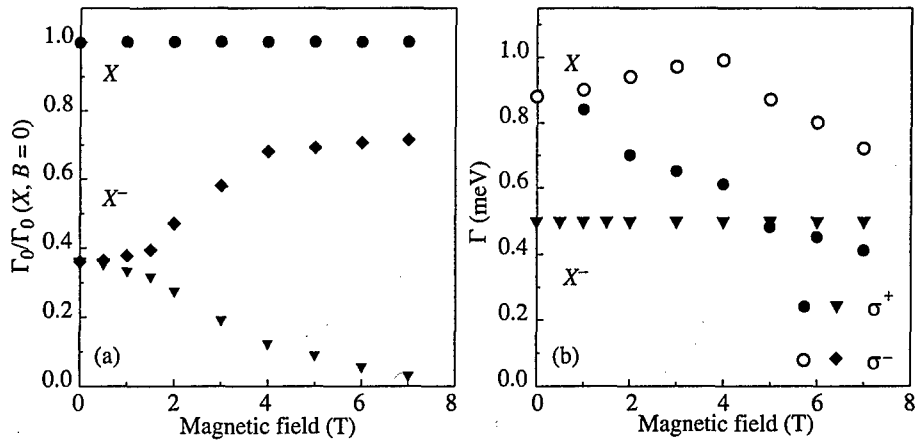

Fig. 3. Magnetic-field dependences of radiative (Γ_0) and nonradiative (Γ) dampings for exciton and trion transitions in a 100 Å thick $ZnSe/Zn_{0.89}Mg_{0.11}S_{0.18}Se_{0.82}$ SQW with $n_e \approx 9 \times 10^{10}\,cm^{-2}$. Results for two circular polarized components of reflectivity spectra are presented at $T = 1.6$ K.

A procedure described in Ref. [12] was used to fit the reflectivity spectra and to deduce the excitonic parameters like radiative damping Γ_0, which corresponds to the exciton oscillator strength, and the nonradiative damping Γ, which in the studied structures is dominated by inhomogeneous broadening. The parameters determined as a function of magnetic fields are presented in Fig. 3. We stress here that Γ_0 for the exciton and Γ for the trion do not vary in magnetic fields. The difference in Γ for the exciton components with opposite circular polarizations is due to an effect of spin-dependent scattering of excitons with 2D electrons [13].

The degree of polarization of the trion transition calculated as $P_c = (\Gamma_0^+ - \Gamma_0^-)/(\Gamma_0^+ + \Gamma_0^-)$ is shown in the inset of Fig. 1(c) by circles. The equilibrium polarization of a nondegenerate 2DEG, calculated with the Boltzmann distribution, $g_e = +1.14$ and $T = 1.6$ K, is traced by a solid line. Experimental points coincide well with the line at fields above 3.7 T. Deviation from the Boltzmann distribution in low magnetic fields takes place for filling factors $\nu > 1$ [14]. In this case the Fermi-Dirac statistic describes the polarization properties of the 2DEG. We conclude from the inset of Fig. 1(c) that the condition $\nu = 1$ is achieved at a magnetic field of 3.7 T. This, in turn, allows to determine the concentration of the 2DEG $n_e = veB/hc = 9 \times 10^{10}\,cm^{-2}$ (for details see [15]).

The X_{lh}^- transition, related to a negatively charged exciton associated with the light-hole exciton states, is observed at 7.5 T as a clearly resolved resonance 4.4 meV below the energy of the light-hole exciton (Fig. 1(c)). It is polarized contrary to the X^-hh states, which is in agreement with optical selection rules. The binding energy of X_{lh}^- is about 20% smaller than that of X_{hh}^- which is 5.5 meV at 7.5 T. To the best of our knowledge no detailed investigation of X_{lh}^- states has been reported so far. Trions associated with the light-hole exciton were observed in PL excitation spectra of GaAs/(Al,Ga)As QWs [3] and in the reflectivity spectra of monomolecular CdTe islands [16]. In both cases the X_{lh}^- binding energy is very close to that of X_{hh}^-.

A shake-up line related to X_{hh}^- has been detected in the emission spectra of the structure with $n_e \approx 10^{10}\,cm^{-2}$ [17] (see Fig. 4(a,b)). It moves towards lower energies with increasing

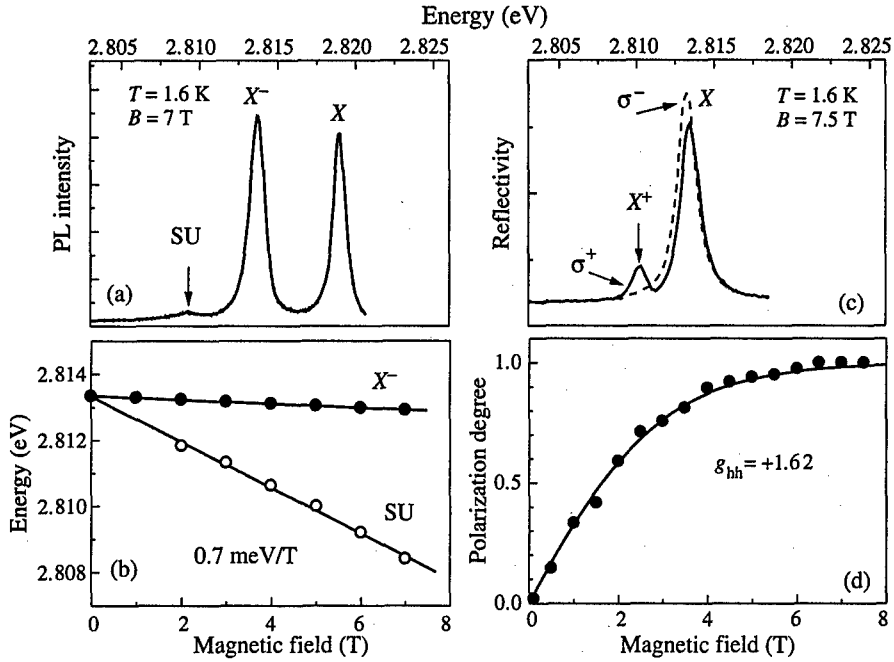

Fig. 4. A shake-up (SU) process in PL spectrum of a 100 Å thick $ZnSe/Zn_{0.89}Mg_{0.11}S_{0.18}Se_{0.82}$ SQW with $n_e \approx 10^{10}\,cm^{-2}$ (a) and magnetic-field dependence of the SU line (b). A positively charged exciton in reflectivity spectra of a 130 Å $ZnSe/Zn_{0.89}Mg_{0.11}S_{0.18}Se_{0.82}$ QW with $n_h \approx 3 \times 10^{10}\,cm^{-2}$ (c) and polarization dependence of X^+ line in magnetic fields: experiment (circles) and calculation for $T = 1.6$ K (line).

magnetic field with a slope of 0.7 meV/T, which is very close to the electron cyclotron energy of 0.725 meV/T (electron effective mass in ZnSe is $m_e = 0.16m_0$). This combined process is based on the recombination of an trion and a simultaneous excitation of a 2D electron from the zeroth to the upper Landau levels.

In Fig. 4(c) reflectivity spectra for the 130 Å thick SQW with a low-dense 2DHG with $n_h \approx 3 \times 10^{10}\,cm^{-2}$ are shown. A line of the positively charged exciton with a binding energy of 3.1 meV is observed in the spectrum. Similar to X^-_{hh} the X^+_{hh} line is totally polarized in magnetic fields above 6 T, but the sign of polarization is opposite. The magnetic-field dependence of the X^+_{hh} polarization degree (see circles in the inset of Fig. 4(d)) coincides remarkably well with the Boltzmann distribution calculated with the heavy-hole g factor $g_{hh} = +1.62$. This g factor value was deduced from the measured $g_{exc} = +0.48$ and $g_e = +1.14$. The value of the X^+_{hh} binding energy of 3.1 meV is close to that for the X^-_{hh} (see Fig. 2(a)), which is in agreement with the results reported for QW structures based on GaAs [6, 7], and CdTe [5].

To conclude, charged excitons shows up brightly in the optical spectra of ZnSe-based QWs. Small inhomogeneous broadening of excitonic transitions combined with a strong Coulomb interaction (5 times stronger than in GaAs-based QWs) allows us to suggest these structures as model objects for the investigation of exciton-electron interaction phenomena in semiconductors.

The high-quality structures for this study were grown at the University of Würzburg by J. Nurnberger, W. Faschinger, M. Keim, G. Reuscher and A. Waag. This work was supported in part by the mutual grant of Russian Foundation for Basic Research (98-02-04089) and the Deutsche Forschungsgemeinshaft (Os98/5 and 436Rus113/428) as well as by the NATO grant HTECH.LG 974702.

References

[1] M. A. Lampert, *Phys. Rev. Lett.* **1**, 450 (1958).
[2] K. Kheng et al., *Phys. Rev. Lett.* **71**, 1752 (1993).
[3] G. Finkelstein and I. Bar-Joseph, *Il Nuovo Cimento* 17D, 1239 (1995).
[4] R. T. Cox et al., *Acta Physica Polonica A* **94**, 99 (1998).
[5] A. Haury et al., *Superlatt. & Microstruct.* **23**, 1097 (1998).
[6] A. J. Shields et al., *Phys. Rev. B* **52**, R5523 (1995).
[7] G. Finkelstein et al., *Phys. Rev. B* **53**, R1709 (1996).
[8] K. Kheng et al., *Superlatt. & Microstruct.* **15**, 253 (1994).
[9] A. V. Platonov et al., *Phys. Solid State* **40**, 745 (1998).
[10] W. Ossau et al., *Physica B* **256-258**, 323 (1998).
[11] A. A. Sirenko et al., *Phys. Rev. B* **56**, 2114 (1997).
[12] E. L. Ivchenko et al., *Phys. Rev. B* **46**, 7713 (1992).
[13] V. P. Kochereshko et al., *Proc. ICPS-23*, Berlin 1996 (World Scientific, 1996), p. 1943.
[14] S. Lovisa et al., *Phys. Stat. Sol. (a)* **164**, 175 (1997).
[15] G. V. Astakhov et al., this conference.
[16] T. Taliercio et al., *Phys. Rev. B* **58**, 15408 (1998).
[17] G. Finkelstein et al., *Phys. Rev. B* **53**, 12593 (1996).

7th Int. Symp. "Nanostructures: Physics and Technology"
St Petersburg, Russia, June 14–18, 1999

Polaron exciton in spherical quantum dot

I. P. Ipatova, A. Yu. Maslov and O. V. Proshina
Ioffe Physico-Technical Institute, St Petersburg, Russia

Abstract. The electron and hole polaron energies are found in a quantum dot made of the materials with high ionicity. It is shown that the energy of hole polaron is larger then the energy of electron polaron due to the degeneration of the valence band. Polaron energies increase with decreasing of the quantum dot radius. In the interband optical transitions, polaron effects are partly compensated, because electron and hole create the polarization potential wells with opposite signs in the process of optical transition. It is shown that there is no total compensation when the degeneration of the valence band structure is taken into account. Therefore the interband transitions are accompanied by the polarization of the medium. The polarization leads to the intensive phonon replicas of the electron transition and to the large Stokes shift of absorption and emission light.

Localization of charge particles in quantum dot results in considerable increase in electrostatic energy of particle interaction. Since longitudinal optical phonons in ionic crystals have also electrostatic nature, the enhancement of the electron–phonon interaction in nanostructures occurs. As a result, polaron effects increase also [1, 2].

If the polaron binding energy is less than the energy of size quantization in the dot, one has the strong confinement regime [3] when

$$\frac{a_0}{R} \gg 1. \tag{1}$$

Here a_0 is the polaron radius and R is the radius of spherical quantum dot.

The binding energies of electron and hole polarons and polaron exciton can be found by adiabatic approach based on parameter (1).

In zero approximation, the electron wave function and energy are defined by Schrödinger equation

$$\hat{H}_e \Psi_e^{(ln)} = \left[-\frac{\hbar^2}{2m_e} \nabla^2 + V_e(\mathbf{r}) \right] \Psi_e^{(ln)} = E_e \Psi_e^{(ln)}, \tag{2}$$

where $V_e(r)$ is the quantum dot potential energy for electron, l is the electron orbital quantum number and n is the radial quantum number. Since the energy in Eq. (2) does not depend on magnetic quantum number m, we do not label the wave function with m for simplicity.

The description of the hole is based on the Luttinger Hamiltonian

$$\hat{H}_h \Psi_h^{(FN)} = \left[\left(\gamma_1 + \frac{5}{2}\gamma \right) \frac{\hat{p}^2}{2m_0} - \frac{\gamma}{m_0} (\hat{p}\hat{j}) + V_h(\mathbf{r}) \right] \Psi_h^{(FN)} = E_h \Psi_h^{(FN)}. \tag{3}$$

Here $V_h(\mathbf{r})$ is quantum dot potential energy for hole,

$$\gamma_1 = \frac{m_0}{2} \left(\frac{1}{m_l} + \frac{1}{m_h} \right), \qquad \gamma = \frac{m_0}{4} \left(\frac{1}{m_l} - \frac{1}{m_h} \right),$$

m_l and m_h being light and heavy hole masses. The quantity j is the effective "spin" of the hole which is equal to 3/2 for typical semiconductors. [Spin–orbit interaction is not taken into account]. The hole wave functions are classified according to total angular momentum $\hat{F} = \hat{l} + \hat{j}$, where $\hat{l}$ is the orbital momentum of the hole. The quantity N is the radial quantum number.

Polaron states of the electron and the hole are described by the following Schrödinger equation

$$\left[\hat{H}_{e,h} + \sum_q \hbar\omega_q a_q^+ a_q + e\sqrt{\frac{2\pi\hbar}{V\varepsilon}} \sum_q \sqrt{\omega_q}\frac{1}{q}\left(a_q e^{i\mathbf{qr}} + a_q^+ e^{-i\mathbf{qr}}\right)\right]\Psi_{e,h} = E\Psi_{e,h}. \quad (4)$$

Here a_q, a_q^+ are the annihilation and creation phonon operators, $\varepsilon^{-1} = \varepsilon_0^{-1} - \varepsilon_\infty^{-1}$ is the optical dielectric permittivity, ω_q is the frequency of longitudinal optical phonon. The second term in Eq. (4) represents the phonon field and the third term is the electron–phonon interaction with longitudinal optical phonons. We consider the electron–phonon interaction to be strong. All three terms in Hamiltonian Eq. (4) have the same order of magnitude (Pekar polaron).

Adiabatic parameter Eq. (1) allows to make an average of Eq. (4) over the fast motion of the electron or hole in the quantum dot. One has for the electron Hamiltonian

$$\hat{H}_e^{(ln)} = E_{ln} + \sum_q \hbar\omega_q a_q^+ a_q + e\sqrt{\frac{2\pi\hbar}{V\varepsilon}} \sum_q \frac{\sqrt{\omega_q}}{q}\left[\rho^{(ln)}(q)a_q + \rho^{(ln)} * (q)a_q^+\right], \quad (5)$$

where $\rho^{(ln)}(q) = \int e^{i\mathbf{qr}}\left[\Psi^{(ln)}(\mathbf{r})\right]^2 d^3r$ is electron density. The unitarian transformation

$$U_e^{(ln)} = \exp\left[\sum_q \frac{e}{q}\sqrt{\frac{2\pi}{V\varepsilon\hbar\omega_q}}\left(\rho^{(ln)}(q)a_q^+ - \rho^{(ln)} * (q)a_q\right)\right], \quad (6)$$

allows to make the diagonalization of matrix $\hat{H}_e$ for Eq. (5)

$$\hat{H}_e^{(ln)} = E_{ln} - \frac{2\pi e^2}{V\varepsilon}\sum_q \frac{\left|\rho^{(ln)}(q)\right|^2}{q^2} + \sum_q \hbar\omega_q a_q^+ a_q. \quad (7)$$

Second term in Eq. (7) is the polaron renormalization of the electron energy

$$\Delta E_e^{(ln)} = -\frac{2\pi e^2}{V\varepsilon}\sum_q \frac{\left|\rho^{(ln)}(q)\right|^2}{q^2}. \quad (8)$$

Further calculations require the knowledge of electronic wave functions $\Psi^{(ln)}(\mathbf{r})$. They were obtained by Al. Efros and A. Efros [3]

$$\Psi_e^{(ln)} = \frac{J_l[C_n(l)r/R]Y_{lm}(\theta,\phi)}{\sqrt{J_{l+1}[C_n(l)]}}, \quad (9)$$

where $C_n(l)$ is nth root of lth spherical Bessel function $J_l(x)$, $Y_{lm}(\theta,\phi)$ is spherical function. Substituting the wave function Eq. (9) for spherical states with $l = 0$ in Eq. (8) results in

$$\Delta E_e^{(0n)} = -\frac{e^2}{2\varepsilon R}\,2\left(1 - \frac{Si(2n\pi)}{2n\pi} + \frac{Si(4n\pi)}{4n\pi}\right), \quad (10)$$

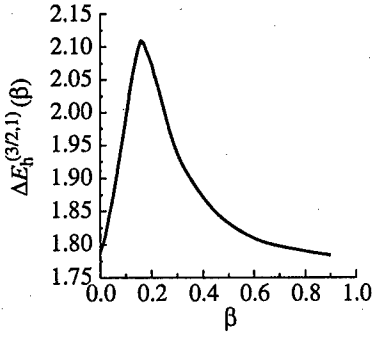

Fig. 1. The dependence of hole polaron energy on the mass ratio $\beta = m_l/m_h$.

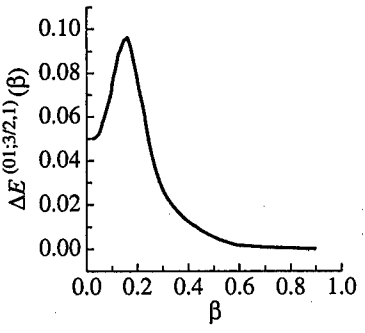

Fig. 2. The dependence of exciton polaron energy on the mass ratio $\beta = m_l/m_h$.

where $Si(x)$ is the integral sinus.

The polarization energy of the hole polaron $\Delta E_h^{(FN)}$ is calculated in a similar way from Eqs. (3) and (4). The wave function of the hole in the spherical dot is taken from [4]. The dependence of the hole ground state energy om the ratio of the light and heavy hole masses, $\beta = m_l/m_h$, is shown in Fig. 1.

The electron and the hole create in the interband optical transition their own potential polarization wells of opposite sign. Nevertheless, the degeneration of the hole band prevent the compensation of polaron effects. There appear the polarization quasiparticle which is called *polaron exciton* [5].

Under condition of strong confinement Eq. (1), the Coulomb interaction of the electron and the hole and their interaction with polar optical phonons are small with respect to the energy of size quantization. The wave function of the electron–hole pair is reduced to the product

$$\Psi(\mathbf{r}_e, \mathbf{r}_h) = \Psi_e^{(ln)}(\mathbf{r}_e)\Psi_h^{(FN)}(\mathbf{r}_h), \tag{11}$$

where wave functions $\Psi_e^{(ln)}(\mathbf{r}_e)$ and $\Psi_h^{(FN)}(\mathbf{r}_h)$ are defined by Eqs. (2) and (3), respectively.

Taking an average over the fast motion of the electron and the hole in a quantum dot and using the wave functions from [3, 4] one can find the polaron exciton energy

$$\Delta E^{(ln,FN)} = -\frac{e^2}{2\varepsilon R} B^{(ln,FN)}(\beta), \tag{12}$$

where dimensionless coefficients $B^{(ln,FN)}(\beta)$ depends on the ratio of light and heavy hole masses β. This dependence for optical transition between the electron ground state ($l = 0, n = 1$) and the hole ground state ($F = 3/2, N = 1$) is shown in Fig. 2. It is follows from Eq. (12) that exciton polaron energy $\Delta E^{(ln,FN)}$ decreases with R.

Polaron exciton in quantum dots manifest itself in multiple phonon replicas of the same intensity as electronic zero–phonon line and in the strong Stokes shift between the absorption and emission lines. Both effects were observed experimentally for A^2B^6 quantum dots in glassy matrix [6, 7].

The work was supported, in different parts, by Russian Foundation for Basic Research, Grant 98-02-18295, by Russian Federal Program "Leading Research Schools" grant 96.15-

96348, and by the Federal Program of the Ministry of Science and Technologies of Russia "Physics of Solid State Nanostructures", project 97-2014.

References

[1] I. P. Ipatova, A. Yu. Maslov and O. V. Proshina, *Phys. Solid State* **37**, 991 (1995).
[2] I. P. Ipatova, A. Yu. Maslov and O. V. Proshina, *Phys. Low–Dim. Structures* No 4–5, 1 (1996).
[3] Al. L. Efros and A. L. Efros, *Sov. Phys. Semicond.* **16**, 772 (1982).
[4] Al. L. Efros, *Phys. Rev. B* **46**, 7448 (1992).
[5] I. P. Ipatova, A. Yu. Maslov and O. V. Proshina, *Semicond.* **33**, (6) (1999).
[6] G. Scamarcio, V. Spagnolo, G. Ventruti, M. Lugara and G. C. Regnini, *Phys. Rev. B* **53**, R10489 (1996).
[7] V. Yungnickel, F. Henneberger and J. Puls, *Proc. 22 Int. Conf. Phys. Semicond.* vol. 3, p. 2011, (World Scientific, Singapore, 1994); V. Yungnickel and F. Henneberger, *J. Luminesc.* **70**, 238, (1996).

7th Int. Symp. "Nanostructures: Physics and Technology"
St Petersburg, Russia, June 14–18, 1999

Magnetooptics of the excitonic states in the shallow GaAs/AlGaAs quantum wells

N. N. Sibeldin†, *M. L. Skorikov*†, V. A. Tsvetkov† and B. Etienne‡
† Solid State Physics Division, P. N. Lebedev Physical Institute, Moscow, Russia
‡ Laboratoire de Microstructures et de Microelectronique, CNRS, Banno, France

Abstract. Photoluminescence (PL) and photoluminescence excitation (PLE) spectra of asymmetric two-well GaAs/$Al_{0.05}Ga_{0.95}As$ structures with tunnel-isolated shallow quantum wells (QW) in magnetic field oriented both perpendicular and parallel to the layers were studied at liquid helium temperatures. In the PLE spectra we observed the lines, which most probably correspond to absorption by excitons, formed by a QW localized carrier and a free carrier of opposite sign, attracted by the Coulomb force. Clear indication of effective excitation transfer between the wide and narrow wells of the structure was observed, which is apparently due to the resonant excitation of the light-hole excitons in the wide well by recombination radiation from heavy-hole excitons in the narrow well.

The nature of electronic states in the structures with shallow quantum wells (QW) that have a single confined state for each type of quasiparticles, is an interesting subject to study. For instance, in type-I structures with shallow wells, additional bound states of excitonic type, formed due to the Coulomb attraction between the charge carriers, one of which resides in the quantum-confined state, and the other one in the continuum, should gain importance due to the limited number of singleparticle discrete levels in such a system. Similar states (the "Coulomb-well excitons") were observed in the structures close to type I – type II transition (i.e., those with nearly zero band offset for one type of the carriers) [1, 2]. It is also convenient that for low-barrier structures the tuning range of the Ti-sapphire laser is quite enough to study both confined and unconfined states by the photoluminescence excitation (PLE) spectroscopy technique.

In this work, we studied the spectra of photoluminescence (PL) and PLE of GaAs/$Al_{0.05}Ga_{0.95}As$ double-well structures, grown by MBE technique at the Laboratoire de Microstructures et de Microelectronique, (Banno, France). Wide and narrow QWs of width $w_1 = 40$ Å, and $w_2 = 30$ Å were separated by the tunnel-untransparent barrier of width $b = 600$ Å. For aluminium concentration in the barrier layer $x = 0.05$, the depth of the potential well for electrons is nearly 45 meV, that for holes is about 30 meV. The PL was excited and PLE spectra were taken with the use of a Ti-sapphire laser. Magnetic field up to 5.5 T was created by a superconducting solenoid. The sample temperature was held at 2 K.

The zero-field PL and PLE spectra are shown in Fig. 1. In the PL spectrum, two narrow lines HH_1 and HH_2 are present; obviously, they correspond to the recombination of heavy-hole excitons in the wide and narrow well, respectively. The PLE spectra were taken by setting the spectrometer approximately at the half-maximum position on the low-energy side of either HH_1 or HH_2 peak. In the absence of any coupling between the wells, one should obtain in these two cases the spectra, typical for the single QWs of corresponding width. Both experimentally observed spectra contain the expected lines, corresponding to excitation of heavy- and light-hole excitons in the wide and narrow QWs (HH_1, LH_1, and

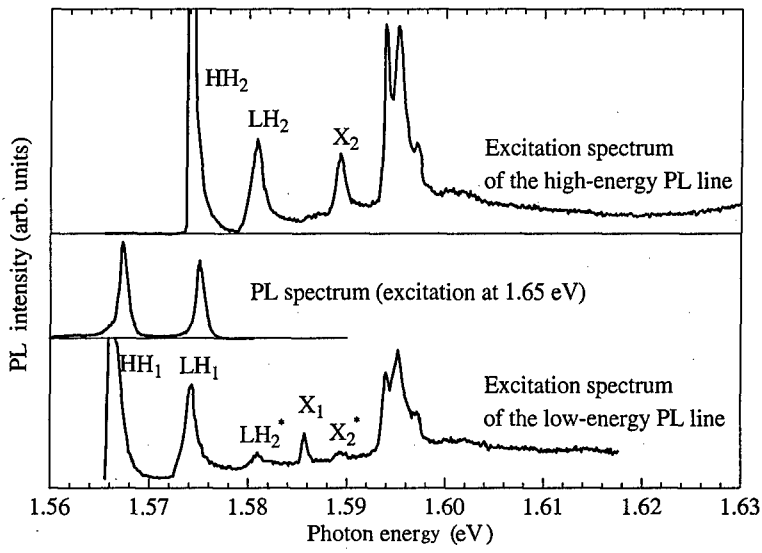

Fig. 1. PL and PLE spectra at zeromagnetic field

HH_2, LH_2, respectively). Besides, one can clearly see additional lines X_1, X_2^*, and LH_2^* in the wide-well, and X_2 in the narrow-well spectra; both spectra contain an intense triplet at 1.593–1.598 eV, as well. Comparing the two PLE spectra in Fig. 1, one can conclude that the energy of the heavy-hole exciton transition HH_2 in the narrow QW nearly coincides with that of the light-hole exciton transition LH_1 in the wide QW ($h\nu \simeq 1.574$ eV). Also, transitions into the excited states of the heavy-hole excitons in each well fall within the corresponding light-hole exciton line; this can be seen from the PLE spectra taken under magnetic field applied perpendicular to the layers (Fig. 2). Magnetic-field dependencies of the energies of the transitions into the $2s$, $3s$, and $4s$ heavy-hole exciton states in each well are outlined there by thin solid lines. Extrapolation to zero field gives the energies of these transitions in the absence of magnetic field, which enabled us to evaluate the binding energies of the heavy-hole excitons in the narrow and wide QWs as 6.4 and 7.2 meV, respectively.

Let us now consider the nature of the additional lines in the PLE spectra (leaving out the discussion of the above-mentioned triplet structure, because this requires extra studies). First, it can be seen from the comparison of the zero-field spectra in Fig. 1 that the line X_1 at $h\nu \simeq 1.586$ eV in the PLE spectrum of the wide QW is related to the state localized in that well, because it is absent in the narrow-QW spectrum. As no transitions between the confined states of electrons and holes, apart from those discussed above, can be expected in our shallow QWs, we believe that this line correspond to the transition between the confined state of one type of particles (most probably, electron) and the unconfined state of the oppositely charged particle. More exactly, an excitonic state should be formed, in which, say, electron resides in the confined state within the QW, and the hole (with single-particle energy above the barrier) is localized near this well by the Coulomb attraction to the electron. Thus, the electron, constituting such an exciton will be quasi-twodimensional, while the hole state will be closer to a three-dimensional one. The fact that the diamagnetic shifts of the HH_1 and X_1 lines in perpendicular field are of the same order of magnitude

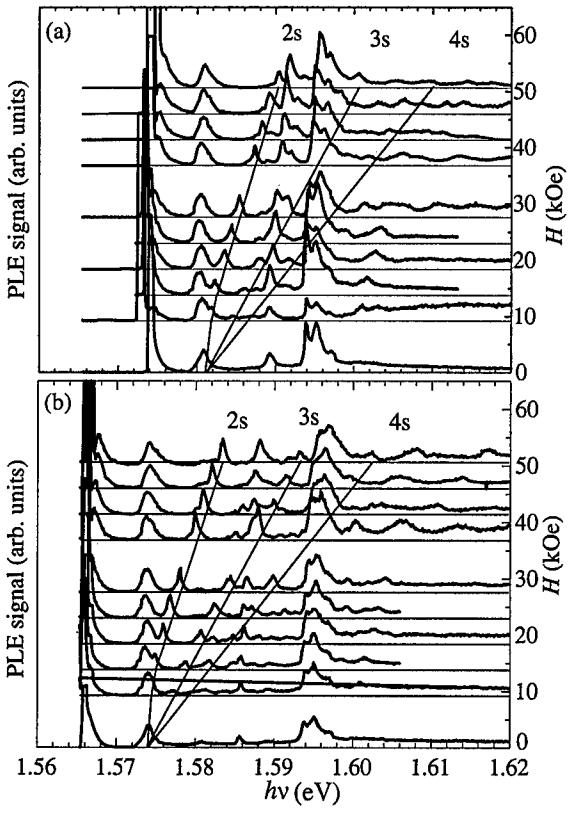

Fig. 2. Excitation spectra of the narrow-well (a) and the wide-well (b) in perpendicular magnetic field. All spectra are normalized to the respective LH peaks. The vertical shift of the curves is proportional to the field strength at which they were taken (right-hand scale).

(about 1.4 and 2.4 meV in the perpendicular field of $H = 5$ T, respectively) seems to corroborate indirectly our interpretation of the nature of the latter. Apparently, the X_2 line in the narrow-well PLE spectrum, whose intensity is comparable to that of the light-hole exciton line, is of the same nature. The diamagnetic shifts of the peaks HH_2 and X_2 in perpendicular field of $H = 5$ T are 1.4 and 2.6 meV, respectively.

Two lines, LH_2^* and X_2^*, in the PLE spectrum of the wide QW coincide very well in their spectral position with the two lines in the narrow QW spectrum, LH_2 and X_2, respectively, although the intensities of the former are significantly lower (Fig. 1). Appearance of the coinciding peaks in the PLE spectra of the two QWs indicates the existing of some sort of coupling between the wells. Tunneling coupling is unfeasible because of the large thickness of the separating barrier ($b = 600$ Å). Non-relevance of the tunneling coupling is further confirmed by the weak influence of the inplane magnetic field, which should reduce the rate of tunneling between the QWs [3, 4], on the intensities of LH_2^* and X_2^* peaks (Fig. 3). Meanwhile, application of the field perpendicular to the layers result in obvious quenching of these peaks (see Fig. 2(b)). We suppose that the most probable explanation of this quite efficient coupling between the wells is the occurence of the resonant excitation of the light-hole excitons in the wide QW (with their further relaxation into heavy-hole excitonic

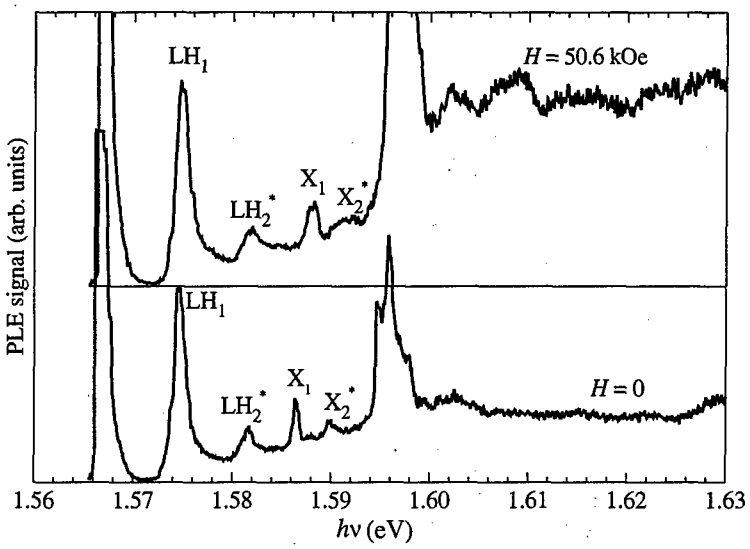

Fig. 3. Influence of the parallel magnetic field on excitation spectrum of the wide-well PL

states) by the recombination radiation emitted by the heavy-hole excitons in the narrow well. As it has been pointed out above, the energies of these two transitions are virtually the same. Under application of perpendicular magnetic field, the difference in diamagnetic shifts results in the detuning of resonance (cf. Figs. 2(a) and 2(b)); in the parallel field, the diamagnetic shifts of both lines are small, and the resonance is conserved.

This work was partially funded by the Russuan Foundation for Basic Research (project No 96-02-18237), Russian Ministry of Science and Technology through the Programs "Physics of Solid-State Nanostructures" (No 97-1050) and "Fundamental Spectroscopy" (No 2.6), and the State Program of Support for the Leading Scientific Schools (No 96-15-96341).

References

[1] J. Warnock, B. T. Jonker, A. Petrou et al., *Phys. Rev. B* **48**, 17321 (1993).
[2] A. V. Kavokin, M. A. Kaliteevski, S. V. Goupalov et al., *Phys. Rev. B* **54**, 11078 (1996).
[3] A. I. Filin, K. v. Klitzing, I. V. Kukushkin et al., *Pis'ma v Zh. Eksp. Teor. Fiz.* **61**, 684 (1995).
[4] M. L. Skorikov, I. I. Zasavitskii, I. P. Kazakov et al., *Pis'ma v Zh. Eksp. Teor. Fiz.* **62**, 500 (1995).

7th Int. Symp. "Nanostructures: Physics and Technology"
St Petersburg, Russia, June 14–18, 1999

Exciton relaxation and quantum mechanical level repulsion

Erich Runge and Roland Zimmermann
Physics Department, Humboldt-University, D-10099 Berlin, Germany

Abstract. Theoretical results for spatially resolved exciton spectra of quantum wells with disorder are discussed. As a consequence of quantum mechanical level repulsion, the autocorrelation of the sharp peaks corresponding to individual quantum states yields information on their spatial extent. Level repulsion is present not only in the density of states but as well in absorption and even luminescence. More generally, the question under what conditions level repulsion can be observed in disordered systems with localized states is addressed.

Introduction

Recent years have seen a strong interest in spatially resolved spectra from both microphotoluminescence (μPL) and near-field scanning optical microscopy (NSOM). The inhomogeneously broadened macroscopic luminescence is resolved into often hundreds of narrow lines with widths of a a few tens of μeV, compatible with the radiative broadening [1]. We show that a statistical analysis of their autocorrelation allows to "measure the size of the wave functions".

First, we discuss in Sec. 1 the phenomenon of level repulsion. In order to study luminescence, we discuss in Sec. 2 the relaxation kinetics of excitons. An illustrative example is given in Sec. 3.

1 Level repulsion in quantum mechanical systems

It was understood early in the development of quantum mechanics that eigenenergies repel each other. Textbook examples include the avoided crossing of two levels as function of an external parameter and random matrix theory [2]. Eugene Wigner and Freeman Dyson proposed the latter as statistical description for spectra of highly excited nuclei. For the model of large Hamilton matrices with randomly chosen matrix elements, they could show that the probability to find a small level spacing is reduced by a factor

$$C_\rho(E) = \left\langle \sum_{m,n} \delta(E - \epsilon_m + \epsilon_n) \right\rangle \sim \left| \frac{E}{\Delta_\rho} \right|^\beta \tag{1}$$

with the average level distance Δ_ρ and an integer exponent $\beta = 1, 2, 4$ depending on the time-reversal properties of the system. For exciton spectra in the absence of magnetic fields, we have real orthogonal matrices (Gaussian Orthogonal Ensemble, GOE) and consequently $\beta = 1$.

If, in contrast to the random matrix model where each state interacts with every other state, the system is composed of M independent compartments not interacting with each other, the level repulsion effect is reduced by a factor $1/M$

$$C_\rho(E) \sim \left(1 - \frac{1}{M}\right) + \frac{1}{M} \left| \frac{E}{\Delta_\rho} \right|^\beta . \tag{2}$$

1.1 Localization and level repulsion

The absence or presence of level repulsion has been proven recently as a very valuable tool in the analysis of numerical simulations for the Anderson localization transition [3]. Thus it might be questionable to look for level repulsion in spatially resolved spectra of two dimensional excitons at all.

We will now argue, that at least three different scenarios allow to see level repulsion in localized systems, in spite of the statement of Eq. (2).

(i) Spatially resolved excitation or detection: μPL or NSOM experiments excite excitons only in a region A_{det} which is not much larger than the area $A_{\rm loc}$ of the excitons center-of-mass wavefunction. Eq. (2) becomes

$$C_\rho(E) \sim \left(1 - \frac{A_{\rm loc}}{A_{\rm det}}\right) + \frac{A_{\rm loc}}{A_{\rm det}} \left|\frac{E}{\Delta_\rho}\right|^\beta \tag{3}$$

which allows to estimate $A_{\rm loc}$.

(ii) Matrixelement-weighted correlations: Many physical processes are determined not by correlations of energy levels, i.e., by the probability to find a given energy spacing, but by the combination of energy spacing and large transition matrix elements. Combinations such as $\left\langle \sum_{m,n} |M_{mn}|^2 \delta(E - \epsilon_m + \epsilon_n) \right\rangle$ can show level repulsion even in disordered systems, because near-degeneracies between spatially well separated regions do not contribute due to vanishing matrix elements [4].

(iii) Expectation values whose uncorrelated part vanish: If the dominant contribution vanishes, the $1/M$ term can survive. Generally, susceptibilities have this form. This has been used by Mott in his classical estimate for the susceptibility of the Anderson insulator. Recently, it has been pointed out that the long-time Rayleigh-scattering signal is of this type. The average electric fields vanish and only the correlated part survives [5].

According to *(i)*, level repulsion should be present in a spatially resolved density of states (DOS). Actual experiments almost exclusively measure luminescence, which differs from DOS in two aspects. First, only optically active states with a large zero-momentum content contribute. Second, luminescence spectra reflect the relaxation kinetics. Low-lying states carry a large weight in luminescence. Both aspects can be expected to decrease the amount of level repulsion: Optical active states are rare and thus one would expect it to be improbable that two states close in energy are both optically active. This effect should already be present in spatially resolved absorption spectra, if they could be measured. Regarding relaxation, one could at low temperature imagine a scenario of only local minima being populated and one might expect local minima to be well separated and thus non-interacting. These two arguments show that a detailed analysis for specific samples and temperatures is needed which includes both optical matrix elements and relaxation kinetics.

2 Relaxation kinetics

We discuss relaxation in terms of a kinetic equation for the occupation N_α of the disorder eigenstates ψ_α [6]:

$$\partial_t N_\alpha = g_\alpha + \sum_\beta \gamma_{\alpha \leftarrow \beta} N_\beta - \left(r_\alpha + \sum_\beta \gamma_{\beta \leftarrow \alpha}\right) N_\alpha \tag{4}$$

with generation rates g_α, radiative recombination r_α, and acoustic phonon scattering rates $\gamma_{\beta \leftarrow \alpha}$ [7]. The generation rate is determined by the specific experimental set-up. All other rates are calculated from numerically determined disorder eigenfunctions.

We focus here on deformation potential scattering involving acoustic phonons ($E = \hbar\omega_q = \hbar uq$), which is thought to dominate the exciton relaxation at least in the III-V materials at low, but not extremely low temperatures where piezoelectric scattering becomes relevant. The factorization approximation for the wave function,

$$\Psi(\vec{r}_e\,\vec{r}_h) = \psi_\alpha(\vec{\rho})\,\varphi_{1s}(\vec{r})\,u_e(z_e)\,u_h(z_h)\ , \tag{5}$$

has been shown to be applicable for typical III-V quantum wells [6].

Apart from thermal phonon occupation, the main ingredient of the scattering rate $\gamma_{\beta\leftarrow\alpha}$ is the center of mass matrix element $\int \psi_\alpha(\vec{\rho})\,e^{i\vec{Q}\cdot\vec{\rho}}\,\psi_\beta(\vec{\rho})$. Similarly, the radiative rate can be written in the factorization approximation as

$$r_\alpha = \frac{4\,e^2\,p_{cv}^2\,n\,E_X}{3\,\hbar^2\,c^3}\,\varphi_{1s}(0)^2\,\langle u_e|u_h\rangle^2\,M_\alpha^2 \tag{6}$$

with the momentum matrix element $p_{cv} = \langle s|\hat{p}|p_z\rangle$, index of refraction n, and exciton energy E_X. A reduction by scattering into dark exciton states is not included here. The confinement wave function overlap $\langle u_e|u_h\rangle$ typically is close to unity for the dominant transition. For strongly localized excitons (neglect of the finite photon momentum and thus polariton effects [8]) the center of mass part of (6) reduces to [9]

$$M_\alpha = \int d^2\vec{\rho}\ \psi_\alpha(\vec{\rho})\ . \tag{7}$$

3 Results

An illustrative example for the solution of Eq. (4) and the resulting autocorrelation is given in Fig. 1. A rather small detection area of 120 nm × 120 nm corresponding to a good NSOM resolution is used. Averaging of the order of 250 spectra should be enough to give a well defined level repulsion dip at small energy difference. Required is however a very good energy resolution of the spectrometer. An almost complete level repulsion such as seen

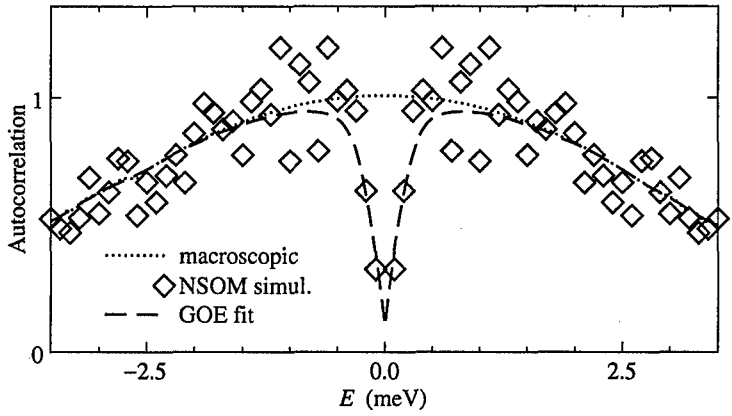

Fig. 1. Simulated spectral autocorrelation for luminescence from 250 NSOM quantum well spectra, each corresponding to an area 120×120 nm. Parameters of a 5 nm wide GaAs/$Al_{.3}Ga_{.7}As$ quantum well with disorder strength $\langle v^2\rangle^{1/2} = 8$ meV are used. GOE-fit (dashed) to the simulation data (diamonds) and corresponding fit to the autocorrelation of the sum of all spectra (macroscopic spectrum) (from Ref. [11].

in Fig. 1 implies, c.f. Eq. (2,3), that almost all wave functions within the detection area interact with each other and A_{loc} is only slightly smaller than A_{det}. This is confirmed by direct analysis of the numerically determined wave functions.

Acknowledgements

This work was financially supported by the Deutsche Forschungs Gemeinschaft in the frame of Sfb 296.

References

[1] H. F. Hess, E. Betzig, T. D. Harris, L. N. Pfeiffer and K. W. West, *Science* **264**, 1740 (1994).
[2] M. L. Mehta, *Random Matrices*, 2. ed., San Diego: Academic Press, 1990.
[3] Proc. of PILS98, ed. Schreiber, M. *Annalen der Physik (Leipzig)* **7** (1998).
[4] E. Runge and R. Zimmermann, in Ref. [3], p. 417.
[5] V. Savona and R. Zimmermann, *Time-resolved Rayleigh scattering of excitons: Evidence for level repulsion in a disordered system*, preprint, 1999.
[6] E. Runge and R. Zimmermann, *Optical properties of localized excitons in nanostructures: Theoretical aspects*, appears in: *Festkörperprobleme / Advances in Solid State Physics* 1998; and references therein.
[7] T. Takagahara, *Phys. Rev. B* **31**, 6552 (1985).
[8] L. C. Andreani, F. Bassani and F. Tassone, in *Optics of Excitons in Confined Systems*, p. 25. (IOP Conference Series Number 123, ed., D'Andrea A., Del Sole R., Girlanda R. and Quattropani A., Bristol, IOP, 1992.
[9] U. Bockelmann, *Phys. Rev. B* **48**, 17637 (1993).
[10] E. Runge and R. Zimmermann, *phys. stat. solidi (b)* **206**, 167 (1998).

7th Int. Symp. "Nanostructures: Physics and Technology"
St Petersburg, Russia, June 14–18, 1999

Temperature-dependent exciton dynamics in quantum wells

S. D. Baranovskii†, H. Cordes†, R. Eichmann‡ and P. Thomas‡
Institute for Physical Chemistry(†) and Department of Physics(‡),
Material Sciences Centre, Philipps-University Marburg,
D-35032 Marburg, Germany

Excitons in quantum wells (QWs) suffer from the disorder potential present in QWs due to the interface roughness and also due to compositional fluctuations in the case of alloy QWs. Numerous studies of optical properties of excitons, in particular of the photoluminescence (PL) have been performed with the aim to characterise the disorder and hence the quality of QWs. Theoretical study in this field is however far behind the experimental and technological progress. To describe the PL properties, it is not sufficient to know the energy distribution of localised states for excitons (DOS) because excitons can move between localised states and the energy distribution of recombining excitons does not coincide with their DOS. The exciton dynamics can be strongly influenced by temperature, as has been shown in various experimental studies. This dynamics is especially pronounced in coupled QWs, where excitons have long lifetimes (see, e.g., [1–4]). Two different models have been treated theoretically in order to describe the dynamics of excitons in coupled QWs. In the first model, excitons were considered as single particles and their hopping relaxation has been studied by a computer simulation [5]. In the second model, temperature-dependent recombination of spatially separated electrons and holes has been studied within particular analytical approximations [3]. None of these models is able to account for the whole variety of experimental data related the temperature-dependent PL of excitons in coupled QWs.

In this report, we discuss the relation between experimental results and theoretical models suggested so far for the temperature-dependent energy relaxation and recombination of excitons in coupled QWs. Physical conditions are discussed that favour each class of theoretical models.

References

[1] T. Fukuzawa, E. E. Mendez and J. M. Hong, *Phys. Rev. Lett.* **64**, 3066 (1990).
[2] J. A. Kash, M. Zachau, E. E. Mendez, J. M. Hong and T. Fukuzawa, *Phys. Rev. Lett.* **66**, 2247 (1991).
[3] V. B. Timofeev, A. V. Larionov, A. S. Ioselevich, J. Zeman, G. Martinez, J. Hvam and K. Soerensen, *Pisma ZhETF* **67**, 580 (1998).
[4] V. B. Timofeev, A. I Filin, A. V. Larionov, J. Zeman, G. Martinez, J. Hvam, D. Birkendal and C. B. Soerensen, *Europhys. Lett.* **41**, 535 (1998).
[5] S. D. Baranovskii, R. Eichmann and P. Thomas, *Phys. Rev. B* **58**, 13081 (1998).

7th Int. Symp. "Nanostructures: Physics and Technology"
St Petersburg, Russia, June 14–18, 1999

Luminescence of HH-excitons in GaAs/GaAlAs superlattices under resonant excitation

Yu. K. Dolgikh†, S. A. Eliseev†, *I. Ya. Gerlovin*†, V. V. Ovsyankin†,
Yu. P. Efimov‡, I. V. Ignatiev‡, I. E. Kozin‡, V. V. Petrov‡, V. Pantukhin‡
and Y. Masumoto¶

† Vavilov State Optical Institute, St Petersburg, Russia
‡ Institute of Physics, St Petersburg State University, Russia
¶ Single Quantum Dot project, ERATO, JST, Japan

Abstract. The spectra and kinetics of photoluminescence decay of GaAs/GaAlAs superlattice were measured under resonant excitation in the temperature range of 5–40 K. A narrow peak resonant with the frequency of excitation radiation was found in the luminescence spectra. This peak can be attributed to the resonant luminescence of excitons. The exciton radiative recombination rate and its dependence on temperature were determined experimentally.

Introduction

The probability of radiative recombination of free excitons in quasi-2D structures (quantum wells and superlattices) is proportional to the number of sites in a crystal lattice participating in collective excitation, i.e. it is determined by the exciton coherence length. According to theoretical estimations [1, 2], in an ideal heterojunction, where this length is limited only by the wavelength of radiation, the time of exciton radiative recombination in GaAs quantum wells is of the order of several picoseconds. These estimates were confirmed by recent pump-probe experiments on high quality GaAs/AlAs superlattices [3]. In the structures of lower quality, the scattering on interface inhomogeneities and internal defects leads to a reduction of exciton coherence length and finally results in its localization. The localization of excitons in GaAs quantum wells was observed in experiments on four-wave mixing [4]. According to the above statements, the radiative recombination rate is defined by the exciton coherence length. This means that a degree of excitons localization in the structure could be directly estimated by the measurement of the excitonic luminescence kinetics. Modern high-speed techniques allow us to perform such measurements in real time, which simplifies the experiments and makes their interpretation more reliable. Such experiments were performed on GaAs/AlAs structures under nonresonant excitation [5].

1 Experimental

In this paper we present a study of luminescence spectra and its kinetics in the GaAs/GaAlAs superlattice under resonant excitation. We investigated a structure of standard quality, grown by solid-source molecular-beam epitaxy (MBE) without interruption on heterointerfaces. The structure consisted of 50 periods of the superlattice 3.0 nm GaAs/3.8 nm $Ga_{0.56}Al_{0.44}As$. Photoluminescence (PL) was excited with a tunable Ti-sapphire laser with a pulse duration of about 7 ps. The resultant PL was dispersed by a double-grating spectrometer (U1000) with a photon counting system. We used a streak-camera for registration

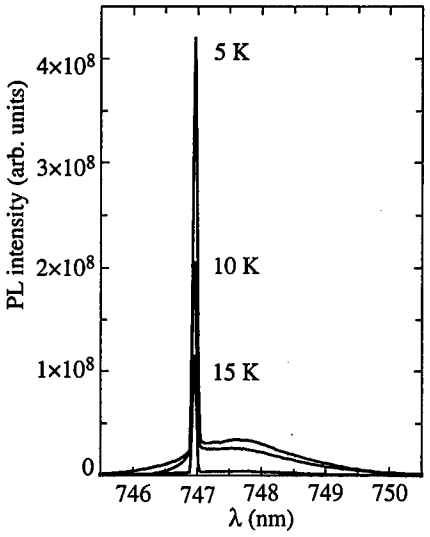

Fig. 1. Temperature-dependent PL spectra (λ_{exc} = 747 nm)

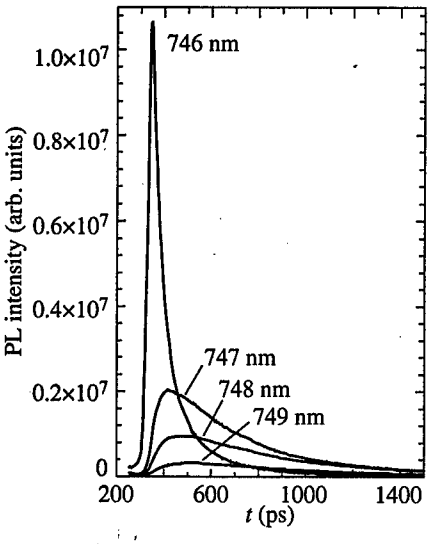

Fig. 2. Time-resolved PL spectra at different detection energies of excitonic band (λ_{exc} = 746 nm)

of luminescence kinetics and a double monochromator with zero dispersion for the spectral selection of PL. The time resolution of this setup was about 40 ps, and the spectral resolution was 0.2 nm.

2 Results and analysis

At low (5–10 K) temperatures the sample exhibits very strong PL with a single excitonic line at ≈ 1638 meV with a half-width of 4.5 meV. The photoluminescence excitation spectrum (PLE) also has an excitonic peak with almost the same half-width (5 meV) and is shifted to a high-frequency range by 3 meV. The Stokes shift comparable to the linewidth indicates a significant inhomogeneous broadening of an excitonic band. The luminescence spectrum under selective resonant excitation is presented in Fig. 1. In addition to the wide band of excitonic luminescence, a narrow peak was observed, the spectral position of which coincides with the frequency of the pumping light. The peak width is equal to the spectral resolution of the registration system. When the temperature increases to 40 K (Fig. 1) the luminescence completely disappears, and the intensity of the narrow peak significantly decreases. It is clear that, at this temperature, the PL is completely quenched and only scattered laser radiation is registered. Since the efficiency of scattering should not depend on temperature, the essential enhancement of the narrow peak intensity at low temperature can be interpreted as a result of a resonant luminescence, spectrally coincident with the laser radiation.

This conclusion was confirmed by the results of time-resolved measurements in which the kinetics of PL as a function of detection wavelength was measured. As is shown in Fig. 2, the PL intensity has a distinctly asymmetric shape—a sharp forward front and a longer tail. Under the resonance conditions, when the excitation and detected wavelengths coincide, the PL response has the shortest duration; however, its decay time still considerably exceeds the time resolution of the recording system.

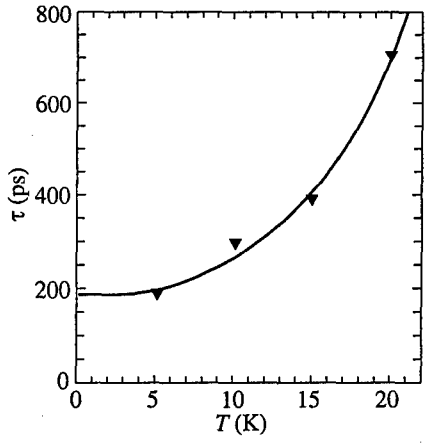

Fig. 3. Temperature dependence of the radiative recombination rate.

From the above discussion it follows that the main contribution to the signal at the resonant frequency is from the luminescence of the sample rather than from a scattered laser radiation. Thus, the narrow luminescence peak is caused by the radiation of excitons resonantly selected from an inhomogeneously broadened band by the excitation radiation. The luminescence kinetics in a wide excitonic band is characterized by the delayed forward front and greatly extended tail. This behaviour of the PL decay is a characteristic attribute of spectral diffusion. The rather high integral intensity of the narrow peak means that the radiative recombination rate under resonant conditions ($1/\tau_r$) does not concede to the rate of the spectral diffusion ($1/\tau_{sd}$). The relaxation time of a resonant PL (τ) which can be obtained experimentally is determined by the equation:

$$1/\tau = 1/\tau_r + 1/\tau_{sd}.$$

The ratio of the integral intensity of the narrow peak to the total luminescence intensity is represented by:

$$I_r/I = (1/\tau_r)/(1/\tau_r + 1/\tau_{sd}).$$

The analysis of the spectral and kinetic measurements provides the value of the exciton radiative recombination rate in the sample to be $1/\tau_r = 1/200$ ps^{-1}. As was mentioned above, the radiative recombination rate strictly corresponds to the exciton coherence length (r_{coher}):

$$\tau_r/\tau_{r0} = (\lambda/r_{coher})^2,$$

where $\lambda = 200$ nm is the wavelength of the resonant radiation in GaAs. Experimentally determined τ_r corresponds to the $r_{coher} = 30$ nm, which is larger than an excitonic Bohr radius in the structure $a_B = 10$ nm.

Based on the above results, we can conclude that the excitons in the studied sample are not totally localized, however, at low temperature, the efficiency of the energy exchange between the excitons, specifying the rate of the spectral diffusion, is not too high.

As the temperature increases, both the relaxation time and PL intensity decrease, which indicates the presence of an additional channel of nonradiative degradation of excitation. At the same time, the analysis shows (see Fig. 3), that with increasing temperature, the exciton radiative recombination rate decreases. The decrease of the 2D-exciton's radiative

recombination rate with temperature was observed by several authors [6–8]. However, up to now these results have no unambiguous interpretation. According to [6, 7], the main reason for this effect is thermal population of nonradiative excitonic states characterized by large magnitudes of the wavevector. Theoretical evaluation predicts, for this case, a linear temperature dependence of τ_r [6], which does not agree with our experimental data (see Fig. 3). Another reason for the increase of τ_r is a decrease of the exciton coherence radius as a result of scattering of excitons by thermal phonons [8]. In this case, the temperature dependence of τ_r can be described by the relation:

$$\tau_r(T) = \tau_r(0)/[1 - A\exp(E_{ph}/kT)].$$

Here, E_{ph} is the energy of the scattered phonon, and the coefficient A is specified by the exciton-phonon coupling. The dependence calculated using this relationship (solid line in Fig. 3) is in excellent agreement with the experimental results (The value E_{ph}, used as a fitting parameter, is about 13 cm^{-1}). Thus, we can conclude that the growth of τ_r with temperature, in our sample, is determined by the exciton-phonon scattering, which reduces the radius of the exciton coherence.

Acknowledgments

The work is supported by Russian Foundation for Basic Research.

Authors are very appressiate to Dr. Nazvanova for a fruitful discussion.

References

[1] E. Hanamura, *Phys. Rev. B* **38**, 1228 (1988).
[2] L. C. Andreani, F. Tassone and F. Bassani, *Solid State Comm.* **77**, 641 (1991).
[3] Yu. K. Dolgikh, *et al*, Proc. *Nanostructures: Physics and Technology*, St Petersburg, p. 370, 1998.
[4] J. Hegarty, L. Goldner and M. D. Sturge, *Phys. Rev. B* **30**, 7346 (1984).
[5] Y. Masumoto, S. Shionoya and H. Kawaguchi, *Phys. Rev. B* **29**, 2324 (1984).
[6] F. Bassani and F. Tassone, *Proc. Int. Conf. Physics of Semiconductors* ed. P. Jiang and H. Z. Zheng. World Scientific, Singapore, p. 1108 (1992).
[7] J. Martinez-Pastor, A. Vinattieri, L. Carraresi et al., *Phys. Rev. B* **47**, 10455 (1993).
[8] J. Feldmann, G. Peter, E. O. Gobel et al., *Phys. Rev. Lett.* **59**, (20) 2337 (1987).

7th Int. Symp. "Nanostructures: Physics and Technology"
St Petersburg, Russia, June 14–18, 1999

Simulation of nanostructures excitonic spectra in an electric field

O. L. Lazarenkova and A. N. Pikhtin
St Petersburg Electrotechnical University
Prof. Popov st. 5, St Petersburg, 197376, Russia

In the most cases the modern quantum electron devices of nanoelectronics and optoelectronics are based on properties of nanostructures in an electric field. The excitonic effects are of considerable importance in the properties of these structures. It is a matter of common knowledge now and it is a reason why consideration of electric field effects on excitonic states in imperfect quantum wells is of great interest.

In general, any quantum system in electric field has continious energy spectrum, but well-known and rather simply formulas describe optical transitions only between discrete energy levels [1, 2]. The approximation of weakly interacted quantum states makes it possible to simulate in an electric field continuous electron spectrum of quantum well by Breit–Wigner resonances [3]. Therefore one can use formulas, which deal with optical transitions between quasi bound states with finite broadening. For example multiple quantum well absorption coefficient taking into account both discrete and continuous excitonic spectrum is given by

$$\alpha(\omega) = \sum_{nm} \frac{q^2 E_p \xi_m}{\pi^2 \varepsilon_0 n_\omega c m_0 \omega a_B^2 \Lambda} \left|\langle \chi_n^e | \chi_m^h \rangle\right|^2 \times \left\{ \sum_{k=1}^{\infty} \left[\hbar \Gamma_{nm} (2k-1)^{-3}\right] \left[\left(E_{nm} - \frac{R_{nm}}{(2k-1)^2} - \hbar\omega\right)^2 + (\hbar\Gamma_{nm})^2\right]^{-1} + \frac{1}{4R_{nm}} \int_{E_{nm}}^{\infty} \frac{\hbar\Gamma_{nm}}{(\hbar\omega - \varepsilon)^2 + (\hbar\Gamma_{nm})^2} \frac{\mathrm{d}\varepsilon}{1 + \exp\left(-2\pi\sqrt{\frac{\varepsilon - E_{nm}}{R_B}}\right)} \right\} \quad (1)$$

where a_B denotes the bulk material of quantum well Bohr radius; n_ω denotes refractive index; Λ denotes the effective absorption width; $E_p = 2/m_0 |\langle S|p_x|X\rangle|^2$ is related with interband matrix element of the velocity operator; $|\langle \chi_n^e | \chi_m^h \rangle|^2$ defines the probability of optical transition between n-th electron and m-th hole states; R_{nm} is a binding energy of nm exciton; $\Gamma_{nm} = \Gamma_n + \Gamma_m + \Gamma_T$, where Γ_T denotes the broadening caused by the exciton-phonon interaction; $E_{nm} = E_g + E_n + E_m$ is an energy of transition between n-th electron and m-th hole states; factor ξ_m depends on light polarization and for normal incidence equals to 1 for heavy hole and 1/3 for light hole.

The field dependence of absorption coefficient may be contained in four parameters, namely E_{nm}, Γ_{nm}, $\left|\langle \chi_n^e | \chi_m^h \rangle\right|^2$, and R_{nm}. For weakly coupled quantum wells R_{nm} depends on electric field much less then E_{nm} does [4]. Consequently we will consider only the first three parameter field dependences.

To universalize the results of our calculations all field dependences are presented in dimensionless form. We purpose to measure electric field in units of

$$F_0 = \frac{V - E_n(0)}{qL}, \quad (2)$$

because of just the distance between energy level and top of well defines its behavior in the field. Here and then L will be the unit of coordinate, and $E_1^{\infty} = (\pi^2\hbar^2)/(2m^*L^2)$ will be the unit of energy. The origin of quasi bound states energies is taken in the center of well bottom.

Field dependences of quasi bound states energies and homogeneous broadening are presented in [3] for different dimensionless well depths. In the presented paper we pay the most attention to the field dependence of excitonic optical transition probability.

Field dependence of excitonic optical transition probability

For calculation of matrix element $\left|\langle\chi_n^e|\chi_m^h\rangle\right|^2$ as a function of electric field it is necessary to use in Eq. (2) the energy $E_n(0)$ of the most closed to continuum in the zero field state. For definition we have purposed that $\Delta E_c/\Delta E_g = 0.5$, $m_{hh} = 10m_e$, $m_{lh} = m_e$. The field dependent probability of optical transitions between n-th electron and m-th light hole states and one between n-th electron and m-th heavy hole states has only quantitative but not qualitative distinctions.

The transformation of envelope wave function symmetry in an electric field leads to existence of some maxima in field dependence of optical transition probability (see Fig. 1). The quantity of them equals to the least quantum number of the corresponding energy levels. There are n (m) maxima in these dependences if $n < m$ ($n > m$). The absolute value of the maxima may be comparable with 1 even for "forbidden" in zero field transitions. The feature in the zero electric field of the field dependences for excitons with heavy hole is their deviation from the unity for transitions between energy levels with the same quantum numbers and nonzero probability of transitions between energy levels with even sum of their numbers. In real structures there is the feature as well for heavy hole as for light hole exciton transitions due to different tunneling of wave functions of particles with different effective mass in barriers of different height.

It's very interesting to compare the probability of optical transitions between n-th electron and different heavy hole states in a wide range of electric field (see Fig. 2). One can see that there are some field values when symmetry-forbidden in zero field transitions are much stronger than symmetry- allowed ones. It may lead to mismatches in identification of experimental peaks. Note that in optical spectra of real structures this effect may be less visible due to the broadening of resonances.

It is possibly, that the effect discussed was the cause of observation of symmetry forbidden transitions in the room temperature photoreflectance spectrum of GaAs/GaAlAs multiple quantum well reported in Ref. [5].

Absorption spectrum of multiple quantum well in graded electric field

In real heterostructures the electric field may be uniform or graded as in optical modulator based on multiple quantum well structure replaced in i-area of $p - i - n$ diode.

In multiple quantum well (MQW) structure it is impossible to neglect by the electric field gradient inside the structure. There are some changes of optical spectra because of signal of quantum wells influenced by different values of electric field interference. In Fig. 3 the calculated by (1) spectra of $GaAs/Ga_{0.32}Al_{0.68}As$ single quantum well (dotted line) and MQW (solid line) structures are compared. The width of well is the same in both structures: $L = 9.5$ nm, barrier width is $L_B = 9.8$ nm, the quantity of quantum wells is $N = 50$. The increasing of electric field in the active region is about 25 kV/cm. The

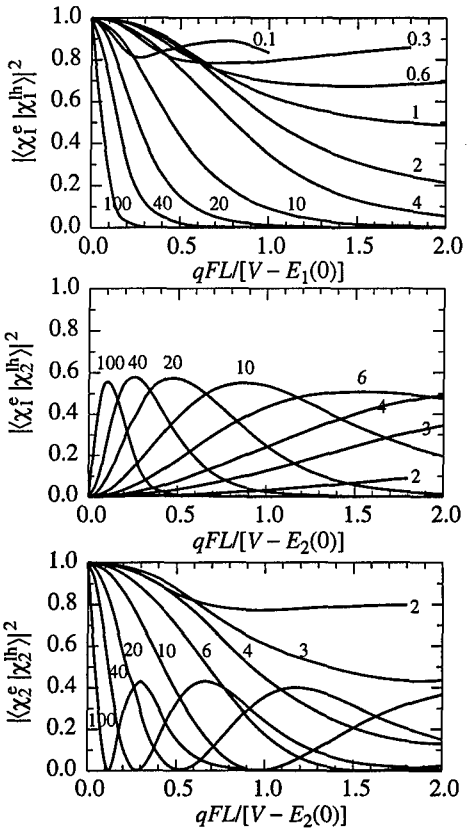

Fig. 1. The field dependence of matrix elements of excitonic optical transitions between n-th electron quasibound state and m-th light hole quasi bound state of single quantum well. Parameter notes the dimensionless quantum well depth.

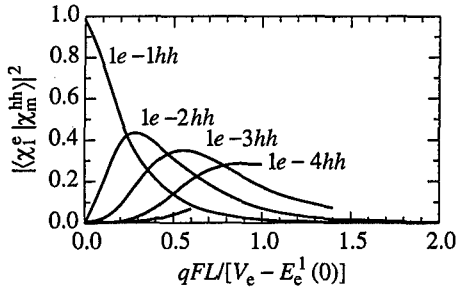

Fig. 2. The field dependence of matrix elements of excitonic optical transitions between n-th electron quasi bound state and m-th heavy hole quasi bound state of single quantum well with following parameters: $E_g = 0.985\,\text{eV}, V_e = 120\,\text{meV}, V_h = 80\,\text{meV}, m_e = 0.06m_0, m_{hh} = 0.5m_0$, $m_{lh} = 0.07m_0$, $L = 20$ nm. The dimesionless quantum well depth is 7.6 for electrons and 42.5 for heavy holes.

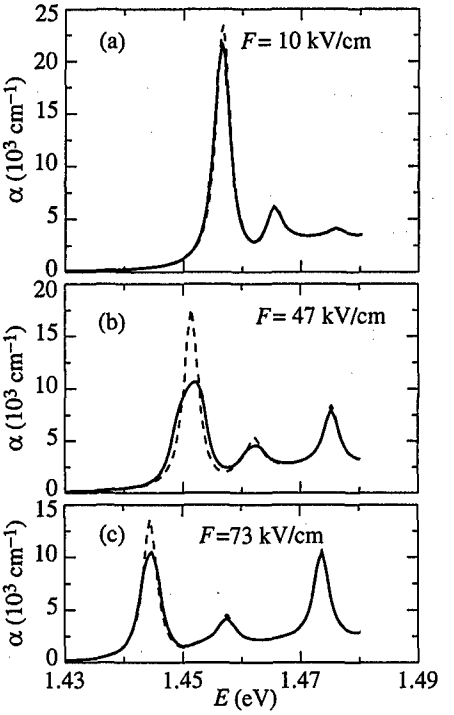

Fig. 3. The effect of gradient electric field on the absorption spectra of GaAs/$Ga_{0.32}Al_{0.68}As$ single quantum well (dotted line) and MQW (solid line) structures for different mean electric field: (a) $F = 10$ kV/cm, (b) $F = 47$ kV/cm, (c) $F = 73$ kV/cm. The width of well is the same in both structures: $L = 9.5$ nm, barrier width is $L_B = 9.8$ nm, the quantity of quantum wells is $N = 50$. The increasing of electric field in the active region is about 25 kV/cm.

comparison of calculated spectra with experimental data reported in [6] has demonstrated their good agreement.

References

[1] G. Bastard, *Wave Mechanics Applied to Semiconductor Heterostructures* France: Les Editions de Physique, 1992.
[2] E. L. Ivchenko and G. E. Pikus, *Superlattices and Other Heterostructures. Symmetry and Optical Phenomena* Springer Series in Solid-State Sciences. Ed. M. Cardona, Springer-Verlag Berlin Heidelberg 1995, 1997.
[3] O. L. Lazarenkova and A. N. Pikhtin, *Semiconductors* **32**, (9) 992–996 (1998).
[4] J. A. Brum and G. Bastard, *Phys. Rev. B* **31**, (6) 3893–3898 (1985).
[5] H. Shen, P. Parayanthal, F. H. Pollak, et al. *Solid State Commun.* **59**, (8) 557–560 (1986).
[6] D. A. B. Miller, D. S. Chemla, T. C. Damen, et al. *Phys. Rev. B* **32** (2) 1043–1060 (1985).

7th Int. Symp. "Nanostructures: Physics and Technology"
St Petersburg, Russia, June 14–18, 1999

The influence of anticrossing of exciton states on exciton relaxation in GaAs/AlGaAs double single quantum wells

K. L. Litvinenko and V. G. Lyssenko
Institute of Problem of Microelectronics Technology RAS,
Chernogolovka, 142432 Russia

It is well known that an external steady electric field shifts the energy position of exciton levels in semiconductor quantum wells. One can choose the particular value of the applied electric field so that the energy positions of different exciton states from neighbouring quantum wells should coincide. The changing of resonant position of each "coinciding" exciton states has been studied both theoretically and experimentally [1]. It was shown that the interaction of these exciton states leads to the mixing of their wave functions and, consequently, modifies their properties.

First of all the mixing of exciton wave functions leads to the strong nonlinear dependencies of the exciton energy position on the applied electric field. Instead of simple crossing due to increasing of the electric field the exciton levels kind of repel of each other and have not any crossing at all. That is why one calls this effect anticrossing. As an example, the anticrossing of heavy holes is shown in Fig. 1 for the structure we used in the experimental part of our work. The anticrossing of the excitons displays absolutely the same behaviour [2]. In Fig. 1 it looks like the interacting particles just exchange their properties. It should really take place, as the calculation shows that the these particles exchange their wave functions [3].

The anticrossing of light hole and heavy hole exciton in GaAs/AlGaAs duble single quantum wells with well width of 80 Å and barrier width of 50 Å was investigated. Radiation with a duration of 150 fs from a tunable Ti-sapphire laser was used in a two beam arrangement to excite states of heavy and light excitons simultaneously and to observe a spectrally resolved four wave mixing (FWM) signal. The sample was located in an optical helium cryostat at a temperature of about 10 K. The FWM spectra with different time delay between two laser pulses were detected with an interval of 50 fs with a spectrometer and an OMA multichannel optical detector with a resolution of 0.1 meV.

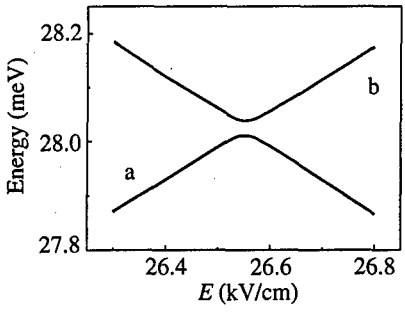

Fig. 1. The behaviour of energy position of the asymmetric ground heavy hole state (a) and the symmetric first excited heavy hole state (b) in the region of anticrossing.

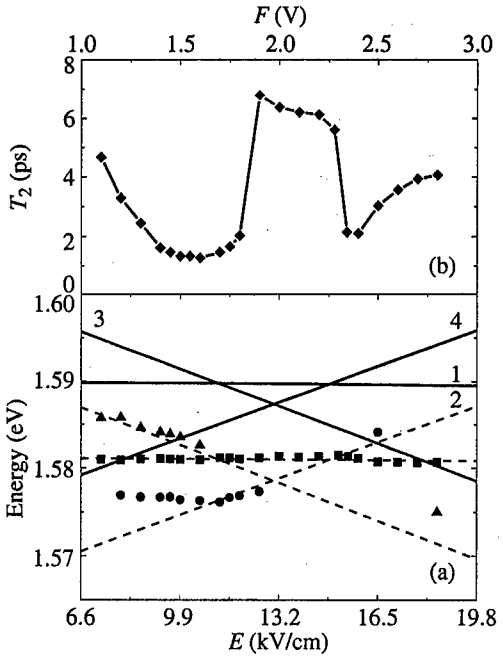

Fig. 2. (a) The energy positions of exciton lines we observed in the spectra of FWM signal for different values of experimental applied electric field (F) are indicated by open circle, square and up-triangle. The theoretical electron–hole transitions which correspond to observed excitons are shown by solid lines. See the text to get further explanation. (b) The dephasing time of light excitons 1 and 2 as a function of applied electric field F.

To get the theoretical energy position of electron–hole optical transitions we used the variational calculation [2]. The result of this calculation is shown in Fig. 2(a) by solid lines. One can see that there are four optical transitions in the region we investigated. The transition between the symmetrical electron state and the asymmetrical ground light hole state is indicated by 1; the asymmetrical electron state and the symmetrical ground light hole state 2; the symmetrical electron state and the asymmetrical first excited heavy hole state 3; the asymmetrical electron state and the asymmetrical ground heavy hole state 4 [4]. The transition 1 and 2 are the same transitions in the different quantum wells. The experimentally measured positions of excitons are shown by opened circles, squares and up-triangles in the same figure. The distance between the exciton and electron–hole transitions allows us to estimate the exciton binding energy. In our experimental condition we get the exciton binding energy of 8.8 meV.

The dependence of the dephasing time T_2 of the light hole excitons 1 and 2 on the applied electric field F are shown in Fig. 2(b). At first T_2 decreases and reaches its first minimum in the region of the anticrossing of the excitons 1 and 2 with exciton 4 ($T_2 = 1.3$ ps). Then T_2 restores its initial value ($T_2 = 6.5$ ps) and keeps it unchanging until the anticrossing with the exciton 3. After that T_2 again slowly restores its unperturbed value. The explanation of such behaviour is the following. The electron–hole transitions number 1 and 2 are the optically allowed, whereas the transitions number 3 and 4 are forbidden [4]. The dephasing time T_2 of the excitons 1 and 2 is much longer than T_2 is for the excitons 3 and 4. So, due

to the mixing of wave functions of the excitons 1 and 2 with optically forbidden states their dephasing time becomes shorter.

In conclusion it was found that the dephasing time T_2 of direct light hole excitons is decreased in 5 times by mixing its wave function with indirect heavy hole exciton wave function. The decreasing and restoring of light hole exciton dephasing time takes place two times for the values of external steady electric field from 1 V to 3 V. We hope this effect will be useful for the designing of new electro-optic devises.

This work was supported by the Russian Fund for Fundamental Research (Grants 97-02-16833, 98-02-16153).

References

[1] T. Meier, G. von Plessen, P. Thomas and S. W. Koch, *Phys. Rev. Lett.* **73**, 902 (1994).
[2] A. M. Fox, D. A. B. Miller, G. Livescu, J. E. Cunningham and W. Y. Jan, *Phys. Rev. B* **44**, 6231 (1991).
[3] K. Litvinenko and V. G. Lyssenko, *JETP Lett.* (to be published in 1999).
[4] W. L. Bloss, *J. Appl. Phys.* **67**, 1421 (1989).

7th Int. Symp. "Nanostructures: Physics and Technology"
St Petersburg, Russia, June 14–18, 1999

Emission and amplification of mid-infrared radiation in quantum well structures under generation of near-infrared light

L. E. Vorobjev†, *D. A. Firsov*†, V. A. Shalygin†, V. N. Tulupenko‡,
Zh. I. Alferov#, P. S. Kop'ev#, I. V. Kochnev#, N. N. Ledentsov#,
V. M. Ustinov#, Yu. M. Shernyakov# and G. Belenky§

† St Petersburg State Technical University, St Petersburg 195251, Russia
‡ Donbass State Engineering Academy, Kramatorsk 343913, Ukraine
# Ioffe Physico-Technical Institute, St Petersburg, Russia
§ State University of New York at Stony Brook, Stony Brook, NY 11794-3800, USA

Abstract. Physical principle of population inversion of electrons between subbands under the electron-hole pair injection into the i-region of p-i-n heterostructure with quantum wells is proposed. The important features of this principle are the simultaneous generation of intraband ($h\nu \gtrsim E_g$) radiation of near-infrared range and presence of "metastable" level. Spontaneous mid-infrared radiation ($\lambda \backsimeq 10 \ldots 20\,\mu$m) is observed from laser structures with InGaAs/GaAs quantum wells. The near-infrared laser diode structures with composite waveguide confining both near-infrared and mid-infrared radiation is designed and grown.

Introduction

The development of quantum cascade lasers [1] based on modified idea suggested in [2] and the development of "fountain" lasers with optical pumping [3] are the great achievements of semiconductor physics in last years. However the realization of quantum cascade lasers is a very complicated technological problem and wide use of "fountain" lasers is limited by optical pumping.

In present work the principle of population inversion of electrons in quantum wells under the electron injection into i-region of heterostructure is considered. The described phenomena permit to develop new mid-infrared (MIR) lasers based on interlevel optical transitions of electrons.

There are three peculiarities of proposed principle. First of all the intraband inversion for QWs is achieved with the help of current injection of electron-hole (e-h) pairs. Then, the second important condition of realization of intraband population inversion (PI) for QWs is the presence of three energy levels and long electron lifetime on upper third level, so this level can be called as "metastable" one. This "metastable" level can be formed by selection of the configuration and parameters of QW (for example, choosing the shape of well as a rectangular funnel). The important role here belongs to the dependence of probability of intersubband electron transitions with emission of polar optical (PO) phonons on extent of wave function overlapping in different subbands and wave vector of emitted phonon. The third condition is simultaneous generation of near-infrared (NIR) radiation ($h\nu \gtrsim E_g$). In this case at rather large current $J > J_{th}$ (J_{th} — threshold current for NIR stimulated emission) the generation of MIR radiation is possible. In QWs with three levels NIR stimulated emission directly does not lead to PI. But its role is very important: NIR stimulated emission supports the constant electron concentration on lower level under

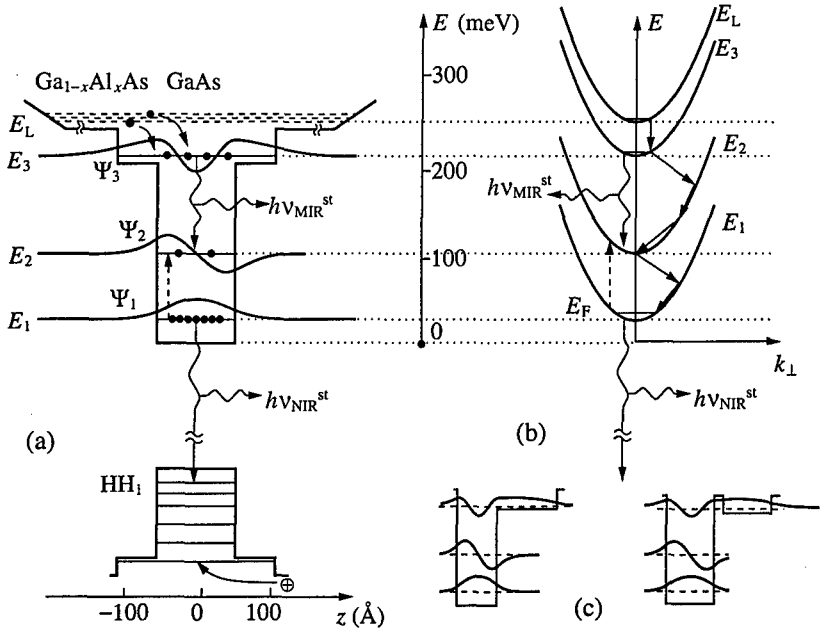

Fig. 1. (a) The diagram of electron transitions in quantum well placed in i-layer of laser n^+-i-p^+ heterostructure, energy levels E_i and electron wavefunctions. (b) The diagram of main inter- and intrasubband electron transitions with emission of optical phonons. (c) The profile of QW providing minimal overlapping the electron wavefunctions, belonging to the upper and two lower levels.

strong current $J > J_{th}$. This fact does not allow to break intraband PI with increase of $e-e$ interaction with current.

1 Principle of intraband population inversion

Let us consider for example n^+-i-p^+ heterostructure with undoped i-layer, having quantum well in the shape of funnel in its center (Fig. 1(a)).

Choosing the well parameters one can obtain the energy distances between levels as it is shown in the Fig. 1.

The injected into i-region electrons get onto the quasidiscrete levels in above barrier region and then they are captured by QW levels E_1, E_2, E_3 as a result of interaction with optical and acoustic phonons or after the elastic scattering by interface roughness.

In the stationary (but nonequilibrium) conditions the electron concentrations on the levels can be found out from system of rate equations, taking into account only main processes:

$$\eta J A_3 - N_3 W_{23} - N_3 W_{13} - N_3 (\tau_{\nu 3}^{sp})^{-1} = 0 \tag{1}$$

$$\eta J A_2 + N_3 W_{23} - N_2 W_{12} - N_2 (\tau_{\nu 2}^{sp})^{-1} + \beta_{12} N_1 = 0 \tag{2}$$

$$\eta J A_1 + N_3 W_{13} + N_2 W_{12} - N_1 (\tau_{\nu 1}^{sp})^{-1} - \beta_{12} N_1 - B_1^{st} N_\nu = 0, \tag{3}$$

where N_1, N_2, N_3 are the surface electron concentrations at levels 1, 2, 3; $\tau_{\nu i}^{sp}$ is the electron lifetime at level E_i relatively for interband radiative recombination under spontaneous emission in QW: electron in conduction band $\rightarrow$ hole in valence band; N_ν is the photon

density; B_1^{st} is a proportional coefficient. The last term in (3) describes the depopulation of level 1 due to stimulated NIR radiation. This term is significant at current J exceeding threshold current J_{th} for NIR radiation generation. Under $J > J_{th}$ this term is proportional to $(J/J_{th} - 1)$. Terms $\beta_{12}N_1$ take into account the thermally ejected electrons, $\beta_{12} = W_{12}\exp\left(-\frac{E_2-E_1}{k_BT}\right)$. Coefficient η describes the part of electrons reaching QW region; A_1, A_2, A_3 are the coefficients determined the electron stream onto levels E_1, E_2, E_3. Lastly, W_{ij} are the probabilities of the transitions from level j to the level i under the interaction with optical and acoustic phonons and interface roughness. We shall consider low temperature $k_BT \ll h\omega_0$ ($h\omega_0$ is PO phonon energy) and take into account only processes with emission of PO phonons.

Calculating the probabilities of inter- and intrasubband electron transitions with emission of optical phonons we have obtained: $W_{13}, W_{23} \ll W_{12}$, $A_1, A_2 \ll A_3$. This is connected with weak overlapping of wavefunctions for appropriate levels and also with small value of phonon wavevector for transitions $E_2 \to E_1$ and $E_L \to E_3$. So, we can call level 3 as "metastable".

The movement of electrons between energy states of QW is shown in Fig 1(b). Fig. 1(c) represents possible well configuration providing weak overlapping the wavefunctions at level 3 and levels 1, 2.

Solving the system (1) and (2) we obtain:

$$N_3 - N_2 = \eta J\left(A_3\frac{W_{12} - W_{23}}{W_{12}(W_{13} + W_{23})} - A_2W_{12}^{-1}\right) - N_1e^{-\frac{E_2-E_1}{k_BT}}. \quad (4)$$

Last term in (4) may be neglected at $T < 200$ K and extent of PI can be evaluated as $N_3 - N_2 = 6 \times 10^8 J/J_{th}$ cm^{-2}.

We calculated optical gain under direct optical transitions between subbands 2 and 3. If optical confinement factor is 10^{-2} (one QW in i-layer), mirror reflection coefficient is 0.3 and resonator length is 1 mm then the threshold current of MIR stimulated emission $J_{th}^{MIR} = 20J_{th}^{NIR}$. Use of set of QWs may essentially improve the situation. So, if the number of QW is 10, $J_{th}^{MIR}/J_{th}^{NIR} = 2$.

2 Experimental results

The first investigation of MIR intraband spontaneous emission from NIR laser diode structures with QW in active layer was carried out in ordinary structures with 0.3 μm wide waveguide and $In_{0.2}Ga_{0.8}As/GaAs$ QW [4]. Intensity of MIR radiation was very small due to strong free carrier absorption of MIR radiation in doped regions. In order to increase this intensity we have designed the heterostructure with composite waveguide. This waveguide confines both MIR and NIR radiation. The diagram of the structure is shown in Fig. 2.

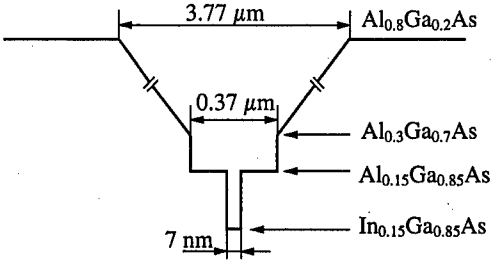

Fig. 2. The band diagram of laser diode structure with wide waveguide.

The structure was MOCVD grown. The active layer for NIR lasing contains 7 nm $In_{0.15}Ga_{0.85}As/Al_{0.15}Ga_{0.85}As$ QW. The width of waveguide for NIR radiation is 0.3 μm. Undoped graded regions of length 1.7 nm form the waveguide for MIR radiation. We found NIR lasing in this structure. The great width of undoped layers leads to the large value of threshold current. The J_{th} values for four-side cleaved samples where external losses are negligible was about 500 A/cm^2. The results of study of MIR spontaneous radiation due to intraband electron transitions in this structure are presented.

This work was supported in part by RFBR, Grants 98-02-16967, 99-02-17102; INTAS-RFBR, Grant 0615i96; INTAS, Grant 97-0751; Russian Program "Integration", Grant 75; UFBR, Grant 2.4/970.

References

[1] J. Faist, F. Capasso, D. L. Sivco, et al. *Science* **264**, 553 (1994).
[2] R. F. Kazarinov and R. A. Suris, *Sov. Phys. Semiconductors* **5**, 707 (1971); **6**, 120 (1972).
[3] O. Gauthier-Lafaye, S. Savage, P. Boucaud, et al. *Appl. Phys. Lett.* **70**, 1 (1997).
[4] L. E. Vorobjev, D. A. Firsov, V. A. Shalygin, et al. *JETP Lett.* **67**, 275 (1998).

7th Int. Symp. "Nanostructures: Physics and Technology"
St Petersburg, Russia, June 14–18, 1999

New type intraband quantum well laser

V. Ya. Aleshkin, A. A. Andronov and *E. V. Demidov*
Institute for Physics of Microstructures, RAS, 603600 N.Novgorod, GSP-105, Russia

Abstract. A universal intraband IR laser scheme on $\Gamma-\Gamma$ and $X-\Gamma$ valley transitions in GaAs-AlAs-like MQW systems under hot electron transfer from Γ valley in GaAs to X valleys in AlAs in a high lateral electric field is proposed, evaluated and simulated by the Monte-Carlo method. For a GaAs-AlAs MQW structure discussed the lasing electric field thresholds were found to be 8 kV/cm and 14 kV/cm with amplification coefficient of 300 cm^{-1} and 50 cm^{-1} near the thresholds at 80 K and 300 K at wavelength $\lambda \approx 9\,\mu m$.

Introduction

For a number of applications there is a need to have a semiconductor source working in the wavelength band from far to mid IR. Existing and emerging semiconductor lasers of the sort: intraband semiconductor lasers — i.e., p-Ge hot hole FIR lasers [1], mid IR quantum cascade lasers [2] and quantum fountain laser [3] for a number of reasons do not meet many of the application needs. So a search for the new sources is still under way.

In this work we propose a new simple universal intraband laser scheme [4] based on hot electron phenomena in GaAs-AlAs-like MQW structures under lateral transport, namely, intervalley transfer (IVT) and real space transfer (RST) of electrons. Also a thorough evaluation of the laser parameters for one specific case is made. Essentially, the scheme provides IR lasing in a planar Gunn-like diode made of the MQW structure. The laser cavity can be produced e.g. by forming of an optical restriction layer between the insulating substrate and the MQW structure and by providing a waveguide on top of the MQW system between the diode contacts. The low frequency Gunn oscillations (which the considered laser systems are potentially subject to) may be suppressed by means known in the planar Gunn devices. The scheme offers diverse possibilities and is flexible; it should provide lasing at any wavelength in a broad band from far to mid IR outside the reststrahlen region of the MQW system.

1 Inversion scheme

The considered MQW structures are such that the lowest electronic level of the system is the GaAs Γ-valley level, while the lowest level in the AlAs layer is the so-called X_z-valley level and the levels of other valleys: X_x and X_y are situated higher (see Fig. 1). The X_z-valley is situated in the Brillouin zone along the [001] growth direction, has a large effective mass along this direction and its states are mixed with the Γ-valley states at a GaAs-AlAs interface [5, 6]. The X_x and X_y are the ones situated in the Brillouin zone along the [100] or [010] directions, have a low effective mass along the growth direction and have no direct interaction with the Γ valley.

Under a high lateral electric field the Γ-valley electrons perform $\Gamma-L$, $L-X$ and $\Gamma-X$ IVT and finally are accumulated at the lowest X_{z1}-valley subband in AlAs layers. The accumulation is stronger than the one in bulk GaAs under the Gunn effect [7] due to a

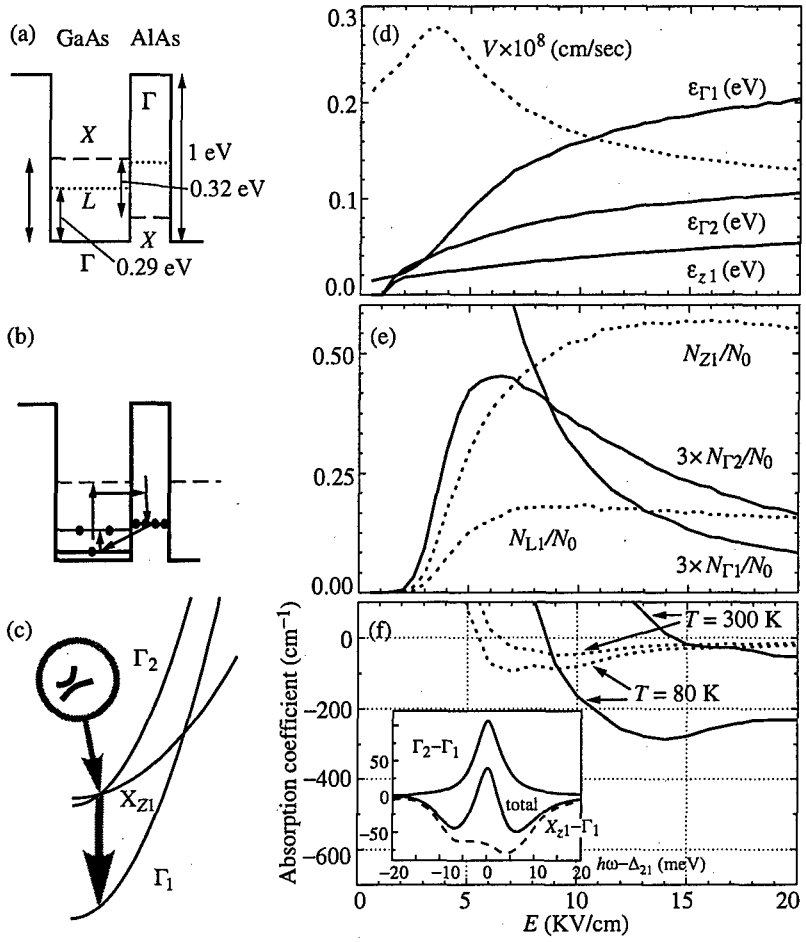

Fig. 1. Conduction band diagram of a single period of GaAs-AlAs MQW structure with positions of Γ, L and X valleys shown (a); schemes of the processes providing electron accumulation in X-valleys of AlAs, $\Gamma_2-\Gamma_1$ and $X_z-\Gamma_1$ inversion and related optical transitions (b); Γ_1, Γ_2 and X_{z1} subbands versus in-plane momentum k; $\Gamma_2-\Gamma_1$ and $X_{z1}-\Gamma_1$ (hatched) laser optical transitions are indicated (c); inset shows "repulsion" of the subbands around the crossing point. Monte-Carlo simulation results at 80 K: drift velocity V and subband Γ_1, Γ_2, X_{z1} average kinetic energies (d); relative subband concentrations N_β/N_0, N_0 is the total electron concentration (e); peaks of absorption coefficient μ for $\Gamma_2-\Gamma_1$ (solid) and $X_{z1}-\Gamma_1$ (dash) transitions calculated from the Monte-Carlo data at $T = 80$ K and at $T = 300$ K and $\chi = 1$; inset shows absorption coefficient spectrum at $E = 8$ kV/cm and $T = 80$ K (f).

substantially lower $X_{z1}-\Gamma$ return rate through GaAs-AlAs interface. The return rate is lower due to low overlapping of the X_z and Γ valley wave functions. For similar reasons direct $X_{z1}-\Gamma$ transfer due to the mixing at the interface is also rather weak. It is this accumulation [8] of electrons at the bottom of X_z-valleys that produces population inversion in the system.

Two inversions are possible here: the inversion between X_{z1} and Γ_1 subbands and inversion between Γ_2 and Γ_1 subbands (see Fig. 1). The latter can arise due to preferable scattering from the X-valley subbands in AlAs to the Γ_2 subband due to larger overlapping of the wave functions of this subband with the X-valley subbands. For the same reason a direct transfer ("injection") of electrons to Γ_2 subband from the lowest X_{z1} subband is also preferable. Both the inversions can be used for lasing: the radiative transition between $\Gamma_2-\Gamma_1$ subbands has a high oscillator strength, while the $X_z-\Gamma_1$ transition is allowed due to the wave functions admixture at the interface and is appreciable in a resonant situation when the Γ_2 level is a little bit lower than the X_{z1} level (see Fig. 1(c)), so that there is an intersection point of these levels at some in-plane wavenumber.

As an example, we consider an AlAs/GaAs MQW structure consisting of AlAs and GaAs layers of 17 Å and 85 Å width, respectively. Conduction band diagram of a single period of the structure is given in Fig. 1(a). To describe $\Gamma-X_z$ admixing at the interface and its effect on the $X_z-\Gamma$ intersubband transfer rates and on the $X_{z1}-\Gamma_1$ optical transition we use the valley intermixing potential $H_{X_z,\Gamma} = \alpha \times \delta(z)$ [6], $z = 0$ is the heterointerface position and $\delta(z)$ is the delta-function. The factor α estimated from the experimental data for the GaAs-AlAs interface is $\alpha \approx 0.155$ eV cm [5]. By using the $H_{X_z,\Gamma}$ one obtains the effective $X_z-\Gamma$ coupling potential $V = \alpha\psi_{X_z}(0)\psi_\Gamma(0)$, where $\psi_{X_z}(0)$, $\psi_\Gamma(0)$ are the wave function values at the interface. For the Γ_2 and X_{z1} subbands shown in Fig. 1(c) $V \approx 1.4$ meV. However, at the subband crossing even small V produces "repulsion" of the subbands (shown in the inset). At the same time, electric field E is important here as well because the field produces tunneling across the gap due to the repulsion. A relative importance of the repulsion and the tunneling is determined by the ratio V/V_{FK}, $V_{FK} = (e^2E^2\hbar^2/2m)^{1/3}$ is the Franz–Keldish energy, m is the reduced mass: $1/m = 1/m_\Gamma - 1/m_{X_z}$ where m_Γ is the effective mass in the Γ valley and m_{X_z} is the in-plane mass in the X_z valleys. For the electric field $E \geq 5$ kV/cm appropriate for the inversion and lasing discussed, $V_{FK} \geq (7-10)$ meV $\gg V$, and the effect of the coupling may be considered as a perturbation.

2 Monte-Carlo simulation results

To demonstrate the laser scheme performance we took into account intervalley scattering, polar optical phonon scattering within quantum wells via the bulk GaAs phonons and the direct $\Gamma-X$ transitions. Results of the Monte-Carlo simulation are given in Fig. 1(d,e,f) for a lattice temperature of 80 K. One can see that electron accumulation at the X_{z1} subband starts immediately after the beginning of intervalley transfer. The condition for population inversion between X_{z1} and Γ_1 is: $n_{z1} > n_{\Gamma_1}$, here n_{Γ_1} and n_{z1} are the occupation numbers of the Γ_1 and X_{z1} subbands at the wave numbers corresponding to the Γ_2-X_{z1} subband crossing. From the simulation results it follows that the $X_{z1}-\Gamma_1$ inversion appears at $E > 6$ kV/cm. The condition for $\Gamma_2-\Gamma_1$ population inversion is $N_{\Gamma_2} > N_{\Gamma_1}$ where N_{Γ_2} and N_{Γ_2} are the surface concentrations. This inversion appears at about $E > 8.5$ kV/cm.

The calculated peaks of the $\Gamma_1-\Gamma_2$ and $X_{z1}-\Gamma_1$ absorption coefficients and an example of the absorption coefficient spectrum found from the Monte-Carlo simulation results are given in Fig. 1(f). One can see that beyond the amplification thresholds the amplification coefficient is quite high (50 cm^{-1}) even at 300 K providing a possibility to achieve a

substantial amplification coefficient even for a low filling factor.

The considered MQW structure is the simplest example of the laser structure. In the MQW system with different layer widths (forms) and compositions one should expect a lower lasing threshold field, higher amplification coefficient and different lasing wavelength.

In particular, lasing at frequencies around transitions between the upper Γ subbands may be achieved. In this case a resonance between the X_{z1} subband and the upper subband of such a transition should occur (whch may be achieved just by increasing the GaAs layer thickness) providing a longer lasing wavelength. On the other hand, a longer wavelength may be achieved also at the $\Gamma_2-\Gamma_1$ subband transition by using an appropriate $Ga_xAl_{1-x}As$ ($x < 0.4$) alloy layer instead of GaAs.

The research described in this publication was made possible due to Grants from the Russian Scientific Programs "Physics of Solid State Nanostructures" (98-02-1098), "Physics of Microwaves" (3.17), the Russian Foundation for Basic Research (99-02-17873) and the INTAS-RFBR (95-0615).

References

[1] *Optical and Quantum Electronics*, **23**, No 2, Special issue *"FIR semiconductor lasers"* (A. Andronov and E. Gornik eds.), 1991.

[2] J. Faist, F. Capasso, D. L. Sivko, A. L. Hutchinson, and A. Y. Cho, *Science* **264**, 553 (1994).

[3] O. Gauthier-Lafaye, P. Boucaud, F. H. Julien, S. Sauvage, S. Cabaret, J.-M. Lourtouz, V. Thierry-Mieg and R. Planel, *Appl. Phys. Lett.* **71**, 3619 (1997).

[4] V. Ya. Aleshkin and A. A. Andronov, *JETP Lett.* **68**, 78 (1998).

[5] J. J. Finley, R. J. Teissier, M. S. Skolnick, J. V. Cocburn, R. Grey, G. Hill and M. A. Pate, *Phys. Rev. B* **45**, R5251 (1996).

[6] H. C. Liu, *Appl. Phys. Lett.* **51**, 1019 (1987).

[7] M. Shur *GaAs: Devices and Circuits*, Plenum Press, 1987.

[8] N. Z. Vagidov, Z. S. Gribnikov and V. M. Ivashenko, *Fiz. Tekh. Poluprovod.* **24**, 1087 (1990).

7th Int. Symp. "Nanostructures: Physics and Technology"
St Petersburg, Russia, June 14–18, 1999

Optical absorption of biased semiconductor superlattices

R. H. J. De Meester†, F. M. Peeters† and M. Helm‡
† University of Antwerp (UIA), Dept. of Physics, 2610 Antwerpen, Belgium
‡ Institut für Halbleiter-und Festkörperphysik, Universität Linz, Austria

Abstract. We report the first experiment which relates electronic transport and intraband optical absorption in a biased superlattice. Wannier–Stark-ladders far in the continuum and strongly coupled by Zener resonances are observed in an n-type GaAs/AlGaAs superlattice using infrared spectroscopy. Additional transport measurements reveal the formation of electric-field domains, with electrons tunneling resonantly to the next-nearest superlattice period. A theoretical description of the optical data is presented and we are able to reproduce most of the important features in the experimental traces.

Introduction

The physics of semiconductor superlattices has been the subject of intense research, in particular in relation to phenomena as Wannier–Stark ladders. If an electric field is applied perpendicular to the layers of a periodic superlattice, the "minibands" are known to split up into a ladder of localized states [1], the Wannier–Stark ladders (WSL). It was not only until recently that a simultaneous investigation of the transport and the intraband optical properties of a biased semiconductor has been performed by Helm *et al* [2].

1 Experimental results

The superlattice (SL) studied consists of 300 periods of GaAs quantum wells (50 Å wide) and $Al_{0.29}Ga_{0.71}As$ barriers (81 Å wide). In this way the system has a rather narrow first subband ($\Delta_1 = 1.2$ meV), but a relatively wide first excited miniband ($\Delta_2 = 30$ meV) which is located in the continuum above the barriers.

Transport by tunneling

By applying an electric field, F, one can measure the current-response of this system (see Fig. 2 in Ref. [2]). At low bias voltage (< 0.5 V) the conduction is ohmic and proceeds by ground-state to ground-state tunneling [3]. At higher voltage the SL breaks up into a low-field and a high-field domain; in the latter electrons tunnel from the ground state in one well to an excited state in a subsequent well. Its extent increases with increasing bias, until the field distribution is again homogeneous and the current rises steeply. In the present SL this occurs at 27 V and the voltage drop per period is (27 V)/300 = 90 meV. Knowing that the energy difference between ground state and first excited state $E_2 - E_1 = 170\,\text{meV} \approx 2 \times 90$ meV, we conclude that the electrons tunnel through 2 barriers (and one well).

Optical IR absorption

For the measurement of the IR absorption spectrum, the transmission change $T(F)/T(0)$ is measured by dividing the signal during a short electric-field pulse, $T(F)$, by the signal a few ten μs after the pulse, $T(0)$. This is shown in Fig. 1 for increasing voltage. Notice that minima correspond to absorption lines induced by the electric field. The positions of the maxima and minima hardly change, but grow in amplitude as the electric field increases.

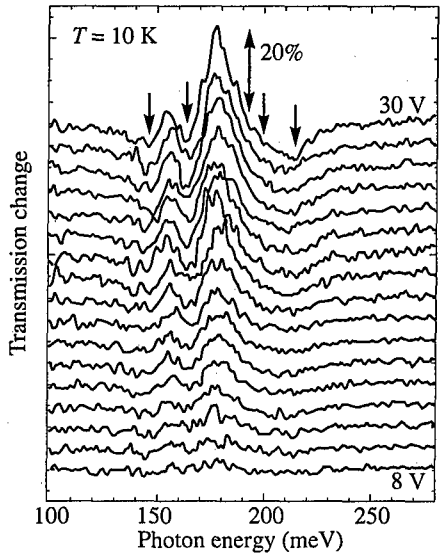

Fig. 1. Differential transmission spectrum ($T(F)/T(0)$) of the superlattice for a series of bias voltages between 8 and 30 V. Minima essentially correspond to electric-field-induced absorption lines.

2 Theoretical calculations

Experimental analysis

In order to obtain an understanding of the IR absorption experiments we have performed energy level calculations for a finite SL system. The results of such a calculation is shown in Fig. 2 together with an absorption spectrum for this system (left). The SL potential is shown in gray, the relevant wavefunctions $\psi_n(z)$ are shown with an offset equal to their energy E_n. The classification (m, p) of the energy levels is as follows: m $= 1, 2, \ldots$ is the (zero field) miniband index, and p $= \ldots, -1, 0, 1, \ldots$ is the spatial index relative to the central quantum well. Notice that only the ground states (1,p) are confined in the wells, all other levels are in the continuum. The main transitions (which are also visible experimentally) are, from low to high energies (3, -1), (2, 0) (main transition), (4, -2) and (3, 0). Besides the two direct transitions, we also observe indirect transitions up to the next-nearest downhill QW.

Biased finite superlattice systems

The effect of the electric field on the energy levels of the SL can be shown by taking a SL with a finite number, N, of quantum wells and plotting the energy for the 3 lowest minibands. This is shown in Fig. 3 for $N = 9$. In this calculation we have taken the experimental parameters for the well width (50 Å), the barrier width (81 Å) and the well depth (232 meV). With these parameters the important features of a finite biased SL are clearly visible. Fig. 3(a) shows the behaviour of all the energy levels in the 3 lowest minibands as the field increases. At an electric field $F = 0$ we show 3 minibands (with band widths: $\Delta_1 = 1.84$ meV, $\Delta_2 = 31.8$ meV and $\Delta_3 = 77$ meV) and there are two degenerate states at 280 meV and 396 meV. These states are the so-called edge states and are intrinsic to a finite system. Notice that the energy of the edge states do not cross the SL

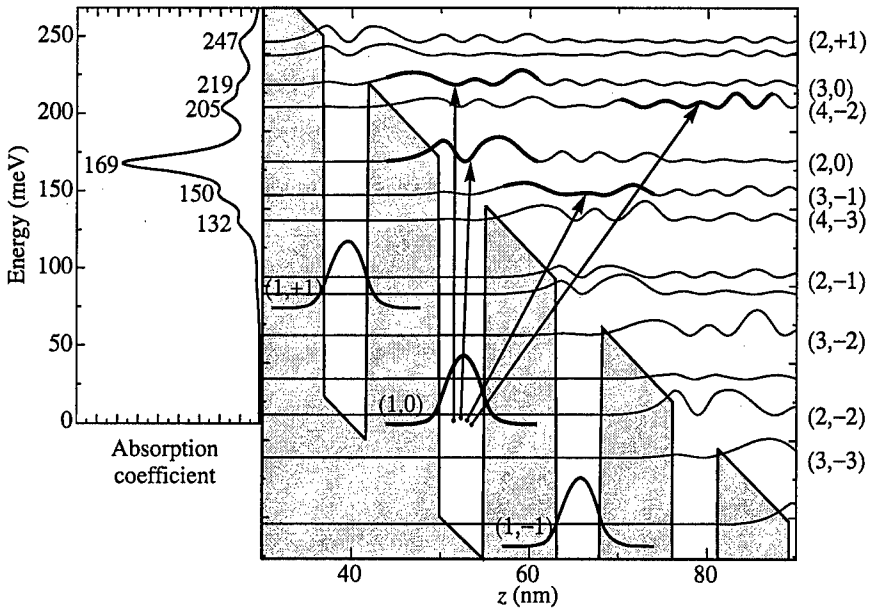

Fig. 2. Conduction profile, energy levels and electron distributions for four superlattice periods with an electric field of 60 kV/cm. The experimental observed transitions are indicated by arrows. The calculated absorption coefficient is shown on the left.

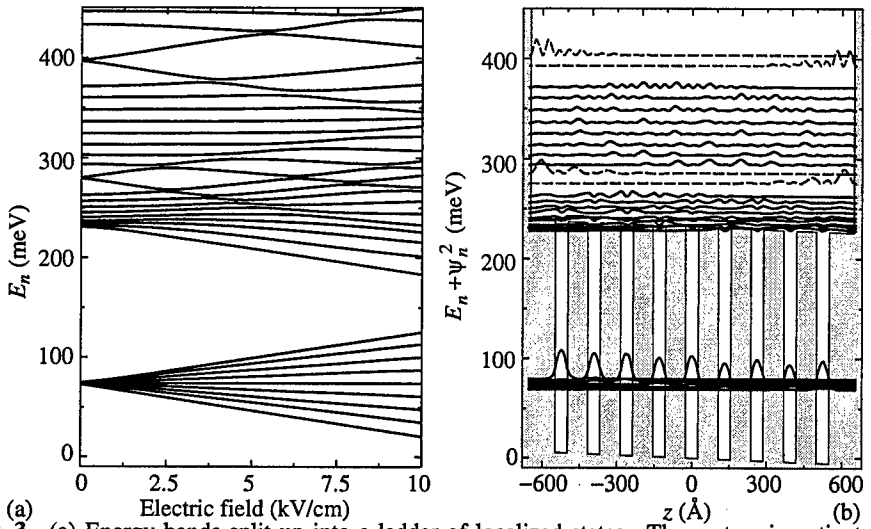

Fig. 3. (a) Energy bands split up into a ladder of localized states. The system investigated is a GaAs/AlGaAs superlattice with well width = 50 Å, barrier width = 81 Å and well depth = 232 meV. We see that each miniband contains about $N = 9$ states, and also observe some extra edge states (at zero field these are at 280 meV and 396 meV). (b) The electron distributions for all states in the 3 lowest minibands are shown at an electric field of 0.5 kV/cm. The edge states are depicted in dashed lines to show the difference with the SL-states (full). The SL potential is shown in gray.

levels, there is a clear anti-crossing. In Fig. 3(b) we have shown the electron distributions of all levels in the 3 lowest minibands at an electric field of 0.5 kV/cm. At this field, the edge states (dashed) can be well distinguished from the SL-states (full).

3 Conclusions

We have performed energy level calculations on biased finite SL systems which reveal the existence of minbands and edge states at zero field. Applying an electric field splits up the minibands in a ladder of localized states, the double degenerate edge states also split up and mix with the localized states without interfering them. By calculating absorption spectra for a GaAs/AlGaAs superlattice we where able to explain the transmission spectra measured by Helm *et al.* [2].

Acknowledgements

This work was partially supported by the Inter-university Micro-Electronics Center (IMEC, Leuven), the Flemish Science Foundation (FWO-Vl) and the IUAP-IV. R. D. M. is supported by "het Vlaams Instituut voor de bevordering van het Wetenschappelijk & Technologisch Onderzoek in de Industrie" (IWT) and F. M. P. is a research director with the FWO-Vl.

References

[1] E. E. Mendez, F. Agullo-Rueda and J. M. Hong, *Phys. Rev. Lett.* **60**, 2426 (1988).

[2] M. Helm, W. Hilber, G. Strasser, R. De Meester, F. M. Peeters and A. Wacker, *to be published in Phys. Rev. Lett.*.

[3] A. Wacker and A.-P. Jauho, *Phys. Rev. Lett.* **80**, 369 (1998).

7th Int. Symp. "Nanostructures: Physics and Technology"
St Petersburg, Russia, June 14–18, 1999

Gunn effect and possibility for FIR radiation in strained 2D InGaAs/AlGaAs structure

Yu. L. Ivánov, V. M. Ustinov, A. E. Zhukov, D. V. Tarkhin, A. A. Prokof'ev, E. Gornik† and R. Zobl†
Ioffe Physico-Technical Institute, St Petersburg, Russia
† Technical University of Vienna, Institute for Solid State Electronics, Vienna, A-1040 Austria

Powerful IR emission of hot holes in a strained 2D InGaAs/AlGaAs structure has been observed in [1]. The emission have clear pronounced threshold with respect to excitation (electric field) against the saturation of the current–voltage characteristic of the structure. It is supposed there that powerful emission can be a manifestation of generation and the saturation is due to a domain of high electric field arising. Both effects are to be suppose due to redistribution of hot holes between quantum subbands under a strong electric field. For check this supposition the more detail transport and FIR emission investigations of the structure have been carried out.

Preparation of the samples under investigations are the same that was used in [1]. A pulse electric field of 1 mcs duration was applied to the samples. Shape of voltage and current was controlled by oscilloscope. Values of voltage and current was measured by means of synchronous detector gate of which can be shifted relatively to the beginning of the pulse. In electric field about 1 kV/cm a downfall of current appears at time of 0.5 μs after beginning of the pulse. With increasing of an electric field the downfall of current becomes bigger but its position in time remains the same. In electric field about 3 kV/cm a new downfall of current appears at time of 1 μs after beginning of the pulse and slowly shifts to the beginning of the pulse with increasing of an electric field (see Fig. 1).

At this situation a view of current–voltage characteristic dependents from time position of synchronous detector gate. Fig. 2 shows the current–voltage characteristics at different gate positions respectively to the beginning of the pulse. One can clear see that at gate position before the first current downfall the current goes to the saturation monotonously. At gate position in time of the first downfall the current–voltage characteristic has a negative part so as at gate position in time of the second current downfall one oscillates with increasing of an electric field which indicates a change of domain velocity.

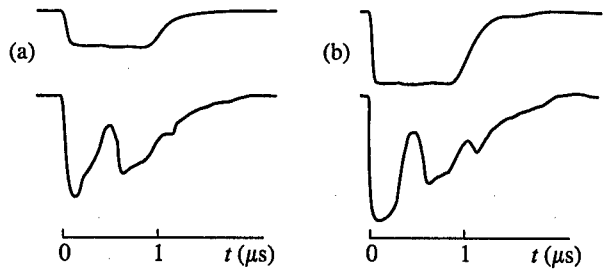

Fig. 1. Shape of voltage (upper curves) and current (lower curves) for electric field of 5 kV/cm (a) and 10 kV/cm (b).

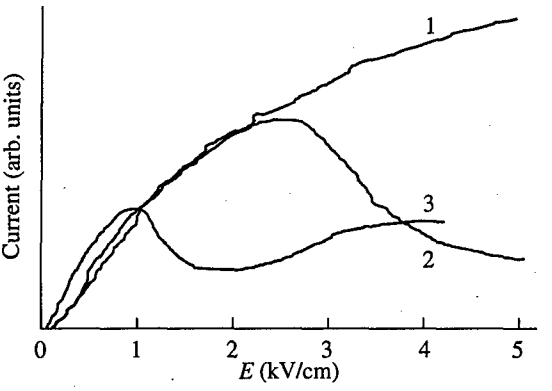

Fig. 2. Current–voltage characteristics at different gate position. Gate position with respect to the beginning of the pulse, μs: 1—0.2; 2—0.5; 3—1.0.

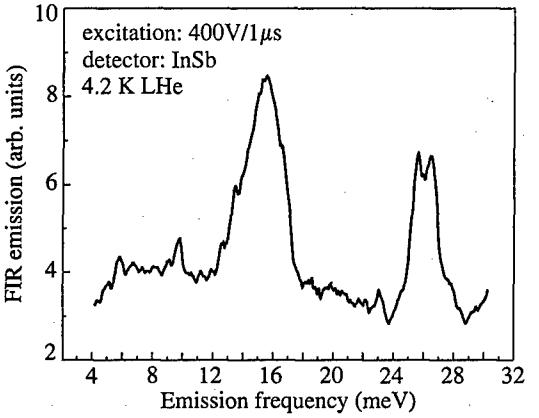

Fig. 3. Spectrum of FIR emission for one of the samples which have superlinear dependence of FIR emission from an electric field (see Fig. 4)

The current oscillations are direct evidence the domain instability existing which can be take place only when the hole effective mass of upper subbands is bigger than one of ground subband like in volume GaAs where the Gunn effect take place. At this situation an accumulation of the holes in upper subbands can occur up to population inversion of hot holes arising. Calculation of hole dispersion curves shows practically isotropic holes at low energy but not parabolic. They effective masses at zero momentum space becomes larger with subband number increasing. The effective mass ratio for first three subbands is 1:1.7:4.4. This is in agreement with experimental data.

In [1] IR emission was observed in wide spectral region of Ge(Ga) photodetector (up to 120 microns including sensitivity of Ge in own region). Now a spectral measurements of the FIR emission have been carried out by means of selective smoothly tuned by a magnetic field InSb detector. The result is shown on Fig. 3. One can see two spectral lines at 16 and 26 meV. The first at 16 meV is sufficiently broad so as second at 26 meV is in three times narrower. Moreover, the second line shape is almost the same for InSb photodetector

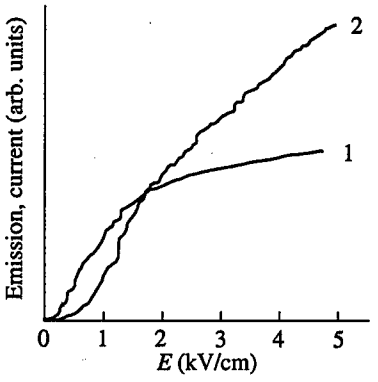

Fig. 4. Dependencies of current (1) and emission (2) vs an electric field.

sensitivity shape obtained independently by means of Fourier spectrometr (spectral width is 1.6 mev) with typical splitting in a magnetic field. It means that this line is a result of InSb photodetectors scanning by a narrow line of emission not more than 0.4 meV. This narrow emission line can be only in the three cases: (i) emission is connected with radiative transition between subbands of cold up to 4.2 K holes, (ii) emission is connected with radiative impurity intracentre transition and (iii) emission is a manifestation of generation. The first possibility can not be realize because a high electric field heats holes at least to 70 K. It one can clear see from the first emission line which has spectral width of 6 meV. The second possibility also can not be realize because impurity concentration in QW is residual and does not exceeds 1.5×10^9 cm^{-2} which is provided by RIBER machine. It is very small value in comparison with concentration of free holes (about 6×10^{11} cm^{-2}). The third possibility seems real.

The most samples of the structure have superlinear dependencies of FIR emission measured in a broad spectral region as it is shown in Fig. 4 so as the current tends to saturation. Superlinear character of FIR emission can be explain by accumulation of holes in upper subbands which can lead to population inversion.

The work is supported by the Russian Foundation for Basic Research, Grant 98-02-18403 and the Interdisciplinary Science and Technology Program of Russia "Physics of Solid-State Nanostructures", Grant 97-1044.

References

[1] Yu. L. Ivánov, C. A. Morosov, V. M. Ustinov and A. E. Zhukov, *Fiz. Tekhn. Poluprovod.* **32**, (9) 1119–1121 (1998).

7th Int. Symp. "Nanostructures: Physics and Technology"
St Petersburg, Russia, June 14–18, 1999

Intraband absorption of far-infrared light by electrons in GaAs/AlGaAs quantum wells

L. E. Vorobjev†, *S. N. Danilov*†, V. L. Zerova†, Yu. V. Kochegarov†,
D. A. Firsov†, R. Kh. Zhukavin‡, S. G. Pavlov‡ and V. N. Shastin‡
† St Petersburg State Technical University, St Petersburg 195251, Russia
‡ Institute for Physics of Microstructures RAS, N. Novgorod 603600, Russia

Abstract. In present work the first results of the investigations of intrasubband absorption of far-infrared polarized radiation ($\lambda \simeq 100\ \mu$m) by equilibrium and hot electrons in GaAs/AlGaAs quantum wells are presented. The electrons were heated by strong longitudinal electric field. The experimental data was compared with theoretical ones taking into account nonequilibrium optical phonon, impurity and interface roughness scattering.

Introduction

Absorption of middle- or far-infrared radiation due to intrasubband indirect transitions of electrons or holes plays an important role in design of optoelectronic devices for these spectral ranges. In particular, in middle- and far-infrared lasers the absorption of this type may limit the value of optical gain. Meanwhile the experimental investigations of absorption of this type in quantum wells (QW), as far as we know, had not been carried out. The published works have mainly theoretical character [1, 2], and deal with classical scattering mechanisms, namely interaction with phonons and impurities. Electron scattering on the nonequilibrium optical phonons and interface roughness were not taken into account.

The aim of this work is to study experimentally and theoretically the intrasubband absorption of polarized far-infrared range (FIR, $\lambda \simeq 100\ \mu$m) radiation by equilibrium and hot electrons in GaAs/AlGaAs quantum wells.

1 The experimental technique

The samples. We studied GaAs/$Al_{0.22}Ga_{0.78}As$ multiple quantum well structure consisted of 150 layers of 6 nm width QW divided by doped 14 nm wide barriers with 4 nm wide spacer. The electron mobility at $T = 77$ K was 3300 $cm^2/(Vs)$. The electron surface concentration was 3×10^{11} cm^{-2} at $T = 300$ K. The diagram of quantum well structure is detailed in Table. 1. Experiment temperature was 4.2 K. Germanium hot hole laser was used as a source of FIR radiation. Photodetector Ge⟨Ga⟩ was used for registration.

Due to small width of quantum well the value of intensity modulation in electric field is also small. The way to increase this value is the use of multiple light passing through the structure. In order to provide this condition we used different techniques of FIR absorption investigations.

Intraresonator measurements. The structure with QWs was placed into the resonator of FIR laser on hot holes in Ge, as it is shown in Fig. 1(a). The electric and magnetic pumping fields applied to laser are chosen in such a way that lasing is absent and only spontaneous emission can be observed. In this case a weak decrease of losses in resonator can lead to

Table 1. Diagram of quantum well structure.

Buffer	5 nm	GaAs	$N_D = 2\times10^{18}cm^{-3}$
150 times (MQW)	6 nm	GaAs	undoped
	4 nm	$Al_{0.22}Ga_{0.78}As$	undoped
	6 nm	$Al_{0.22}Ga_{0.78}As$	$N_D = 1\times10^{17}cm^{-3}$
	4 nm	$Al_{0.22}Ga_{0.78}As$	undoped
Buffer	2 μm	$Al_{0.22}Ga_{0.78}As$	$N_D = 5\times10^{16}cm^{-3}$
	2 μm	GaAs	$N_D = 5\times10^{16}cm^{-3}$
Substrate		semiinsulating GaAs	

significant change of spontaneous radiation intensity. It is very sensitive technique allowing the observation of small changes of light absorption. Unfortunately, this method gives only qualitative information about absorption coefficient variation. It should be noted, that this method is applicable for study of light with s-polarization only but according to selection rules the intrasubband absorption is possible just in this case.

Out of resonator measurements. For the quantitative measurements of light modulation in electric field we use the technique with total internal reflection geometry. The diagram of light transmission through the sample is shown in Fig. 1(b). This technique permits to obtain a value of absorption coefficient modulation, but some problems make difficult the precise calculations. One has to take into account two factors: (i) interference between beam incident on the structure and one reflected from vacuum–semiconductor interface [3, 4] and (ii) reflection from interface substrate-quantum layers. The presence of doped buffer layers in the structure affects both these processes and leads to effective decrease of light intensity inside the QW structure. This is of particular importance for FIR radiation when the structure dimensions are less than wavelength of radiation.

To avoid this difficulties the absorption of FIR radiation in equilibrium conditions was studied in traditional geometry (Fig. 1(c)).

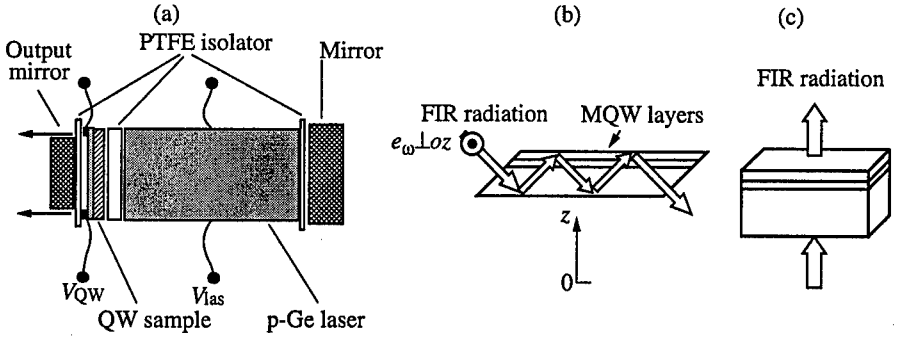

Fig. 1. Diagrams of experimental technique: intraresonator mesurements (a), total internal reflection geometry (b), traditional geometry (c).

2 The experimental results and discussion

The dependence of intensity of FIR radiation from germanium laser with GaAs/AlGaAs QW structures placed into the resonator (see Fig. 1(a)) on the applied electric field is shown in Fig. 2(a). One can see that there is a decrease of FIR absorption of QW structure in longitudinal electric field. Using this method we can not make some conclusion about the value of this decrease $\alpha(E)$, but we find that significant decrease of absorption occurs near $E = 200$ V/cm. These results are consistent with ones obtained from out-of-resonator measurements (see Fig. 1(b)) shown in Fig. 2(b). Some difference between the results shown in Fig. 2(a) and 2(b) can be explain by the presence of strong magnetic field necessary for FIR laser operation in the first case.

The equilibrium absorption in the absence of electric field was measured in traditional geometry (Fig. 1(c)). The value of absorption coefficient $\alpha(0)$ was obtained taking into account reflection from both sides of the sample. These data are necessary for calculating the dependency $\alpha(E)$.

Let us discuss the experimentally observed dependence $\alpha(E)$ (Fig. 2(b)). We carried out the calculations of FIR radiation absorption coefficient due to intrasubband transitions of electrons taking into account nonequilibrium optical phonon, impurity and interface roughness scattering. Nonequilibrium optical phonons generated due to electron heating strongly affect the results of calculations. According to calculations the experimentally observed decrease of absorption coefficient is related to strong impurity and interface roughness scattering at low electron temperature. We suggest to explain the peculiarity of dependence $\alpha(E)$ by the presence of the impurity centers in the barrier near the interface. At low temperature these center can capture the carriers. Depopulation of this centers under electron heating leads to the change of free carrier concentration and to variation of $\alpha(E)$ from theoretically calculated.

The absorption of p-polarized FIR radiation in QW under electron heating in electric field was also investigated. These results have some difference from considered case that also can be explained using model of centers in the barrier.

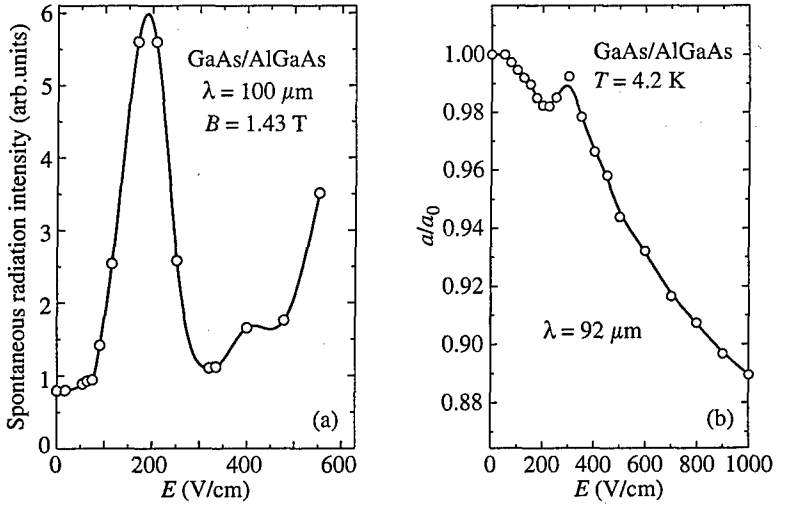

Fig. 2. Results of intraresonator measurements (a); change of the absorption coefficient of QW structure in longitudinal electric field (b).

This work was supported in part by RFBR, Grant 99-02-17102; INTAS-RFBR, Grant 0615i96; INTAS, Grant 97-0856; Russian Program "Integration", Grant 75; Grants of Russian Ministry of General and Professional Education.

References

[1] H. M. Spector, *Phys. Rew. B* **28**, 971 (1983).
[2] V. L. Gurevich, D. A. Parshin and K. E. Shtengel, *Sov. Phys. Sol. State.* **30**, 1288 (1988).
[3] M. J. Kane, M. T. Emeny, N. Apsley et al., *Semicond. Sci. Technol.* **3**, 722 (1988).
[4] T. Fromherz, E. Koppensteiner, M. Helm and G. Bauer, *Phys. Rew. B* **50**, 15073 (1994).

7th Int. Symp. "Nanostructures: Physics and Technology"
St Petersburg, Russia, June 14–18, 1999

Photocurrent under carrier tunneling in GaAs/AlGaAs coupled quantum wells embedded in p-i-n heterostructure

L. E. Vorobjev†, D. A. Firsov†, *V. A. Shalygin*†, I. E. Titkov†, A. M. Tomlinson‡, C. T. Foxon§ and A. M. Fox¶

† St. Petersburg State Technical University, St.Petersburg 195251, Russia
‡ University of Oxford, Oxford OX1 3PU, UK
§ Nottingham University, Nottingham NG7 2RD, UK
¶ University of Sheffield, Sheffield S3 7RH, UK

Abstract. Photocurrent-bias characteristics of coupled quantum well photodiode were studied at different intensities of illuminating light with various spectral range. The optimal conditions for observation of THz radiation emission from such device are established.

Emission and absorption of THz frequency radiation in different nanostructures are intensively studied during last years [1–3]. In this paper we report the results of photoelectric investigations of p-i-n heterostructures with embedded coupled quantum wells (CQWs). We hope that the next step will be the observation of THz radiation emission from these structures. The main feature of studied CQW photodiode implies that the energy separation of the lowest two electronic subbands is voltage-tuned in the THz-frequency range.

The experiments were performed on the device consisted of 25 undoped GaAs/$Al_{0.33}Ga_{0.67}As$ CQW units grown by molecular beam epitaxy in the intrinsic region of a p-i-n diode. The CQW consisted of a narrow well (7.9 nm) and wide well (15.8 nm) separated by a thin barrier (1.7 nm). Adjacent CQWs were separated by a thick barrier (15.3 nm). There are six electronic levels in such CQWs. The states with the energies $E_1 = 15$ meV, $E_3 = 65$ meV, $E_4 = 133$ meV and $E_6 = 242$ meV are generated by the wide well and the states $E_2 = 43$ meV and $E_5 = 179$ meV are connected with the narrow well (these values are calculated for zero bias). For reverse bias up to 7 V the energy separation of the lowest two electronic levels is varied through a range from 10 to 30 meV.

The wafer was selectively etched to produce 400 mm diameter mesa structures. A gold electrical contact with integral grating coupler was deposited onto the surface of the mesa. The experiments were performed at 4.2 K with the sample immersed in liquid helium.

To investigate photocurrent we illuminated the mesa through optical fiber with modulated light of different spectral range and intensity. We used red laser (680 nm), halogen lamp with different optical filters, flash-light lamp. At reverse bias of 1.8 V there was a peak of photocurrent due to resonant tunneling of electrons from 1-st subband of one well to the 2-nd subband of neighbor well. Such resonant tunneling has to be accompanying with emission of THz radiation.

In similar structures the absorption of THz radiation was studied. When the THz photon energy is resonant with the intersubband splitting a direct optical transition is allowed and the absorption of THz photons by carriers is strongly enhanced. Corresponding change of the photocurrent in the device was observed.

In this paper we demonstrate photocurrent-bias characteristics for different conditions of optical pumping. At Fig. 1 the photocurrent-bias characteristics for different intensities

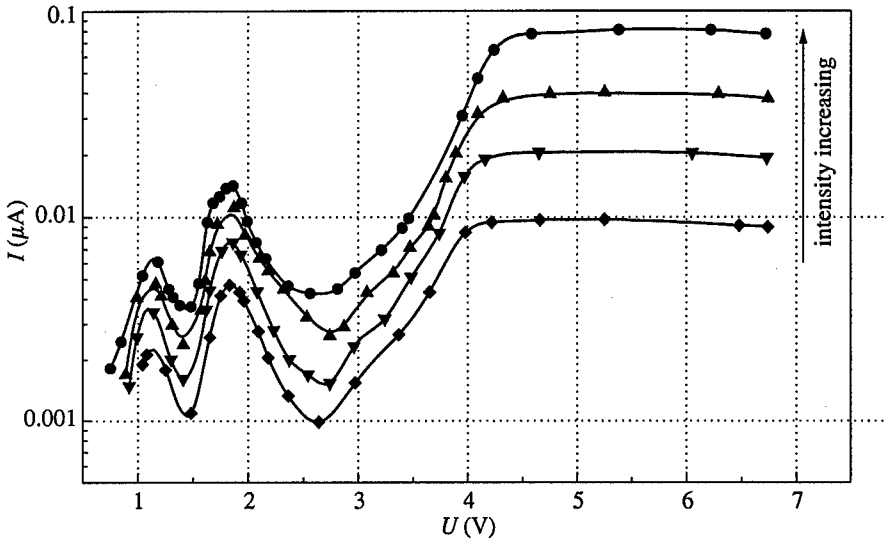

Fig. 1. Photocurrent-bias characteristics of CQW photodiode for different intensities of pumping light (halogen lamp).

of "white" light with the same spectral range are represented. These characteristics and the bias dependence of photocurrent under illumination by light sources with different spectral range are discussed taking into account the energy diagram of CQWs and the possibility of domain formation [4]. Relying on the experimental data we establish the optimum for obtaining THz radiation emission.

This work was supported in part by RFBR, Grant 99-02-17102; INTAS-RFBR, Grant 0615i96, Grants of Russian Ministry of General and Professional Education.

References

[1] H. G. Roskos, M. C. Nuss, J. Shah, et al. *Phys. Rev. Lett.* **68**, 2216 (1992).
[2] B. Xu, Q. Hu and M. R. Melloch, *Appl. Phys. Lett.* **71**, (4) 440 (1997).
[3] A. M. Tomlinson, C. C. Chang, R. J. Nicholas and A. M. Fox, *Proceedings ICPS24, Jerusalem, August 2-7, 1998* (World Scientific, 1998).
[4] H. T. Grahn, R. J. Haug, W. Muller and K. Ploog, *Phys. Rev. Lett.* **67**, 1618 (1991).

7th Int. Symp. "Nanostructures: Physics and Technology"
St Petersburg, Russia, June 14–18, 1999

Wide-miniband superlattice devices for microwave and terahertz frequencies

K. F. Renk
Institut für Angewandte Physik, Universität Regensburg, Germany

Abstract. Wide-miniband superlattice devices are suitable for generation, detection and frequency multiplication of microwaves and for detection and autocorrelation of THz radiation. The devices, operated at room temperature, are based on nonlinear transport properties of the miniband electrons. While the interaction of the miniband electrons with microwaves can be described by the nonlinear current-voltage characteristic, interaction with a THz field is based on a quantum nonlinearity, namely a THz-field induced modulation of the Bloch oscillations of the miniband electrons.

Introduction

The devices are the result of a most successful international cooperation, with four partners, A. Ignatov *et al.* (Nizhni Novgorod) delivering the theoretical basis, P. Kop'ev and V. Ustinov *et al.* (St. Petersburg) providing the MBE growth technique, Pawel'ev *et al.* (Nizhni Novgorod) contributing high-frequency device expertise, and E. Schomburg *et al.* (Regensburg) providing high-frequency and THz experience. The work is based on the ideas of Esaki and Tsu [1], who predicted that semiconductor superlattices should show nonlinear current transport, because of Bloch oscillations [2] of the miniband electrons. With respect to current transport, especially at high current density, transport properties of doped superlattices have been studied by Sibille and Palmier *et al.* [3].

1 Negative differential conductance

First, we consider a superlattice (Fig. 1) of 120 periods each period consisting of 49 Å thick GaAs and 13 Å thick AlAs layers, corresponding to a lowest-miniband width of 22 meV. The superlattice (length 0.74 μm) is homogeneously n doped (1.4×10^{17} cm^{-3}) and is embedded in graded layers and n^+ GaAs layers, grown on a n^+ GaAs substrate. A Au-Ge-Ni layer serves as ohmic contact. The superlattice is mesa structured, with a small-area mesa (dimension 7×8 μm) and a large-area mesa (100×200 μm). In this quasi planar device, with two ohmic contacts in one plane, the small-area mesa is the active device while the large-area mesa is a series resistance.

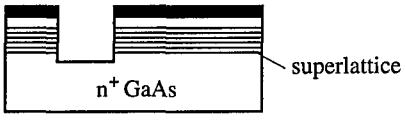

Fig. 1. Superlattice device.

Characteristic for a wide-miniband superlattice is the ability of the miniband electrons to perform Bloch oscillations (Fig. 2). An electron traverses several periods of the superlattice, oscillating back and forth along the superlattice axis, z, being Bragg reflected at the upper

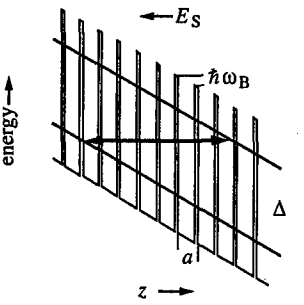

Fig. 2. Bloch oscillation.

boundary of the miniband (width Δ). The oscillation frequency corresponds to the Bloch frequency

$$\omega_B = \frac{ea}{\hbar} E_s \tag{1}$$

where e is the elementary charge, $\hbar$ Planck's constant, a the superlattice period, and E_s the strength of a static electric field along z. The duration of a Bloch oscillation of a miniband electron is limited by the intraminiband relaxation. The Bloch oscillation corresponds to a quantum coherent oscillation within a range of several superlattice periods. After relaxation the coherence is lost and the electron begins a new oscillation. All miniband electrons perform, independently, i. e. without a phase relation to each other, Bloch oscillations.

The current (I)–voltage (U) characteristic of the superlattice (Fig. 3) shows ohmic behavior at small voltage and a negative differential conductance above a critical voltage U_c (~ 1 V). At the critical voltage an electron performs in the average one Bloch oscillation cycle within the relaxation time ($\tau\omega_B = 1$); the critical voltage corresponds to a Bloch frequency $\omega_B/2\pi = 1.6$ THz and the relaxation time τ is $\sim 10^{-13}$s. Overdamped Bloch oscillations ($\omega_B\tau < 1$) are responsible for the deviation of the current-voltage characteristic from ohmic behavior for voltages $U < U_c$. At $U > U_c$ ($\omega_B\tau > 1$) the increasing number of Bloch oscillation cycles within the relaxation time τ reduces the mean path of a miniband electron and therefore the drift velocity, v_d. The drift velocity-field characteristic is given, for a simple tight binding energy dispersion relation for the miniband, by [1]

$$v_d = \frac{ea\Delta}{4\hbar} \frac{2\omega_B\tau}{1+\omega_B^2\tau^2}. \tag{2}$$

The peak drift velocity, $v_p = ea\Delta/4\hbar$, increases linearly with Δ. A more elaborated analysis taking into account the thermal distribution of the electrons in the miniband and, furthermore, elastic scattering, delivers the same inelastic intraminiband relaxation time (10^{-13} s) as the simple analysis and an elastic scattering rate of the same order [4]; the inelastic scattering is due to interaction with longitudinal optical phonons and the elastic scattering mainly due to scattering at the GaAs/AlAs interfaces because of roughness. The jumps in the $I-U$ characteristic (Fig. 3) are the consequence of travelling high-field domains. These are the origin of a current oscillation and of microwave generation [5, 4]. The corresponding charge density is a travelling dipole domain, with a depletion layer followed by an accumulation layer, both extending along the superlattice axis over many superlattice periods.

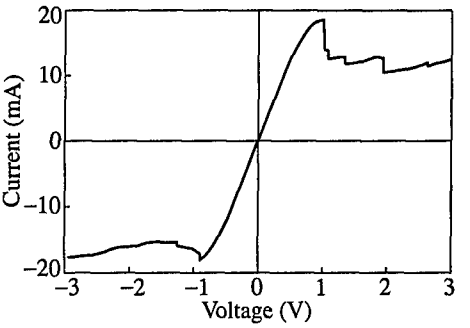

Fig. 3. Current-voltage characteristic.

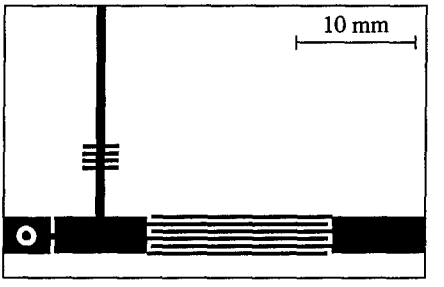

Fig. 4. Superlattice oscillator.

2 Superlattice oscillator

A superlattice device (with the data given in section 1) was integrated into a planar circuit (Fig. 4) with a low-pass port for the direct current supplied by a constant-voltage source, and a high-pass port for the microwaves [6].

The oscillator showed an emission spectrum (Fig. 5) with a fundamental harmonic near 5 GHz and higher harmonics. The fundamental frequency ν_{osc} was equal to the inverse superlattice transit time of the dipole domains, which travelled with a velocity near the peak drift velocity. The occurrence of higher harmonics indicates that the domains had an extension which was shorter than the superlattice length. The power of the oscillator was 1 mW (efficiency 6%).

A weak narrow-band external field is able to phaselock the oscillator [7]. Instead of a bandwidth of about 1 MHz the locked superlattice oscillator now has a bandwidth,

which is comparable with the linewidth ot the external field (e.g. 10 Hz); the locking leads to a suppression of thermal fluctuations occurring in the formation of the domains.

Superlattices with wider minibands show (at comparable superlattice length L) larger fundamental frequencies (Fig. 6). The frequency of the oscillation corresponds to the ratio of the domain velocity and the superlattice length and is approximately given by $\nu_{osc} \sim 0.7 v_p / L$ [4, 8]. Recently, a GaAs/AlAs superlattice oscillator with $\nu_{osc} = 103$ GHz (power 0.5 mW) has been achieved [9]; the miniband width was 120 meV. Other materials such as InGaAs/AlAs [10] should allow to develop oscillators for still higher frequencies. The superlattice can either be integrated into a planar circuit or into a waveguide resonator [11].

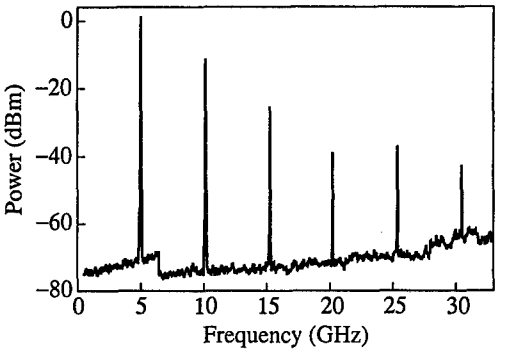

Fig. 5. Emission spectrum of the superlattice oscillator.

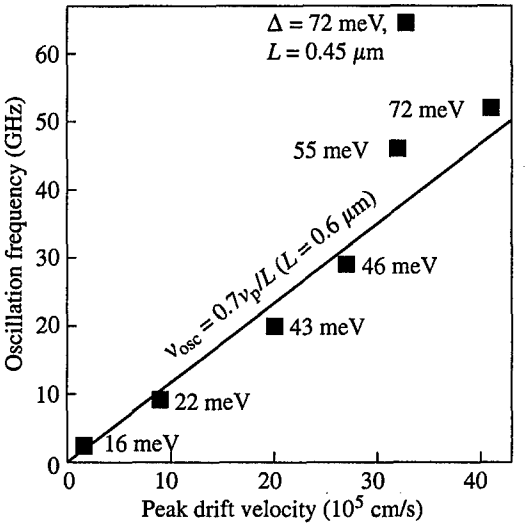

Fig. 6. Superlattice oscillator frequency for superlattices with different Δ.

3 Superlattice detector and frequency multiplier for microwaves

A microwave field influences the current through a superlattice according to the current-voltage characteristic leading to both a direct-current reduction [12] as well as generation of radiation at higher harmonics. Frequency multiplication up to the submillimeter frequency range (320 GHz) has been demonstrated [13, 12].

4 Superlattice detector and autocorrelator for THz radiation

A THz field can directly interact with a blochoscillating electron leading to a modulation of the Bloch frequency according to [14, 15]

$$\omega_B(t) = \frac{ea}{\hbar} E_s + \frac{ea}{\hbar} \hat{E}_\omega \cos(\omega t) \tag{3}$$

where $\hat{E}_\omega$ is the amplitude and ω the angular frequency of the THz field. The modulation leads to a reduction of the drift velocity [14, 15, 16, 17]. Accordingly, the current through a superlattice is reduced during THz irradiation. The response, i.e. the current reduction,

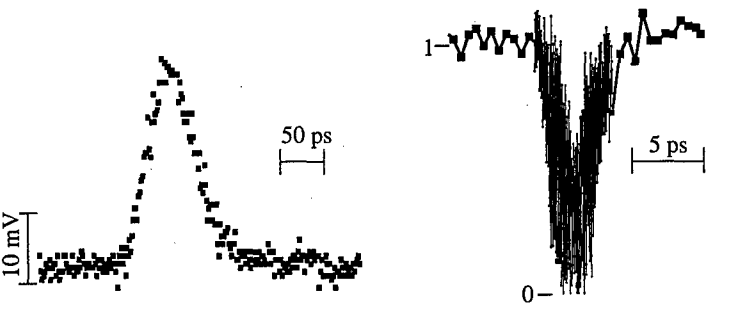

Fig. 7. Signal (left) and autocorrelation signal (right) for 4.3 THz radiation.

is proportional to the power of the radiation. The detection is illustrated in Fig. 7, which shows the response of a superlattice mesa, mounted in a corner cube antenna, on picosecond pulses of the FELIX free electron laser in Rijnhuizen (The Netherlands) [18]. The time resolution (50 ps) was determined by the registering sampling oscilloscope.

The superlattice acts as linear detector over many orders of magnitude of the power of the high-frequency field. At very strong irradiation, the current through the superlattice is almost completely suppressed [15, 16, 17]. This nonlinearity allows to perform autocorrelation experiments. In a first experiment [18] it has been demonstrated that the autocorrelator is able to resolve the 3 ps pulses of the FELIX laser (Fig. 7). The intrinsic time resolution of the detector and the autocorrelator is determined by the intraminiband relaxation time (10^{-13} s).

5 Conclusion

Wide-miniband semiconductor superlattice devices (at room temperature) can be used for generation, detection and frequency multiplication of microwave radiation up to frequencies above 100 GHz and, furthermore, for detection and autocorrelation of radiation at frequencies above 1 THz.

References

[1] L. Esaki und R. Tsu, *IBM J. Res. Dev.* **14**, 61 (1979).

[2] F. Bloch, *Z. Physik* **52**, 555 (1928); C. Zener, *Proc. Roy. Soc. London Ser. A* **145**, 523 (1934).

[3] A. Sibille, J. F. Palmier, H. Wang, J. C. Esnault and F. Mollot, *Appl. Phys. Lett.* **56**, 256 (1990); A. Sibille, J. F. Palmier, H. Wang, and F. Mollot, *Phys. Rev. Lett.* **64**, 52 (1990); M. Hadjazi, A. Sibille, J. F. Palmier, and F. Mollot, *Electron. Lett.* **27**, 1101 (1991).

[4] E. Schomburg, T. Blomeier, K. Hofbeck, J. Grenzer, S. Brandl, I. Lingott, A. A. Ignatov, K. F. Renk, D. G. Pavel'ev, Yu. Koschurinov, B. Ya. Melzer, V. Ustinov, S. Ivanov, A. Zhukov and P. S. Kop'ev, *Phys. Rev. B* **58**, 4035 (1998).

[5] K. Hofbeck, J. Grenzer, E. Schomburg, A. A. Ignatov, K. F. Renk, D. G. Pavel' ev, Yu. Koschurinov, B. Melzer, S. Ivanov, S. Schaposchnikov and P. S. Kop'ev, *Phys. Lett. A* **218**, 349 (1996).

[6] E. Schomburg, K. Hofbeck, J. Grenzer, T. Blomeier, A. A. Ignatov, K. F. Renk, D. G. Pavel'ev, Yu. Koschurinov, V. Ustinov, A. Zhukov, S. Ivanov and P. S. Kop'ev, *Appl. Phys. Lett.* **71**, 401 (1997).

[7] K. Hofbeck, E. Schomburg, J. Grenzer, K. F. Renk, D. G. Pavel'ev, Yu. Koschurinov, B. Melzer, S. Ivanov and P. S. Kop'ev, *IEEE Microw. Guid. Wave Lett.* **8**, 427 (1998).

[8] E. Schomburg, S. Brandl, K. Hofbeck, T. Blomeier, J. Grenzer, A. A. Ignatov, K. F. Renk, D. G. Pavel'ev, Yu. Koschurinov, V. Ustinov, A. Zhukov, A. Kovsch, S. Ivanov and P. S. Kop'ev, *Appl. Phys. Lett.* **72**, 1498 (1998).

[9] E. Schomburg, M. Henini, J. M. Chamberlain, D. P. Steenson, S. Brandl, K. Hofbeck, K. F. Renk and W. Wegscheider, *Appl. Phys. Lett.* **74** (1999).

[10] S. Brandl, E. Schomburg, R. Scheuerer, K. Hofbeck, J. Grenzer, K. F. Renk, D. G. Pavel'ev, Yu. Koschurinov, A. Zhukov, A. Kovsch, V. Ustinov and P. S. Kop'ev, *Appl. Phys. Lett.* **73**, 3117 (1998).

[11] J. Grenzer, A. A. Ignatov, E. Schomburg, K. F. Renk, D. G. Pavel'ev, Yu. Koschurinov, B. Melzer, S. Ivanov, S. Schaposchnikov and P. S. Kop'ev, *Ann. Physik* **4**, 184 (1995).

[12] E. Schomburg, A. A. Ignatov, J. Grenzer, K. F. Renk, D. G. Pavel'ev, Yu. Koschurinov, B. Ja. Melzer, S. Ivanov, S. Schaposchnikov and P. S. Kop'ev, *Appl. Phys. Lett.* **68**, 1096 (1996).

[13] E. Schomburg, J. Grenzer, K. Hofbeck, C. Dummer, S. Winnerl, A. A. Ignatov, K. F. Renk, D. G. Pavel'ev, Yu. Koschurinov, B. Melzer, S. Ivanov, V. Ustinov and P. S. Kop'ev, *IEEE J. Sel. Top. Quantum Electron.* **2**, 724 (1996).

[14] A. A. Ignatov, K. F. Renk and E. P. Dodin, *Phys. Rev. Lett.* **70**, 1996 (1993).

[15] A. A. Ignatov, E. Schomburg, J. Grenzer, K. F. Renk and E. P. Dodin, *Z. Phys. B* **98**, 187 (1995).

[16] S. Winnerl, E. Schomburg, J. Grenzer, H.-J. Regl, A. A. Ignatov, A. D. Semenov and K. F. Renk, *Phys. Rev. B* **56**, 10303 (1997).

[17] A. A. Ignatov, E. Schomburg, K. F. Renk, W. Schatz, J. F. Palmier and F. Mollot, *Ann. Physik* **3**, 137 (1994).

[18] S. Winnerl, W. Seiwerth, E. Schomburg, J. Grenzer, K. F. Renk, C. J. G. M. Langerak, A. F. G. van der Meer, D. G. Pavel'ev, Yu. Koschurinov, A. A. Ignatov, B. Melzer, V. Ustinov, S. Ivanov and P. S. Kop'ev, *Appl. Phys. Lett.* **73**, 2983 (1998); S. Winnerl, S. Pesahl, E. Schomburg, J. Grenzer, K. F. Renk, H. P. M. Pellemans, A. F. G. van der Meer, D. G. Pavel'ev, Yu. Koschurinov, A. A. Ignatov, B. Melzer, V. Ustinov, S. Ivanov, P. S. Kop'ev, *Superlattices Microstruct.* **25**, 57 (1999).

7th Int. Symp. "Nanostructures: Physics and Technology"
St Petersburg, Russia, June 14–18, 1999

Langevin method for shot noise in single-electron tunneling

A. N. Korotkov
Department of Physics, State University of New York, Stony Brook,
NY 11794-3800, USA *and*
Nuclear Physics Institute, Moscow State University, Moscow 119899, Russia

Abstract. The shot noise in correlated single-electron tunneling can be calculated using the Langevin approach. It is equivalent to the Fokker–Plank-type approach in the "orthodox" framework, however, the advantage is a natural possibility to describe also the fluctuations in the quantum frequency range.

Correlated single-electron tunneling [1] remains an attractive topic during last decade. The theoretical study of the shot noise in this regime is interesting because the noise reflects rather directly the correlations in the charge transport, and also because the noise determines the ultimate sensitivity of single-electron devices.

The shot noise in single-electron tunneling is due to the randomness of tunneling events. The earlier developed formalism [2] of noise calculation is of the Fokker–Plank type and is based on the deterministic master equation of "orthodox" theory[1] (we assume sufficiently large tunnel resistances, $R_j \gg h/e^2$):

$$\dot{\sigma} = \Gamma\sigma\,, \tag{1}$$

where the element σ_n of the vector σ is the probability to find the system in the charge state $n \equiv \{n_1, \ldots n_L\}$ (which is characterized by the numbers n_i of excess electrons in each of L internal nodes of the system) and

$$\Gamma_{mn} = \Gamma_{m\leftarrow n} - \delta_{mn}\sum_k \Gamma_{k\leftarrow n}, \qquad \Gamma_{m\leftarrow n} = \sum_j \Gamma^j_{m\leftarrow n}, \tag{2}$$

where $\Gamma^j_{m\leftarrow n}$ are the corresponding tunneling rates and the summation over the junction number j is necessary when an electron can tunnel to (from) an internal node from (to) different external electrodes.

To find the mutual spectral density for two processes $X(t)$ and $Y(t)$ we can calculate first the correlation function $K_{XY}(\tau) = \langle X(t+\tau)Y(t)\rangle - \langle X\rangle\langle Y\rangle$ (brackets denote the averaging over time) and then take the Fourier transform $S_{XY}(\omega) = 2\int_{-\infty}^{+\infty} K_{XY}(\tau)\exp(i\omega\tau)\,d\tau$. If both X and Y are functions of the charge state n (for example, potential of a node) then the correlation function is given by the simple expression

$$K_{XY}(\tau) = \theta(\tau)\sum_{m,n} X(m)\,\sigma(\tau, m|n)\,Y(n)\,\sigma^{st}_n + \theta(-\tau)\sum_{m,n} Y(m)\,\sigma(m, -\tau|n) \times X(n)\,\sigma^{st}_n - \langle X\rangle\langle Y\rangle, \tag{3}$$

where $\sigma(\tau, m|n)$ is the retarded Green's function of Eq. (1) being the probability to find the system in the state m at $t = \tau > 0$ if at $t = 0$ it was in the state n, $\langle X\rangle = \sum_n X(n)\sigma^{st}_n$, and σ^{st}_n is the stationary distribution, $\Gamma\sigma^{st} = 0$, $\sum_n \sigma^{st}_n = 1$.

However, if X and/or Y represent the current through a tunnel junction or in an external lead, Eq. (3) should be modified. For example, if $X(t)$ is the current contribution corresponding to tunneling events $\Gamma^j_{m\leftarrow n}$ while $Y(t)$ corresponds to $\Gamma^{j'}_{m'\leftarrow n'}$, then (similar to Ref. [2])

$$K_{XY}(\tau)/\tilde{e}^j_\pm \tilde{e}^{j'}_\pm = \theta(\tau)\,\Gamma^j_{m\leftarrow n}\,\sigma(\tau, n|m')\,\Gamma^{j'}_{m'\leftarrow n'}\sigma^{st}_{n'} + \theta(-\tau)\,\Gamma^{j'}_{m'\leftarrow n'}$$
$$\times\sigma(n', -\tau|m)\Gamma^j_{m\leftarrow n}\,\sigma^{st}_n - \Gamma^j_{m\leftarrow n}\sigma^{st}_n\,\Gamma^{j'}_{m'\leftarrow n'}\sigma^{st}_{n'} + \delta_{mm'}\delta_{nn'}\delta_{jj'}\delta(\tau)\,\Gamma^j_{m\leftarrow n}\sigma^{st}_n \quad (4)$$

Here the last term is responsible for the high-frequency limit. The effective charges $\tilde{e}^j_\pm$ and $\tilde{e}^{j'}_\pm$ are determined by the direction of electron tunneling, $\tilde{e}^j_+ = -\tilde{e}^j_-$, and by the circuit capacitances [2] (so that $\tilde{e}^j = e$ only if the current through junction j is measured). Any current–current correlation function can be written as a sum of $K_{XY}(\tau)$ given by Eq. (4) over all possible transitions between charge states (such a sum is a counterpart of Eq. (3) in which the sum is written explicitly).

The expressions for spectral densities directly follow from Eqs. (3) and (4) because the Fourier transformation affects only the evolution operator $\sigma(\tau, m|n)$, and the corresponding Green's function in the frequency representation is simply obtained from Eq. (1): $\sigma(\omega, m|n) = [(-i\omega\mathbf{1} - \Gamma)^{-1}]_{mn}$, where $\mathbf{1}$ is the unity matrix. For example, Eq. (4) leads to the following spectral density:

$$S_{XY}(\omega)/\tilde{e}^j_\pm \tilde{e}^{j'}_\pm = 2\,\Gamma^j_{m\leftarrow n}\left[(-i\omega\mathbf{1} - \Gamma)^{-1}\right]_{nm'}\Gamma^{j'}_{m'\leftarrow n'}\sigma^{st}_{n'}$$
$$+ 2\,\Gamma^{j'}_{m'\leftarrow n'}\left[(i\omega\mathbf{1} - \Gamma)^{-1}\right]_{n'm}\Gamma^j_{m\leftarrow n}\sigma^{st}_n + 2\,\delta_{nn'}\delta_{mm'}\delta_{jj'}\,\Gamma^j_{m\leftarrow n}\,\sigma^{st}_n. \quad (5)$$

This method allows to calculate all spectral densities within the framework of "orthodox" theory, and at least for the single-electron transistor the numerical procedure is rather trivial [2] because the matrix Γ is three-diagonal and the matrix inversion is straitforward.

The alternative method of calculations can be based on the Langevin-type approach [3]. Because of the discrete nature of the charge states, the random term cannot be simply added (in analogy with the standard Langevin method) to some evolution equation for the "coordinate" $n(t)$, but should be introduced into the master equation (similar to Ref. [4]). The derivation of the formalism can be understood in the following way. Let us consider the ensemble of M ($M \gg 1$) independent similar circuits, and let us average all magnitudes over this ensemble. Then the average (over time) currents and voltages will not change (due to ergodicity), but the spectral densities of fluctuations (second order magnitudes) will decrease M times. Hence, to calculate spectral densities of the initial system, we can take the leading ($\sim M^{-1}$, $M \to \infty$) order of the spectral density of magnitudes averaged over the ensemble.

In contrast to the single system, the dynamics of the large ensemble is easily described using the Langevin approach. At any moment of time t the ensemble can be characterized by "coordinates" $M\sigma_n(t)$ which represent the numbers of participants being in different charge states n (notice that now $\sigma_n(t)$ is not a probability but the fluctuating coordinate). While in the stationary state the average number of transitions from state m to state n during small time Δt is given by $M\Gamma_{m\leftarrow n}\sigma^{st}_n\Delta t$, the r.m.s. of this number is obviously $(M\Gamma_{m\leftarrow n}\sigma^{st}_n\Delta t)^{1/2}$. Hence, the recipe is the following [4]: for each average flux $M\Gamma^j_{m\leftarrow n}\sigma^{st}_n$ in the space of charge states, we should add in the master equation the

random δ-correlated (white) flux $\xi^j_{m\leftarrow n}(t)$ with the corresponding "seed" spectral density given by Schottky-like formula,

$$\dot{\sigma}_m(t) = \sum_n \Gamma_{mn}\sigma_n(t) + \xi_m(t), \qquad \xi_m(t) = \sum_{n,j} \xi^j_{m\leftarrow n}(t) - \xi^j_{n\leftarrow m}(t), \tag{6}$$

$$S_{\xi^j_{m\leftarrow n}\xi^{j'}_{m'\leftarrow n'}}(\omega) = 2M^{-1}\delta_{mm'}\delta_{nn'}\delta_{jj'}\Gamma^j_{m\leftarrow n}\sigma^{st}_n. \tag{7}$$

For the fluxes in opposite directions ($m \leftarrow n$ and $n \leftarrow m$) we should apply $\xi(t)$ for each direction, so that the random flux does not vanish even if the net average flux is zero.

Because of the linearity of Eqs. (6)–(7) the final spectral densities of the averaged (over M) magnitudes are obviously proportional to $1/M$. Hence, rescaling to the single system can be done formally assuming $M = 1$ in Eqs. (6)–(7). So, instead of keeping M and rescaling at the final stage, we will use $M = 1$ in all equation below.

Using the standard procedure we find the Fourier transform

$$\sigma_m(\omega) = \left[(-i\omega\mathbf{1} - \Gamma)^{-1}\right]_{mn}\xi_n(\omega). \tag{8}$$

Then for the occupation–occupation spectral density we obtain the expression

$$\begin{aligned} S_{\sigma_m\sigma_n} &= \sum_{m'n'}\left[(-i\omega\mathbf{1} - \Gamma)^{-1}\right]_{mm'}\left[(i\omega\mathbf{1} - \Gamma)^{-1}\right]_{nn'} S_{\xi_{m'}\xi_{n'}} \\ &= 2\left[(-i\omega\mathbf{1} - \Gamma)^{-1}\right]_{mn}\sigma^{st}_n + 2\left[(i\omega\mathbf{1} - \Gamma)^{-1}\right]_{nm}\sigma^{st}_m, \end{aligned} \tag{9}$$

which coincides with the result of Fokker-Plank approach (Fourier transform of Eq. (3) without X and Y factors).

The technique is similar for the current–current fluctuations. The case of Eqs. (4) and (5) corresponds to currents

$$X(t) = \tilde{e}^j_{\pm}\left[\Gamma^j_{m\leftarrow n}\sigma_n(t) + \xi^j_{m\leftarrow n}(t)\right], \quad Y(t) = \tilde{e}^{j'}_{\pm}\left[\Gamma^{j'}_{m'\leftarrow n'}\sigma_{n'}(t) + \xi^{j'}_{m'\leftarrow n'}(t)\right], \tag{10}$$

and the straitforward calculations using Eqs. (7) and (8) lead to Eq. (5). Thus, the Fokker-Plank method is equivalent to the Langevin method within the "orthodox" framework. However, in contrast to the former approach, the Langevin method easily allows phenomenological generalization for the fluctuations in the range of high ("quantum") frequencies, $\hbar\omega \sim eV$.

Let us remind that in "orthodox" theory [1] the tunneling rate $\Gamma = I_0(W/e)/e[1 - \exp(-W/T)]$ is determined by the energy gain due to tunneling $W = eV_b - e^2/2C_{eff}$, where $I_0(v)$ is the "seed" *I-V* curve of the junction (in the linear case $I_0(v) = v/R_j$), V_b is the voltage across the junction before the tunneling, C_{eff} is the effective junction capacitance (which also accounts for the environment), and T is the temperature. The generalization of the Langevin method is the substitution of Eq. (7) by the equation

$$\begin{aligned} S_{\xi^j_{m\leftarrow n}\xi^{j'}_{m'\leftarrow n'}}(\omega) &= \delta_{mm'}\delta_{nn'}\delta_{jj'}[\tilde{\Gamma}^+ + \tilde{\Gamma}^-]\sigma^{st}_n, \\ \tilde{\Gamma}^{\pm} &= \frac{I_{0,j}(W^j_{m\leftarrow n}/e \pm \hbar\omega/e)}{e\left[1 - \exp\left(-(W^j_{m\leftarrow n} \pm \hbar\omega)/T\right)\right]}, \end{aligned} \tag{11}$$

which is derived for the individual tunneling event within the standard tunneling hamiltonian technique averaging the quantum current–current correlator and then taking the Fourier transform. Eq. (11) can be considered as a generalization of the fluctuation-dissipation theorem and equations of Ref. [5] for the case of single-electron tunneling. (Actually, the only difference is that we separate fluctuations corresponding to two directions of tunneling. In absence of the Coulomb blockade they could be summed together leading to the standard factor [5] $\coth((W \pm \hbar\omega)/2T)$ instead of the denominator of Eq. (11).)

Equations (6) and (11) represent a phenomenological generalization in which the low frequency behavior is treated by the master equation while high frequency properties are taken into account for individual tunneling events. At high frequencies, $\omega \gg \Gamma$, the occupation–occupation and occupation–current spectral densities vanish, while for the current–current spectral density instead of Eq. (5) we get $S_{XY}(\omega) = \tilde{e}^j_\pm \tilde{e}^{j'}_\pm S_{\xi^j_{m\leftarrow n}\xi^{j'}_{m'\leftarrow n'}}(\omega)$, because the first terms of Eq. (10) are too slow to give a contribution. This result coincides with the result of Ref. [6]. The advantage of the Langevin approach is the possibility to obtain spectral densities in the "orthodox" and "quantum" frequency ranges using the same formalism while before they were necessarily being treated on different footing.

Notice that in the "quantum" frequency range the current spectral density does not correspond directly to the available power because of the contribution from zero-point oscillations. The contribution to be subtracted from $S_{\xi^j_{m\leftarrow n}}$ is equal to $2\hbar\omega \mathrm{Re}G(\omega)$, where the active conductance

$$\mathrm{Re}G(\omega) = \left((\tilde{e}^j_\pm)^2/2\hbar\omega\right)[\tilde{\Gamma}^+ - \tilde{\Gamma}^-] \tag{12}$$

corresponds to the lowest order of photon-assisted tunneling.

Acknowledgements

The author is grateful to S. V. Gantsevich, Sh. M. Kogan, N. E. Korotkov, and K. K. Likharev for the valuable discussions.

The work was supported by US AFOSR and Russian Foundation for Basic Research.

References

[1] D. V. Averin and K. K. Likharev, in *Mesoscopic Phenomena in Solids*, edited by B. L. Altshuler et al. (Elsevier, Amsterdam, 1991), p. 173.

[2] A. N. Korotkov, D. V. Averin, K. K. Likharev, and S. A. Vasenko, in *Single-Electron Tunneling and Mesoscopic Devices*, edited by H. Koch and H. Lubbig (Springer-Verlag, Berlin Heidelberg, 1992), p. 45; A. N. Korotkov, *Phys. Rev. B* **49**, 10381 (1994).

[3] A. N. Korotkov, *Europhys. Lett.* **43**, 343 (1998).

[4] Sh. M. Kogan, A. Ya. Shul'man, *Sov. Phys. JETP* **29**, 467 (1969).

[5] A. J. Dahm, A. Denenstein, D. N. Langenberg, W. H. Parker, D. Rogovin, and D. J. Scalapino, *Phys. Rev. Lett.* **22**, 1416 (1969); A. I. Larkin and Yu. N. Ovchinnikov, *Sov. Phys. JETP* **26**, 1219 (1968).

[6] A. N. Korotkov, D. V. Averin, and K. K. Likharev, *Phys. Rev. B* **49**, 1915 (1994).

7th Int. Symp. "Nanostructures: Physics and Technology"
St Petersburg, Russia, June 14–18, 1999

Single electron transistor of stack design as ultrasensitive electrometer

V. A. Krupenin†, *D. E. Presnov*†, A. B. Zorin‡ and J. Niemeyer‡
† Laboratory of Cryoelectronics, Moscow State University, 119899 Moscow, Russia
‡ Physikalisch-Technische Bundesanstalt D-38116 Braunschweig, Germany

Abstract. We have fabricated and studied the noise characteristics of the stack-junction Single Electron Tunneling (SET) electrometer, in which the island was completely screened from a dielectric substrate. The noise figure of the device was found to be surprisingly low: an equivalent charge noise was less than $8 \times 10^{-6}\, e/\sqrt{\text{Hz}}$ at the frequency 10 Hz or, in energy units, $30\,\hbar$.

Introduction

In the last years the first attempts to define the location of noise sources in metallic Single Electron Tunneling (SET) structures have been done. Noise measurements of SET transistors have detected a trend of the noise increase with the size of an island [1], have shown a correlation of the noise signals of two closely positioned devices [2], have demonstrated that the noise level of the transistor strongly depends on the contact area of its island with a substrate [4]. Recently, it was shown that the transistors of the stack design have the lowest level of the background charge noise measured so far, namely $2.5 \times 10^5\, e/\sqrt{\text{Hz}}$ at the frequency 10 Hz [5]. Although the contact area of an island and substrate in these structures was nominally zero, a possible small-area interface could not be ruled out. In this paper we report on the study of an Al SET transistor of "improved" stack geometry which ensured complete screening of the island from the substrate. Our design allows to eliminate completely the influence of the charge noise sources peculiar to a dielectric substrate on the electrometer noise figure.

1 Fabrications and characterizations of the samples

The Al structure (Fig. 1) was fabricated on a Si substrate buffered by a sputtered Al_2O_3 layer 200 nm thick. The traditional shadow evaporation technique and e-beam lithography were used for the structure fabrication process. There were three successive deposition cycles in-situ at three different angles and two oxidation processes in between to form tunnel barriers. In contrast to the previous stacked samples [4, 5], in this device the *entire* island was placed on a bottom electrode of the structure (see Fig. 1). Since the dimensions of the island (nominally 80 nm by 80 nm) were noticeably smaller than the width of the bottom electrode (150 nm), the island was placed with some margins, it was reliably screened from fluctuating charges located in the dielectric substrate. The I–V curves of the structure, having total resistance $R = 1.25\,\text{M}\Omega$ and capacitance of the island $C_\Sigma = C_1 + C_2 + C_g = 270\,\text{aF}$, were measured at $T = 25\,\text{mK}$. These curves showed a finite conductance within the Coulomb blockade region and this pointed out to the existence of a "shunting" channel $R_{\text{shunt}} = 1.9\,\text{M}\Omega$ for current, namely a conducting tunnel barrier between the outer electrodes of the transistor. This fact ensured against possible contact between the island and the substrate, that might occur at the end edge of the bottom conductor. The resistance $R_\Sigma = R_1 + R_2$ of the SET transistor itself (i.e. the tunnel resistance of its two junctions) was evaluated to be

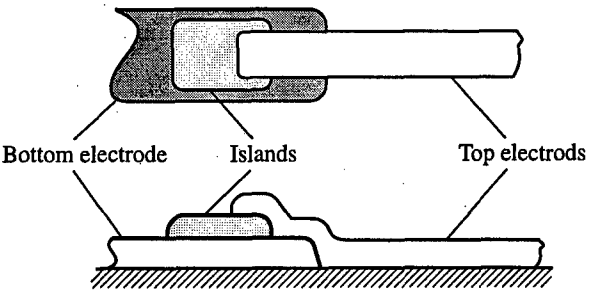

Fig. 1. A geometry of the transistor.

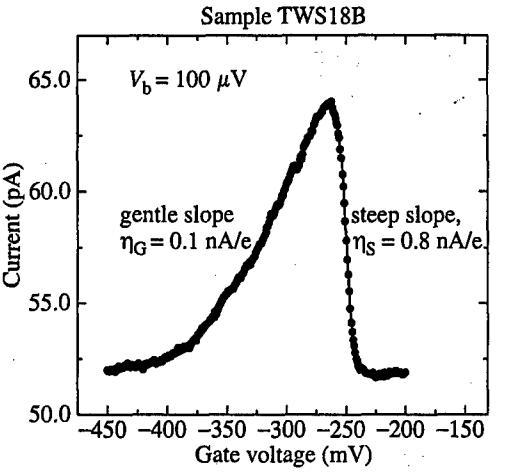

Fig. 2. Modulation curve of the transistor at bias voltage $V_b = 100\,\mu$V.

3.9 MΩ. Expecting a low level of noise in this device and some deterioration of the gain because of shunting channel, we have tried to make the transistor extremely asymmetric in order to get advantage of a steeper slope in the modulation characteristic (see Fig. 2). Fixing of the working point on this slope led to high value of a current-to-charge ratio

$$\eta = \max_{Q_0} \left| \frac{\partial I}{\partial Q_0} \right|_{V=\text{const}}.$$

The values C_1/C_2 and R_2/R_1, evaluated from experimental data, were in our devise as large as 10. The current-to-charge ratio for the steep slopes was in the range $\eta_C \approx 1 - 3$ nA/e depending on voltage across the transistor. These (rather large) values of η had substantially improved the signal-to-noise ratio of our transistor as electrometer.

2 Results and discussion

The transistor clearly exhibited $2e$-periodic modulation characteristics in the superconducting state and e-periodic modulation in the normal state. (That clearly testified to purity of the island material and its interfaces with the surrounding oxide.) The modulation patterns were surprisingly stable against a drift of the background charge. The output noise of this transistor was measured in the frequency range 0.3–100 Hz at different values of transport current I and in different working points of the modulation characteristic. At low I, the

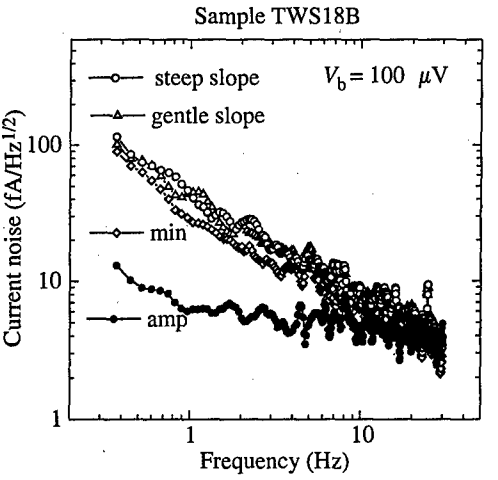

Fig. 3. Noise spectra of the transistor at different points of the modulation curve ($V_b = 100\,\mu$V).

output noise at $f \geq 0.3$ Hz did not show any dependence on the gate voltage (see Fig. 3). This indicated that the charge noise at $I \sim 10$ pA was very small. Thus the noise spectra in the points of the minimum, the gentle and steep slopes of the modulation curve had nearly the same level, which was presumably slightly less than the noise floor of the measuring setup (see the curve marked as *amp* in Fig. 3). The own noise of the preamplifier at 10 Hz was about $5.0 \times 10^{-15}\,\mathrm{A}/\sqrt{\mathrm{Hz}}$. The additional shot noise of the shunting junction, due to a current flowing through it, was estimated to be $\delta I = \sqrt{2eI} \approx 4.0 \times 10^{-15}\,\mathrm{A}/\sqrt{\mathrm{Hz}}$. Hence, the level of the background charge noise at 10 Hz expressed in current units was less than $6.5 \times 10^{-15}\,\mathrm{A}/\sqrt{\mathrm{Hz}}$. The noise figure expressed as an equivalent charge noise δQ_{0x} of the device was found to be less than $8 \times 10^{-6}\,e/\sqrt{\mathrm{Hz}}$ at 10 Hz or, in energy units,

$$\epsilon = \frac{(\delta Q_{0x})^2}{2C_\Sigma \Delta f} = \frac{S_I}{2C_\Sigma} \approx 30\,\hbar$$

To our knowledge, this is the best noise figure of a SET electrometer measured so far. The fundamental noise floor was estimated as $2 \times 10^{-6}\,e/\sqrt{\mathrm{Hz}}$ [3] or $\epsilon \sim 3\,\hbar$. At frequency $f \approx 20$ Hz all noise curves, presented in Fig. 3, have the same level $\delta I \approx 5.0 \times 10^{-15}\,\mathrm{A}/\sqrt{\mathrm{Hz}}$ and we can suggest that noise of the electrometer approached the fundamental noise floor set by stochastic tunneling events. Such delicate regime of the electrometer operation ($I \sim 10$ pA) demonstrates that contribution of the oxide tunnel barriers to the low-frequency noise can be very small. Therefore, this indicates conclusively that the main sources of the background charge fluctuations in metallic SET devices are located in dielectric substrates and the influence of these sources on the performance of SET devices can be considerably eliminated by screening of the islands from the substrate. The stack geometry of our devices shows one of the ways how to solve the problem of the background charge fluctuations.

Acknowledgements

This work is supported in part by the Russian Scientific Program "Physics of Solid State Nanostructures", the Russian Foundation of Fundamental Research, the German BMBF and the EU Project CHARGE.

References

[1] S. M. Verbrugh, *PhD thesis*, Delft University of Technology, 1995; S. M. Verbrugh, M. L. Benhamadi, E. H. Visscher and J. E. Mooij, *J. Appl. Phys.* **78**, 2830 (1995).

[2] A. B. Zorin, F.-J. Ahlers, J. Niemeyer, T. Weimann, H. Wolf, V. A. Krupenin and S. V. Lotkhov, *Phys. Rev. B* **53**, 13682 (1996).

[3] A. N. Korotkov, *Phys. Rev. B* **49**, 10381 (1994).

[4] V. A. Krupenin, D. E. Presnov, M. N. Savvateev, H. Scherer, A. B. Zorin and J. Niemeyer, *CPEM-98, Washington, D.C., U.S.A. July 6–10,* 140 (1998).

[5] V. A. Krupenin, D. E. Presnov, M. N. Savvateev H. Scherer, A. B. Zorin and J. Niemeyer, *J. Appl. Phys.* **48**, 3212 (1998).

7th Int. Symp. "Nanostructures: Physics and Technology"
St Petersburg, Russia, June 14–18, 1999

Processing and characterization of extended InP/GaInAs electron waveguides

I. Maximov, Q. Wang, M. Graczyk, P. Omling, L. Samuelson, W. Seifert and I. Shorubalko

Solid State Physics, Lund University, Box 118, Lund, S-221 00, Sweden

We present fabrication technology and characterization results of InP/GaInAs electron waveguides with lengths between 0.2 and 6 μm. The waveguides, all 100 nm wide, are produced by deep wet etching of high mobility 2DEG MOVPE-grown InP/$Ga_{0.25}In_{0.75}As$ structures. Typical mobility of the initial material is 450 000 cm^2/Vs and electron concentration is 3.5×10^{11} cm^{-2} [1]. The waveguide structures are defined by electron beam lithography at 35 kV and non-selective etchants HCl:CH_3COOH:H_2O_2 (HAP) [2] and a mixture of HBr:HNO_3:H_2O. A 250 nm-thick ZEP520 electron beam resist is used as an etch mask after post-development baking at 120°C to enhance its adhesion to the substrate [3]. These etchants give etch rate 10 and 3 nm/s for the HAP and HBr-based solutions, respectively and produce smooth InP surfaces suitable for immediate regrowth. After etching through the 2DEG layer, the structure is MOVPE-regrown at 600°C by nominally undoped 100 nm-thick InP layer to embed waveguides. To control the Fermi energy, we used a resist-insulated Au top gate made by a lift-off technique. The top view SEM images of 1 and 6 μm-long as-etched waveguides are shown in Figs. 1 and 2. Fig. 3 shows a typical example of the quantized conductance as a function of the top gate voltage in a regrown 100 nm-wide and 1 μm-long electron waveguide at 0.3 K. The effective channel width, calculated from the observed highest quantum number $n = 4$, is about 100 nm, which is equal to the lithographically defined channel width. It suggests no significant depletion of channel walls after epitaxial regrowth. We attribute it to the improvement of quality of the side walls by MOVPE regrowth. Temperature dependent measurements of the samples showthat the first and second conductance plateaus persist up to 7 K, which gives an energy separation between first and second subband at about 2.4 meV. This value is in agreement

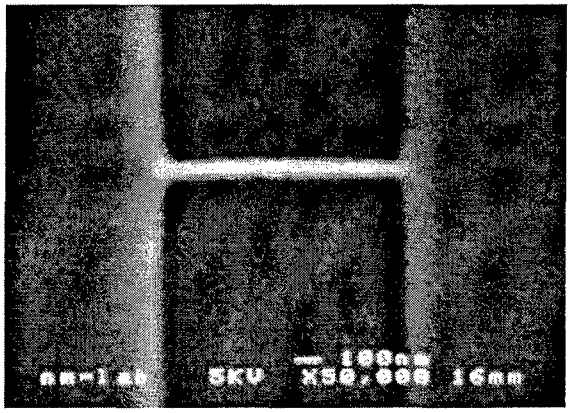

Fig. 1. SEM micrograph of 1 μm long, 100-nm wide electron waveguide produced in InP/$Ga_{0.25}In_{0.75}As$ 2DEG structure. The etching was performed in HCl:CH_3COOH:H_2O_2 solution at 4°C with ZEP 520 resist being an etch mask.

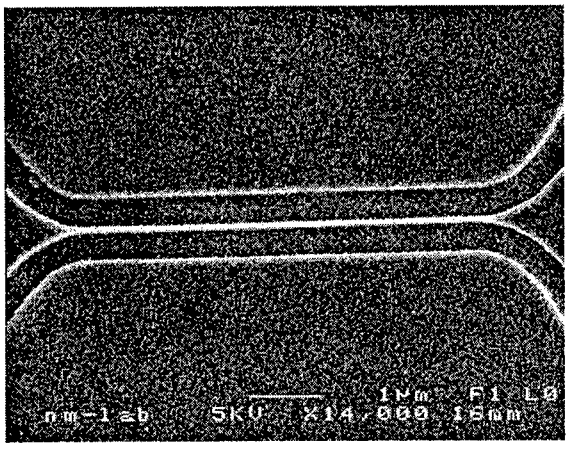

Fig. 2. SEM image of as-etched 6 μm long, 100-nm wide electron waveguide with side gates. Orientation of the waveguide is [110].

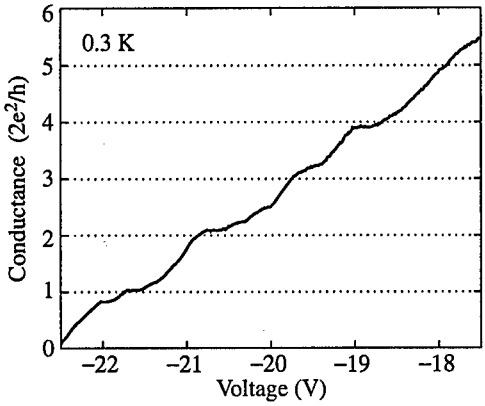

Fig. 3. Conductance, at 0.3 K, as a function of top gate voltage in the 100 nm-wide and 1 μm-long InP/$Ga_{0.25}In_{0.75}As$ waveguide, regrown with undoped InP.

with the calculation for a 100 nm wide channel by using a hard wall square-well potential.

This work is performed within ESPRIT IV Long Term Research, Q-SWITCH program, project number 30960.

References

[1] P. Ramvall, N. Carlsson, P. Omling, L. Samuelson, W. Seifert, M. Stolze and Q. Wang, *Appl. Phys. Lett.* **68**, 1111 (1996).

[2] I. Maximov, N. Carlsson, P. Omling, P. Ramvall, L. Samuelson, W. Seifert, Q. Wang, S. Lourdudoss, E. Rodrigues Messmer, A. Forchel and K. Kerkel, *Proc. 9-th International Conference on Indium Phosphide and Related Materials*, Hyannis, Cape Cod, MA, USA p. 145-148, 1997.

[3] I. Maximov, A. L. Bogdanov and L. Montelius,*J. Vac. Sci. Technol.* **B15**, 2921 (1997).

7th Int. Symp. "Nanostructures: Physics and Technology"
St Petersburg, Russia, June 14–18, 1999

Nanotechnology methods and creation of the terabit storage

V. A. Bykov, A. V. Emelyanov, E. A. Poltoratski and *V. N. Riabokon*
State Research Center Zelenograde State Research Physical Problem Institute,
Zelenograd, Moscow, 103460, Russia

A special direction of research in the field of nanoelectronic devices is creation of storage devices having superhigh density and terabit capacity (terabit storage). The idea that such storage devices can be created appeared soon after STM capable of manipulating separate atoms had been developed — in the US the corresponding patent was granted in 1986. A wide diversity of ways to form local nonuniformities on a great variety of surfaces have been tried, to the point of carrying atoms from place to place and making inscriptions and pictures of them. The most impressing achievements of this "romantic" period were the works of Eigler, Mamin, Aono. However, it became clear rather quickly that the use of STM as a reading tool imposes very stringent requirements on the storage medium. The basis of STM operation — tunnel current — exponentially depends on the probe-substrate gap estimated at several of angstroms. For this reason, recording-reading speeds at a level of 10^5-10^6 bits per second can only be achieved with storage elements being identical practically with atomic accuracy. This means that it is necessary to work either under conditions of superhigh vacuum or under usual conditions, but with atomically smooth and atomically ordered substrates.

To meet these requirements, the concept of using self-organizing ordered atomic-molecular structures as a storage medium was put forward, and the appropriate copyright certificate was received in the USSR in 1989 (A. V. Emelyanov, E. A. Poltoratsky, N. S. Samsonov. Read-only memory and method of writing. USSR Pat. N 1655240. Prior. 30.01.1989). Ordered structures of organosilicon compounds on graphite substrates were tested, and the possibility of recording memory elements of size 0.5 nm was demonstrated. However, the uncontrollability of the STM probe tip at the atomic level and the limited set of substrates allowing work under normal conditions gave no way of going beyond separate successful experiments. Moreover, works performed under conditions of superhigh vacuum on atomically clean surfaces have shown that carrying separate atoms from a substrate to a probe or from a probe onto a substrate is far from being so simple. These processes are of probabilistic character with characteristic times at the level of several to tens of milliseconds, so the necessity for normal storage operation recording validity at a level 10^5-10^6 is out of the question.

The success in development of the atomic force microscopy, and in particular, the opportunity to use micromechanical cantilevers became an essential stimulus to intensification of works on creating terabit storage. By now, impressing results concerning storage media have been obtained: equivalent recording speeds of 0.01–0.1 Mbits per second on a polymeric carrier with a micromechanical cantilever containing a built-in device for warming-up the probe tip and reading speeds of the order of 1 Mbits per second with lightweight cantilevers are possible. Some breadboard models of the terabit storage were tested, the polycarbonate polymer used for manufacturing CD and DVD is a good model of storage medium for them. As a result of the researches carried out by us with the help of AFM (Solver-P4-18RM, Solver-P47, NT MDT Co., Moscow-Zelenograd, www.ntmdt.ru), 10 kbit arrays of bit-by-bit recording (Fig. 1) with a density of 100 Gbit/cm^2 and also arrays

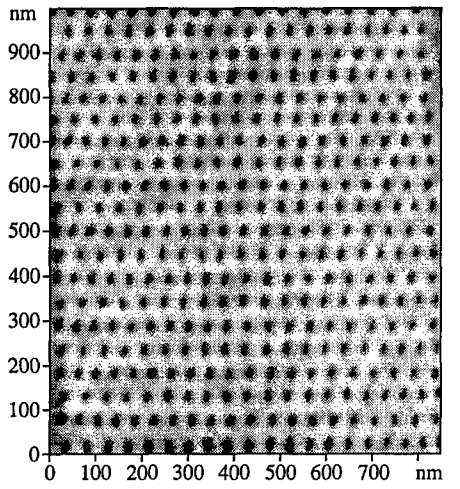

Fig. 1. Example of bit-by-bit recording.

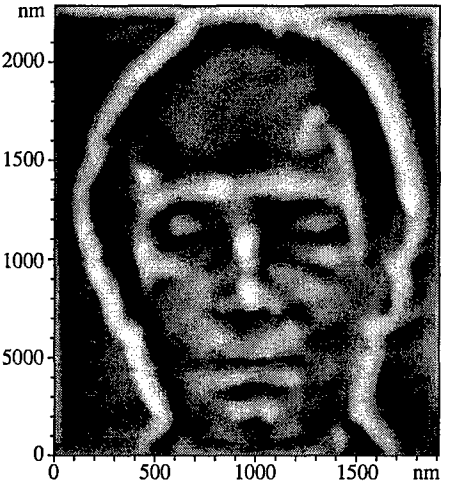

Fig. 2. Example of analog recording.

of analog image recording (Fig. 2) with an equivalent density of 800 Gbit/cm^2 were obtained. A complex approach is necessary for successful development of the terabit storage. This is due first of all to the interdependence of the parameters of a storage device and the micromechanical recording–reading head. A compromise should be reached on a lot of parameters, beginning with those directly associated with the functioning principle of a storage medium (recording on a relief, recording on electrical, magnetic and other nonuniformities), and also including, for example, such parameters, as mechanical properties of the material of the store (wear resistance) and cantilever (rigidity and weight).

Thus, the basic tasks in the initial stage are to develop both a storage device and a microelectromechanical recording–reading head with corresponding characteristics, and then to elaborate technical requirements and ways for creating other elements of the terabit storage: addressing systems, store drive, electronic control units, software etc. It is necessary to note that unlike the storage device, the above units are already present to some extent in atomic force microscopes of the newest types and on CD and magnetic disks, which must ensure a certain continuity of the development of similar storage system units.

The achieved recording and reading speeds are insufficient for successful competition in a set of parameters with the storage systems developed on the basis of traditional methods. Use of multiprobe devices is a natural way to increase the productivity of a recording and reading system. Taking into account the potential opportunity to create micromechanical probe devices with hundreds, up to a thousand of probes, devices with electrical recording and reading seem to be the optimal choice because of the simplest probe design and the system of recording-reading as a whole. Storage media with electrical recording–reading on the basis of arrays of metal clusters located on a semiconductor (silicon) substrate are of interest as storage media for the terabit storage in question. Nanometer-size clusters are made of metals forming silicides rather easily upon heating to several hundred degrees. A writing current pulse warms up the interface between a metal cluster and the silicon substrate and transforms it into silicide. This changes the Schottky barrier height and can be used for subsequent reading. A prototype structure investigated by us was made on the basis of porous silicon, into whose pores a metal, Pd in particular, was electrochemically

deposited. After etching porous silicon, Pd clusters of sizes 100–200 nm remained on its surface. These clusters were used as memory elements. In experiments carried out with Pd clusters at a reverse bias of −1.5 V the current varied between 1.6 and 5.5 nA.

The proposed class of storage devices represents a micromechanical design including plane or linear array of controlled probes with tensoresistive sensitive elements. The recording and reading in such storage devices are carried out by special micromechanical multiprobe heads with a large number of controlled microprobe on disks rotated by micromotors, or cylinders with a layer of a sensitive material specially deposited on the surface. The micromechanical multiprobe head contains very sharp probes with a radius of curvature of 1–2 nm, placed on mobile cantilevers. Such multiprobe heads (with 8 and 16 probes) are being developed by us now and used as sensor controls in atomic force microscopes. With the help of such probes, it is possible to make updating of a film structures surface similar to above mentioned. The density of probes in the multiprobe head can be as high as 100 probes per 1 mm. To enable recording with a step of up to 10 nm, a linear probe array is placed on a single-coordinate scanner (this may be a small piezoelectric table) providing parallel shift of the probe array.

Having an information storage capacity exceeding by two to three orders of magnitude that of modern storage devices based on magnetic and compact discs, comparable speeds of recording–reading and reduced mass and overall dimensional characteristics, the terabit storage devices are especially attractive for use in global (including space-borne) information networks, small spacecraft and unmanned space vehicles.

The above design of the storage device allows us to consider the storage medium based on silicon with a metallic cluster array also a basis for creating digital nanoelectronic devices. In phase transformation occurring during recording, coupling between closely spaced clusters varies together with the conductivity in the system metal cluster-substrate tunnel. This allows forming a certain system of tunnel-coupled quantum wells, which can form a basis for a computing device. This technology of creating digital nanoelectronic systems differs essentially from the traditional operating group methods of microelectronic technology, with technological parameters having some average values over the whole substrate. Thus, dispersion of the characteristics of separate nanoelements is inevitable, which gives no way of creating large computing systems. Application of micromechanical multiprobe nanolithographic heads furnishes essentially new opportunities. The action on a substrate becomes not averaged, but ratyher "intellectually" local. Thus, an opportunity arises to exert not simply local influence, but also to preliminarily define local parameters, to choose local technological modifications and to perform subsequent local control. Thus, it can be expected with greater confidence that large arrays of interacting nanoelements can be created with reasonable dispersion of parameters. The above-mentioned example of analog recording of images with dosed action in each point (Fig. 2) to a certain degree illustrates this approach.

The work was partly supported by the Programme "Physics of Solid State Nanostructures".

7th Int. Symp. "Nanostructures: Physics and Technology"
St Petersburg, Russia, June 14–18, 1999

Charging effects in a quantum wire with leads

V. A. Sablikov and S. V. Polyakov
Institute of Radio Engineering and Electronics, RAS,
Moscow Region, Fryazino, 141120, Russia

Abstract. We have found that a quantum wire in mesoscopic structures is charged as a result of the electron density redistribution between the wire and the reservoirs, which ones this wire connects. Charging of a wire is investigated in the frame of self-consistent field approach. The wire may be charged positively, negatively or be neutral as a whole. Correspondingly to these cases, a quantum well appear in the wire, a barrier arise between the wire and the leads or Friedel oscillations appear in the vicinity of the contacts. Charging of a quantum wire produces a variation in its conductance. This effect is especially important in non-linear transport regime.

Introduction

A great deal of interest is paid now to recent experiments on coherent electron transport in quantum wires [1, 2, 3]. Nonuniversality of conductance quantization [2] and especially the observation of $0.7 \cdot 2e^2/h$ conductance [3] show that new physical approaches based on many-body physics and exchange interaction should be attracted to understand these results. In this paper we draw attention to a charging effect of quantum wires which occurs in real quantum wire structures and, as far as we know, was not considered up to now. We show that together with an exchange interaction effect it has a profound impact on a conductance of mesoscopic quantum wires.

It is usually supposed, that the quantum wire has no charge as a whole (and in general, is locally neutral, if any impurity is absent there). In reality this is not the case. Certainly, a quantum wire (if it could be considered separately from the whole structure, it enters in which one) is neutral. However when a quantum wire is connected to the leads, which are bulky reservoirs of electrons, an equilibrium state of the whole system is established by means of the electron density redistribution between the wire and the leads. This results in charging the quantum wire. The analysis shows that three cases are possible depending on whether the chemical potential in the isolated wire is higher, lower or equal to that of the reservoirs.

(i) Electrons escape from the quantum wire when the equilibrium is established. In this case the wire is charged positively and a potential well for electrons appears there.

(ii) Electrons come into the quantum wire giving rise to a negative charge there. This charge creates a potential barrier appears which hinders the electrons to travel through the wire.

(iii) The electron density is not redistributed between the wire and the reservoirs when the equilibrium is established. In this case, the wire is not charged as a whole, though the Friedel oscillations of the electron density are presented near the contacts.

The charge, accumulated in a wire, and especially its change under the action the applied voltage produces an essential effect on the conductance. In particular, this may be a reason of anomalies observed experimentally.

1 The model

The approach we use here to study the charging effect in quantum wires is based on the consideration of a quantum wire and electron reservoirs as a unified quantum mechanical system with describing the electron-electron interaction within self-consistent Hartree–Fock approximation. Though this approximation underestimates correlation effects, it is very suitable to study charging effects, especially for nonlinear transport. The electron transport is described using one-dimensional Schrödinger equations while the electric field and the electron-electron interaction potential are determined from the solution of a three-dimensional Poisson equation with account of image charges induced on the lead surfaces [4]. For the sake of simplicity we restrict ourselves here with one-mode wires. The one-particle wave functions $\psi_{r,k}(x,t)$ are classified by quantum numbers k and $r = \pm$, where $r = +$ denotes the electrons incident on the wire from the left reservoir and $r = -$ does from the right one, k is wave vectors in the left and right reservoirs, where electron-electron interaction is screened owing to high conductivity. The wave functions are defined by equation

$$-\frac{\hbar^2}{2m}\frac{d^2\psi_{r,k}}{dx^2} + \left[U_0(x) - e\varphi_{\text{ext}}(x) - U_{\text{b}}(x) + U_{\text{H}}(x) + \hat{A}\right]\psi_{r,k} = \varepsilon_r(k)\psi_{r,k}\,, \qquad (1)$$

where U_0 is the built-in potential due to lateral confinement in the quantum wire, $\varphi_{\text{ext}}(x)$ is an external potential, U_{b} is built-in potential of the positive background charge in the wire, $U_{\text{H}}(x)$ is the Hartree potential, $\hat{A}$ is the exchange interaction operator,

$$\varepsilon_r(k) = U_0(-r\cdot\infty) + V_a\delta_{r,-} + \frac{\hbar^2k^2}{2m}\,.$$

The electron density n_{e} (as well as an exchange density) in the wire is defined with using distribution functions in reservoirs $f_\pm(k)$ which are Fermi functions shifted in energy due to the applied voltage

$$n_{\text{e}}(x) = \frac{1}{\pi}\sum_{r=\pm}\int_0^\infty dk'\, f_r(k')\left|\psi_{r,k'}(x)\right|\,.$$

The potentials U_{b}, U_{H} and $\hat{A}$ are defined in terms of Green's function $G(x,x')$ of the Laplace equation in the inter-reservoir space. Thus,

$$U_{\text{b}}(x) = \frac{e^2}{\epsilon a}\int_{-L/2}^{L/2} G(x,x')\,n_{\text{b}}\,dx'\,,$$

where n_{b} is a positive background charge density. n_{b} should be compared with the density $n_0 = 2[2m(\mu_0 - U_0)]^{1/2}/\pi\hbar$. Depending on whether n_{b} is higher, lower or equal to n_0, the chemical potential in the wire μ_{w} is higher, lower or equal to that in the reservoirs μ_0.

We have solved Eq. (1) numerically considering $\psi_{r,k}(x)$ as a function of two continuos variables: x and k. The solution gives the self-consistent distribution of the electron density and the electric current.

2 The equilibrium state

The ground (equilibrium) state is obtained at $V_a = 0$. The potential energy of electrons $U = U_0 + U_{\text{b}} + U_{\text{H}}$, which includes the self-consistent Hartree potential, is shown in Fig. 1

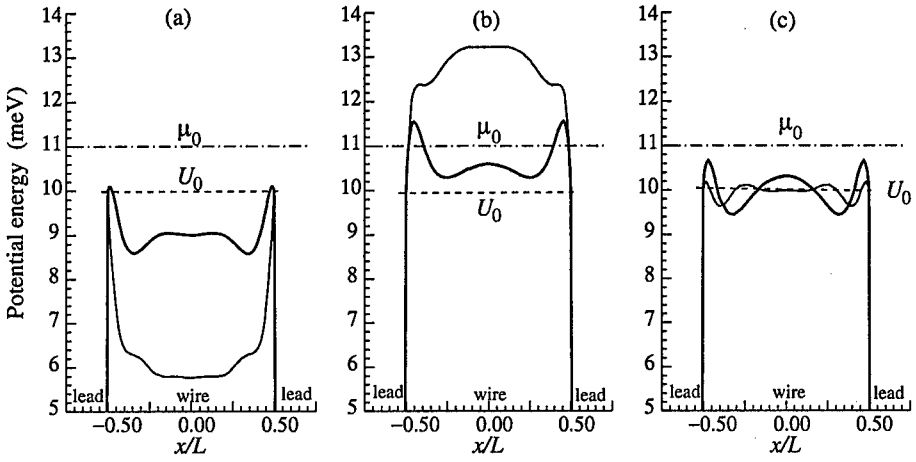

Fig. 1. Potential energy of an electron as a function of distance for cases (a), (b), (c) where $n_b/n_0 = 1.5, 0.5, 1.0$. Thick solid lines were obtained for $\mu_0 - U_0 = 1$ meV, dash-dotted line is the chemical potential, dotted line is U_0 energy. Thin solid lines show the potential energy for $\mu_0 - U_0 = 5$ meV. The parameters used in calculation were: the wire radius $a = 5 \cdot 10^{-7}$ cm, the wire length $L = 10^{-5}$ cm.

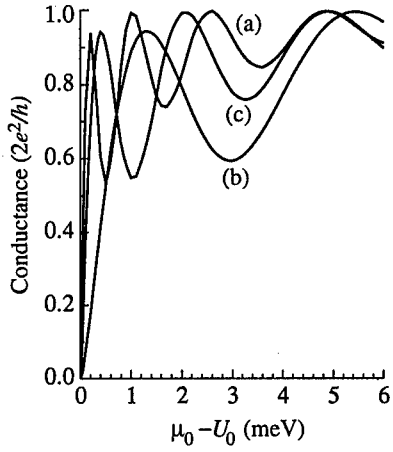

Fig. 2. The dependence of conductance on the chemical potential for the cases (a), (b), (c).

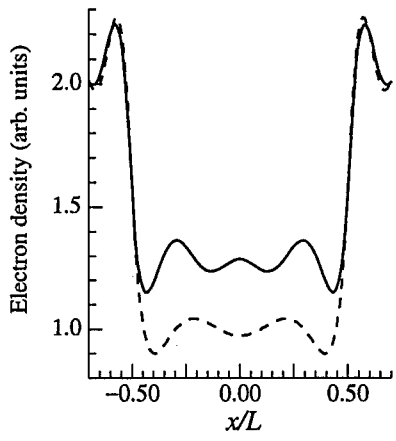

Fig. 3. The electron density distribution calculated with account of the exchange interaction (solid line) and ignoring it (dashed line).

as a function of the distance for three cases: (a) $\mu_w > \mu_0$, (b) $\mu_w < \mu_0$, (c) $\mu_w = \mu_0$. In the first case, the self-consistent potential causes a quantum well to appear in the wire. In the second case a barrier rises between the wire and the reservoirs. When the chemical potential μ_0 is close to U_0 this barrier may be higher than the chemical potential level. This means that the electrons have to tunnel through the self-consistent barrier. In the third case, the Friedel oscillations are only presented near the contacts.

3 The conductance

Figure 2 shows the dependence of the linear conductance upon the chemical potential μ_0 for cases (a), (b) and (c). The conductance is seen to depend on the self-consistent potential, which appear due to the electron density redistribution between the wire and the leads.

Variation of charge piled up in the wire with the applied voltage is a mechanism of non-linear conductance. Under certain conditions it may results in a current instability.

4 Exchange interaction effect

The above results were obtained without inclusion the exchange interaction. Exchange interaction gives rise to an effective electron-electron attraction which results in lowering the energy of the ground state and finally in electron density increase, as is demonstrated in Fig. 3.

Effect of exchange interaction is partially compensated by electron-electron correlation, however the main our result remains as before: the charging of a quantum wire really occurs and produces an essential effect on the conductance.

Acknowledgements

We thank Prof. Markus Büttiker for valuable discussions. This work was supported by INTAS (grant No 96-0721), Russian Foundation for Basic Research (grant No 99-02-18192), Program "Physics of Solid-State Nanostructures" (grant No 97-1054) and Program "Surface Atomic Structures" (grant No 5.3.99).

References

[1] S. Tarucha, T. Honda and T. Saku, *Solid State Commun.* **94**, 413 (1995).
[2] A. Yacoby, H. L. Stormer, N. S. Wingreen, L. N. Pfeiffer, *et al*, *Phys. Rev. Lett.* **77**, 4612 (1996).
[3] K. J. Thomas, J. T. Nicholls, N. J. Appleyard, M. Pepper, *et al*, *Phys. Rev.* **B 58**, 4846 (1998).
[4] V. A. Sablikov and B. S. Shchamkhalova, *Phys. Rev.* **B 58**, 13847 (1998).

7th Int. Symp. "Nanostructures: Physics and Technology"
St Petersburg, Russia, June 14–18, 1999

Single-electron molecular transistors on the base of various types of cluster molecules

E. S. Soldatov†, *A. S. Trifonov*†, S. P. Gubin‡, V. V. Khanin†, G. B. Khomutov†, S. A. Yakovenko†, A. Yu. Obidenov†, V. V. Shorochov† and D. B. Suyatin†
† Faculty of Physics, Moscow State University, 119899 Moscow, Russia
‡ Institute of Generaland Inorganic Chemistry, 119899 Moscow, Russia

Abstract. Effect of single-electron tunneling in double-junction tunnel system based on single molecule was investigated. Molecular single-electron transistor was demonstrated. The comparison of measured characteristics with the similar characteristics of molecular single-electron transistors based on a carborane cluster has shown their qualitative resemblance despite essential differences in a chemical structure and streometry of these molecules.

1 Introduction

The traditional microelectronics schemes construction technologies are limited by resolution of the nanolithography equipment, chemical non-uniformity of layers in which the separate elements are formed and non-uniformity of a substrate. Thereby, searching for new alternate ways of electronics engineering development is actual. One of the perspective solutions for nanotechnology is the use properties of separate molecules, as a rule, organic molecules. The capability of creation a molecular electronics engineering and bioelectronics engineering was motivated [1]. As a simple element for construction of electrical elements the authors offer to use a cluster molecule.

The clusters and cluster molecules differ from other organic and inorganic molecules that they consist of a compact heavy nucleus, as a rule, with spherical symmetry, which is surrounded by ligand from light atoms or elementary molecules [2]. The peculiarities of electron structure of cluster molecule condition on the one hand on occurrence of multiple single-electron reversible transitions [3] and, by the other hand, provide sufficient stability of cluster molecule after addition or removing an electron [4]. The electrochemical properties of many of such molecules are reliably determined enough and vary in rather broad borders.

Main advantage of use a cluster molecules as an element of nanoelectronics:

1. The cluster molecules are synthesized chemically, i.e., all molecules are strictly identical both in electronical structure, and in chemical structure.

2. The size of appropriate for realization a tunnel barrier cluster molecule can be essential less, than in elements formed with classical nanolithography.

3. As chemical and the physico-chemical properties of cluster molecules are already well investigated at the present time, there is a capability to dispose cluster molecules on a substrate not only by physical (deposition), but also by chemical methods.

In our previous activities [5, 6] were demonstrated a double junction single-electron system and single-electron transistor, based on a single carborane cluster molecule. However, the problem is still open: what a minimum set of properties of cluster molecule are enough for possibility of using it as simple element of the single-electron scheme.

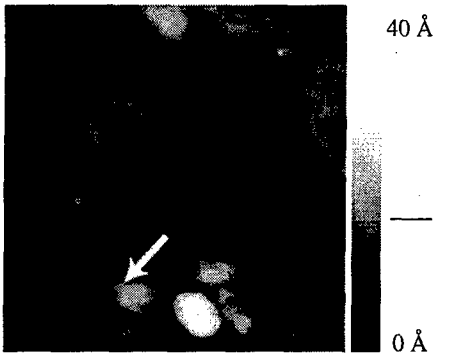

Fig. 1. STM image of $Pt_5(CO)_6[P(C_2H_5)_3]_4$ clusters on graphyte substrate. Arrow point a region where $I-V$ curves and control characteristics was measured. Scan size 550 × 550 Å.

2 Results and discussion

For the comparative analysis of the *SET* — transistor characteristics depending on a type of a cluster molecule, similar [5] experiment was made, where as a working molecule $Pt_5(CO)_6[P(C_2H_5)_3]_4$ was used. Though the molecules $Pt_5(CO)_6[P(C_2H_5)_3]_4$ and the carborane molecule differ entirely by chemical structure, they have a similar structure of energy levels.

For reliability increase of receiving results the samples quantity was increased in comparison with the previous experiments [5, 6], the investigation of measurement regimes influence on the $I-V$ curve and control characteristics (the measure rate, the range of bias voltage, the averaging) was made. The measurements were performed in various characteristic places of a sample (the STM tip above a single cluster on different distances from a gate electrode, above group of clusters and above flat region).

The performed measurements have shown, that

1. The $Pt_5(CO)_6[P(C_2H_5)_3]_4$ molecules have brightly expressed surface — active substance properties, as it forms own (without stearic acid) LB-monolayer.

2. The LB-deposition (at certain parameters) gives a cluster molecules monolayer, and distance between molecules can smoothly be changed over a wide range, for example to do rather large, to consider a separate molecule isolated. (Fig. 1).

3. The $I-V$ characteristics above single clusters differ from $I-V$ curves above flat graphite. (Fig. 2).

4. The control characteristics above single clusters differ from the control characteristics above flat graphite (Fig. 3) by periodicity presence - 2000 ± 200 mV, and this period varies depending on distance between a cluster and a gate electrode.

An observable behavior of $I-V$ curves and control characteristic indicate that in a double junction tunnel system STM tip–cluster–the substrate a regime of single electron tunneling is realized, and the current through this system can be controlled with changing the voltage on a gate electrode.

3 Conclusions

Thus main result of performed research was the realization of the molecular single-electron transistor on the base of a single $Pt_5(CO)_6[P(C_2H_5)_3]_4$ molecule cluster. The comparison of measured characteristics with the similar characteristics of molecular single-electron transistors based on a carborane cluster has shown their qualitative resemblance despite

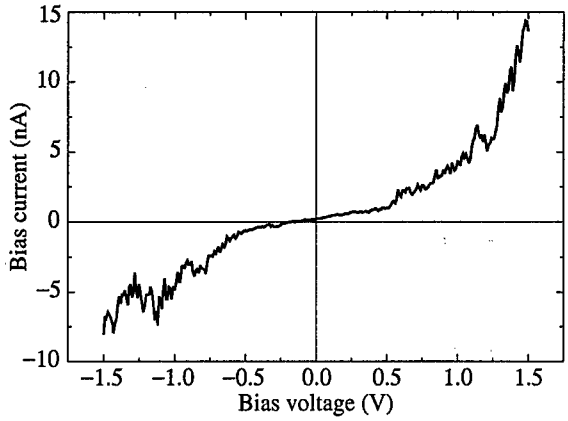

Fig. 2. The typical $I-V$ curve of double junction system STM tip–cluster–substrate.

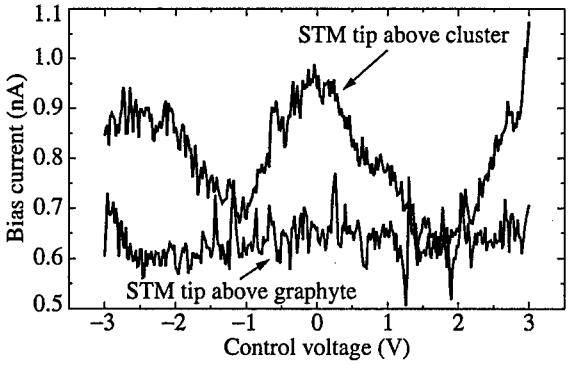

Fig. 3. Control characteristics, measured at STM tip above single cluster molecule and above flat graphite area.

essential differences in a chemical structure and streometry of these molecules.

Acknowledgments

This work was supported in part by Russian Foundation for Basic Research (Grants 96-03-33766a, 97-03-32199a), the Russian Program on the Prospective Technologies for Nanoelectronics (Gr. No 233/78/1-3) and the Russian Program on the Physics of Nanostructures (Gr. No 96-1031).

References

[1] K. K. Likharev, *Microelectronica* **16** No 3, 195 (1987).
[2] S. P. Gubin, *Cluster chemistry*, Nauka, 1987.
[3] V. C. Manning and W. C. Trogler *Coord. Chem. Rev.* **38** No 2/3, 89 (1981).
[4] Trinh-Toan, W. P. Fenhammer and L. F. Dahl, *Amer. Chem. Soc.* **94** No 10, 3389 (1972).
[5] E. S. Soldatov, V. V. Khanin, A. S. Trifonov, D. E. Presnov, S. A. Yakovenko, G. B. Khomutov, S. P. Gubin and V. V. Kolesov, *JETP Lett.* **64** No 7, 556 (1996).
[6] A. S. Trifonov, E. S. Soldatov, V. V. Khanin, S. A. Yakovenko, G. B. Khomutov and S. P. Gubin, *Abstracts of Int. Symp. "Nanostructures: physics and technology"*, St.Petersburg, Russia, p. 494, 1997.

7th Int. Symp. "Nanostructures: Physics and Technology"
St Petersburg, Russia, June 14–18, 1999

Semiconductor nanostructures grown in production MOVPE reactors

Michael Heuken
AIXTRON AG, Kackertstr. 15-17, D-52072 Aachen, Germany

Abstract. Since the invention of the Planetary Reactors® a reliable tool for mass production of various III–V compounds and nanostructures based on MOCVD growth is existing. These reactors have proven to grow extremely uniform films together with a highly efficient utilization of the precursors. Their main features are: an inductive heating system with extremely low thermal mass for precise and fast heating, high flexibility in the reactor size ($15\times2''$, $35\times2''$ to $9\times4''$ wafer load) and the option to use a fully automated cassette-to-cassette wafer loading system. The benefits of this design are very short cycle times, extreme run-to-run stability and even further reduced cost of ownership. Uniformity of thickness, luminescence intensity and composition of the most important III–V compounds such as GaInP, GaInAsP and AlGaInP as well as GaN based materials are shown.

Introduction

Physics and technology of semiconducting materials and structures, in particular GaAs-, InP- and GaN-based ones, have developed tremendously in the last 30 years, triggering development and realization of optoelectronic devices. Such devices like lasers, light emitting diodes, modulators, detectors, photovoltaic solar cells, passive elements and electronic devices using the concept of nanostructures present a driving force of enormous economic growth [1]. Most of them are enabling devices, making systems possible that would not exist or function without that particular device. The present value of an "optoelectronic system" is typically a factor 50–200 larger than the value of the mere device. Typical examples of such systems are compact disc players, laser printers and optical interconnects for the consumer, office, computer and telecommunication markets, optical storage and archive systems. Conservative growth predictions for the opto-electronic component market are 15–25% per year, much higher than the average economic growth [2]. In this paper the focus will be on the MOCVD growth technology to realize compound semiconductor based structures rather than on the physical properties of the ultimate electronic nanostructures and quantum dots.

1 The Planetary Reactor® for the MOVPE growth of nanostructures based on III–V compounds

The requirements for a production machine are high throughput, high efficiency and a good uniformity of composition, layer thickness and doping. These requirements are met by AIXTRON Planetary Reactors® due to their unique design which offers real multiwafer capability at a high degree of flexibility. Depending on the chosen setup, up to $95\times2''$ wafers can be grown simultaneously in one run. Recently, a new fully automated $35\times2''$ or $5\times6''$ type has been introduced. The main carrier gas (N_2 and H_2) and the standard group III elements (TMGa, TMAl, TMIn) and dopants (DEZn, SiH_4) were injected in the center of the susceptor with a rotational symmetry. The second carrier gas and the standard group V elements (AsH_3, PH_3, NH_3) were also injected in the center but separated from

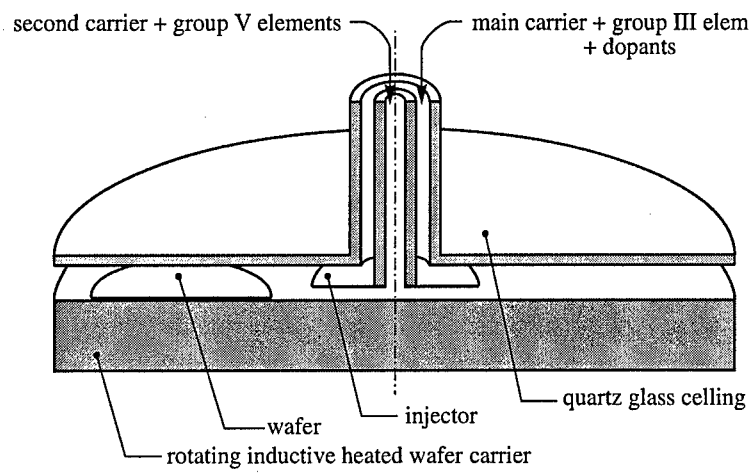

Fig. 1. Planetary Reactor® principle.

the group III elements. This special design of the inlet geometry avoids pre-reactions and allows a very good run-to-run reproducibility and an excellent uniformity. To achieve the good uniformity a precise temperature management of the reactor is necessary. There are several hardware options available to optimize the temperature profile in the reactor for each customer requirement. Absolute growth temperature, gas flow distribution, rotation speed of the main plate and the gas foil rotation of each wafer as well as the gas phase composition are the common parameters which need to be controlled to optimize the layer properties [3]. Details of the reactor performance were investigated by simulation [4].

In this study we discuss results obtained in various types of Planetary Reactors® used for the growth of InP, GaAs and GaN based materials. Standard growth parameters used in this study are low total gas flows between 20 and 30 l/min (depending on the reactor size) and a total pressure around 100 mbar. Typical growth temperatures used were between 675°C and 750°C for GaAs. All epitaxial growth of GaN based material was carried out using an AIXTRON multiwafer planetary MOCVD system which has a 6×2″ capacity. Two inch c-plane sapphire wafers were utilized for all growth and the system was equipped with standard Group III precursors (TMGa, TEGa, TMAl, TMIn) as well as high purity NH_3. Donor and acceptor doping was done using SiH_4 and Cp_2Mg as precursors, respectively. Operating pressures of the system varied from 100–950 mbar and typical growth temperatures were ~ 1000–1100°C for GaN and AlGaN compounds and 750–850°C for InGaN compounds.

2 Results and discussions

2.1 Evaluation of AlGaInP

To demonstrate the capabilities of the AIX 2600G3 reactor we loaded 7×2 inch wafer on one out of 5 satellites with a diameter of 6 inch to grow AlInGaP on GaAs substrates. Room temperature photoluminescence mapping was carried out and the obtained wavelength distribution across one 2″ wafer is shown in Fig. 2. The obtained average wavelength is 592.41 nm with a standard deviation of 0.92 nm which is 0.16%. Basically little variation of composition is observed across the wafer except at the edges. 10 period AlGaInP/AlGaInP multiple quantum wells grown at 750°C with the optimized conditions

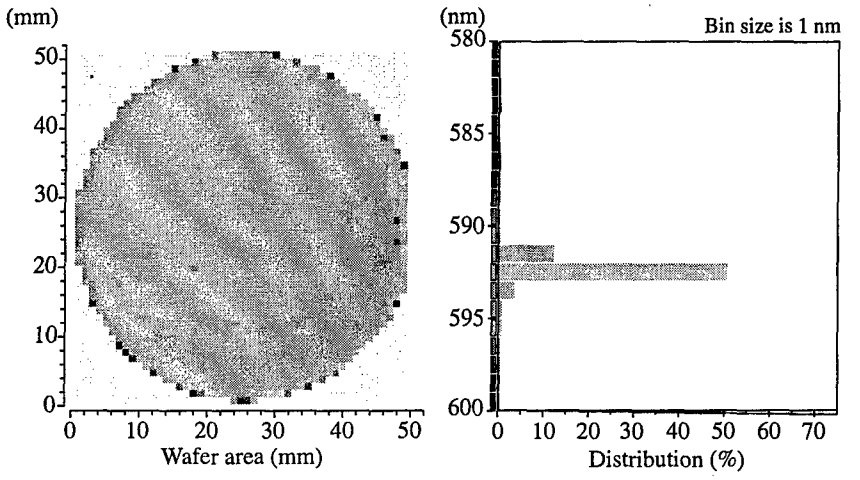

Fig. 2. Uniformity of wavelength of AlInGaP on 2″ GaAs. Average wavelength 590.78 nm, standard deviation 0.80 nm, 0.13%

show a PL-wavelength of 610 nm. The PL-wavelength standard deviation of one 2 inch wafer is less than 2 nm. The standard deviation of the PL-intensity is usually below 15% for one 2 inch wafer.

2.2 Properties of GaInP

The composition uniformity of GaInP has been demonstrated on 4″ GaAs substrates. The PL-wavelength distributions was obtained from automatically performed room temperature photoluminescence measurements. The average wavelength is 665.99 nm with a standard deviation of 1.68 nm which is 0.25%. As an example we demonstrate a good layer thickness homogeneity, represented by a standard deviation of only 0.24%. The average layer thickness of this specific layer is 4135 nm with a standard deviation of 9.8 nm. One can observe a rotational symmetry to the thickness distribution which corresponds to the reactor configuration including the very homogeneous temperature profile together with the well adapted rotation speed of the wafer. The rotational symmetry of the film thickness distribution represents a characteristic of the Planetary Reactor® with individual rotating substrates. The very low number of standard deviation in all important properties (layer thickness as shown, but also composition and PL-intensity) indicate the proper adjustment of the corresponding process parameters. These parameters are temperature and flow profile as well as rotation speed of main plate and wafers. Another important point to increase the device yield is the homogeneity of photoluminescence intensity. Again we will discuss a GaInP layer grown on 4″ GaAs substrates. The room temperature PL intensity distribution was measured. An average of 919 counts was obtained with a standard deviation of 112 counts (12%) which is an excellent value and would permit the use of nearly the whole wafer area to fabricate optoelectronic devices.

2.3 Growth of GaInAsP on 2″ InP

Since no 4″ InP wafers are currently available on a commercial base, GaInAsP was grown on 2″ InP. Since this material is very temperature sensitive, this is the ultimate homogeneity proof. The wavelength distribution of GaInAsP with an average wavelength of 1350.44 nm was measured. The standard deviation is 1.77 nm which is 0.25%. This result demonstrates

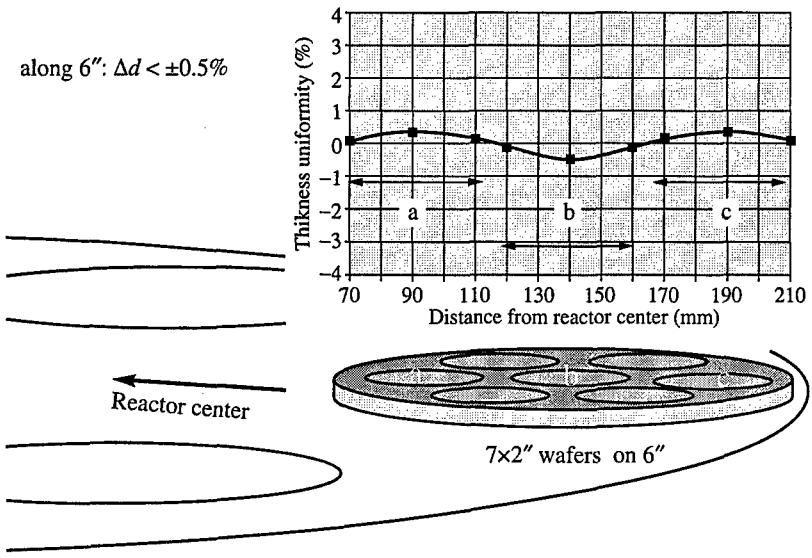

Fig. 3. AlGaAs/GaAs DBR thickness uniformity in the AIX 2600G3 reactor.

the very good uniformity obtainable in this kind of reactors.

2.4 Growth of AlGaAs and GaAs for electronic applications

Since the market for low power and high speed electronics based on GaAs is rapidly increasing we will demonstrate typical material systems in a large scale dimension. The growth of the corresponding layers is performed in the AIX 2600G3 9×4″ configuration. Here we will focus on typical layers used for the design of a AlGaAs based heterobipolar transistors (HBT). The resistivity distribution of a $Al_{0.3}Ga_{0.7}As$:Si layer on 4″ GaAs wafer without edge exclusion was measured and evaluated. Hall measurements show an electron concentration of $3 \times 10^{17}\,cm^{-3}$ and a mobility of 1600 cm^2/Vs. These data fit to the theoretically expected values for $Al_{0.3}Ga_{0.7}As$ to conclude that sufficient low oxygen and carbon levels are present in the sample. In accordance with the Hall data non destructive sheet resistivity measurements with a sheet resistance of 139 Ω/□ were measured. The standard deviation is only 1.4%. The thickness uniformity of this 2 μm thick 30% Al containing layer is below 0.25%. The rapid heating and cooling cycle of the G3 system allows to grow the p-type material at significant lower temperatures than the undoped and n-doped layers. The resistivity distribution of a GaAs:C layer grown below 550°C on a 4″ substrate was used to evaluate the doping uniformity. Using this doping technique we make use of the intrinsic carbon uptake from metalorganic precursors. The high hole concentration of $4 \times 10^{19}\,cm^{-3}$ with a mobility of 99 cm^2/Vs and the sheet resistivity distribution with a standard deviation of only 0.9% proves the ability of this reactor concept to provide excellent doping uniformity in the temperature range lower than 800°C and down to lower than 550°C simultaneously without hardware change. These are the temperature intervals usually employed in HBT growth. These high uniformities in dopant distribution demonstrate the high potential for maximum yield in device fabrication. Unique thickness uniformity was shown as basic demand for the commercial production of electronic and optoelectronic devices like UHB LED, LASER, HBT and HEMT. To achieve the thickness uniformity the unique design of the reactor allows a linear depletion of Al, Ga and In in

the gas phase. We demonstrate the depletion of Gallium along the diameter of a 6 inch satellite. For these investigations we used AlAs/GaAs distributed bragg reflector (DBR) structures grown on wafers which were placed on rotating and intentionally non rotating satellites. Best thickness uniformity on DBR structures of $\pm 0.5\%$ were achieved for a low total carrier gas flow. A scetch of the reactor with the 35×2 inch wafer configuration on one 6 inch satellite together with the measured thickness distribution is shown in Fig. 3. With this total flow we observed a Ga efficiency for the DBR's of more than 40% in the 35×2 inch configuration and more than 50% in the 5×6 inch configuration.

2.5 Development of SQW- and MQW-InGaN/GaN structures for blue and green emitters

Further development of the above described reactor concept was made resulting in InGaN/GaN SQW and MQW structures [5, 6]. Optimization of reactor process conditions has shown that V/III ratios less than 1000 can successfully be employed for the growth of GaN and AlGaN at up to 3 μm/hour without degradation of the electrical and optical properties. Typical background doping of GaN layer is $< 5 \times 10^{16}\,\mathrm{cm}^{-3}$. Thickness uniformity in the range of 1% have been achieved for both GaN and AlGaN films at deposition rates of larger than 2 μm/hour. Low temperature photoluminescence of GaN layers show strong excitonic emission with typical full width at half maximum (FWHM) of 3–4 meV at 4.2 K. For InGaN compounds, V/III ratios smaller than 3000 were employed for the growth of both single layer as well as quantum well and DH structures. In the present work, we investigated different interface treatments of MQW layers consisting of 10 stacks of 7 nm GaN and 5 nm InGaN to study the impact on PL wavelength and intensity. The InGaN-wells were grown under N_2 at 750°C and 200 mbar. The total flow was fixed at 16 slm. The GaN-barriers were grown under either N_2 or H_2 as carrier gas in the range of 750°C to 950°C at 200 mbar with total flow of 14 slm. PL wavelength and intensity were found to be strongly influenced by the introduction of growth interruptions and growth temperature discontinuities. Hence, we varied the barrier temperature while keeping the well growth temperature constant. The emission wavelength of the MQW's shifts with increasing growth temperature of the GaN-barriers to lower values, probably due to enhanced indium losses at higher temperatures. Simultaneously we observe a strong enhancement of emission intensity with increasing growth temperature of the GaN-barriers, due to lower emission wavelengths and an improvement of optical and structural quality of the barrier material. The HR-XRD spectra of the MQW's grown by using growth interruptions exhibit satellite peaks from the -4th to the +3rd order with sharp linewidths. The room temperature PL show single peak transitions without any yellow luminescence at about 470 nm with strong signal intensities depending on the growth conditions. The corresponding line widths (FWHM) ranges from 35 to 40 nm. The wafer to wafer as well as the run to run uniformity is in the range of about 2 nm standard deviation. The intensity distribution ranges around 10% standard deviation. Full wafer mappings of wavelength and intensity show a uniformity of about 2 nm standard deviation in wavelength (Fig. 4) and 20% in intensity for as grown material without any edge exclusion.

3 Conclusion

We presented comprehensive data concerning the growth of GaInAsP, GaInP, AlGaAs, AlGaInP and GaN based materials. Special focus was put on uniformity (typical data: 1% thickness uniformity and 1 nm wavelength uniformity for most of the materials) and electrical and optical characteristics of films grown in these machines. The data prove that AIXTRON Planetary Reactors® are the most flexible and efficient reactors to meet the

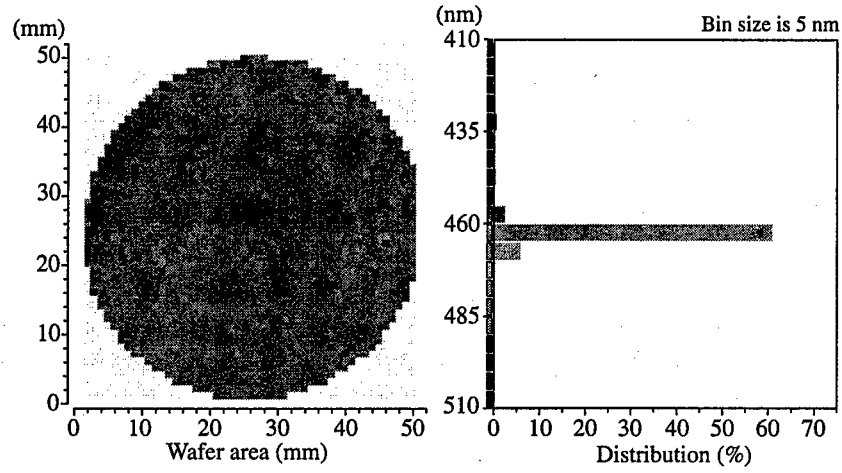

Fig. 4. Room temperature PL wavelength mapping of an InGaN/GaN MQW layer stack. Average wavelength 462.7 nm, standard deviation 1.9 nm.

demands of III–V manufacturing including sophisticated quantum wells and nanostructures for the next decade.

References

[1] D. L. Evans, *Proc. SPIE*, Vol. 3002, pp. 142–153, San Jose, California, February 13-14, 1997.
[2] R. L. Moon, *J. Cryst. Growth* **170**, 1–10 (1997).
[3] M. Deschler, R. Beccard, R. Niebuhr, B. Wachtendorf and H. Juergensen, *Proc. Workshop on Heterostructure Epitaxy and Devices*, Smolenice, October 13-17, 1997.
[4] M. Dauelsberg, L. Kadinski, Yu. N. Makarov, E. Woelk, G. Strauch, D. Schmitz and H. Juergensen, *Inst. Phys. Ser.* Vol. 142, Ch. 12, pp. 887–890, 1996.
[5] R. Beccard, O. Schoen, B. Schineller, D. Schmitz, M. Heuken and H. Juergensen, *MRS Symposium Proceedings*, Vol. 482, pp. 155–160, 1997.
[6] R. Beccard, R. Niebuhr, B. Wachtendorf, D. Schmitz and H. Juergensen, *Proc. LDSD'97*, Lisbon, May 19-21, 1997, *Materials, Science and Engineering B*, Vol. 51, pp. 39–43, Elsevier Science, 1998.

7th Int. Symp. "Nanostructures: Physics and Technology"
St Petersburg, Russia, June 14–18, 1999

Vicinal surface as a tool for QD control: InAs on GaAs

V. P. Evtikhiev
Ioffe Physico-Technical Institute, St Petersburg, Russia

1 Introduction

One of the most promising methods for the preparing of uniform QDs array is the molecular beam epitaxy (MBE) in Stranski–Krastanow growth mode [1]. Many investigations of InAs QDs show that their density and size depends on the growth conditions and QDs arrays in the density range of 10^8–10^{11} cm^{-2} may be received [2, 3]. The formation of InAs QD arrays with a density greater than 3×10^{10} cm^{-2} on a correctly oriented GaAs(001) surface is accompanied, as a rule, by coalescence of a noticeable number of QD into large islands, which leads to a radical broadening of the QD size distribution [3]. So, the independent control of sizes and density of QDs is one of the main problems for the creation QD heterostructures suitable for the devices application.

For the creation of dense arrays of uniform QDs we suggest to use the conventional MBE growth in Stranski–Krastanov growth mode on the vicinal GaAs(001) substrate misoriented to the [010] direction. On such vicinal surfaces there appears a net of small terraces, separated by steps from all the sides. The Schwoebel potential barrier at the step edges may considerably suppress the surface diffusion of adatoms between the terraces [4], and the QDs growth on each terrace will occur primarily from the material deposited on the same terrace.

2 Theory

We have performed Monte-Carlo simulation of the terraces formation on the vicinal GaAs(001) surfaces misoriented to the [010] direction. We took into account the processes of the atom adsorption and desorption on the surface, adatom migration, adatom attachment and detachment to the step. The elemental detachment processes for a different kind of steps configuration are shown in the Fig. 1(a). A Monte-Carlo simulation of the GaAs growth shows that the processes $n3$, $n4$ and $n7$ dominate over the other elemental detachment processes ($n1$–$n10$). The shape of the terraces depends strongly on the variation of the atom detachment activation energies (E_{nx}). The activation energy ratio E_{n3}/E_{n4} controls the ordering of the waves. Parameter E_{n7} controls the abruptness of the wave. With the decreasing of E_{n7} value, terraces become wave-shaped and connected by the gates (see Fig. 1(b)).

In order to reveal the possible role of adatom diffusion between the connected terraces, we estimate the coalescence rate of the QDs located on the neighboring terraces. We simulated the motion of the adatoms by the Monte-Carlo method and determined the number of adatoms which began to move on the edge of one QD and reached the edge of a neighboring QD per unit time. The simulation show that increasing the constriction linearly retards coalescence rate.

3 Technological approach

Experimentally the role of substrate misorientation on the QDs formation was investigated by atomic force microscopy, photoluminescence and electroluminescence. The heterostruc-

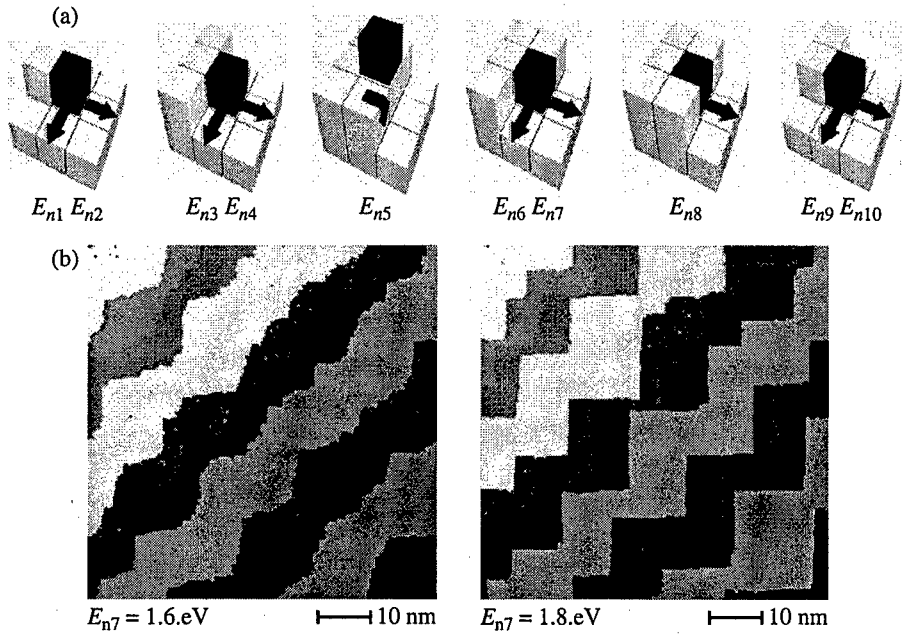

Fig. 1. The elemental detachment processes and results of Monte-Carlo simulation of the GaAs growth on misoriented substrate.

tures for all kinds of measurements were grown in identical growth conditions. Each growth process include two stages. The first stage is the preparation of terraces net during GaAs growth in step flow growth mode and the second—the growth of InAs QDs in Stransky–Krastanow growth mode. The effective thickness of InAs covering was 3 monolayers. Each epitaxy process was performed simultaneously on GaAs(001) surfaces misoriented to the [010] direction by 0, 1, 2, 4, and 6°. The comparatively small range of variation of the misorientation angles was chosen so that the surfaces would differ from one another only in growth-step density without qualitative variation in the surface morphology caused by the approach to new singular faces.

4 Results and discussion

Studying the surface structure of GaAs samples by AFM, we have revealed on the vicinal surfaces the net of wave-like terraces joined by gates as has been predicted by the Monte-Carlo simulation (Fig. 2, upper row). Increasing of the misorientation angle leads to an increase in the density of the terraces and decrease in their mean width from 500 Å for 1° to 250 Å for 6°. These values are considerably larger than the dimensions of the terraces calculated under assumption that the step height is one monolayer. The observed difference is explained by the phenomenon of step-bunching, which in our case increases with increasing of the misorientation angle from 2–3 ML for 1° to roughly 10 ML for 6°.

At InAs coverage of 3 ML (Fig. 2, down row), InAs QDs arrays were found on the terraced surfaces. Also present on the surfaces are large InAs islands formed as a result of the coalescence of InAs QDs. Their number falls dramatically with increase of the misorientation angle and on the surface with 6° misorientation there are scarcely any large InAs islands. Increasing of the terrace density with the misorientation angle leads to the

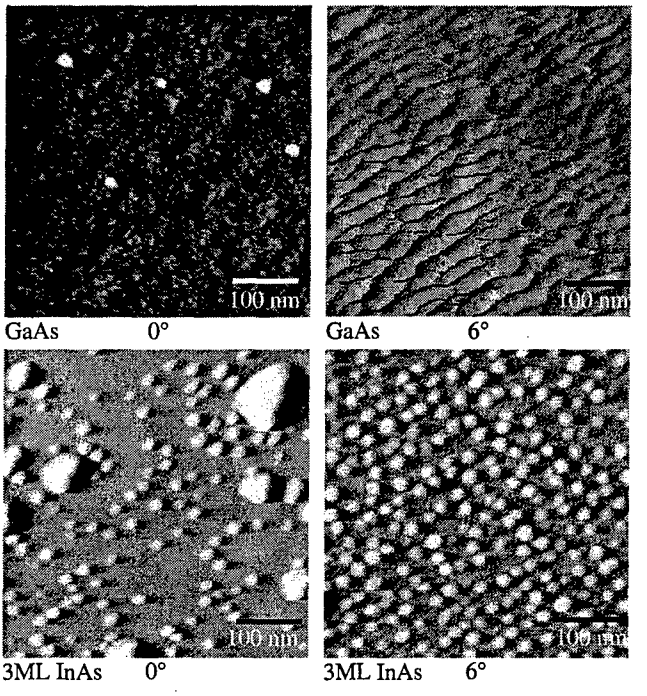

Fig. 2. AFM image of GaAs surfaces (upper row) and InAs QDs (3 ML InAs coverage thickness) (down row) MBE grown on the GaAs(001) surfaces exactly oriented and misoriented by 6° to the [010] directions.

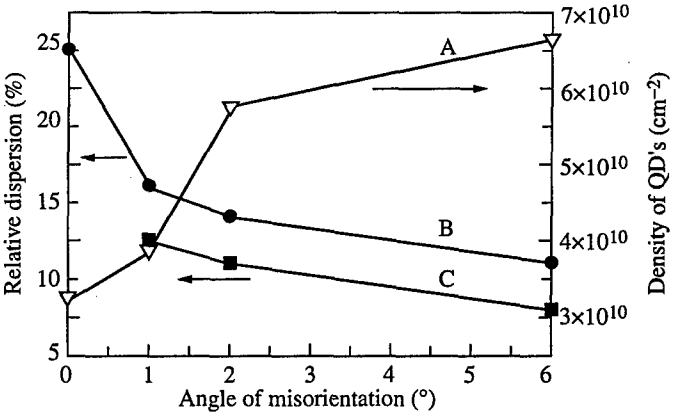

Fig. 3. The relative dispersion of distributions of InAs QD's height (B) and terraces (C) width (left scale) and density of QDs (A) (right scale) as a function of the angle of misorientation.

higher density of QDs (Fig. 3), decreasing of their mean height from 34 Å for 0° to 20 Å for 6° and to the more uniform size distribution.

The similar character of variation of the spread in QDs height and in terraces width with surface misorientation let us conclude that QDs size dispersion is controlled by the terraces areas distribution.

For PL study we prepare two sets of samples. They differ only by the interruption time

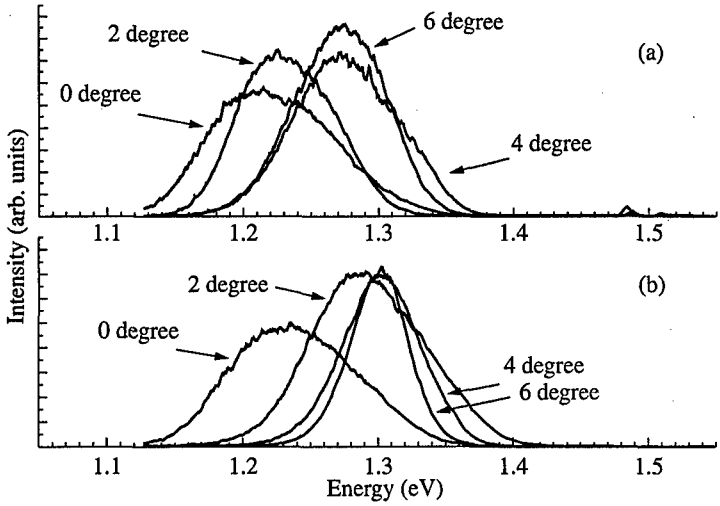

Fig. 4. The PL spectra recorded at $T = 77$ K for the samples with the growth interruption time $t_{int} = 15$ min (a) and $t_{int} = 10$ s (b).

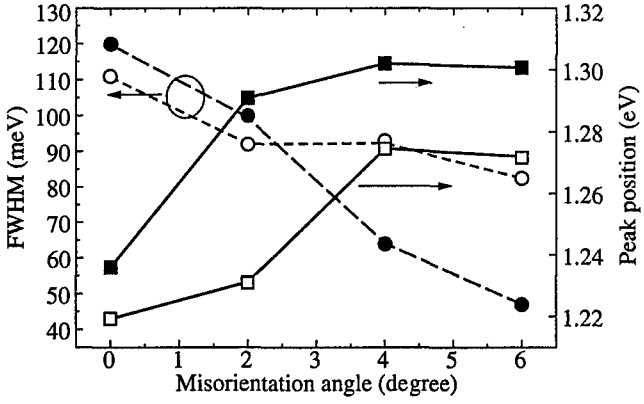

Fig. 5. The maximum position (squares) and the FWHM (triangles) of the PL line for the samples with the growth interruption time $t_{int} = 15$ min (solid) and $t_{int} = 10$ s (open).

(t_{int}) between the end of QDs growth and start of the GaAs layer overgrowth. For the first set $t_{int} = 15$ min and for the second one $t_{int} = 10$ s. In the grown heterostructures the InAs QDs single sheet array was confined by GaAs barriers (200 Å) which were surrounded by the AlAs/GaAs superlatticies and cladding $Al_{0.7}Ga_{0.3}As$ layers. The PL spectra ($T = 77$ K, $\lambda = 514.5$ nm, $P = 200$ A/cm^2) for both the series of samples are presented in the Fig. 4(a) and Fig. 4(b). The position of the PL line maximum and the full width on the height middle (FWHM) of the PL lines versus angle of misorientation are shown in the Fig. 5. For both the series of spectra the misorientation of the substrate leads to blue shift of the maximum and decrease of the FWHM of PL lines. These effects can be naturally explained by the decrease of the sizes and better size uniformity for the InAs QDs on the misoriented surfaces what was revealed by AFM study for the open QDs arrays. The observed effects depend on the growth interruption time t_{int} and are less pronounced in the samples grown with longer t_{int}.

It is natural to connect the dependence of the InAs QDs sizes on the interruption time with the probability of adatom surface migration. On the misoriented surfaces patterned with the dense net of terraces, adatom surface diffusion between terraces should be much slower then on exactly oriented surface, since adatom migration between terraces occurs mainly through the gateways connecting terraces. The increase of the misorientation angle makes terraces and gates smaller and causes progressive suppression of the adatom migration. The effect of interruption time on the PL spectra should be small for exactly oriented surfaces with fast adatom migration and became stronger on the misoriented surfaces. However, with the further increase of the misorientation angle it again may become weaker, when migration will completely supressed on the time scale of chosen t_{int}. The comparison of the data in Fig. 4 shows that in our studies effect of the growth interruption time is stronger for sample with 2 degree misorientation. So, we imply that QDs formation on the misoriented surface comprise two main stages with different characteristic times. First process is very quick. The self-assembled QDs array with high density and high uniformity appear on this stage. On the second, much longer stage QDs increase in sizes due to QDs interactions. This interaction occurs via surface migration of adatoms between QDs. The changes in the QDs morphology on this second growth stage determine variations in the position and width of the QDs PL lines for samples grown with longer interruption time. The misorientation creates a new, much slower time scale for this stage of the QDs formation because of the suppression of the adatom migration between terraces.

We successfully used such substrates for the fabrication of laser heterostructures with a single sheet QDs array. The electroluminescence spectra exhibits the same main features that were observed in PL measurements. As it was predicted by theory [5] the threshold current of the "classical" single sheet QD laser, prepared on these heterostructures shows very strong dependency versus their FWHM. The lowest threshold current density (210 A/cm^2) exhibits the broad area (100 μm) lasers with high reflecting mirror coating made from 4 degree misoriented substrate.

5 Conclusion

We have found that the application of GaAs(001) substrates misoriented to the [010] direction in conventional MBE growth gives an effective tool for the independent control of InAs QDs density and size, permits to improve the QDs sizes dispersion. This possibility originates from special surface patterning which appear on misoriented substrates and may be used in the MBE growth of different types of QDs.

References

[1] I. N. Stranski and L. von Krastanow, *Akad. Wiss. Lit. Mainz Abh. Math. Naturwiss. Kl.* **146**, 797 (1939).

[2] G. S. Solomon, J. A. Trezza and J. S. Harris, *Appl. Phys. Lett.* **66**, 991 (1995).

[3] J. M. Moison, F. Hoozay, F. Barthe, L. Leprince, E. Andre and 0. Vatel, *Appl. Phys. Lett.* **64**, 196 (1994).

[4] J. Tersoff, D. W. Denier van de Gon and R. M. Tromp, *Phys. Rev. Lett.* **72**, 266 (1994).

[5] L. V. Asryan and R. A. Suris, *Semicond. Sci. Techn.* **11**, 554 (1996).

7th Int. Symp. "Nanostructures: Physics and Technology"
St Petersburg, Russia, June 14–18, 1999

Using of self-formed semiconductor micro- and nanotubes as a precise etch mask

V. Ya. Prinz, *A. V. Chehovskiy* and L. A. Nenasheva
Institute of Semiconductor Physics RAS SB, 630090 Novosibirsk, Russia

Abstract. Concepts of making precise etch mask using self-formed tubes have been proposed and realized. The InGaAs/GaAs mask-tubes diameter have been precisely controlled in the range from 4 μm to 8 nm. Using reactive ion etching and these mask-tubes, a mesa-structure and a groove on the GaAs substrate were fabricated.

Realization of recent physical concepts in quantum effect devices as well as in single-electron and atom/molecular switching devices requires further development of nanolithography and nanofabrication methods.

It is required not only to obtain nano- and atomic-scale patterning of semiconductor and metal films, but also to build up device elements with perfectly straight and sharp edges, free of roughness and having precisely controlled sizes.

Despite the extensive use of resist lithography in nanofabrication, it remain difficult to fabricate structures smaller than 10 nm using conventional optical or electron beam technologies, all the more it is impossible to fabricate structures with sharp and straight edges. Self-forming processes for making resistless mask are now proposed as an alternative way to overcome this barrier.

Recently [1–4], self-formed semiconductor nanotubes have been fabricated, and the possibility of precise control over their parameters has been shown. The fabrication process is based on the possibility of self scrolling of highly strained InGaAs/GaAs heterolayers (being debonded from substrate) in a tube shaped scroll. It has been shown that the scrolled up layers get close together, thus forming perfectly bonded tube walls. The tube diameter D is determined by the bilayer thickness d and by the mismatch of lattice parameters $\frac{\Delta a}{a}$ (i.e., by the composition of the InGaAs solution used): $D = \frac{4}{3} \times \frac{d \times a}{\Delta a}$. The InGaAs/GaAs tubes with the tube diameter D as small as 3 nm and length over then 1 mm may be produced. Fabrication of highly ordered arrays of nanotubes was also rendered possible.

Here we introduce a nanofabrication technique, which is based on the use of self formed nanotubes as an etch mask for fabricating high-precision mesa-structures (for example, a bar or a wire of a lateral width determined by the tube diameter).

The following properties of the tubes are important for using them as masks:

1. Ultra-small sizes of the objects, which fall into the nanometer scale range and are highly reproducible.
2. Smooth and straight edges of the scrolled tubes.
3. Possibility of fixing the tubes at a preset place of the structure.
4. Hardness of the tubes to plasma etching.
5. Possibility of formation of tube arrays (using a multi-layered structure).
6. Possibility of successive transformation of sizes (step-by-step pass-over from micro to nanometer scale range along two coordinates using a multi-layered structure).

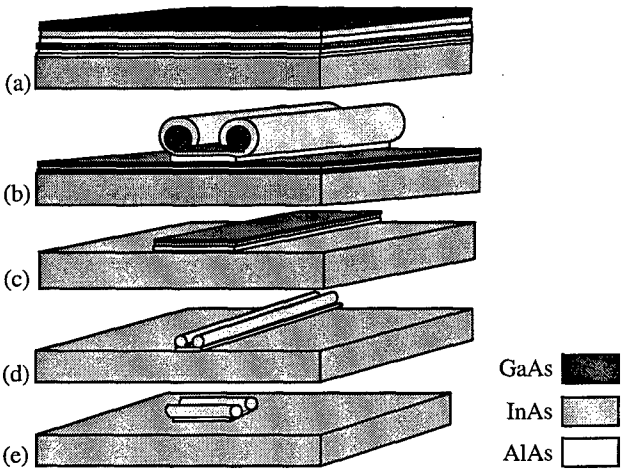

Fig. 1. (a) Initial structure involving thick and thin GaAs/InGaAs/AlAs layers grown on a GaAs substrate; (b) doubled tubes produced using selective wet etching of the thick AlAs layer; (c) mesa-structure produced by reactive ion etching and tube removing by selective etching of thick AlAs; (d) scrolling of the thin GaAs/InGaAs layer contained in the mesa-structure in a tube during AlAs thin layer selective wet etching; (e) the same as (d), with the exception that another direction of scrolling gives ring-shaped tubes.

Let us consider the characteristics of tubes in more detail on the example of formation of mesa-structure. Figure 1 exemplifies steps of transformation from micro- to nano-sizes of self-scrolling tubes. The result of this steps is nanotubes situated in designated place of substrate. This nanotubes were obtained by using wet etching and reactive ion etching only. The double tubes is used as a mask for patterning the underlying layers at reactive ion etching. The most important here is the possibility of etching the structure without causing damages to the tubes. This possibility stems from the following two points:

a. the outer layer of the tubes is the InGaAs one. During reactive ion etching of GaAs with CCl_2F_2- or $SiCl_4/SF_6$-based etchers the tubes are not damaged because InGaAs/GaAs selectivity of etching is more than 1000 [5].
b. In order to destroy the tube, it is required to etch through all the layers forming the multi-coil tube, while the total number of coils closing together can be as high as 40.

Another important point is the possibility of selective removal of AlAs layer by using HF acid etchant which does not attack GaAs and InGaAs layers [6]. It makes possible to obtain tubes, accomplish all technological operations and then remove it out.

It was shown that having a multilayer structure (Fig. 1(a)) containing of a few strained InGaAs/GaAs bilayers separated with sacrificial AlAs layers; one can first fabricate tubes from the upper layer (Fig. 1(b)), then, using them as a mask for reactive ion etching form a pattern on underlayer (Fig. 1(c)), and, finally, scroll up a tube from this layer (Fig. 1(d),(e)). It is possible to choose the proper direction of the scrolling process and fabricate either long tubes (Fig. 1(d)) or ring-shaped tubes (Fig. 1(e)).

We propose to use the self-formation process for successive scaling down of lithographic pattern. By way of example, let us consider a strip of width L formed lithographically from strained bilayer film. After having been freed from bonding with substrate, the strip scrolls

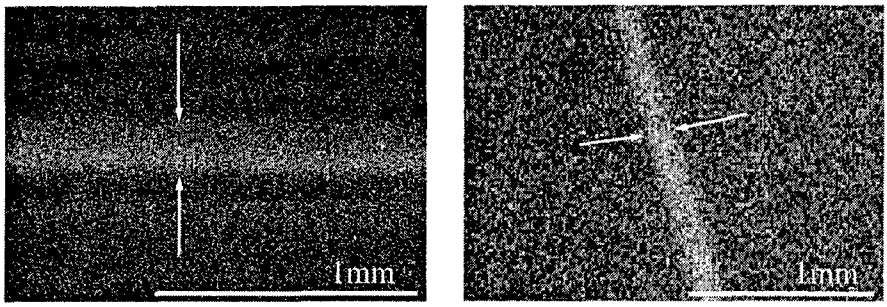

(a) (b)

Fig. 2. (a) The electron microscope image of mesa-structure. The mesa-structure has 300 nm of width and 50 nm of height, (microscope electron beam was directed obliquely); (b) the electron microscope image of groove. The groove has 100 nm of width and 10 nm of depth.

up in a tube of diameter D. Since $L = D \times \pi \times n$, where n is the number of coils, the lateral size the planar structure clearly transforms in an "apparent" (for instance, for ion etching) size D. The scaling factor is $\pi \times n$. In our case, n might be as high as 40, which permitted reduction of the scale by a factor of 100. By successive repetition of the procedure, one can pass over from micro- to nanoscale range. For example, if we have a multi-layered structure containing a few strained bilayer films, which can be successively debonded from substrate, we can pass over from a strip of width L in the upper layer to a tube of diameter $L_1 = \frac{L}{\pi \times n}$ which will serve next as a mask for the formation of a strip of width L_2 in the underlying layer in order to subsequently transform the strip of width L in tube of diameter $L \ll L_1 \ll L_2$, and so on.

The experimental ion reactive etching was performed in a parallel plate capacitance plasma system at a 13.56 MHz frequency. High frequency power of 0.1 W/cm^2 density was supplied to the electrode where samples was situated. The second electrode was the chamber of the reactor. The reactive gases flowed through the chamber from its top uniformly in the time during the whole course of the etching, their pressure being maintained around 5 Pa.

Figure 2(a) shows the obtained GaAs mesa-structure. This mesa-structure was fabricated on the GaAs substrate using reactive ion etching in a CCl_2F_2/O_2 gas mixture and in other reactive gases. The tube lying on the GaAs substrate surface was used as a precise etch mask (this tube of 300 nm diameter was fabricated using a GaAs(4ML)/$In_{0.4}Ga_{0.6}As$(6ML) bilayer). After the tube was removed from substrate, the mesa-structures became opened. This mesa-structure had a width 300 nm and a height 50 nm. The edges of the mesa-structure are straight and sharp.

Figure 2(b) shows the groove obtained on a GaAs substrate. The initial structure consisted of an upper GaAs(2ML)/$In_{0.65}Ga_{0.35}As$(2ML) bilayer, an AlAs (10ML) sacrificial layer and a GaAs substrate. The scratch of width less than 50 nm was made on the surface of the structure and the HF-based etchant could penetrate to the AlAs layer through this scratch. A part of AlAs layer was only etched out because of little time of the etching. As a result, two tubes (20 nm in diameter) have been self-scrolled from that part of GaAs(2ML)/$In_{0.65}Ga_{0.35}As$(2ML) bilayer which had not AlAs underneath. The tubes lied parallel to the scratch and the scratch was between the tubes. Afterwards, a "window" to the GaAs substrate was opened. Then some part of the substrate behind the "window"

was etched out using selective reactive ion etching of GaAs and the creating of groove was finished.

Authors have a circumstantial evidences that tubes of 8 nm in diameter may be used as masks too. In the future, the proposed techniques may be used in combination with the commercial solid-state technology.

Acknowledgements

The authors thank Dr. V. Sh. Aliev for useful consultations and Dr. A. I. Toropov for providing the epitaxial structures. The work was supported by the Russian Foundation for Basic Research (Grants 97-02-18479), Russian Program "Physics of Solid State Nanostructures" (Project No 98-2030) and National Programme "Promising Technologies and Devices for Micro- and Nanoelectronics" (Project No 42).

References

[1] V. Ya. Prinz, V. A. Seleznev, V. A. Samoylov and A. K. Gutakovsky, *Microelectronic Engineering* **30**, 439 (1996).

[2] V. Ya. Prinz, V. A. Seleznev and A. K. Gutakovsky, *The 24th International Conference on the Physics of Semiconductors (ICPS 24), Israel, Eurasalem, August 2-7* Th3-D5 (1998).

[3] V. Ya. Prinz, V. A. Seleznev and A. K. Gutakovsky, *The Physic of Semiconductors, World Scientific Publishing* (1999 in press).

[4] V. Ya. Prinz, V. A. Seleznev and A. K. Gutakovsky, *Submitted to Appl. Phys. Lett.*

[5] C. B. Cooper, S. Salimian and H. F. MacMillan, *Appl. Phys. Lett.* **51** (26), 2225 (1987).

[6] E. Yablonovitch, T. Gmitter, T. Harbison and J. Bhat, *Appl. Phys. Lett.* **51**, 2222 (1987).

7th Int. Symp. "Nanostructures: Physics and Technology"
St Petersburg, Russia, June 14–18, 1999

Growth and characterization of InGaN/GaN nanoscale heterostructures

W. V. Lundin, A. V. Sakharov, V. A. Semenov, A. S. Usikov, M. V. Baidakova, I. L. Krestnikov and N. N. Ledentsov
Ioffe Physico-Technical Institute, St Petersburg, Russia

GaN and related compounds are promising materials for light sources fabrication in the visible spectral range. Blue, green and yellow light emitting diodes (LEDs) and CW blue laser diodes (LDs) have been fabricated utilising InGaN single quantum well (SQW) or InGaN/GaN multi quantum well (MQW) structures as active region [1, 2]. In spite of the remarkable progress in the device development, the further improvement in the LEDs and LDs efficiency and reliability and develop of new type of these devices is connected with understanding and detailed studying of both peculiarities of InGaN growth and the radiate recombination process in this material.

In this report, the growth of InGaN/GaN quantum size heterostructures by metalorganic chemical vapour deposition (MOCVD) and its optical characterisation are presented. The structures under studying consisted of InGaN -based active region embedded between GaN layers. These structures were grown on *c*–plane sapphire in a conventional reduced pressure MOCVD growth machine redesigned for InGaN/GaN growth with a horizontal flow quartz reactor and inductively heated AlN coated graphite susceptor. Ammonia, trimethylindium (TMI), trimethylgallium (TMG) and thrimethylaluminum (TMA) were applied as component precursors. Purified hydrogen and argon were used as carrier gases. Argon was used as a bubbling gas for TMI while hydrogen was used as a bubbling gas for TMG and TMA.

The AlN coating of the susceptor appear to promote the catalytic ammonia decomposition during the low temperature nucleation layer deposition and prevents the destruction of graphite in ammonia ambient [4].

After the substrate heat treatment at 990°C in hydrogen ambient, the temperature was reduced and a 30 nm thick Al-containing GaN nucleation layer was deposited at 530°C [3]. Then, the substrate temperature was raised to 1050°C to grow a 2.5 μm thick GaN layer. During the GaN growth the ammonia and TMG flows were 2.5 sl/min and 36 μmol/min, respectively. The growth rate was 36 nm/min. During these stages the reactor pressure was kept at 200 mbar and hydrogen was used as a carrier gas.

After the GaN growth, the carrier gas was switched from hydrogen to argon, the ammonia flow was increased to 4.5 sl/mim, the TMG flow was ramped down and the reactor pressure was increased to 600 mbar to grow InGaN layers. In accordance with our preliminary experiments, the raise of the reactor pressure during the InGaN growth leads to improvement of material quality and to rise of the indium incorporation efficiency. During switching growth mode from GaN to InGaN and back, the growth process was not interrupted. As in the case of GaN growth, the growth rate of InGaN was found to be proportional to the TMG flow and varied in our experiments in the range of 2.5–6 nm/min.

The structures were characterised by X-ray diffraction (XRD), and photoluminescence (PL) study. Thickness of InGaN layers was estimated on the basis of scanning electron microscope calibration of the growth rate of thick InGaN layers and InGaN/GaN multilayer structures sandwiched between GaN layers. XRD measurements were also employed to determine the period of InGaN/GaN multilayer structures.

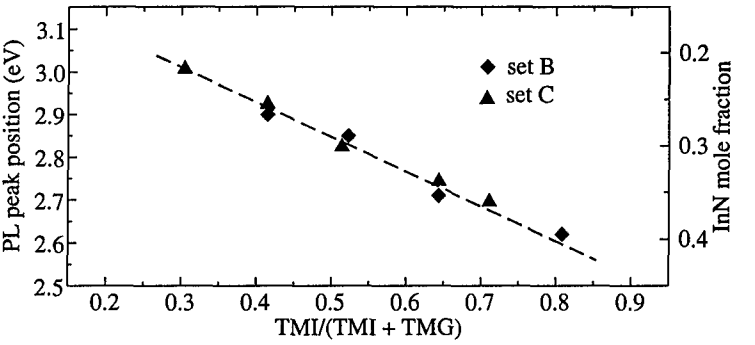

Fig. 1. 77 K PL peak position versus TMI/(TMI+TMG) mole flow ratio for samples from sets B and C.

Three sets of samples with different kinds of InGaN–based active region were prepared. These sets were denoted as A, B and C. The active region of samples of group A consisted of the single thin InGaN layer. During this active layer growth the substrate temperature was reduced to 730°C and then TMI was introduced into the reactor. After the growth of 3 nm of InGaN the substrate temperature was ramped to 1050°C to grow 0.1 μm tick GaN cap layer in hydrogen ambient at pressure of 200 mbar. The TMI flow was switched off from the reactor at the substrate temperature above 800°C.

A strong spatial fluctuations of the InGaN PL peak position from 420 to 500 nm was observed in PL spectra of this samples taken at 77 K. We suppose that this phenomenon is due to nonuniform In content and strain distribution in these lattice-mismatched structures. At the other hand, this effect was not observed for the similar structures with thicker (> 5 nm) InGaN insertions.

The active region of samples of group B consisted of two InGaN layers. First, the substrate temperature was reduced to 800°C to grow 25 nm thick InGaN intermediate layer. Then, keeping all gas flows constant, the temperature was reduced to 730°C and growth of 3 nm InGaN layer was performed. In accordance with our HRD and PL calibrations In content in the intermediate layer was approximately two times lower than in the thin InGaN layer grown at low temperature. The procedure of GaN capping layer growth was the same as in the case of samples of A group.

In the PL spectra of this set of samples no spatial variation of peak position could be observed. Moreover, the PL intensity from InGaN layer was approximately 20 times higher than in the case of A set of samples. The similar effect was previously observed by S. Keller *et al.* [5]. The peak position of PL from InGaN layer was determined by the TMI/(TMG+TMI) mole flow ratio as shown in Fig. 1. This ratio was varied both by TMI and TMG flows change.

The composition of the ternary alloys $In_xGa_{1-x}N$ was calculated using a standard expression: $E_g(x) = x \times E_{g,\mathrm{InN}} + (1-x) \times E_{g,\mathrm{GaN}} - x(1-x) \times b$, where x represents InN molar fraction, $E_g(x)$ represents the peak of the PL emission of $In_xGa_{1-x}N$ alloy, $E_{g,\mathrm{InN}}$ and $E_{g,\mathrm{GaN}}$ represent the band-gap energies for InN (1.95 eV) and GaN (3.49 eV) respectively, and b is a bowing parameter ($b = 1.0$ eV) [1] (see Fig. 1). The indium content in the InGaN layers was found to be independent of growth rate in the experimental range.

The active region of samples of set C was similar to the one of samples of set B excepting that it contained several thin InGaN layers with high In content. After the growth of the intermediate InGaN layer the substrate temperature was cycled from 730°C to 860°C keeping all gas flows constant. We grew a number of 5 and 12 period structures. The

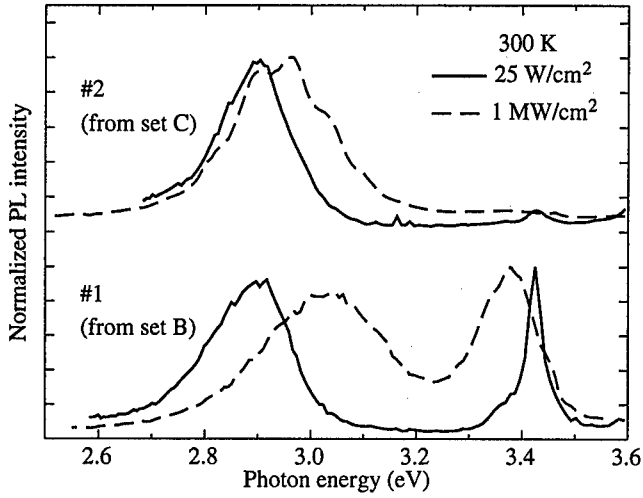

Fig. 2. Room temperature PL spectra at low and high excitation density for samples from sets B and C grown under the same TMI/(TMI + TMG) mole flow ratio of 0.415.

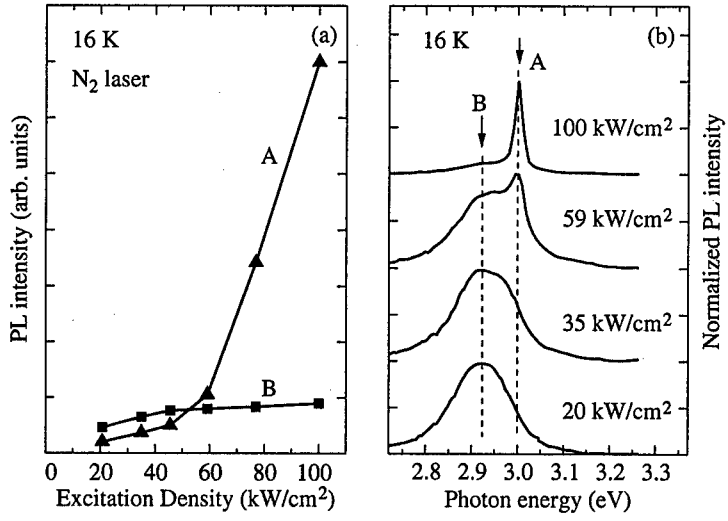

Fig. 3. Photopumped lasing at 16K in sample with cleaved facet mirrors: photoluminescense intensity *versus* excitation density (*a*) and PL spectra (*b*) taken at different excitation densities.

procedure of GaN capping layer growth was the same as in the case of type A samples. The main idea of this growth process was to create a multilayer structure only by growth temperature variation while being other growth conditions unchangeable. Here, the low temperature is needed for increase the indium incorporation in the InGaN layers whereas the high temperature is needed for growth the GaN barrier layers. Indium incorporation in InGaN layer is known to be decreased with the growth temperature increase [2]. The period of the superlattices (SLs) revealed from XRD was 12 nm. This value was in a good agreement with one estimated on the basis of TMG flow. The average In content in the SL from XRD measurements was approximately equal to the In content in the intermediate layers grown at 800°C.

The PL spectra of these samples under low excitation level (He-Cd laser, 25 W/cm^2) were identical to spectra of the samples with single InGaN layer (set B) grown with the same TMI/(TMI+TMG) mole flow ratio (see Fig. 1). In contrast, under high level of excitation (N_2 laser, up to 1 MW/cm^2) the broadening of the PL spectra and the blue shift was lower for samples from set C than for samples from set B (Fig. 2). Moreover, samples with 12 period superlattices grown under moderate TMI/(TMI+TMG) mole flow ratio (0.4–0.5) demonstrated lasing under optical pumping in both vertical and horizontal directions (see Fig. 3) [6] at temperatures up to 200 K.

In conclusion, we show that intensity of InGaN—related photoluminescence increased more than an order of magnitude for structures with intermediate InGaN layer. The growth of the InGaN/GaN SL structures was realized by periodically alteration of the growth temperature in the range between 730°C and 860°C. Lasing under conditions of optical pumping was obtained both in directions perpendicular and parallel to sample surface.

References

[1] S. Nakamura and G. Fasol: *The blue laser diode: GaN based light emmiters and lasers* (New York; London; Berlin: Springer) 1997.

[2] I. Akasaky and H. Konda, *Jpn. J. Appl. Phys.* **36** 5393–5408 (1997).

[3] A. S. Usikov, W. V. Lundin, U. I. Ushakov, B. V. Pushnyi, N. M. Shmidt, B. Ya. Ber, Yu. N. Kudryavzev and V. Yu. Davidov, *Proc. Second Symposium on III-V Nitride Materials and Processes*, Electrochemical Society Proceedings, Vol. 97-34, p. 118, 1997.

[4] W. V. Lundin, A. S. Usikov, A. V. Sakharov and V. V. Ratnikov, *EW-MOVPE VIII, Prague, June 8–11, 1999, (submitted)*.

[5] S. Keller, B.P. Keller, D. Kapolnek, A. C. Abare, H. Masui, L. A. Coldren, U. K. Mishra, and S. P. Den Baars, *Appl. Phys. Lett.* **68**, 3147–3149 (1996).

[6] A. V. Sakharov, W. V. Lundin, V. A. Semenov, A. S. Usikov, N. N. Ledentsov, A. F. Tsatsul'nikov and M. V. Baidakova, *Tech. Phys. Lett.* (1999), *in print*

7th Int. Symp. "Nanostructures: Physics and Technology"
St Petersburg, Russia, June 14–18, 1999

Optical and structural characterization of GaN grown by MBE using Indium as a surfactant

T. V. Shubina†, V. V. Mamutin†, *A. V. Lebedev*†, V. V. Ratnikov†, V. A. Vekshin†, A. A. Toropov†, N. M. Shmidt†, S. V. Ivanov†, P.S. Kop'ev†, M. Karlsteen‡, U. Sodervall‡, M. Willander‡, G. R. Pozina§, J. P. Bergman§ and B. Monemar§
† Ioffe Physico-Technical Institute, St Petersburg, Russia
‡ Chalmers University of Technology and Goteborg University, S-412 96 Goteborg, Sweden
§ University of Linkoping, S-581 83 Linkoping, Sweden

Recently it has been shown that use in GaN MBE growth of surface active agents (surfactants) mediating surface reconstruction can result either in quantum dot formation, as in the case of Si [1], or in a significant improvement of optical and structural quality of epilayers, which is reached by growth under an incident In flux [2, 3]. It has been proposed that the main role played by In atoms is to modify the GaN surface kinetics [3]. The observed phenomena stimulate an enhanced interest in this mode of GaN growth, especially in the case of MBE with its possibility to operate in the very vicinity of $N/III \sim 1:1$ growth conditions. The surfactant mediated GaN growth is conventionally carried out at a typical temperature of 600–800°C, when the theoretically expected incorporation of In is limited by about 4% [4]. The really incorporated portion of In, estimated from the near-band-edge emission energy, is even less, being practically negligible. Due to this fact the epilayers were considered as isoelectronically doped GaN:In [2]. Note that isoelectronic doping is currently considered as a subtle instrument for controlling native point defects and electrically active impurities [5]. For this purpose, a certain critical dopant concentration should be obtained, typically in the range of $4 \times 10^{19}-10^{20}\,\mathrm{cm}^{-3}$, resulting in overlapping the local strain fields induced by the impurities in a crystal lattice. However, until now there are no experimental data elucidating an actual In position in a crystal lattice of GaN layers grown with the additional In flux. Also a mechanism of the In influence on structural properties is not well understood.

In this paper we present the results of structural and optical studies of GaN:In, carried out to elucidate peculiarities of In incorporation in the surfactant mediated growth. The structures studied were grown by MBE on a (0001) sapphire substrates using a EP 1203 MBE setup equipped with a standard ASTEX ECR nitrogen activator. The growth was started from the sapphire nitridation stage at 1000°C during 1 hour. Then the deposition of GaN with an In flux was performed at the temperature varied in the 570–800°C range. The GaN:In was deposited immediately (for absorption measurements) or after about 200 nm thick GaN buffer layer growth.

Secondary ion mass spectroscopy (SIMS) was used for direct determination of In concentration in GaN:In epilayers. The impurity depth distribution in GaN:In and reference GaN samples was measured on a CAMECA IMS 3F instrument using O_2^+ as primary species. InN epilayers of perfect crystal quality, grown in the same MBE setup, were used for calibration of In content, whereas undoped GaN layers gave us the background In level. Figure 1 shows SIMS profiles of 1.15 μm — and 0.28 μm — thick GaN:In samples. In the thicker sample one can see a graded In concentration within the region adjacent to a 0.2 μm — thick undoped GaN buffer. In both samples there is an In increase near the

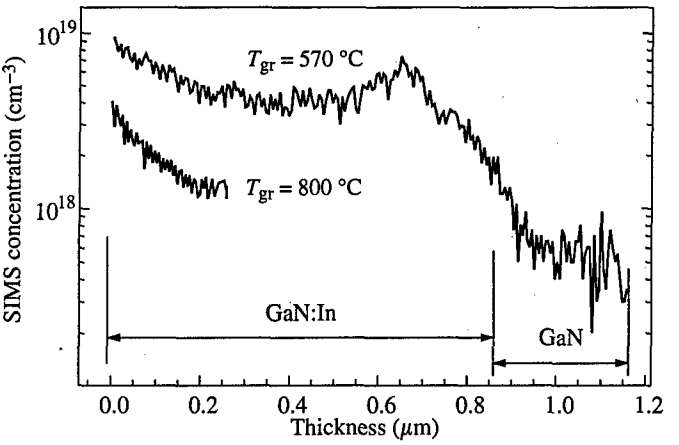

Fig. 1. SIMS profiles of In concentration in GaN:In samples grown at different temperatures.

surface, probably due to a segregation effect. However, in the volume of the thick GaN:In layer the In concentration is almost constant. In the samples studied the value varies in the range of $(1-5) \times 10^{18}$ cm^{-3} corresponding to the In content less than 0.01%.

The In content of in $In_xGa_{1-x}N$ may be independently estimated from x-ray diffraction (XRD) studies [6], assuming a substitutional indium incorporation into the Ga lattice sites. XRD measurements were performed using CuK_{α_1} radiation in double and triple crystal x-ray diffractometers. The details of the XRD studies were described elsewhere [7]. The initial curvature of a one-side polished sapphire substrate was previously measured and taken into account. Surprisingly, the In concentration obtained from XRD data turned out to be much larger than the value given by SIMS. For example, in thick samples grown at 570°C it is about 1020 cm^{-3} ($x \sim 0.3\%$). The discrepancy between SIMS and XRD concentration of In (more than one order) causes us to conclude that under the specific growth conditions In atoms incorporate into interstitials rather than occupy the Ga lattice sites, or even form clusters at surface imperfections like grain boundaries. In this case a larger effect of In on the lattice parameters is expected, which may hardly be estimated using simple models.

To investigate the influence of In incorporation on optical characteristics, low temperature (5 K) photoluminescence (PL) measurements were performed in both the GaN:In samples and the reference 0.35 μm — thick GaN sample. In contrast to the PL spectrum of the undoped GaN, displaying a single narrow near-band-edge PL peak (Fig. 2, dotted line), an additional wide emission band appears in the GaN:In PL spectrum in the 3.35–3.45 eV range. The PL band is clearly composite and, in general, possesses a constant shape in different GaN:In samples with some variation in intensities of constituent peaks (Fig. 2, solid lines). The higher PL intensity corresponds to the higher growth temperature, although the 800°C sample is thinner (0.28 μm instead of 1.15 μm) and was grown without a buffer. Note also that the integral PL intensity in all GaN:In samples is larger than that in the undoped GaN. The band edge sharp peak I_2 (about 7 meV wide) is apparently due to neutral donor-bound exciton D^0X, while the lowest line (3.28 eV) is usually attributed to donor-acceptor pair (DAP) recombination. However, the origin of the 3.428 eV and 3.378 eV wide bands (labelled here as I_x and I_3, respectively) is under question. The intensity of the I_x and I_3 lines drops faster than I_2 with a temperature increase, especially of I_x. The insert in Fig. 2 presents the temperature dependence of the integrated PL intensity

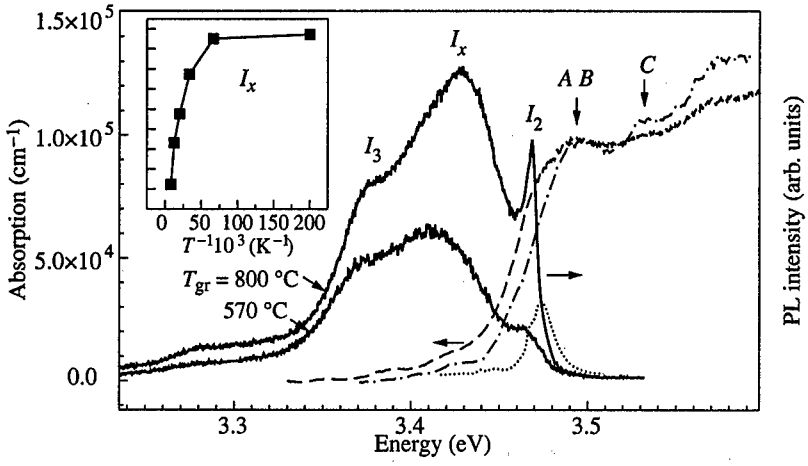

Fig. 2. Low temperature (5 K) PL spectra measured in GaN:In samples (solid curves) grown at different temperatures and in a reference GaN sample (dotted curve). Absorption spectra are shown for a GaN:In sample (dashed curve) and an undoped GaN (dash-dotted curve). The integrated intensity of the I_x peak versus reciprocal temperature is presented in the inset.

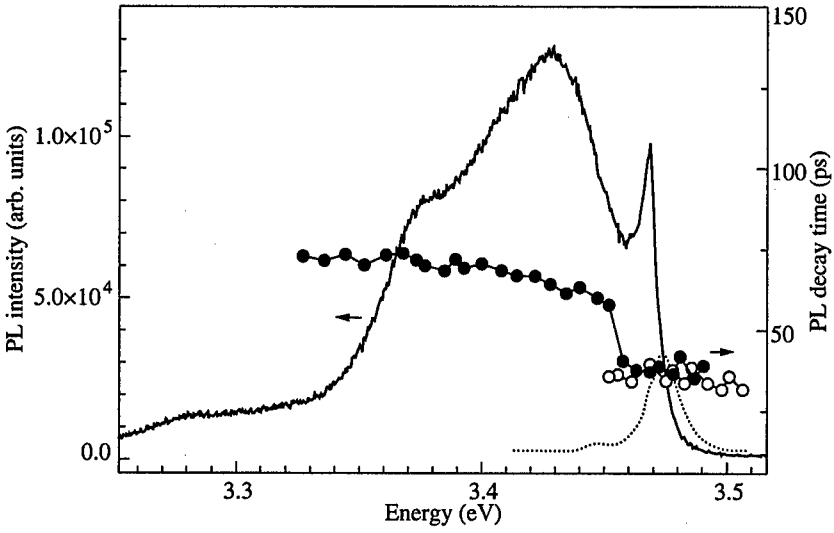

Fig. 3. Decay times of PL in undoped GaN (open circles) and GaN:In (solid circles) samples. *Cw* PL spectra are presented for GaN:In (solid line) and GaN (dotted line).

of the I_x peak, giving a thermal activation energy E_A of 11.8 meV. T he main characteristic of the I3 line is a well-resolved blue shift (about 6 meV in the temperature range from 5 to 50 K), which is typical for PL of thermally-occupied localized states.

To clarify the origin of the complicated PL band, transmission spectra were measured in the 0.28 μm — GaN:In and 0.35 μm — GaN samples, grown without buffer layer. The peculiarities corresponding to unresolved A and B excitons and a separated C exciton are obviously pronounced and are similar in both samples. However, a smooth shoulder below A–B exciton peak is registered in the GaN:In sample, evidencing an additional

inhomogeneously broadened absorption edge, shifted to about 20 meV bellow the A exciton. Assuming formation of $In_xGa_{1-x}N$, it corresponds to $x = 1.3\%$ that is even higher than the value obtained from XRD. To explain this fact, one can suggest formation of $In_xGa_{1-x}N$ clusters. Since the hypothetical $In_xGa_{1-x}N$ and GaN edges coexist in the spectrum, the states forming the absorption edges should be spatially separated.

Time-resolved (TR) PL measurements also confirm the composite character of the PL band in GaN:In. The decay time within the PL contour is not monoexponential. In particular, there is a noticeable contribution of long-living PL (the signal is not vanishing in the 12 ns between the exciting laser pulses). However, the first one-two orders of the PL decay take place in first 100–200 ps with the characteristic decay times plotted in Fig. 3 as diamonds. The time for the low-energy band smoothly depends on the wavelength, increasing to the red side. Accounting for the broadening of the absorption band edge, one possible explanation of this relatively fast contribution to the PL signal may be recombination at the tail localized states, somehow related to the In-rich clusters. Note, that the narrow peak visible in both GaN and GaN:In samples exhibits decay times in the range of 30–50 ps, which is well consistent with the data for D^0X [8].

In conclusion, the structural and optical characterisation of GaN:In epilayers have shown that only a small amount of In is incorporated into the Ga sites, making the layers to be considered as not pure "isoelectronically" doped. The In atoms presumably occupy interstitial positions in the crystal lattice, concentrate on mosaic grain boundaries and have a tendency to form clusters. The In nucleation near structural defects, like e.g. nano-pits, may recover the lattice structure, increasing the integral PL intensity. Besides, like at conventional isoelectronic doping, local strains induced by the inhomogeneous In distribution may activate mechanisms of structure improvement. On the other hand, the possible occupation of interstitials by the In atoms can hardly be considered as a positive factor.

This work has been partly supported by the RFBR grants and the Program of Ministry of Science of RF "Physics of solid-states nanostructures".

References

[1] S. Tanaka, S. Iwai and Y. Aoyagi, *Appl. Phys. Lett.* **69**, 4096 (1996).
[2] C. K. Shu, J. Ou, H. C. Lin, W. K. Chen and M. C. Lee, *Appl. Phys. Lett.* **73**, 641 (1998).
[3] F. Widmann, B. Daudin, G. Feuillet, N. Pelekanos and J. L. Rouviere, *Appl. Phys. Lett.* **73**, 2642 (1998).
[4] I.-H. Ho and G. B. Stringfellow, *Appl. Phys. Lett.* **69**, 2701 (1996).
[5] E. G. Guk and N. M. Shmidt, pp. 5-6, V. V. Chaldyschev and S. V. Novikov, *Semiconductor technology*, 165–194, Part 1, edited by M. E. Levinshtein and M. S. Shur, John Wilay, New York, 1997.
[6] L. T. Romano, B. S. Krusor, M. D. Cluskey, D. P. Bour and K. Nauka, *Appl. Phys. Lett.* **73**, 1757 (1998).
[7] R. N. Kyutt, V. V. Ratnikov, G. N. Mosina and M. P. Scheglov, *Phys. Solid State* **41**, 30 (1999).
[8] C. I. Harris, B. Monemar, H. Amano and I. Akasaki, *Appl. Phys. Lett.* **67**, 840 (1995).

7th Int. Symp. "Nanostructures: Physics and Technology"
St Petersburg, Russia, June 14–18, 1999

Growth of self-assembled GeSi islands with narrow size distribution on Si (001)

A. V. Novikov†, N. V. Vostokov†, I. V. Dolgov†, Yu. N. Drozdov†,
Z. F. Krasil'nik†, D. N. Lobanov†, M. D. Moldavskaya†, V. V. Postnikov†
and D. O. Filatov ‡

† Institute for Physics of Microstructures RAS, Nizhny Novgorod
‡ The Nizhny Novgorod State University

Abstract. The results of the investigation of the self-assembled Ge islands growth on Si (001) at 700°C are presented. The evolution of the islands shape from "hut" to "dome" islands is studied. For Ge coverage of 11 monolayers a narrow distribution of islands sizes is obtained which allowed to use the Raman spectroscopy and X-ray diffraction for determination of Ge content and residual strain in islands.

Introduction

Elastic stress appearing during the growth of Ge on Si (001) causes a series of morphological changes in the growth front. At submonolayer coverages a $(2 \times n)$ reconstruction forms on film's surface then transforming to (2×8) reconstruction at sufficient Ge amounts (> 1 monolayer (ML)). An increase of Ge coverage (d_{Ge}) up to 3 ML results in elongated two-dimensional islands formation. The next stage of elastic sterss relaxation is formation of three-dimensional (3D) coherent (without dislocations) islands. At some critical islands dimensions the dislocations emerge. The total stress relief occurs by development of a misfit dislocation network. Self-assembled 3D islands have been found to be promising material for Si-based optoelectronics. However, such applications require the islands with the uniform size distribution. Therefore determination of the uniform islands growth conditions is of considerable interest.

In this paper we investigate the growth stages of self-assembled Ge islands deposited on Si(001) at 700°C versus Ge amounts. The growth conditions for uniform islands formation were found. Elastic strain and composition of the islands were measured by Raman spectroscopy and X-ray diffraction.

1 Growth of self-assembled islands

All samples were grown on Si (001) substrates at temperature of 700°C by solid source MBE in a "BALZERS" system. The system was equipped with e-gun for Si and Ge evaporation. The growth rate monitored by the quadrupole mass spectrometer was equal to 1.5 Å/c for Si and 0.15 Å/c for Ge. The samples consist of a 200 nm Si buffer with 1 to 11 ML Ge on top. Atomic force microscopy (AFM) images were recorded in the contact and tapping mode, with "Topometrix"-TMX-2100 AFM and "Solver"-P4 AFM in ambient air.

The onset of Ge islands formation at given growth conditions is observed from AFM images at coverages above 4 ML. At the beginning all islands are the so-called "hut clusters" — well shaped prism-like islands with the bases parallel to the [100] or [010] directions and with {105} facets. At 5.5 equivalent ML of Ge deposited a new kind of islands arises;

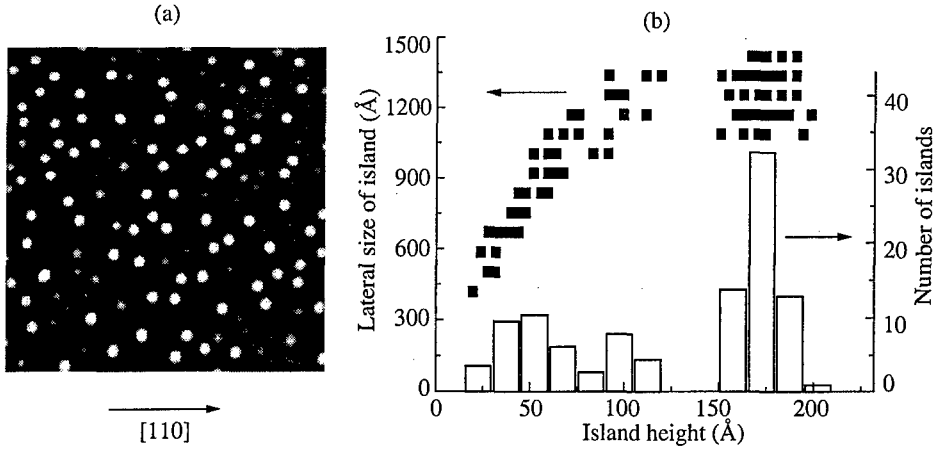

Fig. 1. (a) AFM image (size $2.5 \times 2.5\,\mu m^2$) of the sample with $d_{Ge} = 5.5$ ML; (b) the islands lateral size (D) versus the islands height (H) and histogram of H for this sample.

the so-called "dome-islands" — the islands with fixed lateral size and without clear facets. As an example we show AFM images at 5.5 ML of Ge coverage in Fig. 1(a).

The results of treatment of this image by the special program for determination of the lateral size (D) and height (H) of islands are presented in Fig. 1(b); the bimodal height distribution is clearly seen from the dependence $D(H)$ and from the histogram of the islands height (Fig. 1(b)). We associate the linear relationship on the dependence $D(H)$ with the growth of hut-islands when the lateral size and height of an island increase proportionally. The horizontal region of this dependence corresponds to the growth of dome-islands when the lateral size does not change but the island height gradually increases. From Fig. 2(b) one can estimate the maximal size of hut-islands: $D \approx 1400$ Å, $H \approx 120$ Å. According to the idea suggested in [1] these dimensions define the critical island volume V_c at which the transition from a hut to dome island growth mode occurs. This transition is energetically favourable because at island volume above V_c the dome island energy is less than that of hut-island with the same volume. The chemical potential is decreases step-like in this transition [1], which leads to a rapid growth of dome-islands and to appearance of the bimodal distribution of the island sizes (Fig. 1(b)).

The surface density of islands slightly increases and gradually all hut-islands become dome-ones at an increase of amount of Ge coverage from 5.5 ML to 11 ML. Since dome-islands are of the same lateral size the relative dispersion of D is small (less than 10% at $d_{Ge} = 8$ ML), while the relative dispersion of height distribution is large ($15 \div 20\%$ at the same Ge coverage). An increase of Ge amount up to 11 ML results in remarkable narrowing of both the lateral size and the height distributions (both dispersions are nearly 6%). Such narrow distribution probably results from a local minimum of the dome-islands surface energy or from the energy barrier for generation of dislocation in the islands.

2 Ge content and residual strain in the islands

Determination of Ge content (x) and residual strain (ε) in the islands is important for understanding of their optical properties. However, it is quite difficult to measure either of quantities separately.

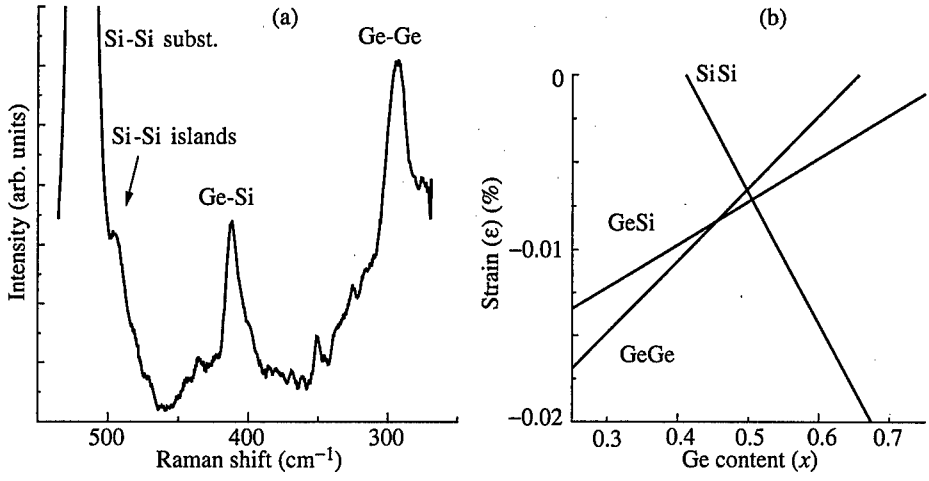

Fig. 2. (a) The Raman spectrum of the sample with $d_{Ge} = 11$ ML; (b) strain (ε) versus Ge content (x) for the sample with $d_{Ge} = 11$ ML.

Uniform islands size distribution in our sample with $d_{Ge} = 11$ ML made it possible to use both the Raman spectroscopy and X-ray diffraction for estimation of x and ε. The Raman scattering and X-ray diffraction measurements were performed at room temperature using DFS-52 spectrometer and DRON-4 diffractometer respectively. Figure 2(a) shows the Raman spectrum of the sample with $d_{Ge} = 11$ ML. Besides the strong Si substrate signal ($\Omega = 520.5\,\text{cm}^{-1}$), the spectrum consists of three peaks which are due to Ge–Ge ($\Omega = 294\,\text{cm}^{-1}$), Si–Ge ($\Omega = 412\,\text{cm}^{-1}$) and Si–Si ($\Omega = 495\,\text{cm}^{-1}$) vibrations [2]. The knowledge of these phonon frequencies allows us to define three linear relationships between x and ε (Fig. 2(b)) [3]. The crossing of any pair of lines in Fig. 2(b) defines a pair of allowed values of x and ε. Note that all the crossing points in Fig. 2(b) are very close to each other. The Ge content and residual strain estimated by this manner are equal to $x = 0.5 \pm 0.05$ and $\varepsilon = -0.7\% \pm 0.05\%$ being in a good agreement with the ones estimated by X-ray diffraction measurements. So one can conclude that at given growth conditions the self-assembled islands at $d_{Ge} = 11$ ML are weakly strained $Si_{0.5}Ge_{0.5}$ alloy. Such a high value of Si content in the islands can not be explained by bulk diffusion of Si at growth temperature especially when the sample does not have a Si cap layer. Thus further experiments are needed for understanding of compositions and strain distribution in self-assembled islands.

Band edges positions of the sample under investigation were calculated using the obtained parameters x and ε [4]. According to this calculations, the energy of the quasi-direct optical transition [4] is about 0.725 eV. A similar structure but with a Si cap layer was investigated by photoluminescence (PL) technique. The peak of PL associated with the islands was observed at the energy of 0.8 eV [4]. The discrepancy between the calculated and the observed values can result from diffusion of Si from the cap layer to the islands and segregation of Ge.

This work has been supported by grant #99-02-16980 from the Russian Foundation for Basic Research, the Russian Academy Science Program of young scientists support #1 and the Russian Scientific Programs: "Physics of Solid State and Nanostructures" and

"Perspective Technologies and Devices for Micro-and Nanoelectonics".

References

[1] F. M. Ross, J. Tersoff and R. M. Tromp, *Phys. Rev. Lett.* **80**, 984 (1998).
[2] M. I. Alonso and K. Winner, *Phys. Rev.* **B39**, 10056 (1989).
[3] J. Groenen, R. Carles et al., *Appl. Phys. Lett.* **71**, 3856 (1997).
[4] V. Ya. Aleshkin and N. A. Bekin, *Semiconductors.* **31**, 171 (1997).
[5] Z. F. Krasil'nik, V. Ya. Aleshkin et al., Proceedings of 6th International Symposium "Nanostructures: Physics and Technology", St. Petersburg, Russia, p. 456, 1998.

7th Int. Symp. "Nanostructures: Physics and Technology"
St Petersburg, Russia, June 14–18, 1999

Self-organized growth of composition-modulated alloys

V. A. Shchukin and A. N. Starodubtsev
Ioffe Physico-Technical Institute, St Petersburg, Russia

Epitaxial growth of semiconductor alloys in open systems can be unstable against fluctuations of composition [1-4]. For such kinetic instability it is typical that the bulk diffusion is negligibly slow compared with the surface diffusion. Fluctuations of composition in the entire thickness of the epitaxial film are "frozen", and these fluctuations create a strain field on the surface which affects the surface migration of atoms. It was shown in [4], that due to the interplay of anisotropic elasticity and anisotropic surface diffusion, the wave vector of the most unstable mode of composition fluctuations can have any direction. However, an important question was still unsolved: How does this interplay depend on key experimental parameters, namely on growth temperature and growth velocity? Moreover, the linear stability analysis of alloy growth [1–4] does not give an answer on the final composition-modulated structure which is being formed during the growth.

In the present paper we, first, perform a linear stability analysis and obtain the wave vector of the most unstable mode as a function of growth temperature and growth velocity. Second, we solve a non-linear problem in the weak segregation regime and obtain a final composition-modulated structure.

We study the growth of a binary alloy $A_{1-c}B_c$ via molecular beam epitaxy at growth temperature above the roughening transition temperature. Then the surface contains a high concentration of steps and kinks. Crystal growth can be described by the propagation of the surface in the normal direction. The growth of an alloy implies coupled fluctuations of alloy composition $\phi(\mathbf{r}_\parallel, z) = c(\mathbf{r}_\parallel, z) - \bar{c}$ and surface profile $\zeta(\mathbf{r}_\parallel) = h(\mathbf{r}_\parallel) - \bar{h}$, where $h(\mathbf{r}_\parallel)$ is the local thickness of the film, and $\bar{h}$ is the average thickness. Let the alloy $A_{1-c}B_c$ be a mixture of two cubic crystals, the homogeneous alloy be lattice-matched to the substrate and the growth occur on the (001)-substrate of a cubic material. The growth of an alloy is described by two coupled kinetic equations. Let the reference frame travel together with the surface with the average growth velocity v. Then kinetic equations are as follows:

$$\begin{aligned} \frac{\partial \phi(\mathbf{r}_\parallel)}{\partial t} &= M^{\phi}_{ij} \nabla_i \nabla_j \frac{\delta F}{\delta \phi(\mathbf{r}_\parallel, \bar{h})} - \frac{v}{a} \phi(\mathbf{r}_\parallel, \bar{h}) \\ \frac{\partial \zeta(\mathbf{r}_\parallel)}{\partial t} &= M^{\zeta}_{ij} \nabla_i \nabla_j \frac{\delta F}{\delta \zeta(\mathbf{r}_\parallel)} . \end{aligned} \tag{1}$$

Here M^{ϕ}_{ij} and M^{ζ}_{ij} are 2D surface atomic mobility tensors related to the substitutional diffusion and to the change of surface profile, respectively. Unlike [3], Eqs.(1) account the anisotropy of surface mobility tensors, their principle axes being [110] and [$\bar{1}$10], which is typical for III-V and II-VI semiconductors; a is the lattice parameter. The free energy F equals $F_{chem} + F_{grad} + E_{surf} + E_{el}$, where F_{chem} is the chemical free energy, F_{grad} is the gradient energy, E_{surf} is the surface energy of a corrugated surface, and E_{el} is the elastic energy depending on the surface profile.

First, we carry out the linear stability analysis by expanding F up to ϕ^2 and ζ^2. We seek Fourier components of fluctuations $\tilde{\phi}(\mathbf{k}_\parallel, t)$ and $\tilde{\zeta}(\mathbf{k}_\parallel, t)$ proportional to $\exp[\omega(\mathbf{k}_\parallel)t]$.

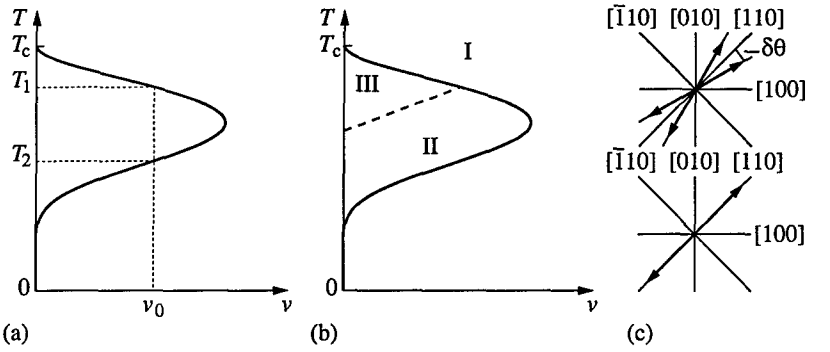

Fig. 1. The phase diagram of kinetic instability in variables "temperature-growth velocity". (a) The boundary of the instability region. For $v = v_0$ the alloy is unstable at $T_2 < T < T_1$. (b) I: stable alloys, II: unstable alloys, most unstable modes are shown in Fig. 1(c) (bottom). III: unstable alloys, most unstable modes are shown in Fig. 1(c) (top). (c) Wave vectors of most unstable modes.

Linearized equations for $\tilde{\phi}(\mathbf{k}_\parallel, t)$ and $\tilde{\zeta}(\mathbf{k}_\parallel, t)$ are decoupled, similar to [2,3]. For fluctuations of composition, $\tilde{\phi}(\mathbf{k}_\parallel, t) \sim \exp[\omega(\mathbf{k}_\parallel)t]$, we obtain the following characteristic equation for ω:

$$\omega = -M(\theta)k^2\left[r(T-T_c) + \kappa k^2 + \sum_{s=1}^{3}\left(\frac{kR_s(\theta)}{k\alpha_s(\theta)+\omega/v} - \frac{R_s(0)}{\alpha_s(0)}\right)\right] - v/a\,. \qquad (2)$$

θ is the angle between $\mathbf{k}_\parallel$ and [100]; $R_s(\theta)$ refer to the anisotropic elastic interaction [1]; $\alpha_s(\theta)$ are attenuation coefficients of static Rayleigh waves; $M(\theta)$ is the effective mobility in the given direction, $M(\theta) = M_1^\phi \cos^2(\theta - \pi/4) + M_2^\phi \sin^2(\theta - \pi/4)$, where M_1^ϕ and M_2^ϕ are mobilities along [110] and [$\bar{1}$10], T_c is the critical temperature of kinetic instability in the slow deposition limit ($v \to 0$) [1]; $r = (\partial^3 f_{chem}/\partial c^2 \partial T)$, where f_{chem} is the chemical free energy density; κ refers to the gradient energy. Given v and T, Eq.(2) determines $\omega(k, \theta)$. Re$\omega > 0$ means the kinetic instability.

To obtain the stability phase diagram of the alloy growth (Fig. 1(b)) we set $\bar{c} = 0.5$, use for f_{chem} the regular solution approximation, $f_{chem}(c, T) = \Omega c(1-c) + T[(1-c)\ln(1-c) + c\ln c]$, and take into account the Arrhenius-type temperature dependence of mobilities $M_{1,2}(T) = M_{1,2}^{(0)} \exp(-E_{1,2}/T)$. The growth of an alloy includes the competition between the surface migration and the burial by the incoming flux. Let temperature T be fixed. Then, if the growth velocity v is larger than a certain critical value, the fast burial does not allow the surface migration to create composition fluctuations. Now, let v be fixed and T decrease. When $T < T_1(v)$, the driving force to kinetic instability appears. When $T < T_2(v)$ the slow surface diffusion does not allow composition fluctuations to occur (Fig. 1(a)).

Anisotropic surface diffusion promotes instability with $\mathbf{k}_\parallel$ along the direction of fast diffusion [110]. Anisotropic elasticity promotes instability with $\mathbf{k}_\parallel$ along the elastically soft direction [100] or [010]. The result of such an interplay is given in Fig. 1(b). In region II there are 2 most unstable modes with $\mathbf{k}_\parallel \parallel$ [110]. In region III there are 4 most unstable modes with $\mathbf{k}_\parallel$ deviated by $\pm\delta\theta$ from [110] (Fig. 1(c)).

Below we seek steady state solutions in the weak segregation regime, i.e. at T and v close to the onset of the instability. For simplicity we consider isotropic surface diffusion. Near the onset of instability we have $(v\kappa)/[aMr(T_c - T)] = 1/4 - \epsilon^2$, where $\epsilon \ll 1$. The fact that in the linear regime, kinetic equations for ϕ and for ζ are decoupled and the

surface remains flat, has two important issues. First, $\zeta \sim \phi^2$. Then, to solve the non-linear problem we expand the free energy up to fourth order terms, i.e. up to ϕ^4 and ζ^2. Second, the relaxation of the surface is a fast process, while the relaxation of the composition profile is a slow process. By using the adiabatic elimination of fast relaxing variables [5] we obtain kinetic equations which contain only ϕ. In the weak segregation regime the solution is a perturbation series in ϵ. The main contribution is given by most unstable modes with $\mathbf{k}_\parallel = \pm(k_0, 0)$ and $\mathbf{k}_\parallel = \pm(0, k_0)$, where $k_0 = (1/\sqrt{2})[r(T_c - T)/\kappa]^{1/2}$. We seek ϕ in the form $\phi(x, y) = \epsilon[(r_4/r(T_c - T)]^{1/2}[\psi_x \cos(k_0 x) + \psi_y \cos(k_0 y)]$, where $r_4 = (\partial^4 f_{chem}/\partial c^4)_{c=\bar{c}}$. Kinetic equations for amplitudes ψ_x and ψ_y are

$$\frac{\partial \psi_x}{\partial \tau} = -\frac{\epsilon^2}{2}\left\{ -\psi_x + a_L \psi_x^3 + a_T \psi_x \psi_y^2 \right\}$$
$$\frac{\partial \psi_y}{\partial \tau} = -\frac{\epsilon^2}{2}\left\{ -\psi_y + a_L \psi_y^3 + a_T \psi_y \psi_x^2 \right\}, \tag{3}$$

where

$$a_L = 1 + \frac{(r(T_c - T))^{1/2}\kappa^{1/2}}{\gamma r_4}\left[\frac{-R_L}{8} - \frac{R_L^2}{2r(T_c - T)}\right]$$
$$a_T = 3 + \frac{(r(T_c - T))^{1/2}\kappa^{1/2}}{\gamma r_4}\left[-R_T - \frac{4R_T^2}{r(T_c - T)}\right], \tag{4}$$

$\tau = (Mr(T_c - T)/\kappa)t$ is a dimensionless time parameter, and γ is the surface energy per unit area, R_L and R_T are characteristic elastic energies. The steady state solution of Eqs.(3) depends on parameters a_L and a_T. If $a_L < a_T$, the stable steady state solution is a 1D composition-modulated structure, $\psi_x = a_L^{-1/2}$ and $\psi_y = 0$ or $\psi_y = a_L^{-1/2}$ and $\psi_x = 0$. If $a_L > a_T$, the stable steady state solution is a 2D modulated structure, $\psi_x = \psi_y = (a_L + a_T)^{-1/2}$. If $a_L + a_T < 0$ or $a_L < 0$, Eqs.(3) do not have stable steady state solutions. This means that the final structure has a finite modulation amplitude already near the onset of instability.

The pattern selection is governed by the interplay of elastic and surface energies. Let the surface energy be very high, $\gamma \to \infty$. Then the surface remains flat even in the non-linear regime; $a_L = 1$, $a_T = 3$, which favors a 1D structure. There is a similarity with alloy decomposition in the bulk [6], where the resulting structure is a mixture of two phases with compositions c_1 and c_2. A two-phase system is consistent with 1D structure and inconsistent with 2D structure. For a moderate γ, the effect of surface corrugation becomes important, which alters a_L and a_T and favors 2D structure. This is similar to the case of lattice-mismatched systems where a 2D corrugation gives a more efficient elastic relaxation than a 1D one [7]. For a low surface energy, $a_L < 0$, $a_T < 0$, and the final structure has a finite amplitude near the onset of instability. Since the interplay of elastic and surface energies depends on $T_c - T$ (Eq.(4)), this yields a phase diagram on Fig. 2. Similar interplay between 1D and 2D structures persists in case of anisotropic surface mobility.

To conclude, we have shown that the alloy growth in open systems can result in both 1D and 2D modulated structure and the orientation of the structure is determined by growth temperature and growth velocity. Principle results, obtained for binary alloys, remain valid for ternary and quaternary alloys. This explains the 1D structure in InAlAs modulated in [110]-direction [8], the 1D structure in MgZnSSe modulated in [100]-direction [9], and the 2D structure in GaInAsP modulated in [100] and [010]-directions [10].

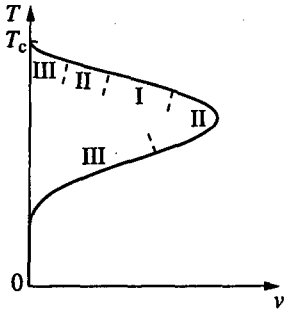

Fig. 2. The phase diagram of final composition-modulated structure near the onset of instability. I: 1D structure, II: 2D structure, III: no solutions in the weak segregation regime, the structure has a finite amplitude.

The work was supported, in different parts, by the Russian Foundation for Basic Research, Grant 98-02-18304, by the Russian Federal Program of Russian Ministry of Science and Technology "Solid State Nanostructures", Project 97-2014, and by the Russian Federal Program "Leading Research Schools", Grant No 96.15-96.348.

References

[1] V. G. Malyshkin and V. A. Shchukin, *Semiconductors* **27**, 1062 (1993).
[2] J. E. Guyer and P. W. Voorhees, *Phys. Rev. B* **54**, 11710 (1996).
[3] F. Leonard and R. C. Desai, *Phys. Rev. B* **57**, 4805 (1998).
[4] I. P. Ipatova, *et al. Phys. Rev. B.* **57**, 12968 (1998).
[5] H. Haken, *Synergetics* (Springer, Berlin, 1983).
[6] A. G. Khachaturyan. *Theory of Structural Transformations in Solids* (Wiley, New York, 1983).
[7] V. A. Shchukin *et al. Phys. Rev. Lett.* **75**, 2968 (1995).
[8] S. W. Jun *et al.* **68**, 3443 (1996).
[9] L. H. Kuo *et al. Appl. Phys. Lett.* **65**, 1230 (1994).
[10] T. L. McDevitt *et al. Phys. Rev. B.* **45**, 6614 (1992).

7th Int. Symp. "Nanostructures: Physics and Technology"
St Petersburg, Russia, June 14–18, 1999

Volmer–Webber epitaxial growth of InAs nanoscale islands on Si(100)

G. E. Cirlin†‡, N. K. Polyakov†, Yu. B. Samsonenko†‡, V. G. Dubrovskii†, V. N. Petrov†, D. V. Denisov‡, V. M. Busov‡ and V. M. Ustinov‡
† Ioffe Physico-Technical Institute, St Petersburg, Russia
‡ Ioffe Institute RAS, St. Petersburg, Russia

Abstract. InAs/Si(100) heteroepitaxial growth is studied with reflection high-energy electron diffraction and scanning electron microscopy methods. It is shown that under certain growth conditions the formation of InAs nanoscale islands on Si(100) surface occurs via Volmer Webber growth mechanism.

Recently we proposed to use coherent narrow gap InAs quantum dots in a silicon matrix for development of Si-based light-emitting devices. By now the possibility to form coherent nanoscale InAs islands on Si(100) surface directly during molecular beam epitaxial (MBE) growth is demonstrated. Photoluminescence (PL) signal was observed for InAs quantum dot array embedded in a silicon matrix up to room temperature. It is shown that the PL band originating from InAs quantum dots is in the 1.3–1.6 micron range depending on the observation temperature [1]. This wavelength range is important for various applications, *e.g.* fiber optics, medicine, biology *etc.*

However, the development of light emitting devices based on the nanoscale islands in the active region requires further basic and technological research. InAs/Si band alignment, the role of strain, size and shape of nanoscale island in designing the necessary bandgap profile is still unclear. In addition, the effect of growth regimes on size and shape of InAs islands is not yet studied in detail.

In this paper we report an effect of the growth conditions on realization of the epitaxial growth mode (Stranski–Krastanow or Volmer–Webber) during heteroepitaxy of InAs on Si(100).

The growth experiments are carried out using EP1203 MBE machine (Russia) or Riber 32 Supra (France) on exactly oriented Si(100) substrates. The Si(100) surface preparation is made in a way similar to that described in [2]. Thermal desorption of silicon native oxide layer is performed at substrate temperature of 800–820 °C during 15 min. After that, well resolved (2×1) or mixed (1×2) and (2×1) surface reconstructions typical for cleaved Si(100) surface has been observed. Then the substrate temperature is gradually decreased to the desired value and the InAs deposition is initiated in a conventional MBE mode. The InAs deposition rate is 0.1 monolayer (ML) per second. A calibration of the growth rate, III–V flux ratio, and monitoring of the surface morphology during growth has been performed using reflection high energy electron diffraction (RHEED) system composed of a high sensitivity video camera, a video tape recorder and a computer, all interconnected via a specially designed interface [3]. Pieces for scanning electron microscopy (SEM) studies are taken from the same wafers, but InAs nanostructures were previously capped with 30 nm silicon.

We have recently shown that the critical thickness T_c for the formation of InAs 3D islands on the Si(100) surface significantly depends on the growth conditions (*e.g.*, substrate temperature and fluxes ratio). We have found that T_c is in the range of 0.7–5.0 monolayers

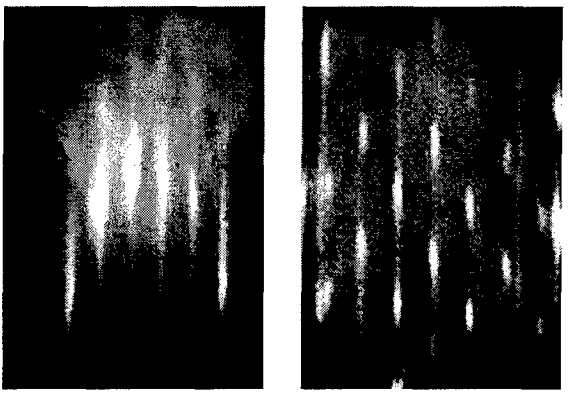

(a) (b)

Fig. 1. RHEED patterns before (a) and after (b) deposition of InAs (2 monolayers) at 10 keV. Images are taken in [011] direction.

of InAs for the substrate temperature range 350–450 °C a fluxes ratio $\sim 2-10$ [4]. We could expect the realization of Volmer–Webber growth mechanism for a case of the critical thickness less then 1 ML. This growth mechanism was observed previously for different heteroepitaxial systems, *e.g.* GaAs/Si.

In Fig. 1(a,b) RHEED patterns for Si(100) surface just before the deposition of InAs (a) and after deposition of 2 ML of InAs at $T_s = 380°$ C and fluxes ratio = 10. For these particular growth conditions we observe a change of 2D to 3D growth mode at average InAs thickness ~ 0.7 ML.

For the pattern in Fig. 1(a) only streaky-like features responsible for a atomic-smooth Si surface are observed. In contrast, in Fig. 1(b) there is coexistence of the peculiarities from both silicon surface (elongated streaks) and nanoscale InAs islands (spots) which began to appear just after the critical thickness is exceeded. There is also evident the difference in lattice constants for substrate and deposited material.

We speculate that for the latter case the situation is the following. After initiation of InAs deposition, on the bare Si substrate the nuclei of InAs start to appear very rapidly. At the continuation of the growth, the island density remains the same with the increasing of their volume only. At the same time the part of Si surface is free from InAs deposit. This is typical for Volmer–Webber growth mechanism. Another situation was observed for Stranski–Krastanow growth mechanism, typical for, *e.g.* InAs/GaAs system or the same InAs/Si, but other growth conditions [5]. Here the formation of nanoscale islands occurs on the top of wetting layer, when first ~ 1.5 ML of deposited material grew via layer-by-layer growth mode. In Fig. 2 SEM image of the sample with the islands growing via Volmer–Webber growth mechanism realization is presented. The coexistence of relatively small ($\sim$ 20 nm) and high ($\sim$ 50 nm) islands pyramidal in shape and smooth silicon InAs-free space in between them is seen (real size of the islands is smaller due to presence of thin Si cap layer). The orientation of sides of the islands is [011] and $[0\bar{1}1]$, opposite to the situation with the islands formed via Stranski–Krastanow mode [5], where dense array of the islands was observed with the preferential orientation along [011] and [001] directions. In conclusion, we have demonstrated the possibility of the formation of InAs nanoscale islands on Si(100) surface via Volmer–Webber growth mechanism that sheds more light in a heteroepitaxial growth processes in this system. This is also important for the tuning of

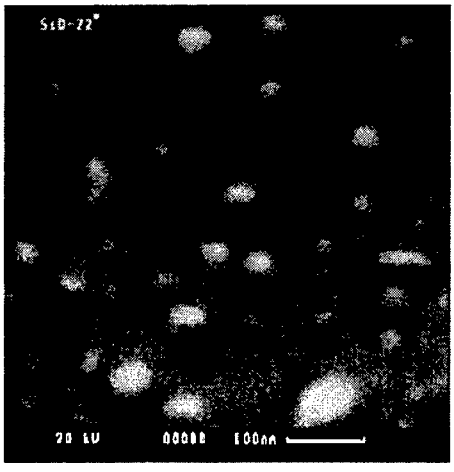

Fig. 2. SEM image of the surface after deposition of 2 ML InAs in a Volmer–Webber growth mode. Sides of the image are parallel to [011] and [0$\bar{1}$1] directions.

the lateral size in order to achieve appropriate geometry of the nanoscale islands.

Acknowledgements

Authors wish to thank V. A. Egorov for the help in preparing the manuscript. This work was partially supported by INTAS Grant No 94-0242, Russian Foundation for Basic Research, National Program "Physics on solid-state nanostructures" and National Program "Advanced devices for micro- and nanoelectronics" in a frame of the project No 02.04.5.1.40.E.46.

References

[1] G. E. Cirlin, V. G. Dubrovskii, V. N. Petrov, N. K. Polyakov, N. P. Korneeva, V. N. Demidov, A. O. Golubok, S. A. Masalov, D. V. Kurochkin, O. M. Gorbenko, N. I. Komyak, V. M. Ustinov, A. Yu. Egorov, A. R. Kovsh, M. V. Maximov, A. F. Tsatsul'nikov, B. V. Volovik, A. E. Zhukov, P. S. Kop'ev, Zh. I. Alferov, N. N. Ledentsov, M. Grundmann and D. Bimberg, *Semicond. Sci. Technol.* **13**, 1262 (1998).

[2] A. Ishisaka and Y. Shiraki, *J. Electrochem. Soc.* **133** 666 (1986).

[3] G. M. Gur'yanov, V. N. Demidov, N. P. Korneeva, V. N. Petrov, Yu. B. Samsonenko and G. E. Tsyrlin, *Tech. Phys.*, **42** 956 (1997).

[4] A. F. Tsatsul'nikov, A. Yu. Egorov, P. S. Kop'ev, A. R. Kovsh, M. V. Maximov, V. M. Ustinov, B. V. Volovik, A. E. Zhukov, Zh. I. Alferov, G. E. Cirlin, A. O. Golubok, S. A. Masalov, V. N. Petrov, N. N. Ledentsov, R. Heitz, M. Grundmann, D. Bimberg, I. P. Soshnikov, P. Werner and U. Gösele, *Proc. 24th Int. Conf. Phys. Semiconductors*, Jerusalem, 1998, World Scientific, Singapoure, 1999, (in press).

[5] G. E. Cirlin, V. N. Petrov, V. G. Dubrovskii, S. A. Masalov, A. O. Golubok, N. I. Komyak, N. N. Ledentsov, Zh. I. Alferov and D. Bimberg, *Tech. Phys. Lett.* **24**, 290 (1998).

7th Int. Symp. "Nanostructures: Physics and Technology"
St Petersburg, Russia, June 14–18, 1999

Growth of InAs self-assembled islands on Ge

S. A. Komarov†, G. S. Solomon‡ and J. S. Harris Jr.†
† Solid State and Photonics Laboratory, Stanford University,
Stanford, CA, 94305, USA
‡ Ginzton Laboratory, Stanford University,
Stanford, CA, 94305-4075,USA

Tremendous amount of research has been devoted to the study of quantum confined structures in the several last years. One of the most popular systems that has been extensively investigated is an ensemble of self-assembled coherently strained nano-sized islands. Despite this effort, complete clarity in understanding mechanisms influencing island formation and evolution is lacking. An important aspect which is not resolved yet is the relationship between the kinetics and thermodynamics of island formation; in particular, what roles strain and surface diffusion play in the islanding dynamics.

To this end, we have investigated an unconventional material system: strain-induced InAs islands on Ge. This is the first time that nanoscale islanding in Stransky–Krastanow mode has been observed and characterized in this a material system. An advantage of this system is close lattice constants of GaAs and Ge, and thus, it becomes possible to compare InAs islanding trends in two systems where the strain state is the same but the underlayer material is different. In addition, understanding the InAs island evolution in this system will give more insight into other systems such as InAs islands on Si.

InAs islands were grown by molecular beam epitaxy (MBE) with a substrate temperature of 420°C, an InAs growth rate of 0.15 μm/s, and a V/III flux ratio of 12. The InAs was deposited on a 10 nm thick Ge layer grown on a 100 nm thick GaAs buffer and (100) GaAs substrate. For comparison, another set of samples were made where the InAs was deposited directly on the GaAs buffer layer under the same conditions. Then surface morphology was examined with an atomic-force microscope (AFM).

We have obtained experimental dependencies of the island density and of the average island size on monolayer (ML) coverage for the two material systems at hand. Based on this data, we have measured saturation island density of $1.3 \cdot 10^{11}$ cm^{-2} and $2 \cdot 10^{11}$ cm^{-2} for InAs on Ge and InAs on GaAs, respectively. For coverages higher than two monolayers InAs islands on Ge were on average larger than those on GaAs. InAs wetting layer thickness was found to be approximately 1.2 ML for islands on Ge and around 1.5 ML for samples with just GaAs buffer. We have also observed island phase evolution, which is quite different in the two systems. A distinct second island phase onset occurred at 2.5 ML coverage in InAs on GaAs system with several phases coexisting up to 3.5 monolayers, while InAs on Ge island distribution stayed relatively uniform throughout this coverage range.

Our data shows that in spite of very similar strain conditions, the islanding dynamics is significantly different in two systems under consideration. Our work suggests that surface diffusion plays an important role in island formation, and that the In adatom surface diffusion length is larger on Ge than GaAs. This fact is in good qualitative agreement with previously reported data for the In adatom binding energy on the Ge surface [1] and on the GaAs surface [2], since diffusion length is inversely proportional to the exponent of the adatom binding energy.

To summarize, we believe that this is the first observation and characterization of self-assembled InAs islands on Ge. Our comparison of islanding dynamics in this system with that of InAs islands on GaAs substantiated the importance of other factors besides the epitaxial strain state, such as surface diffusion, in island formation and evolution.

References

[1] D. H. Rich, et al., *Phys. Rev. B* , **41**, 3004 (1990).

[2] H. T. Dobbs, A. Zangwill and D. D. Vvedensky, *Surface Diffusion: Atomistic and Collective Processes*, Plenum Press, New York, 263 (1997).

7th Int. Symp. "Nanostructures: Physics and Technology"
St Petersburg, Russia, June 14–18, 1999

Optimization of the size distribution of self-organized quantum dots

S. Bose and *E. Schöll*
Institut für Theoretische Physik, Technische Universität Berlin,
Hardenbergstr. 36, 10623 Berlin, Germany

Abstract. We have performed kinetic Monte Carlo simulations which explain the self-organized Stranski-Krastanov growth of quantum dots by the nonlinear interplay of deposition, surface diffusion, and the strain field. The optimization of the size distribution and the spatial arrangement of the quantum dots is discussed with respect to the coverage of the semiconductor surface.

The self-organized growth of quantum dots in strained semiconductor systems has recently become the focus of extensive research because of its great potential for application to nanoelectronic devices. It might help to simplify the fabrication of novel semiconductor devices based on quantum dots, for instance quantum dot lasers. It is widely accepted that the key for understanding this growth lies in the strain fields which are present in the Stranski-Krastanov growth mode [1].

Here we consider the initial stage of growth of quantum dots in regular arrays with a sharp size distribution. While the detailed shape of the fully developed quantum dots [2] is mainly governed by the specific materials the quantum dots are made of, the self-ordering in regular arrays, with sharp size distribution, appears to be a universal feature which is found in the technologically most relevant III-V semiconductor compounds, like InAs/GaAs(001) [3], but has also been observed in the Ge/Si(001) system [4, 5, 6] as well as in Ag/Pt(111) [7]. A theoretical approach based on thermodynamic equilibrium considerations was developed by Shchukin et al. [8].

In this contribution we use a dynamic approach based on kinetic Monte Carlo simulations to discuss the optimization of growth conditions. The main idea is to introduce a strain field around the quantum dots which should have two effects. First, it should destabilize the boundary of the island at which it is centered, similar to the mean field theory by Dobbs et al. [9] or other Monte Carlo simulations by Ratsch et al. [10] or Barabasi [11]. Second, the long range effects of the strain field should provide a medium for the coordination of the quantum dot configuration on the surface. Besides the standard energy terms for the surface binding energy of an atom E_S and the binding energy to a nearest neighbor E_N we introduce an energy correction term due to the strain field $E_C(x, y)$ which depends on the coordinates x and y on the surface, because the strain is high near large islands and decays quite fast with increasing distance from the islands. This correction term depends linearly upon the underlying strain field [12]. The probability for a single atom to jump from one lattice position to another is now given by

$$p = f \exp\left[-\frac{E_S + nE_N + E_C(x, y)}{k_B T}\right] \tag{1}$$

where f is the frequency of attempts per second, n is the number of nearest neighbors, k_B is Boltzmann's constant and T is the temperature.

Due to the strain the atoms are shifted from their equilibrium positions which generally leads to a reduction in binding energy. Therefore $E_C(x, y)$ is a negative quantity. To model

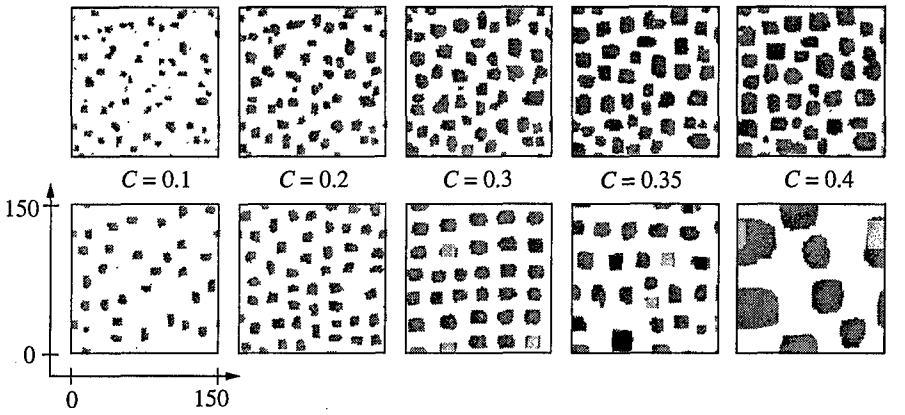

Fig. 1. Monte Carlo simulations of the structure of the surface for different coverage C right at the end of the deposition (upper row) and after 50 s (lower row). The simulation was performed with a growth rate of 0.1 ML/s at 750 K. Atoms in the first and the second monolayer are indicated by dark and light shading, respectively.

the spatial dependence of $E_C(x, y)$ around a single island, we use a phenomenological function which decreases linearly from the boundary of the island, is centered at its center of mass, and has a cubic symmetry and an amplitude depending upon the size of the island. The following parameters are used for the simulations: $E_S = 1.3$ eV, $E_N = 0.3$ eV [13]. The amplitude of the strain field grows by a factor of 0.001 eV per atom and has a range of three times the effective "radius" of the island. We also incorporate a Schwöbel barrier $E_{\text{Sch}} = 0.1$ for atoms jumping up to the next monolayer.

We have performed Monte Carlo simulations with a constant flux of atoms for different temperatures, deposition rates, and growth interruptions. If the temperature is fixed to 750 K and the growth rate is chosen as 0.1 monolayers(ML)/s we get the following sequence of images shown in the upper row of Fig. 1 if we interrupt the deposition at different coverage C. With a growth rate of 0.1 ML/s we reach a coverage of 10%, i.e. 2250 atoms on a 150×150 lattice, after 1 s, a coverage of 20% after 2 s and so on. From the structure of the surface we can extract the size distribution of the islands (quantum dots) which is shown in the upper row of Fig. 2. In the histograms the number of islands is plotted versus the square root of the number of atoms in a dot which is a measure of the mean base length or lateral diameter N of a square island.

It is obvious that at the end of the deposition time the array of self-assembled quantum dots is not of high quality. The size distribution is always broad and the spatial arrangement of the quantum dots on the surface is quite irregular. But there is another notable result. The maximum of the size distribution increases with increasing coverage from about $N = 5$ at $C = 0.1$ to about 15 at $C = 0.35$ beyond which it does not increase any further. This value marks the point where the destabilizing effect of the strain prevents further lateral growth of a single island and the transition from 2D to 3D islands can take place.

During this first stage of the growth a constant flux of atoms keeps the system far from thermodynamic equilibrium. After the growth is interrupted, the simulation is continued without flux; thus the system will evolve towards some state of relative, not necessarily absolute minimum energy. The simulation is stopped after a total simulation time of 50 s. The resulting structures and the corresponding size distributions are shown in the lower

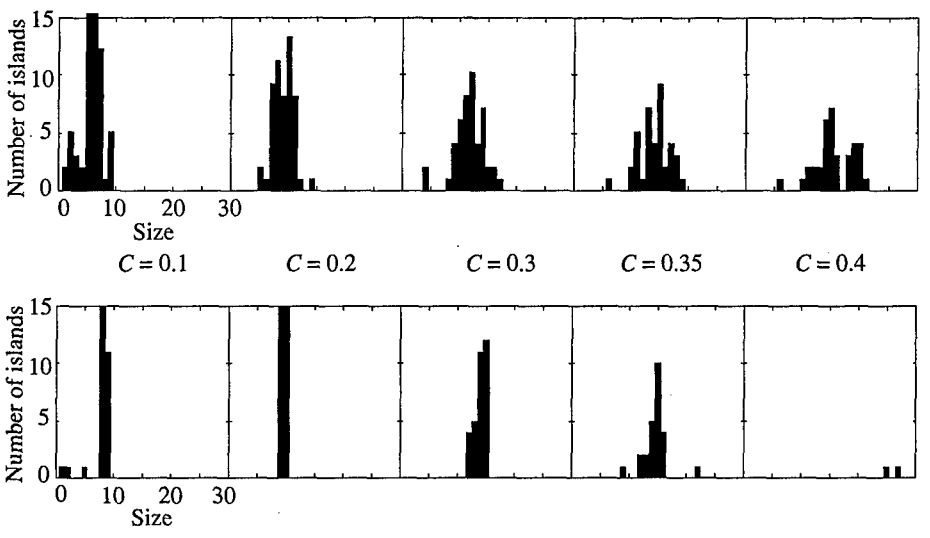

Fig. 2. The distribution of islands sizes for the surface structures shown in Fig. 1.

rows of Fig. 1 and Fig. 2, respectively. Now the different kinds of ordering are clearly visible. The size distribution always becomes sharply peaked, except for $C = 0.4$, and the maximum moves to larger sizes with increasing coverage up to a maximum size of about $N = 15$. The spatial ordering is best at $C = 0.3$, but there are regions of local ordering for $C = 0.2$ and $C = 0.35$ as well. For $C = 0.1$ and $C = 0.2$ the islands are not large enough to interact, and at $C = 0.35$ there occurs already some clustering of islands which spoils the spatial pattern. For a coverage of $C = 0.4$ the islands are completely clustered. The transition from 2D to 3D growth starts at $C = 0.3$ where some islands already consist of two monolayers.

These results show that it is easier to obtain a sharp size distribution than a perfect spatial ordering. There are two reasons for that. First, the interaction which leads to the uniformity of the island sizes is a "long-range" interaction. For example, in the system with a coverage of $C = 0.1$ we have no spatial ordering but a sharp size distribution. The islands are too far apart and too small to interact directly to form a regular spatial pattern, but the destabilizing effect of the strain is stronger for larger islands than for smaller ones, and hence atoms are more likely to move from a large island to a smaller one than vice versa. This consequently leads to approximately equal island sizes. Second, the formation of patterns is a more local effect. If the critical island size and the corresponding critical density for the island-island interaction is reached, the islands start to align locally. If two neighboring islands are too close they will tend to move apart slowly, but sometimes this may be impeded by other close-by islands. It sensitively depends upon how and where the islands nucleate if it is possible for an island to move to a position where it will have the same optimum distance to all its neighbors. In small local regions, the pattern of quantum dots might be very regular, but in larger regions more and more defects may occur in the pattern.

In conclusion, we have presented results of a kinetic Monte Carlo simulation of the initial growth stage of quantum dots. Two different kinds of self-ordering, namely the ordering of the sizes of the dots and their lateral arrangement on the surface, were discussed in

dependence on different surface coverage. Our simulations predict a sharp size distribution up to a critical coverage where the islands start to form clusters. Spatial ordering sets in shortly before the clustering occurs. It has always been found necessary to let the system evolve freely for some time after the end of the deposition to achieve strong ordering.

References

[1] D. Bimberg, M. Grundmann and N. Ledentsov, *Quantum Dot Heterostructures* (John Wiley & Sons Ltd., New York), 1999.
[2] N. Moll, A. Kley, E. Pehlke and M. Scheffler, *Phys. Rev. B* **54**, 8844 (1996).
[3] N. N. Ledentsov, M. Grundmann, et al., *Solid State Electron.* **40**, 785 (1996).
[4] D. J. Eaglesham and M. Cerullo, *Phys. Rev. Lett.* **64**, 1943 (1990).
[5] G. Abstreiter, P. Schittenhelm, C. Engel, E. Silveria, A. Zrenner, D. Meertens and W. Jäger, *Semicond. Sci. Technol.* **11**, 1521 (1996).
[6] O. G. Schmidt, C. Lange, K. Eberl, O. Kienzle and F. Ernst, *Appl. Phys. Lett.* **71**, 2340 (1997).
[7] R. Schuster, H. Röder, K. Bromann, H. Brune and K. Kern, *Phys. Rev. B* **54**, 13476 (1996).
[8] V. A. Shchukin, N. N. Ledentsov, M. Grundmann and D. Bimberg, in *Optical Spectroscopy of Low Dimensional Semiconductors, NATO ASI*, edited by G. Abstreiter (Kluwer, Amsterdam, 1997).
[9] H. T. Dobbs, D. D. Vedensky, A. Zangwill, J. Johansson, N. Carlsson and W. Seifert, *Phys. Rev. Lett.* **79**, 897 (1997).
[10] C. Ratsch, P. Šmilauer, A. Zangwill and D. Vvedensky, *J. Phys. I* **6**, 575 (1996).
[11] A.-L. Barabási, *Appl. Phys. Lett.* **70**, 2565 (1997).
[12] E. Schöll and S. Bose, *Solid State Electron.* **42**, 1587 (1998).
[13] S. Clarke, M. R. Wilby and D. D. Vvedensky, *Surf. Sci.* **255**, 91 (1991).

7th Int. Symp. "Nanostructures: Physics and Technology"
St Petersburg, Russia, June 14–18, 1999

The electric field fluctuations and the δ-layer broadening in semiconductors

N. S. Averkiev, A. M. Coonis, *A. M. Monakhov*,
A. Ya. Shik and P. M. Koenraad†
Ioffe Physico-Technical Institute, St Petersburg, Russia
† Cobra, Eindhoven University of Technology, Netherlands

Delta-layers are objects in which all the impurities are grouped on a few (ideally on a single) crystal planes. Such structures have been thoroughly investigated during recent years. One of the problem being investigated is the δ-layer broadening in the process of its growing [1–3].

In studies of the δ-layer broadening the layer can be considered as a set of dot charges because the screening radius, especially at the growing temperature exceeds the characteristic layer width in tenth times. Thus near such a layer there should be an essential fluctuation of the electric field.

We have considered the electric field distribution function near the plane with randomly arranged dot charges and have shown that this distribution function is not a Gaussian one (see figure) and has an uncommon shape. It has a long tail which is to say that there are profound fluctuation of the electric field near the δ-layer. It is apparent that this fluctuation significantly exceed the mean field value and it should result in the final impurities distribution.

Using the numerical simulation of the impurity diffusion we have shown that the salient features of the distribution function can cause the non-Gaussian (non-Poisson) impurities distribution in the transversal to the δ-layer direction.

The origination of this phenomenon lies in the fact that impurities which occur in the area with the large electric field quickly run away from the δ-layer forming the expanded wings of the final impurities distribution which cannot be fit by the Gaussian distribution function.

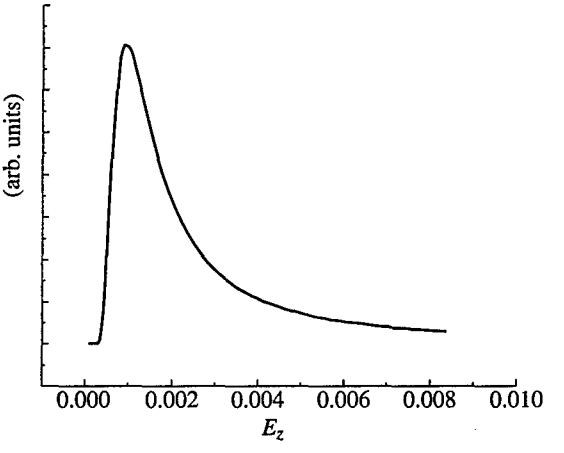

Fig. 1.

The work is supported partly by PSNS No 97-1039 and Nederlandse Organisatie voor Wetenschappelijk Onderzoek (NWO)

References

[1] E. F. Schubert, J. M. Kuo, and R. F. Kopf, *J. Elect. Matt.* **19**, 521 (1989).
[2] A. Ourmazd, J. Cunningham, W. Jan, J. A. Rentschler and W. Scröder, *Appl. Phys. Lett.* **56**, 854 (1990).
[3] P. M. Koenraad et al. *Mat. Sci. Eng.* **B35**, 485 (1995).

7th Int. Symp. "Nanostructures: Physics and Technology"
St Petersburg, Russia, June 14–18, 1999

Nitrogen chemisorbed layers on GaAs(100): formation, properties, applications

V. L. Berkovits†, V. P. Ulin†, T. V. L'vova† and Akira Izumi‡
† Ioffe Physico-Technical Institute, St Petersburg, Russia
‡ Japan Advanced Institute of Science and Technology,
Tatsunokuchi, Ishikava 923-1292, Japan

Abstract. We propose a novel wet chemical technology to form continuous nitride films on GaAs (100). For this nitridation hydrazine (N_2H_4)-based water solutions are used. X-ray photoemission analysis has shown that on the nitridized surfaces Ga-N surface bonds are dominant. We demonstrate that the proposed nitridation improves electronic properties of GaAs(100) and produce an effective surface chemical passivation.

Nitridation of GaAs(100) is known to be a promising way of electronic and chemical surface passivation and also to be a crucial step for epitaxial growth of cubic GaN. However, existing methods of nitridation based on high-temperature treatment of the crystal in atmosphere of nitrogen precursors such as NH_3, hydrazine-related compounds, or N_2 plasma lead to formation of relatively thick, amorphous or defect crystalline GaN-layers [1, 2].

Here we demonstrate that nitridation of GaAs(100) can be successfully performed by a wet chemical treatment of the crystal in alkaline hydrazine (N_2H_4)-based water solutions. The chemistry of this treatment includes the following stages: (i) removal of the natural oxide layer in the alkaline ambient, (ii) formation of the electrophylic adsorption centres on the crystal surface through electron transfer from semiconductor to H_3O^+ or $N_2H_5^+$ cations of the solution, (iii) removal of the surface arsenic atoms and uncovering of Ga-terminated (100) surface, (iv) dissociative adsorption of the hidrazine molecules on the Ga-related centres.

The dissociative adsorption of hydrazine is believed to proceed through several successive stages. At the initial stage one of the nitrogen atoms of hydrazine molecule forms chemical bonds with two neighbouring Ga- atoms in a bridge-site position. At the same time two protons pass into the solution. Shown in Fig. 1 final atomic configurations of nitridized (100) GaAs are allowed to be formed through the pair interactions between the hydrazine admolecules or through their interaction with H_2O. (i) The hydrazine admolecules can interact with H_2O producing chemisorbed NH groups on the surfaces and NH_2OH molecules

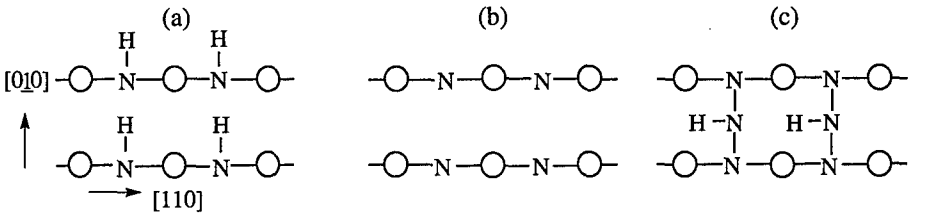

Fig. 1. Allowed atomic configurations of nitridized GaAs(100) (top view).

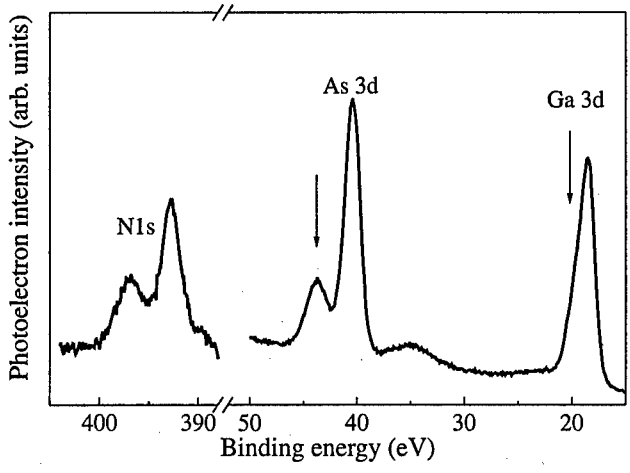

Fig. 2. XPS spectra of N(1s), As(3d) and Ga(3d) from chemically nitridized GaAs. Positions of the chemically shifted components are indicated by arrows.

in the solution (Fig. 1(a)). (ii) Reaction between pairs of hydrazine admolecules can leaves on the surface the nitrogen adatoms themselves (Fig. 1(b)) or with NH-bridge groups on the top (Fig. 1(c)), and correspondingly free N_2H_4 or NH_3 in the solutions.

For nitride treatment of GaAs wafers we used hydrazine-water solutions in the concentration range 3–10 M. We added small amounts of $Na_2S \cdot 9H_2O$ into the solutions to produce SH^- anions. It has been shown [3] that the interaction of the surface arsenic atoms with these anions leads to formation of the soluble thioarsenic acid and, hence, to uncovering of gallium layer. To prevent the interaction of surface gallium with OH^- anions [3] we advisedly decreased pH of the solutions till values 9–12 by adding $N_2H_4 \cdot H_2SO_4$.

Chemical composition of the nitridized GaAs surfaces was analysed by X-ray photoelectron spectroscopy (XPS). These experiments were done in Japan Advanced Institute of Science and Technology (Ishikava).

For excitation of the electron emission monochromatic AlK_α radiation was used. All spectra were observed at the photoelectron take-off angle of 35°. Figure 2 shows obtained XPS spectra. Both As(3d) and Ga(3d) core level spectra clearly demonstrate a presence of the components shifted to high binding energy (BE). Comparison of these spectra with those obtained for oxidized GaAs surface [4] allows to conclude that for Ga(3d) line chemically shifted component is due to Ga-N bonds. This conclusion is directly confirmed by observation of the line at BE = 397 eV corresponding to emission from 1s level of nitrogen. The peak at BE = 392 eV is attributed with gallium LMM Auger signal. For As(3d) line the shifted component occur to be due to As-O bonds. We are speculating that this signal originates from oxydized molecules of thioarsenic acid physisorbed on the surface. Thus we conclude that the proposed chemical treatment, indeed, provides nitridation of the GaAs(100) surface through formation of Ga-N surface bonds.

We found that the nitrogen chemisorbed layer is chemically stable and can serve as a surface mask. Figure 3 shows a profile of (100)GaAs surface after selective (through windows in SiO_2 mask) chemical nitridation and successive treatment in HF and $HCl-K_2Cr_2O_7$ solutions. The nitridized area is seen as the elevated terrace over the etched substrate. This experiment confirms that the chemisorbed nitrogen atoms form a continuous nitride film

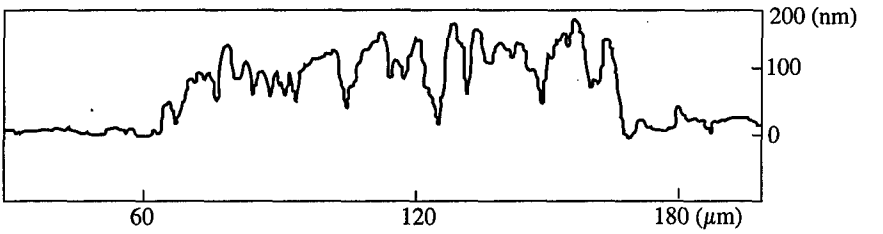

Fig. 3. Profile of chemically nitridized stripe on (100) GaAs after etching.

and therefore produce an effective surface chemical passivation.

To demonstrate the effect of electronic passivation, we studied behaviour of the RT photoluminescence of the nitridized n-GaAs samples taking as a reference the pieces of the same wafer passivated in Na_2S and $(NH_4)_2S$-water solutions. Figure 4 shows the PL spectra of (a) non-treated sample, (b) 1M sodium sulfide, and (c) 3M-ammonium sulfide-passivated samples, (d) chemically nitridized sample. Both sulfide treatments lead to an increasing the photoluminescence intensity (PLI) by a factor of 3–4. However, nitride-passivation produces a stronger PLI increase, by a factor of 7. This analysis unambiguously shows that the hydrazine solutions more efficiently reduce surface recombination velocity than the sodium sulfide and the ammonium sulfide ones.

The chemical stability in air of the nitrogen-passivated surfaces occur to be drastically stronger than of the sulfide-passivated ones. Indeed, we found that in the absence of the external light excitation, nitride passivated surfaces conserved their initial properties *during more than a month.*

Acknowledgements

This work was supported by the Russian Foundation for Basic Research (project No 99-02-18144) and partly supported by the Russian State Program "Surface Atomic Structures" (project No 3.7.99).

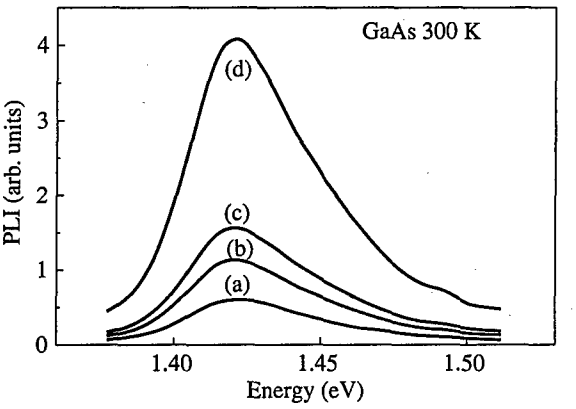

Fig. 4. Photoluminescence spectra of GaAs for untreated (100) surface (a), treated with Na_2S (b), with $(NH_4)_2S$ (c), with hydrazine-based solution (d).

References

[1] H. D. Jung, N. Kumagai, T. Hanada, Z Zhu, T. Yao, T. Yatsuda and K. Kimura, *J. Appl. Phys.* **83**, 5497 (1998).

[2] I. Aksenov, Y. Nakada and H. Okimura, *J. Appl. Phys.* **84**, 3159 (1998).

[3] V. P. Ulin, V. L. Berkovits, V. M. Lantratov and T. L. L'vova, *Proceedings of the 192th Meeting of the Electrochemical Society*, State of the Art Program on Compound Semiconductors XXVII, Paris, Sept. 1997 p. 343.

[4] Akira Izumi, Atsushi Masuda and Hideki Matsumura, *Thin Solid Films*, (1999), (to be published).

7th Int. Symp. "Nanostructures: Physics and Technology"
St Petersburg, Russia, June 14–18, 1999

Optical and structural properties of InGaAsN/GaAs heterostructures

A. Yu. Egorov†, D. Bernklau, M. Schuster, Yu. Sherniakov†, V. M. Ustinov† and H. Riechert

Siemens Corporate Technology, D-81 730 München, Germany
† Ioffe Physico-Technical Institute, St Petersburg, Russia

Semiconductor lasers emitting at 1.3 and 1.5 μm have found wide applications in systems for long-range, high-speed fiber-optical communications. At present, such lasers are fabricated from the InGaAsP heterostructures grown on InP substrates. However, the performance of these devices is limited due to fundamental physical properties of the materials used, i.e. poor temperature stability and weak variation of refraction index leading to problems in the formation of distributed Bragg reflectors for VCSELs. A novel material, InGaAsN lattice matched to GaAs, has been recently proposed to solve this problem [1]. The incorporation of the InGaAsN should be feasible and should lead to GaAs-based lasers emitting at 1.3 μm or longer wavelengths.

We have grown strained and lattice matched GaInAsN/GaAs heterostructures with the N composition of 1–2.3% on GaAs substrates by molecular beam epitaxy. A RF-coupled plasma source was used to incorporate N into layers. The intensity of photoluminescence (PL) observed in the 1.0–1.4 μm spectral range at room temperature was comparable with the PL intensity for GaAs/InGaAs/GaAs quantum wells. The dependences of the PL intensity and the transition energy of the ground state versus quantum well thickness for the GaAs/GaInAsN/GaAs structures with various nitrogen content are presented in Fig. 1. One can see that the increase in nitrogen content or increase in the quantum well thickness leads to the decrease in the photoluminescence intensity. 1.3 μm room temperature photoluminescence was achieved for 8 nm quantum well with the nitrogen content of 1.9% and In content 38%.

We investigated the effect of growth conditions on the crystal quality of the layers and present the results of optical and structural characterization of the grown layers and quantum well structures. We have found that the FWHM of luminescence line is mainly due to nonuniformity of the grown layers. The PL intensity and FWHM as a function of the growth temperature is shown in Fig. 2. The growth of GaInAsN in optimal temperature range significantly improves the uniformity and crystal quality of the structures which results in the decrease in the FWHM of the luminescence line and increase in the intensity.

Post-growth annealing of the structures at elevated temperatures results in more than one order of magnitude increase in PL intensity. The increase in the PL intensity for the annealed sample is accompanied by about 60 nm blue shift of the PL line and decrease in the full width at half maximum to 40 nm. The high resolution XRD measurements have shown that the nitrogen content for the sample after annealing was little higher than before. This fact indicates that there is no diffusion of nitrogen from the quantum well region to the barrier layer. More likely, the reason of the blue shift of the PL maximum with annealing is the decomposition of nitrogen clusters which form nitrogen-rich areas and shift the maximum of the PL line to the longer wavelength.

As the result of the optimization of the growth regimes and post-growth treatment the bright 1.3 μm PL and EL was achieved for the GaAs based heterostructures with InGaAsN active region at room temperature. Fig. 3 shows the electroluminescence spectra

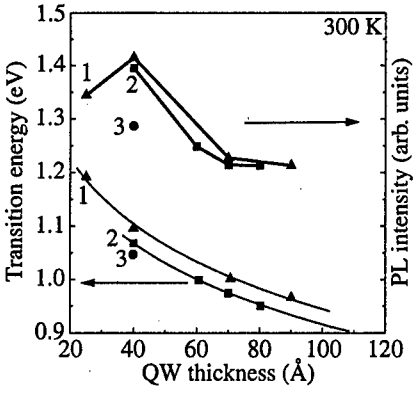

Fig. 1. Photoluminescence characteristics of the heterostructures with quantum wells: (1) $In_{0.38}GaAsN_{0.015}$ (2) $In_{0.38}GaAsN_{0.019}$ (3) $In_{0.38}GaAsN_{0.023}$.

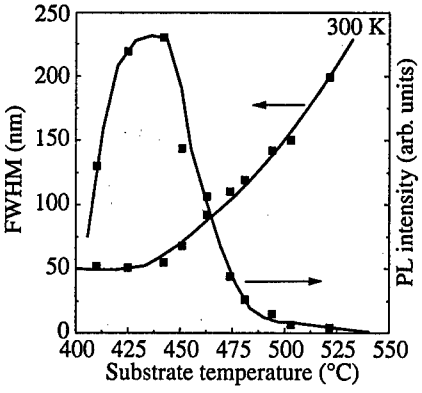

Fig. 2. PL characteristics vs growth temperature for MQW structure $In_{0.3}Ga_{0.7}As_{0.985}N_{0.015}/GaAs$.

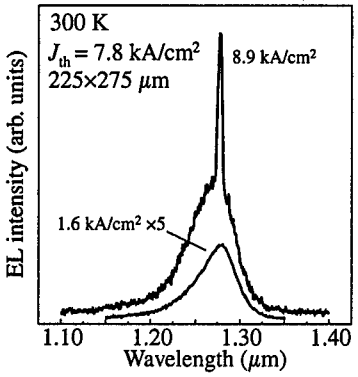

Fig. 3. EL spectrum of InGaAsN based laser diode at 300 K.

of GaAs/InGaAsN heterostructures at 300 K. The lasing with the thershold curent density of 7.8 kA/cm^2 was achieved for the laser based on three InGaAsN quantum wells in the active region and GaAs cladding layers.

This work was supported by the Program "Physics of Solid State Nanostructures" of the Ministry of Science of Russia.

References

[1] M. Kondow, K. Uomi, A. Niwa *et al.*, *Jpn. J. Appl. Phys.*, **35** (1), 1273 (1996).

7th Int. Symp. "Nanostructures: Physics and Technology"
St Petersburg, Russia, June 14–18, 1999

Self-organized InGaAs/GaAs quantum wire nanostructures grown by metal-organic vapor phase epitaxy

I. A. Karpovich†, B. N. Zvonkov§, N. V. Baidus§, *D. O. Filatov*‡,
Yu. Yu. Gushina‡ and S. V. Morozov†

† University of Nizhni Novgorod, 603600 Nizhni Novgorod, Russia
‡ Research and Educational Center for Scanning Probe Microscopy,
University of Nizhni Novgorod, 603600 Nizhni Novgorod, Russia
§ Physical-Technical Research Institute, University of Nizhni Novgorod,
603600 Nizhni Novgorod, Russia

Abstract. We report on observation of a new type of InGaAs self-assembled surface nanostructures grown on (001) GaAs by Metal-Organic Vapor Phase Epitaxy. Atomic Force Microscopy (AFM) studies show presence of a homogeneous system of well ordered shaped rectangular nanoislands extended along the [$\bar{1}$10] direction. Optical properties of the structures studied by photoluminescence (PL) and photoconductivity (PC) spectroscopy indicate presence of 1D electronic states.

Recently a lot of effort was devoted to study of the zero-dimensional semiconductor nanostructures (Quantum Dots, QDs) [1]. The most interest is attracted by the QDs obtained by self-assembling during the epitaxial process. The main advantage of this technique compared to other methods of QDs' preparation (for instance, nanolithography, selective growth, etc.) is that formation of the QDs by self-assembling is a natural process (usually driven by Stranski–Krastanov (S-K) mechanism [2]), and therefore is very promising for commercial device application. However, while for the QDs S-K self organization is well studied and is being used for growth of various 0D structures widely, in the field of using self-organization for formation of quantum wires there is much less success.

In [3] we reported on observation of self-assembled GaAsSb/GaAs quantum wires grown by AP-MOVPE. Here we report on AP-MOCVD growth and characterization of similar structures in InGaAs/GaAs system.

The structures were grown on semi insulating (001) GaAs misoriented by 3.1^o degrees towards [110] direction using trimethylgallium (TMG), trimethylindium (TMI) and arsine as the precursors. The structures were consisting of the 3 layers: a 0.3 μm buffer layer grown at 600 °C, an InAs layer grown at 530 °C, and a 40 nm cap layer. The InAs layer was grown in the altering submonolayer deposition mode switching TMI and arsine flow on for 6 and 2 seconds respectively with a 4 sec pause between each cycle; total 5 cycles.

The surface topography of the structures was characterized by ambient air Atomic Force Microscopy (AFM) on TopoMetrix TMX-2100 Accurex AFM in contact mode. The optical properties were studied by photoluminescence (PL) and by planar photoconductivity (PC) spectroscopy at 77 and 300 K, respectively.

A regular system of well shaped rectangular nanoislands (some kind of a "planch" structure) has been observed on the AFM scans (Fig. 1). The lateral dimensions of the islands are 100×300 nm; the height is about 10 nm. The islands are well ordered along the [110] direction, and are rather homogeneous in size.

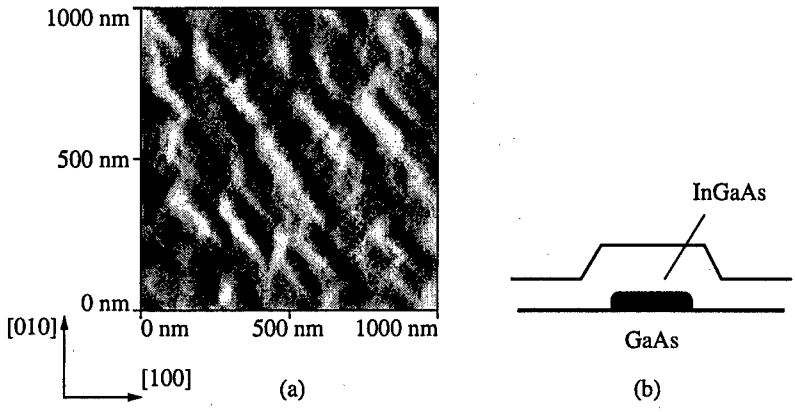

Fig. 1. AFM image of a planch structure (a) and suggested internal structure of a planch (b).

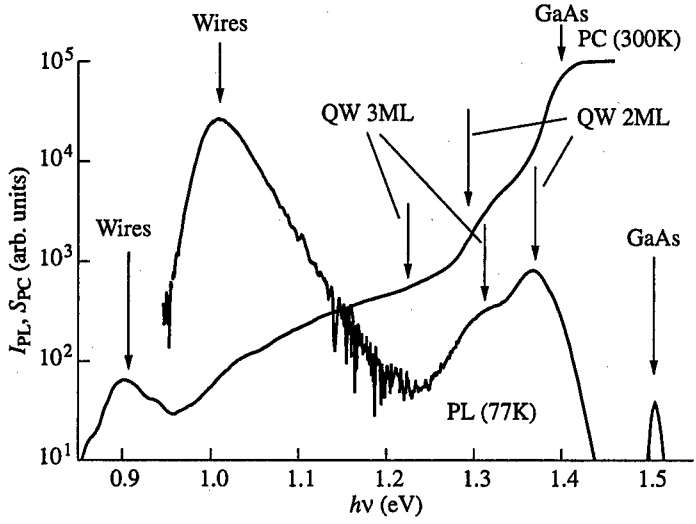

Fig. 2. The photoluminescence (77 K) and photosensitivity (300 K) spectra of a planch structure.

A strong PL line with a maximum at 1.01 eV (at 77 K) is seen in the PL spectrum (Fig. 2). The full width at half maximum of this peak is 55 meV. In the PC spectrum a corresponding photosensitivity peak with a maximum at $h\nu = 0.91$ eV is observed.

The most remarkable feature of the optical properties of this structure is strong polarization dependence both of the PL line and of the PC peak when the PL polarization in the direction perpendicular to the structure surface was analyzed or when the PC was excited by a beam polarized linearly perpendicular to the surface, respectively (Fig. 3). Maximum signal is observed when the electric field strength vector **E** in the emitted/incident light wave is parallel to the [110] direction on the structure surface, i.e. **E** is parallel to the longer axis of the planches. The degree of polarization $P = (I_{max} - I_{min})/(I_{max} + I_{min})$ equals 0.27 for PL and 0.25 for PC. Such polarization dependence allows to suggest existence of one-dimensional electronic states in these planches.

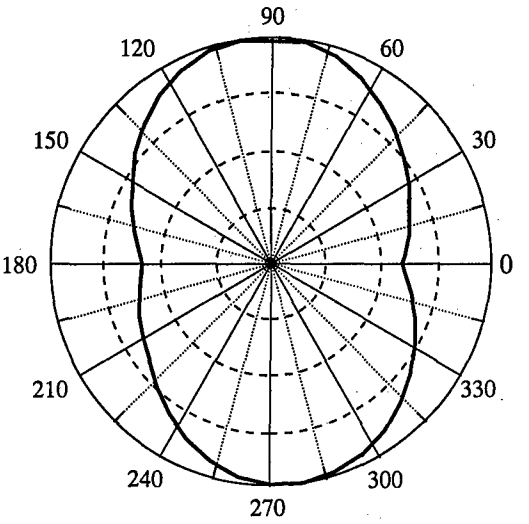

Fig. 3. Dependence of photosensitivity at $h\nu = 0.9$ eV (300 K) on the angle between the electric vector **E** in the incident linearly polarized beam and the [110] direction on the structure surface.

The two PL peaks at 1.4 and 1.3 eV were attributed to $In_xGa_{1-x}As$ quantum wells with $x = 0.9$ and the thickness equal to 2 and 3 monolayers (0.6 and 0.9 nm) respectively on the basis of comparing the calculated transition energies (using model [4]) with the experimental ones.

So far the inner structure of the planches can be suggested to be as shown on Fig. 1(b): plain InAs domains asymmetric in the $x-y$ plain substantially standing on an InGaAs wetting layer with large scale fluctuations in thickness by 1 monolayer. We have to suggest intermixing of In and Ga in the wetting layer since the observed spectral positions of the two QW peaks cannot be explained suggesting pure InAs wetting layer consisting of an integer number of monolayers.

This work was supported by the Russian Foundation for Basic Research, by Ministry of Science (Program "Physics of Solid State Nanostructures"), and by Russian Ministry of General and Professional Education (Program "Universities of Russia: Fundamental Investigations").

The authors are greatful to V. Ya. Alseshkin (Institute of Physics of Microstructures, RAS) for fruitful discussion.

References

[1] N. N. Ledentsov, V. M. Ustinov, V. A. Shchukin. P. S. Kop'ev, Zh. I. Alferov and D. Bimberg, *Semiconductors* **32**, 343 (1998).

[2] I. N. Stranski and L. von Krastanov, *Sitzungsber. Akad. Wiss. Wien IIb.* **146**, 797 (1938).

[3] V. Ya. Aleshkin, S. A. Akhlestina, B. N. Zvonkov, I. G. Malkina and E. A. Uskova, *JETP Lett.* **68**, 91 (1998).

[4] G. Huang, D. Ji, U. K. Reddy and T. S. Henderson, *J. Appl. Phys.* **62**, 3366 (1987).

7th Int. Symp. "Nanostructures: Physics and Technology"
St Petersburg, Russia, June 14–18, 1999

Influence of initial MBE growth stage on properties of hexagonal InN/Al_2O_3 films

V. V. Mamutin, V. A. Vekshin, V. Yu. Davydov, V. V. Ratnikov,
V. V. Emtsev, A. N. Smirnov, S. V. Ivanov and P. S. Kop'ev
Ioffe Physico-Technical Institute, St Petersburg, Russia

Abstract. The InGaN alloys have acquired a lot of interest for using in the active region of light emitting and lasers diodes, as the band gap of this materials can be varied over nearly the whole visible spectral range, when changing In content from 0 to pure InN [1]. However, due to the low dissociation temperature of InN (about 630°C [2]) and the nitrogen equilibrium vapor pressure with a growth temperature (T_s) [3], good quality InN epilayers are still not easily attainable. Taking account of the large lattice mismatch between InN and sapphire, it is also expected that a strain-induced enhanced N re-evaporation at the initial InN monolayer growth [4] would require a 100–150°C decrease of T_s to avoid a liquid In droplet formation followed by a columnar structure growth. As a result, there are only few papers, to our knowledge, on epitaxial InN properties [5–7], and no reports on hexagonal InN films MBE growth.

1 Experimental

InN epilayers were grown on (0001) sapphire substrates by MBE. The MBE chamber (home made EP-1203 setup) with ultimate background pressure $\sim 10^{-10}$ Torr was equipped with a turbomolecular pump with an effective pumping rate of $\sim$ 350 l/s). Metallic In was supplied by a standard effusion cell at a temperature varied within a 750–850°C range in a series of experiments. ASTEX ECR plasma source was used for supplying activated nitrogen with flow rate of about 1–5 sccm, allowing the growth rates of 0.02–0.20 μ/h. The substrates were coated with Ti at back side and mounted on In-free Mo holders. Before loading, sapphire substrates were rinsed in acetone only and then thermally cleaned and nitridated at $\sim$ 1100–1200°C for 30 min, demonstrating finally streaky reflection high energy electron diffraction (RHEED) pattern. T_s for main InN layer growth was varied from 350 to 550°C. Its calibration procedure involved adjusting to several metal melting points, using IR pyrometer and a temperature versus heater power dependence, and provided an $\sim$ 10°C accuracy. Surface structure of the InN epilayers during growth was also monitored by RHEED. The film thickness was in between 0.1 and 0.7 μm.

Three different growth initiation regimes were used. In the first one (I), the growth of main InN epilayer started immediately after high temperature substrate annealing, when T_s was reduced to the working value. In the second regime (II), a $\sim$ 15 nm thick low temperature InN buffer layer was first grown at $\sim$ 300°C, followed by rising T_s to the value of the main InN growth. The third initiation regime (III) differed from the second one by high temperature ($\sim$ 800–900°C) annealing of the low temperature InN buffer before growth of the main InN layer.

Structural and morphological characterization of InN/Al_2O_3 epilayers was performed by high resolution triple-crystal X-ray diffraction (TC XRD), Raman scattering, and scanning electron microscopy (SEM). The symmetrical and asymmetrical Bragg geometry and CuK_α radiation were used for measurements of XRD rocking curves in the vicinity of 0002, 0004 and $11\bar{2}4$ reflections. The full width at half maximum for and $(\Theta - 2\Theta)$ -

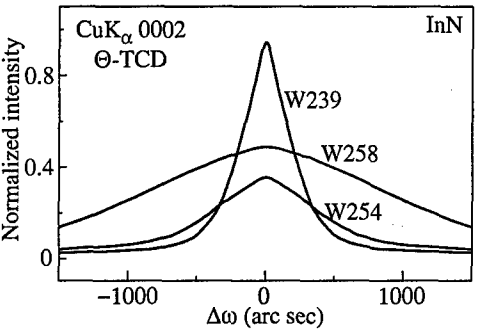

Fig. 1. Θ-TCD curves for MBE InN layers.

scans (ω_Θ and $\omega_{\Theta-2\Theta}$ respectively) was analysed. The curvature radius measurements were employed for a stress calculation in the layers. The Raman spectra of InN layers were measured at room and cryogenic temperatures (at 6 K). Ar^+ ($\lambda_0 = 514$, 488 and 476 nm) and Kr^+ ($\lambda_0 = 647$ and 674 nm) lasers were used for excitation. A carrier concentration was determined by Hall-effect measurements.

2 Results and discussion

MBE growth of complete InN layer in the regime I turns out to be possible at $T_S \sim 350$°C. However, RHEED patterns for the epilayer (W258) corresponds to a polycrystalline or textural 3D-growth (spots, rings and strokes on the rings) from the very beginning of growth. SEM image shows a rough surface and columnar structure at the cleavage. In contrast, regimes II (W254) and III (W239) allow the main InN layer to be grown at maximal possible $T_S \sim 470$°C, when the In/N flux ratio is close to 1:1 and In droplets do not occur. This temperature agrees well with a lower boundary of theoretically estimated region of droplet free InN growth [3]. RHEED for both InN layers demonstrates streaky patterns corresponding to a 2D-growth. Their SEM images show flat surface without columnar structure. However, the InN layer grown in the regime II contains cavities at the InN/Al_2O_3 interface, which are completely recovered after ~ 0.01 μm growth, whereas only the layer III (W239) has a flawless interface with sapphire.

XRD study reveals only hexagonal InN phase for all the samples. The InN layers has a Gaussian shape of rocking curves which is characteristic for III-N's (see Fig. 1). The analysis has shown an asymmetry of diffraction spot elongated parallel to the surface of samples W239 and W254. According to [8] this effect is caused by a small block size anysotropy and specific defect structure of blocks (vertical screw and edge dislocations). The values of lateral block size τ_x and vertical screw dislocation density ρ^{vsd} are given in the Table. For the W258 sample, XRD scattering is almost anysotropical and is mainly determined by small tilted blocks. The stresses σ_a in the layers are biaxial compressive ones (see the Table). The samples W254 and W258 are fully relaxed as a result of layer fragmentation to small blocks.

The analysis of Raman data suggests that the samples under study are epitaxial structures of hexagonal symmetry with the optical axis normal to the substrate plane. No traces of cubic phase have been detected. According to the group-theory analysis, six optical modes, i.e. $A_1(TO) + A_1(LO) + E_1(TO) + E_1(LO) + E_2^1 + E_2^2$, can be observed for the first-order Raman scattering in a hexagonal InN. Some of the spectra taken from InN samples at 300 K, $\lambda_0 = 488$ nm (2.54 eV) are presented in Fig. 2(a). These spectra have been obtained in the scattering configurations allowing the nonpolar E_2^1 and E_2^2 modes for

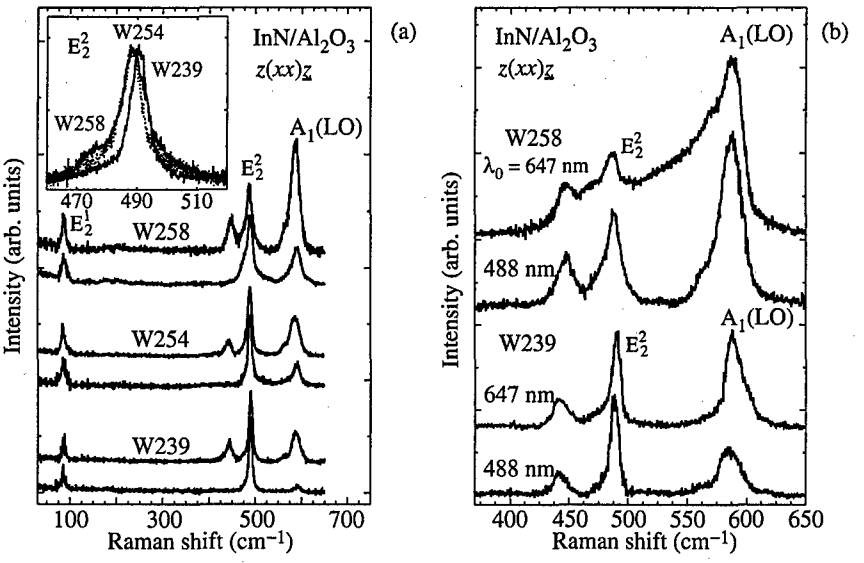

Fig. 2. (a) Raman spectra for InN samples grown in different conditions. (b) Raman spectra obtained with different energies of excitation.

Table 1. The characterization data obtained for InN samples by different techniques

Regime (sample)	σ_a GPa	τ_x 10^{-4} cm	ρ^{vsd} 10^9 cm^{-2}	ω_Θ (0002) arc sec	$\omega_{\Theta-2\Theta}$ (0002) arc sec	FWHM cm^{-1}	n $10^{20}\mu$ cm^{-3}	cm^2/Vs
I-W258	~ 0	< 0.1	$\gg 1$	2140	174	9.6	4	93
II-W254	~ 0	~ 0	1.0	777	80	7.1	2	160
III-W239	-1.23	> 0.5	0.2	350	55	6.2	1	600

both polarizations. However, the longitudinal component of the polar $A_1(LO)$ mode is allowed only in $z(xx)\underline{z}$ polarization. Here the z direction is parallel to the optical c axis. It is clearly seen that the polarized Raman spectra for W239 sample show an excellent agreement with the selection rules, while for W254 and W258 samples selection rules are broken. The inset in Fig. 2(a) shows high-resolution Raman spectra recorded in the region of the E_2 symmetry phonon. The results of fitting of the E_2 line to the Lorentz function (FWHM) are also presented in Table. The large FWHM of E_2 for W258 sample points to the presence of a considerable amount of structural defects in this sample. Using different energies of excitations, we tested different depth of InN layers. Some of the results are presented in Fig. 2(b). It is clearly seen that the Raman spectra of W239 sample are nearly identical for both energies of excitation. This is the evidence of structural uniformity of this sample through the whole thickness. However there is a strong additional band in the Raman spectrum of W258 sample for $\lambda_0 = 647$ nm (1.92 eV) excitation. This band is due to defect induced Raman scattering and shows that the defects are placed near the interface of W258 InN film.

It is known that the E_2 mode is extremely sensitive to the strain in III-N's compounds. For example in GaN layers, the shift of this line by 2.7 cm^{-1} corresponds to the in-plane biaxial stress equal to 1 GPa [9]. The shift of the E_2 line toward higher frequencies

with respect to its position for the strain-free sample W254 ($\Delta = 2.1\,\mathrm{cm}^{-1}$) indicates the compressive in-plane biaxial stress in the sample W239 (see insert in Fig. 2(a)). According to the Raman data, the residual strain in the W258 sample relaxes totally. Thus, the set of all Raman data for investigated InN samples agrees well with the XRD data.

The results of Hall measurements, summarized in the Table, confirm these results, demonstrating the lower electron concentration and higher mobility for the W239 sample, grown with the initiation regime III. As a possible reason of these effects, we suggest that high temperature annealing of the buffer layer results in the formation of an interface nucleation layer of gradual composition (most probably, $Al_xIn_{1-x}N$), which provides a lower lattice mismatch for the main InN layer, preventing the In droplet formation at the InN/AlInN/Al_2O_3 interface at high temperatures. The detailed study of this interface will be published elsewhere. These results can be used for a study of self-organization phenomena in MBE of InN/GaN nanostructures.

3 Conclusion

In summary, we have studied the influence of initial growth stages on the quality of InN MBE layers using SEM, XRD, Raman scattering, Hall-effect measurements. It has been shown that the high temperature annealing of low temperature grown InN buffer layer, followed by the main InN layer growth at maximal T_s permitting In/N = 1:1 growth condition, provides the high quality strained films with featureless InN/sapphire interface.

This work is partly supported by RFBR Grants (No 99-02-17103 and No 99-02-18318), and the Program of the Ministry of Sciences of RF "Physics of Solid State Nanostructures".

References

[1] S. Strite and H. Morkoc, *J. Vac. Sci. Technol.* **B10**, 1237 (1992).
[2] T. Bottcher, S. Einfeldt, V. Kirchner, S. Figge, H. Heinke and D. Hommel, *Appl. Phys. Lett.* **73**, 3232 (1998).
[3] S. Y. Karpov, Y. N. Makarov and M. S. Ramm, *Internet J. Nitride Sem.* Res. 2, Art. 45.
[4] S. V. Ivanov, *et al.*, *Semicond. Sci. Technol.* **8**, 347 (1993).
[5] H. J. Kwon, Y. H. Lee, O. Miki, H. Yamano and A. Yoshida, *Appl. Phys. Lett.* **69**, 937 (1996).
[6] K. Osamura, S. Naka and Y. Murakami, *J. Appl. Phys.* **46**, 3432 (1975).
[7] M. C. Lee, *et al. Appl. Phys. Lett.* **73**, 2606 (1998).
[8] R. N. Kutt, V. V. Ratnikov, G. N. Mosina and M. P. Scheglov, *Solid St. Phys.* **41**, 28 (1999).
[9] V. Yu. Davydov, N. S. Averkiev, I. N. Goncharuk, *et al J. Appl. Phys.* **82**, 5097 (1997).

7th Int. Symp. "Nanostructures: Physics and Technology"
St Petersburg, Russia, June 14–18, 1999

Annealing and morphology transformation effects in MOCVD grown of self-organized InAlAs-AlGaAs quantum dots

A. M. Mintairov†‡, I. Kochnev†, V. M. Lantratov†, J. L. Merz‡, Yu. Musikhin†, A. S. Vlasov†, H. D. Robinson§ and B. B. Goldberg§
† Ioffe Physico-Technical Institute, St Petersburg, Russia
‡ Dept. of Electrical Engineering, University of Notre Dame, Notre Dame, IN 46556, USA
§ Dept. of Physics, Boston University, Boston, MA, 02215

Abstract. We report on MOCVD growth of the (In,Al)As-self-organized quantum dots (QD) on (Al,Ga)As. We demonstrate that dense arrays ($\sim 2 \times 10^{10}$ cm^{-2}) of small ($\sim$ 5 nm) QD are formed during annealing (750°C, 20 min, excess of arsine) of $In_{0.5}Al_{0.5}As$ deposited at 500°C on a $Al_{0.6}Ga_{0.4}As$ surface, as demonstrated by atomic force and transmission electron microscopies and by photoluminescense. We determined that the ripening process continues at room temperature and gives rise to large clusters of submicron size after time of one. In contrast, an identical sample that is not annealed shows low density (2×10^9 cm^{-2}) of the QDs. Aging in this case gives results in a gradual smoothing of the morphology.

Introduction

The self-organized growth of semiconductor zero-dimensional structures usually includes the direct formation of quantum dots (QDs) via the Stranski–Krastanow growth mode. At the same time it has been demonstrated that Ostwald ripening process [1, 2, 3], resulting in an increase of the QD volume and shape transformations from pyramids to domes, can occur during annealing [4, 5, 6, 7] or even at room temperature for some material systems [8]. Here we study and observed similar effects for InAlAs/AlGaAs QDs. Structures in this system have been previously grown by MBE [9, 10]. Here we fabricate and characterize self-organized InAlAs-AlGaAs quantum dots using the MOCVD growth method and report pronounced morphological transformation effects induced in this system by annealing.

1 Experiment

The heterostructures were grown using equipment with a horizontal resistively heated reactor at low pressure (76 torr). Trimethylgallium, trimethylaluminium, ethyldimethylindium, and arsine were used as the sources of materials. The ratio of the group V and group III elements was 75. The growth was carried out with an excess of arsine. Si-doped (100) GaAs substrates were used. Three type of structures were grown. In all cases, after the GaAs buffer-layer growth, a 0.5 μm-thick AlAs layer was deposited and followed by 0.3 μm thick $Al_{0.6}Ga_{0.4}As$ layer. Then a sheet of InAlAs QDs was deposited at 500°C. The average thickness of deposited InAlAs was 2.5 nm and the average In composition was 0.5.

In the one type structure (designated as type A) after the deposition of InAlAs QDs the temperature was increased from 500 to 750°C and growth was interrupted on 20 min. After such *in situ* annealing the 0.1 μm thick $Al_{0.6}Ga_{0.4}As$ layer was deposited at 750°C. In the another structure (type B) no growth interruption occured, and a 0.1 μm thick $Al_{0.6}Ga_{0.4}As$

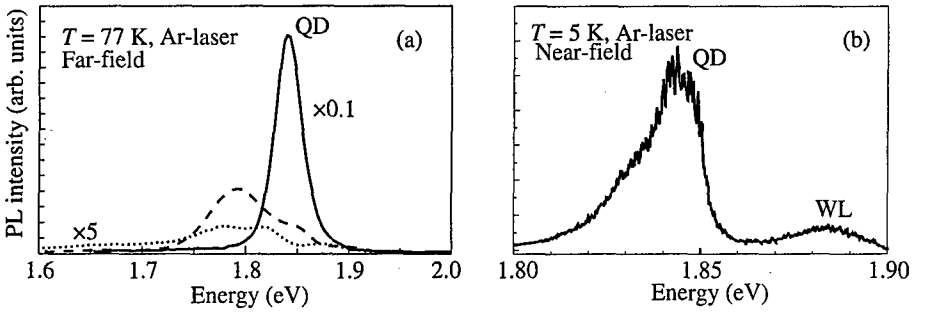

Fig. 1. PL spectra of InAlAs QDs, (a) (far-field): solid curve—structure A, dotted and dashed curves—non-annealed and annealed structure B; (b) (near-field)—structure A.

cap layer was deposited at 500°C. Structures of type A and B were used for PL and TEM measurements.

A third structure (type C) used for AFM measurements had no AlGaAs cap layer. Samples consisting of structure B and C were annealed at 750°C during 20 minutes.

The PL spectra were taken at 77 K under the using 5 mW excitation of the 514.5 nm Ar-laser line. Near-field scanning optical microscope (NSOM) measurements were done at 5 K in illumination mode as described in [11].

2 Results and discussion

2.1 PL measurements

The PL spectra of the structure A and structure B (as grown and annealed) are shown in Fig. 1(a). For the structure A we can see only one very strong band (QD). The relativley small PL linewidth (30 meV) indicates a large size uniformity of the resulting QDs. In Fig. 1(b) we show a NSOM spectrum of the same luminescense line. It is clearly seen that the line consists of multiple ultranarrow peaks with the narrowest ones having a sub-meV halfwidth.

In contrast spectra of structure B contain several broad bands, having very low PL intensity, indicating low density and uniformity of QDs [12]. Annealing of sample B leads to an increase and a redistribution of the PL intensity, and to a blue shift of the bands. This suggests a changing in the island size and in In composition, probably via partial interdiffusion of In and Al [13].

2.2 TEM studies

A cross sectionTEM image of structure A is presented in Fig. 2. The TEM measurements clearly reveal strain-induced contrast characteristic of QDs and point to a typical dot sizes of about 15–20 nm and relative separation between islands of about 40–50 nm. The estimated area density is about 4×10^{10} cm^{-2}.

2.3 AFM measurements

In Fig. 3(a,b) we present the surface morphology of non-annealed and annealed sample C. Self-organized islands are clearly seen in the images. For the as grown sample (Fig. 3(a)) the islands have low density (2×10^9 cm^{-2}). The dominant islands are $\sim$ 40 nm (apparent size $\sim$ 50 nm in AFM image) size islands, while smaller islands of $\sim$ 15 nm ($\sim$ 25 nm in AFM image) size are also presented. After annealing (Fig. 3(b)) the islands density dramatically increased up to 2×10^{10} cm^{-2} and the $\sim$ 15 nm size islands become dominant.

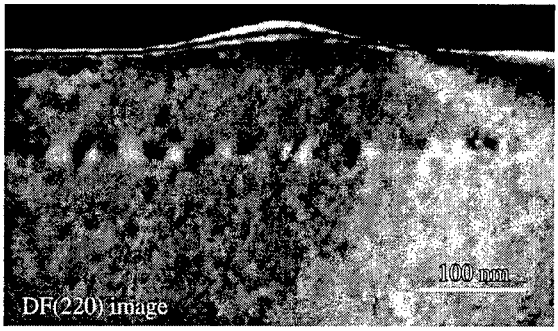

Fig. 2. Cross section TEM image of InAlAs QD structure

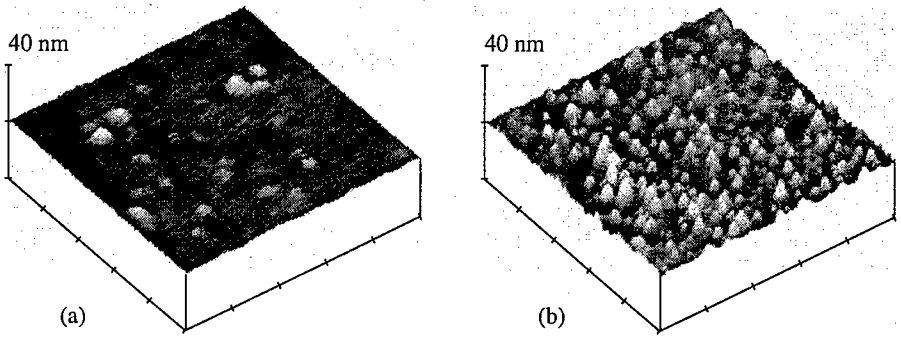

Fig. 3. Surface morphology of as grown (a) and annealed (b) sample C. Scan area 1×1 μm.

In Fig. 4(a,b) we present the surface morphology of the same samples remeasured one year later. No islands are seen in the non-annealed sample. In the annealed sample practically all small islands disappear and big islands (domes) with base ~ 0.3 μm (height 60 nm) and ~ 0.5 μm (height 150 nm) appear.

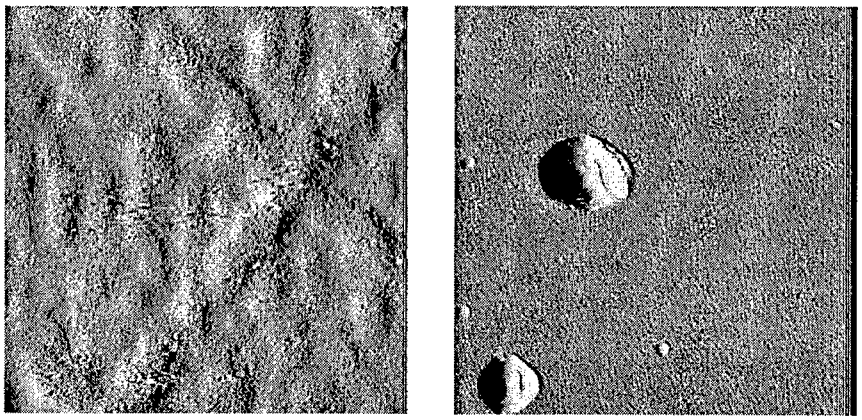

Fig. 4. Surface morphology of non-annealed (a) and annealed (b) sample C, remeasured after one year. Scan area 2×2 μm.

2.4 Discussion

It must first be emphasized that in the annealed samples the structural parameters of the islands, their density, the thickness of the wetting layer are all close to those properties reported for MBE growth [9]. Second, we demonstrate that InAlAs islands obtained via annealing are unstable at room temperature and transform into large clusters as a function of time due to Ostwald ripening. Third, we shown that annealing plays a dominant role in the formation of dense arrays of InAlAs islands by MOCVD. This can be explained as the overgrowth of the wetting layer, delaying the onset of island formation [14]. Upon annealing, such an overgrown wetting layer should lose most of excess material, with atomic rearranment to form strained islands as they tend toward equilibrium. On the other hand, the delay of the onset of island formation can be connected with changing of the value of the critical thickness for 2D-3D growth mode transition. This point of view must assume that as grown InAlAs film has strong non-uniformity of In distribution and annealing changes the distribution of In via diffusion. In this case one may expect the difference in the time evolution of the surface morphology of non-annealed and annealed films which has been experimentally observed.

References

[1] J. Tersoff and F. K. LeGoues, *Phys. Rev. Lett.* **72**, 3570 (1998).
[2] V. A. Schukin, et al., *Phys. Rev. Lett.* **75**, 2968 (1995).
[3] I. Drauka and A.-L. Barabashi, *Phys. Rev. Lett.* **79**, 3708 (1997).
[4] F. M. Ross, et al., *Phys. Rev. Lett.* **80**, 984 (1998).
[5] R. Leon et al., *Phys. Rev. Lett.* **81**, 2486 (1998).
[6] G. Mederiros-Ribeiro et al., *Phys. Rev. B* **58**, 3533 (1998).
[7] B. D. Min et al,, *Phys. Rev. B* **57**, 11879 (1998).
[8] S. Lee et al., *Phys. Rev. Lett.* **81**, 3479 (1998).
[9] R. Leon et al., *Appl. Phys. Lett.*. **64**, 521 (1995).
[10] A. F. Tsatsul'nikov et al., *Appl. Surf. Sci.* **23/124**, 381 (1998).
[11] H. D. Robinson, *Appl. Phys. Lett.* **72**, 2081 (1998).
[12] R. Leon and S. Fafard, *Phys. Rew B* **58**, 1726 (1998).
[13] A. O. Kosogov et al., *Appl. Phys. Lett.* **69**, 3072 (1996).
[14] J. K. Furdyna, S. Lee, A.-L. Barabashi and J. L. Merz, "Self-Organized Low-Dimensional II-VI Nanostructures", in *II–VI Semiconductor Materials and Their Applications*, ed. M. C. Tamargo (Gordon and Breach Science Publishers, 1999) (in press).

7th Int. Symp. "Nanostructures: Physics and Technology"
St Petersburg, Russia, June 14–18, 1999

3D-model of epitaxy on diamond-like crystal (111) surface

I. G. Neizvestny, *N. L. Shwartz*, A. V. Zverev and Z. Sh. Yanovitskaya
Institute of Semiconductor Physics RAS SB, 630090 Novosibirsk, Russia

3D Monte Carlo model of epitaxy growth on {111} surfaces of diamond-cubic materials is presented. In recent papers [1, 2, 3, 4] models for diamond like crystals were suggested. Giving SOS principle up one could simulate three-dimensional surface layer. Atom diffusion could take place on the surfaces with any one orientation. Elementary events in our model are diffusion, adsorption and desorption. Temperature and growth rate are responsible for the rate of 2D nuclei creation and decreasing of intensity flux is equivalent to increasing substrate temperature. So one has every reason to introduce into the model the parameter n_{dif} equal to the number of diffusion hops between two adsorption events. Binding energies E_3 and E_2 between first and second neighbors and parameters E_{1n}, E_{2n}, E_{3n} determining atom hopping probabilities to the sites of first, second and third nearest neighbors are parameters of the model crystal.

Using the experimental STM data on flat Si(111) surface [5] we chose the value of n_{dif} to fit experimental and simulated density of island at the initial stages of growth. This density is scarcely affected by other parameters of the model. With temperature and flux intensity from [5] we estimated surface diffusion energy E_{d} on Si(111) surface as follows: the number of diffusion steps between two acts of adsorption is determined by

$$n_{\mathrm{dif}} = \nu \exp(-E_{\mathrm{d}}/kT)/V, \tag{1}$$

where E_{d} is activation energy for surface diffusion (eV), V rate of growth (bilayer per second) (defined by flux intensity), ν temperature-independent vibration frequency (s^{-1}), k Boltzmann's constant, T substrate temperature (K).

Substituting in this equation experimental temperature and rate of growth and determined by simulation n_{dif} one could obtain E_{d}.

Islands density dependence on model parameter n_{dif} is presented in Fig. 1. Experimental data dependence of island density on temperature and flux intensity [5, 6] are show as well. Both for experiment and simulation temperature ranged from 680 up to 800 K and rate of growth from 0.01 to 0.15 monolayer per minute. When the simulated curve and one of the experimental points from [5] coincided E_{d} was determined. It turns out that all experimental points agree closely with simulated curve for the same E_{d}. Our estimation gives $E_{\mathrm{d}} = (1.75 \pm 0.15)$ eV. All experimental data we used were related to temperature range corresponding to the Si (111) 7×7 surface. So surface diffusion energy estimated in this work refers to this reconstructed surface. Obtained $E_{\mathrm{d}} = (1.75 \pm 0.15)$ eV is close to $E_{\mathrm{d}} = 1.9$ eV in [1] but differ dramatically from $E_{\mathrm{d}} = 0.75$ eV determined in [5]. Such distinction is associated with procedure of data treatment. In [5] E_{d} was defined from the slope of dependence islands density on temperature and flux using Venables theory [7]. In this work we determine E_{d} from correlation of absolute values of simulated and experimental island densities.

With obtained parameters simulation gave steps moving in $[11\bar{2}]$ and $[\bar{1}\bar{1}2]$ directions close to experimental ones during growth on vicinal surfaces. Surface fragment after 0.25 bilayer (BL) deposition at the temperature $T = 690$ K is shown in Fig. 2. Islands

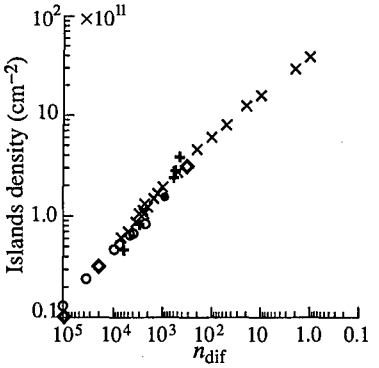

Fig. 1. Islands density dependence on model parameter n_{dif} (×○) simulation results; (◇) experimental data from islands density dependence on temperature; (+) on flux intensity [5]; (•) experimental point from work [6].

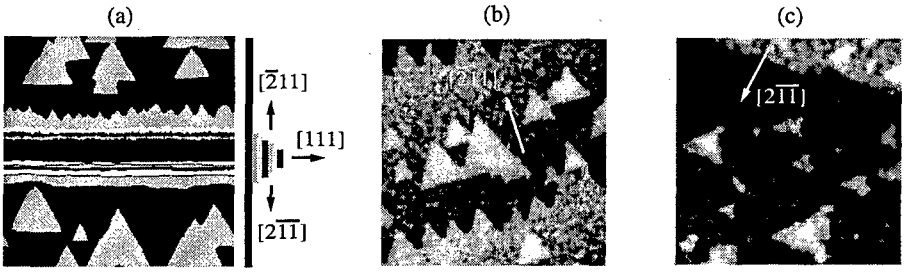

Fig. 2. Si(111) surface view at initial stage of growth. Size of the surface is 300 × 300 lattice sites, $T = 690$ K. (a) Simulated surface after 0.25 BL deposition; on the right initial profile of the echelon like surface; (b) STM view of Si(111) surface with [$\bar{2}$11] the step after 0.25 BL deposition [8]; (c) STM view of Si(111) surface with [2$\bar{1}\bar{1}$] the step after 0.18 BL deposition [8].

created after 0.25 BL deposition on simulated surface are similar in sizes and shape with experimental ones [8]. Initial surface relief represented two echelons of steps of opposite direction. It is clear that steps moving in [$\bar{1}$12] direction are kept flat and on steps moving in opposite direction [11$\bar{2}$] one can see sawtooth shape as it was experimentally observed [8].

We have simulated homoepitaxy process on porous Si(111). Surface fragment with one pore is shown in Fig. 3. Cross-section of the surface before and after 5 BL deposition at temperature $T = 873$ K and high rate of growth equal 60 BL/s. For these conditions it was necessary 10 BL of silicon to be the pore completely overgrown. Simulation results of epitaxy growth on porous surface with 200 × 200 atomic sites with 16 pores at temperature $T = 873$ K and rate of growth equal 1.2 BL/s are presented in Fig. 4. The sizes of each pore are 10 BL in height and 6 atomic sites in diameter. Substrate temperature and epitaxy growth rate were chosen close to experimental ones [9]. Top view and cross-section of the surface before and after 0.5 BL deposition one can see in Fig. 4(a,b). Increasing rate of growth up to 14 BL/s at the same temperature demonstrates continuos layer creation after deposition of 4 BL. Step density oscillations calculated during 10 BL deposition at the same temperature and two different growth rates 14 BL/s (curve 1) and 1.2 BL/s (curve 2) are demonstrated in Fig. 4(c). Comparing oscillation calculated for flat and porous surfaces one could see that for high growth rate their shapes are similar (curve 1). For low growth rate (curve 2) phase delay required for porous overgrow is noticeable. Notice that porous

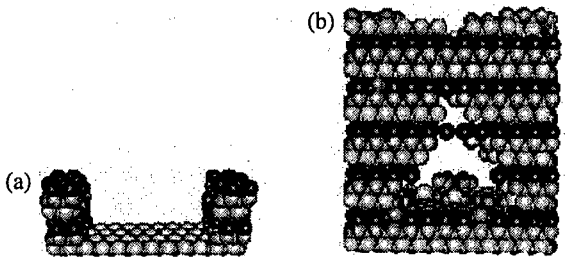

Fig. 3. Simulation of epitaxy growth on the surface with one pore; $T = 873$ K, growth rate 60 BL/s. (a) Initial surface and cross-section before deposition; (b) surface cross-section after 5 BL deposition.

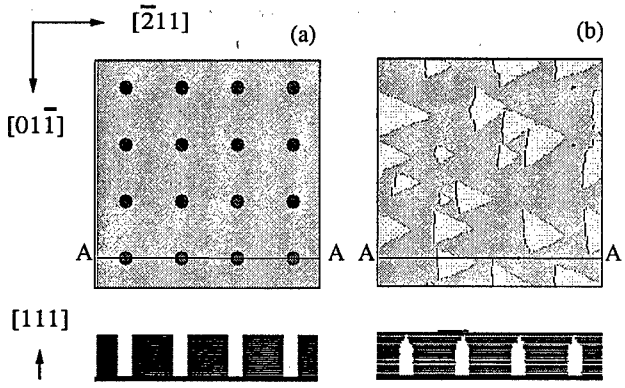

Fig. 4. Homoepitaxy simulation on porous silicon surface at $T = 873$ K. Porous diameter is 6 atomic sites, height is 10 BLs; (a) initial surface: top view and section AA; (b) surface after 0.5 BL deposition at growth rate 1.2 BL/s: top view and section AA.

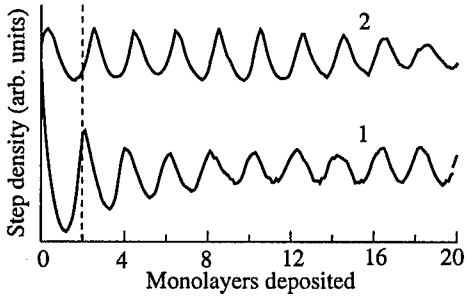

Fig. 5. Step density: curve 1—growth rate 14 BL/s, curve 2—1.2 BL/s; $T = 873$ K.

on the surface synchronize nucleation process that shows up in longer delay curve 2.

Thus the 3D-model for epitaxy on the surfaces of diamond like crystals was created. This model was successfully applied for experimental data analysis of epitaxy on (111) single crystal and porous silicon surfaces. Activation energy of diffusion hop of adatom on flat Si(111) surface was estimated from STM and simulated density of island: $E_d = (1.75 \pm 0.15)$ eV.

This work was supported by the Russian Foundation for Fundamental Research and the State Program "Surface Atomic Structures".

References

[1] M. I. Larsson and G. V. Hansson, *Surf. Sci. Lett.* **321**, 1261 (1994).
[2] S. Kersulis and V. Mitin, *Semicond. Sci. Technol.* **10**, 653 (1995).
[3] D. L. Woodraska and J. A. Jaszczak, Surf. Sci. **374**, 319 (1997).
[4] P. L. Novikov, L. N. Alexandrov, A. V. Dvurecensky and V. A. Zinivev, *JETP Lett. (Russian.)* **67**, 512 (1998).
[5] B. Voigtlander, A. Zinner, T. Weber and H. P. Bonzel *Phys. Rev. B.* **51**, 7583 (1995).
[6] B. Voigtlander, M. Kastner and P. Smulauer *Phys. Rev. Lett.* **81**, 858 (1998).
[7] J. A. Venables, G. D. T. Spiller and M. Hanbucken *Rep. Prog. Phys.* **47**, 399 (1984).
[8] M. Fehrenbacher, H. Rauscher, U. Memmert and R. J. Behm *Surf. Sci.* **398**, 123 (1997).
[9] T. Yasumatsu, T. Ito, H. Nishizawa and A. Hiraki, *Appl. Surf. Sci.* **48/49**, 414 (1991).

7th Int. Symp. "Nanostructures: Physics and Technology"
St Petersburg, Russia, June 14–18, 1999

Effect of laser annealing on optical properties of ZnCdSe/ZnSSe quantum well heterostructures

O. V. Nekrutkina, A. A. Toropov, T. V. Shubina, S. V. Sorokin, S. V. Ivanov and P. S. Kop'ev
Ioffe Physico-Technical Institute, St Petersburg, Russia

ZnSe-based nano-size structures have recently become objects of extensive research activity. In particular, the advanced molecular beam epitaxy (MBE) allows fabrication of high-quality multiple-layer heterostructures grown on a GaAs substrate and including ZnCdSe/ZnSSe quantum wells (QWs) and superlattices (SLs). Nevertheless, the techniques of lateral pattering, resulting in homogeneous arrays of lower-dimensional systems (quantum dots (QDs) or quantum wires) are still not sufficiently developed. The principle problem is supposed to be a simplicity of extended defects formation, which can be activated by any external perturbation during the post-growth process. Note that even application of a standard photolithography for formation of the device functional elements (e.g. narrow laser stripes) usually introduces additional defects, disturbing optical characteristics of these soft-lattice structures [1].

In this paper we study an alternative method of lateral pattering, based on the effect of local interdiffusion induced by a focused laser beam. This technique was previously applied to a single GaAs/AlGaAs single-QW heterostructure, resulting in creation of optically active QDs with perfectly controlled lateral sizes [2]. However, as applied to the wide bandgap II–VI structures, this approach meets a specific problem. The treated layer should be thick enough to provide efficient heating by absorbing the laser emission. Otherwise, most of the light pass the region of interest, heating the thick substrate. This problem is automatically solved in GaAs-based structures by using blue-green lines of a cw Ar^+ laser, efficiently absorbed directly in $\sim$ 1000 Å thick AlGaAs cap layer. As for the strained (Zn,Cd)(S,Se) epilayers on GaAs, the only compound allowing pseudomorphic growth of a reasonably thick layer is the ternary ZnS_xSe_{1-x} solid alloys with $x = 0.04–0.10$ satisfactorily lattice-matched to a GaAs substrate. These alloys possess the room-temperature band gap of about 450 nm and, therefore, are transparent for all blue and green lines of an Ar^+ laser. Most of other available cw laser lines of reasonable power are in the ultraviolet (UV) region, but the UV high-energy quanta are generally supposed to stimulate formation of point defects. We believe that just this assumption has determined the lack of data published (at least, to our knowledge) in the field of laser-induced pattering of the wide-gap II–VI heterostructures.

To overcome this problem, we have used the concept of alternatively-strained SL growth, previously applied to fabrication of extremely thick ZnCdSe/ZnSSe QW structures lattice-matched to GaAs as a whole [3]. The studied structure was grown by MBE on a (100) GaAs substrate at 280°C, using the only shutter-operation technique, as described elsewhere [4]. The sample comprises a 30-period (17 nm-$ZnS_{0.08}Se_{0.92}$/5 nm-$Zn_{0.82}Cd_{0.18}Se$) multiple QW (MQW) structure with a total thickness of 0.66 μm, embedded in $Zn_{0.92}Mg_{0.08}S_{0.09}Se_{0.91}$ quaternary claddings. Such a structure allows, in principle, local heating by the 488 nm Ar^+ laser line with a control over the heating volume in all three dimensions. In the lateral directions, the minimum beam focus size is determined by the diffraction limit as about half of the wavelength, whereas in the vertical direction the heat localization is achieved by the selective light absorption within the MQW region. The

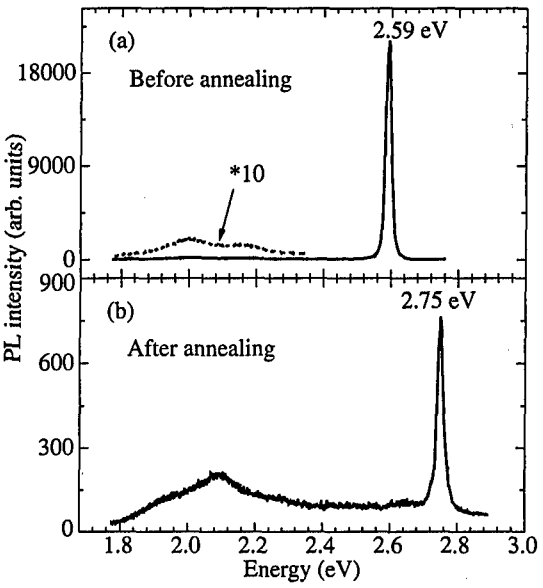

Fig. 1. PL spectra measured at 77 K in unannealed (a) and annealed (b) samples.

dominant expected effect is interdiffusion of the involved elements during the exposure to laser light, modifying the band gap energy (E_g) and, hence, the optical and electronic properties. Thus, the Zn-Cd interdiffusion in the ZnCdSe/ZnSSe QW is to result in an increase of the band gap. In the particular structure studied the local band gap enhancement can be as high as 160 meV, provided the complete intermixing between the well and barrier materials. Using the interdiffusion parameters published for this system in Refs. [5] and [6], one can calculate that observation of the noticeable effect (the 10–20 meV shift of E_g due to about one minute exposure to the laser light) requires local heating over 500–600°C. Simple estimations show that in the sample geometry used this temperature can be achieved by applying the cw laser power density of about 1 kW/cm^2, which can be readily obtained experimentally.

However, the principle problem is whether it is possible to stimulate the large enough changes of E_g without inducing additional defects. To elucidate this question we performed a series of laser annealing experiments changing both the laser power and the exposure time. Figure 1(a) and (b) demonstrate, respectively, photoluminescence (PL) spectra for two extreme cases—unannealed sample and a sample annealed under the conditions resulting in visible degradation of the structure capping layer. To reach this effect we annealed the structure for 5 minutes in air by applying the laser power density of about 1.5 kW/cm^2. PL measurements were made at 77 K with a 325 nm line of a 1 mW He-Cd laser. An iodine tungsten lamp emission dispersed by a single-grating monocromator was used for PL excitation (PLE) measurements.

The resulting effect of the blue shift is well pronounced, being close to a maximum possible value of about 160 meV. The annealing also leads to a decrease of the band-edge PL intensity (by 25 times). The formation of additional defects in the annealed sample is also confirmed by a rise of a red PL line close to 2.1 eV, which is known as a measure of structural perfection. However, the PL linewidth increases only slightly (from 20 to 25 meV), indicating that even the extreme annealing conditions still leave the structure optically active.

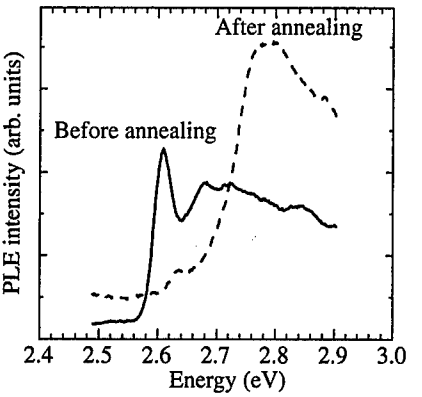

Fig. 2. PLE spectra measured at 77 K in unannealed (solid curve) and annealed (dashed curve) samples. The detection energy is 2.0 eV.

The effect of annealing also reveals itself in the PLE spectra of the samples shown in Fig. 2. The laser treatment results in a drastic blue shift of the fundamental band-edge, followed by broadening and disappearance of the band-edge excitonic line.

In conclusion, we designed and fabricated a (Zn,Cd)(S,Se) MQW heterostructure allowing control over the optical and electronic properties by an exposure to 488 nm Ar^+ laser line. The laser-induced intermixing of elements results in a significant band edge blue shift with a moderate level of introduced defects. By controlling the light pattern on the sample surface this technique allows lateral pattering for fabricating e.g. ultra-narrow stripes or dot-like objects for optoelectronic devices.

This work has been supported in part by the RFBR, the program of MS of RF "Physics of solid-states nanostructures" as well as the Volkswagenstiftung.

References

[1] T. V. Shubina, A. A. Toropov, A. V. Lebedev, S. V. Ivanov, P. S. Kop'ev, H. J. Lugauer, G. Reuscher, M. Keim, L. Worschech, A. Waag and G. Landwehr, *Abstracts of 10th Int. Conference on MBE*, Cannes, France, p. 540, 1998.

[2] K. Brunner, U. Bockelmann, G. Abstreiter, M. Walther, G. Bohm, G Trankle and G. Weimann, *Phys. Rev. Lett.* **69**, 3216 (1992).

[3] A. A. Toropov, S. V. Ivanov, T. V. Shubina, A. V. Lebedev, S. V. Sorokin, G. N. Aliev, M. G. Tkatchman, N. D. Il'inskaya and P. S. Kop'ev, *Proc. Int. Symp. "Nanostructures: Physics and Technology"*, St.-Petersburg, Russia, p. 210, 1997.

[4] T. V. Shubina, S. V. Ivanov, A. A. Toropov, G. N Aliev, M. G. Tkatchman, S. V. Sorokin, N. D. Il'inskaya and P. S Kop'ev, *J. Cryst. Growth*, **184/185**, 596 (1998).

[5] A. Rosenauer, T. Reisinger, E. Steinkirchner, J. Zweck and W. Gebhardt, *J. Cryst. Growth* **152**, 42 (1995).

[6] M. K. Chai, S. F. Wee, K. P. Homewood, W. P. Gillin, T. Cloitre and R. L Aulombard, *Appl. Phys. Lett.* **69**, 1579 (1996).

7th Int. Symp. "Nanostructures: Physics and Technology"
St Petersburg, Russia, June 14–18, 1999

Free-standing GeSi/Si micro- and nanotubes

V. Ya. Prinz, *S. V. Golod* and V. I. Mashanov
Institute of Semiconductor Physics RAS SB, 630090 Novosibirsk, Russia

Abstract. Micro- and nanotubes, as well as free-standing flexible helical microcoils have been fabricated for the first time from strained Ge_xSi_{1-x}/Si bilayers. The scrolling process used for the formation of the nanoobjects proceed in a self-forming manner due to the action of interatomic forces inside the highly strained layers. The obtained tube diameter varied from 1.5 μm to 90 nm depending on the value of lattice mismatch and on the thickness of GeSi/Si bilayer.

Introduction

Nanostructure formation is the forefront of semiconductor science and technology. However, using any traditional fabrication methods (electron or ion beam lithography), it remains difficult to fabricate even planar structures smaller than 10 nm. Fabrication procedures for three-dimensional (3D) nanostructures are far less advanced. However, new interesting physical properties and phenomena can be expected in such structures.

Recently, several new concept of making 3D nanostructures (nanotubes, flexible helical nanocoils, cylindrical quantum well and arrays of nanotubes) have been proposed and realized [1–3]. The concept are based on the possibility of self-scrolling of highly strained InGaAs/GaAs heterolayers (being debonded from substrate) in tube shape scrolls. It has been shown that the rolled up layers get close together, thus forming perfectly bonded tubes walls. The tube diameter could be precisely controlled in the range from 4 μm to 3 nm, depending on the value of lattice mismatch ($\Delta a/a$) and on the thickness d of InGaAs/GaAs bilayer (max $\Delta a/a \approx 7.2\%$) [4].

Results and discussion

We present here 3D micro- and nanostructures fabricated from strained GeSi/Si bilayers using the scrolling process. The use of Ge_xSi_{1-x}/Si heterostructures for the above process (max $\Delta a/a \approx 4\%$, the smallest expected tube diameter ($\sim$ 8 nm) has much potential since: (a) it offers a possibility to obtain conducting tubes with ultra-thin walls (the doping level of Si can be brought up to $\approx 10^{20}$ cm^{-3}, and, in addition, some part of Si layer or even the whole layer can be replaced with $NiSi_2$ or $CoSi_2$ layers having metallic conductivity), (b) the 3D structures fabrication technology matches well the Si-based integration technology.

In the initial pseudomorphic structure, the Ge_xSi_{1-x} layer is compressed. After debonding of the bilayer resulting from lateral undercutting etch of Si substrate through windows on the epilayer side, the interatomic forces (F_1 and F_2—Fig. 1) will act to increase the interatomic distance in the compressed Ge_xSi_{1-x} layer, which tends to bend the bilayer.

The problem of realization of the selective etching was solved by using the well-known chemical-etch stop effect of heavily boron-doped Si ($p^+ \approx 10^{20}$ cm^{-3}). In the case of Ge_xSi_{1-x} films, the effect was even more pronounced, since addition of Ge into Si results in a considerable decrease of the etch rate V [5]. The selective etchant used in this work (selectivity factor $\delta = V_p/V_{p^+} \approx 10^3$) was shown to permit scrolling up of a GeSi/Si in a

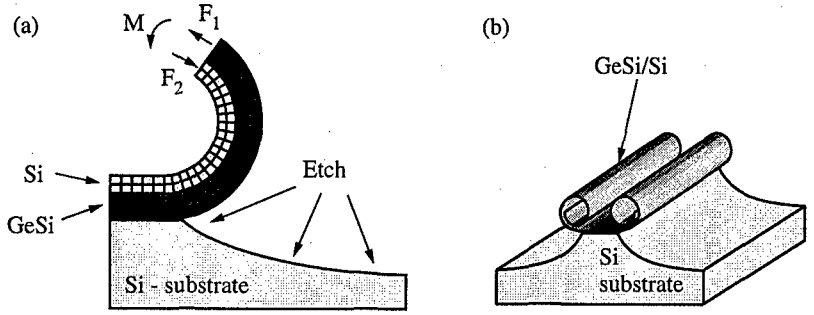

Fig. 1. Schematic illustration of the proposed tube formation technology. (a) Strain-induced bending of the GeSi/Si bilayer after freeing it from bonding with substrate. (b) Self-scrolling of bilayer during removal of substrate. The forces F_1 and F_2 are oppositely directed, and they give rise to a moment of forces M, which tends to bend the bilayer.

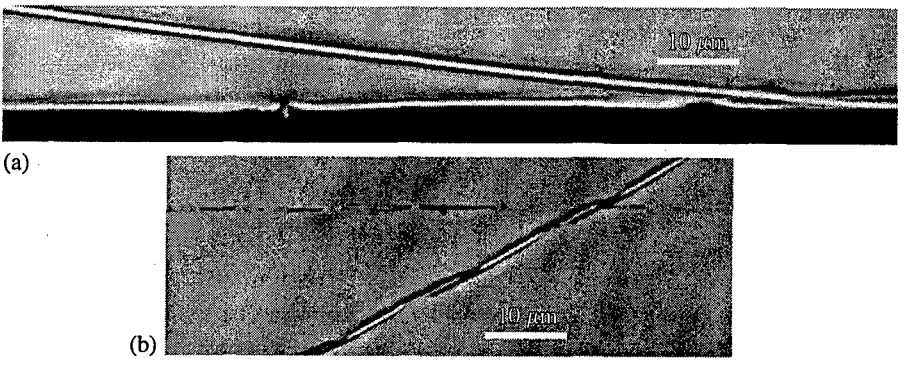

Fig. 2. Photographs of a tube (a) and a helical coil (b) of 1.5 μm in diameter made from a $Ge_{0.4}Si_{0.6}$/Si bilayer. Thicknesses of $Ge_{0.4}Si_{0.6}$ and Si films were 10 and 20 nm, respectively.

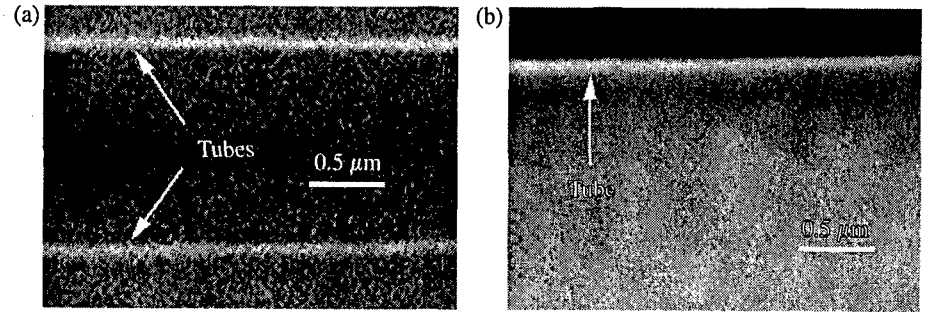

Fig. 3. SEM images of tubes with diameter 90 nm. (a) $Ge_{0.8}Si_{0.2}$/Si bilayer was used. Thicknesses of $Ge_{0.8}Si_{0.2}$ and Si layers were 2 and 5 nm, respectively. (b) $Ge_{0.8}Si_{0.2}$/Si/$Ge_{0.3}Si_{0.7}$ three-layered system was used. Thickness of each layer was 2 nm (the total thickness was 6 nm).

tube, with the thickness of cap silicon layer having been decreased by no more than $\pi D/\delta$, where D is the tube diameter. The latter can be confirmed by the following estimates. Indeed, the length of time required for freeing the bilayer film from bonding with substrate over the distance equal to the scroll circumference can be written down as $t = \pi D/V_{\text{sub}}$, where V_{sub} is the etch rate of substrate. In fact, this duration will be even shorter, since in the cause of etching the scrolling film facilitates the access of etchant towards the substrate. In view of the above, the decrease in the thickness of the cap Si layer will be

$$\Delta d = V_{\text{film}} \cdot t = \frac{V_{\text{sub}}}{\delta} \cdot t = \delta^{-1} \cdot \frac{V_{\text{sub}}}{V_{\text{sub}}} \cdot \pi D = \delta^{-1} \cdot \pi D. \tag{1}$$

In our case this value is less than $10^{-3}\pi D$.

The possibility of formation of Ge_xSi_{1-x}/Si tubes and helical coils with well-defined parameters has been demonstrated on a series of epitaxial structures grown on the MBE "Katun" setup. Using Ge_xSi_{1-x}/Si heterostructures of different thickness, we have fabricated tubes of a preset diameter. Figures 2 and 3 exemplifies a photographs of such tubes and helical coils.

In the last case (Fig. 3(b)), a protective $Ge_{0.3}Si_{0.7}$ cap layer was used. The etch rate of $Ge_{0.3}Si_{0.7}$ is 17 times smaller than that of (100) silicon.

In the future, the proposed technology can be successfully used in combination with the Si technology of ICs.

Acknowledgements

The authors thank A. E. Plotnikov for taking SEM images and O. P. Pchelyakov for interest in the study. The work was supported by the Russian Foundation for Basic Research (Grants 97-02-18479 and 97-02-18408), Russian Program "Physics of Solid State Nanostructures" (Project 98 – 2030) and Russian Program "Promising Technologies and Devices for Micro- and Nanoelectronics" (Project E42).

References

[1] V. Ya. Prinz, V. A. Seleznev, V. A. Samoylov and A. K. Gutakovsky, *Microelectronic Engineering* **30**, 439 (1996).

[2] V. Ya. Prinz, V. A. Seleznev and A. K. Gutakovsky, *The 24th International Conference on the Physics of Semiconductors (ICPS 24), Israel, Eurasalem, August 2-7* Th3-D5 (1998).

[3] V. Ya. Prinz, V. A. Seleznev and A. K. Gutakovsky, *The Physic of Semiconductors, World Scientific Publishing* (1999 in press).

[4] V. Ya. Prinz, V. A. Seleznev and A. K. Gutakovsky, *Submitted to Appl. Phys. Lett.*

[5] R. M. Finne and D. L. Klein, *J. Electrochem. Soc.* **114**, 965 (1967).

7th Int. Symp. "Nanostructures: Physics and Technology"
St Petersburg, Russia, June 14–18, 1999

InAs/GaAs stacked lateral superlattices grown on vicinal GaAs (001) surfaces by molecular beam epitaxy

S. N. Rechkunov, I. A. Panaev, A. K. Gutakovsky and A. I. Toropov
Institute of Semiconductor Physics RAS SB, 630090 Novosibirsk, Russia

Abstract. The MBE growth of strained InAs/GaAs lateral superlattices on 1° vicinal (001) GaAs substrate is reported. The superlattices are produced by depositing alternately fractional monolayers of InAs and GaAs via step flow growth. We demonstrate the growth of stacked InAs quantum wires array embedded in GaAs matrix. Vertical alignment of the InAs wires in stacked array is evidenced and attributed to stress-induced self-organization growth in lattice mismatched InAs/GaAs material system.

Introduction

Low-dimensional carrier-confined nanostructures such as quantum wires (QWR) and quantum dots (QD) are of great interest because of their importance in physics and electronics. For fabrication these structures, novel methods involving self-organization phenomena in epitaxial growth have been proposed and studied extensively. The most important technique for *direct formation of high-density QWR structures* is step flow growth of compound semiconductors on misoriented substrates [1]. The existence of a regular array of equispaced steps on vicinal planes and the precise control of the deposition kinetics and amount of material deposited, insures the growth of a lateral superlattice (LSL) [2]. In this structure, laterally (i.e. in-plane) periodic composition and band gap modulation is achieved by growing alternately fractional monolayers of constituent materials via step flow growth. The serious problem encountered is that the composition modulation is far smaller than ideal in lattice matched systems, such as Ga(Al)As or Ga(Al)Sb, although the transmission electron spectroscopy (TEM) revealed the laterally periodic ordering in the structures.

On other hand, highly strained systems can afford better lateral composition modulation due to the strain-induced self-organizing growth phenomena. Very recently, step flow growth of InAs/GaAs in-plane strained lateral superlattice on misoriented (110) InP substrate have been attempted and excellent spatial composition modulation have been evidenced [3]. In this paper we describe the MBE growth and structural features of strained InAs/GaAs laterally periodic QWR structures fabricated on misoriented (001) GaAs substrates.

1 Experimental and growth results

All structures were performed by molecular beam epitaxy (MBE) using a Riber 32P system. Careful treatment of growth chamber and all molecular sources provided fabrication of AlGaAs/GaAs 2-DEG heterostructures with high electron mobility. The substrates used were epi-ready semi-insulating (001) GaAs tilted on 1° towards the [111]A direction. This value of tilt angle must lead to the formation of a regular lattice of atomic steps with 16 nm mean terrace width. The misorientation direction is chosen to have the steps parallel to the $[1\bar{1}0]$ direction. The formation of step array during growth was monitored *in-situ* with

the reflection high-energy electron diffraction (RHEED) facility. The samples were rotated during growth to improve lateral uniformity of obtained structures.

The structures attempted in this work were AlGaAs/GaAs heterostructures with QWR lattice placed near the heterointerface on GaAs side. High electron mobility 2D system was attempted as a basic structure in order to obtain direct influence of additional lateral carrier confinement, introduced by QWR lattice, on 2-DEG transport properties. The basic structure consisted of following layers, in order of growth from substrate: a 900 nm thick GaAs buffer layer, three monolayers (MLs) of AlAs, a 70 nm thick AlGaAs layer capped with a 10 nm GaAs layer. The short period AlAs/GaAs smoothing superlattice was introduced in buffer layer after the first 100 nm of GaAs have been deposited. All layers in this basic structure were intentionally undoped, except of the AlGaAs layer, which was doped by two δ–planes with sheet Si-donor concentration of about 2.5×10^{12} cm^{-2} placed at distance of 20 nm and 60 nm from the heterointerface. The substrate temperature was kept nearly 620 °C during growth. At this temperature, the RHEED pattern showing single monolayer step ordering was clearly formed and kept during deposition.

For direct formation of the QWR structure in the 2-DEG region of structure described above, we used the following growth sequence. After the buffer layer, 3ML AlAs layer and additional 20 nm thick undoped GaAs layer have been deposited, the growth process was interrupted for 120 s in order to decrease substrate temperature from 620 °C to 420 °C. One, four or ten monolayer cycles of alternate InAs and GaAs half-layer deposition was then performed on separated substrates to obtain InAs/GaAs lateral lattices with different thickness. Low temperature growth stage was completed by depositing eight monolayers of GaAs coating layer in order to weaken possible indium evaporation during growth followed hereafter. The growth rate of InAs and GaAs was about 0.1 ML/s during low temperature growth stage. After this, the growth process was interrupted ones more and substrate temperature was raised to its initial value. An additional 7 ML thick GaAs layer followed by 3 ML AlAs layer was then deposited to separate a fabricated QWR lattice from the heterointerface. The growth was completed by depositing of AlGaAs and GaAs layers. Two AlAs layers served as reference planes in TEM study. Moreover, structural quality of GaAs/AlAs interface may be indicative of heterointerface sharpness in the case of lattice matched GaAs/AlAs system (first AlAs layer) and in that of the same system strained by underlying LSL (second AlAs layer).

During growth of the 1 ML and 4 ML thick lateral structures, step ordering and step flow growth regime were kept, as indicated by RHEED oscillations, when growing InAs and GaAs alternately, and, also, when growing GaAs coating layer at low temperature. On the contrary, it was found, that the step ordering disappeared after deposition of 5 ML thick LSL layer and restored again only after deposition of GaAs coating layer. The TEM plan view image revealed an extra density of dislocations in the sample attempted for the 10 ML LSL stack. This behavior seems to indicate that the deposition of InAs stripes, thicker than 5 ML, leads to termination of the step flow growth regime. To overcome this problem, we attempted growth of a vertically stacked LSL set consisted of two 4 ML thick InAs/GaAs LSLs separated by 2 nm thick GaAs layer. In accordance with the expectations, the equilibrium step ordering was kept during entire growth and the structure produced was free of dislocations.

2 Microscopic study of stacked LSLs and discussion

In order to clarify the structural features, we characterized obtained structures by high-resolution TEM. Cross section samples are prepared using the standard mechanical polish-

ing and ion milling methods. The cross section HRTEM image shown in Fig. 1 illustrates an example of stacked LSL structure obtained by the method described above.

Cross section view $(1\bar{1}0)$ plane is perpendicular to the (001) surface plane and electron beam is directed along surface step edges. The dark areas in the image correspond to InAs-rich regions, while the gray regions indicate a larger GaAs content. The bright line in the [110] direction relates to the 3 ML AlAs layer.

The LSL stack image exhibits well resolved contrast between the constituent LSL and GaAs layers, indicating that these components are well separated. It is clearly seen from contrast-enhanced image (b), that two separate laterally periodic structures are formed in the [110] direction across the surface steps. Lateral period of observed patterns is close related to the mean terrace width of 16 nm, although the insignificant variations of lateral period ranged from 13 nm to 17 nm were also observed.

Surprisingly, a visible contrast exists between the GaAs-rich regions in LSL plane and the GaAs layers (buffer and separating ones), indicating that the indium atoms incorporate in GaAs fraction of the LSL. Because the separating GaAs layer is well resolved in the image, the changes in contrast could not be purely explained by the indium segregation or diffusion. Moreover, the extent of the dark gray regions is limited by LSL plane, indicating that these regions are directly formed during LSL deposition. This, indeed, might occur, if migration length of the indium atoms is less compared with the mean terrace width, i.e. a fraction of the In atoms deposited on surface can not reach the step edges, thus, allowing the In nucleation on the step ledges and leading to the formation of the InGaAs alloy during GaAs fraction growth cycle. The reduced width of well contrasted InAs-rich regions also proves this situation.

The most interesting feature revealed by HRTEM study is an arrangement of stacked LSL structure. Indeed, the InAs-rich regions are not tilted inside the LSL stack and, moreover, these regions are lined up in the growth direction. Thus, we suppose that the surface step arrangement is tuned by stress induced by the InAs regions, so, the In atom nucleation events occur preferably in the InAs-rich regions minimizing misfit stress accumulation. The results obtained here demonstrate a direct evidence on a short-range correlation, when growing the Ga(In)As LSL structures.

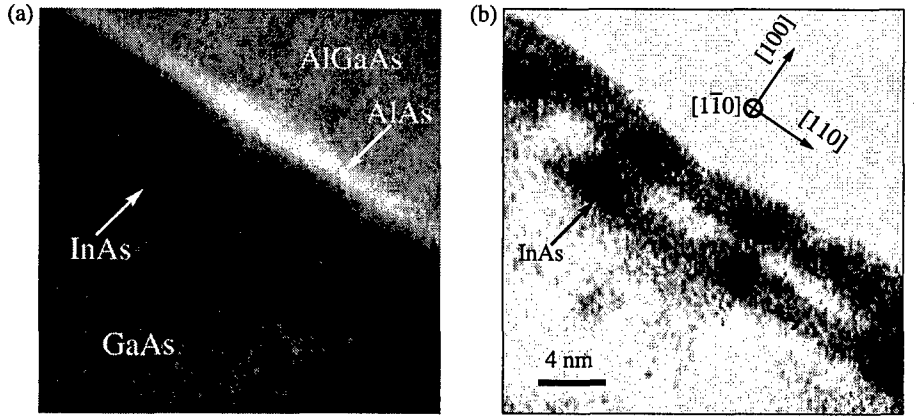

Fig. 1. Cross section HRTEM image of a stacked LSL structure, (a) shows the experimental image, while in (b) the contrast is enhanced by image processing.

3 Summary

We have shown that a modulation of the composition in two directions can be directly introduced by MBE deposition of stacked lateral superlattices via step flow growth. InAs and GaAs compounds can be combined to grow LSL on vicinal GaAs substrate, in spite of a large lattice mismatch. The HRTEM images indicated formation of laterally periodic structure with the period of the mean terrace width of the substrate used. Vertical arrangement of InAs-rich regions was obtained in stacked LSL. This feature may be attributed to the strain-induced self-organization phenomena in step flow growth mode. Close spacing of InAs quantum wires (less than 2 nm) in stacked LSL, we believe may lead to a confinement of electron gas in the InAs coupled wires.

Acknowledgements

This work was supported by the Russian Foundation for Basic Research (Grant 96-02-19371) and Russian Program "Physics of Solid State Nanostructures" (Project 98-2030).

References

[1] P. M. Petroff, A. C. Gossard and W. Wiegmann, *Sov. Phys. Semicond.* **45**, 620 (1984).

[2] J. M. Gaines, P. M. Petroff, H. Kroemer, R. J. Simes, R. S. Geels and J. H. English, *J. Vac. Sci. Thechnol.* **B6**, 1386 (1988).

[3] Y. Nokata, O. Ueda, Y. Nishikawa, S. Muto, N. Yokoyama, *J. Crystal Growth*, **175/176** 168 (1997).

7th Int. Symp. "Nanostructures: Physics and Technology"
St Petersburg, Russia, June 14–18, 1999

The energy of the carbon-flake nanocluster: Pentagon-pentagon distance optimization

Slava V. Rotkin, Robert A. Suris and Stanley F. Kharlapenko
Ioffe Physico-Technical Institute, St Petersburg, Russia

Abstract. The new road of "rolling up" conformation of a graphite fragment into a fullerene is considered in context of the theory of the growth of carbon nanoparticles. The small curved flake-like fragments of the graphite monolayer are investigated as an intermediate step along the conformation path. The optimal shape of the clusters with the small curvature is found within the phenomenological model.

Introduction. The explanation of the experimental distribution (of size and shape) of a huge variety of carbon nanoclusters observed in the standard synthesis is still a challenge for a theoretician for last decade. The nanoclusters have a shape of flat fragments of the graphite, a cylindrical shape (nanotubes), a spherical form (fullerenes). The most complicated question is how to create so symmetric structure, what are the roads of the formation? Let us consider, for example, the rolling up of a flat "flake" (a small monolayer fragment) into a sphere. The lattice of the flat fragment consists from only hexagons like in the simple graphite. In contrast, any closed cluster with 3-armed atoms has to have 12 pentagons besides the arbitrary number of hexagons. What is the intermediate step in the conformation road, which leads to the closed nanosphere from the flake? One interests in the energy of formation of this intermediate state owing to it allows one to understand the optimal condition of the synthesis. The formation energy depends on the distribution of the pentagons over the cluster lattice, though it is not known exactly.

The *ab initio* quantum chemical calculation of the total energy of any cluster remains to be too complicated even it gives accurately the formation energies, because of it demands essential computer resource. The most advanced technique allows one to consider not more than a hundred of atoms.

Instead of time-consuming simulation, the model for phenomenological calculation of the formation energy of carbon nanocluster was introduced in previouse papers [1].

We supposed that a cluster with the small curvature and the large number of atoms does resemble the 2D-graphite sheet fragment. This continual approximation describes the energetics taking into acount three main factors. Namely, the energy of the cluster (more precisely the energy difference between the cluster and the fragment of graphene) contains (*i*) the largest contribution from the dangling bonds. Then, within the continual approach the total length of the cluster perimeter is to be minimized. The next in importance contribution is owing to (*ii*) the topological defects, the 5MRs (five-membered-rings). The less the total body angle covered by the curved surface of the cluster, the less the number of 5MRs, the less the corresponding energy. The last contribution is due to (*iii*) the rehybridization of electron orbits on the surface with the curvature.

The paper [2] applies this continuum phenomenological approach to the problem of instability of the finite piece of graphene (monolayer of graphite) to the rolling up into some curved flake and finally into the closed spherical fullerene. However, the problem of the intermediate step states for the rolling process has been faced.

Energetics of flake fragments. One can assemble the cluster, containing N atoms, as a flat flake, as a closed sphere, and as some intermediate state in this fullerene road. All but flat flake contain 5MRs. The number of 5MRs is less for the cluster with the less curvature.

As believed in the fullerene theory the pentagons are lie as far each from other (in the lattice of cluster) as possible. As the result the regular icosahedral structure of the cluster is formed [3]; its lattice (faces of the icosahedron) is assembled from regular triangular fragments of the graphene with the exception of each sixth fragment (see Fig. 1).

The angles between bonds in this structure do not depend on the size of the cluster and are the simple numbers from school geometry [1]. Therefore the (constant) curvature concentrates along the edges of the icosahedron. In order to minimize the curvature energy, one needs to minimize the total edge length. Henceforth, the minimization is understood to be done at the fixed number of atoms. That means that the conformations between clusters of the same size are to be considered.

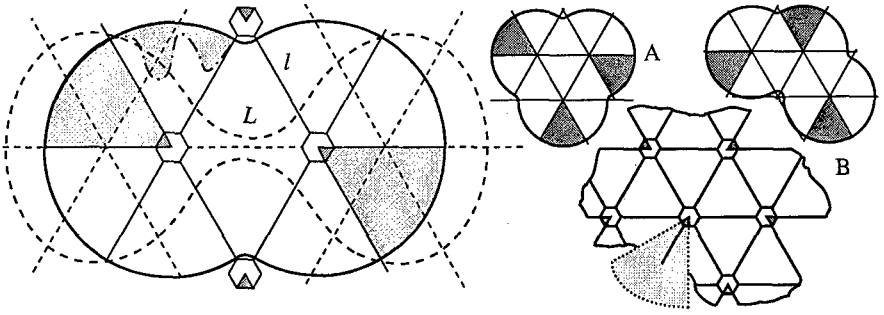

Fig. 1. Left: The optimization of two-pentagon flake. The shaded areas are extracted from the envelope. That forms two 5MRs within the dumb-bell flake. The distance between 5MRs L and the sector radius l define the perimeter and edge length. The variation within a sector is shown as dash-dotted line. The optimal shape is a circular sector. The minimization in the variable L is shown with two triangular superlattices (full and dashed lines). The optimal shape of the flake correspondes to the maximal $l_o = L$ (full line). Right upper: Optimization of two 3-pentagon flakes. The trefoil one (A) is more dense and therefore energetically preferable. Right lower: The triangular superlattice of the carbon flake with any number of 5MRs. Each vertex of the superlattice is the vertex of the polyhedral surface of the fragment of the spheroid. The shaded area depicts the 1/6-th cut from graphene, which makes the 5MR instead of the hexagon and developes the topological curvature of the cluster surface.

The optimal shape of a single triangular sector is known from textbooks (*e.g.* [4]): the isosceles round sector. The optimization is the variation of the perimeter shape, and the solution is the round flake. Naturaly, the round shape follows from the symmetry reasons.

Optimal flake with two 5MRs: dumb-bell shape. In the case of two 5MRs the distance between pentagons L also varies. We divided the problem in two parts. First, we solve the problem for the fixed number of atoms N, *and fixed distance* L. The optimal shape is $\mathcal{S}\ (N, L)$. Then we consider another cluster with the same N and different L' and find $\mathcal{S}\ (N, L')$. Comparing the energies of the optimal clusters E and E' we find the minimal one and, hence, the optimal distance L_o.

The symmetry prompts the optimal shape $\mathcal{S}\ (N, L)$, which consists from six eqiuvalent isosceles sectors (with the radius l) and two concave trapezoids (see Fig. 1). The perimeter is given by the concave-convex line which length depends in both l and L. Now the energy

minimization at the fixed number of atoms (equivalently, at the fixed surface) is performed over the variables l, L. Though, only one variable is independent owing to the bounding condition S =const. The function to be minimized is as follows:

$$\Phi = \mathcal{P}(L,l) + \frac{E_c}{E_b}\mathcal{L}(L,l), \tag{1}$$

where $\mathcal{P}(L,l)$ is the open perimeter. The characteristic dangling bond energy is $E_b \simeq 2.36$ eV per bond, and the curvature is parametrized with the energy $E_c \simeq 0.9$ eV per $1/b^2$ curvature ($b \simeq 1.44$ Å, the carbon bond length). The multiplier E_c/E_b appeared before in Ref. [1] and was abbreviated as $R_\star/3 \simeq 0.38$. $\mathcal{L}(L,l)$ is proportional to the total edge length. We will below make use of the theorem from the calculus of variations, which equals the solution with the minimal perimeter at the fixed area to the solution with the maximal area at the fixed perimeter. Instead of minimization of Eq.(1) one can consider it as a condition bounding L and l. Then implicit dependence $L(l)$ is obtained. We note that in this simplest case the dependence is linear. Then one finds the maximum of the number of atoms (at the function (1) being equal to some constant). The function $N(L(l),l)$ is quadratic in l and grows monothonically. Hence the larger l, the larger N. The optimal shape is that the concave parts of the perimeter are as small as possible. Then the surface consists, approximately, from 6 sectors, with the radius L, and 2 regular triangles with the edge L connecting two 5MRs (Fig. 1). From the other side, this geometry corresponds to the minimal distance L. One can not decrease it without the creation of a new third 5MR. The considerations are general and can be applied to the flake with any number of 5MRs.

Flakes with more than two MRs. In the case of the flake with more than two 5MRs the new parameter is the position of 5MRs in the super-lattice. For 3MRs-flake there are two possible configurations: the trefoil flake and the linear configuration. The minimization procedure is the same. The optimal configuration is the trefoil which has the shorter perimeter and the total edge length as well.

The energy of the optimal flake is the sum of the constant part, $\mathcal{E}_5/12 \simeq 1.48$ eV per pentagon [1], times the number of 5MRs and $E_b\Phi$, the part depending on the optimal distance L. The last is nothing more than the square root from the number of atoms (owing to the surface area depends on L^2). The energy of the round fragment of the flat graphene depends in $\sqrt{N}$ on the same way. The calculation shows that the slope of the flat fragment energy is less than the slope for any curved flake (at chosen E_c, E_b and $\mathcal{E}_5$ parameters. We will discuss the influence of the bond passivation on this result elsewhere). That means that for any number of atoms and the considered number of 5MRs (1-4) the flat fragment is energetically preferable. Simple check shows that the closed polyhedral cluster becomes energetically favourable than the flat flake at the number of atoms $N > N_c$, where $N_c \simeq 70$ is the combination of three energetical parameters of the model and geometrical factors. That means that the flat flake is metastable for rolling up into the polyhedral cluster of the large enough size.

The curvature of the considered clusters was concentrated in the edges of polyhedral super-lattice. Let us consider now the cluster where the curvature is spread over all the surface uniformely. Evidently, the completely closed cluster with the uniform curvature is the spherical one. The shperical cluster has been shown to have the minimal energy between other isomers with the same N [1].

Flakes with uniform curvature of the surface. The spherical fragments of graphene have the lower energy than the polyhedral ones. The curvature energy of the optimal polyhedral flake cluster grows as $\sqrt{N}$ like the dangling bond energy. The same term for

the cluster with the uniform curvature is constant. Therefore, for the large number of atoms the spherical flake is preferable than considered before polyhedral ones.

The more the curvature of the flake (the more the number of 5MRs), the less the slope of the dependence of the energy of dangling bonds on $\sqrt{N}$. Hence, the curved flakes becomes energetically favourable for the large N in respect with the flat graphene. This result in general is consistent with the previouse one obtained in neglection of the pentagon-pentagon distance optimization [2]. The difference appears in the number of atoms corresponding to the "transition" from one-5MR flake to two-5MRs flake. It increases essentially due to the decrease of the perimeter and, hence, of the dangling bond energy.

Summing up, the phenomenological model of the energetics of carbon clusters predicts the rolling up of the flat fragment of the graphene into the closed spheroidal cluster. The continual approach works well in the region of large enough number of cluster atoms. However, the distribution of the pentagons over the surface of the intermediate states of the rolling process is shown to be optimized. We found the optimal geometry of the flake-like clusters with 0–4 5MRs. The optimal cluster perimeter is less than for the open sphere fragments considered in [2]. The distance between pentagons goes to the minimal value owing to the pressure from the dangling bonds along the open perimeter. This also results in that the dense N-foil flake is energetically preferable than the linear (and other less compact) configurations. The curvature energy, owing to the curved carbon bonds along the edges of the polyhedron, is too high to make this cluster optimal one (even in respect to the flat fragment). Contrary, the uniform distribution of the curvature results in the lowering of the formation energy. Due to this optimization, the dangling bond energy term plays less important role in the total energy of formation of spheroidal flake. Hence, the boundary of co-existence of the flat and curved fragments becomes essentially shifted to the larger clusters. That means that more wide region of flat fragments is metastable to the rolling up.

The work was partially supported by RFBR grant No 96-15-96348 and No 98-02-18117.

References

[1] S. V. Rotkin and R. A. Suris, *MRS Symposium Proc.* Vol. 529, p. 175-180 and Refs therein, 1998.

[2] S. V. Rotkin and R. A. Suris, *Phys. Rev. Lett.* (submitted).

[3] According to the Gauss-Bonnet theorem 12 5MRs form the closed spheroid. From the other side, 12 equally-distant points on the surface of the sphere lie in the vertices of the regular icosahedron. It was shown (see *e.g.* V. V. Rotkin, PhD. thesis, St.Petersburg, Russia, 1997) that inserting regular deltagonal graphene faces between 5MRs, we get the closed spheroid (in the same way as assembling the geodesic domes). The actual shape of the cluster is, of course, the truncated icosahedron.

[4] G. A. Korn and Th. M. Korn, *Mathematical handbook for scientist and engineers*, McGraw-Hill Book Company, Inc.: New-York, Toronto, London. 1961.

7th Int. Symp. "Nanostructures: Physics and Technology"
St Petersburg, Russia, June 14–18, 1999

Structural defects due to growth interruptions in ZnSe-based heterostructures

I. V. Sedova, S. V. Sorokin, A. A. Sitnikova, R. V. Zolotareva, S. V. Ivanov and P. S. Kop'ev
Ioffe Physico-Technical Institute, St Petersburg, Russia

Heterostructures based on wide bandgap II–VI compounds and their alloys are currently under intensive studies aiming at fabrication of long-living green laser diodes. After the first demonstration of the room temperature laser many efforts have been made to improve the characteristics and quality of the devices. It is generally known that the main reason of degradation are both extended (misfit dislocations and stacking faults (SFs)) and point defects in the active region of a laser structure [1, 2].

GaAs is a commonly used substrate for ZnSe-based semiconductors growth due to its fairly low lattice mismatch to ZnSe (0.27%). The origin of SFs and dislocations is associated with the heterovalent nucleation of ZnSe on GaAs. Therefore, the properties of the heterointerface between a GaAs substrate and ZnSe are of great importance for the structural quality of the layers. It has been shown that an initial growth stage and the growth conditions of the first few ZnSe monolayers are dominant factors affecting the layer quality and determining the dislocation and SF density [3]. Studies of the initial nucleation of ZnSe on GaAs substrates indicate that stoichiometry of GaAs surface before growth can change the initial growth mode from a 2-dimensional (2D) layer-by-layer to a 3D-island one. The SF density is significantly higher for the films grown on Ga-rich GaAs surfaces in comparison with those on As-stabilized one [1]. The use of a high quality GaAs buffer layer results in a noticeable decrease in the extended defect density [4].

The defects may also arise during the growth process, initiated either by technological stops performed for calibration of the fluxes by ion gauge after a ZnSe-buffer growth or by interruptions at guide/cladding interfaces for necessary variation of substrate temperature or flux intensities. Note that the non-interrupted shutter-operation MBE technique proposed in [5] allows us to produce the structure with improved optical and structural qualities. It has been also suggested that the stands form a specific homo-interface, where the defect formation is simplified, meanwhile this assumption had no experimental confirmation until now. Another serious problem in II–VI growth is penetration of the defects, damaging active region and adjacent layers. To enhance the heterostructure stability much attention has been paid to design and growth of alternately-strained superlattices (SLs) [6]. However, the ability of such SLs to stop defects has not been directly documented for II–VI's.

In this paper we focus on the growth-interruption-induced defects formation as well as on their extinction by a SL. The samples studied were grown by molecular beam epitaxy on GaAs (100) substrates either with or without GaAs buffer layer. All structures were grown on As-stabilised GaAs surface exposed to Zn for 2 minutes prior to the growth of a 20 nm thick ZnSe buffer. The growth conditions and composition control for these heterostructures have been reported elsewhere [7]. To study the defects formation on the interrupted interfaces, the simplest heterostructures were used, containing 50 nm of ZnSe followed by a thin CdSe insertion, capped finally by 20 nm of ZnSe. The total ZnSe thickness was chosen to be less than the critical one. After 20 nm growth of the ZnSe buffer layer the growth interruption took place to calibrate the fluxes with an ion gauge

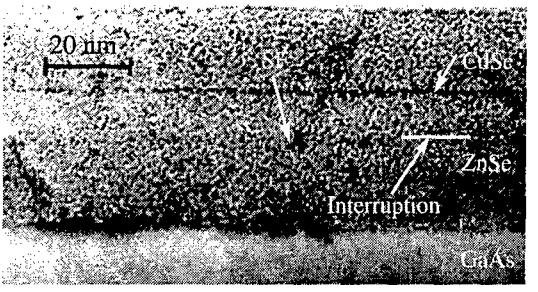

Fig. 1. TEM cross-sectional image of a ZnSe/CdSe/ZnSe structure.

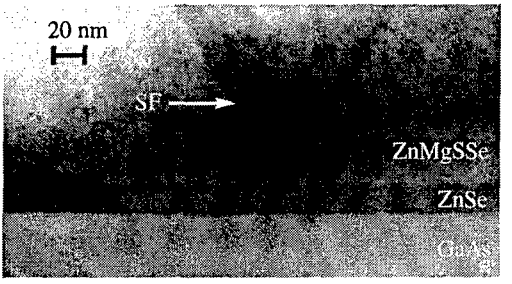

Fig. 2. TEM cross-sectional image taken near a ZnSe/ZnMgSSe interface.

placed in front of the wafer surface at $\sim$ 0.5 cm. A typical laser structure was used to study capability of SLs to quench defects. The structure consists of a 20 nm ZnSe buffer layer, a 0.5 μm thick ZnMgSSe bottom cladding layer, a 0.2 μm ZnSSe/(Zn,Cd)Se short-period SL region centered with a 7 nm wide (Zn,Cd)Se QW, and finally a 0.1 μm ZnMgSSe top cladding layer protected by a 5 nm ZnSe cap. The samples were studied by cross-sectional transmission electron microscopy (TEM) using Philips EM420 electron microscope.

TEM cross-sectional image taken from a ZnSe/CdSe/ZnSe structure is presented in Fig. 1. The structure was grown with an interruption for the flux calibration. The closest to the surface line is a 0.5 monolayer thick CdSe insertion serving as a checkpoint. Below the CdSe layer an additional interface is visible, exactly matching the position of the ZnSe growth interruption. The SF (marked by an arrow) is clearly seen in the figure, originating just from the homo-ZnSe/ZnSe interface and crossing the CdSe insertion. Figure 2 shows a TEM cross-sectional image taken near a ZnSe/ZnMgSSe interface in a sample, characterized by the layer-by-layer growth mode of ZnSe/GaAs on the As-stabilized GaAs buffer. The film is perfectly coherent with the GaAs surface. However, the growth interruption for the flux calibration took place during the epitaxy at the ZnSe/ZnMgSSe interface. The interface is seen in Fig. 2 as a thin dark stripe and the stacking fault nucleates just in this place of the structure.

Figure 3 presents a cross-sectional image of the laser structure with an alternately-strained SL waveguide. The 2D initial growth mode of this structure has provided the low SF density at the ZnSe/GaAs interface, while the growth interruption for fluxes calibration performed at the ZnSe/ZnMgSSe interface results in the SF nucleation. However, the SFs starting from the ZnSe/ZnMgSSe interface are completely suppressed by the SL, which demonstrates a protective ability of the strained II–VI SLs against penetration of the extended defects into the laser active region.

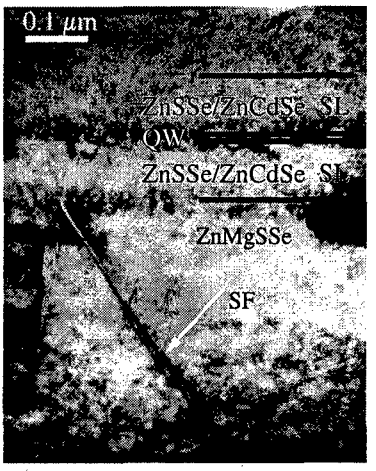

Fig. 3. TEM cross-sectional image of the laser structure with alternately-strained SL waveguide.

In summary, it has been shown that the growth interruption performed for calibration of VI–II flux ratio leads to the additional strain contrast in cross-sectional TEM images. Furthermore, this strain seems to be the driven force for the formation of extended defects immediately at the interruption interface. On the other hand, the developed alternately-strained SLs allow one to enhance the activation energy of the development and propagation of extended defects and protect the laser active region from the defects penetration. This findings, while being qualitative, are important for further decrease of the defects density in ZnSe-based laser structures.

This work has been supported in part by the RFBR, the program of MS of RF "Physics of solid-states nanostructures" as well as the Volkswagenstiftung.

References

[1] L. H. Kuo, L. Salamanca-Riba, B. J. Wu, G. Hofler, J. M. DePuydt and H. Cheng, *Appl. Phys. Lett.* **67**, 3298 (1995).

[2] M. Ehinger, W. Spahn, H. R. Ress, R. Ebel, W. Faschinger and G. Landwehr, Proc. of Int. *Symp. on Blue Laser and Light Emitting Diodes*, Chiba, Japan, 465 (1996).

[3] S. Guha, H. Munekata and L. L. Chang, *J. Appl. Phys.* **73**, 2294 (1993).

[4] S. V. Ivanov, R. N. Kyutt, G. N. Mosina, L. M. Sorokin, S. V. Sorokin, Yu. G. Musukhin and P. S. Kop'ev, *Int. Phys. Conf.* **155**, 223 (1996).

[5] S. V. Ivanov, S. V. Sorokin, P. S. Kop'ev, J. R. Kim, H. D. Jung and H. S. Park, *J. Cryst. Growth* **159**, 16 (1996).

[6] T. V. Shubina, S. V. Ivanov, A. A. Toropov, G. N. Aliev, M. G. Tkatchman, S. V. Sorokin, N. D. Il'inskaya and P. S. Kop'ev, *J. Cryst. Growth* **184/185**, 596 (1998).

[7] S. V. Ivanov, A. Toropov, S. Sorokin, T. Shubina, A. Lebedev, P. Kop'ev, Zh. Alferov, H.-J. Lugauer, G. Reuscher, M. Keim, F. Fischer, A. Waag and G. Landwehr, *Appl. Phys. Lett.* **73**, 2104 (1998).

7th Int. Symp. "Nanostructures: Physics and Technology"
St Petersburg, Russia, June 14–18, 1999

Atom removing from the Si(001)(2×1)-H surface under STM tip. Quantum-chemical approach

E. F. Sheka, E. A. Nikitina and M. Aono†
Russian Peoples' Friendship University, 117923 Moscow, Russia
† Institute of Chemical and Physical Research (RIKEN), Wako-shi, Japan
Department of Precision Science and Technology, Osaka University, Osaka, Japan

Abstract. Appropriate models are suggested for the supercluster simulating the Si(001)(2×1)-H surface as well as for the configuration of the electric field of an STM tip. A series of calculations have been performed for the supercluster in the electric field at different values of the field potentials and at different polarities. The electric field-stimulated desorption of hydrogen and silicon atoms has been observed at both polarities of the tip. The desorption reaction is a threshold one with the threshold potential somewhat higher at positively biased tip. The field impact is in a drastic redistribution of atomic charges in the substrate area under the tip that causes a weakening of interatomic bonding providing atom removing.

The equilibrated spin-singlet structure of the 306-atom supercluster, simulating partially hydrogenated Si(001) surface, is shown in Fig. 1. Initially spaced at 3.82 Å, silicon atoms of two central rows come together forming symmetrical dimers in the course of the total-energy minimum seeking [1]. The electric field was configured by a set of point charges in a model of a sharp one-and-four tungstem atom tip whose position is shown in Fig. 1. The tip was placed 5 Å above the topmost silicon atoms. Its position in the horizontal place varied.

Electrostatic potential $\varphi(x, y, z)$ stimulated by the tip within a substrate is determined as [2]

$$\varphi(x, y, z) = \sum_i q_i / 4\pi\varepsilon\varepsilon_0 [(x - x_i)^2 + (y - y_i)^2 + (z - z_i)^2]^{1/2}$$

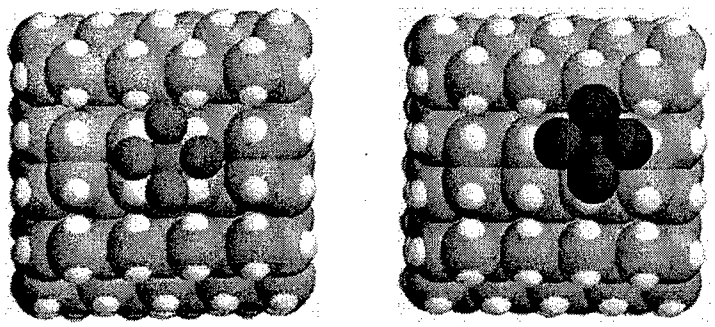

(a) (b)

Fig. 1. Top view on the equilibrated supercluster simulating the Si(001)(2x1)-H surface. Tip in position (a) and (b) is placed 5 Å above the top silicon atoms.

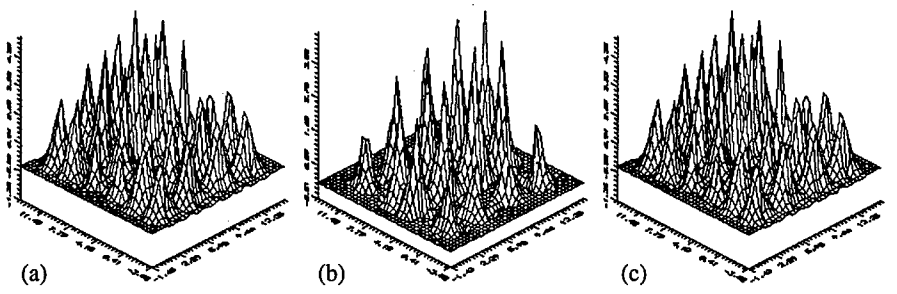

Fig. 2. Tip-stimulated potential distribution over the topmost hydrogen (a), (c) and silicon (b) atoms of the substrate. (a) and (b). Tip consists of five point charges of +0.5 a.u. each. Potential maximum constitutes +7.7 eV. (c). Conical tip is biased by +10 V. Potential maximum is +5.92 eV. Tip is in position (b) of Fig. 1.

where q_i is a point charge positioned at (x_i, y_i, z_i). The components of the electric field vector $\mathbf{E} = -\nabla\varphi$ are determined as

$$E_x = \sum_i q_i(x - x_i)/4\pi\varepsilon\varepsilon_0[(x - x_i)^2 + (y - y_i)^2 + (z - z_i)^2]^{3/2}$$

$$E_y = \sum_i q_i(y - y_i)/4\pi\varepsilon\varepsilon_0[(x - x_i)^2 + (y - y_i)^2 + (z - z_i)^2]^{3/2}$$

$$E_z = \sum_i q_i(z - z_i)/4\pi\varepsilon\varepsilon_0[(x - x_i)^2 + (y - y_i)^2 + (z - z_i)^2]^{3/2}$$

The field on the supercluster atoms had a hill-like configuration with the hill high as bigger as nearer the atoms are to the top layer. As for the atoms positioned in the same layer, the field is non-uniform and depends on a relative position of the tip with respect to the atom considered. The field strength was controlled by the point charge values. Fig. 2 shows the field distribution over the topmost hydrogen and silicon atoms for the tip charged positively. Analogous picture is observed for the negatively charged tip.

Experimentally, one operates with a biased not charged tip. Electrostatic potential $\varphi(x, y, z)$ in a substrate stimulated by a biased tip is determined by the Poisson equation [3]

$$\varepsilon\varepsilon_0\Delta\varphi = e(n - p - N)$$

(n, p, and N are related concentrations of electrons, holes, and impurities) under conditions when the potential at a conical tip $\varphi = V$ is constant while the potential in the space between the substrate and the tip is obeyed to the Laplace equation $\Delta\varphi = 0$.

A series of total-energy minimisation considered in the framework of a quantum-chemical software DUQUFIELD [4, 5] based on a semi-empirical method AM1 has been performed for varied strengths of the field at both polarities of the tip. A removing of one (sometimes two) hydrogen atom is observed at both polarities with somewhat different absolute values of the threshold field (about −6.84 V and +7.70 V). The threshold value depends on the relative position of the tip and the atom considered rather slightly, while being always 10–15% bigger by absolute value for the positively biased tip.

The field impact is in a drastic redistribution of atomic charges in the substrate area under the tip that becomes more pronounced when the potential increases. This causes a

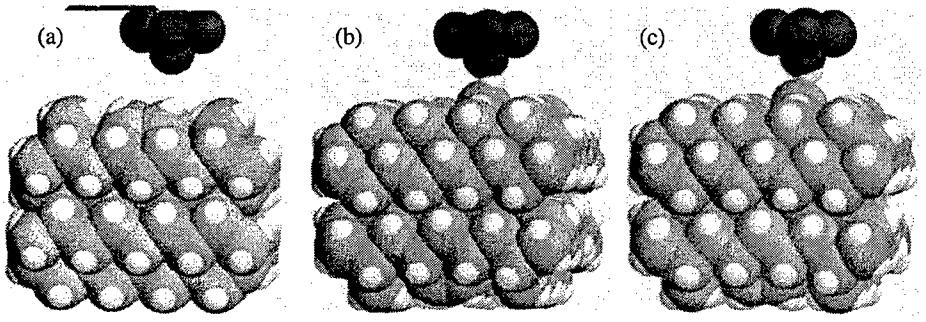

Fig. 3. Successive steps of a hydrogen atom removing at a threshold (negatively biased tip). Starting (a), intermediate (b), and final (c) step, respectively.

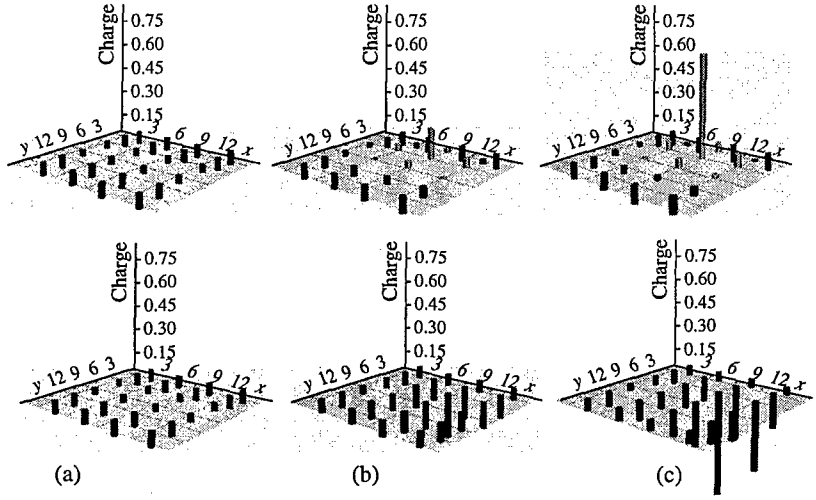

Fig. 4. Distribution of atom charge over the topmost hydrogen atoms under the negatively (top) and positively (bottom) biased tip in position (b) of Fig. 1. Zero (a), intermediate (b), and threshold (c) field.

weakening of interatomic bonding providing atom removing. Fig. 4 shows the effect for the topmost hydrogen atoms under the negatively and positively biased tip. As seen from the figure, the redistribution concerns the same atoms in both cases being, however, opposite by sign.

If the field continues to act after an H atom is going away, a removing of a silicon atom proceeds. Similarly to the hydrogen atoms, the field-stimulated desorption of silicon atoms is caused by a drastic redistribution of the relevant atomic charge when approaching the threshold field.

If the field is switched off after the hydrogen atom removing, a relaxation of the surface structure takes place completed by the formation of energetically stable local defects. Typical defects obtained are shown in Fig. 5. Symmetric dimers are formed in all cases with the difference that the Si–Si spacing in first two cases constitutes 2.42 and 2.38 Å while it is of 2.16 Å in the last case. The former values are typical for a single Si–Si bond while the latter is characteristic for a double Si=Si bond [1] that is formed at the surface.

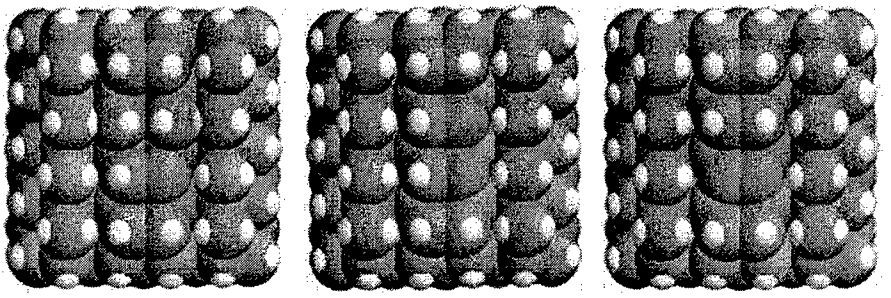

(a) (b) (c)

Fig. 5. Equilibrated defect structures formed after one (a) and two (b,c) hydrogen atom removing. Negatively (a, b) and positively (c) biased tip in position (a) of Fig. 1.

The obtained results on the field-stimulated desorption of hydrogen atoms from the Si(001)(2x1)-H surface are well consistent with recent experimental findings [6–8]. Therefore, the suggested static-field desorption mechanism is a well-supported alternative to the previously discussed dynamic one. The latter relates the atom desorption to vibrational heating of the atom by inelastic scattering of either tunnelling electrons [9] or tunnelling holes [8] with the corresponding resonances on the substrate in the case of negatively and positively biased tip, respectively.

References

[1] E. Nikitina, E. Sheka and M. Aono, (to be published).
[2] I. A. Obukhov, *Coulon field software*, Moscow, 1998.
[3] I. A. Obukhov, *Laplace field software*, Moscow, 1998.
[4] V. D. Khavryutchenko, V. A. Zayetz and A. V. Khavryutchenko Jr, *DYQUAFIELD Dynamical-Quantum Modeling in Electrostatic Field Software for Personal Computers* (Institute of Surface Chemistry, National Academy of Ukraine, Kiev-Dubna, 1995).
[5] E. F. Sheka, V. D. Khavryutchenko and V. A. Zayetz, *Int. J. Quant. Chem.* **57** 741 (1996).
[6] D. H. Huang and Y. Yamamoto, *Scanning Micr.* **10** 717 (1996).
[7] D. H. Huang and Y. Yamamoto, *Jpn. J. Appl. Phys.* **35** 3734 (1996).
[8] K. Stokbro, C. Thirstrup, M. Sakurai, U. Quaade, Ben Yu-Kuang, F. Perez-Murano and F. Grey, *Phys. Rev. Lett.* **80** 2617 (1998).
[9] T.-C. Shen, C. Wang, G. C. Abeln, J. R. Tucker, J. W. Lyding, Ph. Avouris and R. E. Walkup, *Science* **268** 1590 (1995).

7th Int. Symp. "Nanostructures: Physics and Technology"
St Petersburg, Russia, June 14–18, 1999

Growth and structure of $Mn_xCa_{1-x}F_2$ epitaxial films on Si(111)

N. L. Yakovlev, A. G. Banshchikov, R. N. Kyutt, N. S. Sokolov and L. Hirsch†
Ioffe Physico-Technical Institute, St Petersburg, Russia
† Universite Bordeaux 1, 351 Cours de la Liberation, 33405 Talence Cedex, France

Abstract. Molecular beam epitaxy was used to grow films of MnF_2 and CaF_2 solid solutions on Si(111) substrates. The composition of the solutions was measured using oscillations of reflection high energy electron diffraction, electron microprobe analysis and Rutherford backscattering and was in the range from 10% to 45% of MnF_2. In these solutions, step flow growth mode occurs even at relatively low temperature as 400°C in contrast to pure CaF_2. The films have cubic fluorite crystal lattice. Their lattice parameter measured using X-ray diffraction decreases linearly from 0.544 nm to 0.536 nm in the above range.

Introduction

Fluoride films grown by molecular beam epitaxy (MBE) on silicon substrates can be used for matching of lattice constant to that of materials grown above them [1]. The cubic CaF_2, SrF_2 and BaF_2 crystals are good insulators and lattice parameter of their solid solutions covers the range from 0.5463 to 0.620 nm. Smaller lattice parameters can be obtained in mixed $Mn_xCa_{1-x}F_2$ crystals. Though MnF_2 bulk crystals have the tetragonal crystal lattice of rutile ($a = 0.486$ nm, $c = 0.328$ nm), these solid solutions have cubic fluorite lattice up to $x = 0.47$ with lattice parameter linearly decreasing to 0.5372 nm [2].

It was found recently [3] that very thin MnF_2 layers up to 3 molecular layers on the surface of $CaF_2(111)$ can have cubic fluorite lattice. To compare their structure with that of MnF_2 and CaF_2 solid solutions we grew the solution films on Si(111) substrates by means of MBE. We measured their lattice parameters using X-ray diffraction (XRD) and surface morphology using atomic force microscopy (AFM). As a prospective, manganese compound films may have magnetic properties attractive for micro-electronics.

Film growth

The structures were grown at the Ioffe Physico-Technical Institute. After standard chemical cleaning, silicon substrates were loaded into the MBE chamber and cleaned thermally at 1250°C in ultra high vacuum. Reflection high energy electron diffraction (RHEED) images from the Si(111) surface below 830°C showed a clear 7×7 superstructure. Because of molecular mode of sublimation of the fluorides, the stoichiometry of the film is kept automatically, so CaF_2 was deposited from one source, MnF_2 from the other one.

Oscillations of RHEED specular beam intensity were used to monitor the fluoride growth, Fig. 1, which was carried out in 3 stages: (1) CaF_2 7 monolayers (ML) at 700°C to form well ordered interface, then at 400°C (2) CaF_2 several ML and (3) CaF_2 and MnF_2 from the two sources up to the thickness of 300 nm. The change of the oscillation period from (a) to (b), Fig. 1, indicates the mixture composition, which is presented in the table.

The composition of the layers was determined independently by standard electron microprobe analysis (EMA) using Camebax system. In several samples, Rutherford back

Table 1. Structural parameters of the films with different MnF_2 content determined by RHEED, EMA and RBS. All lattice parameters are percents of normalized deviation from respective parameter of silicon: $(a_{film} - a_{Si})/a_{Si}$.

	MnF_2 content (%)			Parameters			Lattice
Sample	RHEED	EMA	RBS	a_{nor}^{111}	a_{nor}^{531}	a_{lat}^{531}	constant
776	0	0		0.560	0.560	0.348	0.46
750	10	11		−0.190			0.10
779	18	19	19	−0.632	−0.663	0.257	−0.20
774	34	35		−1.180	−1.220	−0.526	−0.86
784	40	42	45	−1.320	−1.445	−0.922	−1.13
778	50	43	44	−1.460	−1.536	−0.925	−1.20

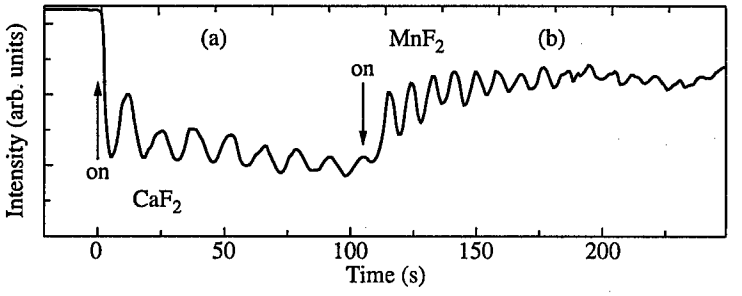

Fig. 1. RHEED intensity oscillations during the deposition of: (a) 8 monolayers of CaF_2, (b) $Mn_{0.34}Ca_{0.66}F_2$. Electron energy 15 keV, beam azimuth [110].

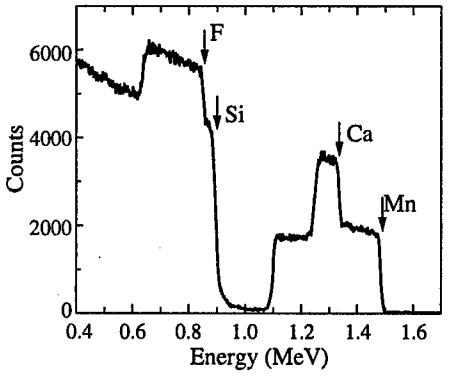

Fig. 2. RBS spectrum from $Mn_{0.4}Ca_{0.6}F_2$ film 300 nm thick in random scattering geometry. The energy of incident $4He^+$ ions is 2 MeV.

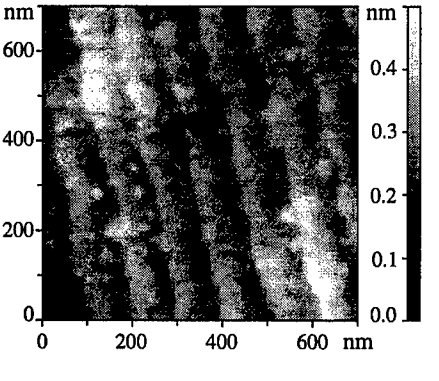

Fig. 3. AFM image of the surface of $Mn_{0.4}Ca_{0.6}F_2$ film 300 nm thick. Tapping mode, resonance frequency 512 kHz.

scattering (RBS) measurements with 2 MeV $4He^+$ ions were carried out at the University of Bordeaux. A random RBS spectrum is shown in Fig. 2. It allows determination of MnF_2 content and indicates also that the distribution of Mn is uniform through the depth of the film. The values of MnF_2 content measured by different methods are quite close, see the table, their deviation can be regarded as the errorbar.

We found that during the growth of the solid solutions in the range of 10% to 40% of MnF_2 content, the growth mode was different from that of pure CaF_2 at 400°C. In the latter case, the surface became rough with 30 nm high hills on a 300 nm film, RHEED image consisted of transmission spots. In the former case, the RHEED image during the whole MBE process contained only two dimensional reflections from (111) face of cubic fluorite lattice. AFM images from these structures showed that step flow growth mode occured, Fig. 3. The large width of the single layer terraces indicates larger migration length of the molecules of the both fluorides here with respect to that in the case of CaF_2. Similar behaviour was observed also during MBE of CaF_2 and MgF_2 solid solutions [4]. This means that the presence of MgF_2 or MnF_2 molecules inhibits nucleation of two dimensional islands. (Molecular surface migration is known for ionic compounds [5].)

Lattice parameters

Lattice parameters of the solid solutions were measured by XRD using a double-crystal two-circle diffractometer with Cu$K\alpha$ radiation. The curves, Fig. 4, are $\theta - 2\theta$ scans (Bragg scans) across 531 reflections, one at the incident grazing angle, the other at the diffracted grazing angle. In this geometry, both normal (a_{nor}^{531}) and lateral (a_{lat}^{531}) lattice parameters can be calculated from the measured positions of the peaks. The normal lattice parameter can be obtained also from $\theta - 2\theta$ scans across symmetric 111 Bragg reflection (a_{nor}^{111}). These parameters normalized with reference to silicon ($a_{\text{Si}} = 0.543$ nm) are presented in the table. The agreement between the values of the normal parameter obtained from different reflections confirms the selfconsistency of the measurement. In the curves of the sample with 10% MnF_2, the peaks from the film and the substrate overlap, thus only normal lattice parameter could be measured.

The difference between the normal and lateral parameters is due to the thermal strain of the films [6]. During cooling of the samples from 400°C to room temperature thermal shrinking of the fluoride crystal is −0.7% because of larger thermal expansion of the fluoride with respect to silicon [7]. Assuming the Poisson ratio for the solid solutions to be the same as for CaF_2 ($p = 0.96$), we can calculate their lattice constants for free crystal,

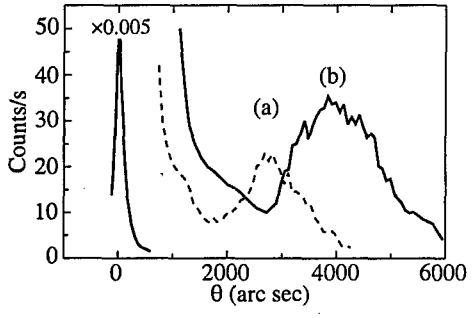

Fig. 4. $\theta - 2\theta$ scans across 531 reflection in XRD of $Mn_{0.34}Ca_{0.66}F_2$ film: (a) grazing diffraction, (b) grazing incidence.

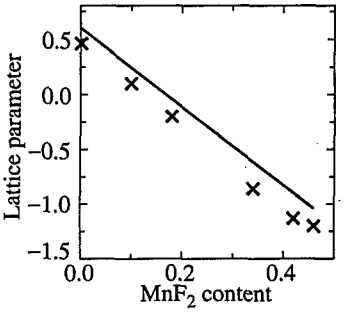

Fig. 5. Lattice parameter versus the composition of CaF_2 and MnF_2 solid solutions.

$a_{film} = (a_{nor} + pa_{lat})/(1 + p)$, see the table. The value of residual planar strain in the films lies in the range between -0.2% and -0.4%. Assuming that it does not fall out of this range also for the sample with 10% MnF_2, we calculated its lattice constant also.

The dependence of the lattice constant of the solid solution films is plotted in Fig. 5. The solid line is the dependence obtained for bulk crystals [2]. The both dependences are close to each other, however in all the films, the lattice constant is smaller than in the bulk. Part of this difference may be due to changes of elastic properties of the crystal with admixture of MnF_2. The other possible reason may be the presence of vacancies which are practically always formed during MBE [8]. Extrapolation of the obtained dependence to $x = 1$ gives the lattice constant of cubic MnF_2 0.527 nm. This value is very close to 0.528 nm extrapolated from XRD measurements of cubic MnF_2 existing at pressure 20 to 50 kbar above 300°C [9], to 1 bar and room temperature.

Acknowledgements

The authors would like to thank M. V. Zamoryanskaya for EMA measurements of Mn content in the films. This work was supported by Russian Foundation for Basic Research, grant No. 98-02-18251 and Programme for Physics of Solid State Nanostructures, grant No. 97-2018.

References

[1] K. Tsutsui, H. Ishiwara and S. Furukawa, *Appl. Phys. Lett.* **48**, 587 (1986).
[2] D. D. Ikrami, P. P. Fedorov, A. A. Luginina and L. A. Olkhovaya, *Zh. Neorg. Khim.* **30**, 1261 (1985) (in Russian); L. Olkhovaya, A. Luginina, V. Sidorov and D. Ikrami, *European Meeting on Crystal Growth,* Prague, 1982, Materials for electronics, p. 179.
[3] N. L. Yakovlev, A. G. Banshchikov, M. M. Moisseeva, N. S. Sokolov, J. L. Beeby and P. A. Maksym, *Asia Pacific Surface and Interface Analysis Conference* 1998 Singapore, Proceedings p. Th-P-14.
[4] N. L. Yakovlev and Yu. V. Shusterman, *J. Cryst. Growth,* **150**, 1119 (1995).
[5] M. H. Yang and C. P. Flynn, *Phys. Rev.* **B41**, 8500 (1990).
[6] N. S. Sokolov, J. C. Alvarez and N. L. Yakovlev, *Appl. Surf. Sci.* **60/61**, 421 (1992).
[7] B. Schumann and H. Neuman, *Cryst. Res. Technol.* **19**, K13 (1984).
[8] D. T. G. Hurle, *J. Phys. Chem. Solids* **40**, 613 (1979).
[9] S. S. Kabalkina, L. F. Vereshchagin and L. M. Lityagina, *Zh. Eksp. Teor. Fiz.* **56**, 1497 (1969) (in Russian).

Author Index